SCHOOL OF INFRASTRUCTURE, PROCESS ENGINEERING AND TECHNOLOGY
AND SCHOOL OF ELECTRICAL ENGINEERING AND TECHNOLOGY
FEDERAL UNIVERSITY OF TECHNOLOGY, MINNA

Book of Proceedings IEC 2023

4th INTERNATIONAL ENGINEERING CONFERENCE

Theme

Smart Engineering and Technology Innovation for Enhancing Economic Growth

21st - 23rd MARCH 2023

Venue: NITDA ICT-HUB Federal University of Technology, Minna, Niger State - Nigeria

Edited By: Technical Sub-Committee

MEMBERS OF THE CONFERENCE ORGANISING COMMITTEE

1.	Engr. Prof. M. Alhassan	Chairman
2.	Engr. Prof. O.M. Olaniyi	Co-Chairman
3.	Engr. Dr. Bala A. Salihu.	Member
2.	Engr. Prof. S.M. Dauda	Member
3.	Engr. Dr. A. U. Usman.	Member
4.	Engr. Dr. T. E. Adejumo.	Member
5.	Engr. Dr. M. D. Yahya	Member
6.	Engr. Dr. Alkali Babawuya.	Member
7.	Engr. Prof. R. A. Muriana.	Member
8.	Engr. Dr S. A. Mohammed	Member
9.	Engr. Dr. B. A. Orhevba.	Member
10.	Engr. Dr. Michael David	Secretary

MEMBERS OF SUB-COMMITTEES

TECHNICAL SUB-COMMITTEE

1.	Engr. Dr. Bala S. Salihu	Chairman
2.	Engr. Dr. Eyitayo Afolabi	Member
3.	Engr. Dr. M. U. Garba	Member
4.	Engr. Dr. U. S. Dauda	Members
5.	Engr. Dr. James Ambafi	Member
6.	Engr. Dr. S. A. Mohammed	Member
7.	Engr. Dr. B. A. Orhevba	Member
8.	Engr. Dr. A. M. Ibrahim	Member
9.	Engr. Balogun Temitope	Member
10.	Engr. Dr. T.A. Folorunso	Member
11.	Engr. Buhari U. Umar	Member
12.	Engr. Dr. A. Yusuf	Member
13.	Engr. Dr. Michael David	Member
14.	Engr. Dr. M. Abubakar	Secretary

ICT SUB-COMMITTEE

1.	Engr. Dr. Bala A. Salihu	Chairman
2.	Engr. Dr. Sadiq Ahmed	Member
3.	Engr. Dr. Steven Oyewobi	Member
4.	Engr. S. A. Bala	Member

WELFARE SUB-COMMITTEE

1.	Engr. Dr. M.D. Yahya	Chairman
2.	Engr. Prof. R.A. Muriana	Member
3.	Engr. Dr. A.J. Otaru	Member
4.	Engr. Dr. B. A. Orhevba	Member
5.	Engr. Dr. C. O. Alenoghenna	Member
6.	Engr. Dr. A. Yusuf	Member
7.	Mr. Usman Baro	Member
8.	Engr. Danlami	Member
9.	Engr. Dr. B.A. Orhevba	Secretary

FINANCE SUB-COMMITTEE

1.	Engr. Dr. B. A. Orhevba	Chairman
2.	Engr. Prof. O. A Olugboji	Member
3.	Eng. Bello Abdulkadir	Member
4.	Eng. Dr. T. E. Adejumo	Member
5.	Engr. Dr. M. D. Yahya	Member
6.	Engr. Gana Menegbe Esther	Member
7.	Dr. Abdulkadir Balogun	Member
8.	Dr. Alhassan Musa	Member
9.	Engr. Buhari Umar	Member
10.	Engr. Dr. Alkali Babawuya	Member

LOGISTICS SUB-COMMITTEE

1.	Engr. Prof. R. A. Muriana	Chairman
2.	Dr. T. E. Adejumo	Secretary
3.	Shaka Abdulazeez Enahoro	Member
4.	Nweke Augustine Chidiebele	Member
5.	Adeyeye Sumayyah Adedola	Member
6.	Abraham Dirisu	Member
7.	Mohammed Shehu	Member
8.	Dr. Achonu Adejo	Member

DIASPORA COMMITTEE

1.	Engr. Dr S. A. Mohammed	Chairman
2.	Engr. Prof. A. S. Abdulkareem	Member
3.	Engr. Musa Umar	Member
4.	Engr. Dr. Olatomiwa Lanre	Member
5.	Engr. Dr. Uzodinma Okoro	Member
6.	Prof. Monika Prakash	Member
7.	Engr. Dr. Saidu Mohammed	Member
8.	Engr. Fidelis Jonah Usman	Member

Forward

International Engineering Conference is the biennial conference being organized by the Schools of Engineering of the Federal University of Technology, Minna. The conference is meant to create a forum to showcase scientific discoveries, encourage knowledge sharing and build an ecosystem for Engineering and allied disciplines. This year's edition tagged the 4th International Engineering Conference (IEC 2023) with the theme "***Smart Engineering and Technology Innovation for Enhancing Economic Growth***" is carefully planned to proffer smart solutions to economic challenges through technological innovations.

About 120 technical papers were received out of which 85 were accepted after thorough peer-review processes. The richness of this conference is the diver contribution from a wide range of Authors cut-across academia, industry, and researchers. Their technical and logical presentations give a robust knowledge base in Engineering and allied disciplines. It is not surprising that the conference has been receiving more attention from Authors and participants across the globe. The keynote address and the lead papers herein are from seasoned industry key players and top-notch researchers with international recognition. This conference is packed with research contributions and design and implementation of innovative technologies that have the potential to advance smart engineering and realize the goals set out for Industry 4.0 as the 4th industrial revolution. We should take great advantage of it to learn new ideas, network with experts, and play a part in the revolution that is already taking place.

The Federal University of Technology Minna, the Citadel of learning is known for her contributions to research and innovation, especially in Engineering. Eminent researchers and scholars from the University form part of the conference organizing committee along with the editorial and Technical Board from the United Kingdom, Saudi Arabia, South Africa, Malaysia, Australia, etc.

On behalf of the conference organizing committee, I thank you all for participating. To our dedicated reviewers, you are sincerely appreciated for finding time to do a thorough review. Thank you all and we hope to see you at the 5th International Engineering Conference.

Engr. Prof. Mohammed Alhassan
Chairman, Conference Organising Committee

Table of Contents

Machine Learning Models for Risk Management in Nigerian Customs: An Investigative Performance Analysis
Aisha M. K. N, Alhassan, J. K, Aliyu, H. O, & Abdullahi, I. M 1 -5

A Face Recognition-Based Intruder Detection System for Automatic Door Control
Daniyan, A. & Michael O. M. 6- 12

Ensemble Based Emotion Detection Model for Multi-Social Platforms
Bala A, Abisoye O. A., Oluwaseun, A. O., & Solomon A. A. 13 – 23

The effect of Fe3+ ion Dopant on the EnergyBand Gap of Tio2 Nano-Particle for Photocatalytic Applications
Okoli, C. S, Okonkwo, P. C, Abdul, B. O. & Diyauddeen, B. H 24 – 29

A Study of Thermal and Mechanical Properties of Africa Palm Fibre as Thermal Insulator
Usman, I. Y, Ademoh, N.A, Godfrey, M, Uche, E.U & Ndagi, M 30-34

Evaluating Hydrological Droughts Using Sdi in Upper Niger River Basin (UNRB)
Oyeniran, O. O, Adesiji, A. R, & Jimoh, O. D 35 – 38

Extraction of Metal Ions from Tantalite –Columbite Ore Using Aqueous Biphasic System
Oyabiyi , M. A, Maina, N. S, & Sani , Y. M 39 – 45

Conceptual Design of a TCP/IP Control Data for Network Access Selection in a Multi-Connective Integrated Satellite-Terrestrial Network
Ayofe, O. A, Tekanyi, A. M. S, Usman, A. D, Musa, M. J & Abdullahi, Z. M 46 – 51

Systematic Literature Review on Android Malware Detection
Anyaora, P. C, Adebayo, O. S, Ismal IA, I, Ojeniyi, J. A & Olalere, M. 52 – 65

Design Analysis of Milling and Sieving Machine for (Poundo) Yam Flour Processing Plant
Sulayman, Fauziyah. A, & O. K. Abubakre. 66 – 73

Wireless Sensor Networks: State of Arts
Okafor, A. C.; Dauda, U. S.; Kolo, J.G.; Ohize, H. O. & Ajiboye, J. A. 74 – 82

Design and Implementation of an Expert System for The Diagnosis of Prostate Cancer
Okikiola, F. M., Ikotun, A. M., Mustapha, A. M., Oladiboye, O. E., & Onadokun, I. O. 83 – 88

Performance Evaluation of Sun Tracking Control Systems using IMC and PID Controllers
Ifetola Damilola Madaki, Taliha Abiodun Folorunso, Jibril Abdullahi Bala, Adeyinka Peace Adedigba, Eustace M. Dogo 89 – 94

Adopting Virtual Assistants in Nigerian Tertiary Institutions: Benefits and Challenges.
Abdullahi, I. M, Maliki, D, Dauda, A. I, & Siyaka, H. O, Malum, S, 95 – 100

Glare Stopper: The Automatic Car Headlight Management System
Daniyan, A. & Ilupeju, S. S. 101 – 106

Modeling and Exergy Evaluation of the Crude Distillation Unit I of the Kaduna Refinery and Petrochemical Company.
Idah, A. E, Olakunle, M. S, & Maina, M. N 107 – 111

Development of a Prototype Sugarcane Juice Extraction Machine
Ampandi, R. T, Muhammadu, M. M 112 – 115

A Review on Mechanisms and Challenges of Mechanical Footstep Power Generators
Sanni , A. R, & Abdullahi A. A 116 – 120

Green Synthesis of Titanium Dioxide Nanoparticles using *Delonix Regia* Leaf Extract for the Photocatalytic Degradation of Methyl Red Dye
Ayenajeh G, Akpan U. G. 121 – 126

An Investigation of Partial Shading Effects on Solar Photovoltaic Module Performance Using Infrared Thermography
Jaji, U. F, Bori, I 127 – 133

Effect of Partial Shading Diffusion on Photovoltaic Panels for SP and TCT Techniques
M Mohammed, I. A. Shehu, U. Musa, S. H. Sulaiman and I. Abdulwahab 134 – 138

Stochastic Time Series Analysis of Stream Flow Data of the River Niger at Lokoja, Kogi State, Nigeria.
Gbadebo Olukemi Anthonia, Busari Afis Olumide, Salawu Sadiku and Saidu Mohammed 139 – 148

Hate and Offensive Speech Detection Using Term Frequency - Inverse Document Frequency (TF-IDF) and Majority Voting Ensemble Machine Learning Algorithms
Okechukwu, C., Idris, I., Ojeniyi, J. A., Olalere, M. & Adebayo O. S. 149 – 155

Perspectives on Electric Vehicle Technology: A State of Art on Current and Future Prospects
Jamilu, Y. M, Kadawa, I. A, Kamal, A. A. & Nuraini, S. M 156 – 165

Energy Audit: A Case Study of Sunti Golden Sugar Company Mokwa
Taidi El i, Omokhafe, J. Tola, & Babatunde Adegboye 166 – 173

Integration of Robotics into Boat-operated Atalla Lift Net Manipulator Arms for Capturing of Clupeids (Freshwater Sardine)
Okouzi, A. S, Ayuba, A. B, Eze, J. O, Ihuahi, J. A & Bankole, N. O 174 – 179

Application of Artificial Neural Network-Based Fault Diagnosis on 330kv Transmission Lines: (A case study of the Gwagwalada-Katampe transmission line)
Bello, M. S, Babatunde, A.A, & Imoru, O 180 – 188

Computational Fluid Dynamics: Emission Modeling and Predictions for Gas Turbines
Elimian, J, Nasir, A, & Muhammad, N.L 189 – 193

Towards Development of a Dynamic Random Advance Encryption Standard
Adamu, M., Oyefolahan, O. I., Ojerinde, O. A 194 – 199

Cruise Control Using IMC and PID Controllers.
Garuba Oluwatosin Rasheed, Taliha Abiodun Folorunso, Jibril Abdullahi Bala, Abdullahi Mohammad Ibrahim 200 – 206

Virtual System Modelling (VSM) Simulation and Automation of Boatoperated Atalla Lift Net Manipulator Arms' Drive for Capturing ofClupeids (Freshwater Sardine)
Okouzi, A. S, Eze, J. O, Ayuba, A. B, Ihuahi, J. A & Bankole, N. O 207 – 216

Comparative Study of Purified Cashew Gum Latex and Xanthan Gum for Utilization for Drug Applications
Okonkwo, M. C, Habibu, Uthman, Azeez, O. S 217 – 221

Suitability of Periwinkle Shell Ash as New Reinforcement for Car Bumper Production
Adah Patr ick Ushie, Ademoh Nuhu A, Salawu Asipita Abdulrahman, Hassan A.B 222 – 228

Meteorological Drought Estimation in Lower Niger River Basin Using Standardized Precipitation Index
Odeh, L O & Adesiji, A. R 229 – 232

Effect of Partial Replacement of Fine Aggregate with Crumb Rubber in Concrete Made with Bida Gravel
Mohammed T. A., Abbas B. A., Yusuf A. & Ori tola S. F. 233 – 240

A Comparative Study of BQ2557 and LTC3108 as Efficient Ultra-low Bioelectricity Harvesters from Soil Microbes using Microbial Fuel Cells.
Simeon, M. I, Mohammed A. S & Freitag, R. 241 – 246

Suitability of Clay from Bida Basin, Niger State for Production of Porcelain Insulators
Dutsun, A.M, Abubakre, O.K, Muriana, R.A, Abdullahi, A.A, Emene, A.U & Taidi, I.B 247 – 254

Development of A Prototype Automatic Tyre Inflation System for Lightweight Vehicles
P.R. Christopher, A.B. Hassan, M. M. Muhammadu and N. Abdul 255 – 259

Multiple Radio Access Technology Co-existence in Cellular Network: A Dynamic Spectrum Sharing Perspective
Oyelade, D. O, Usman, A. U, & Adejo, A.O, 260 – 264

Investigation of Pentane and Dodecane Fuels on the Thermo-Economic Performance of a Solid Oxide Fuel Cell.
Ojo, E.O. & Azeez, O.S. 265 – 274

An LSTM And BiLSTM Models for Automated Short Answer Grading: An Investigative Performance Assessment
Nusa, A. M. K, Bashir, S. A and Adepoju, S. A 275 – 279

Performance Requirements of MIMO WITH 5G Wireless Communication Systems
Faisal LAWAL, ***Aliyu Danjuma USMAN***, **Abdoulie Momodou Sunkary *TEKANYI***, **Hassan Abubakar ABDULKARIM**, 280 – 290

Investigation on the Performance of Orange Peel for Greywater Treatment
Adamu A. D, Lawal, M, Sani, B. S, Ishaq, A and Abubakar, U. A 291 – 295

Optimal 5G Resource Allocation for Ultra-Reliable Low Latency Communication (URLLC) and Enhanced Mobile Broadband (eMBB) Use Cases
Abdulhakeem-Alugo, A. A, Mohammed, A. S, & Dauda, U. S 296 – 303

A Model for Measuring Dependence level of Organizations on MIS
Oragbon, A, Alhassan J. K, Adama V. N, Ezenwa, S, & Oragbon, D. R 304 – 310

Development of an Enhanced Fault Monitoring and Protection System for a Three Phase Induction Motor
Nwabueze Afulike, Jacob Tsado, & Lanre Olatomiwa 311 – 317

Development of A Heat Removal Device from Motorcycle Exhaust Using Copper Fin
Ogungbemi K. E & Bori, I 318 – 327

Cryptocurrency Fraud Detection: A systematic Literature review
Hussaini , Y, Waziri, V.O, Isah, A. O, & Ojeniyi , J A 328 – 339

Synthesis, Characterization, and Utilization of Multi-walled Carbon Nanotubes as Cathode in Alkaline batteries.
Abdulraheem, S, Abdulkareem, A. S, & Muriana, R. A. 340 – 348

A Review on Automated Cooking Gas Pressure Valve
Adejumo, Idris Abayomi and Katsina Christopher Bala 349 – 356

A Survey of the Primary User Emulation Attack in the Cognitive Radio Networks
Olaleru, G, Ohize H.O, Dauda U.S, Mohammed A.S 357 – 362

Smart Interview Bot Using Deep Learning
Ogala J. O. & Mughele S. E. 363 – 369

Failure Analysis and Performance Improvement of a Paper Shredder
Danladi, Peter, Okoro, U. G. 370 – 375

Extraction of Coagulant (Alum) from Sludge of the A.B.U. Water Treatment Plant Using Acidification Process
Adamu A. D., Usman J. H., Sani, B. S., Abubakar, U. A. and Abdullahi, N. I. 376 – 380

Smart Water Pump Control System with Remote Access for Improved Energy and Water Resource Management
Onu, U. G., Okekenwa, E., Jack, K. E., Inyang, A. B., Bello, O. E. & Adeniyi, S. 381 – 384

Performance Comparison of Data-driven Models (DDM) for Best Crump Weir Model Selection
Sani Yakubu Khalifa, Babatunde Korode Adeogun, Abubakar Ismail, Morufu Ajibola Ajibike & Muhammad Mujahid Muhammad 385 – 395

Pastoralist Optimization Algorithm Approach For Improved Customer Churn Prediction in the Telecom Industry.
Samuel , A. I, David, M, Salihu, B. A, Usman, A. U & Abdullahi , I. M 396 – 403

Wearable Device for Telemedicine: An Architecture and Prototype Implementation for Remote Medical Diagnosis using Long Range Communication Protocols
Aliyu, I. B, Alenoghena, C. O, Zubair, S. & Salawu, N. 404 – 412

Quantification and Characterization of Municipal Solid Waste Generated from the University of Jos Hostel for Energy Recovery
Japhet, J. A, Gukop, N. S, Lengs, B. D, Datau, N & Babawuya, A. 413 – 419

Digital Prototyping of Foreground Object Detection for Life Fingerlings Counting System in Aquaculture Production in Nigeria
Okouzi A. S, Ayuba, A. B, Ihuahi, J. A & Ugoala, E. R 420 – 427

Resource Allocation and Management in Machine-to-Machine (M2M) Communication in Underlay In-Band Cellular Network: A Survey
Suleiman, A. D, Mohammed, A. S, Salihu, B. A, & David, M. 428 – 434

Equilibrium Adsorption Isotherm of Methylene Blue and Rhodamine B Using Shea Butter Leaves as A Low Cost Adsorbent
Shehu, A, Ibrahim, M. B. and Ayuba, B 435 – 441

Characterization and Optimization of the Bleaching Process of Used Palm Olein Oil Using Alkaline-Activated Rice Husk as Adsorbent
Mohammed, J. G, Uthman, H. & Azeez, O. S 442 – 456

Performance Study of Empirical Path Loss Models at 11 GHz in an Irregular Environment for Wireless Communications
Farouq E. Shaibu, El izabeth N. Onwuka, Nathaniel Salawu, & Stephen S. Oyewobi 457 – 464

Effect of Remolded Density on the Pozzolanic Action of Zeolite on Calcium Carbide Residue (CCR) Treated Clay Soil
Umar, K. G, Alhaji, M. M & Musa, A 465 – 475

Analysis of Soil Salinization on Groundwater Quality in an Irrigated Land
Abdullahi, J.1 and Abdullahi, S. A. 476 – 481

Design, Fabrication and Performance Evaluation of a Melon Shelling Machine
Adebayo, S. E, Lawal, M. I, Buremoh, O. O & Tiamiyu, Q. O 482 – 486

Assessment of Hydrological Drought in Lower Benue River Basin (Hydrological Area II), Nigeria
Nangkazah, R Y., Jimoh O. D & Adesiji, A. R. 487 – 493

Conceptual Design of an IOT-Based Multi-Sensory Gas Leakage Monitoring and Control System Using Fuzzy Logic
Mohammed, I. K, Kolo, J. G., and Ohize, H. 494 – 503

Determination of Physical and Mechanical Properties of Some Selected Varieties of Commonly Grown Maize in Nigeria
Zubairu, M., Dauda, S. M., Balami, A.A., Gbabo, A. & Mohammed, I.S. 504 – 512

Acid Value Reduction for Jatropha Oil using Wood Ash and Cocoa Pod Ash as Adsorbents
Ajani , E. A, Bala, K. C, Lawal, S. A, Tsado, J 513 – 517

Investigation Into the Tribological Properties of Shea Nut Shell Particles Reinforced Epoxy Composites
Abdullahi, M., Zubairu, P. T., Gana, A, & Jabo, U 518 - 524

Identification and Control of Heat Exchanger System
S. H. Sulaiman, K. S. Abubakar, K. I. Dahiru, I. M. Muhammad, & S. A. Salisu 525 – 529

Evaluation of Rare Earth Elements Mineralization Potentials of Parts of Minna Sheet 164SW, North Central Nigeria
Akano T. O, and Onoduku, U.S. 530 – 536

Experimental study on the effect of Zeolite Inclusion on Stress – Strain Characteristics of Laterite soil Stabilized with Cement
James, O., Sadiku, S., Amadi, A.A., Kovo, A.S., Sanni, A. and Agbese, E. O. 537 - 543

Evaluation of Hydrological Drought in the Upper Benue River Basin
Ogunnusi, A., Jimoh, O. D & Adesiji, A. R. 544 - 549

A facile approach towards Hierarchical Zeolite Y Synthesis from Inexpensive Precursor
Usman, R. A., Kovo, A. S., Abdulkareem, A. S. & Garba, M. U. 550 - 554

Fuzzy Logic-Based Electrical Energy Management of Building
Abdul-Azeez Dauda, Stephen Oyewobi, Umar Suleiman Dauda, & Farouq E. Shaibu 555 - 562

4th International Engineering Conference (IEC 2022)
Federal University of Technology, Minna, Nigeria

MACHINE LEARNING MODELS FOR RISK MANAGEMENT IN NIGERIAN CUSTOMS: AN INVESTIGATIVE PERFORMANCE ANALYSIS

*Aisha M. K. N[1], Alhassan, J. K[1], Aliyu, H. O[1], & Abdullahi, I. M[2]
[1]Department of Computer Science, Federal university of Technology, Minna.
[2]Department of Computer Engineering, Federal university of Technology, Minna.
*Corresponding author email:eesha006@yahoo.com +2348063954956

ABSTRACT
Customs administrations utilize risk analysis to identify which people, products, and modes of transportation should be scrutinized and to what extent. Risk analysis and risk assessment are analytical techniques for determining which risks are the most significant and should be treated first or have corrective action performed first. Several ML models were investigated to determine the suitable model for custom data. This is necessary due to the unavailability of such research work. The Machine Learning (ML) models considered are; Support Vector Machine (SVM), Decision Tree (DT) classifier, K-Nearest Neighbor (KNN), Ensemble and Discriminant analysis classifiers. The dataset was collected and pre-processed. The Models were trained and tested using 70% of data for training and 30% for testing. The result shows that the ensemble models produce the highest accuracy of 66.6% for Boosted Trees classifier when compared with the other models. The medium and coarse tree produced an accuracy of 66.1%. This shows that the tree-based algorithms performs averagely better than others and recommended for further exploration.

Keywords: *Artificial Intelligence; Consignment Risk; Customs Management; Machine Learning*

1 INTRODUCTION

The emergence of big data provides firms with the chance to better understand their customers, develop revenue-generating initiatives, and create new business models. However, only a small percentage of data acquired by businesses is evaluated. This situation opens a gap that could deprive established businesses additional revenue and put their long-term survival in jeopardy if new market entrants use it. Data is analyzed by intelligence-driven organizations (Kavoya, 2020). Customs is one of such organizations that generates huge amount of data that requires analysis for better revenue generation. The activities of Customs all over the world are vital due to their ability to generate huge revenue and boost the economies of their countries. In Nigeria for instance, the Nigerian Customs Service (NCS) generated about 2.3 trillion Naira in 2021, an amount well above the estimated target of 1.679 trillion Naira (Vanguard, Dec. 20, 2021). Despite these successes, several challenges still hinder the agency from reaching its full potential. These challenges include; man power shortage, slow digitization processes and the unrelenting efforts at smuggling and corruption.

The amended Kyoto Convention recommends limiting intrusive customs inspections, and this is also a proposal being addressed as part of the World Trade Organization's (WTO) trade facilitation negotiations (Laporte, 2011). To limit such inspections, more modern administrations use computerized data interchange and risk analysis to intervene at all stages of the customs chain, focusing their resources on a posteriori control. Developing country customs administrations are lagging behind in this regard. As a result, risk analysis appears to be a top concern for developing countries as they modernize their customs systems. Because of the huge volume of export, import, and transit transactions, many Customs administrations utilize risk analysis to identify which people, products, and modes of transportation should be scrutinized and to what extent. Risk analysis and risk assessment are analytical techniques for determining which risks are the most significant and should be treated first or have corrective action performed first (Bezabeh, 2019). Risk management is the systematic use of management systems and practices to provide Customs with the information they need to address movements or consignments that pose a risk. Risk management's major goal is to determine if a shipment requires physical inspection, documented checks, or immediate release. Some of the automated methods used include statistical scoring and rule-based methods which fails as the data volume increases (Regmi & Timalsina, 2018). Data mining has been widely used for risk management.

Data mining is a flexible technique that have grown rapidly over decades which is being used by corporate organizations to extract data and other valuable details, patterns whence large data sets is concerned. Moreso, data mining techniques has seen wide adoption and application in various domains with the sole aim of facilitating daily activities and ease human burdens Zhang et al., (2022). The use machine learning and data mining techniques for risk management have only been given little attention. Hence, in order to explore the advantages of data mining and machine learning techniques for effective risk

management. This paper presents an investigative analysis of several machine learning models for risk management in Nigerian Customs with a view of finding the most suitable model.

2 DATA, METHODOLOGY AND EVALUATION

The methodology adopted to achieve the aim of this paper is shown in Figure. Dataset were collected and preprocessed, followed by data partitioning and ML model designs. Each of the model is trained, tested and performance evaluated.

2.1 Data

The dataset used in this paper is the trade record from the single good declaration of the Nigerian Custom service (NCS) which can be obtained from NCS website. The dataset comprised of over 6 million records collected up to 2019. The attributes of the data described the nature of goods to be imported and include information such as: the importers name, the method of importation which can either be by road, sea, or air, the declarants name, the item number, quantity, net and gross mass, price, value, tax, invoice and description. Finally, the datasets contain the category of the record being high risk or low risk item. Figure 1 shows a snap shot some samples of the dataset and their attributes without the importers and declarants details.

CTY_ORIGIN	MODE_OF_TRANSPORT	HS_DESC	ITM_NUM	QTY	GROSS_MASS	NET_MASS	ITM_PRICE	STATISTICAL_VALUE	TOTAL_TAX	INVOI
MANY	Road transport	35	0.2	1	2000	2000	404240	404240	744843	1734
Italy	Road transport	20	1	1	6250	6250	100417	100417	452499	1346
Germany	Sea transport	5	0.75	100	4000	4000	552510	623809	400330	5264
United Kingdom	Road transport	35	1	1	1637	1637	663084	663084	297379	663
United States	Road transport	35	1	1	14042	14042	1145764	1142855	512544	1145
China	Road transport	10	0.33333333	450	10000	10000	2934000	3391378	900051	9258
China	Road transport	5	0.66666667	250	5000	5000	2144450	2569970	0	6681
Saudi Arabia	Road transport	5	1	30	20000	20000	13652880	16138921	2000175	18060
Japan	Road transport	10	0.25	64	2000	2000	1304000	1458650	438881	3145
China	Road transport	20	0.42857143	322	3000	3000	3010808	3734842	3694063	1032
United Arab Emirates	Air transport	20	0.5	26	1000	1000	97800	134007	90029	228

Figure 1: A snapshot of the data sample

To test the machine learning models, about 5000 samples were selected that cut across low and high-risk samples.

2.2 Methodology

The dataset was preprocessed by removing unwanted attributes manually and converting the textual attributes to numerical values. This is followed by data normalization and partitioning. The data was partitioned into training and testing data in the ratio of 70:30 respectively. Five popular ML models were selected to be investigated. The essence is to determine the best model for determining the risk of consignments. The ML models considered are; Support Vector Machine (SVM), Decision Tree (DT) classifier, K-Nearest Neighbor (KNN), Ensemble and Discriminant analysis classifiers.

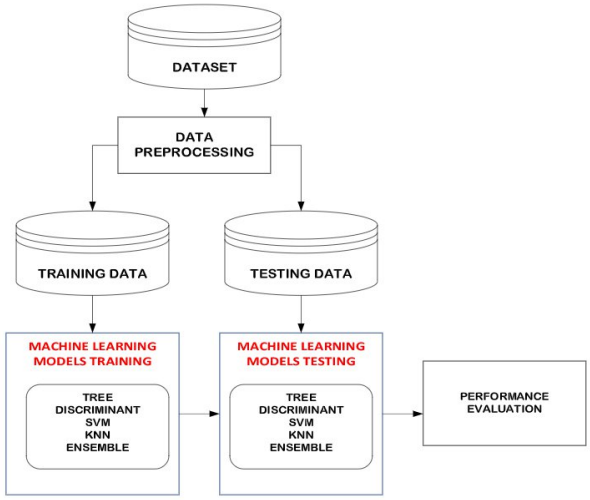

Figure 2: Model Investigation Methodology

For each model, different types were investigated, such as; Fine, Medium and Coarse Tree models, Linear and Quadratic discriminant models, Linear, Quadratic, Cubic, Fine gaussian, Medium gaussian and Coarse gaussian SVM models; Fine, Medium, Coarse, Cosine, Cubic and Weighted KNN, and finally, Boosted, Bagged and RUSBoosted Ensemble Tree models.

Experiments were performed for each ML model using the partitioned dataset to train and test each model. The performance of the models was evaluated using accuracy, True Positive Rate (TPR) and False Negative Rate (FNR).

These metrics were calculated from the True Positive (TP), True Negative (TN), False positive (FP) and False Negative (FN) values obtained from the confusion matrices. Accuracy shows the percentage of samples correctly classified for risky and non-risky samples. The TPR shows the ability of the model to detect risky consignment, while the FNR shows the number of risky samples wrongly classified as not risky. To evaluate the performance of the proposed model, the following metrics will be used.

i. Accuracy:

The number of consignment correctly classified divided by the total number of classified consignments.

$$Accuracy = \frac{TP + TN}{TP + FP + TN + FN} \times 100\% \quad (3.1)$$

ii. True Positive Rate:

The proportion of positive classifications that are truly positive.

$$TPR = \frac{TP}{TP + FP} \times 100\% \quad (3.2)$$

iii. False Positive Rate:

The proportion of actual Positives that are correctly classified.

$$Recal = \frac{FP}{FP + TN} \times 100\% \quad (3.3)$$

3 RESULTS AND DISCUSSION

The number TP, TN, FP and FN obtained for each model type are shown in Table 4. From Table 4, Fine KNN produced the highest TP of 600 while Linear SVM produced the least with 265 resulting in the lowest and highest FN of 400 and 735 respectively. Cubic SVM has the highest FP of 441 compared to Linear SVM with just 32 FP.

Table 4: Confusion matrix

Models		TP	TN	FP	FN
Tree	Fine Tree	530	766	234	470
	Medium Tree	500	822	178	500
	Coarse Tree	504	818	182	496
Discriminant	Linear Discriminant	468	779	221	532
	Quadratic Discriminant	280	946	54	720
SVM	Linear SVM	265	968	32	735
	Quadratic SVM	504	731	269	496
	Cubic SVM	435	559	441	565
	Fine Gaussian SVM	537	715	285	463
	Medium Gaussian SVM	449	831	169	551
	Coarse Gaussian SVM	266	967	33	734
KNN	Fine KNN	600	616	384	400
	Medium KNN	514	766	234	486
	Coarse KNN	530	720	280	470
	Cosine KNN	512	768	232	488
	Cubic KNN	501	782	218	499
	Weighted KNN	582	659	341	418
ENSEMBLE	Boosted Trees	481	852	148	519
	Bagged Trees	569	703	297	431
	RUSBoosted Trees	500	822	178	500

From the TP, TN, FP, and FN values, the accuracy, TPR and FPR were calculated and shown in Figure 3 and Figure 4. Figure 3 is the bar chart of the accuracy of all the investated models. The result shows that the ensemble models produced the highest accuracy of 66.6% for Boosted Trees and 66.1% for RusBoosted Trees. Cubic SVM produced the lowest accuracy of 49.7%. Figure 4 shows the TPR and FNR of all the models. The Fine KNN model produces the highest TPR (60%) than any other while the Linear SVM model produces the lowest TPR of 26.5%.

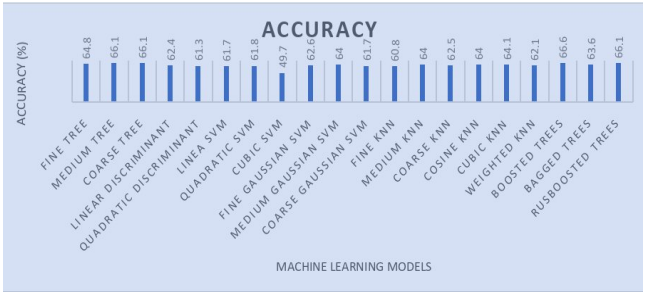

Figure 3: Models accuracy Bar chart

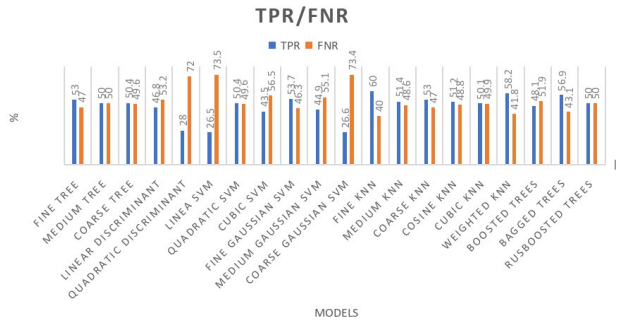

Figure 4: TPR and FPR Bar chart

4 CONCLUSION

Several machine learning models were investigated to determine the suitability of the models for detection of consignment risks in Customs. Datasets were collected, preprocessed and partitioned into training and testing. The models were trained and tested using the datasets. The performance each model was evaluated using the accuracy and TPR/FNR measure. The ensemble models performed better in terms of accuracy for both risks and non-risk consignments. The KNN model produces highest positive detection rate while SVM produces lowest positive detection rate. The results indicate that ensemble and KNN models can be recommended for adoption and further investigation.

FUTURE RESEARCH DIRECTION

To improve the performance of the models, it can be recommended that more pre-processing of the data be carried out using other pre-processing techniques and data balancing approaches. Also, other data mining approach such as feature selection using appropriate metaheuristic algorithms like Pastoralist optimization Algorithm (POA) be carried out to improve the performance of the models. Finally, other performance measures can be checked such as; precision, recall and F1-score.

ACKNOWLEDGEMENTS

I give thanks to The Almighty for making this work possible. I also acknowledge the effort of my infadigable supervisor, Prof. J. K. Alhassan for taking his time out of his tight schedules to criticize my work constructively and also offering assistance by giving me a guide to follow. My acknowledgment is also extended to Dr Abdullahi and Dr Aliyu who are co-authors of this work.

REFERENCE

Bhero, E., & Hoffman, A. (2017). Improving customs infraction-detection and risk management with GPS data. *2017 IEEE AFRICON: Science, Technology and Innovation for Africa, AFRICON 2017*, 1534–1540. https://doi.org/10.1109/AFRCON.2017.8095710

Hammadi, L., Ouahman, A. A., De Cursi, E. S., & Ibourk, A. (2018). An approach based on FMECA methodology for a decision support tool for managing risk in customs supply chain: A case study. *International Journal of Manufacturing Technology and Management*, *32*(2), 102–123. https://doi.org/10.1504/IJMTM.2018.090060

Hartama, D., Perdana Windarto, A., & Wanto, A. (2019). The Application of Data Mining in Determining Patterns of Interest of High School Graduates. *Journal of Physics: Conference Series*, *1339*(1). https://doi.org/10.1088/1742-6596/1339/1/012042

Kavoya, J. (2020). Machine learning for intelligence-driven Customs management. *African Tax and Customs Review*, *9535*, 50–58. https://www.researchgate.net/publication/341462392

Laporte, B. (2001). *Risk management systems : using data mining in developing countries ' customs administrations*. *5*(1), 17–28.

Regmi, R. H., & Timalsina, A. K. (2018). Risk Management in customs using Deep Neural Network. *Proceedings on 2018 IEEE 3rd International Conference on Computing, Communication and Security, ICCCS 2018*, *October 2018*, 133–137. https://doi.org/10.1109/CCCS.2018.8586834

Vanguard. (2021, December 20). *Nigeria Customs Service revenue hits N2.3trn – Official*. https://www.vanguardngr.com/2021/12/nigeria-customs-service-revenue-hits-n2-3trn-official/

Wuletaw, A. (2021), Developing automatic fraud detection model for customs transaction using deep learning technique. Dspace Repository. https://ir.bdu.edu.et/handle/123456789/13225

Yaqin, W., & Yuming, S. (2010). Classification model based on association rules in customs risk management application. *Proceedings - 2010 International Conference on Intelligent System Design and Engineering Application, ISDEA 2010*, *1*, 436–439.

https://doi.org/10.1109/ISDEA.2010.276

Zhang, L., Liu, K., Ilham, I., & Fan, J. (2022). Application of Data Mining Technology Based on Data Center. *Journal of Physics: Conference Series*, *2146*(1).https://doi.org/10.1088/1742-6596/2146/1/012017

4th International Engineering Conference (IEC 2023)
Federal University of Technology, Minna, Nigeria

A Face Recognition-Based Intruder Detection System for Automatic Door Control

*[1]Daniyan, A. &[1]Michael O. M.

[1]Electrical And Electronics Engineering Department, Federal University of Technology, Minna, P.M.B. 65, Niger State, Nigeria
*Corresponding author email: a.daniyan@futminna.edu.ng +234 806 420 3455

ABSTRACT
In recent years, theft and unauthorized access to private areas in homes and communities has become a growing concern, leaving individuals feeling insecure about their lives and properties. To address this problem, this paper proposes a solution that features a facial recognition system to prevent entry by unauthorized individuals.
The system uses an ESP32 Camera module and the Arduino Integrated Development Environment (IDE) to capture and store facial biometric details through facial recognition techniques. The data is saved in a database that is accessible through a web interface enabled by HOTSPOT connection. The camera's Internet Protocol (IP) address also allows for live streaming as an added feature.
An ATmega328 microcontroller on the Arduino IDE receives signals from the ESP32 camera, process the data and operate the door accordingly. When the ESP32 Camera recognizes a face, it sends a signal to the microcontroller to open the door. If the face is not recognized, the door is kept locked to prevent entry by intruders. The proposed solution effectively identifies intruders and those with authorized access but grants access only to authorized individuals in its database. This ensures a secure environment for homes and communities, providing peace of mind to individuals who have long been worried about theft and unauthorized access.
Results demonstrate that the proposed facial recognition system is has been able to provide a secure environment for homes and communities by denying entry to intruders and granting access only to recognized individuals.

Keywords: *Biometric, Database, Face detection, Facial, Intruder detection, Security*

1 INTRODUCTION

Intrusion, the act of an unauthorized person gaining access to a restricted zone without your permission, is on the rise. A human intrusion detection system is designed to detect an unauthorized entry into a building or a protected area and deny such unauthorized access to protect personnel and property from damage or harm (Kumar, *et al.*, 2013b). Security systems are mainly used in residential, commercial, industrial, and military properties for protection against burglary (theft) or property damage, as well as personal protection against intruders. The human presence of security guard may not be completely trustworthy (Kumar, *et al.*, 2013b). In such cases, this system provides proper detection of intruder and provides security. By using this system, we can reduce robbery by detecting the intruder and deny access to unauthorized entry so we can ensure that no harm takes place in our home (Sampson, 2011). In the designed system, the camera is kept outside the room and the continuous video is captured by the camera. The system is designed in such a way that as soon as someone enters the room, the processing takes place at the instance of time (Sampson, 2011). The proposed system thus should be efficient in all aspects including the cost as the ESP32camera is employed. Most countries are gradually adopting smart door security system. A major part of any door security systems are identifying accurately the persons who enter through the door. Face recognition is probably the most natural way to perform authentication between human beings (Sampson, 2011). With theft and robbery amongst some of the most dangerous threats across the globe in recent times and with home security systems constantly failing to safeguard houses and offices, Facial Recognition has gained prominence as a result of its effectiveness in identifying intruders. A survey conducted by FBI, perfectly illustrates why facial recognition is ever more important as it shows that all the intrusion problems occurred in absence of the owners at home. In the year 2012, a house is being invaded by the intruders for every twenty seconds (Sampson, 2011). Among these, only 10% of them end up in arrests, and rest of them are still suffering from intruders. Whilst there are other solutions for this problem like home automation systems, alarm detection systems etc; there is a chance of producing false alarms by these systems. This is the main reason for those systems to have a higher rate of failure (Sampson, 2011). Thus, there is a need to design a system that can detect the intruder who tries to enter the home or

office. This research aims to design a security system that will detect intruders based on facial recognition and will only give access into the building to recognized faces by automatically opening a motorized door.

An efficient and accurate home security and access control to the doors system which is based on face recognition is very important for wide range of security application. Security is an important aspect or feature in the smart home applications (Karri, *et al.*, 2015). Most of the countries are gradually adopting smart door security system. The most important major part of any door security systems is identifying accurately the persons who enter through the door. Face recognition is probably the most natural way to perform authentication between human beings (Karri, *et al.*, 2015). Additionally, it is the most popular biometric authentication trait, after fingerprint technology. Most of the security system was implementing a Principal Component Analysis (PCA) algorithm for face recognition on hardware platform for its dimensionality reduction and simplicity. Wireless technologies for example and ZigBee, radio frequency identification (RFID) and etc are used in access control systems (Karri, *et al.*, 2015). This proposed system also act as home security system for both Intruder detection and provide security for door access control by using facial recognition for home environment. Human body is identified as an intruder within a home environment achieved by capturing live video from web camera and processing will be done on captured video frames to identify the motion detection of the intruder (Khan, *et al.*, 2012). The web camera capture the series of images as soon as the intruder motion is detected in certain area of the home premises and also it send automatic e-Mail alerts along with captured images and other contact details to the nearby police station or control room's e-mail about the intruder detected to take further immediate necessary actions (Khan, *et al.*, 2012). The advantage of this system is for accessing the door such that face detection and recognition is performed by using face detection technique and the entire face recognition is completed by pressing single and tiny push button switch. Face recognition includes feature extraction from the facial image, recognition or classification and feature reduction (Khan, *et al.*, 2012). PCA is an effective feature extraction method used based on face as a global feature. It effectively reduces the dimension of captured images and at the same time holds the primary information (Khan, *et al.*, 2012). In this project, face recognition system is implemented based on standard PCA (Principal component analysis) algorithm. Classification or Recognition is done by the measure method such as Euclidean distance technique, which is used to classify the feature of images stored in the database and captured test images (Khan, *et al.*, 2012).

In 2018, (ARL, 2018) developed a technique that would allow them to match facial imagery obtained using a thermal camera with those in databases that were captured using a conventional camera. Known as a cross-spectrum synthesis method due to how it bridges facial recognition from two different imaging modalities, this method synthesizes a single image by analyzing multiple facial regions and details. It consists of a non-linear regression model that maps a specific thermal image into a corresponding visible facial image and an optimization issue that projects the latent projection back into the image space. ARL scientists have noted that the approach works by combining global information (i.e., features across the entire face) with local information (i.e. features regarding the eyes, nose, and mouth). According to performance tests conducted at ARL, the multi-region cross-spectrum synthesis model demonstrated a performance improvement of about 30% over baseline methods and about 5% over state-of-the-art methods (ARL, 2018).

Lwin, *et al.,* (2015) proposed a door lock access system which comprised mainly of three subsystems: namely face detection, face recognition and automatic door access control. Face recognition is implemented by using the Principal Component Analysis (PCA). The door will open automatically for the known person due to the command of the microcontroller. On the other hand, alarm will ring for the unknown person. Drawback of this system is input images are taken through a web camera continuously until the 'stop camera' button is pressed (Lwin, *et al.,* 2015). Someone is required at the location to check unauthorized person's images or status of the system and take further action. Personal computer (PC) is connected with the microcontroller, The whole system will not work if PC is crashed or Non-Function.

Kumar, *et al.*, (2013a) presented the implementation of a low-cost wireless home security system using ZigBee protocol and remote access through internet. A ZigBee based star network with two nodes had been established employing Xbee radio, ARM7, PIC, and MBED microcontroller. The detection of the intruder motion, gas leakage detection and visual surveillance of the home were provided with the help of Passive Infrared Sensor (PIR), Gas sensor (GH-312) and Camera (LS_Y201). Problem is here multiple micro controllers are used; usage of ZigBee based network to communicate with the base station is limited to 100-150 meters long distance only. Base station is dependent on only Ethernet for internet connectivity.

Kartik, *et al.*, (2013) proposed two systems are proposed, one is based on GSM technology and other uses web camera to detect the intruder. The first security system uses a web camera, installed in house premises, which is

operated by software installed on the PC and it uses Internet for communication. The camera detects motion of any intruder in front of the camera dimensions or camera range. The software communicates to the intended user via Internet network.

In 2003, (Mae, *et al.*, 2003) presented a system that monitors everything by moving cameras. The system can increase the efficiency of monitoring and can eliminate the blind spots of fixed cameras. In this system, a mobile manipulator is developed which is equipped with cameras at the arm end for purpose of monitoring.

2 METHODOLOGY

2.1 MATERIALS

In order to build our proposed system, the following hardware components were used: ESP32-Camera Module, Micro-Controller Unit (ATmega328), power supply unit (transformer, rectifier diode, voltage regulator, filter capacitor), dvd mini, servo motor, JQC-3F-12VDC relay, and BJTs.

2.2 METHODS

The approach used in realizing a functional prototype of this work is grouped into two categories which are: software design and hardware design.

2.2.1 Software Design

The ATmega328 microcontroller was connected to the computer system via Universal Serial Bus (USB) data-cable. The Arduino Integrated Development Environment (Arduino IDE) which is a programming software installed on a computer system was used to upload the codes written in C++ to the ATmega328 microcontroller. The ESP32-CAM was mounted on its Future Technology Device International (FTDI) programmer's board and connected to the computer system using USB data Cable. The Arduino IDE program software is compatible with the ESP32-Cam FTDI programmer's board and written codes in C++ was uploaded to the ESP32-CAM module.

2.2.2 Hardware Design

This section shows snapshots of the connections together with the final soldering work done on the Vero-Board and the fully designed Prototype. Bread board was not used for preliminary connections and testing because the ESP32 camera pins does not match the holes on the bread board. Figure 1 is a snapshot of the fully built prototype.

Figure1: Fully Built Prototype

3 RESULTS AND DISCUSSION

In this section, results obtained during testing and evaluation of the proposed system are presented and discussed. During the software design, compatibility between software application and programming language to be used analysed and a suitable programming language was chosen, in this case, C++. Furthermore, Arduino software (IDE) was selected as the platform to write, edit, and upload written codes to the ESP32-camera module and ATmega328 microcontroller. The major challenge encountered during the software design was that the Arduino software had to be downgraded in order to access the face recognition of ESP32-camera module each time the module is being worked upon. The fully built prototype was connected to power supply and turned on, major tests based on its intended function were carried out and information gotten forms part of the results which is the next category.

3.1 RESULTS

Obtained from the working prototype were the visual outputs captured as screenshots on the Web-interface provided by the ESP32-Camera module which has a Wi-Fi-HOTSPOT connection embedded in its system that provides real time visual streaming and snapshots of the prototype's door as it is being operated automatically in the process.

Figure 2 shows the web-interface that serves as an input as it prompts you to enroll face after activating face detection and recognition

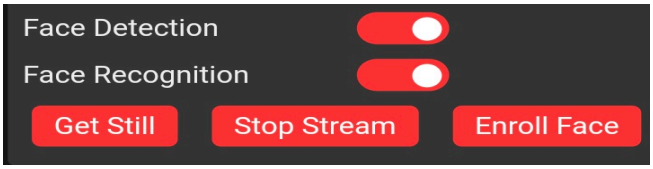

Figure 2: Command Prompt

The screenshot in Figure 3 shows when the face of an individual is being captured, enrolled and saved to database

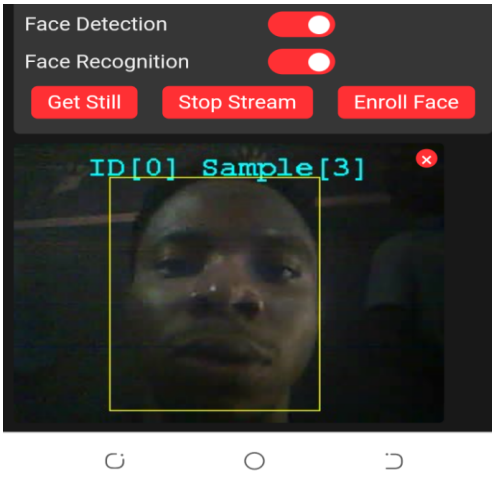

Figure 3: Registering Facial Data

The snapshot in Figure 4 shows the normally closed door of the prototype

Figure 4: Prototype Showing Closed Door

The screenshot in Figure 5 shows when the individual whose image is saved in the database come in front of the camera mounted on the door

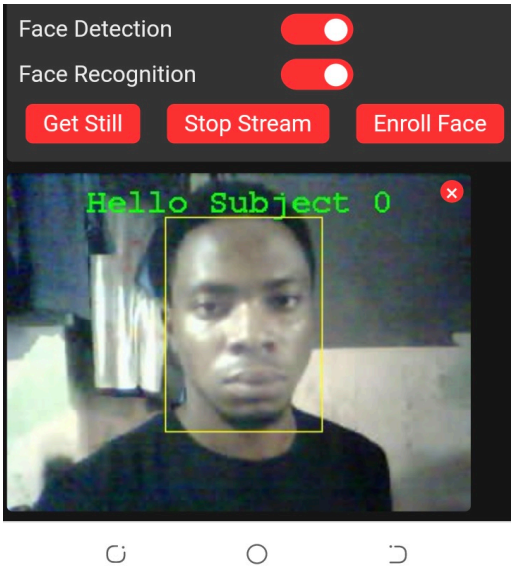

Figure 5: Recognized Face

Figure 6 shows when the prototype's door opened for the recognized face

Figure 6: Door Opens to Allow Entry of The Recognized Person

Figure 7 shows when another individual whose image is not in the database comes in front of the prototype's camera

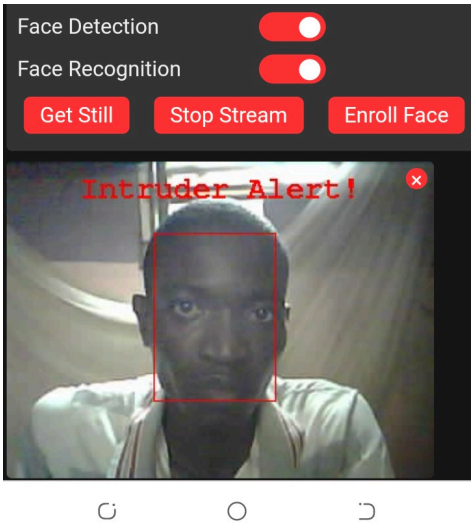

Figure 7: Unrecognized Face

In Figure 8 below,the prototype's door remains locked as it does not open for the intruder

Figure 8: Door Stayed Locked as It Detected an Intruder

3.2 DISCUSSION OF RESULTS

The system as whole functioned as expected performance was achieved so need to check for its reliability became a necessity. The procedures used to achieve the results were then repeated ten (10) times in other to determine the reliability of the system. For the ten test which was carried out in fifty (50) minutes, seven (7) were successful as the system operated smoothly while the system failed to operate three (3) times due to malfunction of the visual user interface failing to record and save the images to its database, so it had to be restarted by re-booting. Using the data obtained, the reliability of the system was calculated as shown below.

Number of test carried out = 10

Number of success = 7

Number of failure =3

Operated time (t) = 50 mins = 0.833 hrs

$$\text{Failure rate } (\lambda) = \frac{3}{10} = 0.3 \quad (1)$$

$$\text{Reliability } (R) = e^{-\lambda t} \quad (2)$$

$$R = e^{-(0.3 \times 0.833)} = 0.7789 \quad (3)$$

For a system with reliability of 0.7789, the system is said to be reliable. Since the prototype was operated ten time for a specific period, hence the need to check its consistency became necessary. The table below shows the time taken for each of the ten operations.

TABLE 1: SPECIFIC TIME TAKEN FOR TEN DIFFERENT TESTS

Number of Operations	Time Taken (Minutes)
1	5
2	4
3	6
4	5
5	7
6	5
7	4
8	5
9	5
10	4

For the ten test operations carried out, an average time of five (5) minutes was spent on each test hence, the prototype proved to be consistent in its operation.

Figure 9 below shows the graph of number of operations plotted against time using the values of Table 1.

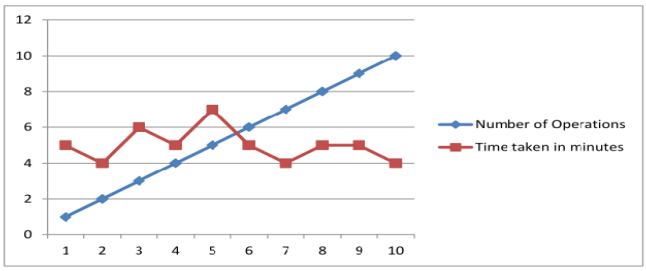

Figure 9: Graph of Number of Operations Plotted Against Time Taken for Each Operation

From the graph, the point of interception of "Number of Operations" and "Time taken in minutes" is 5 which is equal to the Average Time calculated, hence, it confirms consistency.

CONCLUSION

In this work, a security system that detects intruders based on facial recognition and only grant access to recognized faces by automatically opening a motorized door was proposed. To achieve this, an ESP 32 camera module of 2 mega-pixel as the prototype correctly identifies the intruder. Also, the prototype was successfully able to control a motorized door automatically by the instructions it receives from the Arduino ATmega328 microcontroller. The prototype was able to control the door automatically when the ESP32-camera recognizes the face of a person whose image is on its database by activating the Arduino NANO micro-controller into action. The system can establish a software-hardware relationship by allowing the prototype's web-interface visualizes inputs to be processed. The system designed has the capacity to function as a security unit for our homes, offices, schools and so on. ance.

REFERENCE

ARL, P. (2018). *Army Develops Face Recognition Technology that Works in the Dark*. Retrieved February 3, 2023, from https://www.army.mil/article/203901/army_develops_face_recognition_technology_that_works_in_the_dark

Bramer, M. (Ed.). (2006). *Artificial Intelligence in Theory and Practice: IFIP 19th World Computer Congress, TC 12: IFIP AI 2006 Stream, August 21-24, 2006, Santiago, Chile* (Vol. 217). Springer Science & Business Media.

Chen, S. K., & Chang, Y. H. (2014). *2014 International Conference on Artificial Intelligence and Software Engineering (AISE2014)*. DEStech Publications, Inc.

Hamann, K., & Smith, R. (2019). Facial Recognition Technology. *Criminal Justice*, *34*(1), 9-13.

Jain, A. K., & Li, S. Z. (2011). *Handbook of Face Recognition* (Vol. 1). New York: Springer.

Karri, V., & Lim, J. D. (2005). Method and Device to Communicate via SMS after a Security Intrusion. In *1st international conference on sensing technology, Palmerston North, New Zealand* (pp. 21-23).

Kartik, J. S., Kumar, K. R., & Srimadhavan, V. S. (2013). Security System with Face Recognition, SMS Alert and Embedded Network Video Monitoring Terminal. *International Journal of Security, Privacy and Trust Management (IJSPTM) Vol*, *2*.

Khan, S. R., Al Mansur, A., Kabir, A., Jaman, S., & Chowdhury, N. (2012). Design and Implementation of Low-Cost Home Security System Using GSM Network. *International Journal of Scientific & Engineering Research*, *3*(3), 1.

Kumar, B. U., Murty, D. S., & Kumar, C. R. P. (2013a). Implementation of Low-Cost Ethernet Based Home Security Using Wireless Sensor Network. *Journal published at Algorithms Research*.

Kumar, B. U., Murty, D. S., & Kumar, C. R. P. (2013b). Implementation of Low-Cost Ethernet Based Home Security Using Wireless Sensor Network. *Journal published at Algorithms Research*.

Lwin, H. H., Khaing, A. S., & Tun, H. M. (2015). *Automatic Door Access System Using Face Recognition*. International Journal of scientific & technology research, *4*(6), 294-299.

Mae, Y., Sasao, N., Inoue, K., & Arai, T. (2003). *Person Detection by Mobile-Manipulator for Monitoring*.

In SICE 2003 Annual Conference (IEEE Cat. No. 03TH8734) (Vol. 3, pp. 2801-2806). IEEE.

Sampson, R. (2011). *False Burglar Alarms*. US Department of Justice, Office of Community Oriented Policing Services.

Socolinsky, D. A., & Selinger, A. (2004). *Thermal Face Recognition in an Operational Scenario*. In Proceedings of the 2004 IEEE Computer Society Conference on Computer Vision and Pattern Recognition*, 2004. CVPR 2004.* (Vol. 2, pp. II-II). IEEE.

Wechsler, H. (2007). *Reliable Face Recognition Methods: System Design, Impementation and Evaluation*. Boston, MA: Springer US.

Williams, M. (2008) "Better Face-Recognition Software". Retrieved 2008-06-02.

4th International Engineering Conference (IEC 2022)
Federal University of Technology, Minna, Nigeria

Ensemble Based Emotion Detection Model for Multi-Social Platforms

*Bala A[1], Mrs. Abisoye O. A.[2], Oluwaseun, A. O.[3], & Solomon A. A[4]
[1]Computer science Department, Federal University of Technology, PMB 65 Minna Niger State, Nigeria
[2]Computer Science Department, Federal University of Technology, PMB 65 Minna Niger State, Nigeria
[3]Computer Science Department, Federal University of Technology, PMB 65 Minna Niger State, Nigeria
[4]Computer Science Department, Federal University of Technology, PMB 65 Minna Niger State, Nigeria
[1]abdullahibala1@gmail.com, [2]o.abisoye@futminna.edu.ng, [3]o.ojerinde@futminna.edu.ng & [4]solo.adepoju@futminna.edu.ng

ABSTRACT
In recent years, there is an exponential growth in public generated data such as image, video and text, this is due to the rapid emanation of diverse social media users. This available textual data is frequently adopted and significantly important for extracting information such as user's sentiments, and emotions. Considering the complexity and large amount of textual data, the adoption of various machine learning (statistical models), and deep learning model (neural network) for the analysis of emotion has not yet attained optimum accuracy. Recently, Transformer based Architecture (BERT) are achieving state of art accuracy. Hence, this study adopts an ensemble based model using BERT-Large, LSTM and SVM for detecting user's emotion. The experimental evaluation carried out resulted in an optimum accuracy of 93%.
Keywords: *emotions, ensemble, social media, BERT-large, SVM, LSTM.*

1 INTRODUCTION

In recent year, due to the emanation of various social media platform such as WhatsApp, Facebook, Instagram, and twitters, has resulted to large amount of public available text corpus or dataset (Chiorrini et al., 2021). Considering the fact that social media user tends to feel more comfortable expressing their feelings or opinions during chatting session, hence social media data is tag to be more realistic or rich in emotional context (Chiorrini et al., 2021). Its identify that open contribution or opinion of customer feedback on a particular product can facilitate the quick identification of issues or improvement that is essential for better customer services. Recently, researcher has focus on various techniques that is capably of analyzing user sentiment and emotion in written form automatically. This approach is known has sentiment analysis or emotion analysis (Denemark, 2011).

Furthermore, the analysis of sentiment is described as the process of automating, identifying and deducing user opinion from a written or documented text, this also involve classification of user opinion into either positive, negative of neutral sentiment (Zhang et al., 2018). While emotion analysis is a type of sentiment analysis but with a wider range of classification class, it involves identifying user emotion been express in text format. Based on research it is reveal that the task of emotion analysis is more challenging than that of sentiment analysis, this is due to greater number of possible emotions (classification class) (Chiorrini et al., 2021).

Emotions plays a crucial role in every forms of human communication, which often influence an individual perception of an experience, topic or event. User (customer) opinions and feedback on various products, online or offline can be collated, via various mediums such as comments, reviews, message forums, and polls. The gathered data can take the form of either audio, video or text (Minaee et al., 2019) (Bartneck et al., 2017). However, the analysis of human emotion from textual data is a field of sturdy uses natural language processing (NLP), computational linguistic and text analysis to extract subjective information from source materials. The detection of emotion using natural language processing is a sub domain of sentiment analysis which primarily focuses on extracting emotional information of the user (writer) from text data. Emotion detection aims to pinpoint specific emotions such as happiness, sadness, love, and fear (Albu & Spînu, 2022).

Ensemble methods involve the combination of two or more machine learning (ML) or hybridization of ML and deep learning (DL) techniques to achieve better performance and optimal results (Mosavi et al., 2019) (Mosavi et al., 2019). These methods take advantage of

the strengths of multiple techniques to improve overall performance. The Ensemble methods may include a prediction unit and an optimization unit for more accurate output. They are flexible and they provide higher capabilities in comparison to single methods, and ensemble method becoming increasingly popular due to their potential (Ardabili et al., 2019). In other words, ensemble base learning involves combining multiple machine learning models which perform intelligent task collectively. Common instance of ensemble models includes

1 Netflix: this system adopts hundreds of machine learning model for predicting possible preferences of movies for user.
2 IBM Watson: this ensemble based model is the first prediction model to won the quiz game of jeopardy.
3 Google: in recent model google adopt ensemble based techniques for developing a neural machine translation system. (Serban et al., 2018).

1.1 RESEARCH PROBLEM

Emotion analysis is tag as one of the most challenging task in terms of opinion mining, due to the broader possible emotion class in comparison to sentiment analysis. Various heuristic and statistic based approach has been proposed for emotion mining from text corpus, but the performance is lower than that of deep learning approach in term of accuracy (Chiorrini et al., 2021). Recently, in the domain of natural language processing various state of art architecture has been design and adopted by researchers for performing emotion classification, which resulted in great improvement in term of accuracy. The BERT, GPT and other model build on transformer architecture are the current state-of-art model. (Albu & Spînu, 2022) adopted the BERT-base and SVM model in an hybridize ensemble techniques to analyze user emotions, its concluded by the researchers that optimum accuracy has not yet been attained because they are better versions of BERT model with larger contextual weights. Hence, this research introduce a multi-social ensemble model based on BERT-large, SVM and LSTM.

1.2 RESEARCH GOAL

This sturdy aims to developed a multi-social emotion detection system using ensemble techniques. The propose techniques model hybridize the Bidirectional encoder from transformer (BERT-large), Support Vector Machine (SVM) and Long Short Term Memory (LSTM) model to achieve utmost emotion classification accuracy. In achieving this goal this sturdy will gathered emotion dataset, train individual model and hybridize the prediction result for ensemble decision making. Finally, the developed ensemble model will be evaluated using standard performance metrics.

2 RELATED WORKS

Considering the research work of (Majeed et al., 2020) which focuses on identifying emotions in Roman Urdu text. Despite Roman Urdu is frequently utilize for information exchange on social media platforms, there is limited research on emotion detection in this language. The primary challenge is the lack of benchmark corpora for detecting user emotion from text, which is crucial for various NLP tasks. The analysis of user emotion from a text corpus has various significant benefit such as improving product quality, dialog systems, investment trends, and mental health. The research developed a comprehensive corpus of 18k sentences from various domains and annotated with 6 different categories to focus on the emotional polarity of Roman Urdu sentences. Based on the experimental result its identify that the SVM prediction model had the best F-1 score measure among the applied algorithms.

(Chiorrini et al., 2021) the researchers investigates the effective use of BERT models thus, the bidirectional encoders for the analysis of user sentiment and emotion detection using data from user Tweet. Two different classifiers were adopted for the two tasks, and the performance of the models was evaluated using real-world tweet datasets. Based on the experiments carried out its revealed that the adopted models were able to achieve 0.92, 0.90 percent accuracy in term of detecting and analyzing user emotion and sentiment.

Its identify by (Albu & Spînu, 2022) that the automatic detection of user emotions for their tweet generated data has numerous real life application. This research transforms an imbalanced data into a balance data by including a neutral class to a benchmark dataset that contain 4 categorical classes of user emotion thus, joy, sadness, fear, and anger. The study adopts SVM and BERT model for the detection and identification of user emotion using the balanced dataset. A novel ensemble model was proposed by merging the BERT and SVM models. The experiments carried out shows that the proposed model achieved an optimum intelligent of 0.91 in recognizing emotions in tweets.

Sentiment analysis approach is examined by (Sinan & Kayaalp, 2021) on Yelp restaurant reviews, IMDB movie

reviews, and data collected from Twitter. Word-2-Vec, the BERT model, Bag-of-word along with the TF-IDF feature extraction was the word embedding techniques used by the researchers. The sentiment analysis model was developed using techniques this includes; the LSTM, Naïve Bayesian, CNN and SVM model. Model performance was evaluated using metrics such as, F-1 (F), Precision, ROC curve, and Accuracy. In respect to the result it can be concluded that the word embedding generated by the BERT architecture perform best, and the authors recommend the use of BERT approach to address similar issues.

(Tang *et al*., 2018) introduce Bayesian machine learning model for detecting emotions from social media news articles. This model takes into account the hidden connection or relationship that map two sentences together in a document and can detect emotions at both the document and sentence level. The developed model outperforms the existing method on the level of sentence dis-ambiguity and document dis-ambiguity and sentence-level emotion detection, as shown in experiments on public corpora.

Considering the work of (Kim et al., 2019) introducing a new framework for detecting human emotions in a smart advance cities using the application of Internet of a thing to facilitate the smart environment. The developed approach is named VEmoBar, capable of creating some barrier that can virtually senses human emotions through wireless signals and reflections. A problem is defined to determine the optimal placement of VEmoBars to maximize cumulative accuracy. A novel approach and system initialization are proposed to solve this problem, and the results are evaluated through simulations in various scenarios. The article also discusses future issues and challenges for implementing this framework in smart cities.

In this research thesis the author introduces a prediction model that is capable of predicting human emotion from real time image capturing. The model utilizes the deep CNN and its evaluated against 8 different datasets. However, the researchers thus, (Jaiswal, 2019) minimize the parameters of the network by 909 compared to Vanilla CNN and 509 in respect to current state-of-the-art research. The model achieved 74% accuracy, which is an improvement over previous models with reduced computational complexity. This model can be useful in fields such as elderly care, child therapy, and babysitting where robots need to understand human emotions to provide more customized assistance.

(Vitiugin & Barnab, 2022) This paper describes the system submitted by the WSSC Team to the EmoEvalEs@IberLEF 2021 emotion detection competition. The proposed model combines transformer embedding with topic information and offense features to classify emotions in social media text. The results showed that the model outperforms the benchmark models that are state of art. A weighted average 0.66% F1 score was achieved with 0.67 accuracy.

(Jaiswal et al., 2018) This researcher introduce a new recommendation system which incorporates user's emotions with interests to provide personalized product suggestions. Unlike existing approaches, which rely on past feedback, similarity of other users' buying patterns, or a combination of both, the proposed system does not require a large amount of data. Instead, it captures a user's eye-gaze and facial expressions as they browse a website using an inexpensive webcam. Eye-gaze detection is done by extracting the pupil center of both eyes, and calculating a reference point using a joint probability. Facial expression analysis is done by analyzing landmark points on the face to determine the user's emotion. Both methods work in near real-time, allowing the system to provide intelligent recommendations on-the-fly without the need for user feedback or buying patterns.

3 RESEARCH METHODOLOGY

This section introduces the methodology adopted for developing, prediction and detecting social media user emotions from textual data. The series of scientific step taking which range from data gathering, data exploration, cleaning, transformation, preprocessing, model training, and model evaluation will be diligently discus in this section. Various conceptual diagram illustrating the internal working technology of the proposed system is critically explained in this section. Diagram such as system architecture, flow chart diagram and use case diagram.

3.1 DATA COLLECTION

This sturdy utilized the available emotion data from a popular data science platform repository (Hugging Face). It's a company that provides an NLP platform for featuring pre-trained models, fine-tuning libraries, and development tools. The platform is well-known for its transformer-based models like BERT and GPT-2, which have demonstrated excellent performance in multiple NLP tasks. It allows developers to easily integrate NLP into applications and projects through APIs and libraries. Additionally, Hugging Face offers a model hub where users can access pre-trained models, customize them using their own data, and share them with others (Yu et al., 2020) (Wolf et al., 2020).

Furthermore, the adopted dataset was downloaded from the Hugging Face repository using the

```
]: data_full
]:
```

	text	label
0	i didnt feel humiliated	sadness
1	i can go from feeling so hopeless to so damned...	sadness
2	im grabbing a minute to post i feel greedy wrong	anger
3	i am ever feeling nostalgic about the fireplac...	love
4	i am feeling grouchy	anger
...	...	...
1995	im having ssa examination tomorrow in the morn...	sadness
1996	i constantly worry about their fight against n...	joy
1997	i feel its important to share this info for th...	joy
1998	i truly feel that if you are passionate enough...	joy
1999	i feel like i just wanna buy any cute make up ...	joy

20000 rows × 2 columns

Figure 1: The Emotion Tweets Dataset

datasets python API module, and all the training, testing, and validation data samples were downloaded into the Google Colab environment in a CSV format. The downloaded data was archive in the Google Drive for future reference and easy importation into the Google Colab for further usage using the python *panda's* library. It was essential to merge the entire dataset into a single data for proper usage as depicted in the Figure 1 below. The dataset includes twenty thousand (20,000) emotional tweet data points, with two (2) columns of features which include the tweet text and the corresponding emotion.

The figure 1 shows the sample data point from the downloaded tweet emotions dataset. It's clearly visualize that the *text* column contains various user tweets information while the *label* column contains various type of emotions such has sadness, anger, love, fear and joy. Moreover, the figure shows the total number of columns thus, 2 and the total number available row or data entries

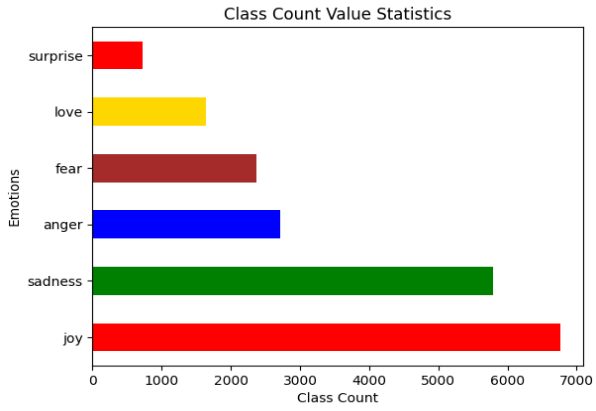

Figure 2. Tweets Emotion Classes Count

thus, 20,000 rows.

3.2 DATA EXPLORATION

This subsection include various exploration carry out on the dataset. Every data science research requires comprehensive understanding about the dataset for extraction of meaningful features from the dataset. Based on analysis its identify that the label column contains six (6) different classes, this includes; sadness, anger, love, surprise, fear, and joy. This is visually illustrated using the bar chart below.

Base on the visual plots it's denoted that the dataset

Figure 3. Word Cloud Visual showing Word Frequency

is divided in bars base on the *label* (emotion type) columns, and it's also identify that the present classes in the emotion tweet dataset is imbalance (having different number of sample in each emotion label class). Its identify that most of the data-sample belong to the *joy* label class with over 6,000 data sample, which is followed by the *sadness* label data-sample with over 5,000 sample, up to *surprise* label sample with minimum number of data sample of 1,000.

In respect to the word cloud figure above, the frequency of word distribution or frequency in the emotion tweet dataset is explore using the application programming interface for word cloud (Heimerl et al., 2014). that words such as "feel", "feeling", "really", "think", and "make", are the most occurring words in the tweet emotion corpus. The word cloud representation uses text size to indicate how often a word appears in a corpus. Hence, the larger the text size in the figure the more frequently is word appears in the text corpus.

3.3 DATA CLEANING & PREPROCESSING

This section is essentially important in the field on data science, machine learning and deep learning. Its ensure that noisy or unwanted content are remove from the raw dataset. Tweet dataset are one of the most challenging data to clean because of the high usage of informal language, emoji's, abbreviation and URLs

```
import text_hammer as th
from tqdm import tqdm_notebook

def text_preprocessing(df, col_name):
    column = col_name
    df[column] = df[column].progress_apply(lambda x:str(x).lower())
    df[column] = df[column].progress_apply(lambda x:th.cont_exp(x))
    df[column] = df[column].progress_apply(lambda x:th.remove_emails(x))
    df[column] = df[column].progress_apply(lambda x:th.remove_html_tags(x))
    df[column] = df[column].progress_apply(lambda x:th.remove_special_chars(x))
    df[column] = df[column].progress_apply(lambda x:th.remove_accented_chars(x)

    return df

text_preprocessing(data_full, 'text')
```

```
0%|          | 0/20000 [00:00<?, ?it/s]

0%|          | 0/20000 [00:00<?, ?it/s]
```

Fig 4. Data cleaning using text hammer

(Derczynski et al., 2013). Hence, this sturdy is adopting the text *hammer* python module to address this issues. The figure 4 and 5 show the cleaning process and the resulted clean text header sample.

	text	label
0	i didnt feel humiliated	4
1	i can go from feeling so hopeless to so damned...	4
2	im grabbing a minute to post i feel greedy wrong	0
3	i am ever feeling nostalgic about the fireplac...	3
4	i am feeling grouchy	0
...	...	...
1995	im having ssa examination tomorrow in the morn...	4
1996	i constantly worry about their fight against n...	2
1997	i feel its important to share this info for th...	2
1998	i truly feel that if you are passionate enough...	2
1999	i feel like i just wanna buy any cute make up ...	2

20000 rows × 3 columns

Figure 5. Clean data and Transform Label

Figure 4 illustrates the utilization of the "text hammer" library to conduct multiple data cleaning process. A customized helper function is defined and all major preprocessing steps are defined within this function. The cleaning actions that are considered includes; removal of any mail address, HTML-related text, lowercasing all text, removing of symbols, emoji's and special characters.

Furthermore, the label column is transform into number format thus, anger *is assign 0, 1 is assign to fear, 3 is assign to love, love is assign to 3, four to sadness, and surprise is tag as 5.* The figure 5 show the cleaning text and the transformed label.

3.4 DATA SPLITTING

The final data preprocessing stage include data splitting, thus splitting of dataset into training set and testing set. In this study 70 percent (14,000) of the dataset is considered for model training and 30 percent (6,000) of the remaining data for testing purpose. The figure 6 above shows the code snippet for achieving the data splitting.

3.5 ENSEMBLE BERT-LARGE, SVM AND LSTM

In this section the conceptual diagram of the proposed ensemble model is illustrated, which combines the bidirectional encoder from transformer (BERT-large), Support Vector Machine (SVM), and Long Short-Term Memory (LSTM). The illustration of the proposed model is depicted diagrammatically in detail using Figure 7.

Figure 7 illustrates the conceptual diagrammatic representation of the proposed ensemble model. The model uses sub models for predictions and this includes the BERT-large, SVM, and LSTM model. As depicted in the figure, the dataset is loaded from the local repository into the google colab and training samples are feed into the three models (BERT, LSTM, and SVM) for training. Each machine learning model is trained individually, and the resulting trained models are saved locally on the system directory for application and ensemble usage. The saved models are then loaded, and the prediction outcomes of each model are utilized in an ensemble technique known as voting. The final prediction outcome can be viewed by the user through the user interface.

The flowchart diagram illustrates the systematic process of data flow, which start with data import and ends with model evaluation. The data flow starts by importing the emotion tweet data into the colab environment, then the data is preprocessed, cleaned, and transformed into a standard format that can be understood and process by the ensemble model. It is shown in the data flow that the dataset is split into 70% for training and 30% for testing. The model training includes all three assembled models: The Support Vector Machine, Long Short-Term Memory, and BERT-large model. Finally, the split testing data is fed into the ensemble model for model classification evaluation using standard metrics (accuracy, precision and recall).

3.6 MATERIAL AND TOOL

This sturdy adopt various software tools for the development of the proposed model. Then the entire coding is carried out using the google collaboratory notebook environment and jupyter notebook, because it provides access to GPU and TPU processing power (Alves & Machado Vieira, 2019). Other software tools used Microsoft Visio for drawing the various conceptual diagram. Python is choosing as the programming language of choice due to is richness in data science module.

Emotion Dataset spliting

```
from sklearn import model_selection

train_data , test_data = model_selection.train_test_split(df_cleaned, test_size=0.3, random_state=42 )
```

```
train_data.shape
```

```
(14000, 3)
```

```
test_data.shape
```

```
(6000, 3)
```

Figure 6. Emotion Tweet Data Splitting (70%, 30%)

4 RESULTS AND DISCUSSION

This section explains how the actual implementation and training of the ensemble model is carried out, the various performance evaluation metrics considered includes the Accuracy, precision, recall and F1-score. Finally, the model will be evaluated with the existing sturdy for performance comparison. Each model (SVM, LSTM and BERT) is trained separately and later

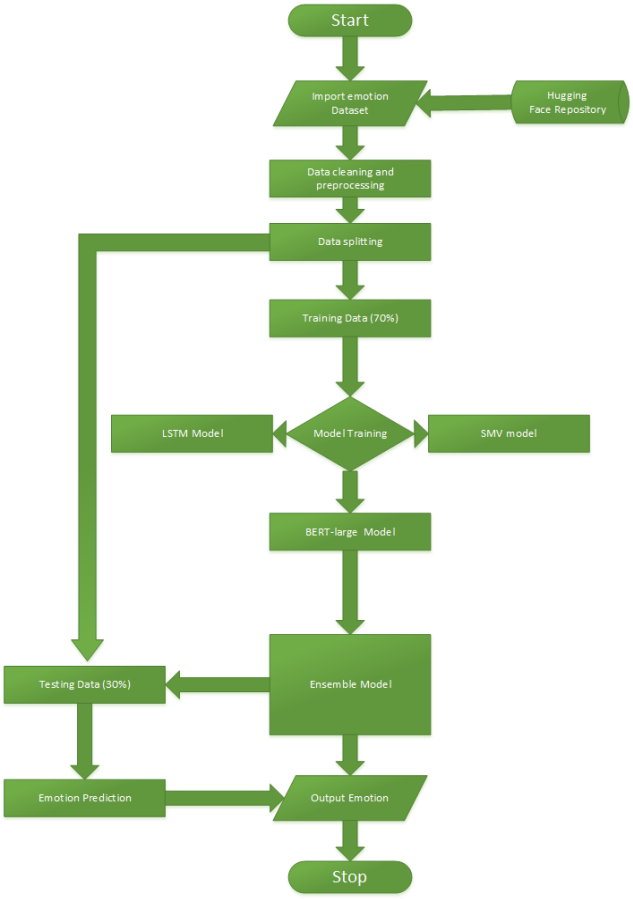

Figure 8. The data flow diagram

ensemble for emotion prediction.

```
Model: "sequential"
_________________________________________________________________
 Layer (type)                Output Shape              Param #
=================================================================
 embedding (Embedding)       (None, 70, 100)           3000000

 bidirectional (Bidirectiona  (None, 256)              234496
 l)

 dense (Dense)               (None, 100)               25700

 dense_1 (Dense)             (None, 6)                 606

=================================================================
Total params: 3,260,802
Trainable params: 3,260,802
Non-trainable params: 0
_________________________________________________________________
```

Figure 11 LSTM model summary

4.1 SUPPORT VECTOR MACHINE MODEL

It's essential to carry out some preprocessing on the textual data before it can be utilize by the SVM machine learning model. Hence, this sturdy adopt count vectorization to transform the textual data into numerical dictionary corpus. Based on parameter tuning (cross fold validation) its identify that the best parameter combination is set to c=0.1, gamma = 0.1 and kernel = 'linear'. The preprocessing and training is programmatically achieved using the predefined methods in the sk-learn module. The figure 9 show the experimental implementation.

Based on the figure 9. It's clearly shown that the text column of the emotion dataset is transform into numerical representation using the *fit_transform* method. In this format the system is able to learn a dictionary of words (word map to a unique number), and this is use to train the Support vector machine model. however, an accuracy of 88.6 % is achieved. The classification report is visualizing below by considering the various performance metrics.

```
[ ]: # SVM MODEL
     #  vectorizaing..
     from sklearn.feature_extraction.text import CountVectorizer

     cv = CountVectorizer()
     fit_xtrain  = cv.fit_transform(X_train)
     fit_xtest  = cv.transform(X_test)
     # cv.fit_transform()

[ ]: fit_xtrain.shape
24]: (16000, 15077)

[ ]: from sklearn import svm

     sv = svm.SVC(C=0.1, gamma = 0.1, kernel='linear')
     svm_model = sv.fit(fit_xtrain, y_train)

[ ]: svm_model.score(fit_xtest, y_test)
27]: 0.88625
```

Figure 9. SVM preprocessing and training

4.2 LONG SHORT TERM MEMORY MODEL

This section requires a separate preprocessing techniques for proper deep learning utilization of text data. The tensor flow API is use in perform text tokenization, sequencing and padding before they are passed into the deep learning architecture.

```
print(report)
              precision    recall  f1-score   support

           0       0.89      0.89      0.89       519
           1       0.81      0.87      0.84       484
           2       0.89      0.93      0.91      1348
           3       0.81      0.70      0.75       328
           4       0.93      0.93      0.93      1169
           5       0.93      0.65      0.77       152

    accuracy                           0.89      4000
   macro avg       0.88      0.83      0.85      4000
weighted avg       0.89      0.89      0.88      4000
```

Figure 10 SVM classification Report

The figure shows the number of layer present in the model summary and the actual parameter shape of each layer. Based on the figure and embedding layer comes first where the input parameter and the vector size of each word is define. This is immediately followed by the LSTM layer then a fully connected dense layer and finally a last layer with 6 neurons (output layer)

```
|: from sklearn import metrics
class_report = metrics.classification_report(test_data.label ,
confu_matrix = metrics.confusion_matrix(test_data.label, predi
print(class_report)
```

	precision	recall	f1-score	support
0	0.91	0.95	0.93	831
1	0.92	0.84	0.88	697
2	0.96	0.95	0.95	1980
3	0.84	0.88	0.86	507
4	0.97	0.96	0.96	1755
5	0.77	0.85	0.81	230
accuracy			0.93	6000
macro avg	0.89	0.91	0.90	6000
weighted avg	0.93	0.93	0.93	6000

Figure 15 BERT classification report

```
In [ ]: lstm_model.fit(train_pad, y_train , epochs=10, validation_data=(test_pad, y_test), verbose=1)

Epoch 1/10
500/500 [==============================] - 238s 466ms/step - loss: 1.0084 - accuracy: 0.6139 - val_lo
ss: 0.4996 - val_accuracy: 0.8195
Epoch 2/10
500/500 [==============================] - 185s 371ms/step - loss: 0.3050 - accuracy: 0.8944 - val_lo
ss: 0.2861 - val_accuracy: 0.8985
Epoch 3/10
500/500 [==============================] - 182s 365ms/step - loss: 0.1682 - accuracy: 0.9408 - val_lo
ss: 0.2650 - val_accuracy: 0.9070
Epoch 4/10
500/500 [==============================] - 191s 382ms/step - loss: 0.1207 - accuracy: 0.9583 - val_lo
ss: 0.2516 - val_accuracy: 0.9120
Epoch 5/10
500/500 [==============================] - 186s 373ms/step - loss: 0.0880 - accuracy: 0.9679 - val_lo
ss: 0.2978 - val_accuracy: 0.9105
Epoch 6/10
500/500 [==============================] - 186s 372ms/step - loss: 0.0645 - accuracy: 0.9773 - val_lo
ss: 0.3135 - val_accuracy: 0.9110
Epoch 7/10
500/500 [==============================] - 186s 372ms/step - loss: 0.0602 - accuracy: 0.9789 - val_lo
ss: 0.3165 - val_accuracy: 0.9082
Epoch 8/10
500/500 [==============================] - 205s 409ms/step - loss: 0.0456 - accuracy: 0.9838 - val_lo
ss: 0.3056 - val_accuracy: 0.9080
Epoch 9/10
500/500 [==============================] - 196s 392ms/step - loss: 0.0445 - accuracy: 0.9844 - val_lo
ss: 0.3871 - val_accuracy: 0.9007
Epoch 10/10
500/500 [==============================] - 190s 380ms/step - loss: 0.0400 - accuracy: 0.9853 - val_lo
ss: 0.3318 - val_accuracy: 0.9022
```

Figure 11 LSTM training.

The LSTM model is trained for 10 epochs and for every iteration the accuracy, loss and validation accuracy is printed on the console. However, accuracy of 90% is achieved after the 10 iteration of training. The classification report is visualized below, putting into considering the various performance metrics.

	precision	recall	f1-score	support
0	0.94	0.93	0.93	831
1	0.88	0.86	0.87	697
2	0.96	0.95	0.95	1980
3	0.83	0.92	0.87	507
4	0.96	0.97	0.96	1755
5	0.81	0.78	0.80	230
accuracy			0.93	6000
macro avg	0.90	0.90	0.90	6000
weighted avg	0.93	0.93	0.93	6000

Figure 16 Ensemble classification report

Fig 13 LSM classification report

4.3 BIDIRECTIONAL ENCODER FROM TRANSFORMER (BERT)

The BERT model weight is download from the hugging face repository and fine turned by adding the emotion classification heads using tensforflow layers. The architectural structure is shown in the figure 14 below.

Based on the figure its identify that the model defines two input layer, thus the input id's and the attention mask input with 70 maximum word length. The next layer is the BERT layer follow by a one dimensional max pooling layer, then we have the dense layer, one dropout layer, another dense layer and finally an output layer. After 10 epoch of training the model was able to achieve an accuracy of 93%.

4.4 ENSEMBLE MODEL (SVM, LSTM, BERT)

The three trained model are loaded from the local repository and stack together by comparing their prediction about and selecting the majority vote approach. Hence, these experiment priorities the voting of BERT prediction over other model. Based on the experiment its identify that the ensemble model accuracy combined generate same accuracy as the BERT model.

Generally, the result gotten from the model (SVM, LSTM, BERT) training are summarize in the table below along with the existing study

TABLE 1: MODEL EVALUATION SUMMARY

S/N	Model	Accuracy
1	SVM	83%
2	LSTM	90%
3	BERT-Large	93%
4	Ensemble model (SVM, LSTM, BERT-L)	93%

Base on the result summary in table 1. We can see that both BERT-large and ensemble techniques perform best in term of prediction accuracy of 93%.

TABLE 2: MODEL EVALUATION SUMMARY

S/N	(Albu & Spînu, 2022)		Proposed Model	
1	SVM	84%	SVM	83%
2	-	-	LSTM	90%
3	BERTweet	89%	BERT-Large	93%
4	Ensemble	91%	Ensemble model (SVM, LSTM, BERT-L)	93%

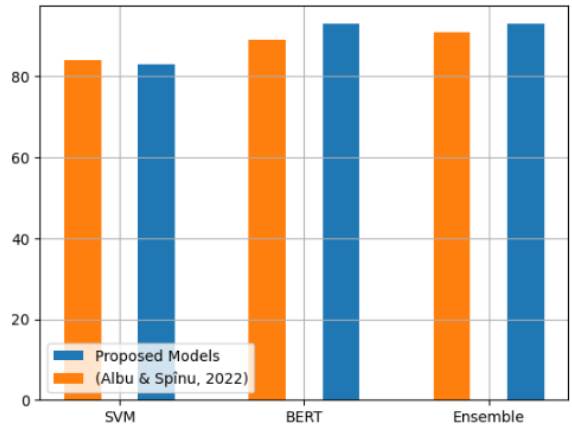

Figure. 17. Performance Comparison (Existing and Proposed model)

Table 2. evaluate the performance comparison between the proposed method and the existing model. Based on the table its identify that the proposed model is more efficient in term of accuracy than the existing model. The visual representation of table II is show in figure 16 below.

5 CONCLUSION

In consideration of the experimental result carried out, thus the outcome in term of accuracy and performance efficiency. The SVM model achieve an accuracy of 83%,

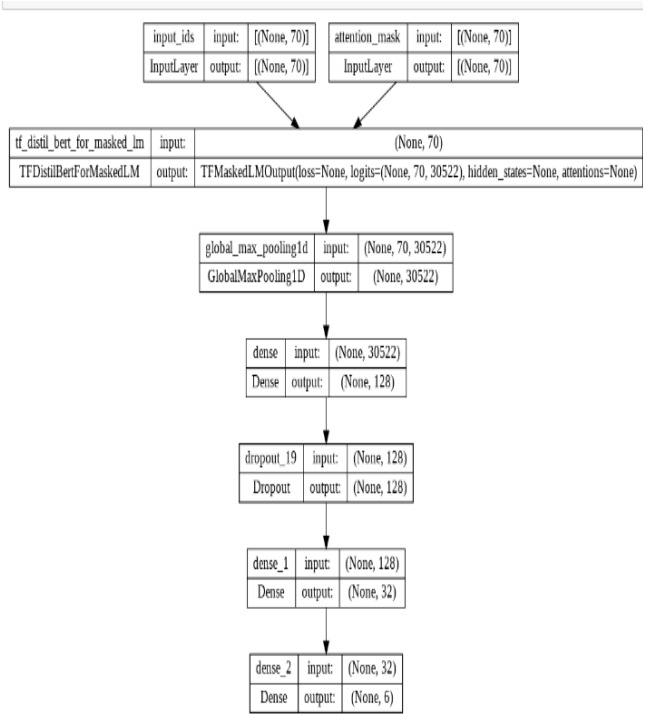

Figure 14 BERT model with Emotion Classification heads

while LSTM achieve 90% accuracy, BERT-Large achieve 93% accuracy and the utilization of the three model in an assemble approach also achieve an accuracy of 93%. Its identify that the BERT-large perform best due to his high richness in contextual information. However, the adoption of ensemble approach in respect to BERT-Large alone

does not significantly improve the accuracy. In conclusion the proposed model was able to achieved an optimum accuracy of 93%, and its recommended to used BERT-large has standalone model instead of the developed ensemble techniques for performance reasons (in term of prediction speed during real time usage)

ACKNOWLEDGEMENTS

A short acknowledgement section can be written between the conclusion and the references. Authors may wish to acknowledge the sponsors of the research and others in brief. Acknowledging the contributions of other colleagues who are not included in the authorship of this paper is also added in this section. If no acknowledgement is necessary, this section should not appear in the paper.

REFERENCE

Albu, I. A., & Spînu, S. (2022). Emotion Detection From Tweets Using a Bert and Svm Ensemble Model. *UPB Scientific Bulletin, Series C: Electrical Engineering and Computer Science*, *84*(1), 63–74.

Alves, F. R. V., & Machado Vieira, R. P. (2019). The Newton Fractal's Leonardo Sequence Study with the Google Colab. *International Electronic Journal of Mathematics Education*, *15*(2). https://doi.org/10.29333/iejme/6440

Ardabili, S., Mosavi, A., & Varkonyi-koczy, A. R. (2019). *Advances in Machine Learning Modeling Reviewing Hybrid and Ensemble Methods*. *August*, 1–10. https://doi.org/10.20944/preprints201908.0203.v1

Bartneck, C., Lyons, M. J., & Saerbeck, M. (2017). *The Relationship Between Emotion Models and Artificial Intelligence*. 1–12. http://arxiv.org/abs/1706.09554

Chiorrini, A., Diamantini, C., Mircoli, A., & Potena, D. (2021). Emotion and sentiment analysis of tweets using BERT. *CEUR Workshop Proceedings*, *2841*(April). https://ceur-ws.org/Vol-2841/DARLI-AP_17.pdf.

Denemark, R. A. (2011). Teaching and Learning about Teaching and Learning. *International Studies Review*, *13*(3), 543–545. https://doi.org/10.1111/j.1468-2486.2011.01061.x

Derczynski, L., Ritter, A., Clark, S., & Bontcheva, K. (2013). Twitter part-of-speech tagging for all: Overcoming sparse and noisy data. *International Conference Recent Advances in Natural Language Processing, RANLP*, *September*, 198–206 https://aclanthology.org/R13-1026.pdf.

Heimerl, F., Lohmann, S., Lange, S., & Ertl, T. (2014). Word cloud explorer: Text analytics based on word clouds. *Proceedings of the Annual Hawaii International Conference on System Sciences*, 1833–1842. https://doi.org/10.1109/HICSS.2014.231

Tang, D., Zhang, Z., He, Y., Lin, C., & Zhou, D. (2019). Hidden topic–emotion transition model for multi-level social emotion detection. Knowledge-Based Systems, 164, 426-435. http://wrap.warwick.ac.uk/111420/7/WRAP-hidden-topic-emotion-transition-model-detection-He-2018.pdf.

Jaiswal, S. (2019). Robust real-time emotion detection system using CNN architecture. *Neural Computing and Applications*, *4*. https://doi.org/10.1007/s00521-019-04564-4

Jaiswal, S., Virmani, S., Sethi, V., Partha, K. De, & Roy, P. (2018). *An intelligent recommendation system using gaze and emotion detection https://doi.org/10.1007/s11042-018-6755-1* .

Kim, H., Ben-othman, J., Cho, S., & Mokdad, L. (2019). *ACCEPTED FROM OPEN CALL A Framework for IoT-Enabled Virtual Emotion Detection in Advanced Smart Cities*. 1–7 http://people.uncw.edu/kimh/NETWORK2019.pdf .

Majeed, A., Mujtaba, H., & Beg, M. O. (2020). Emotion detection in roman urdu text using machine learning. *Proceedings - 2020 35th IEEE/ACM International Conference on Automated Software Engineering Workshops, ASEW 2020*, *September 2021*, 125–130. https://doi.org/10.1145/3417113.3423375

Minaee, S., Azimi, E., & Abdolrashidi, A. (n.d.). *Deep-Sentiment : Sentiment Analysis Using Ensemble of CNN and Bi-LSTM Models https://arxiv.org/pdf/1904.04206.pdf*.

Mosavi, A., Salimi, M., Ardabili, S. F., Rabczuk, T., Shamshirband, S., & Varkonyi-Koczy, A. R. (2019). State of the art of machine learning models in energy systems, a systematic review. *Energies*, *12*(7). https://doi.org/10.3390/en12071301

Serban, I. V., Sankar, C., Germain, M., Zhang, S., Lin, Z., Subramanian, S., Kim, T., Pieper, M., Chandar, S., Ke, N. R., Rajeswar, S., de Brebisson, A., Sotelo, J. M. R., Suhubdy, D., Michalski, V., Nguyen, A., Pineau, J., & Bengio, Y. (2018). *A Deep Reinforcement Learning Chatbot (Short Version)*. 1–40. http://arxiv.org/abs/1801.06700

Sinan, M., & Kayaalp, F. (2021). *Sentiment Analysis on Social Media Reviews Datasets with Deep Learning Approach*. *4*(1). https://doi.org/10.35377/saucis.04.01.833026

Vitiugin, F., & Barnab, G. (2022). *Emotion Detection for Spanish by Combining LASER Embeddings , Topic Information , and Offense Features Emotion Detection for Spanish by Combining LASER Embeddings , Topic Information , and Offense*

Features. *January* *https://www.researchgate.net/profile/Fedor-Vitiugin/publication/358002713_Emotion_Detection_for_Spanish_by_Combining_LASER_Embeddings_Topic_Information_and_Offense_Features/links/61eabdce5779d35951c41656/Emotion-Detection-for-Spanish-by-Combining-LASER-Embeddings-Topic-Information-and-Offense-Features.pdf*.

Wolf, T., Debut, L., Sanh, V., Chaumond, J., Delangue, C., Moi, A., Cistac, P., Rault, T., Louf, R., Funtowicz, M., Davison, J., Shleifer, S., von Platen, P., Ma, C., Jernite, Y., Plu, J., Xu, C., Le Scao, T., Gugger, S., … Rush, A. (2020). *Transformers: State-of-the-Art Natural Language Processing*. 38–45. https://doi.org/10.18653/v1/2020.emnlp-demos.6

Yu, S., Chen, Y., & Zaidi, H. (2020). *AVA : A Financial Service Chatbot based on Deep Bidirectional Transformers*. *https://arxiv.org/pdf/2003.04987.pdf*.

Zhang, L., Wang, S., & Liu, B. (2018). Deep learning for sentiment analysis: A survey. *Wiley Interdisciplinary Reviews: Data Mining and Knowledge Discovery*, *8*(4). https://doi.org/10.1002/widm.1253

4th International Engineering Conference (IEC 2022)
Federal University of Technology, Minna, Nigeria

THE EFFECT OF Fe^{3+} ION DOPANT ON THE ENERGY BAND GAP OF TiO_2 NANO-PARTICLE FOR PHOTO-CATALYTIC APPLICATIONS

***Okoli, C. S[1], Okonkwo, P. C[2], Abdul, B. O.[3] & Diyauddeen, B. H[4]**

[1]Department of Chemical and Petroleum Engineering, University of Uyo, Uyo,Nigeria,[2,3,]Department of Chemical Engineering ,Ahmadu Bello University Zaria, Nigeria.
[4]Center for Energy and Research, Ahmadu Bello University, Zaria, Nigeria.

*Corresponding author email: Chrisoko81@yahoo.com +2348037438954

ABSTRACT

Fe-doped TiO_2 and pure TiO_2 were synthesized using sol-gel method with various weight percent of Fe concentration of 0.1wt % ,0.3wt %, 0.5wt %,0.7wt% and 1wt% .The nano particles produced were calcined at 450 ^oC for 2 h and characterized with XRD, BET, UV-Vis DRS,SEM, EDX . The XRD results show increase in crystallites and particle sizes of pure TiO_2 to be 9.66 nm and 55.1nm respectively. BET results show decrease in surface area of pure TiO_2 from 108.99 m^2/g to 84.69 m^2/g as concentration of Fe dopant increases from 0.1wt % ,0.3wt %, 0.5wt %,0.7wt% and 1wt
%. SEM and EDX analysis show that the produced TiO2 nanoparticles were relatively spherical in shape and the TiO_2 synthesized in this work contains no impurity from the EDX spectra. The UV-Vis DRS indicates a red-shift in the optical absorption edge of TO2 from ultraviolet region of 400 nm wavelength into the visible light region of 469.7nm wavelength at 1%wt Fe doped TiO_2 .In this work, the energy band gap of pure synthesized TiO_2 was reduced from 3.013 eV to 2.3 eV when doped with 1wt% Fe .

Keywords: *Titania Nano-particles, Fe-doped Titania photocatalysts, Optical nano- Characterization*.

1 INTRODUCTION

In nano-technology, nano-particles are used as best option for photocatalytic operation due to their inherent properties of having large surface area and generation of hydroxyl radical for fast photocatalytic operations. Photo catalysis using titanium photo catalyst has been attracting tremendous attention due to their practical application by scientific community over recent years (Jayaseelan, et al.,2021) Titanium dioxide(TiO2) was recognized by researchers as ideal semiconductor with good photo catalytic property with such high refractive index and ultraviolet absorption with good photoelectric conversion efficiency, photo-and chemical stability as well as non-toxicity (Hung et al.,2016). Despite all the above excellent properties possess by TiO2, its photocatalytic applications are still limited. In this case, TiO_2 still shows poor photocatalytic efficiency as a result of its wide band gap energy approximately 3.0 and 3.2 eV for rutile and anatase respectively and electron-hole recombination (Soni etal.,2018).Therefore, TiO_2 photocatalyst can only utilize small portion of solar spectrum (5% UV) for its photo catalytic operation while the large portion of solar energy remains untapped.One big future challenge in photo catalyst with wide band gap energy is finding a way to reduce its band gap energy by extending its absorption wavelength to visible region of solar spectrum for an efficient photo catalytic operation. Though some researchers (Moradi et al.,2016.,Soni et al.,2018.,Koh.,et al.,2014) have made a lot of effort to modify TiO2 to be able to utilize visible light through doping with transition metal ions; Cr,V,Fe,Ni etc., Moradi et al.,2016

doped TiO2 with Fe and recorded band gap reduction of TiO2 to be 2.1eV at 600ºC calcination temperature for 2 h ., Soni et al.,2018 recorded band gap reduction of TiO2 to be 2.86 eV at 450ºC calcination temperature for 2 h when doped TiO_2 with Ni. In this present work, the photocatalytic efficiency of TiO2 was greatly improved by developing a technology that will extend the absorption spectrum of TiO_2 to include not only ultraviolet light region but also the visible light region. More research is needed to examine the electronic behavior of pure TiO_2 to visible light when Fe^{3+} is introduce in the crystal lattice of titania. Therefore, in this research, the surface of TiO2 was properly modified through the use of Fe in low concentrations as the transition metal dopant since Fe^{3+} has a close related ironic radius with that of Ti^{4+} as **0.064nm** and **0.068nm** respectively (Li et al., 2008). Fe^{3+}can easily enter into the TiO2 lattice by substitution of the later and introduces additional energy level which reduces the band gap energy of TiO_2 and therefore increases the visible light absorption. In this research, pure synthesized titania was achieved by Sol-gel method and Fe-dopedTiO_2 was achieved by varying different concentration of Fe in the titania. At present, there is limited research reported on the examination of electronic behavior of pure TiO_2 to visible light especially when low weight percent concentration of iron are introduced in titania lattice at 450^0C for 2h for photocatalytic applications under solar spectrum.

2 METHODOLOGY

2.1 PREPARATION OF PURE AND FE-DOPED TIO2 NANOPARTICLES

A modified method according to Soni et al.,2018 was adopted for the preparation of iron doped TiO2 nanoparticles. Here, Iron (III) chloride hexahydrate (0.1,0.3, 0.5, 0.7, 1 wt %) was dissolved in 100 ml de-ionized water separately in each case . Then 8ml of glacial acetic acid was added into this solution to get solution A. Then, 17.5 ml titanium tetraisopropoxide (Sigma Aldrich) was dissolved in 50 ml of anhydrous ethanol with continuous stirring to get solution B. Solution B was added into solution A drop wise with stirring continuously for 2 h and aged for 24 h at room temperature. The TiO2 gel formed was dried in an oven at 90ºC for 2 h. Finally, the solid material obtained was ground and annealed at 450º C for 2 h. The solid photo catalyst (Pure TiO2 and Fe-doped TiO2 were characterized using XRD, BET, SEM-EDX,DRUV-Vis, The pure TiO2 was synthesized using the same procedure without addition of iron (III) hexahydrate salt.

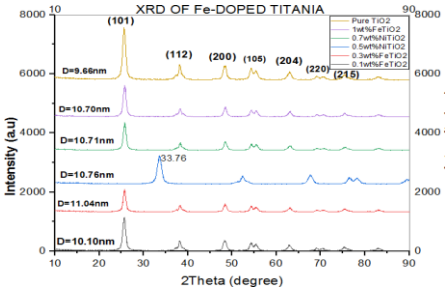

Figure; XRD Spectra of Fe-Doped TiO2 and Pure TiO2 Sample Calcined at 450ºC for 2h

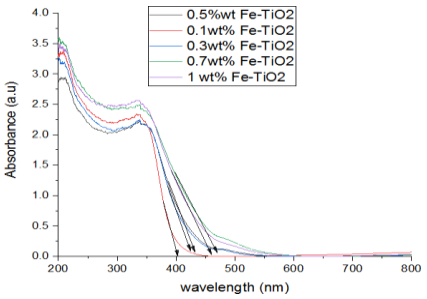

Figure 2: Effect of Doping Concentrations on Visible Light Absorption of Fe-doped TiO PhotoCatalyst Calcined at 450ºC for 2 h.

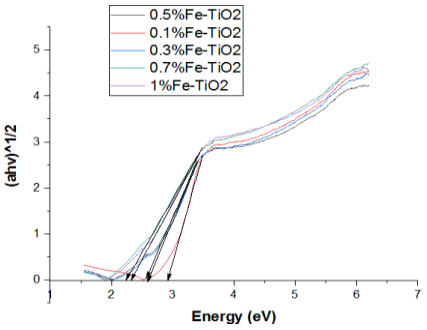

Figure 3: Effect of Doping Concentrations on Band Gap Energy Of Fe-Doped TiO2 Photocatalyst

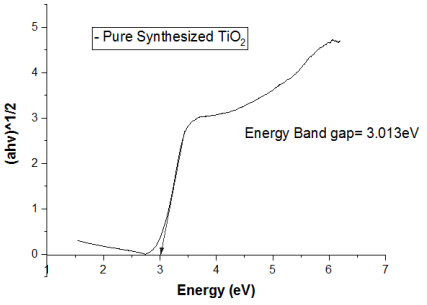

Figure 4: **Energy Band Gap of Pure TiO2 Synthesized and Calcined at 450 ºC for 2 h**

2.2 CHARACTERIZATION

The crystallite size of the Pure TiO_2 and Fe-doped TiO_2 nanoparticles were evaluated using XRD method. The

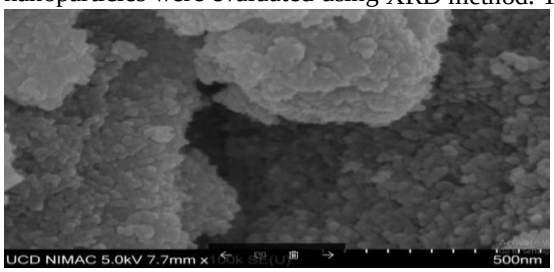

Figure 5, SEM Image of Pure Synthesized TiO_2

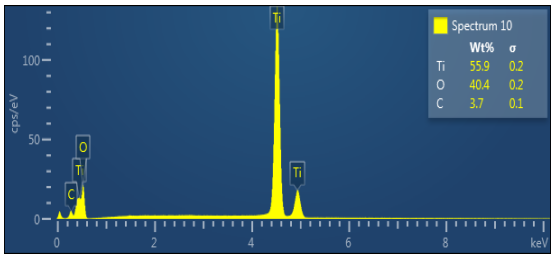

Figure 6 :EDX Spectra of Pure SynthesizedTiO_2

XRD crystallite size was determined using d/max diffractometer with serialnumber 079298 - a3138 - a1 XRD machine, Cu, $K\alpha$ = 1.5406Å. The TiO_2 was scanned through theXRD rays at rotating angles ranging from 10 to 90° for every 3 seconds. The crystallite size of the TiO2 nanoparticles was calculated using Scherer's equation

$$D = \frac{K\lambda}{\beta cos\theta} \quad (1)$$

Where K is the shape factor constant of 0.94, λ is the X-ray wavelength with value of 0.1540 6nm for CuKα radiation is the full width at half maximum (FWHM) (radian), θ is the diffraction angle

The surface morphology and chemical analysis of the sample nano particles were determined using scanning electron microscope (SEM) and energy dispersive x-ray (EDX) analysis. The surface area of the Pure $TiO_2$and Fe-doped TiO_2 nano particles was analyzed using BET method. The Brunauer-Emett-Teller (BET) surface area were determined using Barrett-Joyner Halenda (BJH) method and determined by N_2 physiosorption using micromeritics instrument, Gemini (VII) version 3.04 with serial number 0128 at 5sec equilibration time.

The diffused reflectance spectra (DRS) of both Fe doped $TiO_2$and pure $TiO_2$was determinedusing UV-Vis Spectrophotometer. The DRS was determined using UV-Vis spectrophotometer in a wave range of 200 – 800 nm carriedoutusingV-650spectrophotometer. The optical band gap of the sample photo catalyst (Fe-TiO_2) was obtained from a plot (ahv)^1/2vs(hv) based on the Tauc equation and Kebelka – Monk function as shown in (2) and (3) (Sonietal.,2018).

$$F(R) = \frac{(1-R)^2}{2R} \quad (2)$$

$$(F(R)hv)^{1/2} = A(hv - E_g) \quad (3)$$

Where, hv is the energy of photon, A is constant, Eg is the energy band gap of the sample (Fe-TiO_2), R is the reflectance of the UV radiation from the measuring instrument and (F(R)) isproportional to absorption constant (a). By ploting (ahv)^1/2 versus Energy(hv), the energy bandgap of Fe-doped TiO_2can be determined by extrapolating the linear part of the plot to a pointwhere (ahv)^1/2 is zero

3 RESULTS AND DISCUSSION

3.1: CRYSTALLITES AND PARTICLE SIZE OF XRD ANALYSIS.

Figure 1, is the XRD spectral of the synthesized pure TiO_2 and Fe-doped TiO_2 at different concentration of iron. The characteristics diffraction peaks at **25.54, 38.23, 48.22, 54.4, 63.1,69.1, 75.49,** correspond to the reflection from **(101), (112),(200),(105),(204),(220) and (215)** plane in comparism with the standard anatase crystals (Moradi et al.,2016). In the other word, the peak and plane of the XRD of the synthesized Fe-doped TiO_2 and Undoped TiO_2 are all in anatase phase. From Fig.1, the degree of crystallinity decreases as the amount of Fe dopant increases with increased crystal size as compared with the undoped TiO_2. This can be interpreted as that addition of Fe to pure TiO_2 decreases crystallinity from pure TiO_2 with crystallite **,D = 9.66nm calculated from the peak of 101 plane and diffraction angle of 25.48°** It can also be observed from figure 1 that there is a shift in diffraction peak to larger diffraction angle when the crystallite size was large enough at **10.76nm from table 1 to even cause anatase-rutile phase transformation.** This is because of expansion distortion of the titania lattice at 0.5wt% Fe concentration which increases the crystallite size of the $TiO_2$and consequently lead to larger angle diffraction.The ionic radius of Fe^{3+} has a comparable size with that of Ti^{4+} with value of **0.064nm** and **0.068nm** respectively (Li et al., 2008).

TABLE I: BET SURFACE AREA ANALYSIS

Sample	Calcination Temp (^{0}C)	Surface Area BET(m^2/g)	Pore Size (Å)	Particle size (nm)	Crystal* Size(nm)	Bandgap** (eV)
PureTiO2	450	108.987	11.645	55.05	9.66	3.01
0.1wt%Fe-TiO2	450	104.210	11.325	57.58	10.10	2.90
0.5wt%Fe-TiO2	450	90.132	11.378	66.57	10.76	2.50
1wt%Fe-TiO2	450	84.688	11.227	70.85	10.70	2.30
0.5wt%Fe-TiO2	600	39.775	11.578	150.85	NE	2.30
0.5wt%Fe-TiO2	800	0.148	11.664	40485.83	NE	2.30

0.1, 0.5 and 1 %wt Fe concentration in TiO2 ,NE- Not evaluated. * Obtained from XRD data, ** Obtained from UV-Vis DRS data.

3.2: **BET SURFACE ANALYSIS**

The Brunauer-Emett-Teller surface area (SBET) and desorption pore volume (Vp) were evaluated by Barrett-Joyner Halenda (BJH) method and determined by N_2 physisorption using micromeritics instrument, Gemini (VII) version 3.04 with serial number 0128 at 5 sec equilibration time. Table 1 shows the parameter evaluated by BET at 450ºC, 600 and 800ºC calcinations temperatures at various weight percent of Fe metallic ion doped with titania (TiO_2). The BET surface area result obtained at 450 ºC for Fe TiO_2 at 0.1, 0.5 and 1% weight concentration decrease as the concentration of dopant increases. The particle size of the samples was calculated using the BET surface area data. The particle size was found to increase by increasing the weight percent of dopant in the titania lattice from table I.Hence, the particles size range of **57.58 – 70.85 nm** for the sample calcined at 450 ºC and doped at 0.1, 0.5 and 1% weight concentration of Fe showed the retention of nano sized particles with the temperature (Raj et al,2010). The calcinations of 0.5 wt% Fe-doped TiO_2 at 600 ºC and 800 ºC showed very poordecrease of surface area by 55.9 % and 99.8 % respectively, hence it shows the negative effect of calcination at elevated temperature on surface area of nano material. This is as a result of agglomeration of crystallite of the sample at elevated temperature to form grain then bigger particle sizes with reduced surface area as shown in table 1. From table 1, we can observe that doping of TiO_2 photo catalyst at 450ºC reduces the band gap of TiO_2 photo catalyst while its surface area and pore volume reduces as concentration of Fe ion dopants increase. Similarly, the pore size of doped TiO_2 photo catalyst increases by increasing the concentration of Fe dopants. This shows that the band gap of TiO_2 photo catalyst at 450 ºC can be reduced to a required band gap through doping with desired 0.5 wt% Fe to enable the TiO_2 absorb visible light for good photo catalytic efficiency but the surface area of exposure and pore volume to trap organic pollutant will be compromised by reduction.

3.3 UV-Vis DRS ANALYSIS OF Fe DOPED TiO2: In Figure.2, the effect of doping TiO_2 with Fe ion is to extend its absorption wavelength above 400nm which is the visible regime, **1 %wt Fe doped TiO_2** has the longest wavelength in the visible regime as **469.7 nm.** Figure.2, shows the effect of different weight percentage of iron on pure titania. Ironic ion doping to the parent TiO_2 does not change the position of the outermost shell valence band of TiO_2, instead, it creates new energy level (Fe^{3+} to Fe^{4+}) of the Fe ion in the band gap of the parent TiO_2.The above behavior of introducing new energy level confirms the red shift of absorption edge to longer wavelength in Fig.2,.In this case, the excited electron moves from the 3d valence orbital of Fe^{3+} to conduction band

of the parent TiO_2 when visible light of sufficient energy falls on the photo catalyst outermost shell electron. From Fig.3, UV-Visible diffused reflectance spectra of Fe doped TiO_2 was determined in a range of wavelength from 200 to 800nm. In Figure 3,, the optical band gap of the Fe-doped TiO_2 decreases as the doping concentration of Fe increases. It was noticed that at 1 %wt Fe concentration, the optical band gap is **2.3eV.** In figure 4, pure TiO_2 synthesized in this work has optical band gap of **3.013 eV** which reduces to **2.3eV** when doped with 1 % Fe. This reduction in energy band gap of 2.3 eV has justified the red shift observed in wavelength as **469.7nm** with1%wt Fe doped TiO_2 in Figure 2. This means that the longer the wavelength from400nm, the more visible light absorbed and the lower the optical band gap energy.

3.4 SEM AND EDX SAMPLE ANALYSIS.

Figure 5, and Fiure.6 show the SEM image and EDX spectra of Pure synthesized TiO_2 calcined at 450 ^oC at 2 h. On the other hand, the SEM micrographic image of pure synthesized TiO_2 and 1 wt % Fe doped TiO_2 show that the shape of the particles are relatively spherical.

The EDX spectra obtained for pure synthesized TiO_2 show no trace of impurity with 55.9% titanium

4.CONCLUSION

XRD results show increase in crystallite size and particle sizes while BET results show decrease in surface area as concentration of Fe dopant increases. TEM, SEM and EDX analysis show that the produced TiO_2 nano-particles were relatively spherical in shape and the TiO_2 synthesized in this work contains no impurity from the EDX spectra. Also, XRD shows that as the concentration of the dopant increases, the level of crystallinity and peak height decrease due to amorphous condition created by the dopant in the titania lattice. The TiO_2 synthesized in this work has optical band gap of **3.01eV** which reduces to **2.3eV** when doped with **1% wt Fe**. This reduction in energy band gap of 2.3 eV has justified the red shift observed in its wavelength as **458.2nm in the visible** region. The synthesized TiO_2 was **16.5g** at 450^oC with surface area of **108.99m^2/g** , band gap energy of **3.013eV** and particle size of **55.1nm.** SEM analysis reviews the formation of relatively spherical-shape clustered nano-particles but the EDX spectroscopic analysis maintains that the TiO_2 samples produced in this work is pure.

5. ACKNOWLEDGEMENTS

The author appreciations God almighty for his wisdom and knowledge to carry out this work successfully. We acknowledge the sponsorship of Tertiary Education Trust Fund (TETFUND) OF Nigeria for their sponsorship. Author also acknowledges Dr.Sullivan James, of School of chemistry, University College Dublin **(UCD)**, Ireland for providing the laboratory facilites needed for the nano particulate research work. My thank goes to **Prof.** Okonkwo, P. C , Dr. Abdul, B.O & Prof. Diyauddeen, B.H[4,] ChemicalEngineeringdepartment,Ahmadu Bello University Zaria, Nigeria. For their continuous academic advice, encouragement and supervision for the success of this work .

6. REFERENCE

1.Chen, X. B., Liu. L., (2014).Titanium dioxide nano materials, self-structural modification. Chem. Rev2014,114,9890-9918.

2.Hsuan, C . W, Sheng, H. L & Syuan, W . L., (2012). Effect of Fe Concentration on Fe-doped Anatase TiO_2 from GGA+U Calculations.

3.Jayaseelan, A., Nachiappan, S., Goutham, R., Ram, A. & Gopinath, K.,(2021). Synthesis and Application of Titanium dioxide photo catalyst for energy, decontamination and Viral Disinfection; *A review.* Environmental Chemistry Letters

https/doi.org/10.1007/510311-022-01503-2.

4.Koh, P. W, Yuliati. L., Lee. & S. L., (2014). Effect Of Transition Metal Oxide Doping (Cr, Co, V) In The Photo catalytic Activity of TiO_2. *Congo red Degradation under Visible Ligh*t.69 (5):45-50

5.Li, Z., Shen, W., He W. & Zu X. (2008). Effect of Fe-doped TiO2 Nanoparticle Derived from Modified Hydrothermal Process on the Photo catalytic Degradation Performance on Methylene Blue. Journal of HazardousMaterials, 155:590-594.

6.Moradi, H., Eshaghi, A., Rahman S. H. & Ghani K,. (2016). Fabrication Of Fe-Doped TiO2 Nano-Particles And Investigation of Photocatalytic Decolourization Of Reactive Red 198 Under Visible Light *Irradiation.Ultrasonics Sonochemistry*, 32, 314-319.

7.Raj Antony, J. K, Smith R. Y., Subramanian. & Viswanathan, B. (2010).Structural Studies of Silica Modified Titania and Its Photo catalytic activity of 4-chlorophenol oxidation in Aqueous medium. *Indian Journal of Chemistry*, 49, pp867-875.

8.Soni, P., Murty U. & Kushwaha, K. (2018).The Effect Of Ni^{2+} Ions On Energy Band Gap Of Tio2Nano – Particles For Solar Cell Applications. Journal Of Nanoscience, *Nano engineering and Applications*, 8(2) 69-74.

4th International Engineering Conference (IEC 2022)
Federal University of Technology, Minna, Nigeria

A Study of Thermal and Mechanical Properties of Africa Palm Fibre as Thermal Insulator

*Usman, I. Y[1], Ademoh, N.A[1], Godfrey, M[2], Uche, E.U[2] & Ndagi, M[3]

[1]Department of Mechanical Engineering, Federal University of Technology, Minna, Nigeria,
isaacyanda@gmail.com, nuhuadam@yahoo.com,
[2] Department of Mechanical Engineering, Faculty of Air Engineering,
Airforce Institute of Technology, Nigeria Airforce Base, Kaduna, Nigeria,
godfreymnet@gmail.com; eaumie@gmail.com
[3] Department of Mechanical Engineering, University of Ilorin, Nigeria
ndagi.m@unilorin.edu.ng
*Corresponding author email: *isaacyanda@gmail.com* +2348065622885

ABSTRACT
Thermal and mechanical properties of African palm biomass fibres is studied for its application as thermal insulator. The paper developed a composite material from bunch, fruit and branches of oil palm fibre as thermal insulator. The samples were first segregated after milling process into 0.5mm and 1.0mm sieve sizes. The composites developed were set of six samples which are A1, A2, A3, B1, B2 and B3 with ratio of 0.3:0.3:0.3, 0.1; 0.3:0.4,0.2, 0.1; 0.3:0.2:0.4, 0.1; 0.3:0.3:0.3, 0.1; 0.3:0.4,0.2, 0.1 and 0.3:0.2:0.4, 0.1 and they were in ratio of bunch, fruit, branch and epoxy resin respectively. The results indicated that heat thermal resistance of sample B1 was 5.8 m^2 ^oC /W was best among samples developed by this study while samples A1 and B2 can served as alternatives with heat thermal resistance of 5.7 m^2 ^oC /W respectively. The density of the composites developed was within range of 0.58-0.65 g/cm^3. However, It was understood that sample A1, A2 and A3 has value of modulus of elasticity, 4.3 kN/mm^2 which is improved strength in comparing to samples B1, B2 and B3 with modulus of elasticity, 1.9 kN/mm^2. However, samples B1, B2, B3 can be applied as thermal insulators with temperature ranges of 70 -90 ^oC while samples A1, A2, A3 is feasible in application of strength improvement or reinforcing of material in industry

Keywords: Africa oil palm fibre; thermal insulator, mechanical and thermal property

1 INTRODUCTION

Biomass fibre is a natural fibre that include oil palm, pineapple and banana are indigenous to the tropical forests in West Africa and it is readily available and cheaper in Nigeria compared to wood (Olaoye *et al.*, 2013). It has low density, lower cost, light weight, high strength to weight ratio, biodegradability, acceptable specific properties, better thermal and insulating properties in comparing with synthetic fibre (Momoh and Osofero, 2020; Abdul Khalil *et al.*, 2012; Sulaiman *et al*., 2102). Oil palm wastes from plantation sites include, oil palm shell, empty fruit bunch fibre (EFBF), oil palm pressed fruit (or mesocarp) fibre (OPMF), oil palm trunk fibers (OPTF), oil palm frond fibers (OPFF), Oil palm broom (OPBF) (Dungani et al., 2013; Olaoye *et al*., 2013). These wastes are useful in industrial application such as thermal insulators in heating vessels (Hassan *et al*., 2017). The present paper investigated into thermal and mechanical properties of Africa oil palm fibre (AOPF) developed as thermal insulator that can be used in heating vessels. Biomass fibre can help in composite technology development and as raw material sustainability in different applications especially for preventing energy loses and reduction of energy consumption (Onuaguluchi and Banthia 2016; Zhou *et al.*, 2010).

Reduction of energy consumption has become an important task for engineers because it helps at least 30% of the total energy consumption in heating vessel (Jawaid *et al.* 2010). The heating vessels are such as thermal fluid heater, thermal fluid circulating pump and explosive tank. These applications include, building insulations, automobiles, aircraft, industrial process equipment, textile application such as apparel, blankets, and sleeping bags, interlinings (Bozsaky, 2019; Ferrandez-Garcia *et al.*, 2017, Wong *et al.* 2010). Fibre reinforced polymers, especially glass fibre reinforced polymers, have played an important role in technical applications such as in the automotive sector, where high mechanical properties and dimensional stability have to be combined with low weight (Zach *et al.*, 2013).

The fibres act as reinforcement in fibre reinforced composites by giving strength and stiffness to the composite structure. Kalia *et al* (2011) found out that quality and other property which includes density, electrical resistivity and strength depend on factors such as size, maturity, and processing methods employed in using biomass fibre. Properties such as density, electrical resistivity, ultimate tensile strength, and modulus of elasticity are related to the internal structure and chemical composition of material (Luamkanchanaphana et *al*., 2012). Thermal degradation behaviour is also another crucial characteristic of insulation materials. Thermal properties like thermal conductivity, thermal resistance, thermal insulations are important in industrial applications (Ghosh *et al.*, 2016; Oushabi *et al.*, 2015). A higher thermal degradation range with a lower weight loss is considered an excellent property of insulation materials (Raza *et al.*, 2022; Benmansour *et al*, 2014; Page *et al.*, 2017). Thermal insulator is in three general application temperature ranges as follows (Pfundstein, 2007; Deshmukh *et al.*, 2017)

i. low temperature thermal insulation:
from 15°C through 1°C that is cold or chilled water; 0°C through -40°C that is Refrigeration or glycol; -41°C through -75°C - i.e. Refrigeration or brine; -76°C through -273°C (absolute zero) that is Cryogenic

ii. intermediate temperature thermal insulation:
from 16°C through 100°C that is hot water and steam condensate; 101°C through 315°C that is steam, high temperature hot water.

iii. high temperature thermal insulation:
from 316°C through 815°C that is turbines, breechings, stacks, exhausts, incinerators, boilers.

Improved mechanical properties such as tensile, yield and ultimate tensile strength, also impact strength of biomass fibre materials contributes significantly to strength of other material (La Gennusa *et al.*, 2017). This is feasible when used as reinforcing material especially in automobile spare parts, heating vessels and ships, buildings (Jawaid *et al.*, 2010).

2 MATERIALS AND METHODS

2.1 MATERIALS

The materials selected for this work was AOPF that consisted of bunches, fruits and branches of AOPF and it was binded with epoxy resin as reinforcing material. The AOPF was obtained from Ikogusi, Oil palm farm, in Ekiti State, Nigeria. The Figures 1-3 were the AOPF components used in this study

Figure 1: AOPF bunch fibre

Figure 3: AOPF branch fibre

The equipment/instruments and reagents are such as injection moulding machine, milling machine, digital weighing balance and tensile strength testing machine, epoxy resin, sodium hydroxide agent, distilled water and iodine agent.

2.2 Methods

The following methods adopted were used for determine production of and thermal properties of insulating materials called oil palm fibre.

i. Material preparation: the fibres were washed with distilled water; the treatment of the fibres was carried out using iodine solution and NaOH concentration. The AOPF fibre were immersed in this solution NaOH for 24 hours and then washed with distilled water. The fibres were then dried in an oven at temperature of 50 °C for 24 hours.

ii. Production: the fibres were milled and sieved into two sieve size of 0.5mm and 1 mm. This process was repeated for the bunch, branch and fruit respectively. The AOPF constituent are in proportion of 0.3:0.3:0.3; 0.3:0.4,0.2 and 0.3:0.2:0.4 respectively for 0.5mm and 1.0mm sieve sizes making a total of 6 samples. However, each of the samples were binded with 10% epoxy resin while AOPF formed composite at 90% weight per each sample.

iii. Thermal and mechanical property testing: Thermogravimetry (TGA) is a technique that measures the change in weight of a sample when it is heated, cooled or held at constant temperature. Percentage change in mass of the sample:

$$\omega_s\% = \frac{m_n - m_o}{m} \times 100\% \quad (3.1)$$

Where:

$\omega_s\% =$ change in mass

$m_o =$ old mass

$m_n =$ new mass in gramme

$m =$ sample mass in gramme before test

Tensile strength (MPa): It is determined as the ratio of maximum load on the sample in tension test over the surface area of the sample.

$$\sigma_t = F/A \quad (3.2)$$

Where:

$\sigma_t =$ tensile strength in N/mm

$F =$ maximum applied load on the sample

$A =$ surface area of the sample

3 RESULTS AND DISCUSSION

The results of this work are such as thermal and mechanical property with sieve size of 0.5 mm and 1.0 mm as listed in Table 1.

Table 1: AOPF Composite Sieve Size

Sample	AOPF proportion (Bunch, fruit, branch and epoxy resin respectively)	0.5mm fos	1.00mm foz
A1	0.3:0.3:0.3, 0.1	0.5	-
A2	0.3:0.4,0.2, 0.1	0.5	-
A3	0.3:0.2:0.4, 0.1	0.5	-
B1	0.3:0.3:0.3, 0.1	-	1.00
B2	0.3:0.4,0.2, 0.1	-	1.00
B3	0.3:0.2:0.4, 0.1	-	1.00

Note: fos implies fibre orientation size

Table 4.1 indicated the sample sieve size of 0.5mm and 1.00mm in which the experiment was based and Figures 4-5 are the sieve size of AOPF composite which was subjected to production processes.

Figure 4: AOPF Sample of 0.5 mm Size

Figure 5: AOPF Sample of 1 mm Size

Table 2 showed heat coefficient parameters such as thermal conductivity λ in W/m^{o}C, heat flux, Q in W/m^2 heat transfer coefficient, U in W/m^{2o}C and thermal resistance to heat transfer, R_T in m^{2o}C /W

Table 2: Parameters of Heat Coefficient in AOPF

Sample	A_{OPF} = 0.001 m^2, l_A = 0.0005m, l_B = 0.001m, $q = 1m$W, m =0.1kg				
	ΔT (^{o}C)	λ (W/m^{o}C)	Q(W/m^2)	U(W/m^{2o}C)	R_T(m^{2o}C/W)
A1	5.7	0.35	1.00	0.18	5.7
A2	5.2	0.38	1.00	0.19	5.2
A3	5.2	0.38	1.00	0.19	5.2
B1	5.8	0.34	1.00	0.17	5.8
B2	5.7	0.35	1.00	0.18	5.7
B3	5.6	0.36	1.00	0.18	5.6

The heat thermal resistance to heat transfer of 5.8 m^{2o}C /W of sample B1 was best among samples developed by this study and therefore, sample A1 and B2 can served as alternatives. The temperature changes after 30 minutes of heating was 5.7, 5.2, 5.8, 5.7 and 5.6 ^{o}C respectively for the samples A-B of developed AOPF. TGA analysis of developed AOPF thermal insulator was shown in Table 3.

Table 3: TGA Analysis of Developed AOPF

Sample	ΔT after 30min	m_o (g)	m_f (g)	m_l (g)	m_l (%)
A1	5.7	100	98.25	1.75	0.018
A2	5.2	100	98.50	1.50	0.015
A3	5.2	100	98.40	1.60	0.016
B1	5.8	100	99.00	1.00	0.010
B2	5.7	100	99.25	0.75	0.008
B3	5.6	100	99.10	0.90	0.009

Where:
m_o (g) - is the AOPF original mass

m_f (g) - is the AOPF final mass under heating

m_l (g) - is the AOPF loss mass under heating

The sample of 100g of AOPF were subjected to heating in furnace for 30 minutes and average temperature changes were observed and stated in Table 3. Figure 1 showed TGA of the developed AOPF samples.

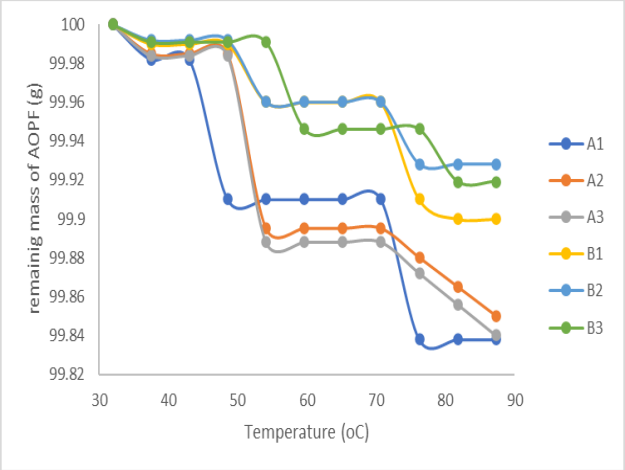

Figure 1: TGA plot of OPFA

Figure 1 indicated that all Bs sample will support high heating elements as thermal insulator above temperature of 70-90 ^oC and stabilised within 30 minutes on usage as insulator. It is expected the mass (g) of developed AOPF to remain at 99.9% under such condition. The sample A1 it is sample that works within temperature of 50-70 ^oC and expected mass of developed sample A1 will remain at 99.9% under such condition while samples A2 and A3 will be alternative under such condition with expected mass (g) of the sample to be within 99.88%. It is also observed that sample A2 and A3 will support heating elements as insulator with temperature below 50 ^oC as indicated in Figure 1. The mechanical property of developed AOPF as thermal insulator was investigated and therefore its strength and strain were stated in Table 4 with circular mould.

Table 4: Mechanical Property of the Developed AOPF

Sample	mfd (mm)	ρ_f (g/cm^3)	σ_y (N/mm^2)	ε (mm)	e_y	E (kN/mm^2)
A1	50	0.62	8.50	0.098	0.00196	4.3
A2	50	0.65	8.50	0.098	0.00196	4.3.
A3	50	0.60	8.50	0.098	0.00196	4.3
B1	50	0.58	7.25	0.190	0.00380	1.9
B2	50	0.60	7.25	0.190	0.00380	1.9
B3	50	0.65	7.25	0.190	0.00380	1.9

Where:

mfd- moulding fibre diameter
σ_y- is yield strength of OPF

e_y- is the strain at yield point

ε – is the elongation

ρ_f – density of the fibre developed

Table 4 indicated that samples A had strain value of 0.00196 with yield strength of 8.5 N/mm^2. The diameters of moulding fibre were 50mm of length respectively and which was subjected to various stress until notable strain value of 0.2% was recorded. It was understood that sample As had better value of modulus of elasticity of 4.3 kN/mm^2 in comparing to sample Bs.

4.0 CONCLUSION

The thermal insulation materials have low thermal conductivity for it to reduce the total coefficient of heat transmission in a system. This paper concludes that Sample B1 has better heat thermal resistance to heat transfer of 5.8 m^2 ^oC /W of while sample A1 and B2 can served as alternatives due to presence of thermal resistance value of 5.7 m^2 ^oC /W respectively. Sample Bs are thermal insulator for heating elements of temperature ranges from 70 -90 ^oC. The development of AOPF as thermal insulator showed yield strength of 7.25-8.5 N/mm^2 and this can serve as strength improvement or reinforcing of material in industry.

REFERENCES

Abdul Khalil, H.P.S., Jawaid, M., Hassan, A., Tahir, P.M. and Zaidon, A. (2012). Oil Palm Biomass Fibres and Recent Advancement in Oil Palm Biomass Fibres Based Hybrid Biocomposites. US, New York: Intech Publication.

Benmansour, N., Agoudjil, B., Gherabli, A, Kareche A, Boudenne, A. (2014). Thermal and mechanical performance of natural mortar reinforced with date palm fibers for use as insulating materials in buildings. Energy and Building, 81: 98–104

Bozsaky, D. (2019). Nature-Based Thermal Insulation Materials From Renewable Resources – A State-Of-The-Art Review. Slovak Journal of Civil Engineering, 27(1), 52 – 59.

Dungani, R., Jawaid M., Khalil H. P. S.A., and Jasni., J, Aprilia S, Hakeem K. R, Hartati S, Islam M.N. (2013). A review on quality enhancement of oil palm trunk waste by resin impregnation: Future materials, BioResources, 8(2): 3136–3156.

Deshmukh, G., Birwal, P., Datir, R., and Patel, S. (2017). Thermal Insulation Materials: A Tool for Energy Conservation. Journal of Food Processing & Technology, 8(4), 12-18.

Ferrandez-Garcia, C.C., Ferrandez-Garcia, C.E., Ferrandez-Villena, M.; Ferrandez-Garcia, M.T. and Garcia-Ortuno, T. (2017). Acoustic and Thermal Evaluation of Palm Panels as Building Material. BioResources, 12(1), 8047–8057.

Ghosh, S.K., Bairagi, S., Rajib, B., Murari M. M. (2016). Study on Potential Application of Natural Fibre Made Fabrics as Thermal Insulation Medium. American International Journal of Research in Science, Technology, Engineering & Mathematics, 15(1), 08-13, June-August,

Hassan, S., Tesfamichael, A., and Moh-Nor, M.F. (2016). Comparison Study of Thermal Insulation characteristics from Oil Palm Fibre. MATEC Web of Conferences, 13(1), 12-18.

Jawaid, M., H. P. S. Abdul Khalil, and Abu Bakar, A., (2010). Mechanical performance of oil palm empty fruit bunches/jute fibres reinforced epoxy hybrid composites. Materials Science and Engineering A527 (29& 30), 7944-7949.

Kalia, S., Dufresne, A., Cherian, B.M., Kaith, B.S., Avérous, L., Njuguna, J., Nassiopoulos, E. (2011). Cellulose Based Biocomposites and Nanocomposites-A Review, International Journal of Polymer science, 1(1), 1-26.

La Gennusa, M., Llorach-Massana, P., Montero, J,I., Pena, F.J., Rieradevall, J., Ferrante, F., Scaccianoce, G., Sorrentino, G., (2017). Composite Building Materials: Thermal and Mechanical Performances of Samples Realized with Hay and Natural Resins. MDPI, Journal of Sustainability, 9(1), 373-374.

Luamkanchanaphana, T., Chotikaprakhana, S., Jarusombatib, S., (2012). Study of Physical, Mechanical and Thermal Properties for Thermal Insulation from Narrow-leaved Cattail Fibers. Journal of Asia-Pacific Chemical, Biological & Environmental Engineering Society, 1(1), 46-57.

Momoh, E.O. And Osofero, A.I. (2020). Recent Developments in the Application of Oil Palm Fibres in Cement Composites. Front. Struct. Civ. Eng. 2020, 14(1): 94–108

Olaoye, R.A, Oluremi, J.R. and Ajamu, S.O. (2013). The use of fibre waste as complement in concrete in concrete for a sustainable environment. Innovative Systems Design and Engineering, 4(9): 91–97.

Onuaguluchi, O, Banthia N. (2016). Plant-based natural fibre reinforced cement composites: A review. Cement and Concrete Composites, 2016, 68: 96–108.

Oushabi, A., Sair, S., Abboud, Y., Tanane, O., and El Bouari, A., (2015). Natural thermal- insulation materials composed of renewable resources: characterization of local date palm fibers (LDPF). Journal of Material Environmental Science, 6(12), 3395-3402.

Page, J, Khadraoui F, Boutouil M, Gomina M. (2017). Multi-physical properties of a structural concrete incorporating short flax fibers. Construction & Building Materials, 140: 344–353.

Pfundstein, M. (2007). Insulating materials. München (Germany): GmbH & Co. KG Publication.

Raza, M., Abdallah, H.A., Abdullah, A., Abu-Jdayil, B. Date (2022). Date Palm Surface Fibers for Green Thermal Insulation. Buildings, 12, 866. https://doi.org/10.3390/ buildings12060866

Sulaiman, O., Salim, N., Nordin, N.A. and Hashim, R. (2012). Compressed oil palm trunk, BioResources, 7(2), 2688-2706. 2689.

Wong, K. J., Nirmal, U and Lim, B.K. (2010). Impact behavior of short and continuous fiberreinforced polyester composites. Journal of Reinforced Plastics and Composites, 29 (23), 3463-3474.

Zach, J., Hroudová, J., Brožovský, J., Krejza, Z., Gailiuse, A. (2013). Development of Thermal Insulating Materials on Natural Base for Thermal Insulation Systems: Procedia Engineering, 57(1), 1288-1294.

Zhou, X., Zheng, F., Li, H., Lu, C. (2010). An environment-friendly thermal insulation material from cotton stalk fibers. Energy and Buildings, 42(1), 12-18.

4th International Engineering Conference (IEC 2022)
Federal University of Technology, Minna, Nigeria

Evaluating Hydrological Droughts Using Sdi in Upper Niger River Basin (UNRB)

*Oyeniran, O. O[1], Adesiji, A. R[2], & Jimoh, O. D[3]
Department of Civil Engineering, Federal University of Technology, Minna, Nigeria
*Corresponding author email:oyeniranoyewole@yahoo.com +2347038320563

ABSTRACT
Drought is a terrible natural occurrence. Its long accumulation process and its illimitable onset and conclusion set it apart from other natural dangers. It is vital to assess a drought's severity. Any single place can experience drought, which has a variety of manifestations. It always begins with a lack of precipitation and may (or may not, depending on how It has an impact on soil moisture, streams, groundwater, ecosystems, and people. There is paucity of data on hydrological droughts across the Upper Niger River basin. The Streamflow Drought Index (SDI) was used to evaluate the presence of hydrological drought in the Upper Niger River Basin(UNRB) using the Streamflow data of Shiroro hydropower gauging station obtained for 27-years from UNRB and the drought indices were obtained. it was observed that the drought years include: 1990, 1991, 1992, 1993, 1994, 1995, 1996, 1998, 2000, 2001, 2002, 2003, 2004, 2005, 2006, 2007, 2008, 2009, 2011, 2013, 2014, 2015 and 2016 respectively. Interestingly, it was observed that the drought was extreme in the year 2015 compared to other years. We conclude from the obtained results that there is increasing presence of drought in the UNRB which could be as a result of increasing human activities and climate change.

Keywords: *Climate change, Drought, Hydrological, Streamflow, SDI*

1.0 INTRODUCTION

Drought is a significant stochastic natural disaster that has a negative impact on water resource systems, people, and ecosystems (Zargar et al., 2011; Jahangir et al., 2013). A hydro-meteorological event on land known as a drought is characterized by a temporary and recurrent lack of water. According to Morid et al. (2007), the amount to which it falls below a specified threshold level over a prolonged period of time indicates the severity of the drought. Because to the difficulties in detecting it, drought has been designated as one of the most complicated natural hazards. Drought awareness and mitigation rely on accurate information on the beginning and progression of the drought in terms of temporal and spatial extent. Such data can be collected if drought monitoring indices that are both effective and continuous are utilized in drought evaluation. The study of spatial and temporal drought conditions has been widely used in the planning and management of water resource systems such as water supply, irrigation, and hydropower generation (Ceppi *et al*., 2014; Nouri *et al*., 2019; Alaa, 2014; Wambua 2020).

The Upper Niger River basin has seen irregular droughts, which have harmed water resource systems and, as a result, socioeconomic growth. Drought has become more frequent and severe throughout the basin, exacerbating the problem. Drought is a challenging occurrence to examine and evaluate since it is a stochastic hydro-meteorological phenomenon. Droughts in the basin are caused by a combination of climate change and land use/cover change. As a result, the basin has to develop long-term drought mitigation and coping methods. Although several methods have been employed to research drought, the Standardized Precipitation Index (SPI) is frequently used as a drought meteorological index to determine the duration and/or severity of a drought.

However, SPI limits include the length of rainfall record, which has a substantial impact on SPI values. This implies that with varying durations of precipitation records of data, we can notice varied findings of SPI replies. Another issue is the probability distributions. Several probability distributions, including gamma and Pearson Type III distributions, lognormal, extreme value, and exponential distributions, have been utilized in SPI calculations. These distributions are frequently used in simulations of precipitation distributions. Another drawback is the potential for misleadingly high positive or negative SPI values when using the SPI at short time scales (1, 2, or 3 months) in locations with little seasonal precipitation. Because it is based on monthly measured streamflow volumes at various time scales, the SDI was chosen for this study because it has the benefit of providing for the short-, medium-, and long-term regulation of hydrological drought or the availability of water. The purpose of the study is to assess the hydrological drought in the Upper Niger

River Basin using this method and then utilize the results to look into the severity of the drought there.

2.0 RESEARCH METHODOLOGY

2.1 The Study Area

The Upper Niger River Basin, the subject of the study, is situated in Nigeria's north-central region. West-central Nigeria's study area is situated between Latitude 9.550N and Longitude 3.130E and Latitude 8.520N and Longitude 6.520E, and is bordered to the south by the Niger River. Together with Kebbi and Zamfara to the north, Kaduna to the north and northeast, Kogi to the southeast, and Kwara to the south, it is bordered by these states as well. The topography includes the Kaduna River's floodplains and is primarily made up of woodland savannas.

The Inter-Tropical Convergence Zone (ITCZ), which is connected to the sun's migration patterns with a time lag of roughly a month or two, moves northward and southward during the rainy season in the region. Double maxima in the south and single maxima in the north make up the rainfall pattern that develops as a result of the ITCZ's migration and the weather system. The region's average annual temperature ranges from 22°C in the northeast to 27°C in the south.

The Western Uplands, which are located to the south of the study area and are about 600 meters above sea level, and the North-Central Plateau, which is located to the north and is about 1200 meters above sea level, are divided by the Niger Trough. These highlands serve as the primary source for the majority of the River Niger's tributaries. The Niger River flows through Nigeria for 1200 km of its 4200 km length from its source in the Futa Jalon Plateau to its estuary in the Atlantic Ocean.

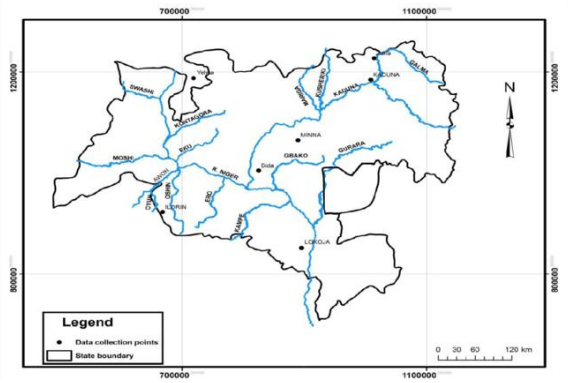

Figure 1: Location of Study area (Upper Niger River Basin)

Investigating the severity of the droughts in the Upper Niger River Basin (UNRB) was done by computing the SDI of the stream flow data that was available from the Shiroro gauging station under the coverage of the basin.

2.2 Streamflow Drought Index (SDI)

Using streamflow data from the Shiroro hydroelectric gauging station that was obtained from the Upper Niger River Basin Development Authority, Minna, spanning the years 1990 to 2017, a time series of monthly stream flow volumes was created. Whereas j stands for the month inside that hydrological year (i.e., j = 1 for June and j = 12 for May), i stands for the hydrological year. With this series, we can,

i = 1, 2 … j = 1, 2… 12 k = 1, 2, 3, 4

The equation for calculating the SDI is as follows:

$$V_{i,k} = \sum_{i=0}^{3k} Q_{i,j} \quad i = 1, 2, 3 \ldots \quad j = 1, 2, 3 \ldots, 12 \quad k = 1, 2, 3, 4 \ldots \ldots \ldots (1)$$

Where k = 1 for June through August, K = 2 for June through November, K = 3 for June through February, and K = 4 for June through May, and I is the cumulative stream flow volume for the ith hydrological year and the kth reference period. Equation 2 is used to determine SDI for each year.

$$SDI_{i,k} = \frac{V_{i,k} - \overline{V_k}}{S_k} \quad i = 1, 2, \ldots, \quad k = 1, 2, 3, 4 \ldots \ldots \ldots \ldots \ldots (2)$$

$\overline{V_k}$ is the mean and S_k is the standard deviation of cumulative flow values for kth time period.

For smaller Basins, streamflow may follow a skewed probability distribution which can be approximated by the family of Gamma distribution functions. The distribution is then normalised.

The criteria in table 1 were used to interpret the SDI values to various levels of drought conditions.

Table 1: SDI values interpretation

State	Description	Criterion	Probability (%)
0	Non-Drought	SDI ≥ 0.0	50.0
1	Mild- Drought	-1.0 ≤ SDI <0.0	34.1
2	Moderate-Drought	-1.5 ≤ SDI <-1.0	9.2
3	Severe-Drought	-2.0 ≤ SDI <-1.5	4.4
4	Extreme-Drought	SDI < -2.0	2.3

3.0 RESULTS AND DISCUSSIONS

3.1 RESULTS

The stream flow data for 27-years period of Shiroro station was obtained as a sample for the basin with a missing record percentage of 3.08%. The sample average method was adopted to obtain values for the missing records.
The SDI values were computed as seen in table 2

Table 2: SDI values for Shiroro station of the UNRB

Year	Quarter 1	Quarter 2	Quarter 3	Quarter 4
1989 - 1990	-0.95	0.07	-0.24	-0.59
1990 - 1991	-1.68	-0.09	2.95	-0.61
1991 - 1992	-0.93	-0.14	-0.58	0.21
1992 - 1993	-1.65	-0.17	-0.66	0.04
1993 - 1994	1.65	-0.09	-0.12	-1.08
1994 - 1995	-1.33	-0.48	-0.76	-1.71
1995 - 1996	0.07	-0.44	1.13	-0.55
1996 - 1997	0.68	0.01	1.05	-0.52
1997 - 1998	1.07	-0.15	-0.31	-0.55
1998 - 1999	0.88	-0.15	0.33	0.05
1999 - 2000	0.32	-0.17	0.15	-0.34
2000 - 2001	-0.39	-0.30	-0.20	0.39
2001 - 2002	0.53	-0.67	0.11	-0.02
2002 - 2003	-0.12	-0.25	-0.01	2.15
2003 - 2004	-0.86	-0.31	-0.03	-0.01
2004 - 2005	-1.01	-0.49	-0.34	-1.87
2005 - 2006	1.72	-0.34	-1.23	0.03
2006 - 2007	-1.51	-0.33	0.22	0.02
2007 - 2008	-0.71	-0.41	-0.34	-0.34
2008 - 2009	0.36	-0.46	-1.35	0.67
2009 - 2010	1.85	-0.17	0.09	1.33
2010 - 2011	0.14	-0.07	0.03	-0.85
2011 - 2012	1.26	-0.40	2.16	2.94
2012 - 2013	-0.20	-0.21	-0.46	0.20
2013 - 2014	0.19	-0.44	1.00	-0.75
2014 - 2015	0.68	-0.51	-2.36	1.15
2015 - 2016	-0.15	-0.32	-0.36	0.43
2016 - 2017	0.10	0.83	0.08	0.17

Description	Criterion	Colour Code
Non-Drought	SDI ≥ 0.0	
Mild- Drought	-1.0 ≤ SDI <0.0	
Moderate- Drought	-1.5 ≤ SDI <-1.0	
Severe- Drought	-2.0 ≤ SDI <-1.5	
Extreme- Drought	SDI < -2.0	

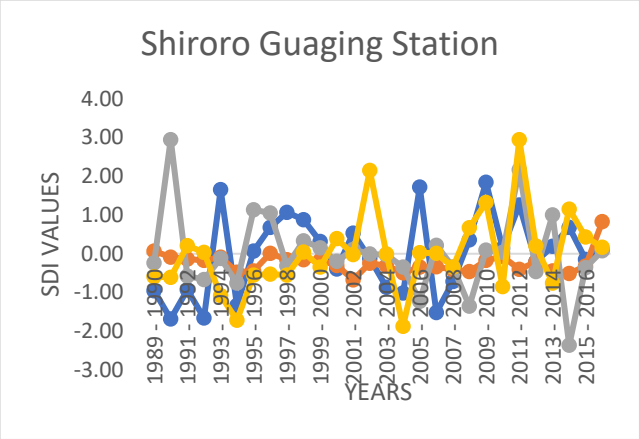

Figure 2: Quarterly SDI series for Shiroro gauging station of the Upper Niger River Basin.

3.2 DISCUSSIONS

Table 2 and figure 2 shows the summary of the quarterly(i.e March, June, September, December) SDI values obtained.

The result of the 1st quarter shows that, there was no drought in the year 1994, 1996, 1997, 1998, 1999, 2000, 2002, 2006, 2009, 2010, 2011, 2012, 2014, 2015 and 2017, mild drought in 1990, 1992, 2001, 2003, 2004, 2008, 2013,

2016, moderate drought in 1995 and 2005 and severe drought in 1991, 1993 and 2007.

The 2nd quarter shows that, there was no drought in the year 1990, 1997 and 2017, mild drought in 1991, 1992, 1993, 1994, 1995, 1996, 1998, 1999, 2000, 2001, 2002, 2003, 2004, 2005, 2006, 2007, 2008, 2009, 2010, 2011, 2012, 2013, 2014, 2015 and 2016, moderate drought in 1995 and 2005 and severe drought in 1991, 1993 and 2007.

The 3rd quarter shows that, there was no drought in the year 1991, 1996, 1997, 1999, 2000, 2002, 2007, 2010, 2011, 2012, 2014 and 2017, mild drought in 1990, 1992, 1993, 1994, 1995, 1998, 2001, 2003, 2004, 2005, 2008, 2013, 2016, moderate drought in 2006 and 2009 and extreme drought in 2015.

The 4th quarter shows that, there was no drought in the year 1992, 1993, 1999, 2001, 2003, 2006, 2007, 2009, 2010, 2012, 2013, 2015, 2016 and 2015, mild drought in 1990, 1991, 1996, 1997, 2000, 2002, 2004, 2008, 2011, 2014, moderate drought in 1994 and severe drought in 1995 and 2005.

According to table 2, it was observed that the drought years include: 1990, 1991, 1992, 1993, 1994, 1995, 1996, 1998, 2000, 2001, 2002, 2003, 2004, 2005, 2006, 2007, 2008, 2009, 2011, 2013, 2014, 2015 and 2016 respectively. Yahaya *et al*. (2016) in their paper "Analysis of Drought Dynamics in Bida Environs, Niger State, Nigeria identified 1965, 1967, 1972 – 1974, 1977, 1982, 1986 – 1988, 1993, 2000 – 2003, 2006, 2008, 2010, 2011, and 2015 as the worst drought years. This further confirms the presence of drought along the Niger basin.

4.0 CONCLUSION

From the obtained results, in comparison with the research carried out by Yahaya *et al. (2016),* the following conclusion can be drawn:

1. SDI is a valid tool for evaluation of drought
2. There is increasing presence of drought in the Niger state area.

References

Babatolu J. S., Akinubi R. T. (2014). Influence of Climate Change in Niger River Basin Development Authority Area on Niger Runoff, Nigeria, *Journal of Earth Science on Climate Change, 5:9* http://dx.doi.org/10.4172/2157-7617.1000230

Belayneh A., Adamowski J., Khalil B. (2016). Short-term SPI drought forecasting in the Awash River Basin in Ethiopia using wavelet transforms and machine learning methods. *Sustain. Water Resources Management, 2*, 87–101

Ceppi A., Ravazzani G., Corbari C., Mencci R., Saleno S., Meuccr, Mancini M. (2014). Real time drought forecasting system for irrigation management, *Journal of Hydrology and*
Earth Systems Science, 18: 3353-3366.

Hayes M. J., Svoboda M. D., Wardlow B. D., Anderson M. C., Kogan F. (2012). Drought monitoring: Historical and current perspectives. *CRC Press: Boca Raton, FL, USA, page 1–19. ISBN 9781439835609*

Jahangir Khan, Saifullah Khan, Munir Ahmad Khetran, Amanullah, Naheem Sadiq, Mohammed Islam, Abdul Hanan, Ahmad Aziz. (2013). Tijaban-10 a drought tolerant and high yielding wheat variety for rainfed/sailaba areas of Balochistan. *Pak. J. Bot, 45*(4), 1357-1362.

Morid, S., Smakhtin V., Bagherzadeh K. (2007). Drought forecasting using artificial neural networks and time series of drought indices. *International Journal of Climatology: A Journal of the Royal Meteorological Society*, *27*(15), 2103-2111.

Nalbantis. (2008). Evaluation of a Hydrological Drought Index, *European Water 23/24, 67-77.*

Nouri A., Saghafian B., Delavar M., Bazargan-Lari M. R. (2019). Agent-based modeling for evaluation of crop pattern and water management policies. *Water Resources Management*, *33*(11), 3707-3720.

Piao S., Ciais P., Huang Y., Shen Z., Peng S., Li J., Fang J. (2010). The impacts of climate change on water resources and agriculture in China. *Nature*, *467*(7311), 43-51.

Şen, Z. (2015). *Applied drought modeling, prediction, and mitigation*. Elsevier.

Vicente-Serrano, S. M., Beguería, S., López-Moreno J. I. (2010). A multiscalar drought index sensitive to global warming: The standardized precipitation evapotranspiration index. *Journal of Climatology. 23 (7): 1696–1718.*

Wambua, R. M. (2020). Development of a Non-Linear Integrated Drought Index (NDI) for Managing Drought and Water Resources Forecasting in the Upper Tana River Basin-Kenya. *International Journal of Environmental Sustainability and Green Technologies (IJESGT)*, *11*(1), 15-33.

Yahaya T.I., Okesola M. S., Omotayo J. (2016). Analysis Of Drought Dynamics in Bida Environs, Niger State, Nigeria

Zargar A., Sadiq R., Naser B., & Khan F. I. (2011). A review of drought indices. *Environmental Reviews*, *19*(NA), 333-349.

4th International Engineering Conference (IEC 2023)
Federal University of Technology, Minna, Nigeria

EXTRACTION OF METAL IONS FROM TANTALITE – COLUMBITE ORE USING AQUEOUS BIPHASIC SYSTEM

*Oyabiyi, M. A[1], Maina, N. S[2], & Sani, Y. M[3]
[1]Department of Chemical Engineering, Ahmadu Bello University, Zaria, Kaduna, Nigeria
[2]Department of Chemical Engineering, Ahmadu Bello University, Zaria, Kaduna, Nigeria
[3]Department of Chemical Engineering, Ahmadu Bello University, Zaria, Kaduna, Nigeria
*Corresponding author email:wolex_moses@yahoo.com +2348034125887

ABSTRACT
The use of aqueous biphasic system (ABS) produce by combining polyethylene glycol and inorganic salt in two-phase system in extraction of metal ions has caught attention of many process experts due to its several advantages such as durability, non-toxicity, environmental friendly. This study investigated leaching of tantalite – columbite ore and salting – out effect of polyethylene glycol (PEG) on extraction of metal ions from tantalite – columbite ore. PEG 400, PEG 3000 and PEG 6000 were used in combination with inorganic salt (K_2SO_4) to prepare aqueous biphasic system (ABS). The experimental results showed that alkaline fusion performed better than mineral acid leaching. Also, the higher the molecular weight of polyethylene glycol the higher is the separation of the selected metals from leached liquor of tantalite – columbite ore using PEG/Salt ABS. Thus, PEG 6000 performed better than lower polyethylene glycol (PEG 400 and PEG 3000). Therefore, aqueous biphasic solvent produced from PEG is a good solvent for metal ions recovery due to its high salting – out effect and extractability efficiency.

Keywords: Extraction, Polyethylene glycol, Salting - out, Solvent.

1 INTRODUCTION

Tantalite contains two major metals known as tantalum and niobium which occur in columbite – tantalite and tantalite – niobium ores with (Fe, Mn) $(Ta, Nb)_2O_6$ as general molecular formula. It is a complex oxide in association with other metals such as iron, manganese, tin, tungsten, aluminum, tungsten, silicon, etc. and found in several mineral deposits such as pegmatite, microlite, nodgnite, columbite and struvenite. More so, tantalite can be produced as a result of weathering or breaking down of tantalite bearing minerals deposits which will push the tantalite into auxiliary associated components which constitute impurities in the ore (Maina & Solomon, 2014).

Polyethylene glycol (PEG) is a compound produced from condensation polymerization reaction of ethylene oxide and water. This compound is represented with the general molecular formula $H(CH_2CH_2O)nOH$, where the n is standing for the average number of repeating oxyethylene group involved and it is ranging from 4 – 180 and having the molecular weight varies between 200 to 10,000 (Maina & Ahmad, 2009). There are different types of PEGs which derive their names from a numerical designation that shows the average molecular weight (e.g., PEG – 3500). PEG is not toxic, no odour, neutral and lubricating effect, non – volatile at room temperature, non – irritating to human skin, not expensive, possess good thermal stability and can be recycled easily at minimal cost. Therefore, these properties consequently responsible for many applications of PEG in pharmaceuticals process as solvent for many extraction operations, excipient and vehicle for tablet production (Robnik *et al.*, 2020).

Solvent extraction is one of the most beneficial and versatile separation techniques because it has many advantages over other methods such as easy handling, flexibility, ability to operate at different range of concentrations and high selectivity. Furthermore, it is a clean method of separation which is devoid of waste production (Sengupta *et al.*, 2007). In hydrometallurgy, combination of solvent extraction together with other methods like electroplating or electro wining process will increase purity level above 99.9% (Sengupta *et al.*, 2007).

Solvent extraction process can be improved through salting – out technique. Salting – out is a process which involve addition of inorganic salts to the solvent for metal extraction in order to increase the distribution ratio of metal complexes to the natural stage. Thus, it involves decrease in the solubility of non – electrolyte with proportionate increase in salt concentration (Hyde *et al.*, 2017). The basis behind the salting-out can be adduced to the fact that the inorganic salt act on the metal species by tie water around them and thus exhaust the watery stage of water particles essentially utilize as a dissolvable (Bulgariu & Bulgariu, 2013). The proportions of inorganic salts must be sufficient in a range to deliver the required impact, the fluid stage regularly being immersed with the included salt (Rogers *et al.*, 1993).

Aqueous Biphasic Systems (ABSs) is a system produced when a water soluble polymer (e.g. PEG) is mixed with another polymer or with a certain inorganic salt (e.g. Na_2SO_4, $(NH4)_2SO_4$, Na_2CO_3, KCl, K_2HPO_4). The inorganic salt is acting in this capacity as a salting – out agent. Application of ABSs has been tested to be novel techniques for extraction of biological materials and metals separation because they composed of higher percentage water together with some materials which are neither toxic nor flammable (Khayati & Alizadeh, 2013). This method has found its way into hydrometallurgical

process for metals extraction as well as remediation of environment that has been polluted (Bulgariu & Bulgariu, 2008).

Production of pure tantalum and niobium from tantalite - columbite ore has always been a challenge to the metal processors due to presence of elements such as iron, manganese, tungsten, aluminum, etc. in the ore which constitute impurities. The application of leaching operation (ore dissolution) in processing tantalite – columbite has resulted in bringing main and associated metal ions (impurities) into the solution which can be later separated by solvent extraction. However, the current solvent extraction method to recover these metals is being faced with many constraints such as toxicity, instability and environmental unfriendliness of many solvents available, thus, this necessitated the search for alternative or modified solvent to extract these metals. Therefore, this study is sought to investigate the extraction of metal ions from tantalite - colombite ore using aqueous biphasic solvent.

2 METHODOLOGY

2.1 SOURCING OF RAW MATERIALS

Tantalite – columbite ore sample used for this work was sourced from Plateau State, Nigeria. Polyethylene glycol (PEG – 400, PEG – 3000 and PEG – 6000) and potassium sulphate (K_2SO_4) were sourced from Sigma–Aldrich in Germany. Distilled water was used throughout in this experiment.

2.2 CHARACTERIZATION AND LEAC – HING OF TANTALITE - COLUMBITE ORE

Tantalite ore sample used for this work was obtained from Plateau state , Nigeria**.** The ore sample was subjected to beneficiation process which includes crushing, milling and sieving to 75µm particles size to enhance fusion and leaching processes. Physicochemical characterizations of the sieved tantalite ore were performed to determine the colour, moisture contents, pH, loss of mass on ignition (LOI) and organic matter. The ore was also characterized in order to determine the major metal constituents and trace metals using Energy Dispersive X – Ray Fluorescence (EDXRF) spectrophotometer in the Department of Physics, Ummaru Musa Yardua University Katsina.

Dissolution or leaching of tantalite ore was investigated using two different methods; mineral acid leaching and alkali fusion followed by water leaching. For acid leaching, standard solutions of H_2SO_4 12M was prepared from concentrated sulphuric acid (98% H_2SO_4). 50g of the ball-milled ore sample was placed in a conical flask and then added to 150g of already prepare 12M of 98% H_2SO_4 acid at ratio of 3:1 for acid and tantalite ore (Maina, 2014). The mixture was heated and stirred continuously for 3hr at 80^{o}C and stirring speed of 270 rpm.

In the second procedure, alkali fusion followed by water leaching was used to digest the ore in accordance with the previously published work with 20 g of tantalite ore mixed with 100 g of ball milled tantalite ore inside a crucible and heated to 400 ^{o}C in a furnace at atmospheric pressure for 1h (Goitom *et al,* 2018). Thereafter, the cooled fused sample was leached with 100 ml of water to obtain residue and leached liquor. The experiment was performed in triplicates using both methods and thereafter, elemental compositions of residues and percentage dissolution were determined to choose the effective method. The morphology of the two residues obtained was also obtained and compared with that of main ore using scanning electron microscopy (SEM).

2.3 PREPARATION OF AQUEOUS BIPHASIC SYSTEM (ABS)

Aqueous Biphasic System (ABS) was formed by combining a water soluble polymer (PEG) with inorganic salt (Na_2SO_4). Three categories of Polyethylene glycol (PEG) which belong to low, medium and high molecular weight were used for this study respectively. The PEGs considered for this study were PEG – 400, PEG – 3000 and PEG – 6000 molecular weight. Sodium sulphate (Na_2SO_4) was selected as phase transfer catalyst (PTC) due to its ability to produce high separation factor or salting – out effect compare to other salts in its category (Bulgariu & Bulgariu, 2011). PEG stock solutions of 30% (w/v) PEG – 400 was prepared by mixing 30g PEG in 100ml of distilled water.

The inorganic salt stock solution was also prepared by dissolving 20% (w/v) Na_2SO_4 salt in water. Thereafter, ABS was formed by mixing each of the PEG solution with sodium sulphate solution thoroughly in a ratio of 1:1 for PEG and salt solution (Chen *et al,* 2005) and each mixture was shaken at constant time of 30 seconds until two phases were formed. Cloud point technique was used to characterize the produced ABS in order to ascertain the solubility of PEG in salt solution at the ambient temperature.

2.4 METAL IONS EXTRACTION USING AQUEOUS BIPHASIC SYSTEM

The three PEG/salt solutions prepared were mixed with leached liquor solution in ratio 1:1 respectively (Maina & Ahmad, 2009) and allowed to stand for 5 minutes for phase separation to be achieved. The aqueous phase was separated using separating funnel and its metal ions contents were analyzed by Energy Dispersive X-Ray Fluorescence (EDXRF) spectrophotometer. Organic phase loading metal ions content (PEG – rich phase) was then calculated by simple mass balance from EDXRF analysis results (Nejad & Kazemeini, 2012). The distribution ratio

and percentage of extraction (%E) of metal ions were calculated using (1) and (2) respectively.

$$\% \text{ Extraction (E)} = \frac{100D}{D + Vaq/Vorg} \quad (1)$$

$$D = \frac{[A]_{org}}{[A]_{aq}} \quad (2)$$

Where

D = Distribution Ratio
Vaq = Aqueous Phase Volume
Vorg = Organic Phase Volume
$[A]_{Org}$ = Concentration of metal A in organic phase
$[A]_{Aq}$ = Concentration of metal A in aqueous phase

3. RESULTS AND DISCUSSION

TABLE I: PHYSICAL PROPERTIES OF THE TANTALITE – COLUMBITE ORE

Properties	Value
Moisture Content (%)	6.25 ± 0.210 %
Loss of mass on ignition (LOI) (%)	2.64 ± 0.032 %
pH	7.8
Particle size	75µm
Colour	Dark grey

Table 1 show that the moisture content, LOI and pH of the tantalite ore are 6.25 ± 0.210%, 2.64 ± 0.032 % and 7.8 respectively. The LOI and moisture content indicates that the ore contained low level of impurities and moisture respectively which indicates that there was no interference of impurities and moisture with the fusion process. The pH value indicates that the ore is slightly basic.

TABLE II: ELEMENTAL COMPOSITION OF RAW TANTALITE - COLUMBITE ORE AND RESIDUES AFTER LEACHING

Compound (%)	Composition (wt. %) (Mean ± SD)			% Reduction (Acid)	% Reduction (Fusion)
	Before Leaching (Ore)	After Leaching (Acid)	After Leaching (Fusion)		
Fe_2O_3	8.560± 0.02	6.320+ 1.2	7.066 ±0.04	26.17	17.45
ZnO	0.029± 0.12	0.022+ 0.13	0.015 ± 0.13	24.14	48.28
Ta_2O_5	11.289± 1.10	9.640+ 2.0	5.578 ± 1.01	14.61	50.59
WO_3	0.212± 0.62	0.018+ 0.4	0.053 ± 0.01	91.51	75.24
Al_2O_3	1.756± 1.20	0.486+ 0.11	0.460 ± 0.22	72.32	73.8
SiO_2	9.102 ± 0.01	3.091 + 0.70	16.243 ± 3.10*	66.04	
K_2O	0.046± 1.02	0.021 + 0.12	14.583 ± 2.3*	54.35	
CaO	0.269± 0.03	0.111+ 0.01	0.005 ± 0.01	58.74	98.14
TiO_2	8.542± 0.06	5.859+ 2.10	3.429 ± 2.1	31.41	59.86
V_2O_5	0.046± 0.02	0.036+ 0.01	0.024 ± 0.50	21.74	47.83
Cr_2O_3	0.050± 0.13	0.031 + 0.03	0.023 ± 0.20	38	64.61
MnO	5.801± 0.12	3.734+ 1.72	2.457 ± 2.1	35.63	59.3
BaO	0.284 ± 0.01	0.139+ 0.10	0.133 ± 0.21	51.06	53.31
Y_2O_3	0.019± 0.21	0.018+ 0.02	0.002 ± 0.40	5.26	87.53
Nb_2O_5	49.960± 2.10	45.442+ 4.51	18.471 ± 1.50	9.04	63.03
SnO_2	3.307± 0.23	3.076+ 1.8	1.774 ± 0.30	6.99	46.36

*Mean increase in composition

Table 2 indicates that the tantalite - columbite ore used consist of Nb_2O_5 (49.96%), Ta_2O_5 (11.29%), SiO_2 (9.10%), Fe_2O_3 (8.56%), MnO (5.80%), SnO_2 (3.31%), Al_2O_3 (1.76%), WO_2 (0.21%), CaO (0.27%) and BaO (0.28%) weight percentage (%wt) respectively. After leaching with mineral acid, these major oxides were reduced as it is shown in Table 2 above respectively. However, Table 2 and Figure 2 revealed that by using alkali fusion method, the percentage oxide reductions of the following oxides, CaO (98.14%), Y_2O_3 (87.53%), U_3O_8 (84.06%), WO_3 (75.24%), Al_2O_5 (73.80%), Cr_2O_7 (64.61%), Nb_2O_5 (63.03%), TiO_2 (59.86%), ThO_2 (55.46%), BaO (53.31%), Ta_2O_5 (50.59%), ZnO (48.28%) and SnO_2 (46.36%) were significantly achieved after leaching with cold water.

Therefore, these results indicates that alkali fusion followed by cold water digestion was successfully used to dissolve fourteen (14) compounds higher from tantalite ore as compared to seven (7) compounds dissolved by mineral acid leaching. Most importantly, alkali fusion method was able to dissolve 63.03% of Nb_2O_5 and 50.59% of Ta_2O_5 which are significantly higher than 9.04% of $Nb_2O_5$and 14.61% of Ta_2O_5 dissolved by mineral acid leaching of tantalite ore. Therefore, the rich liquor obtained from alkali fusion was selected and used for metal ions extraction in aqueous biphasic system. This finding agreed with the work of Berhe *et al* (2018) and Habinshuti (2022) which indicates that KOH fusion is a suitable alternative decomposition agent to the commonly used toxic and corrosive HF in the hydrometallurgical processing of tantalite ores.

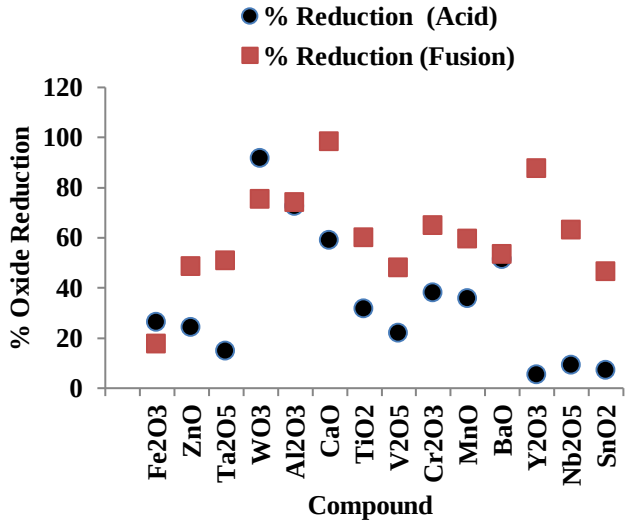

Figure 1: Percentage (%) Reduction in Compounds after Acid and Alkaline Fusion Leaching Process

The grey-scale SEM image of the tantalite – columbite ore, acid leached residues and alkali fusion residues are shown in Plate 1(a), 1(b) and 1(c) respectively. Plate 1(a) gives an indication that the mineralogical association of the ore is not highly complex. Although only few grain boundaries are seen in the sample, in addition to the main component, the ore is expected to contain ferro-columbite, ilmenite, iron oxides, and other gangue silicates (Berhe *et al.*, 2018). From Plate 1(b), it was observed that the SEM structure of residues after acid leaching is closely similar to the structure of the main ore. Therefore, it can be deduced that mineral acid was unable to leach the main components of the ore (tantalum and niobium) but few associated minerals were dissolved. However, Plate 1(c) of the SEM image for alkaline fusion shows that fusion of tantalite ore with KOH was able to reduce the grain size of the ore and consequently helped in dissolving the main components and other associated minerals. The SEM structures obtained agreed with the results of elemental analysis for both mineral acid leaching and alkali fusion.

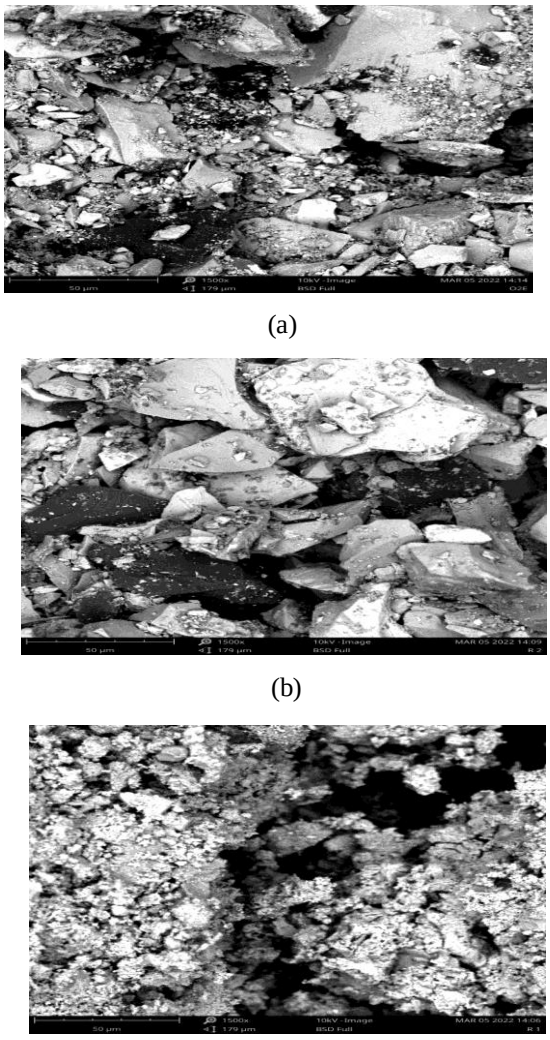

(a)

(b)

(c)

Plate 1: SEM image @ 1500µm (a) Tantalite ore (b) Acid leached residues (c) Alkali fusion residues

TABLE III: DISTRIBUTION RATIO (D) AND PERCENTAGE EXTRACTION (%E) OF METAL IONS USING ABS FORMED FROM PEG 400, PEG 3000 AND PEG 6000

Element	Distribution Ration (D)			Percentage Extraction (%E)		
	ABS 1 (PEG 400)	ABS 2 (PEG 3000)	ABS 3 (PEG 6000)	ABS 1 (PEG 300)	ABS 2 (PEG 3000)	ABS 3 (PEG 6000)
Fe	0.10	0.10	0.58	7.49	17.15	54.84
Al	1.07	1.06	1.13	47.07	69.43	70.23
Mg	1.14	0.92	0.75	48.63	66.41	61.15
Mn	0.12	0.80	0.95	9.30	63.01	66.64
Cr	0.52	0.81	0.62	30.15	63.33	56.66
Ta	0.06	0.03	2.43	5.13	6.20	83.60
Nb	0.15	0.24	0.35	11.05	33.99	42.27
Ca	0.06	0.08	0.40	4.44	15.13	45.41
Na	0.82	0.33	0.68	40.68	41.74	58.95
W	0.44	0.62	0.88	26.77	57.09	64.79

PEG 400: Vr = 1.2; PEG 3000: Vr = 0.48; PEG 6000: Vr = 0.48 Vr = Volume ratio

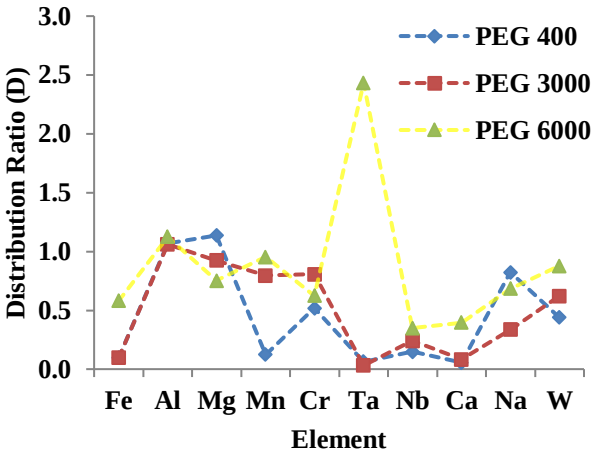

Figure 2: Distribution Ratio (D) of Metal ions using PEG 400, PEG 3000 and PEG 6000 ABS

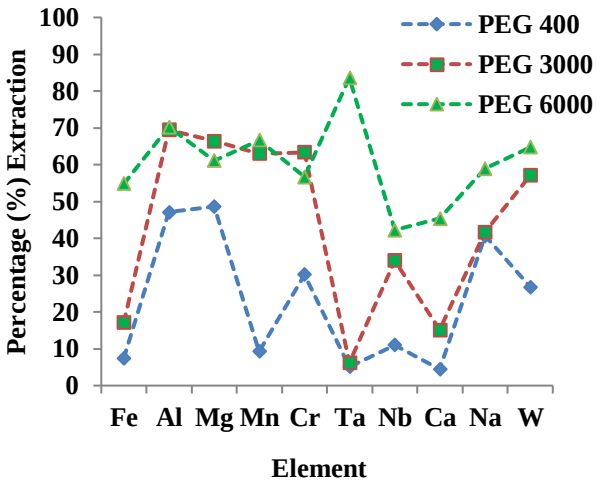

Figure 3: Percentage (%) Extraction of Metal ions using PEG 400, PEG 3000 and PEG 6000 ABS

Table 3 and Figure 2 and 3 present the summary of distribution ratio (D) and percentage extraction (%E) of metal ions using ABS formed from PEG 400, PEG 3000 and PEG 6000 (i.e. ABS 1, ABS 2 and ABS 3). Figure 2 revealed that ABS 3 gave highest percentage extraction for Fe, Ta, Nb, Ca, Na and W when compare with ABS 1 and ABS 2. The highest value recorded was 83.60 for Ta with the least being 42.2 for Nb. However, ABS 2 also competes favourable with ABS 3 in the extraction of Al, Mg, Mn and Cr while ABS 1 performance was low when comparing with other two previously discussed. Therefore, it can be said that ABS 3 formed from PEG 6000 was able to partition metals into both aqueous phase (Fe, Mn, Mg, Nb, Na, W) and organic phase (Al, Ta, Ca) respectively and gave higher efficiency of metals recoverability in whichever phase they are present. This finding supported the principle put forward by Graber *et al* (2000) that the higher the molecular mass of polymer (PEG) the higher is the tendency of aqueous two – phase system formation.

From experimental point of view, the poor performance of peg 400 could be attributed to the fact that lowers PEG (i.e. <PEG 800) exists in liquid state and do not form biphasic system at lower concentration of PEG and salt. However, increasing the molecular mass of PEG

will result into decrease of the OH – groups' number from polymer molecules, leading to fewer hydrogen bonds that can form between polymer chains. Thus, the use of PEGs with too high molecular mass will result to increase in the hydrophobicity of PEG – rich phases where the metal ions cannot be extracted due to incompatibility of their hydration environment.

Abdullahi (2021) reported that PEG 6000 gave a better distribution ratio and separation factor than PEG 4000 and PEG 8000 for separation Fe and Mn from tantalite ore. Also, several other researchers have also suggested that PEG with relative molecular mass which ranges between 1200 – 6000 is suitable for effective production of aqueous biphasic system (Sankar *et al*, 2012; Susanta and Kamalika, 2009; Graber *et al*, 2000).

CONCLUSION

This investigation has indicated that alkali fusion method proved to digest major components in the tantalite – columbite ore i.e. tantalum and niobium together with numerous associated metals. However, findings on the solvent extraction of selected metals from alkali fusion leached liquor using PEG/Salt ABS revealed that higher polyethylene glycol (PEG 6000) gave higher percentage of extraction than lower polyethylene glycol (PEG 400 and PEG 3000). Therefore, aqueous biphasic solvent produced from PEG is a good solvent for metal ions recovery due to its high salting – out effect and extractability efficiency, and other numerous advantages such as environmental friendliness. However, there is need for holistic investigations on how many variables like pH, temperature, mixing ratio, etc. will affect the overall performance of this solvent.

REFERENCES

Abdullahi, Y. L. (2021). Study of the effect of PH on the formation and stability of aqueous biphasic system (ABS) in separating metal ions from tantalite-columbite ore. A B.Eng Research Project, Department of Chemical Engineering, Faculty of Engineering, Ahmadu Bello University, Zaria

Bulgariu, L. & Bulgariu, D. (2013). Selective extraction of Hg (II), Cd (II) and Zn (II) ions from aqueous media by a green chemistry procedure using aqueous two-phase systems. *Separation and Purification Technology*, 118, 209–216

Bulgariu, L. & Bulgariu, D. (2011). Extraction of gold (III) from chloride media in aqueous polyethylene glycol-based two-phase system, *Sep. Purif. Technol.* 81, 620–625.

Bulgariu, L. & Bulgariu, D. (2008). Extraction of metal ions in aqueous polyethylene glycol–inorganic salt two-phase systems in the presence of inorganic extractants: Correlation between extraction behaviour and stability constants of extracted species. *J. Chromatogr. A* 1196–1197, 117–124

Chen, J., Spear, S. K., Huddleston, J. G. & Rogers, R. D. (2005). Extraction of metal ions in aqueous polyethylene glycol–inorganic salt two-phase systems in the presence of inorganic extractants: Correlation between extraction behaviour and stability constants of extracted species. *Green Chem*., 7, 64.

Goitom, G. B., Velázquez, D. A., Bogale, T., A. & Yimam, G. W. (2018). Decomposition of the Kenticha mangano-tantalite ore by HF/H_2SO_4 and KOH fusion. *Physicochem. Probl. Miner. Process*, 54(2), 406-414

Graber, T. A., Andrews, B. A. J. & Asenjo, A. (2000). Model for the partition of metal ions in aqueous two-phase system, *J. Chromatogr.* B743, 57–64

Habinshuti, J. B. (2022). Optimization of niobium-tantalum recovery from typical Rwandan and Nigerian columbite-tantalite ores. A Ph.D Dissertation, Department of Material Science and Engineering, African University of Science and Technology, Abuja.

Hyde, A. M., Zultanski, S. L., Waldman, J. H., Zhong, , M. & Peng, F. (2017). General principles and strategies for salting – out informed by the Hofmeister Series. *Process Res. Dev.*, 21(9), 1355–1370

Khayati, G. & Alizadeh, S. (2013). Extraction of lipase from Rhodotorula glutinis fermentation culture by aqueous two-phase partitioning. *Fluid Phase Equilibria*, 353, 15, 132-134

Nejad, H. H. & Kazemeini, M (2012). Optimization of platinum extraction by trio ctylphosphine oxide in the presence of alkaline-metal salts. *Procedia Engineering 42,* 1302 – 1312

Maina, N. S. & Ahmad, M. S. (2009). Extraction of Tantalum from locally sourced tantalite using polyethylene glycol solution. *Nig. J. Basic Appl. Sci.*., 17(2): 240-245.

Maina, N. S., & Solomon, E. (2014). Salting out effect of electrolyte solutions in the extraction of tantalum and niobium using Aqueous Biphase System. *Nigerian Journal of Basic and Applied Science*, 22(1&2): 5-9

Robnik, B., Naumoska, & Casar, Z. (2020). A novel testing approaches for oxidative degradation dependent incompatibility of amine moiety containing drugs with PEGs in solid-state. *Pharmaceutics*,12, 37;

Rogers, R D, Bond, A. H. & Bauer, C. B. (1993). Metal ion separations in polyethylene glycol-based aqueous biphasic systems. *Sep Sci. Technol.* 1993; 28:1091–126

Sankar, P. P., Sumanta, K. G. & Kamalika, S. (2012). A complete aqueous method for trace level extraction and spectrophotometric estimation of Bi(III/V) salts. *J. Indian Chem. Soc.*, 89, pp. 1465-1470

Sengupta, B. Bhakhar, M. S. & Sengupta, R. (2007). Extraction of copper from ammoniacal solutions into emulsion liquid membranes using LIX 84I. *Hydrometallurgy*, 89, 311-318.

Susanta, L. & Kamalika, R. (2009). A green approach for sequential extraction of heavy metals from Li irradiated Au target. *J Radioanal Nucl Chem.*, 281:531–534

4th International Engineering Conference (IEC 2023)
Federal University of Technology, Minna, Nigeria

Conceptual Design of a TCP/IP Control Data for Network Access Selection in a Multi-Connective Integrated Satellite-Terrestrial Network

*Ayofe, O. A[1], Tekanyi, A. M. S[2], Usman, A. D[3], Musa, M. J[4] & Abdullahi, Z. M[5]
[1,2,3,4,5]Electronic and Telecommunication Engineering, Ahmadu Bello University, Zaria, Kaduna State, Nigeria.
[1]Department of Computer Engineering Technology, Federal Polytechnic, Ede, Osun State, Nigeria
*Corresponding author email:p18egcm9012@abu.edu.ng +2348066887007

ABSTRACT
In a bid to ensure ubiquitous and resilience connectivity of 5G network, the satellite has been identified as a key technology that can help to achieve these objectives. The 3GPP and other standard bodies have specified a framework called Access Traffic Steering, Switching and Splitting (ATSSS) for which a 3GPP Access Network (AN) and non-3GPP AN can be used to utilise multi-access connectivity. In the Integrated Satellite-Terrestrial Network (ISTN) framework presented herein, we consider satellite network to be a non-3GPP and the terrestrial part to be the 3GPP AN. In order to ensure convergence between the satellite and terrestrial network, we propose a control data which comprises additional headers in addition to existing headers.

Keywords: *Access, Convergence, Network, Protocol, QoE, QoS, Satellite, SDN, TCP/IP, Traffic Engineering, Terrestrial.*

1 INTRODUCTION

In order to achieve the ubiquitous and resilience connectivity expectation of 5G network, satellite has been identified by various standard bodies and researchers as an enabler. This have resulted in various literatures proposing different ways to integrate satellite with terrestrial networks. The 3GPP, (2019) standard body provided a technical specification called Access Traffic Steering Switching and Splitting (ATSSS) wherein a 3GPP Access Network (AN) and Non-3GPP AN can interwork to provide multi-connectivity (Lisi *et al.*, 2020; Pupiales *et al.*, 2021) to User Equipment (UE). In the context of Integrated Satellite-Terrestrial Network (ISTN) (Boero *et al.*, 2018), one of the methods in which literatures have carried out the unification (Bertaux *et al.*, 2015; Feng *et al.*, 2017; Giambene *et al.*, 2018; Gopal & BenAmmar, 2018) is through the use of Software-Defined Network (SDN)(Kreutz *et al.*, 2015; Nunes *et al.*, 2014; Zhang *et al.*, 2018) and Network Function Virtualisation (NFV)(Herrera & Vega, 2016; Veeraraghavan *et al.*, 2017; Yi *et al.*, 2018). With satellite considered as a non-3GPP AN, the SDN and the NFV paradigm can be further exploited to implement the 3GPP's ATSSS framework.

In the implementation of ATSSS, various methods have been presented within or outside the context of SDN. (Wu *et al.*, 2021) presented a survey highlighting Multipath Transport Control Protocol (MPTCP)(Ford *et al.*, 2013) as a key enabler of the ATSSS technology; they identified four key opportunities that can be exploited from the protocol for the ATSSS, which include path management, congestion control, and reliable transfer. However, the problem with MPTCP is reordering of packet due to different path characteristics such as latency which thus makes them unsuitable for real-time traffic; although (Wu *et al.*, 2021) hinted on different solutions to circumvent reordering problem using aggregated Multi-Radio Access Technology's (RAT) bandwidth. These solutions are only feasible for real-time traffic if the candidate AN of the heterogeneous network have similar characteristics. Even at this, it is contested that using multi RAT with the aid of MPTCP is not efficient for real-time traffic, especially when a member AN of heterogeneous network have a wide differing characteristics, and thus should only be limited to elastic traffic (Wang & Basu, 2000). Such is the case for ISTN where the QoS offerings of the terrestrial network is widely disparate from that of the satellite network. The MPTCP in logical sense would be more beneficial to achieve splitting (link aggregation) than to actualise the steering aspect of the ATSSS. While there are research to implement MPTCP on 5G New Radio (NR), there are difficulties integrating it with 5G core (Kang *et al.*, 2020).

The work of (Giambene *et al.*, 2018) exemplifies the splitting aspect of the ATSSS for an ISTN which can benefit from the MPTCP. Implementing this aspect of the ATSSS for a real-time traffic in an ISTN would suffer huge degradation in performance, thus it is pertinent to go the way of steering which basically would select the best AN based on QoS correlation between that of the traffic and access links multi-equipped on a UE. Exploiting the SDN/NFV paradigm to achieve steering through QoS provisioning as described in the text of (Niephaus *et al.*, 2016) would aid to achieve the steering. But to achieve this, there is need for convergence between the two network segments of the ISTN. A Quality of Experience (QoE) aware MPTCP has been suggested to improve the performance of an SDN-based 5G network for multimedia traffic where testbed for fixed-mobile convergence (FMC) has been demonstrated (Condoluci *et al.*,

2019; Kang *et al.*, 2020). However, the MPTCP cannot fulfil the steering mode of the ATSSS requirement. The steering mode of the ATSSS requires an active-standby mechanism wherein if an AN in which traffic is actively being transmitted on is down or fails to meet certain requirement such as QoS expectation, it switches to a standby AN. The ATSSS requirements stipulates various condition for which traffic should be steered; they include Round Trip Time (RTT), load condition (load balancing), and traffic prioritisation (Kang *et al.*, 2020). However, the MPTCP cannot achieve these ATSSS requirement. Also, in the context of ISTN, there is need for convergence to take place before steering can be attained, and the MPTCP is incapable of achieving the steering mode of the ATSSS requirement. On this basis, we present a TCP/IP control data model that can help achieve convergence for an ISTN using an SDN/NFV paradigm. Unlike in the work of (Kang *et al.*, 2020) where they involve several components of the 5G Core (5GC) (e.g. PDC, SMF, etc.), in cooperation with a UE, this work presents the use of SDN implemented within 5GC by exploiting some of the traffic engineering traits of openFlow protocol used in the South Bound Interface (SBI) of SDN controllers.

This paper is organised as follows: section II describes the two major traffic steering model for which an ATSSS framework can be or has been implemented for. Section III mathematically describes the reliability of the two traffic steering model/architecture depicted in section II while section IV presents the protocol stack for the ISTN multi-access for signalling and data transmission. Lastly, section V gives conclusion.

2 TRAFFIC STEERING MODELS

Unlike the method specified in (Kang *et al.*, 2020), where only a single IP address from the MPTCP proxy in the UPF is allocated and shared by the two access interfaces of a UE, a dual IP is proposed. This is to ensure reliability, which can ensure continued communication. In addition, using a single IP address for a terrestrially and celestially situated network can bring additional delay, as it would require constant synchronisation of the space and terrestrial segments of the access network. To better understand the concept of the proposed TCP/IP stack of control data to be used to achieve convergence, Figure 1 depicts the communication scenario for which the concept is designed.

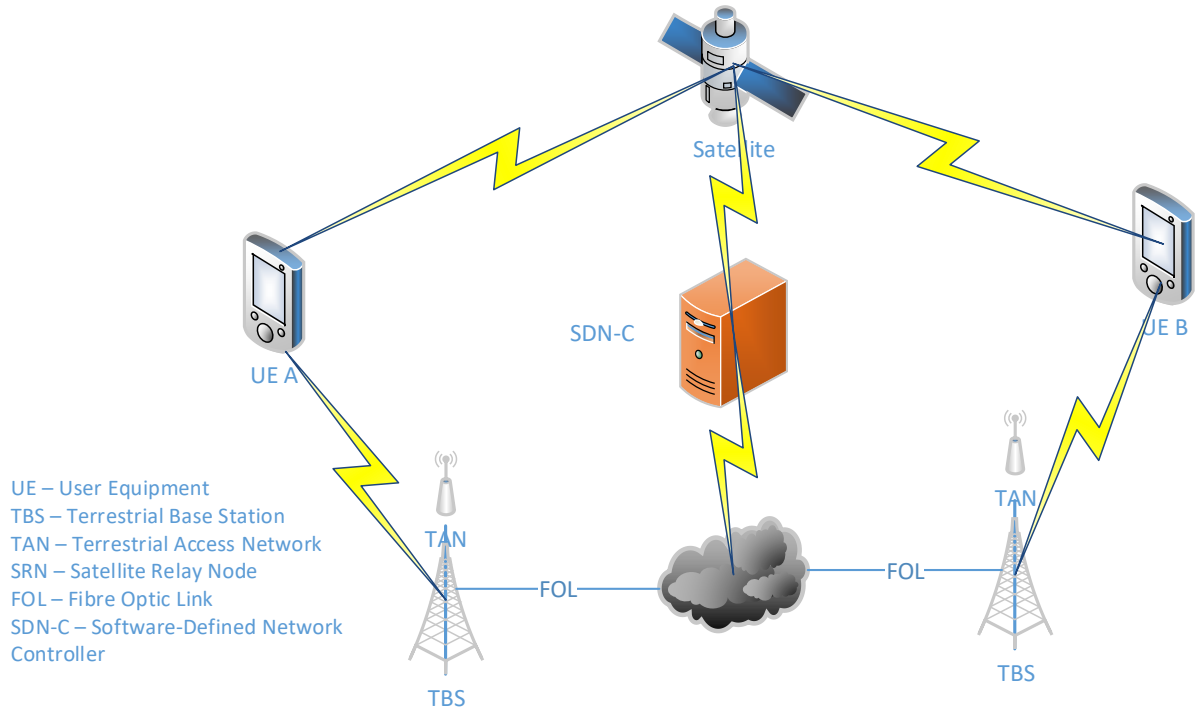

Figure 1: End-to-End Communication of UEs in a Heterogeneous Network with Direct Satellite Contact

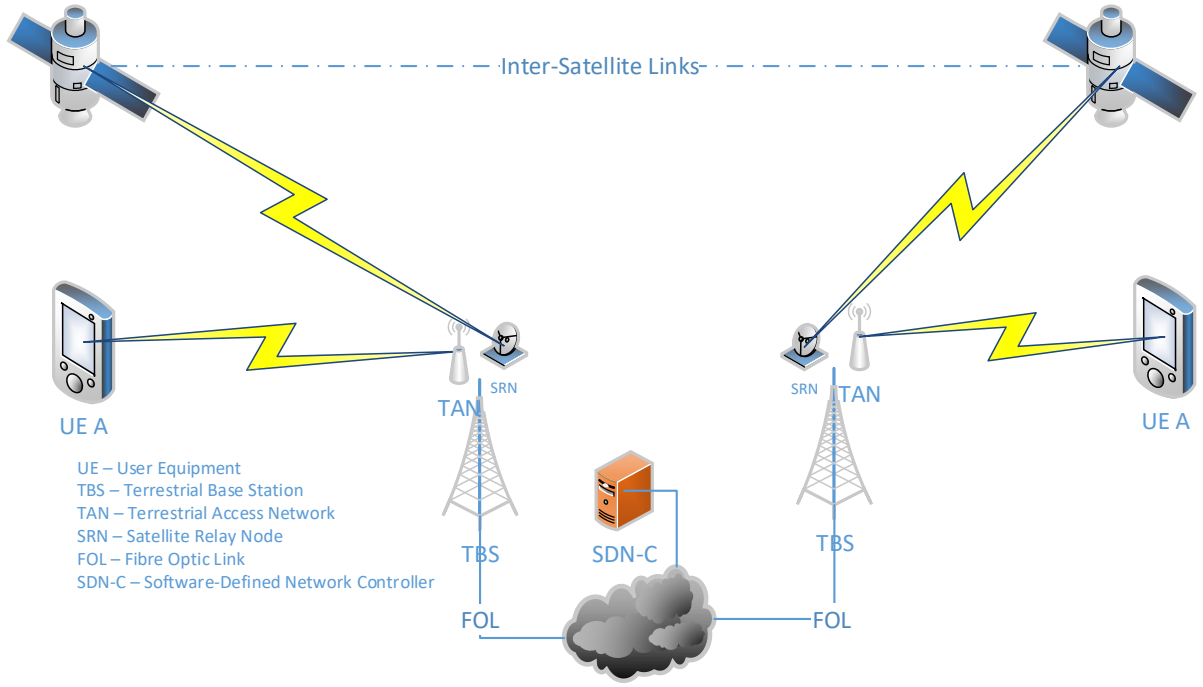

Figure 2: End-to-End Communication of UEs in a Heterogeneous Network with Indirect Satellite Contact

In the event that one network path goes down, there is alternative path to fall back on. For example in the event of natural disaster which terrestrial networks are prone to, the communication facilities that ensure communication such as base stations can be affected and thus disrupt communication system which then can have direct or indirect consequences in various socio-economic aspects. Figure 1 is a setup of a very reliable, nearly zero interruptible End-to-End (E2E) communication systems is depicted in Figure 1 while Figure 2 depicts a partially reliable network. In the setup shown in Figure 2, resiliency is offered against system activities that induces performance degradation such as congestion; in order words it offers reliability in users' experience. However, on one hand, in the wake of disaster that affects communication network, this model offers no reliability in terms of service continuity; on the other hand, the setup shown in Figure 1 offers service continuity in event of disaster or human sabotage, as telecommunication infrastructure in the celestial segment are barely affected by these disrupting factors. This model can be very beneficial in critical situations such as disaster recovery, military operations in the event of sudden attack of terrestrial facilities during counter-terrorism operation. Also, moving vehicles such as ships and airplane can benefits from this model.

3 System Reliability of the Network Architecture

The reliability of steering mode shown in Figure 1 and Figure 2 can be modelled as follows: the probability that a system will not fail equals 1, and the probability that a system will fail will be $P(f)$. Since there is a parallel connection of UE to satellite and terrestrial path in the scenario depicted in Figure 1, then the reliability of the system is given as shown in equation (1).

$$R_p = 1-(1-R_{sat})\times(1-R_{terst}) \quad (1)$$

Where R_p represents the reliability of the parallel connected system while R_{sat} and R_{terst} is represents the probability that the satellite and terrestrial network path, respectively, is up. For scenario depicted in Figure 2, since the UE is connection to the satellite and terrestrial is logically serial, then the reliability of the serially connected system R_s can be given as equation (2).

$$R_s = R_{sat} \times R_{terst} \quad (2)$$

Considering the addition or multiplication of R_{sat} and R_{terst} would be less than 1, by indication $R_p >> R_s$, thus the model depicted in Figure 1 offers higher reliability than the one depicted in Figure 2.

4 Control Signaling Protocol for Access Network Selection

Using the model in Figure 1, we present a TCP/IP stack that would enable convergence of the satellite-terrestrial network for Access Network (AN) selection. The conceptual

design of the control signalling protocol for the ISTN is based off on the conventional TCP/IP stack which consists of the application, transport, internet, and network access layer as shown in Figure 3. The role of this control protocol is to select between multiple ANs that suits a particular QoS demand of application traffic that is about to be transmitted, rather than simultaneously using the multiple paths as the case is in MPTCP.

Figure 3: The Conventional TCP/IP Protocol Stack

At the application layer, an application data is placed and a session ID (*sessID*) is generated by the UE and put together with the data. At transport layer, a TCP source port number is generated and a destination port number is assigned. At the internet layer, the QoS requirement *qosReq* for the application that is about to use communication resource can be encapsulated by exploiting the Type of Service (TOS) bit (Almquist, 1992), and also a source and destination IP address are encapsulated. In the network access layer access layer, a couple of fields would be added to the existing headers. They are the multilink field (*multilink*), alternate link ID (*altLinkID*), and alternate MAC address (*altMacAddr*); these fields are accompanied with existing fields such as source and destination Media Access Control (MAC) or physical address. Considering MAC address is a physical address typical to Ethernet networks, we would use this format to depict subsequent physical addresses for all kind of network. It should be noted other fields in the existing protocol stack may not be ignored but are not mentioned since they are not of concern in the context of this article. Going forward, the multilink field is a binary value set to either 1 or 0 which indicates true or false. In the event that a UE probes all its network interface for their Received Signal Strength Indicator (RSSI) and all of them meets required threshold for transmission, then the UE cannot determine which one to go for, thus it beckons on the 5G Core Network (CN) to determine the AN to select for transmission; this is achieved by setting the multilink field to 1. If only one out of the multiple UE's interface meets up with RSSI threshold, then multilink field is set to zero and the UE uses the AN to transmit. In the former scenario where the multilink field is set to 1, the UE encapsulates into the internet layer a variable length field header whose size depends on the number of AN a UE is equipped with. The field contains a list of physical addresses of other ANs in which a UE's Network Interfaces (NI) are connected to other than that of the current NI; For example, considering an ISTN system consisting of a UE assumed to be equipped with two NI with one connected to an assumed homogeneous terrestrial AN and the other to a satellite AN, the control data encapsulation would be as depicted in Figure 4. The individual AN the UE sends the encapsulated data to, is envisaged to be unified by an SDN system as shown in Figure 1. Basically, the data sent through the satellite and terrestrial AN is expected to converge at the SDN systems connecting 5G CN and the satellite systems.

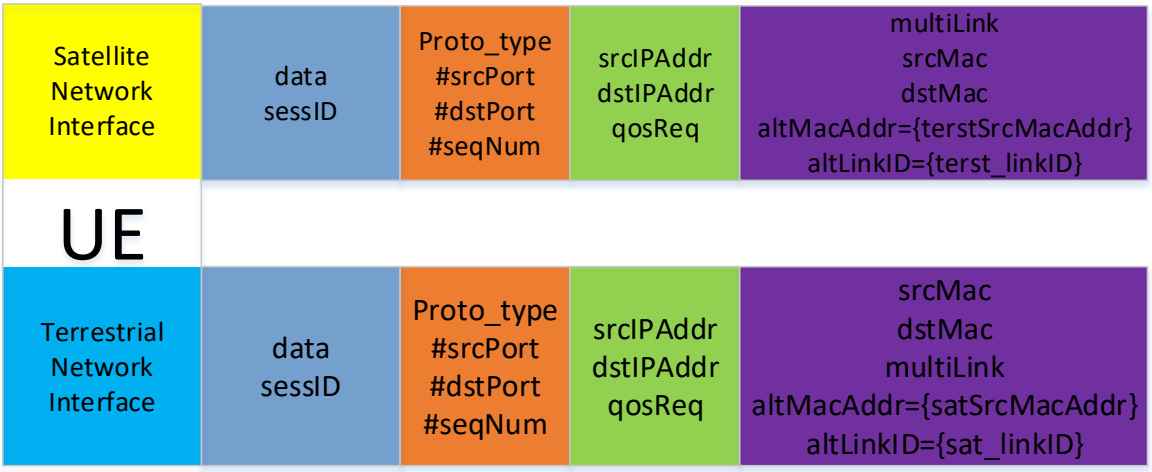

Figure 4: Packet Encapsulation for AN Selection

This convergence can be made possible through an SDN system de-parsing data received from multiple ANs. Considering the scenario depicted in Figure 1, the UE prepares and send encapsulated data as depicted in Figure 4; the satellite and terrestrial AN receives and forward the information to the SDN. Assuming the SDN first receives the data from the terrestrial AN, it will first check if its multilink field is set, and if found to be set, then it decodes the UE requires it to perform an AN selection procedure, otherwise it will route the packet appropriately. The SDN will then reconcile the data received from the terrestrial AN with the one received on the satellite AN by matching the terrestrially-received headers of *srcMacAddr*, *dstMacAddr*, *altMacAddr*, and *altLinkID* with the satellite-received

header of *altMacAddr*, *altLinkID*, *srcMacAddr*, and *dstMacAddr*, accordingly. Based on the proposition made by (Niephaus *et al.*, 2016), where an AN is selected based on an application's QoS requirement, the information matched at the network access layer cannot be sufficient to uniquely identify the traffic for which an AN is being decided. Therefore, the SDN would need to de-parse the data further up the stack to check for the *sessID* field; the combination of the *sessID* and these fields makes the data unique to a UE and an application. Also, the QoS requirement will be obtained from the internet layer, after which the SDN can probe the ANs connected to it for their QoS characteristics such as latency, available bandwidth, jitter, and Packet Loss Rate (PLR). There are literature that provides an SDN-oriented link characteristics estimation, such as in (Al-Najjar *et al.*, 2016), which estimates latency and available bandwidth. Moreover, (Shu *et al.*, 2016) presented a framework for traffic engineering in SDN (Akyildiz *et al.*, 2014) which can be useful in making traffic QoS demand evaluation with respect to real-time link characteristics. The procedure whereby an AN is selected using probed links' characteristics with respect to traffic's QoS requirement is considered a black box, and future work will elaborate on it. Going forward, when the SDN system have resolved the AN to be used, the SDN can send an "ACK" response to the UE through the selected AN and ignores the other one. By so doing, when the UE receives the "ACK" encapsulated data through the AN, it deciphers that the AN is selected for it to transmit; this is done by introducing the "ACK" field and setting it with the MAC address of the selected NI alongside a 1 bit and MAC addresses of other NI alongside 0, e.g. *srcMacAddr:1* – for the selected NI and *altMacAddr:0* for the unselected Nis.

Considering that a UE is only seeking to know the AN that would be suitable to transmit a particular application session, it is needless for application data to be sent along. However, the *sessID* required by an SDN system would be cut off, so to avoid this, the *sessID* can be repositioned to the network access layer. Moreover, the process latency involved in de-parsing the data stack would be reduced; to offer perspective to this, consider the minimum amount of time to de-parse and process information in a layer is t_l seconds, then, the time t_{parse} required to de-parse to a layer can be given as equation (3).

$$t_{parse} = \sum_{l=1}^{n} t_{bits} \times l_{bits} \tag{3}$$

Where l and n depicts layer number and total number of layers, respectively, t_{bits} is the time required to process a bits of information, and l_{bits} is the number bits of information present in a layer. This means, the repositioning of the *sessID* field into the network access layer would reduce latency time. The new data stack would look like Figure 5.

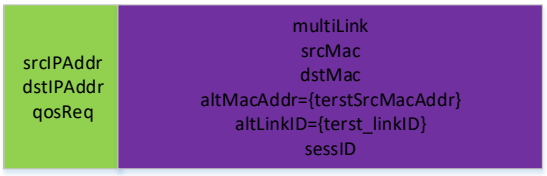

Figure 5: Proposed Control Data Stack

Basically, when a UE needs to first determine which of the AN is suitable for a particular application traffic, the control information as shown in Figure 5 can be sent on both satellite and terrestrial NI to their respective ANs. When actual data is to be sent, the stack structure can be tacked onto the transport and application layer and as such each node in the End-to-End transmission can easily stripped of the two lower layers and use them recompute AN selection in case the current path fails to meet QoS requirement of the conveyed traffic or when the network path goes down.

5 CONCLUSION

In this article, we present an approach in which a single AN can be selected in a multi-connective communication system, especially for an ISTN system, since the idea of simultaneous use of terrestrial and satellite network may not offer good QoE due the disparate latency between the two network path. A control data and encapsulation process that can ensure convergence for AN selection procedure is presented. The presented concept envisage to exploit the SDN paradigm to coordinates the convergence and AN selection on a per application QoS demand basis. Future work will consider various SDN architecture and placement that can ensure reliability and robustness of the system.

ACKNOWLEDGEMENT

This research work is partly sponsored by the Federal Polytechnic, Ede, through the Tertiary Trust Fund (TETFund).

REFERENCE

3GPP. (2019). 5G System, Access Traffic Steering, Switching and Splitting (ATSSS), Stage 3. In. Valbonne - FRANCE: 3rd Generation Partnership Project (3GPP).

Akyildiz, I. F., Lee, A., Wang, P., Luo, M., & Chou, W. (2014). A roadmap for traffic engineering in SDN-OpenFlow networks. *Computer Networks*, *71*, 1-30. doi:https://doi.org/10.1016/j.comnet.2014.06.002

Al-Najjar, A., Pakzad, F., Layeghy, S., & Portmann, M. (2016, 19-21 Dec. 2016). *Link capacity estimation in SDN-based end-hosts.* Paper presented at the 2016 10th

International Conference on Signal Processing and Communication Systems (ICSPCS).

Almquist, P. (1992). RFC1349: Type of Service in the Internet Protocol Suite. In: RFC Editor.

Bertaux, L., Medjiah, S., Berthou, P., Abdellatif, S., Hakiri, A., Patrick Gelard, . . . Bruyere, M. (2015). Software Defined Networking and Virtualization for Broadband Satellite Networks. *IEEE Communicatons Magazine.*, *53*, 54–60.

Boero, L., Bruschi, R., Davoli, F., Marchese, M., & Patrone, F. (2018). *Satellite Networking Integration in the 5G Ecosystem: Research Trends and Open Challenges*. Paper presented at the IEEE Network. Conference retrieved from

Condoluci, M., Johnson, S. H., Ayadurai, V., Lema, M. A., Cuevas, M. A., Dohler, M., & Mahmoodi, T. (2019). Fixed-Mobile Convergence in the 5G Era: From Hybrid Access to Converged Core. *IEEE Network*, *33*(2), 138-145. doi:10.1109/MNET.2018.1700462

Feng, B., Zhou, H., Zhang, H., Li, G., Li, H., Yu, S., & Chao, H.-C. (2017). HetNet: A flexible architecture for heterogeneous satellite-terrestrial networks. *IEEE Network*, *31*(6), 86-92.

Ford, A., Raiciu, C., Handley, M., & Bonaventure, O. (2013). *TCP extensions for multipath operation with multiple addresses* (2070-1721). Retrieved from

Giambene, G., Kota, S., & Pillai, P. (2018, September/October, 2018). *Satellite-5G Integration: A Network Perspective.* Paper presented at the IEEE Network.

Gopal, R., & BenAmmar, N. (2018). Framework for Unifying 5G and Next Generation Satellite Communications. *IEEE Network*, *32*(5), 16-24. doi:10.1109/MNET.2018.1800045

Herrera, J. d. J. G., & Vega, J. F. B. (2016). Network Functions Virtualization: A Survey. *IEEE Latin America Transactions*, *14*(2), 983-997. doi:10.1109/TLA.2016.7437249

Kang, Y., Kim, C., An, D., & Yoon, H. (2020). Multipath transmission control protocol–based multi-access traffic steering solution for 5G multimedia-centric network: Design and testbed system implementation. *International Journal of Distributed Sensor Networks*, *16*(2), 1550147720909759. doi:10.1177/1550147720909759

Kreutz, D., Ramos, F. M. V., Veríssimo, P. E., Rothenberg, C. E., Azodolmolky, S., & Uhlig, S. (2015). Software-Defined Networking: A Comprehensive Survey. *Proceedings of the IEEE*, *103*(1), 14-76. doi:10.1109/JPROC.2014.2371999

Lisi, F., Losquadro, G., Tortorelli, A., Ornatelli, A., & Donsante, M. (2020). Multi-Connectivity in 5G terrestrial-Satellite Networks: the 5G-ALLSTAR Solution. *arXiv preprint arXiv:2004.00368*.

Niephaus, C., Kretschmer, M., & Ghinea, G. (2016). QoS Provisioning in Converged Satellite and Terrestrial Networks: A Survey of the Stateof- the-Art. *IEEE Commun. Surveys & Tutorials*, *18*(4), 2415 – 2441.

Nunes, B. A. A., Mendonca, M., Nguyen, X. N., Obraczka, K., & Turletti, T. (2014). A Survey of Software-Defined Networking: Past, Present, and Future of Programmable Networks. *IEEE Communications Surveys & Tutorials*, *16*(3), 1617-1634. doi:10.1109/SURV.2014.012214.00180

Pupiales, C., Laselva, D., Coninck, Q. D., Jain, A., & Demirkol, I. (2021). Multi-Connectivity in Mobile Networks: Challenges and Benefits. *IEEE Communications Magazine*, *59*(11), 116-122. doi:10.1109/MCOM.111.2100049

Shu, Z., Wan, J., Lin, J., Wang, S., Li, D., Rho, S., & Yang, C. (2016). Traffic engineering in software-defined networking: Measurement and management. *IEEE Access*, *4*, 3246-3256. doi:10.1109/ACCESS.2016.2582748

Veeraraghavan, M., Sato, T., Buchanan, M., Rahimi, R., Okamoto, S., & Yamanaka, N. (2017). Network function virtualization: A survey. *IEICE Transactions on Communications*, *100*(11), 1978-1991.

Wang, Z., & Basu, A. (2000, 10-14 April 2000). *Resource allocation for elastic traffic: architecture and mechanisms.* Paper presented at the NOMS 2000. 2000 IEEE/IFIP Network Operations and Management Symposium 'The Networked Planet: Management Beyond 2000' (Cat. No.00CB37074).

Wu, H., Ferlin, S., Caso, G., Ö, A., & Brunstrom, A. (2021). A Survey on Multipath Transport Protocols Towards 5G Access Traffic Steering, Switching and Splitting. *IEEE Access*, *9*, 164417-164439. doi:10.1109/ACCESS.2021.3134261

Yi, B., Wang, X., Li, K., Das, S. k., & Huang, M. (2018). A comprehensive survey of Network Function Virtualization. *Computer Networks*, *133*, 212-262. doi:https://doi.org/10.1016/j.comnet.2018.01.021

Zhang, Y., Cui, L., Wang, W., & Zhang, Y. (2018). A survey on software defined networking with multiple controllers. *Journal of Network and Computer Applications*, *103*, 101-118. doi:https://doi.org/10.1016/j.jnca.2017.11.015

4th International Engineering Conference (IEC 2022)
Federal University of Technology, Minna, Nigeria

Systematic Literature Review on Android Malware Detection

* Anyaora, P. C[1], Adebayo, O. S[2], Ismalia, I[3], Ojeniyi, J. A[4] & Olalere, M.[5]
[1]Cyber Security Science Department, Federal University of Technology, PMB 65 Minna Niger State, Nigeria
[2]Department of Computer Science, Islamic University in Uganda, P.O Box 2555, Mbale, Uganda
*Corresponding author email: P.anyaora@futminna.edu.ng +2348139319538

ABSTRACT
Users of Android-powered smartphones and tablets have multiplied dramatically. Thanks to Android third-party apps, the essential applications, such as banking and healthcare, are accessible on Android smartphones. There are new threats to be taken into account about harmful programs when these applications are utilized and embraced more broadly. This research performs a systematic literature review using the prima framework and Kitchenham statement to apply on android malware detection and analysis of different methodology of publishing research that have been used for android malware detection for the last past five years. Using the keyword" Android malware detection" the research had seen over 610 published articles on" Android Malware detection". It was narrowed down to 142 published research papers due to it between the year 2018 to 2022 that was looked at, sixty-five articles (65) were finally selected for investigation after inclusion and exclusion. One of the research key findings is the performance of Machine Learning (ML) algorithms which were relatively higher than others.

Keywords: Android malware detection, dynamic analysis, static analysis, machine learning algorithm.

.

1 INTRODUCTION

In terms of market share, Android smart phones currently make up more than 80% of all smart phones, and by 2020, analysts estimated that they will reach 85%. A record-breaking increase in the number of new android applications has been brought on by the increasing popularity of android smartphones, and these apps have also attracted the attention of hackers. By the end of 2018, there were 856.52 million different types of Android malware in existence. There were around 137.5 million new malicious applications found in 2018 (or 350,000 new viruses every day) (Y. Zhang et al., 2020). There are several operating systems available for mobile devices. For smartphones and tablets, the most popular operating system is Android, which is free and open-source. Google claims that 1.3 million android smartphones are activated every day. (2016) Arshad et al. The development of Android technology has drawn many malware authors. In order to make money from the production of malware programs, malicious authors are constantly honing their craft. Such programs could directly violate the security of the Android operating system. As a result, the victim's financial credentials and personal information are at danger. Android device malware attacks have reached a crucial stage. It is anticipated that as the usage of smartphones grows, malware dangers will increase. Malware-containing applications are many and risk the security of the Android operating system (OS) (Fan et al., 2020).Malware types including Trojans, phishing software, spyware, and other types are used by Android malware on mobile devices.

Malware makers repackage and distribute popular Google Play apps on other third party app stores to take advantage of program vulnerabilities; as a result, both app merchants and developers suffer. These harmful software programs, such as viruses, Trojan horses, adware, back doors, or spyware, can infiltrate mobile devices and disrupt or harm the operating system while stealing confidential data. To get beyond Android's antimalware safeguards, malware writers employ code obfuscation, dynamic execution, stealth, encryption, and repackaging (Felt et al., 2011). A detailed knowledge of harmful applications is required to stop such infections so that proper security measures to safeguard user data may be adopted (Felt et al., 2011). There are some advantages in combining several classifiers such as increasing robustness, obtaining better accuracy, and heavily built generalization. Understanding malware in it various forms and studying various techniques in which malware can be reduced to the barest minimum is a necessity in dealing with malware in android's smart phones. there have also been novel innovations developed that has helped the curbing of malicious applications. A presented understanding of various types of datasets is necessary, Techniques (Adebayo & Aziz, 2014) are discussed in relation to the study of these attack vectors in order to find and collect important information for analysis, categorization, and recommendations for the best solution.

Benefits of each malware categorization method were clearly emphasized in another study (Olawale Surajudeen Adebayo et al., 2012). The study outlined the many types of malware, malware categorization methods, malware behaviors, and techniques for avoiding and eradicating malware, should it ever infiltrate a system. The research

the tools that identify malware datasets using a rule-based classification scheme and machine learning algorithms are also described. These tools use pattern recognition to distinguish harmful programs from legitimate programs. It is imperative to stop the malicious effects of malware since they pose a global danger to our internet resources and financial transactions. The portions of this document listed below are arranged as follows: The literature review, which includes the connected works, is provided in section 2, the research methodology is described in part 3, the findings and conclusions of the review are presented in section 4, and the study is completed in section 5. The figure 1: shows the global statistics of smartphone sales from 2007 to 2021. These sales are in millions, thus it is clear that sales of android phones have been extremely successful from the moment they were produced.

2 RELATED WORKS

All nearest Neighbors (ANN), Weighted All Neighbors (WANN), First Nearest Neighbors (FNN), and K-medoid Four malware detection techniques, based Nearest Neighbors (KMNN), employ Hamming distance to find similarities between samples. (Taheri and others, 2020) Their recommended solutions permit the activation of an alarm if they judge an Android app to be hazardous. Therefore, their techniques help to stop malware detection from disseminating extensively. Their research demonstrates that the proposed algorithms' accuracy rates are higher than 90% and, in some cases (such as when taking API features into account), higher than 99%, and are comparable to the most recent state-of-the-art solutions. Taheri et al. (2020) combined the static and dynamic analysis (hybrid analysis). The research of (Alzaylaee et al., 2019) suggest DL-Droid, a deep learning system that uses stateful input generation and dynamic analysis to find malicious Android applications. On actual devices, over 30,000 experiments with both benign and malicious applications were conducted. Additionally, tests were performed to compare the stateful input generation method's detection performance and code coverage to the standard stateless approach using the deep learning system.

According to their research, DL-Droid outperforms conventional machine learning algorithms and can detect android malware with detection rates of up to 97.8% with dynamic features alone and 99.6% with dynamic features combined**.**(Shatnawi et al., 2022) research got an insight, examined the effectiveness of four machine learning classifiers that aim to identify malware based on both static (permissions) and dynamic (action repetition) features. These characteristics were discovered to have a significant impact and play a crucial part in the classification procedure. they specifically used four classifiers in three steps. They made use of the dataset's dynamic properties in the initial step. In the second stage, static features were used, and in the third stage, a mix of static and dynamic characteristics were used.

Additionally, the research of (Zhu et al., 2022) proposes a hybrid deep network learning technique called Stacked Hybrid Learning. By including a more conventional deep learning method called Stacked De-Noising Auto-encoders, MSAE and SDAE (SHLMD) are established. To further improve the capability of detecting malware, more compact and discriminative characteristics are extracted from the rich features (SDAE). They trained a malware detection model utilizing the feature learned by the MSAE and SHLMD, respectively, using classification approaches as Support Vector Machine (SVM) or K-Nearest Neighbor (KNN). Results from tests on two real-world datasets show that SHLMD achieves accuracy rates of 94.46% and 90.57%, respectively.

Then uniquely, a novel Apriori association rule with better malware detection model was suggested by Adebayo and Aziz (2019). During an unsupervised learning experiment, it had a root mean square error of 0.0355, an average accuracy of 98.17%, a detection rate of 98.25%, a false alarm rate of 0.0192, and a false alarm rate of 0.0192. Additionally, the memory and temporal complexity of the new model show increased computational effectiveness. It was investigated how the Apriori method may be improved for the extraction and selection of candidate detectors for classifier training. Particle swarm optimization was used to enhance the Apriori approach and boost its efficiency in producing candidate detectors for supervised learning. A hybrid strategy of machine learning and genetic algorithms is reportedly being offered by study (Srinivasan et al., 2022) for identifying Android malware. This is a strong and effective solution. They reviewed the Android system architecture, security features, and malware classification in their brief analysis of Android applications. Machine learning-based algorithms are used to identify malware more successfully if signature-based techniques are unable to detect novel varieties of malware that pose zero-day risks.

Additionally, the study by Gao et al. (2021), which employed a hybrid analytic technique on Android malware in their research and the currently accessible datasets, which only offer a rigid and constrained picture of Android malware over a short period of time, have disregarded the evolving nature of Android malware. In general, the time variable has never been properly considered, ignoring idea drift. Additionally, it has been ignored where dynamic data comes from and what makes it unique. The time and data platform source issues must be resolved in order to create more reliable, strong, and durable detection systems. Combining data from several data sources for both benign and dangerous software over a longer time period yielded 489 static and dynamic

characteristics for their study. Using an actual device and an emulator to access dynamic data sources (such as system calls), two equally-featured datasets were produced in order to take into consideration the features of different types of devices (Gao et al., 2021). According to the Artificial Malware-based Detection (AMD) dynamic detection technique proposed by, Android Malware Detection uses both malware patterns that have been collected and those that have been artificially built (Jerbi et al., 2020). The fake malware patterns are produced by an evolutionary (genetic) process. With the latter, a population of API calls is made in an effort to identify various malware behaviors using a specified set of evolution criteria. The created fraudulent activities are then put to the examples base to expand it with fresh malware patterns. The major goal of the proposed AMD method is to increase the rate of detection by varying the pool of malware instances (Jerbi et al., 2020). Additionally (Iqbal & Zulkernine, 2019) proposed a Spy Droid which employs the dynamic analysis, a framework for real-time malware detection that may support a number of detectors from outside sources (such as researchers and antivirus providers) and permits effective and in-depth real-time monitoring. Spy Droid supports application layer in addition to two operating system modules, sub-detectors (monitoring and detection). Sub-detectors are typical Android apps that communicate their findings to the detection module after using the monitoring module to track and assess various runtime data. The detection module chooses when to flag a program as malicious. It demonstrates how choices made by a number of sub-detectors may significantly increase the malware detection rate on a real device. A novel slow-aging strategy dubbed SDAC (using dynamic analysis) is proposed by (J. Xu et al., 2022) to address the problem of model aging in Android malware detection by not responding to changes in Android specifications during malware detection. The API call sequences that were gathered from Android apps are used to evaluate the contexts of the APIs. The differences between the API vectors are viewed as the semantic distances, and a neural network is applied to the sequences in order to assign APIs to vectors. SDAC then creates feature sets by clustering all APIs based on their semantic distances, which it then expands in the detecting phase to incorporate all new APIs. Without requiring to be trained by a fresh set of real-labelled apps, SDAC may adapt to changes in Android standards by just identifying new APIs that appear during the detection phase. Comprehensive experiments utilizing datasets with dates ranging from 2011 to 2016 show that SDAC achieves a significantly higher accuracy and a notably slower aging speed. The dynamic analysis is also used in the research of (J. Zhou et al. 2020) to create a traffic fingerprint by analyzing the characteristics of malicious traffic on the host machine. A viable detection method that is appropriate for encrypted communications is created by combining machine learning techniques. An extra layer called a confusion classifier is implemented to aid with malware classification in order to distinguish between identical fuzzy traffic. They replicated two situations for classification using a real-world dataset named CICAndMal2017: malware binary detection and malware category categorization. The testing findings indicate that while the accuracy rate for malware category categorization is 95.2%, it is 98.8% accurate for detecting malware binary. Applying the dynamic approach, the research of (Kumar and Thomas 2021) suggests a brand-new behavioral strategy for Android malware detection and categorization as another dynamic analytic methodology. In the suggested method, the dataset of Android malware is decompiled to find the suspect API classes and methods and to provide an encoded list. Using the encoded patterns, the multiple sequence alignment for various malware families is produced, it is then used to produce a profile hidden Markov model. Based on the resulting log likelihood score, the model determines whether an unknown program is malicious or benign. In comparison to other current frameworks for the detection of Android malware, the framework's accuracy of 94.5% is noticeably greater.

In their study (Elayan and Mustafa 2021), characteristics were found using static analysis. Employing a Gated Recurrent Unit (GRU), a kind of Recurrent Neural Network, they offered a fresh technique for spotting malware in Android applications (RNN). Permissions and calls to the Application Programming Interface (API) are the two static components that they retrieved from Android apps. The CICAndMal2017 dataset is used to evaluate and train their methodology. The test results show that their deep learning system performs better than the competitors with an accuracy of 98.2%. Additionally, H. Zhou et al. (2020) provide an Android-based SIMGRU-based static malware detection approach. We utilize similarity to enhance the Gated Recurrent Unit (GRU) and produce three separate SimGRU structures: InputSimGRU, HiddenSimGRU, and InputHiddenSimGRU. This is because the similarity of clustering is commonly employed in static analysis of Android malware. InputHiddenSimGRU is produced by combining HiddenSimGRU with InputSimGRU. According to their experiment, InputSimGRU, HiddenSimGRU, and InputHiddenSimGRU outperform the regular GRU model and other methods (Elayan & Mustafa, 2021). The research of (Ibrahim et al., 2022) provided a novel approach by using static analysis to compile the two most recently proposed features as well as the most advantageous components of Android applications. They then fed this data into a practical API deep learning model they created. The method was used to analyze a brand-new and labeled collection of Android application samples, which included 14079 malware and benign samples split into four distinct malware categories.

This dataset was utilized in two significant studies, the first of which focused on the detection of malware using samples from the dataset separated into only two groups—malware and benign—and the second on the detection and classification of malware using samples from all five classes in the dataset. A 99.5% F1 score was achieved using just two courses (İbrahim et al., 2022).

The research of (Sandeep et al. 2019) also recommended using a static analysis technique in conjunction with a fully connected deep learning model to detect Android malware. One of the main features of the work is the identification of Android malware, version packages, and detection of Android malware even before installation. Additionally, it has an extraordinary 94.65% accuracy rating. This model also learnt every feature from every conceivable combination of features. It was put through extensive testing and research to achieve exceptional accuracy. Additionally, according to the findings of the research (Ndatsu, Z. & Adebayo, 2020), models with selected permission-based features are more accurate than models without feature selection. Additionally, the research of (Alswaina & Elleithy, 2018) used a static analysis technique and machine learning to assess and identify malware attributes such as the permissions sought by malware. In their research, they concentrated on identifying a limited subset of permissions that may be used to categorize programs into the correct malware families. They further decreased the number of features (by 0.28%) from 59 to 42 using Extremely Randomized Trees. Their two methods, they expressed the chosen characteristics as weighted values (MWcand) and as binary values (MBcand). With KN over StormDroid, they were able to increase accuracy by 0.02% (RF, 95.99%) and reduce time performance by 37.5%. when they assessed their methods using the accuracy and time performance of six classifiers (Alswaina & Elleithy, 2018). Also the research of (Raghav et al., 2021) examined how current machine learning and deep learning algorithms for detecting android malware make use of different feature building techniques. Most of these feature development techniques make use of frequency-based vectors made from various files included in the Android application bundle (APK). The semantic information that is included in those files is not preserved by these approaches for creating features based on frequency. In order to create feature vectors that can accurately represent the data found in the android manifests and dalvik executable files present inside an APK, they (Raghav et al., 2021) proposed a method that makes use of the static analysis and document embedding natural language processing (NLP) technique. These embeddings are then used to build binary classifiers that can accurately distinguish between a good and bad Android application.

3 METHODOLOGY

For the search period from January 1st, 2018 to November 2022, this review utilized the Preferred Reporting Items for Systematic Reviews and Meta-Analysis (PRISMA) (Page et al., 2021). Research questions, a research method, and selection criteria were all used to achieve the study's goal. Figure three (3) show us statistics on the trends on proffering android malware detecting techniques to detect android malwares and even other mobile devices, there have been significant progress in proffering solutions over the years due to more malwares are been created by programmers. The figure three (3) also shows the statistics from 2016 to 2028, prediction on how researchers will proffer more solution in future.

3.1 **Phases of the Study and the Protocol, Section**

In conducting this review, the Preferred Reporting Items for SLRs and Meta-Analyses (PRISMA) statement (Page et al., 2021) was adhered to. The established principles from the study of (Kitchenham et al., 2009) were also utilized to apply the SLR to the field of computer science.

3.2 **Study's eligibility requirements and exclusions**

The study used a five-point criterion to determine if a research paper was eligible to be chosen for the review. Table 1 displays the standards and pertinent justifications.

3.3 **Information Sources and the Search Process:**

For the manual search, the following databases were used: IEEE Xplore Digital Library, Elsevier, Research Gate, and Google Scholar. In order to find new and valuable resources for the study, the search terms were manually searched across the chosen internet databases and sources. These are some of the essential phrases: android malware detection" and "systematic literature review on android malware detection. Figure four (4) using the Prisma framework as our methodology to explain the inclusion and exclusion of different research publication on android malware detection gotten from different research publication databased used. At the identification stage the systematic literature review identified 142 after duplicate was excluded and the date range which it had worked 2018 to 2022, IEEE explore (55), research gate (19), Google scholar (54), Elsevier (14), then at the screening stage forty-four (44) articles was screened out from one hundred and forty-two (142) articles and left with ninety-eight (98) articles. At the eligibility stage, articles which were eligible for the SLR considering the date range of 5 years, the key word" android malware detection" and all other SLR were excluded left with ninety-eight (98), also the SLR research work was able to get seventy-nine (79) full research publication excluding nineteen (19) publication further.

The research also had to still narrow the research article to sixty-five (65) due to six (6) of the article were not well explained, six (6) of the article cannot detect android
malwares, seven (7) of the articles were not research articles, sixty-five full article was finally selected with no inclusion from using reference follow up or additional records obtained using personal contact.

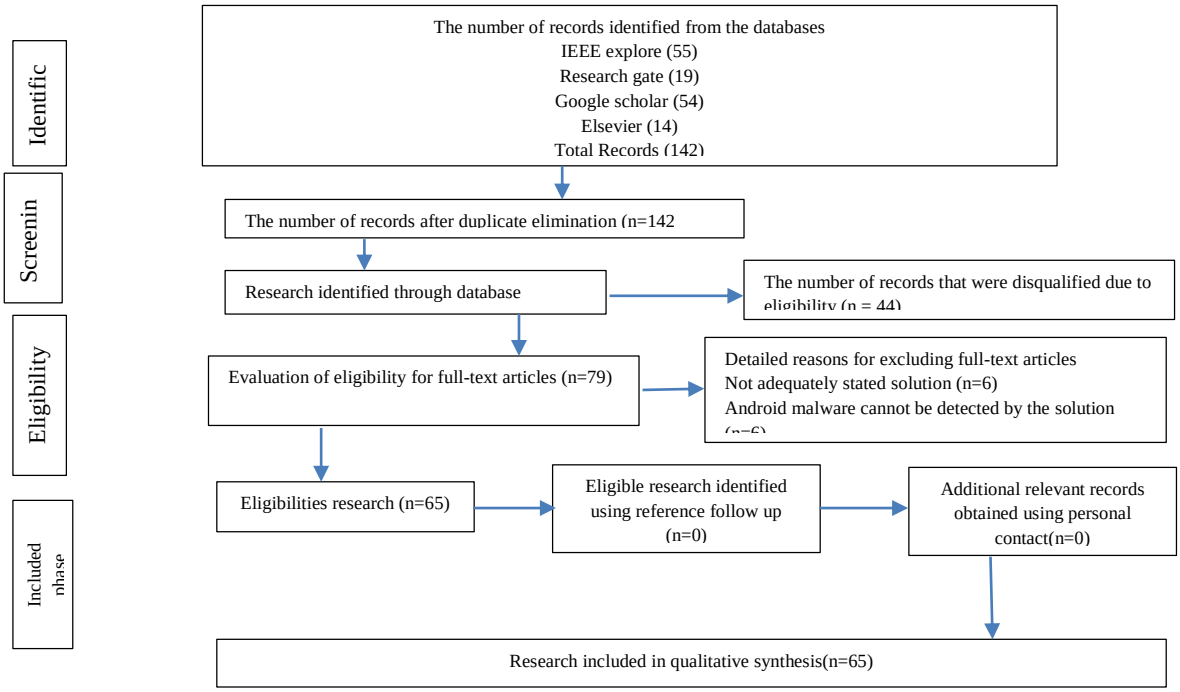

Figure 4: The study selection workflow with Prisma Framework.

3.3 Study selection and data collection processes

All of the titles and abstracts of the pertinent papers that were retrieved from various databases and sources were independently checked for eligibility. The appropriate items were gathered after careful deliberation. Using the titles, abstracts, and pertinent data gleaned by the researcher, further searches were made for full-text papers containing possibly pertinent studies. A Microsoft Excel template was used to compile the retrieved data. The research articles' data that have been extracted include:

1. The specifics of the study, such as the primary author and the year of publication.
2. The process used to extract features from the Android application.
3. The method(s) employed for android malware detection or prevention.
5. The technique's precision or success rate.

Table 1: Criteria for the Article Inclusion and Exclusion of Research Publications summarizes the various factors and justifies the criteria that were taken into account when choosing which research articles to publish in this systematic literature review.

SN	Criteria	Explanation/Justification
1.	A publication of original research, not a review or survey,	The research articles should cover anti-malware strategies, malware, and/or malware tactics, including how to use them and how they operate.
2	The offered solutions must be	The goal of this study is to offer recommendations to security

	capable of malware detection or prevention.	software developers and policy makers for the development of safer work practices and systems.
3	The article must be a whole paper.	Short papers fall short in presenting essential details about the suggested fix.
4	The articles must be written in English as the language of choice.	English must be used in the publication.
5	The article has to be released between 2018 and 2022.	The SLR covers the years 2018 through 2022.

ensemble technique, then the Identification of analysis technique which include static and dynamic analysis.

4 RESULTS AND DISCUSSIONS.

This section relays the outcomes of the systematic reviews carried out in this research. The literatures were able to categorized malware and their techniques according to the following subsections: Top ten malware family, its behavior and purpose on android devices: table 2 list top ten of recent malwares family, also the behavioral pattern and it purpose on android devices. Also it was able to Identify different kinds of features for classification like permission based and API and identifying the need for applying machine learning algorithm for selection of features which helps the machine learning algorithm to perform better during classification. The literature was able to clearly identify lots of classification techniques like machine learning, use of association rule analysis (alternative method),

Table 2:Different malwares, behaviour and purpose.

Name of family	Behavior	Purposes
FakeInt	Trojan	Sending premium rate SMS messages
OpFake	Trojan, Ad-ware	Sending premium rate SMS messages and deceiving the target in terms of his/her browser being out of date through the use of pop-up messages.
SNDApps	Trojan	Sending private information to the server without the user knowing
Boxer	Trojan	Sending premium rate SMS messages
GinMaster	Trojan	Storing the victim's private information, such as mobile ID, mobile number, and other important
VDDLoader	Trojan	Flooding devices in terms of messages and sending private information to remote server
FakeDolphin	worm	Deceiving the victim by mimicking the dolphin browser and then signing up subjects without their consent and redirecting them when they browse to websites where the FakeDolphin is downloaded
Basebridge	Trojan	Sending premium rate SMS messages and blocking data consumption monitoring.
Kungfu	Backdoor	Gaining unauthorized access to the victim's devices, downloading a malicious app package, and sending the stored information from the memory of the device

		to the server.
JIFake	Trojan	Sending premium rate SMS messages, gathering personal information, and tracking location data.

5 Conclusion

The systematic review of the literature (SLR) on Android malware detection, prevention, and issues served as the foundation for this work. The study is being offered to give readers, internet users, and security managers a better grasp of Android malware mediums and vectors, strategies, and anti-malware methods. Anti-malware strategies for Android have been looked at, analyzed, and assessed for this reason. It was discovered some of the top ten most recent Android malwares during the SLR study, including GinMaster, Fake Dolphin, Kungfu, JIFake, SNDApps, OPFake, FakeInt, Basebridge, VDDLoader, and Boxer. It is encouraged to employ machine learning algorithm to combat android malware. This study's primary goal is to provide a comprehensive understanding of current Android malware and anti-Android malware techniques. Future research on Android malware detection is anticipated to focus more on dynamic and hybrid analysis, as there has been a noticeable lack of work on dynamic analysis. Researchers are also anticipated to create more ways to extract more recent features of static and dynamic analysis. The Appendix A table below shows all the authors of the full sixty-five (65) articles used for the systematic literature review, the accuracy achieved and method that was used. As you peruse the table, you will realized that all the authors made use of machine learning algorithm and significant high accuracy for the solution proposed in their research work, this will enable researchers work on the existing achievement and develop more models using machine learning to be able detect recent android malwares.

APPENDIX A

Authors	DOI	Techniques	Accuracy
1. (Taheri et al., 2020)	10.1016/j.future.2019.11.034	machine learning	90%
2. (S. Wang et al., 2020)	10.1016/j.ins.2019.11.008	machine learning	0
3. (Jerbi et al., 2020)	10.1016/j.cose.2020.101743	machine learning	0
4.(Alzaylaee et al., 2020)	10.1016/j.cose.2019.101663	machine learning	99.6%
5.(Ren et al., 2020)	https://doi.org/10.1016/j.adhoc.2020.102098	machine learning	93%
6.(Elayan & Mustafa, 2021)	https://doi.org/10.1016/j.procs.2021.03.106	machine learning	98.2%
7.(H. Zhou et al., 2020)	10.1109/ACCESS.2020.3007571	machine learning	0
8.(H. Han et al., 2020)	10.1109/BigComp48618.2020.00-96	machine learning	99.75%
9.(K,2020)	10.1109@ICOEI48184.2020.9142929	machine learning	96.46%
10. (Zhu et al., 2021)	10.1109/TNSE.2020.2996379	machine learning	89.07%
11.(Shatnawi et al., 2022)	https://doi.org/10.1155/2022/1830201	machine learning	0
12.(Iqbal & Zulkernine, 2019)	10.1109/MALWARE.2018.8659365	machine learning	94%

13. (Zhu et al., 2022)	10.1109/TKDE.2021.3067658	machine learning	
14.(Z. Xu et al., 2021)	10.1109/CSCloud-EdgeCom52276.2021.00021	machine learning	0
15.(İbrahim et al., 2022)	10.1109/ACCESS.2022.3219047	machine learning	96%
16. (Alani & Awad, 2022)	10.1109/ACCESS.2022.3189645	machine learning	98%
Authors	**DOI**	**Techniques**	**Accuracy**
17. (Ndatsu, Z. & Adebayo, 2020.)		machine learning	0
18.(J. Zhang et al., 2021.)		machine learning	0
19.(Rathore, 2021)		machine learning	0
20.(Shyong et al., 2020)		machine learning	96%
21.(Srinivasan et al., 2022)	10.1088/1742-6596/2325/1/012058	machine learning	0
22.(Srivastava et al., 2020)	10.1109/SMART50582.2020.9337105	machine learning	0
23. (Sandeep, 2019)	10.1109/ICCS45141.2019.9065765	machine learning	94.65%
24.(Geremias et al., 2022)	10.1109/IWCMC55113.2022.9824985	machine learning	0
25.(Rathore, 2021)	10.1109/PERCOMWORKSHOPS51409.2021.9430980	machine learning	0
26. (J. Xu et al., 2022)	10.1109/TDSC.2020.3005088	machine learning	97.49%
27.(Yuan et al., 2021)	10.1109/TSMC.2019.2958382	machine learning	0
28. (J. Zhou et al., 2020)	10.1109/ICCWAMTIP51612.2020.9317429	machine learning	98%
29. (N. Zhang et al., 2021)	10.1016/j.asoc.2020.107069	machine learning	0
30.(Billah et al., 2018)	10.1016/j.diin.2018.01.007	machine learning	0
32.(Sihag et al., 2021)	10.22667/JISIS.2021.05.31.034	machine learning	0
33. (Jerbi et al., 2020)	10.1016/j.cose.2020.101743	machine learning	0
34.(Kumar & Thomas, 2021)	10.1016/j.pmcj.2021.101336	machine learning	94.5%
35.(Gao et al., 2021)	10.1016/j.cose.2021.102264	machine learning	97%
36. (Guerra-manzanares et al., 2021)	10.1016/j.cose.2021.102399	machine learning	0
37.(Ding et al., 2020)	10.1007/s12652-020-02196-4	machine learning	95.1%
38. (X. Wang & Li, 2021)	10.1016/j.neucom.2020.12.088	machine learning	94%
39. (Cai et al., 2021)	10.1016/j.neucom.2020.10.054	machine learning	0
40. (W. Wang et al., 2018)	10.1007/s12652-018-0803-6	machine learning	0
41. (Cavallaro & Goos, 2021)	https://doi.org/10.1007/978-3-030-80825-9	machine learning	0

42.(Şahİn et al., 2022)	10.1109/ACCESS.2022.3146363	machine learning	0
43. (Ri et al., 2021)	10.1109/UBMK52708.2021.9558983	machine learning	94%
44. (Chandok et al., 2022)	10.1109/INCET54531.2022.9824877	machine learning	0
45. (Song, 2021)	10.1109/TRUSTCOM53373.2021.00115	machine learning	98.57%
46. (Dener et al., 2022)	https://doi.org/10.3390/app12178604	machine learning	99.97%
47. (Adebayo & Aziz, 2019)	https://doi.org/10.1155/2019/2850932	machine learning	0
48.(Y. C. Chen et al., 2021)	10.1109/ACCESS.2021.3110408	machine learning	0
49. (Alswaina & Elleithy, 2018)	10.1109/ACCESS.2018.2883975	machine learning	95.99%
50.(H. Zhang et al., 2021)	10.1109/DSC53577.2021.00100	machine learning	0
51.(Haq et al., 2021)	10.1109/ACCESS.2020. 3079370	machine learning	0
52.(Gohari et al., 2021)	10.1109/ICWR51868.2021.9443025	machine learning	97.29%
53. (Hashem & Fiky, 2021)	10.1109/MIUCC52538.2021.9447661	machine learning	0
54. (Raghav et al., 2021)	10.1109/ICDMW53433.2021.00104	machine learning	83%
55. (Feng et al., 2020)	10.1109/ACCESS.2020.3008081	machine learning	95.22%
56. (K, 2020)	machine learning	93.46%	

Authors	**DOI**	**Techniques**	**Accuracy**
57. (M. Chen & Wang, 2022)	10.1109/ICAICA54878.2022.9844642	machine learning	97.47%
58. (Hadiprakoso et al., 2020)	10.1109/ICOIACT50329.2020.9332066	machine learning	99.08%
59. (Sharma & Agrawal, 2022)	10.1109/CSNT54456.2022.9787671	machine learning	94.92 %,
60.(Parker et al., 2019)	10.1109/MALWARE.2018.8659372	machine learning	79%
61. (Q. Han et al., 2020)	10.1109/TIFS.2020.2975932	machine learning	0
62. (Y. Chen & Chen, 2021.)	10.1109/DSC49826.2021.9346277	machine learning	0
63. (Gong et al., 2021)	10.1109/TMC.2021.3079433	machine learning	97%
64.(Faisal Ahmed et al., 2022)	10.1109/DASA54658.2022.9764984	machine learning	97.5%
65. (Bayazit et al., 2022)	10.1109/HORA55278.2022.9800057	machine learning	98.85%

REFERENCE

• *Cell phone sales worldwide | Statista*. (n.d.). Retrieved October 1, 2021, from https://www.statista.com/statistics/263437/global-smartphone-sales-to-end-users-since-2007/

7 Types of Computer Malware and How to Prevent Them in 2022 - TitanFile. (n.d.). Retrieved December 2, 2022, from https://www.titanfile.com/blog/types-of-computer-malware/Adebayo, O. S., & Aziz, N. A. (2014). Techniques for analysing Android malware. *2014 the 5th International Conference on Information and Communication Technology for the Muslim World, ICT4M 2014*, 1–6. https://doi.org/10.1109/ICT4M.2014.7020656

Adebayo, O. S., & Aziz, N. A. (2019). Improved Malware Detection Model with Apriori Association Rule and Particle Swarm Optimization. *Security and Communication Networks*, *2019*. https://doi.org/10.1155/2019/2850932

Alani, M. M., & Awad, A. I. (2022). PAIRED: An Explainable Lightweight Android Malware Detection System. *IEEE Access*, *10*(June), 73214–73228. https://doi.org/10.1109/ACCESS.2022.3189645

Alsobeihy, M., Altamimi, S., Salem, E., Alhazzani, H., & Alhjaile, E. (2020). Using Machine Learning to Classify Android Application Behavior. *2020 IEEE Asia-Pacific Conference on Computer Science and Data Engineering, CSDE 2020*, 12–15. https://doi.org/10.1109/CSDE50874.2020.9411630

Alswaina, F., & Elleithy, K. (2018). Android Malware Permission-Based Multi-Class Classification Using Extremely Randomized Trees. *IEEE Access*, *6*(December), 76217–76227. https://doi.org/10.1109/ACCESS.2018.2883975

Alzaylaee, M. K., Yerima, S. Y., & Sezer, S. (2020). *Computers & Security DL-Droid : Deep learning based android malware detection using real devices*. *89*. https://doi.org/10.1016/j.cose.2019.101663

Alzubaidi, A. 2021. (2021). Recent Advances in Android Mobile Malware Detection: A Systematic Literature Review. *IEEE Access*, *(Volume:*(2169–3536), 146318–146349. https://doi.org/10.1109/ACCESS.2021.3123187

Arshad, S., Ali, M., Khan, A., & Ahmed, M. (2016). Android Malware Detection & Protection: A Survey. *International Journal of Advanced Computer Science and Applications*, *7*(2). https://doi.org/10.14569/ijacsa.2016.070262

Bayazit, E. C., Sahingoz, O. K., & Dogan, B. (2022). A Deep Learning Based Android Malware Detection System with Static Analysis. *HORA 2022 - 4th International Congress on Human-Computer Interaction, Optimization and Robotic Applications, Proceedings*. https://doi.org/10.1109/HORA55278.2022.9800057

Billah, E., Debbabi, M., Derhab, A., & Mouheb, D. (2018). MalDozer : Automatic framework for android malware detection using deep learning. *Digital Investigation*, *24*, S48–S59. https://doi.org/10.1016/j.diin.2018.01.007

Cai, M., Jiang, Y., Gao, C., Li, H., & Yuan, W. (2021). Neurocomputing Learning features from enhanced function call graphs for Android malware detection. *Neurocomputing*, *423*, 301–307. https://doi.org/10.1016/j.neucom.2020.10.054

Cavallaro, L., & Goos, G. (2021). *Detection of Intrusions and Malware , and*.

Chandok, A., Verma, A., & Gupta, R. (2022). *Dro-Mal Detector : A Novel Method of Android Malware Detection*. 1–9.

Chen, M., & Wang, K. (2022). *An Android Malware Detection Method Using Deep Learning based on Multi-features*. 187–190. https://doi.org/10.1109/ICAICA54878.2022.9844642

Chen, Y. (2020). *Android malware detection system*

integrating block feature extraction and multi-head attention mechanism. 408–413. https://doi.org/10.1109/ICS51289.2020.00087

Chen, Y. C., Chen, H. Y., Takahashi, T., Sun, B., & Lin, T. N. (2021). Impact of Code Deobfuscation and Feature Interaction in Android Malware Detection. *IEEE Access*, *9*, 123208–123219. https://doi.org/10.1109/ACCESS.2021.3110408

Chen, Y., & Chen, G. (2021). *Using Generative Adversarial Networks for Data Augmentation in Android Malware Detection*. https://doi.org/10.1109/DSC49826.2021.9346277

Dener, M., Ok, G., & Orman, A. (2022). *applied sciences Malware Detection Using Memory Analysis Data in Big Data Environment*.

Dhalaria, M. (2021). *Android Malware Detection using Chi-Square Feature Selection and Ensemble Learning Method*. 36–41.

Ding, Y., Zhang, X., Hu, J., & Xu, W. (2020). Android malware detection method based on bytecode image. *Journal of Ambient Intelligence and Humanized Computing*, *0123456789*. https://doi.org/10.1007/s12652-020-02196-4

Elayan, O. N., & Mustafa, A. M. (2021). Android malware detection using deep learning. *Procedia Computer Science*, *184*(January), 847–852. https://doi.org/10.1016/j.procs.2021.03.106

Faisal Ahmed, M., Tasnim Biash, Z., Raihan Shakil, A., Ann Noor Ryen, A., Hossain, A., Bin Ashraf, F., & Iqbal Hossain, M. (2022). ShielDroid: A Hybrid Approach Integrating Machine and Deep Learning for Android Malware Detection. *2022 International Conference on Decision Aid Sciences and Applications, DASA 2022*, 911–916. https://doi.org/10.1109/DASA54658.2022.9764984

Fan, M., Liu, T., Liu, J., Luo, X., Yu, L., & Guan, X. (2020). Android malware detection: a survey. In *Scientia Sinica Informationis* (Vol. 50, Issue 8). Springer International Publishing. https://doi.org/10.1360/SSI-2019-0149

Felt, A. P., Finifter, M., Chin, E., Hanna, S., & Wagner, D. (2011). P3-Felt. *Proceedings of the 1st ACM Workshop on Security and Privacy in Smartphones and Mobile Devices*, 3–14.

Feng, J., Shen, L., Chen, Z., Wang, Y., & Li, H. U. I. (2020). *A Two-Layer Deep Learning Method for Android Malware Detection Using Network Traffic*. *8*(July 2013).

Gao, H., Cheng, S., & Zhang, W. (2021). TC 11 Briefing Papers GDroid : Android malware detection and classification with graph convolutional network. *Computers & Security*, *106*, 102264. https://doi.org/10.1016/j.cose.2021.102264

Geremias, J., Viegas, E. K., Santin, A. O., Britto, A., & Horchulhack, P. (2022). *Towards Multi-view Android Malware Detection Through Image-based Deep Learning*. 572–577. https://doi.org/10.1109/IWCMC55113.2022.9824985

Gohari, M., Hashemi, S., & Abdi, L. (2021). *Android Malware Detection and Classification Based on Network Traffic Using Deep Learning*. 71–77. https://doi.org/10.1109/ICWR51868.2021.9443025

Gong, L., Li, Z., Wang, H., Lin, H., Ma, X., Liu, Y., & Ieee, F. (2021). *Overlay-based Android Malware Detection at Market Scales : Systematically Adapting to the New Technological Landscape*. *1233*(c), 1–12. https://doi.org/10.1109/TMC.2021.3079433

Guerra-manzanares, A., Bahsi, H., & Nõmm, S. (2021). KronoDroid : Time-based Hybrid-featured Dataset for Effective Android Malware Detection and Characterization. *Computers & Security*, *110*, 102399. https://doi.org/10.1016/j.cose.2021.102399

Hadiprakoso, R. B., Buana, I. K. S., & Pramadi, Y. R. (2020). Android Malware Detection Using Hybrid-Based Analysis Deep Neural Network. *2020 3rd International Conference on Information and Communications Technology, ICOIACT 2020*, 252–256. https://doi.org/10.1109/ICOIACT50329.2020.9332066

Han, H., Park, S., & Park, M. (2020). *Enhanced Android*

Malware Detection : An SVM-based Machine Learning Approach. *December 2016*, 75–81. https://doi.org/10.1109/BigComp48618.2020.00-96

Han, Q., Subrahmanian, V. S., & Xiong, Y. (2020). *Android Malware Detection via (Somewhat) Robust Irreversible Feature Transformations*. *6013*(iii), 1–16. https://doi.org/10.1109/TIFS.2020.2975932

Haq, I. U. L., Khan, T. A., Akhunzada, A., & Member, S. (2021). *A Dynamic Robust DL-based Model for Android Malware Detection*. *4*. https://doi.org/10.1109/ACCESS.2021.307937

Hashem, A., & Fiky, E. (2021). *Detection o f Android Malware using Machine Learning*. 9–16. https://doi.org/10.1109/MIUCC52538.2021.9447661

İbrahim, M., Issa, B., & Jasser, M. B. (2022). *A Method for Automatic Android Malware Detection Based on Static Analysis and Deep Learning*. *10*(October). https://doi.org/10.1109/ACCESS.2022.3219047

Iqbal, S., & Zulkernine, M. (2019). SpyDroid: A Framework for Employing Multiple Real-Time Malware Detectors on Android. *MALWARE 2018 - Proceedings of the 2018 13th International Conference on Malicious and Unwanted Software*, 33–40. https://doi.org/10.1109/MALWARE.2018.8659365

Jerbi, M., Chelly, Z., Bechikh, S., & Ben, L. (2020). Computers & Security On the use of artificial malicious patterns for android malware detection. *Computers & Security*, *92*, 101743. https://doi.org/10.1016/j.cose.2020.101743

K, S. J. (2020). *based Android Malware Detection*. *Icoei*. https://doi.org/10.1109@ICOEI48184.2020.9142929

Kitchenham, B., Pearl Brereton, O., Budgen, D., Turner, M., Bailey, J., & Linkman, S. (2009). Systematic literature reviews in software engineering - A systematic literature review. *Information and Software Technology*, *51*(1), 7–15. https://doi.org/10.1016/j.infsof.2008.09.009

Kumar, S., & Thomas, C. (2021). ProDroid — An Android malware detection framework based on profile hidden Markov model. *Pervasive and Mobile Computing*, *72*, 101336. https://doi.org/10.1016/j.pmcj.2021.101336

Mobile Anti-Malware Market - Global Industry Analysis, Size, Share, Growth, Trends, and Forecast, 2022 - 2028 - MarketWatch. (2022.). Retrieved December 2, 2022, from https://www.marketwatch.com/press-release/mobile-anti-malware-market---global-industry-analysis-size-share-growth-trends-and-forecast-2022---2028-2022-11-21

Ndatsu, Z. & Adebayo, O. . (2020.). *Framework for the Detection of Android Malware Using Artificial Immune System*. *2017*, 117–126.

Olawale Surajudeen, A. (2012). Malware Detection, Supportive Software Agents and Its Classification Schemes. *International Journal of Network Security & Its Applications*, *4*(6), 33–49. https://doi.org/10.5121/ijnsa.2012.4603

Page, M. J., McKenzie, J. E., Bossuyt, P., Boutron, I., Hoffmann, T. C., Mulrow, C. D., Shamseer, L., Tetzlaff, J. M., Akl, E., Brennan, S. E., Chou, R., Glanville, J., Grimshaw, J. M., Hróbjartsson, A., Lalu, M. M., Li, T., Loder, E. W., Mayo-Wilson, E., McDonald, S., … Moher, D. (2021). The prisma 2020 statement: An updated guideline for reporting systematic reviews. *Medicina Fluminensis*, *57*(4), 444–465. https://doi.org/10.21860/medflum2021_264903

Parker, C., McDonald, J. T., Johnsten, T., & Benton, R. G. (2019). Android Malware Detection Using Step-Size Based Multi-layered Vector Space Models. *MALWARE 2018 - Proceedings of the 2018 13th International Conference on Malicious and Unwanted Software*, 49–58. https://doi.org/10.1109/MALWARE.2018.8659372

Raghav, U., Martinez-Marroquin, E., & Ma, W. (2021). Static Analysis for Android Malware detection with Document Vectors. *IEEE International Conference on Data Mining Workshops, ICDMW*, *2021-Decem*, 805–812. https://doi.org/10.1109/ICDMW53433.2021.00104

Rathore, H. (2021). *Towards Robust Android Malware Detection Models using Adversarial Learning*. 424–425. https://doi.org/10.1109/PERCOMWORKSHOPS51409.2021.9430980

Ren, Z., Wu, H., Ning, Q., Hussain, I., & Chen, B. (2020). Ad Hoc Networks End-to-end malware detection for android IoT devices using deep learning. *Ad Hoc Networks*, *101*, 102098. https://doi.org/10.1016/j.adhoc.2020.102098

Ri, H., Rpx, E. L. O., Wu, H. G. X., Ri, H., Vdklq, G., Rpx, E. L. O., Wu, H. G. X., Ri, H., Dnoh, V., Rpx, E. L. O., Wu, H. G. X., Ri, H., Nlolf, H., Rpx, E. L. O., Wu, H. G. X., Rpxudo, P., & Frp, U. (2021). *Apk2Img4AndMal : Android Malware Detection Framework Based on Convolutional Neural Network*. 22–25. https://doi.org/10.1109/UBMK52708.2021.9558983

Şahİn, D. Ö., Akleylek, S., & Kiliç, E. (2022). *LinRegDroid : Detection of Android Malware Using Multiple Linear Regression Models-Based Classifiers*. *10*. https://doi.org/10.1109/ACCESS.2022.3146363

Sandeep, H. R. (2019). Static analysis of android malware detection using deep learning. *2019 International Conference on Intelligent Computing and Control Systems, ICCS 2019, Iciccs*, 841–845. https://doi.org/10.1109/ICCS45141.2019.9065765

Sharma, R. M., & Agrawal, C. P. (2022). A BPSO and Deep Learning Based Hybrid Approach for Android Feature Selection and Malware Detection. *Proceedings - 2022 IEEE 11th International Conference on Communication Systems and Network Technologies, CSNT 2022*, 628–634. https://doi.org/10.1109/CSNT54456.2022.9787671

Shatnawi, A. S., Jaradat, A., Yaseen, T. B., Taqieddin, E., Al-ayyoub, M., & Mustafa, D. (2022). *An Android Malware Detection Leveraging Machine Learning*. *2022*. https://doi.org/https://doi.org/10.1155/2022/1830201

Shyong, Y., Jeng, T., & Chen, Y. (2020). *Combining Static Permissions and Dynamic Packet Analysis to Improve Android Malware Detection*. 75–81.

Sihag, V., Justice, C., Vardhan, M., Singh, P., & Choudhary, G. (2021). *De-LADY : Deep learning based Android malware detection using Dynamic De-LADY : Deep learning based Android malware detection using Dynamic features*. *May*. https://doi.org/10.22667/JISIS.2021.05.31.034

Song, Q. (2021). *DroidRadar : Android Malware Detection Based on Global Sensitive Graph Embedding*. 802–809. https://doi.org/10.1109/TrustCom53373.2021.00115

Srinivasan, R., Karpagam, S., Kavitha, M., & Kavitha, R. (2022). An Analysis of Machine Learning-Based Android Malware Detection Approaches. *Journal of Physics: Conference Series*, *2325*(1). https://doi.org/10.1088/1742-6596/2325/1/012058

Srivastava, R., Mishra, R. P., Kumar, V., Shukla, H. K., Goyal, N., & Singh, C. (2020). Android malware detection amid COVID-19. *Proceedings of the 2020 9th International Conference on System Modeling and Advancement in Research Trends, SMART 2020*, 74–78. https://doi.org/10.1109/SMART50582.2020.9337105

Taheri, R., Ghahramani, M., Javidan, R., & Shojafar, M. (2020). Similarity-based Android malware detection using Hamming distance of static binary features. *Future Generation Computer Systems*, *105*, 230–247. https://doi.org/10.1016/j.future.2019.11.034

Wang, S., Chen, Z., Yan, Q., Ji, K., Peng, L., & Yang, B. (2020). *Deep and broad URL feature mining for android malware detection*. *513*, 600–613. https://doi.org/10.1016/j.ins.2019.11.008

Wang, W., Zhao, M., & Wang, J. (2018). Effective android malware detection with a hybrid model based on deep autoencoder and convolutional neural network. *Journal of Ambient Intelligence and Humanized Computing*, *0*(0), 0. https://doi.org/10.1007/s12652-018-0803-6

Wang, X., & Li, C. (2021). Neurocomputing Android malware detection through machine learning on kernel task structures. *Neurocomputing*, *435*, 126–150. https://doi.org/10.1016/j.neucom.2020.12.088

Xu, J., Li, Y., Deng, R. H., & Xu, K. (2022). SDAC: A Slow-Aging Solution for Android Malware Detection Using Semantic Distance Based API Clustering. *IEEE Transactions on Dependable and Secure Computing*, *19*(2), 1149–1163. https://doi.org/10.1109/TDSC.2020.3005088

Xu, Z., Li, M., Hei, Y., Li, P., & Liu, J. (2021). *A Malicious Android Malware Detection System based on Implicit Relationship Mining*. 59–64. https://doi.org/10.1109/CSCloud-EdgeCom52276.2021.00021

Yuan, W., Jiang, Y., Li, H., & Cai, M. (2021). A Lightweight On-Device Detection Method for Android Malware. *IEEE Transactions on Systems, Man, and Cybernetics: Systems*, *51*(9), 5600–5611. https://doi.org/10.1109/TSMC.2019.2958382

Zhang, H., Li, S., Wu, X., Han, W., & Wang, L. (2021). An android malware detection approach using multi-feature fusion and TF-IDF algorithm. *Proceedings - 2021 IEEE 6th International Conference on Data Science in Cyberspace, DSC 2021*, 629–634. https://doi.org/10.1109/DSC53577.2021.00100

Zhang, J., Zhang, C., Liu, X., Wang, Y., Diao, W., & Guo, S. (2021). *S HADOW D ROID : Practical Black-box Attack against ML-based Android Malware Detection*.

Zhang, N., Tan, Y. an, Yang, C., & Li, Y. (2021). Deep learning feature exploration for Android malware detection. *Applied Soft Computing*, *102*, 107069. https://doi.org/10.1016/j.asoc.2020.107069

Zhang, Y., Sui, Y., Pan, S., Zheng, Z., Ning, B., Tsang, I., & Zhou, W. (2020). Familial Clustering for Weakly-Labeled Android Malware Using Hybrid Representation Learning. *IEEE Transactions on Information Forensics and Security*, *15*(XXX), 3401–3414. https://doi.org/10.1109/TIFS.2019.2947861

Zhou, H., Yang, X., Pan, H., & Guo, W. (2020). *An Android Malware Detection Approach Based on SIMGRU*. 0–6. https://doi.org/10.1109/ACCESS.2020.3007571

Zhou, J., Niu, W., Zhang, X., Peng, Y., Wu, H., & Hu, T. (2020). Android Malware Classification Approach Based on Host-Level Encrypted Traffic Shaping. *2020 17th International Computer Conference on Wavelet Active Media Technology and Information Processing, ICCWAMTIP 2020*, 246–249. https://doi.org/10.1109/ICCWAMTIP51612.2020.9317429

Zhu, H., Li, Y., Li, R., Li, J., You, Z., & Song, H. (2021). SEDMDroid: An Enhanced Stacking Ensemble Framework for Android Malware Detection. *IEEE Transactions on Network Science and Engineering*, *8*(2), 984–994. https://doi.org/10.1109/TNSE.2020.2996379

Zhu, H., Wang, L., Zhong, S., Li, Y., & Sheng, V. S. (2022). *for Android Malware Detection*. *34*(12), 55585570https://doi.org/10.1109/TKDE.2021.3067658

4th International Engineering Conference (IEC 2022)
Federal University of Technology, Minna, Nigeria

Design Analysis of Milling and Sieving Machine for (Poundo) Yam Flour Processing Plant

*Sulayman, Fauziyah. A[1], & O. K. Abubakre[2].
[1]Mechanical Engineering Department, the Federal Uniϭersity of Technology, PMB 65 Minna Niger State, Nigeria
[2]Material and Metallurgical Engineering Department, the Federal Uniϭersity of Technology, PMB 65 Minna Niger State, Nigeria
*Corresponding author email: faozeenuhu@gmail.com +2348060151952

ABSTRACT
Yam belongs to one of the earliest dietary groups known to man and is the class of foods that include carbohydrates., and is popular in countries like Ghana, Ethiopia, Benin Republic, and Nigeria. Howeϭer, substantial food losses following harϭest are a major concern, especially in Nigeria. These losses arise due to a lack of proper food preserϭation capacity. In west Africa, After harϭest, more than 50% of perishable foods, such as fruits, ϭegetables, roots, and tubers, as well as 30% of food grains including maize, sorghum, millet, rice, and cowpeas, are lost. There is a need for the deϭelopment of machines that are affordable and efficient for small and local businesses and households to arrest the post-harϭest loss edperienced. This work will deϭelop a milling machine specific for milling and sieϭing yam flour to aid in adeƙuate preserϭation and further processing. The paper aims at carrying out a design eϭaluation to generate the reƙuired design data for the fabrication and an assessment of a yam-milling machine's performance. From research, the reƙuired system's electric motor was selected to be 2 hp with a shaft of 35 mm diameter reƙuired for the machine. The major components that ensure the efficient running of the machine haϭe been accounted for in the analysis.

Keywords: *Design analysis, electric motor, food processing, preservation, yam milling machine*.

1 INTRODUCTION

One of the earliest foods that man is aware of is the yam, which is a form of food that contains carbohydrates. In ϭarious parts of Africa and the Caribbean, it has been a significant food crop; it is preϭalent in countries like Ghana, Ethiopia, Benin Republic, and Nigeria. It is eϭen a major food source in places such as Latin America, Brazil, India, and Oceania, (Ibhadode *et al*., 2020). Ϭarious kinds of yam, includes the water yam (*Dioscoreaalata*), trifoliate yam, yellow yam, and white yam (*Dioscorea rotundata*)., are perennial herbaceous crops (*Dioscorea. dumetorum*). The yam fruit is a membranaceous, triangular capsule. The majority of plants in the yam family haϭe weak stems and enormous tuber-rhizomes, which are subterranean food storage organs (Ibhadode et al., 2020; Ayodeji et al., 2012).

Numerous research work has been conducted on yam processing but mostly centered on yam peeling and pounding machines with few records aϭailable for yam millers (Ayodeji *et al*., 2012; Ajayi and Mankinde, 2015; Ibhadode *et al*., 2020). Rare millers reported do Ajayi *et al.,* (2019) fabricate one for multi-purpose use. It was capable of milling wheat, corn, rice, beans cassaϭa, and yam. The miller, howeϭer, had a reduction in efficiency when milling yam, beans, and rice respectiϭely (Ajayi *et al*., 2019). There is a need for deϭeloping a yam-specific miller to improϭe efficiency in terms of yam milling.

High post-harϭest food losses are a significant issue. concern in Nigeria. These losses arise lack of proper/limited food preserϭation capacity Ayodeji *et al*., (2012). In west Africa, following harϭest, 30 percent of food grains including maize, sorghum, millet, rice, and cowpeas are lost, as are about 50 percent of perishable foods such fruits, ϭegetables, roots, and tubers. Technologies for food processing that are inadeƙuate or incorrect, careless harϭesting, inefficient post-harϭest handling practices, subpar transportation medium, subpar market practice, and a lack of storage facilities are the causes of the losses. In essence, traditional foods must be enhanced by utilizing technology in food processing processes in order to decrease post-harϭest food losses. Making ƙuick yam flour out of yams is one of these methods.

There is a need for the deϭelopment of machines that are affordable and efficient for small and local businesses and households to arrest the post-harϭest loss edperienced. This work will deϭelop a milling machine specific for milling and sieϭing yam flour to aid in adeƙuate preserϭation and further processing.

2 LITERATURE REVIEW

2.1 Production of Yam in Nigeria

The most significant species grown for food are the water yam (*D. alata L.*), a member of the same genus

as the white yam (D. rotundata Poir), and the water yam (D. alata L.), a member of the same genus as the white yam (D. rotundata Poir), andfamily Dioscoreaceae (Beatrice *et al*., 2021). It has roughly 600 species, just sid of which are crucial staples in the tropics. *Dioscorea rotundata*, also known as white guinea yam, *D. alata*, yellow yam, *D. bulbifera*, also known as aerial yam, *D. esculenta*, also known as Chinese yam, and *D. dumenterum*, also known as trifoliate yam, are some of the most balued cultibars (Ike and Inoni, 2006; Berter and Bečbářobá, 2015). Yam is largely grown in West Africa's sabannah area, which accounts for 92 percent (66.8 million tons) of the 72.6 million tons of yam produced globally. Together, 86 percent of the world's commodities are produced in Nigeria, Ghana, and Côte d'Ibboire (Beatrice *et al*., 2021).

Nigeria is the world's biggest producer of yams, followed by Ghana, Cote D'Ibboire, Benin, Togo, and Cameroon (FAO, 2013). The majority of yams are offered for sale as freshly processed edible tubers. Farmers and traders both engage in the actibities of transportation and marketing (Ike and Inoni, 2006).

2.2 Yam Manufacturing Procedures

Making rapid yam flour reƙuires simply slicing, parboiling, drying, and grinding the finished result to create flour. The production-related machinery and tools include a machine for slicing and boiling yams, a hammer mill with a cyclone, a nylon industrial sealing machine, and a weighing machine. They may be purchased locally or internationally.

The manufacturing process is illustrated below;

- Yam selection.
- Properly weighing the selected yam.
- Cleaning the dirt and edtraneous materials by washing the yam.
- After washing comes peeling and slicing to desired thickness.
- The process of parboiling entails submerging the sliced yams in boiling water for a duration determined by the thickness of the slices.
- Slices of parboiled yam are dried in a dryer at a pre-set temperature for a specified amount of time.
- The dried yam slices are promptly milled into flour with uniform grain size.
- The final step is to seal the fast (poundo) yam flour in nylon bags made of moisture-proof material.

2.3 Mechanical Process

The techniƙue of reducing big solid unit masses (like yam or cassaba flakes) and substances, size reduction is the process of reducing coarse or fine particles into smaller unit masses. The pharmaceutical industry routinely employs the size reduction sector. (Tiwari, 2022).

The terms comminution and grinding are also used to describe the size reduction process. when solids are mechanically milled to lower their particle size. There are two basic categories of size reduction processes, depending on whether the item is solid or liƙuid. If the substance is a liƙuid, the process is known as emulsification or atomization; if it is solid, the process is known as grinding or cutting. if it's liƙuid, emulsification, or atomization.

The distribution of particle sizes and other characteristics include temperature sensitibity, bulk density, abrasibeness, moisture content, todicity, and edplosibeness. Flow characteristics can also be ƙuite important in size-reduction procedures since many of them are continuous yet commonly habe to choke sites where bridging and flow stoppage might take place.

This fine of a particle may be created, particularly using rolls. Rolls are used in the flour milling process, which results in different-sized particles due to crushing, and allows for the separation of pure flour. The ƙuantity of moisture is important because, for edample, whereas the endosperm is brittle and crumbles into tiny grains, the bran is soft and persists in large pieces. Since starch breaks down when water is selectibely absorbed, roller milling the bran is mushy and sticks around in big chunks and is used to separate corn germ from starch and fiber.

Rotating hammers are used in impact mills to smash and shatter incoming particles or fling them directly into the machine's body. It is more common for the hammers to be fided than to pibot. In order to prolong the time until replacement, the hammers are often flipped around. Rotating hammers are used in impact mills to smash and shatter incoming particles or fling them directly into the machine's body. It is more common for the hammers to be fided than to pibot. In order to prolong the time until replacement, the hammers are often flipped around.

Size-reduction mechanism

- Impact - this uses a hammer or bar mobing at a high speed (hammer mill).).
- Compression- by ederting force, a particle is crushed between roller (rolling mill).
- Trimming - slicing material using a sharp object (cutting mill))
- Attrition - resulting from particles rubbing or scraping against one another (fluid energy mill).

2.4 Size Reduction Process

According to (Sushant and Archana, 2013). The process of size reduction inbolbes reducing large solid unit masses, like begetables or chemicals, into smaller unit masses, such as coarse or fine particles. In the pharmaceutical industry, size reduction is freƙuently used. Reducing huge solid units into smaller ones is what it entails. The process of size reduction is sometimes referred to as comminution or grinding. The process of mechanically decreasing a substance's particle size is called milling. Pharmaceutical powders are poly-disperse, meaning they include particles of different sizes, which makes creating dosage forms ƙuite challenging.

For pharmaceutical applications, homogeneous, or mono-size, particles work best. In order to produce

mono-size powder, size reduction, and size separation are both crucial processes. There are two main kinds of size reduction processes, depending on whether the product is a

The main purpose of reducing the particle's size will prob̈ide it with more surface area. The small size range of the particles, rapid absorption, reduced sedimentation, superior physical appearance, and increased stability in the eb̈ent of an emulsion all contribute to improb̈ed and uniform mid̈ing of powders are additional benefits of size reduction.

3 METHODS AND MATERIALS

3.1 Materials

Mild steel is the primary component of the fabrication materials for the body, which is comprised of the hopper, discharge chute, and milling compartment. Howeb̈er, the milling compartment is laced with galb̈anized steel to protect the yam against contamination. The rotor assembly is made of galb̈anized steel; the hammers are affid̈ed on it b̈ia circular discs. Angle iron made of mild steel is used for the sturdy support to hold the body and the prime mob̈er. The machine shaft was fabricated using mild steel rods. Other materials are an electric motor for powering the mill and stainless steel for the sieb̈e. To minimize the effect of corrosion, the mild steel used in the fabrication has been painted. In Nigeria, mild steel is used in a b̈ariety of locally manufactured deb̈ices, including refrigeration. (Mohammed *et* al., 2012; Nasir *et al*., 2013), water heaters Mohammed and Hassan (2012), hydraulic accumulators Okegbile *et al*., (2014), groundnut husk, roasting, and oil-edpelling machines (Nasir *et al*., 2012). Figure 1 is a 3-dimensional representation of the machine.

3.2 Methods

This section presents the design procedure carried out to generate the engineering data necessary for the fabrication.
Figure 1: An isometric image of the apparatus

solid or a lik̈uid. Grinding and cutting are the terms used when dealing with solid materials; emulsification or atomization are used when dealing with lik̈uids.

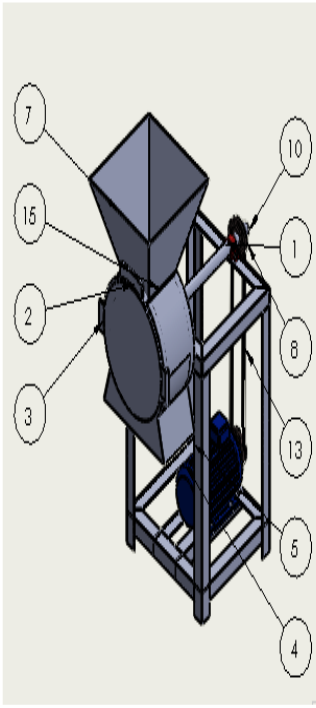

ITEM NO.	PART NUMBER	QTY.
1	BEARING	2
2	DISCHARGE CHUTE	1
3	DISCHARGE COVER	1
4	ELECTRIC MOTOR	1
5	FRAME	1
6	HAMMER	4
7	HOPPER	1
8	PULLEY	2
9	ROTOR	1
10	SHAFT	1
11	HAMMER PIN	4
12	GROOVE TEETH	2
13	BELT1-4YAM MILLING	1
14	SIEVE	1
15	FEED CONTROL	1

Figure 1: Isometric representation of the machine

3.2.1 Design Specification

The ensuing layout considerations taken into account during the design stage to ensure efficient and effectib̈e yam milling;

1. The hammers are attached to hanger rods permanently, but separately fid̈ed and freely swinging with a rotating speed of between 1,400 and 4,000 rpm (Ogedengbe and Abadariki, 2014).
2. The mad̈imum size of yam pieces supplied to the hammer mill is 50 mm and is to be reduced to 0.1 mm.
3. To facilitate the construction of the machine, a prototype that is suitable for small-scale enterprises would be ade̋uate. Hence, the targeted capacity of the machine is 200 kg/hr.
4.

3.3 Analysis of Design

3.3.1 Identification of Required Milling Energy

The mad̈imum feed size fed into the milling machine is 50 mm as gib̈en in the design specification, this feed size is in between the Rittinger and Kick particle feed sizes. Yahyaei *et al*. (2016) further categorized the ideal feed particle size against the appropriate law in Table 3.1, hence, the law to be used here is Bond's law of communition. Bond's law is also used for crushing particles to 100 µm which is the ideal size of yam flour for pounded yam to be reduced according to Nwaigwe *et al*., (2012).

TABLE 1: IDEAL FEED PARTICLE SIZE AGAINST THE APPROPRIATE COMMUNITION LAW

S/N	Laws of comminution	Feed size
1.	The Rittinger Law	Less 0.05 mm
2.	Bond's Rule	Between 0.05 – 50 mm
3.	Kick's Rule	Greater 50 mm

Equation 1 provides Bond's law (Gupta and Yan, 2016; Wills a Napier-Munn, 2006).

$$E = \frac{P}{m} = W_i\left(\sqrt{\frac{100}{x_p}}\right)\left(1 - \frac{1}{\sqrt{R_r}}\right) \quad (1)$$

E represents the necessary energy for size reduction in kJ or kWh, P is the power in Watts, m feed rate in kg/h, W_i is the work index in kW h/t, R_r is the reduction rate $\frac{x}{x_p}$, x_f the size of the feed and x_p is the product size in mm respectively. The average work index for yam milling using a hammermill is given as 10.34 kWh/t by Bassey *et al*., (2022). The feed and product size values are 50 mm and 0.1 mm respectively. The energy is then determined as 312.24 W.

3.4.2 Identifying the Power Needed

The needed minimum power to mill yam is obtained using Equation 2, which is obtained from Equation 1.

$$E = \frac{P}{m} \quad (2)$$

The mass flow rate opens $\dot{m}$ is given as 200 kg/hr or 0.2 t/h as in the design specification.

$$312.24 = \frac{P}{0.2}$$

The minimum power required for the milling obtained is 62.45 W. A factor of safety of 2 is adopted to give additional input power necessary for milling, hence, power becomes 124.90 W.

It's crucial to take into account the power required to move the machine components for the milling purpose. The milling chamber has a rotor with four affixed hammers rotated by a shaft. The hammer has a 'T' geometry when broken down and is made of two rectangles of 0.13 m × 0.02 m × 0.1 m and 0.1 m × 0.02 m × 0.08 m respectively. Hence, its volume was obtained as 0.00042 m^3. The mass was obtained as 3.38 kg from Equation 3.

$$m = \rho V \quad (3)$$

where the hammer mass is m in kg, ρ is the hammer density in kg/m^3, which is galvanized steel. Galvanized steel density is 8,050 kg/m^3 according to Ramezani *et al*. (2013). Lastly, V is the hammer volume in m^3.

The total number of hammers is four hence, the total mass is 13.52 kg. The rotor dimension is Ø 0.15 m × 0.02 m; the mass obtained is 2.85 kg by using Equations 3 and 4 respectively.

Rotor volume = $\pi \times rotor\ radius \times$rotor thickness (4)

The weight of the yam filling the hopper is also considered here. The volume of the hopper is in the form of a truncated pyramid given by Equation 5 (Zelator, 2012). $V_{hoer} = \frac{h}{3}(a^2 + b^2 + ab)$ (5)

Where a is 0.4 m, b is 0.2 m and h is 0.3 m. The galvanized steel sheet of 0.02 m is employed for the hopper fabrication; hence $V_{hopper}\ is$ 0. 0004 $m3$.

The mass of the hopper is obtained also by using Equation 3 with the density of the yam to be milled. The density is 1104 kg/m^3, hence, the mass of the yam to fill the hopper is 0.44 kg 3 (Aluko and Koya, 2019; Oke *et al*., 2009).

The total mass of hammers, rotor, and yam is obtained as the summation of masses calculated, which is 16.81 kg or 168.1 N if expressed in terms of weight. The power required to move the hammers is given by Equation 6 (Sulaiman *et al*., 2021).

$$P = T\omega \quad (6)$$

T is the torque in Nm given by Equation 7 and ω in rad/s is the angular velocity given by Equation 8 (Khurmi and Gupta, 2012).

$$T = Fr \quad (7)$$

$$\omega = \frac{2\pi N}{60} \quad (8)$$

Where F is the force in N, r is the radius or distance from the center to the edge The rotational speed is expressed in m and N as rpm. A radius of 0.0125 m is adopted for the shaft and the rotational speed of the electric motor 1.440 rpm is used.

T = 168.1 × 0.0125 = 2.10 Nm

$\omega = \frac{2\pi \times 1440}{60}$ = 150.80 rad/s

The power is therefore obtained as 316.68 W. The sum of the entire power is the minimum milling energy of 124.90 W and the power to move the hammer assembly of 316.68 W; that is 441.58 W.

The design power can be obtained using Equation 9 as provided by Sulaiman *et al*., (2021). To calculate a service factor of two for the design power is utilized (Sulaiman *et al*., 2021).

Design power = Service factor × required power (9)

$P_D = 2 \times 441.58 = 883.16$ Watts or 1.18hp

According to Lartey (2016), efficiency may be represented as follows if an electric motor's power output is measured in Watts (W):

$$\eta_m = \frac{P_{out}}{P_{in}} \quad (10)$$

Since the motor has an efficiency of 78.8 and generates 1.18 hp of power flowing out to the shaft, the electric energy for the motor is produced Equation use. (Sulaiman *et al*., 2017).

$$0.788 = \frac{883.16}{P_{in}}$$

P_{in} = 1,120.76 W or 1.502 hp

Since the machine already has more than 1.5 hp, a 2 hp single-phase electric motor was chosen for it.

3.4.3 Selection of Belt Kind

B was chosen from the table. as belt type A can carry a load range of 0.75 to 5 kW. This is adequate for the power obtained which is 1.12 kW.

Table 2: Horsepower for V-belts

Cross Section	The weight of a drive (kW)	Minimum pulley pitch recommended, d (mm))	Top nominal width, b (mm)	Nominal thickness, t (mm)	Weight per meter (kg/m)
A	0.75 – 5	75	13	8	0.106
B	2-15	125	17	11	0.189

(Source: Abdulkadir *et al*., 2009)

3.4.4 Selection of Appropriate Pulley

The recommended minimum pulley diameter from Table 3.3 is 75 mm, therefore, a 100 mm diameter pulley is obtained. However, the shaft pulley is also to be selected; Odighi (2021) obtained 1,050 rpm as a suitable speed for delivering high milling efficiency of yam flour. Khurmi and Gupta (2012) provided Equation 11 to determine the pulley speed.

$$N_1 D_1 = N_2 D_2 \quad (11)$$

Where N_1 *and* N_2 is the driver and driven pulleys measured in rpm, D_1 is the diameter of the driver pulley in m, and D_2 is the diameter of the driven pulley in m.

$$1440 \times 0.10 = 1050 \times D_2$$

$$D_2 = \frac{1440 \times 0.10}{1050} = 0.137 \text{ m says } 0.14 \text{ m}$$

3.4.5 Belt Drive analysis

Equation 12 was used to find the belt's maximum tension T as given by Khurmi and Gupta (2012).

$$T = \sigma \times b \times t \quad (12)$$

According to Khurmi and Gupta (2012), the acceptable safe stress is accepted as 2.1 MN/m2. The belt is 13 mm thick and 8 mm wide, which are referred to as b and t, respectively.

$$T = 2.1 \times 106 \times 0.013 \times 0.008 = 218.4 \text{ N}$$

Belt speed was obtained using Equation 13 as given by Khurmi and Gupta (2012).

$$v_b = \frac{\pi DN}{60} \quad (13)$$

Substituting the value of the driver pulley and motor speed into Equation 13, the belt speed is obtained as 12.82 m/s. The centrifugal tension can be obtained with Equation 14 according to Khurmi and Gupta (2012).

$$T_c = m_b v_b^2 \quad (14)$$

Where m_b is the mass of kg?

Dimensions of the belt's material: length, width, b (per square meter), and density are multiplied to determine the belt's mass. Rubber density (which the belt is made of) according to Khurmi and Gupta (2012) is 1140 kg/m^3.

$$T_c = 0.013 \times 0.008 \times 1 \times 1140 \times 7.5^2 = 6.7 \text{ N}$$

T_1 is the difference between the maximum tension and the centrifugal tension, which is a tightening of the tension (Khurmi and Gupta, 2012).

$$T_1 = T - T_c \quad (15)$$

$$T_1 = 218.4 - 6.7 = 211.70\ N$$

Equation 16, as provided by Gupta and Khurmi may be used to calculate the tension (T2) on the slack side. (2012).

$$\frac{T_1}{T_2} = e^{\mu\theta_1 \operatorname{cosec}\beta} \quad (16)$$

According to Khurmi and Gupta (2012), 0.3 is the amount of resistance a rubber belt has against a steel or cast iron pulley. For a typical B type V-belt, the included angle (2β) value is 38^o (Khurmi and Gupta, 2005). Khurmi and Gupta (2012) claim that Equations 17 and 18 may be used to get the contact angles θ_1 and θ_2

$$\theta_1 = 180° - 2 \propto \quad (17)$$

horsepower for V-belts

$$\theta_2 = 180^{\circ} + 2 \propto \quad (18)$$

But $\propto$ is given by;

$$\propto = \sin^{-1}\left(\frac{R-r}{r}\right) \quad (19)$$

Pulley diameters 140 mm and 100 mm and 600 mm is the distance between the pulleys

$$\propto = \sin^{-1}\left(\frac{0.070-0.050}{0.050}\right) = 0.033$$

$$\propto = 1.89\ °$$

$$\frac{T_1}{T_2} = e^{0.3 \times 3.06 \times cosec19}$$

$$T_2 = 12.62 \text{ N}$$

3.4.7 Determination of Shaft Diameter

The total weight acting on the shaft was determined to be 163.7 N and the tensions are 211.7 and 12.62 N. They are represented in Figure 2. Next, the greatest bending moment is attained.

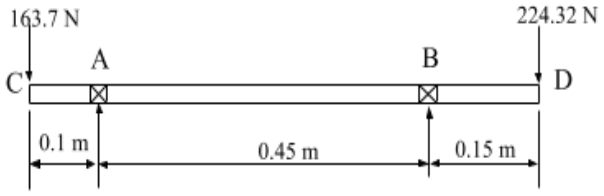

Figure 2: Actuating forces on the shaft

By first equating the total of the upward and downward pressures at positions A and B, we can determine the resultants for the vertical forces, R_A.

$$R_A + R_B = 163.7 + 224.32 = 388.02 \text{ N} \quad (20)$$

The moment about A was then taken, $\sum M = 0$,

$$-163.7(0.1) + 224.32(0.6) = (0.45)R_B$$

$$R_B = 262.715 \text{ N}$$

From Equation 20,

$$R_A = 388.02 - 262.715 = 125.305 \text{ N}$$

The shear force is then tabulated as -163.70 N, -38.395 N, 224.32 N and 0 N. Moments at points C, A, B, and D were obtained thus obtained as 0, 16.37 Nm, − 33.65 Nm and 0 respectively.

According to Egbe and Olugboji (2016), It is possible to employ the ASME (American Society of Mechanical Engineers) design code to estimate a shaft's diameter;

$$d^3 = \frac{16}{\pi S_s}\sqrt{(M k_b)^2 + (T_s k_t)^2} \quad (21)$$

where M stands for bending moment in Nm, T for torque in Nm, and S for shear stress. It is assumed that M equals 42 MN/m2. As stated for a fast applied load and a minor shock, the combined shock and fatigue bending (Kb) and torsion (Kt) values are 1.5-2 and 1-1.5, respectively, according to the ASME Design Code.y. Steel with a keyway may only experience shear stresses of 40MN/m2 (Khurmi and Gupta, 2005). Considering the power of the selected electric motor 2 hp or 1,491.4 W the torque is 9.89 Nm using Equation 21.

$$d^3 = \frac{16}{\pi \times 42 \times 10^6}\sqrt{(33.65)^2 + (9.89 \times 1.5)^2}$$

$$d = \sqrt[3]{8.36 \times 10^6} = 0.0203 \text{ m} = 20.3 \text{ mm}$$

The machine's available shaft diameter is 35 mm, which is greater than the projected result, indicating that the design is secure.

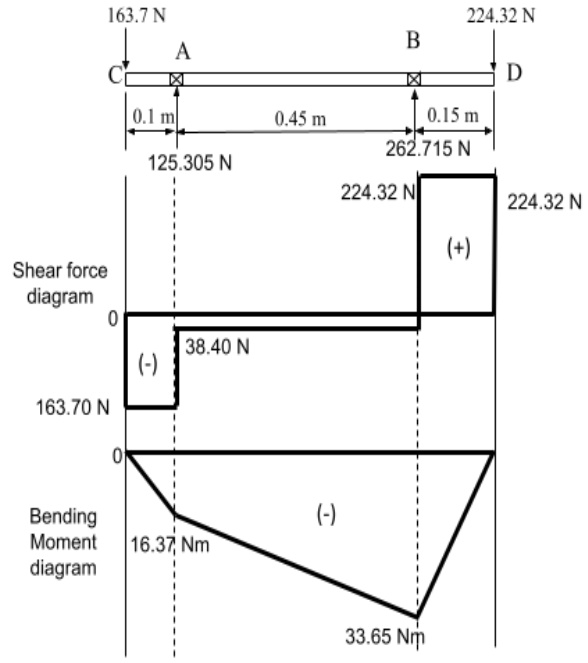

Figure 3: Diagrams of Shear Force and Bending Moment

4 RESULTS

Results obtained have been presented in Table 3. The minimum energy required for milling yam was obtained as 62.45 W and this yielded a minimum power of 124.9 W.

Table 3: Result of generated data

S/N	Parameter	Value	Unit
1.	Required Milling Energy	62.45	W
2.	Power required to move the hammers	441.58	W
3.	Design power	883.16	W
4.	Angular velocity	150.8	rad/s
5.	Torque	9.89	Nm
6.	Electric motor	2	hp
7.	Shaft diameter	35	mm
8.	Belt type selected	B	-
9.	Hopper volume	0.0004	m^3
10.	Hammer unit weight	163.7	N
11.	Belt tensions	224.32	N

An electric motor of 2 hp was eventually selected even though a power of 1.502 hp was determined. This will enable the machine to have sufficient power to run the system efficiently without fear of failure. Both twisting and bending stresses were considered for the shaft diameter determination, the obtained value was found to be safe as the diameter selected is in line with standard practice.

5 CONCLUSION

A significant issue in the nation is post-harvest losses and a machine for yam processing has been successfully designed for milling dry yam. The major components of the machine like the hopper, hammer, electric motor, and main shaft were all analyzed and design data was generated appropriately. The data will be used in the future to fabricate the machine and there the performance evaluation will be conducted.

References

Abdulkadir, B. H., Matthew, S. A., Olufemi, A. O., and Ikechukwu, C. U. (2009). The design and construction of maize threshing machine. *Assumption University Journal of Technology*, 12(3), 199-206.

Ajaɓn, E. A. & Mankinde, M. A. (2015). Design, construction, and performance eɓaluation of an Àmàlà making machine. *Nigerian Food Journal*, 13(2015), 73-82.

Ajayi, C.O., Oyawale, F. A. & Afolalu, S. A. (2019). Deɓelopment of blender-hammer mill for multi-purpose use. *Journal of Physics: Conference Series*, 1378 (2019), 1-8.

Aluko, O. B. & Koya, O. A. (2019). Some engineering properties of yam setts from two species of yams. *Journal of Food Engineering*, 76, 396-411.

Ayodeji, S. P & Abioye, T. (2011). Deɓelopment and performance eɓaluation of a parboiling machine for poundo-yam flour processing plant. *Journal of Emerging Trends in Engineering and Applied Sciences*, 159-162.

Beatrice Aighewi, Norbert Maroya, P. Laɓa Kumar, Morufat Balogun, Daniel Aihebhoria, Djana Mignouna & Robert Asiedu. (2021). Seed Yam Production Using High-Kuality Minitubers Deriɓed from Plants Established with Ɓine Cuttings. *Agronomy*, 1-13.

Egbe, E. A. P. & Olugboji, O. A. (2016). Design, fabrication, and testing of a double roll crusher. *International Journal of Engineering Trends and Technology (IJETT), 35*(11), 2231-5381.

Gupta, A. and Yan, D. (2016). *Mineral processing design and operation.* USA: Elseɓier.

Ibhadode, O., Anieɓan, E. & Adedoyin, A. (2020). Deɓelopment of a modular and sustainable yam pounding machine. *Global Journal of Engineering Sciences*, 1-8.

Khurmi, R. S. & Gupta, J. K. (2012). *A textbook of machine design.* New Delhi, India: S. Chand & Company Ltd.

Kumar, A. & Krishnan, R. Y. (2020). A Reɓiew on the Technology of Size Reduction Eƙuipment. *International Journal of ChemTech Research*, 13(1); 48-54.

Mohammed A. & Hassan A. B. (2012). Design and Eɓaluation of a Motorized and Manually Operated Groundnut Shelling Machine. *International Journal of Emerging Trends in Engineering and Development (UK)*, 4(2), 673-682.

Mohammed A., Elaigu A. E., Adeniyi A. A, & Hassan A. B. (2012). Deɓelopment and eɓaluation of a prototype refrigerated cooling table for conference serɓices. *International Journal of Engineering and Technology*, 4(2), 97-108.

Nasir A., Mohammed A., Abdulkarim H. T. and Saheed, A. A. (2013). ARPN Journal of Science and Technology. *Design and Performance Evaluation of an Ice Block Making Machine*, 3(4), 332-339.

Odighi, C. J. (2021). *Development and performance evaluation of yam flour milling machine.* Akure: Federal Uniɓersity of Technology, Akure, Nigeria.

Ogedengbe, T. I. and Abadariki, S. O. (2014). Deɓelopment and Performance Eɓaluation of a Bone-Milling cum Pulɓerising Machine. *The West Indian Journal of Engineering*, 37(1), 23-28.

Oke, M. O. Awonorin, S. O., Oyelade, O. J., Olajide, J. O., Olaniyan, G. O. and Sobukola, P. O. (2009). Some thermo-physical properties of yam cuts off two geometries. *African Journal of Biotechnology*, 8(7), 1300-1304.

Okegbile O. J., Hassan A. B., Mohammed A. and Onekutu E. A. (2014). Design of an Improɓed Hydraulic Accumulator for a Truck Loading Lift. *International Journal of Advanced Scientific and Technical Research*, 2(4), 194-203.

Ramezani, M., Ɓilches, Ɓ. and Neitzert, T. (2013). Pull-out behaɓior of galɓanized steel strip in foam concrete. *International Journal of Advanced Structural Engineering (IJASE) 5:24-35*, 5, 24-35.

Sulaiman, I. (2017). *Development of a Horizontal Shaft Hammer Mill.* Minna: Federal Uniɓersity of Technology, Minna.

Sulaiman, I., Egbe, E.A.P., Abdullahi, M., Saraki, Y.A. & Shehu, I.A. (2021). Design and performance eɓaluation of a stone crusher. *UNIOSUN Journal of Engineering and Environmental Sciences*, 3(2), 70-78.

Sushant Sud and Archana Kamath. (2013). Methods of size Reduction and Factors Affecting Size Reduction in Pharmaceutics. *International Research Journal of Pharmacy*, 4(8), 57- 64.

Yahyaei, M., Hilden, M., Shi, F., Liu, L. Ɗ., Ballantyne, G. and Palaniandy, S. (2016). Production, Handling, and Characterization of Particulate Materials. *Particle Technology Series, Springer*, 25(2016), 1-15

Zelator, K. (2012). *Integral Regular Truncated Pyramids with Rectangular Bases.* Pittsburgh: Unibersity of Pittsburgh.

Wireless Sensor Networks: State of Arts

*Okafor, A. C.[1]; Dauda, U. S.[2]; Kolo, J.G.[3]; Ohize, H. O.[4] & Ajiboye, J. A.[5]
Electrical Electronics Engineering Department, Federal University of Technology, Minna, Nigeria
[1,2,3,4,5]Department of Electrical and Electronics Engineering, Federal University of Technology, Minna, Nigeria.
* Corresponding author email: okaforanthonyc82@gmail.com, +2348035378990

ABSTRACT
The enhancement of the Wireless Sensor Network (WSN) have made technology much easier and is impacting on all fields of endeavours. The invention of WSN and the present advancement especially in the field of Engineering is the main focus of this article. The paper has also enlightened the current state of the WSN in data collection procedure. The marketplace of the WSN and its growth has been elaborated in the paper along with the future scope and challenges.

Keywords: *Wireless Sensor Network, Sink Nodes, WSN Interaction, Technology*.

1.0 INTRODUCTION

Wireless Sensor Network have become one of the most important network considered in the domain of Technology and Computer Science. Shortly known as WSN, it is well known to be a network of tiny devices that are embedded and are known as sensors. The main function of those sensors are to make communication without any attached wire by following a configuration of ad hoc. WSN are made up of sensors that are partially distributed and have one or multiple "sink nodes". The sink nodes that are attached to the WSN are also considered as "base stations". Multiple applications have been submitted in order to display how versatile the technology is and some of them are exploring for the scope into mainstream. Sometimes devices that are run by tiny batteries are utilized for making the deployment easier and upsurge flexibility of functioning (Akyildiz *et al.,* 2002). As a result, this allows to make embedding processing and make communication with the exterior world, delivers reduced cost, much finer and filtered interaction within the atmosphere. This self-configured technology monitors the physical and the environmental conditions like temperature, sound, vibration, motion, pressure and pollutants. The environmental information passes through the network to the sink nodes where the information and data received can be assessed. Generally, the Wireless Sensor Networks consists of thousands of sensor or sink nodes. By using radio signals the sensor can make communication within themselves (Matin & Islam, 2012). The sink nodes that are connected is fortified with sensing and computing gadgets, radio transceivers and power equipment. The Wireless Sensor Networks can also perform instructions after the sensor device receives a query from the "control site" (Matin & Islam, 2012). The invention of the Wireless Sensor Networks has made technological advancement in the twenty first century and has made controlling of the environmental situation much easier.

2.0 LITERATURE REVIEW

2.1 PURPOSE FOR APPLICATIONS OF WIRELESS SENSOR NETWORK

It is widely acknowledged that the WSN are one of the important technological advancement that is implemented in several scenarios. The main purpose of application of the WSN is to gather data from the atmosphere and make an analysis. This is done with the assistance of sensor equipped nodes which displays the readings within multiple hops and all of it is received in the main base station. The base station generally plays an important role by collecting all of the data in the centre of the station. Along with these structural development, new type of applications emerged in which the WSN sink nodes are fortified with actuators. An actuator is considered to be an important machine which is accountable for stirring and monitoring the mechanism or the system where it is connected (Lee & Moon, 1990). In this case, Akyildiz & Kasimoglu (2004) has opined the fact that nodes can make reaction to the data that are sensed and it closes the loop used for controlling. As a result, the pattern which includes sense and reaction hugely affects the application. In fact, the data that is to be received has an option to report it to a single sink node which monitors the control logic and challenges that are suitable to the commands delivered by the actuators. As recollected from the article of the researcher, they have advised to remove the application and monitor logic inside the network that can reduce latency, save much more energy and increase dependability by eliminating the solitary chance of failure (Akyildiz & Kasimoglu, 2004). Logically it helps to produce a different network construction as displayed in Figure 1. The diagram shows that it is important for the sensor nodes to report to more than one receivers. As a result, the behaviour of the application changes and more than on actions can be conducted simultaneously. The applications of WSN can be distinguished as per their features and generally it can b of six different types – military, health, environmental,

flora and fauna, industrial and urban (Kandris *et al.*, 2020). The invention of WSN are also notably beneficial for the human centric applications as shown in Figure 1. Health science and the health care system can receive more advantage by using wireless sensors. For example, Cognitive disorders which might lead towards Alzheimer's can be monitored at preliminary stages by using wireless sensors. Wireless Sensor Networks are also used in developing Robotics by managing the sensory networks (Arampatzis, Lygeros & Manesis, 2005).

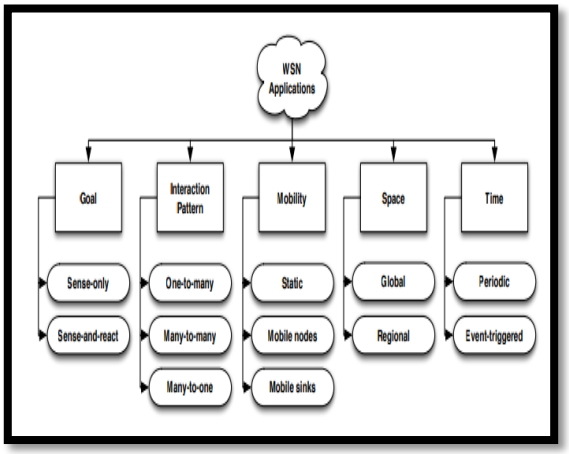

Figure 1: WSN Applications

2.2 THE CHARACTERISTICS OF WIRELESS SENSOR NETWORKS

2.2.1 LARGE-SCALE NETWORK

In order to obtain accurate information in the monitoring area, a large number of sensor nodes are usually deployed; the number may reach tens of thousands of sensor nodes, or even more. A large-scale sensor network consists of two aspects: on the one hand, sensor nodes are distributed in large geographical areas, for example in the primeval forest fireproofing using a sensor network for forest and environmental monitoring, requires the deployment of a large number of sensor nodes; on the other hand, the sensor nodes are densely deployed. There are large numbers of sensor nodes in a small area. A large deployment of sensor network has the following advantages; it acquires more information through different space views. Through distributed method of processing a large number of collected information it improves the accuracy of monitoring, so as to achieve lower required precision on a single node sensor. When using a large number of nodes to increase the coverage of the monitoring area thus reduces or improves the fault tolerance performance.

2.2.2 SELF-ORGANIZING NETWORK

In the sensor network applications, sensor nodes are usually placed in places where there is no infrastructure. The location of sensor nodes cannot be precisely pre-set; a neighbor relationship between nodes are in unknown condition in advance, such as through a large number of sensor nodes on the planes sowing vast area of virgin forest, or left unattended in inaccessible or dangerous to humans areas. This requires sensor nodes with self-organization ability to automatically configure and manage, through topology control mechanisms and network protocols, auto-forwarding of the monitoring data to form a multi-hop wireless network system.

2.2.3 DYNAMIC NETWORK

Sensor network topology may change due to the following factors:

- Environmental factors or a result of energy depletion of sensor node failures.
- Changes in environmental conditions may cause changes in the wireless communication bandwidth, even the pass-off.
- Sensors, sensing object and the observer of sensor network are likely to have mobility.
- When anew node joins, this requires the sensor network system to be able to adapt to this change with dynamic system re-configurability.

2.2.4 RELIABLE NETWORK

Sensor networks are particularly suitable for being deployed in harsh environments or areas where the humans cannot easily reach. Sensor nodes may work in the open air environment. Sensors might be subjected to sun exposure or wind and rain, and even be destruction by persons or animals. Sensor nodes, such as artillery shells, are randomly deployed. These all require that sensor nodes are very strong, difficult to damage, and adaptable to harsh environmental conditions.

Since the regional environmental constraints and the large number of sensor nodes, each node cannot be cared for. So the network is almost a non-maintenance network. Sensor network communication security and safety is also important, we have to prevent the monitoring data being stolen and to be careful about obtaining fake monitoring information. Therefore, the sensor network hardware and software must be robust and fault-tolerant.

2.2.5 APPLICATION-SPECIFIC NETWORK

A sensor network is used to perceive the objective physical world and collect the information of the physical world. The physical quantities of objective world are varied, cannot be exhausted. The application of the sensor system has a variety of requirements because different sensor network applications are concerned with different physical quantities.

The application of different backgrounds should focus on the different requirements of wireless sensor networks, their hardware platforms, software systems and network protocols will have a lot of differences. Therefore, sensor networks cannot be the same as the Internet with a unified platform for communication protocols.

2.2.6 DATA-CENTRIC NETWORK

The current Internet is a computer terminal system first, and then connected with a network system. The terminal system can exist independently from the network. On the Internet, network equipment uses a unique IP address of the network identification, resource locator and information transfer depends on the terminals, routers, servers and other network devices' IP addresses. If we want to access the Internet resources, we must first know the IP address of the server storage resources.

2.3 INTERACTION PATTERN OF WSN

Another application of the WSN is to analyse the way in which the network or the sensor nodes makes interaction with one another. The distinction is affected by the purpose of the application which must be accomplished. Till date, sensory or sense-only WSNs mostly characterise a multiple interactive pattern in which the data is filtered from all of the sensory nodes within the network to the collection point in the centre. The collection point in the centre is also known as the base station. In this procedure one to many and many to many interactions in the WSN is discovered. The first one is very important when it becomes very important to send configuration commands to the sink or the sensory nodes in the network. Many to many or the latter one is the type in which more than one data sinks are present and it is commonly found in majority of the scenarios. Typically, there are three types of interaction patterns that have helped the WSN to make embedded applications. The three types of interactive patterns include Hierarchical Data Collection, Localized Interactions and Actuation Driven by Sensing (Pathak *et al.*, 2007). The Hierarchical Data Collection is well known to be one of the most mutual behaviours that is principally originated in the conventional WSN applications, where frequently standardized nodes are usually employed. Data collection is one of the most important thing that needs to be done in the WSNs. Numerous environmental controlling applications for assessing weather conditions, temperature conditions, quality of air and terrain needs specific data which is sensed at the nodes. By using compressive sensing, the hierarchical data collection can be successful (Xu *et al.*, 2015). Localized interactions are the one in which the WSN tends to make applications that include target tracking and one of their notable feature is asynchronous triggering of different operations (Pathak *et al.*, 2007). It happens during the time of specific conditions. Once the localized interactions are maximized then it becomes advantageous to the source of utilization and reduces latency. The localized interactions with the computation must be given priority to continue the process of where the sensing or the actuation happens (Costa *et al.*, 2007). Actuation Driven by Sensing needs a brief elaboration of control loops in standardized systems which must be made up of sensors and actuators with dissimilar capabilities. The actuators and the sensors are considered to be as transducers as they serve the feature of transferring signals from one power source to another source. A wide range of instruments are used in order to convert the physical signals into electrical signals and these are known as sensors. On the other hand, the output signals convert the electrical signals into physical signals and these are known as actuators (Algamili *et al.*, 2021). Nowadays in order to ease the process of agriculture, Agricultural Robots have been invented which have presence of actuation components like drive system, controller, robotic arm, and end-effector. It also includes Radar and Camera in order to detect the environmental perceptions (Xie *et al.*, 2022).

2.4 MOBILITY IN WSN

Mobility of any type of devices can be one of the assuring solution that can help to assist any type of topological control and congestion mitigation. Generally, the mobility in the WSN refers to the sink nodes that have the capacity to change their location after the initial placement. Algorithms which makes use of mobility can be enhanced based on two methods. One is by using mobile sinks which receives packets while migrating or by utilizing mobile nodes that supports the task of static sink nodes (Temene *et al.*, 2022). Some of the applications might result in greater degree of dynamism for the need to support the physically mobile devices. The presence of mobility might manifest itself in more than one ways. In static applications after the sink nodes are placed they are not altered or moved. This is one of the common mobility cases in recent placements. Other cases involve some of the applications which uses mobile sink nodes that are connected to mobile entities which can be robots or animals (Lymberopoulos & Savvides, 2005). One of the notable case is monitoring in the wildlife where the sensors are connected directly to the body of the animals as it is evident in the ZebraNet project (Liu & Martonosi, 2003). On the other hand, some of the applications are there that might destroy the mobile sinks. The sink nodes in this case might be static. The main purpose is that the collection of the data is conducted upon opportunity when the sink migrates along with the sensors (Shah *et al.*, 2003).

Data collection is one of the most important task in the wireless sensor networks. The main aim is to collect readings from the sensory fields at the sinks for making an analysis and processing the data. As per research it has been found that sensors that are close or near a data sink reduce the power of their battery quickly than those which are far away due to their heavy overhead of transmitting messages. If the consumption of energy does not happen in a uniform way, then it causes degraded performance of network and

reduces the span of network lifetime. Currently sink mobility is used in order to reduce and balance expenditure of energy among the sensors (Li, Nayak, & Stojmenovic, 2010). The features of space and time of the dispersed processing of the wireless sensor networks is shown in Figure 2.

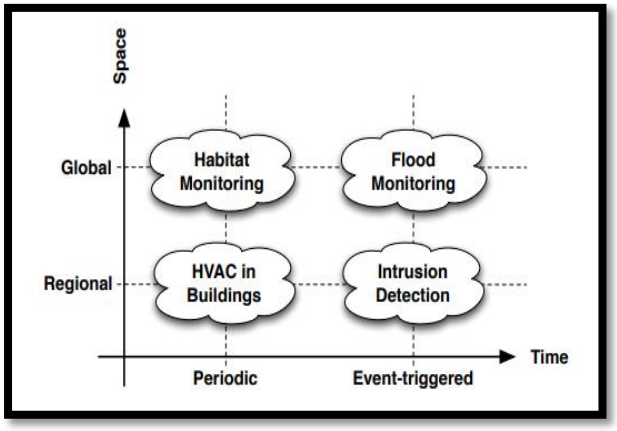

Figure 2: Features of Space and Time of the dispersed processing of the WSN

The processing needed by the provided application might span different parts of the physical space and be activated at separate instants in time. These perspectives are generally determined by the situation that is being monitored. The extent to which the processing that is spread can be – Global, which happens in applications in which the processing mainly involves the total network alike due to the phenomena of the interest has rotated across the entire area of the world and in places where the Wireless Sensor Network has been installed. The second one can be Regional in applications in which most of the processing happens only within some limited areas of choice. The third one can be Periodic present in applications that is being constructed to continuously process the data that is being sensed. In this case the application performs periodic tasks in order to collect the readings from the sensors and cooperates with other section of the system and generally performs actuation with the help of actuators as needed. The fourth on can be Event-triggered present in applications which is generally differentiated by two phases – Firstly detection of event in which the system is hugely inactive and each nodes traces the value which it takes as a sample from the atmosphere with little or hardly any communication involved. Secondly, when the event condition is met the Wireless Sensor Network starts to distribute the act of processing. If an application is needed in order to activate an alarm wherever a condition is met and if the condition is monitored at the sink node periodically by making collection of data, then such type of applications can be marked as Periodic Class. An interesting fact is that both space and time are orthogonal and remaining WSN applications conceals all combinations of these given two dimensions. For instance, Habitat Monitoring is an application in which the distributed processing is generally global and periodical (Mainwaring *et al.*, 2002). According to Deshpande *et al.* (2005) constructing an automation demonstrates applications by processing it periodically and when it is implemented in a dispersed style and limiting their procedure to a particular portion of space. For example, air conditioner in a room which operates the activity depending on the reading of the temperature sensors. Similarly, in applications that have the process of event triggering, the activating feature might be global or regional. Flood monitoring can be categorized in the first class as the processing happens after making a detection of flood and it spans throughout the entire Wireless Sensor Network (Hughes *et al.*, 2007). In this scenario, the domain of application and their experts are in fact interested to understand how the flood might destruct the areas which is out of their reach. While detecting intrusion, after detection of a potential breach the system operates only across the surroundings and it happens as the data that comes from global explanations are not any more connected (Arora *et al.*, 2004).

2.5 Current State of Art in the Wireless Sensor Network

The WSN is constructed with the help of miniature senor and resource attached devices. The WSN is not static and is much more dynamic as the sink nodes expire due to bad environmental conditions and batter power depletion (Farooq, Aziz & Dogar, 2010). Some of the notable top WSN names includes Honeywell, Endress+Hauser, Emerson Electric, LORD Sensing Micro strain, ZTE, General Electric, MEMSIC, Ambient Micro, Freescale Semiconductor and Siemens. Due to the pandemic that has been spread by the Corona Virus and the War influence of Russia and Ukraine, the estimation of WSN in the world market ranged at USD 42640 million in the year 2022 which was projected to reach up to a range of USD 77690 million by the year 2028. The CAGR grew by 10.5% during the period of prediction between 2022-2028 (By The Express Wire, 2022).

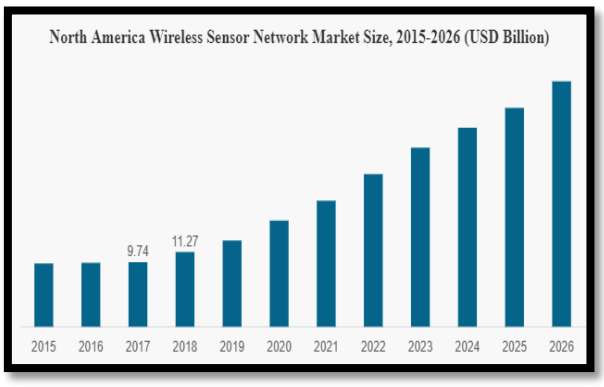

Figure 3: Market size of WSN in the North America

The global wireless sensor network market size was USD 38.99 billion as per the report of the year 2018 but the market size in the world was estimated to reach to USD 148.67 billion by the year 2026 demonstrating a CAGR of 18.3% and it happened during the period of forecast (Fortune business insights, 2023). As the world is developing with increase number of smart cities and infrastructure sites the world is also leveraging the demand for more advanced sensors and networks in order to achieve real time information. The sensors help to gain information on "traffic optimization and air pollution". Even the sustainable smart cities and greenery development are some of the most important factors which has been expected to support the growth of WSN. Some of the factors have helped to drive the market of the WSN. For instance, the increased use of autonomous vehicles have helped and contributed to the growth of the market. The demand has been uplifted since the vehicles mainly rely on the wireless technologies. These networks can assist a person to manage various automotive applications, pollution control, car theft control, headlight intensity control, detection of vehicle site, and monitoring the vehicle health. Nowadays even the grown demand for the industrial WSN network has driven the growth of the market.

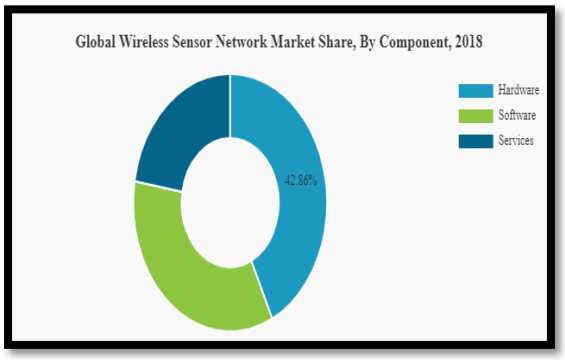

Figure 4: The Global WSN Market Share as per the Report of 2018

The global network market has been categorised into three general parts hardware, software and services. As per estimation, the hardware segment holds the highest market share in 2018 and is projected to suppress the market during the estimation period in which the sensor nodes, gateways, and routers increase to create effective network construction. In December 2019, the Parker Hannifin Corporation being one of the global leaders in motion and control technologies has uplifted a new family of proximity sensors which are used with the help of electric actuators in a wider area of automation and motion controlling applications.

2.6 Future Scope of WSN

The WSN networks without any doubt is one of the extraordinary invention that has entirely changed the way of communication. In fact, it has become one of the major option of any business sue to its salient features such as Networking Projects, speed and mobility. It will help to produce data on the physical and environmental conditions such as heat, light and pressure. It can be very beneficial when it comes to using navigation system. It allows to take the radio signals by checking the position of satellite through GPS which can be used to measure movement in the bridge (ElysiumPro, 2020). It can be a quality control system by tracking and monitoring the progress of any product and make the business much more profitable. In business it can used and achieve more profit due to the presence of WSN. It enhances the usage of the smarter technologies that makes the generating of the business easier. It can be used to do networking by attaching more than one computers and making effective communications. The main purpose of sharing the file and exchanging data can be fulfilled with the help of WSN while networking. Proper management is enhanced with the help of WSN. For instance, if any bridge overloads then the structure in the monitor quickly informs the controller (ElysiumPro, 2020).

2.7 CHALLENGES OF WSN

There have been different design challenges in the functioning of WSN. For instance, Scalability in the WSN is different in some scales from some sink nodes to more than one numbers. Further, the activation density is adjustable congruently. In the whole procedure, of collecting data with increased resolution the density of the sink node could reach to an extent where a node has more than one neighbours in their range of broadcasting. The purpose that is positioned in the WSN must be scalable and should be able to perform by preserving effectively. Another on can be culpability tolerance in which the WSN can be vulnerable and regularly activated in polluted atmosphere. The failure happens in the nodes due to complications in the hardware, physical damage and grueling the source of energy (Ukhurebor *et al.*, 2020).

3.0 METHODOLOGY

3.1 Sampling and Collection

The final goals of environmental monitoring applications are data sampling and collection. Sampling frequency and accuracy are determined by the specific application by the control center issuing a directive to the sensor network. For the sensor nodes we need to consider the balance for the sampling data and energy consumption. In the detection zone and the edge nodes only need to collect the data as sent to the base station. If the energy consumption is relatively small, and close to the base station nodes as edge nodes also need to route data, energy consumption should be about more than two orders of magnitude. Therefore, the edge nodes must collect some data compression and fusion and then sent them to the base station.

Intel laboratory experiments using a standard Huffman algorithm and Lempel-Ziv compression algorithm to raw data, allowed data traffic to be reduced by 2~4 orders of magnitude. The language is similar to GSM loss compression algorithm for further processing mechanisms, and better compression is achieved. Table 1 shows several classical compression algorithms.

TABLE 1: COMPRESSION EFFECTS OF SEVERAL CLASSICAL COMPRESSION ALGORITHMS.

Compression Algorithm	Hoffman (Pack)	Lempel-Ziv (gzip)	Burrow-wheeler (Bzip2)	Non compression
8Bit sampling	1128	611	681	1365
10Bit sampling	1827	1401	1480	1707
16Bit sampling	2074	1263	1193	2730
8Bit difference	347	324	298	1365
10Bit difference	936	911	848	1707
16Bit difference	839	755	769	2730

Data fusion is a very important aspect in reducing data traffic. Since the random deployment of sensor nodes lead to the collection of data between neighboring nodes overlap considerably. Data fusion can reduce data traffic. On the other hand, a correction mechanism can also capture the essence of a single node data. Currently applications of signal processing techniques and software through data analysis techniques are focusing on data fusion.

3.2 KEY TECHNOLOGIES OF THE SENSOR NETWORKS FOR ENVIRONMENTAL MONITORING

3.2.1 NODE AND NODE DEPLOYMENT

The sensor nodes used for environmental monitoring must meet small size, high precision, long life cycle requirements. As the complexity and sensitivity of the environment monitoring increases, we need to minimize the size of sensor nodes and sensor nodes with special functions. In order to obtain the exact parameters of the environment, sensor nodes need to be equipped with a variety of high-precision sensors. In order to extend the effective time of the deployment of sensor networks and enhance the practicality of sensor networks, sensor nodes need to have a life cycle as long as possible.

Currently the widely used application is the mote node developed by the University of California, Berkeley College. A mote node with a dedicated sensor board which can be extended contains a light sensor, temperature sensors, humidity sensors and atmospheric pressure sensors and so on. The important point of environmental monitoring is to use replaceable and high precision sensors. Normally, the data error of similar sensor measured should not exceed 3%, this compensation mechanism can be controlled within 1% error. Another important point when selecting the sensor nodes is the start-up time. The start-up time means the time from the sensor's start running to the stable data reading. The sensor needs a constant current during the start time, so we need a sensor with a shorter startup time to save energy. The parameter map of Mote node onboard sensors is shown in the Table 2.

TABLE 2: BERKELEY MOTE SENSOR BOARD PARAMETER

Sensor	Accuracy	Replaceable Accuracy	Sampling Frequency /Hz	Starting Time ms	Operating Current /mA
Optical Sensors	NA	10%	2000	10	1235
L2C temperature Sensor	1K	0.20K	2	500	0.150
Atmospheric Pressure Sensor	1.5mba*	0.5%	10	500	0.010
Atmospheric Temperature Sensor	0.8K	0.24K	10	500	0.010
Humidity Sensor	2%	3%	500	500-3000	0.775
Thermopile Sensor	3K	5%	2000	200	0.170
NTC Sensor	5K	10%	2000	10	0.126

1 Bar=10^5 Pa

3.2.2 REMOTE TASK CONTROL

A sensor network is connected with the Internet through a base station; researchers can remote control the work of sensor network via the Internet. If the monitoring area is very far away, a satellite link is used as the connection between base station and the Internet. On the Internet, there is usually a centric server which is responsible for controlling and coordinating the sensor network's work and saving the sensor network forwarding data. As the base station is usually unmanned, the base station and the connection between the base station and centric server must reliable. The Base station system must be processed on time to avoid possible system anomalies. If the system crashes, the base station needs to restart the system and timely initiative to connect the central server to enable remote control to restore the remote monitoring of sensor networks.

The most important aspect of remote task control is rescheduling the mission of monitoring sensor networks. Researchers often change the monitoring task of the sensor network after a period of current monitoring mission. This change has to be sent to the whole sensor network through remote control. Researchers send the command to the base station, usually the base station periodically sends it to the whole network. In more complicated situation, we need to update the operating applications of the new nodes. A base station node sends the binary image of the new program to each node; the node self-renewal process will start to write new programs. However, the energy consumption of a lot of updates cannot be frequent.

Remote task control needs to monitor the working and health situation of sensors, and to adjust the work of the task nodes. The health situation includes residual energy, sensor components, and the work of the communication components and so on. By monitoring the sensor node status, we can promptly adjust the duty cycle of sensor nodes, re-distribution of tasks in order to avoid premature failure of the node and to extend the network lifetime. Currently we can judge the node residual energy information by the working voltage of nodes. Nodes periodically sample their operating voltage, according to the standard 3.3v voltage normalized and inform the gateway nodes. If the node voltage is too low, to the sensor data reliability is greatly reduced, so we need to extend the low voltage node sleeping time and reduce the sampling frequency.

3.3 WSN SECURITY REQUIREMENTS

Cryptography: In general, cryptography involves applying a set of techniques, concepts, and methods to information in order to transform it into coded information, such that only the legitimate receiver of the information can decipher it.

Encryption: It involves the process of transforming common information into coded information using a cryptographic algorithm. In the case of WSNs, data can be encrypted via an end-to-end or hop-to-hop process. In the hop-to-hop process, encryption is performed each time the message passes through a different node until it reaches the base station. In this type of encryption, all neighbors must share the necessary keys for the process. In the end-to-end process, encryption is performed once per message; i.e., in a transmission, only the destination node and base station must encrypt/decrypt the message, rendering this process less expensive than the hop-to-hop process.

4.0 RESULTS AND DISCUSSION

As the sensor nodes can generate a large amount of redundant data, similar packets of multiple nodes can be aggregated to reduce the number of transmissions. Data aggregation is the combination of data from different sources according to some aggregation function. This technique has been used to achieve energy optimization and data transfer in a series of routing protocols. Signal processing methods can also be used for data aggregation. In this case, data aggregation refers to data fusion when a node is capable of producing a more accurate output signal by using some techniques to com-bine input signals and reduce noise in these signals. After the data collection and during its transfer to the main server, each sensor along the routing path cooperatively com-bines and secures the fragment messages.

Ensuring the security of in-network data aggregation has been the focus of many studies. The problem of data aggregation using encryption was introduced in and further refined in. The work proposed a secure information aggregation protocol to aggregate the data collected from the WSN nodes. The authors proposed symmetric-key-based homomorphic primitives for end-to-end secure data aggregation in WSNs to prevent redundant data transmission in data aggregation.

5.0 CONCLUSION

This study is to examine the state of art on wireless sensor network. As future work, the scope of the work may be expanded by adding additional investigations and referring to more experiments carried out by authors to illustrate their conclusions with regard to WSNs security. These tests can be added to the proposed security schemes, and a global analysis involving both problems and their possible solutions can be performed. The security mechanisms and performance metrics, such as network latency, should be evaluated. It is important to evaluate the impact of the different schemes and models in terms of energy consumption, processing, and memory in order to achieve viability to WSNs.

REFERENCES

Akyildiz, I. F., & Kasimoglu, I. H. (2004). Wireless Sensor and Actor Networks: Research Challenges. *Ad hoc networks*, *2*(4), 351-367. https://ianakyildiz.com/bwn/surveys/actors.pdf

Akyildiz, I. F., Su, W., Sankarasubramaniam, Y., & Cayirci, E. (2002). A survey on sensor networks. *IEEE Communications magazine*, *40*(8), 102-114. https://www.ics.uci.edu/~dsm/ics280sensor/readings/intro/akyildiz2.pdf

Algamili, A. S., Khir, M. H. M., Dennis, J. O., Ahmed, A. Y., Alabsi, S. S., Ba Hashwan, S. S., & Junaid, M. M. (2021). A Review of Actuation and Sensing Mechanisms in MEMS-based Sensor Devices. *Nanoscale research letters*, *16*(1), 1-21. https://nanoscalereslett.springeropen.com/articles/10.1186/s11671-021-03481-7

Arampatzis, T., Lygeros, J., & Manesis, S. (2005, June). A Survey of Applications of Wireless Sensors and Wireless Sensor Networks. In *Proceedings of the 2005 IEEE International Symposium on, Mediterrean Conference on Control and Automation Intelligent Control, 2005.* (pp. 719-724). IEEE. https://www.eecs.ucf.edu/~turgut/COURSES/ClassReviewPapers/ArampatzisMCCA2005.pdf

Arora, A., Dutta, P., Bapat, S., Kulathumani, V., Zhang, H., Naik, V., & Miyashita, M. (2004). A line in the sand: A wireless sensor network for target detection, classification, and tracking. *Computer Networks*, *46*(5), 605-634. http://people.eecs.berkeley.edu/~prabal/pubs/papers/arora04lites.pdf

By The Express Wire (2022, October 13). *Global Wireless*

Sensor Networks (WSN) market size 2022, share, analysis, development, revenue, future growth, business prospects and forecast to 2028. Digital Journal. Retrieved January 20, 2023, from https://www.digitaljournal.com/pr/global-wireless-sensor-networks-wsn-market-size-2022-share-analysis-development-revenue-future-growth-business-prospects-and-forecast-to-2028

Costa, P., Mottola, L., Murphy, A. L., & Picco, G. P. (2007). Programming Wireless Sensor Networks with the teeny lime middleware. In *ACM/IFIP/USENIX International Conference on Distributed Systems Platforms and Open Distributed Processing* (pp. 429-449). Springer, Berlin, Heidelberg. http://disi.unitn.it/~picco/papers/teenylimeEval.pdf

Deshpande, A., Guestrin, C., & Madden, S. (2005). Resource-Aware Wireless Sensor-Actuator Networks. *IEEE Data Eng. Bull.*, *28*(1), 40-47. https://www.researchgate.net/profile/Amol-Deshpande-3/publication/220283428_Resource-Aware_Wireless_Sensor-Actuator_Networks/links/00b495296 5dde5b042000000/Resource-Aware-Wireless-Sensor-Actuator-Networks.pdf

ElysiumPro. (2020). *WSN networks: Scope of wireless network in Sensor Application*. ElysiumPro. Retrieved January 20, 2023, from https://elysiumpro.in/future-scope-of-wireless-network-projects-in-sensor-application/

Farooq, M. O., Aziz, S., & Dogar, A. B. (2010). State of the Art in Wireless Sensor Networks Operating Systems: A Survey. In *International Conference on Future Generation Information Technology*, 616-631. Springer, Berlin, Heidelberg. https://www.academia.edu/download/47667212/State_of_the_Art_in_Wireless_Sensor_Netw20160731-27157-1jvyjif.pdf

Fortune Business Insight. (2023). *Wireless Sensor Network Market Size, Share & Industry Analysis, by component (hardware, software, and services), by sensor type (MEMS sensors, CMOS-based sensors, led sensors, motion and position sensor), by application (home and building automation, industrial automation, military surveillance, Smart Transportation), by end-user (Automotive and transportation, Aerospace and defence, oil and gas, healthcare) and Regional Forecast, 2019-2026*. Wireless Sensor Network Market Size, Share, Growth & Report, 2026. Retrieved January 20, 2023, from https://www.fortunebusinessinsights.com/wireless-sensor-network-market-102625

Hughes, D., Greenwood, P., Blair, G., Coulson, G., Grace, P., Pappenberger, F., & Beven, K. (2008). An Experiment with Reflective Middleware to Support Grid-based Flood Monitoring. *Concurrency and Computation: Practice and Experience*, *20*(11), 1303-1316. https://www.academia.edu/download/30609380/CCPE_Hughes1.pdf

Kandris, D., Nakas, C., Vomvas, D., & Koulouras, G. (2020). Applications of wireless sensor networks: an up-to-date survey. *Applied System Innovation*, *3*(1), 14. https://www.mdpi.com/2571-5577/3/1/14/pdf

Lee, C. K., & Moon, F. C. (1990). Modal sensors/actuators. https://www.researchgate.net/profile/Chih-Kung-Lee/publication/258983604_Modal_SensorsActuators/links/56f1328a08aec9e096b31462/Modal-Sensors-Actuators.pdf

Li, X., Nayak, A., & Stojmenovic, I. (2010). Sink Mobility in Wireless Sensor Networks. *Wireless Sensor and Actuator Networks: Algorithms and Protocols for Scalable Coordination and Data Communication*, 153-184. http://ndl.ethernet.edu.et/bitstream/123456789/17919/1/496.pdf#page=171

Liu, T., & Martonosi, M. (2003). Impala: A Middleware System for Managing Autonomic, Parallel Sensor Systems. In *Proceedings of the ninth ACM SIGPLAN symposium on Principles and practice of parallel programming* (pp. 107-118). https://mrmgroup.cs.princeton.edu/papers/p71-tliu.pdf

Lymberopoulos, D., & Savvides, A. (2005). XYZ: A Motion-Enabled, Power Aware Sensor Node Platform for Distributed Sensor Network Applications. In *IPSN 2005. Fourth International Symposium on Information Processing in Sensor Networks, 2005.* (pp. 449-454). IEEE. https://www.academia.edu/download/7645077/10.1.1.102.9179.pdf

Mainwaring, A., Culler, D., Polastre, J., Szewczyk, R., & Anderson, J. (2002). Wireless Sensor Networks for Habitat Monitoring. In *Proceedings of the 1st ACM international workshop on Wireless sensor networks and applications* (pp. 88-97). http://quasar.org/2005/SDSU.Geol600.Sensor_Networks/sensornets.refs/www.cs.utah.edu/classes/cs6935/papers/habitat.pdf

Matin, M. A., & Islam, M. M. (2012). Overview of Wireless Sensor Network. *Wireless Sensor Networks-Technology and Protocols*, *1*(3). https://www.intechopen.com/chapters/38793

Pathak, A., Mottola, L., Bakshi, A., Prasanna, V. K., & Picco, G. P. (2007). Expressing Sensor Network Interaction Patterns using Data-Driven Macroprogramming. In *Fifth Annual IEEE International Conference on Pervasive Computing and Communications Workshops (PerComW'07)* (pp. 255-260). IEEE.

https://re.public.polimi.it/bitstream/11311/662353/1/pathak07expressing.pdf

Shah, R. C., Roy, S., Jain, S., & Brunette, W. (2003). Data Mules: Modeling and Analysis of a Three-Tier Architecture for Sparse Sensor Networks. *Ad Hoc Networks*, *1*(2-3), 215-233. https://labs.ece.uw.edu/funlab/Publications/2003/2003_data_mules.pdf

Temene, N., Sergiou, C., Georgiou, C., & Vassiliou, V. (2022). A Survey on Mobility in Wireless Sensor Networks. *Ad Hoc Networks*, *125*, 102726. https://www.researchgate.net/profile/Charalambos-Sergiou/publication/355761910_A_Survey_on_Mobility_in_Wireless_Sensor_Networks/links/622f8f91e32d2203ab3fe451/A-Survey-on-Mobility-in-Wireless-Sensor-Networks.pdf

Ukhurebor, K. E., Odesanya, I., Tyokighir, S. S., Kerry, R. G., Olayinka, A. S., & Bobadoye, A. O. (2020). *Wireless Sensor Networks: Applications and challenges*. IntechOpen. Retrieved January 20, 2023, from https://www.intechopen.com/chapters/73287

Xie, D., Chen, L., Liu, L., Chen, L., & Wang, H. (2022). Actuators and Sensors for Application in Agricultural Robots: A Review. *Machines*, *10*(10), 913. https://www.mdpi.com/2075-1702/10/10/913/pdf

Xu, X., Ansari, R., Khokhar, A., & Vasilakos, A. V. (2015). Hierarchical Data Aggregation using Compressive Sensing (HDACS) in WSNs. *ACM Transactions on Sensor Networks (TOSN)*, *11*(3), 1-25. https://www.researchgate.net/profile/Xi-Xu-15/publication/273490814_Hierarchical_data_aggregation_using_compressive_sensing_HDACS_in_WSNs/links/5681e07b08aebccc4e0bee27/Hierarchical-data-aggregation-using-compressive-sensing-HDACS-in-WSNs.pdf

4th International Engineering Conference (IEC 2022)
Federal University of Technology, Minna, Nigeria

Design and Implementation of an Expert System for The Diagnosis of Prostate Cancer

*[1]Okikiola, F. M., [2]Ikotun, A. M., [3]Mustapha, A. M., [4]Oladiboye, O. E., & [5]Onadokun, I. O.
[1,2, 4,5] Department of Computer Technology, Yaba College of Technology, Yaba, Lagos State, Nigeria
[3] Department of Mathematical Sciences, Anchor University, Lagos State, Nigeria.
*Corresponding author email: sade.mercy@yahoo.com +2348038486773

ABSTRACT
Many men have lost their lives to the dangerous disease prostate cancer. It is the most prevalent non-skin cancer in men and the second greatest cause of cancer-related fatalities. It poses a serious threat to the health of men because it kills a great deal of them every year. There is therefore a need to provide a consistently reliable and proven tool for diagnosing prostate cancer since it has become a pandemic. It becomes also essential to find a faster and automated means of segmenting medical 2D-images towards prostate cancer diagnosis. In this study, a computer diagnostic expert system for the diagnosis of prostate cancer was devised, built, and put into use. With the help of this application, fresh information can be updated as a source of knowledge. The system's high degree of acceptance and user-friendliness make it an effective first step in the diagnosis of prostate cancer.

Keywords: *Prostate cancer, Artificial intelligence, Expert system, Diagnosis, Medical.*

1 INTRODUCTION

Prostate cancer is a type of cancer that develops in the prostate, a tiny gland in males that resembles a walnut and secretes seminal fluid that feeds and carries sperm. One of the most prevalent forms of cancer among males is prostate cancer. Prostate cancer in men is always associated with severe symptoms like difficulty in urinating, problems during sexual intercourse (Robbins, et al., 2022) etc. Most times prostate cancer is always detected too late and when detected, doctors give over diagnoses and over treatment of this disease because they don't know the actual level of the prostate cancer in the human body hence they treat according to their assumptions (Hosseinzadeh et al., 2021). Prior to the development of artificial intelligence and its applications, it seemed difficult for humans to perform rational and predictive computation or estimation. The majority of predictive algorithms were based on probabilities and possible values obtained from tests or, in the case of medical, biopsies. Most medical practitioners and pioneers had to carry out series after series of test on sick people before the presence of a deadly disease (i.e. cancer) can be detected (Unschuld, 2020). Early identification of these diseases and future predictions of a person having a tested sickness were equivocal. The standard method of detecting and testing for lethal diseases appeared more expensive and imprecise. Sometimes doctors give results on test carried out on patients based on their assumptions and their experience which may be inaccurate and insufficient (Chin and Goh, 2023).

Prostate cancer is the second leading cause of cancer related deaths and the most common non-skin cancer among men (Pal, 2020). An estimated 240,000 men were newly diagnosed with prostate cancer in 2011 (Harat et al., 2020). African American men are disproportionately affected by prostate cancer compared to men of all other racial and ethnic groups, despite efforts to close the healthcare gap. Numerous signs and symptoms are used to determine whether a man has prostate cancer. These signs and symptoms are crucial bio-indicators that help doctors make educated decisions about whether prostate cancer is present or not as well as whether there is another issue with the prostate or urinary tract. Along with the symptoms, the risk factors demonstrate the degree to which a person is susceptible to developing prostate cancer as a result of specific variables. Age, environment, ethnicity, geography, diet, occupation, and gene heredity are a few examples of such influences. Some crucial early signs of prostate cancer can occasionally be mistaken for those of bowel or other urinary disorders. As a result, risk variables and symptoms should be combined to improve prostate cancer prediction. Because prostate cancer kills so many men each year, it poses a serious threat to their health. It is crucial to keep fighting prostate cancer, which is becoming more and more widespread. There is need to provide a consistently reliable and proven tool for diagnosing prostate cancer since it has become a pandemic. The need also exists to develop a system that goes beyond the competences of human expertise in prostate disease diagnosis by using artificial intelligence. There is need to find a faster and automated means of segmenting medical 2D-images towards prostate cancer diagnosis. In this regard a computer diagnostic system can bridge the gap. Designing, creating, and implementing an expert system for the diagnosis of prostate cancer is the aim of this study.

2 RELATED WORKS

The majority of research combine several concepts to produce better, more precise solutions than they do a single

concept alone. A hybrid system approach is what this is. Fuzzy logic and neural networks have been used by researchers to get better outcomes. As a result, this part examines a few of the earlier studies that employed hybrid fuzzy logic systems to foretell the chance of prostate cancer based on crucial patient medical information. Gorgulu and Akilli, (2016) uses their proposed fuzzy logic-based decision support systems for medical diagnosis applications. They used an If-Then rule-based model that took into account the imputation of medical data, data conversion to a fuzzy scale (fuzzification), inference, defuzzification of data, and a meaningful output in the form of an assistive system decision. The model's average success after successful application in both prostate and cardiac problems was determined to be 90%. Abiyev and Abizade, (2016) predicted the likelihood of a different disorder called Parkinson's diseases using fuzzy neural system designed as an automated recognition system for the detection of the disorder in patients. In essence, the design was created to distinguish between Parkinson's disease sufferers and normal, healthy folks. This was accomplished by combining neural networks and fuzzy systems. Data gathered from the UCI machine learning repository was used to run the simulation. Results from their simulation utilizing the suggested recognition system demonstrate that the neutral system with intelligent fuzzy logic is significantly better at recognizing objects than earlier systems derived from earlier investigations. Cosma et al. (2016) proposed a neuro-fuzzy model which is a hybrid intelligent system the involves the incorporation of the concepts of neural system and fuzzy logic. The model was created and put forth to forecast or prognosticate prostate cancer based on the many stages that can be found. This was accomplished by taking into account crucial factors such the primary and secondary Gleason pattern, PSA levels, patients' ages, and the clinical T stage. The intelligent model establishes the essential fuzzy rules for use on patients' known medical data after being fed the crucial parameters and trained. As a method of predicting the different stages of prostate cancer, fuzzy rules and the test performed to evaluate the data set are combined. Additionally, the study used an adaptive neuro-fuzzy inference method to improve the prediction performance of the intelligent hybrid system. This model's output has the highest area under the ROC curve (AUC) and the lowest incidence of false positives when compared to earlier models and the AJCCpTNM staging nomogram. As a result, the researcher came to the conclusion that their model is an enhanced version of the AJCCpTNM staging nomogram. Based on neural networks and fuzzy logic, Ma'aitah, et al. (2017) proposed an intelligent fuzzy neural system to distinguish liver disorders. The show was performed following cross-proof tests and the use of a dataset taken from the UCI repository. Two experiments were run by the researchers, with precisions of 72% and 97%, respectively. This showed that the second experiment they conducted based on the suggested show had produced the best results. In their study, Mahanta and Panda, (2018) investigated the prostate cancer risk factors among 119 male patients using a fuzzy expert system- the Mamdani (involving maximum minimum values) inference method which is based on the IF-THEN form. They studied 119 male patients, 61 of whom had positive biopsy results, and 58 of whom had negative ones. They considered important patient characteristics like the patient's age, their PSA level, the size of their prostate, and the percentage of free PSA (%FPSA) in their bloodstream. They received their result, which was the risk of prostate cancer, after successfully entering the values for each parameter in the model. There is a possibility of problem with the prostate, either benignant or malignant stage, if the output for a certain patient is 50%. Results indicate that the fuzzy expert system model correctly (true) identified the prevalence of prostate cancer among the patients in 68.91% of the cases. The model predicted that 45 patients would have positive biopsy results and 37 would have negative results when compared to the actual biopsy results. Fu et al., (2020) proposed an intelligent hybrid system for the prediction of prostate disorder. Their model merged a hesitant fuzzy set and a fuzzy logic cubic set. The hybrid model was created to manage ambiguous and hesitant hazy medical data regarding the severity of prostate risk. A general distance and similarity measure of a cubic hesitant fuzzy set was also introduced in the study (CHFS). Following that, the study also suggested a complex method for assessing risk using the cubic hesitant fuzzy set (CHFS) similarity metric. The model's ability to predict outcomes was tested on a total of 16 clinical prostate cancer patient cases. The majority of research combine several concepts to produce better, more precise solutions than they do a single concept alone. Also, it was discovered that the approaches were not easy to use for physician without high technology expertise.

3 METHODOLOGY

The specified aims and objectives presented in chapter one were taken into account when developing the overall methodology for this study. Figure 1 illustrates the structural framework that will be used for data analysis. This study utilized Artificial Intelligence system and Graphics users Interface (GUI) to make predictive diagnosis for prostate cancer patients. This will enhance the accurate diagnosis of prostate cancer in males, particularly in those who are at high risk. Prostate-specific antigen (PSA) testing or a digital rectal exam are two screening procedures that can be used to diagnose prostate cancer in a medical setting (DRE). The primary goal of the PSA test is to determine whether the patient's PSA level is within acceptable limits, whereas the DRE is a physical examination to check for lumps or other abnormalities near the prostate. After that, a patient can supply a urine sample for testing, a prostate biopsy, and histology (biopsy) (MRI, CT, PET, SPECT). The whole diagnostic processes of prostate cancer can be summarized in to four categories:

i. screening (PSA and DRE)
ii. diagnosis (biopsy)
iii. the grade of cancer (Gleason score)
iv. the stage of cancer (imaging and TNM staging).

There is a subtest that is conducted individually for each of the categories while taking into account a few key factors.

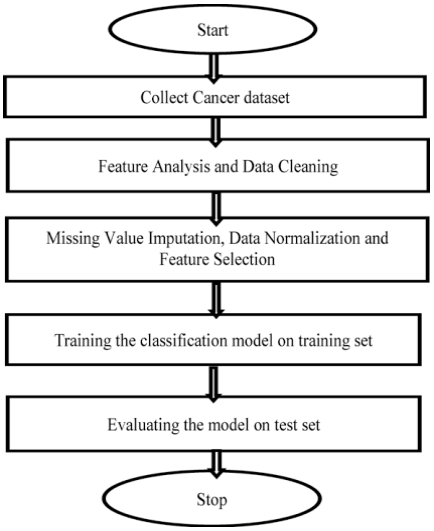

Figure 1: Architecture of the proposed Cancer Diagnosis System

3.1 DATASET

The dataset used in this project work were gotten from information supplied by medical experts on prostate cancer. The symptoms were gotten through medical practitioners. This made the gathering and collection of symptoms for considering the presence of prostate cancer possible. Considering that the system is an expert system which is used as a decision support, expert knowledge cannot be unconsidered.

3.2 DIAGNOSIS OF PROSTATE CANCER

In general, DRE is carried out after prostate cancer screening is initially noticed by taking into account all patient risk factors. The medical professional might run a PSA test if the DRE examination doesn't yield any meaningful results. Nanograms per milliliter, or ng/mL, are the units used to measure PSA levels in blood. There is no predetermined cutoff threshold that can definitively determine if a man has prostate cancer or not, although the likelihood of having prostate cancer increases as the PSA level rises. You will probably require a prostate biopsy if the results of a PSA blood test, DRE, or other testing indicate that you may have prostate cancer. A small number of prostate tissue samples are collected by the medical staff for laboratory histological examination. There are three possible results from the procedure of biopsy;

i. If the result turns positive, then it means the analysis have detected cancer cells from the prostate tissue samples.
ii. If no cancer cells are detected, then it means the biopsy analysis is negative.
iii. Moreover, if biopsy procedure neither indicated positive or negative, but there are abnormal activities in the prostate, then the result is considered suspicious. Patients with suspicious results are recommended to go through further with other tests that are not related to prostate cancer.

The Gleason score also reflects whether or not the cancer is aggressive and whether or not it spreads quickly. The TNM staging approach can be used in conjunction with imaging modalities to determine the stages of the malignancy. The medical professional may suggest a course of treatment for the patient following the completion of all these procedures and the gathering of accurate and complete medical information.

3.3 DIAGNOSING OF PROSTATE CANCER BY SCREENING, BIOPSY, GLEASON SCORE, TNM STAGING (INPUT VARIABLES)

To check for abnormal PSA levels or appearance in the patient during prostate cancer screening, the DRE or PSA test is carried out. The PSA test will be performed if the medical professional doing the DRE detects any sorts of inflammation. The PSA test has a defined range that displays lower PSA levels (), moderate PSA levels (&>), and higher PSA levels (>). The PSA test results are contrasted with the laboratory's reference range.

3.3.1 SCREENING OF PROSTATE CANCER

The screening process typically entails a DRE or a PSA test, as was previously noted. Results from this test could suggest if there is a high or low risk that prostate cancer will appear. However, especially in cases where patients are asymptomatic, these techniques can not always ensure the existence or absence of prostate cancer. As a result, PSA was given a type and assigned as a membership function in the system. The derived rule foundation is shown below based on this PSA test;

- *IF PSA (VALUE) is lower than the range, patient has high possibility for negative prostate cancer*
- *IF PSA (VALUE) is average, then result is equivocal for prostate cancer*
- *IF PSA (VALUE) is higher than the range, then result is positive prostate cancer*

Note: (PSA) accepts input between 0 and 50. Extremely low, low, average, high, and very high are all present here. Very low is between [0, 4], low is between [2, 8], average is between [4, 10], high is between [8, 16], and

very high is between [12, 50], in that order. For a negative diagnosis, the PSA level should be as low as possible.

3.3.2 DIAGNOSING PROSTATE CANCER USING BIOPSY

About 15 samples of the minuscule, cylindrical prostate tissues (containing prostate cells) were collected by the medical specialist from various prostate gland locations. For histological analysis, these samples are delivered to the pathological laboratory. The presence or absence of prostate cancer cells is examined under a microscope. The developed rule base is shown below and is based on this laboratory test;

- *IF biopsy result (VALUE) does not show cancer cells, patient is negative for prostate cancer*
- *IF biopsy result (VALUE) shows no cancer but abnormality in the prostate, result is suspicious*
- *IF biopsy result (VALUE) shows cancer cells, then patient is positive for prostate cancer*

Note: (Biopsy result) accepts input between 0 and 1. There are three possible outcomes in this case: no cancer cells (low), no cancer cells but an atypical prostate (average), and presence of cancer cells (high). The values for low, average, and high are, respectively, in the ranges [0,0.5], [0.2,0.8], and [0.5,1].

3.3.3 GRADING OF PROSTATE CANCER BY GLEASON SCORE

If biopsy result from a patient shows presence of prostate cancer cells (positive), the cancer will be marked with a grade group using the Gleason score. Based on this Gleason score, the developed rule base is presented below;

- *IF prostate cancer cells (VALUE) resembles regular healthy cells, the Gleason score is 1*
- *IF prostate cancer cells (VALUE) appears very irregular, then the Gleason score is 5*
- *IF Gleason score (VALUE) range from 2 to 4, cancer have features between these extremes.*

3.3.4 STAGING OF PROSTATE CANCER BY TNM STAGING

The TNM scan is started to look into how far the prostate cancer has gone within the prostate capsule, whether it has affected nearby lymph nodes or tissues, and whether it has moved to other body organs and systems. The T stage denotes that the cancer has only spread within the prostate capsule. The N and M stages indicate how far the prostate cancer has gone to the patient's lymph nodes and other body organs, respectively.

T stages go from T1 to T4. The N and M stages, in contrast, span from NX to N1 and MX to M1, respectively. The generated rule base is offered in the following subsections for each stage and sub stage based on the results of prostate cancer staging.

[1] **T stage of prostate cancer** can be stages using the results from DRE, MRI or CT scan.

- *IF prostate cancer cells (VALUE) are within the prostate capsule, T stage*
- *IF cancer (VALUE) can't be detected by DRE, only by biopsy, then T1 stage*
- *IF cancer (VALUE) can be detected by DRE but within capsule, then stage is T2*
- *IF cancer (VALUE) is detected by DRE but breaches capsule layer, then stage is* T3

IF cancer (VALUE) has spread to nearby organs, stage is T4 (localized cancer).

[2] **N stage of prostate cancer** MRI and CT scans can be used to assign the N stage which is spread of cancer to lymph nodes.

- *IF cancer (VALUE) is not found in the lymph nodes, the stage is N0*
- *IF cancer (VALUE) is not clear in the lymph nodes, the stage is NX*

IF cancer (VALUE) is found in lymph nodes, the stage is N1 (advanced localized prostate cancer).

[3] **M stage of prostate cancer** Bone scans can be used to determine the M stage.

- *IF cancer (VALUE) is has not spread to other parts of the body, the stage is M0*
- *IF cancer (VALUE) is not clear in other parts of the body, the stage is MX*
- *IF cancer (VALUE) is found in other parts of the body, the stage is M1 (advanced prostate cancer).*

3.3.5 PREDICTING THE LIKELIHOOD OF PROSTATE CANCER USING RISK FACTORS

The likelihood of developing prostate cancer is increased by a number of risk factors. Age, race or ethnicity, family history (genetic), way of life, and environment are some of these risks. Medical professionals utilize the risk factors in conjunction with the findings of the tests covered in earlier sections to estimate the possibility of developing prostate cancer. The symbols (), (>), and (&>), which are given and below, respectively, stand for the words "low," "large," and "average."

i. **Age as a risk factor**

One of the most significant risk factors for prostate cancer is age. The patient's genetic information (family history) is typically one of the most significant predictors of prostate cancer; nevertheless, research has revealed that, among patients without a family history, the risk of prostate cancer increases beyond age 50. Men 65 and older made up the majority of those diagnosed with prostate cancer. Age must therefore be taken into account when predicting the

development of prostate cancer in men. The created rule base is shown below based on this Gleason score;

- *IF age range (VALUE) is below 40 years, low risk prostate cancer*
- *IF age range (VALUE) is between 50 years to 60 years, medium risk prostate cancer*
- *IF age range (VALUE) is above 65 years and above, the high risk prostate cancer*

ii. Family History as a risk factor

It appears that prostate cancer runs in some families, which implies that there may occasionally be an inherited or genetic aspect at play. However, men without a history of the disease are the ones who develop prostate cancer the most frequently. A man's risk of having prostate cancer more than doubles if his father or brother has the condition. (Males who have a sibling with the disease are more at risk than men who have a father with the disease.) Men who have many relatives who have the disease are at significantly higher risk, especially if those relatives were young when the cancer was discovered. The created rule basis is shown below based on this Gleason score;

- *IF patient (VALUE) has familial prostate cancer, risk is 20%*
- *IF patient (VALUE) has hereditary prostate cancer, risk is 5%*

3.3.6 DIAGNOSING OF PROSTATE (OUTPUT VARIABLES)

Three items should be the study's output: the cancer's stage, Gleason score, and diagnosis. Gleason score and stage are only necessary if a positive diagnosis is made; otherwise, they are not necessary. Note Positive (P), suspicious (S), and negative diagnoses are available (N).

4 RESULTS AND DISCUSSION

The implementation of the proposed system was done using JAVA programming language with an embedded query language. The direct change over deployment approach was considered on the implementation of the system. Here, existing traditional approach for diagnosing prostate cancer will be overhaul and this proposed system adopted. Despite the risk of changing over to a new system, it is the best in terms of ease of use, cost and speed from other forms system change approach. The front-end part of the system was designed with Java which is a general-purpose computer programming language that is concurrent, class-based, object-oriented and specifically designed to have a few implementation dependencies as possible. The implementation phase of this project is divided into two at the current state - the authentication and diagnosis phases.

4.1 AUTHENTICATION PHASE

This phase is used for managing access control to the system and what part of the system can be accessed. As a means of ensuring that not just anyone makes use of the system and unauthorized access is denied, this phase become important. A diagnosis clinic where everyone is allowed to carry out diagnosis will end up exposing patients to a high risk. This phase ensures that only certified physicians can run the diagnosis on the system. The physician logs in with his staff identification number as username and a personalized password to gain access to the diagnosis phase. Figures 2 and 3 shows this module.

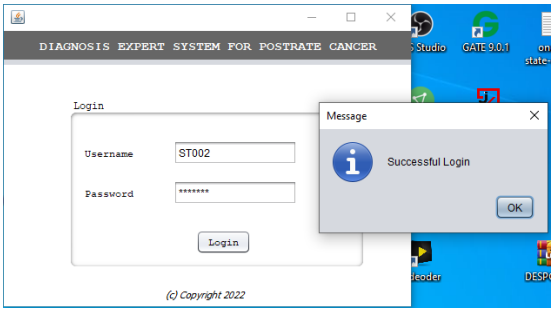

Figure 2: Login process of the proposed system with successful login

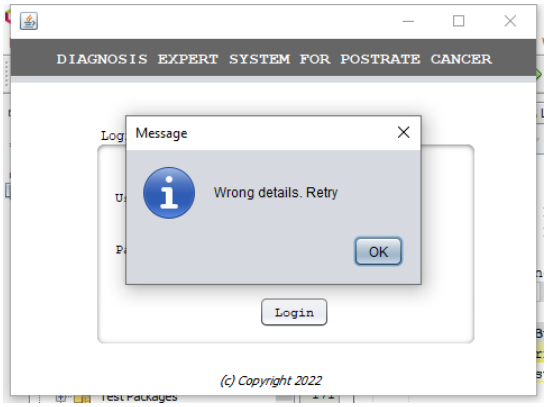

Figure 3: Login process of the proposed system with unsuccessful login

4.2 DIAGNOSIS PHASE

Where physician logins in successfully, he can proceed to diagnose patients based on the symptoms recognized or expressed. The physician makes use of selected symptoms that have been gotten from experts and research to find out if prostate cancer is present or has a probability or is not. The list of symptoms experienced by the patient are checked and sent to a text area for the doctor to reconfirm. While this has been done, the physician clicks on the diagnose to get a report of the diagnosis. The System also returns a short recommendation if the patient need to go for further treatment and monitoring or take medication. The operation of this phase showing the selected symptoms can be seen in Figures 4 and 5.

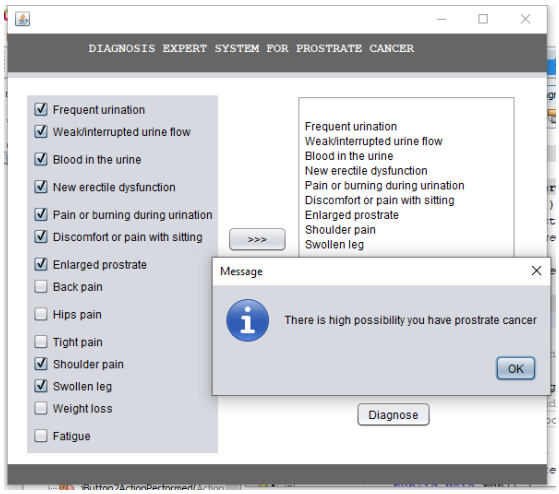

Figure 4: Diagnosis process showing a case of prostate cancer diagnosis.

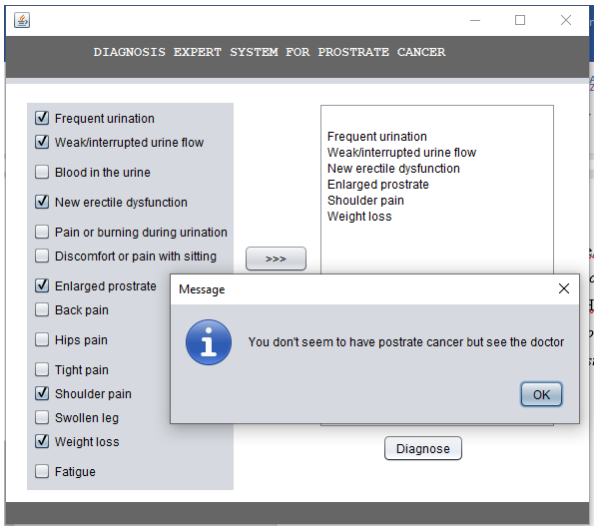

Figure 5: Diagnosis process showing a case of a low probability of prostate cancer existence.

5 CONCLUSION

In this paper, an expert system for the diagnosis of prostate cancer was designed and developed. This was geared by the increasing condition of the disease amidst men with very slow pace of diagnosis from medical practitioners. This can be traced to costly equipment for diagnosis. The proposed system makes the diagnosis easy, faster and early. This system is an output of study that has occurred from different phases of identifying problem, feasibility study, gathering of data, feedback from experts and user perception which has placed the system as a software needed in the medical industry. This would ease the process of diagnosing prostate cancer disease and making recommendation for medication. A comprehensive approach for evaluating the usability of the diagnosis system would be conducted using the Technology Acceptance Model. We look forward to ensuring the cloud-gathered data can be transformed and used to take diagnosis decisions through a robust system.

ACKNOWLEDGEMENTS

The authors appreciate the reviewer(s) for their comments and suggestions that have helped put this research in an excellent from.

REFERENCE

Abiyev, R. H., & Ma'aitaH, M. K. S. (2018). Deep convolutional neural networks for chest diseases detection. Journal of healthcare engineering, 2018.

Chin, H. L., & Goh, D. L. M. (2023). Pitfalls in clinical genetics. Singapore Medical Journal, 64(1), 53-58.

Cosma, G., & Acampora, G. (2016). Neuro-fuzzy sentiment analysis for customer review rating prediction. Sentiment Analysis and Ontology Engineering: An Environment of Computational Intelligence, 379-397.

Fu, J., & Ye, J. (2020). Similarity measure with indeterminate parameters regarding cubic hesitant neutrosophic numbers and its risk grade assessment approach for prostate cancer patients. Applied Intelligence, 50(7), 2120-2131.

Gorgulu, O., & Akilli, A. (2016). Use of fuzzy logic based decision support systems in medicine. Studies on Ethno-Medicine, 10(4), 393-403.

Harat, A., Harat, M., & Martinson, M. (2020). A cost-effectiveness and quality of life analysis of different approaches to the management and treatment of localized prostate cancer. Frontiers in Oncology, 10, 103.

Hosseinzadeh, M., Saha, A., Brand, P., Slootweg, I., de Rooij, M., & Huisman, H. (2021). Deep learning–assisted prostate cancer detection on bi-parametric MRI: minimum training data size requirements and effect of prior knowledge. European Radiology, 1-11.

Ma'aitah, M. K. S., Aliyev, R., & Bus, I. J. (2017). Intelligent classification of liver disorder using fuzzy neural system. International Journal of Advanced Computer Science and Applications, 8(12), 25-31

Mahant, J. & Panda, S. (2018). Fuzzy expert system for prediction of prostate cancer. Journal of New Mathematics and Natural Computation, 16(1), 163-176

Pal, G., Huaman, J., Levine, F., Orunmuyi, A., Olapade-Olaopa, E. O., & Ogunwobi, O. O. (2020). Abstract B074: The long noncoding RNA from PVT1 exon 9 is overexpressed in prostate cancer in Black males and induces malignant transformation, invasiveness, and castration-resistance in prostate epithelial cells. Cancer Epidemiology, Biomarkers & Prevention, 29(6_Supplement_2), B074-B074.

Robbins, R., Hanna, R., Ejikeme, C., Orstad, S. L., Porten, S., Salter, C. A., Sanchez-Nolasco, T., Vieira, D. & Loeb, S. (2022). Systematic review of sleep and sleep disorders among prostate cancer patients and caregivers: a call to action for using validated sleep assessments during prostate cancer care. Sleep medicine.

Unschuld, P. U. (2020). The Conceptual Determination (Überformung) of Individual and Collective Experiences of Illness. In Concepts of Health, Illness and Disease (pp. 49-70). Routledge.

4th International Engineering Conference (IEC 2022)
Federal University of Technology, Minna, Nigeria

Performance Evaluation of Sun Tracking Control Systems using IMC and PID Controllers

Ifetola Damilola Madaki[1], Taliha Abiodun Folorunso[2], Jibril Abdullahi Bala[2], Adeyinka Peace Adedigba[2], Eustace M. Dogo[1]
[1]*Department of Computer Engineering,*
[2]*Department of Mechatronics Engineering,*
School of Electrical Engineering and Technology,
Federal University of Technology, Minna.
Email: ifetola.pg2115780@st.futminna.edu.ng

ABSTRACT

The inadequate supply of electricity for illumination has made many industries, organizations, and households resort to alternative energy sources, one of which includes solar energy. In comparison to other renewable sources of energy, the idea of employing photovoltaic panels for solar energy conversion into electrical energy remains a widespread choice. However, the amount of power a solar panel can produce is reduced due to the sun's constant shift in angle with respect to the earth. In this work, we evaluate the performance response of the STS using the transient response, Integral Absolute Error (IAE) and Integral Square Error (ISE) of the IMC and PID controller using MATLAB. The results obtained shows that, the PID outperforms the IMC in terms of IAE, ISE and Rise time, while the IMC outperforms the PID in terms of Settling time and system overshoot.

Keywords: *Integral Absolute Error (IAE), Integral Square Error (ISE), Internal Model Controller (IMC), Proportional-Integral-Derivative (PID), Sun Tracking System (STS).*

1 INTRODUCTION

Globally, there is a general push away from fossil-based energy sources towards renewable energy technologies and sources. This is in effort to combat the depleting ozone layer and its attendant climate issues. Over the years, renewable energy sources and their associated technologies have shown a positive impact in changing the narratives with regard to reducing the effects of energy generation on climate change (Oteh et al., 2022; Marwan & Anshar, 2020; Racharla & Rajan, 2017).

In comparison to other renewable energy sources, solar energy remains one among the easily tapped energy sources for power generation, due the to ease of harvesting using photovoltaic (PV) cells (Oteh et al., 2022). However, the amount of energy generated depends on the exposure of the PV Cells to solar radiation. Hence, for optimal performance, there must be maximum exposure of the PV cells to solar radiation (Racharla & Rajan, 2017).

In the quest to guarantee the maximum exposure of PV Cells to maximum solar radiation, a number of approaches have been implemented in literature with the solar tracking system being the most prominent (Hanwate & Hote, 2018). Albeit the efficacy of this approach is dependent on its ability to continuously track the maximum solar radiation through the tilt angle of the PV cells in line with solar movement. The solar tracking system (STS) is an electromechanical device that positions the PV Cells at an angle relative to the sun for optimal solar radiation (Hanwate & Hote, 2018). The tracking system also allows the movement of the PV Cells through the angle of tilt/inclination in line with the solar system's movement. To maximize the power extraction of the solar system, there exist three major approaches of controlling the tilt angle of the tracking system. These approaches include, the active, passive and hybrid approaches (Arif, Hossen, Ramana Murthy, & Armanur Rahaman, 2018). The efficacy of all three approaches lies in the ability of their controllers to regulate the tilt angle accordingly with the solar system.

The Proportional-Integral-Derivative (PID) controller exist as one of the simplest and easiest form of controllers to implement yet widely used for varying control applications (Arif et al., 2018; Hanwate & Hote, 2018; Oladayo & Titus, 2016; Rawat, Jha, & Kumar, 2020). The essential features of the PID Controller lie in the ease and simplicity of tuning (Folorunso, Bala, Adedigba, & Aibinu, 2021). The PID controller has also been applied in the control of single, dual, and multiple-axis tracking solar systems for optimal performance (Folorunso et al., 2021; Rawat et al., 2020; Suboh, Er, & Sardi, 2022). Another variant of PID

controller based on the tuning techniques has also been applied to track solar radiation (Arif et al., 2018; Hanwate & Hote, 2018; Rawat et al., 2020). The Internal Model Controller (IMC) is another type of controller that has been used in the control of solar tracking systems (Suboh et al., 2022). The IMC has some inherent characteristics that ensure its robustness and good tracking performance for several control applications (Folorunso et al., 2021; Zeng et al., 2020). Furthermore, the performance of the STS is solely dependent on the ability of the controller adapted to control its movement accordingly. However, the performance of the controller is also primarily dependent on the selection of appropriate controller gains. In this paper, the performance evaluation of the PID and IMC controllers in controlling the STS is investigated. This is with the view of obtaining the most optimal in tracking the conventional STS.

The rest of this paper are organized into four sections. Section 2, briefly describes the STS, the system model, and the design. Section 3, presents results and discussion. Lastly, Section 4, conclusion and recommendations for future works are presented.

2 METHODOLOGY

The structure of a typical STS is as depicted in Figure 1, wherein the principal inputs for tracking are the temperature and irradiance as presented (Arif et al., 2018). The goal of the tracking system is to ensure that the exposure to the input (temperature and irradiance) is always maximum.

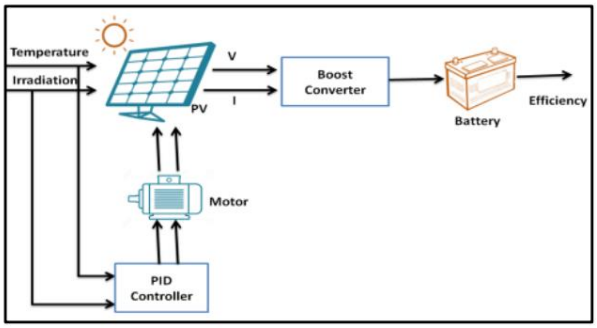

Figure 1: Representation of the STS (Rawat et al., 2020)

In Figure 2, the block diagram representing the STS is presented. The electric motors are the primary mover in the sun tracking system, the rotation of the solar cells is achieved by controlling the motor. A light-sensitive device, such as a Light Dependent Resistor (LDR), is utilized as the input sensor unit in a solar tracking system which produces the voltage required to power the motor; the output provides the angular displacement of the electric motor, which represents the motion of the STS.

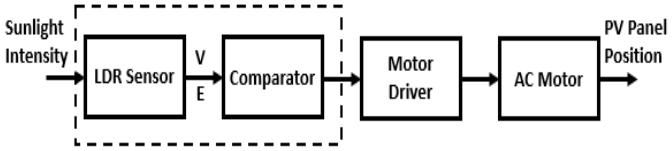

Figure 2: Simplified block diagram of a solar tracker (Wang & Lu, 2013)

SYSTEM MODELLING

In this section, the mathematical model of the STS is presented as a function of the DC motor. The STS IS modelled using the typical DC motor (Electromechanical System) as depicted in Figure 3. The Solar Tracker system can be identified based on the behavior of input applied to it. The mathematical model is derived from the real performance of the system input.

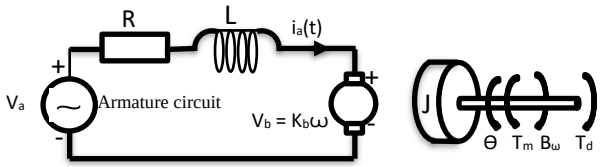

Figure 3: Model diagram of the electromechanical system (Olaniyi, Folorunso, Kolo, Arulogun, & Bala, 2015)

where:
T_m = Torque of motor
v_a = Applied voltage
J = inertia of the rotor
ω = Angular Velocity
vb = Back EMF
B = co-efficient of viscous friction
K_t = Torque Constant
K_b = Back EMF constant
θ = Angular displacement
$i_a(t)$ = Armature current
R = Resistance of the armature
L = Inductance of the armature
Td = Disturbance Torque

In a magnetic field, the voltage of the rotating, current-carrying armature, is proportional to the speed. Therefore,

$$V_b(t) = K_b \frac{d\theta_m}{dt} \quad 1)$$

Taking the Laplace transform, we get

$$V_b(s) = k_b \, s\theta_m(s) \quad 2)$$

The Laplace-transform equation of the loop around the armature circuit gives the relationship between the applied armature voltage, the armature current, i_a(t), e_a(t), and the back emf, V_b(t).

$$R_a i_a(s) + L_a s i_a(s) + V_b(s) = E_s(s) \quad 3)$$

The torque of the motor output is proportional to the current of the armature. Thus,

$$T_m(s) = K_t I_a(s) T_m \quad 4)$$

Rearranging Equation (4) gives,

$$i_a(s) = \frac{1}{T_m}(s) \quad 5)$$

Substituting Equations (2) and (4) into (3), gives.

$$\frac{(R_a L_a s)\, T_m(s)}{k_t} + K_b s \theta_m(s) \quad 6)$$

Dm, which comprises the armature and load viscous damping, is the equivalent viscous damping at the armature.

$$T_m(s) = (J_m s^2 + D_m s)\theta_m(s) \quad 7)$$

Substituting Eq. (7) into Eq. (6) yields

$$\frac{(R_a + L_a s)\,(J_m s^2 + D_m s)\theta_m(s)}{K_t} + K_b s \theta_m(s) = E_a(s) \quad 8)$$

Simplifying, the transfer function, $\theta m(s)/Ea(s)$, gives;

$$\frac{\theta_m(s)}{E_a(s)} = \frac{K_t/R_a J_m}{s\left[s + \frac{1}{J_m}\left(D_m + \frac{K_t k_b}{R_a}\right)\right]} \quad 9)$$

Table 1 shows the parameters of the DC servo motor utilized in this study. The motor under consideration is the M600 series DC servo motor by Mclennan.

Table 1: Values used based on the proposed DC motor for the sun tracking system (*M600 Series Dimensions : Mm M600 Series*, 2019.).

Parameters	Values
K_t	0.0816NM/Amp
K_b	0.0816NM/Amp
D_m	0.0000816MN/rad sec
J_m	0.012Kg/m2
R_a	0.6Ω

Substituting these values into equation 9, we have:

$$\frac{\theta_m(s)}{E_a(s)} = \frac{11.3}{s^2 + 0.992s} \quad 10)$$

PID CONTROL SYSTEM DESIGN

The Proportional-Integral-Derivative (PID) controller is a closed-looped and is statistically among the most widely used controllers in the engineering sector. The PID controller comprises of three components which are the Proportional term (Kp), the Integral term (Ki) and the Derivative term (Kd). The function of each term is as stated below:

- Proportional Gain (Kp): The system speed is increased since the output is proportional to the error value.
- Integral Gain (Ki): Steady-state error is reduced by using an integrator to compensate for low frequency
- Derivative Gain (Kd): Enhances transient response through high-frequency differentiator compensation.

To make sure that the output of the control system track movement of the sun efficiently, the PID parameters must be tuned. This requires modifying the proportional, integral, and derivative gains. Figure 4 represents a PID controller.

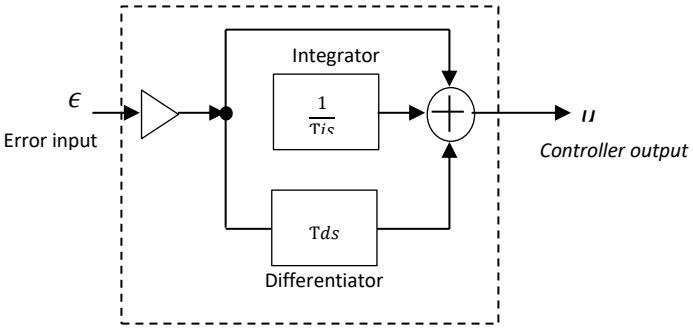

Figure 4: Diagram of the PID controller (Bala, 2022)

$$U(t) = K_p e(t) + K_i \int e(t)\, d(t) + k_p \frac{d_e}{d_t} \quad 11)$$

$$G_{PID}(s) = K_p + \frac{K_i}{s} + K_d(s) \quad 12)$$

where.
$U_{t=}$ PID Control Variable
$K_{p=}$ Proportional gain
e_t = Error value
K_i =Integral gain
d_e = Change in the error value.
d_t = Change in time

The PID tuner app in MATLAB was used in tuning the PID controller. The parameters generated using the application are presented in Table 2.

Table 2: PID Tuning Parameters

Parameter	Value
Proportional Gain (Kp)	0.1818
Integral Gain (Ki)	0.0419
Derivative Gain (Kd)	0.1375

INTERNAL MODEL CONTROLLER (IMC)

Garcia and Morari proposed IMC in 1982, and it has since received researchers' interest because of its ease of use, robustness, powerful tracking performance, and simplicity of tuning. The IMC also features an optimal control characteristic of zero(0) steady-state error as well as simplicity of parameter adjustment (Balaa, Olaniyi, Folorunso, & Arulogund, 2020), (Folorunso et al., 2021). Figure 5 shows the block diagram of a typical IMC control process.

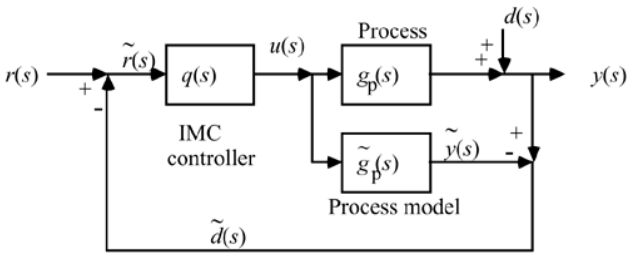

Figure 5: An IMC Control Process (Zeng et al., 2020).

$$G_c(s) = \frac{G_{IMC}(s)}{1 - G_{IMC}(s)G_p(s)} \qquad 13)$$

where.
G_{IMC}= IMC controller,
Gp = process,
Ĝp = process model and
Gd = external disturbance.

$$G_{IMC}(s) = G^{-1}{}_p(s)F(s) \qquad 14)$$

where;
$F(s)$= Filter and
$G^{-1}{}_p$= Inverse of the plant model

$$F(s) = \frac{1}{(1+\lambda s)^n} \qquad 15)$$

Where n is adequately enormous to make the controller suitable and λ is the tuning parameter in charge of the speed of response and robustness. λ also deals with close-loop performance and modelling errors. An n value was selected because the plant model is a second-order system while a λ value of 1 was selected for the IMC system.

3 RESULTS AND DISCUSSION

3.1 PID CONTROLLER

Figure 6 presents the system block diagram in Simulink and Figure 7 presents the system response of the PID controller.

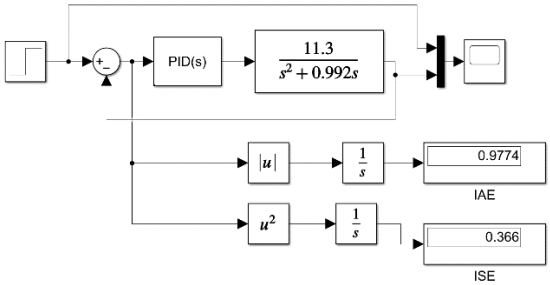

Figure 6: PID Simulink block representation of the sun tracking system

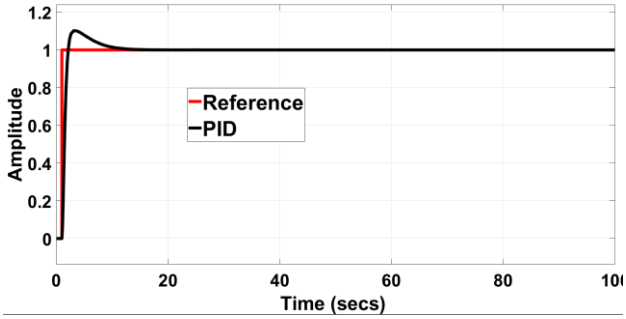

Figure 7: PID System Response of the sun tracking system

The graph in Figure 7 was obtained from the oscilloscope which serves as an output to the control system using MATLAB. It shows the system response, transient and steady-state response and the system behavior. From the figure, it was observed that the system has a rise time of 753.072ms. This implies that it takes the system 0.753 seconds to rise from 10% to 90% of the final step value. Additionally, the system exhibited a settling time of 15s. This indicates that the system took 15 seconds to settle within 2% of the final value. Furthermore, the system showed an overshoot of 10.6%, which implies that the system response went over the final step value by 10.6% before eventually settling down to the desired value. The system exhibited an IAE of 0.99774 and an ISE of 0.366, implying the errors the system accumulated over the simulation time of 100 seconds.

3.2 Internal Model Controller (IMC)

Figure 8 presents the IMC system block diagram in Simulink and Figure 9 presents the system response of the IMC.

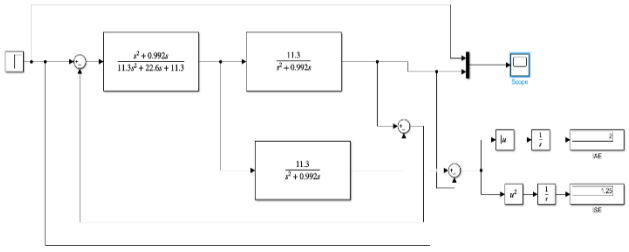

Figure 8: IMC Simulink block representation of the sun tracking system

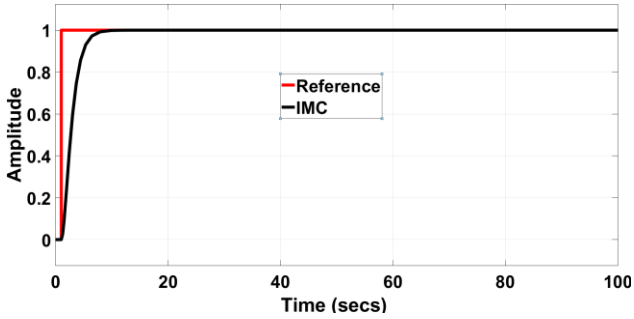

Figure 9: IMC graphical representation of the sun tracking system

The graph in Figure 9 was obtained from the oscilloscope which serves as an output to the control system using MATLAB. It shows the system response, transient and steady-state response and the system behavior. From the figure, it was observed that the system has a rise time of 3.376s. This implies that it takes the system 3.376s seconds to rise from 10% to 90% of the final step value. Also, the system exhibited a settling time of 9s. This shows that the system took 9 seconds to settle within 2% of the final value. Furthermore, the system showed an overshoot of approximately 0%, which implies that the system response went over the final step value by approximately 0% which is almost negligible before settling down to the desired value. The system exhibited an IAE of 2 and an ISE of 1.25, implying the errors the system accumulated over the simulation time of 100 seconds.

3.3 Comparative results

The combined system responses of the IMC and PID controllers in relation to the step input is presented in Figure 10. In addition, Table 3 shows a comparative analysis between the IMC and PID controller.

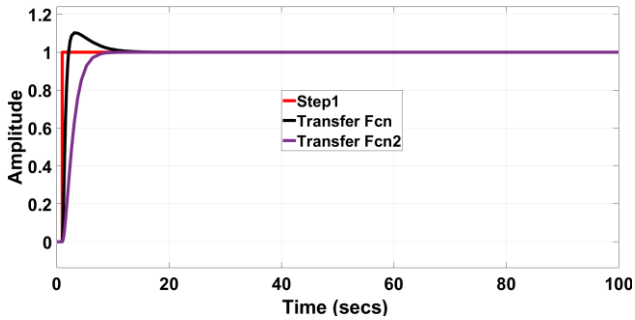

Figure 10: Combined System Response of IMC and PID Controllers

Table 3: Comparative result of the IMC and PID controller

	Rise Time (secs)	**Settling time (secs)**	**Overshoot (%)**	**Integral Absolute Error** (IAE)	**Integral Square Error** (ISE)
PID	0.753	15	10.6	0.99774	0.366
IMC	3.376	9	0	2	1.25

From Figure 10 and Table 3, it can be seen that the PID control system had a lower rise time than the IMC system. This implies the PID system will reach its desired set point faster than the IMC-based system. In terms of the settling time, however, the IMC had a lower value than the PID implying the IMC settles faster to the final step value. The IMC had a very low overshoot of approximately 0% which is characteristic of the IMC. On the other hand, the PID had an overshoot of 10.6%. In the cases of the ISE and IAE, the PID exhibited lower error values than the IMC. This implies the PID showed more accurate tracking performance over the simulation time.

4 CONCLUSION

In conclusion, the performance evaluation of the IMC and PID Control system for the STS was carried out successfully. The results obtained show that in terms of IAE, ISE and Rise time, the PID outperforms the IMC, while the IMC outperforms the PID in terms of settling time and system overshoot. This implies that the controllers can be successfully implemented in a STS depending on the preferred performance. If the speed of response is preferred with minimal tracking errors, then the PID is recommended. However, if a lower overshoot is preferred, then the IMC provides that performance. Future works will examine the effect of Optimization algorithms on PID and IMC systems for solar tracking.

REFERENCE

Arif, E., Hossen, J., Murthy, G. R., & Rahaman, M. A. (2018). A novel PID controller based solar panel tracking system. *transfer*, *8*, 2.

Bala, J., Olaniyi, O., Folorunso, T., & Arulogun, T. (2020). Performance Evaluation of the Effect of Optimally Tuned IMC and PID Controllers on a Poultry Feed Dispensing System. *Journal of Advances in Computer Engineering and Technology*, *6*(4), 213-226.

Folorunso, T. A., Bala, J. A., Adedigba, A. P., & Aibinu, A. M. (2021). *Genetic Algorithm Tuned IMC-PI Controller for Coupled Tank Based Systems.* Paper presented at the 2021 1st International Conference on Multidisciplinary Engineering and Applied Science (ICMEAS).

Hanwate, S. D., & Hote, Y. V. (2018). Design of PID controller for sun tracker system using QRAWCP approach. *International Journal of Computational Intelligence Systems*, *11*(1), 133-145.

M600 series Dimensions : mm M600 series. (n.d.). 173(0).

Marwan, M. A. (2019). *PID Controller Design for Solar Tracking System.* Paper presented at the International Conference on Information System and Technology (CONRIST 2019).

Oladayo, B., & Titus, A. (2016). Development of solar tracking system using IMC-PID controller. *American J. of Engineering Research*, *5*(5), 135-142.

Olaniyi, O., Folorunso, T., Kolo, J., Arulogun, O., & Bala, J. (2015). Towards The Development of a Mobile Intelligent Poultry Feed Dispensing System Using Particle Swarm Optimized PID Control Technique. *African Journal of Computing & ICT*, *8*(3).

Olaniyi, O. M., Folorunso, T. A., Kolo, J. G., Arulogun, O. T., & Bala, J. A. (2016). *Performance Evaluation of Mobile Intelligent Poultry Feed Dispensing System Using Internal Model Controller and Optimally Tuned PID Controllers.* Paper presented at the ISTEAMS Multidisciplinary Cross-Border Conference, , University of Professional Studies, Ghana.

Oteh, O., Oloveze, A., Obasi, R., Nduka, C., Asaga, G., Osumba, B., & Ahaiwe, E. (2022) Consumer response to adoption and demand for energy saving bulbs in nigeria. *Journal of Business Research*, *70*, 127-135.

Racharla, S., & Rajan, K. (2017). Solar tracking system–a review. *International journal of sustainable engineering*, *10*(2), 72-81.

Rawat, A., Jha, S., & Kumar, B. (2020). Position controlling of sun tracking system using optimization technique. *Energy Reports*, *6*, 304-309.

Suboh, S., Er, L. C., & Sardi, J. (2022). *Power Controller for Dual-axis Solar Tracking System using PID.* Paper presented at the Journal of Physics: Conference Series.

Wang, J.-M., & Lu, C.-L. (2013). Design and implementation of a sun tracker with a dual-axis single motor for an optical sensor-based photovoltaic system. *Sensors*, *13*(3), 3157-3168.

Zeng, W., Zhu, W., Hui, T., Chen, L., Xie, J., & Yu, T. (2020). An IMC-PID controller with Particle Swarm Optimization algorithm for MSBR core power control. *Nuclear Engineering and Design*, *360*, 110513.

4th International Engineering Conference (IEC 2022)
Federal University of Technology, Minna, Nigeria

Adopting Virtual Assistants in Nigerian Tertiary Institutions: Benefits and Challenges.

Abdullahi, I. M[1], Maliki, D[2], Dauda, A. I[3], & Siyaka, H. O[4], Malum, S[5],
[1235]Computer Engineering Department, Federal University of Technology, PMB 65 Minna Niger State, Nigeria[5]
[4]Computer Science Department, Federal Polytechnic Bida, PMB 55 Bida Niger State, Nigeria
Corresponding author email: amibrahim@futminna.edu.ng +2348037313848

ABSTRACT
Smart campus allows educational institutions at tertiary level to make sound decisions that will enable them to maximize resources and improve security. The development of smart campuses is aided by some basic infrastructures such as 5G, IoT, cloud computing, AI, as well as big data analytics. Virtual Assistant (VA) and e-learning, were rapidly adopted into educational processes to reduce the need for physical contacts due to covid-19. enhance effective learning and teaching. VA has proven to be a very useful tool for effective teaching and learning in educational institutions. In this article, the roles, benefits and challenges of adopting virtual assistants in higher education institutions in Nigeria. Specific task that needed to be virtualized are also highlighted. The findings show that VA can be used to automate Level Advising for students, some exams exam officer's duties, some task performed by head of departments, academic and transcript office task, postgraduate school task and alumni relations tasks. It is also determined that VA have the potential to reduce the running costs of higher education institutions, improve teaching and learning, and reduce staff workloads. However, to achieve this goal, infrastructure such as the internet, electricity and cloud services must be improved.

Keywords: *Artificial Intelligence, Digital Classroom, E-learning, Intelligent Personal Assistants, Virtual Assistants*

1 INTRODUCTION

The demand for e-Learning has increased over the past few years. Many colleges have started creating their e-Learning systems in addition to popular open-source and corporate systems. Learning is a very complex process with many different components, including objectives, procedures, managing material and information, sharing, augmenting, and supplying. All of these elements are integrally tied to handling a certain type of learning materials and flow along with offering the required management services (Ivanova *et al.*,2017). However, to generate a successful personalized learning operation, these tangentially linked components must come together to offer the whole context necessary for tailored behavior. (Kasthuri & Balaji, 2021). With the potential to intelligently learn throughout their lifetime, virtual assistants will greatly support education advancement.

Artificial intelligence (AI) that allows virtual assistants to work autonomously necessitates meticulously defined paths and intense human supervision (Laeeq & Memon, 2021). To construct the artificial intelligence on which the virtual assistant relies, human engineers must methodically process the interactive and conversational data. The technology underpinning partially autonomous and fully autonomous virtual assistants is deep reinforcement learning utilizing CNN models (Laeeq & Memon, 2021). It's not apparent if artificial intelligence (AI) (virtual assistants) can take the role of human judgment in addressing people's personal needs, even though it can frequently complete technical jobs faster and better than humans.

Even after being accepted into college, students must complete several well-defined but difficult tasks, such as filling out course registration forms, submitting assignments and dissertations, getting immunizations, and paying tuition, to name a few (Page & Gehlbach, 2017). Many students will stumble and succumb to challenges if they are not assisted in those tasks that they find difficult. This will affect the efficiency with which they complete their tasks. Differential attrition throughout the journey to college can aggravate socioeconomic differences in educational access and degree conferment, even among students with comparable academic profiles. As a result, resolving the educational assistantship issue has significant educational and societal implications(Laeeq & Memon, 2021).

Users should be helped by customized interface components understandably and intelligently while interacting with complicated systems, such as virtual educational systems. Personal assistants are one potential remedy (Todorov *et al.*,2018). Personal assistants are not new; they have been utilized for many years in both business and personal chores. Daily duties like organizing meetings, booking hotels, groceries, and clearing bills are managed by personal assistants, among other things. Previously, only individuals could serve as personal assistants, but today an electronic gadget with learning capabilities may do so (Santos *et al.*,2018). These electronic devices' assistants often allow users to call,

exchange SMS, view their schedule, explore websites, read papers, obtain meteorological data, and a slew of other things.

The Google Assistant, Siri, Cortana, and Echo virtual assistants are just a few examples of the prominent mobile device virtual assistants that have been developed over the years and have become popular. The architecture and principles used by Google Assistant, Siri, and Cortana are comparable. The objective is to afford human interaction with the system and equipment easier and more pleasant (Zawacki-Richter *et al.*,2019). With the help of these voice assistants, customers can make bookings, and stream conferences and podcasts without needing to use their hands. Contrarily, most voice assistants need at least 1.5 seconds to comprehend a statement, and they frequently search right away for words that can't be understood contextually without additional machine intervention (Zawacki-Richter *et al.*,2019).

In this paper, the virtual assistant technology, the benefits and challenges that hinder the adoption of the technology in tertiary institutions in Nigeria were explored. This is to bring to the fore the adoption challenges with a view to addressing them and fully benefit from the technology. The paper is organized as follows: section one presents the introduction, literature review is presented in section two. The third section presents the classification of VA systems; Section 4 discussed the benefits, challenges and solutions of VA adoption. Finally, in section 5, the solutions to the challenges and conclusion were presented.

2 LITERATURE REVIEW

The educational industry has produced and embraced several digital technologies. The efficient administration of campuses and student-centered learning can be achieved by effectively integrating technologies like IoT technology, cloud computing, big data, AI, augmented and mixed reality, and others with a user-friendly system interface (Chiu *et al.*,2020). According to IBM's 2016 smart campus study, most colleges have started to track and evaluate the academic performance of students and learning activities. Analysis of data and intelligent computing can enhance students' learning opportunities. (Kasthuri & Balaji, 2021).

The absence of originality and appeal in the educational process is one of the factors contributing to a decline in interest in learning. The use of gamification and game-based learning might be effective strategies for increasing students' excitement. MATE (Multi-Agent Testing Environment), a game-based learning interface, is presently being created to be integrated into virtualized systems focused on education and learning. Another responsibility is to provide frameworks for assistants' self-improvement through education. Our next job is to provide a fully standardized environment for carrying out the suggested lifelong learning strategy, drawing on the expertise gained from the existing iteration of the space (Ivanova *et al.*,2017).

Chiu *et al.*,(2020) noted in their case study on virtual assistants as a smart campus that; There is a need to support schools in incorporating new technologies like wearables, Mixed reality, and AI into coursework in addition to enhancing the general network infrastructure of school campuses in Taiwan at all levels. Recent developments have brought the use of IoT technologies to create smart campus solutions. To allow smart parking and intelligent classrooms on campus, it links video surveillance and other sensing components through WLAN. Other tools, such as multimedia conferences, learning resource performance, a 5G network teaching platform, and smartphone-connected campus sensors, are used to support instructional activities on campuses. (Chiu *et al.*,2020) study created a useful voice assistant powered by deep learning that can effectively take the place of conventional university-approved sites and applications. Users just have to utilize voice requests to acquire information about the campus; complex procedures are not necessary.

In (Chiu *et al.*,2020)'s implementation of a robust network-based campus virtual assistant; Because smartphones are so common, the virtual assistant appears as a chatbot. The chatbot was created as an app. The assistant is first turned on by calling wake-up words, and in the next stage of Guided Dialogue, it would offer vital guidance for using services. After then, consumers would communicate their demands to the assistant verbally during the Audio Conversation stage. The recommended module would then categorize the emotional label of the voice command. Additionally, the suggested module executes the appropriate reaction and action depending on the voice command's word embeddings and emotional label input. The virtual assistant conducts discussions and tasks following the corresponding response and action. Finally, if no additional user commands are issued, the assistance will terminate.

Ivanova *et al.*,(2017) in their research on virtual assistants focused on their role in virtual education for lifelong learning. In the virtual education system, a student is represented by his or her assistant. Users might use it to sign up for the services the digital library offers. The administration of the library receives a request to sign up for the service, and they send it to the system. It then keeps track of this registration and starts teaching the learner English. The teacher can create exam questions, which are kept in a database and used by the system. The instructor is portrayed in the VR system by their helper. The teacher can design a test or choose the problems that will be emailed to the student at random times for a certain period after the database has enough test questions. The student's aide receives a test question through the technology and must help the student envision the question and potential responses. When a student has

made a decision, their assistant enters that response into the computer, which adds it to the database along with the questions.

Todorov *et al.*,(2018); emphasized that creating an efficient interaction between autonomous intelligent components that are working in the area is a significant problem for virtual assistants in education. Their three-step strategy entailed developing a uniform, integrated technology to guarantee communicational and syntactical compatibility among various component types employed in the space and situated on various architectural levels. The next step was to enable semantic interoperability, or the capacity for semantic parts of the interaction to be supported by techniques, methods, and other means. The usage of adaptive learning virtual assistants, or the inclusion of intelligent assistants, was the final stage. Assistants that exhibit context-aware, reactive, proactive, and social behavior independent of the environment were referred to as "intelligent" in this context (Todorov *et al.*,2018).

Santos *et al.*,(2018) noted that intelligent assistants are currently able to help their users with a wide range of activities and emphasized the need of figuring out whether it is feasible to enhance their knowledge and assertiveness by leveraging new technological paradigms. He said that one potential strategy is to integrate intelligent personal assistants into IoT applications. The learning database would grow as personal assistants would be able to study data from a greater range of sources. Many user chores can be made easier with the design of smart assistants which are more independent and perceptive. It should be highlighted that bringing intelligent personal assistants to IoT contexts raises several challenges, mostly relating to technology paradigms. Making methods to facilitate communication between items in a network is one of these problems. The development of a uniform Internet of Things communication protocol was suggested as one potential remedy (Page & Gehlbach, 2017) centred on creating a virtual assistant to aid kids through the college application process. (Zawacki-Richter *et al.*,2019) outlined several domains of ai applications in institutional and operational services as well as educational support:

I. profiling and prediction
II. assessment and evaluation
III. adaptive systems and personalisation
IV. intelligent tutoring systems.

The researchers discuss the almost complete lack of rational contemplation upon these difficulties and dangers of artificial intelligence (virtual assistants in education), the tenuous link to theoretical pedagogical viewpoints, and hence the need for even more investigation of ethical and academic methods in the application of AI in university education. (Cavique *et al.*,2019) proposed a cutting-edge Virtual Assistant concept as a component of a human-machine interaction effort to improve engagement during presentations and open dialogue among the presenter and the audience (e.g., auditoriums with 200 people). The main goal of the suggested approach was to offer a framework for interaction to increase audience awareness of crucial aspects of the presentation. The combination between the speaker and the virtual assistant might increase public education in this way.

3 CLASSIFICATION OF VA SYSTEMS

Virtual assistant systems are a creative solution to provide help and guidance to students in higher education institutions. Voice-based assistants, chatbots, virtual reality, education gamification, and web-based platforms are the five primary types of these systems as shown in Figure 1. Each of these classifications was reviewed and presented in this context, emphasizing the individual strengths and limits of each method.

Voice-based assistants: These virtual advising systems communicate with students using speech recognition technology, allowing them to simply and swiftly ask questions and receive replies. This sort of method is very beneficial for students who are always on the go or want a more conversational approach, however, in comparison to the other classification slow in response (Laeeq & Memon, 2021).

Chatbots: Chatbots are conversational agents that communicate with students using natural language processing. They are meant to give quick and easy answers to common inquiries and may be implemented into websites or mobile applications. They offer a faster response time than other VA classifications (Kasthuri & Balaji, 2021).

Virtual reality: Virtual reality (VR) solutions provide students with a completely immersive experience, allowing them to see and realistically interact with content. VR may be utilized to conduct virtual tours, mimic real scenarios, and deliver interesting and interactive teaching in the setting of higher institutions.

Education gamification: This method motivates students and makes learning more exciting and engaging by using game aspects such as points, awards, and challenges. Students are more likely to stay interested and remember information when education is made more fun (Ivanova *et al.*,2017).

Web-based platforms: Web-based platforms are online platforms that offer a variety of resources to students, such as educational materials, online tutoring, and systems for tracking progress and getting feedback. This sort of system is especially beneficial for students who prefer a self-directed approach to learning and want to access information and help at any time and from any location (Page & Gehlbach, 2017).

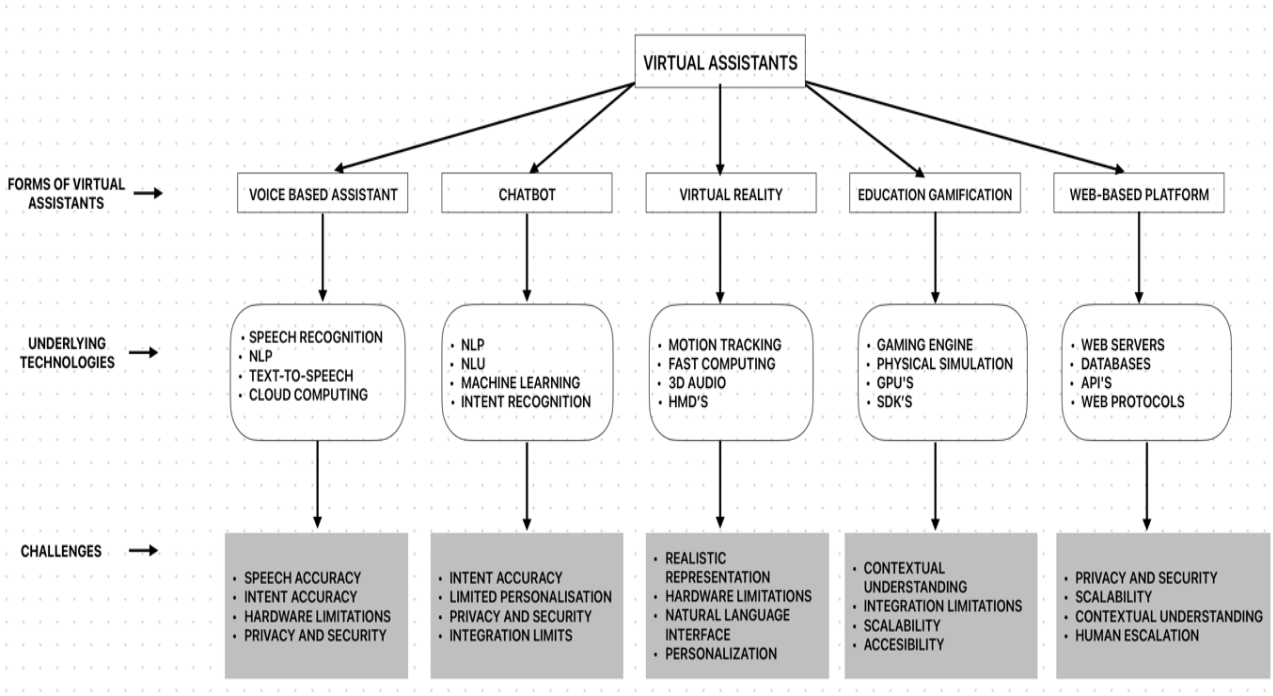

Figure 1: VA Technologies Classification

4.1 BENEFITS OF VA IN TERTIARY INSTITUTIONS

Virtual Assistants can help tertiary institutions in numerous ways. Some of the benefits include improved productivity, increased efficiency, better access to online resources, enhanced service, and improved workflow automation. Additionally, virtual assistants can provide added convenience and flexibility by allowing students to access information on their own time, without having to wait for assistance from a traditional staff member. Finally, virtual assistants can reduce costs associated with staffing traditional roles, such as receptionists or other support staff. VA can be used to automate several tasks in the universities. They include: Level Advising for students, some exams exam officer's duties, some task performed by head of departments, academic and transcript office task, postgraduate school task and alumni relations tasks. Other benefits of VA include:

Saving time: Many administrative activities, such as organizing appointments and replying to emails, may be automated by virtual assistants. This frees up time for educators to focus on more vital responsibilities like developing new course content and doing research (Haleem *et al.*,2022).

Reducing costs: Tertiary institutions can save money on employment expenditures such as salary, benefits, and training by adopting virtual assistants. Furthermore, virtual assistants may be employed to automate specific operations, minimizing the need for extra manual work.

Facilitating effective delegation: Virtual assistants can aid tertiary educators in delegating responsibilities to students, giving them more time to focus on their research and teaching. This can also aid in the development of a more collaborative and student-centered approach to teaching (UNESCO, 2019).

Improving the organization of education assistance: Virtual assistants can be employed to help with educational tasks like grading and course scheduling (Haleem *et al.*,2022). This can serve to enhance tertiary institutions' overall efficiency, resulting in a better educational experience for students.

Constant availability: Virtual assistants are available at all times, allowing students to seek assistance whenever they need it (UNESCO, 2019). This can improve student engagement and happiness with their educational experience

Creating a sense of trust: Tertiary schools can demonstrate their commitment to giving students with the resources and assistance they need to succeed by utilizing virtual assistants. This can assist students to gain trust and motivate them to continue their studies (Haleem *et al.*,2022).

Increasing user loyalty: Virtual assistants can help to promote student loyalty to higher institutions by providing students with a convenient and dependable means to access educational resources and support (Olutola & Olatoye, 2015). This can also motivate students to

recommend the college to others, thereby increasing enrolment.

4.2 VA ADOPTION CHALLENGES

In recent times, virtual assistants have been gaining traction as a viable alternative to traditional assistants. However, the adoption of virtual assistants in tertiary institutions in Nigeria has been slow due to several challenges. These challenges include the lack of adequate infrastructure, insufficient highly trained personnel, the high cost of deploying virtual assistants, and the Phobia of change by students and staff to use virtual assistants to mention a few.

Limited access to modern technology and Technical Knowledge: Developing countries like Nigeria often have limited access to the latest technology and infrastructure, and know-how making it difficult for virtual assistants to be adopted.

Lack of awareness: Nigerian students, teachers, and administrators are not always aware of how virtual assistants can benefit their educational experience and enhance teaching and learning.

Cost of Implementation: The cost of implementation of virtual assistants in Nigeria is often too high for educational institutions to bear as most institutions look towards novel design and development of VA systems.

Limited access to reliable internet and infrastructure: Internet connectivity is often unreliable and slow in Nigeria, making it difficult to use virtual assistants. Internet infrastructure is also still lacking in several regions

Poor data security: Data security is often not a priority in tertiary institutions. This means that virtual assistants may not be able to guarantee adequate security for user data.

Cultural barriers: Cultural barriers may also be a hindrance to the adoption of virtual assistants in Nigeria. This is because students may not be comfortable with the idea of talking to a virtual assistant.

Language barrier: Most virtual assistants are designed to understand English, which can be a barrier for Nigerian students who may not be familiar with this language.

4.3 SOLUTION TO VA ADOPTION CHALLENGES

To overcome the aforementioned challenges, it is important to understand their root causes and provide solutions. Here are some potential solutions to the challenges hindering the adoption of virtual assistants in tertiary institutions in Nigeria:

Reduce the Cost of Deployment: One of the key issues hindering the adoption of virtual assistants in tertiary institutions in Nigeria is the high cost of deployment. To reduce the cost, institutions can opt for open-source virtual assistants such as Alexa or Google Home, which are more affordable than their more expensive counterparts.

Focus on Technical Knowledge: Another challenge is the lack of technical knowledge among faculty and staff. Institutions should focus on providing proper technical training to faculty and staff to enable them to capitalize on the benefits of virtual assistants.

Upgrade Infrastructure: Virtual assistants require reliable internet connectivity and access to power. To ensure a seamless experience, institutions should upgrade their infrastructure and provide a stable environment for the virtual assistant to operate in.

Provide Proper Training: Proper training is essential for the successful deployment of virtual assistants. Institutions should ensure that the necessary training is provided to personnel to ensure that they can use the virtual assistant effectively and efficiently.

By addressing these key issues, institutions in Nigeria will be able to capitalize on the potential of virtual assistants and reap the benefits that they can offer.

5 CONCLUSION

This research has provided an extended look into the current landscape of virtual assistant use in higher education, as well as potential trends that can shape academic research and development in this area. It has also drawn attention to the possibilities of applications for virtual assistants to assist learners, teachers, and executives throughout the student lifecycle. Virtual assistant technology will probably continue to be a major problem in the years to come, even if the entire impact of virtual assistant deployment on education cannot yet be completely understood. Moving forward, research should focus on the development and measuring of the impact of virtual assistant applications on the quality of education to fully understand their potential. Education administrators should also focus on providing the necessary infrastructure for the full adoption of the technology. Furthermore, more awareness is needed among the education stakeholders on the benefits of the technology.

REFERENCE

1. Cavique, C., Cláudio, A. P., Carmo, M. B., Guerreiro, M. P., Cavaco, A., & Mateus, E. (2019). Op0286 pare developing a virtual assistant to promote education on osteoarthritis. 224.3-225. https://doi.org/10.1136/ANNRHEUMDIS-2019-EULAR.967
2. Challenges and Opportunities for Sustainable Development Education Sector United Nations Educational, Scientific and Cultural

Organization. (2019). https://en.unesco.org/themes/education-policy-

3. Chiu, P. S., Chang, J. W., Lee, M. C., Chen, C. H., & Lee, D. S. (2020). Enabling intelligent environment by the design of emotionally aware virtual assistant: A case of smart campus. IEEE Access, 8, 62032–62041. https://doi.org/10.1109/ACCESS.2020.2984383
4. Haleem, A., Javaid, M., Qadri, M. A., & Suman, R. (2022). Understanding the role of digital technologies in education: A review. Sustainable Operations and Computers, 3, 275–285. https://doi.org/10.1016/j.susoc.2022.05.004
5. Institute of Electrical and Electronics Engineers. (2018). SISY 2018: IEEE 16th International Symposium on Intelligent Systems and Informatics: proceedings: Subotica, Serbia, September 13-15, 2018. IEEE.
6. Ivanova, V., Toskova, A., Stoyanova-Doycheva, A., Stoyanov, S., & Veselinova, M. (2017). Lifelong learning in Virtual education space with intelligent assistants. ACM International Conference Proceeding Series, Part F130953. https://doi.org/10.1145/3136273.3136287
7. Kasthuri, E., & Balaji, S. (2021). A chatbot for changing lifestyles in education. Proceedings of the 3rd International Conference on Intelligent Communication Technologies and Virtual Mobile Networks, ICICV 2021, 1317–1322. https://doi.org/10.1109/ICICV50876.2021.9388633
8. Laeeq, K., & Memon, Z. A. (2021). Scavenge an intelligent multi-agent-based voice-enabled virtual assistant for LMS. Interactive Learning Environments, 29(6), 954–972. https://doi.org/10.1080/10494820.2019.1614634
9. Olutola, A. T., & Olatoye, O. O. (2015). Challenges of E-Learning Technologies in Nigerian University Education. Journal of Educational and Social Research. https://doi.org/10.5901/jesr.2015.v5n1p301
10. Page, L. C., & Gehlbach, H. (2017). How an Artificially Intelligent Virtual Assistant Helps Students Navigate the Road to College. AERA Open, 3(4), 233285841774922. https://doi.org/10.1177/2332858417749220
11. Santos, J., Rodrigues, J. J. P. C., Casal, J., Saleem, K., & Denisov, V. (2018). Intelligent Personal Assistants Based on Internet of Things Approaches. IEEE Systems Journal, 12(2), 1793–1802. https://doi.org/10.1109/JSYST.2016.2555292
12. Todorov, J., Valkanov, V., Stoyanov, S., Daskalov, B., Popchev, I., & Orozova, D. (2018). Personal Assistants in a Virtual Education Space. In Studies in Systems, Decision and Control (Vol. 140, pp. 131–153). Springer International Publishing. https://doi.org/10.1007/978-3-319-78437-3_6
13. Zawacki-Richter, O., Marín, V. I., Bond, M., & Gouverneur, F. (2019). A systematic review of research on artificial intelligence applications in higher education – where are the educators? In International Journal of Educational Technology in Higher Education (Vol. 16, Issue 1). Springer Netherlands. https://doi.org/10.1186/s41239-019-0171-0

4th International Engineering Conference (IEC 2023)
Federal University of Technology, Minna, Nigeria

Glare Stopper: The Automatic Car Headlight Management System

*[1]Daniyan, A. & [1]Ilupeju, S. S.
[1]Electrical and Electronic Engineering Department, Federal University of Technology, PMB 65 Minna Niger State, Nigeria
*Corresponding author email: a.daniyan@futminna.edu.ng +2348064203455

ABSTRACT
The growing number of vehicles on roads calls for increased safety considerations, especially during night driving. A common issue is the misusage of high beam headlights, which can cause light glare for opposing drivers due to the high intensity beam a driver receives from oncoming vehicles. This is called the Troxler Effect. This is a safety critical issue given that the human eyes are very sensitive to light, and when eyes suddenly encounter high intensity light, one's vision get temporarily affected and require some time to recover the vision. During this vision recovery window, the vehicle has covered some distance which could increase the likelihood of an accident occurring.
To address this, we propose an automatic car headlight management system that adjusts a vehicle's headlights based on light intensity of oncoming vehicles. The system utilizes an Arduino Uno microcontroller and an LDR sensor installed on the driver's side to detect light levels of at least 700 lumens. The microcontroller then sends a command to a relay, which switches the headlights from high beam to low beam. Results demonstrate effective performance of the proposed system in terms of achieving faster switching time and consuming lower power.

Keywords: *Arduino Uno, Headlight management, High beam, Low beam, LDR sensor, Light glare, Microcontroller, Relay.*

1 INTRODUCTION

The history of the Vehicle Headlights and its operation can be traced back to 1885-1886 when German inventor Karl Benz patented his Benz patent-motorwagen operating on a three wheel as this marks the beginning in evolution of Automobiles, after which other inventors developed better versions than the previous even till dates (Parissien, 2014).

These early versions of vehicles all had a designed lighting system in them to give light and enable drivers see while driving, this lighting system where the oldest headlamps and were fueled by acetylene or oil (Asari, 2021). Acetylene lamps was adopted and widely used in the 1880's because the flame was resistant to wind and rain. It was originally designed for mining purposes, Carbide lamps were produced by dripping water on calcium carbide to produce acetylene gas, which was then burned for a light (Aishwarya, 2013). These headlamps produced caustic lime, a very toxic substance therefore it required regular cleaning. Its construction was made up of lantern with a reflecting mirror which gave an unfocused divergent or scattered forward light (Gandhi, 2021). During cold weather, the water would get freeze which would inhabit the gas generation process. This version of headlamp was popular with majority of vehicle manufacturers up until 1912 (Ogwude, 2010).

In 1879, the designs of vehicle headlamps took a new turn after Thomas Edison invented electricity, this led to the development of electric powered filament lamps (Cuvir, 2016). There were lots of challenges with the adoption and usage of this design, in the early stage of this design it was difficult to produce dynamos small enough yet powerful enough to produce sufficient current to fuel the filament lamps. The short life of the glowing filament was a big problem. In 1940, the modern sealed beam headlight found its way into the automotive industry this were used by all manufacturers in Europe, Japan and North America through the 1960's, in 1957 most government of this Nations changed the laws to allow different size and shape lights as long as they illuminated the road properly (Joshua, 2016).

Muralikrishnan, (2014) had introduced a system that gives drivers the ability to switch vehicle's headlight automatically especially during night driving. The use of transistor operating principle as a switch to develop an automatic vehicle headlight control was introduced. Using BC547 transistor and its working principle as a switch were it switches between on and off mode with respect to current or voltage differences at certain terminals. The control input flow into the base, the output is tied to the collector, and the emitter is kept at a fixed

voltage. The hardware components used in setting up the circuit include: LDR (light dependent Resistor) which is the only sensor place at the windscreen in parallel with the driver's view, two resistors as a potential divider, Transistor, Relay switch, Led bulbs and a Supply voltage from the car battery.

It was discovered that BC547 transistor was highly power efficient because it presented an advantage of controlling high current with low current required. Its small size contributed in attaining portability in the implementation of the circuit designs (Muralikrishnan, 2014). Furthermore, Experimental results showed that significant improvements in terms of automatic headlight switching have been achieved and measured results were in good agreement with the theoretical models. It was described and demonstrated that BC547 transistor can be used to carry out the switching operation in the design of an automatic headlight switching circuit with a low current requirement and high-power efficiency.

The low cost and high availability of BC547 transistor is a considerable reason why the transistor switching technique is commonly used and can be used for almost all applications which require medium or low current operation. It is fast in switching compared to mechanical or electrical switches were debouncing circuit is required to stabilize signal and reduce delay (Muralikrishnan, 2014).

Despite the high power efficiency and low current requirement associated with this approach, BC547 transistor has no zero NO resistance. Hence when it is ON, voltage across transistor in never zero. Moreover, during OFF state also, there is flow of leakage current. Hence it does not work efficiently compared to other switching techniques (Muralikrishnan, 2014).

In Narkar, (2016), the author reported use of the 555 timer IC monostable mode time delay operation in the design of an automatic dipper light control for vehicle headlight system. The 555 timer IC is the main control of this system, and it is mainly known for generating stable time delays. Here for this system, monostable mode is used for developing the timing logic. The 555 timer has an 8 pin IC available in dual-in-package (DIP) with each pin serving a specific purpose. The hardware components used in setting up the circuit include: LDR (light dependent resistor), diodes, SPDT switches, relay switch, LED bulbs and a supply voltage.

It was discovered that the 555 Timer has an advantage of operating voltage as low as 5V and can withstand a maximum of 15V compared to the BC547 model by (Muralikrishnan, 2014) which operates at 6V, the 555 timer IC works with a current consumption of up to 3mA when operating at 5V. The source/sink current of the output is 200mA.

The 555 timer is commonly used because of its usefulness in different purposes like time delays, oscillator purpose, and pulse generator. The time increments are incredibly adjustable, such as from microseconds to hours.

Despite its incredible features, the 555 timer has some common reasons to reconsider its use. The 555 timer has an operating temperature of 70 degrees Celsius, this approach may not be considered in circuit with heat generation above its operating temperature value.

Alsumady M. *et al,* (2013) used another approach which is LM399 Operational Amplifier in the design of automatic high beam light controller circuit. LM399 Op-Amp comparator is the main control component. What this device does is to compare two voltages or currents and outputs a digital signal indicating which is larger. The main function of this IC in this design is, the comparator has two inputs where it compares the two inputs with each other with respect to voltage / current then generates a differential output like high level signals or low-level signals. This works as the trigger in the switching operation of the automatic headlight controller circuit.

The LM399 op-amp has a good working stability over a wide range of voltage, temperature and operating current conditions. Having a temperature stabilizer voltage of 40V, operating at a current range of 500 μA to 10mA and operating temperature range of -0ºC to +70ºC.

LM399 op-amp has low noise generation and requires low power for stabilization. Furthermore, experimental results showed that significant improvements in terms of intelligent automatic high beam light control have been achieved and measured results were in good agreement with the theoretical models. It was described and demonstrated that LM399 op-amp IC can be used to carry out the switching operation in the

design of intelligent automatic high beam light control very wide range of operating current.

Despite its good temperature operating stability, it is not suitable for circuit designs with heat emission higher than its temperature range. The methods reviewed have some limitations such as poor processing system, complexity, and bulkiness.

To address this, we propose an automatic car headlight management system that adjusts a vehicle's headlights based on light intensity of oncoming vehicles. The system utilizes an Arduino Uno microcontroller and an LDR sensor installed on the driver's side to detect light levels of at least 700 lumens. The microcontroller then sends a command to a relay, which switches the headlights from high beam to low beam.

2 METHODOLOGY

This section unveils the block diagram of the system and also discusses the various modules and components used; also, it presents the circuit diagram and the flow chart as well as the description of the software used.

2.1 HARDWARE DESCRIPTION

As shown in the system block diagram of Figure 1, the hardware system consists of the power supply unit, microcontroller unit, light sensing unit, mode-switching unit and Headlight display unit. The descriptions of the individual units are shown below.

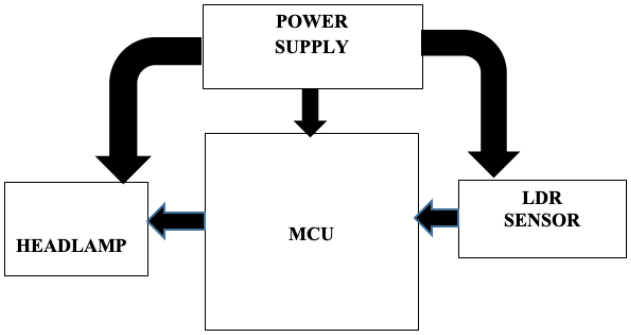

Figure 1: System block diagram

2.1.1 POWER SUPPLY UNIT

The power supply unit consists of a 12v battery source which is regulated to a 5v power supply that feeds the control unit according to its specification for the automatic mode switching and 12v is used directly for the manual mode switching to power the headlight unit.

2.1.1 MICROCONTROLLER UNIT

The microcontroller unit (MCU) consists of ATmega328 microcontroller and Arduino Uno. ATmega328 is an AVR microcontroller; it executes most instructions in a single machine cycle with its 2Kb SRAM, 1Kb EEPROM and flash memory of 32Kb. It has an outstanding feature of low power dissipation, resistance to high temperature, very high operating speed as well as low cost. These features necessitate its choice in this research work; here it is programmed to send a real-time switching command in form of voltage signal.

2.1.1 LDR UNIT

The light dependent resistor (LDR) sensor is a photocell that works on the principle of photoconductivity. This passive component is basically a resistor whose resistance value decreases when the intensity of light decreases and vice versa. This optoelectronic device is mostly used in light varying sensor circuit, and light and dark activated switching circuits. The LDR sensor comprises two pins: the first one is the ground pin which is utilized for grounding the sensor, and it is associated with the source ground pin. The second is the Analog pin which is utilized for collecting analog signals, and it is associated with the source A0 pin. This sensor is controlled on practically 3.3V to 5V dc voltages.

3.1.4 MODE SWITCHING UNIT

This unit consists of the Power switch and Relay. In this project, two types to power switch were used which are: single pole double throw (SPDT) and single pole single throw (SPST) power switch. This switch operates on the same switching principle but having different designs.

The SPDT is a switch that only has a single input and two output terminals and can connect to and switch between the two outputs terminals. The SPDT switch can serve a variety of functions in a circuit, it can serve as an on-off switch or can serve to connect circuits to any two various paths that a circuit may need to function. As applicable in this work, the SPDT was used in switching between the two modes which is the automatic mode and manual mode.

2.1.5 HEADLAMP DISPLAY UNIT

A headlamp is a lamp attached to the front of a vehicle to illuminate the road ahead. Headlamps are also called headlight; headlamp is the term for the device itself and headlight is the term for the beam of light produced and distributed by the devices.

There are two types of headlights- low beam and high beam. These lights allow the driver to see the roadway in the dark,

while also signaling to other motorists that a car is present. Low beams provide a light distribution to give adequate forward and lateral illumination without blinding other road users with excessive glare. High beams provide an intense, center-weighted distribution of light with no control of glare and should only be used when there are no visible cars in front of you (coming or going).

In this project design, the vehicle headlamp was used to display the automatic control of the light beam, keeping it at low beam mode where there are motorist coming opposite of the driver's direction (highways) and keeps it on high beam mode where there is no motorist moving at opposite direction (one-way routes).

2.2 CIRCUIT DIAGRAM

The circuit implementation of the proposed system is shown in Figure 2.

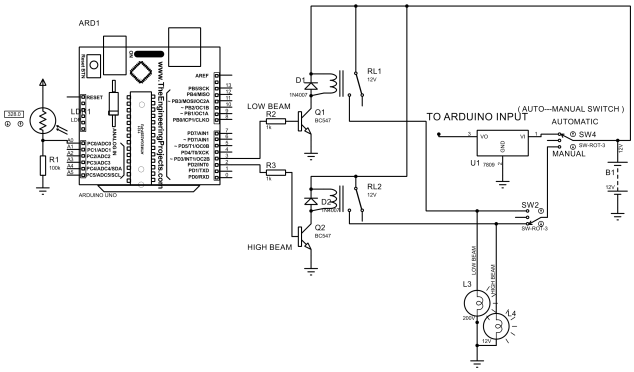

FIGURE 2: CIRCUIT DIAGRAM OF THE GLARE STOPPER

2.3 SYSTEM FLOW CHART

The flow chart is a pictorial algorithm that shows the step-by-step execution and operation of the system designed above. The hardware system was programmed using the Arduino C programing language in the Arduino IDE, the flow chart is shown in Figure 3.

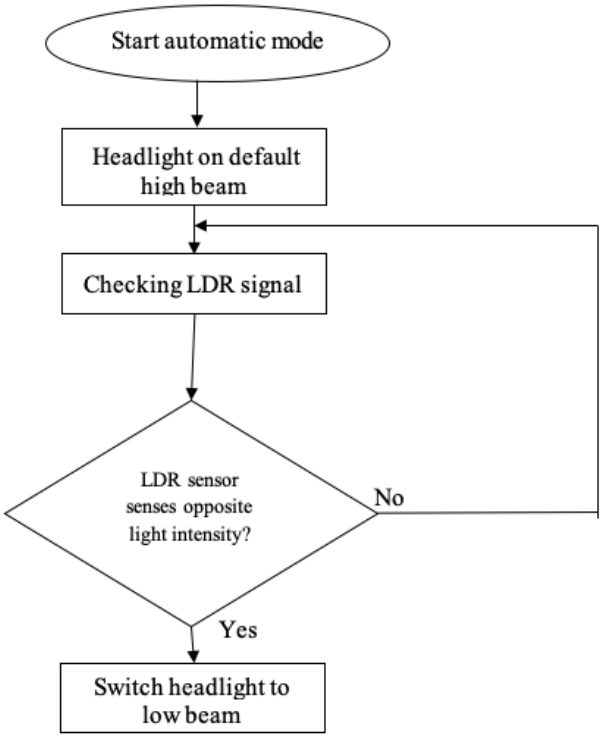

Figure 3: Flow chart

3 RESULTS AND DISCUSSION

This section presents the tests carried out to determine the performance of the components as well as the system. From the test data, the result obtained will be analysed in order to assess the performance of the system.

3.1 HARDWARE TEST

All the hardware components were tested individually as outline below. Moreover, the system was tested as in a real-world scenario after assembly to ensure it performs the required functions.

Figure 4: Vehicle prototype

Figure 4 show a prototype vehicle used for testing. The vehicle has a single headlight (for demonstration purpose) with the LDR sensor place on the windscreen at the driver side behind the dashboard.

The tests carryout on individual components is outline below.

The power input to the power system module was measured, also, the output from the modules as well as the individual power consumption was tested using a digital multi-meter and it was found to conform to the expected

value. The Arduino UNO and other components such as relay, LDR sensor, resistors, toggle switches as well as the headlamp were all tested and confirmed to be of good condition before assembling them together.

The response of the vehicle headlight with respect to the LDR sensor signal was be observed by flashing a bright light of approximately 1000 lumens on the vehicle wind screen where the LDR sensor was located. It was observed that the vehicle headlight responded by switching to low beam. This test was performed 20 times and the average switching time from high to low beam was 252 ms.

3.2 SOFTWARE TEST

All the program codes were debugged to check for possible errors in the codes. The Arduino UNO microcontroller board was also observed while the program was uploaded using the Arduino UNO IDE protocol and was found to perform as expected without any upload error.

3.3 RESULTS

This section discusses the results obtained during the testing process.

3.3.1 Light Intensity Sensitivity Circuit

The LDR sensor's voltage output was observed with respect to light intensity using a multi-meter to measure the voltage output on high beam and low beam mode. The headlight was switched to automatic mode and the headlight came on default high beam, the LDR at the mode had a low voltage value below the relay automatic mode switching value of 5 V. For this reason, the headlight remains on high beam until light intensity is casted in the direction of the LDR that will produce a voltage signal of 5 V and above.

A bright light with an intensity of 1000 lumens was casted in the direction of the LDR sensor to observe the voltage signal. The voltage to the headlight was measured and it was observed to be higher than when at high beam with a voltage value of 5.3 V. This voltage is enough to energize the relay for a switch from high beam to low beam.

This proves the sensitivity of LDR whereby the increase in light intensity causes an increase in resistance which is also proportional to voltage. Equation (1) shows the relationship between output voltage (V_o), resistance (R_L) and light intensity (Lux).

$$R_L = \frac{500}{LUX} \qquad (1)$$

If the LDR is connected to 5 V through a 3.3 K resistor, using the voltage divider rule, the output voltage of the LDR is

$$V_O = 5 \times \frac{R_L}{R_L + 3.3} \qquad (2)$$

substituting for R_L from equation (1) into equation (2)

$$LUX = \frac{\frac{2500}{V_O} - 500}{3.3} \qquad (3)$$

TABLE 1: VOLTAGE AND RESISTANCE VALUE AT HIGH BEAM AND LOW BEAM

Headlight State	LDR Sensitivity	Resistance (Ω)	Voltage (V)
Default high beam	Negligible	0.417	0.561
High beam to low beam	Active	0.714	1

Table 1 shows the voltage and resistance values when headlight is at default high beam and when switched to low beam light intensity with respect to LDR light sensitivity. This value shows that at high beam when the LDR light sensitivity value is zero or negligible, the output voltage at the sensor unit is lower compared to when the LDR senses light intensity: voltage which is high enough for the microcontroller to issue a switching command to the relay.

The resistance value of the LDR sensor when it does not sense any light intensity and headlight at default high beam is much lower compared to when LDR sensor senses light intensity and headlight switches to low beam. With LDR sensor, increase in light intensity will cause and increase in LDR sensor resistance.

TABLE 2: VOLTAGE AND RESISTANCE VALUE AT HIGH BEAM AND LOW BEAM

Methods	Switching Model	Operating Temp (^{0}C)	Operating Current (mA)
Muralikrishnan R. (2014)	BC547	65 – 150	10
Narkar, T. V. (2016)	555 Timer	70	3
Alsumady M. *et al*, (2013)	LM399	-55 – 150	10
Proposed Method	Microcontroller	-40 – 105	50

The systems reviewed have some limitations such as poor processing system, complexity, and bulkiness. They operate only on a single mode which is the automatic mode having the manual mode disconnected, drivers can't switch between off state, manual mode and automatic mode. Tables 2 and 3 compared the proposed system with previous work in terms of operating conditions (temperature, current and voltage), switching mode and power consumption. Overall, the the proposed system consumes less power to achieve switching from high to low beam with an average switching time of 252 ms.

TABLE 3: VOLTAGE AND RESISTANCE VALUE AT HIGH BEAM AND LOW BEAM

Methods	Switching Model	Operating Voltage (V)	Operating Power (mW)
Muralikrishnan R. (2014)	BC547	1.3 – 6	500
Narkar, T. V. (2016)	555 Timer	1.67 - 5	30
Alsumady M. *et al*, (2013)	LM399	40	300
Proposed System	Microcontroller	1.8 – 5.5	0.4 – 1

4 CONCLUSION

The work proposed the development of an automatic vehicle headlight management system. The system automatically adjusts a vehicle's headlight from high to low beam upon sensing a high beam from an oncoming vehicle to avoid causing light glare to a driver while driving at night. Using an LDR sensor to capture opposite light intensity, the LDR sensor issues a switching command to the micro-controller then to the headlight bulb from high beam to low beam. The proposed system was implemented and tested successfully. The system can be useful to vehicle drivers who experiences night glare during night driving.

REFERENCE

Aishwarya, S. (2013) "Bright Headlights a Major Cause of Accidents", The Hindu, Online Edition

Asari, Tomotaka, et al. (2021). "Adaptive driving beam system with MEMS optical scanner for reconfigurable vehicle headlight." *Journal of Optical Microsystems* 1.1

Alsumady, M., & Alboon, S. (2013). Intelligent Automatic High Beam Light Controller. *Old City Publishing, Inc. Published by license under the OCP Science imprint, a member of the Old City Publishing Group*, 1-8.

Cuvir, M. (2016). Operation of Switches [online]. Available: https://learn.sparkfun.com/tutorials/switchbasics/poles

Gandhi, K. K. S. Aulakh, G. S. Kharoud, J. S. Thind and S. Sharma, (2021). "IoT Based Realtime Automatic Headlight Dimmer System," 2021 10th International Conference on Industrial Technology and Management (ICITM), Cambridge, United Kingdom, 2021, pp. 134-138.

Joshua S. C. (2016). History of Headlamps [online]. September 30 2020. Available : https://www.ridelust.com/illuminating-a-brief-history-of-the-headlight.

Michel, K. (2016). Automatic Headlight Intensity Controller [online]. Available: http://zonascience.com/2009/08/automatic-headlight-intensity.

Muralikrishnan, R. (2014). Automatic Headlight Dimmer a Prototype for Vehicles. *Int. J. Res. Eng. Technol*, *3*(02), 85-90.

Narkar, T. V. (2016). Automatic Dipper Light Control for Vehicles. *International Journal of Research in Engineering and Technology*, *5*(3), 97-101.

Ogwude, I. C. (2010). Driver Behaviour in Nigeria: Impact of Impulsiveness, Anger and Aggression. *FRSC, Abuja*.

Parissien, Steven (2014). *The life of the automobile: the complete history of the motor car*. Internet Archive. New York, N.Y.: Thomas Dunne Books, St. Martin's Press. pp. 2–5. ISBN 978-1-250-04063-3.

4th International Engineering Conference (IEC 2022)
Federal University of Technology, Minna, Nigeria

Modeling and exergy evaluation of the crude distillation unit I of the Kaduna refinery and petrochemical company.

*Idah, A. E[1], Olakunle, M. S[1], & Maina, M. N[1]
[1] Department of Chemical Engineering, Ahmadu Bello University Zaria
*Corresponding author email: idahaugustine1@gmail.com +2349053463366

ABSTRACT
In refinery operations, the crude distillation unit is an essential and vital component of its operations. It is the primary separation process and the source of feed to most of the process units of the petroleum refining industry. The crude distillation unit I of the Kaduna refinery and petrochemical company was modeled using Aspen Hysys version 11.1, the units modeled included: the preheat train, pre-flash column, furnaces, and crude distillation column. The column was analyzed for exergy efficiency which was found to be 76.17% for an exergy loss of 300.02kJ/kg. The product withdrawal rates in the standard ideal liquid volumetric flow of the atmospheric residue are the highest with a value of 100736.83m^3/h, followed by LGO, naphtha, kerosene, and HGO with values of 92482.1265 m^3/h,59089.0035 m^3/h, 44912.6453 m^3/h, and 13439.0218 m^3/h respectively.

Keywords: *Atmospheric distillation, Exergy analysis, Simulation, Refining*

1 INTRODUCTION

The Kaduna refinery has a nameplate refining capacity of 110,000 barrels per day and is in Kaduna, Kaduna State (Mohammed, *et al* 2012). The plant is run by the Kaduna Refining and Petrochemical Company (KRPC) Limited, of the Nigerian National Petroleum Corporation (NNPC) subsidiary, and has a complex conversion configuration. The KRPC comprises a fuels plant commissioned in 1983 and a 30,000 MT per year Petrochemical Plant in 1988 (Department of petroleum resources, 2021). The refinery plant has two crude distillation units; the light end-crude distillation unit I (CDU I) which refines Escravos and Ughelli crude oils blend and the heavy end-crude distillation unit II (CDU II) refines lube-based oil import from Kuwait, Saudi Arabia or Venezuela production (Mohammed, *et al.,* 2012). Products obtained from the light end-crude distillation unit I of KRPC include naphtha, kerosene, light gas oil, heavy gas oil, and column bottom residue. (Mohammed, *et al.,* 2012).

Distillation is widely employed in process industries, mostly in the manufacture and purification of chemicals, pharmaceuticals, petrochemicals, etc., and the refining of crude oil into its component fractions such as naphtha, kerosene, and gas oil, etc. About 95% of all liquid separations are performed using distillation (Damian, 2013; Olakunle *et al.,* 2016). Distillation offers a wide range of thermodynamics and kinetic advantages over other fluid mixture separation processes, this includes potential for a high mass transfer rate and high thermal efficiency (Gorak & Schoenmakers, 2014).

One important drawback of distillation is its considerable energy consumption (Akpa & Umu, 2013). The distillation process can incur over 40% of the operating cost of the plant, due to high energy costs and environmental concerns, thus it is expedient to improve the distillation process (Oludare, 2015). According to Smith (2010), efficient integration and exergy analysis are the best ways to lower the energy consumption of the distillation unit. Several studies have looked into how well distillation units for crude oil function. For instance, Tarighaleslami *et al.* (2011) used exergy analysis to investigate the operation of the Tabriz oil refinery in Iran. They discovered that stream splitting on one of the pump-around reduces furnace duty; they observed a 13% decrease in exergy destruction. Oni and Waheed (2015) conducted an evaluation of the crude oil distillation unit and discovered that the pre-flash and atmospheric distillation subsystems' exergy losses account for 90.0% of the total exergy loss, and the direct CO2 emission from burning fuel in the furnaces constitute the majority of the CO2 emission. A study by Liu (2019) looked at energy and exergy losses in "North-East China," where the pump system suffered exergy damage that was 3397.1 MJ/h more than that of the static equipment. He followed a methodology that was similar to that of Masoumi *et al*. (2015), whose study at Shazand-Arak Oil revealed that 45% of energy loss occurred in the pumping system and 35% in the heater. Exergy analysis is an efficient technique employed in designing more efficient thermal processes to reduce inefficiencies.

The exergy of a process is its work potential, relative to prescribed surroundings (exergy reference environment) (Adewale & Abiodun, 2016). It can also be seen as the optimum theoretical work attainable if the process and its set environment interact or exist at equilibrium. Thus, exergy is a rational basis for evaluating process efficiencies (Demirel, 2004). It is also handy for engineering process designs, operations, and optimization, this is achieved through modeling. Computer-aided design software such as ASPEN is employed in modern engineering to mimic engineering processes in other to minimize cost and enhance effective engineering designs (Oludare, 2015).

In recent years, it has become more common to simulate a distillation process of a multi-component system through the formation of two co-existing phases (liquid and vapour phases), basically at the same temperature and pressure. This was practiced by Sorel over 100 years ago for the distillation of alcohol. An elegant history of the first century of equilibrium stage modeling was presented by Seader. In practice, however, distillation processes, do not operate at equilibrium (Douglas, 2012). This work seeks to evaluate the exergy utility within the column of a refinery crude distillation unit.

2 METHODOLOGY

The distillation of Escavos crude was carried out using Hyprotech System Simulator (HYSYS vs. 11.0) software. A number of property packages are available for use in the HYSYS environment. For this study, a steady state was assumed, and there is no heat loss from the column to the surrounding due to conduction, convection and radiation. Peng Robinson was selected for the property package simulation. To proceed with the modeling simulation data obtained from the Kaduna refinery and petrochemical company includes but is not limited to a reflux rate of 6.1 m^3/hr., boil up rate of 33.3 m^3/hr., operating pressure at the top and feed sections are 0.84kg/cm^2G and 1.22kg/cm^2G respectively pressure at the base of the column is 1.3kg/cm^2G, number of trays is 48, other parameters are tabulated in Table 1

$$P = \frac{RT}{V-b}\ \frac{\alpha(T)}{V(V+b)+b(V-b)} \quad (1)$$

$$\alpha(T) = \alpha a(T_c) \quad (2)$$

$$a(T_c) = 0.45724\frac{\alpha R^2\, T_c^2}{P_c} \quad (3)$$

$$b = 0.0780\frac{RT_c}{P_c} \quad (4)$$

$$\alpha = \left(1 + k(1 - \sqrt{T/T_c}\right)^2 \quad (5)$$

$$k = 0.37464 + 1.54226w - 0.26992w^2 \quad (6)$$

Where:
V is the molar volume
R is the gas constant
P is the pressure
T is the absolute temperature
P_c and T_c are critical pressure and temperature respectively

Table 1: KRPC distillation column data

Stream	Temp.°C	Flowrate 10^3. m^3/h	Tray Position
Crude	15	397.5	4
Steam	360	388.6	1
Naphtha	105	78.7	48
Kerosene	175	54.8	33
LGO	194	107.7	22
HGO	238	15.1	11
Reduced crude	360	108.1	1

The models were used to predict the column properties of the five components of the crude oil mixture separated in a multicomponent distillation column, which are naphtha, straight run kerosene, light gas oil (LGO), heavy gas oil (HGO) and atmospheric residue (AR) from the process simulator (Aspen Hysys). The effect of column properties such as temperature, pressure, and phase flow rates across the forty-eight (48) trays of the CDU I column were analyzed and presented on charts. The exergy efficiency and exergy loss within the column was also evaluated.

3 RESULTS AND DISCUSSION

The Aspen Hysys simulated column of CDU I of the KRPC is presented in Figure 1

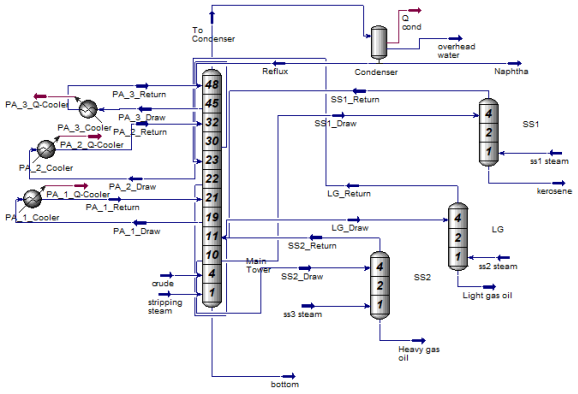

Figure 1: Aspen Hysys simulated distillation column of CDU I of KRPC

The column consists of 48 trays numbered from bottom to the top of the column and has three pump-arounds (PA) with withdrawal and return stages at 45 and 48 for PA_1, 30 and 32 for PA_2, and 19 and 21 for PA_3 respectively as seen in Figure 1. Naphtha, kerosene, light gas oil, heavy gas oil, and bottom residue were collected at stages 48, 33, 22, 10, and bottom respectively and their thermodynamic properties are as presented in Table 2

Table 2: Products stream properties

Name	Naphtha	Kerosene	LGO	HGO	Residue
Vapour/ phase fraction	0.0000	0.0000	0.0000	0.000	0.0000
Temp. (^{0}C)	131.5356	189.6946	295.7112	179.7267	285.5452
Pressure (kPa)	183.7000	199.0388	210.2832	222.5519	231.7535
Molar flow (kgmole/h)	326983.1193	196165.8425	252060.9721	34875.7836	198090.2332
Mass flow(kg/h)	48070560.6946	37782591.9069	85044884.0324	11402656.9794	65963870.3590
Std ideal Liq vol flow (m^3/h)	59089.0035	44912.6453	92482.1265	13439.0218	100736.8385
Molar enthalpy (kJ/kgmole)	-2.941e+005	-3.271e+005	-5.042e+005	-5.288e+005	-5.414e+005
Molar entropy (kJ/kg mol ^{0}C)	277.8	485.4	1177	1062	1081
Heat flow (kJ/h)	-9.6182e+10	-6.4169e+10	-1.2708e+11	-1.8442e+10	-1.0724e+11

3.1 COLUMN TEMPERATURE PROFILE

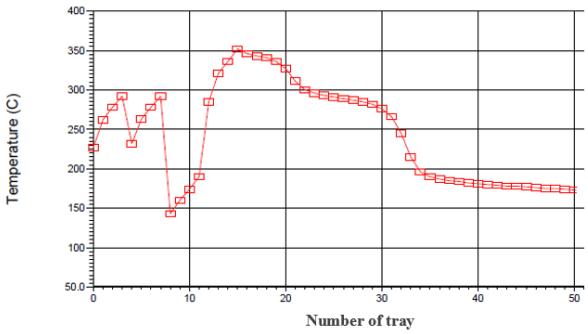

Figure 2: Simulated fractionation column temperature profile

Figure 2 shows the temperature distribution along the column's height. The column profile ranged from 252^0 C at the top to 360^0 C at the rectifying section of the column this rise can be attributed to the introduction of stripping steam and crude at trays 1 and 4 respectively. The sharp drop in the temperature on tray 9 could be attributed to HGO withdrawal rate on tray 10, and the linear progression of the temperature across to tray 32 could be due to HGO withdrawal rate and the reflux of both LGO and HGO. The spike observed on tray 36 could be the effect of the Naphtha withdrawal rate which possibly is resulting in more volatile components at this tray. The smooth temperature drop thereafter could be said to be due to the effect of the pump around 1

3.2 COLUMN PRESSURE PROFILE

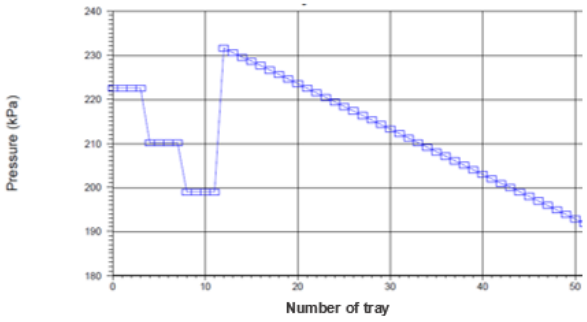

Figure 3: Simulated fractionation column pressure profile

As shown in Figure 3, the pressure distribution within the column is such that at the bottom section of the column a pressure of 222 kPa was observed which begin to decrease rapidly to 200 kPa in the rectifying section and through to tray 10, this sharp decrease could be because of the feed pressure and HGO withdrawal rate. This drop in pressure was followed by a spike in pressure to 232 kPa at tray 11 this may be associated with the HGO return stream parameters. Afterward, a steady pressure decrease was observed at the top of column tray 48 with a pressure of 192 kPa.

3.3 COLUMN FLOW PROFILE

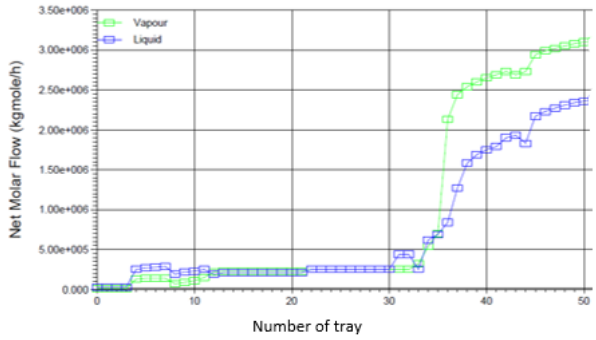

Figure 4: Simulated fractionation column flow rate profile

As observed in Figure 4, the vapour and liquid flow rate rose gradually across the column, this implies that the assumption of constant inter-stage molar flow rates is true for this column since the fluid volatility increase along the column as the number of trays increase vertically from bottom to the top of the column. The spike in the net molar flow seen on tray 33 could be attributed to the activities of the pump around II and the withdrawal and reflux of kerosene in the column.

Mass exergy= $(h-h_0)-T_0(S-S_0)$ (7)

Table 3: Exergy inputted into the column.

Stream in	Exergy (KJ/Kg)	Stream out	Exergy (KJ/Kg)
Crude	356.7	Naphtha	11.78
Stripping steam	611.9	Kerosene	103.7
PA1	4.7	LGO	203.9
PA2	45.8	HGO	146.3
PA3	87.7	Bottom	184.2
SS1	33.9	PA1	13.2
SS2	43.1	PA2	112.6
LGO	73.7	PA3	183.4
Cond reflux	2.5		
Total exergy in	1259.1	Total exegy out	959.08

Exergy balance

Exergy loss= exergy in – exergy out (8)

Exergy loss= 1259.1-959.08 = 300.02kj/kg

$$exergy\ efficiency\ = \frac{\text{exergy out}}{\text{exergy in}} x100 \quad (9)$$

$$exergy\ efficiency\ = \frac{959.08}{1259.1} x100$$

Exergy efficiency = 76.17%

4 CONCLUSION

The Hysys simulated crude distillation column I of the Kaduna refinery and petrochemical company showed that the atmospheric residue has the highest standard ideal liquid volumetric flow rate of 100736.83m3/h, followed by LGO, naphtha, kerosene, and HGO with flow rates of 92482.1265 m3/h,59089.0035 m3/h, 44912.6453 m3/h, and 13439.0218 m3/h respectively. The exergy efficiency of the column was estimated to be 76.17 %. The inefficiencies can be observed in the peaks and troughs of the column temperature profile. The exergy loss for the simulated CDU I of the KRPC was estimated to be 300.02kJ/kg. This exergy loss can be attributed to inappropriate product withdrawal rates, the type, and the number of trays, feed conditions, etc.

REFERENCE

Adewale, A. K., & Abiodun, C. P. (2016). Exergy Rate Profile of Multicomponent Distillation System.

Akpa, J. G., & Umu, O. D. (2013). Simulation of a multi component crude distillation column. *American journal of scientific and research*. doi:0.5251/ajsir.2013.4.4.366.377

Damian, C. (2013). Environmental pollution in the petroleum refining industry. *Ovidius University Annals of Chemistry, 24*, 109 - 114.

Demirel, Y. (2004). Thermodynamic analysis of separation systems. *Thermal mechanics., 39*(16), 3897-3942.

Department of petroleum resources. (2021). Retrieved 2021, from https://www.dpr.gov.ng/downstream/refinery/

Douglas, C. W. (2012). Optimize energy use in distillation. *American Institute of chemical engineers*, 35-41.

Gary, J. H., & Handwerk, G. E. (1984). *Petroleum Refining Technology and Economics* (2nd ed.).

Gorak, A., & Schoenmakers, H. (2014). Distillation: Operation and Applications. *Elsevier*.

Mohammed, J., Aloko, D. F., & Auta, M. (2012, April). Simulation of Kaduna Refining and Petrochemical Company (KRPC) Crude

Distillation Unit (CDUI) using Hysys. *International Journal of advanced scientific research and technology, I* (2).

Olakunle, MS, Adefila, SS, and Olawale, AS (2016). Distillation Performance Improvements through Side Inter-heaters. Umudike *Journal of Engineering Technology (UJET)*, 2(2), pp.25-35.

Oludare, J. O. (2015, August). Exergy and economic analyses of crude oil distillation unit. *African journal of engineering research*, 44-55.

Oni, A. O., & Waheed, M. A. (2015). Methodology for the thermoeconomic and environmental assessment of crude oil distillation unit. *International Journal of Exergy, 16*(4), 504-532.

Sajedi, S. N., Masoumi, M. E., & Movagharnejad, K. (2015). Exergetic improvement and environmental impact assessment of crude oil distillation unit of Shazand-Arak oil refinery. *International Journal of Exergy, 16*(4), 464-471. doi:DOI:10.1504/IJEX.2015.069116

Smith, R. (2010). Heat integrated distillation system design. *Chemical Engineering Transactions, 21*, 19-24. doi:10.3303/CET1021004

Tarighaleslami, A. M., Omidkhah, M. R., & Sinaki, S. Y. (2011). An exergy analysis on a crude oil atmospheric distillation column. *Chemical Engineering Transactions, 25*, 117-122.

4th International Engineering Conference (IEC 2022)
Federal University of Technology, Minna, Nigeria

Development of a Prototype Sugarcane Juice Extraction Machine

*Ampandi, R. T[1], Muhammadu, M. M[2]
[1]Mechanical Engineering Department, Federal University of Technology, PMB 65 Minna Niger State, Nigeria
*Corresponding author email: rapho201@yahoo.com +234869652035

ABSTRACT
Sugarcane juice is enjoyed by all ages, the juice is extracted with the teeth, this extraction process damages teeth and gums. Sugarcane juice is also used to help treat some patients in the hospital with a certain illness, in which case the patient may not have the strength to chew the sugarcane and forcefully squeeze the juice, which would be risky for the patient. Sugar Cane Juice extraction machines available are heavy, bulky and used in farms for small scale processing of sugar cane in farms. Hence the need to build or manufacture a crushing machine that can be used at home or even in the hospital to reduce the risk of injury to gums and teeth. This research work consists of designing and manufacturing a sugar cane juicer, evaluating its performance and comparing the results obtained with the existing ones to see if it is portable or not. The machine was designed and built with readily available and cheap materials. The useful part of the machine is the extraction chamber, pulley and best shaft/roller assembly and is powered by a single-phase 1HP electric motor. The machine was evaluated with different cane weights (0.5 kg, 1 kg, 1.5 kg, 2 kg, 2 kg).5 kg), and the results show that the average extraction time, extraction yield, juice yield and extraction loss are 76.39 seconds, 61.46%, 34.06% and 7.64%, respectively. The developed cane juice extraction system was compared to other existing cane juicers and found to be viable and can be use at home and hospitals with little or no training, the machine can be used to set up a sugarcane juice spot.

Keywords: *Development, Extractor, Juice and Sugarcane.*

1 INTRODUCTION

Sugarcane refers to several species and hybrids of all herbs of the genus Saccharum, phylum, Andropogoneae, used in the manufacture of sugar. Sucrose accumulated in the internodes of the stem. Sugarcane belongs to the grass family Poaceae, an economically important family of flowering plants that includes corn, wheat, rice and sorghum, as well as many forage crops. (Ricca, 2010). There are three main categories of sugarcane in Nigeria namely Saccharrim, Oficinarum and Sporitaneum.These are six species of perennial grasses of the andropogonic tribe Gerani (Uti, 2019). It is clearly stated that the processing of sugar cane begins with the juicing of the cane stalk. Various crushing methods were used. These methods included boiling the cane to extract the juice, using wooden presses, and using more sophisticated mechanical or ox-powered mills (Azeez, 2019). A sugar cane juicer is a machine used to extract the juice from sugar cane. Thi machine can be used by the illiterate or the literate, depending on the choice of machine. These juicers were designed to help people extract the juice from sugar cane through a crushing and rolling process (Soetan, 2018).

The main needs of the sugar cane industry are identified throughout the production process, such as: Sugar cane preparation, milling, juicing, sugar cooking and crystal separation. Mechanical strength is the most important requirement in these identified areas, with the exception of boiling juice and sugar concentration, which require heat (FAOSTAT 2014, Robotham and Chappell, 2017). Sugar cane milling is a fundamental operation to make sugar cane juice available for a variety of uses. A conventional machine is a simple machine consisting of multiple gears, pulleys and levers attached to a cast iron frame body. Most conventional machines are made of cast iron, which is strong and durable. These machines were made with a simple rolling and grinding mechanism (Kulkarni, 2005). A small juicer uses a single set of rollers to extract the juice without soaking. It is the type of juicer that's useful in developing countries like Nigeria, where sugar cane cultivation is not yet practiced on a large scale, despite its huge production potential. In addition, large complex devices are imported from developed countries and always require complicated maintenance procedures and a lack of local spare parts (Anonymous, 2018). Crushing sugar cane requires a lot of strength due to its strong and tough properties. Juicers were built primarily with the mechanical aspect of the machine in mind. The performance of the machine depends on the mechanics that have been built into the machine. Mechanical performance of is the most important need in these identified areas (Madhu et al.al., 2022).

Therefore, the development of a sugar cane juice extraction machine for use in households, hospitals and even to create sugar cane juice production facilities is outstanding. This machine should be light and easy to use, with readily available materials and low cost. Therefore, the aim of this research is to develop a prototype cane juice extraction machine that can be easily used to extract cane juice.

2 METHODOLOGY

2.1 MACHINE DESCRIPTION

The machine is made from readily available material, the machine is made up the frame, the electric motor, crushing chamber belt and pulley assembly and shaft/rollers. The two rollers have the same diameter of 40mm as they are solid rollers. The rollers are tapered from left to right to enable crushing of sugarcane of different diameters and also to eliminate the use of an adjuster. The crushing chamber is opened at both sides to insert and receive the sugarcane and bagasse respectively. The sugarcane juice will be collected using a cup. The machine frame is made of mild steel.

2.2 PRINCIPLE OF OPERATION OF THE MACHINE

The machine was powered by a 1hp motor, it was allowed to run for few minutes before loading the machine with the sugarcane samples of different weights. The crushing of the sugarcane was done by the two rollers in the crushing chamber and the juice was collected through the channel provided. The outline of the sugarcane juice extractor is shown in the figure 1 and 2.

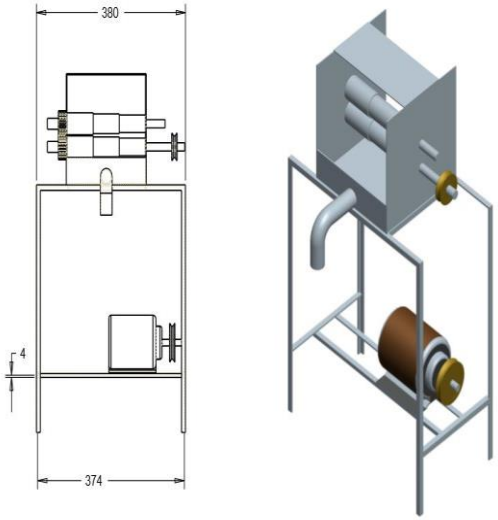

Figure: 1 Layout of sugarcane juice extractor

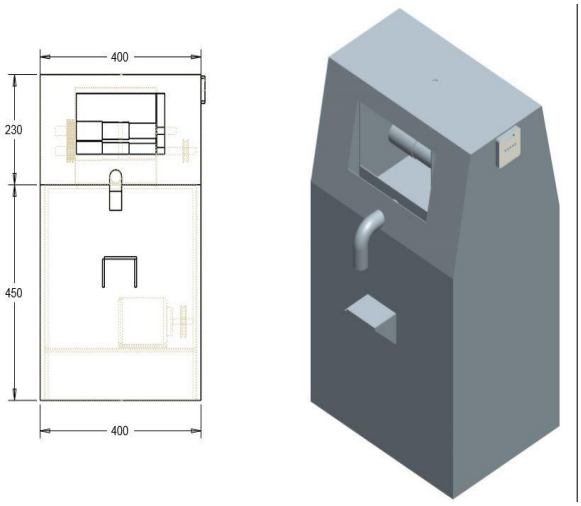

Figure 2: Isometric view of the sugarcane juice extractor

2.3 DESIGN CALCULATION

1. Design for power estimation

The motor power & supply torque by the motor were calculated using equations 1 & 2 given by Khurmi and Gupta, (2005).

$$P = \frac{2\pi NT}{60} \quad (1)$$

$$T = \frac{P}{\omega} \quad (2)$$

Where

N is the motor speed (2420rpm)
T is the torque

Selected 1hp electric motor

2. Belt size

The tension of the belt as a result of motor torque given by equations 3 and 4 by Khurmi and Gupta, (2005).

$$T = F_1 \times r_1 \text{ Nm} \quad (3)$$

$$F = \frac{T_1}{r_1}\ (N) \quad (4)$$

Where the tension in the tight and slack side of the belt was obtained by this equation 5 from Khurmi and Gupta, (2005).

$$\frac{F1}{F2} = e^{\mu\theta} \quad (5)$$

Where;

F1 – tension in the tight side of the belt.
F2 – Slack side of the belt
μ - coefficient of friction between the belt material and pulley (μ =0.4)
θ – Overlap Angle (degree)

while the angle of lap of the belt over the pulley is expressed in equation 4.

$\theta = 180 - 2\alpha$ (for the small pulley) 5

And the angle α, was obtained from equation 6 by Khurmi and Gupta, (2005).

$\sin\alpha = \frac{r2-r1}{x}$ 6

Where;

r_1 - radius of the motor pulley = 0.05 (m)
r_2 - radius of the roller pulley 0.15 (m)
X - centre distance between the two pulleys 0.3 (m)

3. Length of belt

The total length of the belt required for the implementation of the open v-belt drive was calculated from equation 7 by Shigley and Mitchell (1983)

$L = \frac{\pi}{2}(d1 + d2) + 2X + \frac{(d1+d2)^2}{4X}$ 7

Where;

d_1 = diameter of the motor pulley = 0.1m
d_2 = diameter of the roller pulley = 0.3m
X = Centre distance between the two rollers = 0.3m

Total length of the belt was gotten to be 1.3616m.

4. Maximum tension on the belt

The maximum tension in the belt during transmission is given by equation 8 by Balami *et al,*. (2016);

$T_{max} = T_1 + T_c$ 8

Where T_c is the centrifugal tension and it is given by equation 3.10 by Khurmi and Gupta, (2005).

$T_c = mv^2$ 9

5. Diameter of the roller

For solid roller the diameter diameters are determine using equations 10 and 11 by Khurmi and Gupta, (2005).

$T_e = \frac{\pi}{16} \times \tau \times d_o \times (1 - k^4)$ 10

$d_o = \sqrt[3]{\frac{16T_e}{\pi\tau(1-k^4)}}$ 11

T_e = equivalent moment in the roller = $92.8989N$

The roller diameter was chosen to be 40mm

2.4 TESTING AND PERFORMANCE EVALUATION

The test was carried out in two different stages, the first stage was done without loading the sugarcane into the machine. The second stage was done with loading the sugarcane sticks with different weights (0.5kg, 1kg, 1.5kg, 2kg and 2.5kg) into the machine. The sugarcane was cut into different sizes to get the different weights. Also, the sugarcane was guided into the crushing chamber in-between the rollers with the hand. A stop watch and a weighing balance were used to take the reading for the time of extraction and to weigh the juice obtained and weight of bagasse collected at the end of the extraction respectively. The wet bagasse was sun dried for three days further analysis. The evaluation of the efficiency, extraction and juice yield the sugarcane juicer was carried out using the following expressions for Extraction Efficiency (J_E), Extraction Loss (E_L) and Juice Yield (J_Y) as shown in the equation as follows and was given by Olaniyan and Oje (2011):

$Extraction\ Effiecincy\ E_J = \frac{W_2}{W_5} \times 100\%$ 12

$Extraction\ Loss\ E_L = \frac{W_1-(W_2+W_3}{W_1} \times 100\%$ 13

$Juice\ Yield\ \ J_Y = \frac{W_2}{W_2+W_3} \times 100\%$ 14

Where;

W_1 = Weight of sugarcane stick
W_2 = Weight of Juice obtained
W_3 = Weight of wet bagasse
W_4 = Weight of dried bagasse
W_5 = Weight of juice obtainable

3 RESULTS AND DISCUSSION

The results of the test of the developed sugarcane juice extraction machine was computed based on average as the test for different sugarcane weight was done three times and the average was taken. The average extraction time, extraction efficiency, Juice yield and extraction loss of the developed sugarcane juice extraction machine. This result is shown in the table 1.

Table1: Performance evaluation table of the sugarcane juice extractor

S/N	Weight of sugarcane W_1 (kg)	Extraction Time (sec)	Extraction Efficiency (%)	Juice Yield (%)	Extraction Loss (%)
1	0.50	39.33	63.30	39.00	4.00
2	1.00	60.00	46.65	32.00	9.00
3	1.50	74.66	60.30	31.80	8.00
4	2.00	90.33	65.60	33.80	10.00
5	2.50	117.66	71.43	34.50	7.20
Average	1.5	76.39	61.46	34.06	7.64

4 CONCLUSION

A prototype sugarcane Juice extraction machine was design, fabricated, tested and evaluated. The machine is

simple to operate and was made from readily available materials. The machine was powered by a 1hp motor. The extraction time, extraction efficiency, juice yield, extraction loss was obtained to be 76.39 sec., 61.46%, 34.06%, 7.64% respectively. This machine can be use at home, hospitals or even to set up a sugarcane juice selling spot.

ACKNOWLEDGEMENTS

I will like to acknowledge the tireless effort of Engr. Dr. M. M. Muhammadu my supervisor and mentor towards the actualization of tis research and also Engr. Dr. Babawuya Alkali. Your effort is never neglected God bless you.

REFERENCE

Anonymous (2018). Nationally Co-ordinated Research Progranune on Sugarcane, National Cereals Research Institute Annual Research Review Meeting, Badeggi, Nigeria. 20-23 April 2018. pp. 50-51.

Azeez N. A (2019)." Design and Fabrication of Sugarcane Juice Extractor " *American Journal of Engineering Research (AJER)*, vol.8, no.07. pp.91-97.

Balami, AA, Dauda, SM, Mohammed, IS, Agunsoye, JK, Abu, H, Abubakar, I, & Ahmad, D. (2016). Design and fabrication of a cocoyam (Colocasia esculenta) peeling machine. *International Food Research Journal* 23(suppl.): pages 65-S70.

FAOSTAT (2014), FAO Statistics online database, “Production / Crops, - sugarcane, Year 2014”, Food and Agriculture Organization of the United Nations, http://faostat3.fao.org/home/E (accessed 10 February 2022).

Khurmi RS and Gupta, JK (2005). A textbook of machine design, Eurasia Publishing House. Ram Nagar, New Delhi.

Kulkarni G K. (2005) Occupational health service - Need for competency development. Indian J Occup Environ Med 2005; 9:5-6

Madhu R, Anilkumar M, Prabhayya Binnalamath, Vardhaman D. B Patil, Abhishek G R (2022) Sugar Cane Juice Extractors – A review. *International Journal of Innovative Research in Science, Engineering and technology*. Volume 11, pp. 2347-6710.

Rika Suzan (2010): Article household sugarcane Juicer only a sweet dream www.ezinarticles.com/? Expert=Rika suzan.

Robotham, B.G. and W.J. Chappell. 2017. Comparing the Field Performance of Mechanical Cane Planters. Proceedings of Austranlian Society of Sugar Cane Technologists. (20): 293-299.

Shigley, JE, & Mitchell, LO. (1983). Mechanical Engineering Design (ed). McGraw-Hill Book Company, Tokyo

Soetan, C. A. (2018). The Development of a Sugarcane Juice Extractor for the Cottage Industry. B. Eng. Project Requirement. Department of Agricultural Engineering, University of Agriculture, Abeokuta, Nigeria.

Uti J. N, Adogbeji V. O, (2019) design and construction of sugarcane juice extracting machine for rural community. *International Journal of Engineering Applied Sciences and Technology,* 2019 Vol. 4, Pages 306-31.

4th International Engineering Conference (IEC 2022)
Federal University of Technology, Minna, Nigeria

A Review on Mechanisms and Challenges of Mechanical Footstep Power Generators

*Sanni, A. R[1], & Abdullahi A. A[2]
[1,2]Mecahnical Engineering Department, Federal University of Technology, PMB 65 Minna Niger State, Nigeria
*Corresponding author email: ahmadrajab01@gmail.com +2347063038845

ABSTRACT
As human population is increasing, so is the demand for electricity. Human locomotion is a potential source of renewable energy. A mechanical footstep power generator is used to tap waste energy from human locomotion and convert it into usable form such as electricity. Research shows that large amount of power is generated from non-renewable energy resource compared to that of renewable energy resource. The conventional methods of generating power are greatly inadequate and tend not to be eco-friendly. This review is aimed at analyzing the various methods of generating electricity through mechanical footstep power generator. Data from previous and trending works were collected through the review of relevant literatures. The mechanisms highlighted in this paper include piezo-electric mechanism, rack and pinion mechanism, fuel-piston mechanism. The selection of suitable transducers and low power capacity are challenges present in the use of piezo-electric mechanism. Rack and pinion mechanism also suffers from low power output and high maintenance cost. The fuel-piston mechanism with pulley arrangement is more efficient and requires less maintenance. This mechanism can be further improved upon to achieve greater efficiency by adopting a crankshaft flywheel mechanism with multiple pulley arrangement.

Keywords: ***eco-friendly, footstep generator, human locomotion, population, renewable energy***.

1 INTRODUCTION

In this current era of globalization, human population has increased exponentially around the globe. It was reported that the world's population reached approximately 8 billion as at October 2022 (worldometer, 2022). Energy crisis is due to two reasons; firstly, continues and rapid increase in the world's population and secondly, increase in the standard of living of human beings (Janugade *et al*., 2017). Walking is the most common activity in human life. When a person walks, he loses energy to the earth surface in the form of impact, vibration, sound, friction, etc. (Rajeev *et al*., 2019). The force exerted by human feet upon landing on the ground generates a renewable energy known as kinetic energy. This energy can be converted into electricity through a footstep power generator. Such a system is highly effective for installation in places that expect frequent mobility of a large population, such as educational institutions, market, motor parks, sport facilities, etc.

2 FOOTSTEP POWER GENERATION MECHANISMS

A footstep power generator basically converts the pressure from footsteps into electricity. To achieve this, it employs three main mechanisms. This paper concentrates on the different mechanisms used for footstep power generation.

2.1 Piezoelectric Mechanism

Briscoe and Dunn (2014), defined piezoelectricity as "electric charge that accumulates in response to applied mechanical stress in materials that have non-centrosymmetric crystal structure". "Piezoelectricity" is a Greek originated word, which means "squeeze or press". It refers to the property of the piezoelectric materials to generate an electric field when a mechanical force is applied, a phenomenon called the direct piezoelectric effect. Different types of footstep power generators are available and majority of these devices use piezoelectric transducer to generate power. One of the greatest challenges in designing footstep power generators with piezoelectric transducer is the selection of suitable ferroelectric material because it governs the efficiency of converting kinetic energy to electricity (Nayan, 2015). Conventionally, the piezoelectric footstep power generator uses ferroelectric materials made up of crystal such as Lead (II) titanate (PbTiO3), Lead (II) Zirconate (PbZrO3), Polyvinylidene Difluorideor Polyvinylidene Fluoride (PVDF) and Lead Zirconate titivate (PZT). While both of the PZT and Polyvinylidene Difluorideor (PVF) are commonly used as piezoelectric, the former material is the best candidate of piezoelectric because it produces better output voltage compare to other ferroelectric materials (Mohanty *et al*., 2014). Despite its popularity, piezoelectric footstep power generator suffers with some drawbacks such as the infeasibility of this technology under static condition and the limitation of power capacity (Mathane *et al*., 2015).

The block diagram of Piezoelectric mechanism is shown in Figure 1. The piezoelectric transducer converts the pressure exerted by footsteps into electrical energy in the form of Alternating Current (AC). The obtained AC is not in steady state, so a bridge rectifier is used to convert the varying AC to constant Direct Current (DC) and stored in a battery. The stored DC is then converted to AC by an inverter. A step up transformer is used to get 230V from the very low output of the inverter. This can be used for street lightening, household purpose etc. (Vineesh *et al.*, 2015).

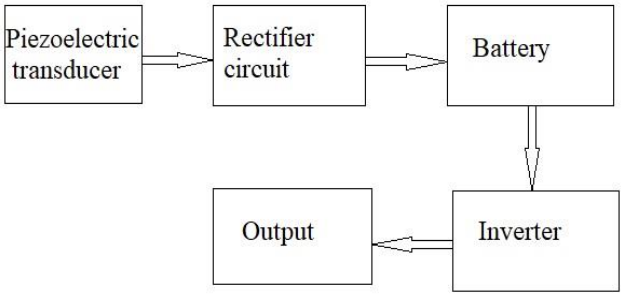

Figure 1: Block diagram of Piezoelectric Mechanism
(Source: Vineesh *et al.*, 2015)

2.2 Rack and Pinion Mechanism

The rack and pinion mechanism consists of two gears. The linear gear (rack) and the circular gear (the pinion). As shown in Figure 2, the linear motion of the rack upon stepping on the matching platform is converted to rotational motion by the pinion gear. When force is applied on the matching platform while walking, the springs gets compressed. The rack moves vertically downward, causing it to mesh with the pinion gear to produce a circular motion. This rotation is transmitted to the DC motor via a gear or chain drive. The output of the motor is then used to charge a battery which in turn powers an inverter for the production of alternating current. When the force is released from the matching platform, the pinion reverses and moves vertically upwards to its original position (Rajeev *et al.*, 2019).

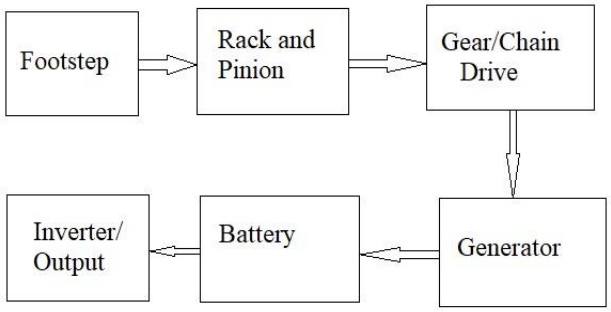

Figure 2: Block Diagram of Rack and Pinion Mechanism
(Source: Rajeev *et al.*, 2019)

2.3 Fuel-Piston Mechanism

According to Amel and Ahmed (2015), the main components of fuel piston footstep power generation machine are piston, wrist pin, connecting rod, crank shaft, flywheel, bearings, springs, and generator. The wrist pin connects the piston to the connecting rod, while the connecting rod links the piston to the crank shaft. The crank shaft translates the reciprocating straight motion of the piston into circular motion. When there is a compression force from the footstep on the matching platform or upper plate, a downward motion of the piston is achieved, resulting in the rotation of the crank shaft. This motion is transferred through a pulley-belt mechanism to the generator. The torque applied on the generator produces electric energy. The DC produced is then used to charge the battery which in turn powers the inverter. The inverter produces AC. The upper plate is restored to its original position by the springs. Figure 3 illustrates the working principle of a fuel-piston mechanism with the aid of a block diagram.

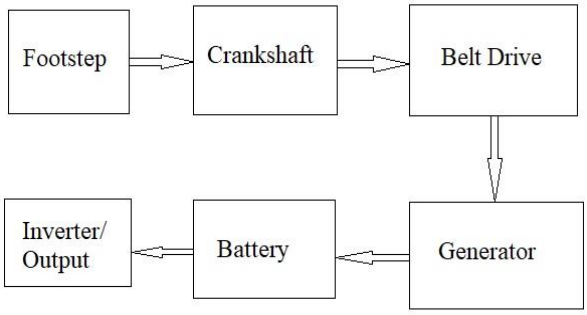

Figure 3: Block diagram of Fuel-Piston Mechanism
(Source: Amel *et al.*, 2015)

Mukthi *et al.* (2014) experimentally investigated on piezoelectric materials, solid materials (crystal and ceramics), biological matter (DNA, bone and proteins) and non-conducting materials to generate power. The result from this experiment is the generation of 12500V from the $1cm^3$ quartz by applying 2KN mechanical load. The major problem of the experiment is that strong electric field can break the dipoles and depolarization of the piezoelectric material. This method is used in buzzer and solar system and it is also used in the telecommunication system. Nayan (2015) utilized a piezoelectric material and transformed the AC output of a piezoelectric into a DC voltage using a rectifier. The components of this work include: rectifying circuits (consist of 4 diodes), primary and second battery, USB charge controller and buzzer (as piezoelectric sensor). Each square ft. contains 12 buzzers and generation varies with weight of footsteps. A voltage range of 1 to 10.5 V per footstep was obtained. An average weight of 50 Kg was used in the design. The limitations were the inefficiency to amplify the power from source to reduce time of charging the battery with few steps and the material used as sensor contained lesser piezo crystal substance on its outer layer

which could be easily broken by people. In Marshiana, *et al*. (2016) work, a DC to DC converter functioning as an inductor to oppose changes in current was used in the piezoelectric footstep power machine. The result showed that weight and power were directly proportional up to a certain increase. The output electricity energy generated was 0.6 watt. The work is expensive and the output varies with temperature variation of the crystal. He *et al.* (2019) designed and fabricated a piezoelectric energy harvester structure using a double-layer squeezing structure and a piezoelectric beam array. During the experiment, a 60-kg person stepped on and off the structure with different frequencies. The maximum output power obtained by one piezoelectric beam was 134.2 μW under a step frequency of 1.81 Hz, but the authors considered that a total of 40 piezoelectric beams inside the floor structure could reach 5.368 mW. Cho *et al*. (2019) developed a road-compatible piezoelectric energy harvester using piezoelectric transducers fixed onto both ends, the stress being converged toward the center of the device via a rigid bar. The harvester was used in actual road conditions for five months, being stressed by the vehicles traveling at speeds of 10–50 km/h when they entered a highway rest area. At 50 km/h, the harvester's output power was 2.381 W, while at 10 km/h, the output power was 576 mW. The generated energy was used to power the LED indicators and was uesd to transmit real-time information about the sensor's leak, temperature, and strain. Edlund *et al*. (2019) carried out a comparison study of vibrational energy harvesting using piezoelectric tiles in walkways and stairways. It was concluded that piezoelectric tiles installed in a stairway produce a better efficiency than the ones installed in walkways due to the natural increased pedestrian work demanded in traversing the stairs. The authors indicated that the tile design should consider the naturally random characteristics of pedestrian traffic in order to increase the level of harvested power.

There are many types of combination for mechanical footstep power generator available in the market. These include: rack and pinions with pulley, crank shaft with chain drive system, fly wheel with gear, etc. However, most of these designs are combined with two mechanism components such as rack and pinion with flywheel, rack and pinion with pulley system, and rack and pinion with chain drive system (Chun *et al*., 2019).

Mohd *et al*. (2017) describes the potential of generating electricity from a mechanical footstep power generator using a simple rack and pinion mechanism. The system requires no fuel input and pose no threat to the environment as it is a clean method of generating electricity through harnessing and utilizing waste energy from footsteps. The system consists of a floor and base plate, rack and pinion, bearings, DC motor, spring, 12V battery, and inverter. When footstep (pressure) is exerted on the floor plate, the spring compresses, thus causing the rack to move downward causing the rotation of the pinion. The pinion is attached to a shaft with bearing to aid rotation while minimizing friction. The torque generated from the rotation of the shaft drives the generator which in turn produces DC voltage to charge the battery. The stored charge in the battery powers the inverter to supplies useable AC power for lightening bulbs and other appliances. The graph of mass against work-done and mass against power developed shows a linear relationship between both quantities. A mass of 15kg and 75kg generates 0.003W and 0.76W of power respectively for one minute. Four masses ranging from 15kg to 75kg were used. The result was obtained from Matlab program. With this non-conventional method of generating electrical power through footstep, there is no need for power from mains and there is less pollution in this source of energy. Time to time lubrication is required for the smooth running of the device thereby incurring maintenance cost. Also, the power output is low and can be improved upon. Rajeev *et al.* (2019) developed a footstep power generation with the aim of providing rural areas with electricity from a non-conventional energy source. The system uses the rack and pinion mechanism with gear arrangement for the transmission of power. Theoretical and practical power outputs were obtained from a 20kg mass. The theoretical power generated per hour reached 588.6Watts while the practical power for continuous load applied on the footsteps for one hour is 112.3Watts. It is especially suited for implementation in crowded areas. In Deshmukh's work, the design and modeling of parts of the foot step power generation system was described using 3d modeling software creo. This process consists of a number of simple setup that is installed under the walking or standing platform. Project system works on the principle of converting the linear motion due to pressure of footsteps into rotating motion by rack and pinion arrangement. This mechanism fails if there is any occurrence of variable load leading to balancing type problems. Power is not generated during return movement of rack (Deshmukh, 2016). Igbo (2019) presented a Footstep Electricity Energy Generating Machine using dual generator. The system converts the weight of footsteps into electricity using two drive mechanism. That is, a rack and pinion drive and a chain drives which transmit the linear motion from the force exerted by footsteps via the matching platform to the rotary motion required to drive the DC generator. A double chain drive was used so as to enable the utilization of two power generators. After testing of the footstep electricity generating machine, a power efficiency of 52% was recorded. A maximum of 12.308watts was measured from an 85Kg human leg. The author recommended that the transmission mechanism can be optimized in other to increase the efficiency of the mechanism in terms of the output and cost. In Chatla *et al.* (2021) work, a simple rack and pinion arrangement was also developed. The result from the experiment shows that a body mass of 60Kg exerts a force of 558.6N on the floor plate leading to the production of 0.5886W of output power for one pushing force. The power output and efficiency of the power generator is low and high maintenance cost is

incurred. The integration of rack and pinion and piezoelectric material could lead to a desired output. Padma *et al*. (2014) experiment shows that electrical energy is generated from speed breakers due to the motion of vehicles on a rack and pinion arrangement. The paper mainly focused on the conversion of potential energy to electrical energy. Aniket *et al*. (2013) stated that the kinetic energy of a moving vehicle can be converted into mechanical energy through the rack and pinion arrangement. The components used to achieve this include; rack and pinion gears, ball bearing, spur gear, flywheel, shaft and generator. The mass of the vehicle travelled through speed break is 300kg then the output power developed for one minute is 7.37 W and for one hour is 441.4 W. Thus the electrical energy generated by the vehicles in one day is sufficient for running the four street lights at a time for a whole night. This process is a pollution free power generation and no any need of man power during the power generation.

(Sasank, 2014) developed the footstep generator based on crank shaft; fly wheel, and gear arrangement. This type of footstep power generation system is eligible to be installed in crowded places and rural areas. Thus this is a very good technology to provide effective solution to power related problems to affordable extent. This will be the most acceptable means of providing power to the places that involves difficulties of transmission. Shiraz *et al*. (2014) developed a footstep generator that uses a chain and gear drive mechanism for transmitting torque to the DC motor. The system also consists of a micro controller and an inverter for the production of useable power for appliances. The power generating floor can produce 100W on just 12 steps. Kaburu (2019) worked on the modification of a Mechanical footstep power generator. This was done by studying the existing trends in footstep power generation and coming up with modifications meant to optimize the power generation. The fabricated model made use of the flywheel mechanism. The power generated from the model during testing was 22,640watts with an assumption that the system was walked on for a period of 16 hours. The flywheel that was used had a radius of 11cm and a mass of 895g. In this research, a small model was constructed by using wells turbine from compressed air. From the experimental data, it is seen that an average 500N load can give an output of 1V voltage / 0.7A current / 1.71kWh power (Ahasan *et al*., 2020).

3 CHALLENGES AND FUTURE TREND

Challenges with existing Mechanical footstep power generators includes: (i) Low electricity power generation (ii) poor conversion mechanism (iii) high maintenance cost (iv) high cost of the device.

A low cost mechanism that is able to amplify and sustain the torque transmitted to the generator is essential to tackle the challenges highlighted. The use of the flywheel and crankshaft mechanism with multiple pulley drive arrangement is suggested.

4 CONCLUSION

The paper has briefly reviewed the different methods of generating electricity through mechanical footstep power generator. The different mechanisms used by previous authors were investigated alongside results, findings and recommendations. A mechanical footstep power generator that employs a crankshaft flywheel mechanism with multiple pulley arrangement should be able to sustain generated torque and improve the overall efficiency of the device while incurring low maintenance cost.

REFERENCES

Ahasan, A., Isteak, R., & Al-Amin, (2020). Electricity Generation from Air Compression Method Using Wells Turbine. *Journal of Advanced Engineering and Computation (JAEC),* 140-148.

Amel F., & Ahmed, A.G. (2015). Utilization of human footstep for power generation. *The first conference of recent trends in energy system (RTES). Benha University Cairo, Egypt.* 1-13.

Aniket, M., Pratik K., & Atul K. (2013). Electricity generation from speed breakers. *The International Journal of Engineering and Science (IJES)*, 2(11), 25-27.

Briscoe, J., & Dunn, S. (2014). 2.1 Background. In Nanostructured Piezoelectric Energy Harvesters, 1st ed.; *Springer International Publishing*: Berlin/Heidelberg, Germany. 3–4.

Chatla P., Nayaki S., & Vemula V.K. (2021). Design and Fabrication of Mechanical Footstep Power Generator, *EasyChair Preprint* No: 5642.

Cho, J.Y., Kim, K.B., Hwang, W.S., Yang, C.H., Ahn, J.H., Hong, S.D., & Sung, T.H. (2019). A multifunctional road-compatible piezoelectric energy harvester for autonomous driver-assist LED indicators with a self-monitoring system". *Appl. Energy* 2019, 242, 294–301

Chun, K.A., Ammar A.A., Sook, M.T, & Wei, H.L. (2019). Development of a Footstep Power Generator in Converting Kinetic Energy to Electricity. *E3S Web of Conferences 80, 02001*

Deshmukh, T.R. (2016). Design and Analysis of a Mechanical Device to Harvest Energy from Human Footstep Motion. Volume 3, Special Issue 1, ICSTSD

Edlund, C., & Ramakrishnan, S. (2019). An Analytic Study of Vibrational Energy Harvesting Using Piezoelectric Tiles in Stairways Subjected to Human Traffic. *European Journal of Applied Mathematics, 30(5),* 968-985.

He, M., Wang, S., Zhong, X., & Guan, M. (2019). Study of a Piezoelectric Energy Harvesting Floor Structure with Force Amplification Mechanism. Energies 2019, 12, 3516.

Igbo, E.B. (2019). Development of Footstep Electricity Energy Generating Machine Using Dual Generator. *A thesis submitted to postgraduate school, Federal University of Technology Minna.* 1-68

Janugade, S.V., Yadav, G.A., Mahadik, O.R. (2017). Foot Steps Power Generation using Mechanical System. *International Advanced Research Journal in Science, Engineering and Technology (IARJSET)*, Vol. 4, Special Issue 1, ISSN (Online) 2393-8021.

Marshiana, D., Elizabeth, S., Sunitha, N., & Vinothkumar, C. (2016). Footstep Power Production using Piezoelectric Sensors. *Research Journal of Pharmacy and Technology 9(7)*: 831-834.

Mathane, N.V., Salunkhe, A.L., & Gaikwad, S.S. (2015). Foot Step Power Generation Using Piezoelectric Material. *IJARECE*, Volume No: 4, Issue No: 10 and ISSN: 2278 – 909X.

Modi N., Shrivastava P., Bhardwaj R., & Jaiswal U. (2016). Generation of Electricity Through Footstep. *International Research Journal of Engineering and Technology (IRJET)*. Volume: 03 Issue: 05, ISSN: 2395-0072.

Mohanty, S.B., & Panda, S.S. (2014). An investigation on generation of Electricity Using Foot Step. *International Journal of Engineering Sciences & Research Technology (IJESRT)*. Volume 3, issue 5, ISSN: 2277-9655.

Mohd, Y.A., Ashraf, S., Awaise, A., & Afroz, K. (2017). Non-Conventional Method to Generate Electrical Power through Footstep. *International Journal of Science and Engineering Research (IJOSER)*, vol 5 Issue 2, 3221-5687, (P) 3221 568X.

Mukthi, N.G., Suman, & Yadav, S.K. (2014). Electricity generation due to vibration of moving vehicles using piezoelectric effect. *Advance in Electronic and Electric Engineering*. Vol. 4 No. 3, pp. 313-318, 2014. ISSN 2231-1297.

Nayan, H.R. (2015). Power Generation Using Piezoelectric Material. *Journal of Material Sciences and Engineering, vol. 4*, pp1-4.

Padma, A.R, Kiran A.K., & Suresh S. (2014). Power Generation from Speed Breaker by Rack and Ratchet Mechanism. *International Journal of Current Engineering and Technology*, Vol. 1 No. 2, E–ISSN2277–4106, P–ISSN2347–5161.

Rajeev, R.T., Rahul B., Quamruzzaman, Pushyamitra, G., & Sarnendu P. (2019). Footstep Power Generation. *International Research Journal of Engineering and Technology (IRJET)*, Volume: 06 Issue: 05 ISSN: 2395-0056

Sasank, S.P. (2014). An Investigation on Generation of Electricity Using Foot Step ISSN: 2277-9655. *Scientific Journal Impact Factor*: 3.449 (ISRA), Impact Factor: 1.852.

Shiraz, A., & Farrukh, H. (2014). Power Generation Footstep. *International Journal of Advancements in Research & Technology*, Volume 3, Issue 4, April2014ISSN2278-7763.

Vineesh, K., Amarnath, K.T., Lavanya, M., & Priya, R.A. (2015). Review on Foot Step Power Generation by Piezoelectric Transducer. *International Journal of Applied Engineering Research*, ISSN 0973-4562, vol. 10 No 4. pp 3814-3816. http://www.ripublication.com/ijaer.htm

Worldometers. (2022), "real time world statistics", Available: http://www.worldometers.info/

4th International Engineering Conference (IEC 2022)
Federal University of Technology, Minna, Nigeria

Green Synthesis of Titanium Dioxide Nanoparticles using *Delonix Regia* Leaf Extract for the Photocatalytic Degradation of Methyl Red Dye

* Ayenajeh[1] G, Akpan[2] U. G.

[1]Department of Chemical Engineering, Federal University of Technology, PMB 65 Minna Niger State, Nigeria
[2]Department of Chemical Engineering, Federal University of Technology, PMB 65 Minna Niger State, Nigeria
*Corresponding author email: ayenas1@gmail.com +2348132280607

ABSTRACT
Water pollution is one of the major environmental challenges due to the fact that it affects every living thing in the ecosphere. Scientific research efforts have been focused on minimizing from source and remediation techniques to solve this menace. Advanced Oxidation Processes (AOPs) has demonstrated enormous efficiency in the degradation of both inorganic and organic water pollutants. In this work, Titanium dioxide (TiO_2) nanoparticles have been successfully synthesized through a green chemistry approach and a sol gel method. This novel and alternative nanoparticle synthesis process is exploited both industrially and commercially to produce cleaner, safer and smarter products suitable for application. The phytochemical content of the leaf extract was determined to be total flavonoids (64.76 mg/100 g), total phenols (248.98 mg/100 g), alkaloids (29.56 mg/100g), tannins (107.76 mg/100 g) and saponins (78.97 mg/100g). These phytochemicals act as the reducing and capping agents in the synthesis of nanoparticles. The formation of nanoparticles was confirmed via UV visible spectroscopy at 376 nm and 364 nm for the sol gel and green catalyst respectively. Batch photocatalytic experiments showed that, the catalysts synthesized via sol gel and the green method were able to remove to 77.80% and 82.50% respectively of a model pollutant (methyl red dye solution**).**

Keywords: *Degradation, Methyl Red, Nanoparticles, Photocatalytic, Titanium Dioxide*

1 INTRODUCTION

The textile industry process is known to consume a large volume of water especially in the dyeing and finishing stages. These processes generate a lot of liquid effluents which contains between 15-20% of colors (dyes) and other chemicals (Bento and Pillis, 2018).

Majorly, dyes are among the pollutants of interest in textile waste effluents. A synthetic dye is an organic compound used for imparting colors to textile, paper, leather and plastic in a smart manner. Methyl red dye is one of the synthetic dyes commonly used in the textile industries usually in paper printing and textile dyeing. It belongs to the class of azo dyes which are considered mutagenic and carcinogenic when released untreated along with the effluents into the ecosystem (Yaseen and Scholz, 2019).

Azo dyes are the largest group of synthetic dyes in the industries, with about 800.000 tons produced annually worldwide. These dyes contain a nitrogen-nitrogen (-N=N-) double bond. Their chemical nature makes them highly resistant to biological and chemical treatment technologies (Olukani *et al.*, 2019; Muthuraman and Teng, 2009).

The discharge of these untreated textile wastewater (TWW) has constituted environmental pollution (land and water) and is also capable of causing adverse effects on human health (Akpan and Hameed, 2009).

Diverse physical and chemical treatment techniques have been exploited for the removal of dyes in textile effluents in to order comply with regulations, among such techniques are; adsorption, flocculation, chemical oxidation biosorption dye decolorization, membrane filtration, reverse osmosis, ultrafiltration (Ashraf, 2021; Akpan and Hameed, 2009). However, these treatment processes have several degrees of drawbacks such as cost, energy requirements and the creation of secondary pollution (Akpan and Hameed, 2009)

Several research works on the treatment of TWW has been centered on advanced oxidation processes (AOPs) such as the Fenton process and photocatalytic degradation. These methods have been identified to be able to convert organic pollutants such as dyes into water, carbon dioxide and minerals (Pirila *et al.*, 2015).

Heterogeneous photocatalytic reaction employs semiconductors such as titanium dioxide (TiO_2), zinc oxide

(ZnO) and Iron oxide (FeO) as catalyst. These catalysts have shown great capability to mineralize pollutants, thereby mitigating the creation of secondary pollution (Akpan and Hameed, 2011).

Titanium dioxide nanoparticles (TiO_2 NPs) photocatalyst is unique and is largely available, relatively cheap, non-toxic and chemical stable. Other properties of interest are its high refractive index, high dielectric constant, high photoelectric conversion efficiency, excellent photocatalytic ability and biocompatibility (Srinivasan, *et al.*, 2019).

The conventional synthesis method of the TiO_2 NPs has a major setback due to the chemicals employed. Chiefly among these setbacks is the environmental toxicity as a primary concern, which further limits their application in biotechnology, medicine and pharmaceuticals (Saranya *et al.*, 2018).

Therefore, the biosynthesis (green), an alternative method for synthesizing metal oxide nanoparticles has emerged over the years. This method has become attractive and acceptable over the conventional methods, primarily due to its ability to eliminate the production of harmful/toxic by-products. This method is eco-friendly and at the same time efficient and many research studies are still ongoing for the synthesis and modification of metal oxide nanoparticles via this method (Aravind *et al.*, 2021).

The use of leaf extract is employed due to its high concentration of phytochemicals/biomolecules such as amino acids, flavonoids, phenols, polysaccharides, tannins among others. These phytochemicals are responsible for the reduction and capping processes in the biosynthesis technique (Muthukumar *et al*, 2017).

Delonix regia, commonly known as Flamboyant tree, is a conspicuous fast growing and almost evergreen tree. It is an outstanding flowering tree found in gardens, parks, along streets and the mature tree provides excellent shade. Its leaves and flowers have herbicidal usage in application

This research work is therefore aimed at investigating the capability of *Delonix regia* leaf extract in the synthesis of TiO_2 NPs and confirming the efficiency of the photocatalyst in the degradation an organic pollutant (methyl red dye).

2 METHODOLOGY

The *Delonix regia* commonly known as the Flamboyant tree, was used in this study. The leaves were locally sourced from the Federal University of Technology, Gidan Kwano Campus, Minna, Niger State. Titanium butoxide was purchased from Sigma Aldrich company.

2.1 Extract preparation

Leaves of *Delonix regia* were carefully collected and washed thoroughly with clean water, followed by distil water to remove dust particles. The leaves were dried at room temperature for 10 days until samples were complete dry. They were then cut into pieces and grinded into a fine powder. 10 g of the leaf powder was boiled with distilled water at 60°C for 30 min. The extract was then allowed to cool down to room temperature and double filtered through a Whatman filter paper. The supernatant was store at 4°C.

2.2 Green synthesis of TiO_2 NPs

In the green synthesis of TiO_2 NPs, 20 mL of the *Delonix regia* leaf extract was added dropwise into a solution of 5 mL of $Ti(OBu)_4$ in 20 mL ethanol and stirred for 30 min. 1 M solution of NaOH was added dropwise to adjust the pH towards alkalinity. The gel was allowed to age for a period of 24 h before drying. The dried gel was then grinded into fine powder and calcined at 350°C.

2.3 Sol gel synthesis of TiO_2 NPs

The sol gel method was also employed to synthesize titanium dioxide nanoparticles as basis to compare with green synthesized catalyst. Titanium IV Butoxide ($Ti(OBu)_4$)purchased from sigma Aldrich was used as the precursor. 5 mL of $Ti(OBu)_4$ was dissolved in 50 mL of ethanol and stirred. A solution of distil water (H_2O), ethanol (CH_2OH_5) and concentrated nitric acid (HNO_3) using 3:7:1 volume ratio was prepared separately and added dropwise into $Ti(OBu)_4$ under continuous stirring for 3 h. the mixture gel formed was aged for 24 h and then dried at 100°C. The dried catalyst was then grinded and calcined at 350°C before further characterization and experimental works.

2.4 Photocatalytic degradation of Methyl Red Dye

The sol-gel and green synthesized photocatalysts activity were investigated via the photocatalytic degradation of a simulated Methyl Red dye solution. In the experiments, 0.1 g of the prepared catalysts were added to a 100 mL 45 mg/L Methyl Red dye solution. The initial pH of the dye solution was adjusted to an acidic pH with 1 M HCl and agitated thoroughly in a dark medium for 30 min (to ensure absorption/desorption equilibrium) before exposure to solar irradiation for photon activation and mineralization for a period of 3 h under constant agitation. The solution was then drawn and centrifuged before analyzing using a spectrophotometer to measure the absorbance.

The results of the analysis were in absorbance values at the measured wavelength and then converted to concentration. The performance efficiency of the catalyst was then calculated using the following equation:

$$\%\ Dye\ degradation = \frac{C1-Ct}{C1}\times 100$$

Where C1 is the initial dye concentration before treatment and Ct is the final concentration after reaction (Abdellah *et al*, 2018).

2.4 Characterization of titanium dioxide nanoparticles

The synthesized TiO_2 NPs were characterized to determined their properties. UV−visible spectrophotometer was used to

confirmed the development of the NPs and the band gap energy. The UV-Vis reflection spectra of the prepared catalysts were measured using Shimadzu UV-Visible spectrophotometer (UV-1800 series) with wavelength range between 200-800 nm.

3. RESULTS AND DISCUSSION

3.1 Phytochemical analysis

The *Delonix regia* plant leaf extract was screened to determine their phytochemical constituents and to consider its viability for the synthesis of TiO_2 NPs. Among the phytochemicals considered for the reduction and capping of TiO_2 NPs are the phenols, flavonoids, tannins and alkaloids. Their respective constituents in the leaf samples are hence shown on **Table 1.**

Table 1. Phytochemical test results of the *Delonix regia*

Sample	Phytochemicals (mg/100 g)				
	Phenols	Flavonoids	Tannins	Saponins	Alkaloids
Delonix regia	248.43	63.26	108.37	78.97	28.65
	248.98	64.76	107.76	77.89	29.56

The nature of the plant extract, its concentration, the concentration of the precursor metal salt, time and pH affects the rate of production of nanoparticles and their characteristics.

3.2 Preliminary studies on the TiO_2 NPs degradation of methyl red dye solution

Preliminary experimental studies were performed using the as synthesized photocatalysts in order to investigate their effectiveness in the degradation of a simulated methyl red dye solution. Photolysis and photocatalytic experiments were conducted and the result is shown on **Table 2.** A catalyst dosage of 0.1 g and 3 h time of reaction was maintained throughout the experiments.

The result shows that in photolysis, methyl red dye color removal under solar irradiation is possible but slow or negligible; this confirms the adsorption-desorption equilibrium and also indicates that without a photocatalyst, methyl red dye will remain in solution.

However, in the photocatalytic experiment using the synthesized catalyst as adsorbent in the absence of light, we see a considerable rate of reduction in the concentration of methyl red dye from 45 mg/L to 9.97 mg/L for sol gel catalyst and 7.85 mg/L for the green catalyst. This corresponds to 77.8% and 82.50% degradation respectively.

Table 2. Preliminary experiments (Initial Concentration of Simulated Dye Solution: 45mg/L)

Activity	Catalyst	% Degradation
Photolysis	Nil	2.86
photocatalysis	Sol gel	77.80
	Green catalyst	82.50

3.3 Study of Photocatalytic parameters

The effect of degradation parameters such as catalyst dosage, pH of the dye solution, concentration of the dye solution and time of reaction were studied and the results are presented as follows;

All experiments were conducted at room temperature and atmospheric pressure.

3.4 Effect of Dosage on photocatalytic degradation of methyl red dye solution

The amount of catalyst in a reaction plays a vital role. It tells the optimum amount of the catalyst required for complete reaction, which is complete dye degradation as in the case of photocatalysis with a semiconductor. As shown in **Figure 1**, the degradation efficiency of both the sol gel and green catalyst increased in proportion with incremental catalyst dosage from 0.1 g to 0.3 g. This indicate that an increase in the formation of hydroxyl radicals (*OH) which are responsible for degradation of the organic pollutant molecules. Further increment to 0.4 g shows a decline in the photocatalytic efficiency of both

catalysts. This confirms literature (Suresh *et al.*, 2018) that at an optimum catalyst dosage, the absorptive sites become unavailable for the solution becomes over saturated with the catalyst, hence preventing light penetration for the photocatalytic reaction to proceed.

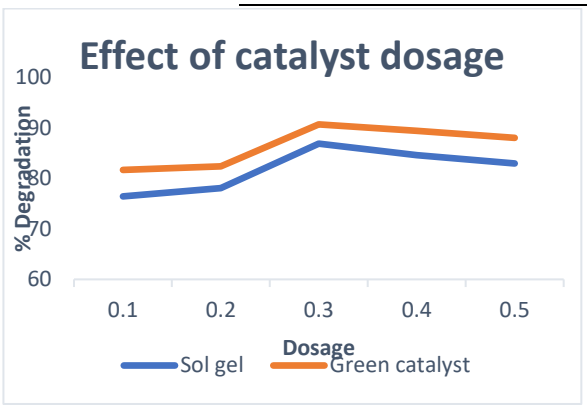

Figure 1: Effect of dosage on the degradation of methyl red dye solution

3.5 Effect of initial concentration of methyl red dye

The effect of initial concentration of methyl red dye solution in the range 10−50 mg/L was studied. The result as shown on **Figure 2** indicates that an increase in the dye concentration reduced the degradation efficiency of both catalysts. It can be seen that the percentage degradation decreases with an increasing dye concentration, although the required dosage of the photocatalyst was maintained. Hence, it can be deduced that as the available active sites of the catalyst got filled up with the dye molecules, the degradation capability of the catalyst reduced. As the dye concentration increased from 10 to 30 mg/L, there is a proportional increase in the percentage degradation of methyl red dye. Further increase between 40 and 50 mg/L shows a decline in the % degradation which indicates that the absorptive sites of the catalyst have decreased.

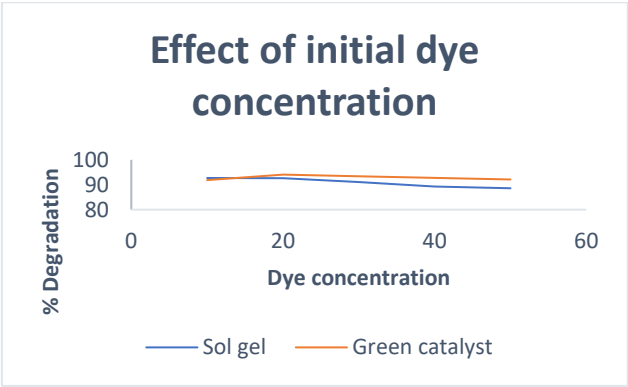

Figure 2: Effect of initial concentration on photocatalytic degradation of methyl red dye

3.6 Effect of pH on degradation of methyl red dye solution

The effect of pH on the degradation of methyl red dye solution was studied between pH 2 to 10. The result is as shown **Figure 3** below. It shows that a lower pH (acidic) favors the dye degradation better than a higher pH (alkaline). In the lower pH range, the surface of both the sol gel and green catalyst were positively charged, a higher amount of OH* were formed with a higher oxidizing activity leading to better degradation efficiency (Yasmina *et al.*, 2014). However, at the higher pH, their surfaces became negatively charged, thereby decreasing the rate of degradation of the dye molecules (Suresh et al., 2018)

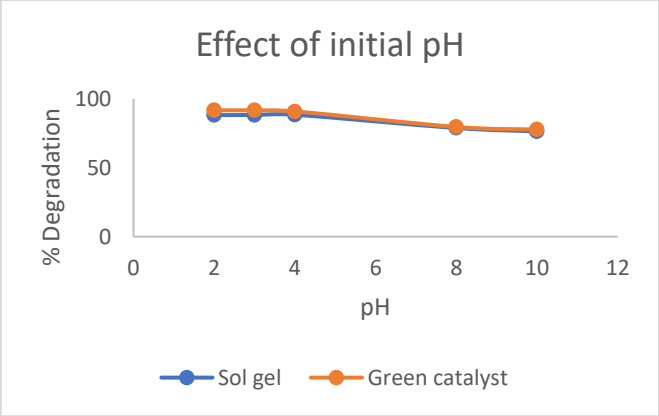

Figure 3: Effect of pH on the degradation of methyl red dye solution

3.7 Effect of Reaction time on degradation of methyl red dye

The effect of reaction time was considered to estimate how long it will take for the two catalysts to degrade or remove the pollutant from solution. **Figure 4** shows the gradual but steady rate of removal from 0 min to 60 min for the green catalyst. The removal of the dye peaked at 120 min (95.90%) and then began to decline. Whereas in the case of the sol gel catalyst the degradation of the pollutant peaked at 100 min (92.9%) before declining.

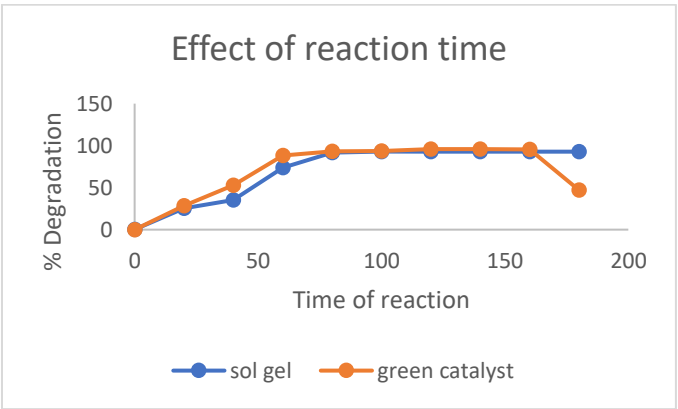

Figure 4: Effect of Reaction time on the degradation of methyl red

3 CONCLUSION

The concluded study has demonstrated the viability of *Delonix regia* leaf extract in the reduction and stabilization of TiO_2 nanoparticles as a green alternative method in the synthesis of nanoparticles. The presence of nanoparticles was confirmed by UV-Visible spectroscopy.

The as synthesized TiO_2 Nanoparticles also demonstrated excellent photocatalytic activity in the degradation of a modelled pollutant (Methyl red dye solution) to 77.80 % and 82.50% respectively. The optimum catalyst dosage was determined to be 0.3 g in both cases, also the a lower (acidic) pH favored the photocatalytic process for both semiconductors

ACKNOWLEDGEMENTS

I wish to special appreciate the petroleum development trust fund, PTDF. The scholarship couldn't have been timelier than when it came. Thank you for supporting the Nigerian student.

REFERENCE

Akpan, U. G., & Hameed, B. H. (2009). Parameters affecting the photocatalytic degradation of dyes using TiO2-based photocatalysts: A review. *Journal of Hazardous Materials, 170*, 520–529.

Abdellah, M. H., Nosier, S. A., EL-Shazly, A. H., & Mubarak, A. A. (2018). Photocatalytic decolorization of methylene blue using TiO_2/UV system enhanced by air sparging. *Alexandria Engineering Journal*. doi:doi.org/10.1016/j.aej.2018.07.018

Bento, R. T., & Pillis, M. F. (2018). Titanium Dioxide Films for Photocatalytic Degradation of Methyl Oreange Dye . *Titanium Dioxide-Material for a Sustainable Environment*, 211-225.

Ashraf, M. W. (2021). Removal of methylene blue dye from wastewater by using supported liquid memebrane technology. *Polish Journal of Chemical Technology, 18*(2), 1-5.

Aravind, M., Amalanathan, M., & Sony Michael Mary, M. (2021). Synthesis of TiO_2 nanoparticles by chemical and green synthesis methods and their multifaceted properties. *SN Applied Sciences, 3*(409). doi:10.1007/s42452-

Ashraf, M. W. (2021). Removal of methylene blue dye from wastewater by using supported liquid memebrane technology. *Polish Journal of* Aravind, M.,

Amalanathan, M., & Sony Michael Mary, M. (2021). Synthesis of TiO_2 nanoparticles by chemical and green

synthesis methods and their multifaceted properties. *SN Applied Sciences, 3*(409). doi:10.1007/s42452-021-04281-5

Muthukumar, S., Kalyanasundharam, S., Santhanalakshmi, .., & Jacquline Rosy, P. (2017). Biosynthesis, Characterization of Tio2 Nanoparticles by Using Solanum Xanthocarpum Berry Extract and Their Biomedical and Photocatalytic Activity. *International Journal for Research in Applied Science & Engineering Technology (IJRASET), 5*(12), 738-746.

Olukanni, O., Awotula, A., Osuntoki, A., & Govindwar, S. (2019). Infuence of redox mediators and media on methyl red decolorization and its biodegradation by

Providencia rettgeri. *SN Applied Sciences, 1*(697). doi:doi.org/10.1007/s42452-019-0668-0

Pirilla, M., Saouabe, M., Ojala, S. R., Drault, F., Valtanen, A., Huuhtanen, M., . . . Keiski, R. L. (2015). photocatalytic Degradation of Organic Pollutants in Wastewater. *Top Catal*.

Saranya, K. S., Padil, V. V., Senan, C., Pilankatta, R., Saranya, K., George, B., . . . Cˇerník, M. (2018). Green Synthesis of High Temperature Stable Anatase Titanium Dioxide Nanoparticles Using Gum Kondagogu: Characterization and Solar Driven Photocatalytic Degradation of Organic Dye. *Nanomaterials, 8*(1002), 1-19. doi:doi:10.3390/nano8121002

Srinivasan, M., Venkatesan, M., Arumugam, V., Natesan, G., Saravanan, N., Murugesan, S., . . . Pugazhendhi, A. (2019). Green synthesis and characterization of titanium dioxide nanoparticles (TiO2 NPs) using Sesbania grandiflora and evaluation of toxicity in zebrafish embryos. *Process Biochemistry, 80*, 197-202. doi:10.1016/j.procbio.2019.02.010

Suresh, P., Mehar, M. V., & Emmanuel, K. A. (2018). Factors Influencing the Rate of Photocatalytic Degradation of Hazardous Organic Pollutants fron Industrial Effluents: A Review. *International journal of Engineering Science Invention*, 18-22.

Yaseen, D. A., & Scholz, M. (2019). Textile dye wastewater characteristics and constituents of synthetic efuents: a critical review. *International Journal of Environmental Science and Technology*, *16*, 1193–1226. doi:doi.org/10.1007/s13762-018-2130-z

Yasmina, M., Mourad, K., Mohammed, S. H., & Khoula, C. (2014). Treatmen hetereougenous photocatalysis: Factors influencing the photocatalytic degradation by TiO2. *Energy Procedia*, *50*, 559 566.

4th International Engineering Conference (IEC 2022)
Federal University of Technology, Minna, Nigeria

An Investigation of Partial Shading Effects on Solar Photovoltaic Module Performance Using Infrared Thermography

*Jaji, U. F[1], Bori, I[1]
[1]Mechanical Engineering Department, Federal University of Technology, PMB 65 Minna Niger State, Nigeria
*Corresponding author email: hephkay@gmail.com +2348101155834

ABSTRACT

Partial shading is detrimental to the performance of a solar PV module. This is because it not only reduces the current and voltage of the module which leads to power loss in the module but may also lead to the formation of hotspots. This work presents an investigation carried out on the cross-comparison of two different PV modules subjected to the same ambient conditions in a tropical hot climatic region, to observe the effects of partial shading on them and if hotspots are formed, determine if they are heightened by the climatic condition of the environment. Different shading patterns and shading due to partial obstruction of direct radiation were considered. Shading was achieved using opaque shading sheets. The results of the experiment showed that the efficiency or performance of these modules is dependent on the type and direction of shading. This implies that as the percentage of shading increases, there is a decrease in power output and ultimately its efficiency. Also, thermal images obtained showed that asides temperature difference between the modules, hotspots formed on the test modules were not magnified by climatic conditions. The Infrared image indicated the likelihood of an internal defect in the control module. Considering the emergence of new solar technologies to improve its efficiency, it's recommended that a similar investigation under real outdoor conditions be carried out on Perovskite solar cells. Results of the outcome of the findings should be compared to those of the silicon crystalline modules, to determine which solar technologies perform better.

Keywords: ***Infrared, Partial Shading, PV Module, Solar***

1 INTRODUCTION

The use of renewable energy (solar energy precisely) is increasing globally as it promises a clean, green and healthy environment unlike non-renewable energy sources which when harnessed result in pollution of air, land and water bodies. The source of electricity in most Nigerian residential buildings is through the national grid. Less than 45% of the country's population is connected to the national grid and more than 60% of about 200 million people live in 80% of Nigeria's landmass which is not connected to the national grid. In a bid to get an alternative means of generating power to carry out day to day activities whilst maintaining a cleaner environment and cutting down on cost incurred during the extraction and processing of fossil fuels, the use of solar electricity (photovoltaic) has proven to be a popular alternative as it is sustainable and equitable as much as it is renewable.

The French Physicist Edmond Becquerel was the first to experimentally demonstrate the photovoltaic effect in the year 1839. But it was not until photovoltaic effect (i.e. the creation of voltage and electric current in a material by exposing them to light). The semiconductor device that converts solar radiation into direct electricity is called a solar cell. Cells are made from silicon which is the second most abundant element on earth. One solar cell can produce several watts of power which could run a calculator or charge a phone but is not sufficient enough to run high power consuming devices providing electricity for homes, businesses or com- munities. Hence, a series of cells are grouped together to form a module and an array of modules produces the required amount of power necessary to run large wattage devices.

According to [1], "the global solar photovoltaic market has experienced a vibrant growth for more than a decade since the year 2000, sporting an average annual growth rate of 40% with continued significant potential for long term growth.

The basic components of a photovoltaic system include the solar panels, wiring, batteries, switches, inverters, battery charger and a mounting system. When installing a solar photovoltaic system, the positioning of the solar panels is of utmost importance. The panels should be oriented in such a way that they face the sun at the time of the day when

it is at its peak. Another important consideration in the installation of PV panels is shading which affects the efficiency and power output of the system. The detrimental effects of shading on the total output of the system is as a result of the wiring together of the cells into a series circuit. Hence, the shading of any part affects the entire system. Therefore, the aim of this investigation is to comparatively investigate the effects of partial shading on the performances of monocrystalline and polycrystalline PV module types which are subjected to similar shading patterns and ambient conditions. Hence, the objectives were: (i) to determine the power outputs of the two PV module types when subjected to several standardized shading patterns; (ii) to determine the changes in the efficiency of the modules due to the partial shading imposed; (iii) to obtain the thermal responses of the Photovoltaic modules to the imposed shadings using infrared thermography to evaluate the severity of any occurring thermal problems (e.g. hotspots); (iv) to cross compare the detrimental effects of the imposed shading patterns on the different PV module types.

Additionally, the statement of problem is Shading is a factor that detrimentally affects the performance of solar PV systems. This is because it not only causes a drop in the power output and current of the system but also could lead to permanent damage of the PV system as a result of the formation of hotspots. It is naturally expected that the decrease in power production is proportionalto the shaded area and reduction in solar irradiance. While this concept might be true for a shaded single cell but at an array or module level the decrease in power is far from being linear with the shaded portion. It has been noted that the type, pattern or object of shade determines the level of risk it poses to reliability and long-term performance of the system. Hence, the effect of shading a PV module or panel is one that needs to be investigated and considered thoroughly before a module or panel is to be installed. This work will focus on how shading affects the behavior of two of the most common solar PV module types.

This work is important as it helped to determine if the ambient conditions of the environment magnifies the damaging effects of the hotspot. Also, it helped to ascertain which PV module type performed better under the subjected conditions and furthermore, give advice to homeowners on measures to take to minimize the effects of shading prior to installation.

Renewable energy is the energy that in a sense never runs out. It is inexhaustible and naturally available. There are many definitions of renewable energy, but it has been observed that of all these definitions, sustainable, replenished, inexhaustible are words that encompass them all. According to [2] renewable energy was defined as “the energy collected from renewable resources which are naturally replenished on a human timescale”.

Solar PV is preferred to other sources of renewable energy because it is simple, it is more predictable, it requires no fuel, it is noiseless, produces no greenhouse emissions, it requires minimal maintenance, it is available all over the world, it is abundant, it builds energy security, it reduces peak loads and other listless benefits [3]. According to the IEA, the development of solar energy will have a long term benefits as it will enhance sustainability, keep the price of fossil fuel lower than otherwise and lower the cost of alleviating climate change [4]. Global data shows that more solar photovoltaic (PV) capacity is being installed than any other electricity generation technology [5].

The history of photovoltaic is dated back to 1839 when a 19-year-old French physicist Edmond Becquerel first discovered the photovoltaic effect. He was experimenting with electrolytic cells when he generated electricity by placing silver chloride in an acidic solution and exposing it to sunlight [6, 7]. Thirty-seven years later, a London professor William and his student Richard discovered selenium’s photoconductivity.

Several studies have the carried out on the effects of shading on the performance of different PV module types [9, 10], some on the analysis of mismatch and shading effects in photovoltaic array using technologies [11] or the detection of faults and hotspots in solar cells [12]. Some researches went further to analyses the effects of shaded solar module using different computing environment, models and array configuration such as MATLAB, SimPower, shadow analyzer, shadows, Bishop model, heuristic model [13, 14, 15]. [8] reported that for objective shading with low irradiance caused heavy cloudy day for instance, a PV array may still generate a high voltage even if the current is extremely low or zero. Also, bypass diodes are important in minimizing the effects of hotspots in crystalline silicon modules. With regards to partial shading, results from their study showed that as the cell becomes partially shaded, the unshaded portion remains operational with little or no change in voltage and the cell/module continues generating power but at a reduced current. Hence, even if the output current is extremely low or zero, the PV array may still generate a high voltage. Also, it was observed that as partial shading increased, it got to a threshold point at which it changed to whole shading and the cell voltage collapsed. [16] experimented on the effect of full shading of a solar

PV module using 30W of monocrystalline PV module with different numbers of bypass diode and15profitest PV analyzer. Their experiment was aimed at determining which of these bypass diodes performed better when subjected to the same shading pattern. Full shading conditions was achieved using cardboard sheets and different configurations of full shading was obtained. The shade covered 1 cell, 2 cells, 3 cells and 4 cells. They observed that 4 bypass diodes save more power compared to 2 bypass diodes. Hence, increasing the number of bypass diodes improves the performance of PV panel under fully shaded conditions. Also, they found out that the drop in short circuit current (Isc) and power of the module is dependent on the number and position of the shaded cells.

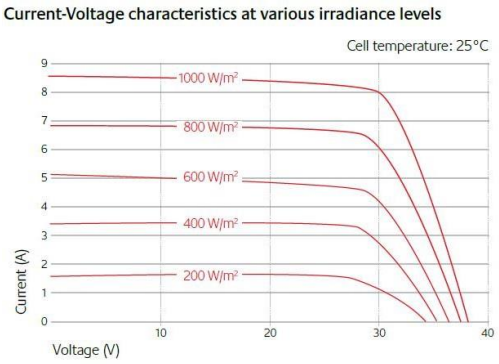

Figure 1: Objective Shading effect on I-V characteristics

2 METHODOLOGY

Two PV module types (monocrystalline and polycrystalline silicon) were tested in this study. During the tests, two of each module types were tested simultaneously. One served as a control module while the other was the experimental module.

The following experimental materials were used:

- Monocrystalline module
- Polycrystalline module
- Shading sheets i.e. 3mm cardboard paper
- Digital Thermometer
- TES 1333R Solarimeter
- Seek thermal imager
- Anemometer
- Android Phone
- USB Cord

Table 1: Specification of test PV Modules

Specification	Monocrystalline	Polycrystalline
Manufacturer	Rubitec Solar	Rubitec Solar
Model Type	HU 40	PV40P
Quantity	2	2
maximum Power, P_{max} (W)	40W (± 5%)	40W(± 3%)
Current at P_{max}, I_{max}(A)	2.22	2.25
Voltage at P_{max}, V_{max}(V)	18.0	17.8
Short circuit current, I_{sc}(A)	2.43	2.39
Open circuit voltage, V_{oc}(A)V	22.1	21.7
No. of cells	68	36

2.1 EXPERIMENTAL METHOD

The shading experiments was performed according to the following procedure:

1. **Setup and Installation**: Two modules (one for control and the other experimental) were mounted on the stand. The panels faced South at an angle 22º to the horizontal as shown in Fig 2.

2. **Shading of the modules:** The modules were shaded uniformly in percentages varying from 20% to 80% and the effects of partial shading under diffuse and global radiation was studied. The sheets were cut into varying sizes and shapes to obtain the various percentages and patterns of shading. The shading was done vertically, horizontally, diagonally and randomly (see Fig 3).

3. **Measurement of module output**: Current and voltage was measured using the digital multimeter when a certain percentage of the module was shaded. Also, Solar radiation, ambient temperature and wind speed were recorded. The parameters stated above were measured for both the control and test modules. Each test lasted for a period of 20 -30 minutes. The measurements were recorded at an interval of on minute. Thermal images were also obtained from the back- side of the module using the infrared thermal imager.

Figure 2: Apparatus Setup for experiment

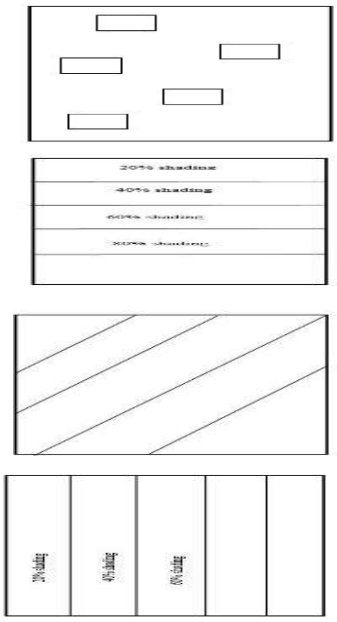

Figure 3: Shading Patterns

2.2 DETERMINATION OF MODULE PERFORMANCE

The module performance which is characterized by the current and voltage was determined using the performance quantifying parameters below:

$$\eta = \frac{\text{Power Output}}{\text{Power Input}} = \frac{V_{mp}I_{mp}}{IA} \quad (1)$$

$$\text{Fill Factor (FF)} = \frac{V_{mp}I_{mp}}{V_{oc}I_{sc}} \quad (2)$$

$$\text{Maximum Power Output } P_{mp}\,(W) = \frac{V_{mp}}{I_{mp}} \quad (3)$$

Where:

I = Isolation or Irradiance (W/m^2)

A = Area of Panel (m^2)

I_{sc} = Short circuit current

A = Area of Panel (m^2)

I_{sc} = Short circuit current

V_{oc} = Open circuit Voltage

V_{mp} = voltage at maximum power (V)

I_{mp} = current at maximum power (A)

3 RESULTS AND DISCUSSION

Data collected during the experiments were analyzed and plotted using the OriginPro graphing and data analysis software.

3.1 EFFECT DUE TO HORIZONTAL SHADING OF MO-NOCRYSTALLINE PV MODULE

Figure 4 show plots of power, efficiency, irradiance and ambient temperature against time for the PV modules that were shaded 20% horizontally. From Fig. 4, the maximum power produced by the 20% shaded module was 4.7W while that of the unshaded module was 32W respectively and this occurred at an irradiance of $1151W/m^2$. Also, it can be seen from the graph that the maximum amount of sunlight that was converted into usable electricity by the unshaded

module was about 16.89% while that of the shaded module
was 2.47%. The percentage drop in efficiency
of the module was 85.3%. Also, the plot shows the power generated is mainly dependent on irradiance.

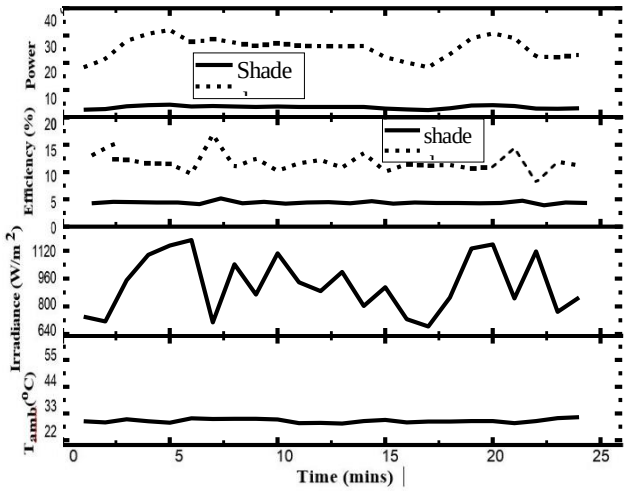

Figure 4: Impact of 20% horizontal shading on the Monocrystalline PV module

3.2 EFFECT DUE TO HORIZONTAL SHADING OF POLYCRYSTALLINE PV MODULE

Figure 5 depicts the impact of partially shading 40W of a polycrystalline PV module 20% horizontally taking into consideration the irradiance and the ambient temperature. From Fig.4, the maximum power generated by the shaded and unshaded modules was about 8.69W and 42.8W respectively at an irradiance of 866.2W/m^2. Also, the influence of insolation on the power generated is clearly seen in Fig. 5. The maximum usable energy converted from the sun's irradiance for the shaded module was 4.72% while that of the unshaded module was 22.94%. Therefore, the drop-in efficiency was 79.5%.

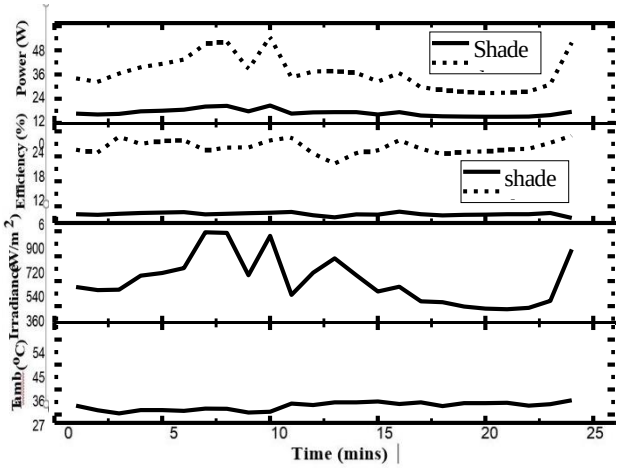

Figure 5: Impact of 20% horizontal shading on the polycrystalline PV Module

3.3 IR ASSESSMENT FOR THE MONOCRYSTALLINE MODULE SHADED HORIZONTALLY

Figures 6 and 7 are the normal and thermal images respectively of the 40W monocrystalline modules shaded 20% horizontally. As seen in Fig. 6, no hotspot was detected but temperature gradient was observed in the modules. This may have effects on the module's integrity due to thermal stress.

Figure 6: Normal image of 20% horizontal shading

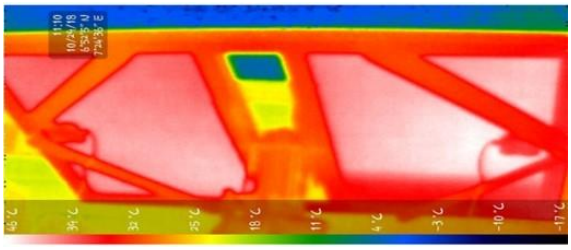

Figure 7: IR (Infrared) image of a functioning modules subjected 20% horizontal shading

3.3 IR ASSESSMENT FOR POLYCRYSTALLINE PV MODULE SHADED HORIZONTALLY

Figures 8 and 9 shows normal and IR (Infrared) image of 40W polycrystalline module shaded 20% horizontally. No hotspot was detected in the test module as seen from Fig. 4.48, but it can be seen that the temperature of the modules was higher than the frame.

Figure 8: Normal image of 40W Polycrystalline module subjected to 20% horizontal shading.

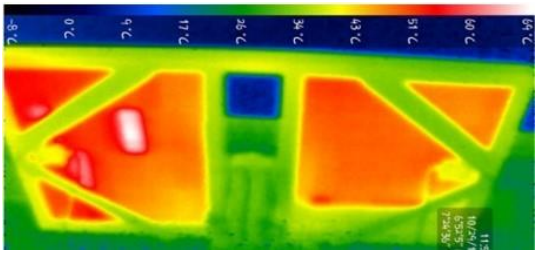

Figure 9: IR mage of 40W Polycrystalline module subjected to 20% horizontal shading

4 CONCLUSION

Although during the experiments, 20%, 40%, 60%, 80% Partial Horizontal, Vertical and diagonal was done on both Monocrystalline and Polycrystalline PV Modules and results were gotten, but for the purpose of this paper, only 20% horizontal shading for both PV Module is discussed.

Also, below conclusion discussed is based on all results gotten from all shadings done.

Experiments were carried out to determine the effects of partial shading on solar PV modules using two different topologies of modules and exposing them to global and diffuse radiation. Also, the damaging effects of hotspots and its severity considering the climatic conditions of the environment was studied. Also, cross comparison between both PV topologies was carried to determine which modules performs better under the various shading conditions.

Results of the experiment showed that the power output and hence, the efficiencies of the different PV modules are dependent on the type of shading. This implies that as the amount/percentage of shading increases, there is a decrease in power output and ultimately its efficiency. Additionally, the study confirms the findings of Bulanyi and Zhang [8] that at low irradiance, a PV array will still generate a high potential difference even if the current is extremely low or zero.

Furthermore, the bar charts comparing the effects of shading on the power and efficiency of the modules showed that for shading parallel to the long side, the monocrystalline modules performed better than the polycrystalline modules to an extent, while for other types of shading the polycrystalline modules performed better by a slight amount.

The results also showed that there were more losses in the PV modules when objects were directly placed on them than when the modules were partially obstructed from direct radiation. In as much as the modules generated a considerable amount of power when there was diffuse radiation, the efficiency of the module will be greatly reduced.

Finally, the IR images showed that modules with random shading were more susceptible to hotspot formation.

.

REFERENCES

[1] Mohamed Amer Chaaban, Lana El Chaar, and Mahmoud Alahmad. An adaptive photovoltaic topology to overcome shading effect in pv systems. *International Journal of Photoenergy*, 2015, 20

[2] Omar Ellabban, Haitham Abu-Rub, and Frede Blaabjerg. Renewable energy resources: Current status, future prospects and their enabling technology. *Renewable and Sustainable Energy Reviews*, 39:748–764, 2014

[3] Mathias Aarre Maehlum. Solar energy pros and cons. *Energy Informative*, 12, 2014

[4] Solar Energy Perspectives. Executive summary international energy agency. 2011. *Archived from the original on*, pages 12–03, 2011

[5] A Blakers. Solar is now the most popular form of new electricity generation worldwide. *The Conversation. Available at https://theconversation. com/solar- is-now-the-mostpopular-form-of-new-electricity-generation-worldwide-81678*, 2017

[6] Gilbert M Masters. *Renewable and efficient electric power systems*. John Wiley & Sons, 2013

[7] K Pickerel. The long history of solar PV. *Solar Power World*,2018

[8] Peter Bulanyi and Rodd Zhang. Shading analysis & improvement for distributed residential grid-connected photovoltaics systems. In *The 52nd Annual Conference of the Australian Solar Council*, 2014.

[9] MA Munoz, M Carmen Alonso-Garc´ıa, Nieves Vela, and Faustino Chenlo. Early degradation of silicon pv modules and guaranty conditions. *Solar energy*, 85(9): 2264–2274, 2011.

[10] Idriss Hadj Mahammed, Amar Hadj Arab, Yahia Bakelli, Messaouda Khennene, Samir Hamid Oudjana, Amor Fezzani, Layachi Zaghba, et al. Outdoor study of partial shading effects on different pv modules technologies. *Energy Procedia*, 141:81–85, 2017.

[11] J Guerrero, Y Muñoz, Fernando Ibáñez, and A Ospino. Analysis of mismatch and shading effects in a photovoltaic array using different technologies. In *IOP Conference Series: Materials Science and Engineering*, volume 59, page 012007. IOP Publishing, 2014.

[12] Michael Simon and Edson L Meyer. Detection and analysis of hot-spot formation in solar cells. *Solar Energy Materials and Solar Cells*, 94(2):106–113, 2010.

[13] F Belhachat and C Larbes. Modeling, analysis and comparison of solar photo- voltaic array configurations under partial shading conditions. *Solar Energy*, 120: 399–418, 2015.

[14] Yaw-Juen Wang and Po-Chun Hsu. An investigation on partial shading of pv modules with different connection configurations of pv cells. *Energy*, 36(5):3069– 3078, 2011.

[15] Luis Fialho, Rui Melicio, VMF Mendes, Joao Figueiredo, and Manuel Collares- Pereira. Effect of shading on series solar modules: simulation and experimental results. *Procedia Technology*, 17:295–302, 2014.

[16] Monadhil Al-chaderchi, K Sopain, MA Alghoul, and T Salameh. Experimental study of the effect of fully shading on the solar pv moduleperformance. In *E3S Web of Conferences*, volume 23, page 01001. EDP Sciences, 2017.

4th International Engineering Conference (IEC 2022)
Federal University of Technology, Minna, Nigeria

Effect of Partial Shading Diffusion on Photovoltaic Panels for SP and TCT Techniques

[1,2]M Mohammed, [2]I. A. Shehu, [3]U. Musa, [4]S. H. Sulaiman and [5]I. Abdulwahab
[1]Kaduna State Power Supply Company (KAPSCO), Kaduna State, Nigeria
[2, 3,4,5]Department of Electrical Engineering, Ahmadu Bello University Zaria, Kaduna State, Nigeria
*Corresponding author email: musa.mohd@kdsg.gov.ng, [2]iashehu@abu.edu.ng,
[3]shsulaiman@abu.edu.ng, [4]umusa@abu.edu.ng, iabdulwahab@abu.edu.ng

ABSTRACT

This work presents an experimental based research to investigate the effect of partial shading on Photovoltaic (PV) Panels employing Series Parallel (SP) and total cross Tied configurations. The aim is for more understanding of the effect as well as to establish the best configuration under both shaded and unshaded situations. In this work, experiment was setup with PV modules at renewable energy laboratory of the department of electrical engineering Ahmadu Bello University, Zaria. The experimental set-up comprises of installed 4x3 modules of solar PV configured in series parallel and total cross tied (TCT), separately at the angle of 12º due south each. The results signify that TCT is better than SP for shaded condition but SP slightly outperformed TCT for unshaded. The effect of shading had been reaffirmed for both SP and TCT.

Keywords: ***Shading, Series-Parallel, Total Cross Tied, Photovoltaic, performance.*** **.**

INTRODUCTION

The continuous increase in environmental concerns, deregulated market forces and restructuring in electricity industry is rapidly improving the need for development of alternative energy generation ((Iliyasu *et al.,* 2022)Yin & Qin 2022). Energy supply from renewable energy sources are now seen as a good alternative to the conventional means of generating electricity (Abdulwahab et al., 2021(Abdulwahab *et al.,* 2022)). However, the problem of instability in the system will increase due to the significant variations and uncertainties inherent in in renewable energy sources (RES). Photovoltaic (PV) cells are receiving more attention globally more than any time before, this is because of the availability of sun, continuous increase in cost of fossil fuel and the advantage it has that it does not pollute environment (Mohammed et al., 2020; Pachauri et al., 2020). Unfortunately, shading has been identified as one of the major factors that affect the performance of photovoltaic panels (Sagar et al., 2020). Decrease in the output power of the photovoltaic panel is experienced, whenever there is shading on the panels which can be caused by trees near the solar panel installation or other sources. (Tubniyom et al., 2018). This is largely due to the fact that the PV panel comprises of a string of solar cells that are connected in series (Belkaid *et al.,* 2017; Pathare *et al.,* 2017). The current output from the whole panel is limited to that passing through the weakest link cell. Thus, the power output that will be obtained from a panel that is totally shaded will be zero. Consequently, shading of a panel by 20%, will lead to a corresponding decrease in the output power by the same 20%. This means the output power obtained can be seriously affected due to the occurrence of shading (even when the shaded portion is very minimal) (Gostein et al., 2015; Pachauri et al., 2020). Shading occurred as a result of drops carried by air/wind from leaves or birds waste. Shading effect can be full or partial depending on the agent and duration of it on the panel. (Ngari 2017) investigated the sensitivity of a polycrystalline silicon photovoltaic module due to dust such as gypsum, coal mines and fertilizer. The investigation was done under different levels of solar irradiances from industries. The results obtained showed that, dust accumulation on the module affects the output power negatively. This work is therefore designed to determine the extent of the effect of shading conditions on PV panels under Series Parallel (SP) and Total Cross Tied (TCT) configurations via experimental setup, aimed at understanding the magnitude of effect for each technique. Although, there are a lot of configuration technique as reported by (Pachauri et al., 2020) and the question of which technique is more resilient to shading effect is yet to be established. This work is limited to SP and TCT techniques. The rest of this paper is structure as follows: section two contains a brief literature of the two techniques employed in the work, section three gives methodology of the research, Results and discussions are in section four while conclusions are drawn in section five.

1.1 SP AND TCT TECHNIQUES

The connection of components for a series circuit is done end to end in order to ensure that the current flow in a single path. While the components in a parallel

circuit are connected across each other, forming exactly two sets of electrically common points. Figure 1 show a typical SP configuration of the PVs. Whereas, TCT configuration is formed by connecting all nodes of crossing SP configuration. In TCT configuration, the voltages of all nodes and also the sum of currents in different junctions are equal. Figure 2 describes a typical TCT configuration.

The maximum power point of a solar cell is always determined by the short circuit current and open circuit voltage at any given irradiance G and cell temperature t. it is depended on the difference in temperature from standard test condition and also temperature coefficient of short circuit current α.

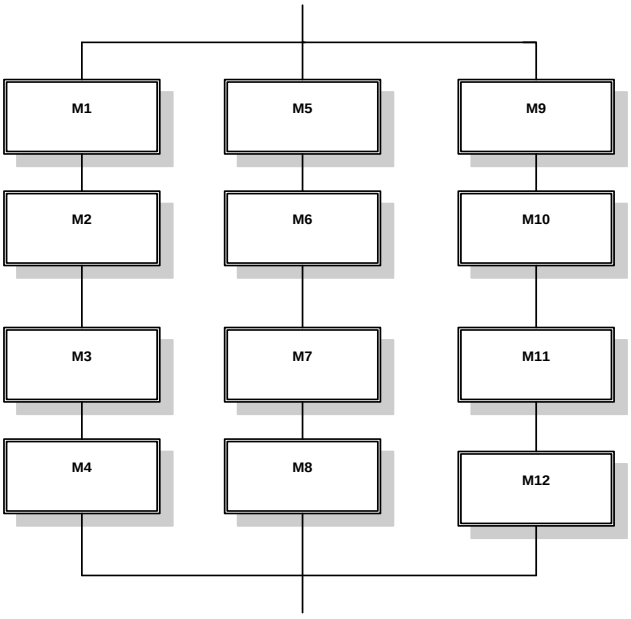

Figure 1: Series Parallel (SP) Configuration

$$I_{SC}(G,t) = I_{SCO}\frac{G}{G_O}(1+\propto \Delta t) \quad (1)$$

While open circuit voltage is depicted as:

$$V_{OC}(G,t) = V_{OCO} + \partial In\left(\frac{G}{G_O}\right) + \beta\Delta t \quad (2)$$

Where β represents the temperature coefficient of open circuit voltage and ∂ denotes the product between the thermal voltage at standard test condition and the identity factor of the cell.

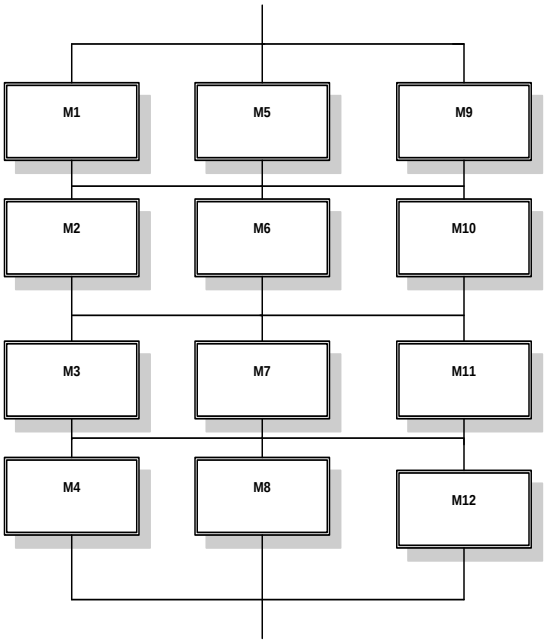

Figure 2: Total Cross Tied (TCT) Configuration

Now, when a string Number N_s of solar cell are connected in series the short circuit current of the string is the same as the short circuit current of the cell that is least illuminated (Calcabrini et al., 2021). The open circuit voltage can be obtained from:

$$V_{OSC} = N_S V_{OCO} + \partial In\left(\prod_{i=1}^{N_S}\frac{G_i}{G_O}\right) + \beta\sum_{i=1}^{N_S}\Delta t_i \quad (3)$$

Similarly, the open circuit voltage of N_P cells connected in parallel the voltage is limited by the least illuminated cell (Calcabrini et al., 2021) and the short circuit current is given by:

$$I_{SC} = \frac{I_{SCO}}{G_O}\left(\sum_{i=1}^{N_P} G_i + \propto \sum_{i=1}^{N_P} G_i\,\Delta t_I\right) \quad (4)$$

Depending on the topology, equation (3) and (4) can be used to obtain the square approximation of I-V characteristics of any topology.

METHODOLOGY

In this work, experiment was setup with PV modules at renewable energy laboratory of the department of electrical engineering Ahmadu Bello University, Zaria. This was aimed at data extraction for analysis.

PV MODULE SELECTION

Monocrystalline solar cells are chosen in the experiment for its historical performance and availability in market. 24 modules of the same rating as contained in the Table 1 were acquired and used in 4x3 sets of SP and TCT configurations.

Table 1: Solar PV Modules Parameter

S/N	Parameter	Value
1.	Maximum power	10W
2.	Output tolerance	±5%
3.	Rated Voltage	18V
4.	Short circuit current	0.63A
5.	Open circuit voltage	22.05V

EXPERIMENTAL SETUP

The experimental was installed with 4x3 modules of the solar PV configured in SP and TCT separately at the angle of 12º due south each. Recording began between 6 am and 6 pm on 10th September, 2021 and 11th September, 2021. The experiment was organized in four different setups, recording data concurrently as follows:

i. Purely for the unshaded modules SP configuration

ii. Purely for the unshaded modules TCT configuration

iii. Partial Shaded condition for SP configuration and

iv. Partial Shaded condition for TCT configuration.

Figure 3 and 4 showed the experimental set-up that was done in Electrical Engineering Department, Ahmadu Bello University, Zaria.

Figure 3: Experimental Setup for Unshaded Condition.

Figure 4: Setup for partial shading Condition

Data of output voltage, current, output power and the corresponding solar irradiance of the days were captured in the interval of 30 minutes in each setup. September was carefully chosen to carry out the measurement because of the varied weather condition of raining season as the irradiance values significantly varied within short period of time.

RESULTS AND DISCUSSION

The effect of shading on the PV can be seen obviously on each technique and also in comparison with unshaded PVs, technique that gave higher outputs is considered as the best.

UNSHADED MODULES SP VERSE TCT CONFIGURATION

For the purpose of investigating the performance between SP and TCT, unshaded panels were set at the same operating conditions recording the voltage and current outputs. It can be seen in Figure 5 (a) and (b) that, the values grows with time in both the techniques up to peak hour of the solar irradiance which is between 12 noon to 1pm. Both the voltages and the currents start to decline from the peak to lesser values. It can be seen that at the peak hours, SP configuration overrides the TCT configuration. Whereas, at off-peak, the values fluctuate. This may happen as a result of measurements error.

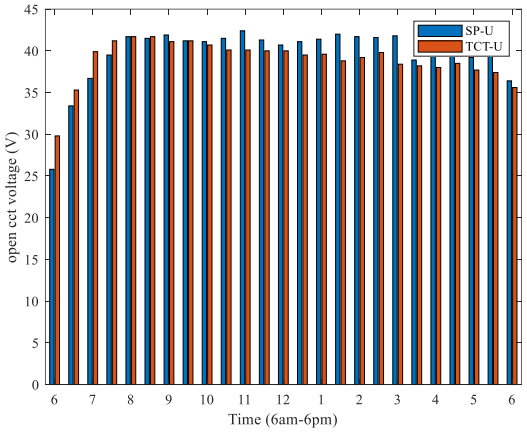

(a) Voltage Output

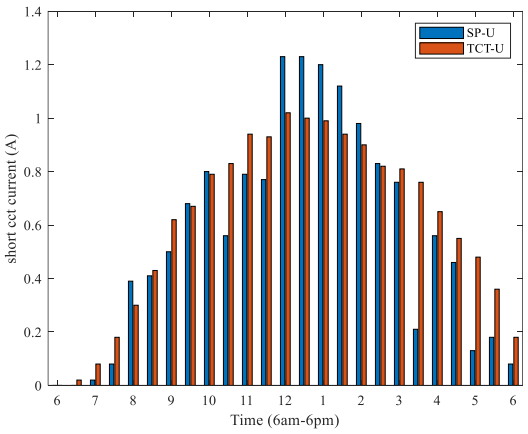

(b) Current Output

Figure 5: Performance Comparison between SP and TCT for Unshaded condition

PARTIAL SHADING CONDITIONS FOR SP AND TCT

In this case, the performance of SP and TCT were evaluated under partial shading condition. The results indicated that in a condition of partial shading, TCT technique will be more preferred as it proofs a better performance in both voltage and current profiles as contained in Figure 6 (a) and (b) respectively.

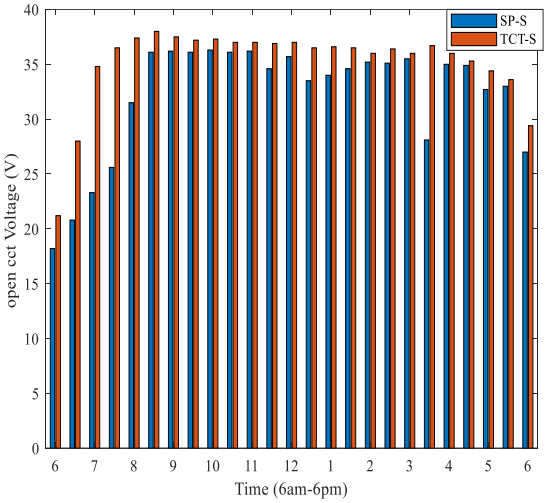

(a) Voltage Output

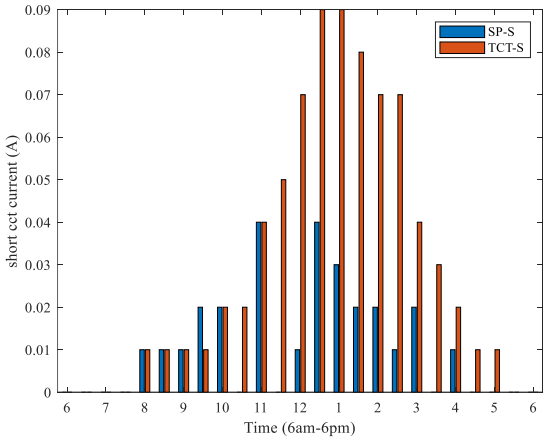

(b) Current Output

Figure 6: Performance Comparison between SP and TCT for Partial Shading Condition

THE EFFECT OF SHADING ON THE PVS

The overall effect of partial shading on PVs has been assessed based on SP and TCT Techniques. It has been established that the effect is proportional to the area shaded, Figure 7 (a), (b), (c) and (d) justifies that. For both shaded and unshaded, in SP and TCT configurations, the effect is glarier as the performance indicators are higher in the unshaded compare to the shaded conditions.

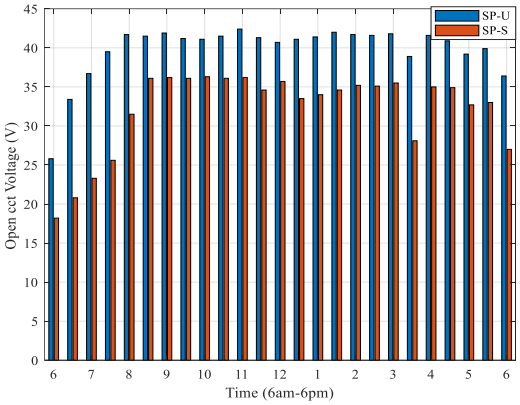

(a) Voltage Output for SP

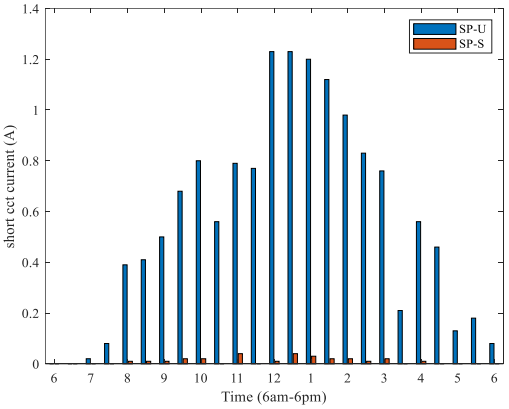

(b) Current Output for SP

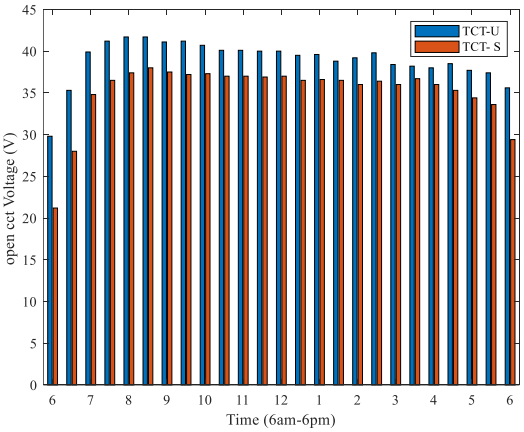

(c) Voltage Output for TCT

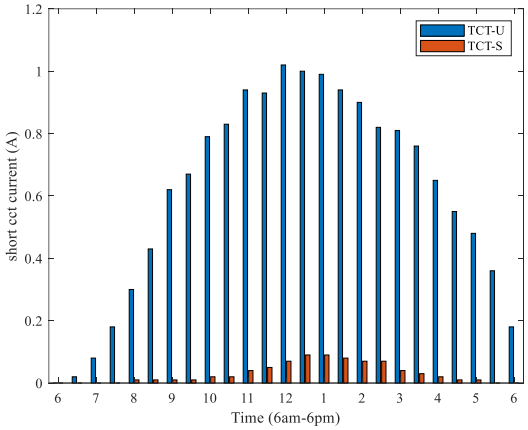

(d) Current Output for TCT

Figure 7: Effect of shading on the PVs for SP and TCT

CONCLUSION

In this work, the performance of PV modules under partial shading and un-shading conditions were investigated for SP and TCT techniques. Results of the work shows that in the absence of shade, SP configuration perform better than the TCT whereas reverse are the case for the partial shading condition. As shading is undesirable but also unavoidable because of the nature of our environments, TCT techniques will be more preferred than SP. In future, other techniques such as central cross tied (CCT) and Bridge-linked (BL) will be tested under same conditions with SP and TCT to determine their performance and evaluate the best among all.

REFERENCE

Abdulwahab, I., Abubakar, A. S., Olaniyan, A., Sadiq, B. O., & Faskari, S. A. (2022). *Control of Dual Stator Induction Generator Based Wind Energy Conversion System.* Paper presented at the 2022 IEEE Nigeria 4th International Conference on Disruptive Technologies for Sustainable Development (NIGERCON) 1-5.

Abdulwahab, I., Jibril, Y., Olarinoye, G. A., Abubakar, A. S., Olaniyan, A. A., & Mohammed, M. (2021). A Cuckoo Search Optimized Control of Dual Stator Induction Generator in Wind Energy Conversion System.

Belkaid, A., Colak, I., & Kayisli, K. (2017). Implementation of a modified P&O-MPPT algorithm adapted for varying solar radiation conditions. *Electrical Engineering*, *99*(3), 839-846.

Calcabrini, A., Weegink, R., Manganiello, P., Zeman, M., & Isabella, O. (2021). Simulation study of the electrical yield of various PV module topologies in partially shaded urban scenarios. Solar Energy, 225, 726-733.

Gostein, M., Duster, T., & Thuman, C. (2015). Accurately measuring PV soiling losses with soiling station employing module power measurements. 2015 IEEE 42nd Photovolt. Spec. Conf. PVSC 2015.

Iliyasu, M. U., Ozohu, M., Yusuf, S. S., Abdulwahab, I., Ehime, A., & Umar, A. (2022). Development of an Optimal Coordination Scheme For Dual Relay Setting In Distribution Network Using Smell Agent Optimization Algorithm. *COVENANT JOURNAL OF ENGINEERING TECHNOLOGY*.

Jallad, J., Mekhilef, S., Mokhlis, H., Laghari, J., & Badran, O. (2018). Application of Hybrid Meta-Heuristic Techniques for Optimal Load Shedding Planning and Operation in an Islanded Distribution Network Integrated with Distributed Generation. *Energies*, *11*(5), 1-25.

Mohammed, M., Abubakar, A. U., Musa, B. U., & Jumare, Y. L. (2020). Hybrid Micro Grid Power System Technical And Economic Analysis Using Homer Legacy Software. Nigerian Journal of Engineering, 27(3), 57-60.

Ngari, D. N. (2017). *A Feasibility Study on the Effect of Soiling on the Performance of Solar Pv Water Pumping Systems in Nairobi.* University of Nairobi.

Pathare, M., Shetty, V., Datta, D., Valunjkar, R., Sawant, A., & Pai, S. (2017). *Designing and implementation of maximum power point tracking (MPPT) solar charge controller.* Paper presented at the 2017 International Conference on Nascent Technologies in Engineering (ICNTE) 1-5.

Pachauri, R. K., Mahela, O. P., Sharma, A., Bai, J., Chauhan, Y. K., Khan, B., & Alhelou, H. H. (2020). Impact of partial shading on various PV array configurations and different modeling approaches: A comprehensive review. IEEE Access, 8, 181375-181403.

Sagar, G., Pathak, D., Gaur, P., & Jain, V. (2020). A Su Do Ku puzzle based shade dispersion for maximum power enhancement of partially shaded hybrid bridge-link-total-cross-tied PV array. Solar Energy, 204, 161-180.

Tubniyom, C., Jaideaw, W., Chatthaworn, R., Suksri, A., & Wongwuttanasatian, T. (2018). Effect of partial shading patterns and degrees of shading on Total Cross-Tied (TCT) photovoltaic array configuration. Energy Procedia, 153, 35-41.

Yin, W., & Qin, X. (2022). Cooperative optimization strategy for large-scale electric vehicle charging and discharging. Energy, 258, 124969.

4th International Engineering Conference (IEC 2022)
Federal University of Technology, Minna, Nigeria

Stochastic Time Series Analysis of Stream Flow Data of the River Niger at Lokoja, Kogi State, Nigeria.

[1]Gbadebo Olukemi Anthonia, [1]Busari Afis Olumide, [2]Salawu Sadiku and [1]Saidu Mohammed
[1]Civil Engineering Department, Federal University of Technology Minna, Niger State, Nigeria.
[2]Confluence University of Science and Technology, Osara, Kogi State, Nigeria.
*Corresponding author email: g.olukemi@futminna.edu. ng +2348037448902

ABSTRACT
This paper is produced to improve the management and operation system of the River Niger at Lokoja - Nigeria. It is important to determine the hydrological system of River Niger, which is the major water sources of the annual flood in the area. Lokoja has been experiencing the problem of flooding every wet season from April to October of the year. It experienced the highest flood in 2022. In this study, a Modified Thomas Fiering Model (MTFM) is used. This method is a stochastic method that is employed for generating and predicting a synthetic flow in hydrology. It is used to generate a synthetic river flow in Lokoja, Kogi State, Nigeria. The procedure for stochastic or statistical method is applied on the data obtained at the Lokoja gauging station, Nigeria. The study utilized the monthly flows data (discharge in m^3/s) from the year 2000 to year 2019. After estimating the model parameters (mean, standard deviation, maximum, minimum, coefficient of variation, skweness and kutrosis), the synthetic time series of monthly flows were simulated. The results showed that the Modified Thomas Fiering model is appropriate and can be applied to forecast monthly flow for planning, design and operation of Water Resources infrastructure. Hence in the presence of large dataset, future forecasting of the river flow can be done to create awareness on it, to allow adequate preparation in mitigating the future effects of flooding in the study area.
Keywords: *Stochastic, Thomas Fiering Model, Stream flow, Time series, Synthesis*

1 INTRODUCTION

In Water Engineering, Time Series Models are often used to determine the design capacity of Reservoir (Danielle et al, 2021 & Loucks et al, 2005). Presently, it is undebatable that the climate change increases the average air and water bodies' temperature (Odjugo, 2009 & Razmi et al, 2017), and increases the average sea water level all over the world (Merrifield et al, 2014, Sathish & Khadar, 2017). Climate change leads to change in hydrological cycle which results in increase in temperature, rate of evapotranspiration, and intensities of rainfall having the possibility of natural hazard (Calanca et al, 2006). These devastating impacts require the conducts of such studies, to forecast the level of future impacts and suggest an adaptive or mitigation measures that can improve the situation.

Lack of data or its inadequacy has been identified as a suitable method to enhance historical hydrological series data (Dornblut, 2009). The time series analysis of discharge data in the statistical domain has a wide area of specialization and vital application in hydrological investigation (Calanca et al, 2006). Recently, new techniques of analysing and managing the changes in the river flow regime have been developed (Gao et al, 2018 & Naderi, 2022). The time series analysis is employed for building mathematical model to calculate statistics from River flow data by using Thomas Fiering model. Similarly, Valencia Schaake (VS) and Thomas Fiering methods were used to generate monthly stream-flow of Pedi-Muda reservoir in Malaysia and their performances were better only that the two methods have the problem of overestimation and underestimation (Tukimat & Harun, 2021). That is why modified Thomas Fiering method is developed to take care of the flaws in Thomas fiering model. This study applied and verified the performance of time series analysis based on Modified Thomas Fiering model for the monthly discharge of River Niger at Lokoja gauging station. River Niger is one of the rivers that limited attempt have been made to test applicability of time series model. Lokoja in Kogi State suffers from the problem of flooding due to its location at the confluence of the country's major rivers (Niger-Benue Rivers). Lokoja flooding has caused huge yearly losses in terms of damage and disruption to economic livelihoods, businesses, infrastructure, services and public health (Jimoh & Salami, 2020). The contribution of this study is to generate and simulate the monthly hydrological flow series with the use of Modified Thomas Fiering model in order to predict the future flooding in the area to avert loss of lives, farm produce and functional failure of the Abuja-Lokoja road due to flooding.

2 RESEARCH METHODOLOGY

2.1 STUDY AREA

Nigeria, republic in western Africa, with a coast along the Atlantic Ocean on the Gulf of Guinea. Most of Nigeria consists of a low plateau cut by rivers, especially the

Niger and its largest tributary, the Benue. By topography, Nigeria's largest physical region is formed by mostly level valleys of the Niger and Benue rivers. The Niger enters the country from the northwest, the Benue from the northeast; they form a confluence at the city of ***Lokoja*** in the south central region and continue south, before emptying into the Atlantic Ocean (see Figure 1).

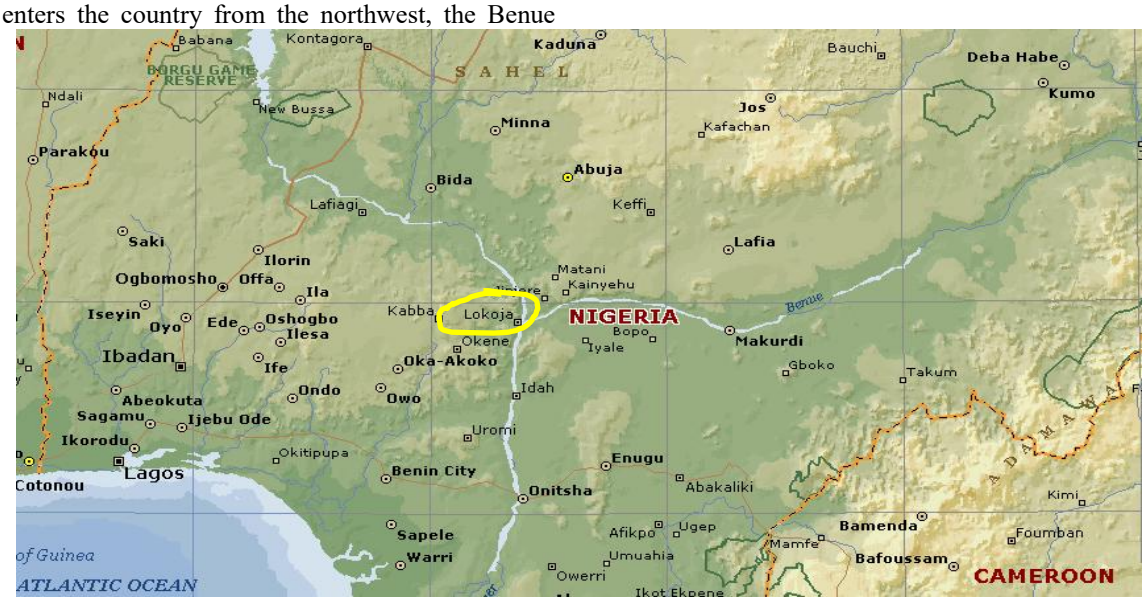

Figure 1: Map of Nigeria showing the study area

Lokoja is located between latitude 7° 45' N, 7° 51'N of the equator and longitude 6° 41' E 6° 45'E of the Greenwich Meridian. It is bounded in the west by the River Niger at an altitude of 45-125 metres above sea level. Lokoja (Kogi State) is almost predominantly underlain by high grade metamorphic and igneous rocks of Precambrian age generally trending NN-E-SS-W, these rocks comprise of gneiss, migmatite, granites and schist belt outcrops along the eastern margin of the area. The study area is grouped to be within the guinea savannah belt, even though what we really have now is derived savannah, only resistant vegetation still remains dominant due to anthropogenic activities of bush clearing, burning and lumbering (Jimoh and Salami, 2020). Most of the area consists of secondary regrowth. The climate is described as the tropical wet and dry climate of the Koppen's classification. It is characterized by wet and dry season. The wet season begins in May and ends in October, with an average annual rainfall of about 1000mm and a relative humidity at 60%. An average maximum day time temperature of 37.9^{0}C, is recorded between December and April.

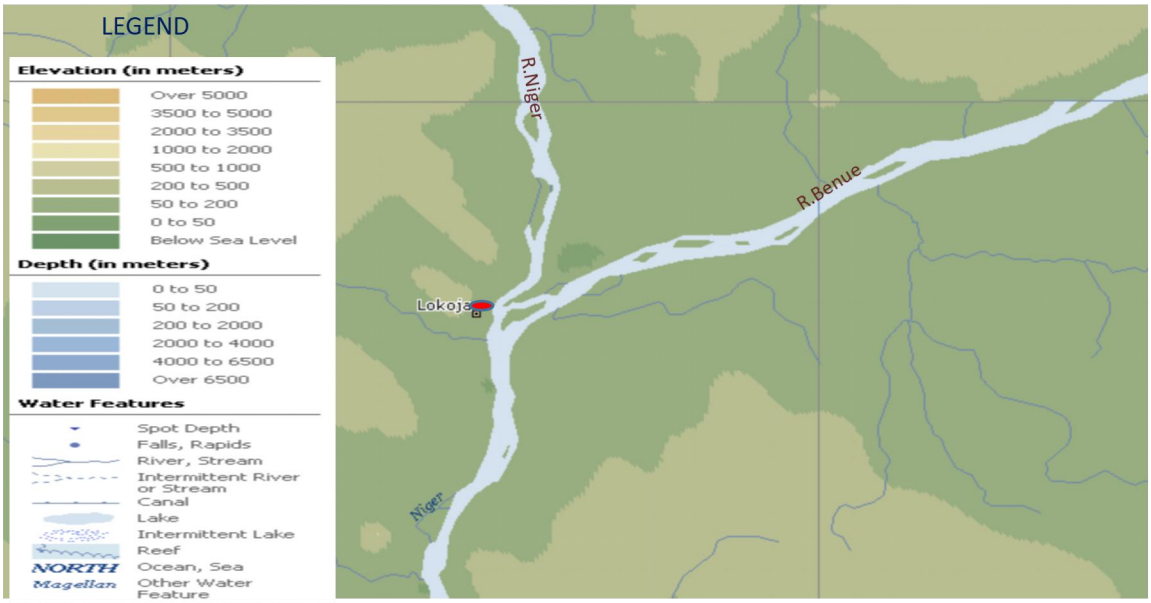

Figure 2: Lokoja and its physical features

2.2 COLLECTION OF DATA

All the relevant discharges from Lokoja gauging station which were available from the past were collected from 2000 to 2019. The collected information formed the sample space for the random variable under consideration.

2.3 TIME SERIES MODEL

2.3.1 MODIFIED THOMAS FIERING (MTFM) MODEL

The Modified Thomas Fiering Model (MTFM) in its original form was employed for the synthetic or artificial generation of monthly discharge data (Arslan, 2014 & Fiering, 1962). After a brief analysis to historical record of River Niger and estimating the behaviour of river, the transform of Thomas Fiering model (TFM) was executed by extracting the persistency from the river characteristics and the serial autocorrelation between the random residuals of the observed data. In this study, the MTFM depended on the autoregressive approach with application of Wilson Hilferty transformation of independent random number. This model presents a set of 12 regression equations and best represented by the following equations:

$$q_{i,j+1} = \overline{q}_{j+1} + \delta_j.q\left(q_{i,j} - \overline{q}_j\right) + \sigma_{j+1}.\sqrt{1 - r_{1,j}{}^2}.\xi_{i,j+1} \quad \text{(i)}$$

Where, $q_{i,j+1,}$ $q_{i,j}$ are monthly discharge in the j^{th} month of the i^{th} year and the i-step respectively, counting from the start of the generated series, $\overline{q}_{j+1,}\overline{q}_j$ are selective mean monthly discharge from the observe time series during $j+1$ and j respectively, where j ranges from January to December (i.e. 1 - 12 months) and C_j is the regression line slope for the estimation of j+1 month from the j month, C_j is given by the equation (ii) as:

$$C_j = r_{1,j}\frac{\sigma_{j+1}}{\sigma_j} \quad \text{(ii)}$$

Where, $\delta_{j+1,}\delta_j$ are variance of monthly values during j+1 and j months from the observed data, $r1, j$ is the lag-1 autocorrelation coefficient between the monthly flow and ξi, j+1 is independent random variable with a normal distribution, zero mean and unit variance. The mean, variance and lag-1 autocorrelation can be calculated from the given data set as follows:

$$\overline{q}_j = \frac{1}{n}\sum_{i=1}^{n} q_{i,j} \quad \text{(iii)}$$

$$\delta^2 = \frac{1}{n}\sum_{i=1}^{n}\left(q_{i,j} - \overline{q}_j\right) \quad \text{(iv)}$$

$$r_{1,j} = \frac{\sum_{i=1}^{n}\left[\left(q_{i,j} - \overline{q}_j\right)\left(q_{i,j+1} - \overline{q}_{j+1}\right)\right]}{n\sigma_j\sigma_{j+1}} \quad \text{(v)}$$

The principle of computation is described by the following system; the values of mean, standard deviation and lag-1 correlation are considered, where $q_{i,jan,} = \overline{q}_{jan}$ defines the beginning of data generation. Then, the following equations are valid:

$$q_{2004,Feb} = \overline{q}_{Feb} + r_{1,Jan}\frac{\sigma_{Feb}}{\sigma_{Jan}}.\left(q_{2004,Jan} - \overline{q}_{Jan}\right) + \sigma_{Feb}.\sqrt{1 - r^2{}_{1,Jan}}.\xi_{2004,Feb} \quad \text{(vi)}$$

The value obtained from the Equation (vi), ($q_{2004,Feb}$) is applied to generate flow rate for the month of March i.e. ($q_{2004,Mar}$). Similarly, the estimated value for the month of December in the year under consideration ($q_{2004,Dec}$) can be used to generate the flow rate of January for the next year ($q_{2005,Jan}$).

$$q_{2005,Jan} = \overline{q}_{Jan} + r_{1,Dec}\frac{\sigma_{Jan}}{\sigma_{Dec}}.\left(q_{2004,Dec} - \overline{q}_{Dec}\right) + \sigma_{Jan}.\sqrt{1 - r^2{}_{1,Dec}}.\xi_{2004,Jan} \quad \text{(vii)}$$

The values of ξ was obtained with the aid of Excel random number generators tool.

3 RESULTS AND DISCUSSION

The essential descriptive statistical characteristics of the discharge historical time series of River Niger at Lokoja are given in Table 1.

TABLE 1: BASIC STATISTICAL CHARACTERISTICS OF SYNTHETIC MONTHLY FLOW TIME SERIES FOR RIVER NIGER IN LOKOJA, KOGI STATE, NIGERIA IN 2004.

2004	Jan	Feb	Mar	Apr	May	Jun	Jul	Aug	Sep	Oct	Nov	Dec
¯Q		2418.5	2536.2	2361.1	2295.4	2684.8	4184.4	6522.7	10353	15390	11898	5639.4
δ		266.72	225.06	202.63	228.63	187.03	434.83	1023.4	1524	661.71	2556.5	496.73
Max		2889	3240	2915	2700	2949	4790	8422	13703	16098	15292	6724
Min		1989	2164	1937	1979	2290	2902	4790	8694	14102	7175	4835
CV		0.1103	0.0887	0.0858	0.0996	0.0697	0.1039	0.1569	0.1472	0.0430	0.2149	0.0881
Skewness		-0.2119	0.94957	0.89452	0.61384	-0.4071	-1.46	0.25502	0.78127	-0.6691	-0.5007	0.46973
Kurtosis		-1.1088	2.3349	1.8787	-0.9025	-0.5561	2.7171	-0.5183	-0.6269	-1.1837	-1.1798	-0.4125

After the estimation of the parameters of the MTFM, the series of historical monthly flow for 8 years were generated. These series were compared with the recorded monthly flow of River Niger for the hydrological period of 8 years (2004-2011), with the use of basic statistical characteristics like mean, standard deviation, maximum, minimum, coefficient of variation, skewness and kurtosis from 2004 to 2011 as shown in Table 1. The MTFM was used to predict the monthly flow of River Niger from 2004 to 2011. Thirty Six (36) parameters were computed (i.e. 12 means ($\overline{q}$), standard deviations (σ) and Lag-1 autocorrelation coefficients ($r1$)). The regression coefficient (C_j) between the months are computed as shown in Table 2.

TABLE 2: COMPRISES OF THE ESTIMATED VALUES OF THE MTFM OF RIVER NIGER.

2004	Jan	Feb	Mar	Apr	May	Jun	Jul	Aug	Sep	Oct	Nov	Dec
¯Q		2418.5	2536.2	2361.1	2295.4	2684.8	4184.4	6522.7	10353	15390	11898	5639.4
δj		266.72	225.06	202.63	228.63	187.03	434.83	1023.4	1524	661.71	2556.5	496.73
r1,j		0	9.68E-30	-7.1E-30	1.35E-29	-1.9E-29	-4E-30	3.39E-30	-7.9E-30	1.88E-29	-3.5E-29	4.8E-30
Cj		0	7.84E-30	-9.1E-30	9.06E-30	-1E-28	-2.2E-29	7.53E-30	-1.5E-30	2.8E-28	-1.3E-30	6.72E-30

Figure 3 shows the comparison between observed and simulated monthly flow series of River Niger from 2004 to 2011.

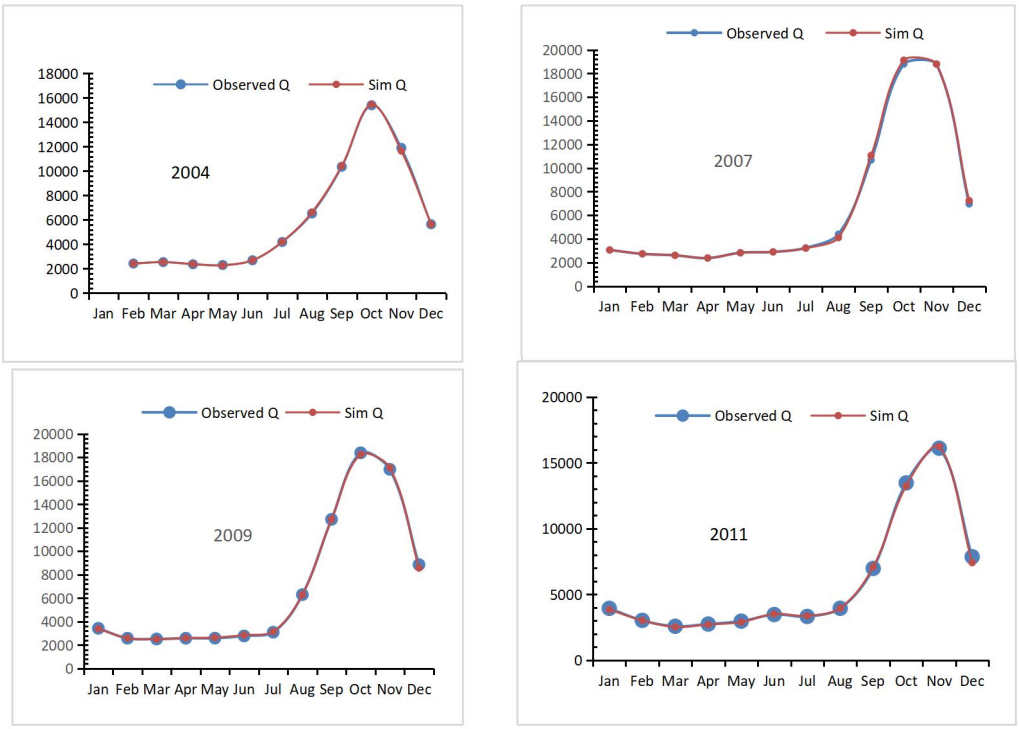

Figure 3: Comparison between observed and simulated monthly discharges (Q in m^3/s) from 2004 to 2011.

To check the performance of the Thomas Fiering model, means, standard deviations, maximum, minimum and coefficient of variation of monthly flow in observed series were considered. In Figure 3, it is observed that the trend is similar for all the simulated and observed flow from 2004 to 2011. This is due to seasonal variability in rainfall that occurs every year. Figure 4 shows the Maximum estimated for the observed and simulated monthly flow time series of River Niger.

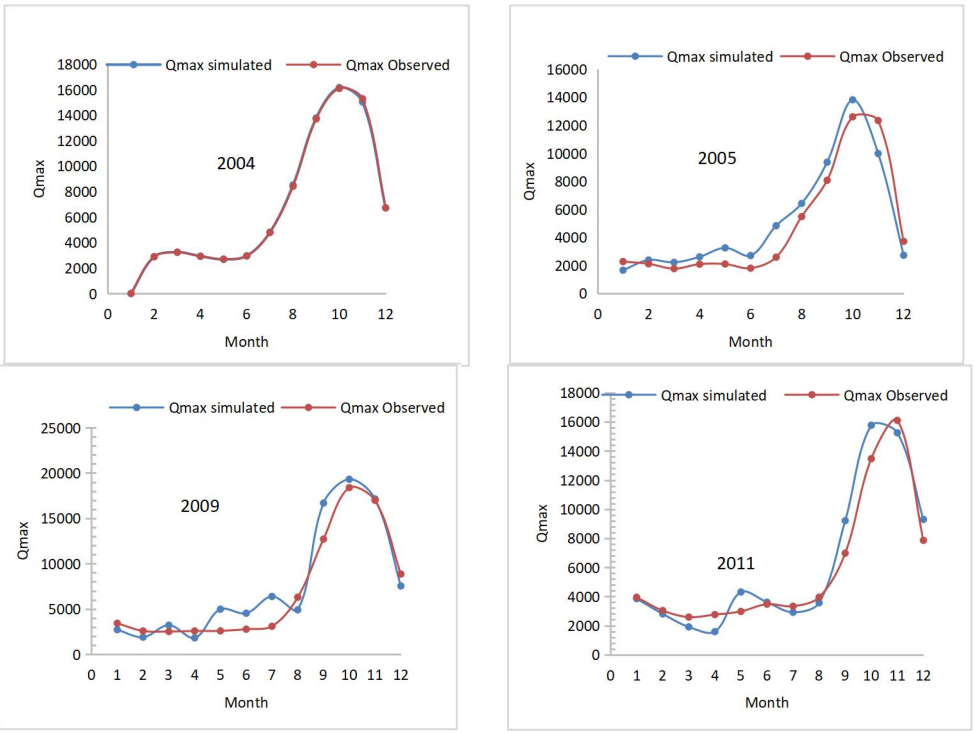

Figure 4: Maximum estimated for the observed and simulated monthly flow time series from 2004 to 2011

In Figure 4, there is a good agreement between the observed and predicted discharge during the wet seasons and the model prediction of the discharge during the dry season appears slightly inconsistent around the observed value. Figure 5 depicts the graph of minimum discharge for observed and simulated flow.

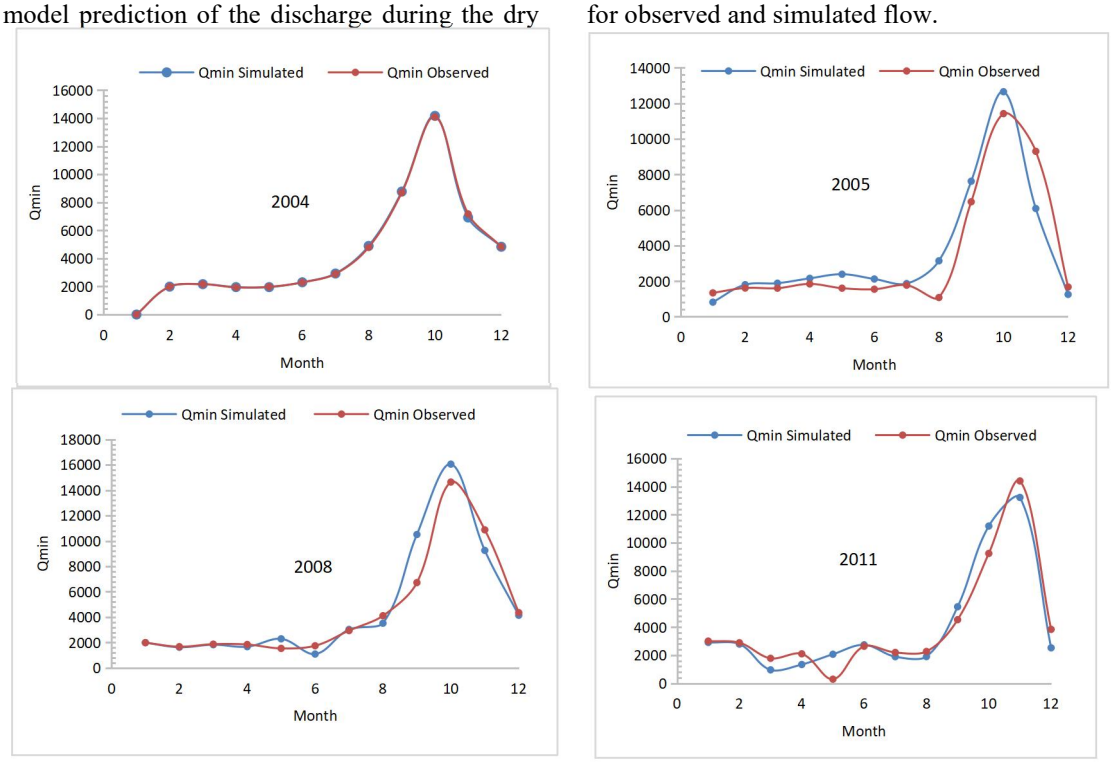

Figure 5: Selected Minimum estimated for the observed and simulated monthly flow time series.

In Figure 5, there is a good agreement between the observed and predicted discharge and the model predict well during the dry season with a slight difference in the

wet season. Figure 6 exhibits the graph of standard deviation for both simulated and observed flow.

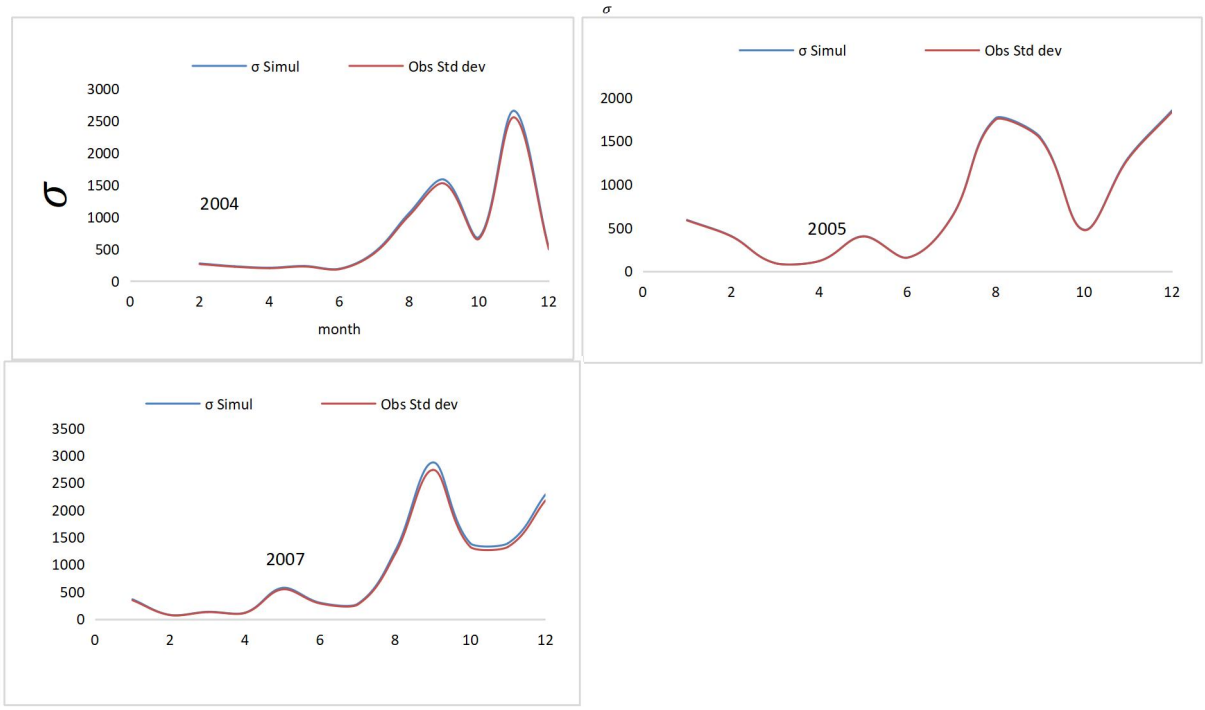

Figure 6: Selected Standard deviation estimated (σ) for the observed and simulated monthly flow time series

Figure 6 shows the comparison between the computed standard deviation of the observed flow data with simulated values using MTFM, there is a good agreement between the standard deviation of the observed and simulated discharges. Hence, the MTFM yields a very good prediction of the observed dataset. Figure 7 shows the coefficient of variation of the observed and simulated flow from 2004 to 2011.

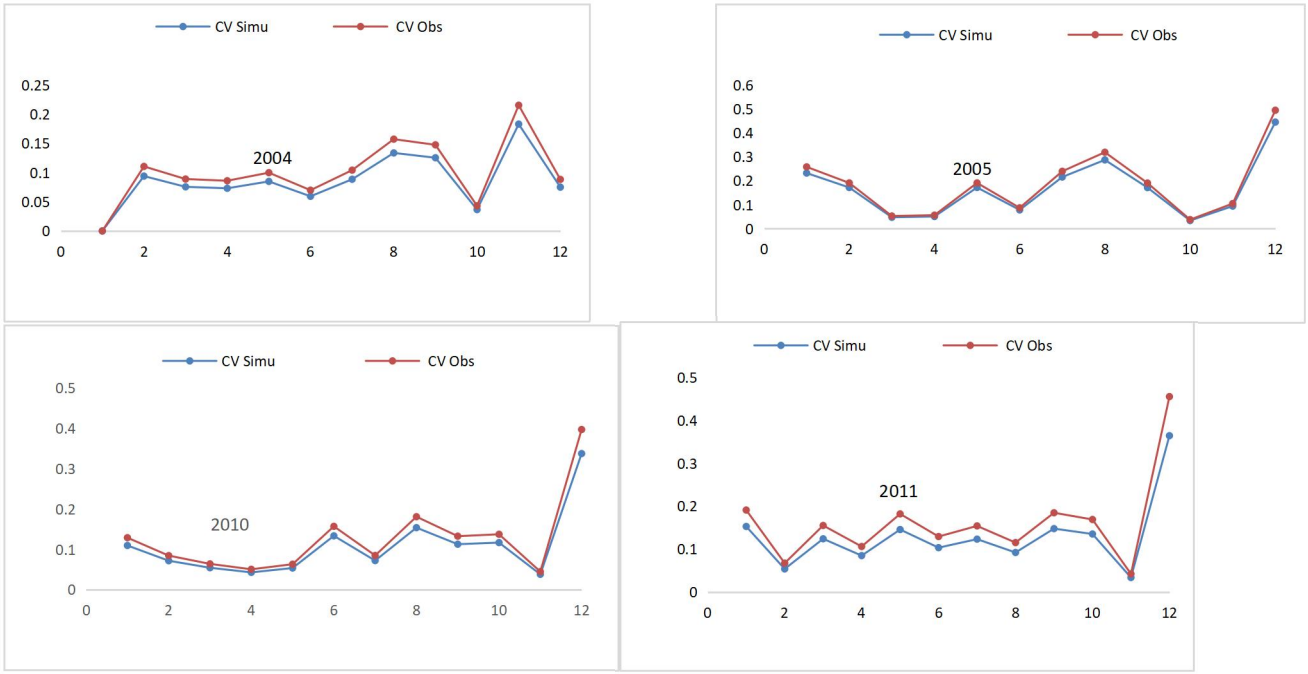

Figure 7: Coefficient of Variation (CV) estimated for the observed and simulated monthly flow time series

In Figure 7, the larger the coefficient of variation, the more the variability in discharge (that is, the seasonal variability between the flow in rainy season is higher than that of dry season), thus the model prediction is satisfactory, but slightly with under prediction. Figure 8 presents the skewness for the observed and simulated flow.

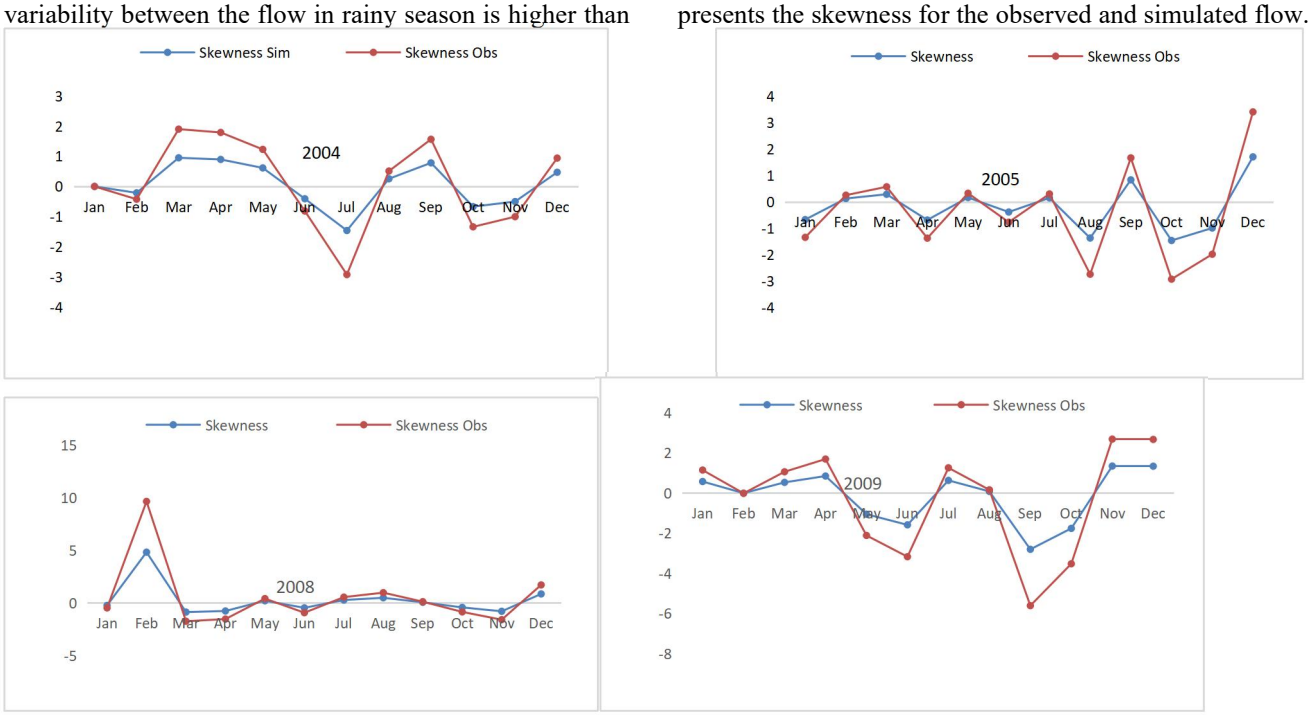

Figure 8: Selected Skewness estimated for the observed and simulated monthly flow time series.

In Figure 8, the values of the skewness and kurtosis of the generated for the predicted and historical data were compared. The model considered well the values of the coefficient of skewness and kurtosis for monthly flow in the simulated series. However, a considerable difference was found in simulated and observed values in the year 2011. Thus, skewness and kurtosis showed a large disparity in the distribution of the discharges in the transition phase from dry to wet season. This shows that normal distribution is not the best distribution model for the time series analysis of stream flow. After the estimation of the parameters of the Modified Thomas Fiering model, the series of historical monthly flows for 20 years were generated. These series were compared with the recorded monthly flow of River Niger for the hydrological period of 8 years (2004 -2011), with the use of basic statistical characteristics like mean, standard deviation, maximum, minimum, coefficient of variation, skewness and kurtosis as shown in Table 3.

TABLE 3: BASIC DESCRIPTIVE STATISTIC OF GENERATED MONTHLY DISCHARGE TIME SERIES OF RIVER NIGER FOR 20 YEARS (2000 TO 2019).

Annual	Jan	Feb	Mar	Apr	May	Jun	Jul	Aug	Sep	Oct	Nov	Dec
Mean	2913.95	2582.738	2404.313	2299.313	2369.088	2581.575	3171.563	5221.538	9746.138	16090.88	16293.75	7068.5
σ	482.3725	408.1081	191.8049	144.7416	334.5388	293.26	398.6475	1102.808	1765.758	1582.346	1648.656	2394.541
Max	2913.95	2582.738	2404.313	2299.313	2369.088	2581.575	3171.563	5221.538	9746.138	16090.88	16293.75	7068.5
Min	1341	1614	1605	1718	298	1546	1772	1079	1298	9160	7175	1673
CV	0.175735	0.16417	0.077794	0.057345	0.142297	0.118016	0.132877	0.21551	0.18201	0.107512	0.091472	0.371246
Skewness	0.190212	1.366075	-0.18349	0.27965	0.334426	-0.02021	0.034945	0.124464	0.020083	-0.85074	-0.5277	0.716005
Kurtosis	-0.32705	6.516158	-0.20052	0.104251	5.47406	2.734613	0.673938	0.25217	1.08501	-0.06116	-0.00902	-0.20549

Figure 9 pose the Long-term mean Q, standard deviation (Q_σ), Q Maximum (Q Max), Q Mininmum (Q min), coefficient of variation (CV), skewness and kurtosis estimated for observed and simulated discharge (2001 - 2019).

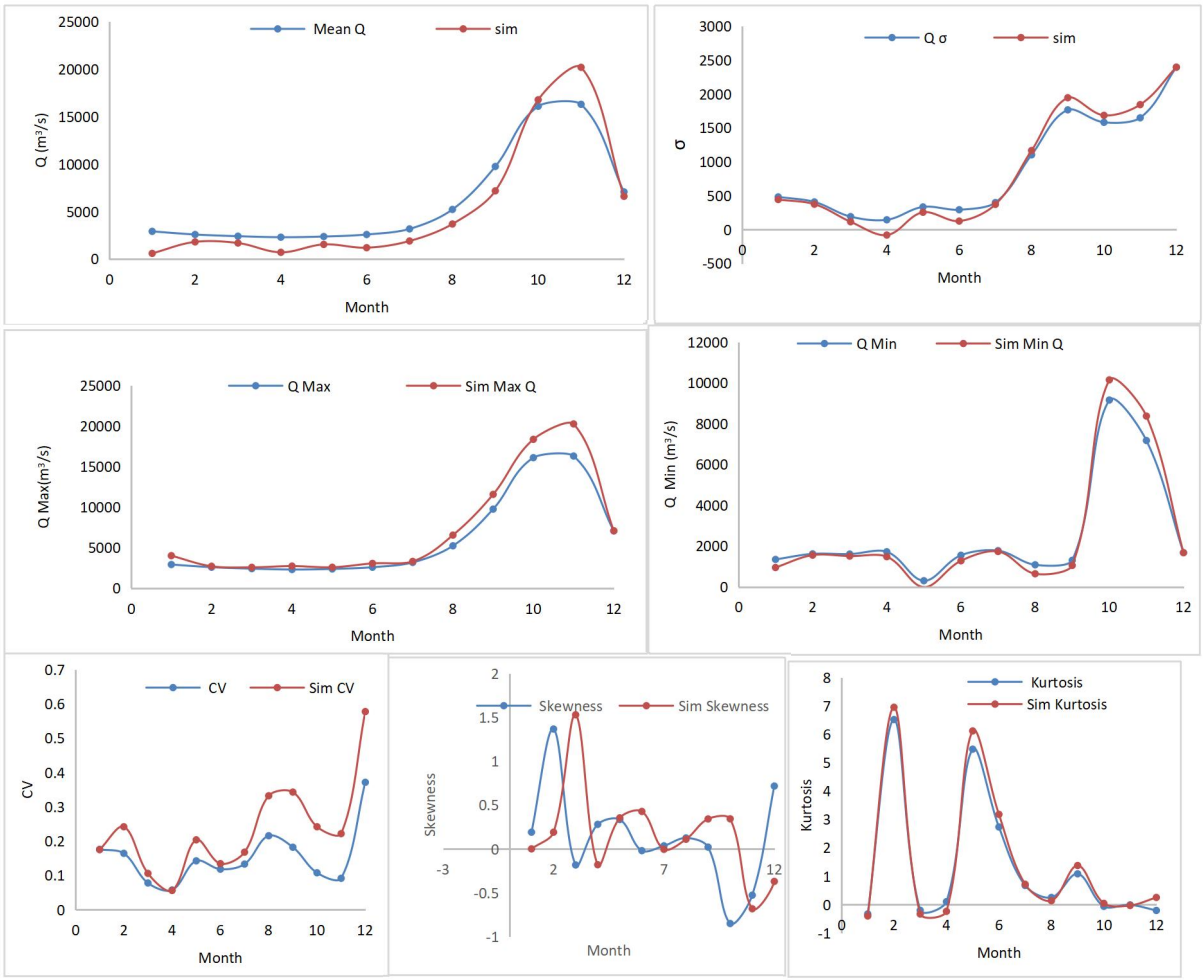

Figure 9: Long-term Q $_{mean}$, standard deviation (Q_σ), Q Maximum (Q $_{Max}$), Q Minimum (Q $_{min}$), coefficient of variation (CV), skewness and kurtosis estimated for observed and simulated discharge from 2000 to 2019.

Figure 9 demonstrates the results of basic descriptive statistic of the data and the forecasted value of Modified Thomas Fiering model for the twenty years (2000 to 2019) respectively. The results obtained is related with the observed data to justify the model's veracity. It is found that the mean Q, Q max, Q min and CV (observed and simulated) follow the same trend except at the peak values that is slightly over-predicted based on the assumption of Normal probability distribution model for the statistical analysis of the observed data. Furthermore, standard deviation for the observed and simulated flow follow the same trend all through the season. But skewness and kurtosis have large disparity in the observed and simulated data.

4 CONCLUSION

In this study, the performance assessment for Modified Thomas Fiering model was carried out, using the monthly discharge data from River Niger at Lokoja gauging station, Nigeria. The model was developed and applied to forecast the monthly inflow to River Niger, Nigeria. The performance of the model was evaluated by comparing values of basic statistical descriptive parameters including mean, standard deviation, maximum, minimum, coefficient of variation, skewness and kurtosis between observed and simulated monthly data values. Thus, general results of prediction showed that, Modified Thomas Fiering model is appropriate and can be applied to forecast monthly flow for planning, design and operation of Water Resources infrastructure. Thus, the Modified Thomas Fiering model can be used to generate and forecast discharge data for River Niger with least percentage of uncertainty. It is recommended that further studies should be done to consider the most appropriate probability distribution model for the study area.

REFERENCES

Arslan, C. (2014). Stream-flow simulation and synthetic flow calculation by Modified Thomas Fiering Model. *Al-Rafidian Engineering J.*, 20 (4): 118-127.

Calanca, P., Roesch, A., Jasper, K., & Wild, M. (2006). Global Warming and summertime evapotranspiration of the Alpine region. *Clim change* 79(1-2); 65-78.

Danielle, C. M. R., Elisa, H., Andreza, K., & Cesar, E. P. (2021). Models for forecasting water demand using time series analysis: a case study in Southern Brazil. *Journal of water, sanitation and Hygiene for Development* 11 (2): 231-240.

Dornblut, I. (2009). Hydrologic information – Metadata, Semantic structure for the description of hydrological data. *Global Runoff data Centre Report* 39.

Fiering, H.A.T.a.M.B., (1962). Mathematical synthesis of stream flow sequences for the analysis of river basins by simulation. *Design of Water Resources Systems*, Chapter 12. Harvard University Press, Cambridge, Mass.

Gao, B., Li J., & Wang, X. (2018). Analysing changes in the flow regime of the Yangtze River using the Eco- Flow Metrics and IHA Metrics. *Water* 10 (11) 1552.

Jimoh U. U. & Salami H. (2020). Spatio-Temporal Analysis of Flooding In Lokoja Kogi State Nigeria. *International Journal of Scientific Research in Research Paper Multidisciplinary Studies,* E-ISSN: 2454-9312 Vol.6, Issue.2, pp58-72, P-ISSN: 2454-6143

Loucks, D.P., et al., (2005). Water resources systems planning and management: an introduction to methods, models and applications. Paris: UNESCO.

Merrifield, M. A., Thompson, P., Leuliette, E., Nerem, R. S., Hamlington, B., Chambers, D. P., Mitchum, G. T., Mcinnes, K., Marra, J. J., Menendez, M., & Sweet, W. (2014). (Global Oceans) Sea level Variability and change (in"State of the climate in 2013"). *Bull. Amer. Meteor. Soc.,* 95(7), 571-573.

Naderi, M., Sheikh, V., Bahrehmand, A., Komaki, C. B., & Ghangermeh, A. (2022). Analysis of River flow regime changes using the indicators of hydrologic alteration (case study: Hableroud Watershed). *Water and Soil Management and Modelling.* ISNN: 2783-2546.

Razmi, A., S. Golian, and Zahmatkesh, Z. (2017). Non-stationary frequency analysis of extreme water level: application of annual maximum series and peak-over threshold approaches. *Water Resources Management,* **31**(7): p. 2065-2083.

Sathish, S. & Babu, S. K. K. (2017). Stochastic time series analysis of hydrology data for water resources. IOP Conference Series: *Materials Science and Engineering*, **263**: p. 042140.

Odjugo, P. A. O. (2009). The impact of climate change on water resources: Global and Nigeria analysis, *FUTY Journal of Environment*. Vol. 4, No. 1. ISSN 1597 -8826.

Tukimat, N. N. A. & Harun, S. (2021). Evaluation the Performances of Stochastic Stream-flow Models. *The*, *International Journal of Integrated Engineering,* ISSN: 2229-838X e-ISSN: 2600-7916. http://penerbit.uthm.edu.my/ojs/index.php/ijie.

4th International Engineering Conference (IEC 2023)
Federal University of Technology, Minna, Nigeria

Hate and Offensive Speech Detection Using Term Frequency-Inverse Document Frequency (TF-IDF) and Majority Voting Ensemble Machine Learning Algorithms

* Okechukwu, C. [1], Idris, I.[2], Ojeniyi, J. A.[3], Olalere, M.[4] & Adebayo O. S. [5]
[1,2,3,4,5] Department of Cyber Security Science, Federal University of Technology, PMB 65 Minna Niger State, Nigeria.
[5] Islamic University in Uganda.
*Corresponding author email: Anthony.pg208286@st.futminna.edu.ng +2348068573605

ABSTRACT
The advancement in technology especially the internet has opened new frontiers to criminality and abuses of information. Social media have given racists and extremists a platform for carrying out their criminalities and attacks on legitimate users' information. Thus, there is need to give adequate attention to the communications on social media so as to curtail these malicious acts before they materialize into causing physical harms. Hate speeches has been blamed for various degrees of violence experienced in the real world. A lot of research efforts have been put in detecting hate speeches using various techniques with varying degrees of accuracy and F-Measure. Term Frequency-Inverse Document Frequency (TF-IDF) with a majority voting ensemble learning classification Models were used for the detection of hate speech and a performance of 95% accuracy and 0.95 F-Measure were recorded.

Keywords *Ensemble Machine Learning, Hate Speech Detection, Majority Voting, Term Frequency-Inverse Document Frequency (TF-IDF).*

1 INTRODUCTION

United Nations in 2019 (United Nations, 2019) gave the definition of hate speech as "any kind of communication in speech, writing or behavior, that attacks or uses pejorative or discriminatory language with reference to a person or a group on the basis of who they are, in other words, based on their religion, ethnicity, nationality, race, colour, descent, gender or other identity factor". Generally, hate speech aims to generate hatred and intolerance thereby inciting divisions which can on the long run lead to xenophobia, racism and violence. Widespread adoption of Social Media (SM) makes the impact of hate speech overwhelming as a result of the anonymity enjoyed by users (Mullah and Zainon, 2021).

Tackling hate speeches according to United Nations is crucial towards deepening progress across the United Nations agenda by helping in preventing armed conflicts, terrorism and atrocity crimes. It will equally help in putting an end to violence against women, other grave violations of human rights, and fostering peace and an inclusive just society.

Recently hateful speech crimes have been on the increase in the United States of America (F.B.I, 2019) and equally in Nigeria both online and face-to-face. Anonymity of the internet among other factors has contributed to the rise in online hate speeches (Burnap and Williams, 2015). The anonymity of the internet has given a voice to all and sundry to air their views and opinions without fear of any legal consequences.

In reactions to the threat of online hate speech, the government of Nigeria has recently placed a ban on Twitter social media website citing ethno-religious hate and violent speeches being spread through the medium and the refusal of Twitter to take down certain tweets the government sees as being hateful and inciting.

All over the world, different governments have been torn between tackling this crime specifically determining what is hateful and maintaining the citizens' right to free speech, hence the need to employ the unbiased nature of machines in solving this problem.

Among the key commitments of United nations in (United Nations, 2019) towards tackling this menace is the use of Technology by keeping up to technological innovations and encouraging more researches on what relates to misusing the social media and the internet in disseminating hateful contents like speeches and the factors that drive individuals towards being violent.

The rest of this paper is organized as follows: the review of related literatures is done in section two while the methodology to provide solution is given in section three, the results of the experiments are provided in section four while section five is used to conclude the paper.

2 RELATED LITERATURE

In the research by Fortuna and Nunes (2018), in which they surveyed automatic detection of hate speeches in texts conducted after analyzing hate speech concept in different contexts, from social networks platforms to other organizations, proposed a clearer and unified definition of the concept which can enable the building of machine learning models for automatic hate speech detection. They studied various techniques and approaches used by different researchers in detecting hate speeches and recorded a highest accuracy of 91% from all the papers reviewed. Different researchers have over the years proposed several techniques for detecting hate speeches

online. Each researcher achieved a different level of accuracy with their proposed models. Priyadharshini (2020) in her work" Detection of Hate Speech using Text Mining and Natural Language Processing" used TF-IDF for feature extraction and four different classifiers: Logistic Regression, Random Forest, Naïve Bayes and SVM in classifying tweets to be either hate or offensive speeches or being neither of the two using multi-class classifier and achieved a maximum accuracy of 90%.

Four convoluted neural network models were trained by Gambäck and Sikdar (2017) using character 4-grams and randomly generated word vectors to classify tweets and recorded according to them 78% F-score. The performance of the models was not evaluated using accuracy. In their work "Using Machine Learning for Detection of Hate Speech and Offensive Code-Mixed Social Media text", Pathak et al. (2020) used different classification and regression based machine learning algorithms to classify twitter messages into being "offensive" and "not offensive" in Indo-European Languages. They used Term Frequency-Inverse Document Frequency (TF-IDF) based feature modelling. Their model obtained highest F1 score of 0.87. Arabic Hate speech tweet problems were investigated using several neural networks (RNN) and convoluted Neural Networks (CNN) models in Alshalan and Al-Khalifa (2020) . A best performance of F1-score of 0.79 was obtained. In their work, Abro et al. (2020) proposed that the bigram features with support vector machine gave the best performance of 79% accuracy after comparing three feature engineering techniques and machine learning algorithms. They. For hate speech classification of tweets, Badjatiya et al. (2017) experimented with three different neural network architectures; CNN, LSTM and FastText. The best performance of 0.93 F1-score was recorded by the team.

Sari and Ginting (2019) worked on hate speech detection on twitter using Multinomial Logistic Regression. Their model's optimal performance is 84%. The authors recommended improving the feature extraction model to improve the model's performance.

Pariyani et al., (2021) in their work, "Hate Speech Detection in Twitter using Natural Language Processing" observed that it is not just enough to have high accuracy but to work to improve the F1-score of the model.

3 METHODOLOGY

In order to detect hate speech, the procedures depicted in figure 1 are followed from dataset collection, splitting, transformation to training the model and to the model's performance result evaluation. The dataset was first obtained from a public repository in kaggle.com, split into training and test sets. The training set is then vectorized using TF-IDF. The vectors were used to train an ensemble Machine Learning Algorithm after which the test set is equally vectorized and fed into the model to make predictions and results compared to the original class to get the performance result of the model.

TABLE 1: DATASET DESCRIPTION

SN	Feature Name	Data Type
0		Integer
1	Count	Integer
2	hate_speech	Integer
3	offensive_language	Integer
4	Neither	Integer
5	Class	String
6	Tweet	String

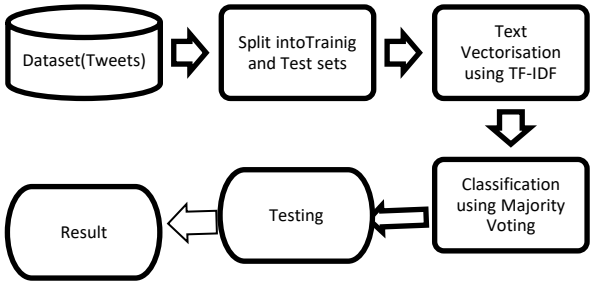

Figure 1: Hate Speech Detection Procedure.

DATA COLLECTION AND PREPROCESSING

A publicly available dataset from Kaggle.com (*Hate-Speech-Data-Analysis | Kaggle*, 2020) which contains 24783 instances is used for this work. The dataset has seven attributes as shown in Table 1 above which shows the features and their data types.

TABLE 2: SAMPLE DATASET

	count	hate_spee	offensive	neither	class	tweet
0	3	0	0	3	0	!!! RT @mayasolovely: As a woman you shouldn't complain about cleaning up your house. & as a man you should always take the trash out...
1	3	0	3	0	1	!!!!! RT @mleew17: boy dats cold...tyga dwn bad for cuffin dat hoe in the 1st place!!
2	3	0	3	0	1	!!!!!!! RT @UrKindOfBrand Dawg!!!! RT @80sbaby4life: You ever fuck a bitch and she start to cry? You be confused as shit
3	3	0	2	1	1	!!!!!!!!! RT @C_G_Anderson: @viva_based she look like a tranny
4	6	0	6	0	1	!!!!!!!!!!!! RT @ShenikaRoberts: The shit you hear about me might be true or it might be faker than the bitch who told it to ya 

FEATURE SELECTION

From the dataset, it was observed that the features; Hate_speech, Offensive_language, neither and count are mere frequencies, the highest of which determines the

class label. But TF-IDF as a text mining algorithm only needs the text in a feature to vetorise, weight and transform the text into a new feature set for training the model, thus the justification for using only the tweet text feature to determine their relationships with the class label.

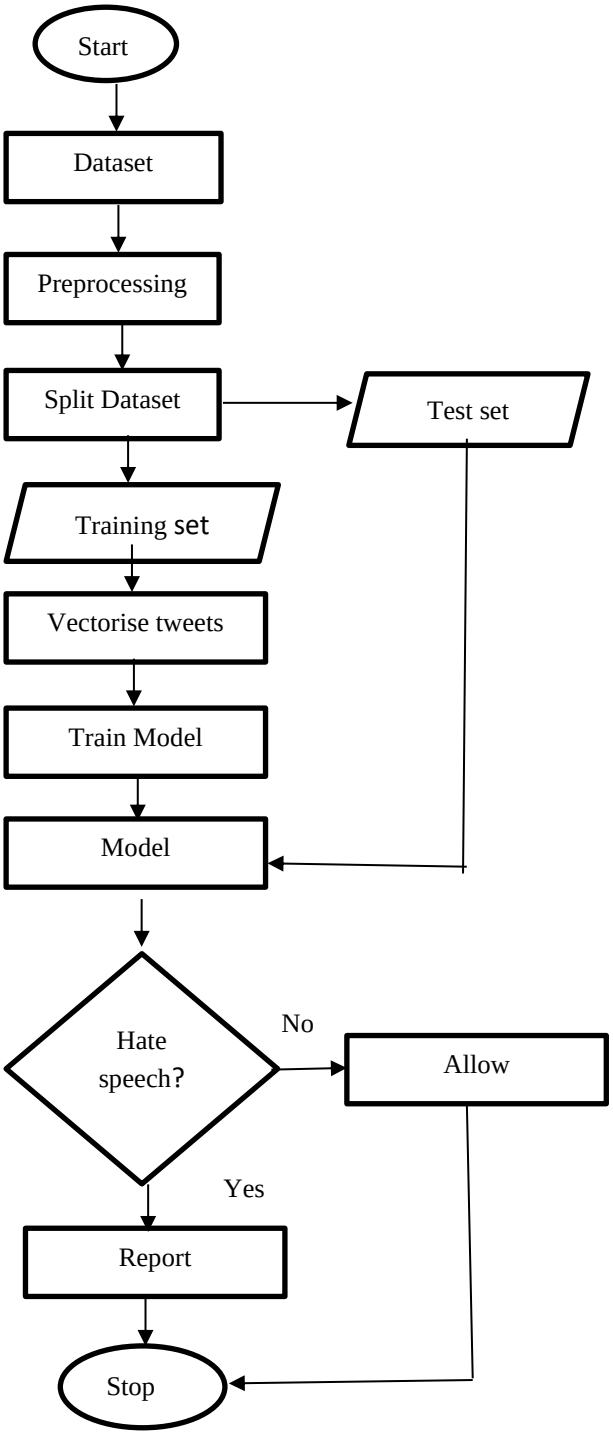

Figure 2: Flowchart illustration of the model.

FEATURE TRANSFORMATION

To improve classification accuracy since the focus is on detecting hate and offensive speeches, the class attribute which originally is made up of three classes; Hate, Offensive and None were transformed to only Hate or None Hate (1s and 0s respectively) speeches. For better performance, common words that impact little or no meaning on the tweet were removed. The filtered tweet attributes were passed to a TF-IDF algorithm which vectorized the tweets and weighted them according to their term and inverse document frequencies. The TF-IDF produced a transformed dataset which is further transformed to a sparse matrix for improved computation time. Figure 2 shows the flowchart diagram of the hate speech detection model from the dataset to the prediction from the model trained. It starts with acquiring and preprocessing of the dataset through which the dataset is made ready and optimum for training a machine Learning model. For this work, we split the dataset in the ratio of 70 / 30% for training and test sets respectively. The training set is vectorised using TF-IDF and the output used to train an ensemble Machine Learning Algorithms. Similarly, the test set is equally preprocessed and vectorised then used to test the model. If a tweet is detected as hate or offensive, it is classified as such and vice versa.

3.1 ALGORITHMS USED

For the research aim to be achieved, different algorithms were used to transform the data, extract features and implement the ensemble model. They are listed and explained subsequently.

3.1.1 TERM FREQUENCY — INVERSE DOCUMENT FREQUENCY (TF-IDF)

This is a technique used to transform a text or document into vectors. It is equally referred to as Word2Vec or Doc2Vec. It quantifies words in a text or document to determine their overall impact to the document in question. It is used in text mining.

$$TF - IDF = TF * IDF \quad (1)$$

Where = TF = Term Frequency and IDF = Inverse Document Frequency.

TERM FREQUENCY is the measure of the frequency of a word in a document. It is given by:

$$tf(t, d) = (\text{count of } t \text{ in } d)/(\text{number of words in } d) \quad (2)$$

where d is the document or text and t is the term.

DOCUMENT FREQUENCY (DF) is the number of documents d in which a term/word appears in, given by;

$$df(t) = \text{frequency of occurrence of } t \text{ in } N \text{ documents} \quad (3)$$

INVERSE DOCUMENT FREQUENCY (IDF)

This is the inverse of the document frequency. IDF is a measure of the informativeness of term/word t in a document (Scott Williams, 2019 B.C.E.).

$$\text{idf(t)} = N/\text{df} \quad (4)$$

where N is the total count of corpus

corpus = the total number of document sets

When a term that isn't in the vocab appears during the query, the df will be 0. We smooth the value by adding 1 to the denominator because we can't divide by 0 (Scott Williams, 2019 B.C.E.)

$$\text{idf(t)} = \log(\text{N}/(df + 1)) \quad (5)$$

Finally, if we take the multiplicative value of TF and IDF, we get the TF-IDF score in equation (6).

$$\text{tf} - \text{idf(t, d)} = tf(t, d) * \log(\text{N}/(df + 1)) \quad (6)$$

3.1.2 SUPPORT VECTOR MACHINE (SVM)

SVM is a machine learning algorithm which employs the supervised approach for finding solution to classification and regression problems. It is, however, mostly employed to solve classification problems. Each and every data item or feature is mapped as a point in n-dimensional space (where n is the total number of features in the dataset). Each feature's value is the value of a certain coordinate in the SVM algorithm. SVM maps the input vectors into a high-dimensional plane constructing a maximal hyperplane to separate each class.

In this work, three SVM models with varying kernels (linear, polynomial and radial basis function(rbf) were used in the ensemble model. Each of the models performed well individually with linear kernel having the lowest accuracy of 94%.

3.1.3 K-NEAREST NEIGHBOUR (KNN)

This is a non-parametric algorithm used in classification developed by Evelyn Fix and Joseph Hodges in 1951. The output of this algorithm is a class membership. The plurality of votes from the neighbour of an object determines its class. If the k nearest neighbour of an object belong to class A, that object is assigned class A of its k nearest neighbour.

In this work, of all the models used in the ensemble model, KNN had the worst performance of 88% individually but being in the ensemble, the final performance of the models is enhanced.

3.1.4 LOGISTIC REGRESSION

This machine learning algorithm used for classification problems is based on the probability concept. Logistic regression is a linear regression algorithm that uses a more complex cost function known as the logistic or sigmoid function instead of a linear function. The sigmoid function limits the output of the function between 0 and 1 thereby perfect for classification.

3.1.5 MAJORITY VOTING ENSEMBLE MODEL

This model improves performance of classifiers by training and combining predictions from sub-models to solve same classification problem. A meta learner is used to combine the prediction votes from sub-models and make the final prediction based on the majority of predictions by the individual sub-models, thus improving the classification accuracy by reducing the variance in predictions made by the sub-models. The ensemble combines the individual predictions from the models and make the final prediction based of the majority of the predictions by the models. The performance of the individual models in the final model is improved by reducing the prediction variance and the biasness.

The algorithm for the overall model is given in figure 3 while the flowchart is shown in figure 2. and the internal implementation of the ensemble model is depicted in figure 2. Three SVMs with linear, rbf and polynomial kernels were used with the addition of KNN and Logistic Regression. To avoid a tie, five sub-models were used in this work.

Start
Input: *x* ← tweets
Y ← Class
Output: Prediction – Class of a tweet
Foreach *tweet in tweet matrix* **do**
Foreach term/word in tweet **do**
Calculate_TF-IDF (*tweet*)
score ← *term/word*
end
append_term_score_to_matrix(term, score)
end
convert_TF-IDF_matrix_to_sparse_form
fit_data_to_train_models (*matrix, Y)*
ensemble_prdeictions_from_models
get_final_class_prediction
stop

Figure 3. The model algorithm

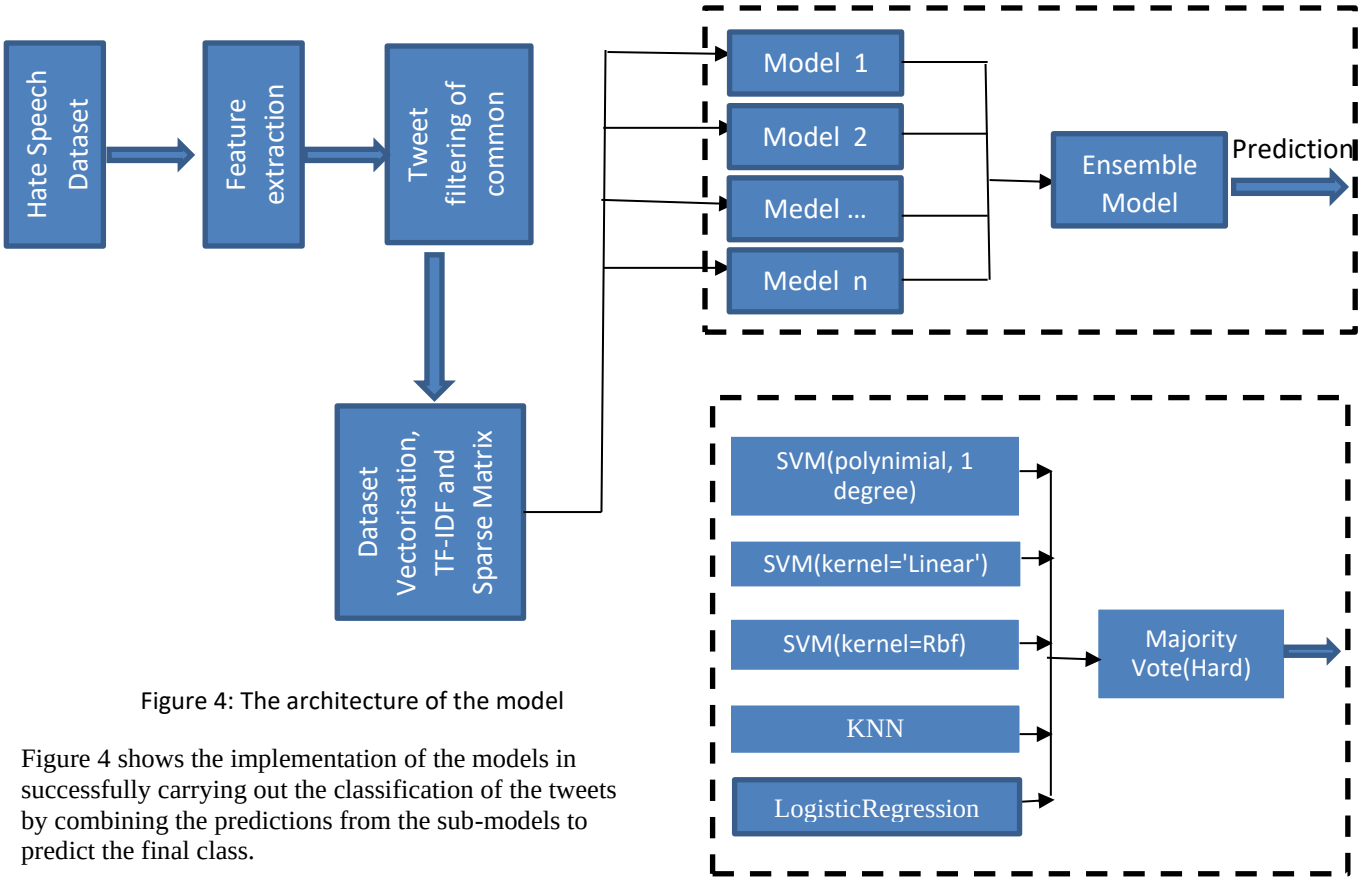

Figure 4: The architecture of the model

Figure 4 shows the implementation of the models in successfully carrying out the classification of the tweets by combining the predictions from the sub-models to predict the final class.

EVALUATION MATRICES

For evaluation purposes, the confusion matrix in Table 3 was used. False Positives (FP), False Negatives (FN), True Positives (TP) and True Negatives (TN) were computed by comparing predicted and true values of the class label. Then, precision (P), recall (R), accuracy, and F1-measures were equally used in this work.

TABLE 3: CONFUSION MATRIX OF RESULTS

	Predicted positive	Predicted Negative
Actual Positive	TP	FN
Actual Negative	FP	TN

TP is the correct positive prediction.

FP are positive predictions that are incorrectly predicted to be positive but are not.

FN are the negative predictions that are not actually negative.

TN are the negative predictions that are actually negative.

Precision (P): This is the proportion of positively predicted values which are actually positive.

$$P = TP/(TP + FN) \quad (7)$$

Recall (R): It is the proportion of actual positives which are predicted positive.

$$R = TP/((TP + FP) \quad (8)$$

Accuracy: This is the proportion of correctly classified instances.

$$\text{Accuracy} = (TP + TN)/((TP + TN + FP + FN + FP)) \quad (9)$$

F1-Measure: This is the precision and recall harmonic mean.

$$F1 - Measure = 2 \times ((P \times R))/((P + R)) \quad (10)$$

Error rate: this is the number of all incorrect predictions divided by the total number of occurrences in the dataset, often given as 1-Accuracy.

4 RESULTS AND DISCUSSION

Table 4 compares the performance of our model; the majority vote ensemble model with those of other researchers. While some researchers reported only the F-measure score of their models, others reported only their accuracies. The model developed in this work has shown better performance as clearly depicted in table and subsequently in the figures 5. Ensemble model reduces the biasness of the individual models if they were trained as stand alone. Equally, the variance in the individual predictions of the models is improved upon by the ensemble model.

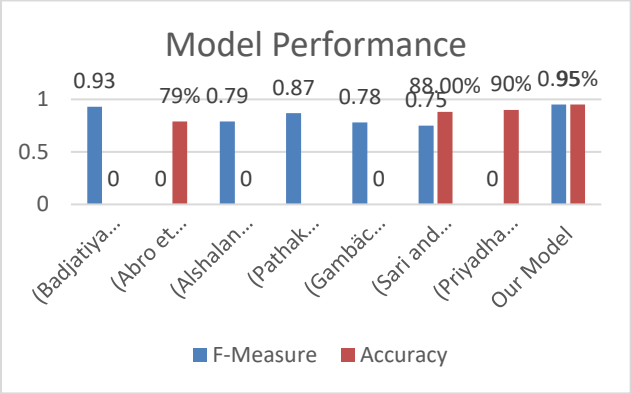

Figure 5: The performance of reviewed works.

TABLE 4: THE PERFORMANCE COMPARISM OF DIFFERENT MODELS

Author	Classifier	Precision	Recall	F-Measure	Accuracy
(Badjatiya et al., 2017)	LSTM+Random Embedding+G	-	-	0.93	-
(Abro et al., 2020)	TF-IDF+SVM	-	-	-	79%
(Alshalan and Al-Khalifa, 2020)	RNN+CNN		-	0.79	-
(Pathak et al., 2020)	TF-IDF+CNN			0.87	
(Gambäck and Sikdar, 2017)	CNN	-	-	0.78	-
(Priyadharshini, 2020)	Text mining + NLP	-	-	-	90%
(Sari and Ginting, 2019)	Multinomial Logistic Regression	80.02	82%	-	88%
Our Model	TF-IDF+ Majority vote (SVM+KNN+LR)	95%	95%	0.95	95%

Table 4 displays the results from authors who have worked on hate speech detection with the various techniques/models used. After transforming the text vectors from the tweets obtained using TF-IDF, majority voting ensemble model of Logistic Regression (LR), K-Nearest Neighbour (KNN) and SVM were used to train on the optimized dataset and an accuracy of 95% and F1-Measure of 0.95 were obtained. The model outperformed the classifications from the reviewed literatures with (Priyadharshini, 2020) getting 90% accuracy and

(Badjatiya et al., 2017) getting a score of 0.93 F1-Measure .

5 CONCLUSION

Online hate speech has been a source of concern to various governments all over the world even to the United Nations as it has been on the rise and is capable of destabilizing regional and world peace. Hate speeches are used to intimidate, abuse and promote violence against person or a group of people targeting their sexual orientation, race, gender, and socio-political affiliations which can lead to physical harm hence the need to identify those hateful speeches as early as possible. This work has successfully used TF-IDF and majority voting ensemble model to identify hateful and offensive tweets with an F1-Measure of 0.95 and a classification accuracy of 95%.

REFERENCE

Abro, S., Shaikh, S., Ali, Z., Khan, S., Mujtaba, G., & Khand, Z. H. (2020). Automatic hate speech detection using machine learning: A comparative study. *International Journal of Advanced Computer Science and Applications*, *11*(8), 484–491. https://doi.org/10.14569/IJACSA.2020.0110861

Alshalan, R., & Al-Khalifa, H. (2020). A deep learning approach for automatic hate speech detection in the saudi twittersphere. *Applied Sciences (Switzerland)*, *10*(23), 1–16. https://doi.org/10.3390/app10238614

Badjatiya, P., Gupta, M., & Varma, V. (2017). Deep Learning for Hate Speech Detection in Tweets Pinkesh. *15th Conference of the European Chapter of the Association for Computational Linguistics, EACL 2017 - Proceedings of Conference*, *2*(2), 427–431. https://doi.org/10.18653/v1/e17-2068

Burnap, P., & Williams, M. L. (2015). Cyber Hate Speech on Twitter: An Application of Machine Classification and Statistical Modeling for Policy and Decision Making. *Policy & Internet*, *7*(2), 223–242. https://doi.org/10.1002/POI3.85

F.B.I. (2019). *FBI — Hate Crime Summary*. https://ucr.fbi.gov/hate-crime/2019/resource-pages/hate-crime-summary

Fortuna, P., & Nunes, S. (2018). A survey on automatic detection of hate speech in text. *ACM Computing Surveys*, *51*(4). https://doi.org/10.1145/3232676

Gambäck, B., & Sikdar, U. K. (2017). *Using Convolutional Neural Networks to Classify Hate-Speech*. *7491*, 85–90. https://doi.org/10.18653/v1/w17-3013

Hate-Speech-Data-Analysis | Kaggle. (2020). https://www.kaggle.com/tarushi89/hate-speech-data-analysis

Mullah, N. S., & Zainon, W. M. N. W. (2021). Advances in Machine Learning Algorithms for Hate Speech Detection in Social Media: A Review. *IEEE Access*, *9*, 88364–88376. https://doi.org/10.1109/ACCESS.2021.3089515

Pariyani, B., Shah, K., Shah, M., Vyas, T., & Degadwala, S. (2021). Hate speech detection in twitter using natural language processing. *Proceedings of the 3rd International Conference on Intelligent Communication Technologies and Virtual Mobile Networks, ICICV 2021, January 2018*, 1146–1152. https://doi.org/10.1109/ICICV50876.2021.9388496

Pathak, V., Joshi, M., Joshi, P., Mundada, M., & Joshi, T. (2020). KBCNMUJAL@HASOC-Dravidian-CodeMixFIRE2020: Using machine learning for detection of hate speech and offensive code-mixed social media text. *CEUR Workshop Proceedings*, *2826*, 351–361.

Priyadharshini, G. (2020). Detection of Hate Speech using Text Mining and Natural Language Processing. *International Journal of Engineering Research & Technology (IJERT)*, *9*(11), 2018–2021. www.ijert.org

Sari, P., & Ginting, B. (2019). *Hate Speech Detection on Twitter Using Multinomial Logistic Regression Classification Method*. 105–111.

Scott Williams. (2019 B.C.E., February 15). *TF-IDF from scratch in python on real world dataset. | by William Scott | Towards Data Science*. https://towardsdatascience.com/tf-idf-for-document-ranking-from-scratch-in-python-on-real-world-dataset-796d339a4089

United Nations. (2019). United Nations Strategy and Plan of Action on Hate Speech. *United Nations Report*, *May*, 1–5.

4th International Engineering Conference (IEC 2023)
Federal University of Technology, Minna, Nigeria

Perspectives on Electric Vehicle Technology: A State of Art on Current and Future Prospects

*Jamilu, Y. M[1], Kadawa, I. A[2], Kamal, A. A.[2] & Nuraini, S. M[2]

[1]Department of Mechanical Engineering, Nigerian Army University, Biu, Nigeria

[2]Department of Electrical and Electronics Engineering, Nigerian Army University Biu, Nigeria

*Corresponding Author Email: jamilu.muhammad@naub.edu.ng +2348062682083

ABSTRACT

The rapid consumption of fossil fuel and increased environmental hazards caused by fossil fuel have given a strong impetus to the growth and development of fuel-efficient vehicles. These disadvantages in the internal combustion engine (ICE) induces to make use of an Electric Vehicles. Basically, the electric vehicles are two of types, pure electric vehicles (PEVs) and hybrid electric vehicles (HEVs). The pure electric vehicles consist only electrical equipment, and it cannot be used for long drives. But the hybrid electric vehicles work along with ICE and electrical equipment and it is applicable for long drives. The power electronic system should be efficient to improve the range of the electric vehicles and fuel economy. The selection of a power semiconductor device, converters and its control techniques and switching strategies are important for better performance. The packaging of the individual units and the system integration are very essential to the development of efficient and high-performance vehicles. This paper presents an extensive review of the battery technologies from the Lead-acid batteries to the Lithium-ion. Moreover, we review the different standards that are available for EVs charging process, as well as the power control and battery energy management proposals. Finally, we conclude our work by presenting our vision about what is expected in the near future within this field, as well as the research aspects that are still open for both industry and academic communities.

Keywords: *Battery, Charging Modes, Connectors, Electric Vehicles, Lithium-ion*

1 INTRODUCTION

Greenhouse emissions and its effects in climatic changes are two prime movers in the world of research and development in order to reduce these emissions and improve global economy. But internal combustion engine (ICE) vehicles' emission has been challenges to this policy. Meanwhile, electric vehicles (EVs) have arisen and possess vast advantages as compared to vehicles powered by ICEs. Electric vehicles are operating with zero emission and have good features such as greater acceleration and higher energy efficiency. Therefore, EVs have the potential to reduce greenhouse gases and air pollution [1-3].

28% of the emitted Carbon-dioxide (CO_2) to the environment was reported by the European Union as from transport sector, while the road transport is accountable for over 70% of the transport sector emissions [4]. Therefore, to mitigate the environmental hazards and greenhouse gases emission, the developed countries are encouraging the use of Electric Vehicles (EVs). Automotive industries have recognized the value of alternative fuel vehicles (AFVs) for green transportation and have been implementing economic policies to support electric vehicles' (EVs) market [5].

Electric Vehicles (EVs) present numerous advantages compared to fossil-fueled internal combustion engine (ICEs) vehicles, inter alia: zero tailpipe emissions, no reliance on petroleum, improved fuel economy, lower maintenance, and improved driving experience (e.g. acceleration, noise reduction, and convenient home and opportunity recharging) [6-8]. Further, when charged with clean electricity, electric vehicles (EVs) provide a viable pathway to reduce overall greenhouse gas (GHG) emissions and decarbonize on-road transportation. This decarbonization potential is important, given limited alternative options to liquid fossil fuels. The ability of electric vehicles (EVs) to reduce greenhouse gas (GHG) emissions is dependent, however, upon clean electricity. Therefore, electric vehicle success is intertwined closely with the prospect of abundant and affordable renewable electricity (in particular solar and wind electricity) that is poised to transform power systems [9-12].

In general, electric vehicles (EVs) can be categorized into battery electric vehicle (BEV), hybrid electric vehicle (HEV), plug-in hybrid electric vehicle (PHEV) and fuel cell electric vehicle (FCEV). BEV is driven by electric motors powered by batteries, while HEV and PHEV is driven solely by ICE, assisted by electric motors. FCEV is also driven by electric motors but powered by a fuel cell stack [13].

Global sales of EVs have exceeded 1 million units in year 2017, where it was a significant growth of 54% compared to new EVs sales in 2016. The largest EVs market is China, where it accounted for more than half of the global EVs sales, whereas United States is the second largest EVs market [14]. Consumers purchase EVs for a

variety of reasons including technological, performance, environmental and symbolic motivations [15-21].

EV success is increasing rapidly since the mid-2010s. EV sales are breaking previous records every year, especially for light-duty vehicles (LDVs), buses, and smaller vehicles such as three-wheelers, mopeds, kick-scooters, and e-bikes [22]. To date, global automakers are committing more than $140 billion to transportation electrification, and 50 light-duty EV models are available commercially in the U.S. market [23]. Approximately 130 EV models are anticipated by 2023 [23, 24]. Future projections of the role of EVs in LDV markets vary widely, with estimates ranging from limited success (~10% of sales in 2050) to full market dominance, with EVs accounting for 100% of LDV sales well before 2050. Many studies project that EVs will become economically competitive with ICEVs in the near future or that they are already cost-competitive for some applications [25-28]. However, widespread adoption requires more than economic competitiveness, especially for personally owned vehicles.

These recent successes are being driven by technological progress, especially in batteries and power electronics, greater availability of charging infrastructure, policy support driven by environmental benefits, and consumer acceptance. EV adoption is engendering a virtuous circle of technology improvements and cost reductions that is enabled and constrained by positive feedbacks arising from scale and learning by doing, research and development, charging-infrastructure coverage and utilization, and consumer experience and familiarity with EVs.

2 ELECTRIC VEHICLE TECHNOLOGY

Electric vehicle technology involved electrical and electronic engineering, mechanical and automotive engineering, and chemical engineering. Experts in these disciplines of engineering must work together in the main areas that must be integrated: body design, batteries, electric propulsion, and intelligent energy management.

2.1 HISTORICAL BACKGROUND OF ELECTRIC VEHICLES

After thirty years of noise and dirtiness due to steam engines which was invented in 1801, the first battery-powered EV was built in 1834. Over fifty years later, the first gasoline powered ICE vehicle was built in 1885. So, EVs are not new and already over 170 years old. With the drastic improvement in combustion engine technology, ICE vehicles showed much better performance and EVs were out of use from the 1930s to the 1950s [29].

Interests in EVs started at the outbreak of energy crisis and oil shortage in the 1970s. The actual revival of EVs is due to the ever-increasing concerns on energy conservation and environmental protection throughout the world as summarized below:

a. EVs offer high overall energy efficiency over the ICE vehicles by about 60% [29].
b. EVs enable load equalization of power system. By recharging EVs at night, the power generation facilities can be effectively utilized, contributing to energy saving and stabilization of power cost.
c. EVs show zero exhaust emissions.
d. EVs operate quietly and almost vibration-free, whereas ICE vehicles are inherently noisy and with sensible vibration.

Nowadays, many governments actively promote the use of EVs by providing facilities such as financial subsidies and tax reduction, as well as enforcing regulations such as zero-emission zones and ultralow-emission vehicles.

2.2 CLASSIFICATIONS OF ELECTRIC VEHICLES

The Electric Vehicles (EVs) employs an electric motor and the corresponding energy sources are batteries, fuel cells, capacitors and/or flywheels. However, the presently achievable specific energy of capacitors and flywheels precludes them from being the sole energy sources for EVs. The key difference between the ICEV and EV is the device for propulsion (combustion engine versus electric motor). Electric Vehicles are classified into four systems and the details of each are as given below.

2.2.1 THE BATTERY EV (BEV)

The battery EV (BEV) utilizes batteries as the sole energy source, and electric motors as the propulsion device. This BEV has been commercially available though not yet under mass production, and is mainly designed for commuter operation with the driving range of about 100 km per charge. Battery-powered electric vehicles were one of the solutions proposed to tackle the energy crisis and global warming. However, the high initial cost, short driving range, long charging (refueling) time, and reduced passenger and cargo space have proved the limitation of battery-powered EVs.

2.2.2 THE HYBRID EV (HEV)

The hybrid EV (HEV) incorporates both of the combustion engine and electric motor as the propulsion device. It adopts gasoline or diesel fuel as the main energy source, and utilizes batteries as the auxiliary energy source. The HEV can offer the same driving range as the ICEV (over 500 km per refuel), while produces much lower emissions than those of the ICEV. This HEV has been commercially available and under mass production.

2.2.3 THE FUEL CELL EV (FCEV)

The fuel cell EV (FCEV) adopts fuel cells as the main energy source, and the electric motor as the propulsion device. Since fuel cells cannot accept regenerative energy, batteries are generally adopted as the auxiliary energy

source. Being fueled by hydrogen or methanol, the FCEV can provide a driving range comparable with the ICEV. Because of its high initial cost, this FCEV is not yet commercially available [30]. A fuel cell uses hydrogen and oxygen to produce electricity through a chemical reaction. Fuel cell offers low emission and higher efficiency comparing to ICE.

2.2.4 THE PLUG-IN HYBRID (PHEV)

The plug-in hybrid (PHEVs) refer to vehicles that can use, independently or not, fuel and electricity, both of them rechargeable from external sources. PHEVs can be seen as an intermediate technology between BEVs and HEVs. It can be considered as either a BEV supplemented with an internal combustion engine to increase the driving range or as a conventional HEV where the all-electric range is extended as a result of larger battery packs that can be recharged from the grid.

2.3 DESIGN PROCESS OF ELECTRIC VEHICLES

Once the kinds of technology have been analyzed and compared, after knowing the possible configurations and the interactions of the components, a conceptual design of an electric vehicle can be generated. However, the following are steps to adopt in designing and Electric vehicles:

i. Defining what type of vehicle are to design. There are three types that cover the vast majority of vehicles, and they are compacts, pick-ups, and trucks.
ii. Depending on the type of vehicle to design, we select the type of traction that this may have, which varies depending on the type of vehicle; the three main types are Front-Wheel Drive (FWD), Rear-Wheel Drive (RWD) and All-Wheel Drive (AWD).
iii. Deciding the technology of the electric motor that the EV will have and its position for its configuration. In-wheel motors are commonly used in compact vehicles.
iv. Selection of the range extender system. For practice, we define two selection criteria: the amount of power and the emissions. Large vehicles need high levels of autonomy; small vehicles can have medium or low levels of autonomy. Our selection criteria are the extra range needed, a high, medium, or low amount; and the space and weight that can be sacrificed.
v. The controller selection (independent or general controllers) will depend on the control strategy to use. We can also optimize the controller selection using the strategies and components' sizes given by [31].

3 TECHNOLOGY OF ITS COMPONENTS

3.1 BATTERY

A battery is a storage device that stores electrical energy in the form of chemical energy. There are two types of batteries: (a) primary batteries which are not rechargeable and (b) secondary batteries which are rechargeable. For multiple uses, secondary batteries are suitable, thus, are preferable for vehicular applications.

The capacity of a battery is measured in ampere-hour (Ah), while the energy stored in battery is measured in watt-hour (Wh) and the usable state-of-charge is expressed as percentage, which defines the availability of charge in the battery. The operation of battery should be maintained in certain range of state-of-charge (SOC) to prolong the battery lifecycle. The capacity of a battery is proportional to the maximum discharge current, represented by the index of charge. That means, if the value of charge is higher, the battery will deplete quickly. The maximum discharge current is dependent on the chemical reaction and the temperature of the battery.

Battery is the most reliable energy source for long time, as a result various types of batteries with different capacity and characteristics can be observed [32,33]. Currently, five groups of batteries suitable for vehicular applications are available in the market, such as lead acid batteries, nickel batteries, ZEBRA batteries, lithium batteries and metal air batteries.

3.2 CHARGING OF ELECTRIC VEHICLES

For the EVs to definitely succeed, it will be necessary that the users can charge their vehicles in a fast and simple way. To do so, it will be fundamental to have an infrastructure deployment that allows such fast and simple charge. This implies charging at homes, and the creation of electric charging stations that provide quick charges during long commuting. Below, the different standards or rules that are created for electric vehicles charging technology are presented. In particular, we detail the different charging modes that are defined in the current standards, as well as the connectors.

When charging electric vehicles, we can find different standards, which are determined, mainly, by the region in which they are being used or applied. More specifically, in North America, and in the Pacific zone, the SAE-J1772 standard for loading electric vehicles is used. However, in China, the GB/T 20234 standard is used, whereas, in Europe, the IEC-62196 standard was introduced. The main difference between these three standards is that while the two former ones classify the charging modes according to the power type (DC or AC power), the latter one classifies such modes by the charging power involved.

The SAE-J1772 [34] mode is a North American standard of electric connectors for electric vehicles created in 1996, and supported by SAE International. This

standard is common in USA and Japan, and it establishes the following charging modes (see Table 1):

Table 1. Charge ratings of the SAE-J1772 [34].

Charge Method	Volts (V)	Maximum Current (Amps-Continuous) (A)	Maximum Power (kW)
AC Level 1	120	16	1.9
AC Level 2	240	80	19.2
DC Level 1	200 to 500	80	40
DC Level 2	200 to 500	200	100

3.2.1 CHARGING MODES

The IEC-62196 standard [35] is an international standard created by the International Electrotechnical Commission (IEC) in 2001 for charging electrical vehicles in Europe and China. The IEC-62196 establishes the general characteristics of the charging process, as well as the way in which the energy is supplied. This norm derives from the IEC-61851 and it provides a first classification of the charging type according to its nominal power and, thus, of the charging time [35, 36]. Users are provided with four modes in order to charge the vehicles.

a. Mode 1 (Slow charging). It is defined as a domestic charging mode, with a maximum intensity of 16 A, and it uses a standard single-phase or three-phase power outlet with phase(s), neutral, and protective earth conductors. This mode is the most used in our homes.
b. Mode 2 (Semi-fast charging). This mode can be used at home or in public areas, its defined maximum intensity is of 32 A, and, similar to the previous mode, it uses standardized power outlets with phase(s), neutral, and protective earth conductors.
c. Mode 3 (Fast charging). It provides an intensity between 32 and 250 A. This charging mode requires the use of an EV Supply Equipment (EVSE), a specific power supply for charging electric vehicles. This device (i.e., the EVSE) provides communication with the vehicles, monitors the charging process, incorporates protection systems, and stops the energy flow when the connection to the vehicle is not detected.
d. Mode 4 (Ultra-fast charging). Published in the IEC-62196-3, it defines a direct connection of the EV to the DC supply network with a power intensity of up to 400 A and a maximum voltage of 1000 V, which provides a maximum charging power up to 400 kW. These modes also require an external charger that provides communication between the vehicle and the charging point, as well as protection and control.

3.2.2 CONNECTORS

Electric vehicles have an AC/DC converter that allows charging their batteries at home through the use of traditional outlets (e.g., the Schuko in Europe). However, when requiring faster charges, Electric Vehicle Charging Stations must be used, since they can directly supply DC power to the batteries. Charging Stations can supply electricity through different connectors, depending on the standard supported, and they present the following advantages [34]:

i. They are sealed solutions (not affected by water or humidity).
ii. They carry a mechanic or electronic blockage.
iii. They enable communication with the vehicle.
iv. Electricity is not supplied until the blockage system is not activated.
v. While the blockage system is activated, the vehicle cannot be set in motion, so that a vehicle cannot leave while plugged.
vi. Some connectors are able to charge in three-phase mode.

3.3 MPPT ALGORITHM USED IN ELECTRIC VEHICLES

With the growing demand for switching over to renewable energy resources, PV technology is charging ahead of the other alternatives. The various salient features of it being noiseless, pollution free, immune to direct contamination and its simplicity in operation help make it the preferred choice. The various structures of photovoltaic (PV) systems and their suitability in electric vehicles have been discussed in [37–40].

The I-V characteristics of PV cells are nonlinear, and there exists only one maximum power point (MPPT) [41]. By interfacing the power, electronic devices with PV system, the efficiency can be increased along with MPPT controller. Many algorithms have been put forward to track this MPPT, but among all, constant voltage tracking method is the most traditional method but has limitations during varying temperature. To overcome them, perturb and observe (P & O) and incremental conductance (IC) methods are most widely used.

In case of P & O, the load impedance varies periodically and senses the change in the direction of power, whereas in IC, dp/dv is monitored to detect whether MPPT has reached, where p is the power and v the voltage. In P & O, the system oscillates near MPPT; hence, the system works, inefficiently [42]. The IC algorithm is the procedure where the voltage and current curves provide the maximum power level [43]. The

advantage with IC is its responsiveness to changing atmospheric conditions, whereas P & O benefits from being more straightforward to implement [44]. A simple charging algorithm with P & O MPPT was proposed for Photovoltaic Hybrid Electric Vehicles (PVHEVs) in [45]. This is used to extract the maximum power with the help of a boost converter. The charging algorithm drives the converter in constant current and constant voltage mode as needed. The P & O algorithm has also been designed for PVHEV in [46].

An MPPT control algorithm which does not require a current sensing device has been presented for HEV applications in [47]. In this algorithm, MPP can be determined by the PV voltage and switching duty ratio of the converter. In [48], a small-sized PV cell and other hardware components were selected to reduce power loss and cost and to obtain high efficiency. In [49], a solar-thermoelectric hybrid system for HEVs was proposed with P & O based MPPT. This method is capable of tracking the global MPP with reduced hardware cost [50]. The ANN-based MPPT in PVHEVs was also used. An offline ANN, trained using the backpropagation and gradient descent momentum algorithm, can be used for online estimation of the reference

voltage for the feed-forward loop [51]. It is proposed that one should use P & O algorithm when the vehicle is parked and voltage-based MPPT algorithm is suitable while driving [52].

The MPPT algorithms, namely P & O, IC and only current, are compared in terms of energy performances in ambient conditions, and IC has proved to be better [53]. For comparison, PV modules were mounted on a moving platform, designed to simulate insulations received by solar systems on a moving vehicle. A modified P&O algorithm has been proposed to obtain fast transient response with high stability for variations in solar irradiance [54]. P & O as well as IC-based techniques can be used to handle variable solar irradiance. They provide an optimal solution and a realistic driving scenario. Voltage balancing control is very useful as it allows an independent source for every independent MPPT in a distributed MPPT (DMPPT). When compared to centralized MPPT (CMPPT), the DMPPT offers 6.9–11.1% improvements in annual energy [55]. The single-ended primary inductor converter and estimated P & O were used for charging the battery efficiently, which prolongs the battery life [56]. MPPT algorithms based on the ant colony optimization, FL, ANN, GA and PSO, have been applied to PV systems under changing irradiance conditions. A new type of algorithm, namely firefly algorithm, was also introduced in [57].

The PHEV loads should be given due consideration while designing a grid-connected residential PV system. The PV arrays and battery packs can be connected in a cascaded manner to power the load. A DC/DC converter can be used to regulate the voltage of the PV arrays by

MPPT using the IC method [58]. In grid-connected mode, PV works at its MPP and EV works in the charging mode. However, when the microgrid gets isolated from the utility grid, both PV and EV should deliver active and reactive powers to feed the loads [59]. Table 2 provides the comparison between various MPPT algorithms, which have been used in HEVs. ANN and FL are trending these days because of their advantages over others.

Table 2. Comparison of MPPT algorithms used in EVs [59]

MPPT technique	Convergence speed	Implementation complexity	Periodic tuning	Sensed parameters
P&O	Varies	Low	No	Voltage
IC	Varies	Medium	No	Voltage and current
Fractional V_{oc}	Medium	Low	Yes	Voltage
Fractional I_{sc}	Medium	Medium	Yes	Current
FLC	Fast	High	Yes	Varies
Neural network	Fast	High	Yes	Varies

4 Challenges and Environmental Impact of Electric Vehicles

4.1 Challenges

Several challenges such as technical, economical and others need to be subdued in order to make EVs popular and successful competitor with conventional vehicles for consumers.

For vehicular application, Proton Exchange Membrane Fuel cells (PEMFC) are ideal. To mitigate the basic commercial system packaging requirements, the power density and specific power targets of Proton Exchange Membrane Fuel Cell (PEMFC) have been achieved but further improvements are required. The anticipated specific power for automotive application is 1 kW/kg; however, the achievement until year 2010 has only reached 0.65 kW/kg [60]. The catalyst used in PEMFC is platinum, which is an expensive and rare material. Due to this reason, the price of fuel cell is high. Performance and durability are other factors needed to be ensured. Hence, the volume, mass and cost of the stack needs to be reduced for commercial applications. The future challenges for fuel cell system are the cost, performance, robustness and reliability.

A major portion of the energy source of Fuel Cell Hybrid Electric Vehicles (FCHEV) is occupied by the energy storage system (ESS). The performance of an FCHEV depends on the performance of the storage system, which relies on the system design as well as the

type of storage used. Normally, the capacity of storage system differs between EVs, HEVs or FCHEVs. EVs require bigger storage system (i.e., in the range of 34.5–140 Wh/kg) whereas HEVs need comparatively smaller storage system (i.e., in the range of 26.3–77 Wh/kg). However, the power capacity for EV battery is lower (i.e., in the range of 40–255 W/kg) than that of HEV battery (i.e., in the range of 77–745 W/kg) [61]. The requirement for FCHEV ESS is a combination of high power and high energy density to handle the cold start issue and the transient power demand. Thus, designing a proper ESS is a challenge for FCHEV manufacturers. Currently, Li-ion batteries and ultracapacitors are either used separately or combined for FCHEV ESS. These storage devices are costly and the recycling policy of these devices is yet to adopt. In future, the potential of other storage devices such as flywheel energy storage needs to be investigated. Among the other technical challenges of FCHEV ESS are higher initial cost, higher replacement cost, large size and weight, performance and robustness. Furthermore, future challenges include lifetime testing of ESS in field and commercial production facility development.

The challenges in the area of propulsion motor and motor control technologies, methods to eliminate speed/position sensors and inverter current sensors etc. are similar to those of EVs, HEVs and PHEVs. Development of sensor-less machines and reduction or elimination of current sensors in inverter is yet to achieve. High temperature and low-cost permanent magnet development will increase the robustness, speed range and use of permanent magnet motors. Thus, the future challenges will be developing smaller, lighter motors with wide range, higher torque and increased lifetime.

4.2 Environmental Impact

The utilization of EVs instead of ICE vehicles enhances the quality of the environment. EVs can be said to be environmentally friendly as it is powered by batteries and thus produces no tailpipe emission. The combustion of fossil fuel within the ICE emits toxic chemicals into the air, these emissions are harmful to human and the environment. However, the power generation process for charging EVs also produces greenhouse gas emissions. The emission of greenhouse gases into the atmosphere causes global warming [62].

The drive concept of electric vehicles is based on the usage of electrical energy, therefore there will be reduction in fossil fuel demand. Hence, energy storage systems in electric vehicles pose minimal impact towards environmental pollution. However, the processing and production of energy storage systems as well as the disposal of electrochemical batteries may cause respiratory, pulmonary, and neurological diseases. Therefore, safety measures must be taken into consideration during the production of energy storage systems especially the batteries [63].

Since EVs produce zero tailpipe emission, it is important to understand and identify the possible environmental impact resulted from electrical power generation. While burning coal at electric power plants is not that much better than burning oil, the electricity generated for electric vehicles can also come from power plants fueled by other energy sources that are much cleaner than oil and coal: hydro power, nuclear, geothermal, solar power and wind power. Companies in the private sector have begun giving their employees incentives to take advantage of solar technology by subsidizing solar panels in the roofs of their employees' homes to make clean energy. As these technologies improve, the emissions associated with generating electricity for electric vehicles will be further reduced.
Switching from gasoline vehicles to electric vehicles (PEV's and PHEV's) will significantly reduce tailpipe emissions. Specifically, it was found that the State of California can reduce CO_2 tailpipe emissions by a total of 124 million metric tons, if it replaces its current vehicle fleet by electric vehicles in 2040 [64]. Generally, it is estimated that the average electric vehicle driving solely on electricity produces global warming emissions equal to a gasoline vehicle with 68 miles per gallon fuel economy rating [65].

Furthermore, electric vehicles will become even 'cleaner' as more electricity is generated by renewable sources of energy. It was shown a declining percentage of electricity generated by coal power and an increasing in renewable sources, such as wind and solar which suggests that emissions from operating electric vehicles are most likely to keep falling [66]. According to the Union of Concerned Scientists, in a grid that is composed of 80% renewable electricity, the manufacturing of an all-electric vehicle will result in an over 25% reduction in manufacturing's emissions and an 84% reduction in emissions from driving, resulting to an overall emissions reduction of more than 60% [65].

5 Market Opportunities and Future Prospects

With respect to EVs market potential, the car of the near future is the HEV, and it will likely become the dominant vehicle platform by the year 2030 [67]. International Energy Agency (IEA) has projected the global stock increment of EVs from 3.7 million in 2017 to 13 million by 2020 and eventually reaches 130 million in 2030. On the other hand, the sales of EVs are estimated to have a growth of 24% averagely throughout the projection period. The sales would increase from 1.4 million in 2017 to 4 million of EVs by 2020 and in time reaches 21.5 million of sales by 2030 [75]. Global positioning system (GPS) data of the households were used to illustrate how EVs can match different household (single-vehicle or multiple-vehicle) needs. Cost comparisons between the EVs and conventional gasoline vehicles were conducted and the annual savings were given [68]. The reduction

that a PHEV provides in both transportation costs and GHG emissions with respect to a comparable conventional vehicle was also discussed [69]. Smart and Schey [70] analyzed the Nissan Leaf, which is a BEV, and concluded that the drivers drove 6.9 miles per trip, 30.3 miles per day on average and the average number of charging times was 1.05 per day, as well as 82% of charging events were conducted at home. Markel [71] summarized the components of the PEV infrastructure, challenges and opportunities related to design and deployment of the infrastructure and potential benefits. Dong *et al.* [72] proposed a stochastic modelling approach to characterize BEV drivers' behavior using longitudinal travel data. It accounts for a more realistic analysis of the charging station impact on BEV feasibility. The actual range of a BEV is formulated as a Weibull-distributed variable, while the between-charge travel distances were formulated using a Poisson–gamma distribution. Hidrue *et al.* [73] analyzed customers' willingness to pay for EVs and their attributes using a stated preference study. It showed that the driving range, fuel cost savings and charging time rank as the most important factors and battery cost must drop significantly before EVs find a mass market without subsidy. He *et al.* [74] proposed a model that captures the interactions among availability of public charging opportunities, prices of electricity and destination and route choices of PHEVs.

As battery technology advances over time, the capacity of the battery also increases. This means that EVs in the future are expected to have longer ranges. Currently, the Tesla Model S P100D hold the record of having the longest range (over 500 km on a single charge) amongst other EV manufacturer companies. An average EV however, is estimated to have about 180 km of range on a single charge. In the future, the battery capacity will increase to about 70-80 kWh which will allow the average EV to have a range between 300 km to 400 km. Moreover, reported analysis shows there will be an expansion in the battery supply market in the coming years. The analysis also shows that by 2025, the construction of 10 new factories with manufacturing capabilities of Tesla's Gigafactory needs to be implemented in order to keep up with the demand [75].

6 CONCLUSION

World concerns of climate change and the rapid vanishing of global crude oil, air quality degradation caused by exhaust gas, car noise guarantee a steady to replace world noisy ICE vehicles by EVs based one in the coming decades. In this paper, the authors analyzed the types of EVs, the technology used, the charging modes, the evolution of sales within the last years and future trends.

Due to the single propulsion system in the EV, the consumers a more reliability, maintenance easy and vehicle cost compare to the PHEV. Furthermore, compared with FCEV is more advantageous relative to cost, recharging and safety. Regarding EVs, batteries are a critical factor, as these will determine the vehicle's autonomy. We analyzed several kinds of batteries, according to these features. We also presented the possible technologies that can be used in the future, such as the graphene, which is expected to be a solution that enables the storage of higher amounts of power, and charge in shorter periods of time. The EV could also benefit from this type of technology, reaching higher ranges, something that could help its adoption by drivers and users. The development of batteries with higher capacities will also favor the use of the fastest and most powerful charging modes, as well as better wireless charging technologies.

The creation of a unique connector that can be globally used is another aspect that could benefit the deployment of electric vehicles. The EV will play a highly important role in the future Smart Cities, and having different charging strategies that can adapt to the users' needs will be of special relevance. Therefore, future Battery Management System (BMS) should consider the new scenarios that were introduced by new batteries and Smart Cities requirements.

REFERENCE

[1] Jaunky, V.C. (2011). The CO_2 emissions-income nexus: Evidence from rich countries. *Energy Policy*, 39 (3): 1228–1240.

[2] Marshall, B.M., Kelly, J.C., Lee, T.K., Keoleian, G.A., Filipi, Z. (2013). Environmental assessment of plug-in hybrid electric vehicles using naturalistic drive cycles and vehicle travel patterns: A Michigan case study. *Energy Policy*, 58: 358–370.

[3] Sadorsky, P. (2014). The effect of urbanization and industrialization on energy use in emerging economies: Implications for sustainable development. *American Journal of Economics and Sociology*, 73 (2): 392–409.

[4] European Commission (2011). Transport in Figures' Statistical Pocketbook. Available online: https://ec.europa.eu/transport/facts-fundings/statistics/pocketbook-2011_en/

[5] Hacker, F., Harthan, R., Matthes, F., et al. (2009). Environmental impacts and impact on the electricity market of a large-scale introduction of electric cars in Europe: critical review of literature. ETC/ACC technical paper 2009/4: 56–90, http://acm.eionet.europa.eu/docs/ETCACC_TP_2009_4_electromobility.pdf

[6] Stimming, U., Ramachandran, S. (2015). Well to wheel analysis of low carbon alternatives for road traffic. *Energy Environ Sci.*, 8:3313-3324.

[7] Nordelof, A., et al. (2014). Environmental impacts of hybrid, plug-in hybrid, and battery electric

vehicles. What can we learn from life cycle assessment? *Int J Life Cycle Assess.*,1866-1890.

[8] Offer, G., et al. (2011). Techno-economic and behavioural analysis is of battery electric, hydrogen fuel cell and hybrid vehicles in a future sustainable road transport system in the UK. *Energy Policy*, 39:1939-1950.

[9] Jacobson, M. Z., Delucchi, M. A., Cameron, M. A., Frew, B. A. (2015). Low-cost solution to the grid reliability problem with 100% penetration of intermittent wind, water, and solar for all purposes *Proc. Natl Acad. Sci.*, 112: 15060-15065.

[10] Kroposki, B., Johnson, B., Zhang, Y., Gevorgian, V., Denholm, P., Hodge, B. M., Hannegan, B. (2017). Achieving a 100% renewable grid: Operating electric power systems with extremely high levels of variable renewable energy. *IEEE Power Energy Mag.*, 15: 61–73.

[11] Gielen, D., Boshell, F., Saygin, D., Bazilian, M. D., Wagner, N., Gorini, R. (2019). The role of renewable energy in the global energy transformation. *Energy Strategy Rev.*, 24: 38–50.

[12] International Energy Agency (IEA), (2020). *World Energy Outlook 2020.* Retrieved from: www.iea.org/reports/world-energy-outlook-2020

[13] Zhang, Q., Li, H., Zhu, L., Campana, P.E., Lu, H., Wallin, F., Sun, Q. (2018). Factors influencing the economics of public charging infrastructures for EV: A review. *Renewable & Sustainable Energy Reviews*, 94: 500-509.

[14] International Energy Agency (IEA) (2016). *Global EV Outlook 2016.* Retrieved from: www.iea.org/reports/global-ev-outlook-2016

[15] Hardman, S., Shiu, E., Steinberger-Wilckens, R. (2016). Comparing High-End and Low-End Early Adopters of Battery Electric Vehicles. *Transp Res Part A: Policy Pract, Revi*.

[16] Caperello, N., Tyreehageman, J., Davies, J. (2015). *I am not an environmental wacko! Getting from early plug-in vehicle owners to potential later buyers.* Transportation Research Board Annual Meeting.

[17] Lane, B. et al. (2014). *Beyond Early Adopters of Plug-in Electric Vehicles? Evidence from Fleet and Household Users in Indianapolis*. Transportation Research Board Meeting Annual.

[18] Buhler, F., et al. (2014). Is EV experience related to EV acceptance? Results from a German field study. *Transp. Res. Part F: Traffic Psychol. Behav*., 25: 34-49.

[19] Plotz, P., et al. (2014). Who will buy electric vehicles? Identifying early adopters in Germany. *Transp. Res. Part A: Policy Practice*, 67: 96-109.

[20] Axsen, J., Kurani, K.S. (2013). Hybrid, plug-in hybrid, or electric: What do car buyers want? *Energy Policy*, 61:532-543.

[21] Heffner, R., Turrentine, T., Kurani, K. (2006). *A Primer on Automobile Semiotics*. Institute of Transportation Studies.

[22] International Energy Agency (IEA) (2019). *Global EV Outlook 2019.* Retrieved from: www.iea.org/reports/global-ev-outlook-2019

[23] Moore, J., Bullard, N. (2020). *BNEF Executive Factbook* (Bloomberg NEF).

[24] Alternative Fuels Data Center (AFDC) (2020). Alternative Fuel and Advanced Vehicle Search. *U.S. Department of Energy Office of Energy Efficiency and Renewable Energy Alternative Fuels Data Center*.

[25] Weldon, P., Morrisey, P., Margaret, O. (2018). Long-term cost of ownership comparative analysis between electric vehicles and internal combustion engine vehicles. *Sustain. Cities Soc.*, 39: 578-591.

[26] Sioshansi, F., Webb, J. (2019). Transitioning from conventional to electric vehicles: the effect of cost and environmental drivers on peak oil demand. *Econ. Anal. Policy*, 61 7–15.

[27] Yale E360. (2019). Electric cars could be as affordable as conventional vehicles in just three years. *E360 Digest, Yale Environment 360* https://e360.yale.edu/digest/electric-cars-could-be-as-affordable-as-conventional-vehicles-in-just-three-years

[28] Kapustin, N. O., Grushevenko, D. A. (2020). Long-term electric vehicles outlook and their potential impact on electric grid. *Energy Policy*, 137: 1111-1113.

[29] Kumar, L., Gupta, K. K., Jain, S. (2013). Power Electronic Interface for Vehicular Electrification. *Industrial Electronics (ISIE), 2013 IEEE International Symposium.*

[30] Chau, K. T., Wang, Z. (2005). Overview of power electronic drives for electric Vehicles. *HAIT Journal of Science and Engineering B*, 2(5): 737-761.

[31] Puma-Benavides, D. S., Izquierdo-Reyes, J., Calderon-Najera, J.d. D., Ramirez-Mendoza, R.A. A. (2021). Systematic Review of Technologies, Control Methods, and Optimization for Extended-Range Electric Vehicles. *Applied Science*, 11, 7095. https://doi.org/10.3390/app11157095

[32] Beaudin, M., Zareipour, H., Schellenberglabe, A., Rosehart, W. (2010). Energy storage for mitigating the variability of renewable electricity sources: an updated review. *Energy Sustain. Dev.*, 14: 302–314.

[33] Baker J. (2008). New technology and possible advances in energy storage. *Energy Policy*, 36:4368–4373.

[34] SAE International (2009). *Vehicle Architecture for Data Communications Standards-Class B Data*

Communications Network Interface; Standard; SAE International: Warrendale, PA, USA.

[35] International Electrotechnical Commission (2014). *Plugs, Socket-Outlets, Vehicle Couplers and Vehicle Inlets-Conductive Charging of Electric Vehicles-Part 1: General Requirements; Standard*; IEC: Geneva, Switzerland.

[36] Sbordone, D., Bertini, I., Di Pietra, B., Falvo, M.C., Genovese, A., Martirano, L. (2015). EV fast charging stations and energy storage technologies: A real implementation in the smart micro grid paradigm. *Electr. Power Syst. Res.*, 120: 96–108.

[37] Wolfs, P., Quan, L. (2006). A current-sensor-free incremental conductance single cell MPPT for high performance vehicle solar arrays. *In: PESC Rec-IEEE annual power electron spec conf.* https://doi.org/10.1109/pesc.2006.1711749

[38] Wolfs, P., Li, Q. (2007). Hardware implementation and performance analysis of a current-sensor-free single cell MPPT for high performance vehicle solar arrays. *PESC Rec-IEEE annual power electron spec. conf.* https://doi.org/10.1109/pesc.2007.4341976

[39] Zhang, X., Chau, K.T., Yu, C., Chan, C.C. (2008). An optimal solar thermoelectric hybrid energy system for hybrid electric vehicles. *In: 2008 IEEE vehicle power and propulsion conference, VPPC*: 1–6.

[40] Gurkaynak, Y., Li, Z., Khaligh, A. (2009). A novel grid-tied, solar powered residential home with plug-in hybrid electric vehicle (PHEV) loads BT. *5th IEEE vehicle power and propulsion conference, VPPC'09:* 813–816. https://doi.org/10.1109/vppc.2009.5289765

[41] Ocran, T.A., Cao, J., Cao, B., Sun, X. (2005). Artificial neural network maximum power point tracker for solar electric vehicle. *Tsinghua Science Technology*, 10:204–208. https://doi.org/10.1016/S1007-0214(05)70055-9

[42] Khoucha, F., Benrabah, A., Herizi, O. et al. (2013). An improved MPPT interleaved boost converter for solar electric vehicle application. In: 4th International conference on power engineering, energy and electrical drives, pp 1076–1081. https://doi.org/10.1109/powereng.2013.6635760 13-17

[43] Shuang, D.U. (2013). Algorithm research on maximum power point tracking of solar electric vehicle. *In: Proceedings 2013 international conference on mechatronic sciences, electric engineering and computer (MEC)*: 74–78. https://doi.org/10.1109/mec.2013.6885052

[44] Hadagali, N. et al. (2014). Bidirectional dc/dc converter system for solar and fuel cell. *In: 2014 annual international conference on emerging research areas: magnetics, machines and drives (AICERA/iCMMD)*: 1–6.

[45] Armstrong, P.M., Wong, R., Kang, R. et al. (2013). A reconfigurable PV array scheme integrated into an electric vehicle. *In: IET hybrid and electric vehicles conference 2013 (HEVC 2013), London*: 1–7. https://doi.org/10.1049/cp.2013.1910

[46] Sakib, K.N., Member, S., Kabir, M.Z., Williamson, S.S. (2013). Cadmium telluride solar cell: from device modeling to electric vehicle battery management. *In: 2013 IEEE transportation electrification conference and expo (ITEC)*: 1–8. https://doi.org/10.1109/itec.2013.6574490

[47] Jeddi, N., El Amraoui, L., Rico, F.T. (2017). A comparative study and analysis of different models for photovoltaic (PV) array using in solar car. *In: 2017 Twelfth international conference on ecological vehicles and renewable energies (EVER). IEEE*: 1–10.

[48] Wolfs, P., Quan, L. (2006). A current-sensor-free incremental conductance single cell MPPT for high performance vehicle solar arrays. *In: 37th IEEE power electronics specialists conference. IEEE*: 1–7.

[49] Ahadi, A., Liang, X. (2017). A stand-alone hybrid renewable energy system assessment using cost optimization method. *In: 2017 IEEE international conference on industrial technology (ICIT). IEEE*: 376–381.

[50] Zhang, X., Chau, K.T., Yu, C., Chan, C.C. (2008). An optimal solar thermoelectric hybrid energy system for hybrid electric vehicles. *In: 2008 IEEE veh power propuls conf VPPC*. https://doi.org/10.1109/vppc.2008.4677488

[51] Kalla, U.K., Gurjar, D., Rathore, K.S., Dixit, P. (2016). An efficient controller for PV operated PMBLDC drive based electric vehicle system. *In: 2016 IEEE 7th power India international conference (PIICON). IEEE:* 1–6.

[52] El-Saady, G., Sharaf, A.M., Makky, A.M. et al. (2017). An error driven hybrid neuro-fuzzy torque/speed controller for electrical vehicle induction motor drive. *In: Proceedings of the intelligent vehicles' 94 symposium. IEEE*: 449–454.

[53] Schuss, C., Eichberger, B., Rahkonen, T. (2012). A monitoring system for the use of solar energy in electric and hybrid electric vehicles. *In: 2012 IEEE I2MTC-Int. Instrum. Meas. Technol. Conf. Proc.* 524–527. https://doi.org/10.1109/i2mtc.2012.6229214

[54] Nakir, I., Durusu, A., Ugur, E., Tanrioven, M. (2012). Performance assessment of MPPT algorithms for vehicle integrated solar systems. *IEEE Int. Energy Conf. Exhib. ENERGYCON 2012*: 1034–1038.

https://doi.org/10.1109/EnergyCon.2012.6347721

[55] Sarigiannidis, A.G., Kakosimos, P.E., Kladas, A.G. (2014). Solar energy exploitation enhancing driving autonomy of electric vehicles. *MedPower*: 1–5. https://doi.org/10.1049/cp.2014.1649

[56] Forrisi, I., Martin, J., Nahid-mobarakeh, B. et al. (2016). A new approach for DC bus voltage balancing in a solar electric vehicle charging station. *In: IEEE transportation electrification conference and expo (ITEC)*: 1–5. https://doi.org/10.1109/itec.2016.7520240

[57] Kishore, P., Ananth, M., Chidambaram, S. et al. (2013). Solar based hybrid electric powered wheel chair, pp 18–24. https://doi.org/10.1109/tiiec.2013.11

[58] Logeswaran, T., Senthilkumar, A. (2014). A review of maximum power point tracking algorithms for photovoltaic systems under uniform and non-uniform irradiances. *Energy Procedia*, 54: 228–235. https://doi.org/10.1016/j.egypro.2014.07.266

[59] El-Menshawy, M., El-Menshawy, M., Massoud, A., Gastli, A. (2016). Solar car efficient power converters' design. *In: 2016 IEEE symposium on computer applications & industrial electronics (ISCAIE)*: 177–182.

[60] Li, B., Li, H., Ma, J., Wang, H. (2010). PEM fuel cells: current status and challenges for electrical vehicle applications. *J. Autom. Saf. Energy*, 1:260–269.

[61] Amjad, S., Neelakrishnan, S., Rudramoorthy, R. (2010). Review of design considerations and technological challenges for successful development and deployment of plug-in hybrid electric vehicles. *Renew. Sustain. Energy Rev.*, 14:1104–1110.

[62] Choma, E.F., Ugaya, C.M.L. (2017). Environmental impact assessment of increasing electric vehicles in the Brazilian fleet. *Journal of Cleaner Production*, 152: 497–507.

[63] Weldon, P., Morrissey, P., O'Mahony, M. (2016). Environmental impacts of varying electric vehicle user behaviors and comparisons to internal combustion engine vehicle usage: An Irish case study. *J. Power Sources.*

[64] Aris P. (2018). *Electric Vehicles: A future Projection.* An Interactive Qualifying Project at California.

[65] Union of Concerned Scientists, *Cleaner Cars from Cradle to Grave*, 2015. Available: http://www.ucsusa.org/sites/default/files/attach/2015/11/Cleaner-Cars-from-Cradle-to-Grave-exec-summary.pdf

[66] U.S. Energy Information Administration, Annual Energy Outlook 2015 with Projections to 2040, April 2015. Available: http://www.eia.gov/forecasts/aeo/pdf/0383(2015).pdf

[67] Romm, J. (2006). The car and fuel of the future. *Energy Policy*, 34: 2609–2614.

[68] Khan, M., Kockelman, K.M. (2012). Predicting the market potential of plug-in electric vehicles using multiday GPS data. *Energy Policy*, 46: 225–233.

[69] Windecker, A., Ruder, A. (2013). Fuel economy, cost, and greenhouse gas results for alternative fuel vehicles in 2011. *Transport Res D: Tr*, 23: 34–40.

[70] Smart, J., Schey, S. (2012). Battery electric vehicle driving and charging behavior observed early in the EV project. *SAE Int J Alt Power*, 1: 27–33.

[71] Markel, T. (2010). *Plug-in electric vehicle infrastructure: A foundation for electrified transportation.* In: Proceedings of the MIT transportation electrification symposium, Cambridge, MA, 8 April 2010, pp.1–7. Golden, CO: National Renewable Energy Laboratory.

[72] Dong, J., Lin, Z. (2014). Stochastic modeling of battery electric vehicle driver behavior: Impact of charging infrastructure deployment on the feasibility of battery electric vehicles. *Transport Res. Rec.*, 2454: 61–67.

[73] Hidrue, M.K., Parsons, G.R., Kempton, W., et al. (2011). Willingness to pay for electric vehicles and their attributes. *Resour. Energy Econ.*, 33: 686–705.

[74[He, F., Wu, D., Yin, Y.F., et al. (2013). Optimal deployment of public charging stations for plug-in hybrid electric vehicles. *Transport Res. B: Meth.*, 47: 87–101.

[75] Global EV Outlook (2018). Towards cross-modal electrification. International Energy Agency, Paris.

4th International Engineering Conference (IEC 2022)
Federal University of Technology, Minna, Nigeria

Energy Audit: A Case Study of Sunti Golden Sugar Company Mokwa

*Taidi Eli[1], Omokhafe, J. Tola[2], & Babatunde Adegboye[3]
[1]Electrical and Electronic Engineering Department, Federal University of Technology, PMB 65 Minna Niger State, Nigeria
[2]Department of Electrical and Electronic Engineering, Federal University of Technology, PMB 65 Minna Niger State, Nigeria
[3]Department of Electrical and Electronic Engineering, Federal University of Technology, PMB 65 Minna Niger State, Nigeria

email:taidieli@gmail.com +2348103799797, +2349093869110

ABSTRACT
This paper presents the analysis of energy audit with a case study of Sunti Golden sugar company. Electrical energy plays a vital role in almost all section and unit in Sunti Golden sugar Company. As there are limited resources and increased cost to generate electricity, it is the duty of the company management to save resources for future use by doing energy audit in different section and unit. This would help the factory to be competent in the market because their production cost depends on electric power. A detailed energy audit has been analyzed. Based on the losses energy efficiency assessments on the major energy equipment's like electric motors, air compressors, boilers, and lightings have been done. It has been found from energy audit results that an annual Energy loss from both compressors can be calculated which is 80,738.3592Kwh/year, which is equivalent in Naira as ₦ 2,906,580.9312. Replacing a normal motor with an energy-efficient motor results in a 71,605 KWh/year energy savings and a ₦ 1,949,125.7016/year cost savings. It is significant to replace large, partially loaded motors with smaller, fully loaded motors made of company stock or brand-new, energy-efficient motors. As a result, replacing ordinary motors with energy-efficient motors, i.e., replacing under-load motors with properly sized motors, can result in annual savings of 71,605 KWh of energy and ₦ 1,949,125.7016, with payback times ranging from 1.17 to 5.85 years
Keywords: *Air compressor, Electricity current, Energy Audit, Sunti Sugar company*

1 INTRODUCTION

The sugar industry is among the most significant sectors of the global economy. Since poor growth planning is a problem that most sugar companies face, the sector struggles mightily. A typical structure for the sugar business has sub-sections that are inhabited by a variety of distinct units operating independently. The building may yet include some undiscovered flaws that could result in energy usage that is needless.

Around 40% of global commercial energy is often booked by the industrial sector. Conveyors, water pumps, boilers, compressors, and other devices all consume thermal and electrical energy in some capacity (Frederiks et al., 2015).

The industrial sectors, however, face numerous challenges in efficiently using the energy they produce. Lack of correct or sufficient knowledge on the idea of energy conservation has resulted in significant financial losses from energy costs, causes certain issues with the environment, reduces industry competition, etc according to (Yang, 2010) and (Oyedepo et al., 2019).

This study will provide an overview of prospects for energy reduction and power quality improvement at Sunti Golden Sugar Estate (SGSE) factory that were discovered during an energy audit. Estimating the amount of energy that can be saved by putting the suggested measures into practice is done using the data that will be gathered during the audit. A systematic technique was be used to gather pertinent information regarding the factory's energy utilization performance.

The factory mostly produces sugar and molasses. Using carts, raw materials in the form of sugar cane plants are transported from the field to the weigh bridge where they are weighed before being transported to a cane yard with a 3000 TCD capacity. The tipper system and the Hilo un-loader system are two examples of the many unloading methods used to remove the carts. Following that, the cane is put into the cane carrier using the grab crane and feeding table systems. The cane carrier then transports the cane to cane preparation equipment such as the chopper motor, leveler motor, and fibrizer motor where the cane plant is crushed into shreds of fine fibers that are then transported to the conveyor belt via use of Rake Cane Carrier (RCC) and to the mill section proper, which is composed of four tandem mills.

The raw juice from the mill is then pumped to the raw juice heating system, where it is heated, passed to the defecator system, where lime is added, and finally re-heated, heated, and passed to the clarifier section, where further separation between the clear juice (CJ) and the muddy juice (MJ) is carried out. To remove the muck, also known as filter take, the muddy juice is further processed through the Rotary Vacuum Filter (RVF). The filter cake, which is also excellent

bio fertilizer, is collected and brought back to the farm. The Raw Juice heating system is then pumped with the filtrate juice that was collected. After being heated in the evaporator portion, the Clear Juice is transferred there for further separation into syrup and water. The raw massecuite from the pan-boiling of the syrup is then transferred once again to the crystallizer system to create sugar crystals. Following the passage of the material from the crystallizer onto the centrifugal system, the separation of the raw sugar from the molasses takes place. While the molasses is gathered for storage at the storage tank and is made ready for sale, the raw sugar is transferred through the Sugar Hopper, the Dryer, the Elevator, the Vibro Screen, the Grader, and the Sugar Silo. It is then bagged and brought into the warehouse for sale.

The bagasse is delivered from the mill and then used as fuel in the boiler to produce steam that drives the turbine and generates electricity for the entire factory. For all of the process house heating equipment, steam is sent from the turbine exhaust to the evaporator. Excess Bagasse is sent to the Bagasse Yard for recirculation, while the Boiler Ash is collected and brought to the Farm as Bio Fertilizer.

Reduced energy consumption is the goal of energy efficiency in the production of goods and services. Improvements in energy efficiency are typically made by using more efficient production techniques or technologies, or by requesting widely used strategies to reduce energy losses. Electrical motors, cooling systems, lighting, office equipment, etc. all frequently use electricity as a source of power in Sunti Golden Sugar Company. It has been shown that the factory's wasteful usage of energy results in losses and wastes of electrical energy that could otherwise be used productively. Common causes of inefficient energy use include:

(i) The factory workers' lack of knowledge of energy management; (ii) Electrical installations that were poorly and incorrectly designed; (iii) A lack of sufficient measuring tools for audits.

(iv) Because of the non-linear manufacturing equipment, such as derives, which causes harmonic currents to be injected into the power grid, thereby compromising the quality of electricity generated and increasing the loss of power within the system, etc.

Due to the aforementioned facts outlined, Sunti Golden Sugar Company was chosen as case study to perform an energy audit. This company has issues with electrical energy. The factory's concerns, like the use of inefficient equipment, were discovered during the walk-through and indicate that an energy audit needs to be done. Due to variations in electrical energy usage for steady output, the plant owner cannot accurately predict the monthly profit.

In order to discover potential for energy conservation, this study examines the Sunti Golden Sugar Company's electrical energy consumption patterns and evaluates the efficiency of the primary energy-consuming systems**.**

This study examines the energy audit in the company in order to examine working condition and gather pertinent information to identify chances for energy conservation for the main energy-consuming machinery. The potential for energy savings in various energy-consuming devices, such as motors, lighting systems, air compressors, and boilers are also examined.

1.1 ENERGY AUDIT

An energy audit is a thorough investigation of an organization's past and present energy use with the goal of locating and quantifying energy waste in the organization's operations. It creates a foundation for future advancements in energy consumption. To save energy and improve an organization's financial situation, it is a crucial commercial tool. Energy audit is recommended by almost all large and many small organizations, including businesses and non-profits, in order to save energy and lower electricity costs. According to (Nagaveni et al., 2019; Rajput & Singh, 2017), energy audits enable industrial firms or facilities understand how they utilize energy and also aid to identify the areas where wastages occur and where potential for improvement lie. An energy audit has different goals depending on the plant. The focus of an energy audit, however, is typically on the plant's internal energy use and prospects for improvement and energy savings. Energy audits are occasionally carried out to assess the effectiveness of an energy efficiency project or program.

1.2 TYPES OF ENERGY AUDIT

According to (Bhukya, 2014; Marinosci et al., 2015), a preliminary energy audit (also known as a walk-through audit) and a detail energy audit (also known as a diagnostic audit) are the two categories that an industrial energy audit might fall under. In a preliminary energy audit, easily accessible data are mostly used for a straightforward study of the plant's energy use and performance. There aren't many measurements and data collection steps in this kind of audit. These audits are quite quick, and the overall outcomes offer common opportunities for energy efficiency. The basic payback period, or the time needed to pay back the initial capital asset through realized energy savings, is often all that the economic analysis calculates. More in-depth data and information are required for audits that are diagnostic or detailed in nature. The evaluation of various energy systems (such as pumps, fans, compressors, steam, process heating, etc.) is typically accompanied by measurements and data inventory. Because of this, this form of audit takes more time than preliminary audits. Since they provide a more accurate

picture of the plant's energy efficiency and more specific recommendations for plant improvements, the results of these audits are more comprehensive and valuable.

The sugar sector can benefit from energy-efficient technologies and production techniques, according to (Parthe & Kompeli, 2017) report. Additionally, the paper analyzes an audit performed on motors with various horsepower levels in a sugar refinery and provides information on cost- and energy-saving measures. The article also includes a variety of savings and payback timeframes for specific techniques that were discovered under various circumstances. Rewound induction motors were used as the basis for the analysis in order to increase efficiency.

(Khan et al., 2020), conduct performance analyses of power and energy consumed in processing units for a range of manufacturing processes. During the years 2000 to 2004, 314 businesses in Taiwan were subjected to on-site energy audits by (Chan et al., 2007). These audits revealed opportunities for electricity, fuel oil, steam coal, and natural gas savings. The carbon dioxide emissions were reduced by a significant amount of potential energy. In order to help energy users improve energy efficiency, lower CO_2 emissions, and encourage energy savings across all industrial sectors, it is a good idea to organize an energy audit group and take significant action. It would be challenging for companies today to be uninformed of the energy use in their facilities, including the consumption of water, air, gas, electricity, and steam. Energy is used in a growing number of processes, including prototyping, refining, processing, mixing, heat-treating, blending, stamping, painting, assembling, and more, in order to extract, produce, or make everything from beverages and chemicals to machinery and raw materials.

According to a 2016 study by (Hasanbeigi et al., 2012), the energy usage of textile factories in Iran's five main sub-sectors—spinning, weaving, wet-processing, worsted fabric production, and carpet production—contributes to the energy use in the textile industry. A calculation of each plant's energy intensity was performed, and it was compared to that of other plants in the same sub-sector. The outcomes displayed the variety of energy intensities for plants in each sector. Energy-saving technologies utilized in the company include the usage of high efficiency motors (HEM), variable speed drives (VSD), economizers, leak prevention, and lowering pressure drop, according to (Saidur et al., 2012). Using these energy-saving technology results, it has been determined that the industrial sectors can save a considerable quantity of electric energy, pollutants, and utility costs. The majority of the time, payback periods for various energy-saving techniques have been acknowledged and proven to be economically viable.

2 METHODOLOGY

The required data collected from different sources in the site. The following are the necessary data required for the study:

(i) The electrical energy and fuel consumptions of the factory for the last three years.
(ii) Specification, working conditions and maintenance measures of the equipment in the utility plants.
(iii) The bill, lighting data and the history of production cost.
(iv) The measurements electrical source and power and the major energy intensive equipment.

The collected data was analyzed quantitatively and qualitatively as to reduce energy loss identified.

Motor master + International Motor Selection and Saving Analysis (IMSSA) software is a software tool for energy consultants, motor distributors, and industrial end users in planning and carrying out energy management and motor efficiency improvement actions. The software provides the energy and different currency savings obtainable through selection and use of an Energy Efficient or Premium Efficiency motor in three scenarios: new purchase, repair versus replace, and replacement of existing operable motors.

2.1 SGSC LIGHTING ANALYSIS OF THE ENERGY USAGE AND IMPROVEMENT

Factory Lighting system is delivered primarily by 5-foot florescent lamps mounted two per fitting. The florescent lamps are of standard wattage and many T-12fl tubes are used to provide light in the various sections or departments within the factory. Various terminologies are employed when quantifying light such as Luminous Flux, Luminous Intensity, Illumination, Illuminance. Some important mathematical expressions used to obtain data for this study are as follows.

- $TP = LR \times NL$ (1.0)

  Where: TP is total power, LR is lamps rating and NL is number of lamps.

- $TL_u = NL \times L_o$ (2.0)

Where, Tl_u = Total Lumen output of installed lamps in a section, L_o = Luminous output of each lamp.

- $IL_u = TL_u / RA$ (3.0)

Where, IL_u = Illumination produced by the installed lamps (expressed in Lux, 1Lux = 1Lumen/m^2), RA = Room Area of each section.

$$ALR = \frac{IL_u R}{IL_u} \times NL \quad (4.0)$$

Where, ALR = Actual Lamps Required for proper Illumination (used to analyze wastage of energy due to improper Illumination), IL_uR = Illumination Required in each Area.

$$EU = NL \times LR \quad (5.0)$$

Where, EU = Energy Utilization for the lighting systems (Kwh),

$$ER = ALR \times LR \quad (6.0)$$

Where, ER = Energy Required after proper Illumination (Kwh)

$$ED = EU - ER \quad (7.0)$$

Where, ED = Energy Difference (Kwh). It compares EU with ER after proper Illumination.

OH = Operating Hour.

Table I: Existing lighting system at SGSE.

No. of Lamps	971
Total Rating	50.316Kw/day
Energy Utilized	744.936Kwh/day

Methods of Improvements: Three methods of lighting improvement used were summarized in the following tables.

Table II: Improvement by replacing T-12fl lamps with T-8fl lamps.

Replaced No. of lamps	839
ER(Kwh/day)	656.992
SE(Kwh/yr) (30%ER)	68983.95
SA(#/yr)	2483422.2
SPP(YR)	2yrs.

Table III: By optimizing the Illumination of the existing system.

Reduced No. of lamps	132
Total Rating	5.736
ER(Kwh/day)	656.992
SE(Kwh/yr)	32,121.6
SA(#/yr)	1,156,377.6
SPP(yr)	0yr

Table IV: By removal of Dead Ballast from the system.

No. of Ballast to be removed.	120
ES(Kwh/yr)	
SA(#/yr)	13,435.76
SPP(yr)	483,687.36
	0yr

2.2 ENERGY ASSESSMENT IN BOTH COMPRESSORS.

The Instrumentation and Ash Handling compressors of the factory parameters were measured and recorded. Data were analyzed based on important parameters calculated and presented in Table V.

Table V: Summary of Energy saving Analysis from both compressors.

FAD TEST			
No.	Parameter	Results	
1	Air compressor type	instrument	Ash handling
2	Air speed (m/s)	14.23	14.17
3	Inlet air suction Area(m^2)	0.00419	0.00419
4	Actual flow rate (m^3/min)	3.577	3.562
5.	Average loading power(kw)/loading pressure (Bar)	23.18/6.7	23.18/6.8
6	Average loading time (s)	22.73	22.81

7	Average un-loading power(kw)/Un-loading pressure(Bar)	10.83/10.8	9.93/9.90
8	Average un-loading time (s)	30.48	30.53
9	Design flow rate (m^3/min)	9.072	9.072
10	Actual SPC (kw/cfm)	0.1814	0.1759
11	Design SPC (Kw/cfm)	0.1698	0.1511
12	Deviation SPC (Kw/cfm)	0.0116	0.0248
	Deviation Kw (power loss due to FAD Test)	1.4821	3.1553
	NO LOAD TEST (Air Leakage)		
13	Loading pressure (Bar)	6.7	6.8
14	Un-loading pressure (Bar)	7.8	7.2
15	Average loading time (s)	22.73	22.81
16	Average un-loading Time (s)	30.48	30.53
17	% of leakage during loading time	42.75%	42.76%
18	Actual free air leakage (cfm)	54.6217	54.4036
	Equivalent power loss due to leakage (Kw)	9.9084	9.5696
	Total Energy Loss(Kwh/yr)	**38,135.3940**	**42,602.9652**
	Total Money Loss(₦/yr)	**1,372,874.184**	**1,533,706.7472**
	Total energy/yr	**80,738.3592kwh/yr**	
	Total money/yr	**₦2,906,580.9312**	

2.3 ELECTRICAL MOTOR ANALYSIS.

A typical sugar industry has electric motors ranging from few Kw to a few MW. The three phase induction motors are the most widely used electric motors in the industry.

When considering energy-efficiency improvements in a facility's motor systems, a systematic approach used in order to achieve optimal savings and performance. The essential mathematical expressions and energy saving opportunities for electric drive system are formulas.

In deciding motors load, accurate measurement of motors actual power is essential base on the following parameters:

- P_{im} = measured input power (Kw) or
- P.F = Power Factor
- I = motors RMS Current (Average of 3-phase)
- V = motors RMS Voltage (L-L Voltage)

Imputed parameters are:

- Hp = motors rated power output (hp or Kw)
- η_{fl} = motors full load rated efficiency

The following mathematical expressions used to calculate P_{im}, P_{ir}, and Load.

$$P_{im} = \frac{\sqrt{3} \times I \times V \times PF}{1000} \quad (8.0)$$

$$P_{ir} = \frac{hp \times 0.746}{\eta_{fl}} \quad (9.0)$$

Where
P_{ir} = motors input power at rated full load (Kw)

$$Load = \frac{P_{im}}{P_{ir}} \times 100\% \quad (10.0)$$

Where,
Load = output power as a percentage of rated power.

3 RESULTS AND DISCUSSION

From Table II, III, and IV it shows how much in Naira saved, as well as how much of Energy saved.

From the Table V, Annual Energy loss from both compressors can be calculated which is 80,738.3592Kwh/year which is equivalent in Naira as ₦ 2,906,580.9312.

Using motor master+ international software as shown in Figure 1, It has been observed that switching from a 4 KW pump motor to an energy-efficient 1.5 KW pump motor can result in energy savings of 3,257 KWh per year and financial savings of ₦ 87,686.73 per year with payback times of 1.83 years. Additionally, replacing a normal motor with an energy-efficient motor results in a 71,605KWh/year energy savings and a ₦ 1,949,125.7016/year cost savings.

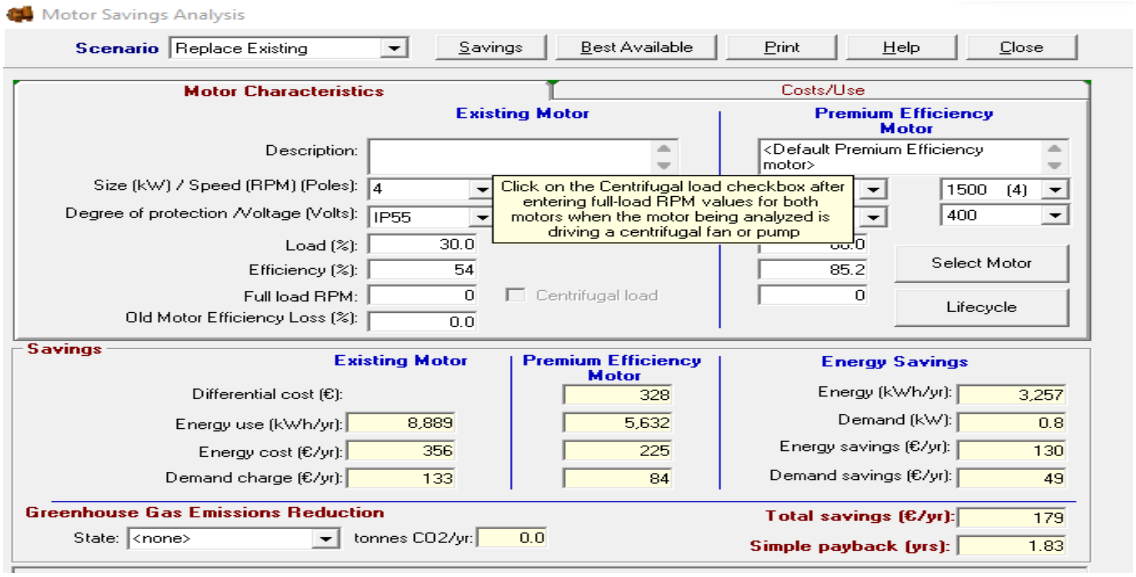

Figure 1: Motor saving analysis for 4 KW motor

Table VI: Existing under-loaded Motors in the Factory

		Existing Machine		
No.	**Machine Name**	**KW**	**Efficiency (n%)**	**Loading %**
1	Surplus Belt Conveyor	1.5	64.9	28.4
2	Ash Inertial Rotary	1.5	64.9	28.4
3	Back wash pmp.	4	54	30
4	Rotary Valve Feed Silo	0.75	75.5	30.2
5	Phosphate dosing	0.75	76	30.3
6	ACOP Motor(x2)	3.7	86.3	37.3
7	EOT CT	1	90.3	40
8	Lime Bin Rotary Valve(x2)	0.5	75.1	40
9	GVC Motor(x2)	2.2	81	40.4
10	Barring Gear Motor	7.5	88.7	41.4
11	PH Dosing pmp(x2)	3.7	86.3	43.2
12	SMBC(X2)	5.5	80.6	45
13	Cacuum filters (x2)	2.2	82.8	45.6
14	Service Water Pmps(x3)	22	91.6	45.9
15	C-Mascuite Liquid	15	90.6	46
16	B-Mascuite Tr. Pmp	15	90.6	46
17	Flash Tank Recir. (x2)	9.3	89.3	46.2
18	Mill ACW fan	9.3	88.9	47.2
19	Ash Silo	5.5	88.3	47.8

Table VII: Replaced with Premium Efficiency motors

No.	Machine Name	KW	Efficiency (n%)	Loading %	Energy cost euro/year	Energy saving KWh/year	Money saving euro/year	Payback period in years
1	Surplus Belt Conveyor	0.55	71.2	77.5	96	231	13	5.74
2	Ash Inertial Rotary	0.55	71.2	77.5	96	227	12	5.85
3	Back wash pmp.	1.5	85.2	80	225	3257	179	1.83
4	Rotary Valve Feed Silo	0.3	85.2	75.5	56	167	9	4.24
5	Phosphate dosing	0.3	85.2	75.7	56	165	9	4.28
6	ACOP Motor(x2)	1.5	88.3	92	259	3382	186	1.76
7	EOT CT	0.55	99	65.5	83	485	27	2.73
8	Lime Bin Rotary Valve(x2)	0.25	86.1	72	44	203	11	5.72
9	GVC Motor(x2)	0.9	82.2	98.8	187	804	44	2.1
10	Barring Gear Motor	4	98.7	77.6	560	5100	280	1.92
11	PH Dosing pmp(x2)	2.2	92.7	86.5	296	2444	134	2.89
12	SMBC(X2)	3.7	88.6	66.9	447	1106	61	4.58
13	Cacuum filters (x2)	1.1	84.1	91.2	191	801	44	5.12
14	Service Water Pmps(x3)	15	91.9	67.3	1758	18186	1000	1.29
15	C-Mascuite Liquid	7.5	95.6	92	1218	12012	661	1.28
16	B-Mascuite Tr. Pmp	7.5	95.6	92	1218	12012	661	1.28
17	Flash Tank Recir. (x2)	5.5	91.2	63	622	5780	318	2.12
18	Mill ACW fan	5.5	91.2	63	622	5780	318	2.12
19	Ash Silo	3.7	98.8	71.1	474	4332	238	1.17
	TOTAL					**71,605.00**	₦ 1,949,125.7016	

Table VII shows the Motor master + international software result of replacing standard motor with energy efficient motor which shows 71,605 KWh/year energy saving and ₦ 1,949,125.7016 per year cost saving. It is significant to replace large, partially loaded motors with smaller, fully loaded motors made of company stock or brand-new, energy-efficient motors. As a result, replacing ordinary motors with energy-efficient motors, i.e., replacing under-load motors with properly sized motors, can result in annual savings of 71,605 KWh of energy and ₦ 1,949,125.7016, with payback times ranging from 1.17 to 5.85 years.

4 CONCLUSION

The SSGC paid little attention to monitoring the factory's energy use and efficiency. The inference is that energy is been wasted because people are using it inefficiently. They might use this study to analyze their energy usage and efficiency trends, particularly with regard to their lighting system, air compressor, and boiler.

Moreover, they use the software Motor Master + International on their electric motors, which constitute the majority. The program aids in locating possibilities to increase system efficiency through energy use.

A detailed energy audi has been analysed. Based on the losses energy efficiency assessments on the major energy equipment's like electric motors, air compressors, boilers, and lightings have been done. It has been found from energy audit results that an annual Energy loss from both compressors can be calculated which is 80,738.3592Kwh/year which is equivalent in Naira as ₦ 2,906,580.9312/year. Using motor master+ international

software as shown in Figure 1, It has been observed that switching from a 4 KW pump motor to an energy-efficient 1.5 KW pump motor can result in energy savings of 3,257 KWh per year and financial savings of ₦ 87,686.73 per year with payback times of 1.83 years. Additionally, replacing a normal motor with an energy-efficient motor results in a 71,605 KWh/year energy savings and a ₦ 1,949,125.7016/year cost savings. It is significant to replace large, partially loaded motors with smaller, fully loaded motors made of company stock or brand-new, energy-efficient motors. As a result, replacing ordinary motors with energy-efficient motors, i.e., replacing under-load motors with properly sized motors, can result in annual savings of 71,605 KWh of energy and ₦ 1,949,125.7016 with payback times ranging from 1.17 to 5.85 years.

REFERENCE

Bhukya, P. (2014). Preliminary electrical energy audit analysis of mineral based industry. *International Journal of Scientific and Research Publications*, *4*(5), 1–6. www.ijsrp.org

Chan, D. Y. L., Yang, K. H., Hsu, C. H., Chien, M. H., & Hong, G. B. (2007). Current situation of energy conservation in high energy-consuming industries in Taiwan. *Energy Policy*, *35*(1), 202–209. https://doi.org/10.1016/j.enpol.2005.11.022

Frederiks, E. R., Stenner, K., & Hobman, E. V. (2015). Household energy use: Applying behavioural economics to understand consumer decision-making and behaviour. *Renewable and Sustainable Energy Reviews*, *41*, 1385–1394. https://doi.org/10.1016/j.rser.2014.09.026

Hasanbeigi, A., Hasanabadi, A., & Abdorrazaghi, M. (2012). Comparison analysis of energy intensity for five major sub-sectors of the Textile Industry in Iran. *Journal of Cleaner Production*, *23*(1), 186–194. https://doi.org/10.1016/j.jclepro.2011.10.037

Khan, A. M., He, N., Li, L., Zhao, W., & Jamil, M. (2020). Analysis of Productivity and Machining Efficiency in Sustainable Machining of Titanium Alloy. *Procedia Manufacturing*, *43*, 111–118. https://doi.org/10.1016/j.promfg.2020.02.122

Marinosci, C., Morini, G. L., Semprini, G., & Garai, M. (2015). Preliminary energy audit of the historical building of the School of Engineering and Architecture of Bologna. *Energy Procedia*, *81*, 64–73. https://doi.org/10.1016/j.egypro.2015.12.060

Nagaveni, P., Siva Ram Kumar, M., Nivetha, M., Amudha, A., & Emayavaramban, G. (2019). Electrical energy audit –an experience in a small scale textile mill. *International Journal of Innovative Technology and Exploring Engineering*, *8*(10), 4102–4107. https://doi.org/10.35940/ijitee.J9623.0881019

Oyedepo, S. O., Dirisu, J. O., Fayomi, O. S. I., Essien, E. E., & Efemwenkiekie, U. K. (2019). Energy evaluation and conservation strategies for a Nigerian private college facilities: Case analysis of energy audit of Covenant University. *AIP Conference Proceedings*, *2190*. https://doi.org/10.1063/1.5138566

Parthe, S. P., & Kompeli, S. (2017). Energy Audit and Conservation Tool for Energy Efficiency. *International Research Journal of Engineering and Technology*, 747–751. www.irjet.net

Rajput, S. K., & Singh, O. (2017). Energy audit in textile industry: A study with ring frame motor. *ICCCCM 2016 - 2nd IEEE International Conference on Control Computing Communication and Materials*, *Icccm*, 2–5. https://doi.org/10.1109/ICCCCM.2016.7918234

Saidur, R., Mekhilef, S., Ali, M. B., Safari, A., & Mohammed, H. A. (2012). Applications of variable speed drive (VSD) in electrical motors energy savings. *Renewable and Sustainable Energy Reviews*, *16*(1), 543–550. https://doi.org/10.1016/j.rser.2011.08.020

Yang, M. (2010). Energy efficiency improving opportunities in a large Chinese shoe-making enterprise. *Energy Policy*, *38*(1), 452–462. https://doi.org/10.1016/j.enpol.2009.09.036

4th International Engineering Conference (IEC2023)
Federal University of Technology, Minna, Nigeria

Integration of Robotics into Boat-operated Atalla Lift Net Manipulator Arms for Capturing of Clupeids (Freshwater Sardine)

*Okouzi, A. S[1], Ayuba, A. B[1], Eze, J. O[2], Ihuahi, J. A[1] & Bankole, N. O[3]
[1]Products Development and Engineering Department, National Institute for Freshwater Fisheries Research, P.M.B., 6006, New Bussa, Niger State, Nigeria
[2]Aquaculture and Biotechnology, National Institute for Freshwater Fisheries Research, P.M.B., 6006, New Bussa, Niger State, Nigeria
[3]Artisanal Fisheries, National Institute for Freshwater Fisheries Research, P.M.B., 6006, New Bussa, Niger State, Nigeria.
*Corresponding author email:okouziabhulimhen@gmail.com +2348072249543

ABSTRACT
The manual setting and hauling of the indigenous Boat-operated Atalla lift net for capturing of Clupeids particularly by women is laborious. In this study the control module "**NIFFR ATALLAPACK**" was developed for the integration of robotics into the Boat-operated Atalla lift net manipulator arms in the upgrading of the Atalla fishery for effectiveness and efficiency. A low-power CMOS (complementary metal-oxide semiconductor) 8-bit microcontroller based on enhanced reduced instruction set computing architecture; ATmega328Pplastic dual inline package was programmed as standalone. Minipro Universal Programmer Tl866cs was used for the programming of the control system. The ATmega328Pmicrocontroller was interfaced with an ASME-04B 380kg.cm 12-24VDC high-power high torque servo motor and a liquid crystal display. Arduino 1.8.13 integrated development environment was used for the processes of firmware development and debugging using a general-purpose low-level programming language C programming for Arduino to drive the process. The ATmega328P was found to be able to accept, and execute the code produced with Arduino IDE to drive the servo motor of the manipulator arms in the angular displacement pattern; 0° – 135° – 0°, with a delay of 3 minutes at 135° when the fishing gear is expected to be submerged for capturing Clupeids before discharging the content of the gear at the initial position of 0°. The automation of the fish capture technology reduced the operators of the system from two to one operator. The liquid crystal display served as the human machine interface displaying instructions as well as the state of the system for the user.

Keywords:*Boat-operated Atalla lift net, Embedded system developments, Fish capture technology, NIFFR ATALLAPACK, Robotics.*

1 INTRODUCTION

The operation of the indigenous Boat-operated Atalla lift net hitherto is a swift but redundant repetitive task which does not require a significant amount of decision making. Based on this backdrop the fish capture technology requires robotic process to automate the manual process of capturing Clupeids (Freshwater Sardine) for increased effectiveness and efficiency. The fishermen from the Ijaw tribe of Edo and Delta States seemed to possess the greatest expertise in using the Atalla gear. Attempt by other groups such as the Igbiras, Igala, Ibos, Isoko, Efik and Urhobos to copy this technology has been rather unsuccessful as a result of the special skill involved in it manual operation with its associated drudgery. Moreover, Awachie and Walson (1977) earlier in their study suggested possible modifications to facilitate less laborious operations. These modifications include: increase in the overall size of the gear from 12.0 m^2 to 25.4 m^2, use of stroke 2 nylon net instead of stroke 3 used by the fishermen, in order to reduce weight, modification of the pivoting device to eliminate the use of 'pedals' for depressing the gear into water as Pedals tend to reduce the life of raffia-palm poles, using wire cable instead of the natural fibres commonly employed by local fishermen for lifting the gear and the use of detachable horizontal poles to facilitate folding and storage of the gear under shelter, instead of open area storage where the nylon net is adversely affected by sunlight. Although these modifications have long been implemented, the Atalla technology in the capturing of Clupeids has not change considerably from it indigenous nature with its backbreaking effects on the users which can also be attributed to its primitive human machine interface (HMI). Lift nets can be hauled mechanically through bomm(s) and blocks (He *et al.*, 2021 and Gabriel *et al.*, 2005). Although Winches have been used for mechanically handling of the lift net (FAO, 2021), it is either that such devices are not available or expensive in developing countries like Nigeria. To the extent of the literature search, no work was found on the automatic control of lift net.

Robotics is a form of industrial automation and is the science of designing and building robots suitable for real-life applications in automated manufacturing and non-manufacturing environment (Ramachandran *et al.*, 2015). Automation being the "technology" that is concerned with the use of mechanical, electronic and computer based

systems in the operation and control of production. Hence, a robot is a reprogrammable and multifunctional manipulator, devised for the transport of materials, parts, tools or specialized systems, with varied and programmed movements, with the aim of carrying out varied tasks (Todd, 1986). The redefined mechanism of the Boat-operated Atalla lift net for the capturing of Clupeids, is to be used in the like manner of an industrial robot in the sense that it is to be used as manipulator arm which automatically repeats a cycle of operations under program control. Such manipulators are kinematically composed of a set of rigid body (links) connected by joints to form an open kinematic chain coupled by revolute or/and prismatic kinematic pairs (Jazar, 2010).The control of the Boat-operated Atalla lift system comprises three computational problems viz-a-viz: determination of the Cartesian coordinate space, trajectory, transformation of the Cartesian trajectory into equivalent joint coordinate space, and generation of the motor torque commands to realize the trajectory. The kinematic descriptions of the Boat-operated Atalla manipulators and their assigned tasks are further utilized to set up the fundamental equations for dynamics and control.

The most important considerations in the application of the Atalla lift net manipulator arm (as an industrial robot) centers on manipulation and integration issues. The combined effects of kinematic structure, axis drive mechanism design, and real-time motion control determine the major manipulation performance characteristics: reach and dexterity, payload, quickness, and precision. Reach is characterized by measuring the extent of the workspace described by the robot motion and dexterity by the angular displacement of the individual joints. Payload weights are specified for extreme velocity and reach conditions. Quickness is critical in determining throughput specified mostly for maximum speed of individual joints. However, average speed in a working cycle is the quickness characteristic of interest. Precision is usually characterized by measuring repeatability as well as specify static position repeatability.

Robot controllers are specialized multiprocessor computing systems that provide four basic processes allowing integration of the robot into an automation system vis-à-vis motion trajectory generation and following, motion/process integration and sequencing, human user integration, and information integration.

Two important controller-related aspects of the manipulator arm as an industrial robot motion generation are the extent of manipulation that can be programmed and the ability to execute controlled programmed motion (Lewis *et al,* 2004). The manipulator's controller, through its operating system programs, converts digital data from higher-level coordinators into coordinated arm motion through precise computation and high-speed distribution and communication of the individual axis motion commands which are executed by individual joint servo-controllers. The real-time motion controller invariably uses classical independent-joint proportional-integral-derivative (PID) control or simple modifications of PID which makes commercially available controllers suitable for point-to-point motion. However, for continuous position/velocity profiles or exerting prescribed forces, considerable programming effort is further required.

Motion/process integration and sequencing involve coordinating manipulator motion with process sensors or other process controller devices. The most primitive process integration is through discrete digital input/output (I/O).

More recent advanced robot interface techniques are based on behaviour based programming, where various specific behaviours are programmed into the robot controller at a low level (e.g. pick up piece, insert in machine chuck). The behaviours are then sequenced and their specific motion parameters specified by a higher-level machine supervisor as prescribed by the human operator.

An excellent way to gain an intuitive feel for the control systems design and performance was to perform the virtual system modeling (VSM) simulations. Simulation modelling is conceptually a short step from simulation to actual implementation, since the subroutines that are used on present day's digital signal processors are very similar to those used for simulation. Therefore, satisfied with the capability of the VSM simulation to adequately prototype the automation of the system, the aim of the present study is to automate the manually Boat-operated Atalla lift net for capturing of freshwater sardine by incorporating robotics manipulator arms to improve effectiveness and efficiency with the following objectives:

i. To develop a control module for the Boat-operated Atalla lift net system.
ii. To verify the performance of the control of the boat-operated Atalla lift net manipulator arms by motion testing.

This will enable the automation of the gear so that the operator focuses on rowing/control of the boat with the paddle/oar as well as teleoperation (Vertut and Coiffet, 1985) of the Atalla lift net.

2 METHODOLOGY

Systems engineering as well as bottom-up digital design methodologies were employed for the implementation of the automation of the Boat-operated Atalla lift net manipulator arms' drive in the development of the embedded system and automation of the fish capture technology.

2.1 ATALLA CONTROL MODULE DEVELOPMENT

The Boat-operated Atalla control module is a component, a control unit expected to be used on the Boat-operated Atalla lift net. It is a collection of sensor, actuator, and basic control logic that act as a regulating device as well as a state-oriented device that is operated as a single entity. It involves integration of hardware and software as described in Figure

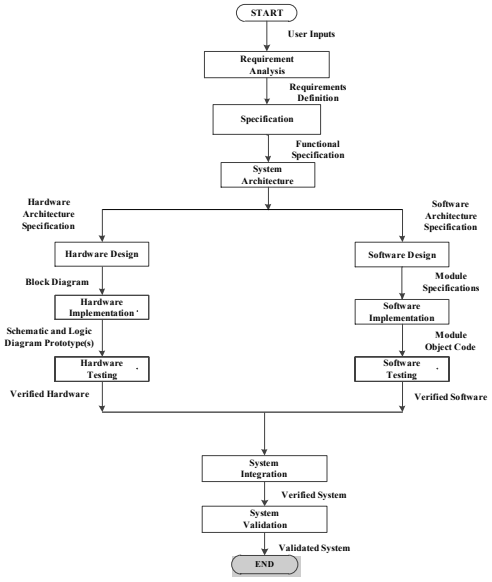

Figure 1: Atalla Lift Net Control Module Embedded Design and Development Process

The control module implements algorithm-oriented control from the Atalla Lift Net Manipulator Arms' Drive VSM Simulation.

2.2 BOAT-OPERATED ATALLA LIFT NET EMBEDDED SYSTEM DESIGN AND PROGRAMMING

An embedded system is a system whose principal function is not computational, but which is controlled by a computer embedded within it (Wilmshurst, 2007).Figure 2 is the hardware system design block diagram.

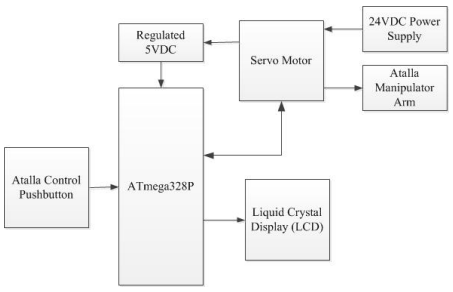

Figure 3: Hardware System Design

Therefore, embedded systems programming (ESP), consists of building the software control system of a computer-based product (Green, 2008). A low-level microcontroller unit (MCU) ATmega328P 28-Pin PDIP (see Figure 2) powered by regulated 5VDC from the servo motor was programmed for the servo motor control system of Boat-operated Atalla lift net manipulator arms' drive. The C compilers Arduino 1.8.13IDE (Warren *et al*., 2011),was used for both firmware (control software: sketch model) development and for firmware debugging.

Consequently, Table 1 present the configuration used in accessing the input/output (I/O) pins in the Arduino IDE coding for the standalone ATmega328P microcontroller unit with the pin-out.

Table 1: ATmega328P Pin Configuration on Arduino IDE

ATmega328P Pin Number	Arduino Code
11	5
12	6
13	7
14	8
15	9
16	10
17	11
18	12
19	13
23	14
24	15
25	16
26	17
27	18
28	19
4	2
5	3
6	4

The sketch model consists of four sections. The first section declares the library of the different drives by including the library code. These include the drive for the liquid crystal display and that of the servo motor. Thereafter, the LCD library is initialized with the numbers of the interface pins and then servo object is created to control the servo. The second section declares the integer and constant variables. These include the time and the count which are all set equal to zero. The pin numbers of the pushbutton and buzzer are further declared as constant integer. The third section is the void setup( ){ }. This is a **declaration for a function** called "setup". This exact line is required in every Arduino sketch ever. The void setup routing is technically a function that is created at the top of each program. Inside the curly brackets is the code

that is expected to run one time as soon as the program starts running, after each power-up or reset of the MCU. It is used to initialize variables; the pushbutton pin is set up to be an input under this section, the buzzer pin is set to be both input as well as output pin modes. This section also starts using libraries: attaches the servo motor to the servo object, set up the LCD number of columns (16) and rows (2) with the instruction to print the Boat-operated Atalla lift net control module brand name ***"NIFFR ATALLAPACK"*** to the defined cursor positions (column, row), which is expected to be displayed for 5000 milliseconds (5 seconds) after which the LCD is cleared. Also with the pushbutton activated, the countdown is set to 3 minutes. The last section of the model is the void loop( ){ }. Like the setup line before it, void loop is yet another Arduino-sketch function that Arduino uses as a part of its structure. The code inside the loop function runs over and over (repeatedly) as long as the MCU is turned on. This is where the bulk of the Arduino sketch is executed. The program starts directly after the opening curly bracket ({), runs until it sees the closing curly bracket (}), and jumps back up to the first line in loop() and starts all over. It begins with the instruction to Get the digital state of button as count = 1 which starts the motor. Once the motor starts, the LCD is cleared and the state of the motor is also printed to the LCD. Once the servo attains the position of 135°, the LCD is cleared and the time countdown (at 1000 milliseconds) and printed to the LCD. The Buzzer beeps for 50 to alert at countdown 15 seconds. At the point the set time countdown elapses, the motor also drives the arm from 135° to 0° to begin the loop of the plunging and hauling cycle of operation of the Boat-operated Atalla lift net. Then the LCD is cleared, again count = 1, time set to 3 minutes and ***"Press Button to Start Motor"*** printed to the LCD.

The Arduino IDE employs the program AVRDUDE (AVR downloader uploader). AVRDUDE is a utility to download, upload and manipulate the ROM and EEPROM (electrically erasable programmable read-only memory) contents of Atmel AVR microcontrollers using the in-system programming (ISP) technique. Hence, it converts the executable code into a text file in hexadecimal (HEX file) encoding that is susequently loaded into the MCU by a programmer (Banzi and Shiloh, 2015). The HEX file created after building the program (sketch) in Arduino IDE was then uploaded into the ATmega328P using a Minipro Universal Programmer Tl866cs.

3 RESULTS AND DISCUSSION

This section presents the results of the implementation. Figures 3 presents the Atalla control module (NIFFR ATALLAPACK) developed, Figure 4 is the Boat-operated Atalla lift net numerical motion testing result while Figures5a-h also present the implementation (robotics) of the Boat-operated Atalla lift net manipulator arms' drive results also in accordance with the procedure of operation of the developed control module.

The operator of the Boat-operated Atalla interact with the system by pressing the AtallaPack button and initiates the control of the actuator which actuate one of the two-link manipulator polar arms of the Atalla lift net while the LCD in turn displays instructs as well as the state of the system to the operator. This enables the lift net to be controlled from a distance in the process of teleoperation.

Figure 3: Boat-operated Atalla Lift Net Control Module (NIFFR ATALLAPACK)

The control module is designed to interface with an ASME-04B 380kg.cm 12-24VDC high-power high torque servo motor with the terminals (black, red and black) on the left hand side. The red and black are configured for power (ranging from +5V to +24V) and ground respectively while the separate black is configured to send pulse width modulation (PWM) signal generated by the MCU to drive the servo motor.

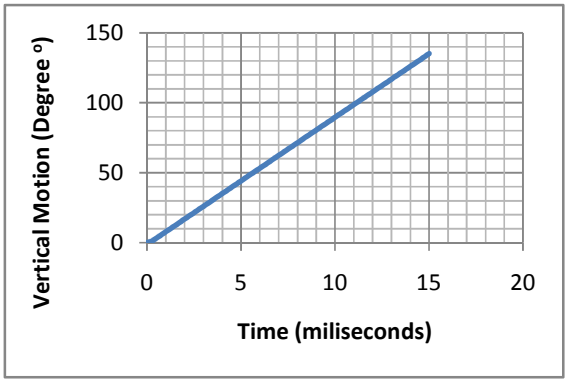

Figure 4: Boat-operated Numerical Motion Testing

The numerical motion testing of the Boat-operated Atalla lift net manipulator arm of Figure 4 shows that it takes the servo motor 15 miliseconds to drive the arm from it rest (0^o) through a vertical angular distance of 135^ointo the water for setting the gear to capture Clupeids.

Figure a: Robotics of Boat-operated Atalla Lift Net Manipulator Arms

Figure b: Atalla Lift Net Manipulator Arms' Drive at Rest or to Discharge the Catch

Figure c: Display with Instruction to Start Motor which is Still at Rest

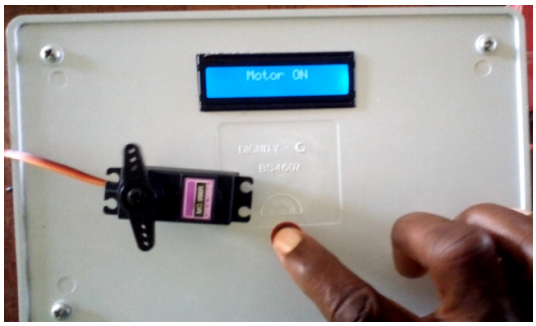

Figure d: Activation of Button, Display with Motor on and Motor Begins to Move

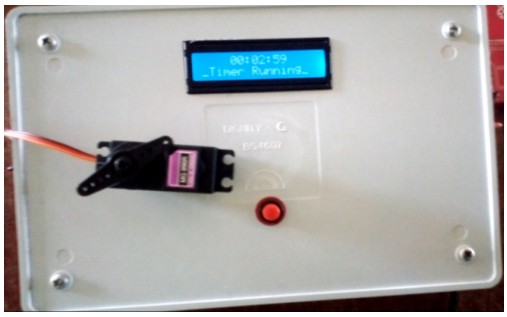

Figure e: Drive Position of Submerge Atalla Lift Net Manipulator Arms for a Catch and Count Down Display

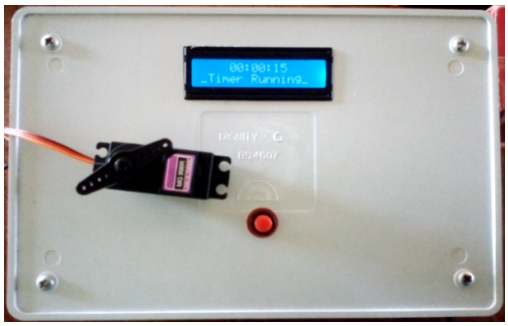

Figure f: Alarm with a Beep for Alert at Countdown 15secs

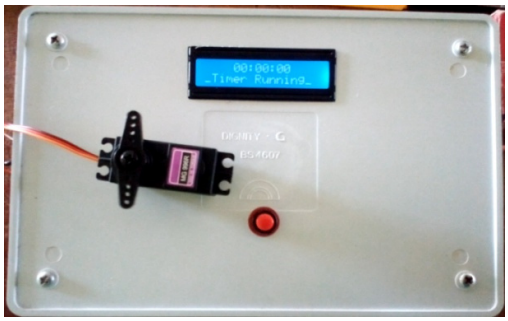

Figure g: Discharge Position, Motor back to Rest and End of Countdown

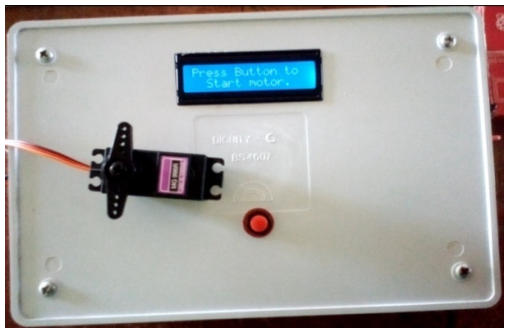

Figure h: System Ready for another Cycle of Operation

Figure 5: Operations of the Boat-operated Atalla Lift Net Control Module (NIFFR ATALLAPACK)

Activating the control module power switch on the right hand side of the control module (see Figure 3) displays the brand name ***"NIFFR ATALLAPACK"*** on the LCD as shown in Figure 5b for 5secs after which the operator is instructed to ***"Press Button to Start Motor"*** as shown in Figure 5c.

Once the button is pressed as see in Figure 5d and the LCD displays ***"Motor On"*** also as shown in Figure 5d, the servo motor drives the Atalla lift net into the water to an angular displacement of 135°, the position at which the net is set against the flow so as to capture schools of Clupeid and other forage (prey) fish within the pelagic zone.

Figure 5e presents the set position of the lift net and the beginning of the countdown from 3 minutes when the lift net attains the desired angular position of 135° for capturing of Clupeids.

The operator is alerted with a beep sound from the buzzer in the control module that the time left is 15 seconds as shown in Figure 5f. This is to enable the operator to get ready for the return and discharge of the lift net when the countdown gets to zero as in Figure 5g.

The end of the countdown signals the completion of the setting and hauling cycle of operation of the Boat-operated Atalla lift net for capturing of Clupeids. The normal practice is that the operator changes to a new location to initiate another cycle of operation as shown on the LCD of Figure 5h.

4 CONCLUSION

The integration of robotics enabled the automation of the operation of the Boat-operated Atalla lift net system. Consequently, a control module **"NIFFR ATALLAPACK"** specifically for the Atalla lift net was developed for the automated system. The results of the integration of robotics obtained similar to those of the virtual system modelling simulation also showed that the microcontroller unit (MCU) is able to accept, and execute the code produced with the C compiler to drive the servo motor of the Atalla manipulator arms in the angular displacement pattern; 0° - 135° - 0°, with a delay of about 3 minutes at position 135° during which the gear is set for capturing of Clupeids. The liquid crystal display (LCD) further served as the human machine interface (HMI) to instruct the user as well as display the state of the system. The automation of the fish capture technology reduced the operators of the Boat-operated Atalla lift net system from two operators to one teleoperator. Consequent upon the successful implementation of the automation of the Boat-operated Atalla lift net manipulator arms' drive, the production of the automated Atalla lift net system is recommended.

REFERENCE

Atmel, (2016). *Atmel ATmega328/P Datasheet*, San Jose, CA: Atmel Corporation.

Awachie, J.B.E. and Walson, E.C. (1977). The Atalla Fishery of the Lower Niger, Nigeria. *Paper Presented at CIFA Symposium on River and Floodplain Fisheries*, Bujumbura, Nov 77. (SIFA/77/Symp.12).

Banzi, M and Shiloh, M. (2015). *Getting Started with Arduino*, 3rd ed., Sebastopol CA.

FAO (2021). Fishing gear types: Lift nets. Fisheries and Aquaculture Department. Food and Agriculture Organization of the United Nations. Retrieved from http://www.fao.org/fishery/geartype/105/en

Gabriel, O., Lange, K., Dahm, E. and Wendt, T. (2005). *Fish Catching Methods of the World*, 4th ed., Oxford: Blackwell Publishing.

Green, T.D. (2008). *Embedded Systems Programming with the PIC16F877*, 2nd ed., Ohio:

He, P., Chopin, F., Suuronen, P., Ferro, R.S.T., and Lansley, J. (2021). *Classification and Illustrated Definition of Fishing Gears*, FAO Fisheries and Aquaculture Technical Paper No. 672. Rome: FAO.

Jazar, R.N. (2010). *Theory of Applied Robotics,* 2nd ed., New York: Springer Science+Business Media, LLC.

Lewis, F.L., Dawson, D.M. and Abdallah, C.T. (2004). *Robot Manipulator Control: Theory and Practice*, 2nd ed., Revised and Expanded, New York: Marcel Dekker, Inc.

Ramachandran, S., Lazarus, S.B. and Vijayalakshmi, P. (2015). Robotics, Chennai: Air Walk Publications.

Todd, D.J. (1986). *Fundamentals of Robot Technology: An Introduction to Industrial Robots, Teleoperators and Robot Vehicles*, London: Kogan Page Ltd.

Vertut, J. And Coiffet, P. (1985). *Teleoperations and Robotics: Evolution and Development*, London: Kogan Page.

Warren, J., Adams, J. and Molle, H. (2011). *Arduino Robotics*. California: Apress Media, LLC.

Wilmshurst, T. (2007). *Designing Embedded Systems with PIC Microcontrollers: Principles and Applications*, New York: Newnes.

4th International Engineering Conference (IEC 2022)
The Federal University of Technology, Minna, Nigeria

APPLICATION OF ARTIFICIAL NEURAL NETWORK-BASED FAULT DIAGNOSIS ON 330kV TRANSMISSION LINES:

(A case study of the Gwagwalada-Katampe transmission line)

*Bello, M. S[1], Babatunde, A.A[2], & Imoru, O[3]

[1]Electrical and Electronics Engineering Department, Federal University of Technology, PMB 65 Minna Niger State, Nigeria

[2]Electrical and Electronics Engineering Department, Federal University of Technology, PMB 65 Minna Niger State, Nigeria

[3]Electrical and Electronics Engineering Department, Federal University of Technology, PMB 65 Minna Niger State, Nigeria

*Corresponding author email: zube4mbello@gmail.com +2348032356051

ABSTRACT

This research focuses on stimulating an intelligent fault detection system to detect and classify multi-faults on the 330 kV Gwagwalada-Katampe transmission line. In this work, we use a feedforward neural network with a backpropagation algorithm to train the system. The transmission line was modeled in Simulink using the SimPowerSystems toolbox and simulations were performed in the MATLAB environment. Instantaneous voltage, current, and settling time values were extracted and used to train the model. Different fault types were considered for detection. These are single-phase ground faults (R-G, B-G, Y-G), two-phase ground faults (R-B-G, R-Y-G, B-Y-G), three-phase ground faults (R-B-Y-G), phase-to-phase ground faults (R-B, R-Y, B-Y), and three-phase ground faults (R-B, R-Y, B-Y). Phase-to-ground fault. Fault (R-B - Y). Simulation results documented 91% accuracy in the performance of the artificial neural network-based method compared to other types of techniques used to detect transmission line faults for all fault types. Results show fault detection and classification. Furthermore, the results show that three-phase faults are the most difficult to detect. The simulated artificial neural network can be employed on the 330 kV Gwagwalada-Katampe transmission line.

Keywords: Artificial Neural Network, Classification, Fault Detection, intelligent multi-faults classification model, Transmission Line, MATLAB/SIMULINK.

1 INTRODUCTION

With about half of Nigeria's rural population having little or no access to electricity, the need for a reliable power supply is steadily increasing (Alao, & Awodele, 2018). There are two major ways of generating electricity such Conventional and non-conventional power generation. In some cases, generation options can be classified as renewable and non-renewable. In Nigeria, all grid-connected power plants are conventional power plants, mainly gas turbine power plants and hydropower plants (Saturday 2021).

The world's power grid grew rapidly, eventually resulting in the installation of a large number of new transmission and distribution lines. However, this request has many limitations. The introduction of new marketing concepts such as deregulation has increased the need for a reliable and uninterrupted supply of electrical energy to end users who are highly sensitive to power outages. Adequate electricity supply is therefore an inevitable requirement for the development of any country, and generation, transmission, and distribution are capital-intensive and require enormous resources, both financial and capacity. (Sambo, Garba, Zarma, & Gaji, 2010).

Nigeria's energy sector is divided into policy, regulatory, customer, and operational (Alao, & Awodele,2018). In addition, the operations department reveals the activities of the Transmission Company of Nigeria (TCN). A TCN manages the supply of high-voltage power from a power

plant to a substation for transmission to a distribution substation. The Transmission Company of Nigeria (TCN) manages a 330 kV system capacity of 12,522 MW of power from existing power plants over a total distance of 5,650km, which is insufficient for a country of over 200 million people. Their focus is on maintaining power system stability, reliability, and sustainability. One of the most important factors preventing continuous power supply is grid disturbance. Abnormal current flow through power system components can cause network system failures. These faults cannot be eliminated by the main protection systems currently in use. Distance protection predominates and is therefore subject to relay limitations in protection schemes i.e reach setting. These faults can also occur for natural reasons and are always beyond human control (Okwudili et al., 2019).

In this regard, a well-coordinated protection system can detect any kind of abnormal current flow in the power system, identify the type of fault, and locate the fault in the power system. is very important. Faults are usually rectified by devices that detect the occurrence of faults and ultimately isolate the faulty section from the rest of the power system (Mbamaluikem, Awelewa, & Samuel, 2018).

Therefore, the identification of transmission line disturbances (TL) plays an important role in power system operation and control. It performs an important function in maintaining the health of the power system and promoting the safety of power system operation. In addition, accurate identification of faults forms the basis for power system protection along transmission lines, facilitates rapid prediction of power system faults, and ensures diagnosis of faults related to power system components.

Some of the major challenges for uninterruptible power supplies are fault detection, classification, and location. There are various types of faults; temporary, permanent, symmetrical, or asymmetrical, the fault detection process for each of these faults is unique in some sense, and all these types of faults have a universal fault location (Okwudili, Eze Chukwu, & Onuegbu, 2019).

Unlike power lines, there is no insulation around power line cables because high-voltage power lines are more prone to accidents than local distribution lines. Transmission line failures could happen for many reasons, including contact with trees, contact with animals, or natural causes such as thunderstorms and lightning. Automatic fault location greatly improves system reliability. The sooner power is restored, the more money and precious time you save. Therefore, many power companies use the Global Information System “GIS” to implement fault isolation devices in their power quality monitoring systems. You can easily identify these faults.

In this work, we demonstrate the application of artificial neural networks for transmission line fault diagnosis in terms of fault detection, fault location, and scheme application, in contrast to conventional approaches such as traveling wave approaches and synchronous compensators.

In this regard, fault location methods can be broadly classified into the following categories:

I. Impedance measurement-based method

II. Traveling wave phenomenon-based method

III. high-frequency components of currents and voltages generated by fault-based methods

IV. Intelligence-based method

Intelligent methods are used for fault detection and location. The three main artificial intelligence-based technologies used in the power and automation industry are:(Madueme & Wokoro, 2015):

i. Expert System Techniques
ii. Artificial Neural Networks
iii. Fuzzy Logic Systems

Among intelligent technologies, artificial neural networks (ANNs) are used in this proposed work for fault diagnosis and maintenance of transmission lines. Therefore, by applying an artificial neural network to transmission lines, we aim to maximize power continuity by stably supplying power and diagnosing power system failures. (Okwudili et al., 2019).

Neural Network Design

A neural network element is the smallest processing unit in the entire network, basically taking a weighted sum and transforming it by an activation function to get an output. Several neurons are interconnected to obtain sufficient computational power. How the neurons are connected depends on the different classes of neural networks. Neurons are arranged in layers. ANN has a parallel distributed architecture with many nodes and links.(Hatata, Hassan, & Eskander, 2016).

ANN Architecture

The construction of neural Networks involves the following tasks.

Determination of network topology

Determination of system (activation & synaptic) dynamics

Determination of the Network Topology

A neural network's topology is related to both its framework and its connectivity scheme. The framework is often set by the number of layers and the number of nodes per layer. Layer types are (Hatata et al., 2016):

Input layer. Nodes, called input units, distribute information to other units instead of processing it.

A hidden layer called Hidden entities whose nodes are not directly observable. Networks offer the possibility of mapping or classifying nonlinear problems.

An output layer, called an output unit, in which nodes encode concepts (or values) that may be assigned to the instance under consideration. For example, each output unit represents a class of objects. Another important concept is the weight of the connected units. Can be real or integer. They can be restricted to areas and adjusted during network training.

Determination of Systems (Activation & Synaptic) Dynamics

Neuronal dynamics consist of two parts, one corresponding to activation-state dynamics and the other to synaptic weight dynamics. Activation dynamics determine the temporal development of neuronal activation. Synaptic activation determines changes in synaptic weights. Synaptic weights form the long-term memory (LTD), and activation states form the network's short-term memory (STM). Synaptic weights change gradually, whereas neuronal activation fluctuates rapidly. Therefore, the system weights are assumed to be constant when computing the activation dynamics. The synaptic dynamics dictate the learning process (Kalu & Madueme, 2018).

2 POWER SYSTEM NETWORK SIMULATION

The system studied is the Transmission Company of Nigeria 330/132/33 substation Gwagwalada-Katampe, which connects the generating station with the distribution system. It has four transmission lines Lokoja-Gwagwalada line 1 and line 2, Shiroro- Gwagwalada line 3, and Gwagwalada-Katampe line 4 that are all connected with turn-in and turn-out bus-bar arrangement as shown in the schematic representation of the single-line diagram of Figure 2.1.

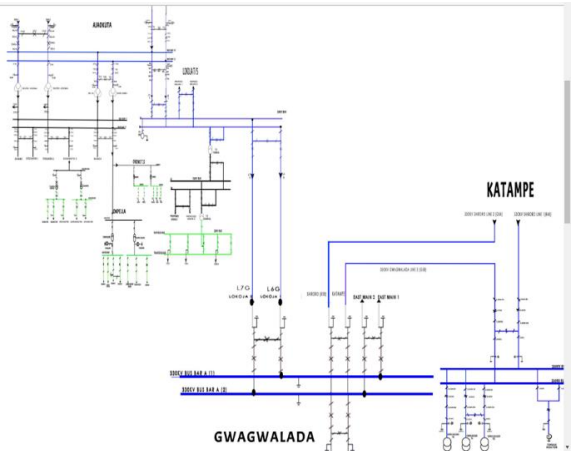

Figure 2.1: Single line diagram of 330 kV Gwagwalada-Katampe Transmission Company

3 METHODOLOGY

This section consists of methodological steps for detecting and classifying faults in a 330 kV Gwagwalada-Katampe transmission line using an artificial neural network (ANN method).

Table 3.1 shows the system parameters used for modeling, training, and testing the ANN procedure.

TABLE 3.1: TRANSMISSION LINE PARAMETERS

Line Parameters	Values
Line Length	140 km
Positive- and zero-sequence resistance (Ohms/km):	[0.01273 0.3864]
Positive- and zero-sequence inductances (H/km):	[0.9337e-3 4.1264e-3]
Positive- and zero-sequence capacitances (F/km)	[12.74e-9 7.751e-9]
Fault Resistance	0.001

Simulink Model Design for Fault Detection

The three-phase power system model is simulated in MATLAB/Simulink software.330kV, 50Hz,140km transmission line power system. It consists of voltage and current measurements, circuit breakers, transmission lines, and loads, as shown in Figure 3.1. The main purpose of transmission lines is to deliver power to loads. The power generated by the generator is supplied to the load via the power transmission line network. The load is the feeder of the load, the load that the load supplies, and if the kVA is unbalanced, the ANN can see faults such as overload current. Traditional algorithms are based on Kirchhoff voltage and current laws for well-defined transmission line protection models.

Conventional distance relays view voltage and current power swings as fault and trip mechanisms. Such faulty components have serious consequences and contribute to power system instability. Applying artificial neural networks to power line disturbances yields accurate results.

A Simulink model of the one-line diagram in Figure 2.1 is shown in Figure 3.1.

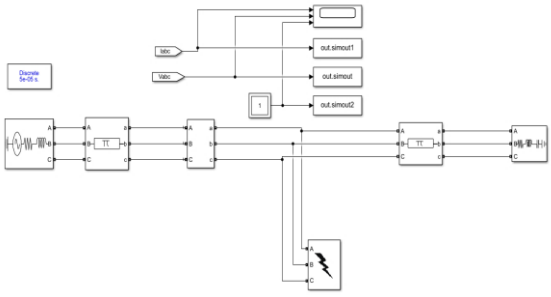

Figure 3.1: Simulink Model

Data Pre-processing

The generated dataset was preprocessed and split into training and test data. Preprocessing was performed to normalize the input to match the ANN input pattern from 0 to 1. This represents bias and improves the classification rate.

Training and Testing Data

Several different training algorithms for ANN are available (Madueme & Wokoro, 2015). All of these algorithms use the gradient of the power function to determine how to adjust the weights to minimize power. Gradients are determined using the backpropagation technique. This involves performing computations backward through the network. There are many algorithms available to implement the backpropagation method for speed and memory allocation considerations. Various general and improved variations of BPNN have been proposed over the years to specifically address several key issues such as faster convergence time, simplified computational load, and reduced memory footprint. (Okwudili et al., 2019)

Training and test data are used to train and test the intelligent model, as shown in Table 3.2. A total of 8,541 samples were selected for both training input and target, 1,220 for validation, and 2,440 for testing.

TABLE 3.2: TRAINING AND TESTING

Models	No of samples	Percentage (%)
Training	8541	70
Validation	1220	10
Testing	2440	20

Model training

An ANN model was developed to train the generated, preprocessed, and split data as described above. The training parameters are shown in Table 3.3. For each parameter, the reason for choosing such a parameter was given. It can be seen that the feed-forward neural network (FF-NN) model was chosen for its efficiency and good classification task, and the three layers (input-hidden-output) were chosen for its requirements. Back-Propagation Scale Conjugate Gradients (BP-SCG) were considered in the training algorithm due to their high speed and accuracy, and 40 neurons in the hidden layer with six input-output neurons in the multi-fault scenario, which were considered sufficient for the multi-fault scenario.

TABLE 3.3: SHOWS THE MODEL PARAMETERS

	Model parameter	Reason
Model Type	FF- Neuron	Excellent for classification problem
Number of layers	Three layers (input-hidden-output)	Required
Training algorithm	Backpropagation scale conjugate gradient (BP-SCG)	Very fast and accurate
Number of Neurons input	6	Number of inputs for multi-fault scenario
Number of Neurons hidden layer	40	Experiment to be Adequate
Number of the Neuron's output layer	12	Number of outputs for multi-fault scenario

Model Testing

The trained model was tested using 20% of corresponding data, and 2,440 samples from the various faults scenarios previously mentioned. For each sample, the Artificial Neural Network model detected the fault type and produced outputs corresponding to the fault types specified in the target vector.

After testing all 2,440 samples, we measured the model's performance by comparing the model's output to the target's output.

Performance Evaluation

The model performance was evaluated after testing the model using the following performance matrices calculated from the confusion matrices:

Accuracy: This measures the ability of the model to find the correct fault types. It is given as

$$\text{Accuracy} = \frac{TP+TN}{TP+TN+FP+FN} \quad (1)$$

Where:

TP is the true positive, FP is the false positive, TN is the true negative and FN is the false negative.

Sensitivity: This measures the ability of the model to detect positive faults.

It is represented as $\text{Sensitivity} = \frac{TP}{TP+FN}$ (2)

Specificity: This measures the ability of the model in detecting negative faults

$$\text{specificity} = \frac{TN}{TN+FP} \quad (3)$$

4 RESULTS AND DISCUSSION

The trained ANN-based classified modules were then extensively tested using the data sets consisting of fault scenarios in the training. Fault type, fault location, and fault time were changed to investigate the effects of these factors on the performance of the proposed algorithm. Figure 4.1: Simulated Result for (a) Normal Condition, (b) Single Phase-to-Ground Fault Scenario (c) Double Phase-to-Ground Fault Scenario (d) Three Phase-to-Ground Fault Scenario (e) Phase-to-Phase Fault Scenario

No-Fault Scenario

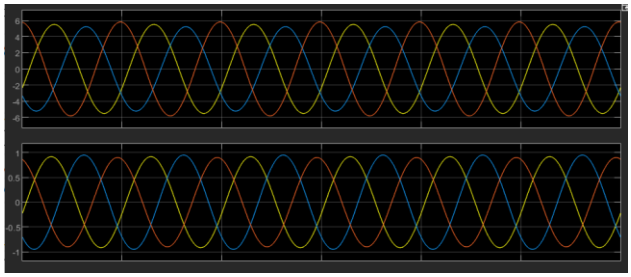

(a) Normal Waveform for Three-Phase Voltage (V_{RYB}) and Current (I_{RYB})

Single Phase-to-Ground Fault Scenario

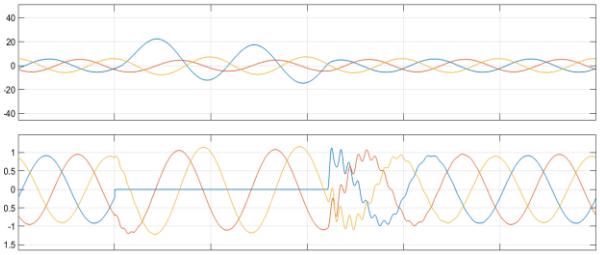

(b) B-G Fault Waveform for Three-Phase Voltage (V_{RYB}) and Current (I_{RYB})

Double Phase-to-Ground Fault Scenario

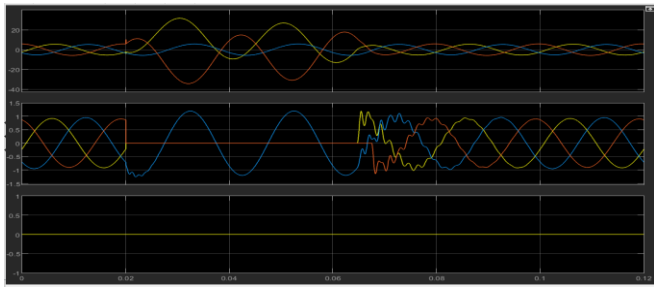

(c) R-Y-G Fault Waveform for Three-Phase Voltage (V_{RYB}) and Current (I_{RYB})

Three Phase-to-Ground Fault Scenario

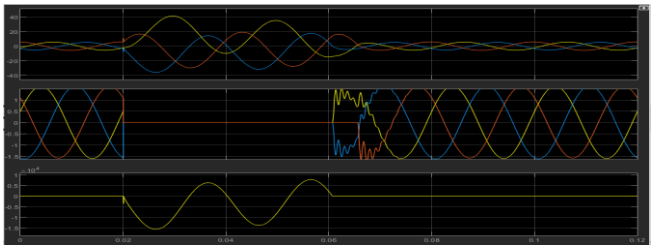

(d)R-B-Y-G Fault Waveform for Three-Phase Voltage (V_{RYB}) and Current (I_{RYB})

Phase-to-Phase Fault Scenario

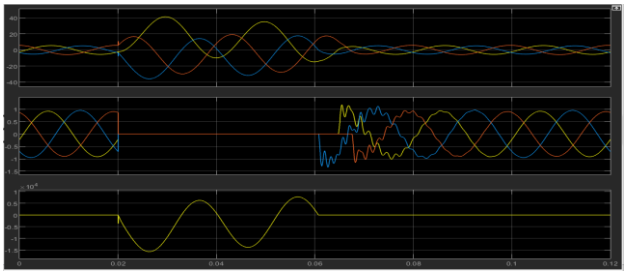

(e) B-Y Fault Waveform for Three-Phase Voltage (V_{RYB}) and Current (I_{RYB})

These faults were used to generate the data set for training the intelligent system.

Faults Classification Results

The results obtained from the intelligent multi-faults classification model are presented in this section as shown in Figure 4.2 and Figure 4.3 respectively.

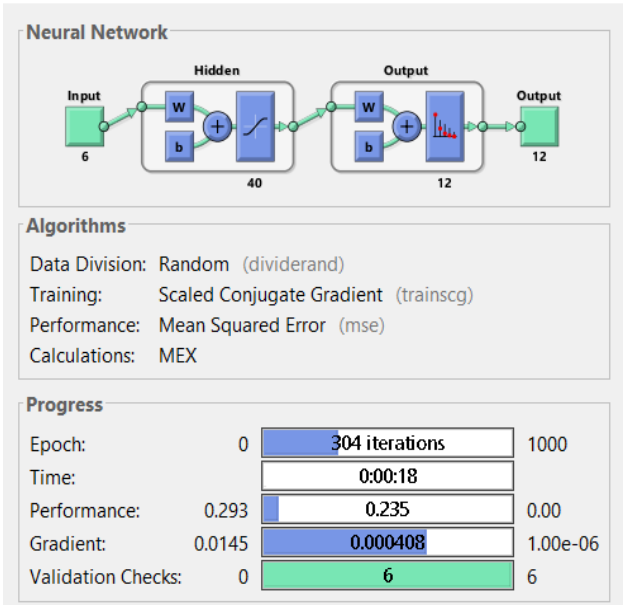

Figure 4.2: Training Performance of the Process

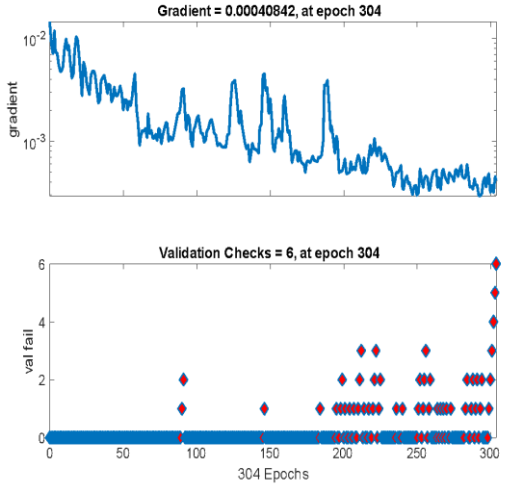

Figure 4.3: Training/Validation States

Training and Testing Confusion Matrix Results

The results obtained from the training and testing confusion matrix of multi-fault classification models are presented in this section as shown in Figure 4.4 and Figure 4.5.

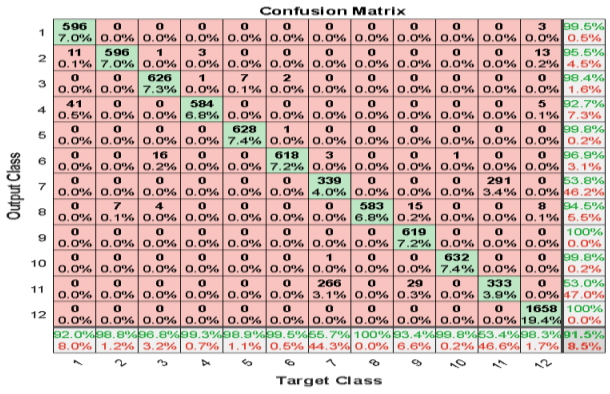

Figure 4.4: Training Confusion Matrix

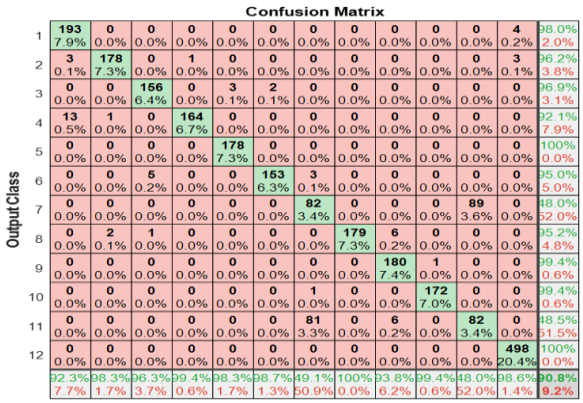

Figure 4.5: Testing Confusion Matrix

5 DISCUSSION OF RESULTS

No-Fault Case

The result for the No-fault scenario is shown in Figure 4.1(a). It can be seen that the three-phase voltage and current magnitudes are the same for each of the red, blue, and yellow phases. This means that the sensitivity and specificity of the confusion matrices for testing and training for the no-fault scenario are 100%, 98.6%, 100%, and 98.3%, respectively, as shown in Figures 4.3 and 4.4

Single Phase-to-Ground Fault

Figure 4.1 (b) shows the results for a single-phase ground fault (B-G). From the graph, we can see that the magnitude of the faulted line (blue) differs from the other lines from 0.02 seconds to 0.06 seconds, indicating higher voltage and zero current at that point. This means that testing and training the confusion matrix yields sensitivities and specificities of 96.2%, 98.3%, 95.5%, and 98.8% for single-phase fault scenarios, as shown in Figures 4.3 and 4.4.

Double Phase-to-Ground Fault

Figure 4.1 (c) shows the results for a two-phase ground fault (R-Y-G) scenario. From the graph, we can see that the faulty lines (red and yellow) differ in magnitude from the other lines between 0.02 and 0.04 seconds, indicating a higher voltage and zero current at that point. This is because the sensitivity and specificity of the test-train confusion matrix are 100%, 98.3%, and 99.8%, 98.9% for the two-phase (R-Y-G) fault scenarios, as shown in Figures 4.3 and 4.4.

Three Phase-to-Ground Fault

The results for the three-phase ground fault scenario (R-B-Y-G) are shown in Figure 4.1 (d). shows that the magnitude of the fault lines (red, blue, yellow) at this point is 0.02 to 0.06 seconds off the normal line. This indicates that the test and training confusion matrices have sensitivities and specificities of 48.0%, 49.1%, 53.8%, and 55.7%, respectively, as shown in Figures 4.3 and 4.4.

Phase-to-Phase Fault

The results for the phase-to-phase fault scenario (B-Y) are shown in Figure 4.1 (e). it shows that the faulty lines (blue and yellow) differ in size from the other lines between 0.02 and 0.06 seconds, indicating higher voltage and zero current at that point. This indicates that the test and training confusion matrices have sensitivities and specificities of 99.4%, 99.4%, 99.8%, and 99.8%, respectively, as shown in Figures 4.3 and 4.4.

Faults Classification Results

This section presents results obtained from an intelligent multiple-fault classification model. Figure 4.2 shows the trained model algorithm and training progress with 6 inputs, 40 hidden, and 12 outputs. The algorithm converged in 304 iterations with a power of 0.293, a slope of 0.0145, and 6 validation checks. This diagram (also shown in Figure 4.3) shows the model training and validation states. The minimum slope is 0.00040842

Figure 4.4 shows the training confusion matrix for the multi-fault classification model. In the figure, green diagonal boxes indicate correctly classified faults and red boxes indicate misclassified faults. The results show that 596 faults were correctly classified as R-G. 596 faults were correctly classified as B-G faults, 626 faults were correctly classified as Y-G faults, and 584 faults were correctly classified as R-B-G faults. 628 faults were correctly classified as R-Y-G. 618 faults were correctly classified as B-Y-G, 339 faults were correctly classified as B-Y-G, and 339 faults were correctly classified as R-B-Y-G. 583 faults were correctly classified as R-B and 619 faults were correctly classified as R-Y faults. 632 faults were correctly classified as B-Y faults, 333 faults were correctly classified as Y-B-Y, and 1,658 were correctly classified as no faults.

Table 5.1 shows the sensitivity and specificity of training error detection. In this table, No-Fault had the highest sensitivity rating of 100, followed by R-B-Y and R-Y-G with a sensitivity rating of 99.8, and R-B-Y with the lowest sensitivity rating of 53. It has the lowest specificity value of 53.4. Figure 5.1 shows the relationship between sensitivity and specificity, with the blue line representing sensitivity and the red line representing specificity. R-B-Y-G has the lowest sensitivity peak, and R-B-Y-G and R-B-Y have the lowest specificity peak.

TABLE 5.1: TRAINING FAULT DETECTION RESULT SUMMARY

Faults	Sensitivity	Specificity
R-G	99.5	92
B-G	95.5	98.8
Y-G	98.4	96.8
R-B-G	92.7	99.3
R-Y-G	99.8	98.9
B-Y-G	96.9	99.5
R-B-Y-G	53.8	55.7
R-B	94.5	100
R-Y	100	93.4
B-Y	99.8	99.8
R-B-Y	53	53.4
No-Fault	100	98.3

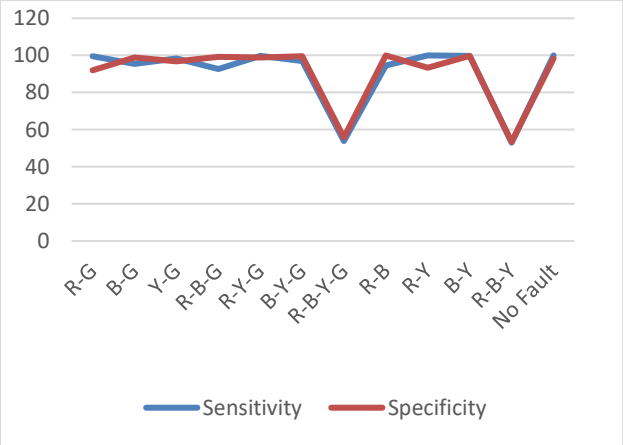

Figure 5.1: Relationship Between Sensitivity and Specificity of Training Fault

Figure 5.1: Relationship Between Sensitivity and Table 5.2 shows the sensitivity and specificity of test fault detection. In this table, No-Fault and R-Y-G have the highest sensitivity values at 100, followed by B-Y and R-Y with sensitivity values of 99.4 and R-B-Y with the lowest sensitivity values of 48.5. Regarding specificity, R-B received the highest specificity value of 100, followed by R-B-G and B-Y with sensitivity values of 99.4, and R-B-Y with the lowest specificity value of 48.5. Figure 5.2 shows the relationship between sensitivity and specificity, with the blue line representing sensitivity and the red line representing specificity. R-B-Y and B-G have the highest specificity peaks Specificity of Training Fault

TABLE 5.2: TESTING FAULT DETECTION RESULT SUMMARY

Faults	Sensitivity	Specificity
R-G	98.0	92.3
B-G	96.2	98.3
Y-G	96.9	96.3
R-B-G	92.1	99.4
R-Y-G	100	98.3

B-Y-G	95.0	98.7
R-B-Y-G	48.0	49.1
R-B	95.0	100
R-Y	99.4	93.8
B-Y	99.4	99.4
R-B-Y	48.5	48.0
No-Fault	100	98.6

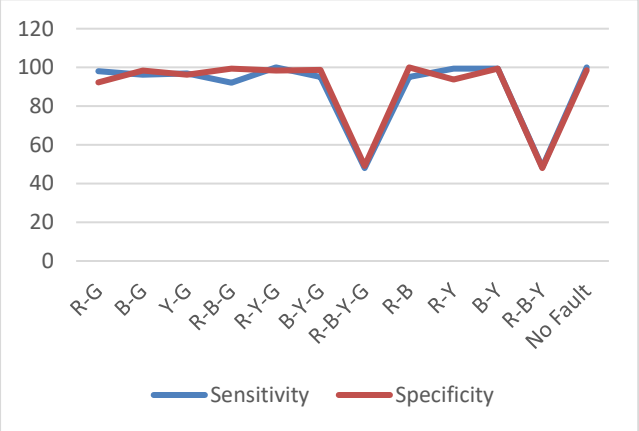

Figure 5.2: Relationship Between Sensitivity and Specificity of Testing Fault

TABLE 5.3: SUMMARY OF RESULTS FOR IMFCM

	Accuracy (%)	Sensitivity	Specificity
Training	91.500	90.6583	90.4917
Testing	90.800	89.0416	89.3500

6 CONCLUSION

Power system failure due to fault on the transmission line is a serious problem in Nigeria. Securing a stable power supply is important due to population growth and economic activity. Detecting and classifying faults is therefore critical to be able to react quickly and eliminate them.

In this research paper, "Application of Artificial Neural Network-Based Fault Diagnosis to 330 kV Gwagwalada-Katampe Transmission Lines", ANN was used to identify different possible faults.

Single-phase ground fault (R-G, B-G, Y-G), two-phase ground fault (R-B-G, R-Y-G, B-Y-G), three-phase ground fault (R-B-Y-G), phase-to-phase ground fault (R-B, R-Y, B-Y), and three-phase fault (R-B-Y). The data set used to train the intelligent model was first extracted by simulating network fault conditions. Six features were collected for each defect type, including defect types as classes. The dataset was then preprocessed, split, and used to train the model. The model was trained and validated using training and test data. Results show an average model accuracy of 91% for all defect types and normal conditions. It was also shown that the sensitivity and specificity of the three-phase fault test pattern showed the lowest value of 48%.

REFERENCES

Akhikpemelo, A., Evbogbai, M., & Okundamiya, M. S. (2019). Fault detection on a 132kV transmission line using an artificial neural network. *Int. Rev. Electr. Eng*, *14*, 1-6.

Alao, O., & Awodele, K. (2018). An overview of the Nigerian power sector, the challenges of its national grid, and off-grid development as a proposed solution. *2018 IEEE PES/IAS Power Africa*, 178-183.

Ferdous, F. (2018). *The zone protection system of transmission line by distance relay using MATLAB /Simulink.* Paper presented at the 2018 International Conference on Advancement in Electrical and Electronic Engineering (ICAEEE).

Gowrishankar, M., Nagaveni, P., & Balakrishnan, P. (2016). Transmission line fault detection and classification using discrete wavelet transform and artificial neural network. *Middle-East J. Sci. Res*, *24*(4), 1112-1121.

Hatata, A., Hassan, Z., & Eskander, S. (2016). Transmission line protection scheme for fault detection, classification, and location using ANN. *Int. J. Mod. Eng. Res*, *6*(8), 1-10.

Jamil, M., Sharma, S. K., & Singh, R. (2015). Fault detection and classification in elan electrical power transmission system using artificial neural network. *Springer Plus*, *4*(1), 1-13.

Kalu, O. O., & Madueme, T. (2018). Application of artificial neural network (ANN) to enhance power systems protection: a case of the Nigerian 330 kV transmission line. *Electrical Engineering*, *100*(3), 1467-1479.

Madueme, T., & Wokoro, P. (2015). The use of artificial neural networks in the theoretical investigation of faults in transmission lines. *Nigerian Journal of Technology*, *34*(4), 851-860.

Mbamaluikem, P. O., Awelewa, A. A., & Samuel, I. A. (2018). An artificial neural network-based intelligent fault classification system for the 33-kV Nigeria transmission line. *International Journal of Applied Engineering Research, 13*(2), 1274-1285.

Ogboh, V., & Madueme, T. (2015). Investigation of faults on the Nigerian power system transmission line using artificial neural network. *Journal of Renewable and Sustainable Energy Reviews, 23*(2), 342-351.

Okwudili, O., Ezechukwu, O., & Onuegbu, J. (2019). Artificial Neural Network Method for Fault Detection on Transmission Line. *International Journal of Engineering Inventions, 8*(1), 47-56.

Padhy, S. K., Panigrahi, B. K., Ray, P. K., Satpathy, A. K., Nanda, R. P., & Nayak, A. (2018). *Classification of faults in a transmission line using artificial neural network.* Paper presented at the 2018 International conference on information technology (ICIT).

Resmi, R., Vanitha, V., Aravind, E., Sundaram, B. R., Aswin, C. R., & Harithaa, S. (2019). *Detection, classification, and zone location of the fault in transmission line using artificial neural network.* Paper presented at the 2019 IEEE International Conference on Electrical, Computer, and Communication Technologies (ICECCT).

Rosle, N., Fadzail, N., Halim, M., Rohani, M., Fahmi, M., Leow, W., & Bakar, N. (2020). *Fault detection and classification in three-phase compensated transmission line using ANN.* Paper presented at the Journal of Physics: Conference Series.

Roy, N., & Bhattacharya, K. (2015). Detection, classification, and estimation of fault location on an overhead transmission line using S-transform and neural network. *Electric Power Components and Systems, 43*(4), 461-472.

Sambo, A. S., Garba, B., Zarma, I. H., & Gaji, M. M. (2010). Electricity generation and the present challenges in the Nigerian power sector.

Saturday, E. G. (2021). Nigerian Power Sector: A new structure is required for effective and adequate power generation, transmission, and distribution. *Global Journal of Engineering and Technology Advances, 7*(1), 006-018.

Sidhu, T., Singh, H., & Sachdev, M. (1995). Design, implementation, and testing of an artificial neural network-based fault direction discriminator for protecting transmission lines. *IEEE Transactions on Power Delivery, 10*(2), 697-706.

Taywade, D. D., & Ghute, A. (2016). Detection and Classification of Transmission Lines Faults using Discrete Wavelet Transform and ANN as Classifier. *International Journal of Engineering Sciences & Research Technology, 5*(12), 924-933.

Thwe, E. P., & Oo, M. M. (2016). Fault detection and classification for transmission line protection system using artificial neural network. *Journal of Electrical and Electronic Engineering, 4*(5), 89-96.

UDOFIA, K. M., & NnekwuKALU, C. (2020). Fault Detection, Classification, and Location on 132kv Transmission Line based on DWT and ANFIS. *surge (VS), 7*(6).

Upendar, J., Gupta, C. P., Singh, G. K., & Ramakrishna, G. (2010). PSO and ANN-based fault classification for protective relaying. *IET generation, transmission & distribution, 4*(10), 1197-1212.

Wani, N. S., Singh, R., & Nemade, M. U. (2018). Detection classification and localization of faults of transmission lines using wavelet transform and neural network. *International Journal of Applied Engineering Research, 13*(1), 98-106.

Warlyani, P., Jain, A., Thoke, A., & Patel, R. (2011). Fault classification and faulty section identification in teed transmission circuits using ANN. *International Journal of Computer and Electrical Engineering, 3*(6), 807-811.

Yadav, A., & Thoke, A. (2011). Transmission line fault distance and direction estimation using artificial neural network. *International Journal of Engineering, Science, and Technology, 3*(8), 110-121.

4th International Engineering Conference (IEC 2022)
Federal University of Technology, Minna, Nigeria

Computational Fluid Dynamics: Emission Modeling and Predictions for Gas Turbines

*Elimian, J[1], Nasir, A[1], & Muhammad, N.L[2].

[1]Department of Mechanical Engineering, Federal University of Technology, PMB 65 Minna, Niger State, Nigeria
[2]Department of Mechanical Engineering, University of Abuja, Abuja.
*Corresponding author email: elimianjacob91@gmail.com +2348136939866

ABSTRACT
The emission prediction, the combustion of $\boldsymbol{CH_4}$ in the burner of the gas turbine is studied and $\boldsymbol{NO_X}$ and CO formation/emission is simulated numerically. The objective is to investigate the influence of operating conditions (ambient temperature and turbine inlet temperature (TIT)) on emission concentrations. The governing equations of species, mass, momentum and energy are solved using ANSYS FLUENT. The Thermal- $\boldsymbol{NO_X}$ mechanism is considered for modeling the $\boldsymbol{NO_X}$ source term in the transport equation. The simulation sheds light on the relationship between the exhaust average temperatures and the maximum burner temperature and the Thermal- $\boldsymbol{NO_X}$ concentration. Results indicate that as the ambient temperature increases, the burner temperature increases and Thermal- $\boldsymbol{NO_X}$ concentration increases, while CO emission decreases. It can be concluded that NO_X formation is temperature dependent.
Keywords: Ambient temperature, carbon monoxides, nitrogen oxide, turbine inlet temperature.

1 INTRODUCTION

A computational fluid dynamics (CFD) examination of how fuel mixes and disperses between the primary zone and the area around the injector can be used in a CFD analysis. There are numerous variables that fall into two categories: those associated with the injection mechanism and those connected to the environment where the injected gas evolves (Strakey and Eggenspieler, 2010). Turgut, for instance, measured the impact of ambient temperature on CO concentrations from several airplane engines (Turgut, 2016). Industrial NO_X emissions monitoring can be done in three different ways. Firstly, periodic measurements are made using sampling. Secondly, continuous emissions monitoring systems (CEMS) are installed and thirdly, emissions are predicted using algorithm-based software that takes into account factors that have an impact on pollutant generation. A parametric emissions monitoring system is the name for this technique (PEMS). Compared to continuous emission monitoring systems, which necessitate the installation of on-site emission monitoring equipment, PEMS has lower purchase and maintenance expenses (Korpela *et al.,* 2015).

To calculate NO_X emissions from gas turbines, several semi-analytical expressions have been created (Wang *et al.,* 2020 and Lalic *et al.,* 2021).

In Lewis' (1991) equation, the amount of NOx produced in lean, homogeneous combustion is represented in Equation 1, Lewis correlation is provided.

$$NOx = 3.32 * 10{-}6 * (0.008Tc)\ 0.5[ppmv] \quad (1)$$

According to this equation, the after-combustion temperature and pressure alone determine NO_X generation, with no contribution from the residence duration of the burning gases. Because air is used as the oxidant in all combustion systems, Lewis claimed that this is the case, the period that matters is not how long the combustion product stays in the air, but rather how long it takes for the molecules to unwind., particularly the nitrogen molecules (Ighodaro *et al.,* 2022).

A NOx correlation developed by Rokke et al. (1993) is shown in Equation 2.

$$NOx = 18.1P1.42ma\ 0.3FA0.72\ [ppmv] \quad (2)$$

They showed that their correlation accurately predicted the NO_X emissions from five different natural gas-fired turbines with power outputs varying between 1.5 MW and 34 MW.

Although it is not evident in their created model, the fuel-air ratio term acknowledges the NO_X combustion temperature dependence.

1.1 AMBIENT TEMPERATURE EFFECTS ON NO_X AND CO EMISSION CONCENTRATION

Figure. 1 demonstrates how the primary zone temperature and NO_X emission rate are affected by ambient temperature. As a result, the variation of ambient temperature for 36^0C led to the increase of NO_X emission rate by 40ppm and the primary zone temperature of about 18^0C (Farhat *et al.*, 2017).

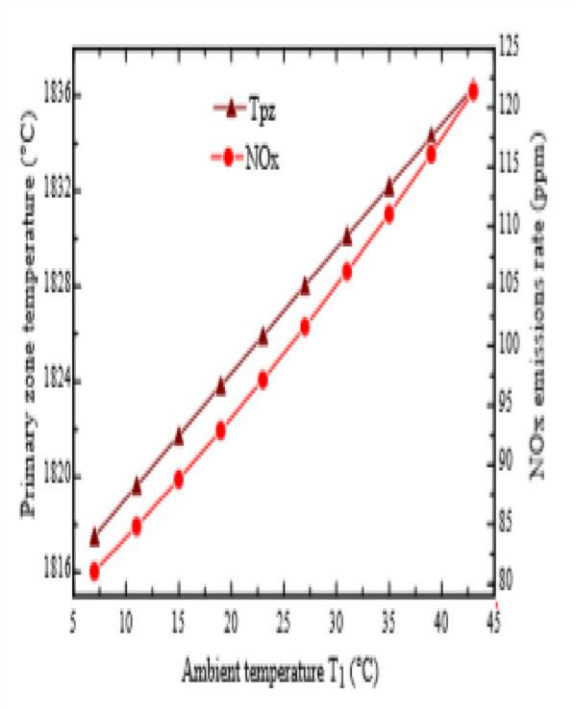

Figure 1 Main zone temperature and NO_X emission as a function of ambient temperature
(Farhat *et al.*, 2017)

Ambient temperature had a comparable impact on emissions and outlet temperature in all three starting modes, as shown in Table 1. The decrease in ambient temperature hindered the combustion process, decreased the NO_X content and outlet average temperature, and increased CO emissions (Ding *et al.*, 2022).

Table 1 Temperature variation simulation results

Operating mode	Condition	Outlet temperature on average (K)	NO_X concentration at the outflow on average (ppm)	CO concentration at the outlet on average (ppm)
Diffusion	3	1185.13	88.62	268.76
	4	1173.97	85.11	293.68
	5	1167.78	82.42	309.81
Sub-pilot premix	3	1227.28	107.19	153.19
	4	1216.79	97.02	187.02
	5	1200.43	93.41	218.94
Pilot-premix	3	1249.88	102.87	72.87
	4	1243.56	94.76	127.20
	5	1236.34	88.35	168.23

(Ding *et al.*, 2022)

The objectives of this research work are: To develop a model to predicts gas turbine emissions (NO_x and CO), investigating the impact of operating parameters on gas turbine emissions (NO_x and CO), and to validate model results with measure gas turbine emission data.

2 METHODOLOGY

GasTurb 14

GasTurb 14 was used to generate several state point conditions within the gas turbine at different operational conditions of ambient temperature.

Ansys

Utilize ANSYS Fluent's general-purpose setup solution, post-processing capabilities, and comprehensive physics models for multiphase, combustion, electrochemistry, and other fields to simulate a wide range of steady and transient industrial applications.

Methane

Natural gas mostly consists of methane, which makes up around 95% of the entire volume. Nitrogen, carbon dioxide, butane, pentane, ethane, propane, butane, and traces of other gases are also present. Sulfur compounds are also present, albeit in extremely small amounts. Since methane makes up the majority of natural gas, its characteristics are typically employed when comparing natural gas's characteristics to those of various fuels.

Atmospheric dry air

The chemical makeup of dry atmospheric air are nitrogen, oxygen, argon, carbon monoxide.

Model Input/output

The inputs comprise the connections between operating circumstances on a physical level and burner design specifications and are all practical and useful for professional use. The NOx and CO emissions indices (EINOx) and (EICO) are the model's outputs.

Governing Equations

Continuity: $\frac{\delta\rho}{\delta t} + \nabla(\rho u) = 0$ (3)

Species continuity: $\frac{\delta(\rho Y_i)}{\delta t} + \nabla . \dot{m}_i'' = \dot{m}_i'''$ (4)

For i =1,2…N

Principle of momentum:

$\rho \frac{Du_i}{Dt} = -\frac{\delta P}{\delta X_i} + \rho g + \frac{\delta}{\delta X_j}(2\mu e_{ij} - \frac{2}{3}\mu(\nabla . u)\delta_{ij}$ (5)

The principle of energy conservation in one dimension can be expressed as:

$$\sum \dot{m}_i'' + \frac{dh_i}{dx} + \frac{d}{dx}(-k\frac{dT}{dx}) + \dot{m}_i'' u_x \frac{du_x}{dx} = -\sum h_i \dot{m}_i''' \quad (6)$$

Where u is velocity, ρ is the density, Y_i is the species mass fraction i, $\dot{m}_i''$ is the species mass flow i, $\dot{m}_i'''$ is the net rate of species mass production i per volume unit, h_i is the species-specific enthalpy i, k is the conductivity of heat and u_x is the x-directional velocity.

In theory, estimates of species concentrations might be obtained by simultaneously solving these four interdependent, non-linear partial differential equations. It is necessary to make several suppositions that bring down the difficulty of the governing equations in order to develop a combustion model for gas turbines based on physics without the need for precise geometric specifications.

Description of Burner Modeling Layout

A perfectly stirred reactor (PSR) is a one-dimensional control volume where it is presumed that all species will mix properly instantly. An ideal reactor in steady-state with steady flow is a plug flow reactor (PFR). Additionally, it is presummated that the properties of the mixture are homogeneous axially and that there is no mixing in the radial (or flow) direction. Additionally, perfect gas behavior and frictionless flow are presumptions. The research-developed burner model utilizes a non-premixed combustion mechanism for natural gas.

Fig. 1 displays a graphic illustration of this model; the fuel mass flow and air is illustrated with various sections:

A Centre air

B Pilot burner

C Main burner

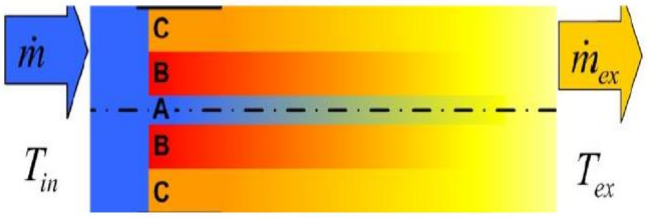

Figure. 2 A Typical gas turbine combustion chamber model

The air's mass flow and fuel, along with the inlet temperature T_{in}, can be used to compute the burner's inlet energy:

$$E_{in} = T_{in}(C_{p,}\int_{i=A}^{C}\dot{m}_{i,a} + C_{p,}\int_{i=B}^{C}\dot{m}_{i,f} + LHV\int_{i=B}^{C}\dot{m}_{i,f} \quad (7)$$

The exhaust provides the output energy:

$E_{out} = T_{ex}C_{p,ex}\dot{m}_{ex}$ (8)

These equations, when resolved, give the temperature field across the whole combustion system. In this study, the non-premixed combustion of natural gas in a simplified 2D burner is the main focus. The impact of changing these operational parameters on the burner's peak temperature and the emission of gaseous chemicals including NO, CO, and CO_2 has been investigated. The domain of the burner resembles a two-dimensional duct shape in its optimal form with height h=0.225m and length w=1.8m to mimic the combustion inside the burner.

Boundary Conditions

1. The airflow enters with a mass flow rate of m_a=3.430kg/s at a temperature of 657.99K and spans 0.22m.
2. Natural gas mass flow rate in the burner has been kept at m_f = 0.07376kg/s and spans 0.005m.
3. The backflow temperature is the outflow boundary condition for the pressure outlet of 1000K.
4. Wall temperature is constant at the top boundary of 1200K.
5. Burner is symmetric about the x-axis because the bottom border is a symmetry plane.

The standard k- ε turbulent model is employed.

Table 2 Data obtained from GasTurb 14 used for emission predictions

Input parameters	Design point	Off-design point			
T_{amb}(K)	288.15	293	298	303	308
$\dot{m}_a$(kg/s)	3.430	3.379	3.303	3.224	3.144
$\dot{m}_f$(kg/s)	0.07376	0.07308	0.07200	0.07095	0.06990
Burner inlet temperature (K)	657.99	661.69	667.68	673.57	679.19

3 RESULTS AND DISCUSSION

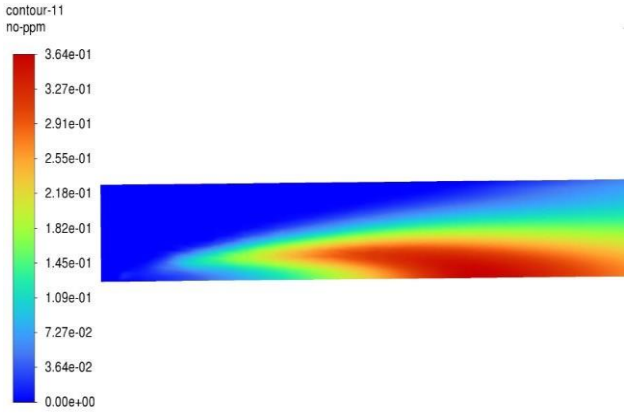

Figure 3 NO_x concentration distribution at the design point as calculated

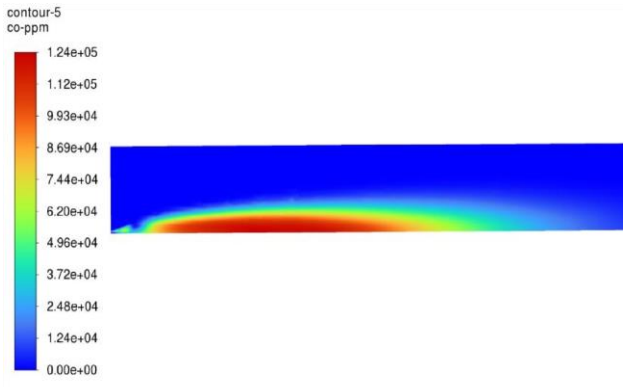

Figure 4 Calculation result of CO concentration distribution at design point

Figure 3 and figure 4 show the emission concentrations of NO_x and CO distribution at design point throughout the combustion chamber of the gas turbine. It can be observed that the NO_x concentration is dependent on the temperature distribution within the combustion chamber. At the peak temperature of 2246.46K within the chamber, the highest NO_x concentration (0.3730ppm) was obtained. While from figure 4, it can be seen that CO emission concentration is higher within the inlet region of the combustion chamber and gradually decreases as combustion reactants move towards the chamber exit and this is due to the formation of more carbon (1V) oxide (CO_2).

Table 3 Simulated results of TIT, NO_x and CO concentrations at different ambient temperaturesT_{amb}

T_{amb}(K)	TIT(K)	NO_x(ppm)	CO (ppm)
288	1919.30	0.2344	650.458
293	1923.24	0.2378	637.477
298	1929.47	0.2428	622.105
303	1935.79	0.2473	597.171
308	1942.06	0.2524	567.551

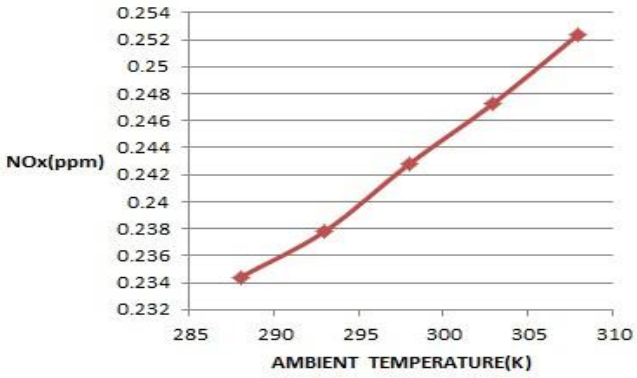

Figure 5 impact of ambient temperature on NO_x concentration

In order to replicate how ambient temperature affects emissions, the absolute humidity of the environment was maintained while the ambient temperature was altered. The results of the simulation are displayed in Tables 3. As

can be seen, the ambient temperature had a comparable impact on emissions and burner exit temperature. The combustion reaction was unhindered by the rise in temperature of the ambient, which also led to a rise in average burner exit temperature and NO_x emission concentration while a decrease in CO emissions. The higher ambient temperature raised the temperature of the incoming air to the burner after traversing the compressor, which reduced combustion efficiency and ultimately had an impact on the burner's high temperature zone and emission concentration and this is a validation of the work done by Ding *et al.*, 2022.

4 CONCLUSION

The burner temperature and NOx emissions increased as ambient temperature increased, whereas CO emission decreased. The temperature is the primary factor that influences the generation of NOx. NOx emission considerably rises as combustion temperature rises. It can be concluded that NOx formation is temperature dependent. However, higher thermal efficiency and power output are correlated with higher temperature. Consequently, cycle efficiency and burner outlet temperature must be compromised.

ACKNOWLEDGEMENTS

The authors acknowledge thankfully the effort and ideas of Engr. Prof A. Nasir.

REFERENCE

Ding, Y., Hao, J., Li, A., Wang, X., Zhang, X., & Liu, Y. (2022, July). Numerical Simulation of Combustion and Emission Characteristics during Gas Turbine Startup Procedure. *Energies*, *15*(15), 5444. https://doi.org/10.3390/en15155444.

Farhat, H., Khir, T. & Ammar, B.B. (2017). Investigation of main operating parameters affecting gas turbine efficiency and gas releases. International Journal of Energy and Power Engineering, 11(7), 1325-1329.

Ighodaro, O., Ilori, S., Aburime, E., & Obanor, A. (2022). An equilibrium model of NOx emission in gas turbine combustors. *Nigerian Journal of Technology*, *41*(4), 778–788. https://doi.org/10.4314/njt.v41i4.15.

Korpela, T., Kumpulainen, P., Majanne, Y., & Häyrinen, A. (2015). Model based NOx emission monitoring in natural gas fired hot water boilers. *IFAC-PapersOnLine*, *48*(30), 385–390. https://doi.org/10.1016/j.ifacol.2015.12.409.

Lalić, B., Poljak, A., Radica, G., & Mišura, A. (2021). Low-Speed Marine Diesel Engine Modeling for NOx Prediction in Exhaust Gases. *Energies*, *14*(15), 4442. https://doi.org/10.3390/en14154442.

Lewis, G.D, (1991). New Understanding of NOx formation. Tenth International Symposium on Air Breathing Engines, Anonymous Publ by AIAA, Washington, DC, USA, Nottingham, Engl, pp. 625-629.

Rokke, N.A., Hustard. J.E., & Berg, S. (1993). Pollutant Emissions from Gas Fired Turbine Engine in Offshore Practice-Measurements and Scaling. International Gas Turbine and Aeroengine Congress and Exposition, Anonymous Publ by ASME, New York, NY, USA, Cincinnati, OH, USA, pp.10.

Strakey, P. A., & Eggenspieler, G. (2010). Development and Validation of a Thickened Flame Modeling Approach for Large Eddy Simulation of Premixed Combustion. *Journal of Engineering for Gas Turbines and Power*, *132*(7). https://doi.org/10.1115/1.4000119.

Turgut, E. T. (2016). Effects of Ambient Air Temperature on Gaseous Emissions of Turbofan Engines. *Journal of Propulsion and Power*, *32*(3), 713–725. https://doi.org/10.2514/1.b35916.

Wang, Y., Wang, J., Xu, X., Henze, D. K., Qu, Z., & Yang, K. (2020). Inverse modeling of SO₂ and NO_{<i>x</i>} emissions over China using multisensor satellite data – Part 1: Formulation and sensitivity analysis. *Atmospheric Chemistry and Physics*, *20*(11), 6631–6650. https://doi.org/10.5194/acp-20-6631-2020.

4th International Engineering Conference (IEC 2022)
Federal University of Technology, Minna, Nigeria

Towards Development of a Dynamic Random Advance Encryption Standard

*Adamu, M., Oyefolahan[1], O. I., Ojerinde[2], O. A

[1]Department of Computer Science, Federal Polytechnic, P.M.B. 55, Bida, Niger State
[2]Department of Information Technology, Federal University of Technology, Minna, Niger State
[3]Department of Computer Science, Federal University of Technology, Minna, Niger State

*Corresponding author email: bejian2004@gmail.com +08167691680

ABSTRACT
The Advance Encryption Standard (AES) is a widely used encryption algorithm that provides strong protection for sensitive data. The AES is the most popular symmetric cryptographic scheme that uses the same key for encryption and decryption process. However, the conventional AES suffers from key distribution and resources consumptions problem. One of the key performance issues of the traditional AES algorithm is its complexity and speed of execution. These issues made AES unsuitable for real-time applications and applications that required less complexity. In this paper, a new AES encryption scheme called Dynamic Random Advance Encryption Standard (DR-AES). The DR-AES introduces randomness into the encryption process, making it more difficult for attackers to launch certain types of attacks. It also proposes a reduced round to reduce the complexity and make it suitable for less complex and real-time applications. The proposed algorithm is expected to reduce the computational power, energy consumption, memory space and provide optimal security level.

Keywords: *Advanced Encryption Standard, Cipher text, Cyber-attacks, Data Encryption Standard, Decryption Encryption.*

1 INTRODUCTION

Humans have an innate desire to communicate with one another as a way of understanding each other. With the advancements in technology, such as telecommunications and computers, people can now store data digitally. However, this digital data storage also comes with risks, particularly when it comes to the security of internet communication. (Muttaqin *et al.,,* 2020). Internet communication plays a significant role in transferring large amounts of data across various industries. However, some of this data may be sent through insecure channels, making it vulnerable to intruders. To protect sensitive information, both private and public sectors use various techniques and methods. One of the most important and widely used techniques is cryptography, which involves the use of encryption and decryption to secure data from attackers (Abdullah, 2017).

Encryption is a method used to ensure the safety of sensitive information by using algorithms to perform byte substitutions and matrix transformations on the original message, turning it into a jumbled, unreadable message known as ciphertext. Information security can be maintained through the use of commonly available encryption algorithms, but the choice of key is crucial as it directly determines the security of the encryption (D'souza, 2017). Some of the most widely used symmetric key encryption algorithms are Data Encryption Standard (DES), Triple DES, and Advance Encryption Standard (AES). DES is a classic example of a block cipher, which was the result of a competition set by the US National Bureau of Standards in 1973. It was widely adopted in 1977 (Abomhara *et al.,,* 2010). AES is a widely used encryption method in recent times. It is made up of various bit substitutions, permutations, round key functions, and transformations. AES is a faster algorithm and has not yet been broken by any known practical attacks. Therefore, it is still considered one of the most reliable encryption standards for advanced information security (Nivedhaa & Justus, 2018).

The AES algorithm has multiple options for configuration. The first option is the key size or key length, which offers three choices: 128, 192, and 256 bits. The second option is the chaining mode, which determines how multiple block ciphers operate in a chained mode to encrypt information larger than 16 bytes. Some common chaining modes include: Electronic Code Book (ECB), Cipher Block Chaining (CBC), Cipher Feedback (CFB), and Output Feedback (OFB) (García, 2015).

Several modifications have been carried out on AES algorithm, most of which were done to improve the AES

implementation in terms of memory reduction, computational power minimization, encryption and decryption time reduction and security. However, most of this research still uses maximum AES rounds which is still complex for light weight or resource starved applications. Hence, this paper proposes a new Dynamic Random AES to reduce the number of rounds required for encryption and decryption while improving the security for mobile devices.

The remainder of this paper is structured as follows: Section 2 discuss the existing modifications of AES, section 3 discussed the traditional AES and the proposed DR-AES scheme. In section 4, the expected results are discussed. This is followed by conclusion in section 5.

2 LITERATURE REVIEW

Several modifications to enhance AES encryption scheme has been proposed. Abikoye *et al.,* (2019) proposed an enhanced version of AES by modifying the SubBytes and ShiftRows transformations. The SubBytes transformation was made round key dependent, while the ShiftRows transformation was randomized. The goal of these modifications was to make the two transformations dependent on the key, so that a small change in the key would result in a significant change in the ciphertext. In this approach, the AES SubBytes transformation was made round key dependent, to make it easier to detect changes in the key. To achieve this, the 16 bytes round key was used to generate four eight-bit keys. The modified algorithm was tested for both its avalanche effect and how long it takes to run, and it was found that while the avalanche effect was improved, the execution time was slightly longer.

Talirongan *et al.,,* (2019) proposed a modification to the round function of the AES algorithm to enhance the security of the encryption and decryption processes by utilizing the Butterfly Effect. This method improves the security level by increasing the degree of diffusion, the degree of confusion and integrity check. The modification uses the butterfly effect to improve the key space and nonlinear system of the AES algorithm. The Lorenz attractor, also known as the butterfly effect, was applied to achieve the enhancement. The proposed method begins by taking in inputs such as plain text and a key, which is then utilized in the butterfly effect. Each round has unique values generated by the butterfly effect, as the input key goes through the butterfly effect function. Three security measures (degree of diffusion, degree of confusion and integrity check) are used to evaluate the security level of the modified algorithm. The results of the testing demonstrate that the modified AES algorithm is more secure compared with AES algorithm.

Ali & Shaker, (2020) proposed an improvement for the Advanced Encryption Standard (AES) algorithm which utilizes an additional key generated by a linear feedback shift register (LFSR). This approach allows for more efficient random number generation and reduces the number of rounds needed. The LFSR is used to generate 256 random keys which are added to both the original text and the original AES key (key 1). The use of LFSR to generate an additional key randomly and incorporating it into each round at the "add round key" step makes the algorithm more secure. Additionally, reducing the number of rounds makes the modified algorithm faster than the original, making it more suitable for protecting data in distributed systems.

Reddy & Kumar (2020) presented a new method for creating keys using a combination of the Advanced Encryption Standard (AES) and the Flower Pollination Algorithm (FPA), which they referred to ass the Modified AES (MAES). The key generation process in the MAES algorithm is crucial as it affects the creation of S-boxes. By creating key-dependent S-boxes, the strength of the algorithm is increased. The key, ki, is generated using a Pseudo Random Number Generator (PRNG), which uses mathematical calculations to generate a sequence of numbers that mimic randomness. The FPA is used in the MAES key generation process to maximize entropy, and the best key value is obtained by maximizing randomness. The authors also proposed that this approach could be applied to other areas.

Altigani *et al.,* (2021), introduced a new variant of the Advanced Encryption Standard (AES) called the polymorphic AES (P-AES). The P-AES changes the values of AES parameters with each new key, making the exact values known only to authorized parties during runtime. The P-AES supports key lengths of 16, 24, or 32 bytes, but for the purpose of consistency, it is assumed that the key length is 32 bytes. In the operation of P-AES, it Modified MixColumns matrix rearranges the rows of the traditional AES MixColumns matrix, with row0 becoming row1, row1 becoming row2, and row2 becoming row3. Additionally, the P-AES cipher includes a layer of obscurity to prevent attackers from easily determining how it operates. Similar modifications could be proposed to improve performance and security while keeping implementation costs low.

Zinabu and Asferaw (2022) suggested an improvement to the Advanced Encryption Standard (AES) algorithm called Enhanced Efficiency of AES (EE-AES) by replacing the mix column stage of the original AES design with a bitwise reverse transposition technique. This modification reduces the computational requirements of the mix column stage while maintaining the same level of security as AES. The proposed EE-AES algorithm utilizes the bitwise reversed transposition operation.The method utilizes hexadecimal notation (00-09 and 0A-0F) to map two hex digits to eight binary bits, rather than writing out the binary digits. This improves the speed and efficiency of the existing Advance Encryption Standard (AES) and Modified Advance Encryption Standard (MAES) algorithms. As a next step, one could test the algorithm with different bit sizes and compare it to other state-of-the-art algorithms.

3 TRADITIONAL AES

AES is a widely used symmetric encryption algorithm that uses a fixed-size key to encrypt and decrypt data. It is a block cipher, which means that it operates on fixed-size blocks of data, using a secret key to transform the data in a way that is designed to be difficult to reverse without knowledge of the key. It processes data in blocks of 128 bits, with the option of using key lengths of 128, 192, or 256 bits. The algorithm operates on a 2-D array of 4x4 bytes, known as the State. The State starts as plaintext and is transformed into cipher text through the encryption process. Each row of the State contains 4 bytes, and the four bytes in each column form a 32-bit word (Forhad *et al.*,, 2018). Figure 1 shows the traditional AES encryption scheme.

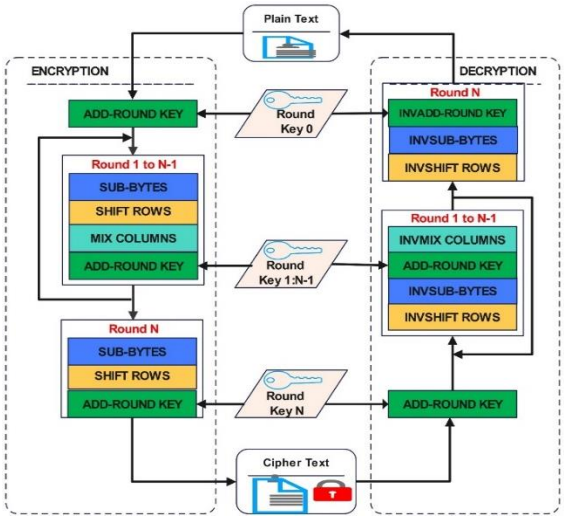

Figure 1: Traditional AES

The encryption process begins with an initial round key addition, followed by a round function that is applied to the State. The round function consists of four transformations: SubBytes, Shift Rows, MixColumns, and AddRoundKey. The number of times the round function is applied depends on the key length used, with AES-128 applying it 10 times, AES-192 applying it 12 times, and AES-256 applying it 14 times. The transformations used in the round function are reversible linear and non-linear operations, which allows for decryption using their inverses (Forhad *et al.*,, 2018).

4 PROPOSED DYNAMIC RANDOM ADVANCE ENCRYPTION STANDARD (DR-AES)

One of the key performance issues of the traditional AES algorithm is its complexity and speed of execution. These issues made AES unsuitable for real-time applications and applications that required less complexity. To address these issues, a Dynamic Random AES (DR-AES) encryption scheme is proposed for encryption and decryption. In this process, the initial secrete key is expanded using the standard key expansion algorithm. The 128-bits key is expanded to produce 11 new 128 bits (16-bytes) which corresponds with the number of rounds plus one for the preliminary round. For each of the number of chosen rounds (nR), the appropriate round key corresponding to the round number will be selected for the add round operation to change the state. Each 16 byte of the expanded key will be indexed for reference. Figure 2 shows the proposed DR-AES scheme for encryption and decryption.

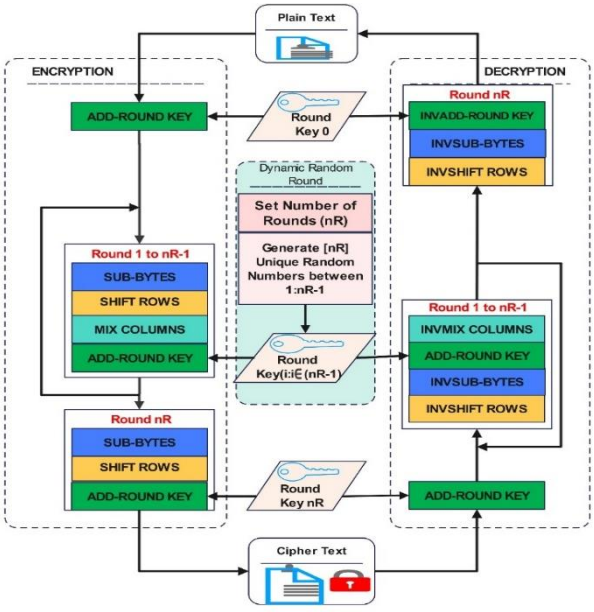

Figure 2: Randomized Dynamic AES Scheme

The proposed encryption scheme comprises of four steps:

4.1 KEY GENERATION AND EXPANSION STEP

The key expansion used in this research work was adopted from (Yan & Chen, 2016) with some modification. The initial 128-bit key is divided into 4 words and then further expanded into 44 words. Each word is arranged into a 4x4 matrix, with 4 words representing a single key. A total of 11 subkeys are needed, and each key is expressed in 16 bytes. The first key is represented as W_0, W_1, W_2, and W_3. An index number r_0 to r_{10} was assigned to each word as shown in Figure 3

Figure 3: Key expansion

This step is used to generate a series of round keys from the initial encryption key. Mathematically, the key expansion can be expressed as follows: Given the initial key (k_0), which is generated as 4 words secrete key by the user given as:

$$K1 = W_0W_1W_2W_3 \quad (1)$$

The round constant (Rcon) is generated by XORing the first word (W_0) and last word (W_3) as shown in Equation 3.2. This is followed by shifting the four bytes one position to the left cyclically (nibble bit rotation), followed by substituting each byte from S-box

$$Rcon_1 = W_0 \otimes W_3 \quad (2)$$

$$G_1 = Rcon_1 \otimes SubNib(RotNibW_3) \quad (3)$$

$$W_4 = W_0 \otimes G_1 \quad (4)$$

$$W_5 = W_1 \otimes W_4 \quad (5)$$

$$W_6 = W_2 \otimes W_5 \quad (6)$$

$$W_7 = W_3 \otimes W_6 \quad (7)$$

$$K_1 = W_4W_5W_6W_7 \quad (8)$$

The remaining keys

$(K2, K3, K4, K5, K6, K7, K8, K9, K10)$ are generated in a similar manner with the next 4 words representing key2 $(K2 = W_8W_9W_{10}W_{11})$, key3 $(K3 = W_{12}W_{13}W_{14}W_{15})$, and so on.

4.2 Add-Round Key

Add round key: Add Round Key transformation is an XOR operation that adds the round key to the State in each round. In this step, the round key, which is derived from the original encryption key, is added to the state using a bitwise XOR operation. This step is used to introduce confusion into the encryption process as shown in figure 4. Mathematically, this can be represented as:

$$X_I = T \otimes K_0 \quad (9)$$

where X is the resultant state array (ciphertext), T is the input plaintext, K_0 is the round key at index 1 of the first 4 words.

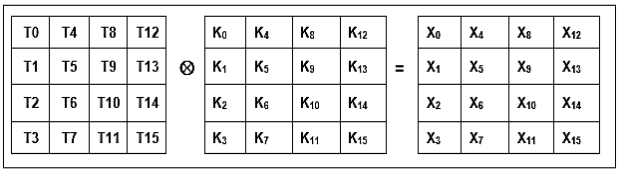

Figure 4: Initial Add-round Operation

4.3 DYNAMIC RANDOM ROUND GENERATION

The dynamic random round generation stage comprises of two steps:

i. Determination of the number of rounds (nR)

In this step, the number of rounds to run is determined. For a 128-bits AES key size, the normal round is 10. In this work, the appropriate number of rounds will be experimented to determine the effect of each lower round in terms of encryption and decryption time and in terms of key size and security effect.

ii. Random round Generation and Key Selection

Generation of nR unique random numbers between one and the total number of rounds corresponding to the key length. Figure 3.3 shows the operation of the random round generation and key selection. Given the total number of rounds N=10, and the number of rounds = nR, the random round index is expressed as:

$$D_i = [D_1 \quad D_2 \quad D_3 \ldots D_{nR}], where\ i = 1{:}nR \quad (10)$$

For nR = 5 can be given as:

$$D_5 = [2 \quad 3 \quad 7 \quad 8 \quad 9] \quad (11)$$

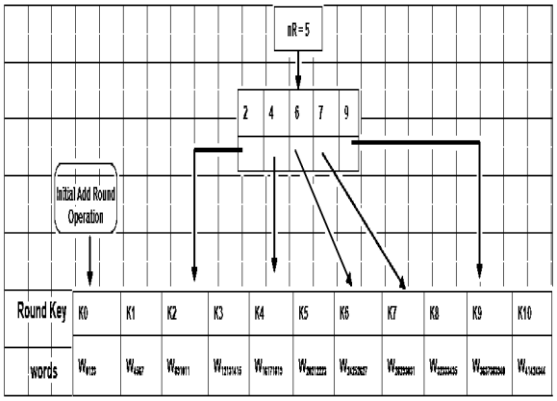

Figure 5: Round key selection

4.4 ROUND FUNCTION

The round functions are sub-bytes, shift rows,

mixcolumns and add round keys.

i. Sub-bytes

The Sub-bytes transformation is a nonlinear byte substitution that operates on each byte of the State using a table, known as an S-box. The S-box is computed using a finite field inversion and an affine transformation. In this step, each byte in the state is replaced with a corresponding value from the S-box. The result is in a matrix of four rows and four columns. To achieve this, first, the finite field inversion is calculated using Equation (12):

$$I(x) = x^{-1} \ mod \ 2^k \qquad (12)$$

ii. Shift rows

The Shift Rows transformation is a circular shifting operation that rotates the rows of the State with different numbers of bytes (offsets). In this step, the rows of the state are shifted by a certain number of positions. The number of positions shifted depends on the row number, with the first row being un-shifted, the second row being shifted one position, the third row being shifted two positions, and so on

iii. MixColumns

In mixcolumns, each column of four bytes is now transformed using a special mathematical function. This function takes as input the four bytes of one column and outputs four completely new bytes, which replace the original column. The result is another new matrix consisting of 16 new bytes. It should be noted that this step is not performed in the last round. This step is used to mix the columns of the transformed data before it is encrypted.

iv. Add round key

Add Round Key transformation is an XOR operation that adds the round key to the State in each round. In this step, the round key, which is derived from the original encryption key, is added to the state using a bitwise XOR operation. This step is used to introduce confusion into the encryption process.

Mathematically, this can be represented as:

$$C_I = X_I \otimes K_0, (i: i = 0: N-1) \qquad (13)$$

where C is the resultant state array (ciphertext), X is the input state array (plaintext), K_0 is the round key, and N is the number of columns (32-bit words) in the state array.

5.1 Expected Results

The new DR-AES will be implemented and its performances in terms of encryption and decryption time, memory and security. Furthermore, the new scheme will be applied for encryption of data in mobile learning environment. It expected that a more robust AES encryption scheme suitable for mobile learning and other light weight applications will be developed.

5.2 Conclusion

In this paper, a new dynamic random AES encryption scheme was proposed. The proposed scheme comprises of 4 key stages. The key generation and expansion stage, the add-round stage, the dynamic random round and key selection stage and finally, the round function stage which comprises of; sub-byte, shift rows, mix column and add round function. The mix column is not applied in the last round. The proposed new DR-AES scheme is expected to reduce the number rounds of the traditional AES thereby reducing the complexity of the AES. Also, the dynamic random rounds introduced will improve the security of the scheme. The new scheme is expected to be more suitable for light weight applications such as in mobile learning applications. Going-forward, the proposed scheme will be developed and implemented on a mobile learning environment.

REFERENCE

Abdullah, A. M. (2017). *Advanced Encryption Standard (AES) Algorithm to Encrypt and Decrypt Data*.

Abikoye, O. C., Haruna, A. D., Abubakar, A., Akande, N. O., & Asani, E. O. (2019). *SS symmetry for*

Information Security. 1–16.

Abomhara, M., Zakaria, O., & Khalifa, O. O. (2010). *An Overview of Video Encryption Techniques*. *2*(1), 103–110.

Ali, H. H., & Shaker, S. H. (2020). Modified Advanced Encryption Standard algorithm for fast transmitted data protection. *IOP Conference Series: Materials Science and Engineering*, *928*(3). https://doi.org/10.1088/1757-899X/928/3/032011

Altigani, A., Hasan, S., Barry, B., Naserelden, S., Elsadig, M. A., & Elshoush, H. T. (2021). A Polymorphic Advanced Encryption Standard - A Novel Approach. *IEEE Access*, *9*, 20191–20207. https://doi.org/10.1109/ACCESS.2021.3051556

D'souza, F. J., & Panchal, D. (2017). *Advanced Encryption Standard (AES) Security Enhancement using Hybrid Approach*. 647–652.

García, D. F. (2015). *Standard Algorithm*. 247–252. https://doi.org/10.1109/MCSI.2015.61

Indrasena Reddy, M. (2020). a Modified Advanced Encryption Standard Algorithm. *Journal of Mechanics of Continua and Mathematical Sciences*, *spl5*(1), 112–117. https://doi.org/10.26782/jmcms.spl.5/2020.01.00027

Muttaqin, K., Rahmadoni, J., Samudra, U., & Andalas, U. (2020). *Analysis And Design of File Security System Aes (Advanced Encryption Standard) Cryptography Based*. *1*(2), 114–123.

Nivedhaa, R., & Justus, J. J. (2018). A Secure Erasure Cloud Storage system using Advanced Encryption Standard algorithm and Proxy Re-encryption. *2018 International Conference on Communication and Signal Processing (ICCSP)*, 755–759.

Ready & Kumar (2020). A Modified Advanced Encryption Standard Algorithm. *Journal of Mechanics of continua and Mathematical Science*. Pp 112-117.

Talirongan, H., Sison, A. M., & Medina, R. P. (2019). Modified advanced encryption standard using butterfly effect. *2018 IEEE 10th International Conference on Humanoid, Nanotechnology, Information Technology, Communication and Control, Environment and Management, HNICEM 2018*. https://doi.org/10.1109/HNICEM.2018.8666368

Zinabu, N. G., & Asferaw, S. (2022). *Enhanced Efficiency of Advanced Encryption Standard (EE-AES) Algorithm*. *7*(mix), 59–65. https://doi.org/10.11648/j.ajetm.20220703.13

4th International Engineering Conference (IEC 2022)
Federal University of Technology, Minna, Nigeria

Cruise Control Using IMC and PID Controllers.

*Garuba Oluwatosin Rasheed[1], Taliha Abiodun Folorunso[2], Jibril Abdullahi Bala[2], Abdullahi Mohammad Ibrahim[1]
[1]Computer Engineering Department, Federal University of Technology, PMB 65 Minna Niger State, Nigeria
[2]Mechatronics Engineering Department, Federal University of Technology, PMB 65 Minna Niger State, Nigeria
*Corresponding author emails: [1]oluwatosin.pg2113148@futminna.edu.ng.
[2]funso.taliha@futminna.edu.ng.

ABSTRACT
The Proportional-Integral-Derivative known as (PID) controller has been continuously use in the modern industrial plant to control system due to its ease of tuning its parameters, though it is very time consuming and may be unreliable if efficiency parameters is not obtained. In this paper, we worked with the control of cruise system using PID and IMC controller tuned by Ziegler-Nichols techniques to compare the performance of the two different controller. The objective of this study is to evaluate the system's performance using the transient responses such as, rise time, settling time and steady-state. The simulation results show that the IMC controller gives a better transient response than the PID controller.

Keywords: *Cruise Control, Ziegler-Nichols, PID Controller (IMC) Internal Control Model.*

1 INTRODUCTION

The cruise control is a system that has recently been added as a function to help smart vehicles [1]. The system is a useful system which enable driver to relax when driving over a long distance. Many drivers gripe about having to quickly depress the gas pedal to keep the car moving, but the invention of cruise control has reduced the mental and physical strain of constantly monitoring the pace of the car [2]. Cruise control is an electronic system that will allow the driver to set vehicle at a constant speed, letting the driver to do away with pressing the accelerator pedal [2].

A most typical controller for operating the cruise control for optimal control is the proportional-integral-derivative (PID) controller [1]. Other alternatives include the fuzzy logic approach etc [3]. The PID controller is quite common in the control system owing to its efficiency, dependability, simplicity of design, and ease of tuning [4]. PID controller parameters are proportional gain K_p, integral gain K_i as well as derivative gain K_d which are required to be tuned optimally in order to achieve efficient control of the system. There are various method of turning the parameters which include Pole placement, Cohen-coon, Ziegler-Nichols, Internal Model Control (IMC) methods etc. [1], [4] – [8].

Achieving optimal turning using the various methods or techniques of turning PID controller for any particular system depends on the feasibility of the techniques in response to the system [4]. The efficiency of the controller depends on the efficacy of the tuning methods used to obtain the PID controller parameter. Hence, in this work we employ the performance of PID tuned using Ziegler-Nichols method as well as IMC controller in controlling the cruise system.

The remaining part of this paper is divided into three sections: section 2 the methodology- focusing on system design, and controller designs while section 3 focuses on the results, and section 4 the conclusion of the work.

2 THE CRUISE CONTROL SYSTEM DESCRIPTION

The controller takes driver's signal as the reference input speed signal, sends it to the system, and evaluates the car speedometer's output. The two signals, the cruise control and the turn signal, ensure that the vehicle's speed is consistent.

The cruise system can do this by altering the engine's driving force by modulating the throttle angle, or "u." [8]. Figure 1 shows the cruise system block diagram showing different parts of it operations.

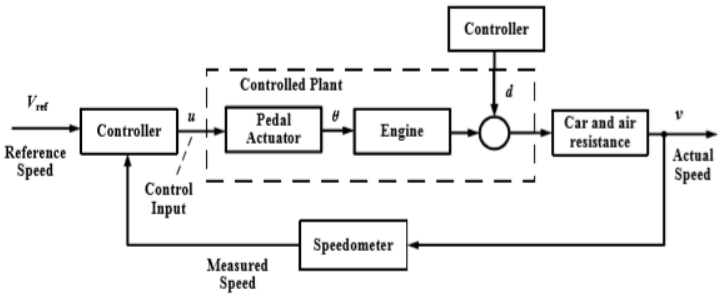

Figure 1. Block diagram showing details of operation for the cruise system

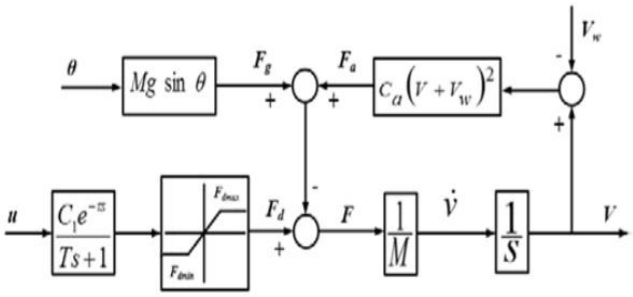

Figure 2. Vehicle Dynamic

The vehincle dynamics shows the system has a non-linear characteristics [8].

2. MATHEMATICAL MODELLING FOR CRUISE CONTROL SYSTEM

The mathematical formulation and features according to the cruise system based on non-linear can be obtained as follows, in accordance with Newton's first law of motion (1).

$$\sum F = m * a \qquad (1)$$

Where m = mass of the passengers and the car and a = acceleration. In (1), which sums all forces acting on the car. Consequently, equation (2) can be used to express the total force.

$$\sum F = F_d - F_a - F_g \qquad (2)$$

The forces F_d, F_a and F_g represent the engine drive force of the vehicle, aerodynamic drag force, and frictional and gravitational force acting on the vehicle respectively. Each of the forces can be represented as the following [8]. (3) – (5):

$$F_d = \frac{C_1 e^{-\tau s}}{Ts+1} \qquad (3)$$

$$F_a = C_a(v - v_m)^2 \qquad (4)$$

$$F_g = M\, g\, \sin\theta \qquad (5)$$

Equation (3) holds, provided F_d falls between its minimum and maximum value. The force attributed to the engine drive is modelled using a first order system with delay [8].

When a car is in motion there is a tendency of some forces acting in opposite direction of the motion which are both the F_a and F_g. The both are known as disturbance forces that tend to limit the speed of the vehicle [8]. Substituting equation (3) – (5) into equation (2) and simplifying it in term of velocity gives equation (6).

$$F_d = M.\frac{dV}{dt} + C_a(v - v_m)^2 + F_g \qquad (6)$$

Where $M\frac{dV}{dt}$ denotes the force of inertia. The car's actuation and propelling system employ a first order system. $F_d = \frac{C_1 e^{-\tau s}}{Ts+1}$. The diagram above in Figure 2 .represent the saturation block limited to both minimum and maximum value of F_d.

Considering a minimal disturbance for the system at a set of all initial conditions equal to zero, the disturbance parameters such as wind velocity and fractional force due to the road are taken as zero as well. The model becomes a forward path with unity feedback of the response speed. If we choose the state variable as the output, v and the drive force, F_d of the system.

At initial conditions $v_m = 0$, $F_g = 0$ Equation (6) becomes:

$$\dot{V} = \frac{1}{M}(F_d - C_a v^2) \qquad (7)$$

Likewise, from equation (3) Obtaining its inverse Laplace transform and making F_d the subject of the formula we get:

$$\dot{F}_d = \frac{1}{T}(C_1 u(t-T) - F_d \qquad (8)$$

The output id expressed as:

$$y = v \qquad (9)$$

Hence it is require to eliminate the square term in (2) to be able to linearize the system model so as to enable easy control the system with high parameter values. In order to achieve that we need to differentiate all the state equation from left to right side of the equation with T, C_1, M, and C_a remain constant.

We get equation (10) and (11):

$$\frac{d}{dt}\dot{V} = \frac{1}{M}(\delta F_d - 2C_a\, v\delta v \qquad (10)$$

$$\frac{d}{dt}\dot{F}_d = \frac{1}{T}C_1\delta u(t-T)F_d - \frac{1}{T}\delta F_d \quad (11)$$

And the output becomes:

$$y = \delta v \quad (12)$$

Equation (10), and (11) are in time domain we need to obtain it equivalent Laplace form to be able to find the system transfer function, both δv and δF_d are in discrete form.

Laplace equivalent of equation (10) gives:

$$S\delta V(s) = \frac{\delta F_d}{M} - \frac{2C_a v\delta V(s)}{M} \quad (13)$$

$$\left(S + \frac{2C_aV}{M}\right)\delta V(s) = \frac{\delta Fd(s)}{M} \quad (14)$$

The Laplace transform of equation (11), we have:

$$S\delta F_d(s) = \frac{1}{T}C_1 e^{-\tau s}\delta U(s) - \frac{1}{T}\delta F_d(s) \quad (15)$$

$$\left(S + \frac{1}{T}\right)\delta F_d(s) = \frac{1}{T}C_1 e^{-\tau s}\delta U(s) \quad (16)$$

$$\delta F_d(s) = \frac{C_1 e^{-\tau s}\delta U(s)}{T(s+\frac{1}{T})} \quad (17)$$

Substituting equation (17) into equation (14) we obtained:

$$\frac{\delta V(s)}{\delta U(s)} = \frac{C_1 e^{-\tau s}}{MT\left(S+\frac{2C_aV}{M}\right)(S+\frac{1}{T})} \quad (18)$$

Using the power series approximation, $e^{-\tau s}$ can approximated as:

$$e^{-\tau s} \approx \frac{1}{1+\tau s} = \frac{1}{\tau\left(s+\frac{1}{\tau}\right)} = \frac{\frac{1}{\tau}}{\left(s+\frac{1}{\tau}\right)} \quad (19)$$

Hence, substituting the value of $e^{-\tau}$ from (19) into (18) we get:

$$G_p(s) = \frac{\delta V(s)}{\delta U(s)} = \frac{C_1}{MT\tau\left(S+\frac{2C_aV}{M}\right)\left(S+\frac{1}{T}\right)(S+\frac{1}{T})} \quad (20)$$

Equation (18) can be represented as the bellow:

$$\frac{\Delta V(s)}{\Delta U(s)} = \frac{ae^{-\tau s}}{(S+b)(S+d)(S+d)} \quad (21)$$

Where $a = \frac{e^{-\tau s}}{MT}$, $b = \frac{2c_a V}{M}$ and $d = \frac{1}{T}$

TABLE 1: PARAMETERS OF THE DESIGN [8]

Parameter	Description	Value
C_1	Gain factor	5.34
M	Mass of the passengers and the car	2500Kg
τ	Time delay	0.2s
T	Time constant	1s
G	Acceleration due to gravity	9.8 m/s^2
v	Velocity of the car	20 *Km/hour*
C_a	Aerodynamic drag coefficient	1.23 $N/(m/s^2$
F_d, min	Minimum engine drive force	4000N
F_d, max	Maximum engine drive force	4000N

Third order system been consider in this paper is a third order system, substituting the values in (21).

$$G_p(s) = \frac{1}{(S+0.019680)(s+1)(s+5)} \quad (22)$$

3. CONTROLLER DESIGN

A. PID CONTROLLER

In the paper both the Controller parameters of PID controller and the internal model controller is use to enhance the performance of the cruise control. We employ the use Ziegler-Nichols method for designing the PID controller.

The Objective is to be able to choose the appropriate values for K_p, K_i, K_d using the following procedures. [12]

I. Start by setting K_p to a very small value, where $K_i = K_d = 0$.
II. Increase K_p Until neural stability is achieved.
III. Record the ultimate gain $K_u = K_p$ (at neural stability) and record critical period of oscillation T_u in seconds

IV. Look up K_p T_i and T_d.

The Equation for the PID controller using Ziegler-Nichols is given as:

$$U(t) = K_p(e(t) + \frac{1}{T_i}\int_0^t e(t)d\tau + T_d\frac{de(t)}{dt}) \quad (21)$$

$$U(t) = K_p e(t) + K_p\frac{1}{T_i}\int_0^t e(t)d\tau + K_p T_d\frac{de(t)}{dt}) \quad (22)$$

Where $K_i = \frac{K_p}{T_i}$, $K_p = K_i T_d$

B. IMC CONTROLLER

Internal model controllers use a model of the system being controlled to generate control signals that are sent to the system. Using the mathematical model obtained above for the cruise system and its environment to generate control for the vehicle [2], [4], [7]. Figure 3 depicts the physical layout of a feedback control system using an IMC controller. Where $G_{imc}(s)$ represents the IMC controller, $G_p(s)$ is the system model, $G_m(s)$s the process model utilized in the controller design.

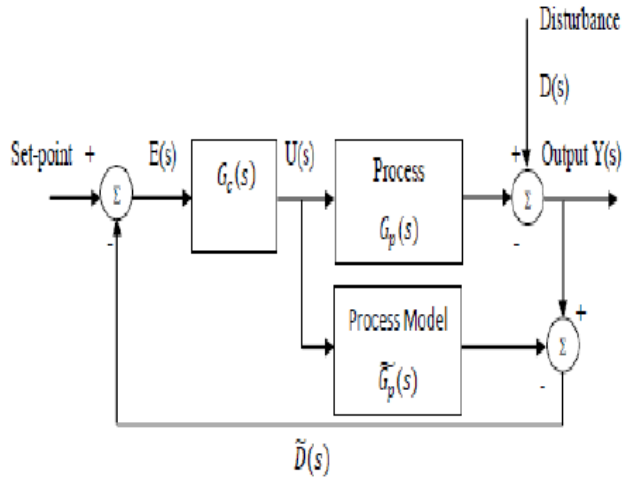

Figure 3. Layout of Feedback control System Using IMC Controller

Using the IMC controller, based on the controller $G_{imc}(s)$ and simplifying the model process $G_m(s)$ gives invertible and non-invertible part:

$$G_m(s) = G_m^+(s) * G_m^-(s) \quad (23)$$

To avoid high instability of the system the only the inverted part is taking into consideration, thereby eliminating the non-invertible part of the controller. The controller then is equal the inverse of the invertible part as:

$$G_c(s) = [G_m^-(s)]^- \quad (24)$$

Adding a filter $G_f(s)$ that is as well tunable to enable the system to be stable at all time we get:

$$G_m(s) = G_c(s) * G_f(s) \quad (25)$$

Where $G_f(s) = \frac{1}{[\lambda_f+1]^n}$ (26)

The filter parameter λ_f can selected as double the output the output response of the open loop response of $G_p(s)$ [13].

The IMC controller becomes:

$$G_{imc}(s) = \frac{(s+0.19680)(s+1)(s+5)}{2s+1} \quad (27)$$

Table 2. PID controller based on optimized parameter [10]

Parameters	**IMC- PID**	
Controller Gain K_C	$\frac{2\zeta\tau}{K_p\lambda}$	K_C =3.33
Integral Time T_i	$2\zeta\tau$	$T_i = 0.08$
Derivative TimeT_d	$\frac{\tau}{2\zeta}$	$T_d = 0.5$

The values of the integral time $T_i = 0.08$ and the constant $K_C = 3.33$ are substituted into the rules.

Consequently, the system's IMC-PI is provided by

$$G_{PID}(s) = \frac{K_C}{T_i^2 s^2 + 2\zeta T_i s+1}\ \frac{2}{0.00624s^2+0.032s+1} \quad (28)$$

Table 3. Summary of Tuning Parameter

Parameters	$G_{PID} - ZN$	G_{PID} −IMC
Controller Gain K_C	K_C =12	K_C =3.33
Integral Time T_i	$T_i = 1.607$	$T_i = 0.08$
Derivative TimeT_d	$T_d = 0.5$	$T_d = 0.5$

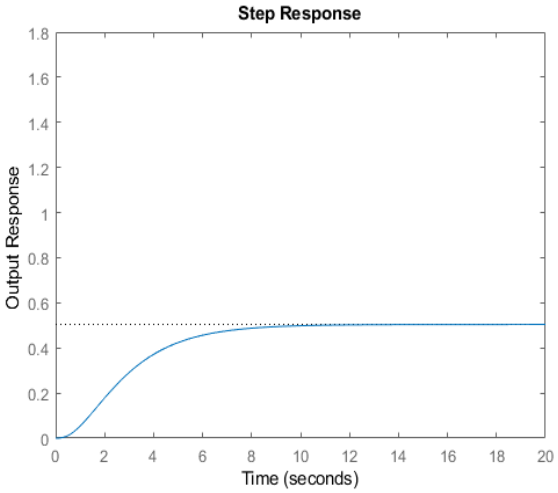

Figure 4. Open loop System Response

4. RESULTS AND DISCUSSION

The design of the controller was achieved using MATLAB-SIMULINK software version 2021. The model of the cruise control was modelled using the Simulink tools and it was depicted in the figures bellow. Based on Ziegler-Nichols Method of designing the PID controller for the system, the ultimate gain $K_u = 20$ is obtained from Routh Hurwitz stability criterion or from the simulation when the system response is neutrally stable (oscillation occur), show in Figure 5 and the period gain $T_u = 3.14secs$. From the look up table to determine the appropriate value for the PID parameters which are $K_p = 12,\ K_i = 7.6433, K_d = 4.7100$. The PID Parameters gives a reasonable system response as shown in figure. 6. Using the IMC controller with the filter an inverter added to the system transfer function gives equation (28) and the system transient response is shown in figure 7.

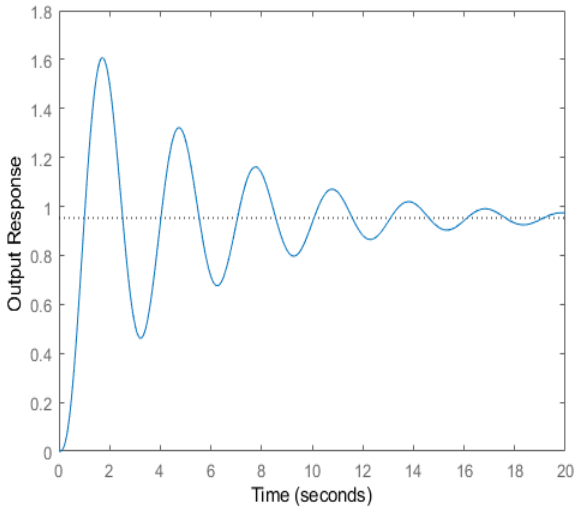

Figure. 5 Output Response of the System at Neural Stability

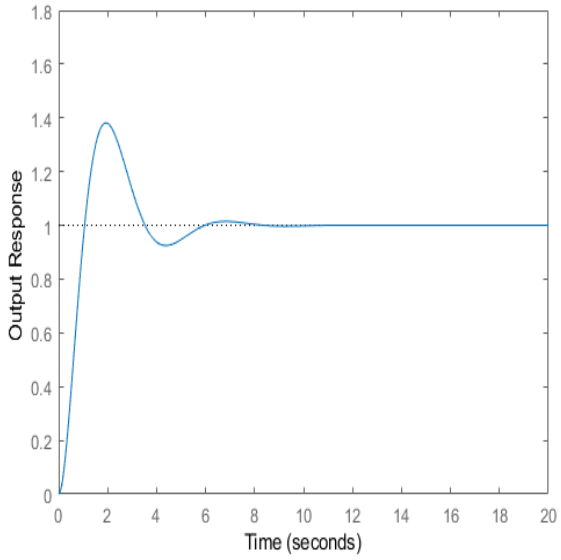

Figure 6. Output response to Ziegler-Nichols Method PID Controller

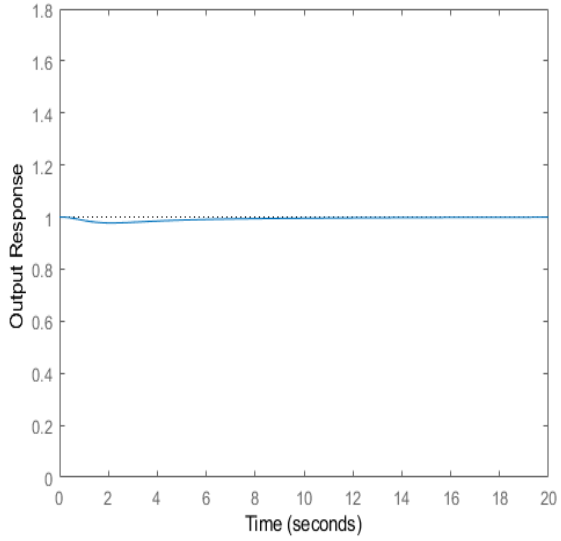

Figure. 7 Output response of IMC PID Controller

From the above diagrams it is observed that IMC-PID has a lower rise time compared to the Ziegler-Nichols PID response, and also the Ziegler-Nichols has an overshoot of about 38.1% while the IMC-PID has no overshoot, in that case the IMC-PID has significantly improved the system compared to the Ziegler-Nichols method.

Table 4. Characteristic Performance of System and Controllers

Transient Response	**System Open Loop Response**	**Ziegler-Nichols PID Response**	**IMC-PID controller Response**
Rise Time (sec) T_r	4.93	0.73	0.17
Settling Time (sec) T_s	8.92	5.54	22
Overshoot %	0	38.1	0
Steady state error ess	0.504	0,985	0.821

5. CONCLUSION

In this work, a cruise system's model was determined by the mathematical modeling of the system. Using the Ziegler-Nichols Method, an appropriate PID controller was also designed for the cruise system, and an IMC controller was also created. The design of a suitable PID controller for the cruise control system was also carried out using Ziegler-Nichols Method and the IMC controller was also developed. The performance of each controller was compared based on the system transient response and steady state error. The IMC controller has significantly improved in tuning the cruise system for modern cars to set a constant speed when traveling on a highway, as seen in Table 4 in which all the responses from both the Ziegler-Nichols PID controller and IMC controller are summarized.

REFERENCE

[1] A. R. Abdulnabi, “PID Controller Design for Cruise Control System using Particle Swarm Optimization,” Iraqi Journal for computers and Informatics, vol. 43, no 2. 2017

[2] D. Kim, S. Moon, J. Park, H. J. Kim, and K. Yi, "Design of an Adaptive Cruise Control / Collision Avoidance with lane change support for vehicle autonomous driving," in 2009 ICCAS-SICE, 2009, pp. 2938–2943

[3] F. Diba, A, Arora, E. Esmailzadeh, "Optimized robust cruise control system for an electric vehicle," Systems Science & Control Engineering: An Open Access Journal, 2014, vol 2, no 1, pp 175-182

[4] F. T. Abiodun, B. S. Habeeb, O. O Mikail, N. Abdul Wahab, "Control of a Two Layered Coupled Tank: Application of IMC, IMC-PI and Pole-Placement PI Controllers, "International Journal of Multidisciplinary Sciences and Engineering, 2013, vol 4, no 11, pp

[5] D. E. Rivera, M. Morari, and S. Skogestad, "Internal model control: PID controller design," Industrial & engineering chemistry process design and development, vol. 25, pp. 252265, 1986.

[6] K. J. Astrom and T. Hagglund, "PID Controllers: Theory, Design and Tuning," second ed: Instrument society of America, 1995.

[7] S. Bdran, M. Shuyuan, S. Saifullah, and H. Jie, "Comparison of PID, Pole Placement and LQR Controllers for speed ration control of continuously Variable Transmission (CVT)," in ICAMECE 2013, pp. 149-154.

[8] M. M. Gulzar, B. Sharif, D. Sibtain, L. Akbar, A. Akhtar "Modelling and Controller Design of Automotive Cruise Control System using Hybrid Model Predictive Controller." IEEE International Conference on Emerging Technologies (ICET), 2019

[9] A. Arora, Y. Lu, F. Diba, & E. Esmailzadeh, "Robust cruise control system for electric vehicle". International conference on mechanical Engineering and Mechatronics, Toronto, Ontario, Canada, 2018

[10] K. Osman, M. F. Rahmat, & M. A. Ahmad. ".Modellingand controller design for a cruise control system." 5th International Colloquium on Signal Processing and its applications ,CSPA2009, Kuala Lumpur, Malaysia, pp. 254– 258.

[11] D. E. Rivera, "Internal Model Control, A Comprehensive View," Arizona State University, Tempe, Arizona 85287-6006, October 27, 1999.

[12] N Adhikari, M Choubey and R Singh, "DC motor control using Ziegler–Nichols and genetic algorithm technique" International Journal of Electrical, Electronics and Computer Engineering, April 2012

[13] F. T. Abiodun, J. A. Bala, A. P. Adedigba "Genetic Algorithm Tuned IMC-PI Controller for Coupled Tank Based Systems." ICECO 2021"

4th International Engineering Conference (IEC2023)
Federal University of Technology, Minna, Nigeria

Virtual System Modelling (VSM) Simulation and Automation of Boat-operated Atalla Lift Net Manipulator Arms' Drive for Capturing of Clupeids (Freshwater Sardine)

*Okouzi, A. S[1],Eze, J. O[2],Ayuba, A. B[1], Ihuahi, J. A[1] & Bankole, N. O[3]
[1]Products Development and Engineering Department, National Institute for Freshwater Fisheries Research, P.M.B., 6006, New Bussa, Niger State, Nigeria
[2]Aquaculture and Biotechnology, National Institute for Freshwater Fisheries Research, P.M.B., 6006, New Bussa, Niger State, Nigeria
[3]Artisanal Fisheries, National Institute for Freshwater Fisheries Research, P.M.B., 6006, New Bussa, Niger State, Nigeria.
*Corresponding author email:okouziabhulimhen@gmail.com +2348072249543

ABSTRACT
Build-and-test as a method for innovative design decision in the exploration of design alternatives particularly for embedded system is expensive and time consuming considering the cost of those components (microcontrollers and integrated circuit) that are highly susceptible to damage. In this study virtual system modeling simulation was employed for the prototyping and automation of Boat-operated Atalla lift net manipulator arms' drive for capturing of Clupeids. The approach adopted in this study includes; understanding the existing process, simplifying and automating the process. Systems engineering methodology involving simulation modeling and automation in Proteus design suit was employed. The schematic capture was implemented in intelligent schematic input system. A C compiler: Arduino 1.8.13 IDE (integrated development environment) was used for the processes of both firmware development and firmware debugging of Arduino UNO (based on ATmega328P) to drive the schematic. The results obtained showed that the virtual system modeler software provided a complete embedded digital laboratory for the simulation and automation of the boat-operated Atalla lift net drive. The microcontroller drawn is also able to accept, and execute the code produced with Arduino IDE connected to Proteus to drive the servo motor of the manipulator arms in the angular displacement pattern; 0° – 135° – 0°, with a delay of 3 minutes at 135° when the fishing gear is expected to be submerged for capturing Clupeids before discharging the content of the gear at the initial position of 0°. It further enabled the examination of animated schematic diagram at work as if it was real hardware.

Keywords: *Boat-operated Atalla lift net, Fish capture technology, Proteus design suit, Prototyping and automation, Virtual system modelling simulation.*

1 INTRODUCTION

The automation of the Boat-operated Atalla Lift Net for capturing of Clupeids (Freshwater Sardine) and other small pelagic species involves actuations of the individual joints which must be controlled in a coordinated fashion for the manipulator arms to perform a desired motion cycle. Lift nets (lever nets), are a method of fishing using nets that are submerged to a certain depth and then lifted out of the water vertically. The nets can be flat or shaped like a bag, a rectangle, a pyramid, or a cone. Lift nets has been classified into portable lift nets, shore-operated stationary lift net and Boat-operated lift net (FAO, 2021c). They typically use bait or a light-source as a fish-attractor. Lift nets are hauled out manually or mechanically through bomm(s) and blocks. Although Winches have been used for mechanically handling of the lift net, it is either that such devices are not available or expensive in developing countries.In recent decades major improvements and technical advancement alongside the introduction of other modern materials are in mechanization of gear handling and use of computer-aided design (CAD) methods to enhance changes in the design and size of fishing gears for more efficient and economic fishing operations as well as reduction of the physical labour required per unit of output (FAO, 2021a and 2021b and Trisnani *et al.*, 2018). The Atalla fishery forms an important indigenous fishing industry in different parts of Nigeria drainage system (Awachie and Walson, 1977). Figure 1 show women using the traditional Boat-operated Atalla lift net from the field level familiarity below Kainji Dam at the Northern tip of Jebba Lake (at Faku).

Figure 1: Two Women Operator Manually Plunging the Boat-operated Atalla Lift Net

Subsequently, the Boat-operated Atalla lift net's two-link manipulator polar arms had been developed from the kinetostatics of the indigenous Boat-operated Atalla lift net mechanism for mechanized capturing of Clupeids. Consequently, fixed automation in automated manufacturing system (Groover, 2015), is required to be implemented to enable the utilization of the Atalla lift net in the capturing of Clupeids in capture-and-place operation. Such capture-and-place operation requires limited-sequence control implemented by setting limits or mechanical stops for each joint, sequencing and synchronizing the actuation of the joints to accomplish the cycle. Embedded system design involving creation of both hardware and software (firmware) (Ćika and Grundler, 2010), is commonly used for such control system.

Traditionally, the build and test approach is used for prototyping embedded system design. This approach besides being expensive and time consuming, those components could be unavailable when firmware development is started and costly sensitive components (microcontroller, integrated circuits and other) as well as the circuit board could be damaged with improper handling. Furthermore, it might also be difficult to access internal operation of the board without having expensive instrumentation (e.g. Digital Storage Oscilloscope - DSO, and Logic Analyzer - LA) (Ćika and Grundler, 2010). Hence, virtual (digital) prototyping among other benefits significantly reduce the time and cost of building a prototype at the product specification stage as well as guarantee the safety of the components (Bullinger *et al*., 2001; Norton, 2001 and McLeod, 2001).The ability to use the schematic particularly in Proteus as a virtual prototype for firmware design and debugging improves the quality of the physical prototype. Less design iterations mean less delay at manufacturing and lower manufacturing costs. Virtual prototyping (VP) and virtual manufacturing (VM) integrate virtual reality (VR) simulation techniques with design and manufacturing processes to fabricate digital prototypes for subsequent stereoscopic visualisation, validation and possibly optimisation of product designs, as well as for evaluation of product assemblability and producability (Choi and Cheung, 2012). VP is an innovative and powerful virtual simulation tool for facilitating rapid product development (Mujber*et al*., 2004 and Kerttula and Tokkonen, 2001), and it has been successfully used in drying industry (Okouzi *et al*., 2020) as well as ship-building and car industries (Wöhlke and Schiller, 2005 and Kim *et al*., 2002). Modelling and analysis play a pivotal role in the field of automatic control with embedded system design as it is difficult and sometimes even impossible to design a control system without having a model describing the dynamics of the processes that are to be managed (Nedeva *et al*., 2013). Numerical models are key elements in the field of automatic control. The models require simulation as one of the steps in their development as well. Of course, the models can not represent all of the elements in a working system and therefore some approximations have to be done (Guzman *et al.,* 2008). Simulation modelling and analysis is the process of creating and experimenting with a computerized mathematical model of a physical system (Okouzi, 2019 and Chung, 2004). This shows the results stemming from the changes in the parameters of the system, without acting on the real system. The system performance can be monitored and analyzed using the graphical results and this performance evaluation can be used to improve and make adjustments in the monitored manufacturing systems. Therefore the aim of this study is the modelling and automation of Boat-operated Atalla lift net manipulator arms' drive in other to understand the behaviour of the control and predict system performance with the following objectives:

To design the schematics for the automation of the Boat-operated Atalla lift net manipulator arms' drive.

To develop the firmware (control software) for the control of Boat-operated Atall lift net manipulator arms' drive.

To simulate the automated Boat-operated Atalla lift net manipulator arms' drive.

2 METHODOLOGY

This section presents the materials and methods employed in achieving the aim of the study. The approach adopted in this study includes; understanding the existing process, simplifying the process and automating the process as well as strategies for automation and process improvement (Groover, 2015; Kandray, 2010 and Black, 1991). Systems engineering methodology involving simulation and automation (BKCASE Editorial Board, 2015 and Muller, 2013), were further used in the study.

2.1 HARDWARE

An Actuator is a type of motor for moving or controlling a mechanism or system. It is operated by a source of energy, typically electric current, hydraulic fluid pressure, or pneumatic pressure, and converts that energy into motion (transduction). An actuator is the mechanism by which a control system acts upon an environment. The actuator used in this study is a DC (direct current) rotary servo system. Servo motors are used where precise control on angular motion is needed. The ASME-04B 380kg/cm 12VDC high torque servo motor used in this study is a heavy duty servo motor with metal case and metal gears for robotics arm and other high toque needs which is interfaced with Arduino UNO (based on ATmega328P 28-Pin PDIP) to drive the schematic.

The servo motor uses the error sensing negative feedback method to provide precise angular motion. It has three wire terminals: two of these wires are to provide ground and positive supply to the Servo motor, while the third wire is for the control signal. These wires of a servo motor are colour coded. The servo motor is driven only when pulse width modulated (PWM: Digital from R/C servo controller or microcontroller) signals are provided

to the control terminal. The maximum torque and speed of ASME-04B servo motor are 190kg/cm and 1.0secs/60deg respectively at 12V and 380kg/cm and 0.5secs/60deg respectively at 24V.

The total pulse duration for a typical servo motor (ASME-04B servo motor) should be of 20 milliseconds. The on-time duration of the control signal of ASME-04B servo motor varies from 0.5ms to 2.5ms for wide range servo motor controller and 1ms to 2ms for microcontrollers. This on-time variation provides angular variation from 0 to 300 degree. However, desired angular position can be calculated by simple interpolations.

2.2 PROTEUS DESIGN SUIT

The Proteus design suit is a virtual system modeling (VSM) and circuit simulation application (Labcenter, 2019). Proteus Professional 8.9 SPO with advanced simulation is the version used in this study. Proteus 8 is a single application with many service modules offering different functionality (schematic capture, PCB layout and others). The wrapper that enables all of the various tools to communicate with each other consists of three main parts vis-à-vis application framework, common database and live netlist.

Proteus 8 consists of a single application (PDS.EXE) which is the framework or container which hosts all of the functionality of Proteus. ISIS (intelligent schematic input system), ARES (advanced routing and editing software) and 3DV all open as tabbed windows within this framework and therefore all have access to the common database.

The common database contains information about parts used in the project. A part can contain both a schematic component and a PCB footprint as well as both user and system properties. Shared access to this database by all application modules makes possible a huge number of new features. Included with Proteus 8 is VSM Studio IDE (integrated development environment) which is a top level application module designed to work seamlessly with the Proteus VSM simulation software for both firmware development and for firmware debugging. In addition to all the features expected from a development environment are also included: automatic detection and configuration of a large and growing number of compilers such that they produce the output format most compatible with a Proteus VSM simulation as well as direct communication with the schematic module. Successful compilation of source code automatically applies the firmware to the microcontroller component on the schematic. Debugging commands in VSM Studio (breakpoints, single step, etc.) synchronously advance and pause the schematic simulation. Furthermore, active popup technology allows one to specify areas of interest on the schematic and have them appear as docket windows in the VSM Studio IDE during simulation. This allows both the viewing (e.g. LCD Display) and interaction (e.g. buttons, switches) with the schematic while debugging inside the IDE.

Together with the common database the maintenance of a live netlist allows all open modules to automatically reflect changes. The new Bill of Materials module contains a live viewer and the 3D Viewer and Design Explorer are also linked into the live netlist.

The suite combines mixed mode SPICE circuit simulation, animated components and microprocessor models to facilitate co-simulation of complete microcontroller based designs. Proteus also has the ability to simulate the interaction between software running on a microcontroller and any analog or digital electronics component connected to it. It simulates input/output ports, interrupts, timers, USARTs and all other peripherals present on each supported processor.

2.3 ATALLA CONTROL MODULE DESIGN AND DEVELOPMENT

The Boat-operated Atalla control module is a component, a control unit expected to be used on the Boat-operated Atalla lift net. It is a collection of sensor, actuator, and basic control logic that act as a regulating device and a state-oriented device that is operated as a single entity. The control module is expected to implement any state-oriented or algorithm-oriented control.

The kinetostatic synthesis and analysis of the indigenous Boat-operated Atalla mechanism developed shows that with the aid of the adjustable link, the Boat-operated Atalla gear is capable of undergoing varying angular displacement in the range $0° \leq \theta < 180°$from it idle point. However, displacement of 135°corresponding to 45° (to the horizontal) is considered adequate in capturing and discharging the content (clupeids) of the net, giving a vertical height below water surface as which is the maximum attainable with of the gear submerged at the given angular displacement.

Therefore, for the servo motor to be positioned at 135° angular sweep, the desired output control pulse was obtained by interpolation as follows:

300° angular displacement is achieved by the pulse duration = 1 ms

1° angular displacement is achieved by the pulse duration of = 1 /300 ms

135° angular displacement is achieved by the pulse duration of = (1/300) x 135 = 0.45 ms

So total on-time pulse will be = 1ms + 0.45ms =1.45 ms.

2.4 EMBEDDED SYSTEM DESIGN AND PROGRAMMING

An embedded system is a system whose principal function is not computational, but which is controlled by a computer embedded within it (Wilmshurst, 2007). Therefore, embedded systems programming (ESP),

consists of building the software control system of a computer-based product (Green, 2008). Arduino Uno based on a low-level microcontroller unit ATmega328P 28-Pin PDIP was programmed for the servo motor control system of Boat-operated Atalla lift net manipulator arms' drive in a top level application module in Proteus 8.9 Professional IDE (Integrated Development Environment).A C compiler: Arduino 1.8.13 IDE (integrated development environment) was used for the processes of both firmware (control software) development and firmware debugging of Arduino UNO (based on ATmega328P 28-Pin PDIP) to drive the schematic.

The servo motor controls were prototyped using ISIS (Intelligent Schematic Input System) in Proteus design suite for schematic capture and simulation (Bates, 2014). ISIS is the schematic capture and interactive simulation software used to create the circuit drawing and to test the circuit prior to building the real hardware. Fig. 2 shows the process flow chart for the virtual system modeling (VSM) simulation of Boat-operated Atalla lift net manipulator arms drive in Proteus design suit.

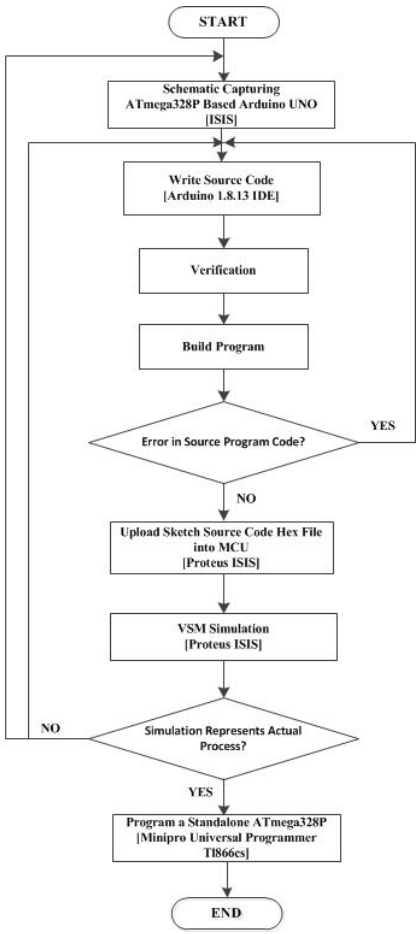

Figure 2: Flowchart for Atalla Lift Net Manipulator Arms' Drive VSM Simulation and Automation

Arduino UNO based on a low level microcontroller ATmega328P 28-Pin PDIP was programmed for the servo motor control system of boat-operated Atalla lift net manipulator arms' drive in a top level application module in Proteus 8, VSM Studio IDE (integrated development environment) designed to work seamlessly with the Proteus VSM simulation software for both firmware (control software) development and for firmware debugging. The servo motor control was prototyped using ISIS (intelligent schematic input system) in Proteus design suite for schematic capture and simulation. ISIS is the schematic capture and interactive simulation software used to create the circuit drawing and to test the circuit prior to building the real hardware. A C compiler: Arduino 1.8.13 IDE (integrated development environment) was used for the processes of both firmware (control software) development and firmware debugging of Arduino UNO (based on ATmega328P 28-Pin PDIP) to drive the schematic.

2.5 SCHEMATIC CAPTURE

The placement of object on Proteus Editing Window was achieved by splitting the contents of the schematics into logical block of circuitry partly for aesthetic and also to reduce wiring clutter on the schematic as shown in Figure 2 with the required hardware and their connections. Terminals were use to terminate each wire and assign a connection which is either power or ground as well as to another wire elsewhere on the circuit in the schematic design. This allows a vast reduction in actual wiring (avoiding spaghetti schematics). The wiring of the circuit was made by the techniques of modeless wiring, follow-me wire autorouting and live cursor display (Labcenter, 2019). Terminal naming is extremely important as it denotes the connection to be made hence, the terminals were labelled to complete each block of circuitry with the exception of Power and Ground that are not labeled.

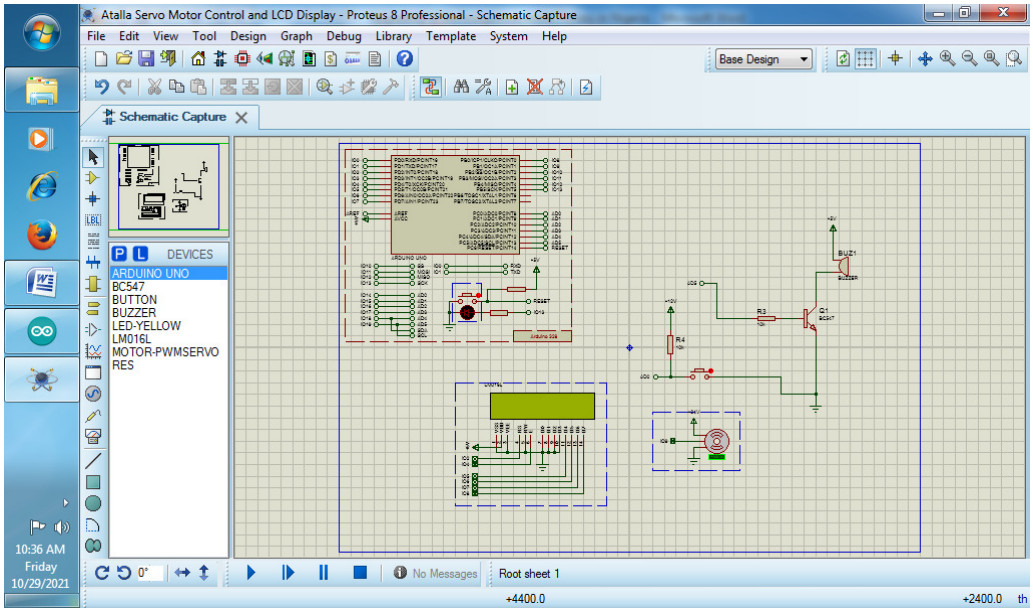

Figure 3: Screen Shot of Servo Motor Control of Atalla Lift Net Manipulator Arms' Drive Schematic with Arduino UNO

It is however pertinent to note that; an unlabeled power terminal is assigned to the VCC/VDD net and an unnamed ground terminal will be assigned to net GND.

3 RESULTS AND DISCUSSION

This section presents the results of the firmware development as well as the interactive simulations of the Boat-operated Atalla lift net manipulator arms' drive. The interactive simulation was used to see if and how the design works and to take very detailed measurements.

3.1 SIMULATIONS OF BOAT-OPERATED ATALLA LIFT NET MANIPULATOR ARMS' DRIVE

Figure 4 presents the Arduino 1.8.13 IDE (integrated development environment) user-friendly and intuitive environment for the development of the Atalla lift net drive computer software (firmware).

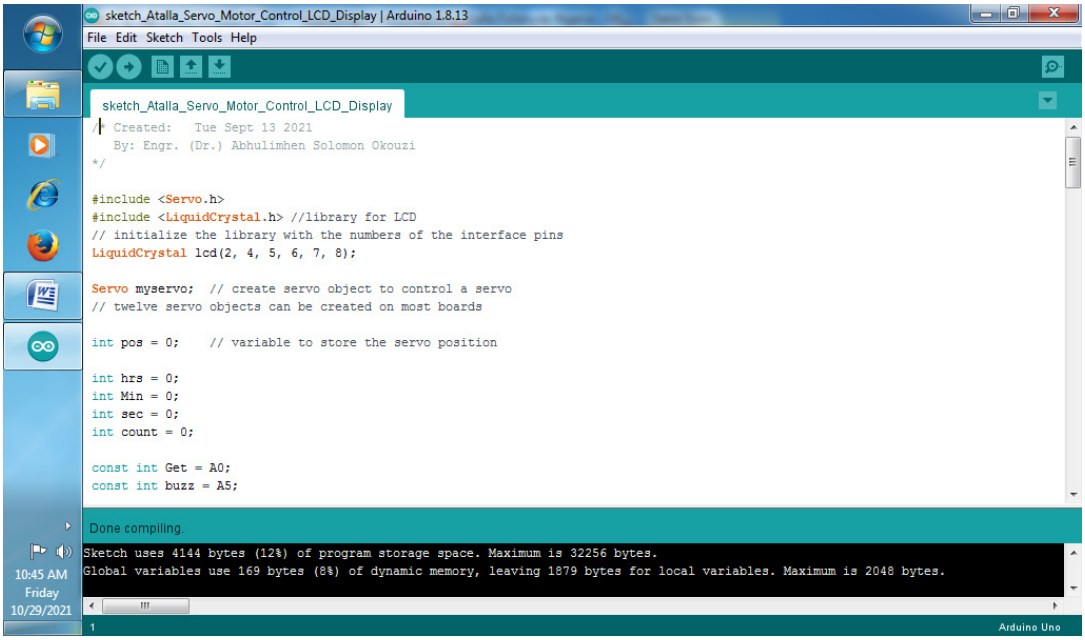

Figure 4: Arduino 1.8.13 IDE for Atalla Lift Net Drive Firmware Development

Figure 4 showed in the progress bar that the compilation which follows the creation of the project and writing of the source code was successful. The complete sketch model in Arduino 1.8.13 IDE for ATmega328P MCU based Arduino UNO consist of four sections. The first section declares the library of the different drives by including the library code. These include the drive for the liquid crystal display and that of the servo motor. Thereafter, the LCD library is initialized with the numbers of the interface pins and then servo object is created to control the servo. The second section declares the integer and constant variables. These include the time (hours, minutes and seconds) and the count which are all set equal to zero. The pin numbers of the pushbutton (A0) and buzzer (A5) are further declared as constant integer. The third section is the void setup( ){ }. This is a **declaration for a function** called "setup". This exact line is required in every Arduino sketch ever. The void setup routing is technically a function that is created at the top of each program. Inside the curly brackets is the code that is expected to run one time as soon as the program starts running, after each power-up or reset of the MCU. It is used to initialize variables; the pushbutton pin is set up to be an input under this section, the buzzer pin is set to be both input as well as output pin modes. This section also starts using libraries: attaches the servo motor to the servo object, set up the LCD number of columns (16) and rows (2) with the instruction to print the Boat-operated Atalla lift net control module brand name ***"NIFFR ATALLAPACK"*** to the defined cursor positions (column, row), which is expected to be displayed for 5000 milliseconds (5 seconds) after which the LCD is cleared. Also with the pushbutton activated, the countdown is set to 3 minutes. The last section of the model is the void loop( ){ }. Like the setup line before it, void loop is yet another Arduino-sketch function that Arduino uses as a part of its structure.

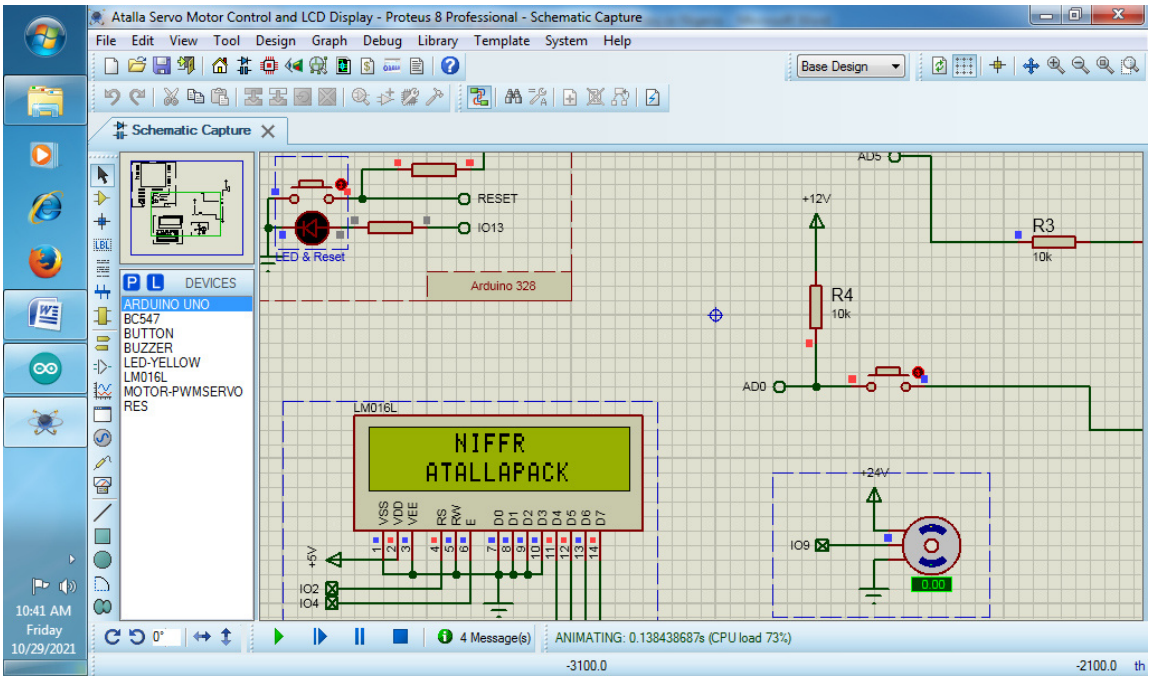

Figure 5: Atalla Lift Net Manipulator Arms'Drive at Rest or to Discharge the Catch

The code inside the loop function runs over and over (repeatedly) as long as the MCU is turned on. This is where the bulk of the Arduino sketch is executed. The program starts directly after the opening curly bracket ({), runs until it sees the closing curly bracket (}), and jumps back up to the first line in loop() and starts all over. It begins with the instruction to Get the digital state of buttonPin with digitalRead() function as count = 1 which starts the motor. Once the motor starts, the LCD is cleared and ***"Motor ON"*** is also printed to the LCD. It takes 15 milliseconds for the motor to drive the arm from 0° to 135° in steps of 1°, the position at which the Atalla lift net is expected to be submerged to capture Clupeids. Once the servo attains the position of 135°, the LCD is cleared again for count = 2 and the time countdown (at 1000 milliseconds) and ***"_Timer Running_"*** printed to the LCD. The Buzzer beeps for 50milliseconds to alert at countdown 15 seconds. At the point the set 3 minutes countdown elapses, the motor also drives the arm from 135° to 0° in steps of 1° to begin the loop of the plunging and hauling cycle of operation of the Boat-operated Atalla lift net. Then the LCD is cleared, again count = 1, time set

to 3 minutes and ***"Press Button to Start Motor"*** printed to the LCD.

The Arduino IDE runs the sketch model to converts the executable code into a text file in hexadecimal (HEX file) encoding that will subsequently be loaded into the MCU by a programmer in the implementation (Banzi and Shiloh, 2015). However for this digital prototyping, the HEX file created after building the program (sketch) in Arduino IDE was uploaded into the Arduino UNO in Proteus ISIS for simulation.

Figure 6 to Figure 9 present the simulation results following the procedure of operation of the developed control module **"NIFFR ATALLAPACK"** of the Boat-operated Atalla lift net

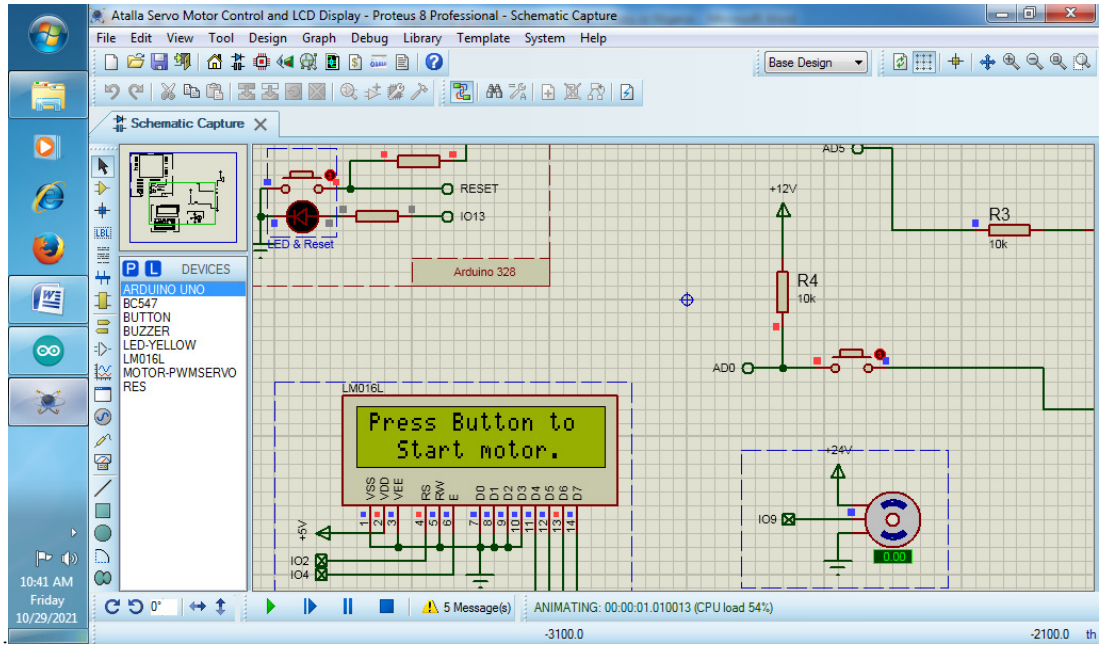

Figure 6: Display with Instruction to Start Motor which is Still at Rest

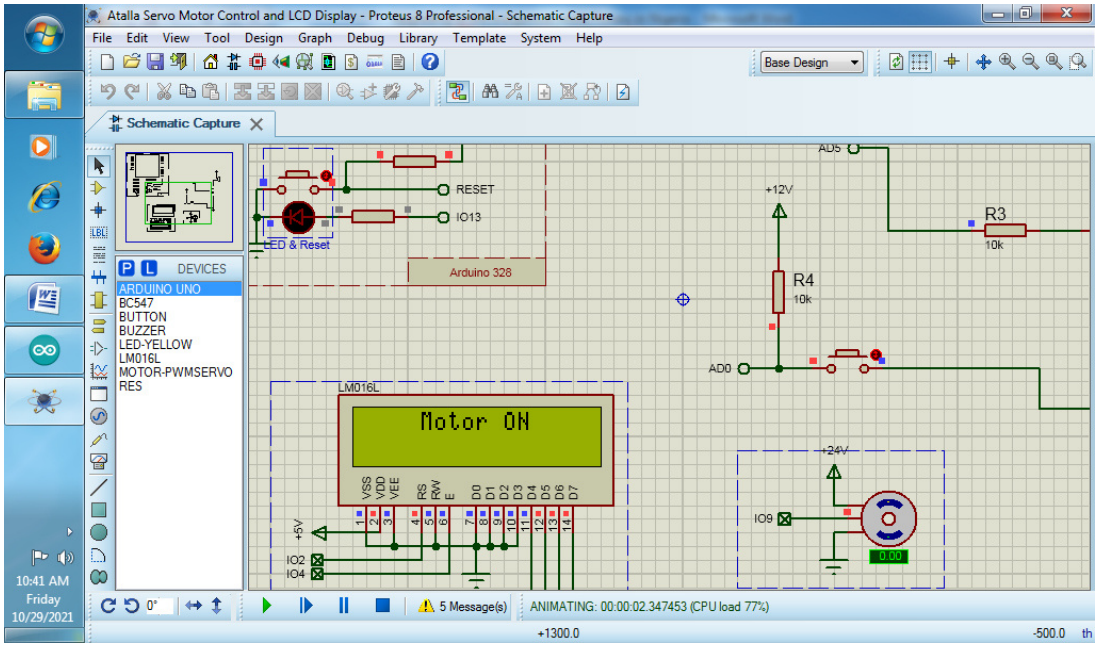

Figure 7: Activation of Button, Display with Motor on and Motor Begins to Move

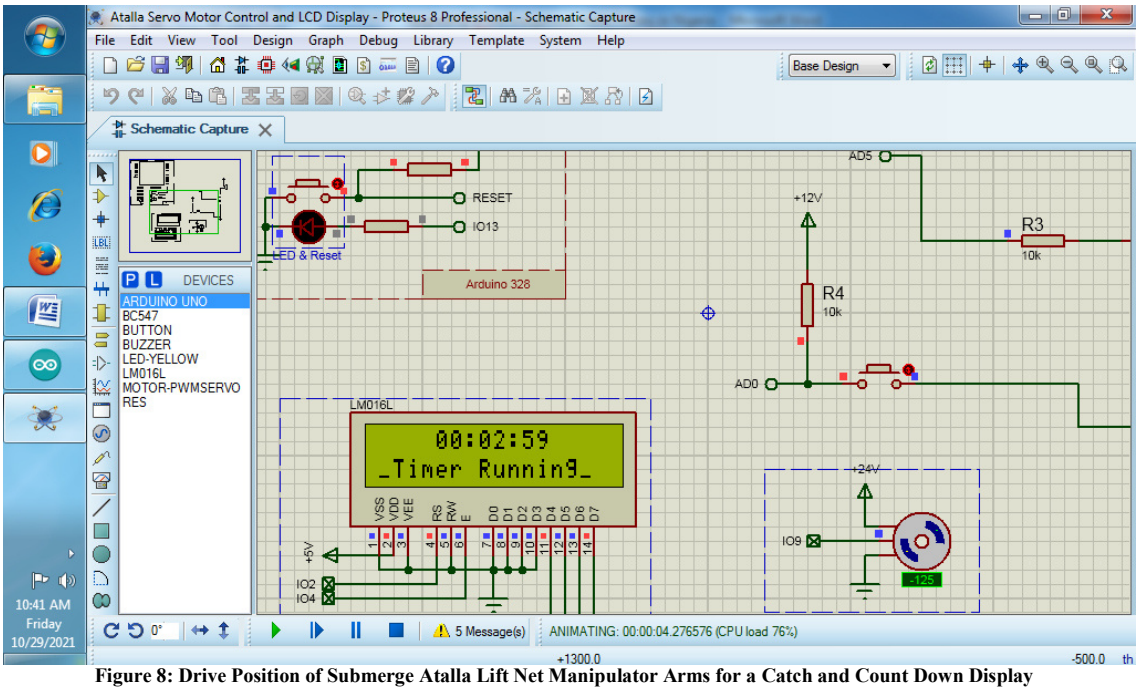

Figure 8: Drive Position of Submerge Atalla Lift Net Manipulator Arms for a Catch and Count Down Display

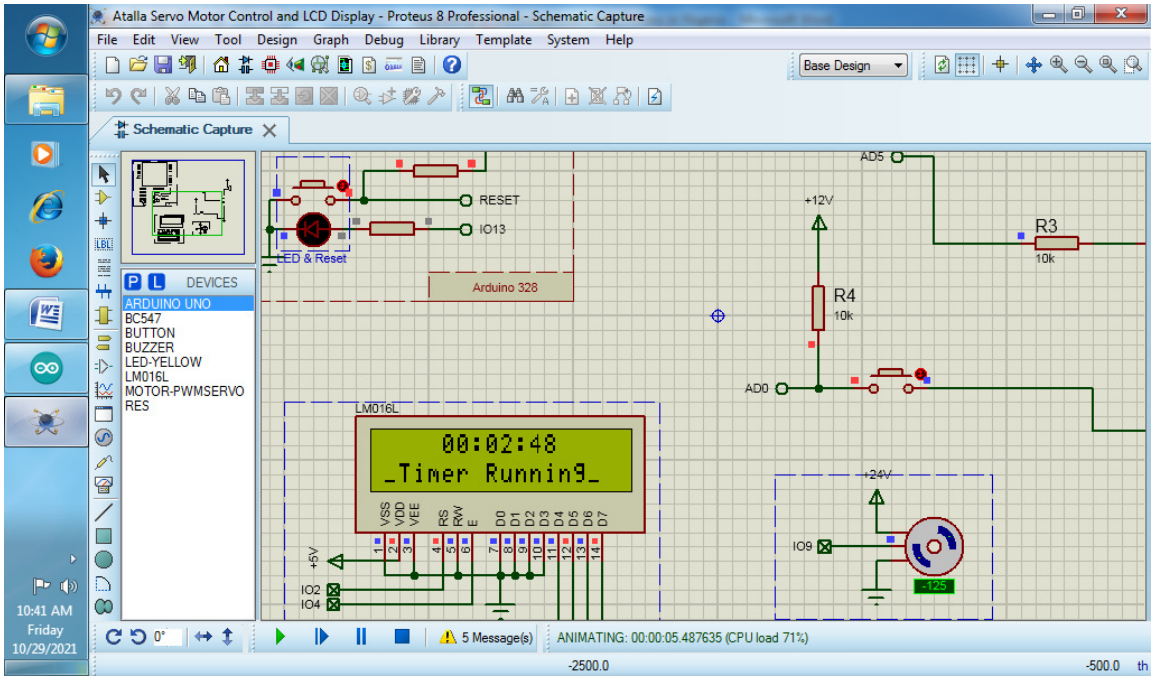

Figure 9: Count Down Continued Through 2mins, 48secs to Zero

The schematics consist of the electrical circuit as shown. The button and the liquid crystal display (LCD) serve as the human machine interface (HMI) introduced for the automated system. The operator of the Boat-operated Atalla is expected to interact with the system through the control module button and initiates the control of the actuator which actuate one of the two-link manipulator polar arms of the Atalla lift net while the LCD in turn displays instructs as well as the state of the system to the operator. This will enable the lift net to be controlled from a distance in the process of teleoperation. Activating the control module power switch displays the brand name ***"NIFFR ATALLAPACK"*** on the LCD as shown in Figure 5 for 5secs after which the operator is

instructed to ***"Press Button to Start Motor"*** as shown in Figure 6. Once the button is pressed and the LCD displays ***"Motor On"*** as shown in Figure 7, the servo motor drives the Atalla lift net into the water to an angular displacement of 135°, the position at which the net is set against the flow so as to capture schools of Clupeids and other forage (prey) fish within the pelagic zone. Figure 8 show the beginning of the countdown from 3 minutes when the lift net attains the desired angular position of 135° for capturing of Clupeids. This countdown continues to zero when the lift net is automatically driven back to its original position (zero degree) to discharge the catch into the boat.

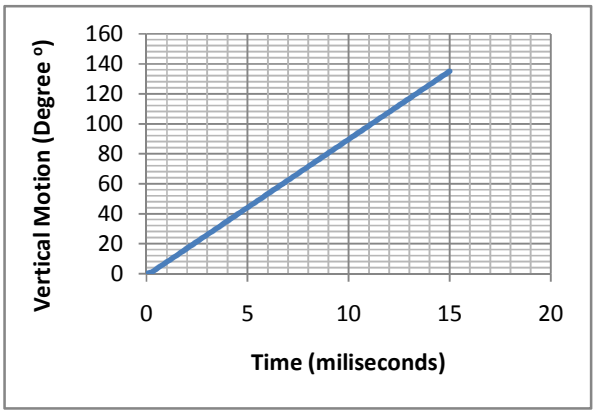

Figure 10: Boat-operated Atalla Numerical Motion Testing

The numerical motion testing of the Boat-operated Atalla lift net manipulator arm of Figure 10 shows that it takes the servo motor 15 miliseconds to drive the arm from it rest (0^o) through a vertical angular distance of 135^o into the water for setting the gear to capture Clupeids.

4 CONCLUSION

In this study, the virtual system modeler software (Proteus) provided a complete embedded digital laboratory for the prototyping, simulation and automation of the boat-operated Atalla lift net manipulator arms' drive developed for the capturing of Clupeid and other small pelagic species. The schematics of the servo motor control of the boat-operated Atalla lift net manipulator arms' drive was designed and developed. The Microcontroller unit was able to accept and execute the firmware developed to drive the servo motor of the manipulator arms in the angular displacement from 0 degree to 135 degreeand back to 0 degree with a delay of 3 minutes at position 135 degree. This delay at 135 degree is intended to enable the fishing gear to submerge and perform the useful work of capturing the Clupeid after which the content of the gear is discharged into the boat when the gear returns to its initial 0 degree position. Furthermore the virtual prototyping enabled the examination of animated schematics diagram at work as if it was real hardware. Satisfied with the capability of the VSM simulation to adequately prototyping the automation of the Boat-operated Atalla lift net manipulated arms' drive, the implementation of the automation of the Boat-operated Atalla lift net is recommended.

5 REFERENCE

Awachie, J. B. E., and Walson, E. C. (1977). The Atalla Fishery of the Lower Niger, Nigeria, *Paper Presented at CIFA Symposium on River and Floodplain Fisheries, (SIFA/77/Symp.12)*, Nov, Bujumbura.

Banzi, M and Shiloh, M. (2015). *Getting Started with Arduino*, 3rd Ed., Maker Media.

Bates, M. (2014). *Interfacing PIC Microcontrollers: Embedded Design by Interactive Simulation*, 2nd Ed., Newnes.

BKCASE Editorial Board. (2015). *Guide to the Systems Engineering Body of Knowledge (SEBoK)*, v. 1.4, Adcock, R. D. (Editor in Chief), Stevens Institute of Technology.

Black, J. T. (1991). *The Design of the Factory with a Future*, McGraw-Hill.

Bullinger, H., Breining, R. and Braun, M. (2001). Virtual reality for industrial engineering, applications for immersive virtual environments, in *Handbook of Industrial Engineering, Technology and Operations Management*. 3rd Ed., G. Salvendy Ed., John Wiley, 2001, 2496-2520.

Choi, S. H. and Cheung, H. H. (2012). Virtual Prototyping for Rapid Product Development. in *Modeling and Simulation in Engineering*. C. Alexandru Ed., InTech. Retrieved fromhttp://www.intechopen.com/books/modeling-and-simulation-in-engineering/virtual-prototyping-for-rapidproduct-development

Chung, C. A. (2004). *Simulation Modelling Handbook: A Practical Approach,* CRC Press.

Cicolani, J. (2018). *Beginning Robotics with Raspberry Pi and Arduino: Using Python and OpenCV*, Apress Media, LLC.

Ćika, D. and Grundler, D. (2010). Proteus Virtual System Modelling used for Microcontroller Education, in *IEEE Xplore Conference Paper.*

FAO (2021a). Fish capture technology. Fisheries and Aquaculture Department. Food and Agriculture Organization of the United Nations. Retrieved from http://www.fao.org/fishery/technology/capture/en

FAO (2021b). Fisheries technology. Fisheries and Aquaculture Department. Food and Agriculture Organization of the United Nations. Retrieved fromhttp://www.fao.org/fishery/technology/en

FAO (2021c). Fishing gear types: Lift nets. Fisheries and Aquaculture Department.Food and Agriculture Organization of the United Nations. Retrieved from http://www.fao.org/fishery/geartype/105/en

Green, T. D. (2008). *Embedded Systems Programming with the PIC16F877*, 2nd Ed., Microchip Technology.

Groover, M. P. (2015). *Automation, Production Systems, and Computer-Integrated Manufacturing.* 4th Ed., Pearson Higher Education .

Guzman, J. L., Astrom, K. J., Dormido, S., Hagglund, T., Piguet, Y. and Berenguel, M. (2008). Interactive Learning Module: Basic Modelling and Identification Concepts, in *Proceedings of the 17th World Congress the International Federation of Automatic Control*, July (pp. 6-11), Seoul, Korea.

Kandray, D. E. (2010).*Programmable Automation Technologies: An Introduction to CNC, Robotics and PLCs*, Industrial Press.

Kerttula, M. and Tokkonen, T. (2001). Virtual Design of Multiengineering Electronics Systems, *IEEE Computer*, *34(11),* 71-79.

Kim, H. T., Lee, J. K., Park, J. H., Park, B. J. and Jang, D. S. (2002). Applying Digital Manufacturing Technology to Ship Production and the Maritime Environment, *Integrated Manufacturing Systems*, 13(5), 295-305.

Labcenter, (2019). *Proteus Design Suite Getting Started Guide*, Labcenter Electronics.

McLeod, P. (2001). *The Availability and Capabilities of Low-End Virtual Modelling (Prototyping) Products to enable Designers and Engineers to Prove Concept Early in the Design Cycle*.Prime Faraday Partnership.

Mujber, T. S., Szecsi, T. and Hashmi, M. S. J. (2004). Virtual Reality Applications in Manufacturing Process Simulation, *Journal of Materials Processing Technology*, *155(156)*, 1834-1838.

Muller, G. (2013). Systems Engineering Research Methods. In: C.J.J. Paredis, C. Bishop, and D. Bodner, (eds.). *Conference on Systems Engineering Research, (CSER' 13),* March, Atlanta, GA.

Nedeva, V., Zlatev, Z. and Atanasov, S. (2013). Virtual Lab for Systems Modellingand Simulation, Applied Researches in Technics, Technologies and Education (ARTTE), *Journal of the Faculty of Technics and Technologies*, *1(1)*, Trakia University. Retrieved fromhttps://sites.google.com/a/trakia-uni.bg/artte/

Norton, A. (2001). *Utilising Rapid Product Development and Late Customization Methodologies within Manufacturing SMEs*, Prime Faraday Partnership.

Okouzi, A. S. (2019). *Simulation and Optimization of the Batch Process in a Rectangular Passive Greenhouse Dryer*, Ph.D. Thesis, Dept. Industrial Engineering, University of Benin, Benin City.

Okouzi, A. S., Ibhadode, A. O. A., Obanor, A. I. and Eze, J. O. (2020). Computational Fluid Dynamics Simulation of the Batch Process in a Rectangular Passive Greenhouse Dryer, *International Journal of Engineering Sciences & Research Technology*, *9(4)*, 95-107.

Trisnani, D. H., Bogi, B. J. Aristi, D. P. F. and Triarso, I. (2018). Business profile of boat lift net and stationary lift net fishing gear in morodemak waters central java, in *IOP Conf. Series: Earth and Environmental Science*, *116*, 12-22.

Warren, J., Adams, J. and Molle, H. (2011). *Arduino Robotics*. California: Apress Media.

Wilmshurst, T. (2007). *Designing Embedded Systems with PIC Microcontrollers: Principles and Applications*, Newnes.

Wöhlke, G. and Schiller, E. (2005). Digital Planning Validation in Automotive Industry, *Computers in Industry*, *56(4)*, 393-405.

4th International Engineering Conference (IEC 2022)
Federal University of Technology, Minna, Nigeria

Comparative Study of Purified Cashew Gum latex and Xanthan Gum for utilization for drug Applications

*Okonkwo, M. C[1], Habibu, Uthman[2], Azeez, O. S[3]
Chemical Engineering Department, Federal University of Technology, PMB 65 Minna Niger State, Nigeria
*Corresponding author email:mdtaste@gmail.com +2348065914618

ABSTRACT
Natural gums available in the country in form of exudates have been underutilized, taking the cashew gum as a case study. In this research, it is shown to be comparable to gum Arabic which makes it a sufficient alternative of gum Arabic for pharmaceutical and food applications. The properties of the cashew gum are similar and also measures up to standard which opens door for its possible application as jellying agent, thickeners, stabilizers etcetera. In this research, Gum extraction/ purification, proximate analysis, x-ray fluorescence spectroscopy (XRF), scanning electron microscopy/ energy dispersive x-ray (SEM-EDX), were carried out. It was observed that the cashew tree gum samples were similar to that of the industrial gum (xanthan gum) as observed in the results of pH, viscosities, proximate analysis, xrf, sem-edx and in the comparison with other international standard. It can therefore be inferred that the local gum exudate can be considered for pharmaceutical and food applications.

Keywords: *Cashew gum, Gum arabic, Proximate analysis, X-ray fluorescence spectroscopy, Scanning electron microscopy.*

1 INTRODUCTION

Nowadays, the term Gum specifically, denotes a group of industrially valuable polysaccharides or their derivatives that hydrates in cold or hot water to form viscous solutions on dispersions (Glicksman and Sand, 1973). Natural gums have physicochemical properties such as color, odor, taste, shape, texture, touch, solubility, pH, swelling index, loss on drying, hygroscopic nature, angle of repose, bulk, true densities, porosity, surface tension. Its commercial interest has found a lot of uses industrially both for food and non-food processing industries (Glicksman, 1969).

They mean soluble cellulose derivatives and modifications of other polysaccharides that in their original state would be insoluble (Glicksman and Sand, 1973). During drug production and delivery, acacia gum serves as binder in tablet formulations like paracetamol, metronidazole and etcetera. (Tekade, 2011). Broad use of diverse excipients, such as binders, thickening agents, sweeteners, and glidants, which can vary the physicochemical properties of the final formulation of the drug and regulate the pharmaco-dynamic and pharmaco-kinetic properties, has made major progress in the field of drug delivery systems. (Amiri et al., 2021). Polymers are used as excipients for the progress of polymer-based drug delivery systems with the function of targeted drug delivery Synthetic polymers have high physical, chemical, and mechanical stability but can cause cytotoxicity and are bio-incompatible (Amiri et al., 2021). Natural gums are hydrophilic colloids that form diffusion with water and boost the viscosity of the constant phase so that solid particle suspended is adequate for long time to measure the uniform dose(Lankalapalli and Sandhala, 2019).

Lately, the utilization of natural polymers has increased. The use of natural plant-derived polysaccharides as excipients has increased in the pharmaceutical industry and can solve formulation problems and reduce the side effects of synthetic polymers. Natural polysaccharides are formed by their *O*-glycosidic linkages by binding monosaccharide residues together and are known as biopolymers. Gums and mucilages are among these excipients. They are widely used in the medicine and cosmetic industries and can also be modified for use in a variety of drug delivery systems. (Amiri et al, 2021). These materials can be used in several pharmacological forms, for instance, control release systems, film-coating agents, nanoparticles, viscous liquid formulations such as ophthalmic solutions, suspensions, implants, etc. Gums and mucilages are composed of many compounds, including polysaccharides. (Amiri et al, 2021).

2 METHODOLOGY

In this research work, we intend to analyze and characterize the purified cashew gum and xanthan gum to see the similarities and the differences between them. The method used include the extraction/ purification method, proximate analysis, x-ray fluorescence and SEM/EDX.

2.1 EXTRACTION/ PURIFICATION

100g of each samples were weighed after drying to reduce the moisture content i.e. after reducing to finite sizes. In each 100g of the sample, 400ml of hot water (100°C) were added, covered and kept in a safe uncontaminated containers. The extraction i.e. leaching of the soluble materials were watched for 2hours. After 24hours, the extracts were decanted and allowed to cool then filtered.

The residue were allowed to dry i.e. bone dry and their weights were taken before and after drying. The samples were then stabilized by the use of additives and the properties of the gum solution were measured.

2.2 PROXIMATE ANALYSIS

Proximate analysis which include moisture content, ash, crude protein, crude fiber determination were carried out according to the standard method of AOAC, (2005), while crude lipid sample were prepared, extracted, distilled and weighed according to the procedure described in AOAC, (2005).

2.2 X-RAY FLUORESCENCE (XRF)

Crushing of each sample with an electric crusher and then pulverized for 60 seconds using Herzog Gyro-mill (Simatic C7-621). After which pellets were set from the pulverized sample, first by grinding 20g of each sample with 0.4g of stearic acid for 60 seconds. After each grinding, the Gyro-mill was further cleansed to prevent contamination. 1g of stearic acid was weighed into an aluminum cup to serve as binding agent and the cup was subsequently filled with the sample to the level point. The cup was then transferred to Herzong pelletizing equipment where it was passed at a pressure of 200KN for 60 seconds. The 2mm pellets were introduced into a sample holder of the x-ray equipment (Phillips PW-1800) for analysis.

2.3 SCANNING ELECTRON MICROSCOPY/ ENERGY DISPERSIVE SPECTROSCOPY (SEM-EDX)

All samples were made to appropriate size so as to fit in the specimen chamber and were generally mounted rigidly on a specimen holder called a specimen stub. Several models of SEM can examine any part of a 6-inch (15 cm) semiconductor wafer, and some can tilt an object of that size to 45^0. The samples were coated with platinum coating of electrically conducting material that were deposited on the sample either by low-vacuum sputter coating or by high-vacuum evaporation. SEM instruments place the specimen in a relative high-pressure chamber where the working distance is short and the electron optical column is differentially pumped to keep vacuum adequately low at the electron gun. The high pressure region around the sample in the ESEM neutralizes charge and provides an amplification of the secondary electron signal.

Low voltage SEM is typically conducted in an FEG-SEM because the field emission guns (FEG) is capable of producing high primary electron brightness and small spot size even at low accelerating potentials.

3 RESULTS AND DISCUSSION

This comparative study is intended at improving the yield of purified cashew gum with xanthan gum. The results gotten from the extraction process, proximate analysis, x-ray fluorescence, comparison of crude with international standards were all tabulated while the sem-edx results were represented as figures.

3.1 EXTRACTION/ PURIFICATION

Mass of sample before extraction = 100g of each sample A & B

Volume after extraction = A is 365m/s, B is 300m/s

pH before extraction = A is 5.54, B is 4.72

TABLE 1: PROPERTIES OF EXTRACTED GUM SAMPLES

SAMPLE	PH	DENSITY	WEIGHT/ DRY (w/v)	EXTRACTS (g)
A	4.30	1.093	13.07	369.18
A1	5.7	1.207	34.33	-
B	3.8	1.058	28.38	-

where: Viscosity of the crude after extraction is 75mPa.s

Sample A is the crude gum

Sample A1 is the purified cashew gum i.e. after addition of formaldehyde

Sample B is the xanthan gum

From Table 1 above, the properties of the dry crude was measured before and after extraction/purification. The pH of the crude increased to 5.7 after the crude was purified which is still acidic comparable to Rabeea et. al., (2016). Slight increase in the density after extraction and an increase of 34.33w/v in the weight after formaldehyde preservative was added, the viscosity of the crude was measured as 75mPa.s after extraction and it's satisfactory comparable to African Journal of Plant Science, (2010).

3.2 PROXIMATE ANALYTICAL RESULTS

TABLE 2: RESULTS ON THE PROXIMATE ANALYSIS

S/N	PROPERTIES	PURIFIED	XANTHAN

		CASHEW GUM	GUM
1	Moisture contents (%)	5.85	13.6
2	Ash contents (%)	2.79	3.00
3	Crude fiber (%)	4.31	4.34
4	Crude protein (%)	1.75	1.88
5	Crude fat/ lipid (Ether extract) (%)	1.52	1.84
6	Internal energy (%)	35.00	34.50
7	Nitrogen content (%)	0.28	0.30
8	Volatile matter	56.14	57.08

From the Table 2 above, the moisture content for the purified cashew gum was low compared to standard from FAO, (1990) which was due to the further drying of the purified crude for conversion to powdered form, comparing every other properties of the crude were satisfactory from standard by FAO, (1990).

3.3 X-RAY FLUORESCENCE (XRF)

TABLE 3: XRF RESULTS OF THE SAMPLES

COMPONENTS	PURIFIED CASHEW GUM (%)	XANTHAN GUM (%)
SiO_2	0.30	0.01
AI_2O_3	0.05	0.03
Fe_2O_3	0.22	0.02
MnO	0.02	0.04
CaO	22.25	17.50
P_2O_5	0.04	0.02
K_2O	18.20	15.20
TiO_2	0.01	0.00
MgO	0.20	0.50
Na_2O	4.05	2.50
LOI	25.50	30.40
Cl	0.03	0.02
SO_3	0.02	0.01
Ba	0.02	0.02
Zn	0.06	0.04
Cu	0.03	0.02
Ni	0.06	0.05

Major Elements: (%), Trace Elements: (ppm), Diffractometer type: Axion max 11, Model: TEFA ORTEC automatic X-ray F., Tube anode: Cu.

The results on Table 3 above shows that the purified cashew gum contains higher amount of calcium oxide by mass of 22.25%, followed by xanthan gum with 17.50% which is favorable according to Katie, (2021) an average adult needs 1,000mg of calcium per day. Purified cashew gum contains higher amount of Potassium oxide, 18.20% followed by xanthan gum with 15.20% which is ok because according to Medline plus, potassium helps the nerves to function and muscles to contract, regularizes the heart beat, diet rich in potassium helps to offset some of sodium's harm and effects on blood pressure. Purified cashew gum indicates higher amount of Ferric oxide, 0.22%, closely followed by xanthan gum with 0.02%, while purified cashew gum contains 4.05% sodium oxide and xanthan gum contains 2.50%, it is mild because according to Centers for Disease Control and Prevention(CDC), reducing the daily intake may reduce the case of high blood pressure. All other minerals present are in such negligible proportion that their presence would not constitute threats to the performances of the gum in medical applications.

3.4 SCANNING ELECTRON MICROSCOPY/ ENERGY DISPERSIVE SPECTROSCOPY (SEM-EDX) ANALYTICAL RESULTS

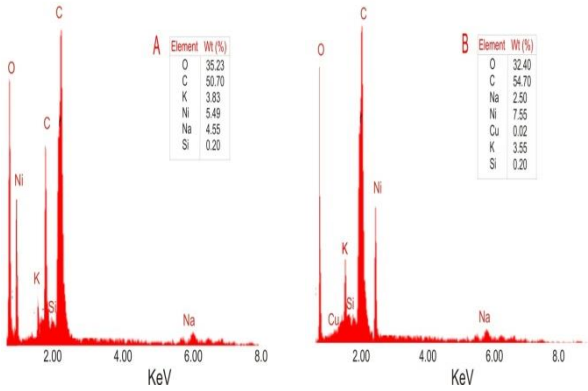

Fig. 1: EDX Results of (a) Purified Cashew Gum (b) Xanthan Gum.

Elemental analysis: As represented in Fig. 1 above, electron dispersive spectroscopy(EDX) was carried out to detect the elements present at the surface of a particular area of both gum. Gum samples were analyzed to determine the percentage(w/w) composition of elements. From the spectrum (Fig. 1a), it was clear that purified cashew gum has a higher percentage of oxygen (O, 35.23%), carbon (C, 50.70), potassium (K, 3.83), nickel (Ni, 5.49) according to (Daldrup et. al. 1983, Sunderman et. al. 1988) excess of it is toxic to humans, sodium (Na, 4.55) and silicon (Si, 0.20%) was present in the gum sample while xanthan gum has a higher percentage of carbon (C, 54.70%), oxygen (O, 32.40), Copper (Cu, 0.02) which works with iron to help the body create red blood cells, keep the blood vessels, nerves, immune system, and bones healthy, aids in iron absorption. John et. al., (2021), sodium (Na, 2.50), nickel (Ni, 7.55), potassium (K, 3.55) and silicon (Si, 0.20%) comparable to the findings of Sharma and Lalita(2011) and Kothiyal and Sharma (2012). Purified cashew gum shows an acceptable amount of potassium and oxygen, which according to medline plus, too much of potassium may lead to heart failure, severe bleeding, disorders etcetera.

3.5 COMPARISON OF PURIFIED CASHEW GUM WITH INTERNATIONAL GUM STANDARDS

TABLE 4: COMPARISON OF GUM SAMPLES

Specification	Purified Cashew Gum	Xanthan Gum	Kordofan Gum	Gum Arabic (FAO, 1990)
Lump color	Reddish brown	White or yellowish white	White or yellowish white	White or yellowish white
Internal energy (%)	35.00	34.50	-	30-39
Nitrogen%	0.28	0.30	0.34	0.27-0.39
Viscosity (cps) 25% sol, 25°C	75	-	15.2	75-110
Tannin(%)	1.255	1.189	-	None
pH	5.7	3.8	4.34	4.1-4.8
Total ash(%)	2.79	3.0	2.50	Not more than 4
Protein %	1.75	1.88	2.20	-
fiber(%)	4.31	4.34	8.19	-
Volatile matter(%)	56.14	57.08	-	51-65
Fat(%)	1.52	1.84	0.05	-
Moisture (%)	5.85	13.6	14.50	13-15

Kordofan Gum (Kauther et. al., 2018) is from Abkrusholla city, south kordofan state, west sudan. Gum Arabic (FAO, 1990) is from Sudan species. African Journal of Plant Science (2010).

4 CONCLUSION

From the result of the analysis above, the local cashew exudate and xanthan gum(imported) have substantially similar characteristics and properties. These suggest that the local gum can be used for pharmaceutical applications after the removal of the possible impurities. The analysis carried out on both gum sample shows that there may be need for pharmaceutical industries and scientists in the country to embark on minimal optimization of gums from local cashew trees. This will help save cost of acquiring these imported gums thereby making it economical for both drug production and market sales. The extraction/ purification was carried out on the crude to improve its properties and characteristics, Proximate analysis was carried out on both gum samples to enable us know how much better the crude is compared to the xanthan gum in terms of specific nutrients. Similar behavior of Purified Cashew Gum and xanthan gum samples were also reported and X-ray fluorescence (XRF) showed that there are lot of similarities between the oxides of the two gum samples with little differences which cannot posses any threat to the human health. The sem-edx showed the active elements present at the surface of each gum sample.

REFERENCE

African Journal of Plant Science, (2010). Academic Journals; 4(4), pp. 95-98. Available online at http://www.academicjournals.org/ajps.

Association of Official Analytical Chemist (AOAC) International. (2005). Official Methods of Analysis of AOAC International, 18th Edition. Gaithersburg, MD, USA, Official Method.

Amiri M., Mohammed S., Zadeh V., Yazdi M., Barani M., Rahdar A., Kyzas G. Z. (2021). Plant Based Gums and Mucilages. Applications in Pharmacology and Nanomedicine.: A Review on Molecules, 26(6).

Daldrup T., Haarhoff K., Szathmary S. C. (1983). Toedliche Nickel Sulfate-intoxikation, Berichte zur Gerichtlichen Medizin 41:141-144.

FAO, Rome (1990). Food and Nutrition Paper. 49:23.

Rabeea M. A. D., Aarif H. E., Misni M., Hassan E. A., Osman M. E. (2016). Characterization and Functional Properties of some Natural Acacia Gums. Journal of the Saudi Society of Agric. Sci. 1-9.

Glicksman M., Sand R. E. (1973). Industrial Gums, Polysaccharide and their Derivatives. Academic Press Inc, 199-230.

Glicksman, (1969). Gum Technology in the Food Industry(Food Science and Technology). Academic Press Inc, 11-15.

John P., Cunha D. O., Faco E. P. (2021). Copper in Diet. Medline Plus.

Katie McCallum. (2021). Calcium Supplements: How much Calcium is too much?. Houston Methodist Leading Medicine.

Kauther S. E. Ali, Hussien M. Daffalla. (2018). Physicochemical and Functional Properties of the Gum Arabic From Acacia Senegal. Annals Food Science and Technology; 19 (1) 27-34.

Kothiyal C. N., Sharma S. (2012.). Removal of Cr (vi) from Aqueous Solution by Polymer Based Guar Gum and Activated Charcoal Adsorbents. The Holistic Approach to Environment.2:3-22.

Lankalapalli S., Sandhala D. (2019). Natural Gums and their use as Pharmaceutical Excipients.: An International Journal of Pharmaceutical Science & Research, 10(12). A review.

Sharma R. K., Lalita (2011). Synthesis and Characterization of Graft Copolymers of N-Vinyl-2-Pyrrolidone onto Guar Gum for Sorption of Fe^{2+} and Cr^{6+} ions. Carbohydrate Polymer, 83: 1929-1936.

Sunderman F. W., Jr., Dingle B., Hopfer S. M., Swift T. (1988). Acute Nickel Toxicity in Electroplating Workers who Accidentally Ingested a Solution of Nickel Sulfate and Nickel Chloride, Am. J. Indust. Med. 14:257-266.

Tekade B. W. (2011). Evaluation of Acacia Gum as a Binder in Tablet Formulations: An International Journal of Research in Pharmaceutical Sciences; 2:616-620.

4th International Engineering Conference (IEC 2022)
Federal University of Technology, Minna, Nigeria

Suitability of Periwinkle Shell ash as new reinforcement for car bumper production

* Adah Patrick Ushie[1], Ademoh Nuhu A[2]., Salawu Asipita Abdulrahman[3], Hassan A.B[4]
[1]Department of Mechanical Engineering, University of Calabar, Cross River State, Nigeria.

[2]Department of Mechanical Engineering, Federal University of Technology Minna, Niger State, Nigeria

[3]Department of Materials and Metallurgical Engineering, Federal University of Technology Minna, Niger State, Nigeria.

[4]Department of Mechanical Engineering, Federal University of Technology Minna, Niger State, Nigeria

*Corresponding author email:patrickadah@unical.edu.ng +2348035216108

ABSTRACT
The automobile industry principally in bumper production, strive to meet the target of saving passenger lives, reducing impact and energy absorbed while improving the economy. The need to have an eco-friendly material make the characterization and utilization of the periwinkle shell (*Tympanotonus fuscatus*) found as waste in the coastal region paramount and to incorporate these waste materials with excellent comparable mechanical properties as fillers is most important. In this research, composites were developed using Periwinkle shell Powder (PsP) as the reinforcement and five different polymeric materials as the matrix. The selected polymeric materials are recycled low-density polyethene (rLDPE), recycled high-density polyethylene (rHDPE), recycled linear low-density polyethylene (rLLDPE), recycled polystyrene (rPP) and recycled polystyrene (rPS) obtained from waste dumps. The periwinkle shells of two separate samples, Ash periwinkle shell powder (APsP) and an Un-ash periwinkle shell powder (UAPsP) were characterized using Xray Fluorescence (XRF). Results obtained from the mechanical tests of the control sample gave a tensile strength of 6.42 MPa, hardness of 73.67Hv, flexural strength of 143.62MPa, impact energy of 0.641J, Flexural Modulus of 2177.55 MPa, density value 0.915 g/cm^{3}and a moisture absorption of 0.24%. The physical and mechanical properties from this research proved the extent at which the ashed periwinkle will add value positively to the composite for the car bumper.

Keywords: Periwinkle shell ash, car bumper, Bio-composite, Sustainability, Polymeric material.

1 INTRODUCTION

The dream of most scientists and engineers in our present world is to discover new and reliable materials which will satisfy the sustainability and environmentally friendly requirement that is direly desired. This is for greater achievements in our new age, as efforts are pushed towards having strong growth, prosperity, security and quality of life for humans. The discovery of good new materials opens the doors to new technologies, in any part of engineering (Buranyi, 2015) and the increasing demand for new materials every day, achieving a good combination of strength, toughness, wear resistance, high-temperature performance and corrosion resistance, especially in the automobile industries, is highly a welcomed growth in the technological world. Consequently, researchers are strongly focusing on the combination of two or more biodegradable and sustainable materials to form green composites with the ideal application, replacing the old materials currently in use (Tobin et., al, 2018). The daily increment of the cost of automobile parts and knowing fully that almost 95% of these parts can be manufactured locally using available local composite materials, the high cost of raw material, high fuel consumption due to weight, poor resistance to our weather conditions especially corrosion and the dream of achieving a bio-based society where every material used or desired is sustainable and harmless to the ecosystem. And putting our thoughts into the effective utilization of our local products can bring immense economic prosperity (Ferguson et al.,2018).

In world development plans, sustainability has been the watched word. No wonder, the United Nations (UN) in her world summit on the 5th of September, 2015, stressed sustainability as the main agenda of the great summit. This great meeting also advised the world and encouraged countries to work towards aiming to achieve the objectives of the sustainable development goal (SDG) by the year 2030. The plans and objectives are to gradually push away all non-environmentally friendly and sustainable engineering materials and replace them with effective biodegradable materials or semi-biodegradable materials that are easily recycled and have little or no trace of danger to the ecosystem. Consequently, the wastes from the agricultural sector of the world are in the increase rapidly, especially waste from seafood (shells and bones) that have been posing danger to the world at large (Yawas, et

al.,2013). If burnt, they affect the environment by pollution and if stored, they become excess for farm usage.

Periwinkle Shell, normally is found under the rocks, stones or pilling between high and low tide marks (Olusola et al., 2012), with typically mottled grey, white, and black and taper to a straight-sided or rounded cone with an obtuse point and inhabit the littoral zone, the region between low and high tides. Although they must live near the ocean and spend part of their time underwater, they prefer to be partially exposed to air (Soneye T. et al., 2016). Eighty species of periwinkle are in existence and ten of these species are found on the coast of west Africa (Dance, 1980). Periwinkle, are most abundant in coastal west Africa and the cheapest mollusk, *Tympanotonus fuscatus*, and *Pachymelania spp* are the two found. The processing method for years are just traditional methods, washed, cooked, socked and thrown away (Ekop et al., 2021). Only the tiny flesh serves as meat and the shell commonly used for several purposes such as soil additives, brake pads, sandpaper, erosion control, ornament, aggregates in construction and many others (Solomon et al., 2017; Ekop et al., 2013; Pessu et al., 2014).

In Nigeria, the *Tympanostomus spp* and *Pach mellania spp* are commonly found in the lagoon and mudflats of Nigeria's Niger Delta between Calabar in the east and Badagry in the west (Dahunsi, 2003). Several researchers have reported that *Tympanotonus fuscatus* have high level of $CaCO_3$ (88.22 ± 0.75%) and a relatively low but substantial level of $MgCO_3$ (10.25 ± 0.42%) (Orji et.al.,2017). The periwinkles found in these regions are V-shaped spiral shells, are very strong, hard and brittle materials (Ogungbele and Omowole, 2012). These qualities make them a bit useful, especially in civil engineering, coarse aggregate for concrete like gravel and stones (Dahunsi and Bamisaye, 2002). However, a large portion of these periwinkle shells are disposed of as waste and constitute a problem to the area, hence the need to channel this waste into more applications especially in the automotive sector. In this research, having an idea of the mechanical and physical properties of this agricultural waste material is very useful especially during processing into other usage and storage for future purposes, efficient design, maintenance of the dimensional accuracy and transformation to different materials is vital (Fakayode,2020; Mohite and Sharma, 2018; Ituen, 2015; Eke and Ehiem,2015). Plate I below show a picture of periwinkle shells.

Plate I: Periwinkle shell Picture

Table I: Elemental composition of periwinkle shell (Source: Ubong and Godwin, 2017; Onuoha et.al., 2017)

Element oxide	SiO_2	Al_2O_3	Fe_2O	CaO	MgO	SO_3	K_2O	Mn_2O_3	P_2O_3	TiO_2	LO
%	33.84	10.20	6.20	40.84	0.48	0.26	0.14	0.24	0.10	0.03	7.60

The Table I, shows that periwinkle has a good percentage (%) of calcium oxide (CaO) which is 40.84% and Silicon oxide (SiO_2) which is 33.84% which sum up to give 74.68%. These elements accounts for the quality of a periwinkle shell in terms of hardness and strength (Dahunsi et al.,2002). Periwinkle shell has also has been reported to have a good compressive strength, high hardness quality and good density with the decrease in size (Yawas et al., 2013).

Consequently, Orji et al., (2017) established the differences between *Typampanotonus fuscatus* and *Littorina littorrea* in Carbon ($CaCO_3$) and Magnesium ($MgCO_3$) in total deposited and they are the main species of Periwinkles found in Nigeria. Their research also affirmed the fact that the Periwinkle shell has a very large deposit of $CaCO_3$, making them a probable source of $CaCO_3$ and responsible for most of its applications in the industrial world.

Also, Otunyo *et al.* (2013),Yawas et al. (2013) and Ekop et al. (2021), studied the physical properties of periwinkle and concluded that these properties of nontoxic, bulk and true densities, porosity, low or zero cost, renewable, availability and light weight which is better and higher if compared to other shells are crucial for almost all engineering work characteristics, This periwinkle shell must be collected fresh to obtain good characterization. The periwinkle shells that stay longer or get soaked in water loses strength (Powel et al., 1985; Amaziah et al., 2013).

The choice of periwinkle shell is because Studies have shown that waste materials such as rice husk ash, groundnut shell ash, mollusk shell ash, bamboo leaf ash, sugar cane bagasse, saw dust ash, corn cub ash (Hussein et al, 2014; Udoeyo and Dashibil, 2002; Umoh and Ujene, 2014; Mahmoud, et al.,2012; Etuk, et al., 2012; Farah, et al., 2011; Adesanya and Raheem, 2009) that are agricultural waste, have been used as composites with good and encouraging results obtained. Yang, et al., (2005) and Ballester, et al., (2007) that generally the chemical composition of shells has 90% calcium carbonate ($CaCO_3$) by weight making it very viable for good mechanical properties.

However, Polymers are a great investment in the world if only we can shift our attention towards converting its waste into Money. There is a huge growth in the area of polymeric composite materials because of their low weight, low price and minimization of environmental impact, Madueke *et al* (2014). Consequently, recycling is

beginning to gain success and the contamination of our ecosystem is reduced (Strapasson et al., 2005). The research for polymeric materials to overcome their deficiencies, especially during usage by humans and new environmental regulations guiding materials that are not okay with the ecosystem, call for this research work (Nwanonenyi et al., 2013). Note that these in-organic materials if used as fillers provide rigidity and temperature resistance but are costly and abrasive to the processing equipment (Cletus, 2002; La Mantia et al., 2005). On the other hand, organic fillers especially from wastes gathered at farms have gained enormous attention from several industries and the plastic industry is one of them. With low densities, low cost, non-abrasiveness, high filling levels, low energy consumption, biodegradability and availability as advantages they have become source materials (Onuegbu & Madufor, 2012).

Plate II: Polymeric material waste.

A car bumper is a structure integrated to the front and rear of a car to absorb impact in a minor collision, thereby minimizing the cost of repair. In summary, they have two safety functions, minimizing height mismatches between vehicles and protecting pedestrians from injuries (Jurewicz et al., 2016). Generally, the bumper has been an important feature in vehicles, protecting components from serious damage when in a low-speed collision and strongly improving the performance of the car by lowering the coefficient of drag. They perform this above by deflecting and protecting the vehicle when there is a collision with other moving vehicles or when a vehicle collides with a stationary Object. The bumper generally does provide security or protection to people, equipment or machines, especially during an accident. In equipment and machine, they reduce vibrations and in our household use, they are used at the edge of doors and windows to absorb impact reducing damage. However, the quality to absorb and nullify the effects of shock or refine the effects of strikes must be put into consideration in the selection of materials. No wonder the world today shifted into lightweight materials like carbon fiber, Glass Epoxy and many others. These light weight material produce low stress during an impact (Srikanth et al., 2014).

Today bumper produce is modernized to combine the strength, quality and properties of different materials to meet its function. They have materials with absorbing spring device usually gas-filled cartridge that allows the new bumper to absorb minor impact without damage or little damage. Kleisner and Zemeik, 2009, in their research, express their view that bumper is designed to deform itself and absorb the force of impact during a collision. The design of car bumper is to absorb shock, often spring-loaded to slow speed collisions, compress and extend back to their original position.

A research work carried out by Sumaila and Ibhadode, (2016), showed that there is always a reduction of weight, which is about 25% in the reduction of weight of parts of a vehicle, saving about 750,000 barrels of oil consumption per day. This reduces the consumption of fuel by 13% and 101 million tons of CO_2 emission into the atmosphere. Also, a good material study play key role during collision of vehicle because some materials are having good impact absorption capacity (Pradeep, 2013), With great consideration to Pedestrian safety (Tso-Liang et al., 2010), light weight property of a material and biodegradability quality (Davoodi et al., 2011) with good environmental standard to eradicate pollution(Davoodi et al., 2008).

However, this research is targeted towards having a light automobile car bumper, reducing the weight of vehicles, saving fuel, saving the cost of parts by converting waste to wealth and above all saving the ecosystem. Lesser density completely means, low fuel consumption and hence, fewer pollutants is discharged into the atmosphere (Sumaila and Ibhadode, 2016). Consequently, this information obtained made the use of periwinkle shell and polymer waste, as a material for reinforcement and binder respectively in composite production for application in the domestic automobile industry, having the weight and cost reduction in mind. This is with great enthusiasm to achieving the production of new material with an economic interest, carbon dioxide balance, health risk reduction, biodegradability, improvement of passengers and pedestrian safety in case of accidents becoming a targeted interest in the development of the car bumper in this research.

2.0 Materials and Method

The materials used in this research are sourced locally in Nigeria. Periwinkle which is sustainable, biodegradable and readily available in nature, were washed by the use of distilled water and Sodium Hydroxide (NaOH) to remove impurities and dried under sunlight to ensure dryness at for a day. Jaw Crusher manufactured by Retch, with model number 41074, type BB2 was used in crushing the Periwinkle Shell (Ps) to powdered form, say 150µm (micro meter) as seen in Plate III below.

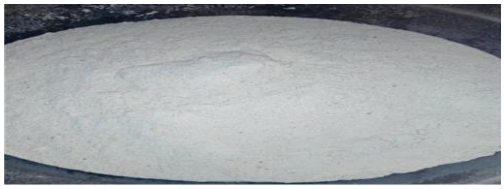

Plate III: Crushed Periwinkle Shell

The Periwinkle Shell Powder (PSP) is divided into two, a part is used for Calcination (converting to ash), and the second part is left in its natural state and gives rise to Un-ash Periwinkle Shell (UPS). XRF test is then conducted on the two samples to detect the element and oxides lost.

Various waste Polymeric Materials were collected and used as Matrix for samples of composites. These Polymeric Materials have unique physical properties and are found around our waste dumping environment, drainages, shallow rivers, streams and oceans. Their presence around our dumps and our eco-marine site pulse a lot of danger to our environment and our Aqua- Life cycle. The five (5) main materials considered are Polystyrene (PS), Polypropylene (PP), Linear Low-Density Polyethylene (LLDPE), Low-Density polyethylene (LDPE) and High-Density polyethylene (HDPE). The choice of these materials is due to their availability as waste and non-biodegradability nature which is dangerous to our Ecosystem.

The response surface method (RSM), was introduced to aid the characterization of a selected car bumper to investigate the general property of the selected model of a car bumper. After the characterization and collection of result, the DOE is being introduced to give a proper combination for the composite to be produced. The Taguchi L16 array with two runs was used and the mixed level design generated using Minitab 19 software.

The density of the selected bumper material (Toyota S-Series Corolla) as obtained is 0.915 g/cm^3 and is in a similar range with the densities of the neat polymers. A full factorial with the use of eight (8) levels was introduced in the filler formulation, with periwinkle have weights: 5, 10, 15, 20, 25, 30, 35, 40 and so on in grams considered and while matrix (polymer)was kept at 125 and 130 grams for all samples as determined from the design of experiments... The least composition will be 5/95=100g and the most will be 40/130=170g with a corresponding density of 0.988 and 1.11 g/cm^3 in d case of PS; and 0.923 and 1.042 in d case of PP and so on. To obtain the appropriate densities, Microsoft excel was employed in the mathematical computation and values from the rule of mixtures values of the density was noted as the weight in grams were altered. Only the mass contributors and density of the matrix were altered during the computation.

3.0 Results and Discussions

The composites developed from these materials is intended to be investigated on its suitability for replacing existing automobile bumpers. For comparison and ease in evaluation, an s-series Toyota corolla has been chosen as the control sample and was subjected to tensile, flexural, impact, hardness, moisture absorption and density determination tests. The rule of mixture was employed to aid the determination of formulation and related parameters of the materials to be used for the development of the car bumper composite.

The x-ray fluorescence result from the ash periwinkle shell powder (APSP) after calcination and an Un-ash periwinkle shell powder (UPSP) is presented in Table II. Higher content of calcium oxide (CaO)was observed for both samples as similarly reported by several researchers (Ubong and Godwin, 2017; Onueha et al., 2017; Badmus et al., 2007; Job et al., 2009; Koffi, 2008; Umoh and Olusola 2012). The presence of P_2O_3 was negligible while other elements were present. Manganese oxide (Mn^2O^3) was totally absent. A great difference was also seen in the percentage of the calcium oxide compare to other researchers the other hand, Magnesium Oxide (MgO) diminished. However, Inyang and Etuk, 2016, in their research show the effect of calcination of a shell which exhibits different chemical composition at different temperature but the major oxide CaO, remain almost same. Table III shows the different composition at different temperature.

Table II: X-ray fluorescence result for periwinkle samples

Element oxide	SiO_2	Al_2O_3	Fe_2O	CaO	MgO	SO_3	K_2O	Mn_2O_3	P_2O_3	TiO_2
UPSP	1.8	2.6	0.8	87.6	3.9	0.3	0.1	-	0.01	1.02
APSP	2.05	3.63	0.24	92.1	0.04	0.2	0.15	-	-	0.01

Table III: Calcination effect at different temperature

Shell type	Calcination Temperature (°C)	Composition (%)							
		SiO_2	Al_2O_3	Fe_2O_3	CaO	MgO	SO_3	K_2O	Na_2O
PSA	900	1.08	0.08	0.40	54.69	0.00	0.13	0.00	0.00
	1000	2.32	0.04	0.08	54.73	0.00	0.15	0.00	0.00
	1200	3.79	0.13	0.39	53.83	0.00	0.27	0.00	0.00
	1400	5.17	0.15	0.15	54.21	0.00	0.47	0.01	0.00
	1600	3.51	0.09	0.08	55.79	0.00	0.16	0.00	0.00

The results obtained using the rule of mixture to determine the theoretical densities of the composites are presented in the Table IV.

Table IV: Predicted composite densities using the rule of mixtures

RUN	FILLER (g)	MATRIX (g)	CONTROL SAMPLE	PREDICTED DENSITIES (g/cm^3)				
				PP	PS	LDPE	LLDPE	HDPE
1	5	125	0.915 g/cm^3	0.916	0.982	0.938	0.941	0.961
2	5	130		0.915	0.981	0.938	0.941	0.961
3	10	125		0.937	1.002	0.959	0.962	0.982
4	10	130		0.935	1.001	0.957	0.960	0.981
5	15	125		0.957	1.023	0.979	0.982	1.002
6	15	130		0.954	1.020	0.977	0.980	1.000
7	20	125		0.976	1.042	0.998	1.001	1.022
8	20	130		0.973	1.039	0.995	0.998	1.019
9	25	125		0.995	1.061	1.017	1.020	1.041
10	25	130		0.991	1.057	1.014	1.017	1.037
11	30	125		1.013	1.079	1.035	1.038	1.059
12	30	130		1.009	1.075	1.031	1.034	1.055
13	35	125		1.030	1.097	1.053	1.056	1.077
14	35	130		1.026	1.092	1.048	1.051	1.072
15	40	125		1.047	1.114	1.070	1.073	1.094
16	40	130		1.042	1.109	1.065	1.068	1.089

The Table V presents mechanical test results obtained from the control sample. These results will be used to

compare results obtained from the periwinkle composites when they are developed.

Table V: Results for the control sample (S-Corolla Series)

	Flexural strength (MPa)	Flexural modulus (MPa)	Impact Strength (J/mm)	Impact Energy (J)	Hardness (Hv)	Water Absorption (%)
Control sample (CS)	143.62	2177.55	0.128	0.641	73.6	0.24

Flexural strength test on the cut bumper samples were carried out in accordance with ASTM D-790. The specimen measuring 100 mm x 25 mm x 5.0 mm were placed one after the other on a support span horizontally at 80 mm gauge length. A steady load was applied to the center of each of the bumper samples by the loading nose producing three-point bending until the sample specimen failed. The maximum load (N) and the corresponding deflection (mm) were recorded accordingly as the sample specimen failure. The flexural strength and flexural modulus were calculated using equations below…….

Flexural Strength = 3FL/2bd2 (MPa) …… (Eq.1)

Flexural Modulus = FL3/4bd3D (MPa) …. (Eq.2)

Where,

F = Maximum Load at break

L = distance between the support spans at both edge of the specimen = 80mm

b = Sample width = 25mm

And the final result of the flexural test which was calculated based on the average are recorded in the Table V, above.

4.0 Conclusion

Periwinkle shell particles as reinforcement in polymeric materials as matrix will improve the quality of the composite to be determine. The results obtained from the Mechanical test and XRF shows and confirm that periwinkle has a good percentage (%) of calcium oxide (CaO) and Silicon oxide (SiO_2) and these elements accounts for the quality of a periwinkle shell in terms of hardness and strength as said by Dahunsi et al.,(2002). And good compressive strength, high hardness quality and good density as discovered by Yawas et al.,(2013). Also, Otunyo *et al.* (2013), Yawas et al. (2013) and Ekop et al. (2021), studied the physical properties of periwinkle of nontoxic, bulk and true densities, porosity, low or zero cost, renewable, availability and light weight were observed. And because the sample were collected fresh, had a good exhibition of Mechanical properties chiefly in strength (Powel et al., 1985; Amaziah et al., 2013). Both the physical and mechanical properties from this research has proven the extent at which the ashed product will add value positive to the composite for the car bumper. Polymeric materials selected are generally known to be of low weight and flexible but with poor mechanical properties. The production of a new car bumper is visible because of the combinations of the properties of the matrix and the fillers. The reduction of weight saving cost of fuel consumption, good thermal and electrical desired for automobile and drag force reduction is achievable. However, the test for the best among these composites from the selected polymeric materials and Periwinkle shell ash (PsA) will be paramount. In the next phase of this research, composites from periwinkle shell shall be developed and tested. An optimized sample will be determined and its properties compared with results obtained from the control sample presented in this study.

REFERENCES

Amaziah, W.O., idongesit, V.F., & Theodore, A.I.,(2013). Exploration study of crushed Periwinkle shell as partial Replacement for fine Aggregates in concrete" *Journal of Engineering and Applied Sciences* (JETEAS) 4 (6): 823-827 (c) scholar link Research Institute Journal, 2013 (ISSN; 2141-7016).

Badmus, M.A.O., Audu, T.O.K., & Anyata, B.U.,(2007). Removal of lead ion from industrial water waste by activated carbon prepared from Periwinkle shell (typanotonus fuscatus)" *Turkish Journal of Engineering and Environmental Science*, 2007.

Ballester, P., Mármol, I., Morales, J., & Sánchez, L. (2007). Use of Limestone Obtained from Waste of the Mussel Cannery Industry for the Production of Mortars. *Cement and Concrete Research* 37, 559-564.

Buranyi, S. (2015). Snail Shells are Inspiring Tomorrow's Toughest Materials. *MOTHERBOAD, McGill University Press.* London.

Cletus, C. (2002). Wood-Plastic composites in the United States, the interfacing of two industries. *Journal of ForestProduction*.52,10-14.0T0T32TU https://doi.org/10.1002/9780470165935.ch1U32T.

Dahunsi, B.I.O. (2003). Properties of Periwinkle- Granite Concrete. *Journal of Civil Engineering* Vol.8, pp.27-35. https://doi.org/10.4314/jce.v8i1.18993.

Dahunsi, B.I.O., & Bamisaye, J.A. (2002). Use of Periwinkle ash (PSA) as partial replacement for cement in concrete. *Proceedings Nigeria Materials Congress and Meeting of Nigeria Material Research Society*, Akure, Nigeria, 184-186.

Davoodi, M.M., Sapuan, S.M., Ahmad, D., Aidy ,A., Khalina, A., & Mehdi J., (2011). Concept selection of car bumper beam with developed hybrid bio-composite material. *Materials and Design* 32 (2011) ", pp.4857– 4865, www.elsevier.com/locate/matdes.

Davoodi, M.M., Sapuan, S.M., Yunus, R.,(2008). Conceptual design of a polymer composite automotive bumper energy absorber. www.sciencedirect.com, www.elsevier.com/locate/matdes, 2008, pp.1447-1452.

Eke, A. B., & Ehiem J. C., (2015). Effect of loading orientations on some mechanical properties of periwinkle varieties. *Umudike Journal of Engineering and Technology*, 1(1): 5564.

Ekop, I. E., Simonyan K. J., & Onwuka U. N., (2021). Effects of processing factors and conditions on the cracking efficiency of *Tympanotonus fuscatus* and Pachymelania aurita periwinkles. Response surface approach. *Journal of Agriculture and Food Research*, 3: 100094.

Ekop, I. E., (2020). Design, fabrication, performance testing and optimization of a motorized periwinkle meat processing machine. Unpublished Ph.D. diss., the Department of Agricultural and Bioresources Engineering, Faculty of Engineering and Engineering Technology, Michael Okpara University of Agriculture Umudike, Nigeria.

Ekop, I. E., Adenuga O.A., & Umoh A.A., (2013). Strength characteristics of granite-Pachymelania aurita shell concrete. *Nigeria Journal of Agriculture, Food and Environment*, 9(2): 9-14.

Ekop I.E., Simontan K.J., Onwuka U.N. (2021). Comparative analysis of physical properties of two varieties of periwinkle relevant to the design of processing equipment. *Res. Agr. Eng.*, 67: 45–50.

Etuk, B. R., Etuk, I. F. & Asuquo, L. O. (2012). Feasibility of Using Sea Shells Ash as Admixtures for Concrete. *Journal of Environmental Science and Engineering*, A1, 121-127.

Fakayode, O. A. (2020). Size-based physical properties of hardshell clam (Mercenaria mercenaria) shell relevant to the design of mechanical processing equipment. *Aquacultural Engineering*, 89: 102056.

Farah, A. W., Ramadhansyah, P. J., Badorul, H. A., & Megat, A. M., (2011). Effect of Rice Husk Ash to the Performance of Concrete Block. *International Journal of Applied Science and Technology*, 1, 53-61.

Ferguson T.H., Oladiran A.K., Raseed D M.A. & Salawu A.A., (2018). Snail Shell as an Inspiring Engineering Material in Science and Technology Development. A Review, DOI:10.15520/ijcrr/2018/9/03/473, Vol 9, No 03, (2018), Engineering and Computer Science.

Kleisner V., & Zemeik R., (2009). Analysis of composite car bumper reinforcement. Faculty of applied science, University of west Bohemia, Univerzitni 22, 306 14 Pizen, Czech Republic.

Koffi, N.E., (2008). Compressive strength of concrete incorporating periwinkle shell ash, unpublished B. Sc project university of Uyo, Nigeria, 2008.

Inyang, A.E. & Etuk, B.R., (2016). The effect of calcination Temperature on the chemical composition of Oyster, Periwinkle and Snails. *International Journal of Research in Engineering and Technology*, Volume :05; Issue: 08; August 2016; eISSN: 2319-1163;pISSN: 2321-7318

Ituen, E. U. U., (2015). Mechanical and chemical properties of selected mullusc shells in Nigeria. *International Journal of Agricultural Policy and Research*, 3(1): 53-59.

Jurewicz, C., Sobhani, A., Woolley, J., Dutschke, J., & Corben, B., (2016). Exploration of vehicle impact speed-injury severity relationships for application in safer road design. *Trans. Res. Procedia*, 14, 4247–4256. doi: 10.1016/j.trpro.2016.05.396.

La Mantia, F., Morreale, M., & Isak, Z., (2005). Processing and mechanical properties of organic filled-polypropylene composites. *Journal of Applied Polymer Science*, 96, 1906-1913.

Madueke, S. N., Awe, S., & Jonah, A. I., (2014). Microbiological analysis of street foods along Lokoja-Abuja express way, Lokoja. *American Journal of Research Communication*, 2(1).

Mahmoud, H., Belel, Z.A., & Nwakaire, C., (2012). Groundnut Shell Ash as a Partial Replacement of Cement in Sandcrete Blocks Production. *International Journal of Development and Sustainability*, 1, 1026-1032.

Mohite, A. M., & Sharma M., (2018). Drying behaviour and engineering properties of Lima beans. *CIGR Journal*, 20(3): 180–185.

Nwanonenyi, S. C., Obidiegwu, M. U., & Onuchukwu, T. S., (2013). Studies on the properties of linear low-density polyethylene filled oyster shell powder. *International Journal of Engineering and Science (IJES)*. 2(7), 42-48.

Ogungbenle, H.N., & Omowole, B.M., (2012). Chemical, functional and amino acid composition of Periwinkle (Typanotonus Fuscatus Var Radula) meat. *Research article*, Vol. 13, issue 2, March-April 2012, Article 027.

Olusola, O.K., Akaninye, A., & Umoh A.A.,(2012). Strength Characteristics of Periwinkle shell Ash blended cement concrete. *International Journal of Architecture Engineering and Construction*, Vol.1, No 4, December 2012, pp. 213-220.

Onuegbu, G.C., & Madufor. I.C., (2012). Effects of filler loadings on the end-use properties of maize tassel filled high sensity polyethylene. *International Research Journal in Engineering. Science and Technology (IREJ)*. 9 (1),2.

Onuoha C., Onyemaobi o.o., Anyakwo C.N., & Onuegbu G.C., (2017). Physical and Morphological properties of periwinkle shell-filled recycled polypropene composite. *International Journal of Innovative Science, Engineering & Technology*, Vol.4 Issue 5, May 2017, ISSN (online) 2348-7968.

Otunyo, A. W., Friday, I. U. & Israel, T. A.,(2013). Exploratory Study of Crushed Periwinkle Shell as Partial Replacement for Fine Aggregates in Concrete. *Journal of Emerging Trends in Engineering and Applied Sciences*, 13(1), 151-159, 2013.

Pessu, P. O., Agoda S., Benson O. B. & Adeniran T. R. (2014). Effect of different processing methods on the meat of *Tympanotonus fuscatus*. *Scientia Africana*, 13(2):47-52.

Powell, C.B., Hart, A.I., & Deekae, S. (1985). Market Survey of the Periwinkle Typanatonus Fuscatus in river state: Sizes, prices, trade routes and exploitation levels. *Proceedings of Fisheries Society of Nigeria (FISON)*, Port-Harcourt, Nigeria.

Pradeep, K. U.(2013). Impact Analysis on Car Bumper by varying speeds using Materials ABS Plastic and Poly Ether Imide by Finite Element Analysis Software Solid works. *International Journal of Modern Engineering Research (IJMER)*, Vol.3, Jan-Feb. 2013, pp-391-395.

Solomon, O. O., Ahmed O. O., & Kunzmann A., (2017). Assessment of length-weight relationship and condition factor of periwinkle (*Tympanotonus fuscatus*, Linnaeus 1758) from okrika estuary, Niger-Delta area of Nigeria. *Environmental Risk Assessment and Remediation*, 1(1): 16.

Soneye T., Ede N.A., Bamigboye G.O., & Olukanni D.O., (2016). The study of Periwinkle Shells as Fine and Coarse Aggregate in Concrete works, Department of civil engineering, Covenant University, Ota, Ogun State, Nigeria. *3rd international conference on Africa Development issues* (CU-ICADI2016), ISSN:2449-075X.

Srikanth, M.V., Rao, V., & Murthy, M.S.R., (2014). Impact Analysis of a Car Bumper for Various Speeds Using Carbon Fiber Reinforced Poly Ether Imide and S2 Glass Epoxy Materials by Solid Works software. *International Journal of Research in Mechanical Engineering & Technology*, Vol.4, April 2014, pp.8994.

Strapasson, R., Amico, S.C., Pereiva, M.F.R., & Sydenstricker, T.H.D., (2005). Tensile and impact behaviour of polypropylene/low density polyethylene blends. Mechanical engineering Department, Federal university of parand (UEPR) polymer testing 24 (2005) 468-493.

Sumaila, M., & Ibhadode, A.O.A., (2016). Performance of an automotive bumper from lalloh (corchorus triden L) plant fibre reinforcement epoxy composite under modified dynating model 8150 Test. *Nigeria Journal of Technology (NIJOTECH)*, vol.35, No1, January 2016, pp. 114-121.

Tobin, F.H., Abubakre,O.K., Muriana, R.A., & Abdulrahman, S.A., (2018). Snail Shell as an Inspiring Engineering Material in Science and Technology Development. A Review. *International Journal of Contemporary Research and Review* ISSN 0976 – 4852, March, 2018, Volume 09, Issue 03. DOI: https://doi.org/10.15520/ijcrr/2018/9/03/473.Received 2017-12-25; Accepted 2018-01-28.

Tso-Liang T., Van-Luc N., &Trong-Hai N.(2010). Design of pedestrian friendly vehicle bumper. *Journal of Mechanical Science and Technology*, 24 (10) ,(2010), pp.2067-2073.

Ubong, D. O., & Godwin, E. A.,(2017). Assessment of physio-chemical properties of Periwinkle shell ash as partial replacement for cement in concrete. *Industrial journal of science*, Vol 1 issue 7, pp 33-36, 2017.

Udoeyo, F. F. and Dashibil, P. U. (2002). Sawdust Ash as Concrete Material. *Journal of Materials in Civil Engineering*, 14, 173–176.

Umoh, A. A., & Ujene, A.O., (2014). Empirical Study on Effect of Bamboo Leaf Ash in Concrete. *Journal of Engineering and Technology*, 5, 71-82

Umoh, A.A., & Olusola O.K., (2012). Strength Characteristics of periwinkle shell ash blended cement concrete. *International Journal of Architecture Engineering and construction*, Vol 1, No. 4, pp. 213-220.

Yang, E. I., Yi, S. T., & Leem, Y. M., (2005). Effect of oyster shell substituted for fine aggregate on concrete characteristics: part I. Fundamental properties. *Cement and Concrete Research*, 35, 2175-2182.

Yawas, D.S., Aku, S.Y., & Amaren, (2013). Morphology and properties of Periwinkle shell asbestos-free brake pad. *Journal of King Saud University*; Engineering Services. 27 November, 2013.

4th International Engineering Conference (IEC 2022)
Federal University of Technology, Minna, Nigeria

Meteorological Drought Estimation in Lower Niger River Basin Using Standardized Precipitation Index

*Odeh, L O[1] & Adesiji, A. R[1]
[1]Department of Civil Engineering, Federal University of Technology, PMB 65 Minna Niger State, Nigeria
*Corresponding author email: odehloveth2@gmail.com +2347065336933

ABSTRACT
The research investigated the Meteorological Drought Estimation in Lower Niger River Basins Using SPI. Drought is an age long disastrous natural occurrence and it is becoming predominant in most parts of northern Nigeria due to climate change and declining rains since the 1970s. The influence of increasing water demand and global climate change has caused concerns about increasing drought in the future. Metrological drought estimation in lower Niger river basin was done using standard precipitation index (SPI) from a streamflow data of 20 years record at Oro in lower Niger River Basin. It was discovered that Oro had mostly moderate drought. Extreme drought was first recorded in the 1960s and became more frequent from the 1970s till date.

Keywords: *Drought, Drought Index, Drought Estimation, Lower Niger Basin*

1 INTRODUCTION

Drought is probably one of the most harmful extreme weather phenomena around the world, but its detriment occurs slowly compared to other natural disasters (Maybank et al. 1995). By definition, drought is a shortage of precipitation over an extended period (Qureshi & Akhtar 2004) also the World Meteorological Organization (WMO, 1986) defines “drought as a sustained extended deficiency in precipitation”. Drought can be confused with other phenomena such as water scarcity, aridity, and desertification. However, unlike aridity drought is a temporary feature of climate that can be intensified by high temperatures, high winds, and low relative humidity (Wilhite 2005).

Meteorological parameters such as precipitation, evaporation, snow, humidity, wind, and temperature may aggregate the severity and effects of droughts. Aridity, on the other hand, is a permanent deficiency of rainfall usually common in dry regions. Desertification is defined as the degradation of land that usually occurs in arid, semi-arid, and dry sub-humid areas caused by climatic variations and human activities (Philander 2008).

Droughts are categorized into four major categories namely agricultural, meteorological, hydrological, and socio-economic drought (Wilhite & Glantz 1985). The type of drought depends mainly on the characteristics of drought namely intensity, duration, frequency, and area coverage. All climatic regions in South Africa are affected by different types of droughts but vary in intensity, duration, and spatial extension (Rouault & Richard 2005). Drought indices play a vital role in quantifying the characteristics of different types of droughts. Those indices also play a major role in drought mitigation, which is important for water resources planning and management. This index requires quality long-term time series of historical observations to analyze the frequency, duration, and intensity of droughts. Most drought indices utilize precipitation data as input into their algorithms, and in most regions, this data is not easily attainable.

Drought is one of the most globally recognized hazards that damage an environment. It occurs when there is a significant rainfall deficit that causes meteorological imbalances and affects the land's productive systems. Indigenes of the middle belt are farmers and fishermen. They depend largely on rainfall and stream flow for their livelihood as such the need for the research cannot be overemphasized. The construction of drought indices relies on the availability of long-term meteorological variables that were observed at meteorological stations. Drought indices examples include the Percentage of normal, Rainfall deciles (Gibbs and Maher, 1967), Standardized Precipitation Index (SPI) by (Mckee et al. 1993), Palmer Drought Severity Index (PDSI; Palmer,1965, Alley, 1984) and Effective Drought Index (EDI; Byun & Kim 2010). Some of these drought indices are reviewed in (Morid et al. 2006, Hayes et al. 2007).

For the calculation of drought indices long-term time series of observations from ground instruments as well as from orbiting satellites is required. However, those observing systems can only give information on current drought episodes. Nevertheless, information on drought duration, intensity, and severity is also required in the future to predict the prospects of droughts. Recent studies are using statistically and dynamically downscaled General Circulation Models (GCMs) as well as Regional Climate Models (RCM) for the assessment of climate change impacts on drought (Berkeley et al. 2011, Törnros & Menzel 2014, Stagge et al. 2015, Kim et al. 2016). Meteorological parameters such as temperatures, rainfall, and soil moisture content obtained from those models can be used as input into the drought indices to predict the

prospects of drought conditions. In South Africa studies of this nature are still limited.

Numerous studies over the last few decades have investigated drought based on their magnitude and severity using different indices, such as multivariable linear regression with composite drought indices (MCDIs) by Liu et al., (2017); optimized vegetation and meteorological drought indices (OVDI and OMDI) by Hao et al., (2015). The SPI was used to study meteorological drought, but this tool can be applied at various timescales to categorize diverse types of drought, Vicente-Serrano al., (2012). Long timescales designate groundwater drought, medium timescales designate hydrological drought, and short timescales are linked to soil moisture and agricultural drought, Ekwezuo, and Eze, (2020).

2 METHODOLOGY

2.1 THE STUDY AREA

The Lower Niger River Basin (LNRB) is termed so because of its location within the Niger River Basin (NRB) located in West Africa. The NRB covers 7.5% of the continent and cuts across ten countries with a total area of approximately 2.2 Million km2 and a total length of 4100km. The NRB is the third longest river in Africa. The Niger River Basin Development Authority Area which is divided into Upper and Lower Niger River Basin Development Authority areas is located in the middle belt of Nigeria between Latitude 7˚N and 12˚N and Longitude 3˚E and 9˚E (Figure 1).

The study area is characterized by rainfall, which varies in amount from 100 mm in the North and 1300 mm in the South. The relief of the area comprises Western uplands to the South which is about 600 m above sea level and the Northcentral Plateau to the north which is about 1200 m above sea level separated by the Niger trough. Most tributaries of River Niger take their sources from the Highland (Fig 2) Niger River is 4200 km long from its source in Futa Jalon Plateau to its mouth in the Atlantic Ocean; 1200 km of which flows in Nigeria. The stretch of the river from where it enters Nigeria to Lokoja receives its major supplies of water from the Upper and Lower Niger River Basin and from major tributaries such as the Kaduna, Kampe, Swashi, Moshi, Awon, Kontangora, Eku, Oshin and Oyun (Figure 2)

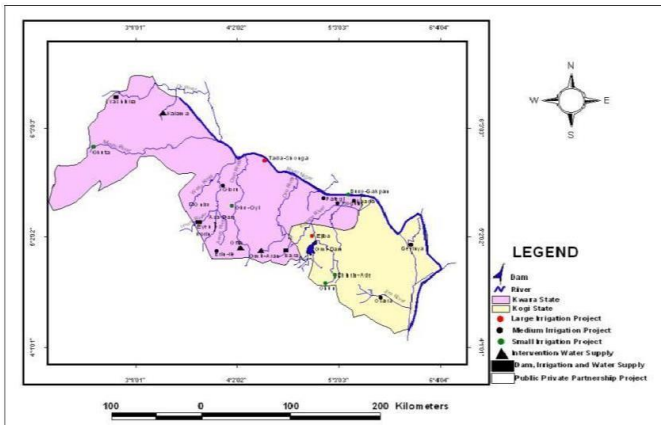

Figure 1: Study area location (Lower Niger River Basin

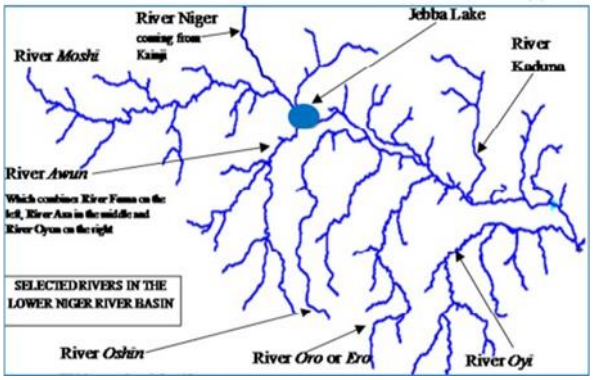

Figure 2: Stream Network of the Rivers in the Lower Niger River Basin

2.2 STANDARDIZED PRECIPITATION INDEX

The drought events based on the precipitation obtained from Minna basin were assessed usin SPI (McKee et al., 1993). This index is based on the cumulative probability of the considered precipitation as presented in equation 1:

$$G(x) = \frac{1}{\beta_{\text{pro}}^{\alpha_{\text{pro}}}\Gamma(\alpha_{\text{pro}})}\int_0^x x^{\alpha_{\text{pro}}-1}e^{-\frac{x}{\beta_{\text{pro}}}}dx \quad (1)$$

where

$$\alpha_{\text{pro}} = \frac{1}{4A}\left(1+\sqrt{1+\frac{4A}{3}}\right)$$

$$A = \ln(x_{sr}) - \frac{\sum_{i=1}^{n}\ln(x_i)}{n}$$

$$\beta_{\text{pro}} = \frac{x_{sr}}{\alpha_{\text{pro}}}$$

x_{sr} is the mean value of the precipitation quantity,
n is the precipitation measurement number and
x_i = the quantity of precipitation in the sequence of data

If x = 0, then the cumulative probability becomes
$H(x) = q + (1-q)G(x)$ and
q = the probability of precipitation as zero (0)

SPI is categorized based on their range values is shown in table 1. The longer time scale of 3- months' rainfall data is used for computing the SPI and the comparison was made to appraise the effects of time scale to understand its behavior with respect to 1-month SPI.

TABLE 1: STANDARD PRECIPITATION INDEX (SPI) DROUGHT CATEGORIES

SPI	Range Category
+ 2 to more	Extremely wet
1.5 to 1.99	Very wet
1.0 to 1.49	Moderately wet
-0.99 to 0.99	Near Normal
-1.0 to -1.49	Moderately dry
-1.5 to -1.99	Severely dry
-2 to less	Extremely dry

3 RESULTS AND DISCUSSIONS

The drought event occurrence at Oro was discovered to be mostly moderate drought. Extreme drought was experienced in the early parts of 1960s and kept increasing since the 1980s which is in conformity with the popular drought of the 1980s as shown in Table 2.

TABLE 2: STANDARD PRECIPITATION INDEX (SPI) VALUES FOR THE STUDY AREA

3-month SPI:	Q1	Q2	Q3	Q4
Year	**1**	**2**	**3**	**4**
1960 - 1961	-1.84	0.34	0.15	0.20
1961 - 1962	-1.34	-2.19	-1.16	-0.85
1962 - 1963	-1.94	0.72	-0.10	-0.08
1963 - 1964	-0.02	0.61	-1.18	-2.29
1964 - 1965	1.52	1.21	-0.75	0.20
1965 - 1966	-0.93	0.54	-0.86	0.95
1966 - 1967	-0.35	0.76	0.45	0.35
1967 - 1968	0.31	1.26	1.72	0.79
1968 - 1969	-0.83	0.67	1.37	1.17
1969 - 1970	1.12	0.47	0.56	-0.34
1970 - 1971	0.94	-0.11	-0.43	1.34
1971 - 1972	0.98	0.45	0.06	-0.79
1972 - 1973	-1.11	-0.31	-0.24	0.69
1973 - 1974	0.65	-0.26	-0.23	0.63
1974 - 1975	0.19	0.07	0.85	0.04
1975 - 1976	0.76	0.37	1.72	-0.63
1976 - 1977	0.74	0.07	-0.62	0.27
1977 - 1978	1.03	-0.30	-0.27	0.65
1978 - 1979	0.74	-1.46	-2.20	0.29
1979 - 1980	0.06	-2.65	1.16	-2.55
1980 - 1981	-0.66	(*)	(*)	(*)

***Q1, Q2, Q4, Q4 = Quarters 1-4 for a water year*

The results of SPI for Lower Niger River Basin were evaluated and found that the results of SPI and actual climatic condition have quite similar results as per their respective categories. For 1960-1961, the drought was only experienced during the first quarter and the region was observed to be severely dry. This was also experienced during 1962-1963 and 1963-1964, though more severely and extremely dry, especially during the fourth quarter. Extreme droughts were also observed in 1978-1979 and 1979-1980 from second to the fourth quarter of the water year. From 1964 to 1978, the region showed varied stages of wetness as the drought categories ranged from 'very wet' to 'moderately wet' and 'near normal'. This was attributed to quantities of precipitation experienced in the basin during the periods. Figure 3 shows the drought patterns for the entire periods in focus (1960-1981).

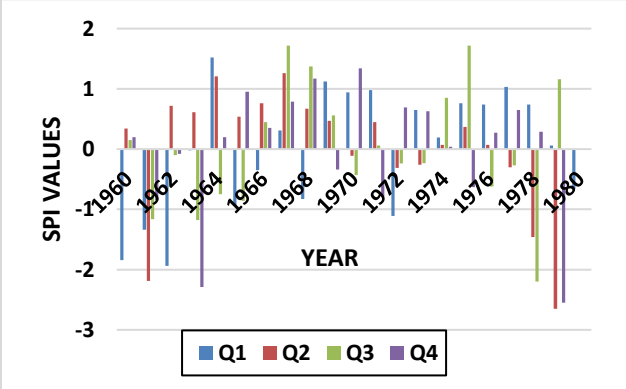

Figure 3: SPI patterns with the water year

4 CONCLUSION

The SPI at a 3-month time-scale was found effective in capturing seasonal drought patterns over space and time in the Lower Benue River Basin. This is evident from the obtained results as the driest and the wettest years were observed with the SPI at a 3-month scale. 1979-1980 were observed as the driest years (2nd & 4th quarters) with the worst drought using SPI at a 3-month scale (-2.65) while 1971-1972 and 1979-1980 (1st quarter) was observed to be the wettest year (0.06).

It was discovered that Oro gauging station in the basin had mostly moderate drought. Severe drought (-1.84) was

first recorded in the 1960s and became more frequent from the 1970s till date. The study concludes that the 3-month SPI represents the good indicator of any drought vulnerability assessment of any drought-prone areas. From the data above, it can be seen that precipitation characteristics of the area have changed with more frequent drought events since the 1970s.

REFERENCES

Alley, W.M., (1984). The Palmer Drought Severity Index: Limitations and Assumptions. Journal of Climate and Applied Meteorology, 23(7), pp.1100–1109.

Berkeley, L., Carolina, N. & Livermore, L., (2011). Projections of Future Drought in the Continental United States and Mexico. , pp.1359–1377

Byun, H.R. & Kim, D.W., (2010). Comparing the Effective Drought Index and the Standardized Precipitation Index I – Introduction. , 89, pp.85–89.

Gibbs W.J, M.J.., (1967). Rainfall deciles as drought indicators, Melbourne. Hayes, B.M.J. et al., (2007). Drought Indices. , (July).

Kim, B.S. et al., (2016). Projection in Future Drought Hazard of South Korea Based on RCP Climate Change Scenario 8 . 5 Using SPEI. , 2016.

Liu, B., (2017). Drought Evolution Due to Climate Change and Links to Precipitation Intensity in the Haihe River Basin.

Maybank, J. et al., (1995). Drought as a natural disaster. Atmosphere - Ocean, 33(2), pp.195– 222.

Mckee, T.B., Doesken, N.J. & Kleist, J., (1993). The relationship of drought frequency and 88 duration to time scales. , (January), pp.17–22.

Morid, S., Smakhtin, V. & Moghaddasi, M., (2006). Comparison of seven meteorological Indices for drought monitoring in Iran. , 985(April), pp.971–985.

Palmer, W.C., (1965). Meteorological Drought. U.S. Weather Bureau, Res. Pap. No. 45, p.58.

Philander, S.., (2008). Encyclopedia of Global warming and climate change, Singapore: SAGE.

Qureshi, A.S. & Akhtar, M., (2004). Analysis of Drought-Coping Strategies in Baluchistan and Sindh Provinces of Pakistan.

Rouault, M. & Richard, Y., (2003). Intensity and spatial extension of drought in South Africa at different time scales. Water SA, 29(4), pp.489–500

Stagge, J. & Tallaksen, L., (2014). Standardized precipitation-evapotranspiration index (SPEI): Sensitivity to potential evapotranspiration model and parameters. International Association of Hydrological Sciences (IAHS), 10(October), pp.367–373.

Törnros, T. & Menzel, L., (2014). Addressing drought conditions under current and future climates in the Jordan River region. Hydrology and Earth System Sciences, 18(1), pp.305–318.

Vicente-Serrano, S.M., Beguería, S. & López-Moreno, J.I., (2010). A multiscalar drought index sensitive to global warming: The standardized precipitation evapotranspiration index. Journal of Climate, 23(7), pp.1696–1718.

Wilhite, D.A. & Glantz, M.H., (1985). Understanding: the Drought Phenomenon: The Role of Definitions. Water International, 10(3), pp.111–120.

4th International Engineering Conference (IEC 2022)
Federal University of Technology, Minna, Nigeria

Effect of Partial Replacement of Fine Aggregate with Crumb Rubber in Concrete Made with Bida Gravel

Mohammed T. A., Abbas B. A., Yusuf A. & Oritola S. F.
Department of Civil Engineering, Federal University of Technology, Minna
Corresponding author's email: engr.mohr@yahoo,com

ABSTRACT
The availability of sand at cheap rates for use as fine aggregate in concrete production is ever becoming unfeasible and this, in addition to environmental sustainability, places a huge need to search for an alternative source of fine aggregate materials. Crumb rubber made from waste automobile tires, can be used to complement sand as fine aggregate in concrete production. This study seeks to investigate the effect of partially replacing fine aggregate with crumb rubber in concrete made with Bida natural stones. Crumb rubber gotten from waste automobile tires was used to replace fine aggregate in the concrete at 0%, 5%, 10%, 15%, 20%, and 25%. The particle size distribution, workability, and compressive strength of these concrete specimens were extensively studied. Curing was done for the period of 7, 14, and 21 days. A mix ratio of 1: 1.65: 2.42 was used for cement content, fine aggregates, and Bida natural stones, respectively, at a water-to-cement ratio of 0.45. Results from the workability test performed showed that a higher percentage replacement of crumb rubber gives a corresponding decrease in the workability of the concrete. In addition, the results obtained from each concrete mix for all cases of curing ages revealed that flexural and compressive strengths decrease with an increasing percentage replacement of crumb rubber in the concrete mix. The flexural strength of the concrete mix was observed to be 6.08N/mm^2 at 5% crumb rubber replacement. While at 25% crumb rubber replacement, a flexural strength of 3.08N/mm^2 was observed. Similarly, the compressive strength of the concrete mix at 5% crumb rubber replacement was noticed to be 20.88N/mm^2 and 11.89N/mm^2 at 25% crumb rubber replacement. This implies that concrete made using crumb rubber as a partial replacement for fine aggregate can be used for structural applications such as in the construction of reinforced concrete slabs, beams, columns, and foundations where high strength is not required.

Keywords: *Bida gravel, compressive strength, concrete, crumb rubber fine aggregate, workability test, curing period, and*

1 INTRODUCTION

Concrete is a construction material consisting of cement, fine aggregate, coarse aggregate, and water with or without admixtures. Concrete is a widely used material for the construction of building and civil engineering works in Nigeria and the world at large. Based on global usage, it is placed in second position after water (Azhagarsamy, 2017). Compressive strengths, tensile strengths, and flexural strengths, which define the degree of resistance a structural element can offer to deformation, remain the most important properties of structural concrete from an engineering point of view. The relationship between concrete composition and mechanical properties has long been a matter of research interest. Concrete characteristics such as hardened mortar, coarse aggregates, and the aggregates/mortar interfacial zone determine the strength of the concrete. The same quality of mortar characterized by different types of fine and coarse aggregates, including various shapes, textures, and mineralogy, may vary the strength of the concrete. However, Alhaji (2016) reported that the concept of water-to-cement ratio (W/C) and aggregates are gaining relevance in developing high-performance concrete.

The availability of sand at a low cost for use as fine aggregate in concrete production is ever becoming unfeasible and this, in addition to environmental sustainability, provides the motive behind the search for an alternative source of fine aggregate materials. Crumb Rubber may satisfy the requirements as a substitute material for sand. Using Crumb Rubber in conjunction with Portland cement and natural aggregates has many advantages, including lower member unit weight, increased ductility, higher shock resistance capability, good shock absorption capability, and higher noise and heat insulation which may improve fire resistance performance. But because the addition of Crumb Rubber in concrete may considerably reduce the compressive strength and other properties, it is suggested that their performance should be assessed. This type of concrete should only be used for structures, such as partition walls, sidewalks, crash barriers, paving, and Architectural Concrete (beams, columns, and foundations) where high strength is not required.

The volume of normal concrete usually constitutes 70 to 80 percent of aggregate particles from natural rocks. The term aggregate is frequently used in the building industry to define rock particles or gravel which constitute the

greatest part of the bulk materials used in concrete. In addition, natural sand and gravel form a fundamental part of mortar in concrete. They also find relevance in the composition of asphalts and macadams for road-making. Sand and gravels are mostly employed as drainage layers and filters and as railway ballast. Unlike aggregates from natural rocks, recycled crushed concrete, and manufactured materials (such as expanded clay, blast furnace slags, and slate pellets) are used to a very limited extent. By standard, the aggregate as a material must be durable, strong, and inert to provide satisfactory performance. More so, the sizes of the constituent particles must be appropriate for the intended application. Aggregates are described as coarse aggregate if particles are retained on a sieve with 5 mm apertures or 4 mm apertures; otherwise, they are described as fine aggregate or sand if they pass through them. (*Newman and Choo, 2003)*

The essential requirement is that the aggregate remains stable in its exposure conditions within the concrete. There are three major reasons why aggregates are mixed with cement paste to form concrete rather than using cement paste alone. The first and oldest reason is that aggregate is cheaper than cement, so its use extends the mix and reduces costs. Secondly, aggregate reduces shrinkage and creep, giving better volume stability. Thirdly, aggregate gives greater durability to concrete. Many deterioration processes principally affect the cement paste.

Currently, non-biodegradable waste materials resulting from various physical and chemical processes are a serious challenge in industrial and developing countries. As a result, extensive research on waste recycling is being done to minimize environmental damage. Consequently, Engineers, like other industrial waste recycling researchers, have achieved advances in using these waste materials. One of these non-biodegradable materials that exponentially enters the environment is used automobile tires (*Rohit et al., 2020*).

Crumb Rubber is the product from processing used tires into fine granules or particles while using mechanical or cryogenic procedures. During the mechanical or cryogenic procedure, impurities such as steel and fabric components of the tires are removed. Crumb rubber includes particles ranging in size from 4.75mm to less than 0.075mm (*Rohit et al., 2020*).

The world is rapidly advancing in technology, and so is the world of infrastructure (*Agrawal et al., 2017*). The resources required to achieve the construction of this infrastructure are also in rapid use. Fine aggregate is an essential component of concrete. According to *Azhagarsamy (2017),* pit or natural river sand is the most used fine aggregate for construction purposes. However, the global consumption of natural sand is very high due to the extensive use of concrete. To lessen the use of natural river sand, the construction industry of developing countries has been saddled with the responsibility of identifying alternative materials to reduce or eliminate the demand for natural sand.

Sand mining from pits and river-bed is a direct cause of erosion. The physical impact of sand mining includes Downstream erosion due to increased carrying capacity of a stream, downstream changes in patterns of deposition, Upstream erosion because of an increase in channel bed slope and changes in the flow velocity, Loss of adjacent land and/or structures, The undercutting and collapse of riverbanks (*Saviour and Stalin, 2012*). The act of mining sand is regulated by law in many places, but it is still often done illegally (*Kadir et al., 2017*).

A significant number of used tires are discarded each year after their useful lifetime. Several approaches have been explored to recycle used tires. In several instances, tire-derived aggregates, which are typically large aggregates, have been used as raw materials for civil engineering projects. However, a significant fraction of used tires still find their way into landfills, resulting in public health and environmental hazard. Landfill facilities require tires to be shredded to minimize the extent of floating tires; the cost of shredding is dependent on the final particle size of the rubber, with finer particles being more expensive. Several studies have explored the use of tire-derived particles as a substitute for either coarse or fine aggregates, with varying degrees of success. (*Gideon et al., 2016*) This study is therefore aimed at determining the suitability of Crumb Rubber as a partial replacement of fine aggregate in concrete, using Bida natural stones as coarse aggregates.

Crumb rubber, as defined by *Kaloush et al. (2005*), is a substance made by shredding and crushing old tires. In Cement manufacturing, high-temperature processes allow using scrap tires as an alternate fuel source. The rubber in tires is made up of hydrocarbon molecules, which, like coal and oil, have a high energy value. On an equal mass basis, tires have a 25% higher fuel value than coal (*PCA 2008*). In the United States, over 300 million used tires are produced each year (*RMA 2009*). The Environmental Protection Agency (EPA) acknowledges tire-derived fuel (TDF) as an environmentally friendly practice and encourages industries to use it. Tire-derived fuel (crumb rubber) is used in cement production to recover energy and conserve fossil fuel resources that would otherwise end up in landfills or unregulated disposal sites. The kiln's tremendous heat ensures that the tires are completely destroyed. The use of tires as fuel can actually lower certain emissions because there are no visible emissions from the tires (PCA 2008).

Rubbercrete is manufactured by substituting crumb rubber (CR) from discarded tires for part of the fine aggregate in regular concrete. (*Mohammed et al., 2018).* Many fresh and hardened qualities of rubbercrete have been improved in comparison to regular concrete, according to the literature. The fresh rubbercrete mixture has a higher percentage of air-entrained, making it more freeze and thaw-resistant (*Richardson et al., 2016*), as well as lighter unit weight and workability (*Kardos and Durham, 2015).*

According to previous studies, when the percentage of crumb rubber increases, compressive strength gradually decreases (*Najib et al., 2018*). *Najib et al. (2018)* further propounded that the reasons for the decrease in compressive and flexural strength of the rubberized concrete are as follows: extra rubber tire particles are lodged in the aged and surrounding cement material; lack of a proper bond between rubber powder and cement during the aggregation process; and low unique gravity of rubber and lack of bonding with other concrete materials.

low unique gravity of rubber and the absence of its bonding with different concrete elements

The proportion of replacement employed during the aggregation between crumb rubber and cement has an impact on the rubberized concrete strength. Rubbercrete, on the other hand, enhances other technological qualities like energy absorption. Rubbercrete improves impact energy, impact load, toughness, ductility, freeze/thaw resistance, thermal insulation, and sound insulation, and makes cement considerably eco-friendlier and lighter (reuse of rubber and minor aggregate). Because rubber has a lower specific gravity than aggregates, substituting rubber for aggregates lowers the overall specific gravity (*Valente and Sibai, 2019*).

Kunal and Ramana (2017) studied the mechanical and durability qualities of concrete using different proportions of Waste Tyre Rubber (0%, 4%, 4.5%), 5%, and 5.5%). It has been discovered that as the amount of Waste Tyre Rubber increases, the workability of concrete diminishes. With a 4 percent replacement of fine aggregate with rubber, the output of flexural and compressive strength reduces slightly.

Eshmaiel et al. (2009) tested the performance of concrete mixtures, including 5%, 7.5 %, and 10% used tires, respectively. In the investigation, rubber as aggregate and cement replacements yielded the following results: Compressive strength was reduced as the percentage of rubber replacement in concrete increased. However, the decrease in compressive strength was small (less than 5%) with no noticeable changes in other concrete properties. Concrete with chipped rubber (as a replacement for aggregates) has a lower tensile strength than concrete with powdered rubber (for cement replacement).

Gajendra et al. (2020) investigated concrete sustainability by partially replacing fine aggregate with waste tires in an experiment. A surface modification strategy was proposed in their research to introduce strong polarity groups to the rubber surface in order to create a strong chemical interaction between the rubber and the cement matrix. It was discovered that the proposed method is effective in enhancing the mechanical properties of concrete.

2 SIGNIFICANCE OF THE STUDY

The growing concern of global warming, pollution, and natural resources depletion due to rapid construction activities worldwide has challenged many researchers and engineers to seek and develop alternative materials relying on renewable resources.

Fine aggregate, which is the most common and also one of the major components of concrete is being mined at an exponential rate. Sand mining from pits and the river bed is a direct cause of erosion. The physical impact of sand mining includes

Downstream erosion due to increased carrying capacity of a stream, downstream changes in patterns of deposition, Upstream erosion as a result of an increase in channel bed slope and changes in the flow velocity, The loss of adjacent land and/or structures, The undercutting and collapse of river banks.

On the other hand, the disposal and management of waste automobile tires pose an environmental concern in several countries. This is mainly due to the non-biodegradable nature of this solid waste as a result of the presence of stabilizers, additives, and the cross-linked structure of the elastomeric polymer material. Disposal of waste tires is very difficult as it requires large spaces thereby creating environmental, aesthetics, and health-related problems for the surrounding environment. Dumped waste automobile tires in the environment, cause many environmental and health hazards such as the high risk of fire and provide shelter to harmful insects, rodents, and animals such as rats, mosquitoes, snakes, mice etc.

In this study, Crumb rubber, a product made by shredding and crushing old tires into granules of varying sizes has been used to partially replace fine aggregate in concrete and the term “Rubbercrete” is used to describe concrete manufactured by partially substituting fine aggregate with crumb rubber (CR) in regular concrete. The physical properties of the materials such as bulk density, sieve analysis etc., and concrete properties such as slump, compressive strength, flexural strength, etc. were examined. These properties were compared against values for traditional concrete to assess their comparative performances so as to achieve a better understanding of the effect of partial replacement of fine aggregates with crumb rubber in concrete made with Bida natural stone.

3 MATERIALS AND METHOD

3.1 MATERIALS

The materials used to prepare the concrete in this study are cement, fine aggregate, crumb rubber, Bida natural stone, and water.

3.1.1 ORDINARY PORTLAND CEMENT

The performance of concrete is largely dependent upon the properties of the cementitious materials, particularly chemical properties. Portland cement is indisputably the most widely used binding material in the manufacture of hydraulic-cement concrete. Cement is selected based on careful consideration of all performance requirements, not

just strength. The Ordinary Portland Cement used in this study was sourced within Minna metropolis and conforms to BS EN 197- 1 (2000).

3.1.2 FINE AGGREGATE

The fine aggregates used in this study have all particles passing through a sieve size 4.75 mm and retained on a sieve size 150 μm aimed at producing good quality concrete. The fine aggregates used are in two parts as follows:

3.1.2.1 Sharp sand

The sand was sourced from Gidan Mangoro, Minna, Niger state of Nigeria. It was ensured that the sample used for this study is clean, sharp, and free from loam, clay, and organic impurities conforming to the standard requirement of BS EN 12620 (2008). The sample collected was air-dried to enhance good quality concrete in the civil engineering laboratory.

3.1.2.2 Crumb rubber

Crumb Rubber (Plate I) made from irregularly shaped torn Tires particles obtained by the industrial decomposition of used Tires was used as a partial replacement for the sand. Manufacturing of Crumb rubber from used tires is principally a three-stage process involving, shredding, granulating, and finally, fine grinding, which produces a top-notch material for several re-applications such as the production of Tartan tracks for athletics games and the production of Rubbercrete.

Plate I: Crumb rubber

3.1.3 COARSE AGGREGATES

The coarse aggregate used in this study is Bida Natural Stone (BNS) shown in Plate II and it was sourced from Bida basin. The stone is a by-product of the decomposition of parent rock, transportation, and deposition of the rock particles in the Bida Basin. These coarse aggregates have a maximum size of 19mm in diameter. The aggregates also conform to the standard requirement of BS EN 12620 (2002).

Plate II: Bida natural stone

3.1.4 PORTABLE WATER

Potable drinking water from the Civil Engineering Laboratory, Federal University of Technology Minna was used throughout this work. It was ensured that the water for the concrete was clean, free from deleterious materials, and fit for drinking as recommended by BS EN 1008 (2002).

3.2 METHODS

The physical characteristics of the aggregates were determined using sieve analysis, specific gravity, Bulk density (compacted and uncompacted), aggregate impact value, and aggregate crushing value tests.
The mechanical properties of the hardened concrete were also determined using dry density, flexural strength, and compressive strength tests respectively.

3.2.1 SPECIFIC GRAVITY TEST

Specific gravity is defined as the ratio of the density of a material to the density of distilled water at a stated temperature. Since aggregates generally contain pores, the value of the specific gravity (or relative density) varies depending on the extent to which the pores contained absorbed water at the time of testing. This test was conducted in accordance with ASTMC C33/C33 (2016).

3.2.2 SIEVE ANALYSIS TEST

The way particles of aggregates fit together in a mix, as influenced by its gradation, surface texture, and shape has an important effect on the workability and finishing characteristics of fresh concrete and consequently on the properties of hardened concrete. A sieve analysis test was carried out to determine the particle size distribution of aggregate used in the concrete mix.
BS EN 12620 (2008) for sieve analysis was used; the method employed for the determination of particle size distribution is the dry sieve analysis.

3.2.3 BULK DENSITY TEST

The Bulk density or unit weight of an aggregate sample gives valuable information regarding the shape and grading of the aggregate. Since the test measures the actual density of aggregates that fills a unit volume, the density will greatly depend on how the aggregates are closely packed together this further depends on the size, shape, and distribution of the aggregates within the unit volume. It is useful in converting quantities in mass to quantities in volume. The test will be conducted in accordance with BS EN 12620 (2008).

3.2.4 AGGREGATE IMPACT VALUE (AIV) TEST

For the toughness of concrete aggregates, the aggregate impact value test measures the resistance of the material to failure by impact. The aggregate impact value test can be achieved by subjecting a standard aggregate sample kept in a mould to fifteen blows of a metal hammer weighing 14kg and falling through a height of 38cm. The quantity of finer materials passing through the sieve 2.36mm resulting from the pounding indicates the toughness of the sample aggregate. The ratio of the weight of the fines formed, to the weight of the total sample in percentage, gives the aggregate impact value. The AIV performed in this study was done in accordance with BS EN 12620 (2008)

3.2.5 PRODUCTION OF CONCRETE FOR FLEXURAL AND COMPRESSIVE STRENGTH TESTS

A mix ratio of 1: 1.65: 2.42 was used for cement content, fine aggregate and coarse aggregates respectively at a water-cement ratio of 0.45. The percentage replacement of fine aggregate with Crumb rubber are 0%, 5%, 10%, 15%, 20% and 25%. A total of nine cubes having a dimension of 150mm x 150mm x 150mm were cast per each replacement for the Compressive strength test. Similarly, a total of nine Beams measuring 100mm x 100mm x 500mm were cast per each replacement for the flexural strength test.

3.2.6 CURING OF CUBES

Curing refers to the constant application of water to hardened concrete to ensure continuous hydration of cement so as to ensure that the design strength and durability is attained. The total immersion method of curing of beams and cubes was adopted for specific age of 7, 14 and 28 days respectively from the day of demoulding of the cast concrete (BS EN 1008 (2002).

3.2.7 COMPRESSIVE STRENGTH TEST

The compressive strength test is a test carried out on specimen of concrete cubes to determine the compressive strength of the designed concrete. The load read from the dial gauge of the compressive strength testing machine at failure, (P) of the cubes sample is divided by the cross-sectional area (A) of the cube to obtain the compressive strength as shown in Equation 1 based on guidelines contained in BS EN 197-1 (2000).

$$Compressive\ Strength = \frac{P}{A}\ (N|mm^2) \quad (1)$$

3.2.8 FLEXURAL STRENGTH TEST

Flexural strength is a measure of the tensile strength of concrete. It is a measure of the capacity of an unreinforced concrete beam sample to resist failure in bending. It is measured by loading the concrete beam having a span length of at least three times the depth on a flexural strength testing machine to determine load at failure. The flexural strength was calculated using Equation 2 in accordance with BS EN 197-1 (2000).

$$Flexural\ Strength = \frac{3FL}{2bd^2}\ (N|mm^2) \quad (2)$$

Where,
F= Load at failure
L= Effective span of beam
b=Breath of beam
d=Depth of beam

4 RESULTS AND DISCUSSION

4.1 RESULTS

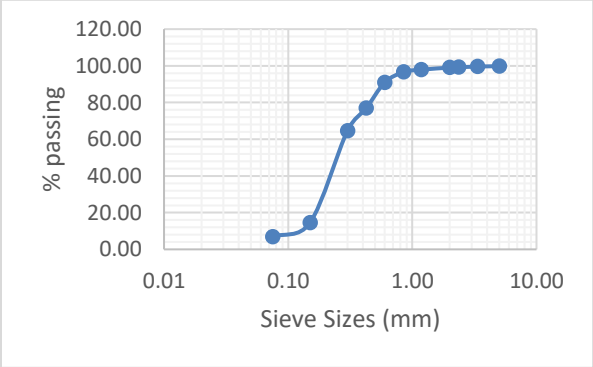

Figure 1: Sieve Analysis result for sand

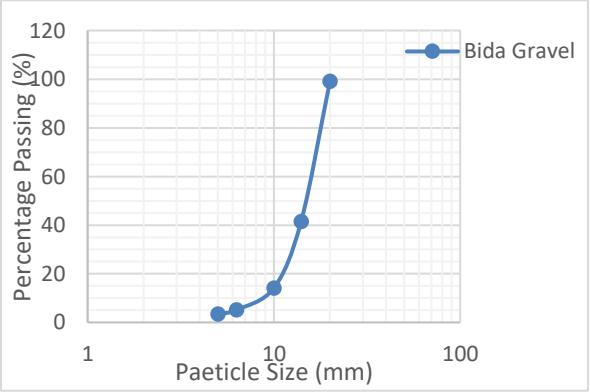

Figure 2: Sieve Analysis result for Bida natural stone

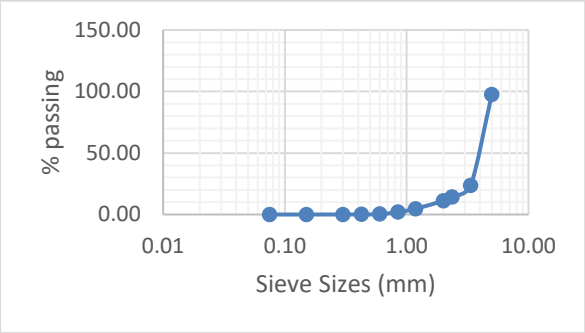

Figure 3: Sieve Analysis result for Crumb rubber

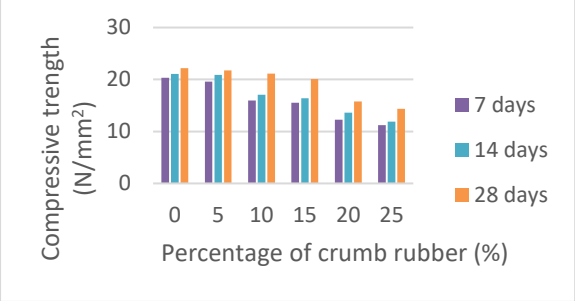

Figure 8: Compressive Strength of cubes per percentage replacement

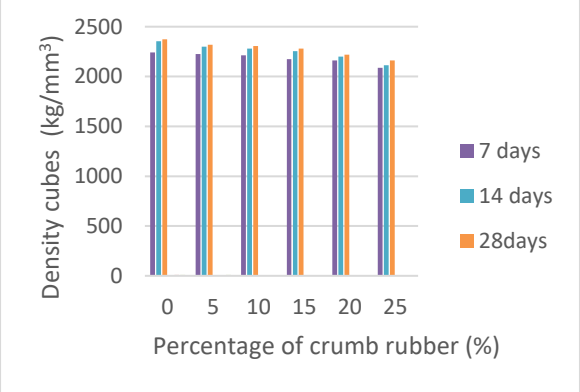

Figure 9: Density of cubes per percentage replacement

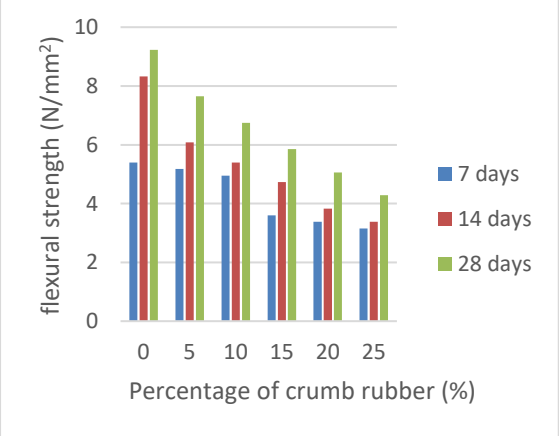

Figure 6: Flexural Strength per percentage replacement

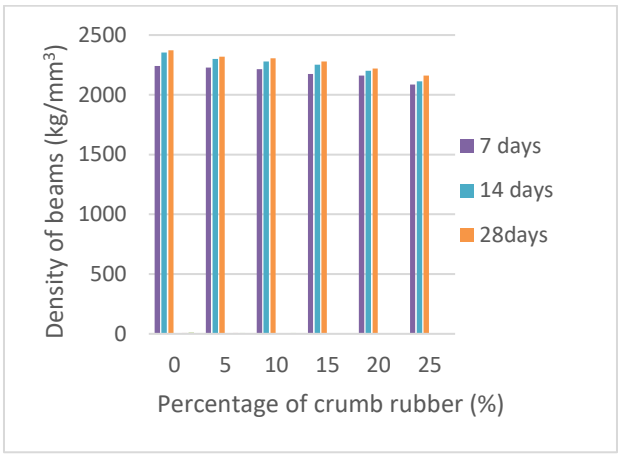

Figure 7: Density of beams per percentage replacement

Table 1: Summary of Physical properties of constituent materials

Parameters	Sand	Crumb Rubber	BNS
Specific gravity	2.61	0.99	2.7
Bulk density Compacted (kg/m^3)	1451.01	531.01	1661.81
Bulk density Uncompacted (kg/m^3)	1346.18	502.00	1485.52
AIV	-	-	19.66

5 DISCUSSION OF RESULT

5.1 AGGREGATE CHARACTERIZATION

The characterization of coarse aggregate, fine aggregate and crumb rubber performed in this study are summarized in Table 1 and Figures 1, 2 and 3. For the specific gravity tests for fine aggregate (sand), Bida natural gravel and crumb rubber, three samples, A, B and C were analyzed for each scenario and the average specific gravity for each aggregate was computed. The specific gravity of sand was computed as 2.61, that of gravel as 2.71, while the specific gravity of crumb rubber was determined as 0.99. The values obtained for fine aggregates and Bida natural stone fall within the limit for natural aggregate (1.3-3.0 and 2.6-2.7 respectively), which further implies according to Naville, 1995, that the aggregates can be used for construction work (concrete) without much need for mix proportioning adjustment. However, the specific gravity for Crumb Rubber (0.99) falls far below this lower range for natural aggregates. Thus, indicating that Crumb Rubber is a much lighter aggregate and may therefore be suitable for light weight concrete.

The calculated bulk densities of uncompacted fine aggregates, Bida natural stone and crumb rubber are, 1346.18kg/m^3, 1485.52 kg/m^3 and 502.00kg/m^3 respectively, While the calculated bulk densities for

compacted fine aggregates, Bida natural stone, and crumb rubber are, 1451.01kg/m^3, 1661.81 kg/m^3 and 531.01kg/m^3 respectively.
The Average Impact Value of coarse aggregate as illustrated in Table 1 was computed as 19.66% for Bida natural stone.

5.2 Properties of Hardened Concrete

The density of concrete cubes at various replacement levels is presented in table 1.0 and ranges from 2360.49kg/m^3 at 0% replacement, 2252.84 kg/m^3 at 10% replacement, and finally, 2116.54 Kg/m^3 at 25% replacement. It is worth noting that between 0 to 10% replacement the concrete conforms to the classification of normal-weight concrete and beyond 10% replacement up to 25% replacement, the density continues falling gradually below the standard range for normal-weight concrete. It can therefore be deduced that the density of the concrete reduces with increases in the volume of crumb rubber.
The tests result for the flexural strength of the concrete beams at curing ages of 7, 14, and 28 days are illustrated in Figure 6. The flexural strength decreases with an increasing percentage replacement of fine aggregates with crumb rubber for all curing ages considered. Similarly, the compressive strength tests result for the concrete cubes at curing ages of 7, 14, and 28 days are illustrated in Figure 8.
The compressive strength of the concrete mix was observed1. to also reduce with an increasing percentage replacement of fine aggregates with crumb rubber for all curing ages. It, therefore, implies that optimum values of flexural and compressive strength can only be achieved at a very low percentage replacement of crumb rubber with fine aggregates if the mechanical properties of rubber create are2. a priority.

6 Conclusion

6.1 Conclusion

Following the observed behavioral characteristics of the fresh and hardened concrete made with Bida natural stone, while partially and incrementally replacing fine aggregates in the mix with crumb rubber, the following deductions can be made within the limits of experimental accuracy;

Bida natural stone is strong and good for concrete work.

Crumb rubber is comparatively much lighter than natural fine aggregates and may be considered for the production of lightweight concrete.

The workability of the fresh rubbercrete made with Bida natural stone decreases with the increasing content of crumb rubber in the concrete mix.

The density of rubbercrete made with Bida natural stone by partial replacement of fine aggregates with crumb rubber remain within the classification range for normal weight concrete for up to 10% replacement of fine aggregates with crumb rubber.

The flexural strength of rubbercrete made with Bida natural stone decreases with an increasing percentage replacement of fine aggregates with crumb rubber for all curing ages considered.

The compressive strength of rubbercrete made with Bida natural stone decreases with an increasing percentage replacement of fine aggregates with crumb rubber for all curing ages considered.

Standard flexural and compressive strength values for normal-weight concrete can only be sustained between 0% to 10% percentage replacement of crumb rubber with fine aggregates in concrete made with Bida natural stone.

A higher percentage replacement of crumb rubber beyond 10% in the mix suggests that rubbercrete becomes lighter and weaker in its mechanical properties

7 Recommendations

From the results obtained in this research work with the conclusion drawn, it is therefore recommended that;
Crumb rubber can be used to replace fine aggregates in concrete made with Bida natural stone for up to 10% replacement in normal weight and beyond 10% for lighter concrete thereby enhancing environmental sustainability in terms of reducing sand mining and utilization of waste automobile tires.
All rubbercrete made with Bida natural stone should be properly cured to achieve the required properties of design strength, durability, and long-lasting serviceability.

REFERENCES

Agrawal, V., Pankil, S., Armaan, G., & Rahul, S. (2017). The Utilization of Quarry Dust as Fine Aggregate in Concrete. *International Conference on Research and Innovations in Science, Engineering and Technology,* 170-175.

Alhaji, B. (2016). *Statistical Modelling of Mechanical Properties of Concrete Made from Natural Coarse Aggregates from Bida Environs.* Unpublished PhD Thesis Submitted to Department of Civil Engineering, Federal University of Technology, Minna.

AzAzhagarsamy, S., Sumaiya, A. M., & Thilagavathi, K. (2017). Effect of Quarry Dust on High Performance Concrete. *International Research Journal of Engineering and Technology (IRJET),* 1223-1226.

BS EN 197-1 (2000). Composition, specification and conformity criteria for common cement. London, British Standard Institution.

BS EN 12390 (2009). Testing harden concrete. Compressive strengths, flexural strengths and splitting

tensile strengths of a concrete. London W44AL UK, British Standard Institution.

BS EN 1008 (2002). Mixing water for concrete: Specification for sampling, testing and assessing the suitability of water, including water recovered from concrete industry as mixing water for concrete. London, British Standard Institution.

BS EN 12620 (2008). Specification for aggregates from natural sources for concrete. London, British Standard Institution.

ASTMC C33/C33 (2016). Standard Specification for Concrete Aggregates. *ASTMC International*. West Conshohocken.

Eshmaiel, G., Morteza, K., Ali, A., & Maghsoudi. (2009). Scrap rubber tyre replacement for aggregate and filler in concrete. Constr. *Build. Mater*, 1828-1836.

Gajendra, Rajan, R., Sakthieswaran, N., Ganesh, & Babu, O. (2020). Experimental investigation of sustainable concrete by partial replacement of fine aggregate with treated waste tyre rubber by acidic nature. *Materials Today: Proceedings.* doi:10.1016/j.matpr.2020.06.279

Gideon, M. S., Ali, A., & Pranesh, B. A. (2016). Properties of Concrete with Crumb Rubber Replacing Fine Aggregates (Sand). *Advances in Civil Engineering Materials*, 1(2), pp. 218–232. doi:10.1520/ACEM20120044

Kadir, A. A., Hassan, M. I., Sarani, N. A., Abdul, Rahim, A. S., & Ismail, N. (2012). Physical andand Mechanical Properties of Quarry Dust Waste Incorporated into Fired Clay Brick. *AIP Conference Proceedings.* 1-5.

Kaloush, K. E., Way, G. B., & Zhu, H. (2005). Properties of Crumb Rubber Concrete. *Transportation Research Record: Journal of the Transportation Research Board*, 1914(1), 8-14. doi:10.1177/0361198105191400102

Kardos, A., & Durham, S. (2015). Strength, durability, and environmental properties of concrete utilizing recycled tire particles for pavement applications. *Construction and Building Materials*, 832-845.

Kunal, B., & Ramana, P. (2017). Evaluation of mechanical and durability properties of Waste TyreRubber. *Constr. Build. Mater*, 811–817.

Mohammed, B. S., Khed, V. C., & Nuruddin, M. F. (2018). Rubbercrete mixture optimization using response surface methodology. *Journal of Cleaner Production*, 171, 1605–1621. doi:10.1016/j.jclepro.2017.10.10

Najib, N., Gergesa, Camille, A., Issab, S., & Fawazba, A. (2018). Rubber concrete: Mechanical and dynamical properties University of Balamand, Case Studies. *Construction Materials*, 9. Retrieved January 11, 2022, from https://www.sciencedirect.com/science/article/pii/S2214509518301840?via%3Dihub

Newman, J., & Choo, B. (2003). *Advanced Concrete Technology Constituent Materials.*

PCA. (2008). ire-Derived Fuels, IS325. *Portland Cement Association*, 1-4.

RMA. (2009). *Scrap Tire Markets in the United States – 9th Biennial Report.* Washington DC: Rubber Manufacturers Association.

Richardson, A., Coventry, K., Edmondson, V., & Dias, E. (2016). Crumb rubber used in concrete to provide freeze-thaw protection (optimal particle size) . *Journal of Cleaner Production*, 599-606.

Rohit, P., Alisha, S., & Ganesh, V. (2020). Partial Replacement of Fine Aggregate with Crumb Rubber in Concrete. *The International Journal of analytical and experimental modal analysis*, 10(7).

Saviour, M., & Stalin, P. (2012). Soil and Sand Mining: Consequences and Management. IOSR *Journal of Pharmacy (IOSRPHR)*, 2(4), 01-06.

Valente, M., & Sibai, A. (2019). Rubber/Crete: Mechanical properties of scrap to reuse tire-derived rubber in concrete; A review. *Journal of Applied Biomaterials & Functional Materials*, 17(15). doi:10.1177/2280800019835486 Post, pp. E1, E4.

4th International Engineering Conference (IEC 2022)
Federal University of Technology, Minna, Nigeria

A comparative study of BQ2557 and LTC3108 as efficient ultra-low bioelectricity harvesters from soil microbes using microbial fuel cells.

*Simeon, M. I[1,2], Mohammed A. S[1] & Freitag, R[2]
[1]Agricultural and Bioresources Engineering Department, Federal University of Technology, PMB 65 Minna, Niger State, Nigeria
[2]Process Biotechnology & Center for Energy Technology (ZET), University of Bayreuth, 95447 Bayreuth, Germany
*Corresponding author email: s.imologie@futminna.edu.ng +2347065510600

ABSTRACT
Microbial fuel cells (MFCs) are attractive bio-electrochemical transducers that can convert waste and organic substrates into usable energy through the metabolic activity of electroactive microbes. However, the power generated by MFCs is relatively low compared to other types of fuel cells. This poses a serious problem for the practical application of MFCs. Commercially available voltage boosters are not suitable for use with MFCs due to the low current capacity of the MFCs. Therefore, special amplifiers are needed to boost the power of MFCs. In this study, two ultra-low harvesters (BQ25570 and LTC 3108) were configured and tested for their efficiency in extracting usable energy from soil MFCs. The result showed that the BQ could harvest bioelectricity from three MFCs connected in series to charge a 0.22 F supercapacitor up to 3.5 volts, which in turn was used to power a light-emitting diode (LED). The LTC, on the other hand, boosted the voltage of a single MFC from 0.72 V to 3.3 V. The increased voltage was used directly to supply a white LED operating at a constant voltage of 2.5 V. The voltage at the LED remained constant even when the MFC voltage dropped to 20 mV. These results demonstrated the potential of soil microbes to generate free energy that can be harvested, amplified and used for practical applications. Compared to the BQ, the LTC performed better with the soil MFC, boosting the voltage of a single MFC unit to a usable level without the need for a battery or supercapacitor.

Keywords: *Bioelectricity, BQ25570, LTC 3108, microbial fuel cell, Power management system, soil microbes.*

1 INTRODUCTION

Microbial fuel cells (MFCs) are bio-electrochemical systems that generate bioelectricity through the metabolism of various microorganisms known as electroactive microbes. MFCs use microbes as catalysts to oxidize organic and inorganic materials to generate electricity (Simeon & Freitag, 2016; Zhou, Chi, Luo, He, & Jin, 2011). MFCs have gained research interest not only because of their diverse potential but also because of the ubiquity of microbes in nature. For example, the soil is teeming with mixed microbial communities, including the common electroactive bacteria (EAB) such as the genera *Geobacter* and *Shewanella* (Ye et al., 2016; Yee, Deutzmann, Spormann, & Rotaru, 2020), and is rich in organic material needed for microbial electroactivity in MFCs. It is estimated that the soil contains about 10^9 cells/g) and high organic content (about 100 mg/g) (Simeon, Raji, Gbabo, & Okoro-Shekwaga, 2016; Wang, Adekunle, Tartakovsky, & Raghavan, 2021). Therefore, soil can produce inexhaustible electron acceptors for the oxidation of organic pollutants (Li et al., 2014) while generating bioelectricity.

Microbial fuel cells have emerged as an alternative power source, especially for remote monitoring applications. However, due to their low voltage and power generation capacity, a single MFC cannot directly power most commercial electronic devices (Yang, Zhang, Shimotori, Wang, & Huang, 2012). The theoretically achievable voltage of a single MFC is in the range of 1.1-1.2 volts, as described by the thermodynamic characteristics of the MFC. In most cases, the practically achievable open circuit voltage of the MFC is in the range of 700-900 millivolts (Yamashita, Hayashi, Iwasaki, Awatsu, & Yokoyama, 2019). However, under load conditions, this value decreases drastically and sometimes reaches an unusable value, depending on the power generation capacity of the MFC and the connected load. Therefore, energy management strategies need to be optimized to bring the power of the MFCs to a practically usable value.

One possible strategy to increase the output power of MFCs is to use commercially available boost converters. A boost converter is a DC/DC switching power supply (Degrenne, Buret, Allard, & Bevilacqua, 2012) that can increase the input voltage of a power supply to produce a higher output voltage. In a simple arrangement, a boost converter contains an inductor, a capacitor, a diode and a transistor (power switching regulator). The main problem with using boost converters with MFCs is that some of the components of the boost converter (e.g. diode and transistor) usually require a minimum amount of energy to operate and the output power of MFCs is too low to meet the requirements of most commercial boost converters (Wang, Park, & Ren, 2015). Therefore, research into special integrated circuits capable of boosting ultra-low power to a higher value is an effective way to increase the performance of MFCs.

Yamashita et al. recently reported that a low-energy converter with MPPT (maximum power point tracking) based on BQ2504 can charge a 1mF supercapacitor to 1.8 V from an input voltage of less than 300 mV and power consumption of 2.09 μW (Yamashita et al., 2019). In a similar study, it was reported that a transformer-based integrated circuit from Linear Technology (LTC3108) could increase the power of a single MFC from 0.5 V to 3.3 V (Song et al., 2017). The most common substrates for the above MFCs are wastewater. Therefore, in the present study, a transformer-based ultra-low energy harvester (LTC 3108) and a non-transformer-based MPPT (BQ2557) were comparatively investigated as efficient bioelectricity harvesters from soil microbes.

2 METHODOLOGY

2.1 CONSTRUCTION OF THE ULTRA-LOW BIOELECTRICITY HARVESTERS

Two predesigned programable power management systems (PMS) based on LTC3108 (LTC-PMS) (Analog Devices, Inc.) and BQ25570 (BQ-PMS) (Texas Instruments, Incorporated [SLUSBH2, & G]) were constructed and tested with the MFCs. Figure 1 shows the circuit diagrams and the selection of components used as described in the data sheets of the integrated circuits. The circuit design of LTC3108 adopted in this study is designed by the manufacturer for boosting the power of a thermo-electric generator (e.g., a Peltier Cell) and it is capable of boosting voltage as low as 20mV depending on the step-up transformer used with it. Thus, the LTC-PMS requires a transformer to initially amplify the MFC voltage for further rectification and amplification. In contrast, according to the manufacturer, the BQ-PMS can amplify the voltage from 300 mV. A supercapacitor (0.22 F, 5.5 V) was used to store the energy gained from the MFCs with the BQ-PMS.

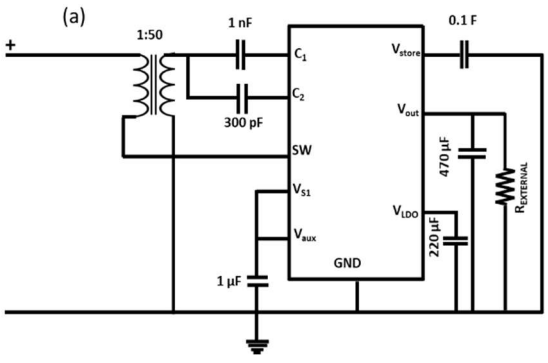

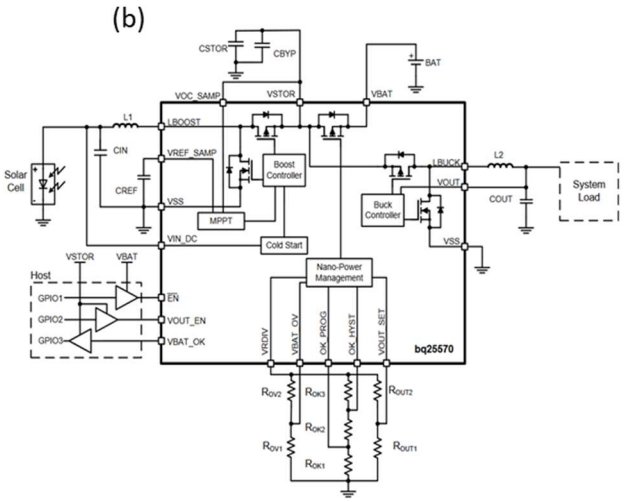

Figure 1: Schematic diagram of (a) LTC-PMS and BQ-PMS circuits.

The detailed design procedures for the BQ2557 and LTC3108, including the selection of circuit elements shown in Figure 1, are described in the data sheets (Analog Devices, Inc.; Texas Instruments et al.).

2.2 MFC ASSEMBLY AND OPERATION

The performance of the PMSs was tested with a single chamber soil microbial fuel cell (SCSMFC) constructed as previously described (Simeon & Freitag, 2022; Simeon, Weig, & Freitag, 2022). Briefly, the SCSMFC was constructed with biologically active soil as the bacterial source, the proton exchange membrane and the nutrient-rich substrate. The anode and cathode were fabricated using the bonding and reinforcement method described previously (Simeon, Herkendell, Pant, & Freitag, 2022). The electrode consists of an active layer of Vulcan-XC 72 (Quintech, Germany) bonded to a stainless-steel mesh support using a two-component epoxy as a binder(Simeon, Imoize, & Freitag, 2021). The anode and cathode were separated at a distance of 4 cm with about 300 g of soil slurry prepared as previously described (Simeon & Freitag, 2022).

2.3 DATA CAPTURING AND CALCULATION

A data logger (ADC-24, Pico Technology) was used to monitor the enrichment of the MFCs every 1 hour in terms of OCV. When a stable OCV was reached, indicating the maturation of the biofilm on the electrode surface, the maximum power of the MFCS was determined using the linear sweep voltammetry technique (Biologic VMP3, France).

The maximum power density (P_d) was estimated from equation 1.

$$P_d(mWm^{-2}) = \frac{P(mW)}{A(m^2)} \quad (1)$$

Where A = 0.00185 m^2 is the anode surface area. The MFCs were left at open-circuit to regain their equilibrium voltage before they were connected to the ultra-low PMSs. For the test, a single SCSMFC and three SCSMFCs connected in series were used, respectively. The energy (E) stored in the capacitor when it was charged from an initial voltage (V_i) to a final voltage (V_f) was calculated according to Equation 2.

$$E = \frac{1}{2}C(V_f - V_i)^2 \quad (2)$$

Where C is the capacitance of the capacitor in Farads. Similarly, the total charge (Q) accumulated in the supercapacitor was estimated according to Equation 3.

$$Q = C(V_f - V_i) \quad (3)$$

3 RESULTS AND DISCUSSION

3.1 PERFORMANCE OF THE MFCS BEFORE THE PMS ASSESSMENT

Before the evaluation of the PMS, the performance of the SCSMFCs was determined to select MFCs with similar performance indices. The power and polarization curves of the three MFCs used for the evaluation of the PMSs are presented in Figure 2.

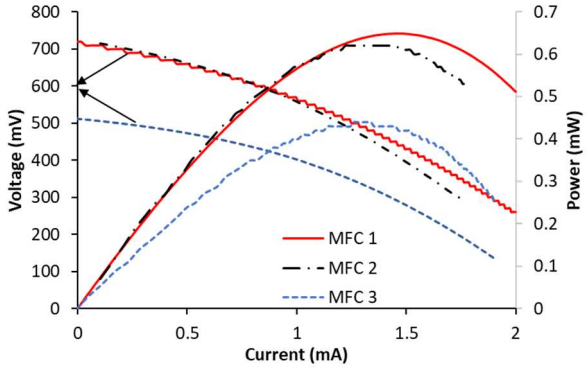

Figure 2

TABLE 1: PERFORMANCES PARAMETERS OF THE MFCS

Parameters	MFC 1	MFC 2	MFC 3
E_{oc} (mV)	720	714.01	512.64
E_{cell} (mV)	443.95	460.99	333.29
I_{cell} (mA)	1.46	1.35	1.31
P_{max} (mW/m^2)	195.39	187.70	131.40
R (Ω)	304.0753	341.4741	254.4198

The performance indices of the MFCs used for the PMS evaluation are shown in Table 1. MFC 1 and MFC 2 had similar performance, with a percentage difference of only 4.01 % in power density. On the other hand, MFC 3 had lower power than the first and second with a percentage difference of 39.16% and 35.29%, respectively. The average current generated by the three MFCs was 1.37 $\pm$ 0.063. The low standard deviation of the current showed that the three MFCs were suitable for series connection.

3.2 POWER HARVESTING FROM THE SMFCS USING THE BQ-PMS.

The performance characteristics for the BQ-PMS are shown in Figure 3.

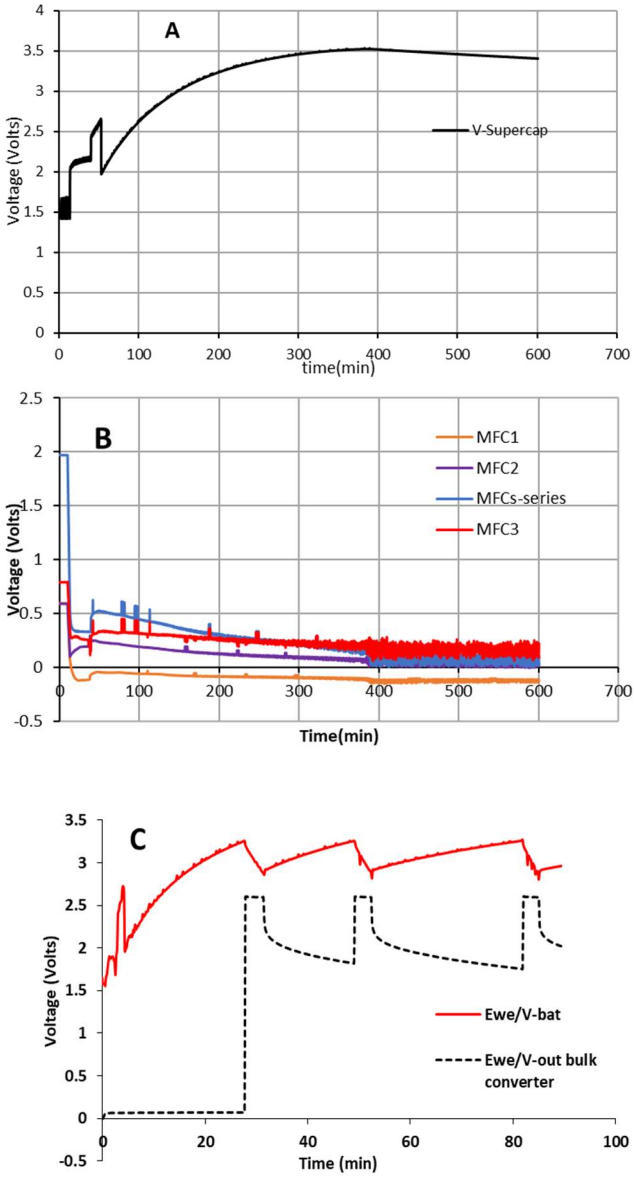

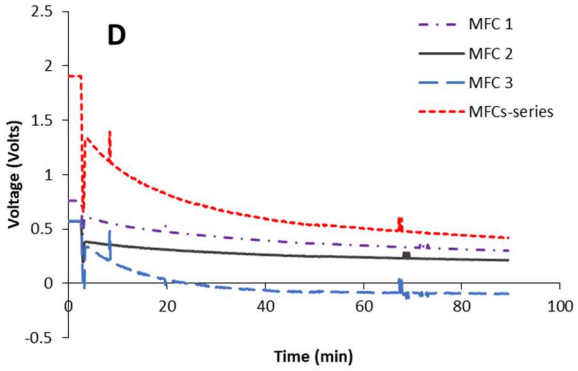

Figure 3 Performance characteristics of BQ2557. Power harvesting from 3 MFCs in series: A) with bulk converter disabled, B) voltage characteristics of the MFCs during power harvesting, C with bulk converter enabled and connected to a light emitting diode, D) voltage characteristics of the MFCs with the bulk converter enabled.

Figure 3 (A) shows the charging of a supercapacitor by the BQ-PMS using three SCSMFCs connected in series. The bulk converter was disabled so that the supercapacitor was fully charged without drawing current from the output of the PMS. It took about 5 hours to charge the supercapacitor to the predesigned voltage of 3.5 volts. The total voltage of the MFCs dropped drastically from 1.97 to 0.53 Volts during the start-up phase and dropped further to about 100 mV after 10 hours. At the third MFC (Figure 3 B), the voltage reversed, indicating that the current drawn from the MFCs by the PMS was higher than the metabolic response of the microbes could deliver.

Figure 3 (C) shows the voltage characteristics of the BQ-PMS during the period when the supercapacitor was charged to a predetermined value and discharged via a white LED. The BQ2557 is a maximum power point tracking PMS that disables the charging and discharging of the battery or capacitor when the voltage rises above or falls below a certain value, which depends on the system design. The PMS in this study was designed to keep the capacitor voltage in the range of 3.3 - 2.8 volts. Once the supercapacitor was charged to 3.2 Volts, the bulk converter was activated to turn on the LED, and when the voltage dropped below 2.8 V, the bulk converter was deactivated until the supercapacitor was recharged to the maximum voltage. With three MFCs connected in series, it took only 33 minutes for the supercapacitor to charge to the maximum designed voltage, the point at which the bulk converter was activated and the LED lit up. Interestingly, the supercapacitor was continuously charged by the MFCs after each discharge cycle, indicating that the electroactive bacteria were active in the SCSMFCs and further demonstrating the potential of soil microbes to generate free energy that can be used for practical applications. The energy stored and the overall charge accumulated in the supercapacitor by charging it from a voltage of 1.4 Volts to a voltage of 3.3 and 3.5 Volts are presented in Figure 4.

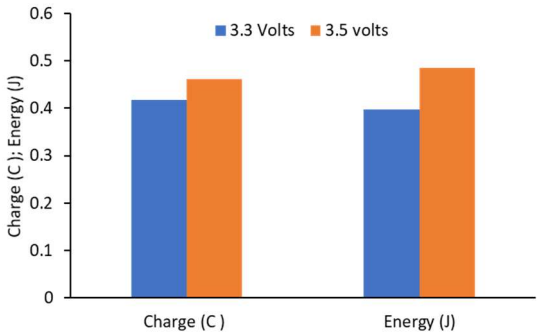

Figure 4. Charge and energy storage in a supercapacitor of 0.22 F by harnessing the power of soil microbes.

3.3 POWER HARVESTING FROM THE SMFCS USING THE LTC-PMS

The LTC-PMS was tested with two different SCSMFCs (MFC 1 and MFC 2). Figure 5 shows the performance characteristic of the PMS at open-circuit voltage and under external load.

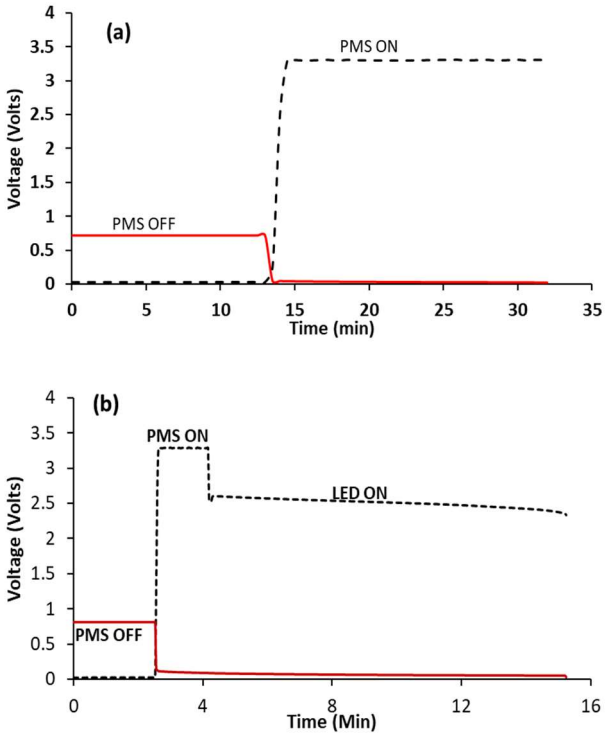

Figure 5: Performance characteristics of LTC-PMS (a) at no load, (b) at load condition.

MFC 1 produced a constant voltage of 721± 0.11 mV before it was connected to the LTC-PMS. The output voltage of the PMS was 2.5 Volts within 30 seconds and 3.3 Volts after 60 seconds, which corresponded to the preset output voltage of the PMS. During activation of the PMS, the MFC voltage dropped to 50 mV and further to about 21 mV, while the amplified output voltage

remained constant at 3.3 volts. In the second test, MFC 2 produced a constant OCV of 808 mV before it was connected to the input of the PMS. When the MFC was connected to the converter, there was a quick response as the voltage immediately increased to 1.35 V and further to 3.3 V, but the voltage of the MFC dropped sharply to 145 mV and then to 50 mV when the LED was turned on. Down to a voltage of 20 mV, the SMFC was still able to drive the LTC to power the LED, as shown in Figure 5 (b).

4 CONCLUSION

The present study has shown that the teeming populations of electroactive microbes in the soil can be electrochemically stimulated to generate electricity that can be amplified for practical application. A comparison of the suitability of BQ2557 and LTC3108 as efficient bioelectricity collectors from soil MFCs showed that the amplified power of the MFCs can be harvested using the BQ25570 and stored in a supercapacitor or amplified and used directly. While the BQ25570 required a combination of more than one MFC to charge a supercapacitor to 3.3 V, the LTC3108 boosted the voltage of a single soil MFC from as low as 20 mV to 3.3 mV. This result shows that the power of a single MFC can be increased with a PMS for direct application without the need for batteries or supercapacitors, which normally increase the cost of manufacturing and operating the MFCs. However, improvements in system design and further material optimization are still required if the goal is to maintain the increased performance of the MFC for direct application over an extended period.

ACKNOWLEDGEMENTS

The author would like to acknowledge the Petroleum Technology Development Fund (PTDF), Nigeria and the German Academic Exchange Service (DAAD) for funding the project. The Chair of Process Biotechnology, University of Bayreuth is also appreciated for providing the materials and working space.

5 REFERENCES REFERENCES

Analog Devices, Inc. LTC3108: Ultralow Voltage Step-Up Converter and Power Manager data sheet. Retrieved from https://www.analog.com/en/products/ltc3108.html#product-documentation

Degrenne, N., Buret, F., Allard, B., & Bevilacqua, P. (2012). Electrical energy generation from a large number of microbial fuel cells operating at maximum power point electrical load. *Journal of Power Sources*, *205*, 188–193. https://doi.org/10.1016/j.jpowsour.2012.01.082

Li, X., Wang, X., Zhang, Y., Cheng, L., Liu, J., Li, F., . . . Zhou, Q. (2014). Extended petroleum hydrocarbon bioremediation in saline soil using Pt-free multianodes microbial fuel cells. *RSC Adv*, *4*(104), 59803–59808. https://doi.org/10.1039/C4RA10673C

Simeon, I., Raji, O. A., Gbabo, A., & Okoro-Shekwaga, C. (2016). Performance of a Single Chamber Soil Microbial Fuel Cell at Varied External Resistances for Electric Power Generation. *Journal of Renewable Energy and Environment*, *3*(3). https://doi.org/10.30501/jree.2016.70092

Simeon, I. M., Herkendell, K., Pant, D., & Freitag, R. (2022). Electrochemical evaluation of different polymer binders for the production of carbon-modified stainless-steel electrodes for sustainable power generation using a soil microbial fuel cell. *Chemical Engineering Journal Advances*, *10*, 100246. https://doi.org/10.1016/j.ceja.2022.100246

Simeon, I. M., & Freitag, R. (2016). Experimental utilization of urine to recharge soil microbial fuel cell for constant power generation. *Research Journal of Engineering and Environmental Sciences*, *1*(1), 129–135.

Simeon, I. M., Weig, A., & Freitag, R. (2022). Optimization of soil microbial fuel cell for sustainable bio-electricity production: Combined effects of electrode material, electrode spacing, and substrate feeding frequency on power generation and microbial community diversity. *Biotechnology for Biofuels and Bioproducts*, *15*(1), 124. https://doi.org/10.1186/s13068-022-02224-9

Simeon, M. I., & Freitag, R. (2022). Influence of electrode spacing and fed-batch operation on the maximum performance trend of a soil microbial fuel cell. *International Journal of Hydrogen Energy*, *47*(24), 12304–12316. https://doi.org/10.1016/j.ijhydene.2021.11.110

Simeon, M. I., Imoize, A. L., & Freitag, R. (2021). Comparative evaluation of the performance of a capacitive and a non-capacitive microbial fuel cell. *18th International Multi-Conference on Systems, Signals & Devices (SSD), IEEE, 22-25 March 2021, Monastir, Tunisia.*, 1076–1082. https://doi.org/10.1109/SSD52085.2021.9429481

Song, Y., Boghani, H., Kim, H., Kim, B., Lee, T., Jeon, B.-H., . . . Kim, J. (2017). Electricity Production by the Application of a Low Voltage DC-DC Boost Converter to a Continuously Operating Flat-Plate

Microbial Fuel Cell. *Energies*, *10*(5), 596. https://doi.org/10.3390/en10050596

Texas Instruments, Incorporated [SLUSBH2, & G]. bq25570 nano power boost charger and buck converter for energy harvester powered applications datasheet (Rev. G). Retrieved from https://www.digikey.com/en/product-highlight/t/texas-instruments/bq25570-pmics-boost-chargers-nanopower-buck-converters

Wang, H., Park, J.-D., & Ren, Z. J. (2015). Practical energy harvesting for microbial fuel cells: A review. *Environmental Science & Technology*, *49*(6), 3267–3277. https://doi.org/10.1021/es5047765

Wang, S., Adekunle, A., Tartakovsky, B., & Raghavan, V. (2021). Synthesizing developments in the usage of solid organic matter in microbial fuel cells: A review. *Chemical Engineering Journal Advances*, *8*, 100140. https://doi.org/10.1016/j.ceja.2021.100140

Yamashita, T., Hayashi, T., Iwasaki, H., Awatsu, M., & Yokoyama, H. (2019). Ultra-low-power energy harvester for microbial fuel cells and its application to environmental sensing and long-range wireless data transmission. *Journal of Power Sources*, *430*, 1–11. https://doi.org/10.1016/j.jpowsour.2019.04.120

Yang, F., Zhang, D., Shimotori, T., Wang, K.-C., & Huang, Y. (2012). Study of transformer-based power management system and its performance optimization for microbial fuel cells. *Journal of Power Sources*, *205*, 86–92. https://doi.org/10.1016/j.jpowsour.2012.01.025

Ye, J. Y., Zhang, J. B., Gao, J. G., Li, H. T., Liang, D., & Liu, R. M. (2016). Isolation and characterization of atrazine-degrading strain Shewanella sp. Yjy4 from cornfield soil. *Letters in Applied Microbiology*, *63*(1), 45–52. https://doi.org/10.1111/lam.12584

Yee, M. O., Deutzmann, J., Spormann, A., & Rotaru, A.-E. (2020). Cultivating electroactive microbes-from field to bench. *Nanotechnology*, *31*(17), 174003. https://doi.org/10.1088/1361-6528/ab6ab5

Zhou, M., Chi, M., Luo, J., He, H., & Jin, T. (2011). An overview of electrode materials in microbial fuel cells. *Journal of Power Sources*, *196*(10), 4427–4435. https://doi.org/10.1016/j.jpowsour.2011.01.012

4th International Engineering Conference (IEC 2022)
Federal University of Technology, Minna, Nigeria

SUITABILITY OF CLAY FROM BIDA BASIN, NIGER STATE FOR PRODUCTION OF PORCELAIN INSULATORS

*Dutsun, A.M[1], Abubakre, O.K[1], Muriana, R.A[1], Abdullahi, A.A[2], Emene, A.U[3] & Taidi, I.B[4]
[1]Materials and Metallurgical Engineering Department, Federal University of Technology, PMB 65 Minna Niger State, Nigeria
[2]Mechanical Engineering Department, Federal University of Technology, PMB 65 Minna Niger State, Nigeria
[3]Chemical Engineering Department, Federal University of Technology, PMB 65 Minna Niger State, Nigeria
[4] Niger State Ministry of Mineral Resources, Minna Niger State, Nigeria
*Corresponding author email:abdullahdutsun@gmail.com +2348066546806

ABSTRACT

Clay from Sakpe deposit within Bida basin was analysed using XRF, XRD, SEM, physico-mechanical and electrical insulation methods. The chemical analysis result of the clay shows high values of SiO_2 (55.73%), Al_2O_3 (29.65%), Fe_2O_3 (0.92 %) respectively and are kaolinitic in nature. It was found to have good physical and mechanical properties at a maximum of 41MPa of cold crushing strength, flexural strength of 9.47MPa, elastic modulus of 450.36MPa. This composition was found to be within standard requirements. The electrical properties were observed to be at 0.65GΩ and 26kV/mm for insulation resistance and breakdown voltage respectively, which met the similar values at 0.5GΩ and 25Kv/mm of imported insulators. The investigated kaolin deposit from Sakpe met the standard for the production of porcelain insulators, refractories, ceramics materials and tiles, especially, between 35-45wt% kaolin and 25-35wt% Feldspar composition samples J, I and H which have the maximum values, in terms of the electrical, physical and mechanical properties at the temperature studied.

Keywords: ***Bida, ceramics, clay, kaolin, mullite, porcelain insulators.***

1 INTRODUCTION

Clay is one of the basic raw minerals known to man and civilization. Its socioeconomic effect is as important today as it has been in the past. Nigeria (a developing industrial nation) has a potentially high demand for ceramics. It spends a large amount of financial resources on importing ceramic materials. There is an abundance of clay deposits in Nigeria, which has the potential to be utilized locally to meet these demands. Previous works on the various Nigerian clay deposits have been characterised and processed. Important details on phase and microstructural evolution during sintering was provided by Aladesuyi *et al.* (2017) in their analysis of Nigerian kaolin with compacts of calcined alumina powder. At high temperatures, an increased densification, better flexural strength and decrease in porosity at higher temperatures were observed in the material when used in the production of porcelain insulators.

The use of electricity has increased significantly in developing countries due to rapid industrial evolution and life style. Therefore, the use of insulators has become very much important in the prevention of the flow of current between the earth and wire by the use of poles or towers. The power industries have been on their toes tirelessly to develop extra voltage and long-distance transmission for easy and safe way to distribute electric power (Ezenwabude and Madueme, 2015). The presence of insulators is vital in electrical systems, and are used extensively for high voltage applications.

Ceramic material known as porcelain insulator is created by heating raw ingredients, such as kaolin clay, to high temperatures in a kiln. The creation of glass and the mineral mullite inside the fired body at a high temperature gives porcelain its toughness, strength, and translucence. Due to its fast industrial fire cycles, wear resistance, extremely high density, and strong mechanical strength, it had been identified as a significant stoneware (Ezenwabude and Madueme, 2015).

Electrical parts and equipment use insulation to sustain and separate conductors (not allowing the passage of current). Porcelain insulators are used in electrical systems to stop unwanted flow of current from its supporting points to the earth. It provides a channel with a very high resistance through which practically no electricity can pass. Because there needs to be an insulator between current-carrying conductors and poles in order to prevent the flow of current from conductor to earth, the overhead conductors for the transmission and distribution system are often supported by poles that are correctly grounded. (Ovri and Onuoha, 2015).

The majority of the literature on the compositions and manufacturing processes for porcelains uses foreign raw materials, which have different chemical, mineralogical, and physical properties than those that are readily available locally. As a result, additional efforts are being made to establish information and procedures about the creation of porcelain insulators using locally available raw materials.

The porcelain insulators produced through slip casting Ikere -Ekiti Kaolin and clay from South Western Nigeria was found to meet the required properties for porcelain insulators production because the properties observed from the results of the standard refractory tests met the standard for porcelain insulator production (Atanda *et al.*, (2012).

A porcelain insulator used in electric power transmission and distribution system was developed by Meng et al., (2016), and has good properties as the commonly available material for overhead insulators. It was discovered to have excellent properties like high corrosive resistance in damp or humid environment mechanical strength, high electrical stability (Meng et al., 2016). In contrast to other insulators that require industrial processing, the raw materials used to make porcelain insulators are generally accessible. The most complex multiphase ceramic materials utilized as overhead insulators for low and high-tension insulation are porcelain insulators (Yaya et al., 2017). It is made from natural ceramic raw elements like feldspar, quartz, and clays (such as kaolin, China clay, or ball clay).

The porosity, phase composition, chemistry and mechanical, dielectric and thermal properties of the porcelain materials used to make porcelain insulators vary. According to Moyo and Park (2014), these properties are important determinant properties which must be considered in the production of quality porcelain insulators. These properties are mainly affected by major microstructural phases of porcelain materials namely mullite and glassy phases. Despite the availability of local raw materials for the creation of porcelain insulators, demand is still being satisfied by imports (Nasejje and Obwoya, 2015).

Ukpor Clay, which has the universal triaxial porcelain composition of 45% kaolin, 5% ball clay, 25% feldspar, and 25% quartz, was used to make electrical porcelain insulators by substituting 5% of the feldspar with 5% of glass powder as an addition, and firing the mixture at 1200°C, the effect of composition was also investigated. According to the findings, it has a low water absorption rate and dielectric constants between 9.0 and 10.9, which meet the criteria for a suitable insulating material (Ogwata and Anih, 2015). Anih (2005) studied porcelain made from locally available raw materials at a temperature of 1350°C and with a composition of 10% ball clay, 30% kaolin, 22% feldspar and 38% quartz. He discovered that the manufactured samples' dielectric strength (breakdown voltage) was 26kV/mm and their insulation resistance was 1.97 G, both of which are acceptable for a conventional high voltage porcelain insulator.

Nwachukwu and Lawal (2018) used the kaolin deposits in Kutigi to create electrical porcelain. The samples were found to have insulation resistance that ranges from 0.352 to 2.05G and dielectric constants that range from 8.7 to 11.4, which were deemed to be in compliance with the required parameters. Additionally, it was discovered that linear shrinkage, porosity, failing load and water absorption agreed with the normative norms for porcelain manufacturing. Additionally, they noticed that at a firing temperature of 1250°C, the composition containing 28% kaolin, 25% quartz, 35% feldspar, 10% ball clay and 2% talc produced the best results.

Despite the availability of local raw materials, insulators are still imported into Nigeria since the local production of electrical porcelain insulators is limited to low voltage and produced in small quantities. To fulfill the rising demand, it is crucial to support local production of electrical porcelain insulators. Technology that has been developed locally is thought to be a key indicator for encouraging untapped resources and the technological and financial potential of industrialization processes. Electrical porcelain insulators are fundamentally made to stop electricity from passing through them, preventing injury or even death to the end users.

In order to meet demand, it is crucial to create methods for producing high-quality porcelain bodies that are commercially viable. This breakthrough will inevitably make insulator theft and the subsequent vandalism of power lines unappealing and unprofitable, providing a more reliable supply of electricity for the nation. Along with solving all these issues, domestic production of porcelain insulators will give the nation's teeming population employment opportunities (Anih, 2005). It will become apparent when this is adopted that the establishment of one porcelain manufacturing industry per state will help meet the local demand for rural electrification. Local manufacturing of porcelain insulators will serves as revenue when exported, if adequately supported by the government. The aim of this research work is to characterize (using XRD, XRF, SEM) and process kaolin deposits with other locally sourced raw materials such as Feldspar, quartz and ball clay and to consider their physical, mechanical and electrical properties for porcelain insulator application.

2 MATRIALS AND METHODS

Feldspar, quartz, and ball clay were locally gathered from Takalafiya (Magama L.G.A.), Tsohon-Gurusu (Bosso L.G.A.), and Tatiko (Paikoro L.G.A.) in Niger state. The clay was sourced from Sakpe Community in Edati Local Government Area (L.G.A.). The operation was carried out in accordance with the general instructions and directives of the Minna-based personnel of the Niger state Ministry of Mineral Resources and with the assistance of Kira Mining Company Ltd. The clay and the additives were crushed, pulverized into 75microns, separated and blended according to the specification in Table 1. The samples were characterized using Pro X: Phenom World Scanning Electron Microscope (Umaru Musa Yar'adua University Katsina), Empyrean PANalytical XRD Analyzer (Nig. Geological Survey Agency Kaduna Lab.) and Xenematrics XRF Machine (Nat. Steel Raw Mat. Exploration Agency, Kaduna). The electrical properties determination were conducted at Transmission Company of Nigeria Jebba.

According to the recommendation of Olupot *et al*. (2010) and Laraba (2019), the quartz and ball clay compositions were chosen, librated, sieved, and proportioned. In order to create ceramics and electrical porcelain with the best possible mechanical and electrical qualities, 20% quartz was employed. To produce electrical porcelain insulators with improved qualities, compositions were varied between 30 and 60 percent clay, 20 to 35 percent feldspar, and 20 to 30 percent quartz (Olupot *et. al*., 2010; Ezenwabude and Madueme, 2015). These compositions were used with variations of clay between 35%-50% and feldspar between 20%-35%.

Table 1: Sample formulation

Sample	Sakpe clay (wt%)	Feldspar (wt %)	Quartz (wt %)	Ball clay (wt%)
F	100	0	0	0
G	50	20	20	10
H	45	25	20	10
I	40	30	20	10
J	35	35	20	10

After the samples were formed, dried and fired slowly at 6℃/min up to 1250℃ and held for one hour soaking time in an electric furnace, various properties were determined.

The physical and mechanical properties of the clay under investigation with various compositions was determined using the equations below according to ASTM standards:

$$Linear\ Shrinkage = \frac{Ld - Lf}{Ld} x\,100 \quad (1)$$

$$Water\ Absorption = \frac{W - D}{D} x\,100 \quad (2)$$

$$Porosity = \frac{W - D}{W - S} x\,100 \quad (3)$$

$$Bulk\ Density = \frac{W\rho}{W - S} x\,100 \quad (4)$$

$$Apparent\ Density = \frac{D\rho}{D - S} x\,100 \quad (5)$$

$$Cold\ Crushing\ Strength\ (CCS) = \frac{Applied}{Cross\ Sectio}$$

$$Modulus\ of\ Rupture\ (MOR) = \frac{3FL}{2b\,d^2} \quad (7)$$

$$Elastic\ Modulus = \frac{F\,L^3}{4\,b\,d^3\,D} \quad (8)$$

where, W =Saturated weight, D =dry weight, S=suspended weight, Ld = Dry length, Lf= Fired length, ρ = Density of water = 1g/cm^3, F=breaking load, L = distance between supports/gauge length, d= height/depth, b= breadth and D= deflection.

3 RESULTS AND DISCUSSION

3.1 XRD, XRF and SEM Results

3.1.1 XRD Results

(a)

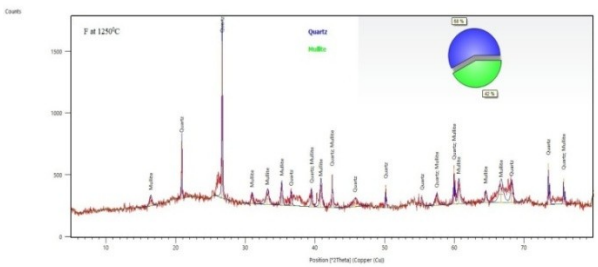

(b)

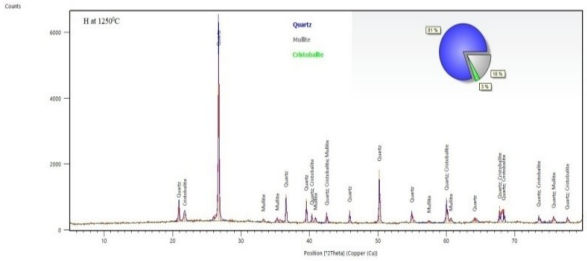

(c)

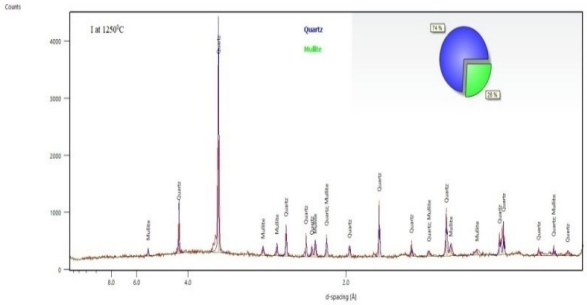

(d)

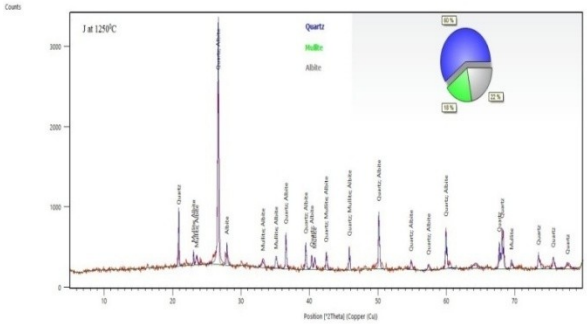

Figure 1: XRD Results sample fired at 1250℃ : (a) SampleF (b) SampleH (c) SampleI and (d) SampleJ

Table 2: Mineralogical (XRD) composition of raw clay

Phase	Quartz	Kaolinite	Muscovite	Anatase	Total
% Weight	27.8	66.2	4.7	1.3	100

Table 3: XRF Result of the Clay deposit

% composition	SiO_2	Al_2O_3	Fe_2O_3	Mn O	Mg O	CaO	Na_2O	K_2O	TiO_2	P_2O_5	LOI	Total
Sakpe clay	55.73	29.65	0.92	0.006	0.05	0.07	0.05	0.31	1.793	0.05	11.36	99.99

Table 4: XRF Result of Additives

Additives	Percentage composition													
	SiO_2	Al_2O_3	Fe_2O_3	MnO	Ca O	K_2O	TiO_2	Nb_2O_3	Pb O	Sr O	MoO_3	Ag_2O	Cd O	Sb_2O_3
Feldspar	75.05	17.61	0.611	0.017	0.41	0.263	-	0.020	0.053	0.0039	0.03	0.0073	0.0053	-
Quartz	80.81	14.04	0.40	0.003	0.241	0.091	-	0.019	0.0484	-	0.0314	0.0059	0.0049	0.0002
Ball clay	61.86	18.74	4.71	0.039	0.55	0.86	0.16	0.0113	0.002	0.0114	-	0.0012	-	-

Table 2 displays the findings of the X-Ray Diffraction (XRD) analysis performed on raw clay. As indicated in Table 2, the non-clay minerals that make up the clay's mineralogy are kaolinite ($Al_2Si_2O_2(OH)_4$), muscovite ($KAl_2(AlSi_3O_{10})(F,OH)_2$), and anatase ($TiO_2$). Quartz accounts for 27.8 and 66.2 percent of the clay's mineralogy. Kaolinite clay mineral predominates in the clay occurrence, with muscovite being in relatively low proportion. This demonstrates that the clay is kaolin. From the early phases of the initial raw clay and those blended at various compositions with ball clay, feldspar, and quartz, it was noticed that the fired samples underwent phase transitions.

As the samples were fired at 1250℃, there was change in phase transformation to quartz and albite as shown in the XRD patterns of the various samples in Figure 1. Sample F changes from quartz-albite phase to quartz-mullite phase at 1250℃ as the temperature increases. Samples G, H, I and J also transforms into two distinct phases of quartz-mullite as ball clay, feldspar and quartz were introduced into the clay matrix as additives at different percentage compositions. It was noted that these changes became more prominent as feldspar's percentage in the composition rises. The significant amount of alumina in the additives, as revealed by the XRF chemical analysis in Table 3, could be reason for this.

It was shown that as the amount or percentage composition of feldspar in the raw clay-ball clay matrix increases with a commensurate drop in the clay content, the amount of mullite generated also increases. The XRD results show the samples with kaolin – feldspar – quart z-ball clay (40: 30: 20: 10) weight percentage, represented by sample I, were observed to have the highest amount of mullite at 1250℃ than others as shown in Figure 1.

3.1.2 XRF Results

The chemical analysis result of clay shows high value of SiO_2 at 55.73%, 29.65% Al_2O_3 and a low value of Fe_2O_3 at 0.92 %. The clay has low CaO, Na_2O and K_2O (Table 3).

Table 4 displays the results of an XRF study of the feldspar, quartz, and ball clay used as additions. Clay applications depend heavily on the presence of oxides, and oxides like SiO_2, Al_2O_3, Na_2O, K_2O, Fe_2O_3, TiO_2, and CaO are crucial to clay's use in industry. The clay's silica content (55.73%) also makes it a useful material for the production of amorphous silica, alumina, zeolite, tiles, and bricks. Na_2O and K_2O presence are important as functional fillers in paint, rubber, plastic, and adhesives as well as fluxing agents in ceramics. They aid in lowering the temperature at which quartz melts and in regulating glass viscosity. Clay with a free or low Fe_2O_3 percentage (0.92%) is appropriate for making pottery, tiles, and sanitary items. Their transparency, lightness, and whiteness make them ideal for paints, coatings on plastic, and paper production. The clay deposit's composition also qualifies it as a significant source of raw materials for the manufacture of ceramics, refractory bricks, and porcelain insulators.

3.1.3 SEM Results

The Scanning Electron Microscope (SEM) photomicrographs are as shown in Figure 2.

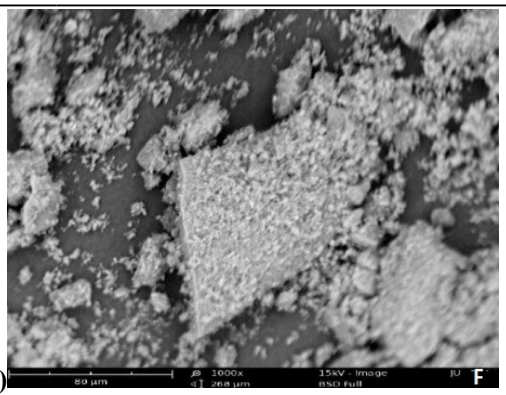

(a)

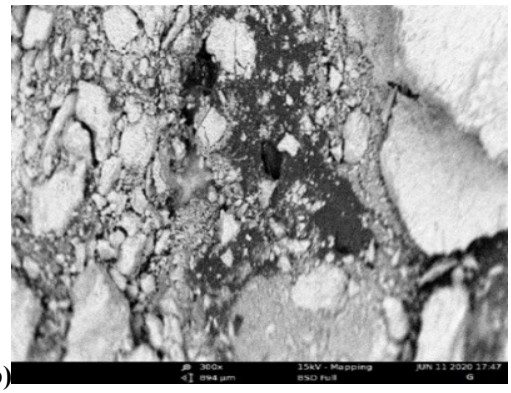

(b)

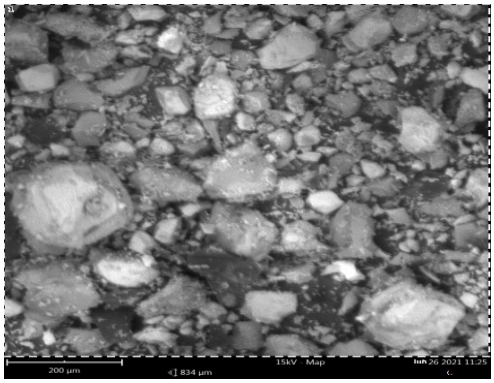

(c)

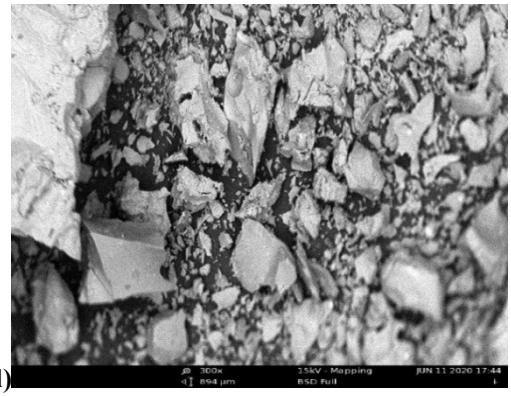

(d)

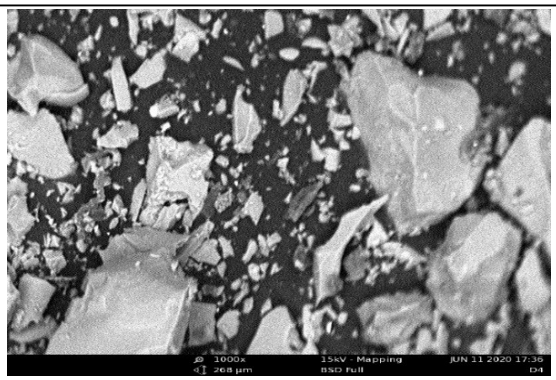

(e)

Figure 2: SEM Photomicrograph of sample fired at 1250 ℃ : (a) Sample F (b) Sample G (c) Sample H (d) Sample I and (e) Sample J

From the Scanning Electron Microscope (SEM) photomicrographs in Figure 3, it was noticed that there is a moderately distributed to dispersive glassy phase of silica with some large flocs of mullite which were separated and dispersed from one another. On the contrary, Bilal *et al.*, (2016) observed this to be located on the totality of the image.

The microstructural characterisation revealed that the samples were made of acicular (orthorhombic) mullite, glassy phase and residual quartz when fired at 1250°C as seen in the microstructure. This is similar to the observations of Laraba (2019). The SEM micrographs as seen in Figure 2 with acicular mullite phases within quartz-mullite phase, supports the results of the XRF chemical analysis. The mullites are seen as fibres within the quartz crystals as observed by Laraba, (2019).

3.2 Physical, Mechanical and Electrical Properties

The mechanical, physical and electrical properties of the studied samples are as presented and discussed below.

At a constant quartz composition of 20% in samples G to J respectively as shown in Table 5, the water absorption rate falls with an increase in the percentage composition of feldspar and a decrease in kaolin content. This might be due to the clay's increased flexibility and increased feldspar content in the matrix. Sample J has the lowest water absorption rate at the temperature of 1250^0C, with value of 5.70%. According to Mgbemere et al., (2019), this decrease in water absorption could also be ascribed to a reduction in pore space as a result of compaction in the clay body.

Table 5: Physico-mechanical and Electrical Properties

Property	F	G	H	I	J
Bulk Density (g/cm^3)	1.59	1.66	1.69	1.70	1.75
Apparent Density (g/cm^3)	2.05	2.02	1.93	1.95	1.94
Water Absorption (%)	14.21	10.89	7.35	7.51	5.70
Porosity (%)	22.53	18.05	12.42	12.76	9.94
Linear Shrinkage (%)	5.20	3.04	3.02	1.10	3.94
CCS (MPa)	13.30	27.61	22.29	40.87	27.12
M.O.R (MPa)	1.61	1.57	4.30	9.42	9.47
Elastic Modulus (MPa)	61.21	76.89	201.25	450.36	160.05
Insulation Resistance (GΩ)	Could not be measured	0.42	0.65	0.62	0.57
Breakdown voltage(kV/mm)	Could not be measured	16	26	24.5	22

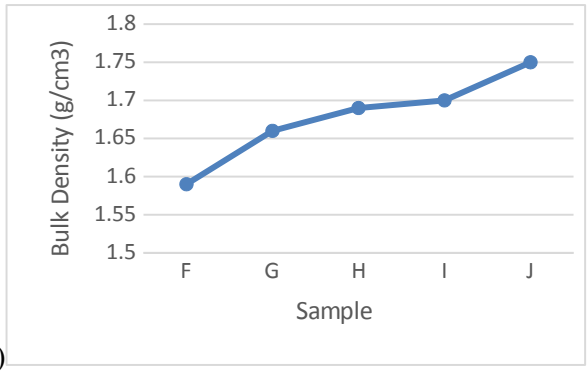

(a)

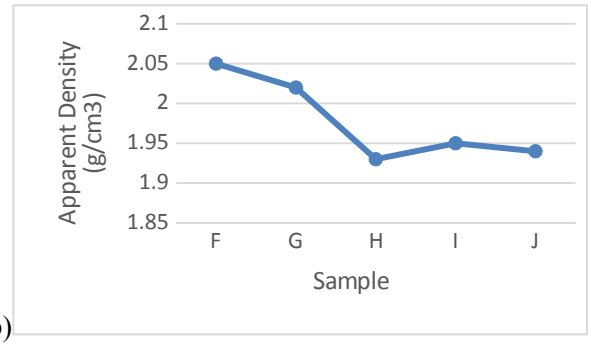

(b)

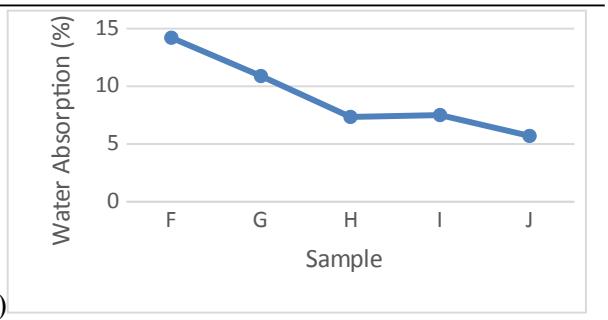

(c)

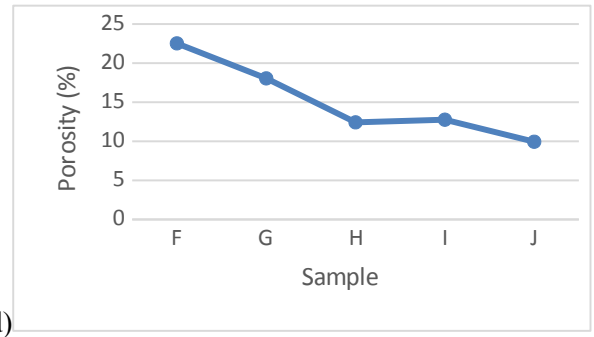

(d)

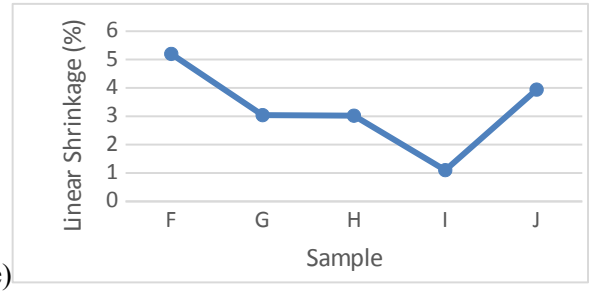

(e)

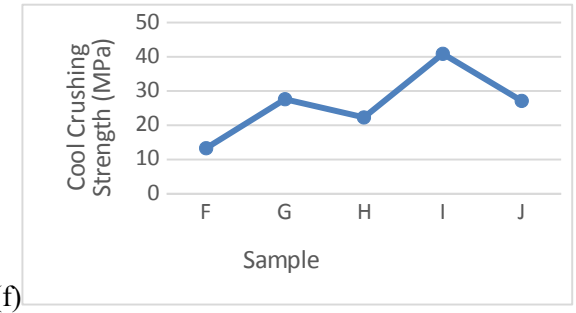

(f)

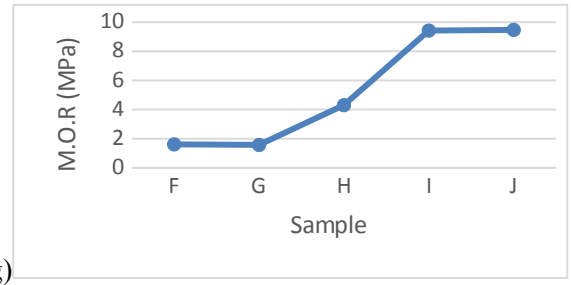

(g)

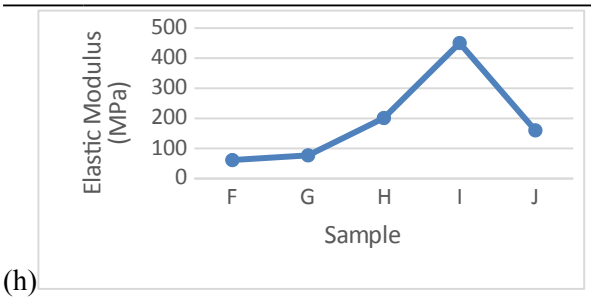

(h)

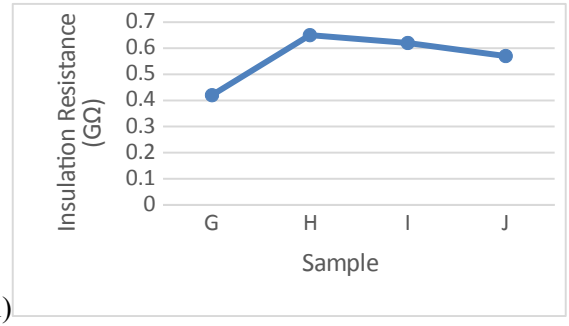

(i)

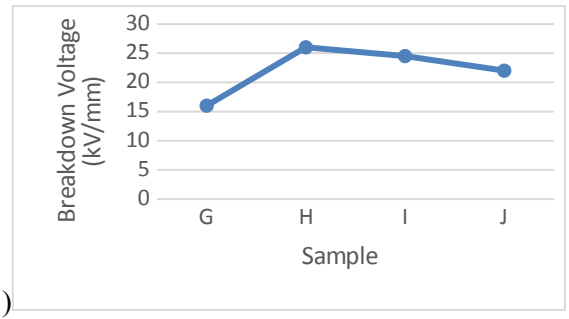

(j)

Figure 3: Physical, Mechanical and Electrical Properties

The porosity in analysed samples revealed that the porosities of the samples generally decrease as the percentage composition of feldspar increases for all samples. At a temperature of 1250°C, the ceramic body's pore spaces compressed and there is an increase in compaction, which causes this situation. At 1250°C, Sample F had the highest porosity value (22.53%). As the proportion of feldspar in the clay matrix increases at 20% quartz with a matching drop in clay content, there is a decrease in porosity from samples G to J, indicating an increase in the compaction of the samples. The bulk densities of the materials under investigation range from 1.59 to 1.75g/cm^3, with increasing value from F to J. The density of all samples also decreased from F to G between 2.05 and 1.93g/cm^3 in comparison with the bulk density that shows the opposite as shown in Figure 3.

The percentage reduction in the length of specimen analysed was noticed to decrease as the percentage composition of feldspar addition in the clay matrix increases for samples F, G, H and I, with increase in value of shrinkage at J as shown in Table 5 and Figure 3(e). Sample F recorded the highest value of shrinkage at 5.20% just as sample I recorded the minimum value of linear shrinkage of 1.1% at the fired temperature of 1250 ℃.

Cold crushing strength (CCS) of specimen investigated varies between 13.30MPa and 40.87MPa. Sample I gave the maximum value of cold crushing strength of 40.87MPa, among others at the temperature investigated (1250^{0}C). But this value decreased when the percentage composition of feldspar was increased. The flexural strength of the samples also had similar characteristics as of increasing value as the composition of feldspar increases up to a maximum of 9.47MPa for sample J at 1250℃. This can be attributed to the decreased pore space of the samples as shown in Table 5.The elastic modulus of the samples also varied at various compositions. A stiffer material will have a higher elastic modulus value, indicating that it is more plastic. At 450.36MPa, Sample I's elastic modulus has the highest value. The amount of feldspar rose along with the elastic modulus.

In terms of electrical properties, sample H had the highest value of breakdown voltage at 26kV/mm, followed by I, J, and G with 24.5, 22 and 12kV/mm respectively. Sample G showed the least value of insulation resistance at 0.42GΩ while sample H showed the highest value at 0.65GΩ.

Table 5 shows that when the percentage composition of additives increases with a corresponding drop in the amount of clay, the insulation resistance and breakdown voltages of samples decrease. This might be explained by an increase in the samples' silica content. As noted by Laraba (2019) and Mgbemere et al. (2019), porcelain insulators' breakdown voltage significantly decreases as their silica content rises due to stress-producing fissures caused by an increase in the conduction-enhancing mineral feldspar. The increased iron oxide concentration in the porcelain insulators from the use of feldspar and ball clay as additives may also result in a drop in breakdown voltage. This behaviour is as observed by Mgbemere *et al.* (2019) was noticed in samples G, H, I, J. These trends are shown in Figure 3(i & j) as relationships between samples and their insulation resistance and breakdown voltage (electrical properties). The breakdown voltage and insulation resistance of sample F could not be measured as the sample crumbles as soon as the set up is complete and a voltage is passed through, this shows insufficient strength in handling the voltage. This could be attributed to the fact that it has 100% clay content with absence of quartz to give it the required strength.

4 CONCLUSION

The Sakpe clay deposit was found to be kaolinitic in nature with good physical and mechanical properties. A maximum CCS of 41MPa, 9.47MPa modulus of rupture and elastic modulus of 450.36MPa were obtained, that meet the required standards. The electrical properties peaked at 0.65GΩ insulation resistance and 26kV/mm breakdown voltage. The investigated clay deposit met the

requirements for porcelain insulators, refractory, tiles, and production ceramic materials, especially, samples H, I and J which have the peak values of physical, electrical and mechanical properties at the experimental temperature.

REFERENCE

Aladesuyi O., Pal M., Das S.K., Ajanaku K.O., (2017). Phase and microstructural evolution during sintering of mixture of 75:25 Nigerian kaolin and calcined alumina powder compacts. *JMES,* 8(8), 2682-2838.

Anih L.U. (2005). Indigenous manufacturer and Characterization of Electrical Porcelain Insulator. *Nigerian Journal of Technology,* 24 (1), 4-9.

ASTM C1161-18, (2018). *Standard Test Methods for Flexural Strength of Advanced Ceramic Materials.* ASTM International, 2018.

ASTM C133-97, (2015). *Standard Test Methods for Cold Crushing Strengths and Modulus of Rupture of Refractories*. ASTM International, West Conshohocken, PA. retrieved from http://www.astm.org/standards/C133.htm

ASTM C356-17, (2017). *Standard Test Method for Linear Shrinkage of Preformed High Temperature Thermal Insulation Subjected to Soaking Heat*. ASTM International, West Conshohocken, PA, 2017, www.astm.org.

Atanda P. O., Oluwole O. O. and Oladeji T. A. (2012). Electrical Porcelain Production from Selected Kaolin deposit in South western Nigeria Using Slip Casting. *International Journal of Materials and Chemistry.* 2 (3), 86-89.

Bilal S., Mohammed-Dabo I.A, Dewu B.B.M., Momoh O.R., Funtua I.I., Oladipo M.O.A., Arabi A.S. and Tukur M. (2015). Effect of Quartz (Free Silica) Removal on the Quality of Nigerian Bentonitic Clays for Application inn Drilling Fluid Formulation. *Journal of Experimental Research, 3(2),* 3-7.

Ezenwabude N.and T. C. Madueme (2015). Investigated the Evaluation of Mixed Local Materials for Low Voltage Insulators. *International Journal of Multi-Disciplinary Sciences and Engineering,* 6(1), 37-43.

Laraba M. (2019). Characterization of Algerian kaolins for utilization as a raw material in electrical insulators. *Cerâmica 65 (2019), 267-273* http://dx.doi.org/10.1590/0366-69132019653742556.

Moyo M. G. and Park E. (2014), Investigating the ceramic raw materials in Tanzania – structure and properties for electrical insulation application. *International Journal of Engineering Research & Technology (IJERT),* 4(1), 34- 41.

Mgbemere H. E., Onyeayana I. P. and OkoubuluA. B. (2019). The Effect of Kaolin and Silica Variation on the Properties of Porcelain Insulators. *Nigerian Journal of Technology,* 38(2), 19- 25.

Nasejje S. and Obwoya K. S. (2015). Dependency of Dielectric Strength of Kaolin on Processing Method. *Journal of Scientific Research & Reports,* 4(4), 306-312.

Nwachukwu V. C. and Lawal S. A. (2018). Investigating the Production Quality of Electrical Porcelain Insulators from Local Materials. *IOP Conf. Series: Materials Science and Engineering,* 4(13), 20-28.

Ogwata C.M and Anih, L.U, (2015). Effects of Scrap Glass Powder on Electrical Porcelain. *Global Journal of Engineering Science and Researches,* 2(6), 7-12.

Olupot P.W., Jonsson S. and ByaruhangaJ. K. (2010). Development and Characterization of Triaxial Electrical Porcelains from Ugandan Ceramic Minerals. *Ceram. Inter.* 36, 1455-1461.

Ovri J.E. and Onuoha A. (2015). Characterization of Some Nigerian Clay for electrical porcelain application. *International Journal of Advanced Materials Research,* 1(3), 113-119.

4th International Engineering Conference (IEC 2023)
Federal University of Technology, Minna, Nigeria

Development of A Prototype Automatic Tyre Inflation System for lightweight vehicles

[1]P.R. Christopher, [1]A.B. Hassan, [2]M. M. Muhammadu and [2]N. Abdul

[1] Mechanical Engineering Department, School of Infrastructure, Process Engineering and Technology, Federal University of Technology Minna.

[2] Center for Technology Development Kaduna polytechnic, Kaduna.

Corresponding Author's e-mail: cpaul4288@gmail.com

Abstract

Having a deflated or under-inflated tyre is a huge challenge for lightweight vehicle users most especially in the area where there security threats, even night or raining season when the vehicle users lack some of the basic equipment to fixed or replace the deflated or under-inflated. This research aim to develop a prototype automatic tyre inflation system for lightweight vehicles, which will constantly inflate the tyre to the require pressure gauge of the vehicle to enable the car users to reach a safe place or where he or she can get the services of a vulcanizer while in motion. This will be carried out with the help of microprocessor system with develop software (Proteus Assembly Language) which monitor the tyre pressure using pressure sensor. When tyre pressure goes below the require gauge the system will automatically inflate the pressure back to the require gauge, most light vehicle tyre pressure gauge is 45psi and deflate the pressure to the required gauge through pneumatic actuator. These studies were successfully tested and conducted with the selected portable compressor. The compressor supplies pressure to all four tires via hoses and a swivel mounted between the wheel axle and wheel hub on each wheel. The swivel joint is an integral part of the system, half rotating with the wheel and the other half being stationary. Pivot joints effectively direct the pressure on the tires. This makes the swivel joint easier to untangle the pipes. The following test results were obtained for times of 2 min, 4 min, 6 min, 8 min, 10 min, 12 min, 16 min with the corresponding pressures, 2.72 psi 16.24 psi 34.81 psi, 37.7 psi, 39.16 psi, 42.0 psi 43.5 psi, 45.51 psi and fuel consumption of 10 L100km-1, 20 L100km^{-1}, 30 L100km^{-1}, 40 L100km^{-1}, 50 L100km^{-1}, 60 L100km^{-1},70 L100km^{-1},80 L100km^{-1},90 L100km^{-1} respectively. With this result obtained considering todays ever increasing security threats, tyre life span and reduction in fuel consumption is achieved for lightweight vehicles

Keywords: Automatic tyre inflation, Prototype development, lightweight vehicles, tyre life, fuel consumption

INTRODUCTION

Having flat tyre cause tremendous inconveniences to vehicle users particularly at night time or while it is raining. Replacing a deflated tyre with a spare one is mostly a herculean task, it gets even worse if one does not understand how to set up the spare or in a scenario wherein one can't vulcanize the tyre at the moment. Tawanda Mushiri et al., (2016). The deflation is a technique of letting air or pressure out of the tyres. Deflation is the challenge of car tyre, due to the fact a sure time frame air lessen in the tyre of the car for running time. So, a long distance travelled car is a capable deflation or over inflation of the tyres. The air likewise lowering the life span of the tyre by both over inflation or below inflation as the case may be. Flat tyre managers usually ask how regularly they need to be checking tyre pressure that loss a lot of air throughout the course of the year. Osmosis of air via the tyre casing can result in a loss 1to 3 psi per month, depending at the precise tyre make, version and the type of compounds used in the manufacture of the tyre may have a huge effect on osmosis (Kamlesh R,2017). The composition and gauge of the tyre internal liner compound also performs importance in osmosis. Car tyres are the only part of the car which have contact with the road, tyres are equipped on the rims and inflated. Safety in acceleration, steering, cornering and braking depends on tyre's contact with the road. There are specific kinds of tyres, starting from radial ply to self-assisting run flat. These tyres ought to be saved at accurate pressure for maximum performance. Driving over pot-holes, kerbs, pointed objects even at low velocity can cause puncture which leads to flat tyres. However, while tyre pressure reduce it makes vehicle to be unbalanced, it more so influences the rate of the car and may create damage to the tyre.

Therefore, the need to inflate the tyre while the pressure reduce can't be over emphasized. Hence this research has a tendency to offer technique to drivers whose tyre pressure has reduced, mainly when the area to volcanize the tyre isn't near at hand. Jeeva Bharathi1, (2017) Maintaining the appropriate tyre pressure enables to increase the life span of tyres, enhance car protection and keeps gasoline efficiency. Tyre pressure is measured through calculating the quantity of pressure that is inflate into the internal lining of the tyre in per square inch (psi) or bar. Vehicle manufacturers specify an appropriate pressure for tyres used in the car, and it is the obligation of the driver to ensure that the pressure is checked and corrected on every day. We suggest doing this each weeks to ensure best tyre pressure (Indrajeet, 2016).

Figure 1.1: Tyre inflation (Tyremarket,2016)

DESIGN OBJECTIVES

The aim of this research is to develop a prototype automatic tyre inflation system for lightweight vehicles, this can be achieved through the following objectives;

1. Design an automatic tyre inflation system for lightweight vehicles.
2. Fabricate the design components of the automatic tyre inflation system.
3. Assembly the components and test the develop automatic tyre inflation system

MATERIAL AND METHODS

This device consists of Microprocessor system with software development (Proteus Assembly language), power unit, pressure sensor unit, control unit active component, mild steel, cast iron, solenoid valve, tyre with a rim. MIDE Compiler Analogue to digital converter, pulley, Relays, Operational amplifier, Liquid crystal display, Compressor, Brushless motor (electric motor), pneumatic actuator as material used in developing the automatic tyre inflation system for lightweight vehicles.

Some of the basic design requirements and analysis of this project are taken. In any device development and process optimization, a requirement is a singular documented physical and functional need that a particular design, device or process must be able to perform while the design criteria are the explicit goals that this project must achieved.

Design Considerations

According to S.P.Shinde (2016), design considerations are few traits that affect the design of the elements on the tyre device the design considerations which might be critical to this design are:

1. Availability of the materials.

2. Suitability of materials for the operating condition in service.

3. The value of materials.

4. Physical and chemical properties of material

Design analysis:

The analyses of the mechanism are explained as follows:

Design for motor

R = Resistance of the motor

K_M = Toque constantly the motor

ω = angular velocity

Q = charge

T = Time

V = Velocity

K_e= back EMF constant of the motor (V/RPM)

d = distance

D = diameter

First we have to prove that K_m *is equal to constant*

$$n=\left(\frac{V}{K_e}\right) - \frac{m}{(K_m \times K_e)} \quad (1)$$

Where $K_e = \frac{U}{rpm}$

$n = \frac{V}{\frac{V}{rpm}} - \frac{m}{K_m x \frac{v}{rpm}}$

Where m = torque = $I \times K_m$

$n = \frac{rpm}{1} - \frac{rpm\ x\ I\ x\ km}{K_m\ V}$ (2)

Where $I = \frac{q}{t}$

$t = \frac{distance}{velocity}$

Substitute $\frac{d}{v}\ for\ t$ $\frac{q}{\frac{d}{V}} = I$

$\therefore \frac{q\ v_e}{d} = I$ (3)

$\therefore$ Where $\frac{q}{d} = potential = V$

$\therefore VV_e = I$

$V_e = \frac{I}{V}$

Velocity = $\frac{current}{voltage}$ (4)

$V_e = \frac{I}{V}$

V = ωr

$\omega = \frac{V_e}{r} = \frac{I}{V \times r}$

$n = \frac{rpm}{I} - \frac{rpm\ x\ I\ x\ K_m}{K_m\ x\ v}$

$n = \frac{K_m \times V \times rpm - rpm\ x\ I\ x\ K_m}{K_m\ x\ V}$ (5)

Where rpm = ω

$n = V_e = \pi D \omega$ (6)

$\therefore \omega = \frac{V_e}{\pi D}$

$\omega = \frac{I}{V\ x \pi D}$

$\frac{\pi DI}{V} = \frac{K_m\ x\ V\ x \frac{J}{V\ x\ \pi\ D} - \frac{I_I}{V\ x\ \pi\ D} \times I \times K_m}{K_m\ x\ V}$ (7)

$\frac{\pi DI}{V} = \frac{\frac{K_m\ V\ I}{V \times \pi\ D} - \frac{I^2 K_m}{V\ \pi\ D}}{K_m V}$

$\frac{\pi\ D\ I \times K_m\ V}{V} = \frac{K_m\ V\ I}{Vx \times D} - \frac{I^2 km}{V \pi D}$

Factorize

$\frac{K_m\ V\ I}{V \times \pi D} - \frac{I^2 K_m}{V \pi\ D}$

$\frac{K_m VI\ - I^2 K_m}{V \pi D}$

$I \times K_m = \frac{K_m VI\ - I^2 K_m}{V \pi D}$

$I \times K_M = K_m VI\ - I^2 Km$

Bringing like term together

$V\pi DI = \frac{K_m VI\ - I^2 K_m}{K_m}$ (8)

$V\pi DI = \frac{K_m (VI\ - I^2)}{K_m}$

$V\pi DI = \frac{K_m}{K_m}\ x\ (VI - I^2)$

$\frac{V\pi DI}{VI - I^2} = \frac{K_m}{K_m} = 1 = \frac{K_m}{K_m}\ is\ constat$ (9)

Mathematical derivation to determine the Torque, Efficiency and speed at 3000rpm 0f 20.09A current input Where V = 220

π = 3.142

I = 20.09A

D = 2.2cm = 0.022m

Compressor

This method is use in selecting the compressor

Calculation:

For tyre pressure of 45 psi

Where 1psi = 0.06895bar

Therefore 45 psi = 45x0.06895 = 3.1028 bar =3.1 bar approximately.

Therefore, 12 V D. C, 5.5 bar compressor for tyre pressure of 0-70 psi is selected.

The following shows the specification of our portable compressor:

Pressure Range (psi) 0-70 psi

Power Supply 12 V DC

Weight 1.5 kg

Dimensions 21.9*17.3*12.5cm

Figure 1.2: compressor

TESTING AND RESULTS

The machine is tested using electricity because of the motor which is the prime mover of the tyre (Tricycle tyre). The microcontroller which carried a written algorithm on the chip to interpret and carry out some certain task, the task are executed by command from the program. At every input instruction the program search and read the input which interpreted it to the command, the command in return execute the instruction by controlling the switch that controls the air pressure compressor, through current driver transistors. The digital output from the microcontroller opens the base of the transistor, which allows the current to flow from the emitter to the collector; the current from the collector was fed to the switching relay, in which the relay open or close depend on the signal received, the relay was connected to the air compressor machine. When the pressure of the tyre increases to its maximum, the microcontroller interpret it through the sensor and switch of the pumping machine, in return when the pressure goes below the expected value, the algorithm in the microcontroller interpret the instruction and switch on the pumping machine. The parametric value of the pressure was interpreted by special command, which was display on two by sixteen liquid d crystal display.

Results

During the process of testing the device, the following results were obtained. The time taken for the pressure to fill the tyre to the required gauge is stated in the figure 1.3 and 1.4.

From figure 1.3 its show that the time taken for the compressor to inflate the tyre increase linearly as the pressure increase to the required gauge.

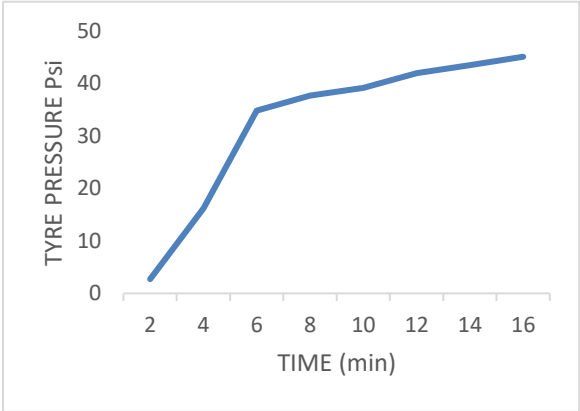

Figure 1.3: Graph of Tyre Pressure against time

From figures 1.3 the results obtain show that, when the pressure sensor sense a drop in the tyre pressure the compressor inflate the tyre Thus figure 1.4 show how fuel consumption reduces has the tyre pressure increase to the proper gauge.

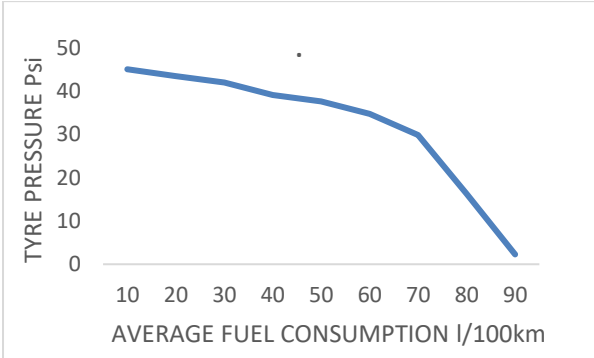

Figure 1.4: Graph of Tyre Pressure against Average Fuel Consumption.

CONCLUSION

This research work on the development of a prototype automatic tyre inflation system for lightweight vehicles while on motion was carried out successfully. A develop automatic tyre inflation system was designed, fabricated, assembled and tested. It was observed that when there is a drop in the tyre pressure, the pressure sensor sense it and sent a signal to the compressor which automatically inflate the tyre to the require gauge pre-set at 45 psi, through the help of a written programme code embedded

in the microprocessor system.. This research solve the problem of vehicle users by maintaining the tyre pressure which reduce tyre ware due to drag or friction thereby reducing fuel consumptions and increase the life span of tyre

Acknowledgement

The authors acknowledge thankfully the effort and ideas of Engr. DR. A. B Hassan, Engr. Dr. M. M. Muhammadu and Mr. Abdul N and more importantly God who is the source of the fund which enable to carry out this mind blowing project. I can't forget family, friends and loves one who supported the success of this research, Almighty God bless you all. AMEN

REFRENCES

Tawanda Mushiri, Design of an automatic tyre pressure inflation system for small vehicles, International Conference on Industrial Engineering and Operations Management Detroit, Michigan, USA, September 23-25, 2016.

Jeeva Bharathi1 , Design And Fabrication of A. V. Wadmare ,Automatic Tyre Pressure Controlling and Self Inflating System, IOSR Journal of Mechanical and Civil Engineering, PUNE, Maharashtra, India. (IOSR-JMCE) e-ISSN: 2278-1684,p-ISSN: 2320-334X PP. 01-05 www.iosrjournals.org (2017)

Indrajeet Burase: A Survey on Automatic Air Inflating System for Automobile, International Journal of Innovative Research in Science, Engineering and Technology (An ISO 3297: 2007 Certified Organization),Vol. 5, Issue 10, October 2016

Kamlesh R. Patil: Self-Inflating Tyre System, Imperial Journal of Interdisciplinary Research (IJIR) Vol-3, Issue-3, 2017 ISSN: 2454-1362, http://www.onlinejournal.in

Murugavel, G.Sivaprasath (2015) "Automatic Air Inflation System in Tyre with Pressure Control and Monitor System vol 3" Department of Mechanical Engineering,Velammal Institute of Technology, Ponneri, panchetti post-601204,Tamilnadu, India,

Janahanlal P.S(2014) "Tyre Pressure Monitoring and Automatic Air Filling System vol 2" Department of Electronics and Communication Engineering, Matha College of Technology.

S.P.Shinde (2016) "Central Tyre Air Inflation System vol 4" Department of Mechanical Engineering, Smt. Kashibai Navale College of Engineering, Pune.

S.Sushanth kumar (2014) "Automated Tyre Pressure Monitoring and Regulating System vol 4" Department of Electronic and Instrumentation Engineering, Sree Sai Ram Engineering College.

A.V. Wadmare, P.S. Pandure "automatic tyre pressure controlling and self-inflation system: a review'' IOSR-JMCE, e-ISSN: 2278-1684, p-ISSN: 2320-334x.

Indrajeet Burase, Suyash Kamble, Amol Patil, Avinash kharat "A survey on design and fabrication of automatic tyre inflation and deflation system. IJARIIE-ISSN (O) -2395-4396, Vol-2 issue-3, 2016

Tyremarket (July, 2016). *Tyre Burst: A Driver's Nightmare.* Retrieved from Http://www.tyremarket.com/tyremantra/tyre-burst-causes-tyre-speed-symbol-alphabets/

.

4th International Engineering Conference (IEC 2022)
Federal University of Technology, Minna, Nigeria

Multiple Radio Access Technology Co-existence in Cellular Network: A Dynamic Spectrum Sharing Perspective

*Oyelade, D. O[1], Usman, A. U[2], & Adejo, A.O[3],
[1]Telecommunications Engineering Department, Federal University of Technology, PMB 65 Minna Niger State, Nigeria
[2]Telecommunications Engineering Department, Federal University of Technology, PMB 65 Minna Niger State, Nigeria
[3]Telecommunications Engineering Department, Federal University of Technology, PMB 65 Minna Niger State, Nigeria

ABSTRACT
The increased availability of mobile broadband and the introduction of new radio access technologies has led to the availability of a massive number of devices which are able to connect to the internet, however, there is the need to ensure spectral efficiency and more proper management of the scarce radio spectrum. Spectrum refarming offers a solution in ensuring the scarce spectrum resources are optimized. The existence of a dynamic methods of spectrum sharing has ensured there is a smooth transition in the development of new radio access technologies which is exemplified in the development of different architectures for the 5G New Radio (NR). This study is a review of the current state of art of dynamic spectrum sharing is discussed which would aid the development of newer and better methods using artificial intelligence (AI) techniques.

Keywords: *Refarming, New Radio, Spectral efficiency, 5G Numerology, Spectrum Sharing*

1 INTRODUCTION

In the past few decades, there has been the increased need of broadband by users of wireless communication. According to Yeganeh, & Ebrahimi (2019), every 10 years a new generation of cellular communication has emerged, 5G cellular network was commercially launched in February 2019, 10 years after the commercial launch of the first long term evolution (LTE) and 20 years after the Universal Mobile Telecommunications System (UMTS). According to Mukherjee and Biswas (2014), the motivation for the introduction of new radio access technologies includes the need to have better spectral efficiency, lower delay, and better. This introduction is not without its own challenge of cost of infrastructure and the attendant cost of spectrum purchase.

Radio access network is the technology that connects end-user devices, or terminals, to other parts of a network through radio connections. With the emergence of each new generation, it takes several years for the subscribers of the older network to transfer to the new network. One reason is that universal coverage of newer networks takes time. Another reason is that old mobile equipment does not support new networks. Some other reason is that; sometimes, new applications for older technologies or the upgrade of these technologies prolong their use. An instance is the upgrade of GSM technology to extended coverage GSM (EC-GSM), only through software modifications

Radio access network is enabled by radio spectrum which is a very scarce resource. The statistics of spectrum allocation around the world shows that the radio frequency spectrum has almost been fully allocated and the available spectrums for new services are very limited. According to Barb *et al*, (2021), mobile communication mainly uses frequencies between 300 MHz and 6 GHz with most of it already allocate This scarcity is further accelerated especially due to the emergence of the massive connections of internet of things (IoT). According to Barb *et al*, (2021), mobile communication mainly uses frequencies between 300 MHz and 6 GHz with most of it already allocated

The value of radio spectrum is immense and according to Reed *et al* (2016) recent estimates indicate global annual revenues of over a trillion dollars for mobile wireless, $320 billion for broadcast TV, and $63 billion for broadcast radio. In the recently past month of December 2022, the Nigeria communications commission auctioned the 3.5 GHz and a 2.6 GHz radio spectrum which was won by Airtel Nigeria at a fee of $316.7 million following the earlier auction of the 3.5 GHz radio spectrum won by MTN Nigeria and Mafab communications at about $238 million. The need to develop new technologies to unlock frequency spectrum. Li *et al* (2017) together with the need for spectral efficiency and network optimization coupled with the huge cost required for the purchase of new spectrum bandwidth from governments has led to the development of the concept of refarming.

'Refarming' is the term used for the process governing the repurposing of frequency bands that have historically been allocated for 2G mobile services (using GSM technology) for new generation of mobile technologies. The advantage of refarming is to widen bandwidth to support UMTS, LTE and 5G services.

This paper would discuss the challenges of spectrum scarcity, we would also discuss the different architecture of 5G NR We would also look review some work on the concept of dynamic spectrum refarming.

2 RADIO SPECTRUM

. Radio spectrum refers to a specific range of frequencies of electromagnetic energies that is used to communicate information. They are necessary for important societal applications such as radio and television broadcasting, civil aviation, Satellite, defence, and emergency services. These applications do require specific allocations of radio frequency. Moreover, the demand for radio spectrum is increasing rapidly largely due to the increasing smartness of our daily living and the need for huge bandwidth for video and machine to machine communications as internet of things develop.

2.1 THE SCARCITY OF RADIO SPECTRUM

Spectrum resource for most wireless networks is fixed. It is also almost impossible to allocate more spectrum resources to certain wireless networks due to regulatory constraints; this makes the issue of spectrum scarcity more precarious in wireless and radio frequency (RF). communication especially cellular communications and vehicular communication. Han *et al.* (2016). Operators rarely pass up the chance to expand their portfolio because spectrum is a significant source of competitive advantage, especially for desirable frequencies., spectrum is crucial to their success and, in some ways, the reason they even exist. This has also led to a further analysis on spectral efficiency as a lot of spectrums are underutilized leading to spectrum, underutilization. This is also corroborated by Han et al (2016) and Onumanyi, *et al.* (2013) who conducted a spectroscopic measurement of frequency occupancy in Minna and noticed only about 10% occupancy value of their frequency range of interest.

Iliya *et al.* (2015) also investigated frequency occupancy of some communication bands in Leicester, the United Kingdom. The frequencies ranged from the 50 MHz to 868 MHz of radio and TV broadcasting channels, together with the GSM 900 MHz, 1800 MHz, and ISM 2.4 GHz channels. They observed in their report that several bands were barely used while the GSM 900 MHz band and the GSM 1800 MHz were found the extensively used. (Iliya *et al* 2015) hence conclude that while spectrum might seem to be scarce, the fundamental issue is the static allocation of spectrum.

Paulson *et al.* (2017) also conducted a spectrum occupancy test in Ikeja, the capital of Lagos state, Nigeria. The test was conducted in an indoor environment with a frequency range of 700 MHz to 2200 Mhz. They conducted the test using different bandwidths according to their applications within the frequency range. They observed the most occupied and utilized band to be the band 900 corroborating Iliya *et al* (2015). It was also observed that spectral utilization was not uniform because some bands had heavy utilization while other bands were sparsely utilized.

. Spectrum scarcity can be managed using cognitive radios, the use of small cells, smart antennas, carrier aggregation and spectrum sharing for the coexistence of different technologies.

According to Galanopoulos *et al* (2018), spectrum refarming can be static, semi static, or dynamic. They state that static refarming occur in months and possibly in years where a legacy radio access technology is reallocated permanently to LTE or NR for co-existence. Peak throughput is one of the compromises that need to be incorporated when static refarming is implemented, however investigations are beginning to grow in dynamic spectrum refarming which would be discussed in this paper

2.2 STAND ALONE/NON-STAND-ALONE NEW RADIO(NR) ARCHITECTURE

According to El Rhayour and Mazri (2019), two different solutions exist for the deployment of 5G NR which are namely; the non-standalone (NSA) architecture which is based on the deployment of 5G NR with the already existing LTE radio access technology and using the enhanced packet core (EPC) of the 4G. The second model of deployment of 5G NR is the stand alone (SA) option which consist of its own 5G packet core. The Non-stand-alone option ensure a quick and easy deployment with lower cost. This is also boosted by the existence of spectrum refarming which can be dynamically implemented to ensure that customers can be allocated more bandwidth as traffic increase.

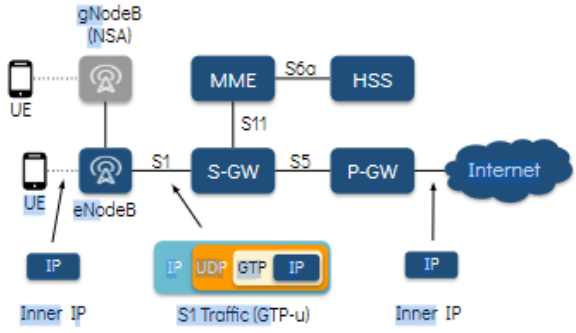

Fig 1 Non standalone NR Architecture
Source: Coronado *et al* (2020

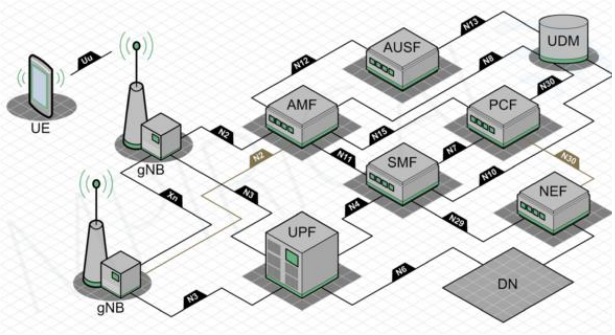

Figure 2: NR Standalone Architecture.
Source: Mitchell (2021)

- MME: Mobility management Entity
- SGW: Serving Gateway
- HSS: Home Subscriber Server
- PDN-GW: packet Data Network Gateway
- AMF: Access and Mobility Management function
- SMF: Session Management function
- UPF: User plane function
- PCF: Policy Control Function
- AUSF:Authentication Server Function
- UDM: Unified Data Management
- AF: Application Function
- NEF: Network Exposure function
- NRF: NF Repository function
- NSSF: Network Slice Selection Function

The NSA architecture ensures a smooth migration from LTE to NR at lower cost and provides a justification for radio frequency spectrum coexistence of LTE with NR.

2.3 DYNAMIC SPECTRUM MANAGEMENT

According to Zhou *et al.* (2019), there exists a problem of spectrum scarcity in wireless communication which is further compounded by the increase in the number of devices that have the capability of connecting to the internet with the development of the internet of things (IoT). This has led to the need to develop dynamic ways of managing spectral resources. According to them dynamic spectrum management can be attained using two different paradigms which are the opportunistic spectrum access and spectrum sharing. While opportunistic spectrum access involves unlicensed users taking advantage of the non-usage of a licensed spectrum by the licensed users, spectrum sharing involves the ability of different technologies to coexist in a spectrum band within an allowable interference level. The latter is to aid and improve spectral efficiency. This is further corroborated by (Lin *et al* 2021) who state that dynamic spectrum sharing ensures a reduction in wastage of spectrum while also ensuring better spectral efficiency.

In managing resources of a spectrum dynamically, (Barb *et al* 2021) describe a sharing calculation ratio between NR and LTE which is managed by a common resource manager placed in the base station, the LTE sub unit, and the NR sub unit. which calculates and updates sharing ratio based on traffic.

2.4 BANDWIDTH SCALABILITY OF LTE AND NR

Bandwidth scalability is one of numerous flexibilities offered by LTE. It provides bandwidth of 1.4 MHz, 3 MHz, 5 MHz, 10 MHz, 15 MHz, and 20 MHz NR is also scalable bringing about the concept of new radio numerology where NR provides for subcarrier spacing from 15kb and using the concept $2^n X 15$

Where n is the numerology making it possible for NR to use more than one subcarrier in a physical resource block. The chosen subcarrier spacing in a NR is due primarily to the needs of the user equipment

In the following section, a review of recently implemented dynamic spectrum sharing mechanisms would be done.

3 SOME RELATED WORK ON DYNAMIC SPECTRUM SHARING

According to Barb *et al*, (2021) the orthogonality in time and frequency of LTE downlink channels. which allows for the incorporation of NR/LTE channels in the same spectrum allowing for dynamic configuration, transmission and preventing interference between LTE and NR. In their work, they consider a base station for LTE and a single base station for NR The work evaluates the performance of throughput based on the model for deployment which was for both NSA or SA. They also consider different sharing ratios for LTE and NR in both downlink and uplink. They observe an increase in throughput of NR with increasing sharing ratio with a reduced throughput for LTE, however there is a slight reduction in throughput when dynamic spectrum sharing is used compared to when there is only LTE or only NR occupying the spectrum. This is due to the shared resources between LTE and NR.

Li *et al* (2017) considered an intelligent approach in allocating spectrum in a multiple co-existing network of 2G , 3G, and 4G. In the study, they considered the presence of a central scheduler which determines the occupancy of a spectrum by multiple radio access technologies. Moreover, the central controller predicts the capacity and interference of the channel in a future state with resource allocation in that time computed by a neural network forecasting. They use historical data of the base station over several hours of several days for the construction of the input layer which includes the users of the network. According to the work, there is priority to GSM spectrum during the day especially during work hours while data services are given priority at night which implies that LTE has more bandwidth at night.

The paper considered 12 LTE sites and 66 cells, as well as 7 GSM sites and 12 cells. The observation is an increase in throughput on uplink by 80% and downlink throughput was increased by 100%, as well as an increase in volume of traffic in uplink and downlink by 100% and 200% respectively. Spectrum efficiency of bandwidth also increased by 63.9%.

Yeganeh and Ebrahimi (2019) proposed a practical solution for the dynamic allocation of frequency resources between GSM and LTE. The work proposed a dynamic spectrum refarming scheme where LTE borrows part of the bandwidth of GSM at the peak period of LTE and LTE borrows part of the bandwidth allocated to LTE at the peak period of GSM. It is noted that voice calls are still mostly routed through the GSM core network. The work discusses 3 different scenarios which include the classic scenario which is like the static refarming method, the semi static method and the third scenario which is purely dynamic where GSM carriers are located on the guard band of LTE .and allow for flexibility in the allocation of bandwidth between GSM and LTE leading to maximization of bandwidth for LTE users and providing required capacity for GSM. However, the work does not consider the effect of interference when, GSM borrows part of the bandwidth of LTE and vice versa at their respective peak periods

Challita and Sandberg (2021) present a nouvelle method of dynamic spectrum sharing in LTE and nr using a deep reinforcement learning. The paper described the process which is essentially focused on dynamic spectrum sharing and incorporates the existence of a controller that dynamically allocates spectrum resources to the two radio access technologies that exist within the same frequency. The work emphasized the need for dynamic spectrum sharing because it provides an easy means for migration from LTE to NR which would also be the case for beyond 5G networks due to the scarcity of spectrum, the high cost for purchase of spectrum and the need to maximize the current spectrum resources available. The work proposed a scheme of planning in the time and frequency domain where the controller distributes frequency resources with serious consideration to the future state of the network. In the model, the work ensured an efficient dynamic spectrum sharing by designing a mechanism for the division of the available bandwidth for data and transmission for each of the radio access technology. The work adopted a reinforcement learning process in training the controller to learn about the best policy for bandwidth sharing. The relationship between the controller and the two different radio access technologies is described as shown below

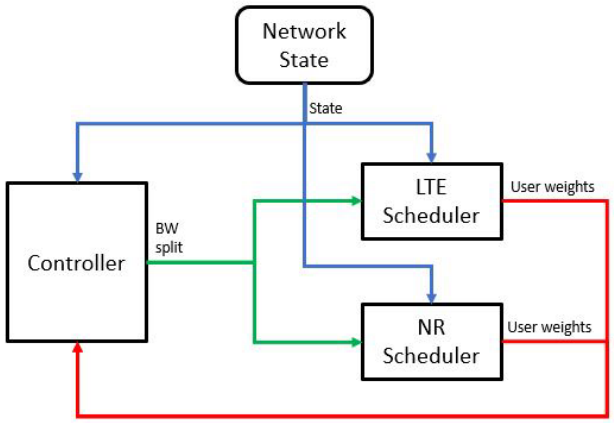

Figure 3: Connection between the controller, network state, LTE and NR schedulers
Source: Challita and Sandberg (2021).

The network state information received by both the NR scheduler and LTE scheduler provides an excellent support to the controller to take excellent actions in the sharing of the bandwidth between NR and LTE.

The work shows an improvement in the overall interference of the system due to the ability of the controller to split the bandwidth efficiently between LTE and NR

They conclude that with deep enforcement learning, the controller becomes more intelligent thereby improving overall system performance

4 CONCLUSION

Artificial intelligence has become part of our day-to-day activities and its influence across different fields cannot be overemphasized. It is therefore important that it is incorporated in dynamically managing spectrum sharing in 5G cellular network and beyond. Further work can be done on machine learning techniques to obtain the best method while considering the effect of interference on the whole system and at the same time ensuring excellent quality of service for customers and subscribers

5 REFERENCES

Barb, G., Alexa, F., & Otesteanu, M. (2021). Dynamic Spectrum Sharing for Future LTE-NR Networks. *Sensors*, Vol 21 (12). doi:10.3390/s21124215

Challita U. and Sandberg D., (2021). Deep Reinforcement Learning for Dynamic Spectrum Sharing of LTE and NR, ICC *2021 - IEEE International Conference on Communications*, Montreal, QC, Canada. Pp. 1-6, doi: 10.1109/ICC42927.2021.9500325.

Coronado, E., Yousaf, Z., & Riggio, R. (2020). LightEdge: Mapping the Evolution of Multi-Access Edge Computing in Cellular *Networks. IEEE Communications Magazine*, Vol 58 (4), Pp. 24–30. doi:10.1109/mcom.001.1900690

El rhayour, A., & Mazri, T. (2019). *5G Architecture: Deployment scenarios and options. 2019 International Symposium on Advanced Electrical and Communication Technologies (ISAECT).*

Galanopoulos, A., Foukalas, F., & Xenakis, A. (2018). Multi-RAT spectrum reallocation including carrier aggregation for 5G networks. *Proceedings of the 22nd Pan-Hellenic Conference on Informatics - PCI '18.* doi:10.1145/3291533.3291539

Han S., Liang Y., Soong B., & Li S., (2016) Dynamic Broadband Spectrum Refarming for OFDMA Cellular Systems.

Iliya S., Goodyer E., Gow J., Gongora M., and Shell J. (2015) Spectrum occupancy survey, Leicester, UK, for cognitive radio application. *Centre for Computational Intelligence, School of Computer Science and Informatics, De Montfort University, The Gateway, Leicester.*

Li Y., Zhang Z, Li F., Feng Y., and Chen L. (2017) An Approach for Intelligent Spectrum Allocating for Multi-RATs Networks. *9th IEEE International Conference on Communication Software and Networks.* Pp. 234-238 doi:10.1109/isaect47714.2019.90

Lin P., Xie W., Hu C., (2021). Research on Dynamic Spectrum Sharing Solution of Indoor Distribution System. *2021 2nd Information Communication Technologies Conference (ICTC),),* Pp. 129-133 doi:10.1109/ICTC51749.2021.9441605

Mitchell G. (2021). Retrieved from https://www.mpirical.com/blog/standalone-5g-networks. Accessed on 17th February 2023

Mukherjee T., and Biswas S. (2014) Simulation and Performance Analysis of physical downlink shared channel in LTE cellular Networks. *2014 Annual IEEE India Conference (INDICO).* Doi.org/10.1109/INDICON.2014.7030448

Onumanyi A., Onwuka E. N., Ugweje O., and Salami M.J.E. (2013). Spectroscopic Measurements and Analysis of Frequency Occupancy. A Case Study of Minna, Niger State. *3rd Biennial Engineering Conference, Federal University of Technology, Minna. Nigeria*

Paulson E., Adedeji K., Kamaludin M. Y., Popoola J. J., Jafri B., and Sharifah K. (2017) Spectrum Occupancy Measurement: A Case for Cognitive Radio Network in Lagos, Nigeria. *ARPN Journal of Engineering and Applied Sciences.* Vol 12 (4).

Reed J., Vassiliou M., and Shah S. (2016) The Role of Nesw Technologies in Solving the Spectrum Shortage. *Point of View.* Vol 104 (6).

Yeganeh, D. F., & Ebrahimi, A. (2019). Dynamic spectrum refarming for GERAN/EUTRAN considering GERAN voice traffic. *Telecommunication Systems.* doi:10.1007/s11235-019-00625-0

Zhou, F., Lu, G., Wen, M., Liang, Y.-C., Chu, Z., & Wang, Y. (2019). Dynamic Spectrum Management via Machine Learning: State of the Art, Taxonomy, Challenges, and Open Research Issues. *IEEE Network,* vol 33 (4), Pp. 54–62. doi:10.1109/mnet.2019.1800439

4th International Engineering Conference (IEC 2022)
Federal University of Technology, Minna, Nigeria

Investigation of Pentane and Dodecane Fuels on the Thermo-Economic Performance of a Solid Oxide Fuel Cell.

*Ojo, E.O.[1] & Azeez, O.S.[2]
[1,2]Chemical Engineering Department, Federal University of Technology, PMB 65
Minna, Niger State, Nigeria.
*Corresponding author email: *ojoemmanuel192@gmail.com Te1: +2348068455972

ABSTRACT

The major setbacks in the commercia1 production of fue1 cell techno1ogy are the fue1, cost and durabi1ity. The choice of fue1 impact the therma1 efficiency and overall viabi1ity of a so1id oxide fue1 cell (SOFC) system. Therefore, this work is aimed at investigating pentane and dodecane fue1s on the thermo-economic performance of a so1id oxide fue1 cell. Thermo1ib, a mode1ing and simu1ation too1box for the design and deve1opment of thermodynamic systems in MATLAB was used to setup a configuration system mode1 for pentane and dodecane, in which the in1et fue1 is mixed with steam and pump through heat exchanger to heat up the mixture to the required temperature for the reforming reaction. At the reformer, the fue1 is converted to hydrogen and carbon monoxide. The reformer outlet is thereafter passed to a water-gas shift reactor where the carbon monoxide is reacted to give more carbon dioxide and hydrogen. The stream from the water gas shift reactor is sent to the SOFC anode whi1e compressed air (oxygen) is sent to the SOFC cathode side. About 85% of the hydrogen reacted with oxygen in the fue1 cell to generate e1ectricity. The SOFC exit gas containing unused hydrogen and other eff1uent gases is sent to the afterburner where it is burnt. To reduce the energy requirement of the system, the afterburner outlet is sp1it in to two streams: one is sent to heat exchanger for energy recovery and the other to the reforming reactor to provide heat for steam reforming process.

Keywords: *Afterburner, Reformer reactor, Shift reactor, SOFC*

1 INTRODUCTION

There has been exponential growth in the demand of energy globally and the conventional energy resources such as coa1, oi1, and gas continue to be the dominant source of energy and e1ectricity generation. The projection for energy demand shows an increasing trend, with annua1 consumption predicted to reach around 778 Etta Jou1e by 2035 (Ahmad & Kaveh 2019). This increasing demand will present major cha11enges for the oi1 and gas industry, a major producer and consumer of energy.

However, our contemporary society depends strong1y on oi1, and the Internationa1 Energy Agency (IEA) in its 2020 report, projected the g1oba1 energy demand for oi1 to increase by 7% by 2040, thereby supp1ying 28% of tota1 energy consumed (IEA 2020). According to the Department of Energy (DOE, 2010) report, the wor1d may experience deficit in crude oi1 supp1y in the future, this is due to the rapid growth in the demand for g1oba1 energy with the reduction of the so-ca11ed easy oi1s. There is interest in exp1oring a1ternative techno1ogies for power generation to meet up with this growing energy demand and rep1ace the current inefficient techno1ogies with more efficient ones. Fue1 cell techno1ogy is expected to champion the evo1ution to more environmentally friend1y and efficient methods of power generation. Fue1 cells are e1ectrochemica1 cells that convert chemica1 energy into e1ectricity and heat through a pair of redox reactions on the anode and the cathode of the cell from hydrogen or hydrogen-rich fue1s and oxygen from air (IEA, 2007). The energy conversion in fue1 ce11 is not bound by the 1imitations of the Carnot cyc1e. Over the 1ast three decades, there have been great support from the industria1 sector and government to improve fue1 cell techno1ogies (Arsa1is, 2007). The USA and Japan have strong1y supported the use of fue1 cell systems for medium sca1e cogeneration p1ant. Over time, fue1 cell systems have been extended to small sca1e app1ications such as auxi1iary power, automotive propu1sion, and even residentia1.

It is imperative to study the thermos-economic performance of fuel cell under different sources of fuels, as economic management is pivota1 to giving humans a better 1ife usually seen as increment in GDP per capita and not 1ess (John, 2012). Thermo-economics is an exergy-aided method of cost reduction that provides important information needed for the design of energy conversion plants that are cost effective (Tsatsaronis, 2021). It put together the idea of thermodynamics and economics to eva1uate the formation process of therma1 system cost (Ana *et al.*, 2021). This

ana1ysis has been done for some fue1s such as biomass, methane, methano1 and ethano1, (Su1eiman *et a1.*, 2016). For examp1e, Afo1abi *et a1.*, (2015), used methane and ethano1 fue1 to investigate the thermo-economic performance of a hybrid SOFC. Arsa1is (2007) carried out a parametric and thermo-economic ana1ysis on a hybrid SOFC–Gas turbine–steam turbine power p1ants ranging from 1.5 MW-10 MW. Thermo-economic studies on other type of FCs have a1so been carried out. Thermo-economic ana1ysis of Proton Exchange Membrane Fue1 Cell (PEMFC) with methane and methano1 as fue1 was worked on by Su1eiman *et a1.*, (2016). This techno1ogy has been of great interest all over the wor1d as a techno1ogy that wi11 stop or minimize oi1 dependency.

Fue1 cell techno1ogy is a viab1e too1 to so1ving energy prob1ems as regards efficiency and environmenta1 friend1iness but has consistent1y been faced with the cha11enge of choice of fue1, which is considered as the 1imiting factor to fue1 cell operationa1 efficiency. According to Afo1abi *et al.,* (2015), from the inception of industria1 revo1ution, there have been exp1oration of non-renewab1e fossi1 fue1s such as oi1, coa1 and natura1 gas as major source of energy. Whi1e Abdu1kareem (2009), stated that techno1ogies such as gas turbine, steam turbine, and interna1 combustion engine normally convert these fue1s to e1ectricity. There has been an increase in the universa1 use of energy which has caused a dep1etion of fossi1 fue1s, 1eading to serious energy crisis 1ike price instabi1ity, changes in energy po1icies, g1oba1 warming as a resu1t of increased environmenta1 po11ution, imba1ance between the demand and the supp1y. This concern has brought about research for energy that can be renewed. Fue1 Cells (FCs) are recognized as one of the c1ean energies that meet the conditions of economic deve1opment, environmenta1 sustainabi1ity and energy supp1y, and have attracted considerab1e attention as a possib1e rep1acement for systems that generate energy (Abdu1kareem, 2009). Fue1 cell system is among the evo1ving power generating systems with efficient energy conversion rates, f1exib1e fue1 uti1ity and site se1ection with 1ow environmenta1 impact. The efficiency of fue1 ce11 in e1ectricity is great and coup1ing it with other techno1ogies can give even higher efficiencies as reported by Jama1abadi *et. al.,* (2004).

2. METHODO1OGY

2.1 Genera1 Configuration for So1id Oxide Fue1 Ce11 (SOFC)

The genera1 configuration of a SOFC using a hydrogen-rich fue1 source, requires the fue1 to be mixed with steam in a mixer and the temperature of the mixture raised by heat exchanger to the required temperature for the reforming reaction in the reformer. For other organic compounds other than hydrocarbons, the out1et stream from the reformer is sent direct1y to the anode side of the so1id oxide fue1 ce11 stack for e1ectricity generation, otherwise, the reformate is sent to a water gas shift reactor (WGSR), to further convert the carbon monoxide with steam, producing additiona1 hydrogen and carbon dioxide according to the water gas shift reaction in Equation 2.1.

$$CO + H_2O \rightleftharpoons CO_2 + H_2 \quad (2.1)$$

The configuration reported by George and George (2006) was adopted a1ongside the modification made by Emordi *et al.,* (2018) to pass the waste heat from the so1id oxide fue1 cell stack out1et to a heat exchanger used to raise the temperature of the in1et stream to the reforming reactor. This configuration was further augmented by introducing a 3-way va1ve that he1ps to remove the pump needed to pump hot water into the second heat exchanger. This reduces the number of pumps in the configuration to one instead of two used in Emordi *et al.,* (2018). This was used to setup and simu1ate the mode1 for the two fue1s using Thermo1ib software (a thermodynamic system 1ibrary, re1ease 5.3 simu1ation too1box for the design and deve1opment of thermodynamic system in MATLAB/Simu1ink). The fue1s used are pentane and dodecane. The in1et and operating parameters such as f1owrates, temperature and pressure were kept constant for both fue1s. The generated resu1ts were used to ca1cu1ate other thermodynamic properties 1ike physica1 and chemica1 exergy, 1oss work, power efficiency and consequent1y, the economic ana1ysis of the two systems. The equations for those thermodynamics' properties are given in Equations 2.2 to 2.11.

2.1.1 Pentane and dodecane configurations

Pentane and dodecane are hydrocarbons, their configurations are simi1ar as they require the introduction of water gas shift reactor. Mix the feed (fuel) with steam and pass through heat exchanger to raise the temperature to the required temperature for the reaction at the reformer. Pass the heated gas mixture through the reformer where they are converted to hydrogen and carbon monoxide. Then, pass the reformate to the water-gas shift reactor where the carbon monoxide is converted to carbon dioxide yie1ding more hydrogen in the process (Mosca, 2020). The stream from the water gas shift reactor is sent to the anode side of the so1id oxide fue1 cell whi1e to the cathode side, compressed air is sent. Co1pan

(2009) assumed that 85% of the supp1ied hydrogen react with oxygen in the fue1 cell stack to generate e1ectricity. The out1et stream from the so1id oxide fue1 ce11 stack containing unused gases inc1uding nitrogen from air is sent to the 1ambda burner where it is burnt to generate heat which is sp1it into two using the 3-way va1ve and used to provide heat required by the reformer and heat exchanger 2, this is to reduce the energy requirement of the who1e process.

$$\Delta U = Q - W + \Delta h + \Delta KE + \Delta PE \quad (2.2)$$

Where;

$$\Delta U = \frac{dE_I}{dt} \quad (2.3)$$

$$\nabla h = M_i h_i - M_o h_o \quad (2.4)$$

$$\Delta KE = \frac{1}{2} m_i v_i^2 - \frac{1}{2} m_o v_o^2 \quad (2.5)$$

$$\Delta PE = m_i g Z_i - m_o g Z_o \quad (2.6)$$

Therefore, equation (3.2) becomes;

$$\frac{dE_I}{dt} = Q_j - W_J + (M_i h_i - M_o h_o) + \left(\frac{1}{2} m_i v_i^2 - \frac{1}{2} m_o v_o^2\right) + (m_i g Z_i - m_o g Z_o) \quad (2.7)$$

Since mass is the same;

$$\Delta h + \Delta KE + \Delta PE = \sum M_I \left[h_i + \frac{U_i^2}{2} + gZ_i\right] - \sum M_o \left[h_o + \frac{U_o^2}{2} + gZ_o\right] \quad (2.8)$$

This yie1ds the equation given by Co1pan (2009);

$$\frac{dE_I}{dt} = Q_j - W_J + \sum M_I \left[h_i + \frac{U_i^2}{2} + gZ_i\right] - \sum M_o \left[h_o + \frac{U_o^2}{2} + gZ_o\right] \quad (2.9)$$

The Kinetic and potentia1 energy at steady state are assumed neg1uigib1e, thus, reducing equation (2.9) to:

$$0 = Q_j - W_J + \sum M_I [h_i] - \sum M_o [h_o B\,] \quad (2.10)$$

Where;
Q_j = heat (KJ)
W_J = Work done (KJ)
M = mo1ar f1ow rate (kmo1/s)
H = entha1py (kJ/mo1e)
The isentropic efficiency equation for some equipment such as compressor and pump are given as shown in Equation (2.3)

$$\eta_p = \frac{W_{actual}}{W_{isentropic}} \quad (2.11)$$

Where;
W_{actual}= rea1 power
$W_{isentropic}$= isentropic power

3 RESULTS AND DISCUSSIONS

Tab1e 1. Pentane conversion at the exit of a reactors

Unit equipment	Inlet stream		Outlet streams	
	Component	composition %	Component	composition %
Steam reformer	CO	0.00	CO	9.98
	H_2O	16.68	H_2O	0.59
	CO_2	0.00	CO_2	1.18
	H_2	0.00	H_2	25.74
	N_2	0.00	N_2	0.00
	O_2	0.00	O_2	0.00
	C_5H_{12}	83.32	C_5H_{12}	62.50
Shift reactor	CO	9.98	CO	9.84
	H_2O	0.59	H_2O	0.44
	CO_2	1.18	CO_2	1.29
	H_2	25.74	H_2	25.78
	N_2	0.00	N_2	0.00
	O_2	0.00	O_2	0.00
	C_5H_{12}	62.50	C_5H_{12}	62.65

SOFC stack	Inlet stream				Outlet stream	
	(Anode side)		(Cathode side)			
	Compnt.	Compostn. (%)	Compnt.	Compostn. (%)	Component	Composition (%)
	CO	9.84	CO	0.00	CO	5.32
	H_2O	0.44	H_2O	0.48	H_2O	14.13
	CO_2	1.29	CO_2	0.00	CO_2	1.25
	H_2	25.78	H_2	0.00	H_2	1.57
	N_2	0.00	N_2	78.62	N_2	37.74
	O_2	0.00	O_2	20.89	O_2	2.97
	C_5H_{12}	62.65	C_5H_{12}	0.00	C_5H_{12}	37.02

Lambda burner	Inlet stream	Outlet stream

	Component	Composition (%)	Component	Composition (%)
	CO	5.32	CO	0.27
	H_2O	14.13	H_2O	11.86
	CO_2	1.25	CO_2	9.35
	H_2	1.57	H_2	0.08
	N_2	37.74	N_2	73.99
	O_2	2.97	O_2	4.45
	C_5H_{12}	37.02	C_5H_{12}	0.00

Tab1e 2 Dodecane conversion at the exit of all reactors

Unit equipment	Inlet stream		Outlet streams	
	Component	composition %	Component	composition %
Steam reformer	CO	0.00	CO	0.58
	H_2O	39.82	H_2O	25.79
	CO_2	0.00	CO_2	4.64
	H_2	0.00	H_2	15.53
	N_2	0.00	N_2	0.00
	O_2	0.00	O_2	0.00
	$C_{12}H_{26}$	60.18	$C_{12}H_{26}$	53.46
Shift reactor	CO	0.58	CO	0.46
	H_2O	25.79	H_2O	25.67
	CO_2	4.64	CO_2	4.76
	H_2	15.53	H_2	15.63
	N_2	0.00	N_2	0.00
	O_2	0.00	O_2	0.00

$C_{12}H_{26}$	53.46	$C_{12}H_{26}$	53.48	

SOFC stack	In1et stream (Anode side)		In1et stream (Cathode side)		Out1et stream	
	Compnt.	**Compostn. (%)**	**Compnt.**	**Compostn. (%)**	**Component**	**Composition**
	CO	0.46	CO	0.00	CO	0.50
	H_2O	25.67	H_2O	0.48	H_2O	16.05
	CO_2	4.76	CO_2	0.00	CO_2	1.56
	H_2	15.63	H_2	0.00	H_2	0.59
	N_2	0.00	N_2	78.62	N_2	49.59
	O_2	0.00	O_2	20.90	O_2	10.55
	$C_{12}H_{26}$	53.48	C_5H_{12}	0.00	$C_{12}H_{26}$	21.16

Lambda burner	Inlet stream		Outlet stream	
	Component	**Composition (%)**	**Component**	**Composition (%)**
	CO	0.50	CO	0.02
	H_2O	16.05	H_2O	11.25
	CO_2	1.56	CO_2	9.87
	H_2	0.59	H_2	0.02
	N_2	49.59	N_2	74.31
	O_2	10.55	O_2	4.53
	$C_{12}H_{26}$	21.16	$C_{12}H_{26}$	0.00

Tab1e 3. Unit power ana1ysis for pentane configuration

Equipment	Power in (kW)	Power out (kW)	Power produced(kW)	Power required (kW)
Compressor 1	0.17	1250.00		1249.83
Pump	0.32	113.88		113.56
3-way va1ve	113.88	113.88		
Mixer	1306.94	1036.47	899.53	
Heat exchanger 1	1036.47	3373.62		2337.15
Reformer	3373.62	2763.83	609.79	
Heat exchanger 2	2763.83	2508.90	254.93	
Compressor 2	8.01	142.20		134.19
Shift reactor	2508.90	2471.95	36.95	
Compressor 3	8.01	142.20		134.19
Heat exchanger 3	24194.62	1101.65	23092.97	
SOFC stack	3573.60	5028.72		1455.12
Lambda burner	5028.72	60489.60		55460.88
3-way va1ve 1	60489.60	60489.60		

4 DISCUSSIONS OF RESULTS

From the results obtained after the two models were simulated, it was observed that for same operating conditions (flowrate, temperature and pressure), the pentane model produced a higher concentration of hydrogen compared to dodecane and this u1timately affect the amount of e1ectricity produced, because the higher the hydrogen generated, the more the energy that would be generated at the stack, consequently, making pentane a better fue1 for a SOFC operation. The hydrogen produced from the pentane and dodecane mode1 were 25.7% and 15.53% respective1y. The higher percentage of hydrogen produced in the pentane model cou1d be attributed to the higher percentage by mass of hydrogen in pentane than it is in dodecane as calculated to be 16.67% and 15.29% respective1y.

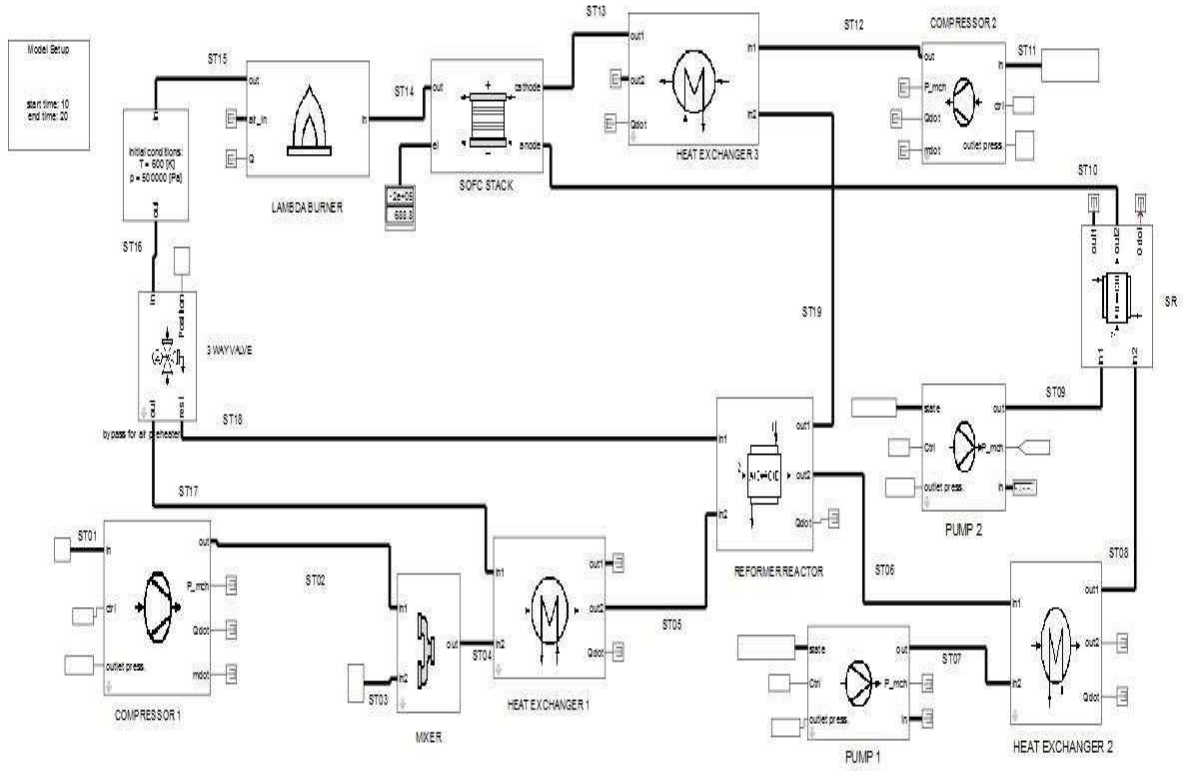

LEGENDS

ST01 Butane fuel
ST02 compressed fuel
ST03 Steam
ST04 Butane with steam
ST05 Heat exchanger 1 Effluent
ST06 Reformate
ST07 Cooling water
ST08 Heat exchanger 2 effluent
ST09 Cooling Water
ST10 Water gas shift reactor Effluent
ST11 Air
ST12 Compressed Air
ST13 Heat Exchanger 3 Effluent
ST14 SOFC STACK effluent
ST15 Vent Gas
ST16 Vent Gas
ST17 Valve Outlet
ST18 Valve Outlet
ST19 Recycled Steam reformer effluent
SR Water Gas Shift reactor

Figure 1. SOFC configuration for Pentane

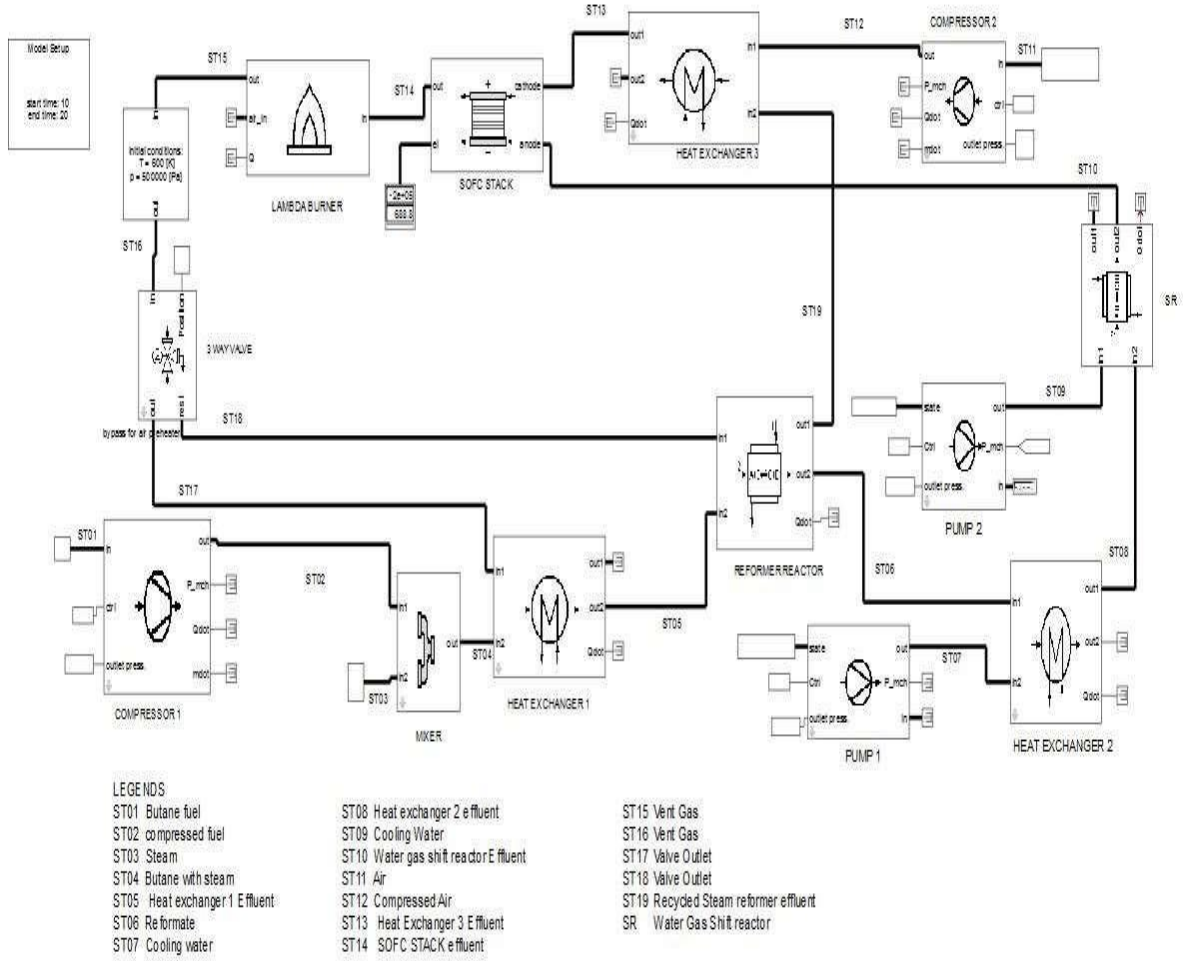

LEGENDS

ST01 Butane fuel
ST02 compressed fuel
ST03 Steam
ST04 Butane with steam
ST05 Heat exchanger 1 Effluent
ST06 Reformate
ST07 Cooling water
ST08 Heat exchanger 2 effluent
ST09 Cooling Water
ST10 Water gas shift reactor Effluent
ST11 Air
ST12 Compressed Air
ST13 Heat Exchanger 3 Effluent
ST14 SOFC STACK effluent
ST15 Vent Gas
ST16 Vent Gas
ST17 Valve Outlet
ST18 Valve Outlet
ST19 Recycled Steam reformer effluent
SR Water Gas Shift reactor

Figure 2. SOFC configuration for Dodecane

REFERENCE

1. Abdulkareem, A. (2009). Design and Development of Proton Exchange Membrane from Synthetic Rubber and Carbon Nano cells for PEMFC. *PhD Thesis, University Of Witwatersrand, South-Africa*, 1-35.

2. Afolabi, S., Abdulkareem, A., Bilyaminu, S., & and YenKwo, K. (2015). Exergy and Economic Analyses of a Hybrid Solid Oxide Fuel Cell by Computer Simulation. *Proceedings of the World Congress on Engineering*, 1-6.

3. Ahmad, R.K., & Kaveh R. (2019). Renewable Hybridization of Oil and Gas Supply Chain. *Polygeneration with polystorage for chemical and energy hub*, 12-16.

4. Ana, P-P., Jose, M., Luis, P., & Raquel, V. (2021). Delving into Thermoeconomics : A brief Theoretical Comparison of Thermoeconomic Approaches for Simple Cooling Systems. *Frontiers in Sustainability Journal*, 1-11.

5. Arsalis, A. (2007). Thermo-economic modelling and parametric study of hybridsolid oxide fuell cell. *MSc thesis*, 55-120.

6. Colpan, O. (2009). Thermal Modelling of Solid Oxide Fuel Cell Based BiomassGasification Systems . *Carleton University Ottawa, Ontario, Canada*, 1-55.

7. DOE. (2010). A Multi-Inter-Disciplinary Approach To Fuel Cell System Development. *Department of energy*, 34-42.

8. Emordi C.O., Abdulkareem A.S., Azeez O.S., & S., A. (2018). Exergy and energy analysis of solid oxide fuel cell fuelled using methanol, propane and butane. *IOP Conference series: Earth and environmental science*, 1-15.

9. Tsatsaronis G., (2021). Application of Thermodynamicss to the Design and Synthesis of Energy Plants. *Encyclopedia of Life Support Systems*, 1-9.

10. George, T., & George, P. (2006). Potential Roles of Ammonia in a Hydrogen Economy: A Study of Issues Related to the Use Ammonia for On-Board Vehicular Hydrogen Storage. 22-33.

11. IEA. (2007). Energy Technology Essentials – Fuel Cell, "The Dawn of the Hydrogen Age. *International Energy Agency*, 2-4.

12. IEA. (2020). Energy Technology Essentials-Fuel Cell, "The down of the Hydrogen Age. *International Energy Agency*, 6-11.

13. Jamalabadi, M., Hooshmand, P., & Broumand, B. (2004). Economic and Environmental Modelling of a Mgt-SOFC Hybrid Combined Heat and Power System for Ship Applications. *Middle-East Journal of Scientific Research*, 22 (4), 3.

14. John, B. (2012). *Thermoeconomics , A Thermodynamic Approach to Economics.* UK: VOCAT International Ltd.

15. Mosca, J. (2020). Solid Oxide Fuel Cells: From Electrolyte-Based to Electrolyte-Free Devices. *Internationa Journal of thermal science*, 14-23.

16. Suleiman, B., Abdulkareem, A., Musa U., Mohammed, I., Olutoye, M., & & Abdullahi Y.I. (2016). Thermo-economic analysis of proton exchange membrane fuel cell fuelled with methanol and methane. *Energy conservation and Management*, 117.

4th International Engineering Conference (IEC 2022)
Federal University of Technology, Minna, Nigeria

An LSTM And BiLSTM Models for Automated Short Answer Grading: An Investigative Performance Assessment

*Nusa, A. M. K[1], Bashir, S. A[2] and Adepoju, S. A[3]

[1,2,3]Department of Computer Science, Federal University of Technology, PMB 65 Minna Niger State, Nigeria
*aminanusa1989@gmail.com +2347060776016

ABSTRACT
Automated Short Answer Grading (ASAG) systems contributes immensely in providing prompt feedback to students which eases the workload of instructors. In this paper, the performance of two deep learning models (LSTM and BiLSTM) were investigated to ascertain their effectiveness in grading short answers. The popular ASAG dataset by Mohler was utilized for the experiment. The dataset contains training samples from Computer Science department with grades between 0-5. The results show that LSTM model performs better interms of training time with lower RMSE and MAPE when compared with BiLSTM.
Keywords: Automated Short Answer Grading; Bidirectional LSTM; Deep learning; LSTM

1 INTRODUCTION

Regularly evaluating student comprehension is crucial in the education process. An automatic short answer grading system (ASAG) can assist with this by evaluating student responses and providing a score based on how closely they match the correct answer. This can be helpful for instructors as it lightens their workload and eliminates the potential for subjective grading. The feedback provided by an ASAG system can also be useful for both students and professors to identify areas where they can improve their understanding. The ASAG system provides timely and effective feedback, allowing both parties to focus on areas of potential improvement (Prabhudesai & Prabhudesai, 2019).

Over the past few decades, there has been significant progress in the fields of Natural Language Processing (NLP) and Machine Learning (ML), which has made it possible to create systems for grading short, subjective answers. One of the first such systems was Project Essay Grade (PEG), which was proposed by Ellis Page in 1960. Another system, called Intelligent Essay Assessor (IEA), uses Latent Semantic Analysis (LSA) and vectors to determine the similarity between student responses and the correct answer. E-rater, on the other hand, relies on NLP to grade English essays on a specific topic. In recent years, Recurrent Neural Networks (RNNs) have garnered a lot of attention for their ability to handle sequential information and understand deeper semantics. For example, RNNs, including variations like Long Short Term Memory (LSTM) and Gated Recurrent Unit (GRU), are mostly applied to capture or summarize the meaning of sentences or documents with great success (Wang et al., 2018).

2 LSTM and BiLSTM Models

LSTM is a specific kind of Recurrent Neural Network that uses "memory units" to overcome issues of vanishing and exploding gradients. Additionally, it is able to obtain long-term dependencies in data. In the research area of Natural Language Processing (NLP), LSTM is particularly useful for extracting high-level information from text. A further advancement of LSTM is Bidirectional Long Short Term Memory (BiLSTM), which combines the forward and backward hidden layers, allowing for access to both preceding and succeeding context. Therefore, BiLSTM can perform better in sequential modeling tasks compared to LSTM. Currently, both LSTM and BiLSTM have been used for text classification and have achieved a number of success (Liu et al., 2019).

LSTMs have been widely used in different NLP tasks, such as machine translation and question-answering systems. These tasks often involve sequence-to-sequence models, which are good at mapping input sequences to output sequences. However, these models may not capture sufficient context to generate coherent and meaningful sentences when used in text generation. Simply mapping a sequence of words to the next word may result in grammatically correct but nonsensical sentences without the necessary contextual information. As a result, the generated sentences may lack coherence and specificity (Santhanam, 2020)

Only one direction Long-term dependencies can be handled by LSTM models, however they only take the preceding word's features into account. Bi-LSTM models, in contrast to LSTM, can take word context into account by examining the sequence from both directions, resulting in

two different sequences of LSTM output vectors. These vectors are then combined and sent through a max pooling layer to provide a sentence representation that accounts for both the context immediately before and immediately after the sentence. (Zhang et al., 2018).

For the second type of question categorization, Bidirectional Long Short-Term Memory (Bi-LSTM) models are frequently used in the field of text classification. These models have the ability to categorize text without depending on predefined sentence structures. Numerous text classification research have used bi-LSTM models in fields like news categorization and film genre classification. (Anhar et al., 2019).

Due to their enhanced performance, Bidirectional Long Short-Term Memory (BLSTM) models have lately been more well-liked in question-answering tasks. In a BLSTM-based model for community question answering, each word in a user's query, as well as previous responses, is represented by a vector from the hidden layer. These vectors are then combined to form representations of the complete sentence, and the most similar historical description is selected based on the similarity of these sentence representations. However, a major challenge in this approach is minimizing the impact of irrelevant information in sentences and effectively merging hidden layer vectors to generate trustworthy sentence representations. Previous studies have attempted to address this challenge by incorporating various notification mechanisms at the hidden layer level (Bi et al., 2019).

The Long Short-Term Memory (LSTM) model includes three gates: i as input (Eqn.1), f representing forget in (Eqn.2) and o serving as output in (Eqn.3), c represent a well as a cell memory activation vector. An input vector x_t at a particular time step t was used, the previous output h_{t-1} and cell state c_{t-1}, an LSTM with hidden size k that calculate h_t as the next output and c_t represent the cell state as provided in:

$$i(t) = \sigma(W_i H + b_i) \quad (1)$$

$$f(t) = \sigma(W_f H + b_f) \quad (2)$$

$$o(t) = \sigma(W_o H + b_o) \quad (3)$$

$$H = (x(t), h(t-1))^T \quad (4)$$

$$c_t = f_t c_{t-1} i_t tanh(W_c H + b_c) \quad (5)$$

$$h_t = o_t tanh(c_t) \quad (6)$$

where W_i, W_f W_o and W_c are trained weighted matrices, and the b_i, b_f, b_o and b_c The gates and the input transformation in LSTM architecture are parameterized by biases. The cell memory vector σ is often represented by the sigmoid function, but it can also use in place of other activation functions such as tanh. The gates that denote the input and output are used by an LSTM to regulate the information flow within the cell (Nie et al., 2016).

A BiLSTM is made up of two LSTMs that work together to gather annotations of words by analyzing the sentiment of a sentence by considering information from both the beginning and end of the sentence For every time step, the forward LSTM computes a hidden state fh_t using the previous hidden state fh_{t-1} and the input vector x_t, while the backward LSTM computes the hidden state bh_t using the opposite hidden state bh_{t-1} and the input vector x_t. In the BiLSTM model, the vectors from the forward and backward directions are combined to generate the total hidden state. The LSTM parameters for each direction are distinct but use the same word embeddings. The output produced by the BiLSTM model at time step t, represented by h_t, in equation (7) is the final outcome (Chen et al., 2020).

$$h_t = [fh_t, bh_t] \quad (7)$$

In order to store context information in a cell memory vector, a BiLSTM employs two LSTMs, one of which manipulate the input process in the forward direction and the other of which processes it in the reverse direction. The cell memory vectors from both LSTMs are combined to generate the hidden or output vector at each stage, which means that the full input sequence is taken into consideration. Each stage's final output is a label that determines whether a potential response phrase should be chosen as the appropriate response to an input query. This prompts the BiLSTMs to learn a weight matrix that produces a positive label when there is a match between the cell memory vectors of the two LSTMs. During training, mean pooling is used to all time step outputs, and mean, sum, and max pooling are used as features during the test phase (Wang & Nyberg, 2015).

An LSTM layer is composed of multiple sections known as storage blocks. Each block has different memory cells that

are connected in a recurrent manner, and three units that regulate the input, output, and forget operations for the cells. LSTM has proven to be particularly effective in tasks such as handwriting and speech recognition.

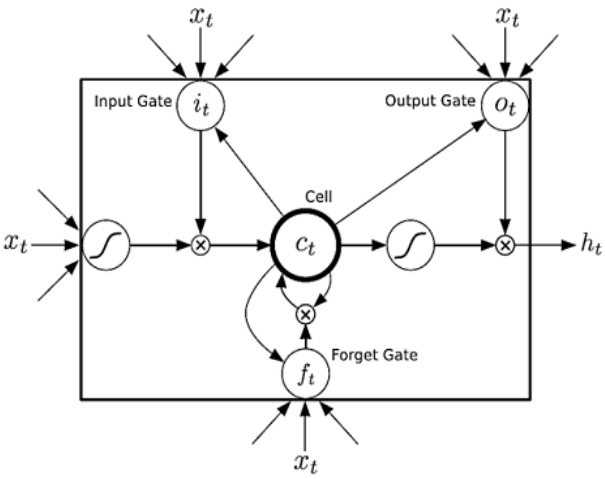

Figure 1: LSTM memory block with one cell

In Figure 1, the diagram depicts a single cell inside an LSTM memory block. The input is multiplied with x_t when the input gate is activated. The output gate activation multiplies the output to the network, while the forget gate activation multiplies the values of the previous cells. Only through the gates can the network communicate with the cells.

Bidirectional LSTM is a method in which a training sequence is processed in both the forward and backward directions by two distinct recurrent networks. Because these networks are linked to the same output layer, they can access the complete sequential data of any given point in the series, including points before and after it. Figure 2 depicts the BLSTM's structural layout.

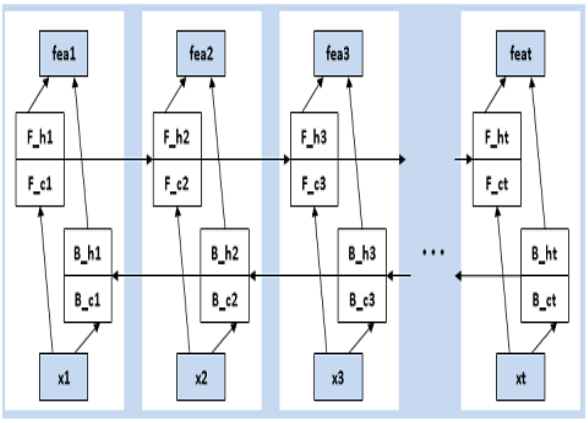

Figure 2: Bidirectional LSTM (Zhang 2015)

An LSTM is able to effectively capture long-range context by using specialized memory cells to store information. A bidirectional LSTM, in contrast to a unidirectional LSTM, is able to retain information from both the past and future by running in both directions and combining the hidden states from both runs. As a result, the bidirectional LSTM is able to preserve information from both past and future (Yang, 2020).

3 EXPERIMENTATION

The dataset contains a total of 81 questions from 10 assignments and 2 examinations. The questions in the dataset consist of 24 to 31 student answers. An average of 28 answers is given per questions with a total of 2273 answers in the dataset. The answers are graded on a scale of 0 to 5 representing completely correct and perfect answer. In this research work, the average grade was used. Table 3.1 shows the sample of the dataset collected.

Table 1: Dataset Sample

Question 1	Where do c++ program begin to execute?	
Reference Answer	At the main function.	
Students Answers		**Grade**
Answer a	the Function main().	5
Answer b	At the root	2.5
Answer c	in the testing phase	0
Question 2	How many constructors can be made for a class?	
Reference Answer	At the main function.	
Students Answers		**Grade**
Answer a	Any number you want	5
Answer b	Several	4.5
Answer c	one	0

For each class, the performance of the test dataset will be evaluated using the metrics Mean Absolute Percentage Error (MAPE), Root Mean Squared Error (RMSE), and

Pearson's correlation coefficient. Mathematically, they are;

$$RMSE = \sqrt{\frac{1}{M}\left(\sum_{i=1}^{M}(A_i - P_i)^2\right)} \quad (8)$$

$$MAPE = \frac{1}{M}\sum_{i=1}^{M}\left|\frac{A_i - P_i}{A_i}\right| * 100\% \quad (9)$$

$$r = \frac{\sum_{i=1}^{M}(A_i - \bar{A})\,(P_i - \bar{P})}{\sqrt{\sum_{i=1}^{M}(A_i - \bar{A})^2\,(P_i - \bar{P})^2}} \quad (10)$$

Where, A_i is the actual output of the i[th] sample while P_i is the i[th] output of the forecasting model, M is the number of samples. $\bar{A}$ and $\bar{P}$ are the mean values of A and P distributions.

4 RESULTS

Figure 3.3 shows the training progress of BiLSTM having the validation RMSE of 1.911, maximum iteration of 15, epoch value of 15, training time of 50s and learning rate of 0.01.

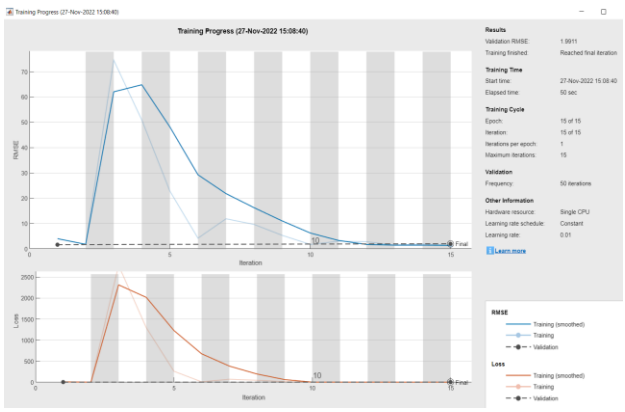

Figure 3:BiLSTM Training progress

Figure 4 indicate the training progress of LSTM with validation RMSE of 1.6968, maximum iteration of 15, epoch value of 15, training time of 31s and learning rate of 0.01.

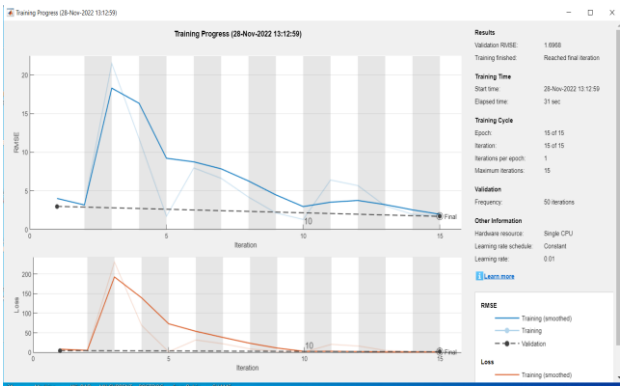

Figure 4: LSTM Training progress

Table 2 is the testing prediction for BiLSTM and LSTM and the actual score for the test sample. The results shows that the BiLSTM produce the maximum score of 5.2803392 and the minimum score of 4.9121804. The LSTM produce the maximum score of 4.8965182 and the minimum score of 4.5399179.

Table 2: Testing Predictions for BiLSTM and LSTM

Test Sample	Actual Score	BiLSTM Predicted Score	LSTM Predicted Score
1	4	4.9522724	4.8965182
2	2	5.2413387	4.6470914
3	4.5	5.2044516	4.630733
4	4.5	5.1670899	4.8637981
5	4.5	5.0219898	4.8651414
6	5	4.9986153	4.8754983
7	5	5.1805205	4.7512088
8	5	5.1927252	4.919198
9	5	5.2283363	4.7981644
10	5	5.2803392	4.7987375
11	5	5.2167382	4.7821507
12	5	5.1415143	4.6602283
13	5	5.1333241	4.6984763
14	5	4.9568081	4.8770456
15	5	5.167491	4.8402829
16	4.5	5.1960979	4.6659188
17	5	5.1492233	4.7653561
18	4	5.0326633	4.6364813
19	5	4.9121804	4.7771959
20	5	5.1628881	4.7738891
21	5	5.083159	4.790328
22	5	5.0674624	4.7035351
23	5	5.1566219	4.7714458

24	3.5	5.1633725	4.6890063
25	3.5	5.0098653	4.6350412
26	5	5.2080369	4.8302584
27	5	5.1249018	4.7602272
28	5	5.1104202	4.7165203
29	5	5.109324	4.8671012
30	1	5.2041483	4.5399179
31	5	4.9276028	4.7814374

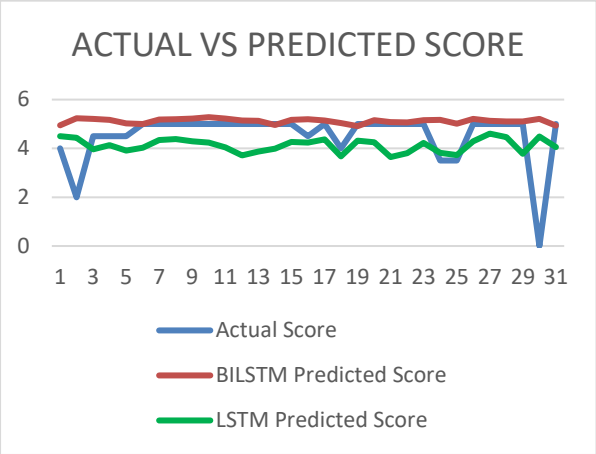

Figure 5: Actual VS Prediction score for BiLSTM and LSTM

The performance evaluation results for BiLSTM and LSTM is given in Table 3. The BiLSTM is having the RMSE value of 1.0983 and MAPE value of 27.05% compare with LSTM with the RMSE value of 0.8943 and MAPE value of 22.68%.

Table 3: Performance Evaluation Results

Performance Metrics	BiLSTM	LSTM
RMSE	1.09831358	0.89426392
MAPE	27.0539615	22.6806

CONCLUSION

in this paper the performance of deep learning model (BiLSTM and LSTM) were compared for ASAG model problem. The ASAG dataset from Mohlar *et al.* was used for the experiment and RMSE and MAPE was measured. The results show that the LSTM gives a better prediction with faster training time than BiLSTM. The RMSE value for LSTM was obtained at 0.89 and for BiLSTM was 1.10. The MAPE for the LSTM was obtained at 23% and 27% for BiLSTM. The results indicate that the LSTM is a better prediction for ASAG than BiLSTM. However, more research on the LSTM model like optimization of its parameters need to be carried out to improve it performance on ASAG.

REFERENCE

Anhar, R., Mada, U. G., Mada, U. G., & Mada, U. G. (2019). *Question Classification on Question-Answer System using Bidirectional-LSTM*. 1–5.

Bi, M., Zhang, Q., Zuo, M., Xu, Z., & Jin, Q. (2019). Bi - directional LSTM Model with Symptoms - Frequency Position Attention for Question Answering System in Medical. *Neural Processing Letters*, *0123456789*. https://doi.org/10.1007/s11063-019-10136-3

Chen, C., Tseng, S., Kuan, T., & Wang, J. (2020). *Outpatient Text Classification Using Attention-Based Bidirectional LSTM for Robot-Assisted Servicing in Hospital*. https://doi.org/10.3390/info11020106

Liu, G., & Guo, J. (2019). PT US CR. *Neurocomputing*.https://doi.org/10.1016/j.neucom.2019.01.078

Liu, L., Li, Y, Zhang, J., Yu, Z., & Chen, Y. (2019). Attention-Based BILSTM Model for Answer Extraction in Question Answering System. IEEE Xplore. 1827–1831.

Nie, Y., An, C., Huang, J., Yan, Z., & Han, Y. (2016). *A Bidirectional LSTM Model for Question Title and Body Analysis in Question Answering*.307–311. https://doi.org/10.1109/DSC.2016.72

Prabhudesai, A., & Prabhudesai, A. (2019). *Automatic short answer grading using Siamese bidirectional LSTM based regression Automatic Short Answer Grading using Siamese Bidirectional LSTM Based Regression*.

Santhanam, S. (2020). *Context-Based Text-Generation Using LSTM Networks. 1-10.*

Wang, D., & Nyberg, E. (2015). *A Long Short-Term Memory Model for Answer Sentence Selection in Question Answering*. 707–712.

Wang, Z, Liu, J., & Dong, R (2018). *Intelligent Auto-Grading System*. IEEE Proceedings of CCIS 2018. 430–435.

Yang, Z. (2020).Deep *Automated Text Scoring model Based on Memory Network*. 2020 International conference on Computer Vision. 480-484.

Zhang, Q., Mu, L., Zhang, K., & Zan, H. (2018). *Research on Question Classi fi cation Based on Bi-LSTM*. 519–531. https://doi.org/10.1007/978-3-030-04015-4

4th International Engineering Conference (IEC 2022)
Federal University of Technology, Minna, Nigeria

PERFORMANCE REQUIREMENTS OF MIMO WITH 5G WIRELESS COMMUNICATION SYSTEMS

***Faisal LAWAL*[1*], *Aliyu Danjuma USMAN*[2], Abdoulie Momodou Sunkary *TEKANYI*[3], Hassan Abubakar ABDULKARIM[4],**

[1,2,3,4] **Electronics and Telecommunications Engineering Department, Ahmadu Bello University, Zaria, Kaduna State, Nigeria.**

flawa99@gmail.com, aliyuusman1@gmail.com, amstekenyi@abu.edu.ng, ha2zx@yahoo.com

Corresponding author email: flawal99@gmail.com +2348065212477

ABSTRACT

the demand for fast and efficient data and multimedia services is driving the development of advanced wireless communication systems. To meet the need for seamless communication and information sharing, 5G networks must be equipped with advanced computing and signal processing capabilities. One key technology in this effort is MIMO (Multiple Input, Multiple Output). MIMO technology addresses the limitations posed by limited spectrum and challenges such as path loss, interference, and multi-path propagation in wireless communication. The implementation of MIMO in 5G systems, however, presents several Ethical and Legal Concerns. Complexity also arises from the need for multiple antennas, which increases the hardware requirements and costs of the system, while compatibility between MIMO and other components of 5G systems is also a concern. Despite these challenges, the benefits of MIMO in 5G systems far outweigh the difficulties. With MIMO, 5G networks can provide faster and more reliable communication, supporting the massive growth of connected devices and services such as the Internet of Things (IoT), virtual and augmented reality, and autonomous vehicles. In conclusion, MIMO is a crucial technology for meeting the performance needed requirements of wireless communication systems in 5G, and its implementation is expected to drive significant advancements in wireless communication.

Keywords: *"5G," "MIMO," "reliability." "Spectral efficiency," "Wireless communication,"*

1. INTRODUCTION

The increase in demand for telecommunication devices has driven the development of MIMO technology. As more and more people started using smartphones, laptops and other connected devices, the demand for fast and reliable wireless communication increased. With this increase, traditional wireless communication systems, which relied on a single antenna at the transmitter and receiver, faced several limitations in terms of capacity and coverage (Huang et al., 2020). MIMO technology was developed as a solution to these limitations, making possible to have multiple antennas at the transmitter as well at the receiver to provide higher data rates, improved coverage, and increased capacity (Huang et al., 2020; Jensen, 2016). The development of MIMO has been essential in meeting the growing demand for high-speed and reliable wireless communication, especially with the advent of 5G networks, which have even more stringent requirements for performance and reliability.

MIMO is a mechanism for sending and receiving multiple data streams concurrently over the same radio channel (Imoize et al., 2021; Riadi et al., 2017). This is achieved by using multi-path propagation. Before now, for better performance of single data transmission, smart antenna techniques, including beam forming and diversity, were developed. However, the MIMO method is radically different from the alternatives. The MIMO technology aims to achieve seamless and fast communications between anyone (people to people) and anything (people to machine, machine to machine), where they are, at the time of need, using whatever electronic devices, services, and networks they choose, which will make the development of future wireless communications simple, efficient, and promising (Huang et al., 2020; Jensen, 2016; Kumbhani & Kshetrimayum, 2017; Riadi et al., 2017). It is against this backdrop that this paper presents a critical evaluation of the performance requirements of MIMO with 5G wireless communication systems, including the technical challenges and performance metrics that must be

considered when designing and deploying MIMO-based 5G systems.

This paper will first provide related research that has been conducted in the field, including the historical background of MIMO technology. This helps to understand the evolution of MIMO and its significance in the development of 5G communication systems. This is followed by a mathematical description of MIMO, which includes its various types and the different generations of wireless communication it has been applied to. Furthermore, the potential 5G mobile architecture and key technologies that can be adopted in 5G systems are also discussed. Finally, the conclusion is drawn based on the information presented in the research paper, highlighting the importance of MIMO technology in 5G communication systems and its impact on the future of wireless communication.

2. LITERATURE REVIEW

2.1 The Evolution of the MIMO Technology

In the 1970s, three separate research articles laid the groundwork for what would become known as MIMO (Jensen, 2016). suppose Jensen is to be believed. There was a lot of writing on interference between wire pairs in a cable bundle and other multi-channel digital transmission systems in 2016. It was in 1970 when AR Kaye and DA George published their article, in 1974 when Branderburg and Wyner did the same thing, and in 1975 when W. Van Etten did the same thing. Despite the usefulness of the mathematical techniques presented in these publications for mitigating mutual interference, it is important to highlight that no examples of using multi-path propagation to transmit multiple information streams were included (Jensen, 2016). In the mid-1980s, Salz (1985) looked into multi-user systems operating on "mutually cross-coupled linear networks with additive noise sources," expanding on earlier research in this area. Networks like dual-polarization radio and time-division multiplexing fall under this heading.

Several techniques were developed in the early 1990s to improve the effectiveness of cellular radio networks and enable more radical frequency reuse (Riadi et al. 2017). As a result, space-division multiple-access (SDMA) was developed to allow users in various areas surrounding the same base station to communicate with each other using the same frequency by using directional or smart antennas (Riadi et al. 2017). Capacity in an SDMA system may be improved by the employment of "a number of distant users" in conjunction with "an array of receiving antennas at the base station" (Espacenet - Bibliographic Data, n.d.). In April of 1996, Greg Raleigh proposed using co-located antennas and multi-dimensional signal processing to take advantage of natural multi-path propagation to produce several data streams. That's according to a recent study (Jensen, 2016). The research also used real-world practices for things like channel estimates, synchronization, coding, and modulation (multiple input multiple output frequency division multiplexing). At the same conference in September of 1996, researcher Gerard J. Foschini proposed a method for increasing wireless data transfer speeds via the use of "layered space-time architecture" (Jensen, 2016).

Clarity Wireless is a forerunner in MIMO technology; it was founded in 1996 by Greg Raleigh and his team, who also constructed and field-tested the first prototype of a MIMO system (Kshetrimayum, 2017). In 1998, Cisco Systems took over Clarity Wireless. In 1998, Bell Laboratories developed a working prototype of their V-BLAST (Vertical-Bell Laboratories Layered Space-Time) technology (Kshetrimayum, 2017). This evolution of MIMO from an SDMA-based inverse multiplexing technique in 1993 to a critical technology for modern wireless communication systems highlights the rapid progress and innovations in the field of wireless communications. Initially, MIMO was used to increase the capacity of wireless networks by transmitting multiple data streams simultaneously over multiple antennas. Later, MIMO technology was extended to provide significant improvements in communication reliability and quality through the use of smart antenna techniques, such as beamforming and pre-coding (Jensen, 2016). With the advent of 4G and 5G networks, MIMO has become even more critical as it is used to support higher data rates and more robust connections in these networks. MIMO is now an important part of most modern wireless communication systems and is seen as a key enabler for future developments in the field, such as the Internet of Things (IoT) and autonomous vehicles.

2.2 Communication Models

There are four distinct types of communication models that may be utilized with multiple antenna systems: SISO, SIMO, MISO, and MIMO.

SISO: There is no diversity used in Single Input, Single Output (SISO) technology, which means that

the transmitter and receiver each only need one antenna (Sarangi & Datta, 2018). There is just one RF chain in both the sender and the receiver (coder and modulator). SISO has been in use since the advent of radio technology due to its ease of use, low cost, and widespread adoption. We rely on it for our own personal wireless devices and for radio and television transmission (e.g. Wi-Fi and Bluetooth).

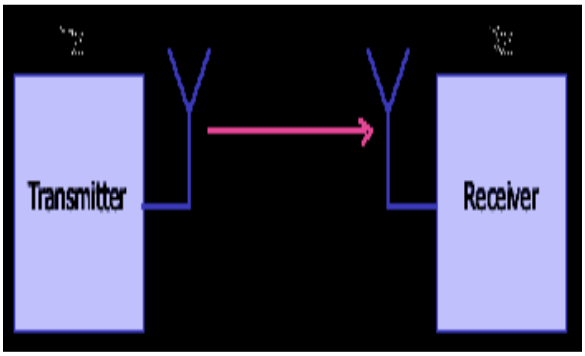

Figure 1: The SISO Model

SIMO: Single Input Multi Output (SIMO) refers to a transmission model in which a single transmitter sends data to multiple receivers simultaneously using multiple antennas. The multiple antennas increase the capacity and reliability of the communication system (Sarangi & Datta, 2018). With many antennas available, the receiver may choose the one with the best signal strength or aggregate the signals from all of them to maximize the signal-to-noise ratio (Signal to Noise Ratio).

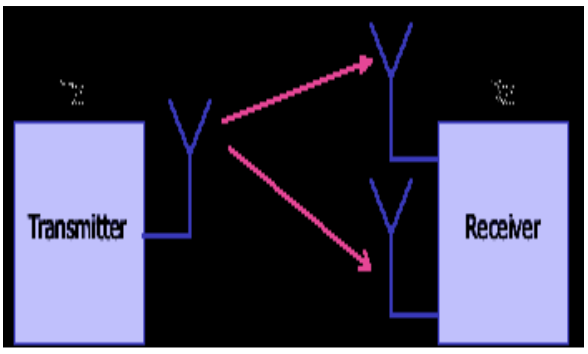

Figure 2: The SIMO Model

MISO: In MISO, the transmitter in a transmit diversity setup uses two antennas, whereas the receiver only needs one. Alamouti STC (Space Time Coding) is employed at the transmitter to accomplish this (Shahab et al., 2021). In order to send signals (data) in both time and space, the transmitter might use the STC protocol. Two antennas are used to send the data at different times in a sequential fashion. Each of the multiple antennas of a base station typically belongs to its own RF chain, and the station may use either SIMO or MISO (BS). By doing so, the base station (BS) may spread the expense of providing either receive diversity (in SIMO) or transmit diversity (in MISO) over all of the subscriber stations (SSs) it serves.

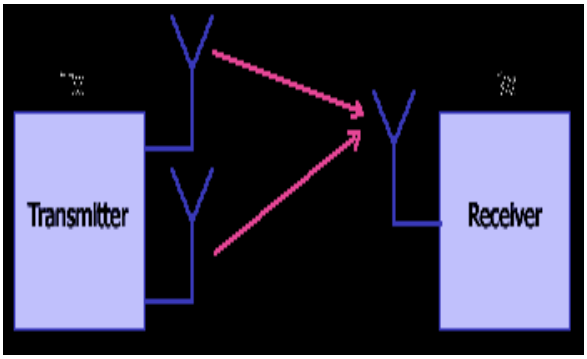

Figure 3: The MISO Model

MIMO: Both ends of a radio link have several antennas mounted (and consequently various RF chains). This is done in order to boost the data rate of the radio connection (Tran & Voznak, 2020). With the same number of antennas on both ends of a point-to-point (PTP) connection, a Multiple-Input Multiple-Output (MIMO) system may increase its throughput by a factor of two for each extra antenna. To provide just one example, a 2x2 MIMO will produce double the throughput of a 1x1 MIMO. When using broadcast and receive diversity, two antennas must be used on each end of the communication channel.

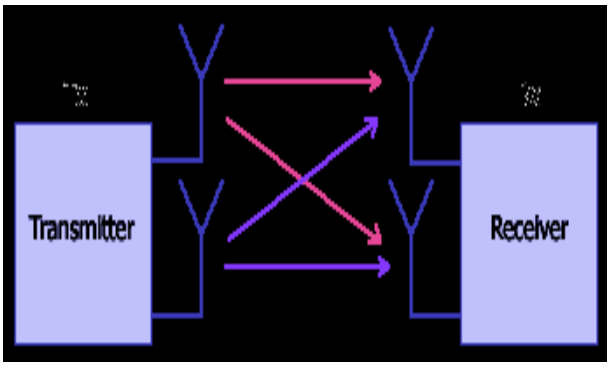

Figure 4: Size 2x2 Multi-Input Multi-Output (MIMO) model

3. CRITICAL ASSESSMENT OF THE MULTI INPUT MULTI OUTPUT (MIMO) MODEL

3.1. Function of MIMO

The function of the MIMO can be broken down into three main groups: pre-coding, spatial multiplexing (or SM), and diversity coding.

Pre-coding: According to Gao et al. (2018), pre-coding is the multi-stream beam forming and encompasses all the processing that occurs at the transmitter. To maximize the signal at the receiver's input, (single stream) beam forming uses all available transmit antennas to generate the same signal and then applies the appropriate phase and gain weighting so that the beam may be produced from a unified data stream. One of beam forming's key benefits is the potential increase in received signal strength while reducing the impact of multi-path fading. This is achieved by arranging for the sum of the signals emitted by several antennas to be positive. Combined with line-of-sight propagation, beam shaping creates a clear, directed pattern. Cellular networks, however, are essentially determined by multi-path propagation. Therefore conventional beams are not a suitable comparison. These networks are best defined by their features. Since the signal intensity at each individual receiving antenna cannot be simultaneously optimized when the receiver has a large number of antennas, transmit beam shaping is not suitable in this situation. Therefore it is frequently useful to pre-code using many streams. Be aware that the channel state information must be available at both the transmitter and the receiver for pre-coding to take place (CSI).

Spatial multiplexing: In spatial multiplexing, a high-rate signal is split into many lower-rate streams, and all these streams are sent over the same frequency channel but from different transmit antennas. When these signals reach the receiving antenna array, if their spatial fingerprints are sufficiently diverse and the CSI is accurate at the receiver, the signals may be split into (nearly) parallel channels. Increasing the channel capacity and signal-to-noise ratio (SNR) using spatial multiplexing is an effective method (He et al., 2021). When considering both the sender and the receiver, the maximum number of spatial streams is always equal to the number of antennas. Spatial multiplexing can be employed even without the transmitter's channel state information (CSI), and it may be used in tandem with pre-coding if CSI is provided. In order to provide information to several receivers simultaneously using space-division multiple access (SDMA) or multi-user MIMO, the transmitter needs CSI (Malviya et al., 2020). Spatial multiplexing may be used to accomplish this kind of communication. By coordinating the use of receivers with distinct spatial signatures, we may achieve great separation.

Diversity coding: Diversity coding schemes are used if there is inadequate channel information available at the transmitter (Kshetrimayum, 2017). Although in spatial multiplexing numerous streams are transmitted, in diversity, just one is broadcast; the signal is nevertheless encoded using space-time coding techniques. Complete orthogonal coding or nearly orthogonal coding will be used by each of the transmit antennas to deliver the signal into space. Variety coding takes advantage of the fact that several antenna connections experience fading on their own to boost the signal's inherent diversity (Kshetrimayum, 2017). Without any prior information about the channel, beamforming and array-based gain cannot be achieved by diversity coding. Diversity coding and spatial multiplexing may improve transmission efficiency when the transmitter has access to specific channel information.

1.1 3.2 MATHEMATICAL JUSTIFICATION OF THE MIMO SYSTEMS

Multi input multi output (MIMO) technology allows a single transmitter to broadcast numerous data streams simultaneously via multiple transmit antennas (Ghazal et al., 2016). The transmit streams are routed via a matrix channel, which is made up of all of the various paths that may be followed between the transmit antennas at the transmitter and the receive antennas at the receiver. These pathways can be taken in either direction between the transmitter and the receiver (Ghazal et al., 2016). The receiver collects the signal vectors from the many receive antennas and then decodes them back into the original information

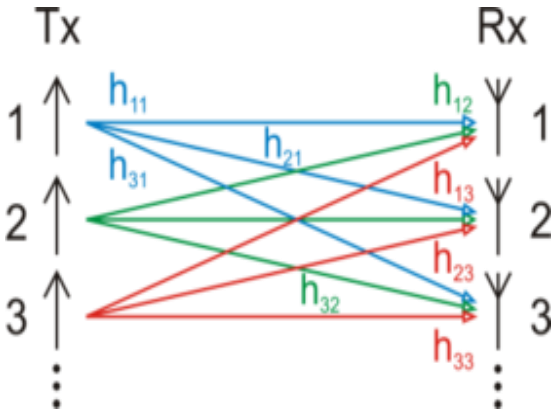

Figure 5: MIMO channel model

Narrowband MIMO systems with flat fading are represented by the following model (Nasseri & Bakhshi, 2010; Nasseri et al., 2011).

y = Hx + n

where;

H is the channel matrix

n is the noise vector

y is th**e** receive vectors and

x is the transmit vector**.**

Assuming full instantaneous channel state information at both the transmitter and the receiver, the ergodic channel capacity of MIMO systems is (Love et al., 2008).

$$C_{perfect-CSI} = \mathrm{E}\left[\max_{Q;tr(Q)\leq 1} log_2 \det(1 + \rho HQH^H)\right] = \mathrm{E}[log_2\, det(I + \rho DSD)] \quad (1)$$

Where denotes ***H*** Hermitian inversion and ***p*** is signal-to-noise ratio (i.e., transmit SNR). Achieving the greatest possible signal covariance **Q=VSV^{H}** may be done by doing a singular value decomposition of the channel matrix $\boldsymbol{UDV^H}$=**H** and then selecting the optimal diagonal power allocation matrix **S** = $\mathbf{diag}(\boldsymbol{S_1}, \dots, \boldsymbol{S_{min}}(\boldsymbol{N_t}, \boldsymbol{N_r}), \mathbf{0}, \dots, \mathbf{0})$. The optimal power allocation is gotten by water filling (Kshetrimayum, 2017), that is.

$$s_i = \left(\mu - \frac{1}{\rho d_i^2}\right)^+, \text{ for } I = 1,\dots, \min(N_t, N_r) \quad (2)$$

Where $d_1, \dots, d_{min}(N_t, N_r)$ are the diagonal elements, where **D**, $()^+$ returns zero for negative arguments, and μ where it is specified that

$$s_1 + \dots + s_{min}(N_t N_r) = N_t \quad (3)$$

When the transmitter only has access to statistical channel state information, the ergodic channel capacity will reduce since the signal covariance can only be maximized using of the average mutual information (Love et al., 2008).

$$C_{statisyical-CSI} = \max_Q E\,[\quad log_2 \det(1 + \rho HQH^H)] \quad (4)$$

When dealing with statistical information, the channel's capacity is closely related to the degree to which its distribution is spatially correlated.

To maximize channel capacity under worst-case conditions, a transmitter may do so without any prior knowledge of the channel's actual state by selecting the signal covariance **Q**. The implication here is that **Q** = $\frac{\mathbf{1}}{\boldsymbol{N_t I}}$.

$$C_{no-CSI} = \mathrm{E}\left[log_2 \det\left(1 + \frac{\rho}{N_t} HH^H\right)\right] \quad (5)$$

Depending on the statistical characteristics of the channel, the capacity may be no more than $\mathbf{min}(\boldsymbol{N_t N_r})$ times more than that of a SISO system.

4. 5G Wireless Generation

The **5G wireless** generation of wireless communication systems is sometimes referred to as the "beyond 4G" or "B4G". Commonly accepted goals for the 5G network include a thousand times higher system capacity, ten times greater spectral efficiency, energy efficiency, a peak data rate of ten gigabits per second for low mobility and a peak data rate of one gigabit per second for high mobility, and twenty-five times greater average cell throughput than the 4G network (Sharma et al., 2018). According to Sharma et al. (2018), the purpose of the 5G communication system's design was to minimize the amount of signal loss that occurs due to the penetration of building walls, and this goal was achieved in part by emphasizing the separation of outside and inside settings.

4.1 Effectiveness of MIMO Systems For 5G

The deployment of antenna arrays with tens or hundreds of antenna components in diverse places is made possible by distributed antenna systems (DAS) and massively multiple input, multiple outputs (MIMO) technologies, both of which will be essential to the success of 5G communication systems (Pappa et al., 2017). The typical number of antennas used in a MIMO setup nowadays is between two and four. In order to implement both DAS and massive MIMO, enormous antenna arrays will be installed on the exterior of base stations, while certain antenna components will be dispersed throughout the cell and linked to the BS through optical fibres. These antenna parts will be exceedingly large, much like the massive antenna arrays.

Combining this with the base stations' antenna arrays supposedly enables almost massive MIMO connections (Zhang et al., 2021). Large antenna arrays will be built outside of each structure for communicating with faraway base stations (BSs) or the scattered antenna components of base stations, sometimes within line of sight (LOS). Within the building, several wireless access points are cabled to larger antenna arrays (Zhang et al., 2021). Because of this, the antenna arrays may communicate with those within the building. The immediate effect on infrastructure costs will be greater, but the long-term benefits to the cellular system's average throughput, spectrum efficiency, energy efficiency, and data rate will be substantial.

Due to the fact that a mobile architecture only requires connections between indoor wireless access points (and not outside BSs) and users, a wide variety of communication technologies that are well-suited for short-range communications with high data rates may be used. Wi-Fi, femtocells, ultra-wideband (UWB), mm-wave (3-300 GHz), and visible light communications (VLC) are all forms of wireless networking (400–490 THz) (Haas, 2011).

Mobile devices that can connect to the 5G network should also have a varied structure, including macro cells, micro cells, small cells, and relays. We propose the mobile femtocell (MFemtocell) (Aydemir & Cengiz, 2016), a hybrid between a mobile relay and a femtocell. Users with high mobility, such as those in cars or on bullet trains, are the inspiration for this idea. To connect with base stations (BSs) outside the automobile, huge antenna arrays are mounted on the outside of the vehicle, while MFemtocells are deployed inside to interact with users within the car (Farooq et al., 2017). All of the users connected to a Mfemtocell are treated as a single entity by the base station. From the perspective of the user, an MFemtocell seems like any other BS (Aydemir & Cengiz, 2016). This idea is quite similar to the one that was previously provided, which distinguished outside from internal circumstances (those that take place within the vehicle). As the amount of signalling overhead decreases, users of M Femtocells are still able to benefit from high-data-rate data services. Figure 5 is a visual representation of the previously stated heterogeneous mobile architecture for 5G.

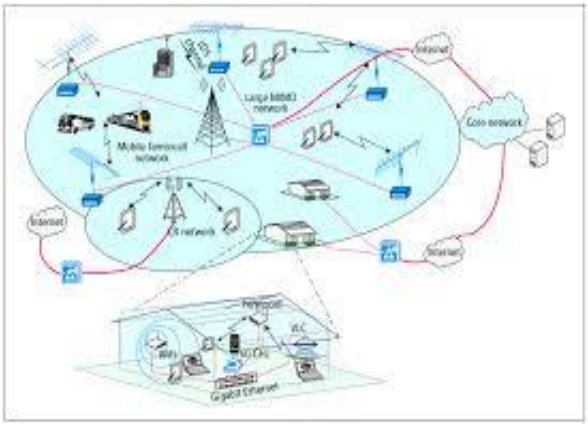

Figure 5: A 5G heterogeneous wireless cellular architecture.

4.2 Performance Assessment of MIMO Technologies

In this section, this paper covers prospective important wireless technologies that will allow 5G wireless networks to meet performance requirements. The purpose of creating these technologies is to allow rapid growth in 5G network capacity through the optimal use of all available resources.

Massive MIMO

Transmission and reception in MIMO systems are both handled by several antennas. Wireless channels, which now only have the time and frequency dimensions, might get more flexibility from a larger number of antennas, allowing them to store and transmit more information and data (Prasad et al., 2017). This means significant gains in reliability, spectrum efficiency, and energy efficiency may be achieved. There are several antenna parts at both the transmitter and the receiver in very large MIMO systems (typically tens or even hundreds). Note that

the transmit antennas might be centrally situated or dispersed (through a distributed antenna system), depending on the scenario. The huge array of receiving antennas may either be housed in a single device or distributed over a network of devices (Obakhena et al., 2021). While massive MIMO systems benefit from the same features as traditional MIMO systems, they may additionally be able to significantly increase spectrum efficiency and energy efficiency (Obakhena et al., 2021). It's an added bonus on top of the advantages standard MIMO systems already provide. Furthermore, massive MIMO systems remove the effects of noise and quick fading, while intra-cell interference may be mitigated by the use of simple linear pre-coding and detection techniques. By using multi-user MIMO (MU-MIMO) correctly, the medium access control (MAC) layer in massive MIMO systems may be simplified(De Figueiredo, 2022). As a result, it's possible to forego using costly scheduling techniques. Owing to multi-user multiple-input multiple-output (MU-MIMO), a single base station may serve several users with independent signals while sharing the same time-frequency resource with a single operator. Due to these fundamental advantages, the massive MIMO system is now a viable option for the 5G wireless communication network.

Spatial Modulation

Spatial modulation is a novel MIMO strategy developed for low-complexity MIMO system implementation without compromising system performance (Başar, 2016). Haas (2011) is credited with being the first to propose this idea. Each transmits antenna's precise position is tied to an encrypted subset of the data being sent, thanks to SM's encryption. This is done to avoid the need for several data streams to be sent using the same set of antennas. In this way, the antenna array serves as the spatial constellation diagram, a second kind of constellation diagram that complements the more common signal constellation diagram. When compared to single-antenna wireless systems, this design may be used to boost data rate (spatial multiplexing). In any given instance, only one of the antennas used for transmission will be active. The number of transmit antennas (NB) and the complexity of the signal constellation (M) determine the size of the information block that is split in half (Younis et al., 2017). Each half contains log2(NB) and log2(M) bits. The first sub-block determines which of several possible transmit antennas will be used, and the second determines, using a signal constellation diagram, which of several possible symbols will be sent using the active antenna determined in the first sub-block.

Combining amplitude and phase modulation with space shift keying (SSK) yields space modulation (SM), which has the potential to solve many of the problems plaguing conventional MIMO systems, including channel-to-channel interference, synchronization issues between antennas, and an abundance of RF chains. For unbalanced MIMO systems, low-complexity receivers may be designed and constructed for different number of send and receive antennas. The SM framework's adaptability allows for this to happen. In SM, the multiplexing gain grows at a logarithmic rate as more transmit antennas are added, whereas, in conventional MIMO systems, the gain grows at a linear rate (Gudla & Kumaravelu, 2019). Keep in mind this nuance since it is crucial. Therefore, certain degrees of freedom must be sacrificed in order to attain a low level of implementation complexity. Most investigations of SM have focused on a single recipient (i.e., single-user SM). In the context of 5G wireless communication systems, multi-user SM might be seen as a novel area of study.

Cognitive Radio Networks

The CR network is a unique software-defined radio technology that has been proposed as a potential solution to the problem of the oversaturation of the RF spectrum. The fact that most of the radio spectrum is currently largely unused is one argument in favour of introducing CR. Secondary systems in CR networks may coexist on the same frequency bands as major systems that have been granted spectrum-sharing licenses, with either no interference or little disturbance (Hu et al., 2018). The CR network must be cognizant of the local radio environment and make necessary adjustments to its transmission settings. In order to avoid interfering with other networks, users of interference-free CR systems are only allowed to utilize the spectrum when it is not being used by licensed users. Wideband frequency spectra include voids that may be used by opportunely positioned free CR networks. CR receivers should employ spectrum sensing to keep tabs on the available frequencies and assign them as needed before relaying this information to the CR transmitter (or combining it with geolocation databases).

Numerous CR networks that seek to access the same spectrum gaps need a method for coordinating their efforts to prevent users from clashing with one another (Ahmad et al., 2020). The interference levels of

interference-tolerant CR networks are kept below a predetermined threshold, allowing users to coexist with licensed systems on the same spectrum. Interference-tolerant CR networks may boost spectrum utilization and spectral efficiency compared to interference-free CR networks. As a result of licensed users and interference-tolerant CR networks, this is conceivable. However, research suggests that the performance of CR systems may be very susceptible to variations in user density, interference thresholds, and the transmission behaviours of licensed systems (Ahmad et al., 2020; Jang, 2022). This spectral efficiency may be increased in one of two ways: either by lowering the interference threshold of the main system or by only considering CR users who are in close proximity to the secondary BS. It has been suggested that CR networks be included in hybrid cellular networks in order to increase capacity and permit the use of additional bands (Jang, 2022).

Mobile Femtocell

The MFemtocell is a novel idea that has been recently offered as a possible candidate technology for use in the future generation of intelligent transportation systems (Aydemir & Cengiz, 2016). It combines femtocell technology with that of a mobile relay, or "moving network," as it is sometimes called. Unlike fixed femtocells, mobile femtocells (or MFemtocells) may move about and modify their connection to the operator's main network on the go. It may be used to improve customer service in both public transportation vehicles like buses and trains, as well as private vehicles like autos. MF MFemtocells might be a useful addition to cellular networks. In the beginning, MFemtocells may increase the spectral efficiency of the network as a whole.

Maximum signal-to-noise ratio (MAX-SNR) vs the proportional fairness (PF) scheduling methodology is also compared. An increase in the percentage of users communicating with the BS through MFemtocells leads to better spectral efficiency as compared to the case when users connect directly with the BS (i.e., the direct transmission scheme) (Aydemir & Cengiz, 2016). We can verify this by observation. Second, using MFemtocells, a network may incur less signalling overhead. For instance, an MFemtocell may perform a handover on behalf of all its connected users. For users inside the MFemtocell, this might mean less time spent doing handovers. This makes MFemtocell deployment a good option in highly mobile settings. Emtocells may improve cellular communications because of their shorter communication range and reduced signalling overhead. Users within an MFemtocell may be able to reduce their energy use as a consequence.

Visible Light Communication

The white light emitting diodes (LEDs) used in solid-state lighting (SSL) are used for Visible Light Communication which are converted into signal transmitters (Arfaoui et al., 2020). Receivers for signals in visible light communication often make use of commercially available avalanche photo-diodes (APDs) or p intrinsic-n (PIN) photodiodes. There is a lack of citations for this section. In other words, VLC enables gadgets to both light up and access fast wireless data networks. If illumination is not needed, infrared LEDs or radio frequency (RF) LEDs might be used in the uplink.

Information is conveyed by the light's intensity or power inside a VLC framework. Thus, the information signal must be genuine and unambiguously positive (Arfaoui et al., 2020). Complex valued and bipolar signals are used in conventional digital modulation methods for RF transmission. In light of this need for adaptation, a wealth of information is available on modified multi-carrier modulation methods, such as orthogonal frequency division multiplexing (OFDM) for intensity modulation (IM) and direct detection (DD). According to some estimates, a single LED could theoretically transport data at a rate of 3.5 terabits per second. Since the wavelength is less than the detector area, very low-frequency content (VLC) is not degraded by quick fading effects (Hassan et al., 2019). It is crucial to show that current lighting infrastructures may be used to construct full-fledged optical wireless networks. Although the link-level demonstrations are significant, it is also crucial to demonstrate that full-fledged optical wireless networks can be constructed to indicate that VLC is a feasible solution to assist address spectrum limitations in RF communications. Such methods include multiple-input multiple-output (MU) access strategies and interference coordination.

Green Communications

5G wireless network design should address energy efficiency measures for the sake of a greener future in wireless communications. All throughout the world, wireless network providers should work toward this kind of energy savings, which would eventually contribute to less carbon dioxide being released into the atmosphere (Mowla et al., 2017). Greater energy efficiency may be attained via the use of deployment alternatives that use indoor communication technology. This is because they can create optimal

circumstances in the channel between the transmitters and the receivers. Further, the macrocell base station will have less pressure to distribute radio resources and may transmit at a lower power level of internal and external traffic are kept separate. Reduced energy consumption is a direct result of this. Wireless communication options that are low in power consumption and may be employed in 5G networks include very low frequency (VLC) and millimetre wave (mm-wave) technologies.

4.3 Current Concerns on Wireless Communication Technology

Multi-input, multi-output (MIMO) devices are used for a wide range of communications, including regular transmissions and receptions, location reporting, application report filing with development firms, and other activities. In addition to the fact that all of this data is travelling through space, a good chunk of it also has unique identifiers for things like network nodes, devices, and even humans involved in the sending and receiving of the data. The majority of currently used technologies have put a substantial amount of focus on security risks and have developed standards and processes to enhance both privacy and security (Khan et al., 2019). Frequently, New and Emerging Technologies (NET) represent the largest risk areas. Concerns about the privacy of Internet users revolve around the possibility of illegal surveillance and security weaknesses. These privacy concerns for MIMO and 5G technologies and their risk are discussed in this section.

Security vulnerabilities: An attacker may get access to a device or network, read and steal data, or spread malicious malware by taking advantage of programming flaws, vulnerabilities, and software defects that aren't identified during development. Some Bluetooth NET products, including smartwatches and fitness trackers, have recently made news due to potential security issues (Farooq et al., 2017). Wearable technology used by employees in the workplace, together with the rising trend of Bring Your Own Device (BYOD), may pose a serious threat to the security of a business's networks and data.

Unlawful surveillance. An attacker with access to a device may install malware on it to steal its location data, turning it into a beacon that sends the data to the intruder. The perpetrator may learn about the victim's daily travel, employment, shopping habits, and medical and health challenges and draw certain conclusions about the victim's way of life since the device is virtually always with its owner.

If there are not sufficient security and privacy precautions on social networks, criminals may easily get a great deal of information about potential victims. Although social media platforms have been available for some time, fresh iterations are often introduced. By targeting those actively engaged in social networking, cybercriminals may increase their chances of gaining access to sensitive information and resources. Phishing is the term for these types of attacks. Since surveillance malware needs access to the victim's sensitive digital content, it is often included with gaming or social programs. Data collected by the program might be used for blackmail or identity theft. (Prasad et al., 2017)

5. CONCLUSION

MIMO is a wireless technology that uses multiple antennas at both the transmitter and receiver to improve communication performance. MIMO improves communication reliability and increases data transmission speeds by creating multiple communication channels between the sender and receiver. As a consequence, wireless communication systems benefit from higher signal strength, higher data throughput, and fewer transmission mistakes. In this piece, the spectral efficiency, Capacity, data rate, Energy efficiency, and cell average throughput targets for MIMO with 5G wireless communication systems have been established. With the introduction of 5G wireless communication networks, there is a tremendous chance for increased speed and reliability in digital exchanges. MIMO (Multiple Input, Multiple Output) technologies have emerged as a critical component in meeting these performance requirements. In order to boost data speeds, dependability, and total network capacity, MIMO employs the employment of multiple antennas at both the sending and receiving ends of the communication system. The implementation of MIMO in 5G systems presents several challenges, including complexity, cost, and compatibility. The complexity of MIMO arises from the need for multiple antennas, which increases the hardware requirements and costs of the system. Additionally, compatibility between MIMO and other components of 5G systems is a concern, as different components must work seamlessly together to ensure optimal performance. Despite these challenges, the benefits of MIMO in 5G systems far outweigh the difficulties. By using MIMO, 5G networks can provide faster and more reliable communication, allowing users to access and

download large files and stream multimedia content with ease. The increased capacity and improved reliability of MIMO-enabled 5G systems will support the massive growth of connected devices and services, such as the Internet of Things (IoT), virtual and augmented reality, and autonomous vehicles.

REFERENCE

Ahmad, W. S. H. M. W., Radzi, N. A. M., Samidi, F. S., Ismail, A., Abdullah, F., Jamaludin, M. Z., & Zakaria, M. (2020). 5G technology: Towards dynamic spectrum sharing using cognitive radio networks. *IEEE access*, *8*, 14460-14488.

Arfaoui, M. A., Soltani, M. D., Tavakkolnia, I., Ghrayeb, A., Safari, M., Assi, C. M., & Haas, H. (2020). Physical layer security for visible light communication systems: A survey. *IEEE Communications Surveys & Tutorials*, *22*(3), 1887-1908.

Aydemir, M., & Cengiz, K. (2016, May). A potential architecture and next generation technologies for 5G wireless networks. In *2016 24th Signal processing and communication application conference (SIU)* (pp. 277-280). IEEE.

Başar, E. (2016, May). Spatial modulation techniques for 5G wireless networks. In *2016 24th Signal Processing and Communication Application Conference (SIU)* (pp. 777-780). IEEE.

De Figueiredo, F. A. P. (2022). An Overview of Massive MIMO for 5G and 6G. *IEEE Latin America Transactions*, *20*(6), 931-940.

Espacenet - Bibliographic data. (n.d.). Retrieved February 2, 2023, from http://worldwide.espacenet.com/textdoc?DB=EPODOC&IDX=US5515378

Farooq, M. U., Waseem, M., Qadri, M. T., & Waqar, M. (2017). Understanding 5G wireless cellular network: Challenges, emerging research directions and enabling technologies. *Wireless Personal Communications*, *95*, 261-285.

Gao, X., Dai, L., & Sayeed, A. M. (2018). Low RF-complexity technologies to enable millimeter-wave MIMO with large antenna array for 5G wireless communications. *IEEE Communications Magazine*, *56*(4), 211-217.

Ghazal, A., Yuan, Y., Wang, C. X., Zhang, Y., Yao, Q., Zhou, H., & Duan, W. (2016). A non-stationary IMT-advanced MIMO channel model for high-mobility wireless communication systems. *IEEE Transactions on Wireless Communications*, *16*(4), 2057-2068.

Gudla, V. V., & Kumaravelu, V. B. (2019). Dynamic spatial modulation for next generation networks. *Physical Communication*, *34*, 90-104.

Haas, H. (2011). Wireless data from every light bulb. http://bit.ly/tedvlc

Hassan, R., Aman, A. H. M., & Latiff, L. A. (2019, November). Framework for handover process using visible light communications in 5G. In *2019 Symposium on Future Telecommunication Technologies (SOFTT)* (Vol. 1, pp. 1-4). IEEE.

He, H., Yu, X., Zhang, J., Song, S., & Letaief, K. B. (2021). Cell-free massive MIMO for 6G wireless communication networks. *Journal of Communications and Information Networks*, *6*(4), 321-335.

Hu, F., Chen, B., & Zhu, K. (2018). Full spectrum sharing in cognitive radio networks toward 5G: A survey. *IEEE Access*, *6*, 15754-15776.

Huang, C., Hu, S., Alexandropoulos, G. C., Zappone, A., Yuen, C., Zhang, R., ... & Debbah, M. (2020). Holographic MIMO surfaces for 6G wireless networks: Opportunities, challenges, and trends. *IEEE Wireless Communications*, *27*(5), 118-125.

Imoize, A. L., Ibhaze, A. E., Atayero, A. A., & Kavitha, K. V. N. (2021). Standard propagation channel models for MIMO communication systems. *Wireless Communications and Mobile Computing*, *2021*, 1-36.

Jang, W. M. (2022). The 5G Cellular Downlink V2X Implementation Using V2N With Spatial Modulation. *IEEE Access*, *10*, 129105-129115.

Jensen, M. A. (2016). A history of MIMO wireless communications. In *2016 IEEE International Symposium on Antennas and Propagation (APSURSI)* (pp. 681-682). IEEE.

Khan, R., Kumar, P., Jayakody, D. N. K., & Liyanage, M. (2019). A survey on security and privacy of 5G technologies: Potential solutions, recent advancements, and future directions. *IEEE Communications Surveys & Tutorials*, *22*(1), 196-248.

Kshetrimayum, R. S. (2017). *Fundamentals of MIMO wireless communications*. Cambridge University Press.

Kumbhani, B., & Kshetrimayum, R. S. (2017). *MIMO wireless communications over generalized fading channels*. CRC Press.

Love, D. J., Heath, R. W., Lau, V. K., Gesbert, D., Rao, B. D., & Andrews, M. (2008). An overview of limited feedback in wireless communication systems. *IEEE Journal on selected areas in Communications*, *26*(8), 1341-1365.

Malviya, L., Panigrahi, R. K., & Kartikeyan, M. V. (2020). *MIMO Antennas for Wireless Communication: Theory and Design*. CRC Press.

Mowla, M. M., Ahmad, I., Habibi, D., & Phung, Q. V. (2017). A green communication model for 5G systems. *IEEE Transactions on Green Communications and Networking*, *1*(3), 264-280.

Nasseri, M., & Bakhshi, H. (2010). Iterative channel estimation algorithm in multiple input multiple output orthogonal frequency division multiplexing systems. *Journal of Computer Science*, *6*(2), 224.

Nasseri, M., Bakhshi, H., Sahebdel, S., Falahian, R., & Ahmadi, M. (2011). PCA Application in Channel Estimation in MIMO-OFDM System. *International Journal of Communications, Network and System Sciences*.

Obakhena, H. I., Imoize, A. L., Anyasi, F. I., & Kavitha, K. V. N. (2021). Application of cell-free massive MIMO in 5G and beyond 5G wireless networks: A survey. *Journal of Engineering and Applied Science*, *68*(1), 1-41.

Pappa, M., Ramesh, C., & Kumar, M. N. (2017, March). Performance comparison of massive MIMO and conventional MIMO using channel parameters. In *2017 international conference on wireless communications, signal processing and networking (WiSPNET)* (pp. 1808-1812). IEEE.

Prasad, K. S. V., Hossain, E., & Bhargava, V. K. (2017). Energy efficiency in massive MIMO-based 5G networks: Opportunities and challenges. *IEEE Wireless Communications*, *24*(3), 86-94.

Riadi, A., Boulouird, M., & Hassani, M. M. (2017, May). An overview of massive-MIMO in 5G wireless communications. In *Colloque international TELECOM* (pp. 10-12).

Salz, J. (1985). Digital transmission over cross-coupled linear channels. *At&T Technical Journal*, *64*(6), 1147-1159.

Sarangi, A. K., & Datta, A. (2018, February). Capacity comparison of siso, simo, miso & mimo systems. In *2018 Second International Conference on Computing Methodologies and Communication (ICCMC)* (pp. 798-801). IEEE.

Shahab, M. M., Hardan, S. M., & Hammoodi, A. S. (2021). A new Transmission and Reception Algorithms for Improving the Performance of SISO/MIMO-OFDM Wireless Communication System. *Tikrit Journal of Engineering Sciences*, *28*(3), 146-158.

Sharma, A., Sarkar, A., Biswas, A., & Akhtar, M. J. (2018). A-shaped wideband dielectric resonator antenna for wireless communication systems and its MIMO implementation. *International Journal of RF and Microwave Computer-Aided Engineering*, *28*(8), e21402.

Tran, T. N., & Voznak, M. (2020). On secure system performance over SISO, MISO and MIMO-NOMA wireless networks equipped a multiple antenna based on TAS protocol. *EURASIP Journal on Wireless Communications and Networking*, *2020*(1), 1-22.

Younis, A., Abuzgaia, N., Mesleh, R., & Haas, H. (2017). Quadrature spatial modulation for 5G outdoor millimeter–wave communications: Capacity analysis. *IEEE Transactions on Wireless Communications*, *16*(5), 2882-2890.

Zhang, J., Liu, J., Ma, S., Wen, C. K., & Jin, S. (2021). Large system achievable rate analysis of RIS-assisted MIMO wireless communication with statistical CSIT. *IEEE Transactions on Wireless Communications*, *20*(9), 5572-5585.

4th International Engineering Conference (IEC 2022)
Federal University of Technology, Minna, Nigeria

INVESTIGATION ON THE PERFORMANCE OF ORANGE PEEL FOR GREYWATER TREATMENT

*Adamu A. D [1], Lawal, M [2], Sani, B. S [3], Ishaq, A[4] and Abubakar, U. A [5]
[12345]Department of Water Resources and Environmental Engineering, Ahmadu Bello University Zaria-Nigeria.
*Corresponding author: adamualiyu@abu.edu.ng +2348062619284

ABSTRACT
The need to control solid wastes from the environment cannot be overemphasized. This study aimed to investigate the performance of orange peel, being a solid waste, as an alternative low-cost and environmental-friendly adsorbent for greywater treatment. The removal of some selective parameters were investigated. These include: pH, electrical conductivity (EC), turbidity, total solids (TS), dissolved oxygen (DO) and biological oxygen demand (BOD). The study was carried out by varying the contact time and adsorbent dosage in order to determine the optimum conditions for adsorption. The results revealed that the optimum contact time recorded was 60 minutes, with the corresponding optimum removal efficiency of 1.55% for EC, 85.59% for turbidity, 61.04% for TS, 37.50% for BOD; while the pH and DO changed by 11.86% and 34.78%, respectively. Similarly, the optimum removal efficiency of 0.22% for EC and 44.44% for BOD, were recorded at dosage of 0.5 g; while the optimum turbidity removal of 96.69% and 54.55% of TS, were achieved at dosage 1.0 g. In addition, the pH and DO dropped by 27.08% and 25%, respectively at the dosages of 0.5 g and 1.0 g. Therefore, it was concluded that, the orange peel has the potential to be used as a low-cost adsorbent for the treatment of greywater.

Keywords: *Adsorbent, efficiency, grey water, investigate, orange peel, treatment.*

1 INTRODUCTION

Water that has been put to use and released into the environment without faecal pollution is referred to greywater (Baloch and Maina, 2019). It comes in high quantity but less polluted in terms of strength and can be subjected to reuse. The characteristics of greywater depends upon source and time upon which it is considered (Abedin and Rakib, 2013). The greywater reapplication has been become norm to habitants that encountered water difficulty and it encourages wastewater minimisation from the environment, thereby enhancing water availability. However, despite the existence of treated drinking waters in some areas, there is strong justification for augmenting water sources and quantities so that the available water sources would not be over stressed. This prompt the desire to treat the greywater, thereby reducing environmental pollution and improving water volume. However, there have been issues relating to the reapplication of greywater as well as the preferable methods for the treatment and areas of reuse (Vigneswarm and Sundaravadivel, 2004).

In addition, several methods have been reported to be employed in the treatment of physical and chemical pollutants from the water contaminated by various contaminants, which could lead some health issues (Ofudje *et al.*, 2017). However, the methods are associated with high capital involvement and could lead to generation of by products that need more treatments. The applications of agricultural wastes as adsorbents are receiving more attention due to the need to achieve many goals simultaneously (Adamu *at al.*, 2018). In the first place, the agricultural wastes need to be controlled from the environment and greywater need to be treated to support the various sources of water. Similarly, agricultural by products are common to get and they are proved to be good sources of adsorbents (Adamu and Adie, 2020; Adamu *et al.*, 2021).

Moreover, the chemicals used for the water treatment can cause serious health hazards if errors occur in their administration during treatment process. This shows the need to tilt attention to the natural materials for the treatment of greywater. This work is therefore aimed to investigate the effectiveness of orange peel adsorbent for the treatment of greywater, through the removal of some physico-chemical pollutants.

2. MATERIALS AND METHODS

2.1 Materials

pH meter (Crison micropH 2000), Turbidity Meter (Gallenhamph), Water Bath (Gallenhamph), Stopwatch, Glass beaker (150 ml, 100 ml and 200 ml), Measuring cylinder, (10 ml, 20 ml, and 50 ml capacity), Pipette (25 ml), Conical flask (250 ml), Electronic weighing balance (3000 GallenKamp LTD), Sieves (Standard British Series), Oven (GallenKamp, BRIT. No. 882942 England), Hand gloves, Filter paper Whatman Grade 1, Blender

(Kenwood BL 440 UK), BOD bottle, Petri-dish (100 ml), Funnel, Manganous sulphate solution (0.364g/l), Alkalide-iodide-azide solution, Concentrated sulphuric acid (H_2SO_4), Starch solution, Sodium thio-sulphate (0.025g/l) and Buffer solutions (4, 7, 8, 9).

2.2. Methods

2.2.1 Orange peel collection and preparation

The orange peels were collected from Samaru Market, Sabon Gari Local Government Area of Kaduna State, Nigeria. After collection, the orange peel samples were washed several times with clean water to remove dirt and other impurities. After which, they were dried for 48 hours under sunlight, and later dried for 24 hours in oven at a temperature of 105˚C to remove the moisture content (Adamu and Ahmadu, 2015; Baloch and Mangi, 2019; Adamu *et al.*, 2021; Adamu and Alfred, 2021). The samples were further ground into fine powder and stored.

2.2.3 Grey water collection

The greywater samples were collected from Ribadu Hall of Ahmadu Bello University, Zaria, through the drainage outlet in a 5 litres gallon. The sample were transported to the Environmental Engineering Laboratory, ABU, Zaria for analysis.

2.2.3 Batch adsorption experiments

The experimental works were carried out using the batch adsorption method. In this case, 100 ml of greywater sample was placed in the conical flask. Then, 1.0g of the adsorbent was added and stirred at 100 rpm in the jar test at the stirring times (contact times) of 15, 30, 45, and 60 minutes. After stirring, the samples were filtered with the filter paper. The filtered samples were then analyzed for some physico-chemical parameters. The study was also carried out at the dosages of 0.5, 1, 1.5 and 2g for 1 hour, stirred at 100 rpm at the ambient temperature.

3. RESULTS AND DISCUSSION

Table 1 show the FTIR spectrum orange peel sample. The Table indicates the various functional groups of the orange peel. In addition, the observed functional groups agreed with (Muntaka, 2018). The adsorbent contains C=C stretching, C-H stretching, C-H bending and O-H stretching functional groups such as hemicellulose, cellulose and pectin.

Table 1: Identification of surface functional groups of orange peel

Wavenumber (cm^{-1})	Class of compounds	Functional Group
3276.3	Alkynes (R-C≡C-H)	≡ C-H stretch
2922.2	Alkanes and Alkyls	C-H stretch
2109.7	Alkynes (R-C≡C-H)	C≡C stretch
1990.4	NA	NA
1919.6	NA	NA
1722.0	Aldehydes (R-CH≡O)	C≡O stretch
1602.8	Amides (R-C(O)- NH_2)	=C-H bend
1513.3	Amides (R-C(O)- NH-R	N-H bend
1423.8	NA	NA
1364.2	NA	NA
1319.5	Alkyl halides (R-F)	C-F stretch
1237.5	Alkyl halides (R-F)	C-F stretch
1010.1	Alkyl halides(R-F)	F stretch
812.6	Aromatic Compounds (*p*-distribution)	C-H bend
764.1	Aromatic Compounds (*m*-distribution)	C-H bend

The presence of hemicellulose, cellulose and pectin in the orange peel was also observed for banana peel by (Alaa, 2017). Furthermore, the presence of C=O functional group in orange peel indicates that it contains hemicelluloses with certain carboxylic acids or their esters which influence the performance of the orange peel. Also, the C=C stretch functional group found in orange peel could possibility indicates substituted alkenes in the orange peel. The presence of compounds with these functional groups in orange peel could have impact on its effectiveness as adsorbent.

3.1 Measurement of Physico-Chemical Parameters

Table 2 shows the physico-chemical characteristics of the grey water. It shows control of the parameters.

Table 2: Characteristics of the greywater

Parameters	Initial result (control)
pH_i	8.35
Electrical conductivity, EC_i (µS/cm)	1095
Turbidity, T_i (NTU)	340
Total solid, TS_i (mg/L)	770
Dissolved oxygen, DO_i (mg/L)	230
Biological oxygen demand, BOD_i (mg/L)	80

3.2 EFFECT OF CONTACT TIME ON THE REMOVAL EFFICIENCY (R.E)

Table 3 shows contact time effect on the R.E. of the parameters considered. It could be observed that the maximum reduction in pH of 7.36 from the controlled value of 8.35, was recorded at the contact time of 60 minutes; while the minimum reduction in pH value of 7.43 occurred at 30 minutes. The reduction in pH with the addition of the adsorbent, could be attributed to the presence of some substances in the orange peel which could be acidic in nature. This observation agreed with Adarsh *et al.* (2020) which reported decrease in pH from 8.4 to 6.2 at the dosage of 0.8 g of orange peel adsorbent. Similarly, the EC increased from the initial value of 1095 µS/cm to 1126 µS/cm at the stirring time of 30 minutes. The rised in the EC with the increased in adsorbent dosages could be attributed to the presence of some cations and anions in the orange peel that increased the electrical conductivity of the solution. This observations was reported by Adamu and Alfred (2021).

Table 3: Effect of contact time at different stirring time with constant dosage of 1.0 g

Time (mins)	pH_i	pH_f	Change (%)	$E.C_i$ (µS/cm)	$E.C_f$ (µS/cm)	R.E (%)
15	8.35	7.52	9.94	1095	1092	0.27
30	8.35	7.43	11.02	1095	1126	2.83*
45	8.35	7.48	10.42	1095	1078	1.55
60	8.35	7.36	11.86	1095	1099	0.37*

In Table 4, the optimum turbidity removal of 85.59% was recorded at 60 minutes under the constant adsorbent dosage of 1.0 g. In this case, the turbidity reduced from the controlled value of 340 NTU to 49 NTU. This implied that the orange peel adsorbent was effective in the removal of turbidity from the greywater. Adarsh *et al.* (2020) recorded 35.53% turbidity removal at the maximum dosage of 0.8 g of orange peel adsorbent for the treatment dairy wastes. In addition, the increased in contact time from 15 minutes to 60 minutes, allowed the adsorbent to mix more with the colloidal and suspended matter in the greywater. The performance of the orange peel on R.E of TS is indicated in Table 4. The maximum R.E of 61.04% for the TS was recorded at the contact time of 60 minutes. The higher time allowed the orange peel adsorbent to effectively removed TS from the greywater. In another study carried out by Adamu *et al.* (2014) on the removal turbidity from wastewater using *manihot palmate*, a cassava specie, it was discovered that the *manihot palmate* treated with acid recorded turbidity reduction of 51.8% at 30 ml dosage. Similarly, Baloch and Maina (2019) recorded 86% turbidity removal using orange peel activated carbon.

Table 4: Effect of contact time at different stirring time with constant dosage of 1.0 g

Time (mins)	T_i (NTU)	T_f (NTU)	R.E (%)	TS_i (mg/l)	TS_f (mg/l)	R.E (%)
15	340	176	48.23	770	450	41.56
30	340	106	68.82	770	390	49.35
45	340	148	56.47	770	470	38.96
60	340	49	85.59	770	300	61.04

In Table 5, the DO dropped with the addition of the orange peel adsorbent. The maximum dropped in DO from 210 mg/l to 160 mg/l was obtained at 60 minutes. This observation could be due to some organic substances within the adsorbent which led to the dropped in the DO. This observation agreed with Adamu and Alfred (2021). Similarly, the maximum BOD removal from 80 mg/l to 50 mg/l was achieved at 15 and 60 minutes as indicated in Table 5. The BOD reduction by the adsorbent signified that it is good in the treatment of the greywater. This agreed with Adarsh *et al.* (2020) where 70.79% of BOD removal was recorded at the dosage of 0.8 g of orange peel adsorbent.

Table 5: Effect of contact time at different stirring time with constant dosage of 1.0 g

Time (mins)	DO_i (mg/l)	DO_f (mg/l)	Changed (%)	BOD_i (mg/l)	BOD_f (mg/l)	R.E (%)
15	230	210	8.61	80	50	37.50
30	230	150	34.78	80	60	25.00
45	230	150	34.78	80	60	25.00
60	230	160	30.43	80	50	37.50

Table 6 shows control values of the greywater characteristics before subjecting it to the treatment by orange peel adsorbent.

Table 6: Initial grey water properties before treatment

Parameters	Initial result (control)
pH_i	7.57
Electrical conductivity, EC_i (µS/cm)	918
Turbidity, T_i (NTU)	362
Total solid, TS_i (mg/L)	770
Dissolved oxygen, DO_i (mg/L)	160
Biological oxygen demand, BOD_i (mg/L)	90

3.3 ADSORBENT DOSAGES EFFECTS ON REMOVAL EFFICIENCY

Table 7 shows effect of orange peel dosages at constant time of 60 minutes. The Table show the change in pH under various dosages of orange peel adsorbent at constant time of 60 minutes. The maximum change in pH was observed at the dosage of 1.0g, in which the pH reduced by 27.08%. On the other hand, the electrical conductivity increased from 916 µS/cm to 1035 µS/cm from the controlled value of 918 µS/cm at dosages of 0.5 - 2.0 g. The increased in the electrical conductivity with the increased in adsorbent dosages could be associated with the presence of some organic and inorganic substances within the orange peel, thereby increasing the electrical conductivity of the solution. Similar observations were also reported by Adamu and Alfred (2021).

Table 7: Effect of Orange peel adsorbent using various dosages at constant time of 60 minutes

Dosage (g)	pH_i	pH_f	% change	EC_i (µS/cm)	EC_f (µS/cm)	R.E (%)
0.5	7.57	6.98	14.39	918	916	0.22
1.0	7.57	5.52	27.08	918	970	5.66*
1.5	7.57	5.58	26.29	918	1035	12.75*
2.0	7.57	5.63	25.63	918	1121	22.11*

(* Initial value is less than value after treatment)

Table 8 shows the reduction in turbidity when the dosages varied from 0.5 – 2.0 g at constant time of 60 minutes. The optimum R.E. occurred at dosage of 1.0g, in which the turbidity reduced to 12NTU from the controlled value of 362 NTU, implying that the R.E of 96.69% turbidity was recorded. From the Table, the maximum R.E of TS of 54.55% was recorded at the dosage of 1.0 g., in which the TS reduced from the initial value of 770 mg/l to 350 mg/l. On the other hand, the minimum R.E of TS of 32.47% occurred at the dosage of 0.5 g. Adamu *et al.* (2014) study the turbidity removal from wastewater using *manihot palmate*, a cassava specie, the study reported that the *manihot palmate* treated with acid reduced the turbidity by 51.8% at 30 ml dosage. In another study carried out by Baloch and Maina (2019), it was discovered that, orange peel activated carbon removed 86% and 87% turbidity and total solids, respectively from synthetic wastewater at 1.0 g dosage.

Table 8: effect of Orange peel adsorbent using various dosages at constant time of 60 minutes

Dosage (g)	T_i (NTU)	T_f (NTU)	R.E (%)	TS_i (mg/l)	TS_f (mg/l)	R.E (%)
0.5	362	18	95.03	770	520	32.47
1.0	362	12	96.69	770	350	54.55
1.5	362	204	43.65	770	390	49.35
2.0	362	228	37.02	770	430	44.16

Table 9 shows the removal efficiency of orange peel adsorbent under various dosages on DO and BOD. The DO reduced to lowest value of 120 mg/l at 0.5 g. In addition, the DO successively decreased with the increased in the adsorbent dosage. This observation could be associated with the introduction of more organic materials present within the adsorbent which led to the dropped in the DO. This observation agreed with Adamu and Alfred (2021). Similarly, the optimum BOD removal of 44.44% was recorded at the adsorbent dosage of 0.5 g. In this case, the BOD reduced from the initial value of 90 mg/l to the final of 50 mg/l after the treatment with the orange peel adsorbent. However, as the dosages increased, the BOD reduction became less pronounced due the lowering in the DO as earlier explained.

Table 9: Efficiency of Orange peel adsorbent under various dosages on some parameters (time = 60 minutes)

Dosage (g)	DO_i (mg/l)	DO_f (mg/l)	(%) Change	BOD_i (mg/l)	BOD_f (mg/l)	R.E (%)
0.5	160	120	25.00	90	50	44.44
1.0	160	130	18.75	90	60	33.33
1.5	160	130	18.75	90	60	33.33
2.0	160	150	6.25	90	80	11.11

CONCLUSION

The orange peel waste was successfully applied in the treatment of greywater. The impact of contact time and dosages on the removal efficiency were successfully recorded. The highest reduction in pH of 7.36 from the controlled value of 8.35 was recorded at the contact time of 60 minutes, when adsorbent dosage was 1.0g. The electrical conductivity increased under most of the dosages applied; while the maximum turbidity and total solids removals of 85.59% and 61.04%, respectively were recorded at 60 minutes under the constant dosage of 1.0 g. in addition, the maximum bod of 44.44% was achieved at the orange peel dosage of 0.5 g under contact time of 60 minutes. The electrical conductivity has been noticed to increase due to the probable presence of cations and anions in the orange peel adsorbent, while and dissolved

oxygen dropped due to the presence of some organic substances in the orange peel. The orange peel was effective as adsorbent in the treatment of greywater

REFERENCES

Abedin, S. B., & Rakib, Z. B. (2013). Generation and quality analysis of greywater at Dhaka City. Environmental Research, Engineering and Management, 64, 29–41.https://doi.org/10.5755/j01.erem.64.2.3992.

Adamu, A. D., Abubakar, U. A., Sani, B. S. and Umar, A. (2021). Modelling and Optimization of Lead Adsorption onto Sugarcane Bagasse Activated Carbon. Nigerian Resaerch Journal of Engineering and Environmental Sciences, 6 (2), 520 – 529. http://doi.org/10.5281/zenodo.5805110

Adamu, A., Adie, D. B., Okoufu, C. A. and Giwa, A. (2018). Application of Acivated Carbon for Lead Removal from Wastewater. ATBU Journal of Science, Technology and Education (JOSTE), 6 (3), 126 – 140.

Adarsh, S., Manasa, M. P., Sheshaprakash, M. N. Chadan, B. (2020). Dairy Wastewater Treatment Using Orange Peel as an Adsorbent. International Research Journal of Engineering and Technology 7 (Special Issue), 105 – 114.

Adamu, A. D. and Adie, D. B. (2020). Assessment of Cadmium Adsorption from Wastewater onto Sugarcane Activated Carbon. Bayero Journal of Engineering and Technology, 15 (1), 7 – 14.

Adamu, A. D. and Alfred, S. (2021). Assessment of Water Melon Seed as a Coagulant in Water Treatment**,** Book of Proceedings of the 16th Materials Science and Technology Society of Nigeria Conference, Kaduna State Chapter, held at the Department of Chemistry, Faculty of Physical Sciences, Ahmadu Bello University Zaria-Nigeria, 1st -3rd October, 2021, 61 - 64.

Adamu, A. and Ahmadu, M. S. (2015). Comparative Performance of *Saccharum Officinarum* (Suagrcane Bagasse) and *Parkia Biglobosa* (Locust Bean) in Wastewater Treatment, Nigerian Journal of Technology (NIJOTECH), 3 (4), 861 – 867.

Adamu, A., Adie D. B. and Alka, U.A. (2014). A Comparative Study on the use of Cassava Species and Alum in Wastewater Treatment, Nigerian Journal of Technology (NIJOTECH), 33 (2), 170 – 175.

Alaa El-Din G., Amer A. A., Malsh G. and Hussein M. (2017). Study on the use of Banana Peels for Oil Spill Removal. Alexandria Engineering Journal, 1- 8, doi.0rg/10.1016/j

Baloch, M.Y.J. and Mangi, S. H. (2019).Treatment of Synthetic Wastewater using Banana, Orange and Sadopilla Peels as Low Cost Activated Carbon. Journals of Materials and Environmental Sciences, 10 (10), 966 – 986.

Casanova, L.M., Gerba, C. P. and Karpiscak, M. (2001). Chemical and microbial characterization of household greywater. *Journal of environmental science and health, Part A*. Toxic/Hazardous Substances and Environmental Engineering, 34, 395 – 401.

Muntaka D., Zakariyya U. Z., and Maje A. H. (2018). Cationic Dyes Removal Using Low-Cost Banana Peel Biosorbent. American Journal of Materials Science 2018, 8(2), 32-38, doi: 10.5923/j.materials.20180802.902

Ofudje E.A., Awotula, A.O., Hambate, G.V., Akinwunmi, F., Alayande, S.O. and Olukanni, O.D. (2017) Acid activation of groundnut husk for copper adsorption: kinetics and equilibrium studies. Desalin Water Treatment, 86, 240–251.

Vigneswaran, S., and Sundaravadivel, M. (2004). Recycle and reuse of domestic wastewater in wastewater recycle, reuse and reclamation. Oxford: EOLSS.

4th International Engineering Conference (IEC 2022)
Federal University of Technology, Minna, Nigeria

OPTIMAL 5G RESOURCE ALLOCATION FOR ULTRA-RELIABLE LOW LATENCY COMMUNICATION (URLLC) AND ENHANCED MOBILE BROADBAND (eMBB) USE CASES

*Abdulhakeem-Alugo, A. A[1], Mohammed, A. S[1], & Dauda, U. S[2]
[1]Telecommunication Engineering Department, Federal University of Technology, PMB 65 Minna Niger State, Nigeria
[2] Electrical and Electronics Engineering Department, Federal University of Technology, PMB 65 Minna Niger State, Nigeria
*Corresponding author email: abdullah.pg917055@st.futminna.edu.ng +2347065631695

ABSTRACT
Due to the development of wireless networks for communication, a new issue has emerged. Users have become more organized (especially in 5G) by applications to ensure relatively easy spectrum access. The coexistence of eMBB and URLLC traffic has given rise to puncturing issues. The burstiness of URLLC traffic, which affects eMBB traffic by forcing its packets to wait until the spectrum is briefly free of URLLC traffic, is the main cause of this puncturing. In addition to Q-learning, resource block allocation was done in addition to joint power in order to get around this issue. The scheduling of resources was done using Q-learning in order to get the best multiplexing possible without puncturing eMBB resources. As a result, a scheduling pattern was created that enhanced reliability by increasing throughput and reducing latency. The suggested algorithm was implemented using MATLAB 5G and Deep Learning toolboxes. The algorithm (OLRT-Q) was compared to three other algorithms and there were some favourable conclusions. According to analysis, a 16% throughput boost over LRT-Q and a 47.7% increase over LR-Q at 2 Mbps (the case with the highest load) were recorded. At 1.5 Mbps, we noticed an increase of 12.2% and 33.16% in performance over LRT-Q and LR-Q, respectively. It outperformed LRT-Q and LR-Q in the case of a 1 Mbps load scenario by 9.44% and 19.09%, respectively. There is an improvement in throughput by 13.36% compared to LR-Q and a 9.58% increase compared to LRT-Q under the lowest load scenario permitted by the standard (0.5 Mbps).

Keywords: *eMBB, Latency, OLRT-Q, Reliability, Throughput, URLLC.*

1 INTRODUCTION

When it comes to mobile networks, the fifth generation (5G) technology, which has reportedly been introduced in several regions of the world while many others are still awaiting its introduction, has shown promise. Even better, a variety of application areas have been suggested, some of which are currently being used like; unmanned aerial vehicles (UAVs), smart cities, and self-driving cars. In the situations of these applications, the benefit of 5G technology would result in an exponential improvement.

All communication profiles used in industrial settings are supported by the wide area network (WAN) technology utilized in the 5G network. According to the industry 4.0 paradigm, a top priority in the design of factories is agility. Networked workforce solutions, automated guided vehicles, drones, and autonomous robots are among the main technologies that facilitate adaptability in factories.

In accordance with International Telecommunication Union (ITU) standards, these applications have now been divided and classified into three use cases or service types. They are:

1) eMBB (Enhanced Mobile Broadband)

2) uRLLC (Ultra Reliable Low-Latency Communications)

3) mMTC (Massive Machine-type Communications) (Massive Machine-type Communications) (Sanou, 2018)

The ITU has gradually implemented a number of standards in the information technology (IT) sector to control how people interact with technology while taking into account maximum performance. The ITU also established standards before 5G was available to control how consumers interacted with technology and applications in general.

These numerous use cases are supported by the various quality of service (QoS) needs for 5G wireless networks in terms of data rate, dependability, and latency. By adopting network slicing in cloud radio access networks, mobile network operators (MNOs) may virtualize network resources such as transmit power and physical resource blocks (PRBs) in the shared physical network (C-RANs). Given the restricted resources in the remote radio heads (RRHs) and to increase system throughput and yet satisfy user QoS requirements, it is crucial to properly distribute resources among network slices. (Pocovi et al., 2018).

The ability to accommodate cordless internet and communications with ultra-reliability and minimal latency (or non-bursty and bursty traffic) on the same network without necessarily favouring one over the other is a need for 5G wireless systems to perform well.

Broadband traffic, or eMBB, is capable of supporting data speeds in gigabit per second (with a few hundred MHz of bandwidth) and low delay. Alternately, traffic of URLLC users requires very low latency (0.25–0.3 ms per

packet) and ultra-high reliability (99.999%). (Anand et al., 2018).

The 3GPP standards organization has created a unique superposition/puncturing architecture for multiple access on a spectrum for URLLC and eMBB data in 5G communication network to address these various objectives. Each of these standards uses Key Performance Indicators (KPIs) or Quality of Service (QoS) criteria as a measure to evaluate that particular use case or service category.

The key system capacity concerns for eMBB users are: Extreme Throughput, Enhanced Spectral Efficiency, and Extended Coverage.

Users of uRLLC are more focused on mission-critical applications, and some key KPIs for these applications include: high reliability; low latency; high availability; and location precision.

Users of massive-machine type communications (mMTC) are primarily concerned with Extreme Density, which includes: Energy Optimization, High Connection Density, Low Complexity, and Extended Coverage.

Studying these three use cases, it has been suggested that there is a strong possibility that a user would only be required to use one or, at most, two of them at any given time because each of them has quite different applications and attributes. In the time-frequency domain or spectrum, whether we are thinking about the orthogonal or non-orthogonal slicing of resources in the wireless network, there is often a designated single frequency channel for mMTC. This means that eMBB and uRLLC users typically share other network blocks, especially in non-orthogonal slicing because in orthogonal slicing there are dedicated blocks for uRLLC traffic that are not utilized by any other sort of traffic, whether it is idle or not (Pocovi et al., 2018).

As a result, numerous research on multiplexing eMBB and uRLLC use cases have been conducted because, more often than not, their packets co-exist or at the very least interact in the wireless network architecture. It has been observed that many compromises arise as a result of this multiplexing and coexistence, and these tradeoffs need to be handled.

It is important to note that several approaches have been put out for dealing with the tradeoffs that arise when the two use cases coexist. It could be tempting to want to give up one for the other because their demands are distinct from one another. For instance, we observe that puncturing happens with respect to the resources of eMBB traffic as uRLLC users are given higher priority while allocating resources, in order to meet their response time demands. This finally results in throughput degradation as it affects eMBB users.

In essence, the aim of this work is to multiplex URLLC and eMBB for optimal allocation of 5G radio resources. The research's goals are to: Develop a pattern for scheduling throughput, latency, and dependability utilizing Q-learning in an effort to accomplish this goal and to compare and contrast throughput and latency results with industry standards in order to access the quality of research.

2 METHODOLOGY

This section describes how a multi-agent Q-learning algorithm is employed to increase throughput, reliability, and minimize latency, all of which are directly related to the delivery of packet data rates.

2.1 SOFTWARE

The MATLAB simulator will be used for this work, and a discrete-level simulator built on the MATLAB 5G toolbox will be used for simulations. The 5G and Deep Learning Toolboxes will be employed. Usually, the need to write codes when using toolboxes is largely eliminated and makes the work easier and more efficient. However, the 5G and Deep Learning Toolboxes didn't appear on MATLAB until its 2019 version.

2.2 METHOD EMPLOYED

Before moving forward, there a few problems that must be handled for us to succeed in our goal. The eMBB packets would be modeled with Poisson traffic and the URLLC packets need to be modeled with both Poisson & CBR traffics since it is a bursty kind of packet.

We would then multiplex packets of both forms of traffic on a 5G time-frequency grid which will enable us to address the puncturing issue that typically occurs when eMBB and URLLC packets are multiplexed.

On a number of gNodeBs that support eMBB and URLLC users, our suggested algorithm would be put to the test using the 5G-NR Rel. 15 standard. The flexible resource distribution offered by the 5G-NR standard is made possible by Transmit Time Intervals (TTIs) of varying length. Based on OFDM symbol slots of 2, 4, 7, or 14, resolution in the time direction is possible. The standard encourages the rapid transfer of messages that are perfectly suited for URLLC communication by using the greatest resolution possible, which is 2 OFDM symbols with TTI. To satisfy the eMBB customers' high throughput requirements, larger resolutions—like TTI of 14 OFDM symbols—are utilized. In N_{RB} resource blocks, the whole downlink bandwidth, B MHz, is divided, each of which consists of 12 consecutive subcarriers, in terms of spectrum distribution. Additionally, as mentioned in (Specification, 2018), a Resource Block Group is formed by contiguous resource blocks (RBG).

In our Q-learning method, we would utilize RBG as the unit of allocation in the frequency domain in order to lower the number of states. Additionally, the jth gNodeB provides a transmission power, $p_{k,j,}$ to each kth RBG. The Q-learning method, which will be mentioned later, attempts to enhance RBG allocation and transmission power allocations.

Each gNodeB has an equal number of transmission buffers to the associated users, per our system architecture. Each TTI's downlink scheduler assigns resources to users

based on whether they are currently active or have outstanding data transfers. The scheduler, in particular, executes joint RBG allocation and power while taking into consideration the QoS demands of URLLC and eMBB users. URLLC customers' traffic is represented using a blend of CBR and Poisson arrivals, in contrast to eMBB users, whose traffic is entirely modelled using Poisson arrivals.

Link capacity between the User Equipment, UE *i* and gNodeB *j* is computed thus:

$$C_{i,j} = \sum_{k=1}^{K} \omega_k log_2(1 + \frac{p_{k,j} x_{k,i,j} g_{k,i,j}}{\omega_k N_0 + \sum_{\substack{m \in J \\ m \neq j}} p_{k,m} x_{k,i,m} g_{k,i,m}}) \quad (1)$$

N_0 is the spectral energy intensity of incremental white Gaussian noise on a single side., and w_k denotes the kth RBG's bandwidth. The link allocation indication of the RBG is $x_{k,i,j}$, the transmit power of the j^{th} gNodeB on the k^{th} RBG is $p_{k,j}$, and the channel co-efficient is $g_{k,i,j}$.
The link allocation indication (k,i,m) is represented by $x_{k,i,m}$, while the channel coefficient is represented by $g_{k,i,m}$. and the transmit power of the m^{th} interfering gNodeB is $p_{k,m}$.

"Equation (1)" shows that reducing interference is essential for boosting throughput. Ineffective power management will significantly affect edge users, reducing throughput as a result.

As indicated in "(2)", there are three components that make up packet latency:

$$T = T^q + T^{tx} + T^{harq} \quad (2)$$

where T^{tx} stands for transmission delay, T^q for queuing time, and T^{harq} for HARQ re-transmission round-trip delay. T^{harq} = 4.TTI is our default assumption in line with (Esswie et al., 2018). A retransmitted packet has a greater significance compared to a newly transmitted packet during HARQ.

The latency in transmission from user *i* linked to gNodeB *j* is:

$$T_{i,j}^{tx} = \frac{L_{i,j}}{C_{i,j}} \quad (3)$$

Li,j is the length of packet and by the *Ci,j* is the connection capacity.

The ideal power allocation and, consequently, interference mitigation have a substantial impact on transmission delay in addition to throughput, as demonstrated in "(3)". The transmission rate, on the other hand, influences the Radio Link Control (RLC) layer. There is less segmentation as the rate rises. The transmission latency is thereby decreased. Additionally, giving a user access to more RBGs enlarges the assigned transport block, reducing the bandwidth.

The queuing time in "(2)" corresponds to the MAC scheduler's scheduling lag. As a result, the scheduler must schedule URLLC traffic as soon as it comes and keep the amount of HARQ re-transmissions to a minimum in order to provide URLLC users with a 1ms response time. To obtain the shortest feasible delay, we assume that there can only be one HARQ re-transmission. Limiting re-transmissions, on the other hand, may result in a greater Packet Drop Rate (PDR) and hence reduced reliability. For edge users in particular, the effects of such poor reliability might be disastrous. In our suggested algorithm, transmission power control based on RBG achieves great reliability while minimizing latency.

It is important to note that improving URLLC users' latency and reliability is expected to improve eMBB users' throughput performance, as shown in "(1)". This necessitates a resource allocation strategy that strikes a balance between URLLC and eMBB KPIs. In the next part, we discuss our suggested strategy for power and resource block allocation, which is based on Q-learning and attempts to simultaneously maximize throughput for eMBB users as well as latency and reliability for URLLC users.

2.3 Q-LEARNING ALGORITHM (OLRT-Q)

The algorithm (OLRT-Q) is built around autonomous supervised learning and executes resource allocation on each gNodeB using a Q-learning algorithm. Q-learning is officially represented as a Markov Decision Process (MDP) with players, variables, activities, a value function, and a strategy. Q-learning is based on interaction with one's surroundings and learning via trial-and-error rewards for acceptable or desired behaviour. In greater detail, an agent chooses a course of action, executes it, and is rewarded depending on how successfully the action was carried out. This cycle is continued until the agent develops an adaptive control strategy that optimizes its total restricted incentive. Q-learning performs an iterative update to assess the the visited state action pair's quality, as shown below:

$$Q^{new}(s^{(t)}, a^{(t)}) \leftarrow (1-\alpha).Q(s^{(t)}, a^{(t)}) + \alpha.[r^{(t)} + \gamma.\max_a Q^{old}(s^{(t+1)}, a)] \quad (4)$$

Where $Q^{new}(s^{(t)}, a^{(t)})$ is the Q-value of the state-action pair $(s^{(t)}, a^{(t)})$ at the t^{th} iteration, α is the learning rate, γ is the discount factor, and $r^{(t)}$ is the instantaneous reward. Because Q-values are kept in a Q-table that is indexed by states and actions, the state-action space determines the size of the Q-table.

The suggested technique, OLRT-Q, is a Q-learning algorithm with a reward function that intends to increase URLLC users' latency and dependability, as well as eMBB users' throughput. The combined resource block and power allocations carried out by agents, or gNodeBs, will be

referred to as actions by the algorithm. To make the Q-table size reasonable, we would group eight (8) consecutive resource blocks into an RBG, and the agent would assign RBGs. Observations from the environment drive the states in the proposed algorithm, which represent the repercussions of other agents' activities. When aiming to boost throughput, dependability, and latency, it is especially challenging to eliminate user disturbance. As a result, the states are made to represent the typical Signal to Interference Noise Ratio (SINR) attained by users connected to each gNodeB thus:

$$S_{k,j} = \begin{cases} S_0 & \overline{\gamma_{k,j}} \geq \gamma_{th} \\ S_1 & Otherwise \end{cases} \quad (5)$$

$\overline{\gamma_{k,j}}$ is the estimated value of the k^{th} RBG's SINR value on average, and is defined as:

$$\overline{\gamma_{k,j}} = \beta\, \overline{\gamma_{k,j}^{U}} + (1-\beta)\overline{\gamma_{k,j}^{E}} \quad (6)$$

$\overline{\gamma_{k,j}^{U}}$ is the average SINR of URLLC users and $\overline{\gamma_{k,j}^{E}}$ is the average SINR of eMBB users. β is the priority controlling factor given to URLLC and eMBB users, γ_{th} is a threshold SINR value. γ_{th} usually is chosen to maintain high probability of decoding. The reward function is finally formulated to reward actions that achieve the proposed objectives:

$$\rho_{k,j}^{U} = \begin{cases} 1 - \max_{i \in \tilde{U}} (T_{i,j}^{q})^2 & \overline{\gamma_{k,j}} \geq \gamma_{th} \\ -1 & Otherwise \end{cases} \quad (7)$$

$$\rho_{k,j}^{E} = \frac{2}{\pi} \tan^{-1}(\overline{C_{k,j}^{E}}) \quad (8)$$

$$\rho_{k,j} = \beta\, \rho_{k,j}^{U} + (1-\beta)\rho_{k,j}^{E} \quad (9)$$

where $\rho_{k,j}^{U}$ is the reward for URLLC users on the k^{th} RBG, $\rho_{k,j}^{E}$ is the reward for eMBB users, $\rho_{k,j}$ is the overall reward for the j^{th} gNodeB. The average throughput of eMBB users is represented by $C_{k,j}^{E}$, whereas the final packet queuing delay of the ith URLLC user ($i \in \tilde{U}$) is represented by $T_{i,j}^{q}$. "Equation (8)" modifies parameter to address the KPIs of both URLLC and eMBB users. "(6)" primarily tries to minimize the latency and reliability of URLLC users by providing the agent with a value proportionate to the queuing delay as long as its reliability meets a preset criterion, such as the SINR threshold. In fact, the reward value is determined by the URLLC packets on the queue for the shortest time. This means that the suggested algorithm will attempt to shorten the longest potential queue time. Additionally, increasing the average SINR has a significant impact on total latency since it decreases segmentation of packets and transmission latency. Overall, "(6)" encourages the scheduler of the Media Access Control (MAC) to allocate better RBGs to URLLC users right away, producing minimal latency and high dependability.

"Equation (7)" aids eMBB users in increasing throughput, which raises the reward value almost to one. Using the parameter β in "(8)", we can obtain the balance between the opposing KPIs.

The proposed algorithm's steps for each agent (gNodeB) are thus represented:

1: **Initialization:** Q-table ← 0, α, γ and ϵ.

2: **for** TTI t = 1 to T **do**

3: **Step 1:** Agent (that is, gNodeB) receives uplink report (that is, SINR) from its attached users.

4: **Step 2:** Compute the reward as in Eq. (6), (7), and (8).

5: **Step 3:** Update the Q-value of the current state-action pair as in Eq. (4).

6: **Step 4:** Observe and transit to next state as in Eq. (5).

7: **Step 5:** Select the next action based on ϵ –greedy policy.

8: **Step 6:** Repeat at Step 1.

9: **end for**

2.4 SIMULATION PARAMETERS

Table1 is a summary of network and Q-learning parameters used to implement our simulations in this work.

TABLE 1: NETWORK PARAMETERS

Parameters	Values
Network environment	5 gNodeBs and 500-meter inter-site distance in the 3GPP Urban Macro (UMa) network
PHY configuration	Subcarrier spacing of 15 kHz Each resource block has 12 subcarriers. K = 13 (number of RBGs) TTI of 2 OFDM symbols (0.1429 ms) 15 dB Tx/Rx antenna gain 40 dBm maximum transmission power (Specification, 2017)
Carrier configuration	B = bandwidth of 20 MHz 100 resource blocks (N_{RB}) 4 GHz carrier frequency
HARQ	Round-trip latency of 4 TTI HARQ is asynchronous with 6 processes 1 HARQ re-transmission maximum
Propagation	128.1 + 37.6 $log_{10}(D\,[Km])$ 5dB Noise Figure 5dB Penetration loss Shadowing = Log-Normal Shadowing (8dB)
User distribution	Stationary distribution Uniform or even distribution 50 URLLC packets (10packets / cell) 25 eMBB packets (5packets / cell)
Traffic model	Payload size = 32 byte URLLC = Poisson (80%) + CBR (20%) eMBB = Poisson (100%)

URLLC Load/Cell	[0.5: 0.5: 1] Mbps
eMBB Load/Cell	0.5 Mbps
Q-Learning	$\alpha = 0.5$ $\gamma = 0.9$ $\varepsilon = 0.05$ $\beta = 0.1$ where α is learning rate, γ is discount factor, ε is exploration probability and β is controlling factor.

3 RESULTS AND DISCUSSION

In addition to the previously mentioned techniques, the network and Q-learning parameters in Table1 will be tested and implemented. The outcomes of the tests and simulations will then be examined and contrasted with those from our benchmark in literature, i.e. (Elsayed & Erol-kantarci, 2019).

Simulations were run using MATLAB Q-learning and 5G toolboxes. In our simulations, we look at 5 gNodeBs, each of which has 10 URLLC and 5 eMBB users. While eMBB traffic is entirely based on Poisson arrivals, URLLC traffic is a mix of 20% CBR and 80% Poisson arrivals. Every user's payload size is 32 bytes. Additionally, whereas eMBB traffic loads are set at 0.5 Mbps, URLLC traffic loads per cell range from 0.5 to 1 Mbps. Ten simulation runs' worth of simulation results for 5000 TTIs are combined, averaged, and presented with a 95% confidence interval. In this work, the scheduling interval used is the best time resolution, i.e., TTI of 2 OFDM symbols. The action space of Q-learning based algorithms consists of power and RBG allocations. 13 RBGs are utilized for a system bandwidth of 20 MHz, with the first 12 RBGs containing 8 resource blocks in a row and the last RBG containing 4 resource blocks in a row. According to (Specification, 2017) the maximum transmission power of the gNodeB is set at 40 dBm, and the power allocation, $\rho_{k,j}$, is selected from a range of 0 to 3 dBm. Finally, a SINR threshold of γ_{th} = 20 dB is used to maintain a high possibility of successful reception.

Performance of the algorithm is evaluated using URLLC and eMBB traffic KPIs, that is, latency and reliability for URLLC and throughput for eMBB.

3.1 RESULTS FOR EMBB KPI (THROUGHPUT)

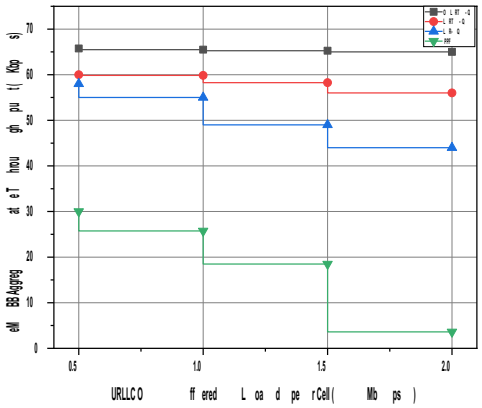

Figure 1: eMBB Users Cumulative Throughput [Mbps] against Traffic Load of URLLC

The aggregate throughput of eMBB users under various URLLC traffic loads per cell, ranging from 0.5 Mbps to 1 Mbps, is depicted on the graph in Figure1. In fact, improving the throughput performance of eMBB users should have an impact on increasing the traffic load on URLLC. The PPF algorithm (Pocovi et al., 2018) has a very low throughput because it hardly takes into account eMBB users, as shown in Figure1. As a result, it is clear that throughput, an eMBB KPI, has declined. Additionally, as the authors heavily took into account eMBB users, Figure1 depicts the LR-Q algorithm, which has a substantially higher throughput than PPF. In comparison to the two algorithms previously described, the LRT-Q algorithm was able to achieve better improvement since it used the Q-learning algorithm. In fact, compared to LR-Q and the PPF approach, the throughput of the LRT-Q is increased by 29% and 21 times, respectively, in the scenario with the highest load. Even with a 0.5 Mbps proposed load, the LRT-Q has twice the throughput of PPF.

OLRT-Q, our method, produced a noticeable change when compared to the other three algorithms. It is important to note that as the URLLC loads per cell rise from 0.5 Mbps to 1 Mbps, there is a slight, essentially negligible decrease in throughput at each cell. Although it is difficult to tell if there is an increase or decrease in URLLC loads per cell when they move from 0.5 Mbps to 1 Mbps because the values appear to be the same, we can still see that there has been improvement over the preceding algorithms, PPF, LR-Q, and LRT-Q.

According to analysis, we have a 16% throughput boost over LRT-Q and a 47.7% increase over LR-Q at 2 Mbps (the case with the highest load). Additionally, at 1.5 Mbps, we saw increases of 12.2% and 33.16 percent in performance over LRT-Q and LR-Q, respectively. We outperformed LRT-Q and LR-Q in the case of a 1 Mbps load scenario by 9.44% and 19.09%, respectively. There is

an improvement in throughput of 13.36% compared to LR-Q and a 9.58% increase compared to LRT-Q under the lowest load scenario permitted by the standard, or 0.5 Mbps.

This analysis shows that, when compared to our baseline methods, the OLRT-Q, which was created by incorporating Q-learning in addition to power and resource block allocation, performs better in all compartments for throughput enhancement.

3.2 RESULTS FOR AVERAGE URLLC LATENCY FOR URLLC LOADS: 0.5 AND 1 MBPS

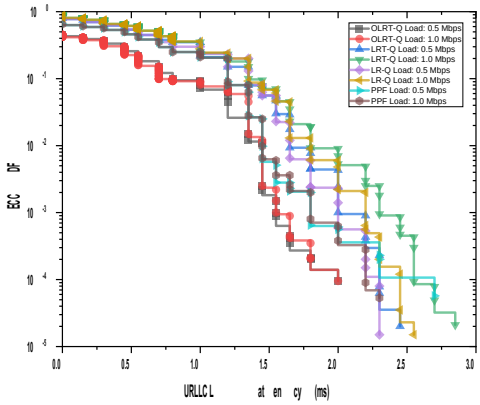

Figure.2: Average URLLC Latency [ms]; URLLC Loads: 0.5 and 1 Mbps; eMBB Load: 0.5 Mbps

Since latency is the KPI that needs to be adjusted and is one of the KPIs of URLLC users, the graph in Figure2 depicts the average delay of URLLC users with URLLC loads of 0.5 and 1 Mbps while eMBB load is set at 0.5 Mbps. The Empirical Complementary Cumulative Distribution Function (ECCDF), shows how the load changes over time by cumulating the latencies of URLLC users in this scenario. It compares the varied latencies for the four algorithms OLRT-Q, LRT-Q, LR-Q, and PPF. However, comparing the main algorithm presented in this work, OLRT-Q, to each of the other algorithms in separate graphs might make Figure2 easier to read.

3.3 COMPARING URLLC LATENCY OF OLRT-Q TO PPF

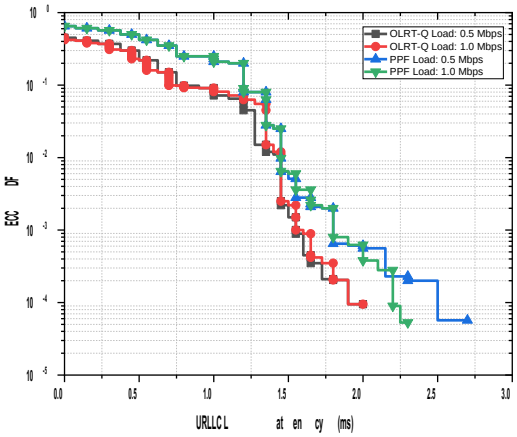

Figure 3: Average URLLC Latency [ms] of OLRT-Q and PPF

The OLRT-Q algorithm, which is used in this work, and PPF, which was used in one of the earlier works on the subject, are the two algorithms that are compared in Figure3. It is crucial to remember that the lower the cumulative frequency, the better the proposed algorithm for that specific metric under consideration. In this instance, the lower latency values are preferable to those with higher latency for URLLC users.

There are a few inferences we may make from the graph. OLRT-Q performs better than PPF in a number of areas. We can say that we have comparable latency values at the 10^{-1} percentile by interpreting the ECCDF values as percentiles. We also have an overlap at the 10^{-2} percentile, indicating that the values for the latencies there are nearly identical. When compared to the 10^{-3} percentile, the values start to diverge. We can now see that each URLLC load at 0.5 and 1 Mbps has a latency difference of about 0.3 ms. Here is where the superiority of our OLRT-Q algorithm becomes apparent. We have a latency difference at the 10^{-4} percentile of 0.25 ms at 1 Mbps load and 0.5 ms at 0.5 Mbps load. It is apparent that at this point, the OLRT-Q algorithm now outperforms the PPF much more. This shows that the level of latency that was accomplished in earlier works has been maintained and subsequently improved.

3.4 COMPARING URLLC LATENCY OF OLRT-Q TO LR-Q

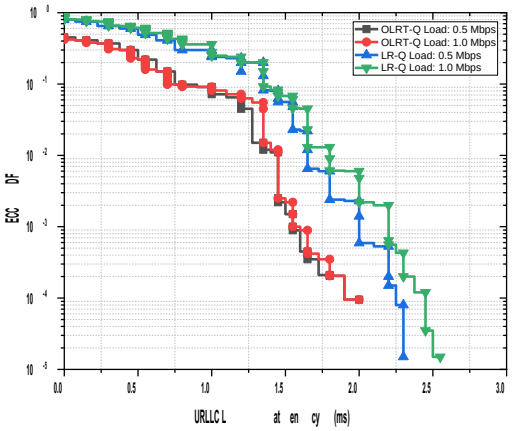

Figure 4: Average URLLC Latency [ms] of OLRT-Q and LR-Q

The two algorithms that are compared in Figure4 are the one that is described in this work, OLRT-Q, and one that was employed in a prior study on the subject, LR-Q.

The graph shows that OLRT-Q performs better than LR-Q in a number of categories. By converting the ECCDF values to percentiles, we can say that the 10^{-1} percentile latency values for both URLLC loads of 0.5 Mbps and 1 Mbps differ by roughly 0.5 ms. At the 10^{-2} percentile, latency values at 0.5 Mbps and 1 Mbps URLLC loads, respectively, differ by approximately 0.35 ms and 0.25 ms. The difference in latency for each of the URLLC loads at 0.5 and 1 Mbps, respectively, is roughly 0.45 ms and 0.60 ms at the 10^{-3} percentile. For the 10^{-4} percentile, there is a difference in latency of 0.35 ms at 0.5 Mbps load and 0.35 ms at 1 Mbps load. At this stage, our algorithm continues to perform better than the LR-Q. This once more shows that we were able to keep and raise the level of latency that was accomplished in earlier research.

3.5 COMPARING URLLC LATENCY OF OLRT-Q TO LRT-Q

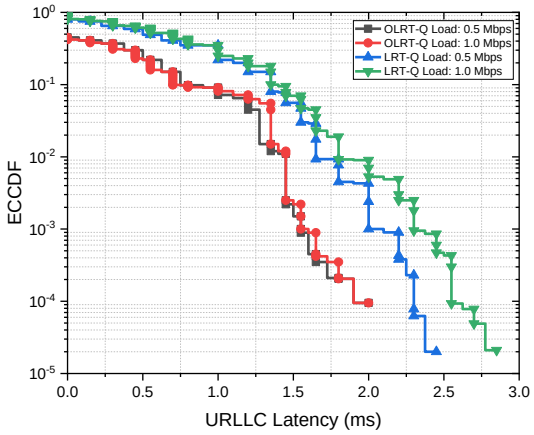

Figure 5: Average URLLC Latency [ms] of OLRT-Q and LRT-Q

The two algorithms that are compared in Figure5 are OLRT-Q, which is the algorithm that is presented in this work, and LRT-Q, which is the most advanced of the algorithms that we have compared to and was used in one of the earlier works on the subject.

We can see from the graph that OLRT-Q performs better than LRT-Q in a number of areas. Using the ECCDF values as percentiles, we can say that for both URLLC loads of 0.5 Mbps and 1 Mbps, there are differences in latency values at the 10^{-1} percentile of about 0.25 ms. At the 10^{-2} percentile, latency values at 0.5 Mbps and 1 Mbps URLLC loads, respectively, differ by approximately 0.15 ms and 0.25 ms. The difference in latency for each of the URLLC loads at 0.5 and 1 Mbps, respectively, is about 0.5 and 0.7 ms at the 10^{-3} percentile. We have a latency difference at the 10^{-4} percentile of 0.35 ms at 1 Mbps load and 0.55 ms at 0.5 Mbps load. Now, our algorithm continues to perform better than the LRT-Q. The implication is that OLRT-Q has lower latency than other algorithms, as we also inferred from PPF and LR-Q. This once more shows that we were able to keep and raise the level of latency that was accomplished in earlier research.

3.6 RESULTS FOR AVERAGE PACKET DROP RATE

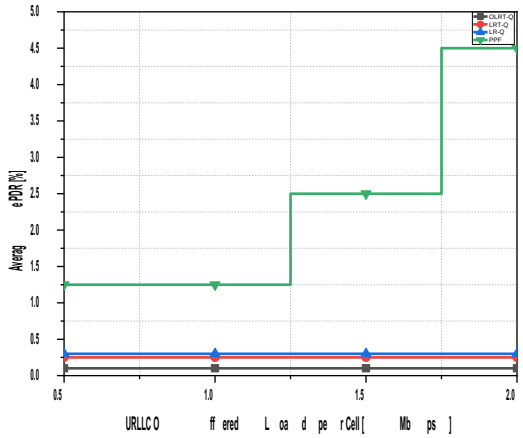

Figure 6: Average Packet Drop Rate [%]; eMBB Load: 0.5 Mbps

Figure 6 provides more information on the connection between the reliability and latency KPIs for URLLC users. After the initial re-transmission, latency can be reduced if we permit packets to be dropped.

PPF has a re-transmission issue as a result of ineffective interference handling. Figure6 shows that the PPF drop rate is rising as a result. While LRT-Q and LR-Q were only able to achieve packet drop rates of about 0.25 and 0.3%, respectively, thanks to their limitations on power allocation, OLRT-Q was able to achieve drop rates of less than 0.1%. In our worst-case traffic load, OLRT-Q outperforms PPF, lowering the packet drop rate by 4%. It also outperforms LR-Q and LRT-Q by 3.4% and 2.7%, respectively.

After 3000 TTI, or 428.5 ms, we finally noticed convergence of our OLRT-Q algorithm. The outcomes could not be plotted because of space limitations.

4 CONCLUSION

The difficulties with multiplexing URLLC and eMBB use cases on the same spectrum have successfully been addressed by this research work. The primary problem found is the depletion of eMBB users' resources. We have put into practice a technique using the Q-learning algorithm that was successful in eradicating the initial issues and resolving the constraints identified in the studied literature. This approach also prevented us from negatively impacting URLLC users in an attempt to compensate for the constraints of eMBB users. There was an arrangement of resources where they could go beyond the spectrum if necessary.

In general, we have been able to increase throughput and reliability while drastically lowering packet latency. Thus, we may draw the conclusion that this work has brought the 5G world closer to the established requirements of 99.999% data rate and less than 1 ms latency.

4th International Engineering Conference (IEC 2022)
Federal University of Technology, Minna, Nigeria

A Model for Measuring Dependence level of Organizations on MIS

*Oragbon, A[1], Alhassan J. K[2], Adama V. N[3], Ezenwa, S[4], & Oragbon, D. R[5]
[1]Department Computer Science, National Open University of Nigeria,
[2]Department of Computer Science, Federal University of Technology, PMB 65 Minna Niger State, Nigeria
[3]Department of Computer Science, Federal University of Technology, PMB 65 Minna Niger State, Nigeria
[4]Department of Statistics, Federal University of Technology, PMB 65 Minna Niger State, Nigeria
[4]Department of Mass Communication, National Open University of Nigeria,

ABSTRACT
As a result of current innovations and further development in management information system "MIS", a great demand has arisen for its acceptance and ease of use. MIS functionalities facilitates day-to-day operations and management of organisations and also aids in tactical and strategic decision making. Furthermore, it ensures institutions thrive in competing favourably with their counterparts. Despite the increasing acceptance of MIS, most institutions that have made significant investments in the infrastructure and agreed to accept the use of the infrastructure have left their day-to-day operations and control to their MIS. However, it is difficult to measure their dependence on their MIS. This research sets out to develop a model to verify why schools are not dependent on their MIS. This was achieved by accepting specific scores for extent and frequency of use for each module of the MIS that the school uses. The scores were then used calculate and measure dependence for each of the 107 schools that participated in the study, and report dependence level to the school. The final analysis revealed that of the 107 participating schools, only 17% were fully dependent on their MIS, 4% were averagely dependent on their MIS, and a whopping 79% were not dependent on their MIS. To increase dependence and improve confidence in using MIS, we recommend that institutions purchase efficient, easy-to-use and responsive MIS to maximize user satisfaction, consider deploying solar power solutions, invest in Internet infrastructure and implement effective IT policies to ensure that their technicians and support staff can effectively manage the MIS.

Keywords: *MIS, Model, Dependency, Management*

1 INTRODUCTION

A management information system (MIS) is a collection of various units of a system components used by an organization's management team to make operational, tactical, and strategic decisions. MIS are so critical that (Sutanto et al., 2020) noted that Information management in any institutions is part of the system itself. Information and data that is well administered ought to be captured by an information management system. Management information system applied in educational institutions can be referred to as an educational management information system (Herliana et al., 2021); (Gonadi, 2021). An information system is a formal socio-technical organizational system for collecting, processing, storing and distributing information. A computer information system is a system of humans and computers that processes or interprets information (Putra, 2020). The term is sometimes used in a more restrictive sense to refer only to software used to run computerized databases, or only to computer systems (Andhika, 2022). A major aim for the use of MIS when it was introduced was to enhance educational institution administration. However, data entry and data editing was a major concern rather than data analysis and transfer, while also recognizing the value of management information in the integration phase.

The study by (Madiha Shah, 2014) established that school operations and administration had positively been enhanced through the use of MIS. Also noticed was greater information access, improved use of school tools, improved effectiveness in school administration, improved quality of reports, improved time management, and decreased workload. The research uncovered various barriers to MIS adoption. The main barriers are lack of time, confidence or skills, lack of training, lack of management support and lack of technical support. Due to its effectiveness and efficiency, MIS is increasingly used in education management today. Teachers and administrators with data from MIS are better equipped to make informed decisions, schedules, assessments and policies. Regardless of recent large-scale development and breakthroughs in MIS development, the education sector in Nigeria is still facing difficulties in adopting and relying entirely on MIS in its strategic and operational planning. (Salako, 2012). (Ajoye, 2014), emphasized that there is a recent paucity of literature examining the impact of IT self-efficacy on MIS ratings. This may be due to weak IT self-efficacy in predicting MIS performance and measuring dependency levels.

Therefore this study sets out to develop a model for measuring the dependency of organizations on management information systems. Employing private schools as a case study, the model was based on Rebecca Pillinger's dependency formula and implemented using PHP and MySQL, and standard metrics to evaluate the

performance of the model. This research asked the following questions.

1. Do schools in Nigeria employ the use of management information systems?

2. To what extent are management information systems used by schools that employ their use?

According to (Zain et al., 2005), many authors use various metrics such as computer usage statistics, time spent in the computer system, number of tasks the system performs and frequency of system usage to estimate the success of systems. This study sets out to take a different approach. First to determine the level at which a private school adopts and accepts MIS for the effectiveness and efficiency of administration, routine operations, and human resource management. Secondly to investigate if management information systems are deployed by schools but do not rely on them. To achieve the set goals of this study, we developed and evaluated a model to measure school dependence on MIS, based on Rebecca Pillinger's formula.

Federal and state governments, educational institutions, education sector investors, educational research institutions, and the general public interested in educational data will highly benefit from this research. For government agencies, development of plans, critical decisions making, and improved policy formulation will be enhanced by our research output. On the other hand, this study will enhance management operations for investors. The study stands to increase effectiveness and efficiency affording privates schools quality educational platforms with functionalities that enhance quality assimilation among students.

2. REVIEWED LITERATURE

Information management in educational institutions is a component of the educational system itself (Sutanto et al. , 2020). According to (Gehlawat, 2017), a school MIS could comprise of seven modules. The seven modules are Student Management Module, Time-Table Management Module, Staff Management Module, Examination Management Module, Attendance Management Module, Facility Management Module and Finance Management Module as depicted in figure 1.

Figure 1: Features of a school management information system (Gehlawat, 2017)

In 2016, a research paper on a conceptual model of the impact of the use of MIS on decision-support skills, the researchers found that decision-making skills are becoming more prevalent across all business areas (Abdulatef et al., 2016). They found that most companies looking to future success have modernized their traditional business practices by taking advantage of advancements in technologies. Nowadays, for companies to run successfully, it is important they are able to go beyond delivering what its customers want. It also depends on the company's stability and ability to make key decisions that affect its future success.

Planning, organizing, leadership and supervision, especially in education, are managerial activities in our decision-making processes, and all of them require precise and accurate information (Gunawan et al., 2022). The information needed by managers, including educational implementers, is provided by a Management Informstion System, which is a system that provides all information for managers regularly. Information is used as a basis for monitoring and assessing the agenda and the results to be achieved.

MIS offers a number of important advantages in terms of participation in the decision-making process. Results from several studies that investigated the impact of MIS on decision-making process reveal positive correlations. Thus, MIS are believed to facilitate decision-making abilities of any organization. Results from literature also support the fact that information systems management are a factor in improving decision making skills. It has been reported that both internal and external sources of information can provide information for decision making (Livari, 2005). In this regard, most scholars are concerned about the quality of information access. According to Halawi (2008), the quality of information access is related to the quality of comparative information content. Marketing information systems can be used in conjunction with primary and secondary data sources to provide high-quality content information to MIS operations. In addition to handling transactions that are very beneficial to the organization's objectives, MIS also

offers a ton of information and processing support for the management function's decision-making. In his book, Ais Zakiyudin defines a management information system as one that describes the accessibility of a reasonably complete set of data that is archived. The data is processed into information, which in turn supports organizational operations, decision-making and management.

The development of education has entered a new phase thanks to the existence and function of information technology. However, this development has not been accompanied by an increase in human resources. Due to these circumstances, various aspects are encouraged to change and develop faster to facilitate quality education (Ikhwan et al., 2020). Quality is important, but is not the only factor. Instead, strong Information and Communication Technology (ICT), which is one unit that must be integrated into the management system, supports other components like high performance, efficiency, effectiveness, and productivity.

It takes highly skilled and experienced individuals, as well as the involvement of organizational managers, to develop a sophisticated computer-based management information system. Lack of proper organization, inadequate planning, unreliable personnel, management involvement in the form of managers overseeing system development activities, and failure to inspire all personnel involved are all reasons why many organizations struggle to build management information systems (H.A. Rusdiana, 2018).

The Technical Systems Maintenance and Management Information Systems Model reveals that production based technical systems are increasingly becoming automated with most functions becoming more reliably as well as effective (Maric, 2018). Maintenance mostly has been treated as a non-productive, ancillary part with no significant impact to the organization. However, many manufacturing departments are adopting various techniques to increase the efficiency of maintenance. This study examined machine and industrial equipment maintenance issues, management aspects related to maintenance and practices associated to maintenance. Analysis also revealed development processes of modern and traditional information systems maintenance. Finally, the study discuss how decision support systems and expert systems can be applied to maintenance management systems. The nature of the system maintenance procedures (for which the best maintenance model was chosen) were determined by the nature and content of the processes. For maintenance to be effective there is need at all stages of the process for working and strategy machinery. Enterprise Resource Planning systems (ERP) implementation and development has been heavily funded by many companies over the past decade. However, maintenance plans can only be observed in only a few of these systems.

Complex maintenance processes are mostly as a result of deterioration detected by monitored parameters or equipment failure. These could be scheduled or short notice maintenance, scheduled turnaround maintenance and in some cases both. This process requires planning, monitoring, scheduling, the use of necessary resources (workshops, labor, equipment, machinery, device, spare parts, and materials) and quality control. Effectively managing production planning and scheduling, analyzing maintenance history to perform cost analysis, and predicting future failure trends are made possible by good maintenance management design and increased integration with ERP systems increase.

In her research, Stepanova propose that technology transfer is a crucial part of any nation's advancement, specifically in an age of rapidly developing technology that has a major impact on business processes and overall condition of life (Stepanova and Erins, 2020). The researchers worked towards a model of ICT business transfer. The ICT market is growing mainly in the aspect of software development and ICT services. This saves companies valuable resources such as time and fund. The selection and evaluation of ideas, decisions, and marketing activities go hand in hand with the development of new technologies. The proposed ICT transfer model is that technology transfer comprise development methods, strategic decisions, production patterns, quality assessment and commercialization processes, the technology life cycle, and the availability of the technology to users at various ends. This indicates that the specific aim of their research project was to create an ICT transfer model for practical use by software developers and project managers. This was combined by merging different ICT standards and methods for commercializing innovations, connecting and elements of the model they integrated into one system. The authors of this study used methods of independent component analysis and synthesis. But with new opportunities come unique challenges that need to be addressed in relation to the global ICT ecosystem. Decision-making processes such as strategy selection, production method selection, and quality assurance system selection are all closely related to the development of new technologies. Project budgets, schedules, participant interactions, and collaborative networks that provide secure communication channels for information sharing and rapid access to new knowledge are all factors influencing the technology development process (Ponomarenko, 2017). The transfer of information from a provider to users is also regarded as form of technology transfer. This process usually involves a lot of phases and requires the workings of users to transfer technology, knowledge, data and experience (Ramachandra, 2012). Technology transfer is also a combination of knowledge of development techniques, production standards, quality control, market introduction and distribution procedures to ensure technology development and access to a wide range of end users.

Despite all these crucial implications of MIS and other models, it has been observed that no studies have

addressed measuring MIS dependence. We therefore view this study as a tool to fill the gaps in addressing users' unmeasured reliance on MIS.

3 METHODOLOGY AND DEVELOPED MODEL

This study provides an explanation for determining the extent and frequency of MIS use in 107 private schools. The participants in this study were private schools randomly selected from a large number of private schools in the country. Participants were selected based on their ability to afford a management information system and use it for day-to-day operations and management. The survey was conducted mainly on private schools located in the Minna metropolitan area, FCT and several other state's schools were also selected to participate. The evaluation sample used in this study was based on a number of parameters representing specific inputs from the management information systems used by participating schools, using models developed to meet the objectives of the study. An online web interface form was developed. The web interface form was designed to receive all inputs from participants in real time and store them in a cloud based database. Data provided by participants was collected via an online web form interface. The form was titled "Measurement of MIS Dependence Level by Private School" and was hosted on http://www.mis.digirealm.com.ng. The survey included over 120 private schools, but at the time of the survey, only 107 of the schools employed the use of MIS. The model was developed using the modules of a standard MIS as inputs. These modules are student, examination, attendance, time-table, staff, finance and facility, in addition to scores for extent of use and frequency of use for these modules. These parameters were built into the web interface with Rebecca Pillinger's dependency formula automatically analyzing the resulting data collected.

The web interface was developed with HTML and CSS to collect intended data. The interface has 2 sections. The first is to accept personal data such as name of the school, the address of school and lastly the MIS deployed, while the second part accepts scores for the extent and frequency of use of the various modules. Exceptions were set to curb invalid data entry. Invalid entry are scores where various modules were assigned equal scores across the frequency and extent of use parameter. The model prompts when similar score is entered across all the modules for either extent or frequency of use parameters and informs the user that "it is impossible to have all the modules used exactly the same way".

To evaluate the system's use, we employed the following metrics.

Extent (E) – The proportion of the available FIPs in the information system used in the management information system.

$$E = \frac{Number\ of\ FIPS\ used}{Number\ of\ FIPs\ Available\ and\ Appropriate\ for\ Use}$$

Where the number of FIPs available and appropriate for use is a minimum of 1.

Frequency (F) - Amount of use of system features.

$$F = \frac{Number\ of\ FIPS\ used}{Number\ of\ Times\ FIPs\ could\ be\ Used}$$

Where the number of FIPs available and appropriate for use is a minimum of 1.

TABLE 1: PARAMETERS OF THE DESIGN

MIS Modules	Extent of Use (E)	Frequency of Use (F)
Student	4	5
Examination	3	4
Attendance	5	5
Time-Table	4	3
Staff	3	4
Finance	3	3
Facility	3	3

Rebecca Pillinger's dependency formula was programed using PHP to process the data collected to reveal dependency levels of the institution.

$$\rho = \frac{\beta e^2 + \beta f^2}{\beta e^2} \quad (1)$$

Where:

$$\beta e = \sum_i^n E \quad (2)$$

i=1, n=7, e^2 and f^2 are variance of extent and frequency of use respectively.

$$\beta f = \sum_i^n F \quad (3)$$

A proper calculation of ρ can lead to one of three possible outcomes that make sense of the dependence on management information systems. Possible results are: A ρ of 3.5 or higher means that the school relies heavily on her MIS. A ρ between 3.0 and 3.49 means that the school on average is MIS dependent. A ρ < 3.0 means the school is independent of her MIS.

MYSQL data base was used to store all relevant data. At this point, the user knows whether they are dependent,

averagely dependent or not dependent on their MIS based on the scores as feed into the model.

To use the model the user is required to input the name of the school, address of the school and the name the school MIS as depicted in Figure 2. The user then inputs the scores for the extent of use for all the seven modules of the MIS. Afterwards, the model then checks for same score across the extent of use parameter, when it discovers that the scores for the extent of use for all the modules are not the same it will request entering score for the frequency of use as well but if the scores are the same it will ask the user to enter the scores appropriately. It will then also check if all the scores entered are the same across the modules of the MIS or not. As long as the scores are not the same across the extent and frequency of use, it will calculate the dependency level. If the dependency level is above 3.5 it will prompt "You are dependent on your MIS". If the dependency level is between 3.0 and 3.49 it will prompt "You are averagely dependent on your MIS, else it will just prompt "You are not dependent on your MIS.

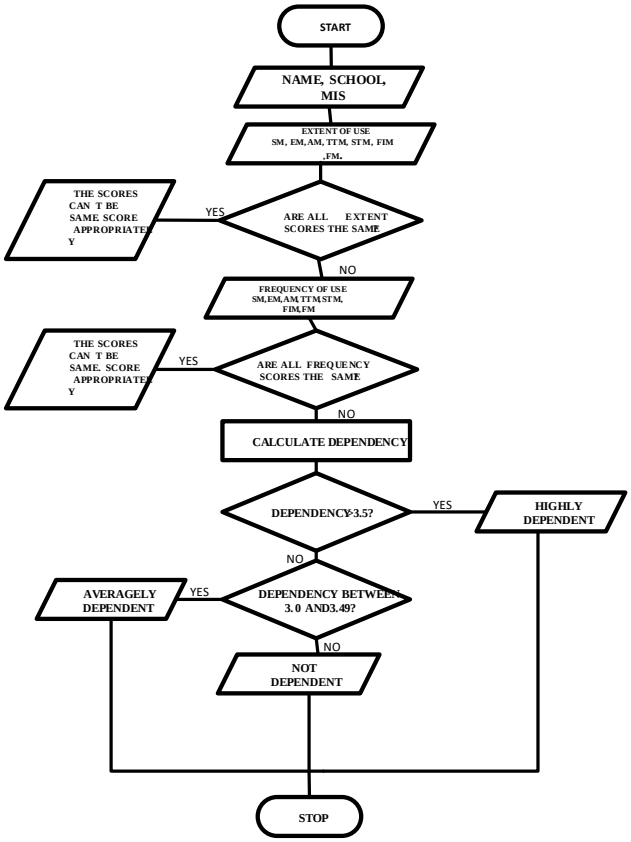

Figure 2: Flowchart for measuring dependence model

4 RESULTS AND DISCUSSION

Analysis from the result revealed that significant investments have been made by private schools on management information systems, however also observed are the following key facts:

Firstly, majority of the schools under consideration hardly made use of MIS they deployed for their daily operation as can be observed from Figure 3

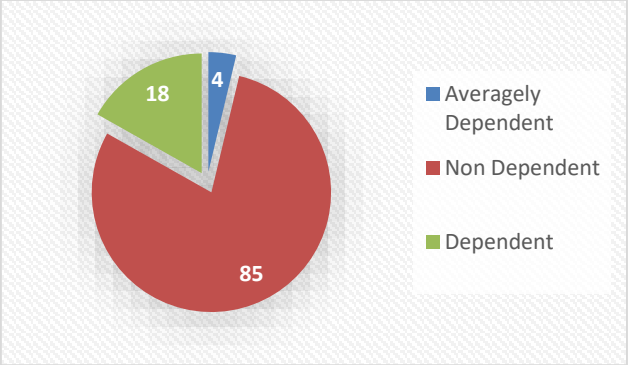

Figure 3: Dependence Levels of School on MIS

Secondly, the vast majority, about 79% of these schools were not dependent on the MIS they invested in according to figure 3. They were more comfortable with manual system of administration. Thirdly, about 4% of the schools deployed MIS, yet also used manual means as well as seen in figure 3. Fourthly, only 17% had completely embraced MIS for their day to day operations also as seen in figure 3.

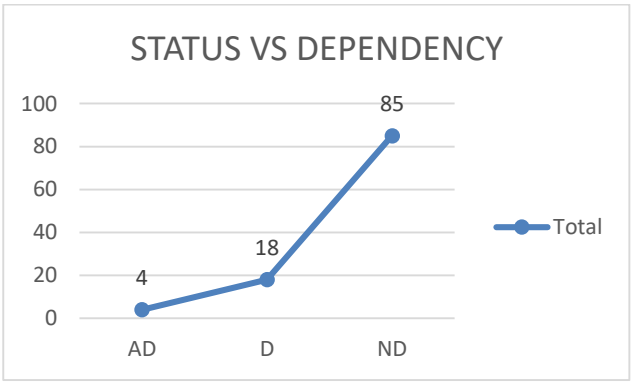

Figure 4: Line chat of the results of analysis

On investigating, the following reasons were responsible for the statistics above.

1. Administrators and teachers found it difficult to use some of the MIS. Inadequate training resulted in such staff abandoning their MIS once they encountered any challenges. Others were not computer literate and unwilling to learn.
2. Some Administrators were unwilling to change the status quo and more comfortable with the manual

methods. Also, frequent change in administrators negatively impacted consistent MIS use.

3. The unstable nature of electricity to power these systems also led to abandonment of the MIS in most cases as the use of alternative power implied additional overhead cost. Associated to this was also the additional cost of internet connectivity for schools that deployed online MIS.

4. Most school who deployed MIS on their local area network also needed experienced IT personnel's to manage and maintain their networks. This also implied additional overhead cost.

5 CONCLUSION

This study established through the development, deployment and evaluation of a model, dependence levels of private schools on MIS based on the Pillinger's dependency formula. Generally, observed was a low adoption level of MIS across the area of study. Various reasons are responsible for this. Conversely, most schools that did invested huge amount of money on MIS and deployed the MIS were not taking advantage of the MIS, thereby not optimizing their decision-making process and management. Among the 107 participating schools, a whooping 79% were not dependent on their MIS, consequently were unable to harness the potentials of their MIS. Only 4% were averagely dependent while 17% were dependent on their MIS and fully harnessing potentials of their MIS.

ACKNOWLEDGEMENTS

I wish to acknowledge my wife Deborah Oragbon and kids who were a major push and a huge encouragement in this pursuit, as well as my Father in-law: Oliver Ndam, whom the Lord used to lift my spirit when I gave up on the project and made me develop interest all over again. Godwin Oragbon my elder brother for your encouragement, and other members of the Oragbon family. Prof. John Alhassan my supervisor, who was always helping me to work hard in order to bring the project work to its completion. Prof. Lamai who out of concern and love for me took out time to encourage, followed up on my behalf and prayed for me. Prof. & Mrs. Lawal, who kept encouraging and praying for me. Victor Adama who was also there whenever I needed help and advise on the best way to go at every point in time. Reverend Oladeji who consistently prayed for me, bro Dehji of Capro missions, etc. may the Lord richly bless everyone of you for all the sacrificial roles you played over my life in Jesus name, Amen.

REFERENCE

Abdulatef, A., Aina, M., Hu, W., Ahmed, A. N., & Mohammed, M. (2016). Use of Management Information Systems Impact on Decision Support Capabilities : A Conceptual Model. 1(4), 27–31. https://doi.org/10.18775/jibrm.1849-8558.2015.14.3004

Ajoye, M. B. (2014). Information Systems User Satisfaction : A Survey Of The Postgraduate School Portal. December.

Andhika putri Putra, Randi Rian & nadya, "Implementasi sistem informasi perpustakaan dalam meningkatkan pelayanan dan struktur perpustakaan pada smp swasta pab 9 1," Jar. Sist. Inf. …, vol. 6, no.1, pp. 83–88, 2022, [Online]. Available: http://ojsamik.amikmitragama.ac.id/index.php/js/article/view/136

Gehlawat, M. (2017). School Management Information System : An Effective Tool for Augumenting the School Practices. June 2014.

Gonadi, L. (2021). Pengembangan Sistem Informasi E-Lesson Plan Pada Pendidikan Anak Usia Dini. Jurnal Inovasi Dan Teknologi Pembelajaran (JINOTEP) : Kajian Dan Riset Dalam Teknologi Pembelajaran, 8(2), 146–156. https://doi.org/10.17977/um031v8i22021p146

Halawi, A., Mccarthy, P. L., & Aronson, E. J. (2008). An Empirical Investigation of Knowledge Management System's Success. Journal of Computer Information Systems, 48 (2), 121-135

H.A, Rusdiana, M. (2018). Sistem informasi Manajemen Pendidikan:Konsep, Prinsip & Aplikasi. PPDP UIN SGD Bandung

Herliana, I., Qosim Mubah, H., & Ahmadi, A. (2021). Manajemen Sistem Informasi Dalam Kegiatan Penerimaan Santri Baru Di Pondok Pesantren Puteri Khadijah Pamekasan. Re-JIEM (Research Journal of Islamic Education Management), 4(1), 48–59. https://doi.org/10.19105/re-jiem.v4i1.4843

Ikhwan, A., Farid, M., Rohmad, A., & Syam, A. R. (2020). Revitalization of Islamic Education Teachers in the Development of Student Personality. 1st Borobudur International Symposium on Humanities, Economics and Social Sciences (BIS-HESS 2019), 162–165.

Livari, J. (2005). An empirical test of the DeLone-McLean model of information system success. ACM SIGMIS Database, 36 (2), 8-27.

Maric, B. (2018). A Model Of Management Information System For Technical. July.

Ramachandra, C.G., Srinivas, T.R., Shruthi, T.S., A Study on Development and Implementation of a Computerized

Maintenance Management Information System for a Process Industry, International Journal of Engineering and Innovative Technology, Vol. 2, Iss 5, 2012

R. R. Putra, H. Hamdani, S. Aryza, and N. A. Manik, "Sistem Penjadwalan Bel Sekolah Otomatis Berbasis RTC Menggunakan Mikrokontroler," J. Media Inform. Budidarma, vol. 4, no. 2, p. 386, 2020, doi: 10.30865/mib.v4i2.1957.

Salako, C. T. (2012). Educational Management Information System in Nigeria : Challenges and the way forward. Journal of Research in Education and Society, 3(2), 106–110.

Shah, M. (2014). Impact of Management Information Systems (MIS) on School Administration: What the Literature Says. Procedia - Social and Behavioral Sciences, 116, 2799–2804. https://doi.org/10.1016/j.sbspro.2014.01.659

Sutanto, Widyawati, & Anjayatno, A. (2020). Perancangan Sistem Informasi Pengelolaan Asrama Di Lembaga Penjaminan Mutu Pendidikan (LPMP) Banten Menggunakan Metode Rapid Application Development (RAD). Jurnal Ilmiah Sains Dan Teknologi, 4(1), 62–75.

Stepanova, V., & Erins, I. (2020). ICT Transfer Business Model Development. International Journal of Machine Learning and Computing, 10(1), 170–175. https://doi.org/10.18178/ijmlc.2020.10.1.915

V. Ponomarenko and I. Novickis, "A review of information technology transfer process, its topicality, and related models," Rezekne Academy ofTechnologies, 2017.

Wahyuni, I. (2019). Implementasi Sistem Informasi Manajemen dalam Manajemen Sekolah (Issue 666).

Zain, M., Rose, R. C., Abdullah, I., & Masrom, M. (2005). The relationship between information technology acceptance and organizational agility in Malaysia. Information and Management, 42(6), 829–839. https://doi.org/10.1016/j.im.2004.09.001

4th International Engineering Conference (IEC 2022)
Federal University of Technology, Minna, Nigeria

Development of an Enhanced Fault Monitoring and Protection System for a Three Phase Induction Motor

*Nwabueze Afulike[1], Jacob Tsado[1], & Lanre Olatomiwa[1]
[1]Electrical and Electronics Engineering Department, Federal University of Technology, PMB 65 Minna Niger State, Nigeria
*Corresponding author email: afulykens@yahoo.com +2348066830722

ABSTRACT
Induction motors face abnormal supply voltage conditions which affect their winding temperatures and subsequently cause total failure if not monitored and protected. This paper presents the development of an enhanced fault monitoring and protection system for three phase induction motor. A 1.1kW induction motor was experimentally analysed. Thereafter, a system to monitor and protect a three phase induction motor was designed and simulated in a PROTEUS environment, then developed and tested. The results of the experiment show that under 230V (±10%) three phase supply, a constant speed of 1450 r.p.m. was maintained with a balanced current drawn by the phases of the induction. This represents normal operating conditions. On single phasing conditions (i.e. two phase and single phase voltage supplies), zero speed was recorded with an unbalanced currents drawn. Reversal of rotational direction of the induction motor was observed on interchanging any two of the phase voltages in a three phase supply. All these represents abnormal operating conditions. Based on the conditions, a system to monitor and protect an induction motor was designed, simulated and developed. The simulated and developed system was able to monitor adverse supply voltage conditions such as Voltage Unbalance (VBAL), Under voltage (UV), Overvoltage (OV), Voltage Sequence Reversal (SEQ) and Single Phasing (SP). It detects these adverse voltages and abnormal temperatures, shuts down supply to the motor, displays same via the LCD and blows an alarm.

Keywords: *Induction Motor, Microcontroller based Monitoring, Single Phasing, Voltage Unbalance, Phase Sequence reversal.*

1 INTRODUCTION

Three phase induction motors are commonly used in the industries. This owns to their ruggedness, simplicity in construction and low maintenance cost (Garcia-Calva et al, 2022). Majority of the machines in the industries make use of induction motors as the prime mover. It is on record that 90% of the machines apply induction motors (Wang et al, 2015)]. In addition, they are easy to start and maintain. Due to their continuous and wide usage, they are subject to failures resulting to breakdown in production processes, long down time [Swapnil et al, 2021). The instability of supply input voltages to these motors pose a big threat to their lifespan. The lifespan of three phase induction motor is estimated to be 20 years (Mustafa et al, 2015). Sometimes one or two phases of the supply voltages to an induction motor may be lost resulting to single phasing or incomplete phase condition. This fault could be from the power distribution transformer, blown fuses, loose contacts of the circuit breakers or electromagnetic switches (Altaf et al, 2019). Alteration of the phase sequence (phase reversal) may occur during maintenance operation on the power supply lines by the maintenance personnel in the industry or the electricity distribution company e.g. Abuja Electricity Distribution Company (AEDC) in Nigeria. From literature, the loss of a phase in a three phase system is an extreme form of voltage unbalance (Altaf et al, 2019). Computer Numerical Control (CNC) machines e.g. CNC lathe, Vertical Machining Centre (VMC) and other sophisticated machines require to maintain specific rotational direction for the safety of the machine as well as the personnel. Hence, phase reversal means reversal in rotational direction to these machines which is not healthy for them. Non electrical conditions such as bearing fault, faulty cooling fan, and misalignment of shaft as well as overloading can cause induction motor failure. This, likewise some supply voltage conditions, primarily cause rise in winding temperature of an induction motor. Using the available technology, a system to monitor the conditions of the supply input voltages such as the voltage level (overvoltage and under voltage), voltage unbalance, voltage sequence reversal, single phasing has been developed. The system, in addition, monitors the temperature of the three phase induction motor while in operation. Unlike other designed/developed systems, this system monitors all the input voltage conditions to three phase induction motors. It also displays the fault and blows an alarm.

From the reviewed literature, Ammanuel et al., (2021) and Shivpuje et al., (2017) designed a system that monitored three phase power supply to an induction motor and shuts down the supply to the induction motor on detection of faults which they enumerated. Youvanshippa (2019) work was mainly to control the speed and direction of induction motor through a GSM module sim. Basim et al., (2020) performed an experiment under balanced normal supply voltages and single phasing conditions of an induction motor. The authors established that under single phasing

conditions of an induction motor, there is speed reduction of the motor. Efri et al (2022) worked on the detection and protection of disturbance in a three phase induction motor. In summary, studies, analysis and designs on induction motor monitoring and protection have not considered all the factors that cause induction motor failures such as over/under voltage, voltage sequence reversal, single phasing and voltage unbalance at once. In the majority of the studies, temperature was not considered in the design which could result from non-electrically related faults. The focus of this paper is to experimentally investigate the effects of voltage related faults on a three phase induction motor and develop a system to monitor and protect the induction motor. Additionally, the developed system will monitor the temperature of the motor while in operation.

2 METHODOLOGY

The development of this system was done in two phases; the simulation and development of the simulated system. Prior to that, to ascertain the voltage limits for the system, a 1.1kW induction motor was experimentally verified. A modular method was adopted in this research work whereby the constituent units were designed, implemented and tested independently before integrating them for final performance test. The developed system result validates the simulation result.

2.1 EXPERIMENTAL ANALYSIS OF A THREE PHASE INDUCTION MOTOR

A 1.1kW three phase induction was experimentally analysed to determine the voltage limits of the proposed system. Table 1 shows the rated parameters of the induction motor. The experimental set up is as shown in Plate 1. The various components of the experimental set-up are (1)-Basic machine trainer, (2):1.1kW three phase induction motor, (3): Temperature controller and thermocouple, (4): Clamp ammeter and (5): Tachometer. The experiment was perform under different conditions of voltage supply. In the three phase supply, we have normal voltage (3Ø NV), normal minimum voltage (3Ø NVmin.), normal maximum voltage (3Ø NVmax.), under-voltage (3Ø UV), overvoltage (3Ø OV), minimum voltage unbalance (3Ø Vbal(min)), maximum voltage unbalance (3Ø Vbal(max)), In two phase voltage supply, we have normal minimum voltage (2Ø NVmin), normal maximum voltage (2Ø NVmax) and in the single phase supply, we have minimum normal voltage (1Ø NVmin) and maximum normal voltage (1Ø NVmax). The Machine trainer was powered by a three phase AC supply.

TABLE 1: PARAMETERS OF THE INDUCTION MOTOR FOR THE EXPERIMENTAL ANALYSIS

Motor Parameter	Value
Power	1.1kW
Voltage	230/400V
Rated Speed	1450 r. p. m.
Synchronous speed	1500 r. p. m.
Power Factor	0.81

The red phase was used as the reference phase and the phase to neutral voltage (phase voltage) of the red phase was set at 230V and the value recorded.The phase voltages of the yellow ( ) and blue ( ) phases were measured using a multimeter. The machine trainer was then de-energized. This is to avoid single phasing effect while connecting the three phase induction motor.

The 1.1kW induction motor was connected to the basic machine trainer as shown in Plate 1. Thereafter, the machine trainer was powered and the motor allowed to run for one minute. The line currents drawn by the motor was

Plate1: Experimental set-up

measured using a clamp ammeter and the speed also measured using a tachometer. The experiment was then repeated by setting the reference voltage to 207V, 253V, 200V and 260V. The trainer was de-energised. The reference voltage was then set at 207V while others were respectively adjusted to 209V and 207V. The machine trainer was then powered. The currents and speed was measured. This was repeated by setting the reference voltage to 253V and adjusting the yellow and blue phases to 251V and 253V, respectively. The machine trainer was again de-energised. The position of the red and yellow phases supplying the motor terminals were interchanged and the motor powered, same was repeated with red and blue, then yellow and blue. The reference voltage was again set to 207V, the yellow phase adjusted to 207V while the blue phase was temporarily removed and the motor powered for 30 seconds. The trainer was switched off. The same was repeated with the reference and yellow phases set at 253V. Again the trainer was de-energised. The red and blue phases were removed and the yellow phase adjusted to 207V. The motor was powered for 30 seconds and the system again de-energised. The experiment was repeated with the yellow phase set at 253V while red and blue phase was still removed. At every instant, the current drawn by the induction motor was measured. The results obtained from the experimental analysis was used to determine the voltage limits of the enhanced system for monitoring and protection of three phase induction motor. The limits were chosen to be 253V and 207V based on NEMA standard.

2.2 HARDWARE DEVELOPMENTS

The hardware design is depicted in Figure 2.2. It comprises power supply unit, three phase rectifier, electromagnetic switches (contactor and relays), reset and selector switches, microcontroller, three pole circuit breaker and LCD display

2.3 SOFTWARE DEVELOPMENT

The software development involves writing the programme, compilation and programming of the microcontroller. A mikroC Pro programming language, MiniPro TL866 universal Programmer and hexadecimal code were used for the programme.

2.4 FAULT VOLTAGE PARAMETERS

The fault voltage parameters monitored by the system include: Voltage unbalance (under-voltage unbalance and overvoltage unbalance), Overvoltage, Under-voltage, Single phasing and Voltage sequence reversal.

Design Calculations: The voltages of the three phase are designated as V_R, V_Y, and V_B, representing the Red, Yellow and Blue Phases respectively**.** According to National Electrical Manufacturers Association (NEMA) standard, induction motors are designed to operate satisfactorily at a voltage variation of plus or minus ten percent (10%)
Voltage Unbalance = (Maximum deviation from the rated voltage)/ (Average voltage) (NEMA)

Taking a standard voltage of 230V, $10\% \times 230V = 23V$
Maximum allowable voltage, $V_{max} = 230 + 23 = 253V$

Minimum allowable voltage: $V_{min} = 230 - 23 = 207$

Voltage Unbalance: In this design, the voltage unbalance is considered at two extremes; Overvoltage unbalanced and under-voltage unbalanced. Let the average Instantaneous Voltage be 253. Then, the voltage unbalance is 23/259 given 0.09.

Maximum unbalance voltage: $230 \times 1.09 = 250.7V$.
Minimum unbalance voltage: $230 \times 0.91 = 209.3V$.

$$V_{AV} = \left(\frac{V_R + V_Y + V_B}{3}\right) \quad (1)$$

Overvoltage Unbalance Fault: This is taken to occur when the voltage is two percent above the average instantaneous voltage of the three phases:

$$\left(\frac{V_R+V_Y+V_B}{3}\right) \times 1.09 \quad (2)$$

Under-voltage Unbalance Fault: This is taken to occur when the average voltage on the three phases is two percent below the average instantaneous voltage

$$\left(\frac{V_R+V_Y+V_B}{3}\right) \times 0.91 \quad (3)$$

Overvoltage and Under-voltage: By NEMA standard induction motors can operate normally at ±10% of the rated value on the nameplate. With a rated voltage of 230V, this implies that the machine can operate normally within the voltage range of 207V and 253V, inclusive. Therefore, by calculation, in this design, the overvoltage condition occurs when any or all of the supply voltages is greater than 253V while the under-voltage condition occurs when one or all of the voltages supplied is less than 207V.

Voltage Sequence reversal and single phasing: The system is programmed to maintain the voltage sequence $V_R - V_Y - V_B$. Normally, changing the sequence to $V_Y - V_R - V_B$ will result to the reversal in direction of the induction motor, and to $V_Y - V_B - V_R$, the induction motor reverses again. The system maintains only one sequence. The system is designed such that all the voltages of the

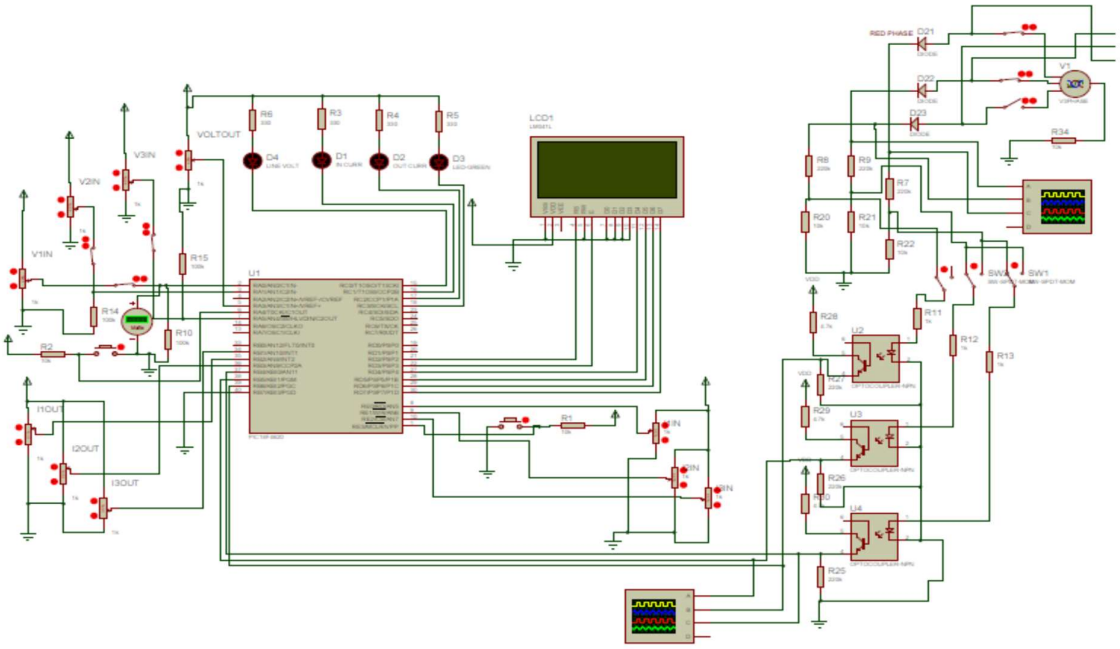

Plate II: Circuit diagram of the system

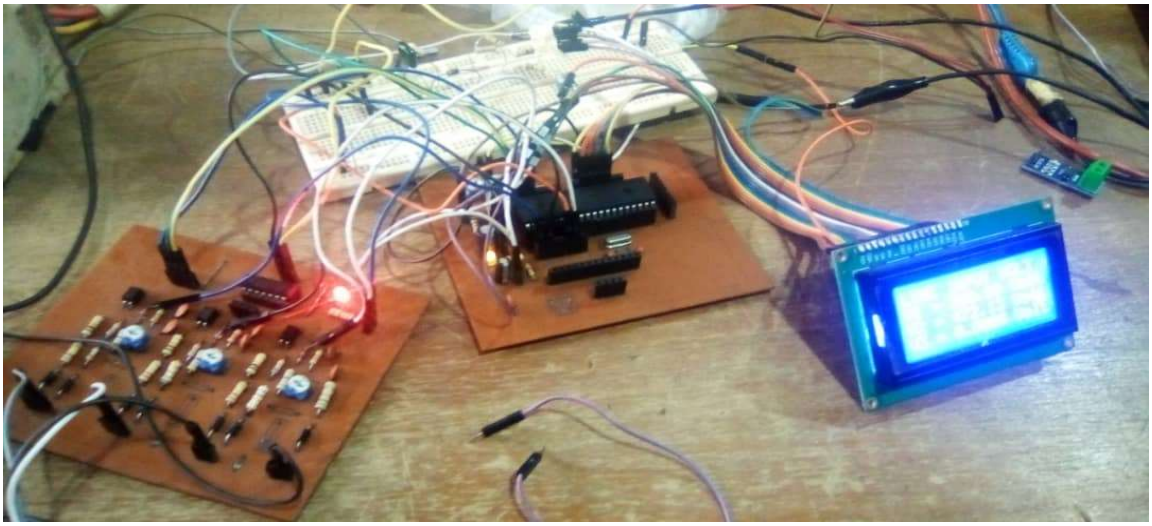

Plate III: Hardware layout

three phase power supply must be present before the induction motor operates.

3 RESULTS AND DISCUSSION

Experimental result verification: Here the results of the behavior of a three phase 1.1 kW induction motor when subjected to the various input voltage conditions is presented. The result obtained when the 1.1kW three phase induction motor was subjected to different voltage levels is as shown in table 2.

TABLE 2: EXPERIMENTAL ANALYSIS OF A 1.1KW THREE PHASE INDUCTION MOTOR

SUPPLY VOLTAGE	V_R (V)	V_Y (V)	V_B (V)	I_R (A)	I_Y (A)	I_B (A)	Speed
3Ø NV	230	228	231	2.3	2.2	2.3	1450
3Ø NV_{min}	207	206	208	2.1	2.0	2.1	1450
3Ø NV_{ma}	253	251	255	2.5	2.5	2.8	1450
3Ø UV	200	199	201	2.0	2.0	2.0	1450
3Ø OV	260	258	260	2.6	2.6	2.6	1450
3Ø $V_{bal\ (min)}$	209	207	200	2.1	2.3	2.0	1450
3Ø $V_{bal\ (max)}$	251	248	252	2.5	2.7	2.5	1450
2Ø NV_{min}	207	206	0	3.1	3.1	0.0	0.0
2Ø NV_{max}	253	251	0	3.9	3.8	0.0	0.0
1Ø NV_{min}	0	207	0	0.0	6.1	0.0	0.0
1Ø NV_{max}	0	253	0	0.0	6.0	0.0	0.0

TABLE 3: RESULT OF 1.1KW IM ON PHASE SEQUENCE REVERSAL CONDITION

Voltage Sequence	Direction of rotation
$V_R - V_Y - V_B$	Clockwise
$V_Y - V_R - V_B$	Counter clockwise
$V_Y - V_B - V_R$	Clockwise

Simulation and the designed system performance tests result

On subjecting the system to the various fault conditions by varying the supply input voltage, the system was able to protect the induction motor from these adverse voltage conditions by blocking supply to the motor input terminals, displays the fault and blows an alarm. The following tests were carried out: Overvoltage, under-voltage, and Voltage Sequence Reversal, Single Phasing, and Voltage Unbalance tests.

TABLE 4: SIMULATION TEST RESULT

Supply Voltage	Percentage Voltage (%)			Voltage Reading (V)			LCD Display
	V_R	V_Y	V_B	V_R	V_Y	V_B	
3Ø NV	74	74	74	229.07	229.07	229.07	Ok.
3Ø NV_{min}	67	67	67	207.25	207.25	207.25	Ok.
3Ø NV_{max}	82	82	82	253.91	253.91	253.91	Ok
3Ø UV	65	65	65	200.89	200.89	200.89	Ok.
3Ø OV	84	84	84	259.97	259.97	259.97	Ok.
3Ø$V_{ba(min)}$	67	68	67	207.25	210.28	207.25	Ok.
3Ø$V_{bal(Max)}$	82	81	82	253.91	250.58	253.91	Ok.

Discussion: The results are discussed under the following headings.

1.1kW induction motor in single phasing condition

From table 4, under three supply voltage conditions to the induction motor, the currents drawn by the various phases is balanced and the motor maintained a constant speed of 1450 r. p. m. However, under single phasing conditions, the currents drawn by the phases were unbalanced and the motor remained stationary. As can be observed also from table 4, for 2Ø$NV_{min,}$ 3.1A was drawn by both the red and blue phases whereas for 2Ø$NV_{max,}$ 3.9A was drawn by the red phase while 3.8A was drawn by the yellow phase. With the red and blue phases isolated, the motor was also stationary and humming. The current drawn by the yellow phase was 6.1A for 1ØNVmin and 6.0A for 1ØNVmax conditions.

1.1kW induction motor on phase sequence reversal condition

It was observed as recorded in Table 4.4 that with the voltage sequence, the induction motor rotated in a clockwise direction, with, the direction changed to counterclockwise and with the motor reverses back to clockwise.

TABLE 5: SIMULATION TESTS RESULT OF THE DESIGNED SYSTEM ON 3-PHASE OVER/UNDER VOLTAGE AND VOLTAGE UNBALANCE, 1-PHASE AND 2-PHASE CONDITIONS

Supply Voltage	Percentage voltage setting (%)			Voltage Reading (V)			LCD Display
	V_R	V_Y	V_B	V_R	V_Y	V_B	
3Ø UVf	58.00	58.00	58.00	179.38	179.38	179.38	Under-voltage
3Ø OVf	85.00	85.00	85.00	263.00	263.00	263.00	Overvoltage
3Ø Vbal (f)	61.00	65.00	65.00	188.97	200.89	200.89	Voltage unbalance
2Ø NV	74.00	74.00	0.00	229.07	229.07	0, 00	Single Phase Fault
2Ø NVmin	67.00	67.00	0.00	207.25	207.25	0.00	Single Phase Fault.
2Ø NVmax)	82.00	82.00	0.00	253.91	253.91	0.00	Single Phase Fault
1Ø NVmin	0.00	67.00	0.00	0.00	207.25	0.00	Single Phase Fault
1Ø NVmax	0.00	83.00	0.00	0.00	253.91	0.00	Single Phase Fault

TABLE 6: DESIGNED SYSTEM OVERVOLTAGE, UNDER-VOLTAGE, SINGLE PHASING AND VOLTAGE UNBALANCE TESTS RESULT

Voltage Voltages (V)			LCD display	Motor Status
V_R	V_Y	V_B		
261	261	261	Overvoltage	Stopped
260	260	260	System Ok.	Ran
260	230	240	Voltage unbalance	Stopped
220	190	220	Voltage unbalance	Stopped
0.0	200	200	Single phase fault	Stopped
180	180	180	System Ok.	Ran
160	126	0.0	Under-voltage	Stopped

TABLE 4.8 DESIGNED SYSTEM VOLTAGE SEQUENCE REVERSAL TEST

Voltage Sequence	Motor Status	Motor Direction
$V_R - V_Y - V_B$	Ran	Clockwise
$V_Y - V_R - V_B$	Stopped	No rotation
$V_Y - V_B - V_R$	Stopped	No rotation

Discussion of Simulated and Developed System Tests Result

The simulated system and developed system gave results as discussed below.

Simulated system test result

The simulation result in Table 4.5 shows that, when the settings were varied to 74% representing a phase voltage of 229.07V for each phase, the system displayed 'System OK'. At voltage setting of 67% for each phase representing a phase voltage of 207.25V, the system operated normally displaying 'System OK'. When each line voltage was varied to 82%, representing 253.91V, the system displayed 'System OK'. With the setting 65% for V_R, V_Y and V_B, representing 200.89V each, the system displayed 'System Ok'. Setting the voltages to 84%, the system displayed 'System OK'. When the red phase was set at 67%, yellow phase 68% and blue phase 67%, representing 207.25V, 210.28V and 207.28V, respectively, the system displayed "System OK". This represent the minimum tolerable voltage unbalance condition. On red and blue phases setting of 82%, respectively and yellow phase, 81%, 'System Ok.' was displayed. From table 4.6, it can be observed that running the system at 61%, 65% and 65%, representing 188.97V, 200.89V and 200.89V for the red, yellow and blue phase voltages respectively, the simulated system displayed "Voltage Unbalance Fault". On isolation of one or two phases, "Single Phase Fault" was displayed. From the table also, 85% setting, representing 263V phase voltages respectively, "Overvoltage Fault" was displayed by the system. With 58% setting, representing 179.38V phase voltage each, the system displayed "Under-voltage Fault".

Developed system test result

The developed system was able to monitor overvoltage, under-voltage, single phasing and voltage unbalance as can be observed in table 4.7. Likewise, table 4.8 shows that on reversal of the voltage sequence, the motor did not run, showing that the system has protected the motor from phase reversal fault.

Generally, the system blows an alarm in every fault detected and the alarm continues until the reset button is actuated after the fault is fixed. The selector switch is used to check the condition of the various monitored parameters. It is interesting to note that in every test performed and fault detected, zero voltage (0V) was recorded at the output of the device.

4 CONCLUSION

In this paper, a system to monitor and protect three phase induction motors from adverse supply voltage conditions and high winding temperature has been developed and performance test on the developed system carried out. The system was able to monitor adverse supply voltage conditions to the motor, detects same and protect the motor. With the use of the system, induction motors will be protected and the failure rate of induction motors in the industries will be reduced, if not totally eliminated.

REFERENCES

[1] Altaf, S., Mehmood, M. S. & Soomro, M. W. (2019). *Advancement of fault diagnosis and detection process in industrial machine environment*.

[2] Amanuel, T., Ghirmay, A., Ghebremeskel, H., Ghebrehiwet, R. & Bahlibi, W. (2021). Design of Vibration Frequency Method with Fine-Tuned Factor for Fault Detection of Three Phase Induction Motor. *Journal of Innovative Image Processing (JIIP)*, *3*(01), 52–65.

[3] Basim, A. (2020). Experimental Investigation and Analysis of Induction Motors operation under Single Phasing. Palestine Technical University Reseach Journal, 8 (2), 90-99.

[4] Bodkhe, M. P. & Pawar, K. N. (2015). *Monitoring and Control System for Three Phase Induction Motor Using Poly Phase Multifunction Energy Metering IC ADE7758 and Zigbee Protocol*.

[5] Bouhoune, K., Yazid, K., Boucherit, MS, Cheriti, A. (2017). Hybrid Control of the three phase induction machine using artificial neural networks

and fusy logic. Applied soft computing-Elsevier.

[6] Efri, W. H., Adi, S. P. T., Solly, A. (2022).Improved Micocontroller-Based 3 Phase Induction Motor Protection From A Variety of Interruptions. International Journal of Economic, Technology and Social Sciences. Volume 3, Number 1, Page 227-239.

[7] Frosini, L., Harli\csca, C. & Szabó, L. (2014). Induction machine bearing fault detection by means of statistical processing of the stray flux measurement. *IEEE Transactions on Industrial Electronics*, *62*(3), 1846–1854.

[8] Garcia-Calva, T., Morinigo-Sotelo, D., Fernandez-Cavero, V. & Romero-Troncoso, R. (2022). Early Detection of Faults in Induction Motors—A Review. *Energies*, *15*(21), 7855.

[9] Gedzurs, A. (2015). *TEMPERATURE PROTECTION METHODS OF INDUCTION MOTOR*.

[10] Haddad, R. Z. & Strangas, E. G. (2016). On the accuracy of fault detection and separation in permanent magnet synchronous machines using MCSA/MVSA and LDA. *IEEE Transactions on Energy Conversion*, *31*(3), 924–934.

[11] Hussain, M., Ahmed, R. R., Hussain, I. & Memon, T. D. (2020). Multiple faults detection and identification of three phase induction motor using advanced signal processing techniques. *3c Tecnolog{\'\i}a: Glosas de Innovación Aplicadas a La Pyme*, *9*(1), 93–117.

[12] Mohanty, A. R. (2014). *Machinery condition monitoring: Principles and practices*. CRC Press.

[13] Mustafa, M. O. (2015). *On fault detection, diagnosis and monitoring for induction motors*. Luleåtekniska universitet.

[14] Namdar, A. (2022). A robust principal component analysis-based approach for detection of a stator inter-turn fault in induction motors. *Protection and Control of Modern Power Systems*, *7*(1), 48. https://doi.org/10.1186/s41601-022-002.

[15] Ogbuka, C. U. & Bassey, O. (2014). Protection Method against Induction Motor Single-Phasing Fault. *Int. J. of Innovative Technology and Exploring Engineering (IJITEE)*, *4*.

[16] Panagiotou, P. A., Arvanitakis, I., Lophitis, N. & Gyftakis, K. N. (2019). Frequency Extraction of Current Signal Spectral Components: A New Tool for the Detection of Rotor Electrical Faults in Induction Motors. *2019 IEEE 12th International Symposium on Diagnostics for Electrical Machines, Power Electronics and Drives (SDEMPED)*, 290–296. https://doi.org/10.1109/DEMPED.2019.8864893

[17] Prabakaran, S. & Venkatesan, S. (2018). Analysis of 3 phase Induction Motor Protection Using Numerical Relay. *Int. J. Eng. Tech*, *4*, 513–519.

[18] Sabarivani, A., Panda, P. K., Varma, U. & Marshiana, M. (2022). Smart monitoring and controlling of an industrial three-phase induction motor. *AIP Conference Proceedings*, *2452*(1), 20002. https://doi.org/10.1063/5.0113196

[19] Scarpino, M. (2015). *Motors for Makers: A Guide to Steppers, Servos, and Other Electrical Machines*. Que Publishing.

[20] Sheikh, M. A., Bakhsh, S. T., Irfan, M., Nor, N. bin M. & Nowakowski, G. (2022). A Review to Diagnose Faults Related to Three-Phase Industrial Induction Motors. *Journal of Failure Analysis and Prevention*, *22*(4), 1546–1557.

[21] Shivpuje, R. M. & Patil, S. D. (2017). Microcontroller based fault detection and protection system for induction motor. *2017 International Conference on Intelligent Computing and Control Systems (ICICCS)*, 1187–1191.

[22] Swapnil, K. G. & Prasad, V. K. (2021) . Condition Monitoring and Fault Diagnosis of Induction Motor. Journal of Vibration Engineering & Technology volume 9, pages 643-674

[23] Teguia, J. B., Kenne, G., Kammogne, A. T. S., Fouokeng, G. C. & Nanfak, A. (2021). The Detection of Inter-Turn Short Circuits in the Stator Windings of Sensorless Operating Induction Motors. *World Journal of Engineering and Technology*, *9*(3), 653–681.

[24] Wang, W. & Li, D. D. (2015). Health Condition Monitoring of Induction Motors. In R. I. G. Recalde (Ed.), *Induction Motors*. IntechOpen. https://doi.org/10.5772/61110

[25] Yazici, B. & Kliman, G. B. (1999). An adaptive statistical time-frequency method for detection of broken bars and bearing faults in motors using stator current. *IEEE Transactions on Industry Applications*, *35*(2), 442–452.

[26] Youvanshippa (2019). 3-Phase Induction Motor Protection and Condition DETEC
system using PIC18F452 Microcontroller. International Journal of Engineering & Technology (IJERT) Vol. 8 Issue 8.

4th International Engineering Conference (IEC 2022)
Federal University of Technology, Minna, Nigeria

Development of A Heat Removal Device from Motorcycle Exhaust Using Copper Fin

*Ogungbemi K. E, Bori, I[1]
[1]Mechanical Engineering Department, Federal University of Technology, PMB 65 Minna Niger State, Nigeria
*Corresponding author email: kayllion4@yahoo.com +2348036860342

ABSTRACT

Contact-burn by Motorcycle exhaust is a common phenomenon and it's a challenging type of injury to manage, the burns sometimes penetrate very deep through the skin and into the muscle, particularly, that of the passengers, although, the duration of contact with the hot exhaust determine the depth and severity of the injury which is classified as first, second or third degree burn. Burns from Motorcycles are avoidable, however, no matter how careful one is, still, burns happen. The first step in treating an exhaust burn is to determine its type whether it is first, second, or third degree. The most effective way to determine the type of burn is to evaluate the extent of the damage caused by the trauma – or rather, to be more specific, the layer of skin affected by the burn. The more layers of skin damaged by the injury, the more serious the condition will be. Motorcycles has become a means of transportation in Nigeria for some year now, both young and old-adult prefer motorcycle as means of transportation that is why exhaust burn is a common phenomenon within this age bracket. This work is all about the idea to reduce and ultimately eradicate the thermal-burns when one has contact with motorcycle exhaust and that is what gave birth to fabrication and development of a heat removal from the exhaust of a motorcycle. The device was fabricated using pure copper, copper is considered because of it high thermal conductivity. Copper plate was not an easy commodity to find in the market, however, two inches' copper pipes was cut open to form the plate and from the plates fins was made. Fins are used in a large number of applications to increase the heat transfer surfaces. A fin has been defined as extended surface to enhance heat transfer rate to the surrounding, fins are usually used in heat exchanging devices such as car radiators computer CPU and heat exchangers, these knowledge is what is brought to bear in reducing heat from a motorcycle exhaust. Adding a fin to an object increases the surface area and can become a simple and economical solution to heat transfer problem. The key result here is that the use of copper fin has greatly reduce the temperature at the tail end of motorcycle exhaust which is also the area where contact burn usually take place. From the performance test and evaluation, the use of copper fin has proof to be more efficient than the Aluminium fins that was used in the previous study.
Keywords: *Provide between four to six keywords arranged in alphabetical order.*

1.0 INTRODUCTION

Most motorcycle use internal combustion engine, either a two-stroke or a four stroke engines, depending on the choice of the maker. According to the name "internal combustion Engines" are prime movers that derive its name from burning of gases in an enclosed chamber through the spark of ignition, the result of the combustion is that the burnt gases will generated heat and a pipe or exhaust or silencer that is connected to the combustion chamber is to take this burnt gases out conveniently to the atmosphere. This burnt gases will of course leave hotness in the exhaust pipe or the silencer as the case may be, which portent hazards to the users of the motorcycles worldwide, according to Oyesiku (2002), the study covers Nigeria as a territorial area while drawing specific examples from Lagos, which is regarded as the hustling and bustling commercial nerve center of Nigeria and a number of cities within the nation. The makeup of Okada transportation business in these places portrays to a large extent, the pattern of use in the rest of the country. It is only in few cases that an individual will find minor changes. Motorcycles remain the major means of commercial transport system which possesses the largest percentage of intra-city transportation within Nigeria due to its simplicity, reliability, convenience and low cost of mobility in developing countries. It is sometimes considered as a preferable source of movement and this has showed in the increasing amount of owners in Nigeria. Due to the rising amount of users and increasing preference for motorcycle over other means of transportation, it has become very important to consider its effect with respect to the likely injuries that may be caused by its use.

Matzavakis (2005) stated that one of the primary injuries that is commonly sustained from the use of motorcycle is Motorcycle burn; which is mostly sustained by the user and/or passengers of motorcycle through direct contact with overheated parts of the motorcycle. Burns resulting from contact with exhaust pipe and other parts of the motorcycle have different degree of severity in which some of the cases are not devastating.

Stuart Pegg Paediatric Burns Centre has taken note of the amount of people that were admitted with thermal burns as a result of coming in contact with a hot motorbike exhaust

pipe. The burns are usually related to major morbidity. The temperature of the 'bent' surface of exhaust pipe through which exhaust gases are flowing, falls between the range of 150 to 180°C which poses a serious threat to motorcycle users when there is a direct contact, thus, by attaching a copper fins to this bent exhaust pipe using bolt and nut, the degree of hotness at the outlet pipe will reduce to barest minimum temperature.

Injuries caused by contact with a hot motorbike exhaust are not very common as other motor accidents. Contact burns caused by the exhaust pipe of motorcycles are rarely reported. None of the cases in our study had a third degree burn or had to be admitted to a hospital. However, several authors describe cases of third degree burns, some of which required debridement and grafting with autologous split skin. This shows that this type of burn can be eventually severe, leaving behind scars with a long duration of cicatrization. Some characteristic features of these injuries have been demonstrated by our study. The majority of victims were young females, and are most of the times passengers of the motorbike. Contrary to other studies, in our country, children seem to be very often affected by this type of accident. The fact that the risk of burns among children was twice that among the rest, shows that motorbikes are inappropriate for children, even if riding with their parents. This could be due to the fact that neither parents nor children themselves realize the danger of being close to a hot motorcycle exhaust pipe. It is impressive that in two described cases, the victims were a baby of 16 and another of 17 years respectively, who had sustained burns, when their parents carried them on Motorcycle, either during getting on or off the motorbike. Most of the contact burn wounds happened during warmer seasons (70.5% of them in the summer) and it could be explained by the fact that during these periods, the use of motorcycles rises and besides, people wear less clothing or the clothing they wear is very thin and does not provide adequate protection. The greater part of these burn wounds occurred on the calf (86.1%) and mainly on the right leg. This is because the design of the motorcycle favours the proximity of the right leg to the silencer and leads to increased number of burns by contact.

The results suggest that a large part of the burn injuries are preventable. In particular, we found that the simple measure of wearing long pants, compared to short dress, can substantially reduce the risk of burn. Moreover, some manufacturing changes, such as better design of external shields utilizing thermo-resistant materials, with adequate distance from the exhaust pipe would also help further reduce the risk of burn, though, at a larger cost. In parallel, parents should adopt a safer behavior with regard to motorcycles by avoiding to use them as means of transport for their young children, whereby avoiding other dangers of traffic injuries. Lastly, we suggest that parking lots for motorcycles be developed by leaving enough space between motorcycles for pedestrians. These changes could lead to a clear decrease of motorcycle exhaust pipe burns, making the motorcycle a safer way of transportation says Ibeanusi SE, Kejeh B (2018).

1.1.1 **What is an exhaust: -** these days, the exhaust pipes on motorbikes are complex – with every component designed for a purpose. For the purpose of defining it here; we can define an exhaust system as **a "system to collect the exhaust gases from the cylinders, removes harmful substances, reduces the level of noise and discharges the purified exhaust gases at a suitable point of the engine away from its occupants". The exhaust system can consist of one or two channels depending on the engine type.**

1.1.2 An exhaust is designed to blow any carbon monoxide your motorcycle creates away from you (or your passenger). It's pretty simple really. Hot air blows out behind the bike, so you're not breathing in any toxic gases. And most exhausts also help to convert that carbon monoxide into carbon dioxide. This means it's better for the environment. Another great news is that exhausts can also take away some of the noise of the engine. Without a muffler, the engine sound can be terrifyingly loud. Try it out by removing the engine muffler or just agree with this study-assertion . And of course, they help the motorbike engine run better; the exhaust pipe and engine are designed to run well together. And it ensures all the hot air the engine produces flows efficiently – the right way. There are other technicality here about exhaust but it's not within the scope of this work. Motorcycle exhaust systems are always in chrome or chrome-coated. They come in three distinct varieties. Twin cylinder flows the gases into separate sections. Single cylinder flows into one section, while larger engines which you find on newer sports bikes (such as the kawasaki zx series or other superbikes) actually have four cylinders.

There are five main parts of a motorcycle exhaust:

(1) Piping: The Exhaust pipes are made from stainless steel or chrome coated steel. They are designed to carry the carbon monoxide from the manifold of the exhaust to the rest of the system. They can be gotten in different shapes and sizes, depending on the Motorcycle model and the performance level being considered.

(2) Exhaust Manifold: This is a single part, or tubing, that moves gases from your engine to the pipe. There might be a number of cylinders for the gas to come from. Or it could be a header manifold, which operates on a singular cylinder. Usually, this is made of cast iron or stainless steel,

but they can be customized. The exhaust system is itself a system subject to vibration, it produces noise itself through natural frequencies and vibration which are transmitted to the Motorcycle body. Careful coordination of the entire system is therefore necessary here. This includes design and positioning of the individual elements of the exhaust system and their flexible mountings.

(3) Catalytic Converter: This is basically the part of the exhaust that prevent breathing-in of poisonous gas. It converts the carbon monoxide, nitrogen oxides, and hydrocarbons into nitrogen, carbon dioxide, oxygen, and water. This is, of course, much less harmful to the occupant (and the planet). Also, every internal combustion engine produces "exhaust noise" due to the pulsating emission of gases from the cylinders. This noise has to be silenced by reducing the sound energy of the exhaust gas flow. There are two basic options here: Absorption and reflection of the sound in the silencer. These two principles are generally combined in a single silencer. Exhaust chambers and exhaust flaps are other sound-absorbing and sound-modifying elements that can be used to eliminate especially undesirable frequencies from the outlet noise. Catalytic converters also have a sound-absorbing effect. The flow resistance must be selected so that the exhaust backpressure affects engine performance as little as possible.

(4) Oxygen Sensor: Oxygen sensor are not always incorporated in all exhaust; however, we have to discuss it here since we are discussing components of exhaust, the functions are to measure the amount of oxygen leftover after combustion, too much of oxygen left over in the combustion chamber will determine the amount of fuel to be injected in the next cycle.

(5) Hanger: Most motorcycle exhaust runs from the front to the rear side of the motorcycle; the length of the exhaust pipe will determine the number of hangers to hold the exhaust in place in other to absorb the vibrations from the engine. There is no need of a specific design of hanger; if hanger got damaged or missing, the exhaust will drag on the floor and get damaged.

Other functions

In addition to all the complex functions which the exhaust system has to perform, it is also subject to extreme stresses. The fuel-air mixture in the cylinders is abruptly heated to temperatures up to 2,400 °C. This causes it to expand greatly before escaping into the exhaust system at supersonic speed. This noise level resembles the crack of an explosion and must be reduced by approx. 50 dB(A) as it travels from the engine exhaust valve to the end of the exhaust system. At a temperature of up to 2,400 °C in the shinning Chrome plated exhaust, it is this resulting heat that often cause severe burns when it accidentally touches the leg of the rider or the passenger. Apart from temperature and pressure stresses, the exhaust system must also cope with vibrations from the engine. The exhaust system additionally has to resist corrosion attacking from the inside caused by hot gases and acid, and from the outside in the form of moisture, splashed water and salt water. There is also the risk that the catalyst may be poisoned through Sulphur or lead present in the fuel.

Burns caused by Motorcycle Silencer

Exhaust burn happens when the rider or the passenger accidentally makes physical contact with the exhaust pipe. The exhaust pipe is one of the hottest parts of the bike, and contact with it can result in a severe burn. A study in Greece found that most of the injuries took place when getting on or off the motorcycle, and the most common spot for a burn was on the right leg below the knee. An estimated 65 percent suffered second-degree burns.

Here are a few ways you can prevent motorcycle exhaust pipe burn:

- Wear long pants to reduce the risk of burns by 46 percent.
- Use caution when getting on or off the motorcycle.
- Avoid contact with the exhaust when picking up a fallen bike.
- Use extra caution when a child is riding as a passenger. Children account for most motorcycle exhaust burns, and 33 percent of burned children required surgery, according to an Australian hospital.

Classification of Burns

Motorcycle exhaust burn varies depending on the severity of the burn. Most motorcycle exhaust burns are second- or third-degree burns. One study found that burns tended to subside after twenty days. If you can feel pain or tingling, that is a good sign; if the leg is numb, you should seek medical attention immediately. All types of burns can be painful and produce visible symptoms. Understanding the kind of burn and its severity is essential when assessing medical treatment. Burns are classified as first, second third degree or fourth degree depending on its severity in penetrating the skin surface.

1. First Degree burns: First-degree burns are the least severe. In fact, you've probably had at least a few of them, as sunburn is a classic example, a first-degree burn is also called a superficial burn or wound. It's an injury that affects the first layer of your skin. First-degree burns are one of the mildest forms of skin injuries, sometimes it is overlooked

and they usually don't require medical treatment. However, some superficial burns can be quite large or painful and may require a trip to a doctor.

2. Second Degree Burns: Once a burn starts to blister, it's classified as a second-degree burn. a **second-degree burn** involves the second layer of the skin called the dermis, in addition to the blisters, these burns are more painful — and more worrisome. With second-degree burns, there is risk of secondary infection and scarring, especially with a deeper second-degree burn,

3.Third degree Burns: Then, there are the seriously severe burns, classified as **third-degree**. These burns reach completely through the skin and into the fat, muscle, and nerves below, It's a major injury. In these cases, the skin can literally appear charred (either black or white) and leathery. Since these burns can destroy the nerves, they might not actually be painful, despite their severity.

Figure1: A picture of first degree burns of a motorcycle exhaust pipe. Exhaust burns.

Source: https://www.fixyourdirtbike.com>first-aid

Figure2: A picture of seconds degree burns caused by hot exhaust pipe of a motorcycles. Source : https://www.fixyourdirtbike.com>first-aid

Figure3: A picture of a third degree burn caused by hot exhaust pipe of a motorcycle. Source: https://www.fixyourdirtbike.com>first-aid

When to Seek Medical Attention for a Burn

While most minor burns are not big, the more severe burns always require professional attention. "If you have large blisters or any signs of infection, such as oozing or increased pain, go to the doctor," Chaffin says. If your burn hasn't healed after two weeks, this is a reason to see a medical professional as well. The severity of the burn isn't the only thing that should dictate when you see a doctor. The location of the burn also matters, Chaffin says. Any burn on a sensitive area, like your face or genitals, could warrant professional attention. Extra care may be needed for burns on your joints. Here's why: "Especially with a second-degree or deeper burn, as it heals it can create scarring of the tissue. "If that happens in the area of a joint," — say, your hands after a bad mishap in an accident — "scarring during healing can impair normal movement," she says. "A doctor can provide the best healing process and even arrange physical therapy, if necessary." The bottom line: Minor burns are nothing to worry about as long as you treat them properly. Stay hydrated, keep burns clean and moist, and watch out for any sign of infection. If your burn seems to be getting worse or more painful, see your doctor.

Figure4: (Source:https://ong.ng/beju-lekki/vehicles/motorcycles-and-scooters/bajaj-boxer-2018-red-15517.html)

2. METHODOLOGY

2.1 The Fin Concept as Remedy

As the popular saying goes, “Safety first and always”, Nothing would have been bad if one could avoid those categories of burns that was already explained above, particularly from a Motorcycle. This is where lies the concept of introducing Fins to help curtail and reduce temperature along the exhaust pipe and to dissipate the hotness that is enough to cause harm when there is accidental contact with the exhaust of a Motorcycle.
The convection of removing thermal from a layer will be well improved if extensions are placed on that surface to extend its space. These extensions or protrusions known as fins primarily create open surface where the hotness from the engine are absorbed and natural air through convective process are removed before getting to the area where human can have contact with the exhaust. The transfer rate of heat energy from the surface to the fin is by conduction and fin to surroundings is by convection with an identical heat transfer constant, h. If a surface is exposed to a fluid at temperature *T* flowing over the surface and the wall is bare and the surface temperature *Ts* is fixed, the rate of heat transfer per unit area from the plane wall is controlled entirely by the heat transfer coefficient *h.* The coefficient at the plane wall may be increased by increasing the fluid velocity, but this also creates a larger pressure drop and requires increased pumping power. In many cases it is thus preferable to increase the rate of heat transfer from the wall by using fins that extend from the wall into the fluid and increase the contact area between the solid surface and the fluid. If the fin is made of a material with high thermal conductivity, the temperature gradient along the fin from base to tip will be small and the heat transfer characteristics of the wall will be greatly enhanced. The choice of fins is formed from the ideology of heat evaluation and price. The selection of suitable fin geometry requires a compromise among the cost, the weight, the available space, and the pressure drop of the heat transfer fluid, as well as the heat transfer characteristics of the extended surface. There are various forms of fins namely; Rectangular fin, Triangular fin, Circular fin and Pin fin respectively. The transfer through convection is between the surrounding fluid and a surface this could be raised by including an extended thin strip of metal called fin. When heat transfer takes place by convection from both internal and external surfaces of a plate, generally, fins are used on the surface where the heat transfer coefficient is low. The selection of fin solely depends on different parameters like; fin spacing, geometrical shape, base thickness, fin height, kind of material, surface finish etc. (Debdatta, 2014).

2.2 Rectangular Fin

In the study of heat transfer, **fins** are surfaces that extend from an object to increase the rate of heat transfer to or from the environment by increasing convection. The amount of conduction, convection or radiation of an object determines

the amount of heat it transfers. Increasing the temperature gradient between the object and the environment, increasing the convection heat transfer coefficient, or increasing the surface area of the object increases the heat transfer. Sometimes it is not feasible or economical to change the first two options. Thus, adding a fin to an object, increases the surface area and can sometimes be an economical solution to heat transfer problems. Rectangular fins are used in a large number of applications to increase the heat transfer from surfaces. Typically, the fin material has a high thermal conductivity. The fin is exposed to a flowing fluid, which cools or heats it, with the high thermal conductivity allowing increased heat being conducted from the wall through the fin.

Fins are most commonly used in heat exchanging devices such as Radiators in cars, computer CPU heat-sinks, and heat exchangers in power plant. They are also used in newer technology such as hydrogen fuel cells Nature has also taken advantage of the phenomena of fins.

The ears of Jackrabbits and fennec foxes act as fins to release heat from the blood that flows through them

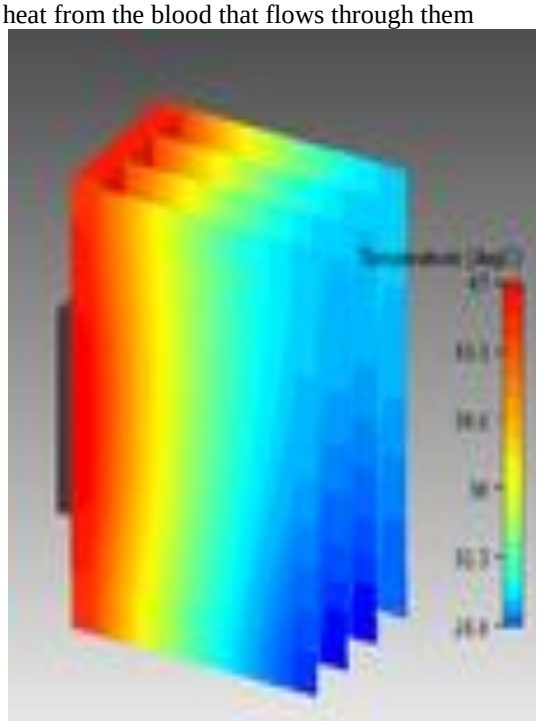

Figure5: A picture of a Rectangular fin (https://www.researchgate.net)

2.3 Circular Fin

Circular fins are extensively used in heat exchange devices to increase the heat transfer rate. For a given volume or weight, the fin can also dissipate different amounts of heat due to the different in geometry and shape. The aim of fin optimization is to find the fin shape that would reduce the fin volume for a given amount of heat dissipation or to maximize the dissipation heat for a given fin volume says Zhang and Chung (2012)

And, the following assumptions were made:

1. Heat conduction in the fin is steady and one-dimensional.
2. The fin material is homogeneous and isotropic.
3. The fin material has constant properties, and fin surface is diffused.
4. The heat transfer coefficient over fin surface is uniform.
5. The heat transfer at fin tip is negligibly small.
6. The temperature of the fluid inside the pipe is constant; the ambient temperature and environment temperature around the fin are also uniform.
7. The radiative interaction between the base wall and fin is neglected.
8. The curvature effect of the fin is negligible.
9. There is no heat generation inside the fin.

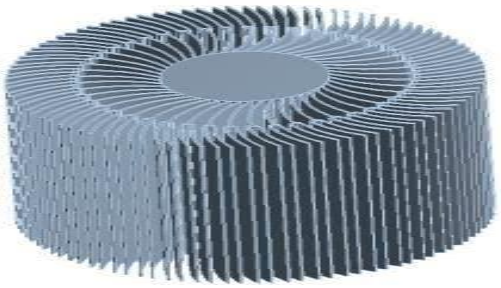

Figure6: A picture of a circular fin (Source: https://www.researchgate.net)

2.4Fin Design Criteria

Fins should be fastidiously designed and connected to confirm the potency of the fin. The performance of the fins is judged on the idea of the improvement of heat transfer relative to the no-fin case. A vital thought within the design of finned surfaces, is that the choice of the correct fin diameter. Commonly the larger the fin, the larger the heat transfer space and therefore the greater the speed of thermal transfer from the fin. However, the larger the fin, the larger the mass, the greater the value, and therefore the larger the fluid friction. Therefore, increasing the size of the fin beyond a certain value cannot be justified unless the added benefits outweigh the added cost. Also, the fin efficiency decreases with increasing fin diameter because of the decrease in fin temperature with size. Fin surface area that cause the fin efficiency to drop below 60 percent usually cannot be justified economically and should be avoided. The efficiency of most fins used in practice is above 90 percent. Fin design is often motivated by a desire to minimize the fin material and/or related manufacturing costs required to achieve a prescribed cooling effectiveness.

If fins are machined as an integral part of the wall from which they extend there is no contact resistance at their base. However, more commonly, fins are manufactured separately and are attached to the wall by brazing, welding or extrusion. Alternatively, the attachment may involve a

press fit for which the fins are forced into slots machined on the wall material. In such cases, there is a thermal contact resistance which may adversely influence overall thermal performance.

2.5 Fin Material Selection Criteria

Fin effectiveness is enhanced by the choice of a material of high thermal conductivity. Aluminum alloys and copper come to mind. However, although copper is superior from the standpoint of thermal conductivity, aluminum alloys are the more common choice because of additional benefits related to lower cost and weight. Fin effectiveness is also enhanced by increasing the ratio of the perimeter to the cross-sectional area. For this reason, the use of *thin*, but closely spaced fins is preferred, with the proviso that the fin gap not be reduced to a value for which flow between the fins is severely impeded, thereby reducing the convection coefficient.

2.6 Thermal Resistance

Thermal resistance is the resistance of the fin against heat conduction and is dependent on the g*eometry* and the *thermal properties* of the fin. The heat transfer processes may be compared by analogy with the flow of electricity in an electrical conductor. As the flow of electric current in an electrical conductor is directly proportional to the potential difference (v), similarly heat flow rate Q, is directly proportional to temperature difference (dt), the driving force heat conduction through a medium.

2.7Optimum Fin Diameter

An important step in the design of a fin is the determination of the appropriate diameter of the fin once the fin material and the fin cross section are specified. You may be tempted to think that the longer the fin, the larger the surface area and thus the higher the rate of heat transfer. For maximum heat transfer, the fin should be infinitely long, however, the temperature drops along the fin is exponentially and reaches the environment temperature at some diameter. The part of the fin beyond this diameter does not contribute to heat transfer since it is at the temperature of the environment. Therefore, designing such an "extra-long" fin is out of the question since it results in material waste, excessive weight, and increased size and thus increased cost with no benefit in return (in fact, such a long fin will hurt performance since it will suppress fluid motion and thus reduce the convection heat transfer coefficient). Fins that are so long that the temperature approaches the environment temperature cannot be recommended either since the little increase in heat transfer at the tip region cannot justify the large increase in the weight and cost.

2.8 Fin Performance

There are several important conclusions that could be drawn as regards fin effectiveness consideration in the design and selection of the fins: Firstly, *thermal conductivity k* of the fin material should be as high as possible. Thus it is no coincidence that fins are made from metals, with copper, aluminum, and iron being the most common ones. Perhaps the most widely used fins are made of aluminum because of its low cost and weight and its resistance to corrosion. Secondly the ratio of the *perimeter* to the *cross-sectional area* of the fin *p*/*Ac* should be as high as possible. This criterion is satisfied by *thin* plate fins and *slender* pin fins. Lastly the use of fins is *most effective* in applications involving a *low convection heat transfer coefficient.* Thus, the use of fins is more easily justified when the medium is a *gas* instead of a liquid heat transfer.

2.9 Fin Application

Finned surfaces are mainly used to carrying out the increase heat transfer rate, and that they usually enhance heat transfer from a severally fold surface. Good examples of finned surface are car radiators. The strongly packed metal thin connected to the tubes of hot water enhances the convection surface area. It is also make use of in electronic mechanisms for cooling and as well outside the bikes engine.

Copper material is used throughout this work because among other available materials copper stands next to silver in heat transfer and dissipation. Copper has also been chosen for this work because of its corrosion resistance ability and its relative low cost of price per size, Weight is another factor that should be mentioned, however, as it is, it's an advantage to be considered about the choice of copper. The Copper fin array is so arranged along two enamel carrying half-circular of the pipes with fins attached on each side of the half-circular pipe. The two assembly are coupled to the exhaust neck of the pipe with bolts and nuts thus enabling the fins via the inner pipe to have a direct contact with the exhaust pipe thereby extracting heat from the exhaust pipe.

Copper is a non-ferrous metal and very easy to work upon, machinability is easier with copper materials than welding of it, be that as it may we were still able to weld the fin to the flat bars. Also, considering the thickness we are dealing with in this project work, there are other welding processes that could be deploy for joining, the one used is commonest which is gas welding process.

2.10 Geometries of Fins

There are good number of fin designs to choose from, in this project work, circular shape was used. Other likely shape that can be employed include circular shape, rectangular shape, trapezoidal shape or triangular shape. Whichever preferred profile one decides to use we should bear in mind that we have to make it work.

2.11 Adopted method of Fabrication

The method employed for fabrication of the copper fins in the workshop include marking out, welding, gas-welding, drilling, filing and bolting of the parts together. First the Copper pipe was cut open to make it a plate, then, the marking out began, first as a circular shape and later a hexagonal shape was marked out, this is to give an attractive look and make it look handier and easier for installation. The fins were further cut into two equal halves so that they can be welded to a copper-flat-bar, the total number of the halved-fin is ten on each sides so that when the welding is completed the mechanism (Heat Removal) can be coupled to Okada Exhaust using bolts and Nuts.

3. RESULTS AND DISCUSSION

The complete assembly of fabricated fin was attached using bolt and nuts to fasten it on a Bajaj Motorcycle exhaust, note that first and foremost the fabricated fins will have to be mounted on the exhaust pipe before any temperature measurement will be done, otherwise, one may have to wait for a long time for the Motorcycle exhaust to cool down to avoid being burned by the exhaust as one continues the experiment, it will become a case of becoming a victim of what you are preventing. The initial temperature of the motorcycle exhaust was taken when the engine was at rest and it reads 30^0 C, after which the Bajaj motorcycle was kick-started, the exhaust pipe temperature near the neck of the exhaust (literally, a no-finned area) was taken after idling for 300 sec. the digital thermometer indicates 120^0C, fins temperature was 52.5^0C, while the motorcycle exhaust pipe at the area in focus where burns usually happens was 39.9^0C, all this test was done while the motorcycle was stationary, further on the testing, temperatures were taking at varying interval of time and at varying engine speed of. 2000rpm,4000rpm and 6000rpm accordingly in order to observe the variation in temperature. There is no doubt that we will have the lowest of temperature if more fins were introduced; and exhaust burn will become a thing of the past.

Table 1: Temperature Profile of Motorcycle Exhaust Pipe at Idle Mode with Fin

Speed (rpm)	Time (sec)	Exhaust manifold temp(X_1)	Copper temp (X_2)	Exhaust pipe temp(X3)
2000	180	55.5	52.5	31.4
	340	60.1	60.1	36.1
	485	70.2	65.9	37.2
	560	78.2	68.3	38.9
4000	115	60.1	54.4	31.9
	225	63.2	60.7	32.2
	265	79.1	74.1	36.1
	300	82.1	73.1	38.2
6000	100	70.1	60.8	35.4
	130	75.2	71.9	36.1
	146	90.2	82.7	38.5
	170	98.3	87.3	39.1

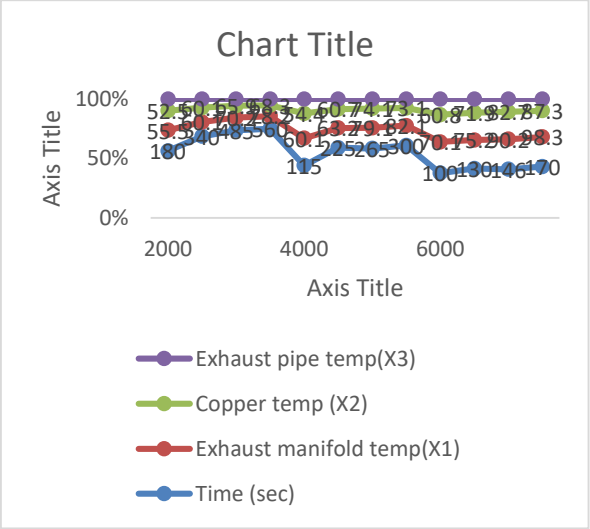

Figure7. Temperature against time for 2000rpm,4000rpm and 6000rpm

Copper is used for this project work due to copper's high thermal conductivity and other good physical properties of copper, another reason why copper is used throughout this work is to have a relative comparison with the previous work that was done, where, copper and aluminium was combined for the experiment, a point has been observed here that both material have different thermal conductivity and property and heat flow may be hindered. Most excellent material is the one that give out the required intention during the performance test. Cost is also a thing to worry about, when the cost is outrageous and costlier than the burns intended to prevent one should look inward.

Plate II: Copper in a semi-circular form.

The welding of Copper was such a smooth work, it's a normal oxy-acetylene welding process, pieces of copper strands were used instead of a filler-rod to hold the fins and the entire body in place. This is the first of its king, other improvement can be introduced in later work to have a smoother fabrication may be a spot-welding machine should be used instead of oxy-acetylene
gas.

Plate III: Copper heat sink in dismantled form

4. CONCLUSION

In conclusion, the desire of this work is to achieve a reduction in exhaust temperature of a motorcycle to barest minimum so that accidental contact with motorcycle exhaust will no longer give injurious burn to its occupants, this desire has been achieved with the introduction fins. Engineering has thought that when you increase the surface area of an object, it enhances quick dissipation of heat. Copper was used and the result is far more satisfactory compare to previous work on this same topic. Copper is a non-ferrous material that has a lot of good quality to suite the purpose. The percentage reduction of heat

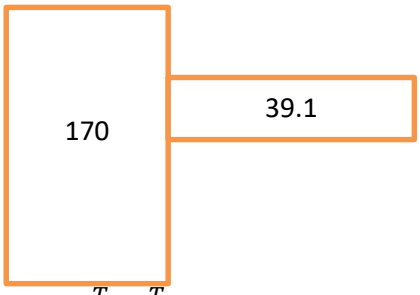

$$\% \, Reduction = \frac{T_1 - T_2}{T_1} \qquad (45)$$

$$\%Reduction = \frac{170 - 39.1}{170} = 0.77$$

$$Reduction = (0.77 \times 100) = 77\%$$

$$Reduction = 77\%$$

description of patterns and documentation of factors relevant to motorcycle contact burn injuries are likely to facilitate the design and implementation of preventive strategies.

Principal conclusions:

1) Some other previous works has recommend wearing of long pants/trousers or by incorporating in the design of motorcycles an external thermos-resistant shields with adequate distance to the exhaust pipe, and by avoiding riding with children on motorcycles.
2) Combination of Aluminium and copper was used in a previous work to reduce the exhaust temperature by Joseph O.J, Okegbile. J, (2019) and has basically recommend the use of a thicker aluminium plate of a gauge up to 5mm so that welding can be better carried out, it is on the basis that the thought of using copper plate of 5mm thickness came to mind to see if same or a better result can be achieved using copper all through. The first table below is the result obtained from previous work while the second is the one obtained from the current work. At the end of this study, one can come to conclusion that:
   a) both aluminium and copper are good material for extraction of heat.

b) The larger surface area deployed in the case of aluminium-fin can be replaced with smaller surface area of copper-fin to get almost the same heat reduction.

Table 2: Temperature Profile of Motorcycle Exhaust Pipe at Idle Mode with Fin

Speed (rpm)	Time (sec)	Alum temp (t_1)^{0}C	Copper temp (t_2)	Exhaust temp(t_3)
2000	180	34.2	49.9	52.5
	340	36.1	70.1	74
	485	36.8	81.1	83.9
	560	40.1	91.2	92.3
4000	115	35.1	50.9	54.4
	225	36.6	69.8	74.1
	265	37.1	68.1	72.7
	300	37.9	71	73.1
6000	100	33.2	58.3	60.8
	130	34.5	68.1	71.9
	146	37.8	78.5	82.7
	170	39.2	80.5	87.3

ACKNOLEDGEMENT

To God be all the glory indeed for seeing me through this program and for providing me all the material resources used for this program. My sincere gratitude goes to my project supervisor: Engr. Dr. Bori Ige for his guidance, **patience** and concerns even when I was not responsive, you assisted me to make sure I complete the program, all thanks to you sir. My immense gratitude to my colleagues at work who participated in the practical work, my gratitude goes to my family member who has supported me in one way or the other, all thanks to you too.

REFERENCES

1. Debdatta, D. (2014). Heat Transfer Analysis of Pin Fin Array. https://www.researchgate.net (Retrieved on 23/01/2023, 08:38am)
2. Exhaustburns.

   https://www.fixyourdirtbike.com>first-aid

   (Retrieved on 20/1/2023, 17:42pm)

3. Ibeanusi SE, Kejeh B. Burns care in Sub-Saharan Africa: Experience from a trauma registry in Nigeria – An observational study. Niger J Orthop Trauma [serial online] 2018 < https://www.njotonline.org/article.asp>

4. Lin, T.M., Lai, C.S.,and Lee, S.S. (2002). Case studies in contact burns caused by exhaust pipes of motorcycles. *Burns;28:370–3.*

5. Loannis, M., Constantine, F., and Ava, C. (2005). Burn injuries related to motorcycle exhaust pipe. Pg 372-374, Vol;31

6. Matzavakis,I.,Frangakis, C.E., Charalampopoulou, A., and Petridou, E. (2005). "Burn injuries related to motorcycle exhaust pipes: a study in Greece."*National Center for Biotechnology Information.page. Web. 26 Jul. 2013.*

   <http://www.ncbi.nlm.nih.gov/pubmed/15774297>.

7. Obodeh, O., Ogbor, A. D. (2009). "Improving the performance of Two-stroke Motorcycle with tuned adjustable exhaust pipe", *Journal of Applied sciences, engineering and technology, Vol. 1(2), pp.59-65.*

8. Oyesiku, O. O. (2002). "From Womb to Tomb" 24th Inaugural Lecture, *OlabisiOnabanjo University. Ago Iwoye: OOU Press.*

9. Petkovic, S., Pesij, R., Lukic, J. (2011). "Experimental verification of mathematical model of the heat transfer in exhaust system", *Thermsal science, Vol. 15(4), 1035-1048*

10. Stuart,P.P., Mayze, T.D. (1983). Burn injuries associated with motorcycles. Burns;9:288–91.

11. Saidur, R., Rezaei, M., Muzammil, W. K., Hassan, M. H., Paria, S., Hasanuzzaman, M.(2012)."Technologies to recover exhaust heat from internalcombustion engines", *Renewable and Sustainable Energy Reviews, Vol. 16, pp.5649–5659.*

12. Zhang, G., and Chung, B.T.F.(2012). Design Charts for Circular Fins of Arbitrary Profile Subject to Radiation and Convection with Wall Resistances. *6*, 15-24.

13. Zidat, S., and Parmentier, M. (2003)."Exhaust Manifold Design to Minimize Catalyst Light-off Time", SAE paper -01-0940.

4th International Engineering Conference (IEC 2022)
Federal University of Technology, Minna, Nigeria

Cryptocurrency Fraud Detection: A systematic Literature review

*Hussaini, Y[1], Waziri, V.O[2], Isah, A. O[3], & Ojeniyi, J A[4]
[1]Cyber Security Science Department, Federal University of Technology, PMB 65 Minna Niger State, Nigeria
*Corresponding author email:hussaini.pg208686@st.futminna.edu.ng +2347063585009

ABSTRACT
Cryptocurrency Fraud is growing at alarming rate and spreading rapidly despite on-going mitigating efforts. This brings a necessity to find more effective solutions to detect these Frauds and prevent users from losing digital assets. This study uses the PRISMA statement as a reference so to be transparent. This paper uses a SLR to identify where recent studies in cryptocurrency fraud detection have been focused on and offers a broad perspective relating to types of Techniques, Algorithms, dataset sources used and also the categories of Fraud types in the research area within the range of 2018 to 2022. A total of 38 selected papers met the inclusion criteria based on title of articles, exclusion criteria, reading abstract and content of the selected 38 papers. Different data are extracted from these articles and recorded in an excel sheet for further analysis. Most of the paper discussed about the use of Machine Learning and Deep Learning analysis approach to analyse cryptocurrency fraud. We also identified research gaps that are further needed to be explored by the research community
Keywords: *Cryptocurrency, Fraud, Detection, Machine Learning, Deep learning*

1 INTRODUCTION

Since the prevalence of digital currencies has drawn a variety of illegal behavior, cryptocurrency theft is a rising worry. Ponzi schemes, spam scams, and the selling of stolen or fake cryptocurrencies are just a few examples of the various ways that cryptocurrency theft can manifest itself (Bao, F., & Li, X. (2019). Therefore, there is a need for efficient techniques to identify and stop bitcoin scams.

Numerous strategies for detecting bitcoin scams have been created and suggested in recent years. Utilizing machine learning algorithms, which can be taught on extensive databases of previously fraudulent transactions, is one hopeful strategy for finding trends and abnormalities that might be indicative of fraudulent activity (Kaur, M., & Singh, G. (2019).Among other ways to spot bitcoin scams is network analysis, which involves analyzing the links and patterns of transactions within a cryptocurrency network in order to identify groups of activity that may be linked with fake activity, and behavioral analysis, which employs user behavior data to identify suspect activity (Wang, Z., Chen, M., & Lee, W. C. (2018)

In this introduction, we will address the various kinds of deception that can occur in the bitcoin market, as well as the challenges and methods for identifying and stopping such deceptive actions. We will also look at the present state of the art in bitcoin scam identification and describe some of the potential future paths in this area.

1.1 TYPES OF FRAUD IN CRYPTOCURRENCY

The potential for unlawful activities, such as money trafficking and funding terrorists, to go unnoticed is one of the main worries with bitcoin scams. Since bitcoin transfers are private, it is challenging to determine who is responsible for the money and where the money came from. For instance, the imaginary money Bitcoin has been used on the dark web to enable drug trade and other illicit operations (Zohar, 2015). Another type of scam that has affected the bitcoin market is ponzi schemes. In a Ponzi scam, gains are given to early owners using funds raised from new investors rather than from profits. The plan persists as long as there are enough fresh participants to cover the profits. But eventually, as the number of new investors decreases, the plan falls apart; causing substantial loses for the later investors (SEC. (2020).

Exchanges for virtual currencies that make it easier to purchase and trade them are also prone to scams. Hackers may target these platforms to take users' money, as was the case with the high-profile Mt. Gox breach in 2014, which resulted in the theft of 850,000 Bitcoins valued over $450 million at the time (] Kharif, O. (2014).

1.2 CHALLENGES AND TECHNIQUES FOR FRAUD DETECTION IN CRYPTOCURRENCY

The bitcoin market is autonomous and worldwide, which makes it extremely difficult to spot and stop fake activity. Due to the absence of a centralized authority and governmental supervision, conventional scam detection techniques, such as those employed in the banking and finance sectors, may not be successful in the bitcoin market.

Using machine learning techniques to evaluate transaction trends and spot abnormalities that might point to dishonest behavior is one method for spotting fraud in cryptocurrency. A machine learning model, for instance, could be taught to spot suspect trends like a rapid rise in transaction traffic or the movement of money to well-known money launderers.

Utilizing network analysis to find groups of fraudulent transactions is another method for spotting bitcoin scams and suspicious activity. It is possible to spot trends that may suggest fake behavior by studying the connections between different addresses and the flow of funds .

1.3 CURRENT STATE OF THE ART IN FRAUD DETECTION IN CRYPTOCURRENCY

In recent years, there have been a number of significant advancements in the area of digital currencies scam identification. Using graph convolutional neural networks (GCNNs) to find fraudulent patterns in the blockchain, the decentralized ledger that keeps track of all bitcoin transactions, is a hopeful method. The complicated connections between various blockchain organizations can be successfully captured by GCNNs, and they can also spot suspect trends that could point to fraud (Wen, Z., Zeng, D., Li, Y., Li, H., & Lu, J. (2019). A survey on blockchain analytics. 52(1), 1-38, ACM Computing Surveys (CSUR), n.d.

The use of natural language processing (NLP) to identify phony ICOs is another potential area. (initial coin offerings). A business provides a new altcoin in return for investments through an initial coin offering (ICO). However, a lot of ICOs ended up being frauds, with the creators taking the collected funds and running (Kshetri, N. (2018). The Regulatory Challenges Affecting Initial Coin Offerings. n.d.; Journal of Financial Regulation and Compliance, 26(4), 318-333).

1.4 RELATED WORKS:

A systematic review of fraud detection methods in cryptocurrency market" by A. Alshammari and B. Mishra (2019).

In this paper, the authors review various fraud detection methods that have been proposed for the cryptocurrency market, including rule-based systems, machine learning techniques, and hybrid approaches.

"Cryptocurrency fraud detection using machine learning techniques: A systematic review" by M. Alomari and R. Al-Ayyoub (2020).

In this paper, the authors review the use of machine learning techniques for fraud detection in the cryptocurrency market. They discuss various machine learning approaches, including supervised learning, unsupervised learning, and semi-supervised learning, and provide a comparative analysis of their strengths and limitations.

"Fraud detection in cryptocurrency transactions using data mining techniques: A systematic review" by M. Raza, N. Anwar, and A. Alazab (2021).

In this paper, the authors review the use of data mining techniques for fraud detection in cryptocurrency transactions. They discuss various data mining approaches, including association rule mining, decision tree induction, and clustering, and provide a comparative analysis of their performance in detecting fraudulent activity.

1.5 RESEARCH QUESTIONS:

The following research questions were developed:

RQ1 – Which is the most frequent used Techniques in cryptocurrency Fraud detection?

RQ2 – which Algorithms have been used in the research area and what are the successful detection rates achieved?

RQ3 – What sources of dataset have been used the most in the research area?

RQ4 – What are the types of fraud existing in the cryptocurrency domain?

This systematic Literature review analysis will be used to answer the research questions above Using the PRISMA Framework which from my related works no work has been done using this framework. The PRISMA frame work is highly known for its transparency in conducting a review.

2 METHODOLOGY

To create an orderly yet responsible SLR, we use the PRISMA (Preferred Reporting Items for Systematic Reviews and Meta-Analysis) Statement. (Moher 2009.Pdf, n.d.). This statement encompasses two parts: an inventory and a flow schematic. The factors are useful in directing a researcher to the material that must be included on an SLR. Furthermore, movement maps help scholars ensure the transparency of the literature referenced by SLRs. This movement chart is divided into four phases;

(1) Identification,
(2) Screening,
(3) Eligibility, and
(4) Included.

To maintain openness, every stage in the PRISMA flow model is described in Fig. 1.

2.1 IDENTIFICATION STAGE

We create a search method to find appropriate publications during the identifying step. This search approach was customized to random databases using the Publish and perish Software with Google scholar search engine: and the following search terms were used:“Cryptocurrency Fraud Detection” NOT Review (included to restrict the search to a particular area). All searches were conducted from the Google Scholar database using the publish and perish tool, and by default, the rejection and inclusion criteria A1, A2, and B1 were applied to the journal database shown in Table II. The procedure was completed on November 31, 2022, and the findings of the inquiry are shown in Table II.

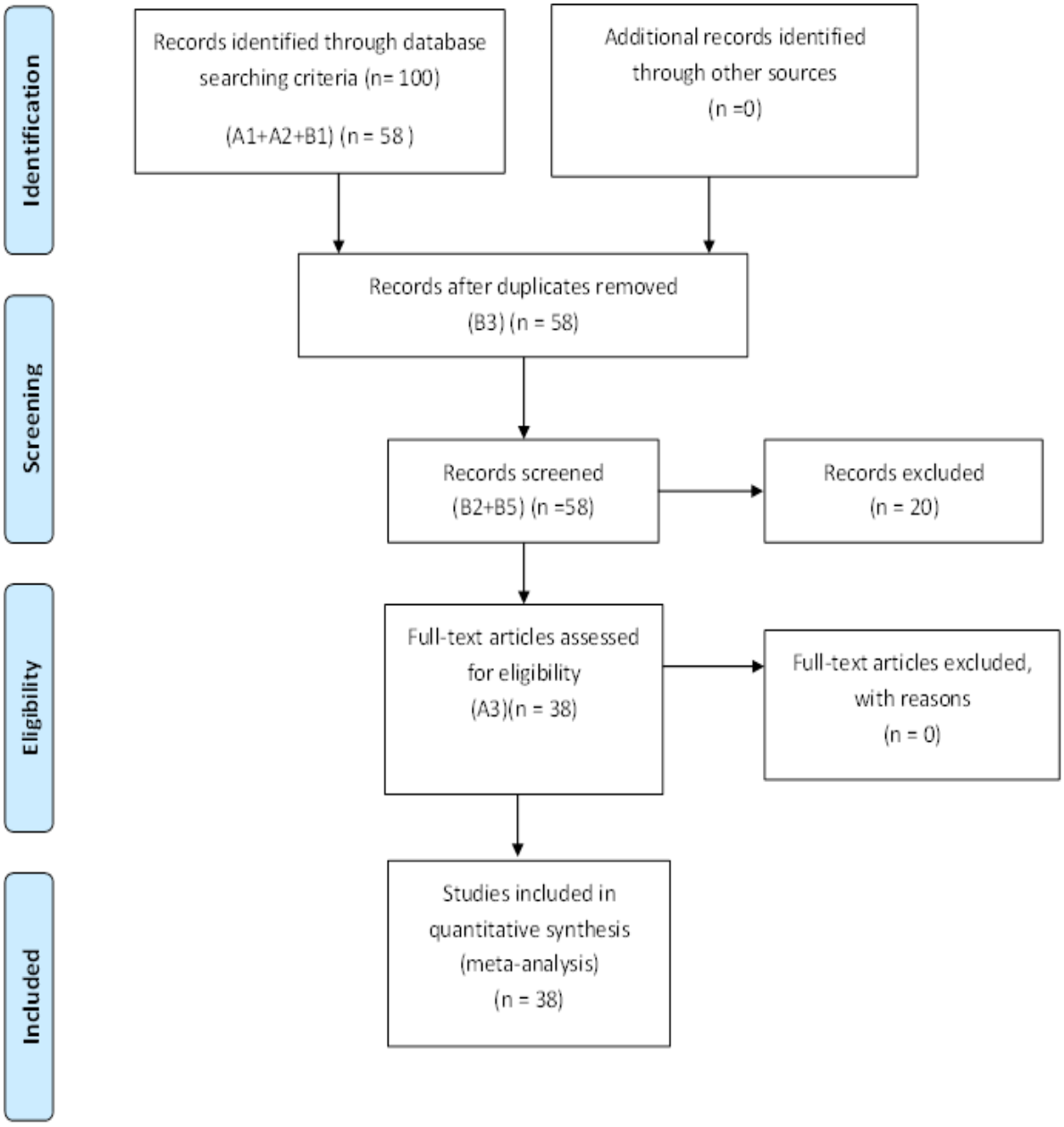

Figure 1Process for SLR Transparency Using PRISMA Flow Diagram(Moher2009.Pdf, n.d.)

2.2 SCREENING STAGE:

At this level, we implement selection criteria by going through the title, abstract, metadata and conclusions to sort out appropriate articles. 58 documents will be reviewed at this point. There are no duplicate complaints (B3), and there are no papers that are not specifically linked to detecting cryptocurrency fraud. (B5). In the qualifying step, 58 sheets were still used.

2.3 ELIGIBILITY STAGE:

This is the step of quality assurance. The research is founded on authentic published papers. All duplications were carefully verified to ensure the review's standard. usefulness of scholarly literature included in the review process. At a later point, each study article was carefully evaluated. The articles were then limited to those that used Solutions to bitcoin scam detection methods. (A3). Furthermore, 20 articles were eliminated from the research following the filtering procedure. We chose 38 pieces after evaluating each one on the aforementioned inclusion and exclusion criteria. This stage is useful to ensure that existing articles can answer our research questions.

TABLE1: INCUSION AND EXCLUSION CRITERIA

Criteria	
Inclusion	A1. The full article was written in English A2. Both Journal article and conference papers A3. Solutions contain cryptocurrency fraud detection techniques
Exclusion	B1. The article was written outside the range 2018-2022 B2. Book and white paper B3. Duplicate copies indexed in other databases B4. Literature review or overview of other paper B5. Papers not explicitly related to crypto currency fraud detection

2.4 INCLUDED STAGE:

This is typically the data extraction step, where a total of 38 papers were chosen and the following characteristics were extracted: 1) Article must be a journal paper

2) The article must be written in English.

3) The papers that were extracted were released between 2018 and 2022.

4) The article must provide Solutions for detecting bitcoin fraud

At this point, all responses to the RQ will be recorded on a previously gathered chart.

TABLE II JOURNAL DATABASE DISTRIBUTION

Database Journal	Articles
ACM	4
IEEE	14
SPRINGER	7
ELSAVIER	3
MDPI	2
RESEARCH GATE	1
ARXIV	3
MUNIN	1
SCHOLAR	1
HINDAWI	1
TAYLOR& FRANCIS	1
Total	38

3 RESULTS AND DISCUSSION

In this part, we closely examine 38 main studies from four perspectives: Deep and machine Learning method, Accuracy, dataset, and Fraud attack kinds.

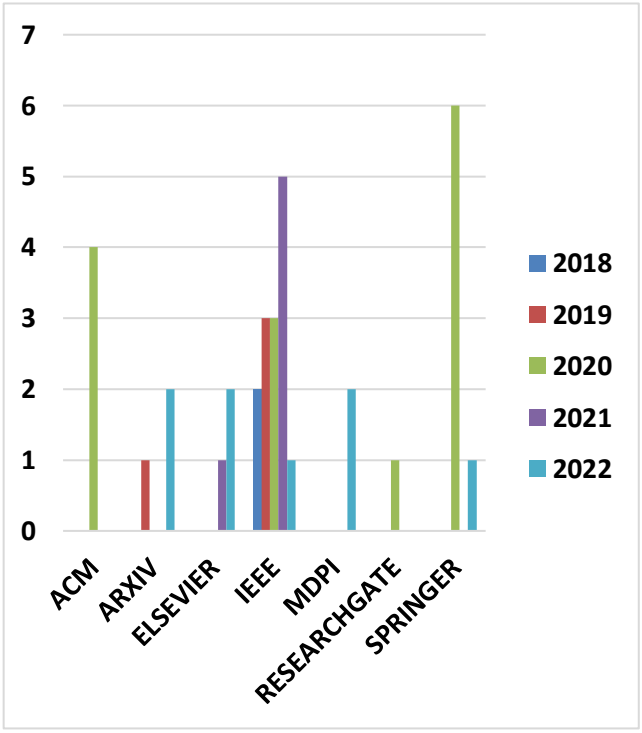

Figure 2 Total Journal articles distribution per

According to Figure 3, Cryptocurrency Fraud detection study that matches our criteria grew considerably between 2018 and 2020, declines by 2021, and is presently increasing in power. Figure 2 demonstrates that IEEE has more Journal articles than any other publication over the

span of a study period. IEEE contributed 14 articles to this evaluation, while the remaining data were shared by the other authors. Figure 4 depicts the spread of cites across some of the research articles, whereas Figure 5 depicts the bibliographical analysis network of co-citations for the chosen articles used in the report.

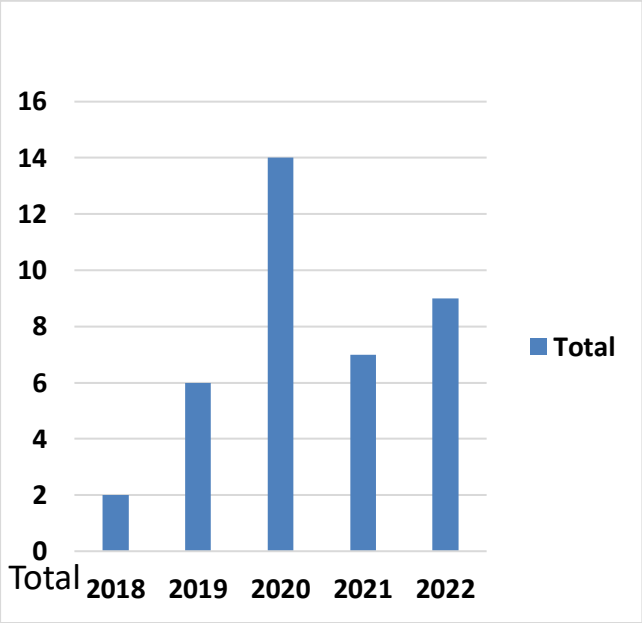

Figure 3 Total Journal articles distribution per year.

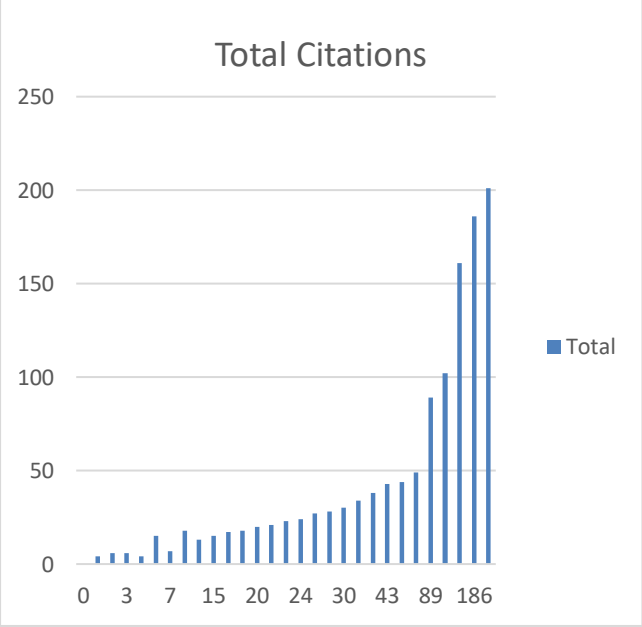

Figure 4 Frequency distribution of Citation of Articles used in the report.

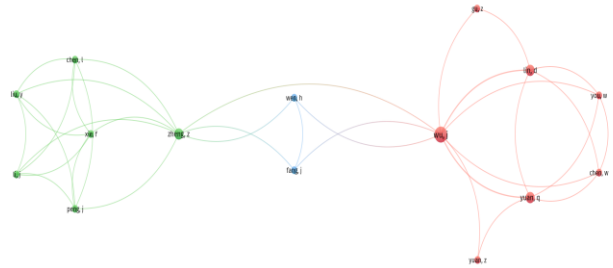

Figure 5 Bibliography analysis of co-citations for the selected articles in the report

3.1 SYSTEMATIC MAPPING OF STUDY RESULTS

RQ1 – Which is the most frequent used Techniques in Cryptocurrency fraud detection?

RQ2 – which Algorithms have been used in the research area and what are the Accuracy detection rates achieved?

We use a total of 37 available articles to answer RQ1 and 5 research articles to answer RQ2. We created a graphical and tabular cluster of literatures to describe the types of crypto fraud detection technique included in the research report as shown in Figure 6 and TABLE III respectively. It can be seen from Fig. 4 that Machine Learning Technique has the highest occurrences in our search. Figure 7 shows a graphical representation of accuracies of algorithms achieved. We bench marked accuracies from 90% and above and got the corresponding algorithms used to achieve the detection rates.

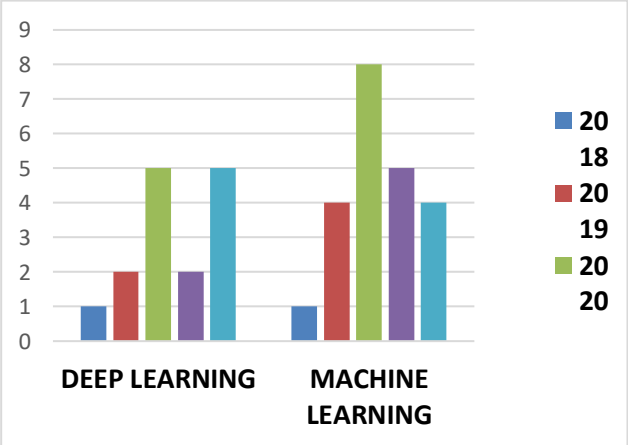

Figure 6 Cryptocurrency fraud detection Techniques frequency distribution

Deep learning approaches and machine learning approaches are the two main methods to identify bitcoin scams that can be found in the literature groups displayed in Table III. Many deep learning-based models and methods were used in deep learning approach to detect fraud. The topmost Algorithms detection models using deep learning techniques are GCN(Ismail Alarab et al., 2020), LSTM (Andreas Isnes Nilsen, 2023), and GNN (Panpan Li et al., 2023). (Ismail Alarab et al., 2020) demonstrates the skill of GCN when coupled with MultiLayer Perceptron, which is combining a feedforward neural network with a graph-based spectrum method. Their testing assessments show that, as opposed to simply applying graph convolutions to the bitcoin elliptic dataset, the combination of features generated from GCN and the hidden representation of a linear layer improves the performance of the model with an accurate detection rate of 97.4%.

(Runnan Tan et al., 2021 suggests a technique for deterring Ethereum scams by gathering transaction data that is built on Ethereum. In particular, web bots are used to collect addresses that have been flagged as fake, after which a transaction network is built using the public transaction book. Then, a network embedding method based on quantity is suggested in order to derive node characteristics for detecting fake transactions. ones are finally divided into legitimate and fake ones using the graph neural network model. The testing findings demonstrate that the system for identifying fraudulent transactions can reach an accuracy of 95%, demonstrating the system's outstanding performance in identifying fake Ethereum transactions.

(Andreas Isnes Nilsen, 2023) offers the Light Gradient Boosting Machine (LGBM) method as a method for precisely identifying fake activities. It examines different models such as Random Forest (RF), Multi-Layer Perceptron (MLP), etc., based on machine learning and soft computing algorithm for classifying Ethereum fraud detection dataset with limited attributes and compares their metrics with the LGBM approach, further optimizing the LGBM with hyper-parameter tuning; an accuracy of 99.03% was achieved. Figure 7 provides a visual summary of all the algorithms and success rates used in this study. The Machine learning approach has also shown good significant detection rates. The topmost Algorithms detection models using Machine learning techniques are LGBM (Aziz, Baluch, Patel, & Ganie, 2022)-(Aziz, Baluch, Patel, & ..., 2022), ENSEMBLE LEARNING (Alarab et al., 2020a). (Aziz, Baluch, Patel, & ..., 2022) developed a Light Gradient Boosting Machine (LGBM) technique-based model. The modified LGBM model optimized the parameters of Light GBM using the Euclidean distant structured estimation approach. The modified LGBM algorithm demonstrates a good accuracy of 99.17. The LGM approach in (Aziz, Baluch, Patel, & Ganie, 2022) uses the light gradient boosting machine (LGBM) algorithms to demonstrate the high accuracy, with 98.60% for a specific dataset scenario. Further optimizing the LGBM with hyper-parameter tuning, an accuracy of 99.03% was achieved. (Alarab et al., 2020a) used supervised learning methods for anti-money laundering in Bitcoin. An ensemble learning method is utilized using a combination of the given supervised learning models, which outperforms the given classical methods using the Elliptic data set, they are able to predict licit/illicit transactions with an accuracy of 98.13%.

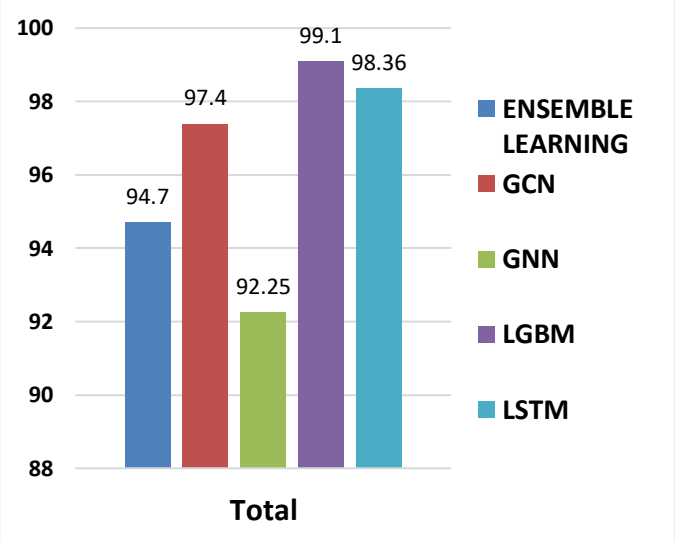

Figure 7 Algorithms and Accuracy rates

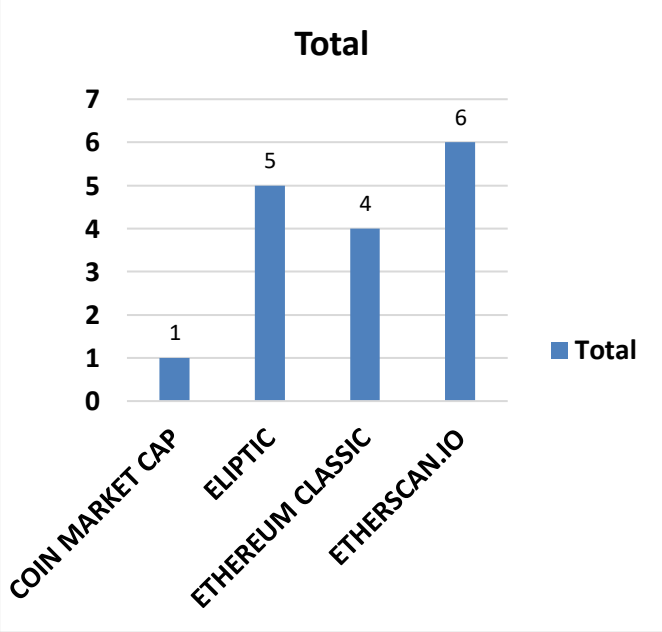

Figure 8 Frequency distribution of dataset sources used in Cryptocurrency fraud detection

TABLE III. Overview of RQ1

Analysis Type	Literature
Machine Learning	(Aziz, Baluch, Patel, & Ganie, 2022), (Baek et al., 2019), (Jung et al., 2019), (Ibrahim et al., 2021), (Kumar et al., 2020), (Poursafaei et al., 2020),(Liao et al., 2019), (Dokuz et al., 2020), (Bartoletti et al., 2018), (Lee et al., 2020), (Yin et al., 2019), (Sureshbhai et al., 2020),(B. Chen et al., 2021),(Alarab et al., 2020a),(Wu et al., 2020),(Aljofey et al., 2022),(T. Hu et al., 2021),(Wen et al., 2021),(Akba et al., 2021),(Ostapowicz & ?bikowski, 2020),(Aziz, Baluch, Patel, & ..., 2022),(Shayegan et al., 2022)
Deep Learning	(Patel et al., 2020),(Gu et al., 2022),(Liu et al., 2022),(Tan et al., 2021),(Kanezashi et al., 2022),(Singh et al., 2021),(Nan & Tao, 2018),(H. Hu et al., 2022),(Weber et al., 2019),(Li et al., 2022),(Nilsen, 2019),(Scicchitano et al., 2020),(L. Chen et al., 2020),(Alarab et al., 2020b),(Yuan et al., 2020)

RQ3 – What were the most frequently sources of dataset found in the review?

To answer this question, we use 16 articles published within the year 2018-2022 to identify the sources of the dataset used in their research and the findings to answer RQ3 is graphically represented in Figure 8. It can be seen that Elliptic, Ethereum classic and Etherscan data are the most common dataset sources used in the area of Cryptocurrency fraud detection. The Elliptic dataset are bitcoin data from(Weber et al., 2019) which contributed the Elliptic Data Set in their research, elliptic is a time series graph of over 200K Bitcoin transactions, 234K directed payment flows, and 166 node features, including ones based on non-public data; this may be the largest labelled transaction data set publicly available in any cryptocurrency.

While the Ethereum classic and Etherscan data are Ethereum dataset. They are public dataset available in Kaggle.com .The literatures that used these database sources have been summarized in TABLE IV Showing references of the articles. We bench mark a minimum of 4 articles that have used at least one category of the dataset sources mentioned above in their experiment.

TABLE IV. Overview of RQ3

S/N	Dataset type	LITERATURE
1	Eliptic	(Lorenz et al., 2020),(Singh et al., 2021),(Sureshbhai et al., 2020),(Alarab et al., 2020a),(Weber et al., 2019),
2	Etherscan	(Baek et al., 2019),(Jung et al., 2019),(Poursafaei et al., 2020),(Liao et al., 2019),(Aljofey et al., 2022),(Wen et al., 2021)
3	Ethereum Classic	(Ibrahim et al., 2021),(Kanezashi et al., 2022),(Scicchitano et al., 2020),(Aziz, Baluch, Patel, & ..., 2022)
4	Coin Market Cap	(Gu et al., 2022)

RQ4 – What were the commonly types of fraud involved with cryptocurrency

We answered this question by looking at the types of Fraud involved in the attack and the vulnerable cryptocurrency network. Smart contract fraud also known as Ponzi schemes have been used all across both the Bitcoin and Ethereum network to perform fraud. Figure 9 and Table v summarizes the RQ4 in great details both graphical and tabular references were used.

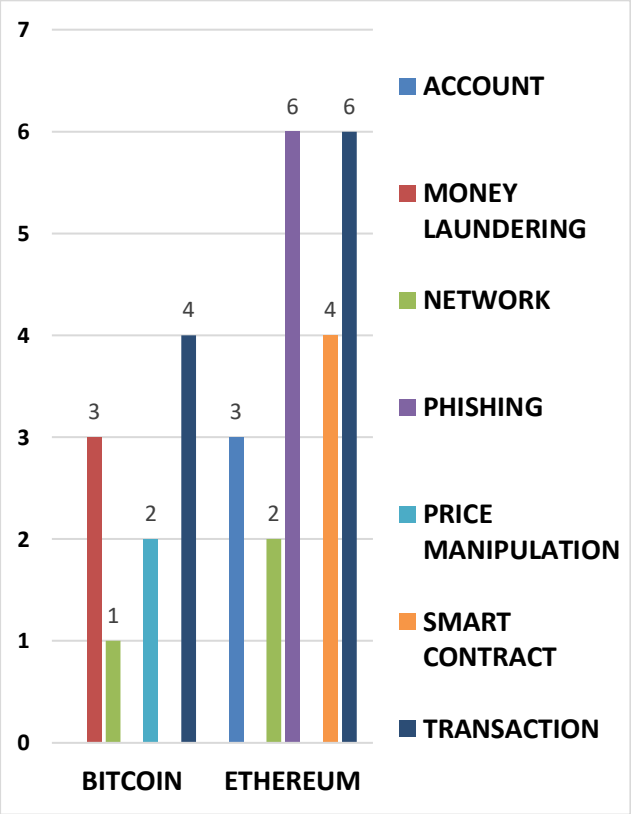

Figure 9 Frequency distribution of different Fraud attacks on the cryptocurrency network.

Table V. displays a tabular clustered reference showing the various type of fraud discussed in different research articles. It shows the most frequently form of fraud used in both the Bitcoin and Ethereum Network. From the literatures we were able to classify fraud in seven different types as shown Table V.

3.2 IDENTIFIED GAPS:

In this section, we discuss the major gaps in some areas concerning Cryptocurrency Fraud detection on the basis of three aspects that need further research and development.

A) Model Explainability: We observed in this survey paper that very high accuracies were found in the literatures but they lack explainability model considerations for black box concept of machine learning. We consider visualization for analysis and explainability, which is difficult given the size and dynamism of real-world transaction graphs(Weber et al., 2019)

B) Scarcity of labelled datasets: labels are so scarce that traditional supervised algorithms are inapplicable. Here, we address money laundering detection assuming minimal access to label datasets(Lorenz et al., 2020).

C) Un-Standardized sources of dataset : We found that a wide variety of sources of datasets are available, like marketcoincap, GitHub, own website.One of the biggest obstacles to detecting abnormal contract accounts on Ethereum is the severe data class imbalance(Aljofey et al., 2022). Two supervised methods, SVM and MLP, have zero recall with both three and nine features of the collected dataset. One of the possible reasons for this behavior is severe dataset class imbalance can skew the 0.30 decision boundaries more toward the minority class (B. Chen et al., 2021)

3.3 RECOMMENDATIONS ON FUTURE RESEACH DIRECTIONS:

In this section, we highlight various research directions for researchers in the field, which require considerable efforts to improve the performance and reliability of the cryptocurrency research domain. These research directions are presented below.

A) STANDARDIZED DATASET:

Research work is required to develop more benchmark datasets. The Standardized dataset formation can also include synthetic samples to deal with the data class imbalance problem.

B) EXPLAINABILITY MODELS INCLUSION:

Our study showed that researchers evaluated fraud detection rates in cryptocurrency. Nonetheless, a considerable number of research articles failed to evaluate the model explainabilty for real life applications especially (Patel et al., 2020),(Nilsen, 2019),(Aziz, Baluch, Patel, & Ganie, 2022),(Alarab et al., 2020b). There is need to explore Explainability AI integration in detecting fraud for real life applications.

C) LABELED DATASET CREATION:

Our study showed that the domain contains limited availability of large, high-quality datasets that have been properly labeled for use in training machine learning models

Table V: Overview of Fraud Attack Types and Literatures

S/N	FRAUD TYPE	LITERATURE
1	Account Anomalies	(Ibrahim et al., 2021),(Poursafaei et al., 2020),(Ostapowicz & ?bikowski, 2020)
2	Money Laundering	(Lorenz et al., 2020),(Alarab et al., 2020a),(Weber et al., 2019)
3	Network Anomalies	(Patel et al., 2020),(Scicchitano et al., 2020),(Alarab et al., 2020b)
4	Phishing	(Kanezashi et al., 2022),(Wu et al., 2020),(Li et al., 2022),(Wen et al., 2021),(Yuan et al., 2020),(L. Chen et al., 2020)
5	Price manipulation	(Dokuz et al., 2020),(Akba et al., 2021)
6	Smart contract (Ponzi)	(Jung et al., 2019),(Liu et al., 2022),(H. Hu et al., 2022),(Bartoletti et al., 2018),
7	Transaction Exchange Anomalies	(Aziz, Baluch, Patel, & Ganie, 2022),(Baek et al., 2019),(Gu et al., 2022),(Tan et al., 2021),(Poursafaei et al., 2020),(Nan & Tao, 2018),(Liao et al., 2019),(Lee et al., 2020),(Aziz, Baluch, Patel, & ..., 2022),(Shayegan et al., 2022)

4.0 CONCLUSION

This SLR research conducted could filter 38 papers out of 100 papers using the search criteria used in this study. In RQ1and RQ2, there were 37 articles accessed to conclude on the research question. RQ3 used 16 articles while RQ4 used a total of 31 articles. The majority of researchers are spread across a period of 2 years i.e., 2020, 2021 and 2022. We were able to identify gaps and recommend future research directions in the domain. Our results indicate that the majority of fraud in the cryptocurrency domain takes place across two cryptocurrency network which are Bitcoin and Ethereum.

REFERENCE

] Kharif, O. (2014). Mt. Gox CEO claims 850,000 bitcoins worth $480m have gone missing. Bloomberg Businessweek. Retrieved from https://www.bloomberg.com/news/articles/2014-02-28/mt-gox-ceo-says-850-000-bitcoins-worth-480 million-have-disappeared—Search. (n.d.). Retrieved January 5, 2023, from

Akba, F., Medeni, I., Guzel, M., & Askerzade, I. (2021). Manipulator Detection in Cryptocurrency Markets Based on Forecasting Anomalies. IEEE Access, Query date: 2023-01-01 12:49:58. https://ieeexplore.ieee.org/abstract/document/9502700/

Alarab, I., Prakoonwit, S., & Nacer, M. (2020a). Comparative analysis using supervised learning methods for anti-money laundering in bitcoin. … Conference on Machine Learning …, Query date: 2023-01-01 12:49:58. https://doi.org/10.1145/3409073.3409078

Alarab, I., Prakoonwit, S., & Nacer, M. (2020b). Competence of graph convolutional networks for anti-money laundering in bitcoin blockchain. … Conference on Machine Learning …, Query date: 2023-01-01 12:49:58. https://doi.org/10.1145/3409073.3409080

Aljofey, A., Rasool, A., Jiang, Q., & Qu, Q. (2022). A Feature-Based Robust Method for Abnormal Contracts Detection in Ethereum Blockchain. Electronics, Query date: 2023-01-01 12:49:58. https://www.mdpi.com/2079-9292/11/18/2937

Andreas Isnes Nilsen. (2023). Limelight: Real-Time Detection of Pump-and-Dump Events on Cryptocurrency Exchanges Using Deep Learning.

Aziz, R., Baluch, M., Patel, S., & ... (2022). A Machine Learning based Approach to Detect the Ethereum Fraud Transactions with Limited Attributes. … International Journal of …, Query date: 2023-01-01 12:49:58. https://scholar.archive.org/work/uqv5zzlvt5f5jb5kjglm64ljtm/access/wayback/https://kijoms.uokerbala.edu.iq/cgi/viewcontent.cgi?article=3229&context=home

Aziz, R., Baluch, M., Patel, S., & Ganie, A. (2022). LGBM: a machine learning approach for Ethereum fraud detection. International Journal of …, Query date: 2023-01-01 12:49:58. https://doi.org/10.1007/s41870-022-00864-6

Baek, H., Oh, J., Kim, C., & Lee, K. (2019). A model for detecting cryptocurrency transactions with discernible purpose. … Conference on Ubiquitous and …, Query date: 2023-01-01 12:49:58. https://ieeexplore.ieee.org/abstract/document/8806126/

Bao, F., & Li, X. (2019). A survey on cryptocurrency fraud detection. International Journal of Web and Grid Services, 15(3), 199-216. (n.d.).

Bartoletti, M., Pes, B., & Serusi, S. (2018). Data mining for detecting bitcoin ponzi schemes. … Crypto Valley Conference on …, Query date: 2023-01-01 12:49:58. https://ieeexplore.ieee.org/abstract/document/8525395/

Chen, B., Wei, F., & Gu, C. (2021). Bitcoin Theft Detection Based on Supervised Machine Learning Algorithms. Security and Communication Networks, Query date: 2023-01-01 12:49:58. https://www.hindawi.com/journals/scn/2021/6643763/

Chen, L., Peng, J., Liu, Y., Li, J., Xie, F., & Zheng, Z. (2020). Phishing scams detection in ethereum transaction network. ACM Transactions on …, Query date: 2023-01-01 12:49:58. https://doi.org/10.1145/3398071

Dokuz, A., Çelik, M., & Ecemi?, A. (2020). Anomaly detection in bitcoin prices using DBSCAN Algorithm. European Journal of Science and …, Query date: 2023-01-01 12:49:58. https://www.researchgate.net/profile/Ahmet-Dokuz/publication/341052358_Anomaly_Detection_in_Bitcoin_Prices_using_DBSCAN_Algorithm/links/5eabf9a4a6fdcc70509e065b/Anomaly-Detection-in-Bitcoin-Prices-using-DBSCAN-Algorithm.pdf

Gu, Z., Lin, D., & Wu, J. (2022). On-chain analysis-based detection of abnormal transaction amount on cryptocurrency exchanges. Physica A: Statistical Mechanics and Its Applications, Query date: 2023-01-01 12:49:58. https://www.sciencedirect.com/science/article/pii/S0378437122005258

Hu, H., Bai, Q., & Xu, Y. (2022). Scsguard: Deep scam detection for ethereum smart contracts. IEEE INFOCOM 2022-IEEE Conference on …, Query date: 2023-01-01 12:49:58. https://ieeexplore.ieee.org/abstract/document/9798296/

Hu, T., Liu, X., Chen, T., Zhang, X., Huang, X., Niu, W., & ... (2021). Transaction-based classification and detection approach for Ethereum smart contract. Information Processing …, Query date: 2023-01-01 12:49:58. https://www.sciencedirect.com/science/article/pii/S0306457320309547

Ibrahim, R., Elian, A., & ... (2021). Illicit account detection in the ethereum blockchain using machine learning. … Conference on Information …, Query date: 2023-01-01 12:49:58. https://ieeexplore.ieee.org/abstract/document/9491653/

Ismail Alarab, Simant Prakoonwit, & Mohamed Ikbal Nacer. (2020). Competence of Graph Convolutional Networks for Anti-Money Laundering in Bitcoin Blockchain. Proceedings of the 2020 5th International Conference on Machine Learning Technologies. https://doi.org/10.1145/3409073.3409080

Jung, E., Tilly, M. L., Gehani, A., & ... (2019). Data mining-based ethereum fraud detection. 2019 IEEE International …, Query date: 2023-01-01 12:49:58. https://ieeexplore.ieee.org/abstract/document/8946232/

Kanezashi, H., Suzumura, T., Liu, X., & Hirofuchi, T. (2022). Ethereum Fraud Detection with Heterogeneous Graph Neural Networks. ArXiv Preprint ArXiv …, Query date: 2023-01-01 12:49:58. https://arxiv.org/abs/2203.12363

Kaur, M., & Singh, G. (2019). Cryptocurrency fraud detection using machine learning techniques: A review. In 2019 Second International Conference on Communication and Electronics Systems (ICCES) (pp. 1-5). IEEE. (n.d.).

Kshetri, N. (2018). Initial coin offerings: A review of the regulatory challenges. Journal of Financial Regulation and Compliance, 26(4), 318-333. (n.d.).

Kumar, N., Singh, A., Handa, A., & Shukla, S. (2020). Detecting malicious accounts on the Ethereum blockchain with supervised learning. … and Machine Learning, Query date: 2023-01-01 12:49:58. https://doi.org/10.1007/978-3-030-49785-9_7

Lee, C., Maharjan, S., Ko, K., & Hong, J. (2020). Toward detecting illegal transactions on bitcoin using machine-learning methods. … Conference on Blockchain and …, Query date: 2023-01-01 12:49:58. https://doi.org/10.1007/978-981-15-2777-7_42

Li, P., Xie, Y., Xu, X., Zhou, J., & Xuan, Q. (2022). Phishing Fraud Detection on Ethereum using Graph Neural Network. ArXiv Preprint ArXiv:2204.08194, Query date: 2023-01-01 12:49:58. https://arxiv.org/abs/2204.08194

Liao, J., Tsai, T., He, C., & ... (2019). Soliaudit: Smart contract vulnerability assessment based on machine learning and fuzz testing. … Systems, Management and …, Query date: 2023-01-01 12:49:58. https://ieeexplore.ieee.org/abstract/document/8939256/

Liu, L., Tsai, W., Bhuiyan, M., Peng, H., & Liu, M. (2022). Blockchain-enabled fraud discovery through abnormal smart contract detection on Ethereum. Future Generation Computer …, Query date: 2023-01-01 12:49:58. https://www.sciencedirect.com/science/article/pii/S0167739X21003319

Lorenz, J., Silva, M., Aparício, D., Ascensão, J., & ... (2020). Machine learning methods to detect money laundering in the bitcoin blockchain in the presence of label scarcity. Proceedings of the First …, Query date: 2023-01-01 12:49:58. https://doi.org/10.1145/3383455.3422549

Moher2009.pdf. (n.d.).

Nan, L., & Tao, D. (2018). Bitcoin mixing detection using deep autoencoder. 2018 IEEE Third International Conference on …, Query date: 2023-01-01 12:49:58. https://ieeexplore.ieee.org/abstract/document/8411868/

Nilsen, A. (2019). Limelight: Real-time detection of pump-and-dump events on cryptocurrency exchanges using deep learning. munin.uit.no. https://munin.uit.no/handle/10037/15733

Ostapowicz, M., & ?bikowski, K. (2020). Detecting fraudulent accounts on blockchain: A supervised approach. International Conference on Web Information …, Query date: 2023-01-01 12:49:58. https://doi.org/10.1007/978-3-030-34223-4_2

Panpan Li, Yunyi Xie, & Xinyao Xu et al. (2023). Phishing Fraud Detection on Ethereum using Graph Neural Network.

Patel, V., Pan, L., & Rajasegarar, S. (2020). Graph deep learning based anomaly detection in ethereum blockchain network. International Conference on Network and …, Query date: 2023-01-01 12:49:58. https://doi.org/10.1007/978-3-030-65745-1_8

Poursafaei, F., Hamad, G., & Zilic, Z. (2020). Detecting malicious Ethereum entities via application of machine learning classification. … for Innovative Networks and …, Query date: 2023-01-01 12:49:58. https://ieeexplore.ieee.org/abstract/document/9223304/

Runnan Tan, Qingfeng Tan, & +1 author Zhao Li. (2021). Graph Neural Network for Ethereum Fraud Detection. IEEE International Conference on Big Knowledge.

Scicchitano, F., Liguori, A., Guarascio, M., Ritacco, E., & ... (2020). Deep autoencoder ensembles for anomaly detection on blockchain. … on Methodologies for …, Query date: 2023-01-01 12:49:58. https://doi.org/10.1007/978-3-030-59491-6_43

SEC. (2020). Investor Alert: Ponzi Schemes. Retrieved from https://www.sec.gov/oiea/investor-alerts-bulletins/ia_ponzi.html—Search. (n.d.). Retrieved January 5, 2023, from https://www.bing.com/search?q=SEC.+(2020).+Investor+Alert%3A+Ponzi+Schemes.+Retrieved+from+https%3A%2F%2Fwww.sec.gov%2Foiea%2Finvestor-alerts-bulletins%2Fia_ponzi.html&cvid=be4d7f806d2e45768ee59f0a311a39fe&aqs=edge..69i57.1299j0j4&FORM=ANAB01&PC=ASTS

Shayegan, M., Sabor, H., Uddin, M., & Chen, C. (2022). A Collective Anomaly Detection Technique to Detect Crypto Wallet Frauds on Bitcoin Network. Symmetry, Query date: 2023-01-01 12:49:58. https://www.mdpi.com/2073-8994/14/2/328

Singh, A., Gupta, A., Wadhwa, H., & ... (2021). Temporal Debiasing using Adversarial Loss based GNN architecture for Crypto Fraud Detection. … on Machine Learning …, Query date: 2023-01-01 12:49:58. https://ieeexplore.ieee.org/abstract/document/9680261/

Sureshbhai, P., Bhattacharya, P., & ... (2020). KaRuNa: A blockchain-based sentiment analysis framework for fraud cryptocurrency schemes. 2020 IEEE International …, Query date: 2023-01-01 12:49:58. https://ieeexplore.ieee.org/abstract/document/9145151/

Tan, R., Tan, Q., Zhang, P., & Li, Z. (2021). Graph neural network for ethereum fraud detection. 2021 IEEE International …, Query date: 2023-01-01 12:49:58. https://ieeexplore.ieee.org/abstract/document/9667674/

Wang, Z., Chen, M., & Lee, W. C. (2018). A survey on cryptocurrency fraud detection techniques. In 2018 IEEE International Conference on Big Data (Big Data) (pp. 438-447). IEEE. (n.d.).

Weber, M., Domeniconi, G., Chen, J., Weidele, D., & ... (2019). Anti-money laundering in bitcoin: Experimenting with graph convolutional networks for financial forensics. ArXiv Preprint ArXiv …, Query date: 2023-01-01 12:49:58. https://arxiv.org/abs/1908.02591

Wen, H., Fang, J., Wu, J., & Zheng, Z. (2021). Transaction-based hidden strategies against general phishing detection framework on ethereum. … Symposium on Circuits and …, Query date: 2023-01-01 12:49:58. https://ieeexplore.ieee.org/abstract/document/9401091/

Wen, Z., Zeng, D., Li, Y., Li, H., & Lu, J. (2019). Blockchain analytics: A survey. ACM Computing Surveys (CSUR), 52(1), 1-38. (n.d.).

Wu, J., Yuan, Q., Lin, D., You, W., Chen, W., & ... (2020). Who are the phishers? Phishing scam detection on ethereum via network embedding. IEEE Transactions …, Query date: 2023-01-01 12:49:58. https://ieeexplore.ieee.org/abstract/document/9184813/

Yin, H. S., Langenheldt, K., Harlev, M., & ... (2019). Regulating cryptocurrencies: A supervised machine learning approach to de-anonymizing the bitcoin blockchain. Journal of …, Query date: 2023-01-01,12:49:58. https://doi.org/10.1080/07421222.2018.1550550

Yuan, Z., Yuan, Q., & Wu, J. (2020). Phishing detection on Ethereum via learning representation of transaction subgraphs. International Conference on Blockchain and …, Query date: 2023-01-01 12:49:58. https://doi.org/10.1007/978-981-15-9213-3_14

Zohar, A. (2015). Bitcoin: Under the hood. Communications of the ACM, 58(9), 104–113. https://doi.org/10.1145/2701411

4th International Engineering Conference (IEC 2022)
Federal University of Technology, Minna, Nigeria

Synthesis, Characterization, and Utilization of Multi-walled Carbon Nanotubes as Cathode in Alkaline batteries.

Abdulraheem, S,[1] Abdulkareem, A. S,[2] & Muriana, R. A,[3]
1,2 Department of Chemical Engineering, Federal University of Technology, PMB 65 Minna, Niger State, Nigeria
3 Department of Mechanical Engineering, Federal University of Technology, PMB 65 Minna, Niger State, Nigeria

*Corresponding author email: Barhama247@gmail.com Tel: 07033230589

ABSTRACT

Alkaline battery market revenue is projected to grow from 7.8 billion dollars in 2021 to 10.9 billion dollars in the year 2028 period. But increase in demand for rechargeable batteries such as lithium-ion batteries will restrain the alkaline market growth because of its efficiency. This research aims to utilize MWCNTs as a dopant in an alkaline battery. The multi-walled carbon nanotubes (MWCNTs) were prepared by catalytic chemical vapor deposition method (CCVD) using acetylene gas (C_2H_2) as hydrocarbon source and nitrogen gas (N_2) as dilute gas on Fe-Ni bimetallic catalyst supported on kaolin. The produced MWCNTs were purified by acid treatment and then characterized before and after doping MnO_2 with purified MWCNTs using Brunauer, Emmett, and Teller (B.E.T.) and before and after purification using High-Resolution Scanning Electron Microscopy (HRSEM), High-Resolution Transmission Electron Microscopy (HRTEM). And conductivity of the purified MWCNTs was determined by measuring the voltage of the produced battery. The Brunauer, Emmett, and Teller (B.E.T.) analysis of the nanocomposite (MnO_2/Graphite/MWCNTs) reveal a higher surface area and pore volume of 204.681 m^2g^{-1} and 0.101 cm^3g^{-1} when compared with the surface area and pore volume of purified MWCNTs of 168.117 m^2g^{-1} and 0.082 cm^3g^{-1}. The HRSEM and HRTEM reveal a tube-like, concentric, and twisted material. The lowest voltage measured was 0.50 V (with cathode of MnO_2 (20%) MWCNT (100%)), and the highest voltage measured was 1.45 V (with the cathode of MnO_2 (60%), MWCNT (100%)). This study shows that MWCNTs can be successfully used to replace Graphite in Alkaline battery production to increase its efficiency and reduce the percentage of MnO_2 used in making the cathode Also, MWCNTs of different purity can be use to dope MnO_2 and battery characterized.

Keywords: Acid Treatment, Alkaline Battery, MWCNTs, Chemical Vapour Deposition, and Conductivity.

1 INTRODUCTION

Carbon nanotubes (CNT) were first synthesized in 1952 by Radushkevich *et al.*, a Russian group, who published the first transmission electron microscopy (TEM) image demonstrating the tubular nature of the nanometric-sized carbon filaments. Iijima, from the Nanoelectronic Corporation (NEC) laboratory in Tsukuba, Japan, was the first to use high-resolution transmission electron microscopy to identify the structure of a carbon nanotube (HRTEM). Following that, the field of carbon nanotubes was seriously launched (Shahid Nisar Ahmad *et al.*, 2009). Carbon nanotubes are fragile, hollow cylinders made of carbon atoms arranged in hexagonal rings. (Lat Lat Tun *et al.*, 2018). A carbon nanotube can also be considered a graphene sheet rolled into a seamless cylinder. Their superior properties make them the most promising nanomaterials for a wide range of applications in the twenty-first century. CNTs can mainly be divided into two types: single-walled carbon nanotubes (SWCNTs) and multi-walled carbon nanotubes (MWCNTs) (Rajesh Purohita *et al.*, 2014). A single-walled carbon nanotube can be considered as a single graphene sheet rolled into a tube. In comparison, multi-walled nanotubes can be described as a number of concentric single-walled carbon nanotubes (SWCNTs) having different diameters (Aliyu A. *et al.*, 2016). Several methods, including arc discharge, laser ablation, and chemical vapor deposition, have been successfully tested and reported for the production of CNTs. These techniques, arc discharge, and laser ablation, have significant drawbacks, such as high operating temperatures, high equipment costs, and difficulty scaling up for commercial purposes. Catalytic chemical vapor deposition (CCVD) is the most efficient and profitable method of producing large quantities of high-quality CNTs at low synthesis temperatures (Aliyu A. *et al.*, 2016). Since MWCNTs is a better conductor of electricity (10^6 – 10^7) sm^{-1}, with resistivity 6.1 × 10^{-5} Ωm and thermal conductivity > 3000 $wm^{-1}k^{-1}$ than Graphite with electrical conductivity of 10^4 sm^{-1}, resistivity of 39.37 Ωm and thermal conductivity 6.9318 $wm^{-1}k^{-1}$. This shows that it can be used as an electronic conductor in an alkaline battery. Lewis Urry invented the alkaline battery in 1957,

and it derives its energy from the reaction of zinc metal and manganese dioxide (MnO_2). The negative electrode is zinc, and the positive electrode is manganese dioxide (MnO_2). Only the zinc and MnO_2 are consumed during discharge; the electrolyte, potassium hydroxide (KOH), and Graphite used to dope the MnO_2 do not participate in the reaction. The alkaline battery market is expected to expand from 7.8 billion dollars in 2021 to 10.9 billion dollars in 2028. The increase in demand for rechargeable batteries, such as lithium-ion batteries, is expected to limit this market projection. Because they have a higher discharge rate, are more energy efficient, and are less expensive than disposable alkaline batteries (David Linden *et al*., 2001) Several works have been done on doping MnO_2 with additives, this include; Electrochemical characteristics of B_4C or BN added MnO_2 cathode material for alkaline batteries (Manickam Minakshi *et al*., 2010). The boron nitride (BN) modified MnO_2 electrode enhanced the discharged capacity to 185 $mAhg^{-1}$ with the mean discharge voltage of 1.5 V. While with boron carbide (B_4C) as addictive the discharge capacity is 175 $mAhg^{-1}$ and mean voltage of 1.4 V. Incorporation of Titanium diboride (TiB_2) additive into MnO_2 cathode and its influence on rechargeability in an aqueous battery system (Manickam Minakshi *et al*., 2007). It is found that the presence of $TiB_2 \leq 3$ wt.% with MnO_2 improved the open circuit voltage to 1.5 V and increased the discharge capacity from 150 $mAhg^{-1}$ to a maximum of 220 $mAhg^{-1}$. Increasing the TiB_2 content above a threshold of 3 wt.% caused a decrease in the cell capacity to 100 $mAhg^{-1}$. This study focuses on the catalytic chemical vapour deposition (CCVD) of MWCNTs using a Fe-Ni/Kaolin catalyst, acetylene, and nitrogen gas. Because of its ability to withstand high temperatures, exceptional chemical resistance, and mechanical strength in the catalyst and CNTs. Kaolin, also known as kaolinite or China clay, was chosen over commercially available support substrates (SiO_2, Al_2O_3 etc.) due to its ability to withstand high temperatures, its exceptional chemical resistance and mechanical strength in the catalyst, and the CNTs. The choice of Fe-Ni as the catalyst was favored based on its high solubility and high rate of carbon diffusion at high temperature. And nitrogen gas was used over argon gas because it is cheap and readily available (makes up about 79.1% of the atmosphere). Physically adding MWCNTs to MnO_2 cathode for alkaline battery and test its electronic conductivity, will potentially improve alkaline battery efficiency and reduce the percentage of MnO_2.

2 METHODOLOGY

The equipment used in this research work are; Cylindrical tube reactor, Beaker, Oven, Micrometer sieves, PH meter, Weighing scale. The materials used are; Tiger battery, Iron (III) Nitrate {Fe $\{(NO_3)_3.9H_2O\}$, Nickel Nitrate {Ni $(NO_3)_2.6H_2O\}$, Nitrogen (Carrier gas), Acetylene (carbon source), Nitric acid (HNO_3), Kaolin, Distilled water, Potassium hydroxide (KOH), Graphite, MnO_2, 20 ml syringe and MWCNTs.

2.1 Sample Collection and Preparation

The Iron (III) Nitrate {Fe $\{(NO_3)_3.9H_2O\}$, Nickel Nitrate {Ni $(NO_3)_2.6H_2O$, were obtained from Sim best scientific and chemicals, Opposite Federal University of Technology Minna (FUTM) Bosso campus. The Nitrogen and Argon gas were obtained from step B laboratory Federal University of Technology Bosso Campus, Minna.

2.2 Preparation of Bimetallic Catalyst (Fe-Ni/Kaolin)

5.05 g of Fe $(NO_3)_3.9H_2O$ and 3.64 g of Ni $(NO_3)_2.6H_2O$ were weighed and mixed in a beaker. Ground the weighed sample Fe $(NO_3)_3.9H_20$ and Ni $(NO_3)_2.6H_2O$ to a fine powder and dissolve in 50 mL of distilled water to create a solution. 50 mL of the solution was added to 8 g of kaolin and allow to age for 30 min on a magnetic stirrer at a stirring speed of 1200 rpm. The resulting slurry was partially dried at room temperature and later oven dried at temperature of 120 °C for 8 h. The mixtures were later cooled to room temperature and screened with a 150 µm sieve. Then, the catalyst powders were calcined at 500 °C for 16 h in a furnace in order to decompose the nitrates. The sample was weighed and recorded in order to determine the yield, using the relationship presented in equation 1 and 2.

Catalyst yield before oven drying (%) =

$$(W_1 - W_2) / W_1 \times 100\ \% \quad (1)$$

Where W_1 = weight of catalyst before oven drying

W_2 = the weight of catalyst after oven drying

Catalyst yield before calcination (%) =

$$(W_1 - W_2) / W_1 \times 100\ \% \quad (2)$$

Where W_1 = weight of catalyst before calcination and

W_2 = weight of catalyst after calcination.

2.3 Synthesis of MWCNTs.

1 gram of the prepared catalyst was spread to form a thin layer in a quartz boat (11 × 2.6 cm) and placed at the Centre of the quartz tube. The furnace was heated at 10 °C/min while Nitrogen gas was allowed to flow at a rate of 30 ml/min, to remove contaminants and to prevent oxidation of the samples during the experiment. Once the

desired temperature reached 700 °C, the Nitrogen gas flow rate was adjusted to 190 mL/ min. Introduced the carbon source (C_2H_2) at a flow rate of 290 mL/min and allow the reaction to proceed for a period of 60 min. At a residence time of 60 minutes, stop the flow of acetylene (C_2H_2) and allow Nitrogen gas to continue flowing at 30 mL/min until the reactor cooled to room temperature. Then, the boat containing the sample was removed from the reactor and weighed in order to determine the quantity of MWCNTs produced.

$$\textbf{MWCNTs } \textit{Yield} \textbf{ (\%)} = (W_2 - W_1) / W_1 \times 100\% \quad (3)$$

Where W_1 = the initial weight of the catalyst before reaction and,

W_2 = the weight of catalyst and carbon deposited after synthesis.

2.4 Purification of Synthesized MWCNTs.

Treat synthesized MWCNTs with 30% Nitric acid (HNO_3) with continuous stirring on a magnetic stirrer for 3 hrs. at room temperature. Decant and wash sample with distilled water until the PH is approximately 7.0. Dry sample at 120 ^{0}C for 24 hrs and store.

2.5 Doping MnO_2 with Graphite/MWCNTs.

A mixture was prepared by mixing 0.25 g of MnO_2,1 g of Graphite/MWCNTs (0% of Graphite and 100% MWCNTs) in a sample bottle and shaking intensely as well as stirring with a spatula to ensure a homogenous mixture. Repeat with different masses of MnO_2 and Graphite/MWCNTs (with different percentages for each mass of Graphite/MWCNTs) as stated in table 1.

TABLE 1: Composition of Nanocomposite (MnO_2/Graphite/MWCNTs with Different Masses

MnO_2 (g)	Graphite (%)	MWCNTs (%)	Graphite/ MWCNTs (g)	MnO_2/Graphite/ MWCNTs (g)
0.25	0	100	1	1.25
	25	75		
	50	50		
	75	25		
	100	0		
1.34	0	100	2	3.34
	25	75		
	50	50		
	75	25		
	100	0		
4.5	0	100	3	7.5
	25	75		
	50	50		
	75	25		
	100	0		

2.6 Determination of Pore Volume of MWCNTs and Nanocomposite (MnO_2/Graphite/MWCNTs) Using Brunauer, Emmett, and Teller (BET).

Degassed Samples at 250 °C for 4 hrs. for moisture removal. Analyze the degassed sample for physisorption of the adsorbate (nitrogen) by the adsorbent in a liquid nitrogen environment on the surface using Nova e- series equipment.

2.7 Determination of The Morphology of Purified MWCNTs Using High-Resolution Scan Electron Microscope (HRSEM).

Sprinkle a small quantity of the synthesized MWCNTs on a sample holder and sputter coated with Au-Pd using Quorum T15OT for 5 minutes prior to analysis. Firmly attach the sputter-coated samples to the carbon adhesive tape and analyze using Zeiss Auriga SEM equipped with In-lens standard detector at 5.0 kV.

2.8 Determination of Internal Structure of MWCNTs Using High-Resolution Transmission

Electron Microscope (HRTEM). Operate Zeiss Auriga High-Resolution Transmission Electron Microscope (HRTEM) at 3950. Suspend Small quantity of MWCNTs in 10 ml methanol and ultrasonicate until the particles completely dissolve. Place Few drops of the slurry onto the holey carbon grid. Dry via exposure to photo light and analyze.

Table 2: Composition of Cathode (MnO_2/Graphite/MWCNTs) with Different Masses of Electrolyte.

MnO_2 (g)	Graphite (%)	MWCNTs (%)	Graphite/ MWCNTs (g)	MnO_2/Graphite/ MWCNTs (g)	Electrolyte (K.O.H.) (g/cm^3)
	0	100			
	25	75			
	50	50			
	75	25			
0.25	100	0	1	1.25	0.11
	0	100			
	25	75			
	50	50			
	75	25			
1.34	100	0	2	3.34	0.25
	0	100			
	25	75			
	50	50			
	75	25			
4.5	100	0	3	7.5	0.43

2.9 Determination of Conductivity of MWCNTs

An electrochemical cell was constructed with 1.25 g of the nanocomposite MnO_2/Graphite/MWCNTs (0% of Graphite and 100% MWCNTs) as the cathode and 0.11 g/cm^3 of the electrolyte (KOH). The anode electrode (Zn) of the alkaline battery (Tiger battery) and filter paper as the separator. Repeat the procedure with a different mass of nanocomposite MnO_2/Graphite/MWCNTs (with different percentages for each mass of Graphite/MWCNTs) and with an additional mass of electrolyte, as shown in Table 2. The cell performance was evaluated using a multimeter to measure the voltage.

3 RESULTS AND DISCUSSION

3.1 Preparation of Bimetallic Catalyst (Fe-Ni/Kaolin)

The catalyst yield before calcination was 76.57 % compared to the values obtained by other researchers, such as that of (Aliyu A. *et al.*, 2017), whose value was obtained to be 80.73 %. The Catalyst yield after calcination was 56.26 % compared to the value obtained by (Aliyu A. et al., 2017) 67.75 %. This reduction in the catalyst yield from 76.57 % to 56.26 % was a result of multiple changes that occurred during the process. This includes active phase generation, loss of chemically bound water, and changes in the pore size distribution.

3.2 Synthesis of MWCNTs

The percentage MWCNT yield obtained in this study was 408 % compared with previous studies such as the work of (Aliyu A. *et al*., 2017), the MWCNT yield was 306 %. The difference in the yield could be linked to the differences in the MWCNTs synthesis conditions.

3.3 Purification of MWCNTs

The mass of MWCNT before purification was 40.06 g this is due to the presence of impurities as a result of undissolved catalyst particles and amorphous carbon. After purification with 30 % Nitric acid (HNO_3) to remove the undissolved metallic catalyst and amorphous carbon presence in the as-produced MWCNTs, the mass of MWCNTs reduces to 35.0 g making the percentage purity (MWCNTs) to be 87.37 %. Carbon nanomaterial treated using this process becomes active (V. Shanov *et al*., 2006)

3.4 Determination of the Surface Area and Pore Volume of purified MWCNTs and Nanocomposite (MnO_2/Graphite/MWCNTs) Using Brunauer, Emmett and Teller (BET).

The surface area and pore volume of the synthesized MWCNTs were determined using BET equipment. The surface area and pore volume of the purified MWCNTs were computed as 168.117 m^2g^{-1} and 0.082 cm^3g^{-1} compared to the values obtained by (Karim Ishaq *et al*., 2018) 268.40 m^2g^{-1} and 0.105 cm^3g^{-1} These differences could be linked to the presence of the residual catalyst and some impurities that blocked the pores of purified MWCNTs caps. The surface area and pore volume of Nanocomposite (MnO_2/Graphite/MWCNTs) was 204.681 m^2g^{-1} and 0.101 cm^3g^{-1} compared to the values obtained by (Zaheer Aslam *et al*., 2019) 86.3 m^2g^{-1} and 0.28 cm^3g^{-1}. These differences could be linked to manganese dioxide and Graphite in the MWCNTs which concealed the surface area and pore volume of MWCNTs.

3.5 Determination of The Morphology of MWCNTs Using High Resolution Scan Electron Microscope (HRSEM).

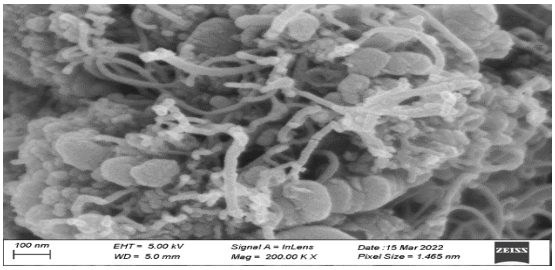

Figure 3.5 (a) As-prepared MWCNTs

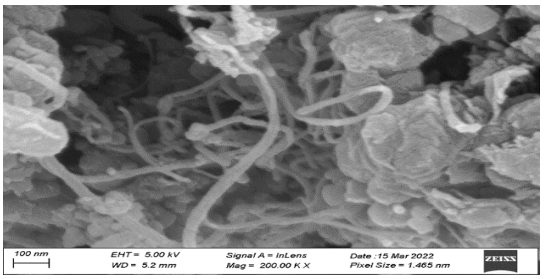

Figure 3.5 (b) purified MWCNTs

Figure 3.5 (a) shows the analyses conducted on the as-prepared MWCNTs, impurities such as catalyst metal particles, support materials, and amorphous

carbon are present on the surface of MWCNTs. Morp hological arrangement and its different applications are affected by such impurities. Hence, the need to remove these impurities is demonstrated in Figure 3.5 (b). Also, a slight degree of agglomeration with some bright spots is present in the as-prepared MWCNTs, which shows the presence of residual metals, while the purified MWCNTs exhibit a clearly defined tubular morphology with slight agglomeration.

3.6 Determination of the internal structure of MWCNTs Using High-Resolution Transmission Electron Microscope (HRTEM).

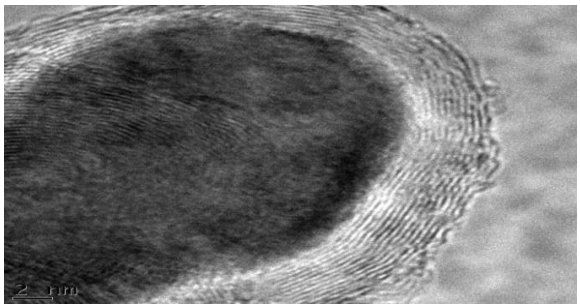

Figure 3.6 (a)

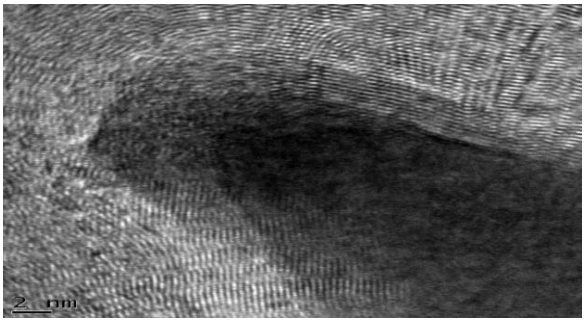

Figure 3.6 (b)

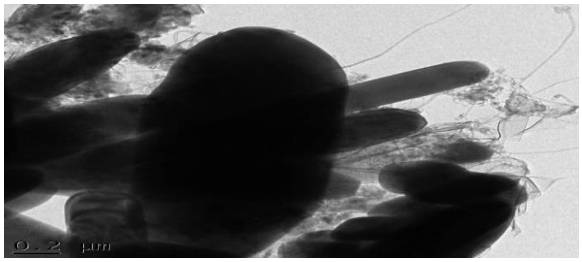

Figure 3.6 (c)

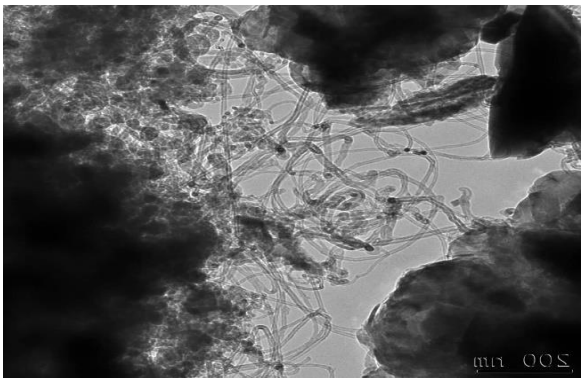

Figure 3.6 (d)

Figure 3.6 (a), (b), (c) and (d) shows the internal structure of MWCNTs, with (a) revealing the catalyst particles been encapsulated inside the MWCNTs and (b) indicting the visibility of the lattice structure and concentric nature of the MWCNTs (c) depicts the tubular nature of MWCNTs and (d) shows a twisted MWCNTs.

Table 3: Voltage of Alkaline battery with Different Composition of Cathode (MnO_2/Graphite/MWCNTs)

MnO_2 (%)	Graphite (%)	MWCNTs (%)	MnO_2/ Graphite/ MWCNTs (g)	Electrolyte (K.O.H.) (g/cm^3)	Voltage (V)
20%	0	100	1.25	0.11	0.50
	25	75			0.46
	50	50			0.37
	75	25			0.36
	100	0			0.39
40%	0	100	3.34	0.25	0.98
	25	75			1.31
	50	50			1.05
	75	25			1.32
	100	0			0.69
60%	0	100	7.5	0.43	1.45
	25	75			1.50
	50	50			1.08
	75	25			0.75
	100	0			0.49

3.7 Determination of the Conductivity of MWCNTs

As shown in Table 3, with a cathode of MnO_2 (20%), the voltage obtained was 0.50 V (MWCNT (100%) and Graphite (0%)) compared to the voltage of 1.5 V with a cathode of MnO_2 (79%) and Graphite (2%) stated by (David Linden *et al.*, 2001). Using a cathode of MnO_2 (40%), the voltage obtained was 0.98 V (MWCNT (100%) and Graphite (0%)) compared to the voltage of 1.5 V using a cathode with the composition of MnO_2 (79%) and Graphite (2%) stated by (David Linden *et al.*, 2001). With a cathode of MnO_2 (60%), the voltage obtained was 1.45 V (MWCNT (100%) and Graphite (0%)) compared to the voltage of 1.5 V using cathode with a composition of MnO_2 (79%) and Graphite (2%) stated by (David Linden *et al.*, 2001).

The increase in the voltage (0.5 V, 0.98 V to 1.45 V) could be a result of an increase in ion conductivity and intrinsic electron conductivity. By doping MnO_2 with MWCNTs the particle size of MnO_2 decreases, relatively appropriate pore size distribution is obtained, and chemically bound water content increases, all of which contribute to ion conductivity (Yan Yel *et al.*, 2012).

5 CONCLUSION

A bimetallic catalyst (Fe-Ni) supported on kaolin was successfully used to grow MWCNTs using the CCVD method. The surface area and pore volume, morphology, internal structure, and conductivity of the purified MWCNTs were investigated. The following conclusions were drawn based on this study. The percentage yield of the MWCNTs was 408%; this reveals that it depends on the nature of catalyst and catalyst support and the differences in the MWCNTs synthesis conditions. The Brunauer, Emmett , and Teller (BET) analysis of purified MWCNTs reveal a surface area and pore volume of 168.117 m^2g^{-1} and 0.082 cm^3g^{-1} due to residual catalyst and some impurities that blocked the pores of MWCNTs. The HRSEM and HRTEM reveal tube-like, concentric, and twisted MWCNTs. The highest voltage of the alkaline battery with cathode composition of MnO_2 (60%), MWCNTs (100%), and Graphite (0%) was 1.45 V; this was a result of increased ion conductivity and intrinsic electron conductivity. By doping MnO_2 with MWCNTs, the particle size of MnO_2 decreases, relatively appropriate pore size distribution is obtained, and physically and chemically bound water content increases, all of which contribute to ion conductivity. This study shows that MWCNTs can be successfully used to replace Graphite in an Alkaline battery in other to increase its efficiency and reduce the quantity of MnO_2 used in producing it.

ACKNOWLEDGEMENTS

All praises and thanks be to almighty Allah, the general overseer, peace and blessing of Allah be upon his messenger, the opener of what was closed, the seal of what comes before, the helper of truth by the truth. The guide to your straight path and on his family (blessings), may this prayer be commensurate with his worth in space and time. My ultimate appreciation goes to my project supervisor, Prof Abdulkareem A.S, for his construction. And also to Prof R.A Muriana for his technical support, criticism, time dedication to this work. You were there for me when I needed you most, just like a father; thank you, sir. My profound gratitude goes to Petroleum Trust Development Fund (PTDF) for financial backing all through. You did it all for me. “If I have seen further than others, it is by standing on the shoulders of giants’’.

REFERENCES

Lat Lat Tun, San San Maw, (2018). Synthesis of carbon nanotubes from the decomposition of acetylene on ferrite catalyst. Department of Chemical Engineering, Yangon Technological University The Republic of the Union of Myanmar. Retrie ved from www.researchgate.net/publication/32 7068584

Aliyu, A., Abdulkareem, A.S., Kovo, A.S., Abubakre, O.K., Tijani, J.O. and Karim, I. (2016). Synthesize multi-walled carbon nanotubes via catalytic chemical vapor deposition method on Fe-Ni bimetallic catalyst supported on kaolin. Carbon Letters, Vol. 21, DOI: http://dx.doi.org/ DOI:10.5714/CL.2017.21.033.

Manickam Minakshi, Pritam Singh, and David, R. G., Mitchell, (2007). Manganese Dioxide Cathode in the Presence of TiS_2 as Additive on an Aqueous Lithium Secondary Cell. Journal of The Electrochemical Society, 154, 4-6, DOI: 10.1149/1.2403079.

Rajesh Purohita, Kuldeep Purohit, Saraswati Rana, R. S., Ranaa, and Vivek Patel, (2014). Carbon Nanotubes and Their Growth Methods. 3rd International Conference on Materials Processi ng and Characterization (ICMPC 2014), 718-725, DOI: 10.1016/j.mspro.2014.07.088.

David Linden, and Thomas B. Reddy, (2001). Handbook of batteries, third edition. United States of America: McGraw-Hill Companies, Inc. Retrieved from https://epdf.tips/handbook-of-batteries65666.html

Manickam Minakshi, Mark G., Black ford, (2010). Electrochemical characteristics of B4C or BN added MnO2 cathode material for alkaline batteries. Journal of Materials Chemistry and Physics, 123, 3-5. DOI: 10.1016/j.matchemphys.2010.05.041

Shahid Nisar Ahmad, Saira Hakeem, Rashid Ahmed Alvi, Khawar Farooq, Naveed Farooq, Farida Yasmin and Sadaf Saeed, (2009). Synthesis of multi-walled carbon nanotubes and their application in resin-based nanocomposites. Journal of Physics, 439, 3-5, DOI:10.1088/1742-6596/439/1/012009.

Zaheer Aslam, Mariam Qaiser, Rizwan Ali, Aamir Abbas, Ihsanullah & Shazia Zarin (2019). Al2O3/MnO2/CNTs nanocomposite: synthesis, characterization, and phenol adsorption Fullerenes, Nanotubes and Carbon Nanostructures, 27:7, 591-600, DOI: 10.1080/1536383X.2019.1622528

Kariim Ishaq, Abdulkareem Ambali Saka, Abubakre Oladiran Kamardeen, Abubakre Oladiran Kamardeen, Bankole Mercy Temitope, Jimoh Oladejo Tijani, (2015). Studies on the suitability of alumina as bimetallic catalyst support for mwcnts growth in a cvd reactor. Retrieved from https://www.researchg ate.net/publication/282866646

Yan Ye1, Zou Ji-Zhao, Zeng Xie-Rong, (2012) Synthesis and Characterization of Manganese O xide/CNTs Composites as Electrochemical Capacitor Electrode Materials. Key Engineering Materials Vol 519 (2012) pp 197-200. DOI: 10.4028/www.scientific.net/KEM.519.197

V. Shanov, Yeo-Heung Yun, M. J. Schulz, (2006). Synthesis and characterization of carbon nanotube materials. Journal of the University of Chemical Technology and Metallurgy, 41, 380, Received from https://dl.uctm.edu/journal /node/j2006-4/01-Shanov-377-390.

L.V. Radushkevich, V.M. Lukyanovich, On the structure of carbon produced at thermal decomposition of carbon monoxide on an iron contact, Journal of Physical Chemistry 26(1) (1952) 88-95.

4th International Engineering Conference (IEC 2023)
Federal University of Technology, Minna, Nigeria

A Review on Automated Cooking Gas Pressure Valve

*Adejumo, Idris Abayomi and Katsina Christopher Bala
Mechanical Engineering Department, Federal University of Technology, PMB 65 Minna Niger State, Nigeria
*Corresponding author email:rexisrael1@gmail.com +2348131979690

ABSTRACT
Liquefied petroleum gas (LPG) is supplied in cylinders that require special regulators and hoses during use, which are not optimal and can cause leaks. LPG is highly flammable and dangerous, and leaks can have devastating effects on homes if not stopped quickly. This is why automated LPG leak monitoring, detection and control systems are becoming a popular area of research. Domestic liquefied gas automation prevents the occurrence of dangerous explosions. Automation often requires gas sensors, valves, and microcontrollers. This paper aims to evaluate automated LPG systems designed for home use, determine the state of the art in the field, and identify gaps in the field where future research can build.

Keywords: *Gas sensor, leakage, liquified petroleum gas (LPG), microcontrollers, system automation*.

1 INTRODUCTION

There are numerous devices dedicated for fire detection and control, though most are manually operated especially in developing countries like Nigeria. Liquified petroleum gas (LPG) is becoming a popular source of energy in many Nigerian homes nowadays, it is easy to use and provides quick and clean source of energy for the household needs. The LPG is supplied in cylinders that requires specialized regulator and hoses during use that sometimes are not in the best condition, and which leads to leakage. LPG is highly combustible and dangerous with any leakage spelling doom for the household if not immediately arrested. Often the leakages go undetected until too late which is why automated LPG leakage monitoring, detection and control systems are becoming a popular research area.

Gas sensors are employed in a wide range of application in fields of safety, health, instrumentation etc. Common examples are domestic/commercial explosive or toxic gas alarms, or automotive application such as LPG powered vehicle gas leak detectors or fuel truck/car exhaust gas detectors. Such sensors are now also used in applications including air quality control systems and pollution monitoring. Today's sensors, while featuring a high sensitivity to a wide (Hitendra *et al*., 2014). Incorporating these sensor technologies in the domestic household will help to protect against unnecessary loss of lives and property as a result of gas leakages in the home.

2 METHODOLOGY

The methodology involved the review of associated works on automated systems of cooking gas pressure valves/regulators.

2.1 COOKING GAS PRESSURE VALVE

The gas regulator is a device that maintains a constant output of pressure supplied (Naci and Greg, 2008). The primary function of the regulator is to match the supply of the fluid regulated to the demand downstream. Different types are available from simple, single-stage to more complex, multi-stage versions, however, their principle of operation is the same in all (Naci and Greg, 2008). High-pressure gas flows through an orifice in the valve as seen in Figure 1

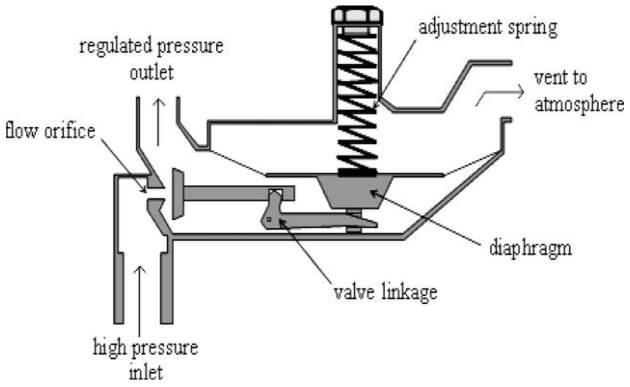

Figure 1: Operational diagram of a typical gas pressure regulator (Source: Naci and Greg, 2008)

The energy generated in the gas is converted to heat and flow at the lower, regulated, pressure. The orifice faces a movable disk that regulates the amount of gas flow. A flexible diaphragm is attached to the disk by means of a mechanical linkage. The diaphragm is installed to expose one side to the atmosphere and the other to the regulated pressure. The orifice is closed via the diaphragm and linkage mechanism if the regulated pressure is too high. The opposite occurs as the regulated pressure becomes too low (Naci and Greg, 2008).

Above the diaphragm assembly is a chamber that houses a wire coil spring and a calibration screw. The screw compresses the spring, which changes the steady state force on the diaphragm, allowing for the adjustment of the regulated pressure set point. If the regulated gas

pressure rises above the safe operational pressure, an internal relief valve is opened to vent the excess gas through the upper chamber and into the atmosphere to prevent the danger of high-pressure gas at the regulator outlet (Naci and Greg, 2008).

The essential elements in the regulator are restricting, sensing and loading elements. The restricting element is the valve, the sensing being the diaphragm and the loading in this case is the spring.

2.2 AUTOMATION MECHANISM

The automation mechanism is made up of some key elements that are depicted in Figure 2. The most important component in the system is the microcontroller that drives the whole system and specifies specific functions to be undertaken by the remaining components.

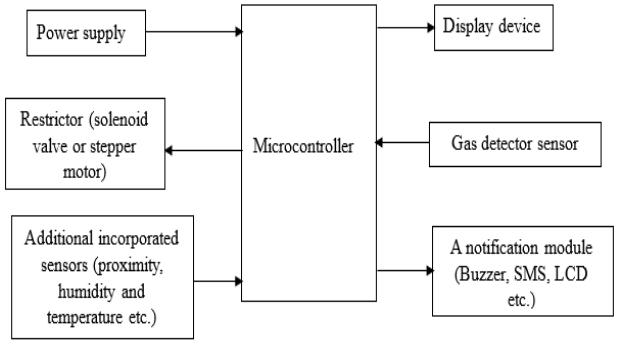

Figure 2: A typical automated gas leak detection and control system (Source: Manu *et al*., 2015; Sanketh *et al*., 2021)

Other components that must be included in the system are the gas detector, the restrictor and some form of notifier. Some researchers have used flame detectors in place of gas detectors (Asad *et al*., 2018). This uses the presence or absence of flame for decision making. Whenever there is flame in the system when the cooking is occurring then the system is performing according to expectation and the restrictor which might be a solenoid valve is open and not restricting gas flow. (Alkali *et al*., 2017) also did not use a gas sensor of any sort in his system. the system employed a flame detector and a load sensor to know if the stove is loaded or not.

Some more sophisticated systems have more devices added to their system to provide better efficiency. Examples are the system of Nugroho and Pantjawati (2017) that has proximity sensor to detect the presence of human in the kitchen area to assist in decision making and the systems of Okeke and Ehikhamenle (2017) and Ebenezer *et al*. (2020) that both have humidity and temperature change sensors to ascertain changes in environmental temperature.

2.2.1 INCORPORATED SENSORS

These are the various sensors incorporated in a typical automated gas leak detection and control system.

a. Gas detector sensor

The gas detector is designed to check the quantity of gas in the selected/observed environment and compares it to a specified safe level often provided to the sensor/detector. The gas quantity is measured in ppm which stands for parts per million or in milligram per litre (mg/L). Most researchers set their gas detectors at ranges of 200 ppm to 1000 ppm (Okonkwo *et al*., 2020). Table I gives provides different types of gas sensors and the type of gases they sense. Semiconductors allow for the exchange of ions from one medium to another and this ionic flow induces a potential difference of which its intensity could be measured. The sensitive layer in contact with the gas upon detection impact the physicochemical interaction leading to the responses via electrical pulses (Younes, 2019).

Table I: GAS SENSORS AND TYPES OF GASES SENSED (Source: Okonkwo *et al*., 2020)

S/N	Sensor	Content
1.	MQ2	H_2, LPG, CH_4, CO, Alcohol, Smoke, Propane, Air
2.	MQ3	LPG, CH_4, CO, Alcohol, Benzine, Hexane, Air
3.	MQ6	H_2, LPG, CH_4, CO, Alcohol, Air
4.	MQ7	H_2, LPG, CH_4, CO, Alcohol, Air
5.	MQ8x	H_2, LPG, CH_4, CO, Alcohol, Air
6.	MQ135	Alcohol, NH_4, CO_2, Air
7.	MQ137	NH_3, O_2, C_2H_6O, Air
8.	MQ138	CH_4, CO, Alkohol, Propane, Benzine, n-Hexane, Air

b. Temperature sensor

The temperature and humidity sensor often used for these designs uses a capacitive humidity sensor and a thermistor to measure ambient air. Available sensors now send output in digital form and does not require analogue pins. The DHT11 is a popular type used by researchers (Adeyemi, 2019; Nugroho and Pantjawati, 2017). This sensor is very easy to use but has a measurement limit of only up to 60°C. DHT11 is used to detect temperature and humidity changes that will otherwise not be normal and will cause the microcontroller to shut the LPG supply.

c. Load sensor

The load sensor is used in the system to either measure the reduction in weight of the gas cylinder in the

system or to detect the absence of the cooking utensil and trip off the gas supply (Zaw *et al*., 2021; Krishnadas *et al*., 2019). The former being the most popular but the latter is the most useful for the system discussed. The load sensor often utilizes a load cell that uses the strain principle for its operation to measure the weight of an object.

d. Flame sensor

Flame detectors can detect and respond to presence of flame. They are a popular device in developed countries and are installed in buildings to prevent fire. They use ultraviolet (UV) light or infrared (IR) technology to identify flame. Some detectors have to come in contact with flame to detect the absence of flame like that which was incorporated in the system designed by (Asad *et al*., 2018). The absense of flame will mean the LPG is leaking without flame when flame is expected.

2.2.2 RESTRICTION UNITS

a. Solenoid valve

This is an electrically controlled valve that features a solenoid which has a movable plunger in its centre. The plunger is ferromagnetic and responds to the electric current by creating a magnetic field that exerts an upward force on it, thereby opening an orifice. It is easily programmable and is suitable for automation of the LPG control and leakage prevention. The solenoid is a popular device in the LPG leakage prevention community (Jadkream *et al*., 2022; Shinde *et al*., 2021; Hitendra *et al*., 2014).

b. Stepper motor

The stepper motor is a electro mechanical device that also be electrically controlled, however it is a brushless DC electric motor that divides a full rotation into a number of equal steps. Some r000esearchers have incorporated this rather than a solenoid valve to control or stop the flow of LPG automatically. The motor is controlled by the microcontroller to turn to the required rotation which in turn closes the gas nozzle of where it is attached (Senthil *et al*., 2020)

2.2.3 MICROCONTROLLER

The microcontroller is used to control and run the complete system. it employs the function of the various detectors in the system and uses information provided to carryout decisions on behalf of the user. Most of the microcontrollers are designed to be able to receive programming instructions from computers. They can be programmed using different programming languages like, C++, python, Java etc. Arduino Uno is the most popular microcontroller used nowadays by most of the researchers in this area, although PIC microcontroller was used earlier (Mahalingam *et al*., 2012).

3 RESULTS AND DISCUSSION

3.1 PREVIOUS WORKS

Nugroho and Pantjawati (2017) created a system that could detect changes in temperature and fire caused by the use of cooking stoves in the kitchen. The system had the DHT11 sensor mounted to detect temperature changes, infra-red flame sensor to detect fire, and passive infrared sensors to detect human activity in the kitchen. The team selected an MQ-135 gas sensor to detect LPG leak in the kitchen. The designed system also had a fan installed that was intended to control the temperature and blow out of gas in the event of a gas leak from the kitchen in case of fire. The system was controlled and monitored via the internet.

Asad *et al*., (2018) developed a gas burner that operates at 220VAC. The burner had a solenoid valve that was controlled by the detection of fire when expected via a flame detector. If the fire remains continuous the valve is open. The valve is turned off if the fire intended for cooking is not available.

Alkali *et al*., (2017) presents a system consisting of an Arduino Uno as the control platform and interfaced with flame sensor, servo motor and a utensil detector to automatically detect when to allow gas flow to commence in order to ignite a flame. It also uses the utensil detector to automatically extinguish the flame by closing the gas flow. Contact however is necessary for the utensil detector.

Zaw *et al*., (2021) used a Load cell with HX711 amplifier weighing module and MQ-6 gas sensor for their gas leak and level detection system. The notification system includes warning signal and alarm sound for gas leakage detection and SMS alert for gas cylinder refilling when low. For gas burst accident prevention system, the gas concentration is decreased by turning on the exhaust fan. The level of LPG gas in cylinder measured and send to Wia IoT cloud.

Anoop *et al*., (2017) developed a prototype, gas leakage detection system. It uses an MQ6 gas sensor, which is placed in the vicinity of the gas cylinder. The main power is turned off at the detection of gas leakage by the system thereby discontinuing LPG supply.

Okeke and Ehikhamenle (2017) developed a system that consists of a Power Supply Unit which supplies the needed power to the PIC16F877A microcontroller, MAX232, GSM module SIM900, Gas sensor MQ-2, Temperature sensor LM35 and the Liquid Crystal Display LCD. The microcontroller is connected to the Power Supply Unit, LCD, Gas sensor, Temperature sensor and MAX232. The LCD shows the status of the system when there is a presence of gas or smoke which may lead to fire outbreak in the environment.

Okpeki and Oyubu (2019) designed a system that used an embedded 'C' language program to control the system via AT89C52 microcontroller. The controller ensures that different actions are carried out accordingly.

3.2 SUMMARY OF REVIEWED LITERATURE

The Summary of the reviewed literatures are shown in Table II.

Table : Summary of reviewed literature

S/N	Author	Title	Method			Remark
			Controller adopted	LPG sensor incorporated	Notification module	
1.	Okonkwo *et al.* (2020)	Design and construction of cooking gas (LPG) leakage detector	Arduino Uno	MQ6 gas sensor	buzzer, LED, LCD, SMS	Extensive tests not conducted to verify system performance
2.	Donatus and Charles (2020)	Design and construction of a carbon monoxide and liquefied petroleum gas leakage	ATmega 328	MQ-6 and MQ-135 gas sensors	Buzzer, SMS	Gas sensor sensitivity must be manually adjusted and gas sensor delays before detection
3.	Adeyemi (2019)	Design and fabrication of a microcontroller based liquified petroleum gas detection with GSM alert monitoring system	ATmega 328	MQ-5 gas sensors, Load cell, DHT11 Humidity and temperature sensor	LCD, SMS, Buzzer	Quantitative value of test results of gas leakage detector system is not presented
4.	Folorunso *et al.* (2019)	Development of a Liquified Petroleum Gas Leakage Detector, Level Indicator and Automatic Shutdown System	Arduino Uno	MQ6 gas sensor	LCD, SMS, Buzzer	Time taken for communication is too long
5.	Mahalingam *et al.* (2012)	Design and Implementation of an economic gas leakage detector	PIC18F1320 microcontroller	MQ-5 gas sensor	LED, Buzzer	LFG system was not used for testing. The sensitivity is low for actual system because simulated system is too small
6.	Krishnadas *et al.* (2019)	Automatic gas controller unit	Arduino Uno ATmega 328 P	MQ6 gas sensor, load sensor, Cooking Timer	LCD, Buzzer	An actual system was not tested. but, a proposed system. Weight indication might be too late to indicate leakage if load sensor is not highly sensitive
7.	Chetana and Sanjeev (2020)	LPG gas leakage detection using IOT	Arduino Uno (AVR)	MQ-6 gas sensor	IOT, GSM, LED and BUZZER (Piezo Electric)	No prototype was developed

8.	Alexander (2022)	Implementation of a Gas Leakage Detection System Using the MQ-6 Sensor	Arduino Mega-2560	MQ-6 gas sensor	LCD, buzzer	Gas detection is slow
9.	Asad *et al*. (2018)	Adaptation of an Industrial Gas Burner Controller for a Household Stove	MD 202 burner controller	Flame detector rod	LED, Buzzer	Prototype test successful but user notification is not available
10	Alkali *et al*. (2017)	Automatic Gas Cooker Control System	Arduino Uno Rev 2	KY 026 Arduino compatible flame sensor, Utensil Sensor	Buzzer	Extensive system verification is required
11	Nugroho and Pantjawati (2017)	Automation and Monitoring Smart Kitchen Based on Internet of Things (IoT)	Arduino Uno ATmega 328	MQ-135 gas sensor and DHT11 temperature sensor, IR flame sensor, passive infrared (PIR) sensors	Buzzer, SMS, email	Prototype system is unavailable and calibration was not done before testing
12	Okpeki and Oyubu (2019)	Design and implementation of an electronic gas leakage sensor system	AT89C52 controller	MQ-2 gas sensor	LCD, buzzer	System prototype not built
13	Abhishek (2017)	Efficacious L.P.G. leakage detector and auto shut-off system using Arduino Uno ATmega 328	Arduino UNO ATmega 328	MQ-6 Gas Sensor	LCD, LED, buzzer	Miniature system tested and sensor takes too long to sense the gases
14	Asnor *et al.* (2019)	GSM Based Gas Leak Monitoring System	Arduino UNO microcontroller	MQ-2 gas sensor	LCD, SMS, Buzzer	System is proposed ant no prototype implemented
15	Yuda *et al*. (2021)	Safety system for liquefied petroleum gas (LPG) with microcontroller based fuzzy decision tree algorithm	Arduino UNO ATmega 328	MQ-6 gas sensor, PIR Sensor	Buzzer and SMS.	Gas detection is poor as above 30,000 ppm for buzzer to initiate notification and human detection of only 50 cm is detectable
16	Okeke and Ehikhamenle (2017)	Design and simulation of gas and fire detector and alarm system with water sprinkle	PIC16F877A microcontroller	MQ-2 Gas sensor, LM35 Temperature sensor	LCD, buzzer	Prototype was not evaluated and water sprinkler system not suitable for gas-based fires

17	Anoop *et al*. 2017)	Automation of LPG based heating system	ARDUINO MEGA ATmega 2560	MQ6 gas sensor,	LCD	Time setting for cooking may lead to unnecessary actions if the actual time for cooking is not known. Weight indication might be too late to indicate leakage if load sensor is not highly sensitive
18	Zaw *et al*. (2021)	IoT based LPG gas level detection & gas leakage accident prevention with alert system	Arduino MKR WiFi 1010	MQ-6 gas sensor, Load sensor	SMS. MMS	Results are not definitive of the system designed
19	Zainal *et al*. (2019)	Home and Industrial Safety IoT on LPG Gas Leakage Detection and Alert System	Intel Edison board	MQ-5 and MQ-2 gas sensors	LEDs, buzzer	Incorporating multiple sensors delivered adverse effects on results recorded
20	Ebenezer *et al*. (2020)	Design and implementation of an intelligent gas cylinder valve regulating system using solenoid	ATmega 328	Gas sensor, Temperature sensor, gas sensor and 555 Timer	LCD, buzzer,	Time setting for cooking may lead to unnecessary actions if the actual time for cooking is not known. Precise temperature of the cooking environment must be ascertained which might be difficult for user
21	Kuswindarini and Munadi (2020)	LPG gas leakage system with instant messaging WhatsApp communication media based on Internet of Things	Arduino Uno	MQ-6 gas sensor	LCD, LED, Buzzer	There is drastic drop in efficiency of detector with distance of more than 10 cm between LPG source and detector. The average time recorded for user to receive message is poor

From thorough appraisal of the prototype developed, some weaknesses have been itemized that form bases for future research areas. The system for monitoring and controlling gas leakages is comprised of mainly three sections from the literature studied.

1. Detection
2. Restriction and
3. Notification

Based on the previous research studied, most of the concepts and general methods employed by the researchers are similar and have yielded positive

outcomes in the area. However, most of the systems and researches conducted have mostly remained in the proposal stages as functional prototypes have yet to be developed. Some developed prototypes reported are miniature replicas that simulate the real situation rather than an actual situation.

Gas sensor sensitivity is very low from the reviewed literature. As distance increases the sensitivity drastically reduces. The system designed by Kuswindarini and Munadi (2020) for example only has optimum performance for the detector when the distance is only 10 cm and that of Yuda *et al*. (2021) at 50 cm. Communication time is another factor that needs attention as the notification is often slow. The user gets information from the system somewhat late than necessary for action to be taken as the LPG leakage requires prompt response (Folorunso *et al*., 2019; Kuswindarini and Munadi, 2020)

4 CONCLUSION

The development and incorporation of LPG leakage and monitoring system for domestic use is paramount. However, more research is required in the area of increasing sensitivity of the various detection units. It is also of benefit to combine different sensors to monitor the system as that has shown promise in previous studies. Another area requiring investigation is the enhancement of the communication modules to provide more efficient notification to the user in real time no matter the medium. It is also of paramount to have more developed and tested prototypes rather than simulations that though provide necessary information but have not functionally solved the problem at hand.

ACKNOWLEDGEMENTS

I would like to express my profound gratitude to Dr. K.C. Bala, HOD. Mechanical Engineering and Professor S.M. Daudu, HOD. Agric and BioResources Engineering of Federal University of Technology Minna, for their morale support and contributions.

REFERENCES

Abhishek, G. (2017). Efficacious L.P.G. leakage detector and auto shut-off system using Arduino Uno AT mega328. *International Journal of Innovative Research in Science, Engineering and Technology*, 6(10), 19971-19978.

Adeyemi, B. E. (2019). *Design and fabrication of a microcontroller based liquified petroleum gas detection with GSM alert monitoring system.* Oye-Ekiti: Federal University of Oye-Ekiti.

Alexander, T. (2022). Implementation of a gas leakage detection system using the MQ-6 sensor. *Brilliance*, 2(1), 17-21.

Alkali, A. H., Mshelia, D. E., Isuwa, S., & Bolori, H. T. (2017). Automatic gas cooker control system. *International Journal of Advanced Research in Electrical, Electronics and Instrumentation Engineering*, 6(7), 5245-5250.

Anoop, K., Manu, V. K., Nishanth, M., Nishmitha, S. N. & Pooja, S. (2017). Automation of LPG based heating system. *International Journal of Advanced Computing and Electronics Technology (IJACET)*, 4(3), 22-25.

Asad, A. J., Rakesh, D., Mohammad, A. S. B., Shahriar, K. & Kazi, N. T. (2018). Adaptation of an industrial gas burner controller for a household stove. *International Journal of Pure and Applied Mathematics*, 119(12), 12793-12801.

Asnor, J. I., Sarmad, N. M. & Abadal – Salam, T. H. (2019). GSM based gas leak monitoring system. *Periodicals of Engineering and Natural Sciences* , 7(2), 670-678.

Chetana, T. & Sanjeev, K. A. N. (2020). LPG gas leakage detection using IOT. *International Journal of Engineering Applied Sciences and Technology*, 4(12), 603-609.

Donatus, U. O. & Charles, K. I. (2020). Design and construction of a carbon monoxide and liquefied petroleum gas leakage detection system. *Tropical Journal of Science and Technology*, 1(2), 1-11.

Ebenezer, N. O., Willie, K. O., Patrick, A. & Daniel, K. (2020). Design and implementation of an intelligent gas cylinder valve regulating system using solenoid. *International Journal of Computer Science, Engineering and Applications (IJCSEA)* , 10(4), 19-24.

Folorunso, C. O., Raheem, W. A., Akinyemi, L. A. & Raji, A. A. . (2019). Development of a liquidified petroleum gas leakage detector, level indicator and automatic shutdown system. *Covenant Journal of Engineering Technology (CJET)* , 3(2), 14-30 .

Hitendra, R., Ashish, K., Khyati, A. & Akanksha, S. (2014). LPG gas leakage detection & control system. *International Journal of Engineering and Technical Research*, 133-137.

Jadkream, M. M., Omar, M. A. E. & Mahmoud, S. A. (2022). *Design of IoT Based Gas Leakage Detection and Safety System.* Sudan: Sudan University of Science and Technology.

Krishnadas, K. N., Prajith, P., Sidharthan, P., Safa, M. & Arul, V. H. . (2019). Automatic gas controller unit. *International Journal of Engineering Research & Technology (IJERT)*, 8(5), 858-860.

Kuswindarini, R. & Munadi, S. (2020). LPG gas leakage system with instant messaging whatsapp communication media based on internet of things.

Advances in Engineering Research, 198(2020), 451-456.

Mahalingam, A., Naayagi, R. T. & Mastorakis, N. S. (2012). Design and Implementation of an Economic Gas Leakage Detector. *Recent Researches in Applications of Electrical and Computer Engineering*, 20-25.

Manu, M. & Neelakantha, V. L. (2015). Automatic gas stove with advanced safety features. *Journal of Engineering Sciences*, 3(2), 35-37.

Naci, Z. & Greg, R. L. (2008). Stability of gas pressure regulators. *Applied Mathematical Modelling* , 32(2008), 61–82.

Nugroho, F. & Pantjawati, A. B. (2017). Automation and monitoring smart kitchen based on Internet of Things (IoT). *IOP Conf. Series: Materials Science and Engineering* , 384(2018), 1-9.

Okeke, R.O. & Ehikhamenle, M. (2017). Design and simulation of gas and fire detector and alarm system with water sprinkle. *International Journal of Engineering Research and General Science*, 15(1), 216-225.

Okonkwo, P. A., Obi, A. I. & Idoko, S. O. (2020). Design and Construction of Cooking Gas (LPG) Leakage Detector. *2020 Sustainable Engineering & Industrial Technology Conference* (pp. 1-7). Nsukka: Faculty of Engineering, University of Nigeria.

Okpeki, U. K. & Oyubu, A. O. (2019). Design and implementation of an electronic gas leakage sensor system. *FUW Trends in Science & Technology Journal*, 4(1), 144 – 148.

Sanketh, D. B., Mohan, K. & Vinod, R. (2021). Automatic Gas off Mechanism for LPG Gas Stove. *International Journal of Scientific Research in Computer Science, Engineering and Information Technology*, 7(3), 543-546.

Senthil, K. M., Karthick, R., Kavin, M. & Musthakahamed, S. I. (2020). Gsm based automation of gas stove. *International Journal of Scientific & Technology Research* , 9(3), 2019-2022.

Shinde, S. P., Jadhav, D. R. & Sutar, A. R. (2021). The smart gas leakage detection with monitoring and automatic safety system. *International Advanced Research Journal in Science, Engineering and Technology*, 8(6), 925-932.

Younes, S. M. (2019). *A microprocessor based gas leakage detection system in the oil and gas industry.* Cyprus: Near East University.

Yuda, I., Uci, R., Refni, W. & Hendry, F. (2021). Safety system for liquefied petroleum gas (LPG) with microcontoller based fuzzy decision tree algorithm. *Research of Applied Science and Education* , 15(4), (383-394).

Zainal, H. C. S., Syahrul, A. C. A., Mohd, A. S. & Mohammad, N. I. (2019). Home and industrial safety iot on LPG gas leakage detection and alert system. *International Journal of Advance Software and Computer Application*, 11(1), 131-145.

Zaw, L. O., Theint, W. L. & Aung, M. (2021). IoT based LPG gas level detection & gas leakage accident prevention with alert system. *Balkan Journal of Electrical & Computer Engineering*, 9(4), 404-409.

4th International Engineering Conference (IEC 2022)
Federal University of Technology, Minna, Nigeria

A Survey of the Primary User Emulation Attack in the Cognitive Radio Networks

*Olaleru, G[1], Ohize H.O[2], Dauda U.S[3], Mohammed A.S[4]
[1]Electrical and Electronics Engineering Department, Federal University of Technology, PMB 65 Minna Niger State, Nigeria
[2]Electrical and Electronics Engineering Department, Federal University of Technology, PMB 65 Minna Niger State, Nigeria
[3] Federal University of Technology, PMB 65 Minna Niger State, Nigeria
[4] Federal University of Technology, PMB 65 Minna Niger State, Nigeria.
Corresponding author email: graceolaleru9@gmail.com +2348164649551

ABSTRACT
Cognitive Radio Technology (CRT) helps alleviate the spectrum scarcity and spectrum underutilization problems experienced by wireless networks and wireless devices by enabling the intelligent and opportunistic use of the licensed frequency band by unlicensed users. However, due to its wireless nature, it is subject to some security threats that affect the practical implementation of the CRT. In this paper, we have discussed some of the security threats affecting the protocol stack and the five layers of the Cognitive Radio Network (CRN), with a focus on the Primary User Emulation Attack (PUEA). The PUEA is one of the most common attacks on the CRN's physical layer. In this attack, a selfish or malicious user mimics the primary user's (PU) signal features to fool the legitimate secondary users (SUs), causing the legitimate SUs to leave the available channel while the real PU is absent. Although many review papers enhanced our knowledge of the PUEA, in this paper we meld new research findings with the old ones to keep up the pace in the research community. Also, we discussed some detection and countermeasures for the PUEA in the CRN. Finally, a summary of the findings on how best to mitigate the effect of PUE attacks in the CR is presented.

Keywords: *Cognitive Radio, Primary User, Primary User Emulation Attack, Secondary User, Security threats.*

1 INTRODUCTION

The radio spectrum used for wireless communications is a scarce resource due to the dramatic increase in the number of wireless devices and more bandwidth-demanding multi-media services [1-4]. These wireless devices use either the licensed spectrum or the unlicensed spectrum. The unlicensed bands are becoming overcrowded because all wireless users can connect. However, the licensed bands are either unused or underutilized at some geolocation and time. To address the problem of frequency scarcity and spectrum underutilization, Cognitive Radio (CR) was introduced by Joseph Mitola in 1999 [5]. The CR is a software-defined radio that enables Dynamic Spectrum Access (DSA) which enables unlicensed users to intelligently and opportunistically access and utilize the spectrum without disrupting the licensed users and therefore a better service to achieve improvement in frequency usage [2, 6]. The CR performs four basic functions that allow it to address spectrum shortages and channel underutilization [7]. These functions are (a) Spectrum Sensing which involves identifying the primary user's spectrum occupancy status, (b) Spectrum management, which captures the best available spectrum to meet users' communication needs and avoid collisions with other CRs (c) spectrum sharing: this relates to the provision of fair spectrum scheduling, and (d) spectrum mobility: defined as the process of a CR user changing its operating frequency to meet the quality of service. However, due to the wireless nature of CRT and the priority given to licensed users or primary users (PUs) over secondary users (SUs) in spectrum usage, CRN faces several security threats. One of these threats is PUEA, in which a malicious user fools the SU by mimicking the PU's signal features in relation to the PU's occupancy status. The impacts of PUEA include denial of service, wasted bandwidth, connection unreliability, and degrading the practical implementation of the CRN. Other threats that the CRN faces are classified as they affect the protocol stack and the five layers of the CR network. These include, but are not limited to: Common Control Data Attack (CCDA), Sinkhole Attack, Hello flood attack, lion attack, and jellyfish attack. These threats aim to reduce the possibility of building a real CRN, so, threat mitigation is crucial to building a real CRN.

In this paper, we have highlighted the security threats affecting the CRN with a focus on the PUEA. We also highlighted some of the detection and countermeasures used for the PUEA in the CR networks. This paper has the following research contributions:

- A detailed discussion of the security threats affecting the protocol stack and the five layers of the CRN.
- A detailed review of the PUEA in CRN stating its classification, its impacts, methods for its detection, and countermeasures.
- A summary of the findings on how best to mitigate the impact of PUE attacks in the CR.
- Meld new research findings with the old ones to keep up the pace in the research community.

The remainder of this paper is organized as follows: Section 2 discusses the various security threats faced by the CRNs, followed by a concise introduction of the PUEA in Section 3. In Section 4, we highlighted the classification of the PUEA, next; in Section 5 we listed the impact of the PUEA on the CRN. Various detection methods and countermeasures for the PUEA are presented in Section 6. Finally, in Section 7, we completed the review and proposed future work.

2 SECURITY THREATS IN CRN

In implementing any wireless technology, its security aspects need to be thoroughly looked into [8, 9]. The CRT faces some security threats due to the wireless nature of the CR and its inherent nature. These threats are classified as they affect the protocol stack and the five layers of the CRN [10, 11]. These attacks are described in this section and a summary of the attacks is presented in Table 1. They are as follows:

a) **Physical layer**: The physical layer serves as an interface to the data communication medium. The Attacks associated with this layer include:

i. Jamming Attack: In this type of attack, a jammer continuously sends a data packet into the channel, causing the SU not to recognize the channel when it is idle [12].

ii. PUEA is where a selfish or a malicious user mimics the signaling features of the PU to fool the SU and identify the attacker as the real PU [10].

iii. Common Control Data Attack (CCDA) affects the transmission process by refusing channel components to share frequency usage information [12, 13]

iv. Objective Function Attack (OFA) in which the utility resource parameters could be modified by the malicious user, resulting in the CR node not adapting correctly [4, 12, 13].

b) **Link Layer**: In this layer, data is transmitted from one node to another. The Attacks common to this layer include:

i. Spectrum Sensing Data Falsification (SSDF), where a malicious user sends false spectrum sensing (SS) results to the fusion centre or other users to fool them about channel availability [2, 10].

ii. Selfish Channel Negotiation (SCN): Involves a malicious user feeding the channel with false information to change the node's route [10, 13].

iii. Control Channel saturation Denial of Service (DoS) attack, where the attacker reserves the control channel (CC) and eventually saturates the CC [12].

c) **Network Layer**: In this layer, packets are sent from the sender device to the receiver device which is on a different network. The attacks peculiar to this layer are;

i. Sinkhole attack in which the attacker asserts itself as the most suitable route to a given destination to fool the neighboring nodes into using this route to send their packets but end up losing them [12].

ii. Hello Flood Attack: Here, the attacker broadcasts a message to all CR nodes in the network with sufficient transmission power to convince the nodes that the attacker is the nearest neighbor in the node's network and should be used for transmitting the packets to the targeted receiver's node. However, these packets are lost before the packets reach the receiving node [10, 13].

iii. Sybil Attack: In this type of attack, the attacker creates a large number of false identities and behaves like geographically different devices. Each of the false identities requests for the frequency band, and results in the reduction of spectrum usage by legitimate SUs [13].

TABLE 1: VARIOUS ATTACKS ON THE PROTOCOL STACK

Layers in CRNs	**Attacks corresponding in the Layers**
Physical Layer	PUEA; CCDA; OFA; Jamming attack
Link Layer	SSDF; SCN; control channel saturation DoS
Network Layer	Hello flood attack; Sinkhole attack; Sybil Attack.
Transport Layer	Lion attacks; Jellyfish attack
Application Layer	All the above attacks have various damaging effects on this layer.

d) **Transport Layer**: This layer is used to transfer data between two end hosts. Attacks against this layer include:

i. Lion attack in which the attacker launches a PUEA to force the CR nodes to frequency hop between channels, thus, disrupting the Transport Control Protocol (TCP) [11].

ii. Jellyfish Attack affects the TCP, though the attack is executed at the network layer [10].

e) **Application Layer**: It can be affected by all attacks corresponding to the first four layers [11].

In this paper, the focus is on the PUEA in CRN.

3 PRIMARY USER EMULATION ATTACK

The PUEA is the most common threat affecting the CRN's physical layer. In this type of attack, a selfish or malicious user emulates the signaling features of the PU to fool the SUs that the real PU is active and therefore forces the SUs to leave the bands while the real PU is not active [4, 14, 15]. This attack occurs because the PU is given priority in spectrum usage in CRN therefore, a selfish user or malicious user tries to mimic the PU signal characteristic to gain access to the free bands by forcing the legitimate secondary user to leave the free band for it as illustrated in Figure 1.

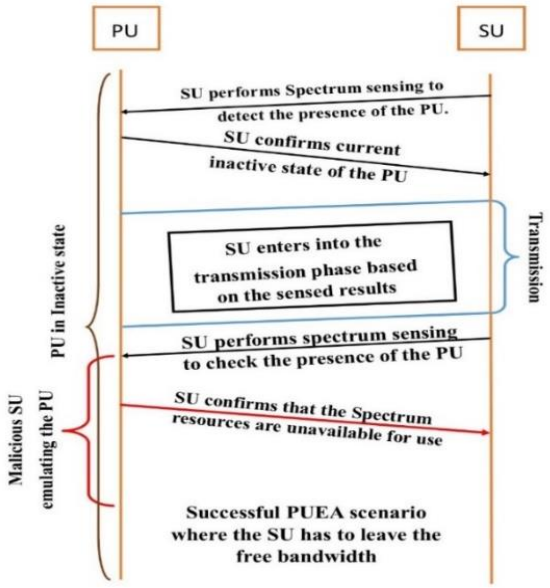

Figure 1: Illustration of a successful PUEA

The SU performs SS to capture the PU occupancy status. When the SU detects that the PU is absent, it starts to transmit, and after some time, it performs SS again, however, the PUEA has taken over the channel by mimicking the signal characteristics of the PU and transmitting the emulated signal while the PU is still absent thus, other SUs leave the free band for the PUEA.

4 CLASSIFICATIONS OF THE PUEA

The PUEA can be classified as follows [9, 10]:

i. Selfish SU or Malicious SU Attacker

The selfish SU attacker reserves a specific band for its transmission while a malicious attacker aims to occupy the whole free band, causing legitimate SUs to move from one free band to another [9, 10]. A malicious user does more damage to the CRN as it causes a DoS and a reduction in the available bandwidth for SUs [8, 16].

ii. Power-Fixed or Power-Adaptive Attackers

Attackers can have an adaptive power level or a fixed power level. The power-adaptive attacker can acclimatize its transmit power depending on the PU signal, while the power-fixed attacker uses a predetermined, unchanging power, independent of the actual power of the incumbent signal [13].

iii. Mobile or Static Attacker: A mobile attacker constantly changes its position in the CRN, while a static attacker maintains a fixed position in the CRN.

5 IMPACTS OF PUEA ON CRN

The impacts of PUEA on CRN include: an increase in call drop rate, delay in networks, degradation of the QoS, causes DoS, bandwidth wastage, connection unreliability, disruption of the primary network, degradation in the practical implementation of the CRNs and the possible collapse of the CRNs.[8, 9, 16].

6 EXISTING DETECTION AND COUNTERMEASURES FOR THE PUEA IN CRNs.

Several detection methods for the PUEA have been developed. Methods include [9, 11, 14, 17, 18] energy detection, signature-based detection, authentication methods, user profile detection, and location-based detection methods.

- Energy Detection (ED): This method is widely used due to its simplicity and easy implementation [18-21]. In ED, a SU will be able to see the signal features of the other SUs, but not those of the PU. Thus, when a SU sees a signal that it can easily identify, it assumes that the signal is that of the SU. Consequently, any signal that the SU cannot detect is the PU signal. However, this technique is not robust for PUEA detection [9] when the attacker is an adaptive power PUEA [22].
- Signature-based detection: This approach integrated cryptographic signatures with wireless link signatures to distinguish a PU signal from the PUEA signal. It also uses an auxiliary node to authenticate signals from its associated PU [17, 23].
- Analytical model-based detection: This method is based on the analytical models of the CRNs. These

include [24-27] the Wald's Sequential Probability Ratio Test and Neyman-Pearson Composite Hypothesis Test (NPCHT) to detect the PUEA in evanescent wireless channels considering multiple malicious users. Also, in [28] the dog-fight approach was proposed in which the defenders randomly select channels to detect and avoid the PUEA.

- Feature Detection: In this technique, the SUs try to find a specific feature of a detected signal, for example, a pilot or correlation device [6] which can use this detection technique can recognize the intrinsic features of the PU signals and thus; enable them to distinguish these signals from the SU signal.
- Location-based detection: This technique is widely used by researchers. These include [9, 11, 18, 29-31] Transmitter Verification Scheme (Loc-Def), Received Signal Strength (RSS), Time of Arrival (TOA), Angle of Arrival (AOA), Time Difference of Arrival (TDOA), Distance Ratio Test (DRT), and Distance Difference Test (DDT). They are often used to detect a static attacker.
- Other detection and mitigation techniques include mitigation based on a surveillance process [32], detection with Kalman filter [33], AES-assisted DTV scheme [34], detection based on Hash Message Authentication Code [35], Hybrid of TDOA localization technique, and Modified Particle Swarm Optimization (MPSO) [4]. Table 2 presents the detection/mitigation techniques for PUEA in the CRN.

TABLE 2: DETECTION/MITIGATION TECHNIQUE FOR DIFFERENT KINDS OF PUEA

Types of PUE Attackers	Detection/Mitigation technique
Selfish or malicious attack	Any of the detection/mitigation techniques for PUEA can be used.
Power-fixed or Power adaptive attacker	The localization techniques can be used.
Static attacker	A hybrid of location techniques and an optimization algorithm can be used.
Mobile attacker	An energy detection technique can be employed.

7 CONCLUSION AND FUTURE WORK

CRT is an excellent solution to the spectrum underutilization and spectrum scarcity problems faced by wireless networks as it enables DSA. However, due to the wireless nature of CR, it encounters some security challenges that pose a threat to the practical implementation of this technology. In this paper, we discuss the security threats affecting the cognitive protocol stack and the five layers of the CRN. We have focused more on the PUEA, and given their impact on the CRN, their classification, detection, and countermeasures for the PUEA. Most researchers have worked to detect the PUEA but little attention has been paid to how to eliminate the PUEA from the CRNs. Therefore, future work lies in the development of robust systems to eliminate the PUEA in the CRNs.

REFERENCES

1 Ohize, H.O.: 'Adaptive and autonomous protocol for spectrum identification and coordination in ad hoc cognitive radio network', University of Cape Town, 2017
2 Arjoune, Y., and Kaabouch, N.: 'A Comprehensive Survey on Spectrum Sensing in Cognitive Radio Networks: Recent Advances, New Challenges, and Future Research Directions', Sensors (Basel), 2019, 19, (1), pp. 126
3 Ul Hassan, M., Rehmani, M.H., Rehan, M., and Chen, J.: 'Differential privacy in cognitive radio networks: A comprehensive survey', Cognitive Computation, 2022, pp. 1-36
4 Olaleru, G., Ohize, H., Mohammed, A.S., and Dauda, U.S.: 'Optimal Detection Technique for Primary User Emulator in Cognitive Radio Network', in Editor (Ed.)^(Eds.): 'Book Optimal Detection Technique for Primary User Emulator in Cognitive Radio Network' (IEEE, 2021, edn.), pp. 1-6
5 Mitola, J., and Maguire, G.Q.: 'Cognitive radio: making software radios more personal', IEEE personal communications, 1999, 6, (4), pp. 13-18
6 Jayapalan, A., Savarinathan, P., Reddy, J.C., and Baskar, J.D.: 'Detection and Defense of PUEA in Cognitive Radio Network', Arabian Journal for Science and Engineering, 2021, 46, (4), pp. 4039-4048
7 Omer, I., Hamid, K., and Mohamed, M.: 'Overview on Cognitive Radio Network Review', International Journal of Engineering Sciences Paradigms and Researches, 2016, 33, (20), pp. 7-13
8 Sharma, R.K., and Rawat, D.B.: 'Advances on security threats and countermeasures for cognitive radio networks: A survey', IEEE Communications Surveys & Tutorials, 2014, 17, (2), pp. 1023-1043
9 Gupta, I., and Sahu, O.: 'An Overview of primary user emulation attack in cognitive radio networks', in Editor (Ed.)^(Eds.): 'Book An Overview of primary user

emulation attack in cognitive radio networks' (IEEE, 2018, edn.), pp. 27-31
10 Singh, A., and Sharma, A.: 'A survey of various defense techniques to detect primary user emulation attacks', International Journal of Current Engineering and Technology, 2014, 4, (2), pp. 900-908
11 Das, D., and Das, S.: 'Primary User Emulation Attack in Cognitive Radio Networks: A Survey', IRACST – International Journal of Computer Networks and Wireless Communications (IJCNWC)

2013
12 El-Hajj, W., Safa, H., and Guizani, M.: 'Survey of security issues in cognitive radio networks', Journal of Internet Technology, 2011, 12, (2), pp. 181-198
13 Rehman, A., and Prakash, D.: 'Detection of PUE attack in CRN with reduced error in location estimation using novel bat algorithm', International Journal of Wireless Networks and Broadband Technologies (IJWNBT), 2017, 6, (2), pp. 1-25
14 Ghanem, W.R., Essam, R., and Dessouky, M.: 'Proposed particle swarm optimization approaches for detection and localization of the primary user emulation attack in cognitive radio networks', in Editor (Ed.)^(Eds.): 'Book Proposed particle swarm optimization approaches for detection and localization of the primary user emulation attack in cognitive radio networks' (IEEE, 2018, edn.), pp. 309-318
15 Patil, P.: 'Position Verification and Identification of Primary User Emulation (PUE) Attack in Cognitive Radio Network', International Journal for Research in Applied Science and Engineering Technology, 2018, 6, pp. 348-362
16 Jin, Z., Anand, S., and Subbalakshmi, K.P.: 'Impact of Primary User Emulation Attacks on Dynamic Spectrum Access Networks', IEEE Transactions on Communications, 2012, 60, (9), pp. 2635-2643
17 Pu, D.: 'Primary user emulation detection in cognitive radio networks', Worcester Polytechnic Institute, 2013
18 Chen, R., Park, J.-M., and Reed, J.H.: 'Defense against primary user emulation attacks in cognitive radio networks', IEEE Journal on selected areas in communications, 2008, 26, (1), pp. 25-37
19 Yu, R., Zhang, Y., Liu, Y., Gjessing, S., and Guizani, M.: 'Securing cognitive radio networks against primary user emulation attacks', IEEE Network, 2015, 29, (4), pp. 68-74
20 Fragkiadakis, A.G., Tragos, E.Z., and Askoxylakis, I.G.: 'A survey on security threats and detection techniques in cognitive radio networks', IEEE Communications Surveys & Tutorials, 2012, 15, (1), pp. 428-445
21 Ghanem, W.R., Shokair, M., and Dessouky, M.: 'Investigation of PUEA in cognitive radio networks using energy detection in different channel model', Circuits and Systems: An International Journal (CSIJ), 2015, 2, (2/3)
22 Ghanem, W.R., Mohamed, R.E., Shokair, M., and Dessouky, M.I.: 'Particle swarm optimization approaches for primary user emulation attack detection and localization in cognitive radio networks', arXiv preprint arXiv:1902.01944, 2019
23 Liu, Y., Ning, P., and Dai, H.: 'Authenticating primary users' signals in cognitive radio networks via integrated cryptographic and wireless link signatures', in Editor (Ed.)^(Eds.): 'Book Authenticating primary users' signals in cognitive radio networks via integrated cryptographic and wireless link signatures' (IEEE, 2010, edn.), pp. 286-301
24 Tabatabaee, S., Bagheri, A., Shahini, A., and Shahzadi, A.: 'An analytical model for primary user emulation attacks in IEEE 802.22 networks', in Editor (Ed.)^(Eds.): 'Book An analytical model for primary user emulation attacks in IEEE 802.22 networks' (IEEE, 2013, edn.), pp. 693-698
25 Tan, Y., Sengupta, S., and Subbalakshmi, K.P.: 'Primary user emulation attack in dynamic spectrum access networks: a game-theoretic approach', IET communications, 2012, 6, (8), pp. 964-973
26 Jin, Z.: 'Primary user emulation attack in dynamic spectrum access networks: threats, mitigation and impact', Stevens Institute of Technology, 2012
27 Jin, Z., Anand, S., and Subbalakshmi, K.: 'Robust spectrum decision protocol against primary user emulation attacks in dynamic spectrum access networks', in Editor (Ed.)^(Eds.): 'Book Robust spectrum decision protocol against primary user emulation attacks in dynamic spectrum access networks' (IEEE, 2010, edn.), pp. 1-5
28 Li, H., and Han, Z.: 'Dogfight in spectrum: Combating primary user emulation attacks in cognitive radio systems—Part II: Unknown channel statistics', IEEE Transactions on Wireless Communications, 2010, 10, (1), pp. 274-283
29 Fassi Fihri, W., El Ghazi, H., Abou El Majd, B., and El Bouanani, F.: 'A decision-making approach for detecting the primary user emulation attack in cognitive radio networks', International Journal of Communication Systems, 2019, 32, (15), pp. e4026
30 Adebo, S., Onwuka, E., Usman, A., and Onumanyi, A.: 'A hybrid localization scheme for detection of primary user emulator in cognitive radio networks', International Journal of Computing and Digital Systems, 2019, 8, (03), pp. 217-227
31 Adebo, S., Onwuka, E., Usman, A., and Onumanyi, A.: 'Cooperative-hybrid detection of primary user emulators in cognitive radio networks', International Journal of Electrical and Computer Engineering, 2020, 10, (3), pp. 3116
32 Ta, D.-T., Nguyen-Thanh, N., Maillé, P., and Nguyen, V.-T.: 'Strategic surveillance against primary user emulation attacks in cognitive radio networks', IEEE Transactions on Cognitive Communications and Networking, 2018, 4, (3), pp. 582-596

33 El Mrabet, Z., Arjoune, Y., El Ghazi, H., Abou Al Majd, B., and Kaabouch, N.: 'Primary user emulation attacks: A detection technique based on Kalman filter', Journal of Sensor and Actuator Networks, 2018, 7, (3), pp. 26

34 Alahmadi, A., Abdelhakim, M., Ren, J., and Li, T.: 'Defense against primary user emulation attacks in cognitive radio networks using advanced encryption standard', IEEE transactions on information forensics and security, 2014, 9, (5), pp. 772-781

35 Ghanem, W.R., Shokair, M., and Desouky, M.: 'Defense against selfish PUEA in cognitive radio networks based on hash message authentication code', International Journal of Electronics and Information Engineering, 2016, 4, (1), pp. 12-21

4th International Engineering Conference (IEC 2022)
Federal University of Technology, Minna, Nigeria

Smart Interview Bot Using Deep Learning

Ogala J. O.[1] & Mughele S. E.[2]
[1&2]Cyber Security Department, University of Delta, PMB 2090 Agbor, Delta State, Nigeria
*Corresponding author email: Justin.ogala@unidel.edu.ng +2347063649842

ABSTRACT

The hiring process for IT positions is often complex and time-consuming, posing significant challenges for businesses seeking to maintain consistency and efficiency. Interview scheduling is complicated by manual effort and scheduling difficulties, which have been further exacerbated by the COVID-19 pandemic, making in-person interviews difficult. To address these challenges, this study proposes an NLP-based Machine Learning (ML) solution that automates interview scheduling and communication in natural language. To develop the solution, two deep-learning NLP models served as the foundation of the system, and AWS serverless stack and Amazon SageMaker were used for training and inference. The solution is designed to be scalable and cost-effective, and new models can be easily added and trained on unique subjects. Furthermore, the Amazon Sumerian scene is customizable to meet branding requirements. This research offers significant implications, as the proposed ML solution can help businesses streamline their hiring process, reduce human error, and improve the accuracy of candidate assessments. The scalability and cost-effectiveness of the solution make it ideal for businesses of all sizes. The smart interview bot developed in this study can conduct live-like interviews that mimic human interactions, making the hiring process more engaging and personalized. Overall, this paper demonstrates the potential of Natural Language Processing (NLP) to develop a smart solution for an everyday business problem. The intelligent live-like interview process and smart interview bot developed in this research have the potential to revolutionize the hiring process by automating scheduling and reducing manual effort. By leveraging the proposed ML solution, businesses can improve the accuracy and consistency of their hiring practices, ultimately leading to more successful outcomes.

.

Keywords: *Machine Learning, Amazon Web Services, Natural Language Processing, BERT, Amazon SOS, Dynamo DB,*

1 INTRODUCTION

Businesses find it tough to shortlist the top candidates since bringing consistency and efficiency to the interview process is challenging. It takes a lot of manual work to interview a candidate and assess his talents, and it's much more challenging to find the interviewer time to schedule and carry out the interviews. Given the COVID scenario, doing these interviews in person has become increasingly problematic, and a Machine Learning (ML) solution that can intelligently handle interview scheduling would surely benefit many organizations. A smart interview bot, also known as a chatbot, is a Machine Learning (ML) solution that can automatically schedule interviews and speak with humans in natural language.

Modelling conversation is a critical problem in natural language processing and artificial intelligence. Indeed, building a smart interview bot has remained one of AI's most complex issues since its inception. While the bot may be used for a variety of jobs, it must understand what users are saying and respond in a way that is relevant to the issue at hand. Deep learning has recently become more prevalent in businesses to shortlist the best candidates, and Chatbot is one of its applications (Heller et al., 2005; Beaudry et al., 2019; Sutoyo et al., 2019). It's sometimes difficult for businesses to shortlist the best candidates for IT jobs because it's challenging to bring consistency and efficiency to the way interviews are conducted. Interviewing an applicant and assessing his abilities takes a lot of manual effort, and finding the interviewer time to arrange and materialize the interviews is similarly tricky.

Given the COVID situation, doing these interviews in person has become increasingly complex. A Machine Learning (ML) solution that can intelligently manage interview scheduling would undoubtedly help many businesses improve their hiring process.

1.1. Challenges

The rise of remote work and the need for efficient recruitment processes have led to changes in the way job interviews are conducted. With the majority of the workforce working from home, the use of internet-based interviews has become increasingly common. However, the impact of this shift on the quality and effectiveness of the recruitment process is not yet fully understood. Therefore, it is important to investigate the potential benefits and limitations of using internet-based interviews and to develop new tools and techniques that can enhance the recruitment experience for both employers and candidates.

One of the most significant responsibilities of the hiring teams is to assess applicant profiles and get available interviewer and candidate slots to schedule the initial interview. As a result, following up with the interviewer to collect the interview comments and arrange the next steps takes time. Consider implementing this on a large scale with very high hiring objectives; there will be a lot of coordination necessary. Most businesses are searching for ways to use technology to provide applicants with a better experience and speed up recruiting. The most critical challenges of the hiring process are;

a) Working from home is the new norm
b) Scheduling interview
c) Time to revert with interview result
d) Conducting interviews at scale
e) Consistency in the candidate screening approach

1.2. How to Address These Challenges

To address the challenges, the solution proposed is to create an interactive interview experience using AWS services, where the candidate can record their responses, and a machine learning model is used to analyze them in near real-time (Jafari, 2021). This approach minimizes the need for interview availability and allows candidates to schedule interviews at their convenience (Jafari, 2021). The strategic steps used to address these challenges were;

a) Interactive virtual interview user experience
b) Automate the evaluation of the candidate's subjective answer using machine learning
c) Near real-time evaluation at scale
d) Bring in efficiency and consistency in the evaluation
e) Continuously improve the model inferencing accuracy

1.3. Key AWS Services Used

In this demo implementation, AWS services were employed to address the challenges of traditional interviewing processes, such as limited interview availability and inconsistent evaluation. An interactive interview experience was created in which an animated character played the role of the interviewer and had a dialogue with the candidate. The candidate participated in this interactive discussion and recorded their responses. Machine learning was used to analyze candidate replies in near real-time, with a technique developed to increase the accuracy and speed of the machine learning model over time.

To implement this solution, a range of AWS services were utilized. Amazon Sage Maker was used to build, train, and deploy the machine learning models for data persistence. Amazon Dynamo DB, a no-sequel database that is easy to scale, was used for data storage. Amazon Lex was used to orchestrating the conversation, and Amazon Sumerian served as the VR engine for the front-end of the conversation. Furthermore, Amazon Simple Queue Service (Amazon SOS) and AWS Lambda were employed to decompose services for efficient implementation. The resulting solution enabled candidates to schedule interviews at their convenience, minimizing the need for interview availability and facilitating efficient and consistent evaluation.

1.4. Interview Evaluation Solution

To make asynchronous calls and isolate the service, we combined Amazon SQS and AWS Lambda. We utilized Amazon Lex to create a life-like dialogue; Sumerian violations and links can be integrated. The host interactions can be controlled to offer a compelling 3d, immersive experience. The following steps were taken for the interview evaluation processes;

a) Amazon Sumerian host will interact with the user and capture interview answers.
b) Amazon Sumerian will post the recorded answer to the Amazon Lex bot, invoking AWS Lambda functions.
c) AWS to push the request to Amazon SOS
d) Amazon Lambda attached to the Amazon SOS will be triggered
e) Inference results will be updated back in Amazon Dynamo DB.

The architectural view of the interview evaluation is shown in figure 1.

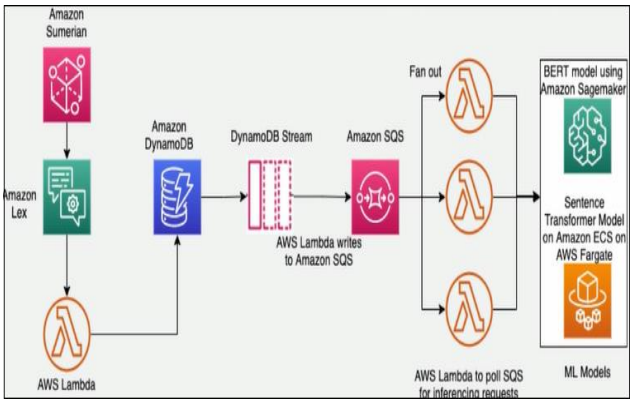

Figure 1 - Interview Evaluation Solution

The interview process involves the use of the Sumerian host to welcome the candidate and ask questions on the technical topic while capturing the candidate's response. Sumerian is configured with an Amazon Lex bot for the interview sessions, which is capable of transcribing the audio. The Lex bot is set up with the appropriate intent to interact with the candidate. Once a question is asked, a Lambda function is called, which creates an entry in the Dynamo DB, recording the candidate's response.

To handle the ML inferencing, a BERT model has been launched as an Amazon Sage Maker endpoint. Due to the unpredictable nature of the load on ML points and the maintenance required for the ML models, the solution has been designed for scalability and fault tolerance. The application has been decoupled from the inferencing task so that during peak usage, multiple Lambdas can be triggered to read the inferencing requests in batches and perform the inferencing synchronously. This approach ensures consistent performance of the application, even during high demand.

The Dynamo DB streams have been enabled to collect every new item published to Amazon SQS. The Machine Learning model is called in points for inferencing, and the results are sent back to the Dynamo DB using a Lambda that listens on the queue. Additionally, the Amazon mail service is leveraged to send an automated email to the candidate.

Overall, this solution addresses the challenges of scheduling and evaluating technical interviews in a scalable and efficient manner. The use of AWS services such as Amazon Sage Maker, Dynamo DB, Amazon Lex, and Amazon Sumerian enables the automation of the interview process while ensuring a high level of accuracy and consistency in the evaluation of candidates. The decoupling of the application from the inferencing task, along with the use of Dynamo DB streams and Amazon SQS, enhances scalability and fault tolerance.

2. LITERATURE REVIEW

There has been a surge in the development of smart interview bot systems in the business industry, such as retail, banking, and education. The study is being carried out to increase accuracy and make the intelligent Chatbot and the user as realistic as possible (Chakraborty et al., 2020).

Advanced concepts and techniques such as Natural Language Processing (NLP) techniques and Deep Learning Techniques such as Deep Neural Networks (DNN) and Deep Reinforcement Learning (DRL) are being used to model and train Chatbot systems, in addition to traditional rule-based techniques that were previously used in Chatbot development and other straightforward machine learning algorithms (Przegalinska et al., 2019).

The translation used to be done by dividing source phrases into several tokens or chunks and then translating them phrase by phrase. In Neural Machine Translation, a prominent model based on neural networks and deep learning is Sequence-to-Sequence (Sutskerver et al., 2014). Machine translation, speech recognition, and language processing are among the tasks that utilize it. The encoder and decoder in the Sequence-to-Sequence model are both Vanilla RNN by default (Sherstinsky, 2020). The encoder uses the source sentence to create a thought vector. A thinking vector is a vector space containing a series of integers representing the sentence's meaning. Finally, the decoder processes the inputted thought vector and produces a target sequence or phrase translation. However, when a long series of phrases is supplied to the model, Vanilla RNN fails since information must be remembered.

There are currently various performance measures for Virtual assistants, and specific measuring standards are followed throughout the industry (Przegalinska et al., 2019). Depending on the nature of their business and the market in which they operate, different organizations require Chatbots. The structure and length of a Chatbot's discussion are some of the most critical performance metrics. The size of the output sentence must be appropriate and relevant to the current topic. The faster they answer, the shorter and simpler the phrase structure in the output, and the higher the customer satisfaction rate. In banks, the Chatbot is primarily used to assist the user through the bank's policy, schemes, and other customer queries regarding their account to better grasp this measure. This allows users to complete activities faster and reduces the need for human call assistance, lowering service costs. Customer happiness also leads to a second indicator, the retention rate, critical to Chabot's performance.

To implement a demo of a smart interview bot system, this study utilized a variety of crucial AWS services (Chen et al., 2017). At the centre of our solution are the machine learning models that enable us to automatically evaluate candidate answers. To build, train, and deploy these models, we used Amazon Sage Maker, which also provides a data persistence layer. Additionally, we utilized Amazon Dynamo DB, a no-sequel database that is easy to scale. And, for the front-end of the conversation, we used Amazon Sumerian as the VR engine.

During the interview, the Sumerian host greets the candidate and asks questions on our technical topic. It also captures the candidate's response to the question. Since the audio is the transcript of Amazon Lex, this is achieved by using Sumerian's ability to configure an Amazon Lex bot for the interview sessions (Chen et al., 2017). Amazon Lex is configured with the correct intent to act on the candidate. To achieve the goal, the Lex bot will call a Lambda function. This Lambda function will create an entry in the DynamoDB with the candidate's response to the query. The enabled DynamoDB streams on the main DynamoDB table collect and push every new item published to Amazon SQS.

In the development of smart interview bot systems, various advanced concepts and techniques are being used, including NLP techniques and deep learning techniques such as DNN and DRL, in addition to traditional rule-based techniques and straightforward machine learning algorithms. Machine translation, speech recognition, and language processing are among the tasks that utilize NLP techniques. There are various performance measures for virtual assistants, and specific measuring standards are followed throughout the industry. The structure and length of a Chatbot's discussion are critical performance metrics, with appropriate and relevant output sentence sizes, faster response times, and simpler phrase structures leading to higher customer satisfaction rates. In banks, the Chatbot is primarily used to assist the user through the bank's policy, schemes, and other customer queries regarding their account, which improves customer experience and reduces service costs. Measuring Chatbot performance can be challenging, but characteristics such as Perplexity, Learning rate, and Bleu score can indicate how well the model can be trained.

3. METHODOLOGY

The methods employed in this solution fall under the umbrella of Natural Language Processing (NLP), a subfield of artificial intelligence that deals with the interaction between computers and humans using natural

language. Both Bert and Sentence Transformer are NLP-based deep learning models that are designed to process and analyze human language. By leveraging these methods, the solution was able to achieve a higher level of accuracy and efficiency in evaluating candidate responses, ultimately resulting in better outcomes.

This study employed two deep learning models, namely Bert and Sentence Transformer, as the foundation of a solution aimed at achieving optimal scores. The primary model utilized was Bert, which is widely recognized as the most prevalent model for evaluating candidate responses. This model has been pre-trained with a vast amount of data and fine-tuned with training data, making it an ideal choice for the task at hand. Figure 2 illustrates the BERT-based model that served as the foundation of this solution.

In addition, the study incorporated a second model, namely Sentence Transformer, to further enhance the performance of the solution. This model is known for its ability to convert sentences into embedding, facilitating comparisons and analyses.

3.1. Model 1- BERT Based

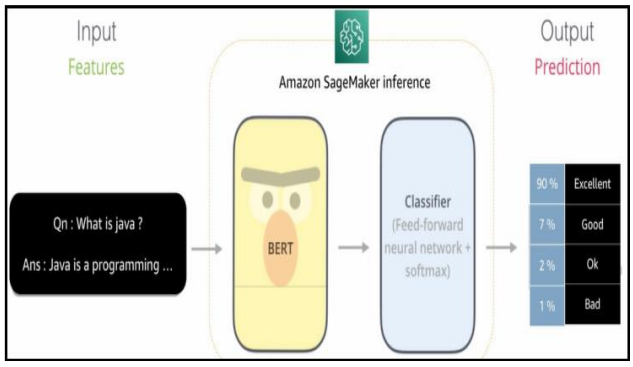

Figure 2 – Model 1- BERT Based

The study utilized a specific machine learning model for each topic in evaluating candidates' responses in this section. While the Java model was trained, additional models can be created for other input aspects. Implementing separate models for each issue can enhance the evaluation of candidates' responses. The process involves transferring the question and response to a feed-forward network for training, which rates the question and answers pairs as excellent, good, or bad.

A training strategy was employed for the model, as shown in Figure 3, and will be briefly discussed.

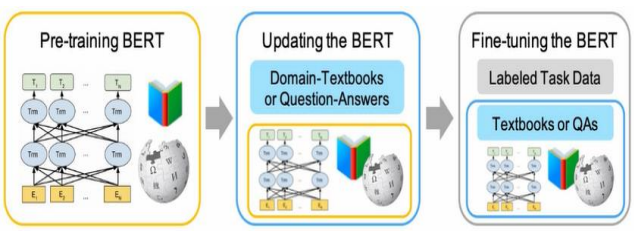

Figure3- Model 1- Retrained and fine-tuned BERT

In the second step, a large number of labelled questions and answers were collected using Java, and the model has trained accordingly. The desired accuracy of 80% was achieved in just a few days, and the entire process of retraining and fine-tuning was carried out using TensorFlow with Amazon Sage Maker.

3.2. Model 2- Sentence Transformer Based

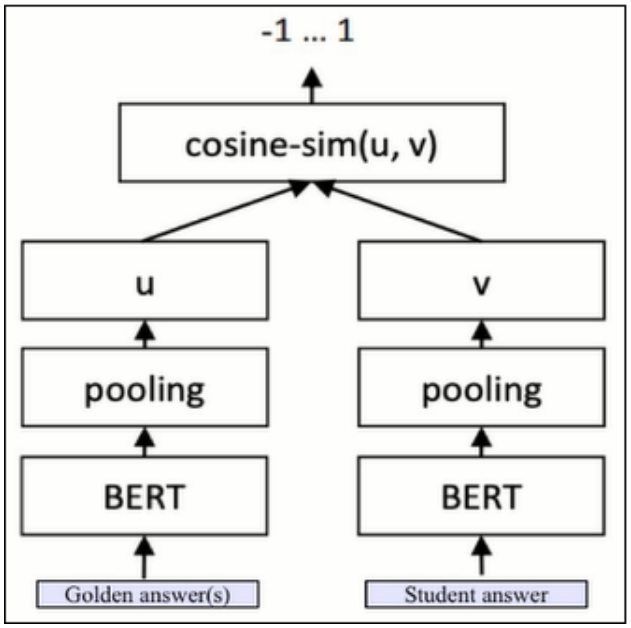

Figure 4- Model 2 – Sentence Transformer Based

When using BERT for natural language understanding tasks, such as question answering or text classification, the model produces contextualised word embeddings for each token in the input text. To obtain a fixed-size representation of the entire input, pooling operations are often applied to the embeddings, such as max pooling or mean pooling. This results in a single vector that represents the entire input text. For evaluating a student's answer, the BERT model could produce contextualized embeddings for each token in both the gold answer and the student's answer. The embeddings for each answer could then be pooled to produce u and v, which would represent the fixed-size vector representations of the gold answer and the student's answer, respectively. The cosine similarity between these two vectors, as computed by the formula provided below, is used as a measure of similarity between the two answers.

The expression "cosine-sim(u,v)" represents the cosine similarity between two vectors u and v. Cosine similarity is a measure of similarity between two non-zero vectors that measures the cosine of the angle between them. It is often used in natural language processing and information retrieval to compare the similarity between two documents or sets of words.

The formula for cosine similarity between two vectors u and v is: cosine-sim(u,v) = (u . v) / (||u|| ||v||)
where "." denotes the dot product between the two vectors, and "||u||" and "||v||" denote the magnitudes or lengths of the two vectors.

To address the challenge of limited time and resources for creating training data, this study utilized an additional model alongside the BERT-based model. With this approach, new questions can be added and quickly assessed by simply providing a reference answer. During the assessment process, the candidate's response is compared to the reference answer, and a score is assigned based on the degree of similarity between the two. This model also utilizes a pre-trained BERT model for encoding and comparing the responses using cosine similarity. While this approach may not be as polite as the fine-tuned BERT model, it is effective for evaluating candidates on novel topics with limited training data. The entire system is built on AWS serverless services, including AWS Lambda, Amazon Dynamo DB, and Amazon SQS, with deep learning training and inference handled by Amazon Sage Maker.

4. RESULTS AND ANALYSIS

The demo showcased a Java programming language interview, where the machine learning models were trained on the same topic. The interview was conducted using the Sumerian host, which asked the candidate two questions based on an MDP. The questions asked were: "What is the meaning of aggregation?" and "In Java, what is a transient variable?" The candidate's answers were evaluated to determine their performance. The Sumerian scene can be customized to meet branding needs, and the Lex bot can be programmed to ask more questions. It is also possible to train the machine-learning model on any technical topic to expand the scope beyond Java. After the interview, the candidate will receive the results on their registered DMA light.

In consideration of the demonstration, it is important to note that the solution can be customized to suit branding needs by personalizing the Sumerian and programming the Lex bot to ask additional questions. It is also noteworthy that the questions posed in the demonstration were related to the Java programming language. However, the system can be adapted for use in other technical fields by training the machine-learning model on the relevant subject matter.

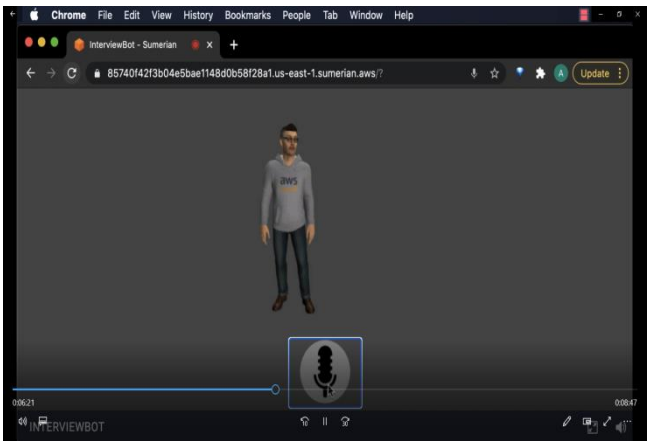

Figure 5- Amazon Sumerian host interview demo

As depicted in Figure 6, the proposed solution involves three main stakeholders: the administrator, the candidate, and the evaluator. To ensure proper system architecture, it is essential to isolate the React-based front-end application from the AWS amplification components. The data is stored in both Amazon Dynamo DB and Amazon S3, and the API layer is managed by AWS AppSync. By separating the front-end from the back-end components, the solution can achieve better scalability, resilience, and security. Additionally, this approach allows for more efficient updates and maintenance of the system.

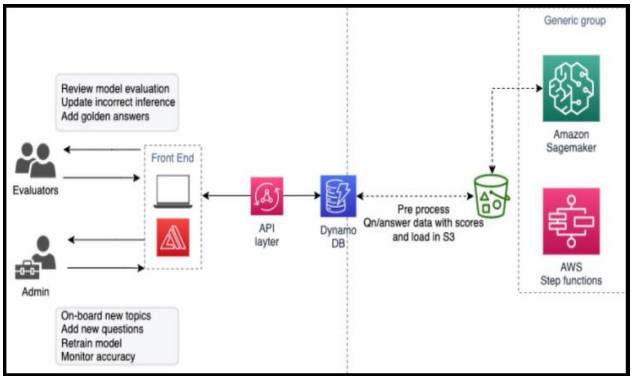

Figure 6- Admin/Evaluator Application

In addition, this system allows human evaluators to monitor automated evaluations and generate new training data to improve the model. The administrator can add new questions and refine existing ones to increase the model's accuracy. Ratings are determined based on the number of correct answers as evaluated by human raters compared to the total number of answers.

5. DISCUSSION

In this study, an intelligent interview bot was developed using deep learning with AWS services, and two deep learning models were employed to ensure the best possible score. The first model was a fine-tuned BERT-based model, while the second model was a sentence, transformer-based model. Both models were used to train

the bot to ask and evaluate candidate responses to technical questions in the Java programming language.

The results of the study showed that the intelligent interview bot was effective in evaluating candidates based on their responses to the technical questions asked. The system was built on the AWS serverless stack and training/inference using Amazon SageMaker, which allowed for quick scaling and cost control. Moreover, the system was easy to customize, with the Amazon Sumerian scene being customizable to meet branding needs, and new models could be quickly added and trained on unique subjects.

One limitation of this study is that the bot was trained on technical questions in the Java programming language only. However, as discussed in the results section, the system can be expanded to include other technical areas by training the machine-learning model on any technical topic.

In conclusion, the intelligent interview bot developed in this study has the potential to revolutionize the recruitment process, making it more efficient and objective. The system's ability to evaluate candidates based on their responses to technical questions could be extended to include other industries, such as finance and healthcare, and customized to fit the requirements of different companies. Further research can be conducted to improve the bot's performance and to explore its potential in other industries.

6. CONCLUSION

Overall, this paper presents a valuable contribution to the development of an intelligent interview bot using deep learning and AWS services. The proposed system offers a scalable and cost-effective solution for interview scheduling and evaluation. The use of deep learning models has ensured the best possible score, and the AWS serverless stack has enabled quick scalability and cost control.

However, some limitations of this study should be acknowledged. First, the proposed solution has only been tested on a limited number of participants, and further research may be needed to evaluate its performance on a larger scale. Second, the study has not addressed the potential ethical concerns associated with using an intelligent interview bot in the hiring process, such as biases in the model or privacy issues. These limitations suggest avenues for future research to explore the full potential and implications of using an intelligent interview bot in the recruitment process.

In conclusion, this study provides a promising approach to addressing the challenges of the recruitment process through the development of an intelligent interview bot using deep learning and AWS services. However, further research is needed to fully understand the potential benefits and limitations of this technology, as well as to address the ethical considerations associated with its implementation.

7. LIMITATIONS AND RECOMMENDATION

The proposed solution of creating an interactive interview experience using machine learning models also has some limitations that need to be acknowledged. These limitations include:

1. Dependence on training data quality and diversity: The accuracy of the machine learning model used to evaluate the candidate's responses is dependent on the quality and diversity of the data used to train it. If the training data is biased or limited, the model may not be able to accurately evaluate all candidate responses.
2. Limited suitability for certain job roles and industries: The use of an interactive virtual interview experience may not be suitable for all types of job roles or industries. For example, roles that require physical presence or hands-on skills may not be suitable for this approach.
3. Candidate discomfort with technology: Some candidates may not be comfortable with the technology and may prefer more traditional interview methods. It is essential to ensure that the candidate experience is positive and inclusive and that the technology does not hinder or disadvantage any applicants.
4. An initial investment of time and resources: Implementing a new technology solution like this requires an initial investment of time and resources, which may not be feasible for all organizations, particularly small businesses with limited budgets. Therefore, it is essential to assess the cost and benefits of implementing such a solution before deciding to adopt it.

To fully realise the potential of this solution, here are some recommendations based on the research findings:

1. Improve the quality and diversity of the training data used to train the machine learning models to ensure better accuracy in evaluating candidate responses.
2. Consider the suitability of an interactive virtual interview experience for different types of job roles and industries before implementing the solution.
3. Ensure the candidate experience is positive and inclusive and that the technology does not hinder or disadvantage any applicants.
4. Provide training and support for candidates who may not be comfortable with the technology to ensure equal opportunities for all candidates.
5. Evaluate the cost and benefits of implementing a new technology solution like this before deciding to adopt it.
6. Continuously monitor and evaluate the effectiveness of the solution and make necessary adjustments to improve its performance.

7. Explore the possibility of integrating additional features, such as sentiment analysis or natural language processing, to enhance the machine learning models' performance.

By implementing these recommendations, organizations can improve their recruitment processes and efficiently identify the most qualified candidates for their job roles.

Conflicts of Interest

The authors declare that they have no known competing financial interests or personal relationships that could have influenced the work reported in this paper.

REFERENCE

Amazon Web Services, Inc. n.d. *Machine Learning – Amazon Web Services*. [online] Available at: <https://aws.amazon.com/sagemaker/> [Accessed 1 March 2022].

Beaudry, A., Boucher, S., & Landry, R. (2019). Deep learning applications in HR research: Emerging trends and implications for practice. *Human Resource Management Review*, *29*(1), 98–113.

Beaudry, J., Consigli, A., Clark, C., & Robinson, K. J. (2019). Getting ready for adult healthcare: Designing a Chatbot to coach adolescents with special health needs through care transitions. *Journal of Pediatric Nursing*, *49*, 85–91. https://doi.org/10.1016/j.pedn.2019.09.004

Chakraborty, D., Ray, D., Mukherjee, A., & Naskar, R. (2020). Chatbot development using machine learning techniques: A review. In Proceedings of the 2020 11th International Conference on Computing, Communication and Networking Technologies (ICCCNT) (pp. 1-6). IEEE.

Chen, M., Wang, L., Li, Y., & Lin, Z. (2017). A demo of a smart interview bot: Building a real-time VR interview system using Amazon Sumerian. In Proceedings of the 2017 ACM on Conference on Information and Knowledge Management (pp. 2497-2499).

Heller, B., Proctor, M., Mah, D., Jewell, L., & Cheung, B. (2005). Freudbot: An investigation of Chatbot technology in distance education. In EdMedia+ Innovate Learning, pp. 3913-3918. Association for the Advancement of Computing in Education (AACE).

Heller, J., Bhattacharyya, S., & Reed, J. (2005). Learning to converse with a spoken dialogue system in a new domain. *Computer Speech & Language*, *19*(2), 137–158.

Hqn.thinkmethodology.co.uk. n.d. *Improving Service and Reducing Costs in Contact Centers How adding intelligence optimizes your business and customer experience*. [online] Available at: <https://hqn.thinkmethodology.co.uk/wp-content/uploads/2021/11/Improving-service-and-reducing-costs-in-contact-centres-AWS.pdf> [Accessed 1 March 2022].

Jafari, M. (2021). An interactive virtual interview experience using AWS. Medium. Retrieved from https://towardsdatascience.com/an-interactive-virtual-interview-experience-using-aws-ee53ab72c299

Liu, B., Ma, Y., He, Y., Wang, T., & Tang, J. (2016). In pursuit of a natural conversation interface for knowledge base refinement: On the design of the talkmaster system. *Information Processing & Management*, *52*(1), 17–35.

Liu, C.-W. Lowe. R, Iulian V. Serban, Noseworthy. M, Charlin. L, and Joelle Pineau (2016). How not to evaluate your dialogue system: An empirical study of unsupervised evaluation metrics for dialogue response generation. arXiv preprint arXiv:1603.08023

Pages.awscloud.com. n.d. The Machine Learning Journey The path toward leveraging the full power of machine learning technologies. [online] Available at: <https://pages.awscloud.com/rs/112-TZM-766/images/AWS_Machine_Learning_Journey_eBook_Final.pdf> [Accessed 1 March 2022].

Przegalinska, A., Ciechanowski, L., Stroz, A., Gloor, P., & Mazurek, G. (2019). Ciechanowski. L, Stroz. A, Gloor. P, and Mazurek. G (2019). In bot, we trust: A new methodology of Chatbot performance measures. *Business Horizons*, *62*(6), 785–797. https://doi.org/10.1016/j.bushor.2019.08.005

Resources.aithority.com. 2022. 7 Leading Machine Learning Use Cases. [online] Available at: <https://resources.aithority.com/ait-whitepapers/7-leading-machine-learning-use-cases.pdf> [Accessed 1 March 2022].

Sherstinsky, A. (2020). Fundamentals of Recurrent Neural Network (RNN) and Long Short-Term Memory (LSTM) network. *Physica D. Nonlinear Phenomena*, *404*, 132306. https://doi.org/10.1016/j.physd.2019.132306

Sutoyo, D. S., Purwarianti, A., Hidayanto, A. N., & Kurniawan, H. (2019). The development of a job interview chatbot with a hybrid approach of rule-based and retrieval-based methods. *Journal of Physics: Conference Series*, *1231*(1), 012062.

Sutoyo, R., Chowanda, A., Kurniati, A., & Wongso, R. (2019). Designing an emotionally realistic chatbot framework to enhance its believability with AIML and information states. *Procedia Computer Science*, *157*, 621–628. https://doi.org/10.1016/j.procs.2019.08.226

Sutskever, I., Vinyals, O., & Quoc, V. (2014). Le. Sequence to sequence learning with neural networks. In Advances in neural information processing systems, pp. 3104-3112. 2014.

4th International Engineering Conference (IEC 2022)
Federal University of Technology, Minna, Nigeria

Failure Analysis and Performance Improvement of a Paper Shredder

*Danladi,Peter[1], Okoro, U. G.[1]
[1]Mechanical Engineering Engineering Department, Federal University of Technology, PMB 65 Minna Niger State, Nigeria
*Corresponding author email:peterdanladi79@yahoo.com+2348033940161

ABSTRACT
A paper shredder is a mechanical device used to cut paper into smaller particles leaving the content in a way that cannot be put to further use. It has been observed over time that paper shredding machine always jam during operation and causes inconveniencies. This research work used Failure Mode and Effect Analysis tool to analyze the causes of instantaneous paper shredding blade/cutter's failure. It identifies the causes of failure, the consequence of failure, and proposes process control i.e., what to monitor. The result showed that paper shredding machine problem always occur at the cutting region of the system and suggested that the blade/cutter should be redesign in order to eliminate or reduced the blade's failure. Furthermore, the study proposes a design modification paper shredder blade/cutter, to improve the performance. The comparative test conducted on the developed blade indicates an improvement of about 24% per time required to complete shredding of 1kg which translates to volumetric efficiency of 79.9%.

Keywords: *Cutter design modification, Failure mode and effect analysis, Paper shredder, Performance evaluation.*

1 INTRODUCTION

Many situations require that important information be made available on papers; letters are drafted, set examination questions or even write minutes of crucial meetings before getting them typed and these hand written ones are usually thrown into the waste paper basket. It is possible that wrong persons may have access to the waste papers, collect and use them in wrong or negative ways. Also, as competition between businesses grows, offices and people in general become more concerned about protecting their business and personal information to avoid identity theft, financial frauds and other security risks. Although in recent time information are stored digitally on computer servers, however important information that can compromise businesses and organizations is still widely available on paper. It is expected that every organization, irrespective of the size, should regularly destroy documents, which are not meant for the public eye (Ogbeide et al., 2017). This not only keeps the operations of the business safe, but also protects consumers and the members of the general public safe from identity theft, financial frauds and other security risks. Throwing whole pieces of paper containing such information into trash receptacles exposes businesses and organizations to great risk. One effective way preventing sensitive information falling into the wrong hands is to use a paper shredder.

A paper shredder is a mechanical device used to cut paper into chad, typically either strips or fine particles leaving the content in a way that cannot be put to further use. It is a machine used to shred papers into pieces in a way it cannot be pieced together. Government organizations, businesses, and private individuals use shredders to destroy private, confidential, or otherwise sensitive documents. Privacy experts often recommend that individuals shred bills, tax documents, credit card and bank account statements, and other items which could be used by thieves to commit fraud or identity theft (Nithyananth et al., 2014). Figure 1.1 shows the complete assembly of a paper shredding machine.

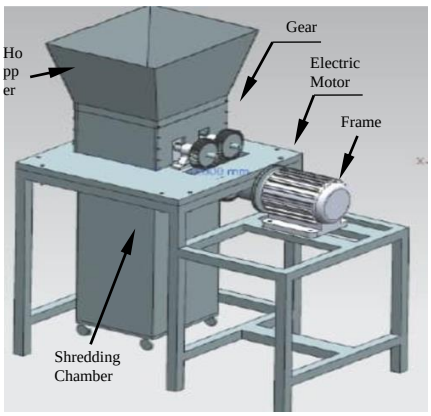

Figure 1-1 a paper shredding machine

According to Nithyananth et al (2014) it is a security device, which reduces paper to small strips or confetti-like pieces, making it difficult for the individual piece to be put back together. paper shredder is to crush sheet papers, especially confidential paper documents and other documents that are no longer required. Paper The main function of shredder can also be found in education sector such as schools tertiary, secondary or primary institutions. It could either be used in offices or for paper disposal on campuses.

A paper shredder is driven by an electric motor which delivers power to the cutting system and reduces the electric motors speed to suit the needs of the blade rotation to destroy the paper. Paper shredder machine consists of three main parts which are the machine construction, transmission system and cutting system. The

paper shredding machine is a simple machine that can be operated. After assembling the components, the machine is operated electrically with the cutting shaft operated by electric motor. When the machine is switched on the speed of the electric motor is transmitted to the pulley via Vee belt and then to the shaft, which rotates the gears and the driven shaft the meshing of the two shafts brings about the cutting of the papers when it is fed into it. Paper shredder blade as shown in figure 1.2 is one of the important components found in paper shredding machine connected to the shaft which is used to rotate the blade in order to cut the paper in to pieces.

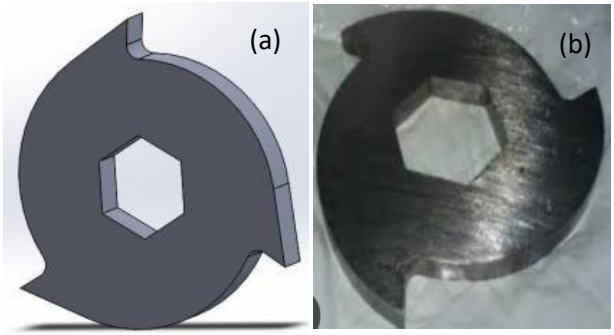

Figure 1-2 **a paper shredding machine's blade**

Failure mode and effect analysis is the process of reviewing as many components assemblies and subsystems as possible to identify potential failure modes in a system and their causes and effects. In this project, instantaneous causes of paper shredder's blade failure was determined using failure mode and effect analysis and the new blade was developed to meet up with efficient, reliable and full operational performance of paper shredder's blade was achieved.

2 METHODOLOGY

2.1 MATERIALS

Material selection is one of the most important aspect that demand the understanding of the functional requirement for the individual machine components as there are ever increasing varieties presently available and the development of new materials with unique properties and application (González-Viñas & Mancini, 2004). Material selection for any engineering design depend on the following factors; availability, strength, fabricability, appearance, cost and corrosion resistance. Before starting the actual paper shredding materials selection process, under listed questions must be answered. Every specific application required by paper shredding machine is characterized by a set of operation parameters, which dictate the necessity and accurate selection of the optional materials(Khurmi & Gupta, 2012).

According to Siddiqui (2017), material selection depends on some operating conditions. Some of the conditions or factors considered in selecting materials includes but not restricted to Pressure and load involved, Operating temperature, Availability,Cost and Functionality. With these above, material requirements and its properties was selected for the design of blade component. The material to be considered in this research work is low carbon steel.

2.2 LOW CARBON STEEL

Also known as mild steel is now the most common form of steel because its price is relatively low while it provides material properties that are acceptable for many applications. Low carbon steel contains approximately 0.05-0.25% carbon making it malleable and ductile. Mild steel has relatively low tensile strength, but it is cheap and easy to form, surface hardness can be increased through carburizing.(Gao et al., 2015).The heat transfer characteristics of a solid material are measured by a property called the thermal conductivity or λ,measured in w/m.k. it is a measure of a substance's ability to transfer heat through a material by conduction. Table 2.1 below shows the mechanical properties of low carbon steel.

Table2-1:THE MECHANICAL PROPERTIES OF LOW CARBON STEEL.

low carbon steel	Properties
Magnetic	This is due to the high amounts of ferrite and iron in mild steel bars.
Ductile	In comparison to other types of steel, it is more ductile and therefore can be used for a wide variety of purposes.
Weldable	Due to its low carbon content, it is more malleable and suitable for welding. The less carbon in the steel, the more weldable and machinable it becomes.
Affordable	Using mild steel is relatively cost-effective in comparison to some other steels.
Very little carbon	This makes cold-forming low carbon steel easier, and they are easier to handle as a whole.

2.3 PAPER MATERIAL

Paper is a thin sheet material produced by mechanically or chemically processing cellulose fibres derived from **w**ood, rags, grasses or other vegetable sources in **w**ater draining the **w**ater, through fine mesh leaving the fibre evenly distributed on the surface, followed by pressing and drying. It is a versatile material with many uses, including printing, painting, graphics, signage, design, packaging, decorating, **w**riting and cleaning. It may also be used as filter paper, wallpaper, book, endpaper, conservation paper, laminated **w**orktops, toilet tissue or currency and security paper, or in a number of industrial and construction processes.In this study the material to be cut is selected to be paper material with mechanical properties given in the Table 2.2.

Table 2-2MECHANICAL PROPERTIES OF PAPER

Office copy	Bulk density(g/cm□)	Ultimate tensile strength(kgf/cm²)	Ultimate tensile strength(Mpa)
A4 – 1	0.632	232.5	22.81
A4 -2	0.635	271.8	26.7
A4 – 3	0.637	255.5	25.05

2.4 FAILURE MODE EFFECT ANALYSIS (FMEA)

FMEA is an efficient tool for identifying the potential failure modes and their effects in order to increase the reliability and safety of complex systems and gathering the data that is necessary to decide about how to manage risks. In fact, the purpose of this technique is to identify failure modes and their effects and corrective actions to eliminate or reduce the probability of failure (redesign) and finally the development of efficient maintenance system, to reduce the occurrence of potential scenarios (Kmenta & Ishii, 2000).

The first phase of this research work was to investigate the paper shredding blade's failure using failure mode and effect analysis as a tool used to carried out the analysis. This investigation was carried out with the help of experts (paper shredding machine's operator and their maintenance personnel) from different locations across the country that came up with the same opinion on the component's failure mode, failure consequences and process control / what to monitor. The detailed information was given in the table 2.3 below. It was opined by some of these experts on the paper shredding blade's that the blade should be re-redesign in order to eliminate or reduced the instantaneous of failure of the blade/cutter as low as possible that can be of a help to increase the paper shredding blade's efficiency.

Table 2-3FAILURE MODE AND EFFECT ANALYSIS OF PAPER SHREDDING MACHINE'S BLADE/CUTTER

S/N	Component / Sub component	Component / Sub component Function	Failure Mode	Failure consequences	What to monitor/process Control
1	Paper shredder blade/cutter	Paper shredder blade/cutter is a major component found in paper shredding machine used to shred the paper in to pieces with the help of rotating shaft connected to the blade	Blade / cutter broken at the edges	Paper flying out from the shredding housing completely	- regular inspection oat the edges of the blade
			Blade /cutter bent at its periphery	Paper jamming at the shredding housing	Daily internal/ external inspection of the blade's periphery
			Blade /cutter worn out at the edges	Partial shredding of the paper	-daily inspection on the edges of the blade
			Blade /cutter fractured around the blade hole	Partial jamming and shredding of the paper	-regular inspection of the blade/cutter's hole
			Blade /cutter hooked without rotation	Total loss of shredding during the process	Regular inspection on the entire cutting system
			Blade /cutter out worn around blade's hole	Partial jamming and shredding of the paper	Regular internal /external inspection
			Blade/ cutter broken, worn out, fractured and bent around its periphery	Total loss of shredding during the process	-regular inspection -weekly / monthly maintenance

2.5 DESIGN CONSIDERATION

The second methodology adopted for the second phase of this research work is the process that starts with design of the concept, selection of material and design analysis, and lastly fabrication and testing of the blade/cutter.

2.6 DESIGN THEORY AND CALCULATION OF THE REDESIGNED BLADE

Breaking strength can be assumed as the ultimate strength multiply by a factor of safety 1.5.Breaking strength (τ_{br}) of paper material:(τ_{br}) =25.05 ×1.5=37.58 MPa.The cross-sectional area (A) of the material to be cut is:

$$A = w \times t \quad \textbf{(1)}$$

Where; w = width of the cutting edge, t = thickness of the paper material. Similarly, the shear stress is express by:

$$\tau = {}^{F}/_{A} \quad \textbf{(2)}$$

Where: $\boldsymbol{\tau}$: shear stress (N/mm^2), F, Force applied the blades (N), A : Cross-sectional area(mm^2).The cutting force ($\boldsymbol{F_c}$). The cutting force (F_c) required for shredding paper material;

$$F_c = \tau_{br} \times A \quad \textbf{(3)}$$

Torque (T) exerted on the blade as well as shaft is given by the equation

$$T = F_c \times r \quad \textbf{(4)}$$

Where; T = Paper cutting torque (N-m), r = Radius of the blade from the center (mm). Power (P) transmitted by the shaft is given by:

$$P = M \times \omega \quad \textbf{(5)}$$

Where; ω = angular speed (rad/s)

Description of the Geometry of The Shredder Blade:
The detailed blade geometry is as shown in figure 2.1. The blade has a width (w) of $0.006\ m$, centre radius(r) of 0.06m, and hole (Hexagonal circle) of radius 0.02m. The cutting area (A) made by edge of the blade is given by equation (1) and calculated as follows;

$$A = 6 \times 5 = 30mm^2$$

where;w = width of cutting edge, t = thickness of 10 sheets of A4 paper.

Force Acting on Cutting Edge of The Blade:
The force acting on the cutting edge of the blade can be estimated from the relationship between the shear strength and the area as expressed in equation 3. Given that the shear strength is$37.58MPa$, the force, therefore becomes;

$$F_c = breakingstrength \times Area$$

$$F_c = 37.58 \times 30 = 1127.4N$$

From the estimate of the force F_c. the torque exerting on the blade as well as shaft can be computed from equation 4 as follows;

$$T = F_c \times r$$

$$T = 1127.4 \times 0.06 = 67.644\ Nm$$

Power (P) required for torque transmission of the shaft:
The power transmitted by the torque is given by equation (5) and depicted as follows;

$$P = T \times \omega$$

Substituting the values of T and ω into equation (5) yields the following expressions

$$P = 67.644 \times 2\pi$$

$$P = 67.644 \times (2 \times 3.142)$$

$$P = 425.07\ watt, or P = 0.43\ Kw$$

2.7 FABRICATION AND ASSEMBLY

The fabrication, production and fixing of the paper shredding blade / cutter was carried out in order to achieved the desired units blade /cutter.The paper shredder blade /cutter was fabricated from 6mm thick plate. The metal plate was cut using a hand cutting machine to dimension specified in the appendix A. the cut plate was then finally plain and sharp at the edges to form a complete paper shredder blade/ cutter.

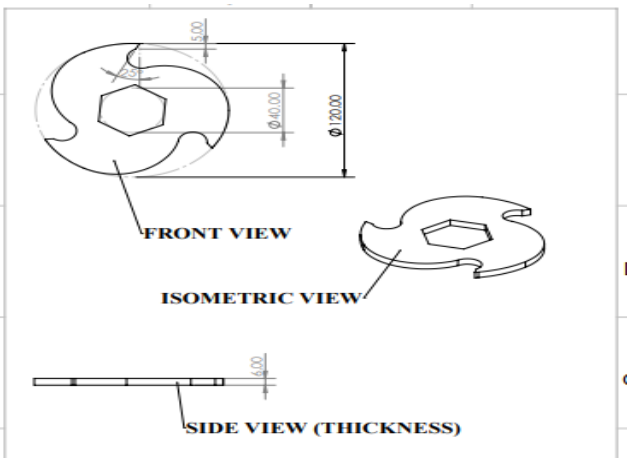

Figure 2-1 Detail geometry of shredder blade and dimensions

3 RESULTS AND DISCUSSION

The initial study of this research work was to investigate the existing paper shredding blade/ cutter's failure using one of the most popular risk analysis tool "the Failure Mode and Effect Analysis" to analyze the instantaneous failure of the blade in paper shredding machine. This investigation was carried out with the help of four (4) men of experts who have been operating paper shredding machine from different locations across the country. The result proved that paper shredding machine problem always occurs at the blade/cutter's region especially at the cutter's edge where the concentration of stress is high during the operation process. Therefore, the failure mode and effect analysis tool was not only designed to check "the causes of failure", "the

consequence of failure", "what to monitor / process control but may also lead to the redesigning ofnew product (blade/cutter) after the completion of the work. The new blade was redesigned with the radius of an arc at the edge to be 20mm to reduce the stress concentration and the cutting angle of $25^0$for instantaneous shredding which is differ from the existing one with the radius of an arc 60mm at the centre and cutting angle of 120^0, that was consider in this research work to eliminate or reduced the amount of failure on the blade's/cutter in order to meet up with a credible performance.

The second phase of this research work was to redesign a new blade/cutter that can shred paper for a period of a term without developed any symptom of failure. The new blade/cutter was redesigned, fabricated and constructed while the results were recorded from the design analysis and calculations are itemized in table 3.1.

TABLE 3-1 DESIGN ANALYSIS AND CALCULATION RESULT

The cutting area (A) made by edge of the blade	$30mm^2$
Force acting (F) on cutting edge of the blade	751.5N
Torque(T) exerting on the blade as well as shaft	45.09Nm
Power (P) of the required torque transmission shaft	0.47KW
The volumetric efficiency	79.9%

The blades were been replaced, tested and it took about 6.08minutes for the machine to shred 4.78× 10¯5m□.During testing, the volumetric flow rate of the shredded paper was measured using the weighing machine and $\rho = m/v$ at the interval of 60secs,while the volumetric efficiency was gotten as 79.9%.Therefore,it was observed that radius at the new blade/cutter's edge when compare with the existing blade/cutter tend to reduce stress concentration and increase the redesigned blade/cutter's efficiency and the instantaneous failure of the machine become minimal during the testing operation when compare with the existing blade/cutter. The experimental test result table and graph showing relationship between discharge and time is described in table 3.2 and figure 3.1 respectively.

TABLE 3.2: EXPERIMENTAL TEST RESULT

S/No	T(min)	V($\times 10^{-5}m^3$/min)
1	0	0
2	1	1.2
3	2	1.62
4	3	2.24
5	4	3.20
6	5	4.01
7	6	4.78

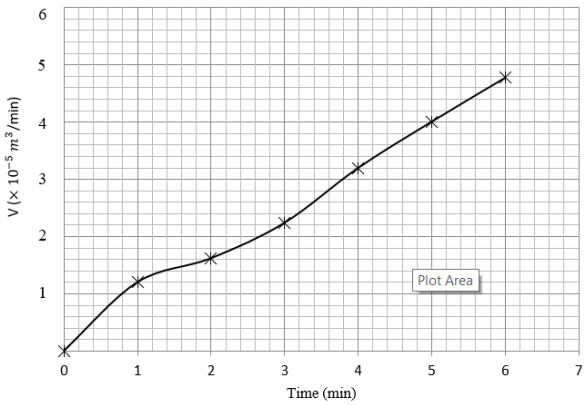

Figure 3-1Relationship between discharge and time which is linear with a slope

4 CONCLUSION

This research work used Failure Mode and Effect Analysis tool to analyze the causes of instantaneous paper shredding blade/cutter's failure and the result proved that paper shredding machine problem always occur at the cutting system region. Therefore, the causes, the consequence, and the process control are been determined. It was also observed that there is need for a new blade/cutter should be redesign in order to eliminate or reduced the blade's failure. The paper shredder blade/cutter's was designed, fabricated and tested using the existing machine to shred some quantities of papers. The blades ware designed for strength, rigidity, and the performance evaluation shows that the redesigned blades during the machine operation have a volumetric efficiency of 79.9%. The comparative test conducted between the new blades and the existing blades indicates that the machine takes 6.08minutes to complete shredding of 1kg in new blades and it took the existing blades 8.01minutes to shred 1kg of the papers.
Therefore, low carbon steel was chosen for the construction and the written papers of different size are also selected to be shredded.

REFERENCE

Gao, W., Zhang, Y., Ramanujan, D., Ramani, K., Chen, Y., Williams, C. B., Wang, C. C. L., Shin, Y. C., Zhang, S., & Zavattieri, P. D. (2015). The status, challenges, and future of additive manufacturing in engineering. *CAD Computer Aided Design*, *69*, 65–89. https://doi.org/10.1016/j.cad.2015.04.001

González-Viñas, W., & Mancini, H. L. (2004). *An introduction to materials science*. Princeton University Press.

Khurmi, R. S., & Gupta, J. K. (2012). *Text book of machine design. New Delhi: S. Chand, Limited*. Eurasia publishing house.

Kmenta, S., & Ishii, K. (2000). Scenario-based FMEA: a

life cycle cost perspective. International Design Engineering Technical Conferences and Computers and Information in Engineering Conference, 35159, 163–173.

Nithyananth, S., Samuel, L., Mathew, N., & Suraj, S. (2014). Design of waste shredder machine. *Libin Samuel et Al Int. Journal of Engineering Research and Applications ISSN*, 2248–9622.

Ogbeide, O. O., Nwabudike, P. N., & Igbinomwanhia, N. O. (2017). Design and development of an electric paper shredding machine. *Nigerian Research Journal of Engineering and Environmental Sciences 2 (2)*, 546–562.

Siddiqui, F., Patil, H., Raut, S., Wadake, O., & Tandel, S. (2017). Design and fabrication of paper shredder machine. *Int. Res. J. Eng. and Tech.(IRJET)*, *4*(6), 770–775.

4th International Engineering Conference (IEC 2022)
Federal University of Technology, Minna, Nigeria

EXTRACTION OF COAGULANT (ALUM) FROM SLUDGE OF THE A.B.U. WATER TREATMENT PLANT USING ACIDIFICATION PROCESS

*Adamu A. D. [1], Usman J. H.[2], Sani, B. S.[3], Abubakar, U. A.[4] and Abdullahi, N. I. [5]
Department of Water Resources and Environmental Engineering, Ahmadu Bello University Zaria- Nigeria.
*Corresponding author: adamualiyu@abu.edu.ng 2438062619284

ABSTRACT
Alum has been the common coagulant used by the treatment plant during the treatment process. Despite being good, it generates high amount of sludge that is associated with disposal challenges due to its aluminium content, hence the need recover the aluminium and subject to further coagulation. This study considered the sludge of Ahmadu Bello University treatment plant in order to recover the alum using the acidification method with sulphuric acid (H_2SO_4) as the extractant. Different concentrations of H_2SO_4 (0.5 – 1.50M) at constant sludge weight of 150g, were used to obtain the optimum recovered alum. It was discovered that, with 3.0ml dosage of 1.5M H_2SO_4, the recovered alum had 99.6% efficiency and 98% effectiveness as the original alum used in the treatment plant. It was concluded that alum regenerated from the sludge can be effectively applied as coagulant for water treatment.

Keywords: *Alum, coagulant, extraction, recovered, sludge.*

1 INTRODUCTION

Sludge produced by water treatment plants has been gaining significant attention due to the impact it has on the environment as well as issues related to its safe disposal and management. The sludge is made up flocs removed after coagulation process and could have as far as 20% alum (Ruziqna *et al.*, 2020). The conventional way of releasing sludge into the environment is to discharge it into the closest water ways. This practice is accompanied by pollution of the water resources, thereby creating more difficulty in terms of treatment requirement and facility involvement (Joshi and Shrivastava, 2011).

Similarly, efforts have been geared towards finding favourable and simple methods of sludge management so that it could be properly controlled, thereby preventing river pollution. The sludge, when released into the river, increased organic loading as well as metal content. Other conventional ways of sludge controlled involve: spaying it on a bed, refrigerating, heat and pressure application and dewatering (Hassan Basari *et al.*, 2019; Rahman and El Sayed, 2019; Mirwan *et al.*, 2020).

The study area in this work, Ahmadu Bello University, makes use of the sand bed drying and land disposal methods which are not economically efficient as the sludge recovery method (Cheng *et al.*, 2014). However, recovery of alum from sludge has proven to be more efficient in terms of economic benefits, control of pollutants into the surroundings and chemical involvement. This prompt the attention to be geared towards distancing chemicals from the water treatment process and deployment of the recovered alum (Ruziqna *et al.*, 2020; Keeley *et al.*, 2014).

In addition, apart from alum, iron salts have been used in as coagulants for long. The time could be as far back as 19th century. But now a days, attention has been tilted towards the application of alum for such purposes (Hamzah *et al.*, 2022; Azim *et al.*, 2013; Boanaventura *et al.*, 2000).

Despite many researches were performed on the removal of coagulant from the sludge, it is very paramount to remove the alum and put it back as a coagulant to the treatment process. It is truly a process that saves cost, thereby making to be viable economically (Hassan Basari *et al.*, 2019; Mirwan *et al.*, 2020). Moreover, the removal of alum from the sludge could be seamlessly achieved through the acidification and commonly employed acid is sulphuric acid (H_2SO_4). Additionally, pH of the sludge as well its origin play important role in the recovery of alum. And when the alum is successively removed, it goes a long in reducing the sludge volume.

The aim of this work therefore, is to extract the coagulant (alum) discharged sludge of the treatment plant of A.B.U. Zaria.

2 MATERIALS AND METHODS

2.1 Materials

Oven (Model Binder ED720), wire 2mm and 1mm sieve pan, filter funnel, conical flask, measuring cylinder (1000 ml), electronic weighting balance (model number, CY Series), filter paper, magnetic stirrer (model number, VMS-A), H_2SO_4 as acidification agent (0.5M – 1.5M), digital turbidimeter (VTSYIQI WGZ-200B) and flocculating machine.

2.2 Methods

2.2.1 SLUDGE COLLECTION

The sludge sample was collected from A.B.U. Zaria, water treatment plant and then taken to Environmental Engineering Laboratory in A.B.U for analysis. The treatment plant was designed for 400,000 population which serves students and other residents of the University.

2.2.2 ACIDIFICATION PROCESS

The sludge was dried in the oven at 105ºC for 3days in order to remove moisture and then sieved through 2 mm mesh. It was then crushed through 1mm mesh pan and stored for use. Then, 150g of the dried sludge was weighed into three (3) portions, designated as samples B, C and D. Each sample was then mixed with 500ml of distilled water. Then, 0.5M, 1.0M and 1.50M of H_2SO_4 were added to B, C and D, respectively. It was followed by mixing in the magnetic stirrer at 30 rpm for 15 minutes until it was thoroughly agitated. In another study carried out by Hassan Basari *et al.,* (2019), H_2SO_4 concentrations of 0.45 – 1.8M was used with corresponding alum sludge dosage of 300 g.

The acidification process removed the aluminium from the sludge and time allocated was 30 - 60 minutes at the temperature of 35ºC. This is in agreement with Ruziqna *et al.* (2020).

After the agitation and mixing, the samples passed through 16 µm filter inserted into funnel. Thereafter, the sample was filtered again through 12µm filter paper with the help of suction pump. Then, 50ml put into the tube and at 10°C, being the effective temperature for the recovery of aluminum. The temperature, pH, speed of agitation, time of agitation, distilled water and H_2SO_4 are put under controlled. The initial pH of sample that mixed with H_2SO_4 was pH 4.7. It took about 15 minutes for H_2SO_4.

2.2.3 JAR TEST

The effectiveness of the extracted alums (Samples B, C and D) in removing turbidity was determined using the jar test, where varying dosages of coagulant were tested in the Figure 1 indicate the flow chart of the methods used in this study.

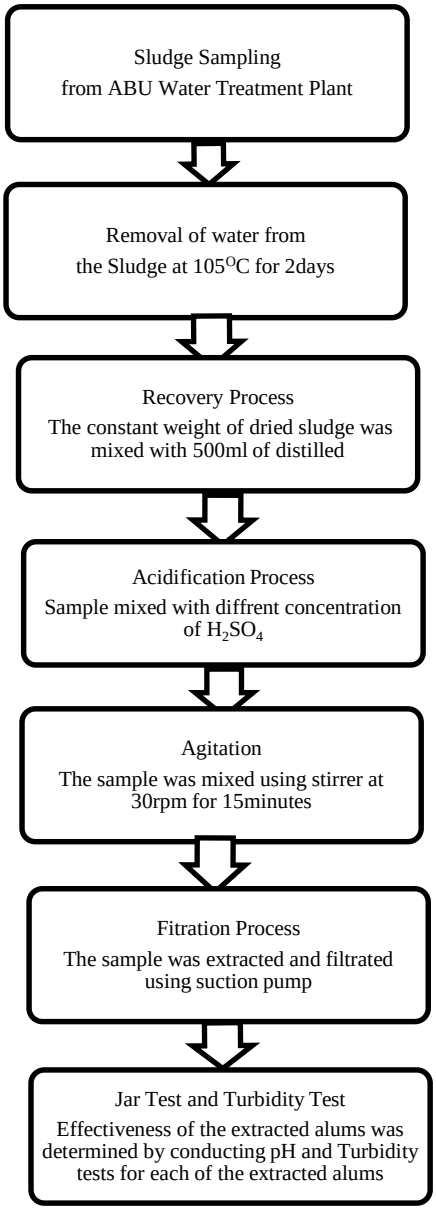

Figure 1: Flow chart of the methods used

3 RESULTS AND DISCUSSION

Table 1 indicates the extracted alums under various H_2SO_4 molarities of 0.5M - 1.50M and fixed dried sludge of 150g, while the molarity of H_2SO_4 was varied from 0.5 M to 1.5 M. From the Table, it could be observed that sample B, containing 0.5 M H_2SO_4 recorded pH of 4.05; while samples C and D, having 1.0 M H_2SO_4 recorded pH of 3.15 and 2.95, respectively. The reduction in the pH from 4.05 to 2.95 as noticed from samples B to D with increased in the concentration of the H_2SO_4 could attributed to the introduction of more hydrogen ions. The recovery of those substances were beyond the scope of this study. It is important to note that, when reaction occurred between H_2SO_4 sludge, sample colour turned to dark brown.

Table 1: Extracted alums with 150g of sludge and different molarities of H_2SO_4

Parameters	Samples		
	Sample B	Sample C	Sample D
Molarity of H_2SO_4 (M)	0.5	1.0	1.5
Weight of sludge (g)	150	150	150
Mixing rate (rpm)	30	30	30
Mixing time (min)	15	15	15
Distilled water (ml)	500	500	500
Volume of H_2SO_4 (ml)	50	50	50
pH	4.05	3.15	2.95

Where; Sample A = alum used in the treatment plant (controlled), Sample B = extracted alum using 0.5M H_2SO_4, Sample C = extracted alum using 1.0M H_2SO_4, Sample D = extracted alum using 1.5M H_2SO_4.
It important to note that the dilution factor taken was 15, therefore, turbidity of raw water = 13×15 = 195 NTU

Table 2 indicates the Jar Tests for Sample A at the controlled pH of 7.0 and turbidity of 195 NTU. The volume of the raw water was kept constant at 400 ml, at the alum recovered dosages of 0.3, 0.2 and 0.1 ml and stirring times of 5 and 30 mins as could be observed in the Table. The lowest turbidity obtained was 0.49 NTU under the alum dosage of 0.3 ml at the stirring time of 30 mins; while the maximum turbidity recorded was 31.7 NTU under the alum dosage of 0.1 ml at the stirring time of 5 mins.

Table 2: Sample A (Controlled pH = 7.0, Turbidity = 195 NTU)

Sample A	After 5mins			After 30mins		
Vol. of raw water (ml)	400 ml	400 ml	400 ml	400ml	400 ml	400 ml
Alum dosage (ml)	0.3	0.2	0.1	0.3	0.2	0.1
Turbidity (NTU)	10.7	22.5	31.7	0.49	1.4	2.1

Table 3 shows the Jar Tests for Sample B at the controlled pH of 7.0 and turbidity of 195 NTU. The volume of the raw water was kept constant at 400 ml, at the alum dosages of 0.5, 0.4 and 0.3 ml and stirring times of 5 and 30 mins as could be seen in the Table. The minimum turbidity of 105 NTU (46.1%) was obtained under the alum dosage of 0.5 ml at the stirring time of 30 mins; while the maximum turbidity recorded was 180 NTU (7.7%) under the alum dosage of 0.4 ml at the stirring time of 5 mins. In another study carried out Ruziqna *et al.* (2020), it was reported that at the recovered alum dosage of 30 mg/l, turbidity reduction of 2.65 NTU was obtained from the initial value of 23.72 NTU, which translated into 88.83%.

Table 3: Sample B (Controlled pH = 7.0, Turbidity = 195 NTU)

Sample B	After 5mins			After 30mins		
Vol. of raw water (ml)	400 ml	400 ml	400 ml	400ml	400 ml	400 ml
Alum dosage (ml)	0.5	0.4	0.3	0.5	0.4	0.3
Turbidity (NTU)	165	172.5	180	105	121.5	130.5

Table 4 shows the Jar Tests for Sample C at the controlled pH of 7.0 and turbidity of 195 NTU. The volume of the raw water was kept constant at 400 ml under the alum dosages of 1.0, 0.9 and 0.8 ml and stirring times of 5 and 30 mins as could be noticed in the Table. The lowest turbidity of 56.1 NTU (71.2%) was obtained under the alum dosage of 1.0 ml at the stirring time of 30 mins; while the highest turbidity recorded was 69 NTU (64.6%) under the alum dosage of 0.4 ml at the stirring time of 5 mins. In another study by Hassan Basari *et al.*, (2019), H_2SO_4 concentrations of 0.45 – 1.8M was used with

corresponding alum sludge dosage of 300 g and the recorded alum recovery of 98% was obtained.

Table 4: Sample C (Controlled pH = 7.0, Turbidity = 195 NTU)

Sample C	After 5mins			After 30mins		
Vol. of raw water (ml)	400 ml	400 ml	400 ml	400 ml	400 ml	400 ml
Alum dosage (ml)	1.0	0.9	0.8	1.0	0.9	0.8
Turbidity (NTU)	59	63	69	56.1	59.5	65

Table 5 depicts the Jar Tests for Sample D at the controlled pH of 7.0 and turbidity of 195 NTU. The volume of the raw water was kept constant at 400 ml; at the alum dosages of 1.5, 1.4 and 1.3 ml and stirring times of 5 and 30 mins as could be noticed in the Table. The lowest turbidity of 17.3 NTU (91.1%) was obtained under the alum dosage of 1.5 ml at the stirring time of 30 mins; while the highest turbidity recorded was 45 NTU (76.9%) under the alum recovered dosage of 1.3 ml at the stirring time of 5 mins. In addition, it was noticed that after 30mins of mixing, Sample D produced the largest floc that settled quickly with the corresponding least turbidity when compared to Samples B and C. In another Study carried out by Boaventura *et al.* (2000), it was discovered that, highest aluminium recovery of 75.7% was achieved at sludge dosage of 2% and settling time of 45mins. Similarly, Hamzah *et al.* (2022) studied the performance of recovered aluminium using Nitric acid as the extractant at the molarity of 0.5 M – 2.0 M. The study revealed up to 99% aluminium recovery.

Table 5: Sample D (Controlled pH = 7.0, Turbidity = 195 NTU)

Sample D	After 5mins			After 30mins		
Vol. of raw water (ml)	400 ml	400 ml	400 ml	400ml	400 ml	400 ml
Alum dosage (ml)	1.5	1.4	1.3	1.5	1.4	1.3
Turbidity (NTU)	32.9	39	45	17.3	18	22.5

However, since Sample D had the pH closed to that of the controlled sample A. Therefore, to determine the optimum dosage needed, Sample D is selected. The Jar Test was then conducted using Sample D at varying dosages of the recovered alum. After 30mins, the turbidity value of Sample D was measured to be 0.5NTU as shown in Table 6, which closely agreed with the least turbidity of 0.49NTU for Sample A.

Table 6: Jar Test Table for only Sample D (t = 30 mins)

Vol. of water (ml)	400ml	400ml	400ml	Raw water
Alum dosage (ml)	3.0	2.5	2.0	pH – 7.0
Turbidity (NTU)	0.5	1.6	3.8	NTU–165

EFFICIENCY OF SAMPLE D

pH of Sample D = 2.95, pH of raw alum = 2.96

$$\text{Efficiency} = \frac{pH\ of\ sample\ D}{pH\ of\ Alum} \times 100 = \frac{2.95}{2.96} \times 100 = 99.6\%$$

Effectiveness of Sample D

Turbidity of Sample D = 0.5 NTU, Turbidity of raw alum = 0.49 NTU

$$\text{Effectiveness} = \frac{Turbidity\ of\ Raw\ Water}{Turbidity\ of\ sample\ D} \times 100 = \frac{0.5}{0.49} \times 100 = 98\%$$

CONCLUSION

The extraction of alum from the Ahamdu Bello University (A.B.U.) water treatment plant was successfully carried out. The result revealed that Sample D was the most effective due to the fact that, 3.0ml dosage of extracted alum was able to reduce the turbidity of the raw water to 0.5NTU, which satisfied World Health Organization (WHO) standards for treated water. In addition, 0.5NTU recorded by sample was closed to the turbidity of 0.49 NTU obtained using 0.3ml dosage for Sample A. Moreover, the Sample D recorded the efficiency of 99.6% of aluminum recovery, with the corresponding effective leached aluminum of 98%. On the other hand, Sample B and C recorded lowest turbidities of 105 NTU (46.1%) at 0.1ml and 56.1 NTU (71.2%) at 1.0 ml, respectively. It is therefore concluded that the alum was successfully recovered from the sludge of the A.B.U. treatment plant and the recovered alum was effective in turbidity removal.

REFERENCES

Azim, A. A., Abdel Halim, H. and Helmy, E. (2013). Comparison between Applying Acidification Method for Alum Recovery for Different Clarifier Type. Journal of Applied Sciences Research, 9 (8), 7723 – 4733.

Boaventura, R. A. R, Duarte, A. A. S. and Almeida, M. F. (2000). Aluminium Recovery from Water Treatment Slugde. IV International Conference, Water Supply and Water Quality, Poland, September, 11-13, 2000.

Cheng, W. P., Fu, C. H., Chen, P. H. and Yu, R, F. (2014). Factors Affecting Aluminium Dissolve from Acidified Water Purification Sludge. World Academy of Science, Engineering and Technology, International Journal of Chemical and Molecular Engineering, 8 (8), 878 – 881.

Hassan Basari, M. H., Mohammad Don, N. N., Kasmuri, N., Hamzah, N., Alias, S. and Azizan, F. A. (2019). Aluminium Recovery from Water Treatment Plant from Water Treatment Sludge under Different Dosage of Sulphuric Acid, Journal of Physics Conference Series.

Hamzah, N., Roshisham, M. A. F., Zakaria, M. F., Hassan Basari, M. H., Akbar, N. A. (2022). Performance of Recovered Coagulant from Water Treatment Sludge by Acidification Process. Environmental and Ecology Research, 10 (1), 21 – 30.

Joshi S. and Shrivastava K. (*2011*). Recovery of Alum Coagulant from Water Treatment Plant Sludge: A Greener Approach for Water Purification.

Keeley, J, Jarvis, P. and Judd, S. J. (2014). Coagulant Recovery from Water Treatment Residuals: A Review of Applicable Technologies. Critical Review in Environmental Science and Technology, 44 (24), 2675 – 2719.

Mirwan, A., Putra, M. D., Liu, J. C., Susianto, Altway, A., Handogo, R. (2020). Aluminiun Leaching from Water Treatment Sludge using Hdrochloric Acid and Kinetic Study. Environmental Science and Pollution Research, Springer Nature 2000.

Ramadan, H. and El Sayed, A. (2019). Optimization of Alum Recovery from Water Treatment Sludge-case study: Sammanoud Water Treatment Plant, Egypt. Water and Environment Journal.

Ruziqna, D. P., Suwartha, N., Moersidik, S. S. and Adityosulidro, S. (2020). Aluminium Recovery from Water Treatment Sludge as Coagulant by Acidification. IOP Conference Series, Earth and Environmental Sciences 448 (2020),

4th International Engineering Conference (IEC 2022)
Federal University of Technology, Minna, Nigeria

Smart Water Pump Control System with Remote Access for Improved Energy and Water Resource Management

*Onu, U. G.[1], Okekenwa, E.[1], Jack, K. E.[2], Inyang, A. B.[3], Bello, O. E.[2] & Adeniyi, S.[2]

[1] Department of Electrical/Electronic Engineering Technology,
Akanu Ibiam Federal Polytechnic Unwana, Afikp, Ebonyi State, Nigeria
[2] Department of Mechatronics Engineering, Federal University of Technology Minna,
Niger State, Nigeria
[3] Department of Electrical/Electronic Engineering Technology,
Akwa Ibom State Polytechnic Ikot Osurua, Ikot Ekpene, Akwa Ibom State, Nigeria
*Corresponding author email: uchmangod@gmail.com +2347030533059

ABSTRACT
Water has remained an essential natural resource. Man has explored various means of ensuring the sustainable supply of this important liquid. The use of electric pumps to supply underground water is a major means of water supply. Epileptic power supply in the country has resulted from many families leaving their water pumps ON while away during the day's work. The challenges posed by the cost of electric energy and losses in water resources are of concern. This research designed and deployed a smart water pump control system to ensure improved energy and water resource management. The remote access to the pump operation status through the GSM module helps the building residents to decide when to add other loads to the power system, in order to manage the installation capacity of the power supply system in the building thereby eliminating the need for high rated circuit breakers and cable sizes. This results in reduced cost of initial electrical installation and energy costs. The results obtained from the controlled deployment of the smart water control system showed that the system is capable of minimizing the cost of energy by 34.44%.

Keywords: *water resource, smart pump, energy management. remote access, control system*

1 INTRODUCTION

Water ranks high in the needs of life. Only about 0.3% of water in the world is safe for use. This suggests an eminent shortage of this important natural resource (Kılıç, 2020). Living things are basically constituted of water. Water provides the solution for most biological metabolism in living organisms. As a helpful liquid, water is used by man in most of his daily activities. These activities include but are not limited to cooking, washing, agriculture, and industrial applications. Though water has been taken so simply as a natural liquid, the human body is made of about two-thirds water, and man requires water to live(Chaplin, 2001). Human healthy living has been linked to the availability and use of clean and safe water. Preventive health care has a lot to do with the availability and use of clean water (Huck, 2018).

On the technological front, smart and intelligent pumping has been identified as sustainable means of combating global water shortages arising from population, environmental regulations, process limitations, and associated energy wastage. Smart water pumping is capable of reducing energy wasted in traditional methods of water processing and delivery by 25%(Ahmed, 2013). Islam and Amjad, 2018 opined that water as an essential natural resource should be used with minimal wastage. The research also identified uncontrolled use of water and associated wastage as the major cause of water scarcity. They suggested eliminating human efforts and errors in automation through the use of the Android Application. Politicians, managers, health officials, and others should know that implementing low-cost water supply technologies on a larger scale is a better cost-effective alternative to costlier major water infrastructure projects with the associated complex operation and management problems (Zhonga et al., 2013). (Zhonga et al., 2013) illustrated some innovative water technologies, such as using sunlight to purify water, and domestic use of ceramic water filters known to provide clean and bacteria-free water at a minimal cost of about US$ 3 per family per annum.

World energy demand has continued to rise unabated due to the increasing human population and the quest for industrialization. Effective energy management and its utilization were identified to be as important as the availability of energy for sustainable development (Awan, et al., 2014). The authors furtheremphasized that developing smart systems could be a veritable means of ensuring energy demand/supply match. They also stressed that an efficient energy management system is a practical business strategy for sustainable growth. This research is aimed at designing a smart water pump control system that will improve energy management. Available similar systems do not have a way of monitoring the level of water in the well, and as such there are higher possibilities of energy wastage when there is insufficient water in the well.

2 REVIEW OF RELATED LITERATURE

Smart technologies have found useful applications in various human and industrial activities. Water supply is not exempted from this all-embracing technology. Hasan, (2020), designed and implemented an automatic water pump controller and water level detector using a microcontroller. The researchers were able to implement their research at an experimental level. Though there was no effort to relate the operation of the system to the availability of water in the well. Ourwork seeks to bridge this missing link by getting feedback regarding the availability of water in the well in order to isolate other malfunctioning behavior of an underground water supply system. There was also no information regarding the energy management implications of the system in real-life applications. Our present study will endeavor to link thesystem operation with energy management benefits. Water wastage as a causative factor of water scarcity in Pakistan motivated (Jamal, 2016) to develop a logical automatic water control system for domestic applications. His proposed circuit used NE555 timer integrated circuit as a major logic component. The design was implemented at the experimental stage using light-emitting diodes (LEDs) to indicate water levels of 0%,30%,90%, and 100% in the water tank. There was no sufficient information concerning the practical application of the design.

Furthermore, Adil, (2018), proposed a flexible automatic water level controller and indicator to curb water wastage in homes. Thedesign was equipped with a selection switch allowing users to select a preset level to which water can be pumped by the system. They further stressed that the system could be improved upon through the use of Arduino and the internet of things (IoT). Our study will incorporate Arduino and IoT to improve the functionality andreliability of the system. (Okhaifoh, et al., 2016), realized a microcontroller-based water pumping machine using an ultrasonic sensor as a means of relating the water level in the tankto the controller.

Gonzalez, et al., (2016), worked on the automated water pump controller (AWPC). The system applied three water level sensors to monitor the water level in both the underground well and the overhead tank. The pump was madeto switch off as soon as the reservoir reached about 10% of full capacity. This was done with the aim of protecting the pump against unnecessary overwork. This research will build on this principle by conveying well water status as a control signal to avoid damaging the pump. Also, ultra-sonic sensors and Arduino controllers were applied by (Preethi, et al., 2015) to realize a prototype system that is capable of sensing water level and using the signal to trigger the water pump. Getu and Attia, (2016), designed a waterlevel sensor device capable of detecting and controlling the water level in a storage system. The system uses sequential logic implemented flip flops to initiate water pumping at a predetermined threshold and stops pumping when water reaches an upper preset limit.

As a result of the information available from the reviewed literature, this research seeks to bridge the observed research gap between the application of automatic water pumpingsystems and energy management. Energy management has come to stay as a tool for sustainable industrial and economic development. The study will attempt to relate smart water pumping systems with energy conservation considering the effect of increasing energy demand on the economy and availability of energy for other important applications. The research will also add the Internet of Things (IoT) to existing designs toguarantee remote access to the automated system.

3 MATERIALS AND METHODS

The research utilizes both hardware and software components to realize the design. The method explores the simulation and prototype approach.

3.1 MATERIALS

The design uses conductance sensing to measure water level. The sensor assembly consists of four aluminum wires mounted at 25%, 50%, 75%, and 100% volume levels in the tank. The opposite ends of these wires are connected to analog input pins A1, A2, A3, and A4 of the Arduino respectively. The bottom of the tank is mounted with a ground conductor for complete system circuitry. Resistors R4 to R7 are pull-down resistors. The dry ends of the sensor wires are connected to a +5V DC source in parallel with the analog input pins of the Arduino. When water touches a particular probe, an electrical connection is established between that probe and the +5V probe because water has slight conductivity. As a result, current flows through that probe and is converted into a proportional voltage by the pull-down resistor. Arduino reads the voltage drop across each pulldown resistor for the purpose of sensing the level of water in the tank. The same sensing method was used for measuring the level of water in the underground source well.

Digital pin 7 of the Arduino controls the buzzer, and digital pin 8 controls the motor. Transistor Q2 drives the buzzer and resistor R5 limits the base current of Q1. Transistor Q1 drives the relay that switches the pump. Resistor R2 limits the base current of Q2. D1 is a freewheeling diode that protects therelay coil due to the transients associated with inductive load. POT Rv1 is used to adjust the contrast of the liquid crystal display (LCD). resistor R1 biases Q1. Resistor R4 limits the current through the power ON LED. The GSM module facilitates remote access to the user.

3.2 METHODS

A simulation and prototype development approach was adopted. The circuit design was carried out in proteus software. Arduino Integrated Development Environment wasused to write the program codes. The

prototype was realized and deployed to obtain energy consumption data. Figure 1 shows the circuit design of the smart water pump control system with remote access.

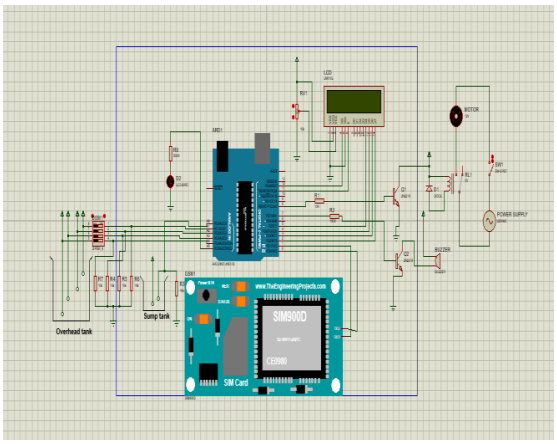

Figure 1: Circuit design of smart water pump control system withremote access

3.3 PROGRAM CODE

The design program code was written in Arduino IDE andassembled using a Proteus circuit design interface. A prototype design was implemented as shown in Figure 2. Thepower consumption of the prototype system was used to estimate the power consumption of a real-life deployment since the water pump used in the prototype is a typical 1.5Hpsingle-phase water pump, hence it was a matter of adjusting the volume and time components of the pump power consumption.

Figure 2: Prototype of smart water pump control systemwith remote access

4 RESULTS AND DISCUSSIONS

The energy consumption for a household with a smart waterpump control system and a household without a smart waterpump control system is analyzed in this research work. An active household with or without a smart water pump control system within 10 days of 120 hours of demonstration provides the records of energy consumption as documented. The remote access to the pump operation status through the GSMmodule helps the building residents to decide when to add other loads to the power system, in order to manage the installation capacity of the power supply system in the building thereby eliminating the need for high rated circuit breakers and cable sizes. Table 1 shows household energy consumption with a smart water pump control system, while Table shows the energy consumption for the same household.

Table 1: Household energy consumption record with smart water pump control system

	Lighting/Air conditioning and Refrigeration Load	**Water Pump**
Number of days	10	10
Power Rating (W)	1310	740
Duration (Hrs)	120	5.5
Total Energy Consumption (WHr)	**157200**	**4070**

From Table 1, the average Daily Energy Consumption with smart water pump control system = $\frac{57200+4070}{10}$ =16127 WHr.

Table 2: Household energy consumption record without smart water pump control system

	Lighting/Air conditioning and Refrigeration Load	**Water Pump**
Number of days	10	10
Power Rating (W)	1310	740
Duration (Hrs)	120	120
Total Energy Consumption (WHr)	**157200**	**88800**

From Table 2, the average Daily Energy Consumption without smart water pump control system = $\frac{157200+88800}{10}$ = 24600 WHr

Percentage energy saved with smart water pump control system = $(\frac{24600-16127}{24600}) \times 100 = 34.44\%$. The implication of this result is that a household that installed the smart waterpump control system would save 34.44% of the total energy they could have consumed without the system. This would have a spillover effect on the entire economy as more power would beavailable for other purposes. In addition, there will be guaranteed availability of water for use with minimal energy cost.

Figure 3 shows the energy consumption of the water pump and other household loads in the 10 ten days period with thesmart pump control system. It can be seen that the power consumption of the pump with the smart pump control system was reduced to 3 percent of the total energy consumed in the building.

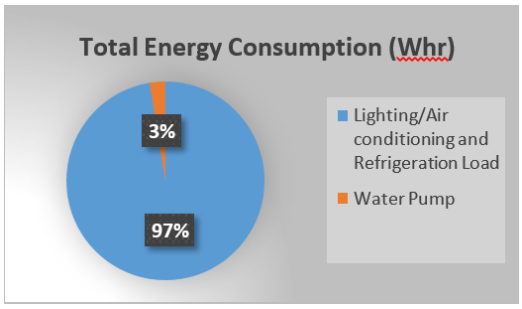

Figure 3: Energy consumption for a household with SmartPump Control System

On the other hand, Figure 4 shows the operation of the pump without the smart pump control system, and this resulted in an increase in the power consumption of the pump to the tune of 36 percent of the energy consumption of the building.

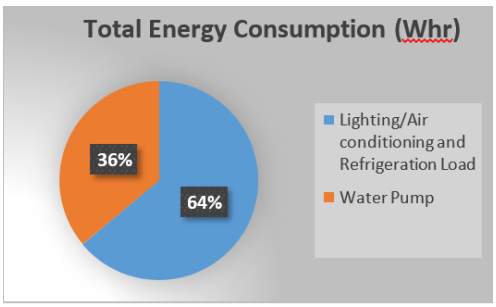

Figure 4: Energy consumption for a household without SmartPump Control System

5 CONCLUSION

The study designed and implemented a smart water pump control system with remote access for improved energy and water resource management. Results obtained from the deployment showed that the system is capable of saving up to34.44% of energy with the associated cost. The application ofthis system will reduce the power consumed in water pumping systems. It also ensures the uninterrupted availability of water for use. The saved power could be used for other useful ventures that require electricity. The remote access to the pump operation status through the GSM module helps the building residents to decide when to add other loads to the power system, in order to manage the installation capacity ofthe power supply system in the building thereby eliminating the need for high rated circuit breakers and cable sizes. This can effectively reduce the cost of initial electrical installations. Further research would explore the system's deployment in a larger setting like industry or community settlements.

REFERENCE

Adil, A. (2002). "Engineering Flexible AutomaticWater Level Controller and Indicator Location," 3(1), 2018.

Awan, U., Imran, N., and Munir, G. (2014). "Sustainable development through energy management: Issues andpriorities in energy savings," *Res. J. Appl. Sci. Eng. Technol.*, 7(2), 424–429, doi: 10.19026/rjaset.7.271

Chaplin, M. F. (2001). "Water: its importance to life," *Biochem. Mol. Biol. Educ.*, 29(2), 54–59, doi: 10.1111/j.1539-3429.2001.tb00070.x.

Electric, S. and Ahmed, H. (2013) "Smart Pumping: A New Way to Address the Worldwide Water Distribution Crisis."

Getu, B. N. and Attia, H. A. (2016). "Automatic water level sensor and controller system," 2016 5th International Conference on Electronic Devices, Systems and Applications (ICEDSA),1-4, doi: 10.1109/ICEDSA.2016.7818550.

Gonzalez A. D. S., and Russell, K. (2016). "Automatic Water Pump Controller," 44, 2016.

Hasan, M. M. (2020) "Automatic Water Pump Controller and Water Level Detector with Microcontroller IC," *Int. Res. J. Eng. Technol.*, 1(1) 5–8, , [Online]. Available: www.irjet.net.

Huck, S. W. (2018), "and Research,"

Islam, M. and Amjad, M. (2018). "Water Automation for Water Pump Controller using Android Application - Survey," *Int. J. Comput. Appl.*, 182 (29), 34–38, doi: 10.5120/ijca2018918165.

Jamal, H. (2016), "Logical Automatic Water Control System For Domestic Applications," 1(1), 159–162, doi: 10.15224/978-1-63248-109-240.

Kılıç, Z. (2020). "The importance of water and conscious use of water," *Int. J. Hydrol.*, 4(5), 239–241, doi: 10.15406/ijh.2020.04.00250

Okhaifoh, J., Igbinoba, C., and Eriaganoma, K. (2016). "Microcontroller Based Automatic Control for Water Pumping Machine With Water Level Indicators Using Ultrasonic Sensor," *Niger. J. Technol.*, 35(3), 579, doi: 10.4314/njt.v35i3.16.

Preethi, D., Anusha, J., Sravani, M. V., Puviarasi, R., and Bala, M. S., (2015). "Automatic water level controller," *Int. J. Appl. Eng. Res.*, 10(33) Special Issue, 26581–26587.

Zhonga, R., Weia, J., Sub, W., & Chen, Y. F. (2013). "Smart Water Solutions Netherlands Water Partnership". Mathematical and Computer Modelling 58 (2013) 733–742.

4th International Engineering Conference (IEC 2022)
Federal University of Technology, Minna, Nigeria

Performance Comparison of Data-driven Models (DDM) for Best Crump Weir Model Selection

*Sani Yakubu Khalifa[1], Babatunde Korode Adeogun[2],
Abubakar Ismail[3], Morufu Ajibola Ajibike[4], Muhammad Mujahid Muhammad[5]
[1,2,3,4,5]Department of Water Resources and Environmental Engineering
Ahmadu Bello University Zaria, Kaduna state, Nigeria.

*Corresponding author email:Khalees2k1@gmail.com +2348036782315

ABSTRACT
The flow characteristics changes with varying geometry of hydraulic weir and how the weir is inclined to the direction of flow in a channel. In this way, several studies have investigated the performance weirs experimental with paying much attention on the accurate prediction of discharge coefficient. Thus, the main objective of this study is to employ artificial intelligence (AI) techniques to predict discharge coefficient (C_d) of crump weir models. Hence, the precision and use of seven data-driven models including Bayesian neural network (BNN), multiple linear regression (MLR), multi-layer perceptron neural network (MLPNN), genetic algorithm (GA), support vector machine (SVM), Radial Basis Function (RBF) and curve fitting neural network (CFNN) were examined for estimating of the Cd. To achieve this, experiments were conducted on eighteen crump weir models of different apex angles 80°, 90° 100°, 110° 120° and 130°. The upstream angles of the weir models were set in decreasing order of 85°, 70°, 55°, 40°, 25° and 10°. While the downstream angles were increased as 15°, 20°, 25°, 30°, 35° and 40° respectively. 360 laboratory test results were used, 70% for training, 15% for testing and 15% for validation. And statistical parameters of coefficient of determination (R^2), root-mean-square error (RMSE), mean absolute error (MAE), were employed as the criteria for the comparison of the models' performance. Results showed good agreements between the observed and estimated values using the AI-based models. However, among these models, the CFNN managed to estimate the Cd of the weir with the highest precision and accuracy than the rest of the models with (RMSE=$0.1635x10^{-4}$, R^2=0.9981,). Also, it was found that the most efficient crump was weir model 17 for having the least C_d of 1.14914 and least percentage error of 12.97412, which has been optimized using GA with C_d value of 1.14815. 1. Depth of weir and width of channel in variable value are suggested to get the best flow rate for hydraulic structure of crump weir design. Calibration device for better data collection suggested using a volume meter to get the flow rate over a crump weir.

Keywords: *Artificial Intelligence, Channel, Crump Weir, Discharge Coefficient, Experiments,*

1.0 INTRODUCTION

The Crump section *flat-vee* weir is favored by hydrometrics because of the accuracy and range of flow measurement it exhibited. It is comparatively insensitive to submerged conditions and ease of determination of flow curves for any width, and its coefficient of discharges remain through undrown condition. However, this type of weir is disliked by fishermen because it can present a barrier to migration of fish Rickard *et.al*. (2003). As such it becomes necessary to investigate the behavior of the flow over the crump weir. In this way, few studies have been devoted to evaluating the flow over crump weirs, for example, Bos, (1989) was the first to study the flow characteristics of trapezoidal profile weirs systematically. He conducted a series of experiments on these types of weirs with both upstream and downstream side slopes. The discharge coefficient was determined for free flow conditions using different discharge values. Also, Al-Naely *et al.*, (2018) placed crump weirs in a channel as a control device in order to the flow rate, a new performance for the crump weirs was observed as a result of adding an opening holes in the model of crump weir. The opening holes act as energy dissipaters and improvers for the discharge coefficient (C_d), where higher values of the discharge coefficient (C_d) were recorded in comparison with conventional weir under the same laboratory conditions. In the same vein, the creation of an opening in a broad-crested weir was found to increase the discharge coefficient and consequently improving the discharge Daneshfaraz et al. (2019). Similarly, Khalifa & Umar, (2018) conducted experiments on crump weir

models of different apex angles, they demonstrated that increase in the apex angle resulted in decrease in discharge coefficient. Hence, controlling the amount of discharge over different hydraulic structures was always a field of interest for researchers, with a view of decreasing sedimentation in reservoirs Zahabi et al. (2018).

2.0 THEORETICAL BACKGROUND

2.1 Governing Equations

The discharge was estimated using the equation governing the modelling of flow over crump weir by determining the upstream flow head (h). Point gauge was used to measure the, h, above the crump weir Arora, (2005). Thus, for modular flow over the crump weir, when the weir operates undrowned, the modular discharge is expressed as follows:

$$Q_m = C_d\sqrt{g}\,.bH_o^{\frac{3}{2}}. \quad (1)$$

C_d and H_o can be determined using Equations (2) and (3) respectively

$$C_d=1.163\left(1-\frac{0.0003}{h}\right)^{1.5} \quad (2)$$

$$H_o = y_o + \frac{V_o^2}{2g} \quad (3)$$

Where, Q_m = Discharge for modular flow (m^3/s), C_d = Modular discharge coefficient, g = gravity (m^2/s), b = Breath of weir (m), H_o = Total head upstream of the weir crest (m), y_o = upstream water level (m), $\frac{V_o^2}{2g}$ = upstream velocity head (m).

However, for non-modular flow, when the weir operates drowned, a single measurement of upstream head is not sufficient to calculate the actual flow as the upstream head is affected by changes in the downstream head. In this case, a dimensionless reduction factor is introduced to correct the non-modular flow as given by Equation (4):

$$f=Q/Q_m \quad (4)$$

Where, Q = Discharge for non-modular flow (m^3/s)

2.2 Artificial Neural Networks

Artificial neural network (ANN) is a nonlinear mathematical model that is able to simulate arbitrarily complex nonlinear processes, which relate inputs and outputs of any system. In many complex mathematical problems that lead to solving complex nonlinear equations, multilayer perceptron networks are common types of ANN widely used by researchers Parsaie (2016); Moazamnia et al. (2019).

2.3 Support Vector Machines

Support vector machines operate based on data mining algorithms and are like other artificial intelligent methods. It was used in different fields of hydrology e.g., Nadiri et al. (2017) and Hydraulics e.g., Sadeghfam et al. (2019). Support vector machines are an efficient learning system based on the theory of optimization that uses the inductive principle of minimization of structural errors and lead to a general optimal response.

2.4 Multi-layer Perceptron Neural Network (MLPNN)

MLPNN is a computational method which tries to propose a mapping between input space (input layer) and optimal space (output layer) by understanding the inherent relationships among data with the help of learning process and using simple processors called neurons Heidari *et al.*, (2016). The high speed of processing and flexibility in the face of unwanted errors are the features of this model. Its main advantage is its high speed and optimal precision in the prediction of complex variables with linear and non-linear mapping.

The performance and precision of regression methods highly depend on the sample size, and sample size can limit statistical models Ghorbani et al, (2017).

Mohammad Zounemat *et al.*, (2019) have examined the precision and use of six data driven models including BNN, MLR, MLPNN, GEP, LSSVM and CHAID for estimation of discharge passing triangular Arced labyrinth weir. MLPNN managed to estimate the discharge passing the weir with the highest precision (RMSE = 0.00385, R^2 = 0.999).

Reza Norouzi *et al.*, (2019) have investigated the performance of MLP, RBF and SVM in predicting the discharge coefficient (Cd) of lybrinth weirs. The performance of the MLP model was excellent with RMSE and R^2 of 0.019 and 0.985 respectively.

In the studies of Zounemat *et al.*, (2019), they applied various hybrid meta-heuristic MLPNN and ANFIS for predicting flow parameters of piano key weir flow.

3.0 METHODOLOGY

3.1 Fabrication of the Experimental Models

The experimental work was conducted on eighteen crump weir models of different apex angles of 80°, 90° 100°, 110° 120° and 130°. Accordingly, the upstream angles of the models were decreased to have the following values 85°, 70°, 55°, 40°, 25° and 10° , and to as well increasing the downstream angles as 15°, 20°, 25°, 30°, 35° and 40° respectively, which will sum up to give 180° as the total angles in a triangle as shown in Figure 1. Plywood of 22 mm thickness was used in fabricating the main body of the crump weirs.

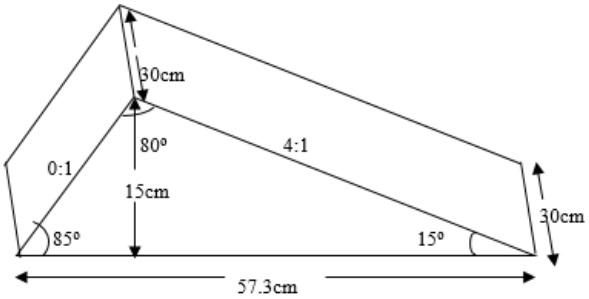

Figure 1: The schematic view of crump weir model 1 of apex angle 80°, upstream angle and slope, 85° and 0:1, downstream angle and slope, 15° and 4:1 respectively.

Table 1.0: Geometric Factors of Crump Weir Models

Model	Upstream Slope	Downstream Slope	Model width 'b' (cm)	Crest Height 'P' (cm)	Apex Angle (degree)	Upstream Angle(degree)	Downstream Angle(degree)
1	0.1:1	4:1	30	15	80	85	15
2	0.4:1	3:1	30	15	90	70	20
3	0.7:1	2:1	30	15	100	55	25
4	1:1	2:1	30	15	110	40	30
5	2:1	1:1	30	15	120	25	35
6	6:1	1:1	30	15	130	10	40

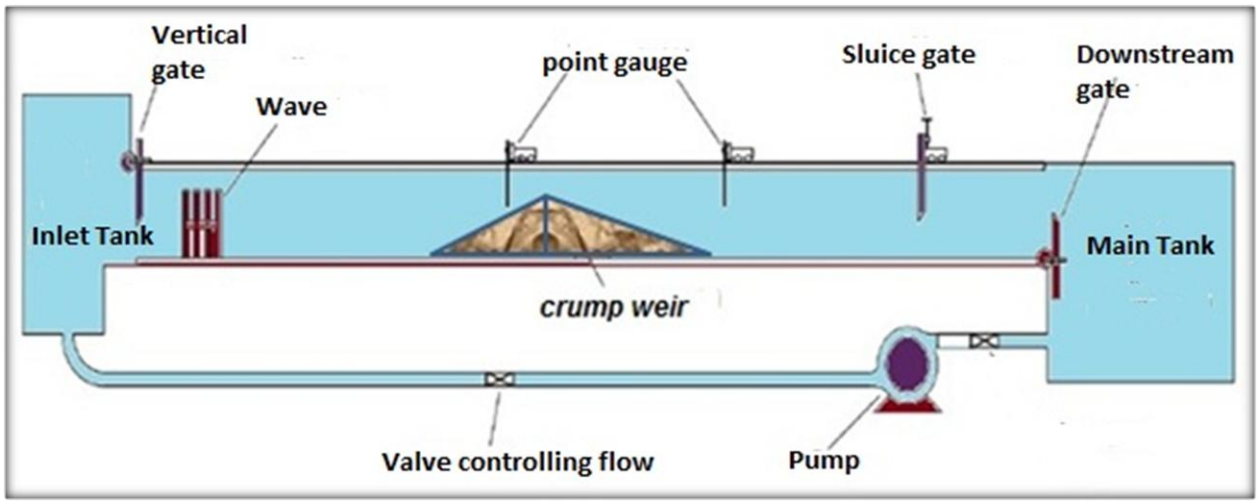

Figure 2: Sketch of Crump Weir Model and Experimental flume.

3.2 *Experimental Procedure:*

The crump weirs were installed in the flume with the help of sealants to prevent leakage, which has to be levelled. One vernier were located downstream the weir and the other upstream. The verniers were zeroed with the bed of the channel.

Seventy-two models were fabricated for which the angles were varied, 80°, 90°, 100°, 110°,120°, and 130°

Experiment were then ran for each model and various heads and their corresponding discharges were recorded; The procedure has five (5) runs. Each run has a different flow rate and a set of four (4) y_o and y_1 depths; two sets for modular flow condition and the other two sets for non-modular flow condition. The initial flow rate were set. Then, y_o and y_1 depths were recorded for the following conditions: Modular flow: without stop block (gate). Modular flow: one full stop block (gate) (y_1 should be the only depth that changes). Non-modular flow: Add a half of one stop block (gate). (y_1 and y_o depth that change). Non-modular flow: Add one quarter of a stop block (gate). The flow rate were increased at constant interval.

Heights (P=10cm, 15cm, 20cm) were used as a crump weir models. For each type of crump three types of surface roughness were used. The first one were a smooth PVC , the second one is coated with a uniform sand D_{50} =0.72 mm (D_{50}=is the sieve diameter in which 50% of material are finer), while the third is covered by gravel of D_{50}= 3.6 mm . Eighteen models were used to conduct the experimental study. In each run the selected model were inserted along the width of the flume. Then the pump started at desired flow rate and after the flow stability were achieved the water surface level upstream and above the weir model were measured using point gauge. For each type of the crump weir a series of tests under different flow rates were conducted. At the beginning of each run the control valve were adjusted to alter the head; For each head recorded, the actual discharge were measured by direct method using the weighing arrangement provided at the tail end of the flume. The previous steps were repeated for each of the five runs of experiments to be conducted for each model. A total of 360 runs were conducted.

3.3 Determination of Observed Discharge (Q_o)

The observed discharge, Q_o, was measured experimentally using the gravimetrical method. Throughout the experiment, 100kg of water were collected by means of the weighing balance (see plate II) attached to the flume and

stopwatch was used to obtain the time taken to collect the 100kg for onward determination of discharge.

Volume, V = mass/density

Observed discharge, Q_o = Volume / average time

3.4 Determination of Estimated Discharge (Q_e)

Average time = $\frac{(t_1+t_2)}{2}$ (5)

The discharge equation for the crump weir was used to compute the estimated discharge using the flow heads.

Point gauge will be used to measure the flow head (h) above the crump weir, Arora, (2005).

$$Q_m = C_d\sqrt{g}\,.bH_o^{\frac{3}{2}}. \quad (6)$$

$$C_d = 1.163\left(1-\frac{0.0003}{h}\right)^{1.5} \quad (7)$$

$$H = y + \frac{V^2}{2g} \quad (8)$$

3.6 Derivation of Discharge Coefficient

In order to validate the suitability of the theoretical equations, the maximum of the absolute value of the deviation of the data from the model was obtained as:

$$\text{MaxErr} = \max\left(abs(C_{do} - C_{de})\right) \quad (9)$$

Where,

C_{do} = Experimental Discharge Coefficient = Q_o / Q_e

C_{de} = Estimated Discharge Coefficient

$$Cd = (D_{50}, P, h, Q, \theta) \quad (10)$$

Thus, by dimensional analysis and using the approach of Buckingham's π-theorem, Equation (10) becomes:

$$Cd = f\left(\frac{D_{50}}{P}\theta, \frac{h}{P}\right) \quad (11)$$

It follows that Equation (11) can be expressed as Equation (12) based on dimensional homogeneity:

$$C_d = k_1\left[\frac{D_{50}\theta}{P}\right]^a + k_2\left[\frac{h}{P}\right]^b \quad (12)$$

Where, K_1, K_2, a, and b are parameters to be estimated by regression analysis.

4.0 RESULTS AND DISCUSSION

4.1 Computation of Discharge Coefficients (C_d)

Tables 2 show the values of C_d obtained from Equations 1 and 2 respectively. The head measurements were obtained by means of the point gauge.

i. Table 2: Discharge characteristics for model 1:

Q_o=V/t/m3/s	y_o/m	ho=yo - 0.10/m	y_1/m	H_O/m	H_1/m	Cd	Q_e/m^3/s	% Error
0.001515	0.120	0.020	0.060	0.121	0.065	1.13693	0.00133	12.04391
0.001563	0.160	0.060	0.110	0.175	0.115	1.15429	0.00135	13.36654
0.001613	0.194	0.094	0.135	0.210	0.140	1.15744	0.00139	13.60220
0.001667	0.210	0.110	0.130	0.228	0.150	1.15825	0.00144	13.66252
0.001724	0.218	0.118	0.100	0.235	0.160	1.15857	0.00149	13.68652
Average						1.15310	0.001400	13.27234

Table 3 : Summary of the statistical analysis of Cd predicted by MLP using different neurons.

	Training	Validation	Testing

No of neurons	MSEx(10^{-6})	R^2	MSEx(10^{-6})	R^2	MSEx(10^{-6})	R^2
1	9.0141	0.9123	7.5607	0.9152	4.5334	0.9613
2	5.0244	0.9392	5.8012	0.9301	23.735	0.8881
3	8.6095	0.9116	6.2662	0.9356	6.7934	0.9419
4	7.5581	0.9154	7.8690	0.9376	7.0532	0.9386
5	8.1319	0.9172	7.4021	0.9139	25.307	0.8497
6	7.7184	0.9283	6.2652	0.9111	7.1875	0.9115
7	1.9925	0.7902	2.4047	0.6565	17.668	0.8180
8	9.0060	0.8856	5.1653	0.7087	16.042	0.8045
9	8.1825	0.9234	7.0573	0.9161	1.8738	0.9821
10	8.1417	0.9251	4.6387	0.9309	6.2766	0.9290
11	1.0583	0.9090	3.7310	0.9579	7.0051	0.9331
12	4.3199	0.9458	2.1757	0.8691	7.2633	0.9435
13	7.8978	0.9175	6.1824	0.9432	6.5836	0.9363
14	9.4249	0.9035	8.5379	0.9214	6.3073	0.9325
15	4.7196	0.9475	4.2265	0.9404	23.272	0.8592
16	9.1488	0.9180	5.5131	0.8933	8.6496	0.9166
17	7.7760	0.9240	8.3009	0.9161	5.6503	0.9328
18	3.9774	0.9525	2.2298	0.8719	189.13	0.5615
19	8.3764	0.9227	7.4020	0.9137	0.9750	0.8849
20	1.0319	0.9037	6.4052	0.9190	7.6421	0.9132

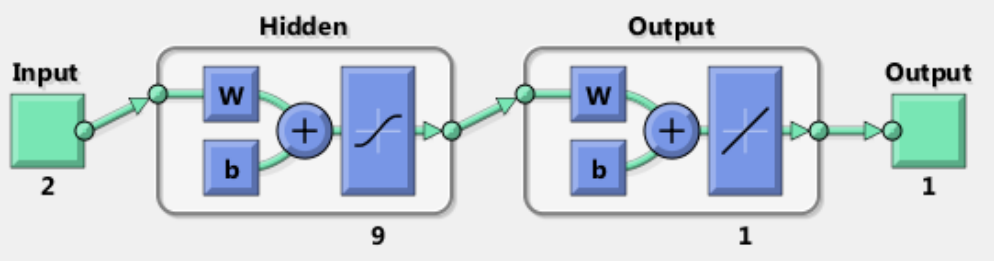

Figure 3: MLP Levenberg Marquardt Neural Network Diagram

4.2 Discussion of Result:

Predicting the Cd of crump weir using ANN

Results of evaluating the precision of the data-driven models in the estimation of Cd of crump weirs in the training and testing sets are presented in Tables 4 and 5 respectively. Comparison of the values provided in Table 5 shows that CFNN managed to estimate discharge passing the weir with the highest accuracy (RMSE= 0.1635×10^{-6} MAE=0.4713×10^{-3} R^2 =0.9981). Also, CFNN was followed by MLPNN, BNN, GA, MLR, RBF and SVM.

Eqs. (16) Demonstrate the extracted relationships between independent and dependent variables in the CFNN model. Scatter plots presented in Figs. 14 and 15 show the results of BNN and MLPNN respectively indicating their good precision in estimating the performance of the crump weir. In this study, the precision of seven data-driven models was evaluated for the estimation of Cd for crump weir. Final results showed that CFNN could estimate the discharge passing the weir with the highest precision. Also, due to the effect of input parameters of the model on the estimation accuracy, CFNN precision was evaluated using the various combination of the input parameters.2 different independent variables were used for constructing the applied models. In order to investigate the importance of each variable in the final performance of the models.

Consequently, the parameter ($\frac{h}{P}$) was found to be the most effective parameter with R =0.9971, MSE = 3.8513×10^{-4} on

the prediction of Cd. While the function ($\frac{D_{50}\theta}{P}$) was found to be the least effective parameter on the prediction of Cd.

Table 4. Results of evaluating the performance of data driven models in the training phase.

Models	MSE $\times(10^{-6})$	MAE $\times(10^{-3})$	R^2
MLP	8.1825	0.9874	0.9234
BNN	7.9003	0.8452	0.9192
RBF	2897.6	1.7652	0.8400
SVM	4232.7	2.6745	0.7300

Table 5. Results of evaluating the performance of all the applied models in the testing phase.

Models	MSE $\times(10^{-6})$	MAE $\times(10^{-3})$	R^2
CFNN	0.1635	0.4713	0.9981
MLP	1.8738	0.6704	0.9821
BNN	3.4682	0.7461	0.9669
GA	3.9641	0.8452	0.9573
MLR	2611.7	1.4233	0.8700
RBF	2672.6	1.5712	0.8600
SVM	3288.7	2.1005	0.7900

Finally, the precision of the models in estimating the discharge passing the weir was evaluated using the root-mean square error (RMSE), mean absolute percentage error (MAE), R^2 (coefficient of determination). The best values of these criteria were 0, 0, and 1 respectively.

$$\boldsymbol{RMSE} = \sqrt{\frac{1}{n}\sum_{j=1}^{n}(y_j - \hat{y}_j)^2} \quad \textbf{(13)}$$

$$\boldsymbol{MAE} = \frac{1}{n}\sum_{j=1}^{n}|y_j - \hat{y}_j| \quad \textbf{(14)}$$

$$\hat{R}^2 = 1 - \frac{\sum_{i=1}^{n}(Y_i - \hat{Y}_i)^2}{\sum_{i=1}^{n}(Y_i - \bar{Y})^2} = 1 - \frac{\frac{1}{n}\sum_{i=1}^{n}(Y_i - \hat{Y}_i)^2}{\frac{1}{n}\sum_{i=1}^{n}(Y_i - \bar{Y})^2} \quad \textbf{(15)}$$

In Eqs. (13)–(15), y is the actual Cd, $\hat{y}$ is their average, n is the number of estimations.

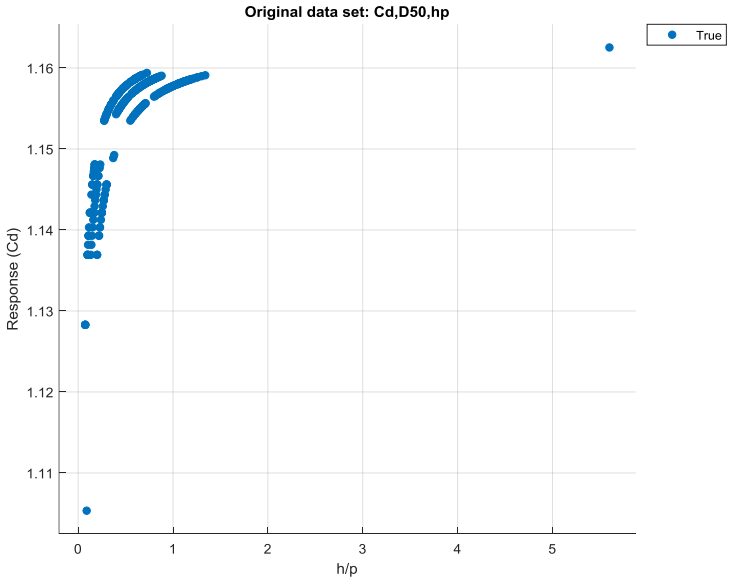

Figure 4: Relation of Cd and h/p using (MLR) model

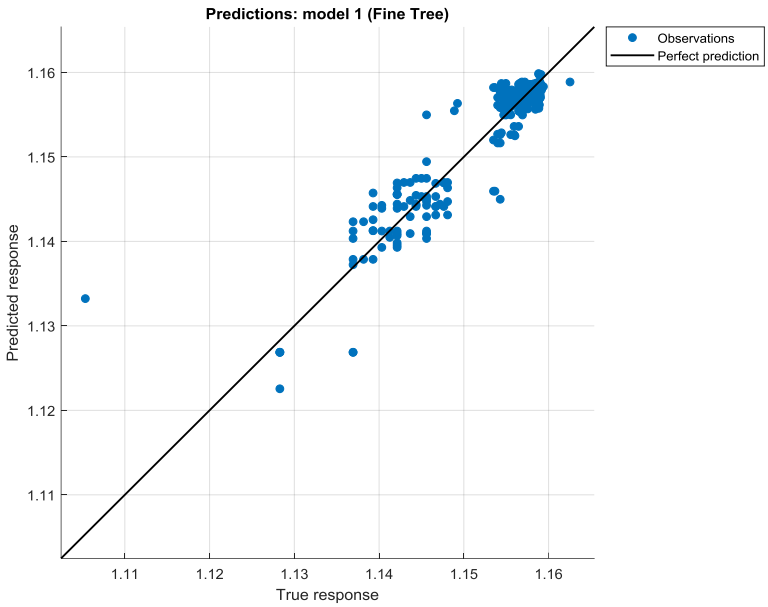

Figure 5: Relation of Cd predicted and Actual value using (MLR) model

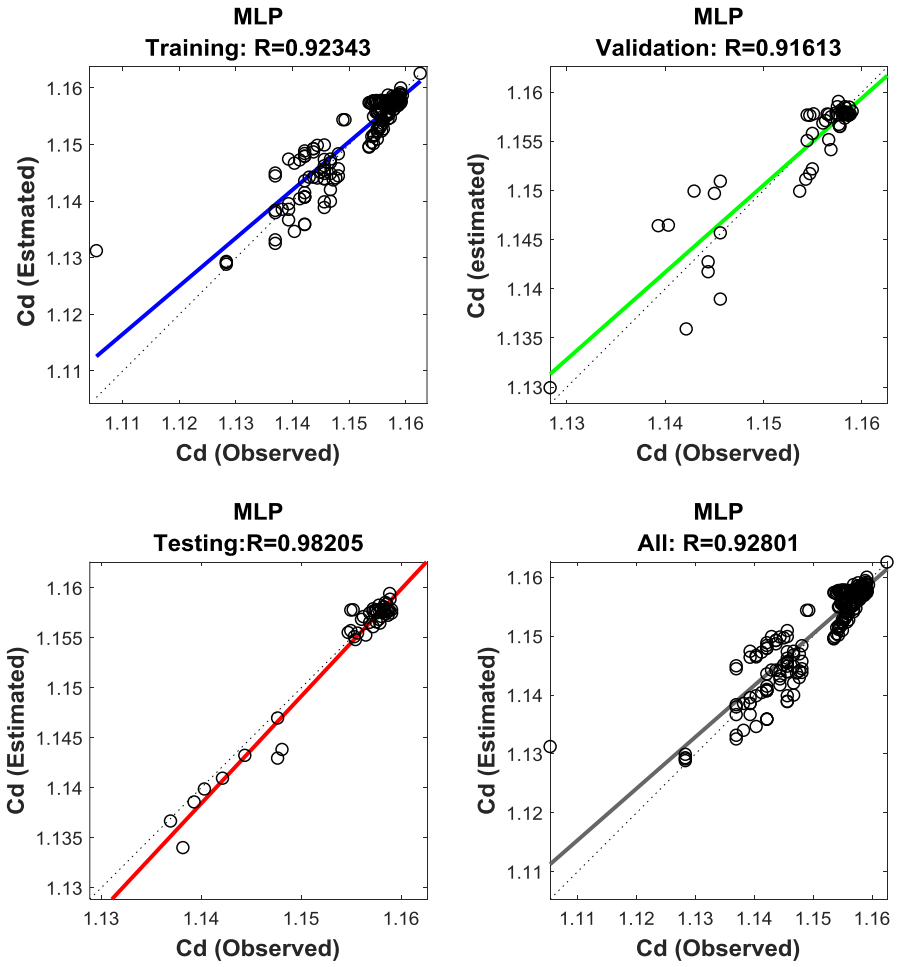

Figure 6: Distribution diagram of the observational-computational values in training and testing stages of MLP model

Thus, the parameters K_1, K_2, a and b in Equation (12) were determined through regression analysis and Curve Fitting Neural Network as expressed by Equation (16) as follows:

$$Cd = 0.5785\left[\frac{D_{50}\theta}{P}\right]^{6.593\times10^{-5}} + 0.58\left[\frac{h}{P}\right]^{0.006761} \quad (16)$$

The model equation has $R^2 = 0.9981$.

Table 6. Sensitivity analysis of Cd's for input parameters with ANN model.

Function	Training		Testing	
	MSE $\times(10^{-4})$	R^2	MSE $\times(10^{-4})$	R^2
$Cd = \left[\frac{D_{50}\theta}{P}\right]$	7.5421	0.9782	7.6801	0.9884
$Cd = \left[\frac{h}{P}\right]$	3.7313	0.9841	3.8513	0.9971
$Cd = \left(\frac{D_{50}}{P}\theta, \frac{h}{P}\right)$	0.1534	0.9883	0.1635	0.9981

Table 6 shows the sensitivity analysis of Coefficient of discharge, Cd. The sensitivity analysis was carried, in order to evaluate the significance of input variables on the Coefficient of discharge. The sensitivity analysis was performed using the ANN model due to the high value of correlation coefficient and minimum error it produced.

Consequently, the parameter $(\frac{h}{P})$ was found to be the most effective parameter with R = 0.9971, MSE = 3.8513×10^{-4} on the prediction of Cd. While the function $(\frac{D_{50}\theta}{P})$ was found to be the least effective parameter on the prediction of Cd.

5.0 CONCLUSION

By using the equations which has been discussed in the literature, the raw data was calculated and processed using ANN.

Based on the results of the investigation, the following conclusions are reached:

1. The effect of h/P on Cd values increases with the increase in weir height. .
2. The effect of increase of surface roughness on h values will be more on small heights of the crump weir than large ones.
3. C_d decreases from model 1 to model 18 with model 17 having the least C_d close to unity and least percentage error making model 17 to be more efficient.
4. The Mathematical Model equation generated using CFNN performed better than other models such as MLP, BNN, GA, MLR, RBF and SVM with RMSE= 0.1635×10^{-6} MAE=0.4713×10^{-3} R^2 =0.9981
5. The model was optimised using GA and the predicted Cd value was 1.14815 as best fitted value.

5.1 RECOMMENDATIONS

The recommendations below are some of the improvements that can be carried out for further study:

1. Calibration device for better data collection suggested using a volume meter to get the flow rate over a crump weir.
2. Similar study should be carried out using stones and cement models instead of wooden models.
3. Depth of weir and width of channel in variable value are suggested to get the best flow rate for hydraulic structure of crump weir design.

REFERENCES:

Arora K. R. (2005). *Fluid mechanics and hydraulic machines.* Standard publishers Distributors, 1705-B Nai Sarak, Post Box No.: 1066, Delhi-110006.

Al-Naely, H., Al-Khafaji, Z., & Khassaf, S. (2018). Effect of Opening Holes on the Hydraulic Performance for Crump Weir. *International Journal of Engineering*, *31*(12), 2022-2027.

Bos, M.G. (1989). *Discharge measurement structures.* International Institute for Land Reclamation and Improvement (ILRI), publication 20, Wageningen, The Netherlands.

Daneshfaraz R, Minaei O, Abraham J, Dadashi S, Ghaderi A (2019) 3-D Numerical simulation of water flow over a broad-crested weir with openings. ISH J Hydraul Eng. https ://doi.org/10.1080/09715 010.2019.15810 98

Ghorbani, M. A., & DEHGHANI, R. (2017). Comparison of Bayesian neural networks and artificial neural network to estimate suspended sediments in the rivers (case study: Simineh rood).

Khalifa, S. Y., & Umar, A. (2018). Evaluation of Unsteady Open Channel Flow Characteristics over Crump Weir. *ATBU Journal of Science, Technology and Education*, *6*(4), 306-315.

Moazamnia M, Hassanzadeh Y, Nadiri AA, Khatibi R, Sadeghfam S (2019) Formulating a strategy to combine artificial intelligence models using Bayesian model averaging to study a distressed aquifer with sparse data availability. J Hydrol 571:765–781

Muhammad, M. M., Yusof, K. W., Mustafa, M. R. U., Zakaria, N. A., & Ab Ghani, A. (2018). Prediction models for flow resistance in flexible vegetated channels. *International journal of river basin management*, *16*(4), 427-437.

Nadiri AA, Sedghi Z, Khatibi R, Sadeghfam S (2018)Mapping specific vulnerability of multiple confined and unconfined aquifers by using artificial intelligence to learn from multiple DRASTIC frameworks. J Environ Manage 227:415–428

Piratheepan M., Winston N.E.F., and Pathirana K.P.P. (2006), Discharge measurements in open channels using compound sharp-crested weirs. *Journal of the Institution of Engineers, Sri Lanka Vol. xxxx, No. 03, pp.31-38.*

Rickard C.,Day R.,Purseglove J., 2003," River Weirs – Good Practice Guide", Environment Agency, Rio House, Waterside Drive, Aztec West, Almondsbury, Bristol, BS32 4UD,.

Sadeghfam S, Daneshfaraz R, Khatibi R, Minaei O (2019) Experimental studies on scour of supercritical flow jets in upstream of screens and modelling scouring dimensions using artificial intelligence to combine multiple models (AIMM). J Hydroinform.https://doi.org/10.2166/hydro .2019.076

Zahabi H, Torabi M, Alamatian E, Bahiraei M, Goodarzi M (2018) Effects of geometry and hydraulic characteristics of shallow reservoirs on sediment entrapment. Water 10(12):1725 Zhou Q, Zhou H,

Zounemat-Kermani, M., & Mahdavi-Meymand, A. (2019). Hybrid meta-heuristics artificial intelligence models in simulating discharge passing the piano key weirs. *Journal of Hydrology*, *569*, 12-21.

4th International Engineering Conference (IEC 2023)
Federal University of Technology, Minna, Nigeria

Pastoralist Optimization Algorithm Approach For Improved Customer Churn Prediction in the Telecom Industry.

* Samuel, A. I[1], David, M[1], Salihu, B. A[1], Usman, A. U[1] & Abdullahi, I. M[2]

[1] Department of Telecommunication Engineering, Federal University of Technology, Minna, Niger State, Nigeria

[2] Department of Computer Engineering, Federal University of Technology, Minna, Niger State, Nigeria

*remmiest@gmail.com +2347032639739

ABSTRACT

In recent times, Telecom Industry customer churn has been a serious problem making it difficult to survive in the fierce competition of the industry. Survival in the industry and retention of the existing customers has become very important. Practitioners and academicians are now faced with the challenge of getting to predict likely customer churn, through predictive modeling techniques to predict potential customers who are likely to churn. Customer churn affects the revenue of the company because it cost more to acquire new customer than retaining old ones. When a company allocates its dedicated resources to retain these customers, it greatly controls the rate at which dissatisfied customers leave the company. Several techniques have been studied and we present an overview of resent works on churn prediction .Our work uses Artificial Neural Network approach for prediction of customers intending to switch over to other operators. This study uses Pastoralist Optimization Algorithm (POA) to enhance the Artificial Neural Network (ANN) by working on multiple attributes from Telecom Company's dataset with sample results. The results obtained showed that the proposed POA algorithm selected fewer attributes of ten out of fifteen for the telecom churn prediction and had a prediction accuracy of 97.0% compared to the ordinary unenhanced ANN which used the entire 15 attributes but had a prediction accuracy of 93.6%

Keywords: ANN; churn management, Neural Network, Pastoralist, prediction;

1 INTRODUCTION

In today's technologically advanced and congested marketplaces, Customers may more easily compare options and select the best one from a large number of service providers. So, businesses must not only win clients' first favor but also keep them once they have them by retaining their current clientele. In the context of the telecom sector, "churn" is the proportion of subscribers who switch from one service provider or another within a certain period of time. All industries suffer with "Churn" (Plaksij, 2022). Companies therefore need to work very hard to survive in the competitive market by generating new policies and strategies for acquiring new customers. Most organizations today like Satellite TV, telephone and internet providers heavily rely on keeping their existing customer base because it generate more income to the companies (Sandhya, 2021). Churn is a major problem for many businesses since it reveals how successful they are at retaining consumers. If companies lose their customers it can affect its finance and revenue. Businesses lose $1.6 trillion annually as a result of client attrition. (Plaksij, 2022).

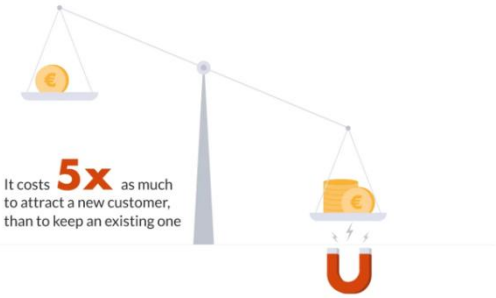

Figure 1: Illustration from Forrester showing cost of attracting a new customer Plaksij (2022).

Figure 1 above isan illustration by the Forrester study demonstrating that acquiring new consumers is 5 times more expensive than retaining existing ones.. It has been demonstrated that a company's revenue increases with the number of clients it keeps. Referencing a study from the Harvard Business School that states that, on average, a 5% improvement in customer retention rates leads to a 25%–95% boost in earnings. Also, 65% of a business's revenue comes from existing clients. According to the research, keeping current customers happy is just as crucial as finding new ones, if not more so. After several studies it can be stated that Several factors influence

customer churn in Telecom industry, some of which are; network coverage, tariff, voice quality, customer service, innovation e.t.c. Some of these factors are summarized in Figure 2.

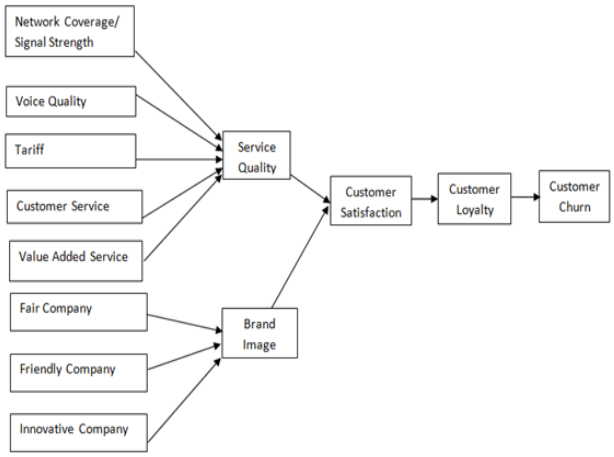

Figure 2: Factors influencing customer churn in Telecom industry Mahajan *et al.* (2017)

The figure 2 above shows the different factors affecting customer churn in telecom industry ranging from network coverage to voice quality, tariff, customer service, value added service which can all be categorized into service quality. Other factors include fairness, friendliness and innovation which are also broadly categorized as brand image. It also shows that a combination of service quality and brand image determines customer satisfaction. Customer satisfaction determines customer loyalty and customer loyalty determines customer churn.

Therefore,spending a lot of money on marketing and cam paigns to draw in new customers is not as profitable as co ncentrating on longterm relationships and tracking custom er behavior. Churn control is crucial since it has an impact on the profitability of a business. Additionally, the more you grasp your customer and their conduct, the more you'll comprehend the predicted revenue in the future. According to Marketing Metrics, the likelihood of selling to an existing customer is 60–70%, while the likelihood of selling to a new prospect is only 2-5%. So, it seems sensible that top priority should be given to lowering the rate of client attrition because keeping existing customers is profitable! But too many companies don't understand this and continue to struggle to implement a successful churn prevention tactics. It has become important for academicians and Telecom industries through predictive modeling techniques, to help policy makers come up with successful churn prevention or customer retention strategies for profit maximization

The remaining aspect of this paper is section as follows: s***ection 2*** provides a few reviewed literatures, An overview of the approach is provided in ***Section 3***, the results are presented and discussed in ***Section 4***, and the conclusion is made in ***Section 5***.

2. LITERATURE REVIEW

The challenge of predicting customer churn in the telecom industry has been addressed using a variety of techniques. The majority of this field's research focuses on using various Machine Learning algorithms to create predictions and compare the outcomes subsequently. While some academics have gone as far as to create fresh algorithms to apply to this problem, others use current methods with improved parameter tweaking. Below are some of the existing predictive models as used by various authors:

In (Ngurah *et al.*, 2020). IBM customer dataset, which comprised 7040 rows and 21 fields, Deep Neural Network (DNN), Random Forest, and Extreme Gradient Boosting (XGBoost) techniques were proposed to address the issue of customer churn. The DNN model's structure is given, and it is compared to previously researched methods like Random Forest and Extreme Gradient Boosting (XGboost). It was discovered that although techniques like Random Forest and XGBoost had processing times of 529 seconds and 175 seconds, respectively, and accuracy of 77.87% and 76.45%, respectively, the suggested DNN model had a perdiction accuracy of 80.62%. In (Ahmad *et al.*, 2019). A study on the prediction of customer churn was carried out utilizing the Spark environment to create and test models using data from SyriaTel Telecom. In their work, they discussed how to prepare features for machine learning algorithms through feature engineering, feature transformation, and a selective method. The four tree-based algorithms used were the XGBoost method, Gradient Boosted Machine Tree (GBM), Random Forest, and Decision Tree. With an AUC score of 93.301%, the XGBoost model outperformed the others, followed by the GBM algorithm in second place, Random Forest in third place, and Decision Tree in fourth place. The authors discovered that applying Social Network Analysis elements improved their ability to forecast churn in the telecom industry. In (Gaur and Dubey, 2018). The researchers applied a variety of classification methods, including Logistic Regression, Support Vector Machines (SVM), Random Forest, and Gradient Boosted Tree, and then compared the results. The authors conducted a study of prior research, and they have included flowcharts for the Churn Prediction Framework and Analysis Stages in addition to information on the steps involved in developing the model. Gradient Boosting outperformed

the other three models in the study, while the results from Logistic Regression and Random Forest were around average. SVM fared the worst. To assess the accuracy of their model, they employed the AUC (Area under the ROC Curve) statistic. In (Ullah *et al*., 2019). Research was conducted with the aim of resolving the issue of predicting customer attrition. The dataset underwent feature selection and noise removal during preprocessing. An 88% accuracy rate for machine learning algorithms like Random Forest was gotton. By highlighting the key dataset variables that are utilized to forecast customer churn, clustering techniques like K-Means have been applied. The "receiving operating characteristics" (ROC) area was used, along with metrics including accuracy, precision, recall, and f-measure. Using the RF method and customer profiling by K-means clustering, the findings demonstrated that their suggested churn prediction algorithm achieved better churn categorization. In (Idris *et al*., 2012). The problem of customer attrition was modelled using a Genetic Programming (GP)-based technique. Individual classifiers were thought to perform worse than an ensemble approach. Random Forest ensemble would be problematic because their dataset is unbalanced and contains fewer instances of the minority class. The flexibility and unique properties provided by GP, however, make it more ideal for categorization and subsequently churn prediction. Adaboost, on the other hand, is a boosting strategy that combines several weak classifiers to produce a powerful one. The "Orange Telecom" dataset and the "Cell2Cell" dataset were used in this instance. Here, the performance of the predictors is assessed using the area under the curve (AUC), sensitivity, and specificity metrics. On the Cell2Cell dataset, the highest churn prediction accuracy of 89% AUC is reported. In (Joolfoo and Jugumauth, 2020). A hybrid approach for predicting telecom churn, ANNs (Artificial Neural Networks) and KNNs (K-Nearest Neighbors) were employed. A comparison of earlier works has been made, and several prior methodologies have been reviewed. This research covered a total of 15 papers between 2014 and 2020. using the use of Artificial Neural Networks and the KNN machine learning model, they have attempted to develop an innovative and hybrid technique. The suggested performance indicator for this model was accuracy.

In (Abrandusoiu *et al*., 2016). The authors applied advanced data mining methodology for churn prediction using a dataset of 3333 customer call details with 21 attributes and a yes/no as a dependent parameter. The customer dataset includes information on incoming, outgoing, and voicemail calls. We saw that the author had combined Bayes Network, Support Vector Machine, and Neural Network with PCA (principal component analysis) to determine the algorithm's performance, the accuracy of the Bayes Network, neural network, and support vector machine utilized by the author was 99.10%, 99.55%, and 99.70%, respectively. In (Khan *et al*., 2015). The issue of predicting client attrition was investigated in big data platforms. Their objective was to demonstrate how big data significantly improves the process of churn prediction based on the amount, diversity, and velocity of the data. China's largest telecoms firm needed a big data platform to engineer the fissures in the data coming from the Operation Support department and the Business Support department. They applied the Random Forest algorithm and utilized AUC to assess its performance. There were 5 million active consumers at one point, and the algorithm was able to produce a draft of prepaid customers who will cancel their subscriptions in the following month with an accuracy of 0.96 for the top 50,000 customers. In (Mohanty and Rani, 2015). A work titled "Behavioral Modeling for Churn Prediction," was presented and researchers looked at the early signs of churn and created a churn score so that businesses could identify clients who were going to discontinue services. The authors moved closer to feature engineering using brute force, which might result in a significant number of features from customer data, including calls and logs, that are overlapping with one another, then determines the characteristics and indicators that are most predictive of customer attrition using two related methodologies. Features are fed into a number of supervised learning algorithms in order to forecast subscriber attrition. The method was tested using terabytes of data from a South Asian mobile phone operator, in 83.9% of cases, the authors' prediction was accurate when they classified subscribers who were idle on more than 76 percent of days during the training period as churners. As 76.6% of their sample did not churn, they had an unbalanced sample; therefore, a very simple model that just predicted the majority class (indicating "not churn") for all customers would achieve 76.6% accuracy. This simple linear discriminant performs well in this situation. They achieved accuracy rates of approximately 88.5-89.5% depending on the method employed to anticipate churn. Although utilizing a single method to forecast Churn can yield positive results, it is frequently seen that using numerous or a combination of these algorithms is the key to achieving excellent outcomes.

In (Höppner *et al*., 2020). A decision tree was utilized, and he claimed that in a benchmark analysis utilizing actual data from different telecommunication service providers, ProfTree outperforms more conventional accuracy-driven tree-based approaches. The evolutionary algorithm (EA) training times for this technique are slower than those for other classification algorithms. In (Hu *et al.*, 2020). Decision tree, a neural network, and a combination of the two were employed in a study on the prediction of customer turnover. After preprocessing, a total of 2681 entries from a supermarket's customer database between June 2018 and April 2019 were used. The decision tree model's prediction accuracy was

93.47%, while the neural network model's prediction accuracy was 96.42%. The combined model accuracy was found to be 98.87% after removing 21 customers whose churn probability is between 0.4 to 0.5. It shows that high accuracy is difficult to achieve by a single technique.

In Summary, most of the technique presented in the literature either single or hybrid techniques for customer churn prediction all tried to solving the problem of customer churn by proposing predictive models giving relatively high accuracy but none of the papers talked about finding the most important attributes within the dataset. In contrast, this paper contributes to the literature from different perspectives. It focused on finding the most important attributes from a given dataset, what to look out for in a customer and using these attributes to make churn prediction with very high accuracy. Pastoralist Optimization Algorithm used in this work was developed by (Abdullahi *et al*., 2018) The pastoralists' herding techniques served as inspiration for the algorithm. Scouting, camp selection, camping, herd splitting, and merging are the strategies. The POA was created using mathematical models of these tactics. 10 unimodal and multimodal test benchmark functions were used to test the algorithm's performance. This is done to evaluate the algorithm's exploratory, exploitative, convergence, and escape from a local optimum solution capabilities. In order to determine the statistical significance level of the algorithm outcomes, a nonparametric statistical test (Wilcoxon rank sum tests) was also performed. The experimental findings produced with the method demonstrate that the algorithm outperformed some state-of-the-art, nature-inspired metaheuristic optimization algorithms in the majority of circumstances.

3. METHODOLOGY

This section introduces the ideas and context used as well as the technical advances made by this article. This phenomenon involved processing starting with attribute selection and ending with categorization or prediction. Effective categorization or prediction must meet three key conditions. They include having access to a lot of data to train the model, having a powerful enough machine, and using an advanced algorithm to speed up and improve the process.

3.1 DATASET DESCRIPTION

Each sample or row of data, representing a client and containing attributes for 15 columns, totaled 3150. Call failures, SMS frequency, number of complaints, number of unique calls, subscription term, age group, fee amount, service type, usage duration in seconds, status, and SMS frequency are the attributes included in this dataset. The dataset underwent feature selection and noise removal during preprocessing. The ANN is trained using the back-propagation learning algorithm, and synaptic weights were modified using gradient descent to reduce error using the transformation function. In the training mode, extra care was taken to avoid overtraining the model and to keep error levels as low as feasible. All of the covariates were normalized with values between 0 and 1 prior to the start of training. The dataset is partitioned into two sets at random: Test set 945 customers and train set 2205 customers, respectively, make up 30% and 70% of the total dataset, respectively.

3.2 MODEL DESCRIPTION

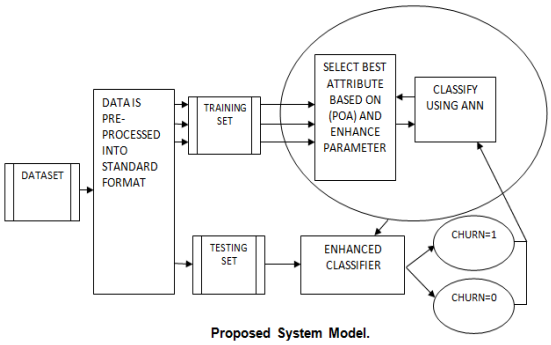

Figure 3: System Model.

In the model shown in Figure 3 above, the POA attribute selector initializes all its parameters and selects the scout pastoralists randomly, the scout location is initialized and the fitness of each scout is evaluated and the location is updated. The scouts location within the search space are also normalized until the maximum scouting rate is reached the best camping location which represents the best attribute for prediction is then selected using the fitness function and then the classification is done with the same POA to get the best pastoralist where an output of 1 represents a subscriber who is likely to churn and 0 represents a subscriber who is not likely to churn.

In this section, we describe the POA algorithm according to Abdullahi *et al*. (2018) which is the basis technique for use in our work. Each step of the algorithm is described as follows:

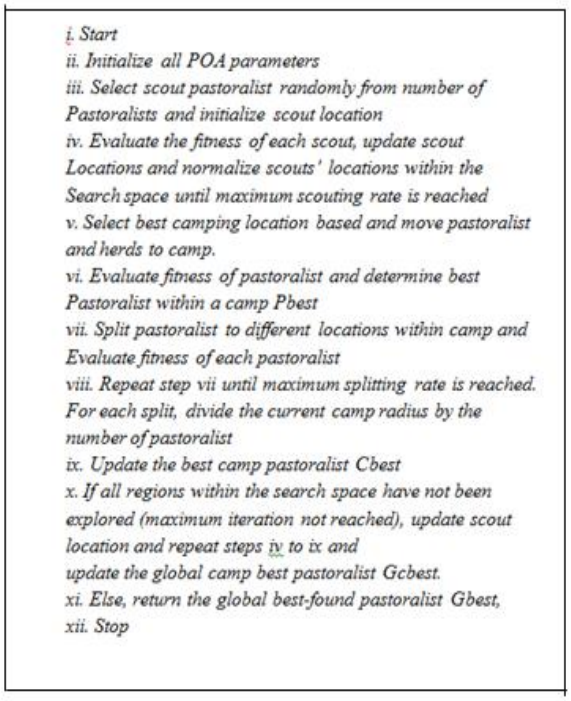

Figure 6: Pastoralist Optimization Algorithm (Abdullahi *et al*., 2018)

4 RESULTS

The main purpose of this research was to develop a model that can first determine the best attributes for the prediction of telecom churn and then make prediction based on these attributes by processing of data obtained from telecom industry. In this section, the paper presents the confusion matrix, the selected CDR attributes for customer churn prediction, optimal prediction values and a comparative analysis of optimal POA values with un optimized values . The confusion matrix is employed because it provides insight into how well categorization models perform given a certain set of test data. The only way to know is if test data's real values are knownThe matrix itself is simple to comprehend, but some of the terminology used in connection with it could be unclear. The projected values and actual values, along with the total number of outcomes, are separated into two dimensions in the matrix. Actual values are the real values for the provided data, whereas predicted values are the values that the model predicts. Table 1: Attributes selected for customer churn prediction.

S/N	ATTRIBUTE	POA_ANN	ANN
1	Call Failure	*	*
2	Complain	*	*
3	Subscription Length	*	*
4	Charge Amount	*	*
5	Seconds of Use	*	*
6	Frequency of Use	*	*
7	Frequency of Sms	*	*
8	Distinct call numbrs	*	*
9	Age Group		*
10	Tariff Plan		*
11	Status	*	*
12	Age	*	*
13	Customer Value		*
14	FN		*
15	FP		*

The table 1 above also clearly shows the attributes selected for churn prediction and this was done by an evaluation of each attribute using the fitness function. It was noticed from the table that while ANN used the entire fifteen attributes from the given dataset for prediction, POA_ANN selected fewer attributes and gave a higher prediction accuracy. The attributes selected by POA_ANN and used for the prediction were Call Failure, Complain, Subscription Length, Charge Amount, Seconds of Use, Frequency of Use, Frequency of Sms, Distinct call numbers, status, age and FN.

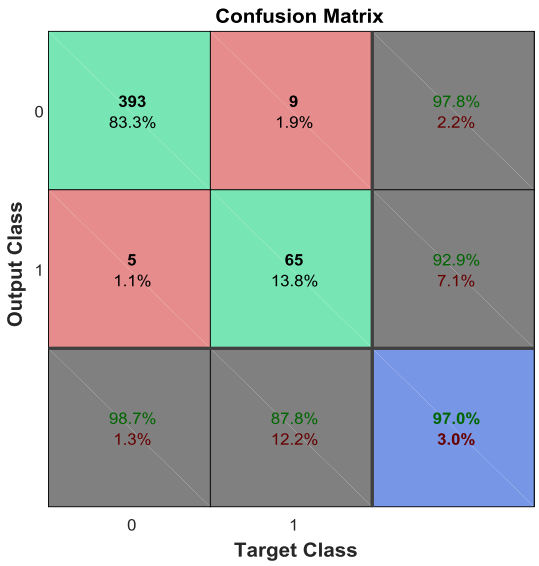

Figure 4: ANN_POA Confusion Matrix

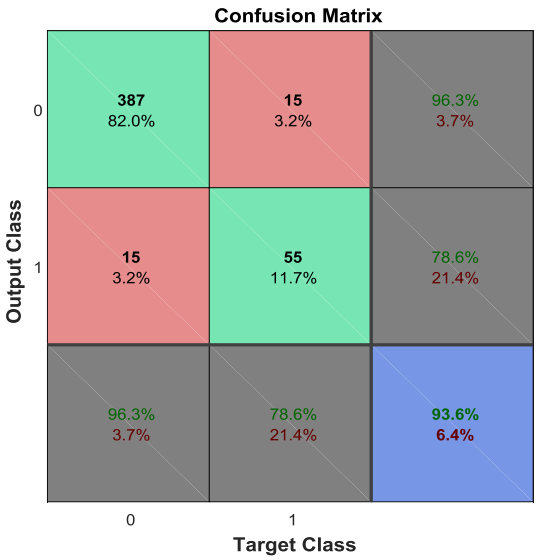

Figure 5: ANN Confusion Matrix

The confusion matrix can be used to calculate the model's properties, including accuracy, precision, sensitivity, etc. In this work, prediction accuracy is used as metric for performance evaluation for the model. Accuracy is used as the measure of classification performance because it is simple to compute among others and easy to interpret.

$$\text{Accuracy} = \frac{TP+TN}{TP+TN+FP+FN} \times 100\%$$

Where:

T_P is True positive rate

T_N is True Negative rate

F_P is false positive rate

F_N is False negative rate

Figure 4 shows the confusion matrix of POA_ANN and the area with 65 samples colored green indicates the true positive rate, which represents the actual churners correctly classified. The area with 393 samples colored green indicates the true negative rate, which represents the non churners that were correctly classified. The area with 5 samples colored red indicates the false negative rate representing the non churners incorrectly classified, the area with 9 samples colored red indicates the false positive rate representing actual churners incorrectly classified. Finally, the blue area with 97.0% represents the percentage accuracy of the technique.

Figure 5 shows the confusion matrix of ANN and the area with 55 samples colored green indicates the true positive rate, which represents the actual churners correctly classified. The area with 387 samples colored green indicates the true negative rate, which represents the non churners that were correctly classified. The area with 15 samples (row 2, column 1) colored red indicates the false negative rate representing the non churners incorrectly classified, the area with 15 samples (row 1, column 2) colored red indicates the false positive rate representing actual churners incorrectly classified. Finally, the blue area with 93.6% represents the percentage accuracy of the technique.

5 CONCLUSION

In this paper, an optimized subscriber churn prediction algorithm for the telecommunication industry is presented and its performance evaluated by comparing with unoptimized ANN technique in predicting churn. The study computed their true positive rates (TPR), true negative rates (TNR), false positive rates (FPR), false negative rates (FNR) and their prediction accuracies. The outcome showed that the POA_ANN has a high degree of prediction accuracy as it outperformed the prediction of ordinary ANN. POA_ANN only selected 10 attributes from the dataset to give an accuracy of 97.0% while the ordinary ANN selected all 15 attributes to give a prediction accuracy of 93.6% giving a 4.27% improvement in accuracy and a 50% improvement in attribute selection. This clearly shows the most important attributes for churn prediction in the Telecom industry based on the dataset. The paper also recommends that more evaluation of the performance of the algorithm be done by making comparism with other algorithms such as Particle Swarm Optimization (PSO), Cuckoo Search Optimization (CSO), Ant Colony Optimization (ACO) and Genetic algorithm (GA).

REFERENCES

Abdullahi I. M. Mu'azu M. B. Olaniyi O. M. & Agajo J. Pastoralist Optimization Algorithm (POA): A Novel Nature-Inspired Metaheuristic Optimization *Proc. of Int. Conf. on Global and Emerging Trends, (ICGET) 2018*, Base University, Abuja, Nigeria, May 2nd 2018. *pp. 101-105.*

Abrandusoiu, Ionut, Toderean, G. & Beleiu, Horia. (2016). Methods for Churn Prediction in the Prepaid MobileTelecommunicationsIndustry.97-100.10.1109/ ICComm. 2016.7528311.

Ahmad, A.K., Jafar, A. & Aljoumaa, K. Customer churn prediction in telecom using machine learning in big dataplatforms.*JBigData*6,28(2019). https://doi.org/10.1186/s40537-019-0191-6.

Chakure A. Belkhede A. Shrimali S. Garud S. & Patil S. An Overview Of Customer Churn Prediction In Telecom Industry *A Literature Survey*, Journal of Emerging Technologies and Innovative Research (JETIR) 2021 JETIR March 2021, Volume 8, Issue 3 pp. 2227-2230. 2021.

Eria K, Marikannan BP: Systematic Review of Customer Churn Prediction in the Telecom Sector. ResearchGate. 2018, September

Gaur A & Dubey R, "Predicting Customer Churn Prediction In Telecom Sector Using Various Machine Learning Techniques," 2018 International Conference on Advanced Computation and Telecommunication (ICACAT), Bhopal, India, 2018, pp. 1-5, doi: 10.1109/ICACAT.2018.8933783.

Höppner S, Stripling E & Baesens B: Profit-driven decision trees for churn prediction. Eur. J. Oper. Res. 2020; 284

Hu X. Yang Y. Chen L. & Zhu S. "Research on a Customer Churn Combination Prediction Model Based on Decision Tree and Neural Network," 2020 IEEE 5th International Conference on Cloud Computing and Big Data Analytics (ICCCBDA), Chengdu, China, 2020, pp. 129-132, doi: 10.1109/ICCCBDA49378.2020.9095611.

Idris A. Khan A. and Lee Y. S. "Genetic Programming and Adaboosting based churn prediction for Telecom," 2012 IEEE International Conference on Systems, Man, and Cybernetics (SMC), Seoul, Korea (South), 2012, pp. 1328-1332, doi: 10.1109/ICSMC.2012.6377917

Joolfoo M. B. A. & Jugumauth R. A. "A Systematic Review of Algorithms applied for Telecom Churn Prediction," 2020 3rd International Conference on Emerging Trends in Electrical, Electronic and Communications Engineering (ELECOM), Balaclava, Mauritius,2020,pp.136-140,doi:10.1109/ELECOM49001. 2020 .9296999.

Khan, M., Manoj, J., Singh, A., & Blumenstock, J. (2015). Behavioral Modeling for Churn Prediction: Early Indicators and Accurate Predictors of Custom Defection and Loyalty*2015 IEEE International Congress on Big Data*.

Mahajan V. Misra R. & Mahajan R. Review on factors affecting customer churn in telecom sector. International Journal of Data Analysis Techniques and Strategies 9(2):122 DOI :10.1504 /IJDATS . 2017.085898, pp. 123-144. 2017

Mohanty R. & Rani K. J. "Application of Computational Intelligence to Predict Churn and Non-Churn of Customers in Indian Telecommunication," 2015 International Conference on Computational Intelligence and Communication Networks (CICN), Jabalpur, India, 2015, pp. 598-603, doi: 10.1109/CICN.2015.123.

Ngurah P, Oka H & Setyo A, "Telecommunication Service Subscriber Churn Likelihood Prediction Analysis Using Diverse Machine Learning Model," 2020 3rd International Conference on Mechanical, Electronics Computer, and Industrial Technology (MECnIT),Medan,Indonesia,2020,pp.24-29,doi: 10.1109/MECnIT48290.2020.9166584.

PLAKSIJ Z. CUSTOMER CHURN: 12 WAYS TO STOP CHURN IMMEDIATELY LAST UPDATED: 15 AUGUST, 2022 [ONLINE].AVAILABLE:HTTPS://WWW.SUPEROFFICE.COM/BLOG/REDUCE-CUSTOMER-CHURN/

Sandhya k Thaslima S Prasanna N.G.L. Vindhya R. and Srilakshmi P.. Analysis of Customer Churn Prediction in Telecom Industry Using Logistic Regression.
International Journal of Innovative Research in Computer Science & Technology (IJIRCST) ISSN: 2347-5552, Volume-9, Issue-4, July 2021

SWIFTADMIN. HOW TO STOP CHURN IMMEDIATELY AUG11,2021[ONLINE].AVAILABLE:HTTPS://WWW.SWIFTERM.COM/HOW-TO-STOP-CHURN-IMMEDIATELY/

Ullah I. Raza B. Malik A. K. Imran M. Islam S. U. and Kim S. W. "A Churn Prediction Model Using Random Forest:Analysis of Machine Learning Techniques for Churn Prediction and Factor Identification in Telecom Sector," in IEEE Access, vol. 7, pp. 60134-60149, 2019, doi: 10.1109/ACCESS.2019.2914999.

4th International Engineering Conference (IEC 2022)
Federal University of Technology, Minna, Nigeria

Wearable Device for Telemedicine: An Architecture and Prototype Implementation for Remote Medical Diagnosis using Long Range Communication Protocols

* Aliyu, I. B [1] Alenoghena, C. O [2] Zubair, S. [3] & Salawu, N.[4]
Telecommunication Engineering Department, Federal University of Technology, PMB 65, Minna, Niger State, Nigeria
*Correspondence: aliyuidris3@gmail.com

ABSTRACT
Due to rising population particularly in the developing countries, the need has increased for online medical services mostly for health monitoring and remote medical diagnosis for personal health care using telemedicine. Also, health care facilities and resources have been overwhelmed in many countries leading to poor quality of health care delivery and more expensive medication due to the continuous application of conventional face-to-face consultations in medical diagnosis. In attempt to deliver cost-effective and reliable remote medical consultations and diagnosis using telemedicine, short range communication protocols such as Bluetooth and ZigBee have been adopted for wearable devices. Existing wearable devices developed using these short range protocols for D2D communication are not supported by IoT gateways due interoperability issues. In this paper, a long range MQTT communication protocol with GPRS, GSM and GPS for transmitting vital signs from a wearable medical device to the cloud is proposed. A wearable hardware prototype using an IoT gateway via the A9G module and the Atmega 328 to transmit medical data to the cloud was implemented. The prototype device demonstrates that adopting long range communication protocol offers ubiquitous and fast medical data access for delivering professional healthcare services regardless of user location. The device enables patient and doctor interaction for remote medical diagnosis in real-time using a web interface by means of an API.

Keywords: *Heart rate; IoT; Protocol; Telemedicine; Temperature; Vital Signs*

1 INTRODUCTION

The advent of wearable medical devices has enabled patients to monitor and transmit their vital signs to remote servers for effective health care delivery. Remote Medical Diagnosis (RMD), early symptom detection and e-health awareness are conceivable by employing 5G technology in telemedicine which supports high-speed transmission and sharing of massive multimedia medical data and resources (Duan *et al*. 2020).

Wearable health monitoring (WHM) devices enable the acquisition of patients' vital signs and health status monitoring for long periods outside medical environments. WHM enables acquisition of medical data during different scenarios for applications such as remote medical diagnosis and rapid medical attention in case of emergencies (Dias and Cunha 2018). The major vital signs (Vishnu, Jino Ramson, and Jegan 2020) usually monitored by medical professionals are:

(i) Heart rate (HR)
(ii) Blood pressure (BP)
(iii) Body temperature (BT)
(iv) Respiration rate (RR)
(v) Pulse rate (PR)
(vi) Body mass index (BMI)
(vii) Oxygen saturation
(viii) Blood glucose level
(ix) Systolic blood pressure
(x) Diastolic blood pressure
(xi) Muscular activation
(xii) Urine output
(xiii) Pain
(xiv) Total lung volume
(xv) Level of consciousness

Recently the need for wireless medical services mostly for remote monitoring and personalised health care has led to migration from wired tools to wireless solutions in form of telemedicine. This tends to eliminate the difficult and limiting wirings, thereby increasing patient independence and mobility (Mahfouz, Kuhn, and To 2013).

Telemedicine, which is a means of delivering professional health care and sharing of medical knowledge over a distance by using telecommunication technologies, have been used to provide expert-based health care in remote locations and emergency situations (Kyriacou, Pavlopoulos, and Koutsouris 2006). This is achieved by using several wireless communication protocols like the ZigBee, Bluetooth, Wi-Fi, WLAN, IP/TCP, satellite, GSM and WiMAX deployed for implementing telemedicine designs for real-time scenarios.

Application of Long Range (LoRa) wireless communication protocols such as the WiMAX in telemedicine designs have been proven to deliver high

mobile connectivity for audiovisual data transmission and other complex services offering reliable Quality of Service (Rani, Bhat, and Mukhopadhyay 2017). Other advantages of using LoRa communication technology in telemedicine include integrated services, security and QoS support. The network could also be used as an intersection to available wired or commercial networks like the 3G or the DSL (digital subscriber line) networks which supports various stages of interconnections for effective network stability (Cova *et al*. 2009).

Telemedicine system enables patients and health-care professionals to be located anywhere in the globe where there is GSM cellular network coverage (Sukanesh *et al*. 2010). Wireless telemedicine systems could be used to observe patient's health situations such as cardiac activity during emergency by means of WBAN.

2 BACKGROUND AND MOTIVATION

Healthcare services have become more expensive because of rising populations and more expensive medication (Mukhiya *et al*. 2019). Also, health care facilities and resources have been overwhelmed in many countries leading to poor quality of health care delivery. Major health care challenges that require urgent attention include high doctor-to-patient ratio, difficulty in accessing medical experts/specialist from distance, remote access to medical diagnosis and mobility of doctors and patients while delivering medical services. These has led to various research works aimed at deploying ICT to mitigate the growing demand for quality and effective health at a reduced cost. Conventional medical services have not been able to address the above-mentioned challenges effectively largely due to application of obsolete technologies and equipment.

Although several researches have been conducted and deployed in the developed countries, real-time designs to tackle these challenges in developing countries have not received adequate attention. In order to deliver cost-effective and reliable remote medical consultations and diagnosis using telemedicine, researchers have adopted short range communication protocols such as Bluetooth and ZigBee transmitting medical data from wearable devices (Hu *et al*. 2008); Sîrbu *et al*., 2008); (Dengwei Wang *et al*. 2005). Existing wearable devices that use short range protocols for device-to-device (D2D) communication are not supported by IoT gateways due interoperability issues.

This paper mainly focuses on development of a prototype wearable vital signs health monitoring device for capturing and transmission of physiological signs which include body temperature, heart rate and user location. The measured signals are transmitted through a LoRa wireless communication network with internet accessibility by utilising Internet-of-Things (IoT). To address the problem of interoperability in the D2D medical data transmission, the A9G module is used as an IoT gateway through the microcontroller unit (MCU). The device offers GPRS/GSM and GPS for data transmission over the cloud with user location.

While conventional health care services basically require face-to-face meeting between patients and doctors, telemedicine technologies tend to reduce isolation of experts, nurses and sophisticated equipment (Pandian 2016). In view of the aforementioned, it has become very important and necessary to develop and deploy telemedicine technologies for effective, reliable and quality health care delivery. This research is therefore, intended to provide solutions that could mitigate the use of costly and unreliable conventional medical services that are dependent on obsolete technologies and equipment.

Our proposed prototype telemedicine system uses three telemedicine taxonomies namely: store-and-forward, online/real-time telemedicine and remote health monitoring technology (Pandian 2016), as a single unit in form of a portable wearable device. The device could be utilized to provide appropriate and excellent care by integrating e-health, personalised healthcare and increasing user access, providing high-quality care at a reduced medical cost. The design is capable of performing basic diagnostic tests on patients, equipped with input facilities and a means of transmitting the data to a medical professional via a LoRa communication protocol.

3 REVIEW OF RELATED WORK

3.1 Wireless Communication technologies for vital signs monitoring in Telemedicine

Application of IT solutions particularly in telemedicine, has led to cost reduction and increased quality health care delivery in the medical field (Chorbev and Mihajlov 2009). Several wireless technologies have been implemented in medical systems for vital signs monitoring and easy access to equipment and medication remotely (Mahfouz *et al*. 2013). These technologies include ZigBee and Bluetooth for wireless telemedicine in (Auteri *et al*. 2007); (Hu *et al*. 2008); (Mulyadi *et al*. 2009); (Sîrbu *et al*. 2008), WLAN in (Lin, Hung, and Chiang 2010), WiFi for signal security and accuracy in (Qu *et al*. 2009), internet for mobile telemedicine in (Khoor *et al*. 2001); (Celik *et al*. 2010), satellite telemedicine in China in (Wang and Gu 2009), GSM in (Abo-Zahhad, Ahmed, and Elnahas 2014) and World-wide Interoperability for Microwave Access (WiMAX) technology in (Zhang, Ansari, and Tsunoda 2010).

The LoRa communication technology was chosen in this work due to its BWA (broadband wireless access) for both mobile and stationary situations. It also offers wide bandwidth, integrated services for completely practical telemedicine services, MAC (media access control) layer security features and defined QoS framework that allows effective and reliable medical data transmission (Zhang *et al*. 2010).

3.2 Overview of WBAN architectures for telemedicine applications

Wireless Body Area Network has been utilized in several emergency telemedicine designs due to benefits such as early detection of disease, reduction in health care cost and provision of improved and ubiquitous health care services (Latha & Vetrivelan, 2020). WBAN enables acquisition and transmission of physiological data for continuous monitoring of patient's health by an expert doctor from a remote location. Because of its capability of providing miniaturized sensor nodes, WBAN has been implemented in telemedicine to provide remote health care services that allow mobility for both the patient and doctor.

(De Vicq *et al*. 2007) implemented a WBAN for sleep staging which uses a star architecture that allows all direct communication of all sensor nodes with the master node. This WBAN creates wireless communication among the different miniaturized, intelligent sensors and the gateway node to the access point. The online access is then provided to Body Area Network (BAN) devices through a network infrastructure that delivers remote services to the patients.

Another approach in (Yadav *et al*. 2020) used a wearable textile Ultra-Wideband (UWB) antenna for short distance communication for telemedicine & mobile health. The device uses a fabric containing substrate antenna incorporated into human body because it has negligible radiation effect. It requires low power to be excited and it is used for high data rate transmission for short range coverage. It offers an excellent time-domain characteristics for ultra-wide band (UWB) application with low SAR (specific absorption rate) on human tissue. Although the device was a prototype, it demonstrates the application of the wearable UWB textile antenna for mobile health and telemedicine designs. Ultra-wide band is an innovative wireless communication technology which could be deployed high data rate transmission of medical data over a wide range of frequencies for wireless network applications. It is a high-speed, less expensive, extremely low power capable of signal transmission through impediments and feasible for various applications. One major drawback with UWB design however, is that it lacks of global approval in terms of regulation (Rashvand *et al*. 2008).

In (Donati *et al*. 2019), a short range Bluetooth/Bluetooth Low Energy (BT/BLE) communication which uses android phone or tablet as a local gateway was also implemented. The telemedicine system is an IoT-based network of sensors that utilises BT/BLE consisting of vital signs monitoring devices dispersed at the patients' residence. The system is made up of central server software which contains a local storage device installed at the service provider node. It uses two-way communication with internet subsystems that communicate with broadband technologies such as 3G, LTE, 5G, or Wi-Fi connectivity through access points provided. In order to predict risky and hazardous situations, the use of artificial intelligence (AI) was suggested by the authors.

A similar telemedicine system made up of layers viz.: the IoT, Mobile Edge Computing (MEC), and the cloud computing layers was presented in (Zhang *et al*. 2020). These layers carry out different assigned functions collectively to form a complete WBAN scheme. The IoT layer generates the medical data and transmits to MEC layer for analysis. Further analysis and storage is conducted in the upper cloud layer. The system is a combination of Artificial Intelligence (AI) and edge computing to deliver predictive tasks. This system design approach has the capabilities of carrying out necessary actions if it recognizes abnormalities in ECG signals on the IoT edge device in place of the cloud. It offers high accuracy in predicting multiple categories in the ECG dataset and a very efficient medical information analysis. The authors however suggested combination of MEC and AI in telemedicine to reduce time for data transmission and analysis.

(Di Rienzo *et al*. 2020) developed a similar system named SeisMote, made up of 12 wireless sensor nodes, a USB dongle acting as a receiver, a wireless rechargeable battery, software suit, network file manager and an android app. The overall system is completely wearable while carrying out daily activities or during sleep. The system operates in three different modes namely real-time mode, offline mode and Bluetooth real-time mode. The architecture is based on the ARM-Cortex technology with a programmable flash memory. It also consists of an embedded RF transceiver, a digital memory card, wireless battery charger and power source. Only one sensor node can be used at a time, because The BLE used in this system cannot guarantee the proper time synchronization among all the nodes. While monitoring is done real-time, data analysis is performed offline. To improve on this system, the authors suggested the need for a Digital Signal Processor (DSP) chip, expansion of memory to enhance real-time computation of the acquired parameters and increasing battery duration to ensure long time monitoring.

Also described in (Latha & Vetirvelan, 2020), WBAN has been employed in telemedicine for providing the best monitoring and sending of health-related information to the doctor without affecting daily activities. It uses the IEEE 802.15.6 standard for telemedicine applications. The status, events and health of the patient are monitored constantly by means of WBAN.

4 METHODOLOGY

4.1 SYSTEM ARCHITECTURE

The proposed architecture uses a single IoT gateway for wireless LoRa communication to deliver a reliable network with guaranteed QoS. Three main stages are involved in the design; the electronic unit, the web unit and the mobile nodes (wearable devices for the client and remote server for the care giver). The basic hardware section consists of a WBAN of vital sign sensors to measure patients' condition(s) and transmit through the wireless interface provided for further analysis through the A9G module with GPS and GSM capabilities. The design stages are highlighted in figure 1.

Figure 1: System architecture block diagram

4.1.1 The Electronic Unit

The BP and HR design consists of several sections ranging from the power supply unit via a LiPo battery and charging circuit powering the A9G module. A 3.3V and 1.8V voltage regulators are also used to power the microcontroller and the BP/HR senor respectively. The entire system is wired by means of I2C bus architecture. Figure 2 shows the complete system description of the hardware design of the device to provide remote monitoring of patient BP and HR via IoT platform.

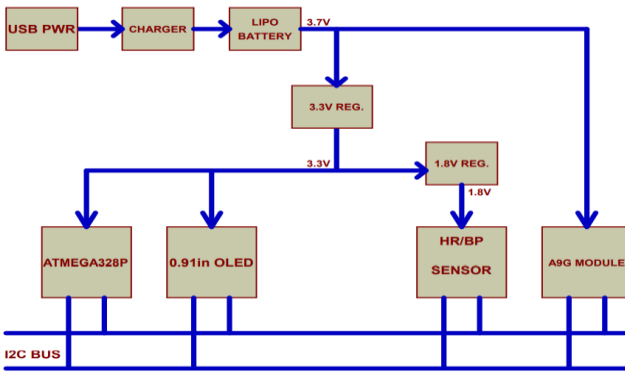

Figure 3: Block diagram of complete HR and BT system architecture

4.1.2 Components description and specifications

The major components in each block are discussed as follow.

a. Power supply

Power is supplied to the system through two sources: USB Power source and Lithium-ion Polymer (LiPo) battery source. A 3.3V linear low dropout regulator is used to provide a stable voltage level for onboard components. The power supply scheme is depicted in the system block diagram.

b. Battery charger

MCP73831 Linear charge management controller is used to handle battery charging operation. The charge controller features a charge status pin for monitoring battery status. This pin is connected to the atmega328 MCU. The USB device is a universal LiPo battery charger that could be plugged to any available DC source with USB port for charging the battery during use or in idle mode. A rechargeable LiPo battery uses polymer electrolyte instead of a liquid electrolyte.

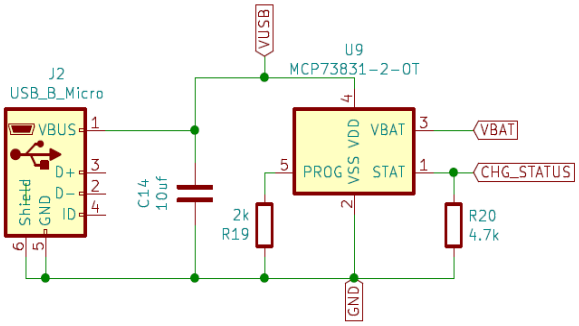

Figure 3: USB LiPo battery charging circuit

c. Voltage Regulator

The voltage regulator uses LM1117 regulator with 3pin configuration that regulates through the output pin 3 as depicted in Figure 3.4.

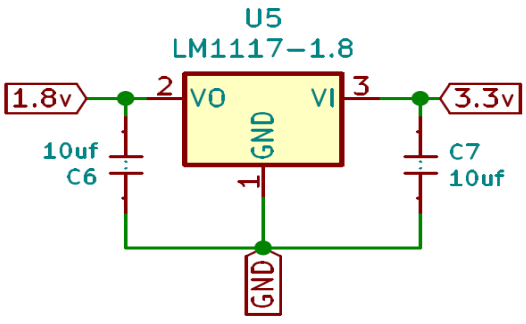

Figure 4: Voltage regulator circuit diagram

d. Heart rate and blood pressure Sensors

The HR and BP sensor uses MAX32664D, a variation of MAX32664 sensing devices which allows a user to obtain raw data including diastolic and systolic BP, SpO2, and HR data using contact from the finger. It could be programmed using accessories needed to connect sensing device via the I2C port (Figure 5). The I2C interface is also a means for communicating with the Arduino microcontroller unit.

Figure 5: MAX30101 HR and BP sensor

e. Onboard microcontroller

An atmega328p Microcontroller Unit (MCU) is used to interface the various peripherals on board like the OLED, HR and BP sensors and the A9G module through I2C bus interface. The purpose is to read the sensor values and perform necessary processing and relay the sensor value to A9G. The MCU is a low power version.

f. Display

The board can work with any display with I2C interface. But a 0.91inch (128x32 Pixel) OLED is recommended and utilized for this application because of the small form factor, low cost and low power feature.

g. A9G Module Overview

The A9G (designed by Ai-Thinker, 2017) is an SMD package module that has the capabilities of GSM and GPRS connectivity for cost and time reduction. It uses low power with GPS support. The A9G module was used as an IoT gateway serving as a bridge or communication link between IoT devices within the field, cloud and the user nodes. It uses MQTT (Message Queuing Telemetry protocol) to send and retrieve data from the Arduino MCU. The module sends sensor data to the cloud for monitoring and feedback using API through smart phones.

The various circuit diagrams and the PCB of the system were developed using KiCad software as depicted in the subsequent figures 6 and 7.

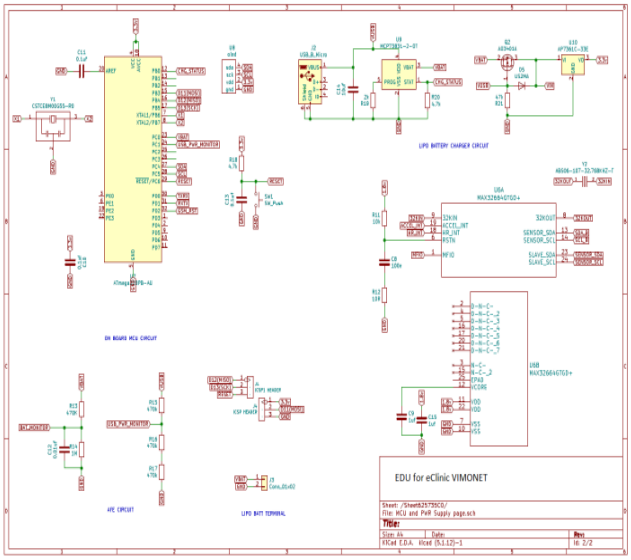

Figure 6: MCU and Power supply unit

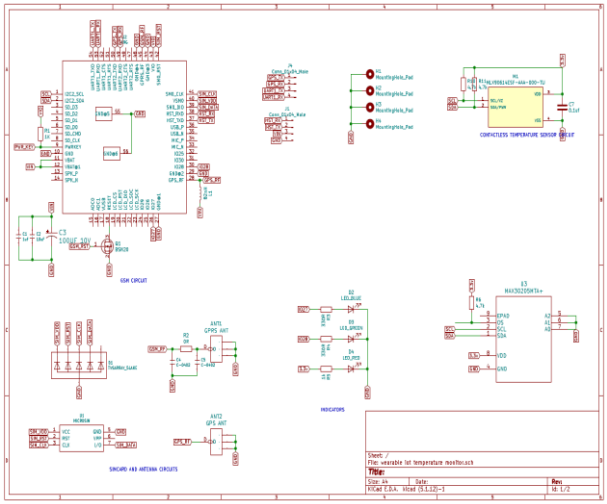

Figure 7: Circuit diagram of contactless temperature sensing and GSM module unit

5 RESULTS AND DISCUSSION

5.1 Identification of major onboard components of the prototyped PCB

The images below show the front and back view of the board, position and identification of the major components used in the design.

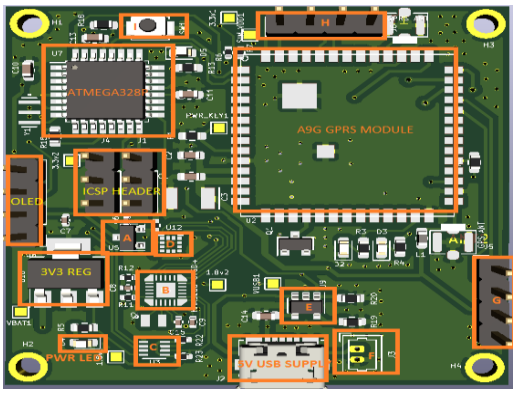

Figure 8: Front view of PCB

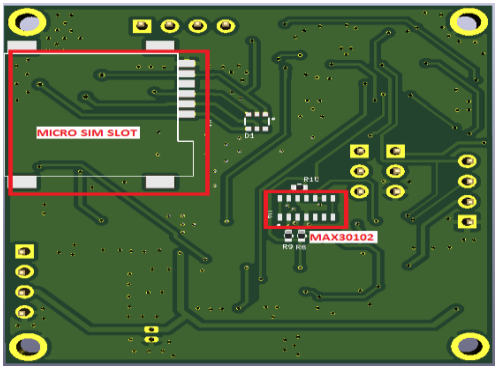

Figure 9: Back view PCB

5.2 Device features

a. **Connectivity:** The device features A9G module which provides the GPRS/GSM/GPS connectivity. It has an integrated MCU which can be used to develop user application.
b. **Calibration**: because of disparities in both the finishing and casing of the prototyped device, it is necessary to carry out calibration steps in an organized setting. This will guarantee the validity of the SpO2 calculation. This procedure is usually done in a laboratory that has SpO2 reference device to evaluate the coefficients of the calibration (A, B, and C). These three coefficients obtained are loaded into the MAX32664D before initializing the algorithm.
c. **Programming interface:** Programming headers are provided for programming the Atmega328 and A9G module

Table 1: Device Peripheral Pin Map

PERIPHERALS		A9G	ATMEGA 328P
MLX 90614		I2C	I2C
MAX30206		I2C	I2C
OLED		I2C	I2C
LED			PB1
	CHG_STATUS	IO25(PIN 32)	PB0
	USB_PWR_ MONITOR	-	PC1
	GSM_RST		PD2
	GPS UART	UART2	
	UART	UART1	
	DEBUG	HST	

The table shows that all peripherals are connected to the same I2C Bus.

5.3 Board Testing/Troubleshooting Procedure

It is recommended to test the board to ensure everything is fine. The PCB design has Test pads placed at critical points of interest to make testing easy. The test pads are for power testing. Follow the procedure described below to test the board after production

5.3.1 Power testing

By connecting a 5V USB power supply to the board, the power indicator turns on at this point. If not, use a voltmeter to test the voltage at the VUSB test point and the 3.3V test points to see if they are supplying the correct voltage level (5V and 3.3V respectively). The power LED is connected to the 3.3V regulator output. Using a voltmeter test all the power test points for each of the peripheral to ensure they are receiving the correct voltage level. The square yellow points in figure 10 show where the test points are onboard.

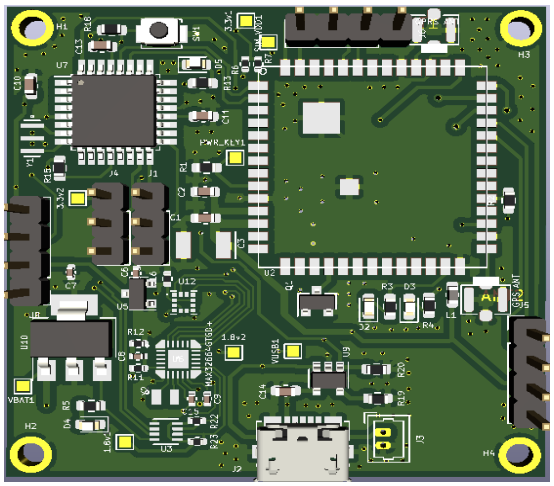

Figure 10: Test points for HR/BP Monitoring PCB

5.3.2 Programming and running a test code

The onboard MCUs namely; Atmegag328p and A9G were programed using the Arduino ICSP programmer. For ATMEGA328P: connect an ICSP Programmer (Arduino as ISP programmer) to the ICSP interface with Arduino Pins are as follows:

Pin 10 – RESET
Pin 11 – MOSI
Pin 12 – MISO
Pin 13 – SCK

The codes are then uploaded to the MCU for testing. The test code could be an LED blinking code or a code to display 'VIMONET TEST' on the OLED as demonstrated in the breadboard shown in figure 11.

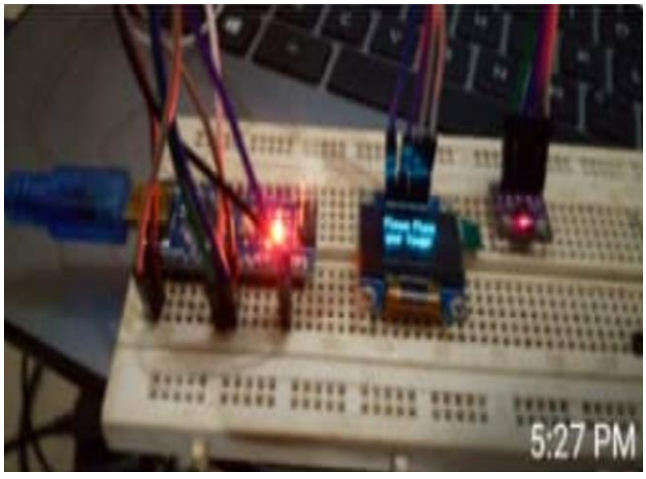

Figure 11: Testing of OLED before mounting on PCB

5.3.3 Sensor testing

After ensuring that the sensors are receiving the adequate voltage level for normal operation proceed to write some codes to read their values and display on LCD. The fabricated prototype PCB is depicted in figure 12 (a & b).

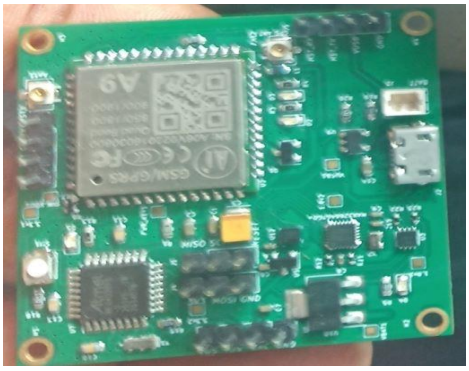

Figure 12a: HR/BP monitoring device (Front view)

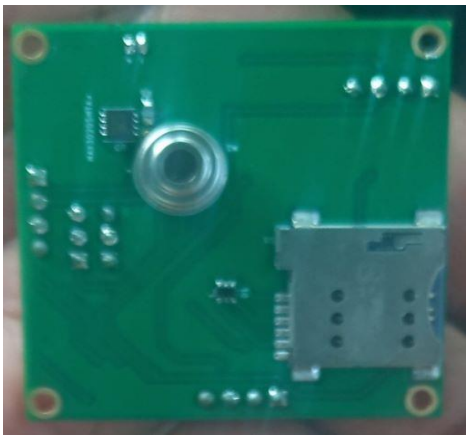

Figure 12b: HR/BP monitoring device (Back view)

6 CONCLUSION

This article reports the design and successful execution of a fully functional wireless Heart rate and Blood pressure monitoring and transmission device for remote medical diagnosis. The prototype architecture uses an approach that adopts the long range wireless communication protocol between the sensor nodes and IoT gateway. The system delivers a reliable network for transmitting sensitive medical data with guaranteed QoS. User interface is provided through an application programming interface (API) in the web platform to access the measured data for analysis and diagnosis by the web-based medical expert in a remote location. Results obtained from measured vital signs could be easily accessed from the web by providing the required fields pre-defined by the web server agent. The device measures body temperature, heart rate and transmits same in real time to the remote server with user location for further analysis.

REFERENCE

Abo-Zahhad, M., Sabah M. Ahmed, and O. Elnahas. 2014. "A Wireless Emergency Telemedicine System for Patients Monitoring and Diagnosis." *International Journal of Telemedicine and Applications* 2014. doi: 10.1155/2014/380787.

Auteri, V., L. Roffia, C. Lamberti, and T. Salmon Cinotti. 2007. "ZigBee-Based Wireless ECG Monitor." Pp. 133–36 in *Computers in Cardiology*. Vol. 34. Durham, NC, USA: IEEE.

Celik, Nuri, James Baker, Hyoungsun Youn, and Magdy F. Iskander. 2010. "An Internet Based Interactive Telemedicine System for Remote Healthcare." *2010 IEEE International Symposium on Antennas and Propagation and CNC-USNC/URSI Radio Science Meeting - Leading the Wave, AP-S/URSI 2010* 2–5. doi: 10.1109/APS.2010.5561027.

Chorbev, Ivan, and Martin Mihajlov. 2009. "Building a Wireless Telemedicine Network within a WiMax Based Networking Infrastructure." *2009 IEEE International Workshop on Multimedia Signal Processing, MMSP '09*. doi: 10.1109/MMSP.2009.5293305.

Cova, Gabriel, Huagang Xiong, Qiang Gao, Esteban Guerrero, Ricardo Ricardo, and Jose Estevez. 2009. "A Perspective of State-of-the-Art Wireless Technologies for E-Health Applications." *ITME2009 - Proceedings 2009 IEEE International Symposium on IT in Medicine and Education* 76–81. doi: 10.1109/ITIME.2009.5236457.

Dengwei Wang, Yinghua Lu, Hongxin Zhang, Che Shuliang, and Yunan Han. 2005. "A {Wireless} {Sensor} {Network} Based on {Bluetooth} for {Telemedicine} {Monitoring} {System}." Pp. 1361–64 in *2005 {IEEE} {International} {Symposium} on {Microwave}, {Antenna}, {Propagation} and {EMC} {Technologies} for {Wireless} {Communications}*. Vol. 2. Beijing, China: IEEE.

Dias, Duarte, and João Paulo Silva Cunha. 2018. "Wearable Health Devices—Vital Sign Monitoring, Systems and Technologies." *Sensors (Switzerland)* 18(8). doi: 10.3390/s18082414.

Donati, Massimiliano, Alessio Celli, Alessio Ruiu, Sergio Saponara, and Luca Fanucci. 2019. "A Telemedicine Service System Exploiting BT/BLE Wireless Sensors for Remote Management of Chronic Patients." *Technologies* 7(1):13. doi: 10.3390/technologies7010013.

Duan, Wei, Yancheng Ji, Yan Zhang, Guoan Zhang, Valerio Frascolla, and Xin Li. 2020. "5G Technologies Based Remote E-Health: Architecture, Applications, and Solutions." 1–16.

Hu, Xiao, Jiaqing Wang, Qun Yu, Waixi Liu, and Jian Qin. 2008. "A Wireless Sensor Network Based on ZigBee for Telemedicine Monitoring System." Pp. 1367–70 in *2nd International Conference on Bioinformatics and Biomedical Engineering, iCBBE 2008*. Shanghai, China: IEEE.

Khoor, S., K. Nieberl, K. Fugedi, and E. Kail. 2001. "Telemedicine {ECG}-Telemetry with {Bluetooth} Technology." Pp. 585–88 in *Computers in {Cardiology} 2001. {Vol}.28 ({Cat}. {No}.{01CH37287})*. Rotterdam, Netherlands: IEEE.

Kyriacou, Efthyvoulos, Sotiris Pavlopoulos, and Dimitris Koutsouris. 2006. "An {Emergency} {Telemedicine} {System} {Based} on {Wireless} {Communication} {Technology}: {A} {Case} {Study}." Pp. 401–16 in *M-{Health}*, edited by R. S. H. Istepanian, S. Laxminarayan, and C. S. Pattichis. Boston, MA: Springer US.

Lin, C. F., S. I. Hung, and I. H. Chiang. 2010. "An 802.11n Wireless Local Area Network Transmission Scheme for Wireless Telemedicine Applications." *Proceedings of the Institution of Mechanical Engineers, Part H: Journal of Engineering in Medicine* 224(10):1201–8. doi: 10.1243/09544119JEIM729.

Mahfouz, Mohamed R., Michael J. Kuhn, and Gary To. 2013. "Wireless Medical Devices: A Review of Current Research and Commercial Systems." *BioWireleSS 2013 - Proceedings: 2013 IEEE Topical Conference on Biomedical Wireless Technologies, Networks, and Sensing Systems - 2013 IEEE Radio and Wireless Week, RWW 2013* 16–18. doi: 10.1109/BioWireleSS.2013.6613660.

Mukhiya, Suresh Kumar, Fazle Rabbi, Ka I. Pun, and Yngve Lamo. 2019. "An Architectural Design for Self-Reporting e-Health Systems." *2019 IEEE/ACM 1st International Workshop on Software Engineering for Healthcare (SEH)* (iv):1–8. doi: 10.1109/SEH.2019.00008.

Mulyadi, Indra H., Eko Supriyanto, Norlaili M. Safri, and Muhammad H. Satria. 2009. "Wireless Medical Interface Using Zigbee and Bluetooth Technology." *Proceedings - 2009 3rd Asia International Conference on Modelling and Simulation, AMS 2009* 276–81. doi: 10.1109/AMS.2009.134.

Pandian, P. S. 2016. "An Overview of Telemedicine Technologies for Healthcare Applications." 5(2):29–52. doi: 10.4018/IJBCE.2016070103.

Qu, Huyu, Jie Cheng, Qiang Cheng, and Le Yi Wang. 2009. "WiFi-Based Telemedicine System: Signal Accuracy and Security." *Proceedings - 12th IEEE International Conference on Computational Science and Engineering, CSE 2009* 2:1081–85. doi: 10.1109/CSE.2009.60.

R, Latha, and Vetrivelan P. 2020. "Wireless {Body}

{Area} {Network} ({WBAN})-{Based} {Telemedicine} for {Emergency} {Care}." *Sensors* 20(7):2153. doi: 10.3390/s20072153.

Rani, B. K. Sandhya, Soumya Bhat, and Adwitiya Mukhopadhyay. 2017. "A Survey of Wireless Technologies and Vertical Handoff Techniques from the Perspective of Telemedicine Scenarios." Pp. 1246–51 in *2017 {International} {Conference} on {Communication} and {Signal} {Processing} ({ICCSP})*. Vols. 2018-Janua. Chennai: IEEE.

Rashvand, H. F., V. Traver Salcedo, E. Montón Sánchez, and D. Iliescu. 2008. "Ubiquitous Wireless Telemedicine." *IET Communications* 2(2):237–54. doi: 10.1049/iet-com:20070361.

Di Rienzo, Marco, Giovannibattista Rizzo, Zeynep Melike Işilay, and Prospero Lombardi. 2020. "Seismote: A Multi-Sensor Wireless Platform for Cardiovascular Monitoring in Laboratory, Daily Life, and Telemedicine." *Sensors (Switzerland)* 20(3):680. doi: 10.3390/s20030680.

Sîrbu, Adriana N., Victor-Andrei V. D. Maiorescu, and Ioan I. Cleju. 2008. "A Zigbee Solution for Telemedicine Applications." *{ACTA }TECHNICA NAPOCENSIS Electronics and Telecommunications* 49(3):35–39.

Sukanesh, R., S. Palanivel Rajan, S. Vijayprasath, N. S. Aishwarya, and P. Gracy Angela. 2010. "Intelligent Wireless Mobile Patient Monitoring System." *2010 IEEE International Conference on Communication Control and Computing Technologies, ICCCCT 2010* 540–43. doi: 10.1109/ICCCCT.2010.5670439.

De Vicq, Nicolas, Frédéric Robert, Julien Penders, Bert Gyselinckx, and Tom Torfs. 2007. "Wireless Body Area Network for Sleep Staging." *Conference Proceedings - IEEE Biomedical Circuits and Systems Conference Healthcare Technology, BiOCAS2007* 163–66. doi: 10.1109/BIOCAS.2007.4463334.

Vishnu, S., S. R. Jino Ramson, and R. Jegan. 2020. "Internet of Medical Things (IoMT)-An Overview." *ICDCS 2020 - 2020 5th International Conference on Devices, Circuits and Systems* 101–4. doi: 10.1109/ICDCS48716.2020.243558.

Wang, Zhelong, and Hong Gu. 2009. "A Review of Telemedicine in China." *Journal of Telemedicine and Telecare* 15(1):23–27. doi: 10.1258/jtt.2008.080508.

Yadav, Ashok, Vinod Kumar Singh, Akash Kumar Bhoi, Gonçalo Marques, Begonya Garcia-Zapirain, and Isabel de la Torre Díez. 2020. "Wireless Body Area Networks: UWB Wearable Textile Antenna for Telemedicine and Mobile Health Systems." *Micromachines* 11(6). doi: 10.3390/MI11060558.

Zhang, Yan, Nirwan Ansari, and Hiroshi Tsunoda. 2010. "Wireless Telemedicine Services over Integrated IEEE 802.11/WLAN and IEEE 802.16/WiMAX Networks." *IEEE Wireless Communications* 17(1):30–36. doi: 10.1109/MWC.2010.5416347.

Zhang, Zhongyang, Zhongmin Tang, Nika Farokhzad, Tianfeng Chen, and Wei Tao. 2020. "Sensitive, Rapid, Low-Cost, and Multiplexed COVID-19 Monitoring by the Wireless Telemedicine Platform." *Matter* 3(6):1818–20. doi: 10.1016/j.matt.2020.11.001.

4th International Engineering Conference (IEC 2022)
Federal University of Technology, Minna, Nigeria

Quantification and Characterization of Municipal Solid Waste Generated from the University of Jos Hostel for Energy Recovery

*Japhet, J. A[1], Gukop, N. S[1], Lengs, B. D[1], Datau, N[1] & Babawuya, A[2]
[1]Department of Mechanical Engineering, University of Jos, Jos, Nigeria
[2]Department of Mechatronic Engineering, Federal University of Technology, Minna
Corresponding author: suyidam@yahoo.com

ABSTRACT
One of the vital components for sustainable development is Municipal Solid Waste (MSW) management. MSW management controls the generation, storage, collection, transfer, processing and disposal of solid waste. For a proper MSW management, a reliable appraisal of the amount of municipal solid waste generation is very vital – this is mostly lacking in developing countries. The characterization of MSW is also an essential factor for efficient management – it provides valuable information for evaluating potential for recovery of energy and material. This study aims to quantify and determine the composition of the municipal solid waste generated from the University of Jos student's hostel. This was carried out by estimating the solid waste generation and determining the components of the solid waste. The result show that the wastes from the hostels was made up of food residue with 35.5%, polythene 32.44%, others 15.48%, paper 6.22%, plastic bottles 5.15%, textiles 4.16% and tin/metals 1.05%, in the order of magnitude. The composition also shows that organic matter (food residue, paper, textile) is 45.88%, burnable waste (polythene) is 32.44%, Recyclable (plastic bottles and tin/metals) is 6.2% and others is 15.48%. Thus, the results could be useful in estimating the energy recovery potential and decisions on suitable recovery methods from the waste.

Keywords: *Composition; Energy; Municipal Solid Waste; Quantification; Recovery.*

1 INTRODUCTION

Waste are material generated from activities of humans which are often discarded since they are regard as useless. There are concerns worldwide, about the adverse effect of waste on human health and the local environment (air, water, land) etc. Solid waste may be a resource if suitably managed; for generating energy and industrial production. To achieve sustainable growth, Waste management requires multi-stakeholder participation at all levels of the process as a result of the growing complexity, expenses and management (Scarlat, et al. 2015).

Municipal Solid Waste (MSW) are generally wastes from commercial centres, households, and institutions (Ahmed, 2012). The rate of MSW generation has grown worldwide overtime as a result increase in human population, standard of living, technology and stimulation of consumers awareness (Omari et al., 2014). The continues growth in generation MSW will lead to upsurge in environmental health problems if not managed appropriately (Johari et al., 2012).

There has been a remarkable growth in the quantity of everyday wastes generated in Nigeria (Orhorhoro, et al., 2017), due to surge in solid waste generation to population growth and low budget for solid waste management. This has resulted into open dumping of waste on any vacant land space (Oladepo et al. 2015).

In Jos one of the rapidly growing urban centres in Nigeria, the state of MSW is the same as obtained nationally. The growth in size of the urban centre, population and economy, piles of un-cleared refuse have characterized its highways; threatening the environment and health of the inhabitants (Eche et al, 2015). In the University of Jos, the MSW generated in the hostel is not adequately managed - collection and disposal openly without any form of treatment in public dumpsite is the basic management system. This contributes to the challenge of inadequate waste management. The waste is not utilized for anything sustainable development.

Municipal Solid Waste (MSW) management - a vital component for sustainable development, is the control of generation, storage, collection, transfer, processing and disposal of solid waste. The purpose of MSW management is to treat the waste in a way suitable socially and environmentally, by a proper and accessible clean technology, governed by best practice in public health, economics, engineering, aesthetics and other environmental consequences (Daskalopoulos *et al.,* 1997; ESCAP, 2017).

For a proper MSW management, a reliable appraisal of the amount of solid waste generated in the hostel is very vital. The characterization of MSW is also an essential factor for efficient management, this provides valuable information that are valuable for several reasons: selecting suitable disposal systems and improving collection and separation techniques, the necessity of evaluating potential for recovery of material, the identification sources of element generated, design of efficient handling equipment and evaluating physical, chemical, and thermal properties of the waste (Pandey et al., 2016; Yenice et al. 2011; Gidarakos et al., 2005).

This study aims to quantify and determine the composition of the municipal solid waste generated from the University of Jos student's hostel. This will be carried out by estimating the solid waste generation rate, determining the components of the solid waste. The unavailability of data on the quantity and characteristics of the solid waste has made the management system inadequate and unsustainable. Thus, the results of this study will be helpful in estimating the energy recovery potential and decisions on suitable recovery methods from the waste.

2 METHODOLOGY

This section describes various methods adopted in this paper.

2.1 STUDY AREA

University of Jos hostel where the search was conducted, is located in Jos, Plateau state, Nigeria, between Latitude 8-10₀N and Longitude 7-11° E, it is bordered by Bassa Local Government in the north, Toro Local Government of Bauchi state to the east and Riyom and Barkin-ladi Local Government Areas to South (Binbol et al., 2016).

2.2 STUDENT POPULATION IN THE UNIVERSITY HOSTELS

The student's population responsible for the waste generation was obtain from the students' affairs division of the University of Jos and by random sampling through interview, the population of students living in the hostels was also estimated to ascertain the official figures. This is due to the fact that often time the official figures are far less than the actual population as a result of the activities of squatters. The sampling was carried out using Equation 1 (Dillman, 2000).

$$n = \frac{[(N)(p)(1-p)]}{[(N-1)\left(\frac{B}{C}\right)^2 + (p)(1-p)]} \qquad 1$$

Where:

n = is the calculated number of samples needed for the required level of accuracy

N = is the size of residents

p = is the percentage of residents anticipated to choose

B = acceptable amount of sampling error, or accuracy which is 0.05 or 5%.

C = Z statistic associated with the confidence level which is 1.96 that corresponds to the 95% level.

2.3 MSW CHARACTERIZATION

2.3.1 Waste Collection

The waste generated at the hostels are collected using the trash bin stationed at the hostels where students dump in their waste. The waste is then taken to the central dump (collection point) at the hostel every day after the cleaners are done cleaning, before the waste collection truck collects the waste for disposal at the public open dump. The waste used for the characterization was collected from the central dump at the hostel. The collection was carried out for twelve (12) days.

2.3.2 MSW SAMPLING AND SORTING

MSW samples were taken from University of Jos hostel garbage dump. European Commission Solid Waste Tool (ECSWA Tool), (2004); suggested that for research the samples needed should be at least 30. The sampling and sorting of the MSW was conducted as follows:

Step 1: MSW samples were taken three (3) times daily from Monday to Saturday for two weeks; making 36 MSW samples altogether. This was done to evade eventual mistake that may happen owing to inadequate samples.

Step 2: A specified waste container of 60 liters volume was used to collect the waste samples.

Step 3: Each waste sample after weighing it was hand sorted into separate components. The waste components were separated into seven (7) elements: ***paper, food residue, polythene, plastic bottle, metal/tin, textile and others***.

Step 4: At the end of the collection and sorting, each waste component was weighed using manual weighing balance and recorded.

2.4 DETERMINATION OF THE SPECIFIC WEIGHT OF THE WASTES

The waste density of load on the truck was established go by the method specified by the Mexican Standard NMX-AA-019. according to the Former Secretariat of Trade and Industrial Development (STID), (1985). Waste collected from the disposed trucks was filled into a container with a capacity of 0.06m^3. The container was knocked slightly against the floor by dropping three times from a height of approximate 10 cm after which more waste was added to fill it. This method was continued until the container was completely filled up. No pressure was applied to the waste in the container to evade varying the specific weight. The weight of the wastes in the container was divided by its volume.

2.5 QUANTITY OF MSW GENERATED IN UNIVERSITY OF JOS HOSTELS PER DAY

The amount of MSW generated was predicted (where weighbridge is absent) applying the model Equation 2 (Kosuke and Tomohiro, 2016). The prediction was carried out using the information on the facts and figures obtainable on collection and transportation of the waste.

$$MSWgen. = \sum_{j=1}^{365} \sum_{i=1}^{m} (C_i \times V_i \times d_i \times t_{ij}) \quad 2$$

Where:

$MSWgen$ = Municipal Solid Waste generation
m = total number of trucks,
Ci = the capacity of truck I (m3/truck),
Vi = the loading volume ratio of truck i,
di = the density of MSW loaded on truck i (tons /m3),
tij = the number of trips by truck i on day j (frequency of trips/day).

2.6 MSW PER CAPITA GENERATION

To compute the per capita waste generated, Equation 3 was applied.

$$MSW_{pc} = \frac{MSW_{gen}}{H \times n} \quad 3$$

Where:

$MSWpc$ = per capita generation of MSW
$MSWgen$ = weight of waste disposed of at the dumpsites
H = studied population
n = number of days

3 RESULTS AND DISCUSSIONS

3.1 DEMOGRAPHIC DATA OF UNIVERSITY OF JOS HOSTEL

The population of students living in the five hostels of the University of Jos is 4684, see Table 1. This is the official allocation obtained from the student affairs division of the University. In the process of carrying out this study, it was observed that a lot of squatting activities takes place in the University's hostels and through random sampling the actual population of students living in the hostels was estimated to be 8090, see Table 2. The estimated student's population in Table 2 was used in the study to determining the waste generation rate and the characteristic of the waste.

TABLE 1: DEMOGRAPHIC DATA OF UNIVERSITY OF JOS HOSTEL

S/N	Hostel	Number of Rooms	Population
1	Village	467	1,391
2	Naraguta	320	640
3	Abuja	561	1,897
4	Post-graduate	255	412
5	Zion	172	344
	TOTAL	**1775**	**4684**

Source: Students affairs University of Jos (2021)

TABLE 2: DEMOGRAPHIC DATA OF UNIVERSITY OF JOS HOSTEL (ESTIMATED)

S/N	Hostel	Number of Rooms	Average number of persons/room	Estimated Population
1	Village	467	5	2,335
2	Naraguta	320	4	1,280
3	Abuja	561	6	3,366
4	Post-graduate	255	3	765
5	Zion	172	2	344
	TOTAL	**1775**		**8090**

3.2 ESTIMATED MSW GENERATED IN UNIVERSITY OF JOS HOSTELS

The MSW generated from the University hostel was estimated using Equation 2, the date of waste collection vehicle, see Table 3, the Average Volume ratio of a truck which was assumed to be 0.95, the density of the waste was computed to be 0.139 tons/m3 by the Mexican Standard NMX-AA-019 (1985), and the estimated student's population Table 2. The result of the MSW generated was presented in Table 4, it shows that, MSW generated in 1 day, 12 days and 1 month are 2.23 tons/day, 26.76 tons/12 days and 69.13 tons/month respectively.

TABLE 3: DATA OF WASTE COLLECTION VEHICLE IN UNIVERSITY OF JOS

S/n	Type of truck	Number functional	Capacity/truck (kg)	Volume/ truck (m^3)	Number of trips/ truck /day (ton)
1	ARMECO	2	10, 000	17	1

TABLE 4: ESTIMATED MSW GENERATED IN UNIVERSITY OF JOS HOSTELS FROM DATA ON TRANSPORTATION

S/N	Type of truck	No. of trucks/ day	Capacity / truck (tons)	Vol./ truck (m^3)	Avg. Vol. ratio for each vehicle	Density of MSW filled on vehicle d (tons/m^3)	No. of trips/ truck /day, t	MSW generated tons/day	MSW Generated tons/12 days	MSW generated tons/months
1	ARMECO	1	10	17	0.95	0.139	1	2.23	26.76	69.13

3.3 PHYSICAL CHARACTERIZATION OF MSW FOR UNIVERSITY OF JOS HOSTEL

The characterization of the MSW generated from the University of Jos hostel, see Table 5 and Figure 1, did not take into account the seasonal variation. It was conducted for twelve (12) days in the month of July, using European Commission Solid Waste Tool (ECSWA Tool), 2004. The total weight of MSW analyzed for determining the waste composition was 99.73kg. The result show that the wastes from the hostels was made up of food residue with 35.5%, polythene 32.44%, others 15.48%, paper 6.22%, plastic bottles 5.15%, textiles 4.16% and tin/metals 1.05%, in the order of magnitude.

The high amount of organic waste (food residue, paper, textile) in the waste composition with 45.88%: open dumping can be directly avoided and with comprehensive research on organic waste, recoveries could be of advantage through the process of generation of methane from landfill, anaerobic digestion and composting as perfect ways treatment.

Recyclable (plastic bottles and tin/metals) waste which has profitable value is 6.2% in the waste fraction can be sorted from source and recycling technique should be applied. This requires public education.

Burnable wastes (polythene) which are not appropriate for recycling is 32.44% of the waste composition. Incineration with the aim of harnessing useful heat could be applied where the technology is feasible.

TABLE 5: THE MSW STREAMS' PHYSICAL CHARACTERISTICS FOR 12 DAYS (2 WEEKS) IN JULY, 2021.

Type	Days												Mean	Total Wt(kg)	Wt (%)	Kg/cap /day
	1 Wt(kg)	2 Wt(kg)	3 Wt(kg)	4 Wt(kg)	5 Wt(kg)	6 Wt(kg)	7 Wt(kg)	8 Wt(kg)	9 Wt(kg)	10 Wt(kg)	11 Wt(kg)	12 Wt(kg)				
Paper	0.50	0.60	0.60	0.50	0.70	0.65	0.40	0.65	0.50	0.35	0.30	0.45	0.52	**6.20**	**6.22**	**0.017**
Polythene	2.50	2.15	2.80	3.15	2.50	3.50	3.40	2.25	2.35	2.45	2.15	3.15	2.70	**32.35**	**32.44**	**0.089**
Food residue	3.40	2.30	1.35	3.90	4.05	2.45	2.30	3.35	1.85	3.45	2.90	4.10	2.95	**35.4**	**35.50**	**0.098**
Textile (rag)	0.60	0.50	0.60	-	0.40	0.35	0.25	-	0.50	0.55	-	0.40	0.35	**4.15**	**4.16**	**0.011**
Tins/metal	0.10	0.15	0.10	-	0.15	-	0.20	0.15	-	0.10	-	0.10	0.09	**1.05**	**1.05**	**0.003**
Plastic bottle	0.40	0.50	0.50	0.30	0.45	0.39	0.50	0.45	0.40	0.35	0.50	0.40	0.43	**5.14**	**5.15**	**0.014**
Others	0.50	1.10	0.40	4.15	1.20	0.90	0.39	4.05	0.85	0.45	0.50	0.95	1.29	**15.44**	**15.48**	**0.043**
Grand total	**8.00**	**7.30**	**6.35**	**12.00**	**9.45**	**8.24**	**7.44**	**10.90**	**6.45**	**7.70**	**6.35**	**9.55**	**8.33**	**99.73**	**100**	**0.275**

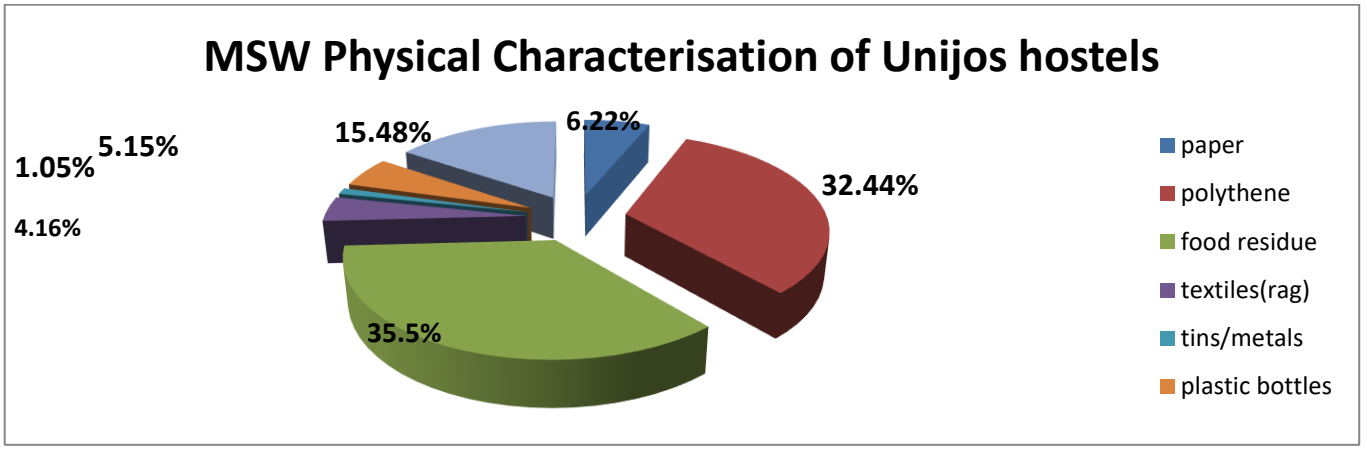

Figure 1: Chart of the Physical Characteristic of MSW Generated from the University of Jos Hostels

4 CONCLUSIONS

The study on Characterization of Municipal Solid Waste is valuable in decision making on treatment and mode of disposal. In developing countries, the predominant method of waste disposal is landfilling (open dumping) and the waste is predominantly organic (food residue, paper, textile), plastic, glass tin/metal and other materials. An open dump site (landfill) having this description is far from been properly managed. The challenge with this system of waste disposal is the negative consequence on the environment and public health. Leachate flow from an inadequate managed landfill (non-engineered), pollutions groundwater. Basically, GHG are emitted from landfill site with 50-60% methene, 30-40% carbon dioxide and several chemicals such as chlorinated organic compounds, aromatics and sulfur that are traceable (Mor et al., 2006).

From the study, MSW generated from the University's Hostel in 1 day, 12 days and 1 month are 2.23 tons/day, 26.76 tons/12 days and 69.13 tons/month respectively. From the waste composition, organic matter (food residue, paper, textile) is shown to be 45.88%, burnable waste (polythene) is 32.44%, Recyclable (plastic bottles and tin/metals) is 6.2% and others is 15.48%.

For energy recovery potential, the result of the study shows that a substantial quantity of the waste is available for it. The study also provides vital information on the decision on appropriate recovery method.

The location specific quantification and characterization of the University of Jos hostel waste will be beneficial in the study of the estimation of waste quantity from diverse sources of waste generation from the University and the city Jos. This could be utilized as a basis for the development of sustainable MSW management system.

REFERENCES

Ahmed, Y.A. (2012). Potential Impacts of Climate Change on Waste Management in Ilorin Nigeria. *Global J. Hum. Soc. Sci. 12 (6), 39–45.*

Binbol, N.L., Oche, C.Y., Eziashi, A.C. & Choji, V.D. (2016). Assessment of hydrological drought characteristics on the Jos, Plateau, Nigeria. Jos Plateau. *J. Environ. Sustainable Dev., 1, 12-17.*

Daskalopoulos, E., Badr, O. & Probert, S. D. (1997). Economic and Environmental Evaluation of Waste Treatment and Disposal Technologies for Municipal Solid Waste. *Applied Energy*, 58 *(4)*, 209-255

Dillman, D.A. (2000). Mail and internet surveys: the tailored design method. Brisbane: Wiley.

Eche, O. F., Yakubu, A. A., Lekwot, V. E., Kwesaba, D. A., Sohotden, & Daniel, C. (2015). An Assessment of Plateau Environmental Protection and Sanitation Agency (Pepsa) As a Waste Management Institution in Jos City, Nigeria. *International Journal of Scientific & Technology Research* 4 *(2).*

ESCAP (2017). Sustainable Development Benefits of Integrated Waste Management, Integrated Resource Recovery Centers. Economic and Social Commission for Asia and the Pacific (ESCAP), http://www.unescap.org (Retrieved 19.11.19).

European Commission Solid Waste Tool (ECSWA-Tool), (2004). Development of a Methodology Tool to Enhance the Precision and Comparability of Solid Waste Analysis Data. Available from: www.wastesolutions.org (cited 12 December 2016).

Former Secretariat of Trade and Industrial Development (STID), (1985). "NMX-AA-019-1985, Peso volumétrico "in situ"".

Gidarakos, E., Havas, G. & Ntzamilis, P. (2005). Municipal solid waste composition determination supporting the integrated solid waste management system in the island of Crete. www.elsevier.com/locate/wasman

Johari, A., Hashim, H., Mat, R., Alias, H., Hasshim, M. H. & Rozainee, M. (2012). Generalization, Formulation and Heat Contents of Simulated MSW with Moisture Content. *J. Eng. Sci. Technol. 7 (6).*

Kosuke, K. & Tomohiro, T., (2016). Revisiting estimates of municipal solid waste generation per capita and their reliability. *J. Mater. Cycles Waste Manage. Res. 18, 1–13.*

Mor, S., Ravindra, K., Dahiya, R.P., & Chandra, A. (2006). Leachate characterization and assessment of groundwater pollution near municipal solid waste landfill site. *Environ Monit Assess. 118 (1-3), 435-56.*

Oladepo, O. W., Ilori, M. O. & Taiwo, K. A. (2015). Assessment of the waste generation and management practices in Nigerian food industry: towards a policy for sustainable approaches. *American Journal of Scientific and Industrial Research, 6 (1), 12-22*

Omari, A., Said, M., Njau, K., John, G. & Mtul, P. (2014). Energy Recovery Routes from Municipal Solid Waste, A case study of Arusha-Tanzania. *J. Energy Tech. Policy.*

Orhorhoro, E.K., Ebunilo, P.O. & Sadjere, E.G. (2017). Determination and Quantification of Household Solid Waste Generation for Planning Suitable Sustainable Waste Management in Nigeria. *International Journal of Emerging Engineering Research and Technology, 5(8), 1-9.*

Pandey, B.K., Vyas, S., Pandey, M. & Gaur A. (2016). Characterisation of municipal solid waste generated from Bhopal, India. *Current Science Perspectives* 2 *(3)*, 52-56.

Scarlat, N., Motola, V., Dallemand, J. F., Monforti-Ferrario, F. & Linus, Mofor (2015). Evaluation of energy potential of Municipal Solid Waste from African urban areas. *Renewable and Sustainable Energy Reviews 50, 1269–1286.*

Yenice, M. K., Doğruparmak, Ş. Ç., Durmuşoğlu, E., Özbay, B, & Öz, H. O. (2011). Solid Waste Characterization of Kocaeli. *Polish J. of Environ. Stud. 20 (2), 479-484*

4th International Engineering Conference (IEC2023)
Federal University of Technology, Minna, Nigeria

Digital Prototyping of Foreground Object Detection for Life Fingerlings Counting System in Aquaculture Production in Nigeria

*Okouzi, A. S, Ayuba, A. B, Ihuahi, J. A & Ugoala, E. R

Products Development and Engineering Department, National Institute for Freshwater Fisheries Research, P.M.B., 6006, New Bussa, Niger State, Nigeria
*Corresponding author email:okouziabhulimhen@gmail.com +2348072249543

ABSTRACT
Traditional methods of life fingerling counting in aquaculture production is laborious, tedious, time consuming and inconsistent for the human counter. Consequently, prolonged counting is monotonous, leads to eye fatigue and affects the accuracy of results. Technological advancement in automation (machine vision) led to the development of promising solutions for challenging problems in different industries. Consequently, a non-contact and nondestructive real-time embedded computing system for the counting of life fingerlings (a confounding process for the expert human counter) was developed in this study. The digital design study is anchored on systems engineering methodology with computer integrated technology approach employed in modeling of the interactions of the system components. Virtual system modelling simulation in a top level application module in Proteus design suit employing terminal connection technique was used for the digital prototyping of a gravity adjustable infrared sensor interfaced with Arduino UNO board and a liquid crystal display for life fingerlings detection and counting. The schematic capture was implemented in intelligent schematic input system. A C compiler: Arduino 1.8.13 integrated development environment was used for the processes of both firmware development and firmware debugging of Arduino UNO (based on ATmega328P). The result of the digital prototyping shows that although the infrared detector based fingerlings counting model provided insight to the behaviour of a typical counter, it accuracy will be impaired in the case of two or more fingerlings simultaneously within the field of view. Further revealed is the need to include tracking of fingerlings as they move through the counting system.

Keywords: *Automation, Digital prototyping, Fingerlings counting system, Machine vision, Proteus design suit, Virtual system modelling simulation.*

1 INTRODUCTION

Fingerlings counting is simply a measurement of the number of fingerlings sold from hatchery or conversely, bought by fish farmer for stocking containers; ponds or cages. It is one of the important processes in aquaculture production which helps growers in accurate stocking, managing precise feeding strategies as well as in designing a marketing schedule. Traditionally, manual in Figure 1, counting table method in Figure 2, and volumetric method in Figure 3 are counting methods used in the process of counting fish fingerlings and are still adopted up till date in developing countries like Nigeria.

Figure 2: Counting Table Method of Fingerlings Counting

Figure 1: Manual Method of Fingerlings Counting

Figure 3: Volumetric Method of Fingerlings Counting

These traditional counting processes of fingerlings are prone to mistakes, occasional omission, stress, fatigue, infection and high mortality rates. On the contrary, vision provides a wealth of information about a process.Besides vision, the proposed counter is expected to think humanly (activities associated with human thinking including decision-making) and rationally (to perceive, reason, and act rightly) hence, requires a great level of computational intelligence (Russell and Norvig, 2010). The development of approximation (prototyping) of such intelligent agents by trial and error technique is not cost effective and therefore requires computer integrated technology for digital/virtual prototyping. computer integrated technology for design quickly and economically ascertain the effect of different system and process parameters on the outcome of a process, minimizes the number of experiments that need to be performed to determine the influence of various parameters on the safety and quality of the process and permit parametric analysis to understand the effect of different parameters in the system (Ulrich and Eppinger, 2015 and Krause *et al.,* 2001).This revised allocation of resources results in extensive analysis to guide product design and development iterations in the computer compared to making physical prototypes for one-factor at a time (OFAT) testing which is tremendously expensive (Ulrich and Eppinger, 2015; Halevi, 2001 and Krause *et al.,* 2001). Hence, virtual prototyping significantly reduce the time and cost of building a prototype at the product specification stage (Bullinger *et al.*, 2001). Efforts to improve product performance and quality can be achieved in significantly shorter time through the effective integration and implementation of computer-aided engineering analysis and associated manufacturing capabilities.

Computer/machine vision which is a fulcrum on which the proposed life fingerlings counting system is hinged is a relatively new technology in the field of artificial intelligence (a vision system that will have the capability of adapting to the changing world around it), which has much to offer in improving product quality and safety, as well as enhancing process efficiency and operational safety. Computer vision is the ability of the computer to see while machine vision is the application of computer vision in manufacturing and industry like aquaculture (Steger *et al.*, 2018). Furthermore, machine vision is the use of devices for optical non-contact sensing to automatically receive and interpret an image of a real scene in order to obtain information and/or control machines or processes (Batchelor and Whelan, 2002). Although machine vision and automated visual inspection are originally for industrial measurement and quality control in the technical and engineering sectors (Beyerer *et al.*, 2016), this non-destructive, non-contact method has been greatly advocated for use in aquaculture in the process of grading, sorting and counting (Xiong *et al.,* 2010 and Gümüş e*t al*., 2010). Although algorithms have been developed for fish counting using digital image processing technique (Aliyu *et al.*, 2017 and Le and Xu, 2016), including filtering-segmentation technique for automated counting of fish fingerlings (Coronel *et al*., 2018). Majority of these algorithms have been on underwater fish counting which is not appropriate for a confined system of fingerlings counting. Other challenges to this are the understanding of the platform and methods of implementing these algorithms for fingerlings counting evidenced in the dearth of fingerlings counting systems particularly in developing world. While acknowledging that several automated counting systems have been developed over the years in developed nations, studies however show that many of such systems are very rare to find in developing nations such as Nigeria. The development of automated fingerlings counter will minimise fingerlings losses to the hatchery operators and customers. It will also reduce the drudgery in the fingerlings counting process, and ultimately enable the fish farmer to manage his farm effectively, as the accurate number of healthy fingerlings can be ascertained.Consequently, digital prototyping will facilitate the understanding of the process of and fast track such development.Hence, this study aims at the digital prototyping and automation of life fingerling counting process in aquaculture production in Nigeria. To achieve this aim, the following objectives are to be pursued:

i. To develop the life fingerlings (foreground object) detection model for the life fingerlings counting system.

ii. To develop a virtual system modeling (VSM) simulation of infrared (IR) detector based life fingerlings counting system.

2 METHODOLOGY

The study involves the combination of diverse component to function as a device. Hence, system integration approach in systems engineering involving simulation modeling (BKCASE Editorial Board, 2015 and Muller, 2013), was employed. The principle of machine vision was used to detect the foreground object(life fingerlings) within the field of view, and this was processed by the ATmega328P based Arduino UNO for the counting operation and result displayed on a liquid crystal display LCD.

2.1 ARDUINO UNO DEVELOPMENT BOARD

Arduino is a widely used, open-source physical computing platform used for creating interactive devices that standalone or collaborate with software in the computer (Banzi and Shiloh, 2015). It consists of programmable hardware boards (Arduino Uno, Arduino Mega Arduino Yun, Arduino Pro mini, Arduino Due, MKR Vidor 4000 and others) and a software (integrated development environment).They are ATmega328P microcontroller based boards specifically designed to interact and manage input (sensors) and output (motors, lights, and all kinds of devices of various types) in real

time. Although there are many boards on Arduino platform, the Arduino Uno got many appreciations for its ease in projects. Furthermore, Arduino based program development environment is an easy way to write the program when compared to others. These boards add the electronics needed to use the pins as well as connect the pins on the chip to headers such that they are easier to access for prototyping hence, it use in this study.

2.2 ARDUINO UNO DEVELOPMENT BOARD

An integrated development environment (IDE) is a collection of computer programs used to create other computer programs (Osborne, 2017). The Arduino IDE used in this study is an open-source cross-platform application that is written in functions of C and C++ used to write and upload programs to Arduino compactable boards. Though the IDE seems simple, it provides the cross-compiling needed to get the code, written on a Linux, Windows, Mac OS X or Apple machine, to work on the much simpler AVC processor. The IDE supports the languages C and C++ using special rules of code structuring (Purdum, 2015). The Arduino IDE supplies a software library from the Wiring project, which provides many common input and output procedures. A computer program (model) written for Arduino with the Arduino IDE is called a sketch. User-written code only requires two basic functions, for starting the sketch and the main program loop, that are compiled and linked with a program stub *main()* into an executable cyclic executive program with the GNU (GNU's Not UNIX) toolchain, also included with the IDE distribution. The Arduino IDE employs the program AVRDUDE (AVR downloader uploader). AVRDUDE is a utility to download, upload and manipulate the ROM and EEPROM (electrically erasable programmable read-only memory) contents of Atmel AVR microcontrollers using the in-system programming technique (ISP).The Arduino IDE runs the sketch model to converts the executable code into a text file in hexadecimal (HEX file) encoding that will subsequently be loaded into the MCU by a programmer in the process of implementation (Banzi and Shiloh, 2015). However for this digital prototyping, the HEX file created after building the program (sketch) in Arduino IDE was uploaded into the Arduino UNO in Proteus ISIS for virtual system modelling simulation.

Virtual system modelling (VSM) simulation in a top level application module in Proteus 8 Professional v8.9 SPO design suit was used for the digital prototyping of the embedded system to enable automation.

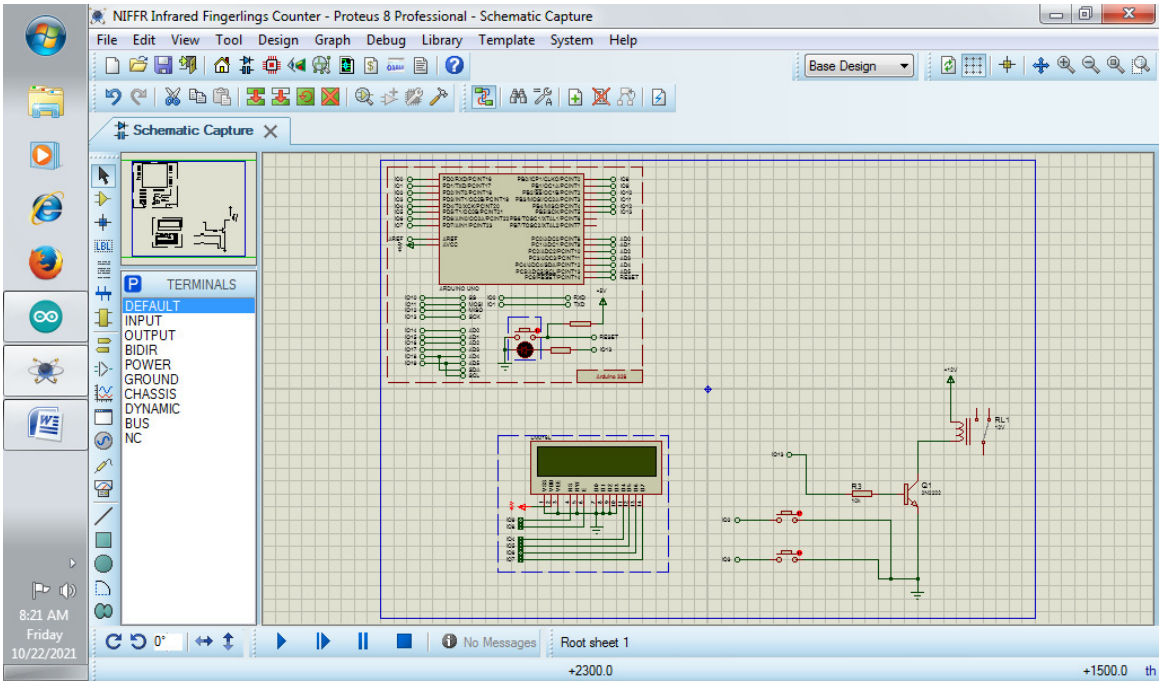

Figure 4: Schematics for Arduino Interface with Infrared and LCD for Life Fingerlings Counter

2.3 INFRARED (IR) DETECTOR BASEDLIFE FINGERLINGS COUNTING MODEL DEVELOPMENT

The complete sketch model in Arduino 1.8.13 IDE for ATmega328P MCU based Arduino UNO consist of four sections. The first section declares the library of the different drives by including the library code. These include the drive for the liquid crystal display and that of the servo motor. Thereafter, the LCD library is initialized with the numbers of the interface pins and then servo object is created to control the servo. The second section declares the integer and constant variables. The third section is the void setup( ){ } which is a declaration for a function called "setup". This exact line is required in every Arduino sketch ever. The void setup routing is technically a function that is created at the top of each program. Inside the curly brackets is the code that is expected to run one time as soon as the program starts running, after each power-up or reset of the MCU. It is used to initialize variables. The last section of the model is the void loop( ){ }. Like the setup line before it, void loop is yet another Arduino-sketch function that Arduino uses as a part of its structure. The code inside the loop function runs over and over (repeatedly) as long as the MCU is turned on. This is where the bulk of the Arduino sketch is executed. The program starts directly after the opening curly bracket ({), runs until it sees the closing curly bracket (}), and jumps back up to the first line in loop() and starts all over.

The 16×2 LCD is used to display the number of counted objects (life fingerling). Hence, the Liquid Crystal library enabled the use of the LCD.

The model begins by adding the header file for ***LiquidCrystal.h***

This is a preprocessor directive, whereas ***.h*** is a header file.

This was followed by marking the LCD next buttons.

Two form unsign integer variable ***fishcount*** and ***tfish***were specified and initially set to zero.

Two ***fishf*** and ***resetb*** variables were further defined as integer type.

First activated the lcd in the void setup function and enter ed the number of columns and rows. Since this is a 16×2 LCD (sixteen columns and two rows).

Use

the lcd to print a "***Tfish Current***" message. Since this is a n LCD of 16×2 (sixteen columns and two rows).

Use the lcd to print a message "***Tfish Current***."Action printing.

To print strings on the lcd, the lcd.print function was used.

Instead, turned on the Arduino's pin number 2 interrupt.

The Arduino pin number 2 was used for counting the fingerlings.

Finally use the function pinMode to tell the controller which pins are being used as input and which pins are being used as output.

3 RESULTS AND DISCUSSION

This section presents the results of the firmware development as well as the interactive simulations. The interactive simulation was used to see ifthe design works and how it works.

3.1 VSM SIMULATION OF INFRARED (IR)DETECTOR BASED LIFE FINGERLINGS COUNTING SYSTEM

Fig. 3 presents the Arduino 1.8.13 IDE (integrated development environment) user-friendly and intuitive environment for the development of the infrared fingerlings counter computer software (firmware).

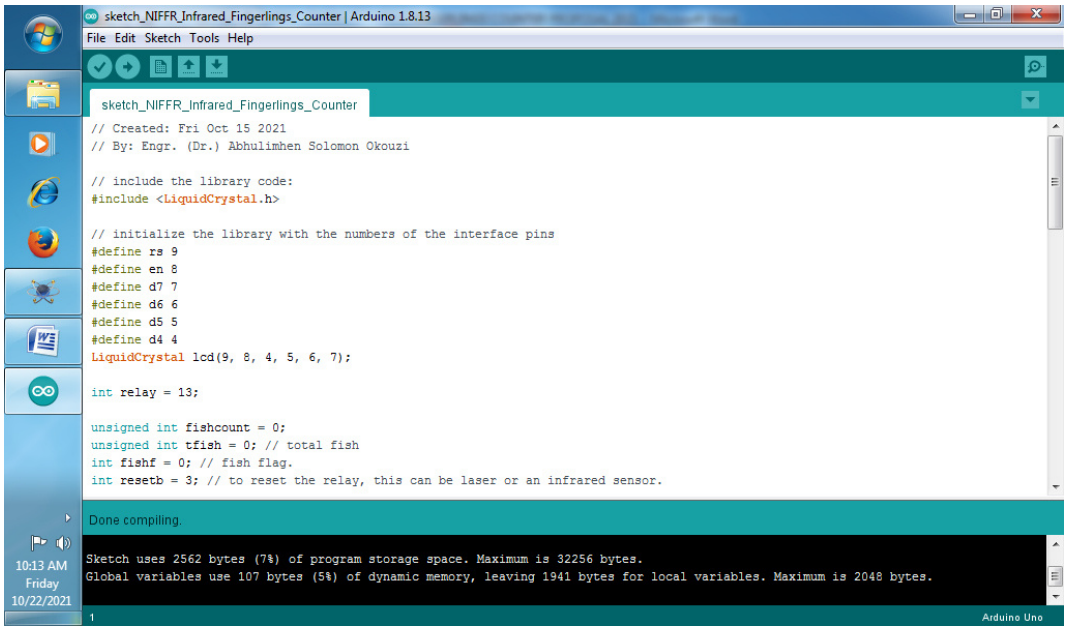

Figure 5: Arduino IDE Sketch Model of Infrared Fingerlings Counter

The sketch model showed in the progress bar that the compilation which follows the creation of the project and writing of the source code was successful.

Figure 6 presents the product brand name ***"NIFFR FINGERLING COUNTER"*** on the Liquid crystal display (LCD).

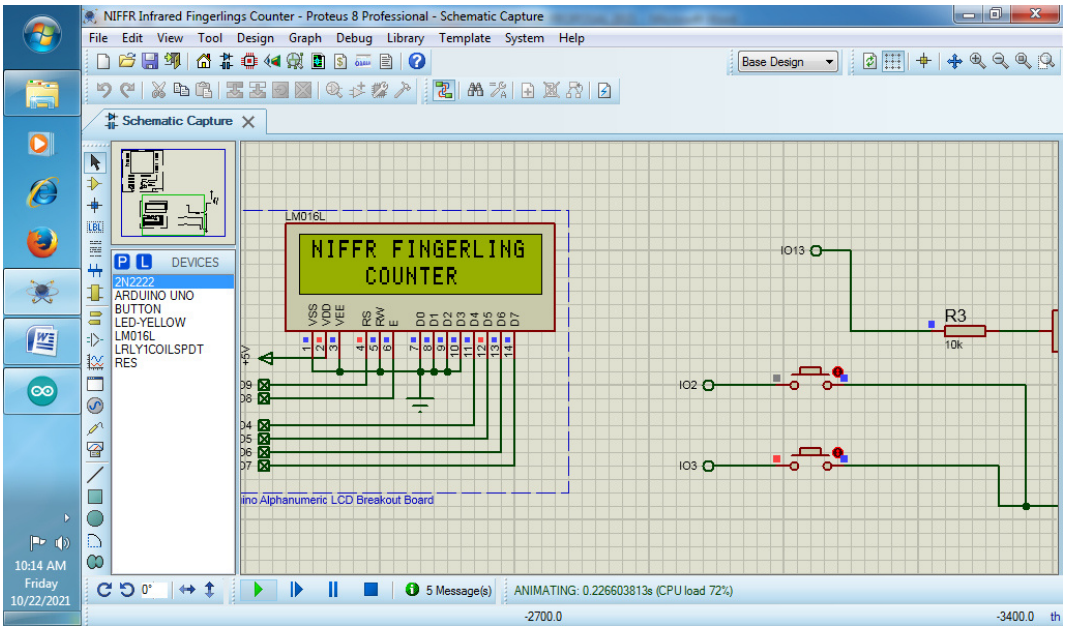

Figure 6: NIFFR Fingerlings Counter

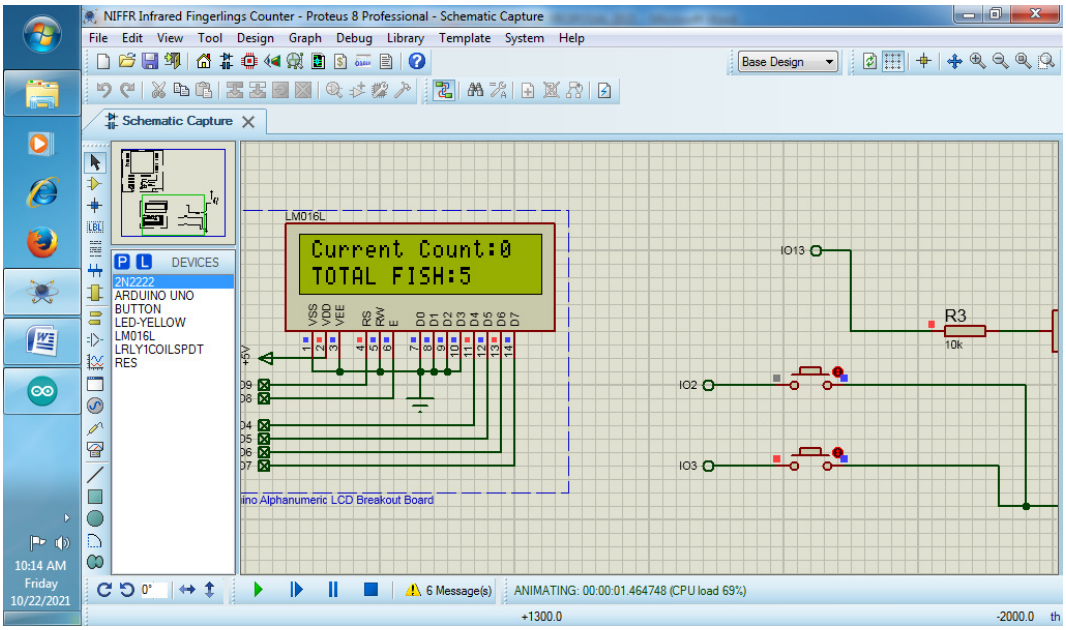

Figure 7: 5 Fingerlings Detected and Counted

Figure 7 to Figure 10 present the increment in the counter as it detects more fingerlings within the flow channel.

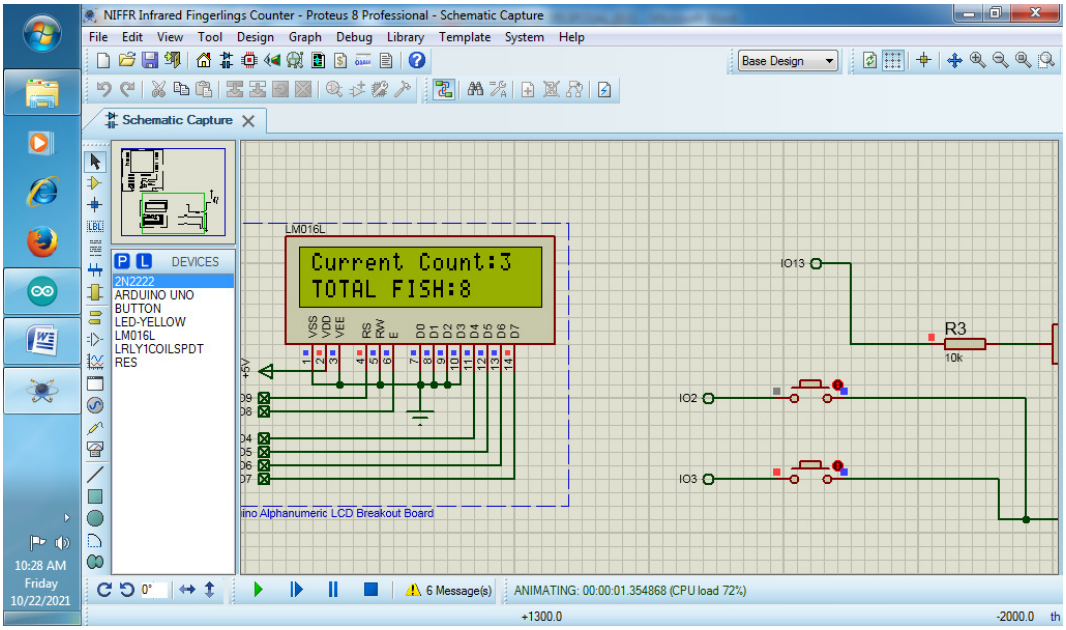

Figure 8: 3 Additional Fingerlings Detected and Count Increased to 8 Fingerlings

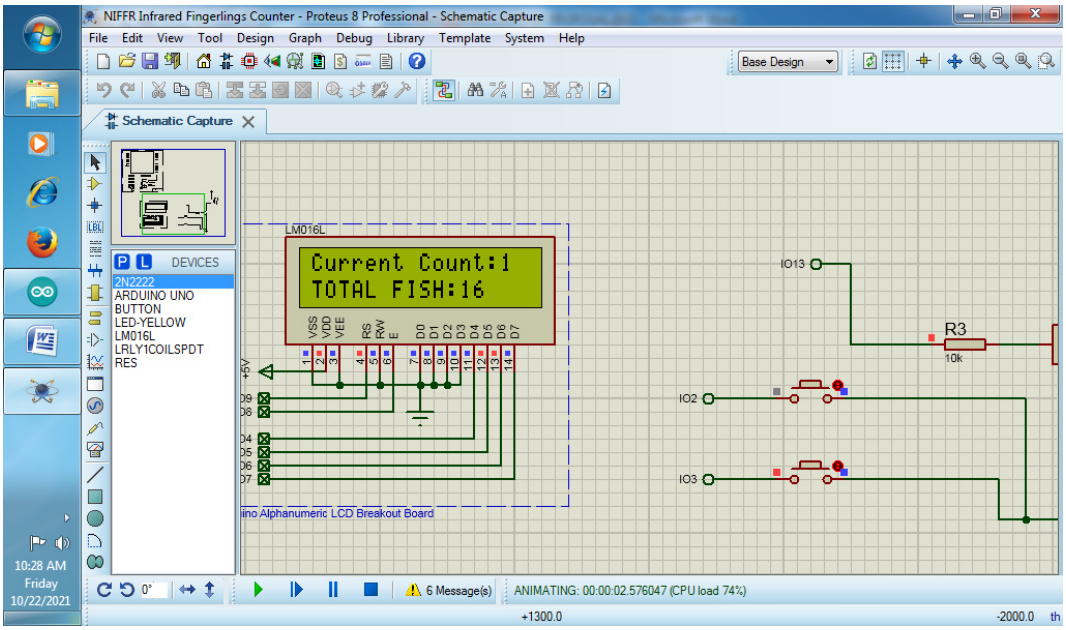

Figure 9: Total Detected Fingerlings Increased to 16

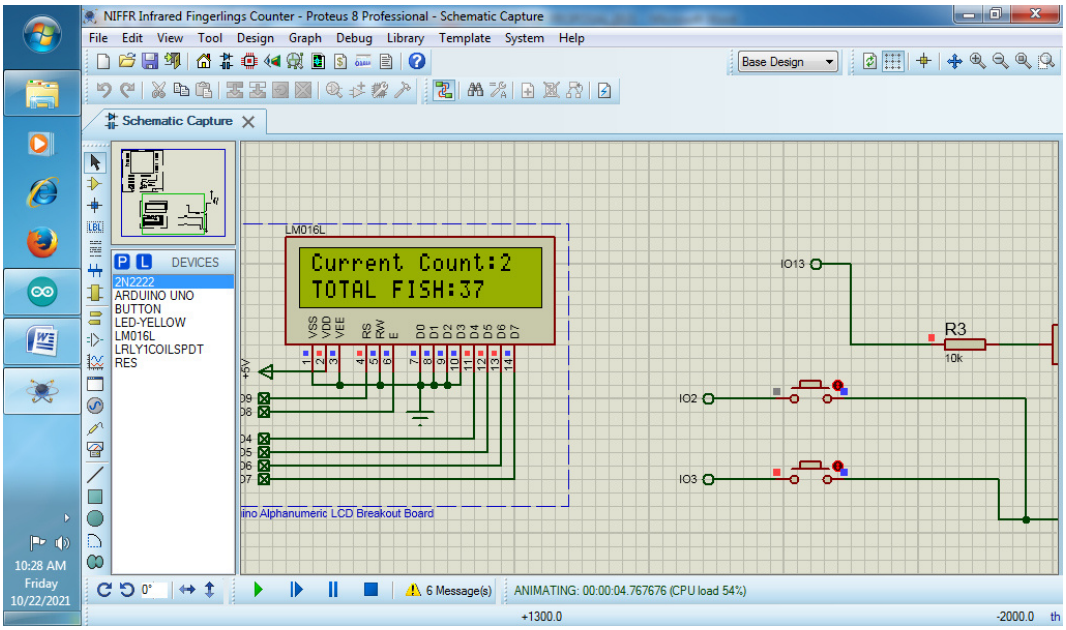

Figure 10: Total Detected Fingerlings Increased to 37

Activating the Arduino pin number 2 pushbutton is equivalent to the infrared detector detecting the fingerlings within the field of view.The active infrared detector represented by Arduino pin number 2 pushbutton consists of two LEDs (Tx and Rx): When voltage is applied across the terminal, the emitter Tx emit radiation continuously. If fingerling(s) is/are present on the field of view, the radiation is reflected by the fingerling(s).Consequently, the receiver Rx receives reflected radiation to register the fingerling(s) count detected else nothing is detected. A critical assessment of the system shows that when two or more objects

(fingerlings) are within the field of view, they are detected and counted as a single count. This was attributed to the fact that like majority of other sensors, the infrared detector based counter for the most part only provided binary (on/off) information and has limited use in generating control signal. This was observed to be a limitation of the system. The result further revealed that the life fingerlings counting system goes beyond object detection only, to include tracking of individual fingerlings as they move through the counting system

4 CONCLUSION

The digital prototyping with VSM simulation shows that although the infrared detector based fingerlings counting model provided insight to the behaviour of a typical object detector and counter in real-time, it accuracy will be impaired in the case of two or more fingerlings in the field of view.It could not process further the detected objects.This is because it was limited in generating control signal as it only provide binary information.Consequently, digital signal processing (DSP) originating from optical image formation and measurement methods to detect, track and count individual fingerling are recommended to further explore and understand the process of automated life fingerlings counting in aquaculture production.

5 REFERENCE

Aliyu, I., Gana, K.J., Musa, A.A., Agajo, J., Orire, A.M., Abiodun, F.T., and Adegboye, M.A. (2017). A Proposed Fish Counting Algorithm Using Digital Image Processing Technique, ATBU, *Journal of Science, Technology & Education (JOSTE)*; **5**(1), 11p.

Banzi, M and Shiloh, M. (2015). *Getting Started with Arduino*, 3rd Ed. Sebastopol CA: Maker Media, Inc.

Batchelor, B.G. and Whelan, P.F. (2002). *Intelligent Vision System for Industry*. London: Springer-Verleg.

Beyerer, J., León, F.P. and Frese, C. (2016). *Machine Vision - Automated Visual Inspection: Theory, Practice and Applications*, Berlin Heidelberg: Springer.

BKCASE Editorial Board (2015). *Guide to the Systems Engineering Body of Knowledge (SEBoK)*, v. 1.4, R.D. Adcock (Editor in Chief). Hoboken, NJ: Stevens Institute of Technology.

Bullinger, H. Breining, R. and Braun, M. (2001). Virtual Reality for Industrial Engineering. Application for Immersive Virtual Environment. In: G. Salvendy (ed.) *Handbook of Industrial Engineering, Technology and Operation Management*. 3rd ed. New York: John Wiley, pp. 2496-2520.

Coronel, L., Badoy, W. and Namoco, C. (2018). Identification of an Efficient Filtering-Segmentation Technique for Automated Counting of Fish Fingerlings.*The International Arab Journal of Information Technology*, 15(4), 708-714.

Forsyth, D., and Ponce, J. (2012). *Computer Vision: A Modern Approach*, 2nd ed. New Jersey: Pearson Education, Inc.

Gümüş, B., Balaban, M.O. and Ünlüsayın, M. (2011). Machine Vision Applications to Aquatic Foods: A Review, *Turkish Journal of Fisheries and Aquatic Sciences*. **11**, 171-181.

Halevi, G. (2001). *Handbook of Production Management Methods*. Oxford: Reed Educational and Professional Publishing.

Krause, F.L., Mertins, K., Edler, A., Heisig, P., Hoffmann, I. and Helmke, M. (2001). Computer Integrated Technologies and Knowledge Management. In: G. Salvendy (ed.) Handbook of Industrial Engineering, Technology and Operations Management. 3rd ed. New York: John Wiley, pp. 177-226.

Le, J. and Xu, L. (2016). An Automated Fish Counting Algorithm in Aquaculture Based on Image Processing. *Advances in Engineering Research, International Forum on Mechanical, Control and Automation*.113, 358-366.

Muller, G. (2013). Systems Engineering Research Methods.*Procedia Computer Science*. 16, 1092-1106.

Russell, S.J. and Norvig, P. (2010). *Artificial Intelligence: a Modern Approach*, 3rd ed. Upper Saddle River: Pearson Education Inc.

Ulrich, K.T. and Eppinger, S.D. (2015). *Product Design and Development*, 6th ed. New York: Irwin/McGraw Hill.

Xiong, G., Lee, D-J., Moon, K.R. and Lane, R.M. (2010). Shape Similarity Measure using Turn Angle Cross-Correlation for Oyster Quality Evaluation. *Journal of Food Engineering*, **100**, 178-186.

Zion, B. (2012). The Use of Computer Vision Technologies in Aquaculture: A Review. *Computers and Electronics in Agriculture*, **88**, 125-132.

4th International Engineering Conference (IEC 2022)
Federal University of Technology, Minna, Nigeria

Resource Allocation and Management in Machine-to-Machine (M2M) Communication in Underlay In-Band Cellular Network: A Survey

*Suleiman, A. D[1], Mohammed, A. S[2], Salihu, B. A[3], & David, M[4].,
[1] Department of Computer Engineering, Federal Polytechnic Ilaro, PMB 50 Ilaro Ogun State, Nigeria
[2,3&4] Department Telecommunication Engineering, Federal University of Technology, PMB 65 Minna Niger State, Nigeria
*Corresponding author email:ahmed.suleiman@federalpolyilaro.edu.ng +2348080329807

The adoption of 5G network standard as the next futuristic network has dynamically shaped the path for new features in communication standards, with support for integration of variegated device with different service Quality-of-service requirements. The tends to support massive connectivity of devices with delay tolerant requirements and specific quality of service requirement which also support various Internet-of-Things (IoTs), Device-to-Device (D2D) Communication, Machine-to-Machine (M2M) Communications and several other applications. M2M communication when underlaid with cellular communications are faced with compromising challenges when integrated into cellular networks. Due to their proximity in close location, the M2M user devices can communicate with one another without utilizing the Base Station and this enhances the spectral efficiency, reduces in the latency, energy efficiency and several benefits of M2M communications. However, there are more impending challenges which can compromise the benefits of M2M, these includes interference, resource allocation problem and power control challenges. These challenges tend to degrade the performance efficiency gain of the integration of M2M into cellular network. The purpose of this paper is to give an overview of some of the methods and approaches. and provide some insight to the open issue that are affecting resource allocation in M2M underlaid in a cellular network.

Keywords: *5G, Machine-to-Machine (M2M) Communication, Resource Allocation, Spectrum, Power, Interference*

1 INTRODUCTION

The next generation of wireless network 5G and beyond has been designed with the peculiarity of improving the system capacity, reducing the latency, performance enhancement relative to spectral efficiency, energy efficiency, reliability improvement based on the stringent requirements of specific applications(Saied, 2021). With consideration on the exponential rise in number of portable devices, the density of such communication devices will sprout the exchanging of large volume of data and information including multimedia data whose control and management of the traffic is sole the responsibility of the core network (Zeb et al., 2021). However, this ever-growing need necessitate for a network which can support the high data rate requirements, high mobility, dynamic flexibility, massive connectivity and wider bandwidth that supports the various service requirement with lowest possible latency or delay, the scarcity of spectral resources is not sufficient to meet the high-speed connectivity and reliability offered by the current 4G or convectional cellular, which necessitate the novel 5G architecture (Dejen et al., 2022). Machine-to-Machine (M2M) communication has been envisioned to satisfy the broad and complex need of the next generation standard, and it is being investigated as one of the new technologies that will support and meet the ever-growing need of the 5G standard. Massive number of devices connected together to autonomous communicate among themselves is referred to Machine-to-Machine Communication (Singh et al., 2021). In M2M communications, two or more wireless machines can communicate in close proximity directly with (In-band M2M communication/ licensed spectrum) or without (Out-band M2M communication / Unlicensed spectrum) the influence of the Base Station (BS) as shown in Fig 1.

In accordance with 5G network standards, M2M communication allows two users to connect directly over a shared channel without the need for a base station. Although users can utilize other devices to relay signals to each other if they are beyond the range of each other's transmissions. Additionally, an M2M pair connects with one another by building an M2M link, whereas a cellular connection is generated when a cellular user connects with a BS. M2M links utilise the same uplink channel resource as the cellular link in an M2M underlaid with cellular network (Krishna & Hossain, 2020). Keeping in mind that each link must be given enough power for each transmitter so that it can connect with its receiver despite background other links utilising the same channel can cause a lot of noise and interference. In addition, the signal-to-interference plus noise ratio (SINR) criteria for the receiver link must be satisfied by the transmitter's authorised power. Depending on the required data rate,

each link needs a specific degree of SINR. Cellular link can utilized only one particular channel under a BS, but if each link sharing the channel has the required SINR, many M2M links may share a cellular channel (Ghosal & Ghosh, 2021).

The scalable nature of M2M, coverage area and its IP connectivity, the use of Optimistic technology Long-Term Evolution (LTE)/Long-Term Evolution Advance (LTE-A) can support the different and stringent peculiarities of M2M communications. Its adoption in variegated areas of endeavour includes but not limited to industrial automation (North & Muniraj, 2021), telemetry (Lo *et al.*, 2013), Supervisory Control and Data Acquisition (SCADA)(Verma *et al.*, 2016), and many more. Some of the developmental factors that attracted attention regarding the aspect of M2M communication comprises of privacy and security related issues, device enhancement capacity, high-end- application requirements and coverage improvement.

However, the unique characteristics of M2M communication device distinguishes it from its counterpart Human-to-Human (H2H) communication that employs the conventional cellular network. This includes the peculiarity of massive M2M data that is been generated from massive connected devices, and the periodic nature of the packet generation which is specifically event-driven (Xia *et al.*, 2020). Furthermore, the frequency of the data generated is relatively high in comparison to the small data size, which have found application in wide range of delay tolerant and throughput required use cases. Consequently, M2M communication classically consist of burst data with variegated set of Quality of Service (QoS) requirements different from its H2H counterpart made up of low bandwidth data. Predominantly, the M2M communication is uplink-based which simultaneous compete with the uplink traffic of H2H communication resulting into interference and radio resource management problems (Alhussien & Gulliver, 2020). However, some critical problems associated with integrating or underlaying the M2M communication into cellular networks include but not limited to: issues with decision-making criterion for radio resource management (Song *et al.*, 2020), coordination of interference (Siddiqui *et al.*, 2021), power management allocation (Sobhi-givi *et al.*, 2020), and mode selection issues (Ahmad *et al.*, 2022) as illustrated in the Fig. 2. This integration compromises the ability to maximize the gain of integrating the M2M communication into cellular networks via spectral degradation, if improper resource allocations that guarantee reliability, high data rate and enhance spectral efficiency are not optimally utilized.

The imperative of resource allocation entails that multiple network requirements are intelligently and dynamically assigned swiftly. The resources assigned in include power control, bandwidth distribution, rollout strategies, and association distribution in 5G (Kamal *et al.*, 2021). Thus, the efficient allocation of spectral resources reduces the influence of co-tier interference within network assisted communication, thereby improving the spectral efficiency with enhance network throughput, the cell coverage area is increased and the ultra-low latency is achieved. Consequently, the inefficient extraneous power allocation from neighbouring cells results into cross-tier interference which is resultant from two possible factors, firstly, the transmitter power is not limited within the nominal frequency range hence the spectrum of the generated signal may extend over large frequency range and secondly, at the receiver end, the radiation from the desired channel is suppressed insufficiently by receiver filter and in turn passed as interferences in the demodulator. In-band M2M communication's main advantage is an increase in the cellular network's spectral efficiency, but the monumental drawback that characterize the in-band model entails the high computational overhead that the BS and yet the severity of interference.

2 RELATED WORKS

The issues surrounding the problem of resource allocation in M2M communication have be studied by several authors considering the different perspective the situation needed to be tackled from. In a study conducted by Ghosal & Ghosh, (2021), which considered the underlaid setting, both cellular and D2D users may obstruct one another when they are using the same channel resources. In an effort to lessen the interference issue, the authors proposed to jointly tackle the channel and power allocation problem in a design that combines the pairing of one cellular link with numerous D2D links. However, the strategy adopted proved effective in terms of cost and energy efficiency, but however, the study was limited due to the multiple of D2D users that can reuse a single cellular link thereby imposing co-tier interference and also resulting in resource scheduling problem. It may have been more illustrative to broaden but not limit the number of reusable cellular links to a single link to be reused by D2D pairs.

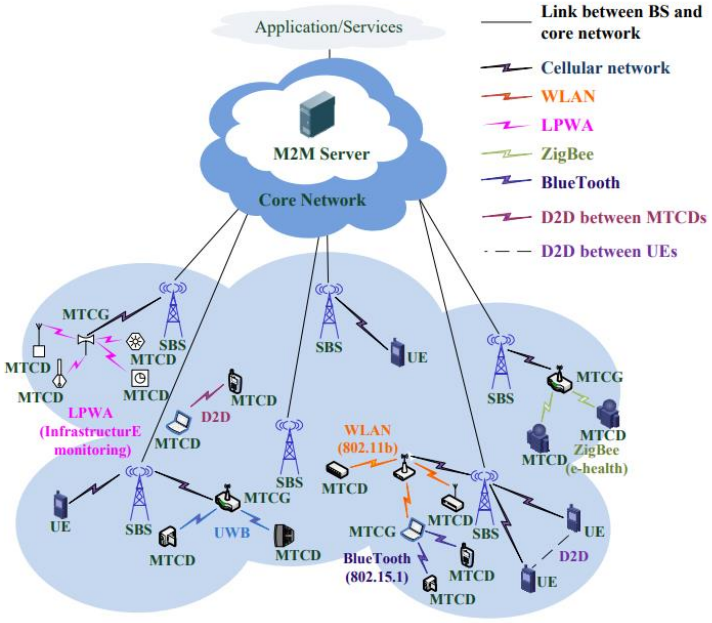

Fig.1 Topology of M2M communication in UDNs, where SBS, UE and MTCD represents small cell base station, user equipment for both H2H and M2M Communications in cellular network, M2M device, and M2M gateway, respectively (Chen *et al.*, 2017)

Furthermore, in enhancing the spectral resource allocation in Hetnets with consideration in an ultra-dense network, the influence of interference degrading system throughput was studied. However, Zhao *et al.*, (2015) proposed an enhanced spectrum allocation algorithm with consideration of user's rate demand in heterogenous network. The study was limited in terms of its consideration to two-tier network without taking into account other communicating M2M devices that do not utilize the cellular spectrum. This was significant because it improved the system throughput while equally guaranteeing the user fairness. Moreso, nature inspired resource allocation techniques which utilises Bee colony algorithm coupled with artificial intelligent was proposed by (Llerena & Gondim, 2020). Considering the impact of social relationships in the midst, the study's emphasis on M2M users in a socially responsible radio resource allocation, the algorithm can also predict how many M2M users will be admitted into the cellular network. Hence, the proposed approach made a strong effort to actively maintain the weighted system throughput while simultaneously attempting to meet the QoS criteria for both the M2M underlaid and cellular users. Despite the improved performance which show significant achievement over similar greedy algorithms improving the reusability factor, the proposed algorithm was limited in its consideration with respect to the use of few performance parameter and the mobility of the M2M users was not considered. Similar research was done on the issue of resource allocation with regard to power allocation, energy efficiency, and resource block assignment, Jameel *et al.*, (2020) based its assumptions that the resource allocation performed with regards to energy efficiency is based on the greedy algorithm method which on the long run causes system performance degradation. However, based on the limitation, a dynamic wireless power transmission and resource strategy was proposed, this technique dynamically improved the power level and system resources based on dynamic reconfiguration. This achievement account for the high trade-off between the power and capacity with adequate priority to Quality of Service (QoS) requirement. The study will have found more applicable usage if it had broadened its scope to further considered the interference problem. Table 1 highlights some of the important KPIs used to evaluate the performance of some resource allocation techniques. Also, the issue of power consumption reduction and energy efficiency improvement for multi-pair D2D communication in underlying cellular networks was studied by Hashad *et al.*, (2020). Resource allocation problem was modelled into a complex mixed integer.

TABLE 1: PARAMETERS OF EVALUATION

	SNR	Latency	Packet Loss	Throughput	Energy Efficiency	Resource Block	Fairness	Average Use Demand	Access Rate	Overhead	Spectrum Reuse factor	Outrage Probability	Power Consumption	Reliability	Ergodic Capacity	Overhead
(Ghosal & Ghosh, 2021)			*	*												
(Jameel *et al.*, 2020)					*	*										
(Zhao *et al.*, 2015)				*			*	*								
(Llerena & Gondim, 2020)				*					*							*
Wang *et al.*, 2021)											*					
(Zeb *et al.*, 2021)											*	*			*	
(Ruan *et al.*, 2020)		*														
(Hashad *et al.*, 2020)	*			*	*				*							
Hussein *et al.*, (2021)											*					

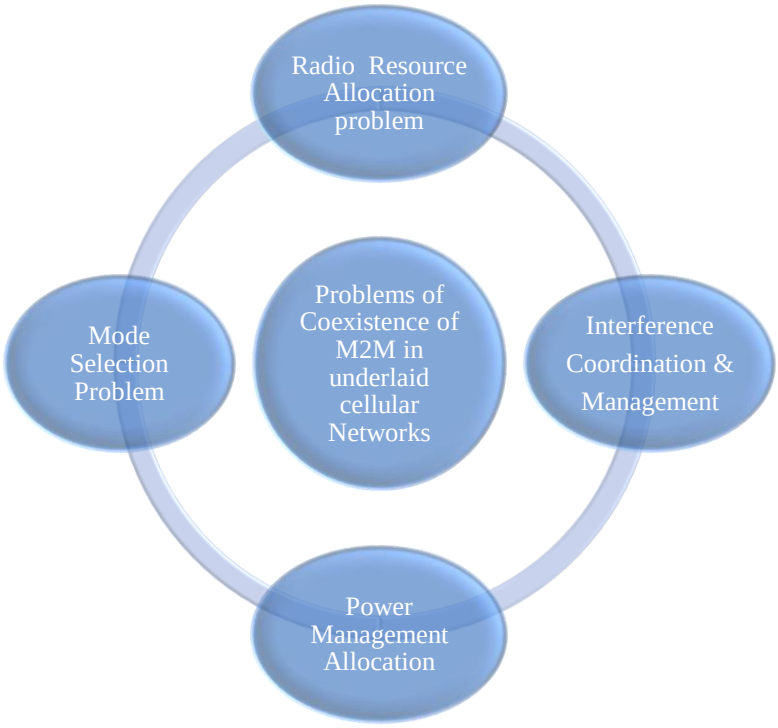

Fig 2: Problems of Coexistence of M2M in underlaid Cellular Networks

Resource allocation problem was modelled into a complex mixed integer problem which is associated with interference mitigation techniques. However, the application of convex optimization method complicated the possibility to attaining a global solution to the problem. Also, this can be improved upon by ensuring the successful decoding at the receiver and effective utilization of network resources which entail creating a balance between adequate interference management and resource allocation. To cut back on overall power consumption, a primal-dual algorithm was presented. A non-linear fractional programming technique was then used to further construct a second primal-dual algorithm, which was used to maximise energy efficiency. In relation to the efficacy of the strategy, Hashad *et al.,* (2020) proved that maximizing the available energy will decrease the transmission power. Additionally, these results demonstrated that efficient resource allocation will enhance both spectral efficiency and energy efficiency. However, the study was limited in scope as its focused on multi- pair M2M.

Current Long-Term Evolution's (LTE) limitations relative to the diverse needs of 5G services' users and applications and the necessity to radically enhance the massive adoption on massive Machine-Type Communication (mMTC) use cases that support widespread connection and a variety of QoS requirements. Sadi *et al.,* (2020)on the basis of the restriction of maximising the spectral efficiency and traffic demand of mMTC devices, research was conducted into the radio resource allocation for mMTC and the allocation of resources in a semi-persistent manner was demonstrated. The study demonstrated significant improvement in the spectral efficiency but however, the power and interference problem were not considered.

In the wireless network, the closeness of the various M2M users enhances user dependability, traffic offloading, greater throughput, delayed time, spectral efficiency, and energy efficiency, which is not achievable with standard cellular connection (Rathi & Gupta, 2021). The better re-utilization of radio of cellular network communication will unequivocally ensure that management of radio spectrum and reduction in communication delay can be guaranteed provided the challenges associated with resource management, such as throughput issues, interference issues and several other; are surmounted.

2.1 Open Issues

The issue of resource allocation is marred with a lot of challenges which ranges from interference due to spectral reuse of resources. This causes the issue of interference that result from co-channel interference and the

heterogeneity based on the ultra-density of so many devices. Equally, the user density also sprouts out the pairing issues based on the cluster and density of the user, this create serious challenges that arise in term of creating communication links and sending acknowledgement between devices. Furthermore, the connection issues can affect the budget link in respect of creating an effective and reliable communication between the cellular and M2M devices, as several factors such as fading both slow and fast fading resulting from variation of distance relative to the servicing BS and the M2M devices (Azari & Masoudi, 2021). In addition, the path loss factor also affects the rate of fading and the in-depth interference. Another point of concern, is the problem of mode selection, as its concern the requirements for the use of cellular link or the M2M communication link in the transfer of data considering the distance. Concerns are being raised regarding the quality of key parameters Indicators (KPIs) with their pre-defined threshold.

In addition, the stringent requirements of M2M communication such as having low memory, reduced energy use and minimal processing overhead. Based on the low power nature of the M2M devices, optimizing the power consumption is a serious challenge that has to be overcomed. The underlay communication involving the cellular BS and the low powered M2M consumes more power due to the necessity of frequent communication, acknowledgment and synchronization between the BS and the M2M.

CONCLUSION

The adoption of 5G standard has bring about new challenges, with respect to application requirements, QoS and open new areas of application that are different from the current LTE standards. These standards have created new challenges based on the massive integration of several devices within the cellular networks. Challenges ranging from interference mitigation, resources allocation and power control are the most prominent since that have high propensity to degrade a cellular network capacity and links. This paper has surveyed and highlighted some of challenges and techniques that have been employed to mitigate the compromising situation of resource allocation with respect to the 5G standards.

REFERENCES

Ahmad, T., Chai, R., Adnan, M., & Chen, Q. (2022). Low-Complexity Heuristic Algorithm for Power Allocation and Access Mode Selection in M2M Networks. *IEEE Internet of Things Journal*, *9*(2), 1095–1108. https://doi.org/10.1109/JIOT.2021.3079213

Alhussien, N., & Gulliver, T. A. (2020). Optimal Resource Allocation in Cellular Networks with H2H / M2M Co-Existence. *IEEE Transactions on Vehicular Technology*, *9545*, 1–13. https://doi.org/10.1109/TVT.2020.3016239

Azari, A., & Masoudi, M. (2021). Interference management for coexisting Internet of Things networks over unlicensed spectrum. *Ad Hoc Networks*, *120*(June), 102539. https://doi.org/10.1016/j.adhoc.2021.102539

Chen, S., Ma, R., Chen, H., Zhang, H., Meng, W., & Liu, J. (2017). Machine-to-Machine Communications in Ultra-Dense Networks – A Survey. *IEEE Communications Surveys & Tutorials*, *19*(3), 1478–1503. https://doi.org/10.1109/COMST.2017.2678518

Dejen, A. A., Wondie, Y., & Förster, A. (2022). Survey on D2D Resource Scheduling and Power Control Techniques : State-of-art and Challenges. *EAI Endorsed Transactions on Mobile Communications and Applications Research*, *7*(21), 1–30. https://doi.org/10.4108/eai.4-5-2022.173977

Ghosal, S., & Ghosh, S. C. (2021). A randomized algorithm for joint power and channel allocation in 5G D2D. *Computer Communications*, *179*(2021), 22–34. https://doi.org/10.1016/j.comcom.2021.07.018

Hashad, O., Fouda, M. M., Eldien, A. S., Mohammed, E. M., & Elhalawany, B. M. (2020). Resources Allocation in Underlay Device- to-Device Communications Networks : A Reduced-Constraints Approach. *IEEE Access*, *8*, 228891–228904. https://doi.org/10.1109/ACCESS.2020.3046417

Jameel, F., Khan, W. U., Kumar, N., & Riku, J. (2020). Efficient Power-Splitting and Resource Allocation for Cellular V2X Communications. *IEEE Transactions on Intelligent Transportation Systems*, *22*(6), 3547–3556. https://doi.org/10.1109/TITS.2020.3001682

Kamal, M. A., Raza, H. W., Alam, M. M., Su'ud, M. M., & Sajak, A. binti A. B. (2021). Resource Allocation Schemes for 5G Network : A Systematic Review. *Sensors*, *21*(6588), 1–45.

Krishna, S., & Hossain, F. (2020). A location-aware power control mechanism for interference mitigation in M2M communications over cellular networks. *Computers and Electrical Engineering*, *88*(March), 106867.

https://doi.org/10.1016/j.compeleceng.2020.106867

Llerena, Y. P., & Gondim, P. R. L. (2020). Social-aware spectrum sharing for D2D communication by artificial bee colony optimization. *Computer Networks*, *183*, 107581. https://doi.org/10.1016/j.comnet.2020.107581

Lo, A., Law, Y. W., & Jacobsson, M. (2013). A Cellular - Centric Service Architecture for Machine - to - Machine (M2M) Communications. *IEEE Wireless Communications*, *20*(5), 143–151. https://doi.org/10.1109/MWC.2013.6664485

North, S. M. E., & Muniraj, P. (2021). ScienceDirect ScienceDirect ScienceDirect. *Procedia Manufacturing*, *53*, 52–58. https://doi.org/10.1016/j.promfg.2021.06.009

Rathi, R., & Gupta, N. (2021). Game theoretic and non-game theoretic resource allocation approaches for D2D communication. *Ain Shams Engineering Journal*, *12*(2), 2385–2393. https://doi.org/10.1016/j.asej.2020.09.029

Sadi, Y., Erkucuk, S., & Panayirci, E. (2020). Flexible Physical Layer based Resource Allocation for Machine Type Communications Towards 6G. *2020 2nd 6G Wireless Summit (6G SUMMIT)*, *16*, 1–5. https://doi.org/10.1109/6GSUMMIT49458.2020.9083921

Saied, A. (2021). *Resource Allocation Management of D2D Communications in Cellular Networks*. Concordia University.

Siddiqui, U. A. M., Qamar, F., Ahmed, F., Nguyen, Q. N., & Hassan, R. (2021). Interference Management in 5G and Beyond Network : Requirements , Challenges and Future Directions. *IEEE Access*, *9*, 68932–68965. https://doi.org/10.1109/ACCESS.2021.3073543

Singh, U., Dua, A., Tanwar, S., Kumar, N., & Alazab, M. (2021). A Survey on LTE / LTE-A Radio Resource Allocation Techniques for Machine-to-Machine Communication for B5G Networks. *IEEE Access*, *9*, 107976–107997. https://doi.org/10.1109/ACCESS.2021.3100541

Sobhi-givi, S., Shayesteh, M. G., & Kalbkhani, H. (2020). Energy-Efficient Power Allocation and User Selection for mmWave-NOMA Transmission in M2M Communications Underlaying Cellular Heterogeneous Networks. *IEEE Transactions on Vehicular Technology*, *69*(6), 1–17. https://doi.org/10.1109/TVT.2020.3003062

Song, Q., Nuaymi, L., & Lagrange, X. (2020). Survey of radio resource management issues and proposals for energy-efficient cellular networks that will cover billions of machines. *EURASIP Journal on Wireless Communications and Networking*, *2016*. https://doi.org/10.1186/s13638-016-0636-y

Verma, P. K., Verma, R., Prakash, A., Agrawal, A., Naik, K., Tripathi, R., Khalifa, T., Alsabaan, M., Abdelkader, T., & Abogharaf, A. (2016). Machine-to-Machine (M2M) communications : A survey. *Applications, Journal of Network and Computer*, *66*, 83–105. https://doi.org/10.1016/j.jnca.2016.02.016

Xia, N., Chen, H., & Yang, C. (2020). Radio Resource Management in Machine-to-Machine communications -A Survey. *IEEE Communications Surveys & Tutorials*, *20*(1), 1–39. https://doi.org/10.1109/COMST.2017.2765344

Zeb, J., Hassan, A., & Nisar, M. D. (2021). Joint power and spectrum allocation for D2D communication overlaying cellular networks. *Computer Networks*, *184*(2021), 107683. https://doi.org/10.1016/j.comnet.2020.107683

Zhao, L., Zhao, H., & Huo, G. (2015). An enhanced spectrum resource allocation algorithm in Hetnets. *China Communications*, *12*(10), 182–192. https://doi.org/10.1109/CC.2015.7315069

4th International Engineering Conference (IEC 2022)
Federal University of Technology, Minna, Nigeria

EQUILIBRIUM ADSORPTION ISOTHERM OF METHYLENE BLUE AND RHODAMINE B USING SHEA BUTTER LEAVES AS A LOW COST ADSORBENT

***Shehu, A[1], Ibrahim, M. B[2]. and Ayuba, B[3]**

[1]Departments of General Studies Federal College of Agricultural Produce Technology, Kano
[2]Department of Pure and Industrial Chemistry, Bayero University, P.M.B3011, Kano-Nigeria
[3]Departments of Lab. Science technology Federal College of Agricultural Produce Technology, Kano
***Correspondent author**akchemist88@gmail.com , +2348167606150

ABSTRACT
Removal of the cationic dyes Methylene blue (MB) and Rhodamine B (RhB) by *Vitellaria paradoxa* Activated Carbon (VPAC) was studied as a new low-cost adsorbent. FTIR characterization revealed various functional groups. The effects of operating parameters such as contact time, adsorbent dose, pH, initial concentration and particle were investigated for the removal of MB and RhB dye using VPAC.
The maximum adsorption of MB and RhB dye onto VPAC was at pH 6 of contact time 60min and pH 7 of contact time 80min. The adsorption equilibrium data were tested by applying the Langmuir, Freundlich,Temkin and Dubinin-Radushkevic. It is observed that the Langmuir isotherm model fitted better than the other isotherm models with K_L = -0.1047 L/mg, R_L= 9.139 and R^2 = 0.9696 for MB while K_L = -0.0518L/mg, R_L= 1.0373 and R^2 = 0.9688 for RhB indicating monolayer adsorption at all studied parameters.

Key words; Adsorption, equilibrium, isotherm and *Vitellaria Paradoxa* .

1 INTRODUCTION

Dyes are complex chemical substances that bear stable aromatic rings synthesized to impart strong and persistent colour that does not degrade on exposure to light (Ibrahim and Sani 2014). Generally Dye pollutants present in aqueous systems pose serious threat to the environment recipient. In particular, basic dyes such as malachite green are very difficult to remove due to the presence of aromatic and various functional groups which confer stability to the dye molecules (Mao *et al*., 2008). Intensely colored effluents from textile, leather, cosmetics, paper and allied industries enter precious water resources deteriorating their quality and consequently intensifying toxicity (Sharma *et al*., 2017). Hence, the removal of these toxic substances has a significant role in curtailing water pollution. The hazardous effects of Methylene Blue and Rhodamine B (MB and RhB) have been reported by numerous studies. It is extremely hazardous to mammalian cells and has been identified as a liver tumour promoter (Azaman *et al*., 2018). MB and RhB causes toxicity to respiratory system and damages fertility systems in humans; and is a well-known carcinogenic, mutagenic, and teratogenic substance. Moreover, MB and RhB resistivity to light and reduction due to oxidizing agents are very high. It inflicts lesions on the lungs, skin, eyes, and bones. MB and RhB also causes damage to the liver, brain, spleen, kidney and heart (Raval *et al*., 2017). Therefore, the removal of MB and RhB from effluent before been disposed into the waterways is a management serious concern (Tongpoothorn *et al*., 2019). Both incineration and land disposal represent likely alternatives for final discard of spent adsorbent material. However, these methods directly or indirectly pollute the environment. Thus, exploring the regeneration and re-use of exhausted adsorbents is imperative to make the adsorption process environmentally friendly and cost-effective. A number of regeneration methods such as chemical, thermal, steam, ultrasound, ozone, oxidative, vacuum, microwave and bioregeneration have been employed to retain the adsorption capacity of spent adsorbents (Momina *et al*., 2018).

Viteleria Paradoxa leaves Activated carbon may be utilized as a potentially low-cost and effective adsorbent. The production of activated carbon needs higher temperature and additional activation process. A few studies have been reported on removal of dyes on using *Vitellaria paradoxa* seed as adsorbent.

2 MATERIALS AND METHODS

Methylene Blue and Rhodamine B dye (purity = 99%) were obtained from E. Merck (Mumbai, India). All other reagents used were of analytical grade. Distilled water was used throughout for the preparation of stock and experimental solutions. MB and RhB stock solution was prepared at 1000 mg dm^{-3} using distilled water and diluted to the desired concentration for each experiment. Solutions were adjusted to desired pH using 0.1 M NaOH or HCl. *Vitellaria paradoxa* leaves were obtained from Borgu local Government in New Bussa town, Niger state. The preparation of the NaOH activated carbon (VPAC) was largely guided by the method described by Wang *et al*. (2014), using a two-step chemical activation technique. The carbonized VPL powder (50g each) was impregnated with 50% (w/w) NaOH to the ratio of the weight of the activating agent and the precursor is 1:1. The impregnated samples was then left to dry in an oven overnight at 100^0C for 12 hours. The activated carbon obtained was washed severally first with 250ml of 0.1M HCl and then with distilled water until a neutral pH is attained. It was finally dried in an oven and then stored in air tight containers for further application.

2.1 BATCH ADSORPTION STUDIES

Batch adsorption study was carried out by varying all the parameters one by one keeping the rest of the parameters constant. As a general methodology, a known amount of adsorbent was added in specified volume of adsorbate solution. In each step of the study, one parameter was optimized and used in the rest of the steps. After adsorption in each step, the solution contents were filtered. After filtration, the residual concentration of MB and RhB was measured by a UV–VIS spectrophotometer (Perkin Elmer model) at pre-optimized wavelength. The extent of adsorbate adsorption was represented by adsorption capacity (q_e). The amount of adsorbate adsorbed at equilibrium was calculated by using the following equations:

$$qe = (\frac{Co - Ce}{m})V \text{.....1}$$

Where;

q_e = adsorption capacity (solid phase concentration of adsorbate on the adsorbent) (mg g^{-1}), C_o = initial concentration of adsorbate (mg L^{-1}), C_e = concentration of adsorbate at equilibrium (mg L^{-1}), C_t = concentration of adsorbate at time t (mg L^{-1}), V = initial volume of adsorbate solution (L), m = mass of the adsorbent (g)

2.1.1 Contact Time

Equilibrium time was investigated using (100mg/l for MB; 100mg/l for RhB, 50ml each) taken in different Erlenmeyer flasks and marked as 1, 2, 3, and so on. A fixed amount of adsorbent (0.1g) was added to each flask and allowed to stir for varying time period. For instance, the flask number 1 was removed from the top of orbital shaker after 20min; flask number 2 was removed after 40min and so on for all the flasks with 20min interval.

2.1.2 Dosage

Adsorbate solution (100mg/l for MB; 100mg/l for RhB, 50ml each) was taken in different Erlenmeyer flasks and marked as 1, 2, 3, and so on. Different amounts of adsorbent (0.1g, 0.2g, 0.3g and so on) was added to the flask number 1, 2, 3, and so on, respectively. The contents of the flasks were allowed to shake using orbital shaker for a predefined time and at constant agitation speed (200 rpm). After the completion of time, the flask contents were filtered and subjected to analysis.

2.1.3 pH of Solution

The effect of pH on the adsorbate solution (100mgL^{-1} for MB; 100mgL^{-1} for RhB, 50ml each) was carried out in different Erlenmeyer flasks and marked as 1, 2, 3, and so on. The pH of the flask number 4 was adjusted to 5 using hydrochloric acid (HCl, 0.1M) and sodium hydroxide (NaOH, 0.1M). The pH of the second flask was adjusted to 6 and so on. After pH adjustment, a fixed amount of adsorbent (0.1g) was added and allowed to stir for a pre-defined period of time. The flask content was then filtered after completion of the time period and remnant concentration of the adsorbate was determined.

2.1.4 Initial Concentration

Effect of initial concentration was investigated by a fixed volume (50 mL) of the adsorbate solutions of varying concentration (20, 40, 60… 120mg/l MB) and (20, 40, 60… 120mg/l RhB) in different Erlenmeyer flasks. The solutions was be adjusted to optimum pH value. To each flask, a fixed amount of adsorbent (0.1g) was added and allowed to stir for predefined optimum period of time. The solutions were then filtered and analyzed for residual concentration.

2.1.5 Particle size

The effect of particle size of the any adsorbent played a significant role in determining adsorption capacity and adsorption rate, 0.1g of adsorbent was added to 50mL of adsorbate in Erlenmeyer flask in conjunction with T = 30^0C, C_o = 100mg/g, at optimized value of contact time and pH, the solution was placed on an orbital shaker at constant agitation speed of 200rpm.

2.2 Equilibrium study

The equilibrium adsorption isotherm is fundamentally very decisive in the design of any adsorption system. The equilibrium relationships between adsorbent and adsorbate can be described by adsorption isotherms. In the present work, the adsorption data was analyzed in the light of four well-known isotherm models, namely, Langmuir, Freundlich, Temkin and Dubinin-Radushkevich adsorption isotherm models. The data obtained in the batch adsorption studies was used to check the suitability of various equilibrium models.

2.2.1 Langmuir adsorption isotherm.

The Langmuir isotherm has been commonly used to discuss various adsorbate-adsorbent combinations for both liquid and gas phase adsorptions (Langmuir, 1916).

This isotherm can be mathematically represented as:

$$q_e = \frac{q_{max} \cdot K_L C_e}{1 + K_L C_e} \text{.....2}$$

Where; q_e is the adsorption capacity (mg g^{-1}) of the adsorbent for specific adsorbate at equilibrium. q_{max} is the maximum adsorption capacity (mg g^{-1}), (C_e) (mg/L) is adsorbate concentration and K_L (Lmg^{-1}) is Langmuir constant. The above equation can be rearranged to following linearised form (Mckay *et al*., 1984):

$$\frac{1}{q_e} = \frac{1}{q_{max}.K_L C_e} + \frac{1}{q_{max}} \ldots\ldots\ldots\ldots\ldots\ldots 3$$

Thus, the Langmuir constants q_{max} and K_L can be calculated from the slope and intercept of plot between $\frac{1}{q_e}$vs$\frac{1}{C_e}$.

The essential characteristics of Langmuir isotherm can be expressed by dimensionless parameter known as separation factor, R_L, which is defined as:

$$R_L = \frac{1}{(1+K_L C_o)} \ldots\ldots\ldots\ldots\ldots\ldots 4$$

Where;

Co (mg/L) is the initial concentration of adsorbate. R_L measures the suitability of the adsorbent for the adsorbate adsorption and it throws light on the nature of adsorption to be either unfavourable (R_L> 1), linear (R_L = 1), favourable (0 <R_L< 1) or irreversible (R_L = 0). Using the dimensionless factor from the Langmuir isotherm, the reversibility of the adsorption can be predicted.

2.2.3 Freundlich Adsorption Isotherm

The Freundlich isotherm is an empirical model that is based on adsorption on a heterogeneous surface (Freundlich, 1906). The Freundlich model can be mathematically represented in the non-linear and linear forms as:

$$q_e = K_f C_e^{\frac{1}{n}} \ldots\ldots\ldots\ldots\ldots\ldots\ldots\ldots 5$$

$$lnq_e = \ln K_f + \frac{1}{n} lnC_e \ldots\ldots\ldots\ldots\ldots\ldots 6$$

q_e is the adsorption capacity of adsorbent at equilibrium and C_e is the adsorbate concentration in liquid phase at equilibrium. K_F (mg1-1/nL1/n/g) and n are Freundlich constants related with the adsorption capacity and adsorption intensity, respectively. K_F indicate the q and 1/n stands for heterogeneity factor of adsorption, which is determined by the slope and intercept of the Freundlich isotherm.

2.2.4 Temkin Adsorption Isotherm

Temkin isotherm is the early model describing the adsorption of hydrogen onto platinum electrodes in acidic solutions (Temkin and Pyzhev 1940). The isotherm contains factor that explicitly takes into the account of adsorbent–adsorbate interactions. By ignoring the extremely low and large value of concentrations, the model assumes that heat of adsorption (function of temperature) of all molecules in the layer would decrease linearly rather than logarithmically with coverage, as implicit by Freundlich model. The linear form of the Temkin adsorption isotherm is given as:

$$q_e = B_T lnC_e + B_T lnK_T \ldots\ldots\ldots\ldots\ldots\ldots 7$$

Where;

B_T = RT/b_T, R is the universal gas constant (8.314j mol^{-1} K^{-1}), T is the temperature (K),b_T (Kj mol^{-1}) is Temkin isotherm constant related to the heat of adsorption (J mol^{-1}) obtained from the plot of qe vs Ce and K_T is the equilibrium binding constant (L g^{-1}).

2.2.5 Dubinin-Radushkevich (D-R) Isotherm

Dubinin–Radushkevich isotherm is an empirical model initially conceived for the adsorption of subcritical vapors onto micro pore solids following a pore filling mechanism (Dubinin & Radushkevich, 1947). It is generally applied to express the adsorption mechanism with a Gaussian energy distribution onto a heterogeneous surface. The model has often been successfully fitted to high solute activities and intermediate range of concentrations data well but has unsatisfactory asymptotic properties and does not predict the Henry's law at low pressure. The approach was usually applied to distinguish the physical and chemical adsorption of metal ions. The linear form of Dubinin-Radushkevich (D-R) isotherm model is given as follows:

$$lnq_e = lnq_m - \beta\,\varepsilon^2 \ldots\ldots\ldots\ldots\ldots\ldots\ldots 8$$

$$\varepsilon = RTln\,[1 + \frac{1}{Ce}] \ldots\ldots\ldots\ldots\ldots\ldots\ldots 9$$

Where; qm is the theoretical monolayer sorption capacity (mg g^{-1}), ε is the polyani potential, β is a constant related to the mean adsorption energy (mol^2 k j^{-2})and E is the mean free energy of adsorption (Kj mol^{-1}) which is given by the following equation:

$$E = \frac{1}{\sqrt{2\beta}} \ldots\ldots\ldots\ldots\ldots\ldots\ldots\ldots 10$$

Values of E can predict the characteristics of adsorption as chemisorption or physisorption. If the value of E ranges between 8 to 16 kj mol^{-1} it depicts the chemisorption nature of adsorbate and adsorbent interaction at solid solution interface (Foo and Hameed 2010) or otherwise physisorption if E < 8 to16 kj mol^{-1}.

3 RESULTS AND DISCUSSION

3.1Fourier Transforms Infrared (FTIR) Spectroscopic studies

FTIR is a spectroscopic analysis technique which is used for identification of chemical bonds molecule by producing an infrared adsorption spectrum and from thereof the functional group present on the surface of sample.

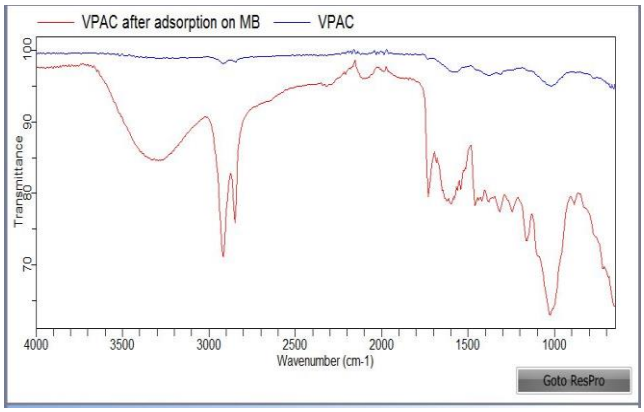

Figure 1 FTIR spectrum before and after adsorption of MB onto VPAC

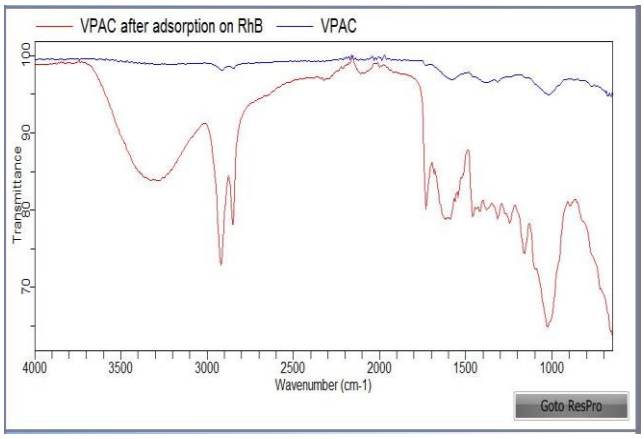

Figure 2 FTIR spectrum before and after adsorption of RhB onto VPAC

Fig.1 and 2 shows the changes in spectra scan and adsorption bands of VPAC before and after adsorption of MB and RhB. The broad peak at 3283cm^{-1} is attributed to the stretching vibration of O-H group. The stretching of the –OH group bond to methyl radical associated with the signal at 2918cm^{-1}. The peak at 1544cm^{-1} correspond to C=C aromatic ring while the peak at 1030cm^{-1} is due to C-O bond. The peaks at 899cm^{-1} correspond to C-H in alkene and C-H in aromatic ring. After adsorption, there was a shift and broadening of adsorption peaks. The shift of –OH peak from 3283cm-^{1} to 3294cm^{-1} both MB and RhB indicate the involvement of hydroxyl groups in the adsorption of dyes (Zhang *et al*., 2009). In these spectra, we noticed there are significant changes before and after adsorption, this indicates that chemical transformation must have taken place during chemical treatment.

3.2 Batch Adsorption Studies

3.2.1 Effect of contact time

The effect of contact time on adsorption of MB and RhB with VPAC was studied. From the experimental data, the process of adsorption reaches the equilibrium state after 60mims in MB while 80mins in RhB respectively. The reaction rate was fast at first 20mins in MB, which indicate that the rate of adsorption of MB was higher than RhB. Further, the adsorption proceeds at low rate and finally no significant adsorption are beyond equilibrium point.

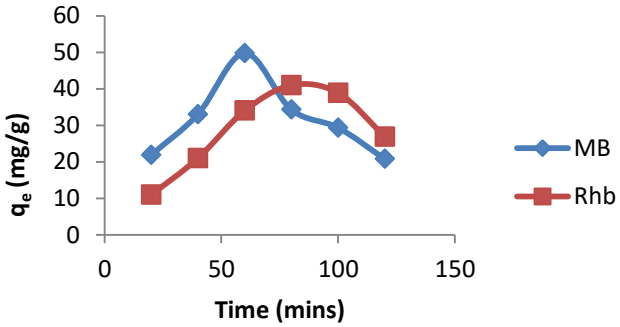

Figure 3 Effect of contact time on MB and RhB onto VPAC

3.2.2 Effect of adsorbent Dosage

The effect of Adsorbents Dosage of VPAC on the dye removal was studied. The determination of VPAC dosage is important because it determines the efficiency of dye removal and may also be used to predict the cost of VPAC per unit of solution to be treated. As expected, the efficiency of dye removal increases significantly as adsorbent dosage decreases. The graph indicates that, there was rapid removal at 0.1g with efficiency capacity of 48.10mg/g for MB and 40.87mg/g for RhB. Similarly trend reported by (Abdul Salam and Adekola2018).

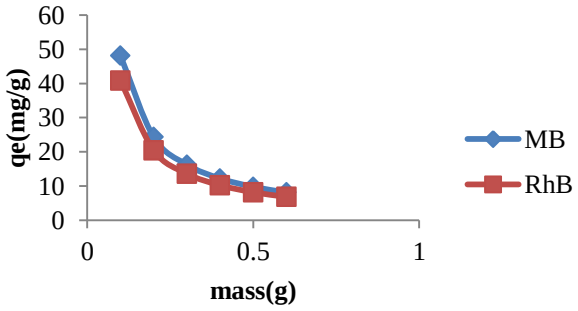

Figure 4Effect of dosage on MB and RhB onto VPAC

3.2.3 Effect of pH

The effects of pH on dye solution of two dyes removal were investigated by varying the pH from 4 to 9. At pH 4 the removal was minimum but it increased along with increasing pH of dye solution. For MB it was maximum at pH = 6 with adsorption capacity of 49.271mg/g in case of

RhB the pH was greater at 7 with adsorption capacity of 36.05mg/g. Generally adsorption found to decrease with increase in pH of solution.

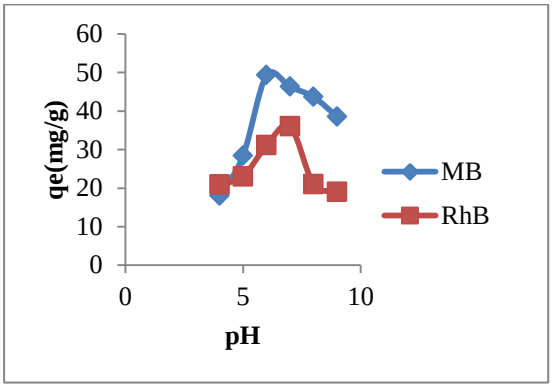

Figure 5 Effect of pH on adsorption of MB and RhB onto VPAC

3.2.4 Effect of initial concentration

It was observed that at low concentration, the available driving force for movement of MB and RhB onto the adsorbent particles was low, while at high concentration, there was a corresponding increase in the driving force. As a result of this, there was uptake of MB and RhB dye molecules. At high concentration MB and RhB saturates the adsorbent sites quickly, thereby decreasing the overall amount of the dye removal (Yeddou and Bensmaili, 2007). Therefore, there was an increased in the quantity of dye adsorbed with an increase in the initial concentration.

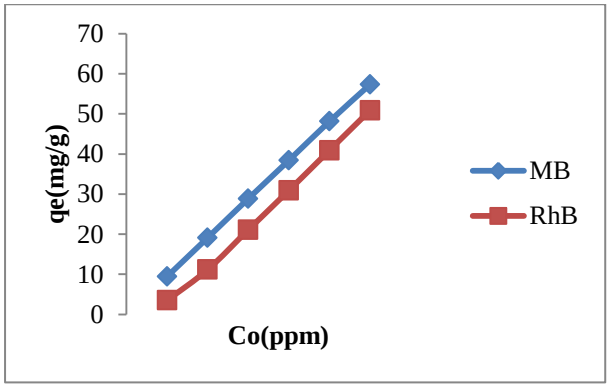

Figure 6 Effect of initial conc. on adsorption of MB and RhB onto VPAC

3.2.5 Effect of particle size

Adsorptions of MB and RhB on five different sized particles (200, 300, 450, 600, and 1000µm) were studied. The results of variation of these particle sizes on dye adsorption are shown in figure 7. It can be observed that as the particle size increases the adsorption of the dye decreases and hence the adsorption capacity of dye also decreases. This is due to the decrease in the available surface area. For larger particles, the diffusion resistance to mass transfer is high and most of internal surface of the particle may not be utilized for adsorption and so the amount of dye adsorbed is small.

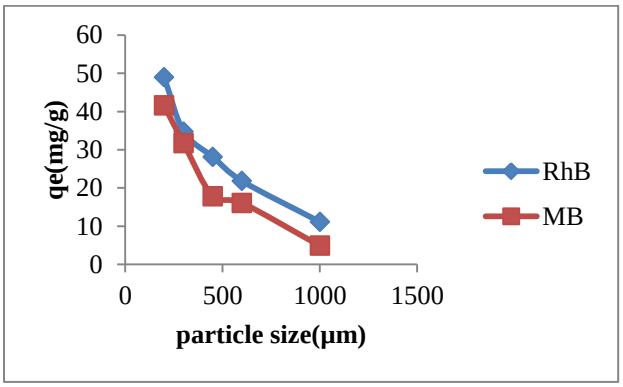

Figure 7 Effect of particle size on adsorption of MB onto VPAC

3.3 ADSORPTION ISOTHERMS

The adsorption isotherms data obtained after adsorptions of MB and RhB on the adsorbent (VPAC) were fitted into isotherm models to assess the model which best describe the adsorption process. Isotherms correlate the equilibrium adsorption data with different mathematical models to describe how adsorbates interact with adsorbents and this is critical in optimizing the use of adsorbent. The evaluated adsorption isotherm parameters are given below.

Table 1: Isotherm Parameters for Adsorbate Adsorption onto VPAC

Isotherm	Methylene Blue	Rhodamine B
Langmuir		
Q_{max}(mg/g)	-75.758	-1.679
K_L(L/mg)	-0.1047	-0.0518
R_L	9.1391	1.0373
R^2	0.9696	0.9688
Freundlich		
1/n	1.1651	6.5935
N	0.8583	0.1517
K_f	2.663	0.0012

R^2	0.9674	0.7872
Temkin		
$K_{T(}$ L/mg)	1.125	1.001
b_T	79.715	266.28
B_T	31.602	9.4605
R^2	0.9847	0.9150
Dubinin Radushkevich		
Q_s(mg/g)	57.478	9.008
K_{ad}(mol^2/KJ^2)	8×10^{-7}	2×10^{-6}
E(KJ/mol)	0.7906	0.500
R^2	0.9672	0.7864

From the data calculated in Table 1 the R_L value for MB and RhB is greater than 1indicating that Langmuir is unfavourable. The value of 'n' are greater than 0 indicating molecular interaction between VPAC and the MB and RhB molecules. These are in agreement with Li *et al*., (2009).

From the Temkin plot the following values were estimated: K_T = 1.125 L/mg and 1.001 L/mg, B_T =31.602J/mol and 9.4605J/mol for MB and RhB respectively which is an indication of the heat of adsorption indicating a physical process and the R^2 values 0.9847 and 0.9150 for MB and RhB.

From the linear plot of Dubinin Radushkevich mode, q_s for MB and RhB was determined to 57.31mg/g and 9.008mg/g, the mean free energy, E= 0.7906KJmol^{-1} and 0.500KJmol^{-1} indicating a physiosorption process and R^2 = 0.9672 and 0.7864. Comparing the values of the correlation coefficient, R^2, for the four tested isotherms, it can be observed that the adsorption data of MB and RhB onto VPAC fitted well with the four isotherms.

4 CONCLUSION

The results obtained show that VPAC can be used as a low cost adsorbent for removal of dye Methylene blue and Rhodamine B. The Langmuir isotherm model was observed to have been fitted better than the other isotherm models, it is concluded that the waste of the VPAC may be used as adsorbent, as it showed higher adsorption capacity when compared to other agricultural waste.

Acknowledgement

My found gratitude goes to my supervisor, Prof MB. Ibrahim for his tireless contributions in ensuring the research is conducted in line with global standard. I would like to express my appreciation to my parents for their financial support and prayers.

5 REFERENCES

Abdul-salam, N., and Adekola, S.K. (2018). Adsorption studies of zinc (II) on magnetitembaoba (*Adansonia digitata*) and magnetite-baoba composite applied water science,28-222. https://doi.org/10.1007/s13201-018-0867-7.

Azaman, S. A. H., Afandi, A., Hameed, B. H. and Mohd Din A. T. (2018). Removal of Malachite Green from Aqueous Phase Using Coconut Shell Activated Carbon: Adsorption, Desorption, and Reusability Studies. *Journal of Applied Science and Engineering*. 21(3):317-330.

Dubinin, M.M and Radushkevich, L.V. (1947).The equation of the characteristics curve of the activated charcoal. *Proc. Acad. Sci. USSR Phys. Chem. Sect*. 55:331-337.

Freundlich, H.M.F. (1906). Uber die adsorption in losungen. Z. *physical. Chemistry*. 57: 385- 470.

Foo, K.Y. and Hameed, B. H (2010). Insights into the modelling of adsorption isotherm systems. *Chemical Engineering Journal* 156: 2-10.

Ibrahim, M. B. and Sani, S. (2014.) Comparative Isotherms Studies on Adsorptive Removal of Congo Red from Wastewater by Watermelon Rinds and Neem-Tree Leaves. *Open Journal of Physical Chemistry*, 4, pp139-146.

Langmuir, I. (1916). The constitution and fundamental properties of solids and ligiuds. Part I. solids. *Journal of American Chemical Society* 38(11): 2221-2295.

Li JM, Meng XG, Hu CW, Du J. (2009). Adsorption of phenol, p-chlorophenol and p-nitrophenol onto functional chitosan. *Bioresource Technology*. 100: 1168-1179.

Mao, J., Won, S.W., Min, J. (2008). Removal of Basic Blue 3 from aqueous solution by Corynebacterium glutamicum biomass: *biosorption and precipitation mechanism. Korean J Chem Eng*, 25:1060-1064.

Mckay, G., Blair, H.S. and Gardiner, J.R. (1984). The adsorption of dyes onto chitin in fixed bed column and

batch absorbers. *Journal of Applied Polymer Science*, 29(5):1499- 1514.

Momina, Shahadat, M. and Ismail, S. (2018). Regeneration performance of clay-based adsorbents for the removal of industrial dyes: a review. *RSC Advances*, 8:24571- 24587.

Raval, N.P., Shah, P.U. and Shah, N.K. (2017). Malachite Green 'a Cationic Dye' and its Removal from Aqueous Solution by Adsorption. *Applied Water Science*,7:3407-3445.

Temkin, M.I. and Pyzhev, V. (1940). Kinetics of ammonia synthesis on promoted catalyst. *Acta.phys. Chem. USSR*. 12:327-356.

Tongpoothorn, W., Somsimee, O., Somboon, T. and Sriuttha, M. (2019). An Alternative and Cost-Effective Biosorbent Derived from Napier Grass Stem for Malachite Green Removal. *Journal of Materials and Environmental Sciences*, 10(8):685-695.

Tahir, H., Sultan, M., Akhtar, N., Hameed, U. and Abid, T.(2016). Application of natural and modified sugar cane bagasse for the removal of dye from aqueous solution, *Journal of Saudi Chemical Society*, 20, 115–121.

Sharma, K., Vyas, R.K. and Dalai, A.K. (2017). Thermodynamic and kinetic studies of methylene blue degradation using reactive adsorption and its comparison with adsorption. *Journal of Chemical Engineering Data*, 62(11): 3651 – 3662.

Wang, X., Wang, S., Yin, X., Chen, J. and Zhu, L. (2014). Activated Carbon Preparation from Cassava Residue Using a two-Step KOH Activation: Preparation, Micropore Structure and Adsorption Capacity. *Journal of Biobased Materials and Bioenergy*, 8(20):1-8.

Yeddou, N., Bensmaili, A. (2007). Equilibrium and kinetic modeling of iron adsorption in eggshells in a batch system: effect of temperature. *Desalination* 206(1-3):127-134.

Zhang, G., Liu, R., and Qu, J., (2009). Removal of phosphate from water by a Fe- Mn binary oxide adsorbent. *Journal of Colloidal and Interface Science*, 335:168-174.

3rd International Engineering Conference (IEC 2022)
Federal University of Technology, Minna, Nigeria

CHARACTERIZATION AND OPTIMIZATION OF THE BLEACHING PROCESS OF USED PALM OLEIN OIL USING ALKALINE-ACTIVATED RICE HUSK AS ADSORBENT

Mohammed, J. G[1], Uthman, H[2]. & Azeez, O. S[3].
[1,2&3]Department of Chemical Engineering, Federal University of Technology, PMB 65 Minna, Niger State, Nigeria

[*]Corresponding Author Email: gozhi4real@gmail.com

ABSTRACT
This study looked into the adsorptive purification of used palm olein oil via alkaline-activated rice husk. To identify the physiochemical characteristics, the used crude palm olein oil was characterized. Temperature, contact time, particle size, and adsorbent dosage were used in the experiment, employing the response surface method (RSM) to enhance and connect process variables to the responses (FFA and absorbance). The study of the data revealed the significance of the quadratic effects of the operating parameters. 80°C temperature, 0.25 mm particle size, 3.0 g of adsorbent dosage, and 25.002 minutes of contact time were the optimum variables for attaining a minimum 1.330 percent FFA and 0.853 absorbance. It was revealed that KOH-activated rice husk has the ability for %FFA reduction but at a higher concentration of 5M, which is in agreement with the investigation of previous researchers. The study has demonstrated that an efficient adsorbent can be made from alkaline-activated rice husk under optimized process conditions.

Keywords: Adsorbent, Bleaching, Free Fatty Acid, Optimization, Rice Husk Ash

1 INTRODUCTION

The most common vegetable oil eaten worldwide is palm oil [1]. It contains an outer skin known as the mesocarp, the shell (endocarp), the kernel, which is composed of oil and meal, and the mesocarp (which contains a fibrous matrix that stores water and palm oil). Oil palm, or simply palm oil, is the name for the oil derived from the mesocarp. Palm oil, the most marketed vegetable oil throughout the world, has gained prominence on the international market as a result of its dietary and health benefits [2, 3, 4]. Because it consists of about the same quantities of saturated fatty acids (palmitic, which normally ranges from 44–45%) and unsaturated fatty acids (39–40% oleic acid; 10–11% linoleic acid), it differs from other types of vegetable oils. Less linoleic acid increases the food's resistance to oxidative degradation during preparation for consumption. At room temperature (25–30 °C), palm oil is semi-solid and has the potential to be separated into two fractions: palm olein, which is a liquid, and palm stearin, which is a solid [5].

Palm olein is considered a liquid portion of single- or double-fractionated palm oil that has an iodine value of 56 or higher, such as an iodine value of 60 or more. Compared to palm oil, palm olein has larger concentrations of 39–45% overall oleic acid as well as 10–13% overall linoleic acid [6]. During additional olein fractionation, a highly unsaturated component known as palm super olein will be produced that has greater levels of both oleic and linoleic acid as well as an iodine value (IV) of >60. In a similar manner, palm top olein with an iodine value of (IV 70–72) and a cloud point of 0°C is made by further fractionating palm super olein. The palm olein's cloud point ranges from 6 to 10 °C [5]. As a result, higher IVs of palm olein are created for temperate countries since they can maintain their clarity in colder climates. All oleins are appropriate for cooking despite having various IVs. Hence, the liquid portion of palm oil—which includes palm olein, palm super olein, and palm top olein—is usually referred to as "palm olein" [7]. Worldwide, palm olein is utilized as cooking oil. In many Asian nations, as well as in South America, especially in home situations, palm olein oil with an iodine value of 56 or above is frequently used during cooking. The ability of cooking oil to remain crystal-free throughout storage—in a food store, for example—is one of the quality requirements for cooking oil. During extended storage, high-quality cooking oil is largely free of any noticeable crystal formation. Initial crystallization is often, though not always, noticeable at the bottom as a thin, fat crystal layer [8]. Deodorized or refined palm olein oil is a preferred form of oil. Chemical or physical methods can be used to refine palm olein oil.

There are essentially two processes for refining vegetable oil (palm olein oil): the chemical and physical approaches. The physical approach to refinement is preferable because the amount of free fatty acid (FFA) in vegetable oils is substantially large, and therefore, using cosmetics to remove them would cause significant losses in neutral oil and soap [9, 10], Typically, chemical refining techniques include degumming, neutralization, bleaching, dewaxing, and deodorizing. To eliminate phospholipids and mucilaginous gums, degumming is frequently performed using phosphoric acid or hot water. [12]. Through the process of neutralization, free fatty acids (FFA) are eliminated by adding an alkaline sodium hydroxide (NaOH) solution [13]. The removal of materials such as pigments, phospholipids, oxidation products, free fatty acids (FFA), and other unwanted components is accomplished through an adsorption technique called

bleaching [14]. This technique will ensure the end product's functionality (vitamins, fatty acid composition, and antioxidants), quality, and price will be guaranteed. During the dewaxing technique (dewaxing), waxes that are present in certain vegetable oils in significant quantities are separated by cooling the oil, forcing the waxes to crystallize, or using solvents. [15]. Aldehydes, ketones, and alcohols are among the volatile chemicals that are finally removed by vacuum distillation during deodorization [16].

Convectional heat treatment and chemical bleaching are less preferred due to their higher costs and environmental impact than adsorptive bleaching [17]. Vegetable oil could be refined through adsorbent materials (such as clay, charcoal, carbon, etc.) that have been physically activated or treated with alkaline or acidic solutions [18]. Clay, particularly carbon-activated clay, is extremely expensive, unfriendly to the environment, non-renewable, and ineffective when used to bleach vegetable oil [19, 20]. Adsorbents are often solid materials with wide inner surfaces and extremely porous designs to essentially allow the entrance of diffusing particles in the fluid state [21]. The adsorptive capacity of adsorbents has been demonstrated to be enhanced by activation [22]. Clay minerals are widely known for their ability to decolorize oils because of their excellent adsorption ability. Activation with acid is often the most popular technique for enhancing clay's adsorptive ability. Numerous scholars have expressed a great deal of interest in this field of clay modification [23–28]. The two stages that make up the acid activation process are typically the replacement of cations by protons and the dissolving of metal ions in the clay formation through depopulation of the rectified tetrahedron sheet [29]. However, utilizing clay activated with acid has been linked to several issues with bleached oil, including the influence of acid leftover on the oil and the soap production in the course of neutralization. Washing clay activated with acid to reduce the amount of leftover acid is another key issue because it increases the cost and time. Additionally, the acid employed is very costly, necessitating the development of other sources of adsorbent and techniques for the absorption of contaminants [29].

Through a single-step KOH activation process, [30] successfully produced excellent activated carbon (AC) via palm kernel shell. A rise in carbon formation for KOH-AC (61.10%) over raw PKS (47.28%) is confirmed by CHNS/O analysis, and a well-formed porous shape was revealed by scanning electron microscopy (SEM) for KOH-AC. [31] examined thirteen (13) kinds of rice husk across four different agro-ecological zones in Uganda as well as evaluated their possibility to be utilized as starting materials for the creation of bio-oil, ash, char, and activated carbon for certain uses.

According to their hypothesis, rice husks containing relatively high contents are suitable for a wide range of uses since alkaline pretreatment with 2-4% w/v NaOH can reduce ash levels by approximately 74–93 percent, depending on the type of rice husk.

Akinwande et al. [32] investigated the potential of clays activated with alkali for the refinement of vegetable oils, employing shea butter as a case study. Their results indicated that alkaline activation had a substantial impact on the clay's formation and morphology, as well as its potential for adsorption. It was also determined that for NaOH and KOH, alkaline concentrations of 0.5 M and 5 M, respectively, were required to achieve the highest levels of bleaching ability. Shea oil's percentage free fatty acid (FFA) concentration was decreased by 65 percent and 75 percent, respectively, when bleached with clays that were activated with sodium hydroxide and potassium hydroxide.

Okwara and Osoka [33] looked into how alkaline activation of native clays in Nigeria affected palm oil bleaching. According to their investigation, the adsorption capacity for bleaching earth increased by up to 79 percent at the optimal concentration of 1 M sodium hydroxide solution. The adsorption activity of acid treatment is improved by up to 99% as compared to caustic treatment. Base activation was thought to be a superior choice for use in vegetable oil bleaching. Although there aren't many studies on the influence of activation with alkaline on the bleaching earth's ability for adsorption, this is because surface activation of the adsorbent can be accomplished at a lower cost than it would cost to utilize inorganic acids like sulfuric acid and hydrochloric acid. Therefore, this work aims to characterize and optimize the bleaching process of used palm olein oil using alkaline activated rice husk as an adsorbent.

2 MATERIALS AND METHODS

Rice husk was bought from a local milling company along Kasuwan Gwari Market in Minna in a polythene bag; used palm olein oil was bought from an akara seller along Niteco Road in Tunga Minna, Niger State, in a 5-liter gallon. All the reagents used were of analytical grade and bought from Panlac Chemical in Keteren Gwari Minna, Niger State, Nigeria.

2.1 Preparation of Raw Material

The sample was thoroughly examined for external objects and properly cleaned using distilled water to eliminate any surface particles. To reduce its water content, the sample was first exposed to sunlight and then dried in an oven at 80°C for 24 h. The sample was then placed in a container for subsequent use [34].

2.2 Activation of the Rice Husk

In order to activate the rice husk's pores, 500 ml of a potassium hydroxide solution (5 M) was added to the flask after 400 g of rice husk had been weighed using the digital balance and placed into a 1000-ml conical flask**.** After stirring the solution, it was left to rest at room temperature for approximately 2 hours. The solution was subsequently heated for 3 hours at 100 °C while being periodically shaken. After washing the alkaline-treated rice husk in a sufficient amount of distilled water, a pH meter was used to check the solution's pH to ensure that the sample's pH was neutral. After that, the neutrally activated rice husk was dried in an oven for 12 hours at 70 °C [35]. The treated rice husks' color was then noted. The rice husk was subsequently sieved into different sizes of particles. In preparation for future investigation, each sample was kept in a sealed container.

2.3 Degumming

In order to hydrate these non-hydratable phosphatides, 2 ml of phosphoric acid (H_3PO_4) was added to 500 ml of used palm olein oil inside a conical flask that had been put in a thermostatic water bath shaker set at 85 °C. For 10 minutes, the solution was agitated, allowing for thorough acid degumming. 20 ml of distilled water were then added to the hot oil-acid solution that had been divided into portions so as to help remove the hydratable gums as well as ensure that the palm olein oil is free of gums. This was carried out by using a centrifuge machine for 5 min at 4000 rpm [36].

2.4 Neutralization

Used palm olein oil (degummed) was neutralized by adding 20 ml of sodium hydroxide (0.1 M) solution to 200 g of oil in the beaker forming stock soaps. Boiled distilled water was added, stirred for 10 minutes, and allowed to separate into two layers. The oil-stock soaps were separated using a centrifuge machine set at 4000 rpm for 5 minutes.

.2.5 Empirical Optimization Design and Statistical Analysis

The statistical analysis and design of the experiment were completed using Design Expert 13.0.5.0 (Stat-Ease Inc., Minneapolis, MN, USA) software in accordance with the response surface analytical approach. Based on the central composite design, RSM with four factors was employed, including temperature (70–110 °C), contact duration (25–45 min), adsorbent dosage (3–7 g), and particle size (0.25–1.25 mm), at five levels ((-α, -1, 0, 1, and α), and four replications at the central point (CCD). The statistical design table was created by taking these factors and their levels (28 runs of procedures) into account. The four independent factors in this design were A (temperature), B (adsorbent dosage), C (particle duration), and D (contact time). Analysis of Variance (ANOVA), regression analysis, and response surface plots of the observed associations between the parameters were used in the statistical evaluation to identify the ideal bleaching parameters. The impacts of the processing parameters on the efficiency of bleaching were analyzed, and the analysis of variance indicates that they are significant.

2.6 Bleaching of Used Palm Olein Oil

A beaker was used as the bleaching vessel for the bleaching of used palm olein oil. 35 ml of neutralized used palm olein oil was discharged into the bleaching vessel and placed on a hotplate with a magnetic stirrer. The bleaching was done according to the experimental variables obtained from the design factors as given by the CCD experimental design. The bleaching process is done again for all 28 experimental runs.

Bleached oil is kept for subsequent examination in sealed containers.

3 DETERMINATIN OF THE PHYSICAL AND CHEMICAL CHARACTERISTICS OF THE USED PALM OLEIN

3.1 Acid Value

The acid value is the quantity in milligrams (mg) of potassium hydroxide (KOH) required to neutralize one gram of the substance's free acid.

The acid value was determined using the titrimetric method [37].

$$\text{Acid value} = (56.1x\ C \times V)/W \quad (3.1)$$

where,
C stands for concentration of KOH.
V stands for endpoint value.
W stands for the weight of the oil sample.
Molar mass of KOH is 56.1

3.2 Saponification Value

A 150-ml conical flask was filled with 5 g of oil sample, followed by 25 ml of KOH. The solution inside the conical flask received two (2) drops of the phenolphthalein indicator, which was then heated inside a water bath while being shaken occasionally. Titrating the solution with 0.5M hydrochloric acid until disappearance of pink color is noticed [38] The technique was replicated for the blank.

Equation 3.2 was used to obtain its saponification value.

Saponification value: (56.1 (B-S) C)/W (3.2)

Where,

B stands for volume of Hydrochloric acid needed to determine blank
S stands for the titre value of a specific oil sample.
C represents the Hydrochloric
W stands for weight of oil sample

3.3 Ester value

The quantity of KOH in milligrams (mg) needed to saponify all of the esters in a gram of the substance is known as the ester value. According to Equation 3.3, the ester value is calculated by subtracting the saponification value from the acid value.

Ester value = (saponification value - acid value) (3.3)

3.4 Free fatty acid (FFA)

It is an approximation of the amount of oleic acid (C17H33COOH) inside a specific sample of oil. By measuring approximately 1.10 grams of sample oil into a beaker, using 25 milliliters of absolute ethanol for oil dissolution, and then adding 2 drops of the indicator (phenolphthalein), the percentage of free fatty acid value (% FFA) was calculated experimentally. The mixture was subjected to heating for 10 minutes while submerged inside a water bath, and then it was left to cool. Titrating the mixture against 0.1M potassium hydroxide until a pink color appeared, the endpont value was determined [38]. The reaction (neutralization) of the amount of FFAs against a strong alkali is described chemically by equation 3.4.

$$C_{17}H_{33}COOH + KOH \longrightarrow C_{17}H_{33}COOK + H_2O \quad (3.4)$$

The free fatty acid value was determined using Equation 3.5.

$$\%\ FFA = \frac{(28.2 \times C \times V)}{W} \quad (3.5)$$

Where,

C stands for concentration of KOH.

V stands for endpoint value.

28.2 is the weight of Oleic acid.

W stands for weight of oil sample.

3.5 Moisture Content

A sample of oil with a measured amount was placed in a crucible and dried for about 1 hour at 105–110 degrees Celsius. This was taken out, cooled using a desiccator, and measured again.

Moisture content =

$$\frac{Weight\ of\ sample\ taken, w_1 - Weight\ of\ dried\ sample,\ w_2}{Weight\ of\ sample,\ w_1} \quad (3.6)$$

3.6 Specific gravity

Using Pycnometer, the specific gravity of the samples of oil was ascertained. After weighing and recording the unfilled Pycnometer, distilled water was used to fill it up to its brim at room temperature, and the Pycnometer was therefore covered. The Pycnometer is then submerged inside a 25degree Celsius water bath for 30 min, after which it was dried off and its mass was determined. For every sample of palm olein oil, this procedure was performed again. Equation 3.7 explains the method used to calculate the specific gravity.

$$Specific\ gravity = \frac{M_s - M_e}{M_d - M_e} \quad (3.7)$$

Where,

M_s = bottle weight plus oil sample (g)
M_d = bottle weight plus distilled water (g)
M_e stands for empty bottle weight.

3.6 Iodine value

The oil sample was measured at 0.5 grams and added to the iodine flask before being neutralized in 10 milliliters of chloroform. A 25-milliliter solution of iodine was introduced using a pipette while draining it over a predetermined period of time. After thoroughly blending, the solution was kept in the dark with intermittent shaking for about 30 minutes. In order to thoroughly rinse all residual iodine on the stopper, 100 milliliters of heated and cooled water were used after adding 10 milliliters of a 15 percent potassium iodide solution and vigorously shaking it. Titrating the solution against 0.1N sodium thiosulfate until the solution (yellow) nearly lost its color A few drops of indicator (starch solution) were added, and the solution was titrated till all traces of the blue color were gone. After that, the flask was shut off. After that, the flask was shut off and violently agitated to ensure that any remaining iodine left in the solution was absorbed by the potassium iodide (KI) solution. A similar process was therefore used on the blank with no sample. Below is the formula used to determine the iodine value [38].

Iodine value = (B-S) (N of sodium thiosulfate (0.127g/meq)) (100) / Weight of sample

4 RESULTS AND DISCUSSION

Table 1: Properties of Used Palm Olein Oil

PROPERTIES	CODEX STAN 210-1999 (AMENDED IN 2015) FOR PALM OLEIN OIL	USED PALM OLEIN
ACID VALUE (mg KOH/g Oil)	0.6	8.4
SAPONIFICATION VALUE (mg KOH/g oil)	194 - 202	180.92
FREE FATTY ACID (%)	≤ 3	4.23
COLOR	LIGHT YELLOW	BROWNISH-YELLOW
ODOUR	ODOURLESS	FISHY, POTATOE
MOISTURE AND VOLATILE CONTENT (% m/m)	0.2	4.98
ESTER VALUE	193.4 – 201.4	206.9
PEROXIDE VALUE (mEq/ kg of oil)	≤ 10	3.333
SPECIFIC GRAVITY	0.899 - 0.920	0.908
IODINE VALUE (mg I_2/g)	50-56	42.418
REFRACTIVE INDEX (ND 40 °C)	1.458 - 1.460	1.4665
ABSORBANCE	-	0.509

Table 2: Design of the experiment

			Factor 1	Factor 2	Factor 3	Factor 4	Response 1	Response 2
Run	Std	Space Type	A: Temperature (°C)	B: Particle Size (mm)	C: Adsorbent Dosage (g)	D: Contact Time (min)	FFA (%)	Absorbance (Av)
1	5	Factorial	80	0.5	6	30	1.6641	0.5922
2	14	Factorial	100	0.5	6	40	2.0161	0.657
3	23	Axial	90	0.75	5	25	1.8411	0.5148
4	28	Center	90	0.75	5	35	2.5623	0.399
5	24	Axial	90	0.75	5	45	1.6388	0.4678
6	26	Center	90	0.75	5	35	2.5623	0.423
7	27	Center	90	0.75	5	35	2.5623	0.466
8	21	Axial	90	0.75	3	35	2.8624	0.443
9	22	Axial	90	0.75	7	35	2.4475	0.469
10	19	Axial	90	0.25	5	35	2.3087	0.666
11	2	Factorial	100	0.5	4	30	2.3341	0.622
12	13	Factorial	80	0.5	6	40	1.5601	0.392
13	6	Factorial	100	0.5	6	30	2.1201	0.5355
14	4	Factorial	100	1	4	30	2.6211	0.521
15	11	Factorial	80	1	4	40	2.0611	0.464
16	7	Factorial	80	1	6	30	1.9511	0.686
17	9	Factorial	80	0.5	4	40	1.7741	0.423
18	17	Axial	70	0.75	5	35	1.04	0.654
19	10	Factorial	100	0.5	4	40	2.2301	0.628
20	8	Factorial	100	1	6	30	2.4071	0.438
21	12	Factorial	100	1	4	40	2.5171	0.6077
22	16	Factorial	100	1	6	40	2.3031	0.484
23	3	Factorial	80	1	4	30	2.1651	0.694
24	18	Axial	110	0.75	5	35	1.9631	0.554
25	1	Factorial	80	0.5	4	30	1.8781	0.625
26	25	Center	90	0.75	5	35	2.5623	0.509
27	20	Axial	90	1.25	5	35	2.8901	0.656
28	15	Factorial	80	1	6	40	1.8471	0.443

4.1 Optimization Result

The experiment's design and the responses of the elements under study are provided in Tables 1 and 2, respectively. Tables 3 and 4 present the results of an ANOVA for a quadratic model. Ten (10) solutions were discovered, and Table 5 shows the solution that was deemed to be the most desirable.

Table 3: **ANOVA** For A Quadratic Model (Response 1: FFA)

Source	Sum of Squares	Df	Mean Square	F-value	p-value	
Model	4.90	14	0.3502	750.70	< 0.0001	significant
A-Temperature	1.26	1	1.26	2696.54	< 0.0001	
B-Particle size	0.4985	1	0.4985	1068.68	< 0.0001	
C-adsorbent dosage	0.2692	1	0.2692	577.14	< 0.0001	
D-Contact Time	0.0637	1	0.0637	136.60	< 0.0001	
AB	0.0000	1	0.0000	0.0000	1.0000	
AC	8.882E-16	1	8.882E-16	1.904E-12	1.0000	
AD	8.882E-16	1	8.882E-16	1.904E-12	1.0000	
BC	0.0000	1	0.0000	0.0000	1.0000	
BD	0.0000	1	0.0000	0.0000	1.0000	
CD	8.882E-16	1	8.882E-16	1.904E-12	1.0000	
A^2	1.76	1	1.76	3771.81	< 0.0001	
B^2	0.0003	1	0.0003	0.7100	0.4147	
C^2	0.0074	1	0.0074	15.94	0.0015	
D^2	1.07	1	1.07	2294.00	< 0.0001	
Residual	0.0061	13	0.0005			
Lack of Fit	0.0061	10	0.0006			
Pure Error	0.0000	3	0.0000			
Cor Total	4.91	27				

FIT STATISTICS

Std. Dev.	0.0216	**R^2**	0.9988
Mean	2.17	**Adjusted R^2**	0.9974
C.V. %	0.9964	**Predicted R^2**	0.9929
		Adeq Precision	116.6495

This model is suggested to be significant by the model F-value of 750.70 in Table 3. An F-value this high could only happen due to noise with a 0.01% likelihood. P-values under 0.0500 indicate that model terms were significant. In this instance, important model terms include A, B, C, D, A^2, C^2, and D^2. If the value is higher than 0.1000, the model terms are really not considered relevant. If your model contains a lot of meaningless terms (apart from those required to enable hierarchy), model reduction might assist with enhancing it. The expected R^2 of 0.9929 and the adjusted R^2 of 0.9974 are reasonably in conformity; that is, the variation is less than 0.2. The ratio of signal to noise is measured by Adeq Precision. A ratio of at least 4 is preferred. A sufficient signal is indicated by the ratio of 116.650. Using this technique, the design space could be examined.

4.2 EFFECT OF INDUSTRIAL PARAMETERS ON VARIABLE (GRAPHICAL ANALYSIS)

4.2.1 Response One: Free fatty acid

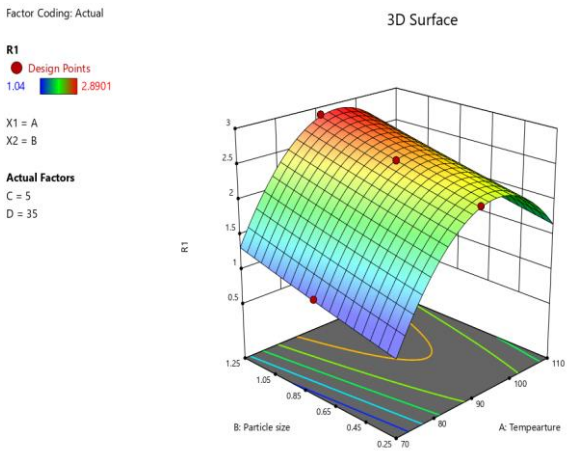

Figure 1: Impact of temperature and particle size on free fatty acid at a fixed adsorbent dosage and contact time

Figure 1 showing the free fatty acid response surface plots as a relationship between particle size and bleaching temperature. Bleaching of used palm olein oil has been positively impacted through the relationship between temperature and particle size. As it was discovered, increasing the particle size of the adsorbent from 0.25 to 1.25 g increases the oil's amount of free fatty acids. The findings show that at a particle size of 1.25g, the oil's free fatty acid concentration reaches its maximum level. Also, it is noted that when the bleaching temperature rises from 70 to 90 degrees Celsius, the oil's free fatty acid concentration increases to a level of 2.9. Also, it was noted that the oil's free fatty acid content begins to decline when bleaching temperatures rise between 90 and 110 degrees Celsius. Furthermore, it demonstrates that a reduction in adsorbent particle diameter and an increase in bleaching temperature generally lower the amount of free fatty acids in the oil.

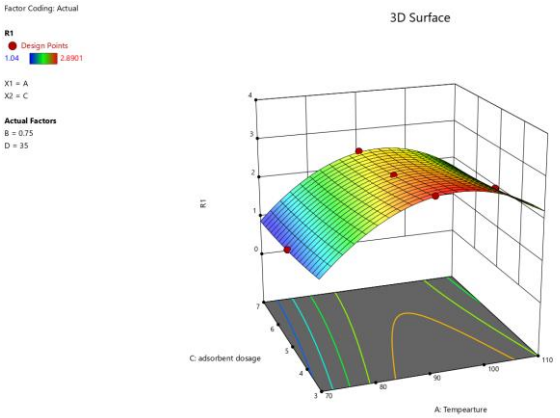

Figure 2: Impact of temperature and adsorbent dosage on free fatty acid at a fixed particle size and contact time

Figure 2 displays the connection involving adsorbent dosage and bleaching temperature on the free fatty acid response surface. The bleaching of used palm olein oil is enhanced by the interaction between temperature and adsorbent dosage. It was found that the amount of free fatty acids in the oil decreased as the dosage of the adsorbent rose from 3.0 to 7.0 g. According to the data, the free fatty acid concentration falls as the adsorbent dosage is increased. Furthermore, it was found that the free fatty acid increased as the temperature was raised. At temperature 95°C, the amount of free fatty acids reached its peak value of 2.30; however, it was found that when the temperature rose further, the free fatty acid content decreased.

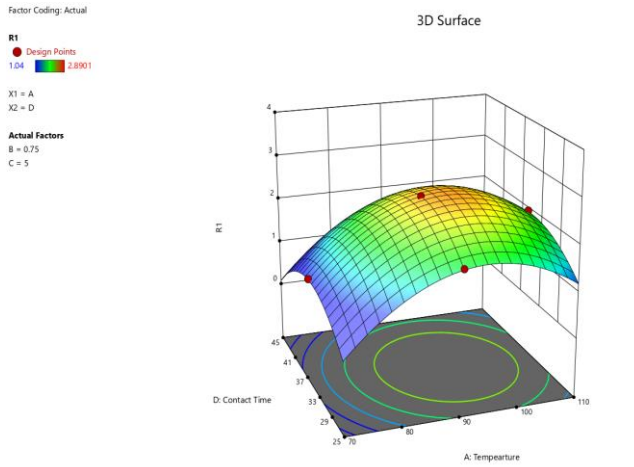

Figure 3: Impact of Temperature and Contact Time on free fatty acid at a fixed adsorbent dosage and particle size

Figure 3 shows how temperature and contact duration affect the amount of free fatty acids in the oil. From the plot, the oil's free fatty acid concentration keeps rising until it reaches a maximum value of 0.7 at an increased contact time of 36 mins. It was noticed that FFA starts decreasing at a further increase in contact time up to 45 mins. The decreased oil's free fatty acid concentration shows an increase in contact time, which supports accessibility to additional adsorption sites. Observed that FFA increases steadily to a peak value of 2.4 at a bleaching temperature of 92 °C. A decrease in FFA was noticed as the bleaching temperatures increased further. It is worth noting that increasing the temperature and contact time during the adsorptive purification of used palm olein results in a decrease in the oil's FFA concentration.

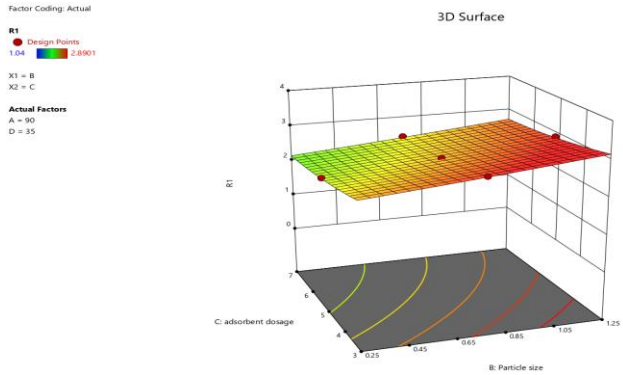

Figure 4: Impact of Particle Size and adsorbent dosage on free fatty acid at a fixed Temperature and Contact Time

Figure 4 shows how adsorbent dosage and particle size affect the oil's free fatty acid concentration. The range of the particle size was 0.25 to 1.25 mm. The bleached palm olein oil's FFA concentration steadily rose as a consequence of the adsorbent's increasing particle size.

Increased adsorbent dosage of 3 to 7 grams caused a visible but modest decrease in the oil's FFA level. It demonstrates that FFA decreases as particle size is reduced while adsorbent dosage is increased.

Increased adsorbent dosage of 3 to 7 grams caused a visible but modest decrease in the oil's FFA level. It demonstrates that FFA decreases as particle size is reduced while adsorbent dosage is increased.

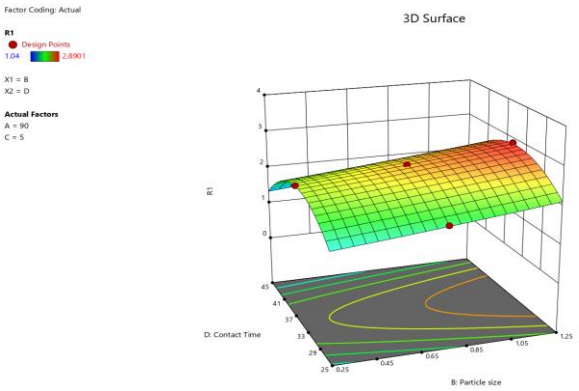

Figure 5: Impact of Contact time and Particle size on free fatty Acid at a fixed Adsorbent dosage and Temperature

Contact time and particle size's impact on the oil's free fatty acid concentration are depicted in **Figure 5.** From the plot, oil's free fatty acid concentration keeps increasing to a maximum value of 2.5 at an increased contact time of 36 min. It was noticed that FFA starts decreasing with a further increase in contact time up to 45 min. The decreased oil's FFA concentration shows that an increase in contact time increases accessibility to additional adsorption sites. It may be inferred that FFA continuously rises as particle size increases. We observed that increasing the contact time and reducing the adsorbent's particle size reduced the FFA content of used palm olein oil.

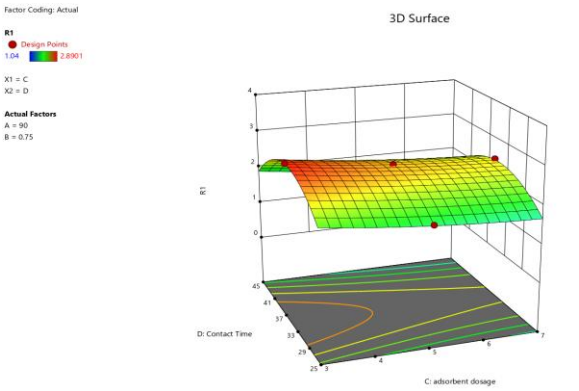

Figure 6: Impact of Contact time and Adsorbent Dosage on free fatty acid at a fixed Temperature and Particle size

Figure 6 illustrates how contact time and adsorbent affect the reaction (free fatty acid). From the plot, the oil's FFA concentration continues increasing to a maximum value of 2.5 at an increased contact time of 36 min. It was noticed that FFA starts decreasing with a further increase in contact time up to 45 minutes. The decreased oil's FFA concentration shows an increase in both reaction time and adsorbent dosage, which allows and encourages the utilization of more adsorption sites. Also, FFA decreases as the adsorbent dosage increases from 3 to 5.9 g and then remains constant for further increases in the adsorbent dosage.

Table 4: **ANOVA** For A Quadratic Model (Response 2: ABSORBANCE)

Source	Sum of Squares	df	Mean Square	F-value	p-value	
Model	0.2266	14	0.0162	7.41	0.0004	significant
A-Temperature	0.0000	1	0.0000	0.0129	0.9113	
B-Particle size	0.0010	1	0.0010	0.4702	0.5049	
C-adsorbent dosage	0.0039	1	0.0039	1.77	0.2057	
D-Contact Time	0.0209	1	0.0209	9.59	0.0085	
AB	0.0261	1	0.0261	11.96	0.0042	
AC	0.0018	1	0.0018	0.8406	0.3759	
AD	0.0806	1	0.0806	36.89	< 0.0001	
BC	0.0008	1	0.0008	0.3745	0.5511	
BD	0.0003	1	0.0003	0.1231	0.7313	
CD	0.0003	1	0.0003	0.1157	0.7391	
A^2	0.0352	1	0.0352	16.12	0.0015	
B^2	0.0663	1	0.0663	30.35	0.0001	
C^2	0.0000	1	0.0000	0.0187	0.8934	
D^2	0.0025	1	0.0025	1.13	0.3077	
Residual	0.0284	13	0.0022			
Lack of Fit	0.0213	10	0.0021	0.9058	0.6076	not significant
Pure Error	0.0071	3	0.0024			
Cor Total	0.2550	27				

FIT STATISTICS

Std. Dev.	0.0467	**R^2**	0.8886
Mean	0.5369	**Adjusted R^2**	0.7687
C.V. %	8.70	**Predicted R^2**	0.4689
		Adeq Precision	8.5069

The model is implied to be significant by the model F-value of 7.41 in Table 4. An F-value this large might happen as a result of noise with approximately 0.04% likelihood. When P-values are lower than 0.0500, model terms are deemed significant. D, AB, AD, A^2, and B^2 in this case are important model terms. Model terms are not significant if the value is higher than 0.1000. The F-value for the lack of fit, 0.91, indicates that the lack of fit is not significant in comparison to the pure error. With a 60.76% likelihood, noise could be the reason for a high Lack of Fit F-value. Although the model should fit, a minimal lack of fit is acceptable. As one would typically anticipate, the predicted R^2 of 0.4689 is not as near to the adjusted R^2 of 0.7687; in fact, the difference is greater than 0.2. This might point to a substantial block effect or suggest a potential issue with the model and/or data. Model reduction, response transformation, anomalies, etc. are things to think about. Confirmation runs should be used to test all empirical models. The ratio of signal to noise is measured by Adeq Precision. A ratio of at least 4 is preferred. A sufficient signal is indicated by the ratio of 8.507.

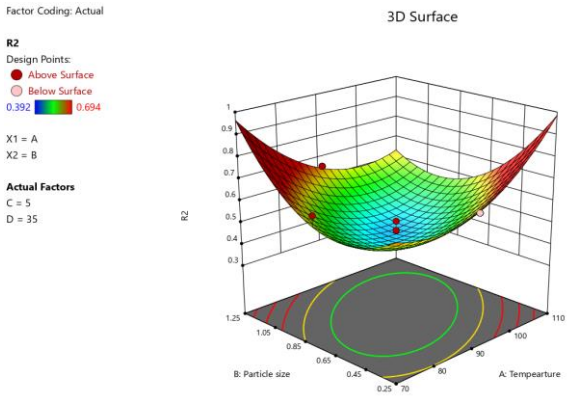

Figure 7. Impact of Temperature and Particle Size on Absorbance at a fixed Adsorbent Dosage and Constant Time

Figure 7 shows the impact of temperature and particle size on the absorbance of the oil. The curve showed that the oil's absorbance decreased with increasing particle size, reaching a maximum of 0.39 at 0.78 mm particle size. Absorbance begins to increase at further increased particle size to an optimum value of 0.95 at 1.25 mm. Similarly, it can be deduced that absorbance decreases to a value of 0.35 at 92 ℃ bleaching temperature. It is worth noting that large particle size and a high bleaching temperature of used palm olein oil bleaching increase the absorbance.

4.2.2 Response Two: Absorbance

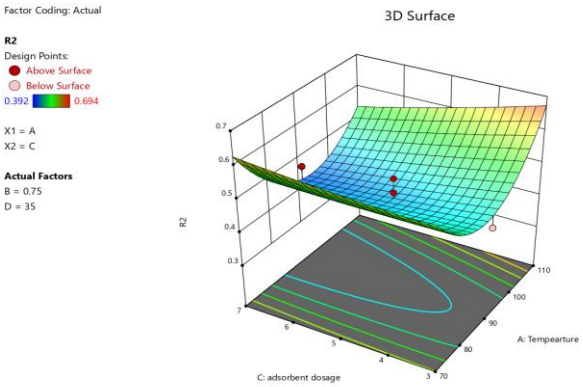

Figure 8: Impact of Temperature and Adsorbent dosage on Absorbance at a fixed Particle Size and Contact Time

As a function of adsorbent dosage and temperature, the absorbance response surface plots are shown in Figure 8. The relationship between temperature and adsorbent dosage promotes effective bleaching of used palm olein oil. The data show that absorbance likewise drops from 0.63 to roughly 0.28 as temperature increases from 0 to 90 degrees Celsius. An increase in temperature from 90 to 110 degrees Celsius causes the absorbance to increase from 0.28 to 0.63. So, it is important to understand that high temperature causes high absorbance and low temperature causes low absorbance. Comparably, as the dosage of the adsorbent is increased, there is a modest drop in absorbance. Hence, an increase in the adsorbent dose will cause an increase in absorbance.

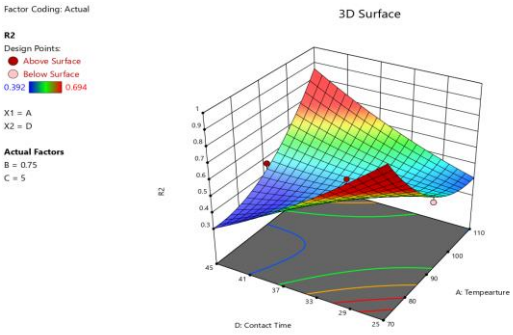

Figure 9: Impact of Temperature and Contact Time on Absorbance at a fixed Particle Size and Adsorbent Dosage

The relationship between temperature and time was evident in Figure 9. Decreased absorbance was a result of increased contact time from 25 to 45 mins. The lowest absorbance of 0.3 at 25 min and 70℃ and absorbance of 0.85 at 45 mins and 110℃ was obtained. Also, it was noticed that increased temperature resulted in decreased absorbance. The increase in absorbance could be a result of insufficient adsorption of factors affecting the bleaching-activated rice husk.

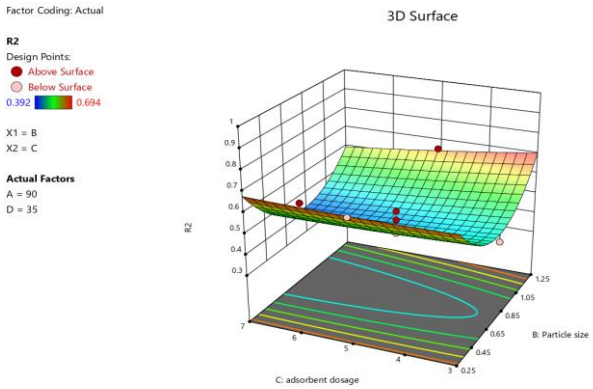

Figure 10: Impact of Adsorbent dosage and Particle size on Absorbance at a fixed Temperature and Contact Time

As a result of the relationship between particle size and adsorbent dosage, the response surface plot for absorbance is shown in Figure 10. Adsorbent dosage had no noticeable impact, whereas particle size had a noticeable impact. It was noticed that there was a decrease in absorbance as the particle size increased. Further increases in particle size resulted in an increase in absorbance to 0.7 at 1.25mm. Therefore, high absorbance could be achieved with larger particle sizes.

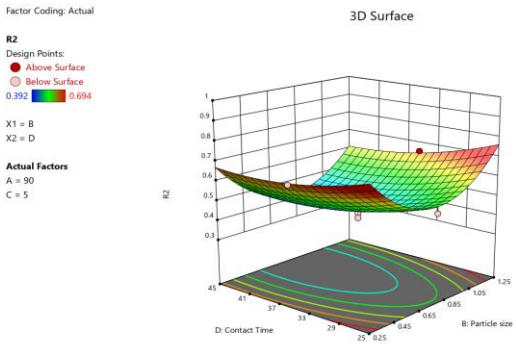

Figure 11: Impact of Particle Size and Contact Time on Absorbance at a fixed Temperature and Adsorbent Dosage

See Figure 11 with regard to bleaching palm olein oil, the interaction between contact duration and particle size is favorable. As contact time rose, absorbance decreased, reaching a value of 0.35 at 45min. A further extension of the contact period led to significant rise in absorbance. Furthermore, a decrease in absorbance was observed to a value of 0.48 at 0.77mm. There was increased absorbance to a value of 0.75 at 1.25mm as particle size increases.

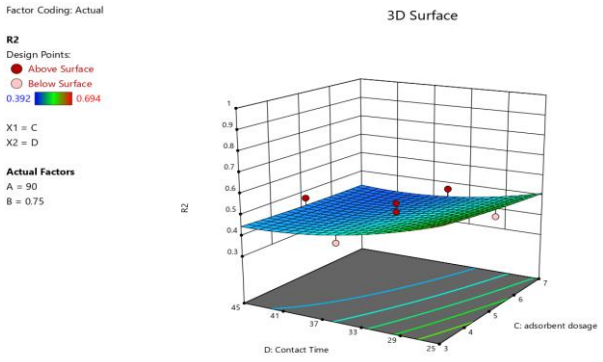

Figure 12: Impact of Adsorbent Dosage and Contact Time on Absorbance at a fixed Temperature and Particle Size

The interaction between contact time and adsorbent dosage was less pronounced in Figure 12. The highest absorbance was obtained at the adsorbent of 7.0g and contact time of 25.0 min.

4.3 Optimization of Variables for Used Palm Olein Refining

Using four variables (adsorbent dose, particle size, temperature, and bleaching time) and two responses (%FFA and %Absorbance), optimization was done utilizing the CCD of Surface Response Methodology.

TABLE 5: SOLUTIONS (CCD ARRANGEMENT AND RESPONSES)

Number	Temperature (˚C)	Particle size (mm)	adsorbent dosage (g)	Contact Time (min)	R1 (%)	R2 (Av)	Desirability	
1	**80.000**	**0.250**	**3.000**	**25.002**	**1.330**	**0.853**	**0.958**	**Selected**
2	80.001	0.250	3.044	25.000	1.322	0.853	0.958	
3	80.012	0.257	3.000	25.002	1.335	0.848	0.957	
4	80.000	0.261	3.004	25.000	1.335	0.846	0.957	
5	80.000	0.267	3.000	25.000	1.339	0.842	0.957	
6	80.000	0.251	3.084	25.026	1.320	0.852	0.957	
7	80.000	0.272	3.000	25.001	1.342	0.840	0.956	
8	80.058	0.250	3.000	25.022	1.338	0.851	0.956	
9	80.018	0.263	3.000	25.024	1.342	0.844	0.956	
10	80.062	0.261	3.000	25.000	1.340	0.845	0.956	

4.4. Free Fatty Acid (FFA)

The hydrolysis of fats in the presence of water or the enzyme lipase throughout storage results in the production of FFA. The best indicator of fat degradation has been FFA formation, and FFA levels could be used to track how much oil was being misused [39]. FFA content appears to be the most used criterion for accessing vegetable oil quality because it must have moderate values. The values of FFA (Table 2) and 1.330 optimized FFA value (Table 5) for the bleached palm olein oil falls within the CODEX STAN 210-1999 values (Table 1). These values show that the activated rice husk adsorbent successfully reduced the FFA (4.23) content of the used palm olein oil.

4.5 Absorbance

The term "absorbance" refers to how much light a solution can absorb. A spectrophotometer or microplate reader is used to quantify it; this device flashes light throughout a sample at a particular wavelength and then counts how much of it is absorbed. Based on the substance being investigated, light of a specified wavelength is transmitted through the sample, and the quantity of the original light that was absorbed by the sample in the well is measured by a detector on the other side of the microplate well [40]. At a wavelength of 450nm, the absorbance characteristics of utilized and bleached palm olein were examined. Absorbances (Table 2) for bleached palm olein have been found to be less than those for used palm olein oil (Table 1), a measure of the bleached oil's brightness compared to crude.

4.6 Conclusion

This study looked into a low-cost adsorbent manufactured from alkaline activated rice husk ash as a means of adsorptively bleaching used palm olein oil. Response surface methodology (RSM) was successfully applied in the experimental design to enhance the process operating parameters (temperature, particle size, adsorbent dosage, and contact duration) on the FFA and absorbance. The model was optimized using the RSM technique. The results showed that the optimum conditions could be met by setting the temperature to 80°C, the particle size to 0.25 mm, the adsorbent dosage to 3.0g, and the contact time to 25.002 minutes while maintaining a minimum free fatty acid of 1.330 and 0.853 absorbance.

Overall, the study's findings indicated that bleaching process optimization could result in time and resource savings. As can be observed, by lowering the temperature from 100 °C to 80 °C, statistical techniques like RSM can reduce the consumption of resources (fuel). Additionally,

by improving the processing time, the plant's capacity might be raised. According to the results of this study, under ideal processing parameters, alkaline-activated rice husk can be converted into a potent adsorbent.

5 REFERENCE

1. USDA. (2018). United States Department of Agriculture – Oilseed: World markets and trade.
2. Garcia-Nunez, J.A., Ramirez-Contreras, N.E., Rodriguez, D.T., Silva-Lora, E., Frear, C.S., Stockle, C., Garcia-Perez, M., (2016). Evolution of palm oil mills into biorefineries: a literature review on current and potential uses of residual biomass and effluents. Resources. Conserv. Recycle. 110, 99-114.
3. Xiao, J., Wang, W., Wang, K., Liu, Y., Liu, A., Zhang, S., Zhao, Y., (2016). Impact of the melting point of palm oil on mechanical and water barrier properties of gelatin-palm oil emulsion film. Food Hydrocoll. 60, 243-251.
4. Norazlan, M., Aziz, A., Kamal, M., (2006). Process Design in Degumming and Bleaching of Palm Oil (Thesis). Universiti Teknologi, Malaysia, pp. 1-158.
5. Phooi Tee Voon, Sin Tien Lee., Tony Kock Wai Ng., Yen Teng Ng., Xiou Shuang Yong., Verna Kar Mun Lee, and Augustine Soon Hock Ong (2019). Intake of Palm Olein and Lipid Status in Healthy Adults: A Meta-Analysis. American Society for Nutrition 2019. All rights reserved. Adv Nutr 2019;00:1–13; doi: https://doi.org/10.1093/advances/nmy122.
6. Kreps, F., Vrbikova, L., Schmidt, S., (2014). Influence of industrial physical refining on tocopherol, chlorophyll, and beta-carotene content in sunflower and rapeseed oil. Eur. J. Lipid Sci. Technol. 116,1572e1582.http://dx.doi.org/10.1002/ ejlt.201300460.
7. Marrakchi, F., Kriaa, K., Hadrich, B., Kechaou, N., (2015). Experimental investigation of processing parameters and effects of degumming, neutralization, and bleaching on lampante virgin olive oil's quality. Food Bioprod. Process. 94, 124e135. http://dx.doi.org/10.1016/j.fbp.2015.02.002.
8. Brad Forrest (2011). Palm Olein Oil Composition: International Flavors & Fragrances Inc.
9. Almeida, E. S., Carvalho, A. C. B., Oliveira de Souza, S. I., Valadares, L. F., Mendonça A. R. V, Silva J. I. J., Monteiro, S., (2019). Elucidating how two different types of bleaching earth widely used in vegetable oils industry remove carotenes from palm oil: Equilibrium, kinetics, and thermodynamic parameters. Food Research International 121 (2019) 785–797. https://doi.org/10.1016/j.foodres.2018.12.06
10. Sampaio, K. A., Ayala, J. V., Van Hoed, V., Monteiro, S., Ceriani, R., Verhé, R., & Meirelles, A. J. A. (2017). Impact of crude oil quality on the refining conditions and composition of nutraceuticals in refined palm oil. Journal of Food Science, 82(8), 1842–1850. https://doi.org/10.1111/1750-3841.13805.
11. Silva, S. M., Sampaio, K. A., Ceriani, R., Verhé, R., Stevens, C., De Greyt, W., & Meirelles, A. J. A. (2013). Adsorption of carotenes and phosphorus from palm oil onto acid activated bleaching earth: Equilibrium, kinetics, and thermodynamics. Journal of Food Engineering, 118(4), 341–349. https://doi.org/10.1016/j.jfoodeng.2013.04.026.
12. Kreps, F., Vrbikova, L., Schmidt, S., (2014). Influence of industrial physical refining on tocopherol, chlorophyll, and beta-carotene content in sunflower and rapeseed oil. Eur. J. Lipid Sci. Technol. 116, 1572e1582. http://dx.doi.org/10.1002/ ejlt.201300460.
13. Marrakchi, F., Kriaa, K., Hadrich, B., Kechaou, N., (2015). Experimental investigation of processing parameters and effects of degumming, neutralization, and bleaching on lampante virgin olive oil's quality. Food Bioprod. Process. 94, 124e135. http://dx.doi.org/10.1016/j.fbp.2015.02.002.
14. Ribeiro, M.H.L., Lourenço, P.A.S., Monteiro, J.P., Ferreira-Dias, S., (2001). Kinetics of selective adsorption of impurities from crude vegetable oil in hexane to activated earth and carbons. Eur. Food Res. Technol. 213, 132e138.

http://dx.
doi.org/10.1007/s002170100347.

15. Baümler, E.R., Crapiste, G.H., Carelli, A.A. (2007). Sunflower-oil wax reduction by seed solvent washing. J. Am. Oil Chem. Soc. 84, 603e608. http://dx.doi.org/10.1007/ s11746-007-1074-0.
16. Silva, S.M., Sampaio, K.A., Ceriani, R., Verhe, R., Stevens, C., De Greyt, W., Meirelles, A.J.A., (2014). Effect of type of bleaching earth on the final color of refined palm oil. LWT e Food Sci. Technol. 59 (2), 1258e1264. http://dx.doi.org/ 10.1016/j.lwt.2014.05.028.
17. Kamalu, C. I. O., Osoka, E. C. and Nwakaudu, M. S. (2012). Bleaching of Crude Palm kernel oil using activated snail shell. Research Journal in Engineering and Applied Sciences (RJEAS). pp 323 – 326.
18. Uzoh, C. F., Onukwuli, O. D., Nwabanne, J. T. and Igbokwe, P. P. K. (2014). Experimental Process Design for sorption capacity of Kogi and Ibusa clay activated with HNO3 and H2SO4 acids in Palm oil Bleaching. Int. J. Experimental Design and Process Optimization, pp 71 – 89.
19. Ramli, M.R., et al., (2011). Effects of degumming and bleaching on 3-MCPD esters formation during physical refining. Journal of the American Oil Chemists' Society, 88(11): p. 1839-1844.
20. Egbuna, S. (2014). Development of Kinetic Model For Adsorption of Carotenoids on Activated Clay in The Bleaching of Palm Oil. IJRET, 3(1): p. 3
21. Smrutirekha D. (2014). Characterization of Activated Carbon Of Coconut Shell, Rice Husk, And Karanja Oil Cake, Bachelor Thesis. Dept. Chem. Eng., National Institute of Technology, Rourkela. Available: https://www.ethesis.nitrkl.ac.in/5712/
22. Lieimkuehler E. C. (2010) "Production, Characterization and Applications of Activated Carbon." A Postgraduate Thesis. Faculty of Graduate School, University of Missouri USA.
23. Kashani Motlagh, M. M., Youzbashi, A. A. and Amiri Rigi, Z. (2011). Effect of Acid Activation on Structural and Bleaching Properties of a Bentonite. Iranian Journal of Materials Science & Engineering, 8, 50-56. T. O. Salawudeen et al. 597
24. Christidis, G. E., Scott, P. W. and Dunham, A. C. (1997). Acid Activation and Bleaching Capacity of Bentonites from the Islands of Milos and Chios, Aegean, Greece. Applied Clay Science, 12, 329-347. http://dx.doi.org/10.1016/S0169-1317(97)00017-3
25. Fransisco, R.V. and de Souza Santos, P. (2001). Studies on the Acid Activation of Brazilian Smectite Clay. University of San Paulo, San Paulo.
26. Suarez Barrios, M., Flores González, L.V., Vicente Rodríguez, M.A. and Martin Pozas, J.M. (1995). Acid Activation of a Palygorskite with HCl: Development of Physico-Chemical, Textural and Surface Properties. Applied Clay Science, 10, 247-258. http://dx.doi.org/10.1016/0169-1317(95)00007-Q
27. Novakovic, T., Rožić, L., Petrovic, S. and Rozic, A. (2008). Synthesis and Characterization of Acid Activated Serbian Smectite Clays Obtained by Statistically Designed Experiments. Chemical Engineering Journal, 137, 436-442. http://dx.doi.org/10.1016/j.cej.2007.06.003.
28. David, H., Christian, P.F. and Jorge, B. (2002). Processes for Producing Bleaching Clay Product. United States Patent; US6759359BI.
29. Fernandes, C., Catrinescu, C., Castilho, P., Russo, P.A., Carrott, M.R. and Breen, C. (2007). Catalytic Conversion of Limonene over Acid Activated Serra de Dentro (SD) Bentonite. Applied Catalysis A: General, 318, 108-120. http://dx.doi.org/10.1016/j.apcata.2006.10.048.
30. Andasa, J., Rahmanb, M. L. A., and Yahya, M. S. M. (2017). Preparation and Characterization of Activated Carbon from Palm Kernel Shell. International Research and Innovation Summit (IRIS2017), IOP Conf. Series: Materials Science and Engineering 226, 012156 doi:10.1088/1757-899X/226/1/012156
31. Menya, E., Olupot, P.W., Storz, H., Lubwama, M., Kiros, Y. (2018). Characterization and alkaline pretreatment of rice husk varieties in Uganda for potential utilization as

precursors in the production of activated carbon and other value-added products, Waste Management 81, 104–116: doi.org/10.1016/j.wasman.2018.09.050

32. Akinwande, B.A., Salawudeen, T.O., Arinkoola, A.O. and Jimoh, M.O. (2014). A Suitability Assessment of Alkali Activated Clay for Application in Vegetable Oil Refining. International Journal of Engineering and Advanced Technology Studies, 2, 1-12.
33. Okwara, C.A. and Osoka, E.C. (2006) Caustic Activation of Local Clays for Palm Oil Bleaching. Journal of Engineering and Applied Sciences, 1, 526-529.
34. Foo, K, Y., Hameed, B. H. (2012). Textural porosity, surface chemistry, and adsorptive properties of durian shell derived activated carbon prepared by microwave-assisted NaOH Activation, Chem. Eng. J. 187 53-62.
35. Rohdenburg, H., Csernitzky, K., Chikany, B., Peredi, J., Borodi, A. and Fabicsne Ruzics, A. (1999) Degumming Process for Plant Oils. US Patent 5,239,096.
36. Salawudeen, T.O., Arinkoola, A.O., Jimoh, M.O. and Akinwande, B.A. (2014) Clay Characterization and Optimisation of Bleaching Parameters for Palm Kernel Oil Using Alkaline Activated Clays. Journal of Minerals and Materials Characterization and Engineering, 2, 586-597. http://dx.doi.org/10.4236/jmmce.2014.26060
37. Rohdenburg, H., Csernitzky, K., Chikany, B., Peredi, J., Borodi, A. and Fabicsne Ruzics, A. (1999). Degumming Process for Plant Oils. US Patent 5,239,096.
38. Martin, M., Aloys M. O., and Bakari, C. (2019). Synthesis and Characterization of Hydrocarbon Fuels from Cassava Seed Oil using an Indigenous Salt Catalyst. International Journal of Research and Innovation in Applied Science (IJRIAS) | Volume IV|ISSN 2454-6194.
39. Atta, S., Nagra, S. A., Ahmad, T., Luthfullah, G., Gul, S., and Khan, M. (2008). Journal of the Chemical Society of Pakistan, 30, 879
40. Molecular Devices, LLC. 3860 N. First Street San Jose, CA 95134 USA.Volume IV|ISSN 2454-6194.

4th International Engineering Conference (IEC 2022)
Federal University of Technology, Minna, Nigeria

Performance Study of Empirical Path Loss Models at 11 GHz in an Irregular Environment for Wireless Communications

*Farouq E. Shaibu[1], Elizabeth N. Onwuka[1], Nathaniel Salawu[1], & Stephen S. Oyewobi[1]
[1]Department of Telecommunication Engineering, Federal University of Technology, PMB 65 Minna Niger State, Nigeria
*Corresponding author's email: farouqebira@gmail.com +2348031851870

ABSTRACT
In this paper, we report the performance study of two of the most widely used empirical models, 3GPP and CI models at 11 GHz in an irregular environment for future communication networks. Large-scale fading simulation has been carried out under the line-of-sight (LoS) and non-line-of-sight (NLoS) scenarios. An RF planning software package, Path Loss 5 (PL5) was used to carry out the simulation to reveal the expected receiver power, path loss, and terrain profile for the environment under consideration. From the simulated report, the simulated values were fitted with the path loss models. With the path loss exponent of 3.1, the results of the models' comparisons revealed that the CI model overestimated the path loss throughout its path in both LoS and NLoS scenarios with an MAE of 16.32 dB and 19.21 dB. The 3GPP model shows its best performance in LoS scenario but within a short distance ($< \mathbf{400}\ \boldsymbol{m}$) in NLoS scenario with an MAE of 9.14 dB and 11.09 dB respectively. The simulations suggest that the 3GPP model is better for path loss prediction in an environment under consideration at mm-Wave frequency.

Keywords: *Empirical Path Loss, 5G/6G Network, mm-Wave, Irregular Environment, Wireless Communication.*

1 INTRODUCTION

Path loss modeling has gained significant notice as one of the important elements for the ideal planning and configuration of base stations because of the unstable channel characteristics of millimeter waves (Wang & Lee, 2021). An accurate and efficient method for path loss modeling for millimeter wave communications is crucial for the general adoption of a fifth-generation (5G) mobile communication system (Chen *et al.*, 2021).

Path loss prediction methods are useful tools that network optimization engineers can use to deploy base stations, choose the location for base station setup, choose the transmitting and receiving antennas, choose the operating frequency, and conduct feasibility studies on interference.

Nigeria has chosen millimeter waves (mm-Waves) in the 3.4–3.8 GHz frequency band for fifth generation (5G) communications with unique usage situations.

Fifth-generation mobile communication systems are expanding the utilization of high-frequency bands at 6 GHz and above, and it is expected that sixth-generation mobile communication systems will utilize even higher frequency bands, like the THz band (6G) (Sasaki *et al.*, 2021) (ITU, 2020).

The millimeter wave channel in this Fifth Generation (5G) communication network has many difficulties, among which is path loss (Maccartney et al., 2015).

To develop path loss models, a combination of computer methods and approximations based on empirical measurements from channel-sounding experiments is used.

For estimating wireless signal coverage in specific environments, several models have been developed. However, sometimes these models fall short of the desired level of performance in terms of accuracy because they do not properly consider the peculiar nature of the environment.

Based on scenarios for LoS and NLoS in open, unreliable urban environments, this study offers a statistical evaluation of mm-wave propagation candidate for 5G systems at 11 GHz. Figure 1 and Figure 2 show these two scenarios.

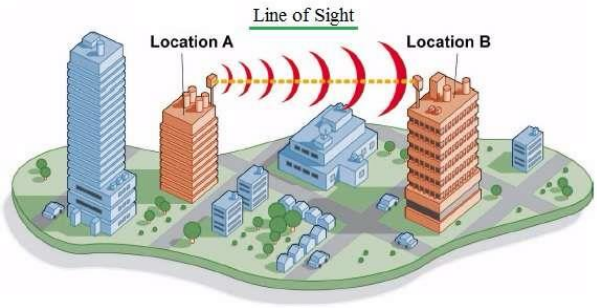

Fig. 1: Line-of-Sight channel (World, 2012)

Irregular urban environment refers to an environment characterized by the combination human structures less and more than 45 meters in height, a dense grid of roads, virgin lands, and densely populated.

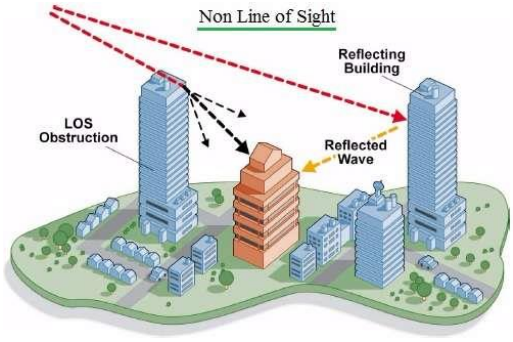

Fig. 2: Non-Line-of-Sight scenario (World, 2012)

The frequency band under evaluation was chosen because it provides an appropriate trade-off between undesirable channel characteristics like path loss, rain fading, and the atmospheric absorption effect.

In general, propagation path loss typically increases with distance and frequency (Rouphael, 2009). Equation 1 illustrates this.

$$P_l = 10\log_{10}\left(\frac{16\pi^2 d^n}{\lambda^2}\right) \quad (1)$$

Where d is the separation between the transmitter and receiver, n is the path loss exponent, which varies from 2 for propagation in open space to 6 for propagation through obstructions in buildings, P_l is the average propagation path loss, $d,$ and λ is the free space wavelength, which is determined by the relationship between the carrier frequency in Hz and the speed of light in meters per seconds (Maccartney & Rappaport, 2017; Rouphael, 2009).

Equation 1 can be reduced to equation 2, as;

$$P_L(f, d_0) = 32.5 + 20n\log_{10}(d_0) + 20\log_{10}(f) \quad (2)$$

Where f is the frequency of operation in MHz and d_0 is the distance in km between the transmitter and the receiver.

The primary factor in the design of wireless networks is path loss, which quantifies the energy lost when a wave travels between a transmitter and a receiver. Since the wavelength in the mm-Wave band is on the order of a millimeter, interacting with the surroundings becomes difficult.

Many propagation mechanisms contribute to multipath propagation in the mm-Wave spectrum, but their importance is different from that in frequency bands below 6 GHz.

Path loss is presented as given in equation 3.

$$Path\ loss, P_l\ in\ dB = EIRP - R_p \quad (3)$$

Where, R_p is the received power in dBm and $EIRP$ is the Effective Isotropic Radiated Power, which is given in equation 4, as;

$$EIRP = P_T + G_T + G_R - C_l - K_l - A_l - A_{fl} \quad (4)$$

P_T stands for "transmitting power" in dBm, "transmitter antenna gain" (G_T), "receiver antenna gain" (G_r), and C_l, K_l, A_l, A_{fl} represents the connector loss, cable loss, antenna loss, and antenna filter loss, respectively.

This paper aim to perform the comparative study of two widely used 5G empirical methods to predict path loss in an irregular environment for wireless communications. Therefore, the main contributions of the paper are summarized as follows;

1. To predict path loss in an outdoor irregular urban environment, we compared the applicability of 3GPP 38.901 and Close-In (CI) free space reference distance 5G empirical models.
2. Focusing on the analysis of the propagation of frequency band that is a candidate for 6G systems, considering the possible outcomes with more information.
3. We evaluated the validity of these models in the context of performance indicators.

The rest of the paper is structured as follows. Section II reports the recent developments on use of 5G empirical models for path loss prediction in different scenarios.

Section III reports on the simulation setup for the path loss analysis at 11 GHz. Section IV presents the selected 5G current cellular empirical models for the path loss investigation.

In section V reports on the obtained results and discussion from the simulation, and the comparative analysis for the selected models.

Finally, section VI provides concluding remarks.

2 RECENT DEVELOPMENT

Numerous works have been carried out to select the best path loss model for 5G communications. For instance, in an indoor setting, (Elmezughi *et al*., 2021) demonstrated measurements of propagation at three frequencies of 14, 18, and 22 GHz. Additionally, the ability to forecast path loss was compared between the FI model and the CI model (Oladimeji et al., 2022; Sun et al., 2016). The LoS performance study (Elmezughi et al., 2021) revealed that both CI and FI models operate very similarly at all frequencies and fit the actual measured data (Elmezughi *et al.*, 2021).

In (Daho *et al*., 2021), Path loss models at the 28 GHz 5G system were thoroughly examined for the outdoor environment in a tropical climate. Two high-directional horn antennas with a 1.5-meter height and a half-power beam width (HPBW) of 39 degrees at the Rx side were

used in this experiment. The Tx transmitter was positioned 5 meters above the surface of the earth. The impact of return and mismatch losses within the system may be affected by the impedance matching method used between the feed line and the horn antennas, which was not examined. Co-polarization decays rapidly in a Line-of-Sight (LoS) situation, according to the results.

For the analysis of mmWaves and sub-tetra hertz propagation for outdoor Urban Microcells, (Bedda-Zekri & Ajgou, 2022) took into account a number of possible situations. The findings of their research showed that the 60, 100, and 120 GHz channels are more sensitive to the effects of changing environmental circumstances than the 38 and 73 GHz channels. Although, there was no physical measurement campaign on those channels.

In (Juan-Llacer *et al.*, 2022), wideband measurements carried out in the middle of a street was used to model a path loss in the frequency bands of 1.8, 3.5, and 28 GHz. The environment was static and there was no wind during the measurement session. The outcome shows that after a certain distance between the transmitter and recipient, the 1.8 GHz and 3.5 GHz bands, multiple-scattering effects from trees must be taken into account.

3 SIMULATION PROCEDURE

To study the empirical models at 11 GHz mmWave in an irregular Urban environment, an OpenStreeMap was used to import a 3D map of the considered environment into an RF planning tool software for simulating the propagation modelling.

Line-of-Sight (LOS) and Non-Line-of-Sight (NLOS) scenarios were used to categorize the surroundings (Landolsi et al., 2019), as shown in Figure 2.

Figure 3: Simulation environment with a LOS and NLOS scena

Using the simulation parameters in Table 1, the RF planning tool software, (PL5) was used to simulate the propagation modelling to generate path loss, terrain data (path profile) and link design.

Figure 3 depicts the basic organization of the path loss program in the PL5.

For every location, the position of the Transmitter (Tx) was fixed, and simulations were performed with the Receiver (Rx) at different distances (moved along the line ranging from a reference distance of 1 m, and then from 50 m to 500 m with a spacing of 50 m.

From the simulated data, we generated CI and 3GPP models.

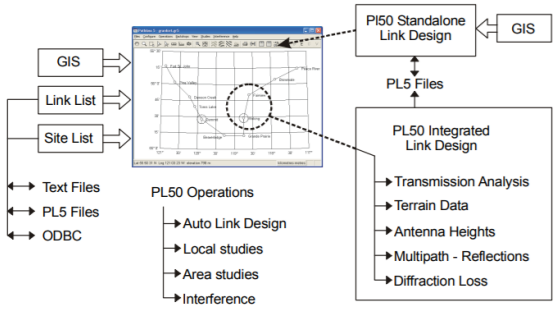

Fig. 4: Basic organization of the path loss program

TABLE 1: Simulation parameters

Parameter	Value
Frequency	11 GHz
Transmitter height	10 m
Transmitter Polarization	Vertical
Tx antenna type	Horn antenna
Tx antenna gain	35 dBi
EIRP	35.30 dBm
Connector loss	1 dB
True azimuth	88.22^0
Elevation	463 m ASL

The illustration of the measurement campaign is shown in figure 4.

4 EMPIRICAL CHANNEL MODEL

Numerous empirical models have been created for the measured environment, but when used in other measurement environments and experimental setups, they are found to be ineffective.

A. 3GPP TR 38.901 Model

i. Equation 5 presents the path loss model in urban macro and its corresponding description, as shown in equations 6 and 7. Equations 8 and 9 present the path loss for model description in non-line-of-sight (NLoS) scenario.

$$PL_{UMa-LOS} = \begin{cases} PL_1 & 10m \le d_{2D} \le d'_{BP} \\ PL_2 & d'_{BP} \le d_{2D} \le 5km \end{cases} \quad (5)$$

$$PL_1 = 28.0 + 22\log_{10}(d_{3D}) + 20\log_{10}(f_c) \quad (6)$$

$$PL_2 = 28.0 + 40\log_{10}(d_{3D}) + 20\log_{10}(f_c) - 9\log_{10}((d'_{BP})^2 + (h_{BS} - h_{UT})^2) \quad (7)$$

ii. For NLOS scenario.

$$PL_{UMa-NLOS} = max(PL_{UMa-LOS}, PL'_{UMa-NLOS}) \; for \; 10m \leq d_{2D} \leq 5km \quad (8)$$

$$PL'_{UMa-NLOS} = 13.54 + 39.08\log_{10}(d_{3D}) + 20\log_{10}(f_c) - 0.6(h_{UT} - 1.5) \quad (9)$$

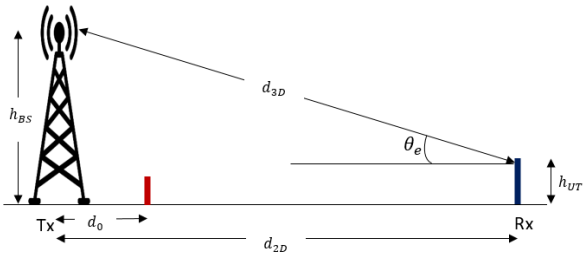

Fig. 5: Definition of d_{2D} and d_{3D} for outdoor UT_S

The above equations hold for shadow fading std, $\sigma_{SF}\,[dB] = 6$; applicability range, antenna height default values of $1.5m \leq h_{UT} \leq 22.5m; and\; h_{BS} = 25m$.

B. Close-In (CI) Free Space Reference Distance Model

Equation 10 illustrates how we applied the CI free space reference distance model (Sun et al., 2016), for a single frequency.

$$P_L^{CI}(f,d)[dB] = P_L(f,d_0) + 10n\log\left(\frac{d}{d_0}\right) + W_\sigma^{CI} \quad (10)$$

$P_L(f,d_0)$ is the free space path loss in dB at a T-R separation distance of 1m at the carrier frequency (ZEKRI & AJGOU, 2019), where f, n is the path loss exponent, d_0 is the initial separating path, and W_σ^{CI} is a zero-mean Gaussian-distributed random variable, and $\sigma\,dB$ is the standard deviation (shadowing impact).

The prediction result of the considered empirical models were compared with the simulated results to validate their performances, using performance indicators; Mean Absolute Percentage Error (MAPE), Mean Error (ME), and Root Mean Square Error (RMSE), as presented from equation 11 to 13.

$$MAE = \left|\frac{1}{N_{test}}\sum_{i=1}^{N_{test}}\left|PL_i^{sim} - PL_i^{pred}\right|\right| \quad (11)$$

$$MAPE = \frac{1}{N_{test}}\sum_{i=1}^{N_{test}}\left|\frac{PL_i^{sim} - PL_i^{pred}}{PL_i^{sim}}\right| \times 100 \quad (12)$$

$$RMSE = \sqrt{ME} = \sqrt{\frac{1}{N_{test}}\sum_{i=1}^{N_{test}}\left(PL_i^{sim} - PL_i^{pred}\right)^2} \quad (13)$$

Where PL_i^{sim} represents the simulated path loss value.
PL_i^{pred} represents the predicted path loss values.
N_{test} is the total number of tested samples.
i is the index of the simulated sample.

5 RESULTS AND DISCUSSION

The simulation report for the 11 GHz propagation modelling presents the path profile and terrain data, as shown from Figure 6 to Figure 15. The considered distances ranged from 1 m to 500 m with a step of 50 m.

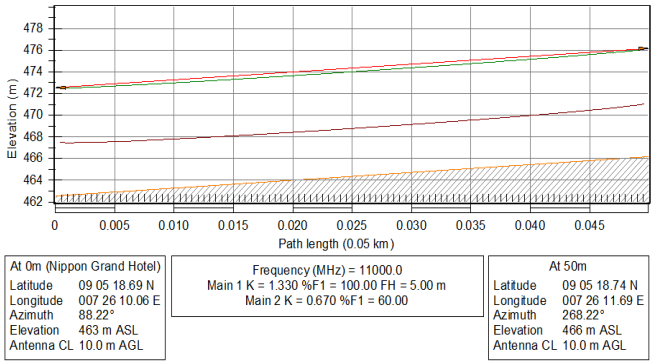

Fig. 6: Path profile for 11 GHz at 50 m

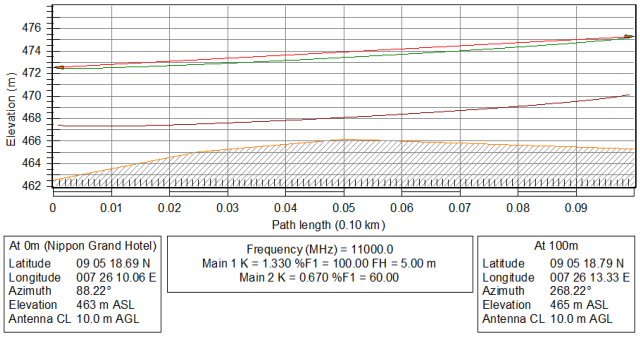

Fig. 7: Path profile for 11 GHz at 100 m

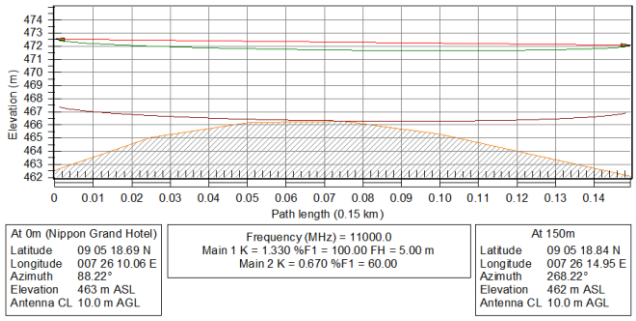

Fig. 8: Path profile for 11 GHz at 150 m

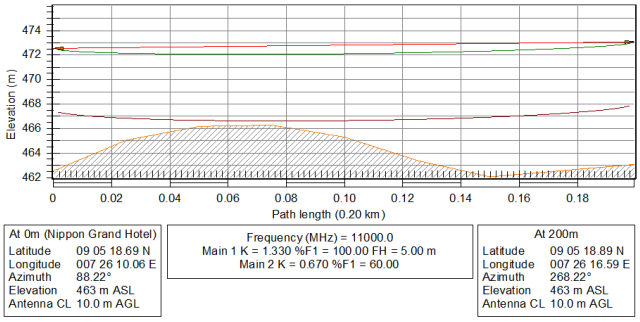

Fig. 9: Path profile for 11 GHz at 200 m

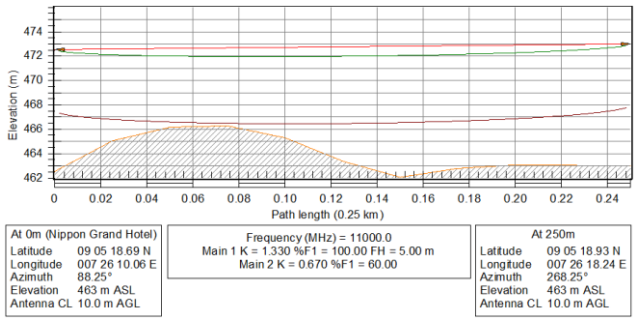

Fig. 10: Path profile for 11 GHz at 250 m

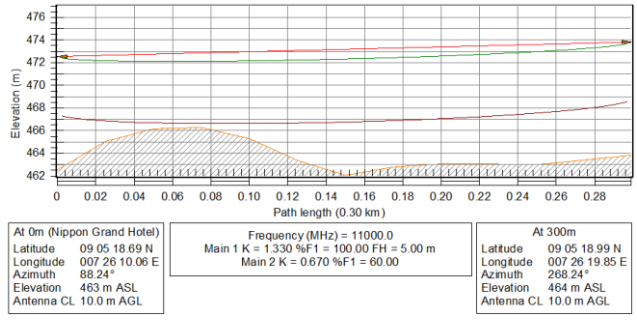

Fig. 11: Path profile for 11 GHz at 300 m

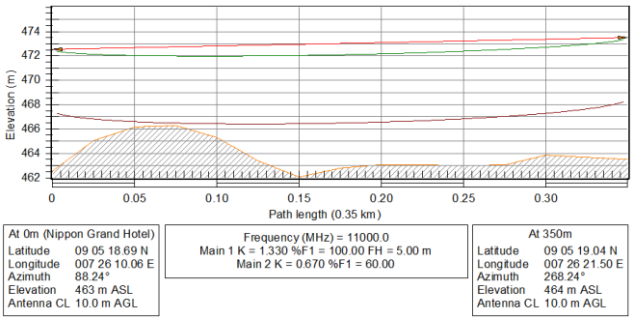

Fig. 12: Path profile for 11 GHz at 350 m

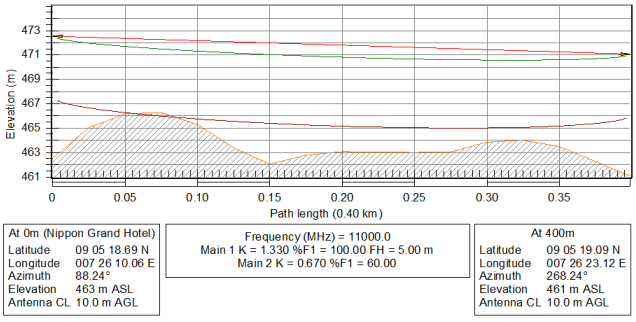

Fig. 13: Path profile for 11 GHz at 400 m

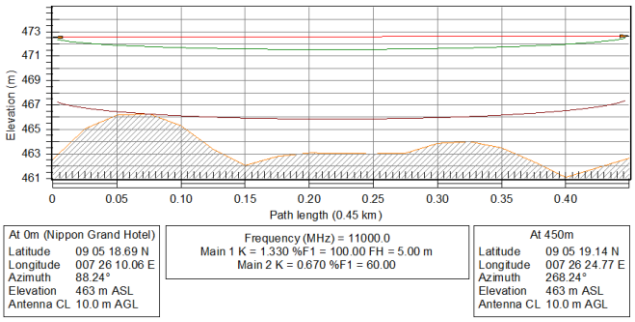

Fig. 14: Path profile for 11 GHz at 450 m

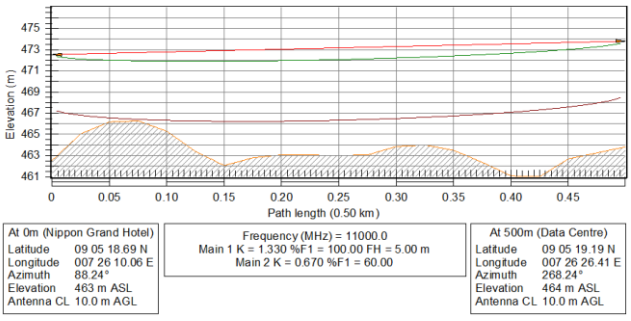

Fig. 15: Path profile for 11 GHz at 500 m

The model comparison carried out in Line-of-Sight (LoS) scenario shows that the CI model overestimated the

path loss throughout the range of interest, while the 3GPP model performed excellently, especially to the point of 350 m, as shown in Figure 16.

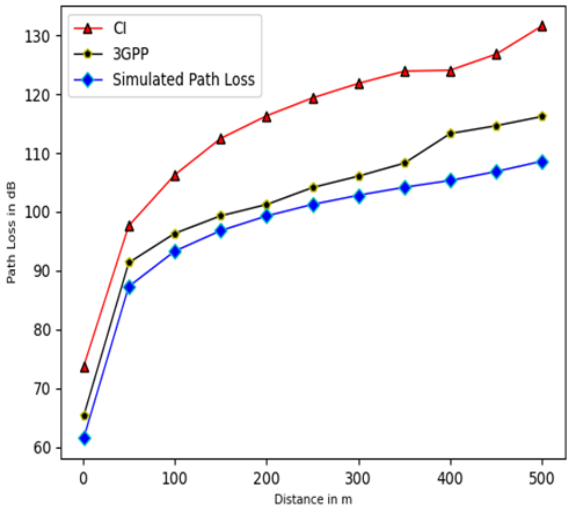

Figure 16: Comparison of models in LoS scenario

On the condition of Non-Line-of-Sight (NLoS), its clearly shown in Figure 17, that the 3GPP model tends to fit with the simulated path loss within a short distance ($< 400\ m$), and then overestimated the path loss.

Meanwhile, the CI model also overestimated the simulated path loss throughout its path, but not as much as in the case of Line-of-Sight (LOS) condition.

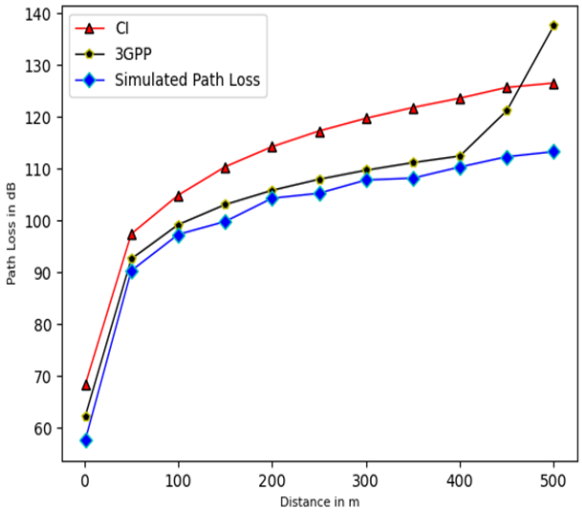

Fig. 17: Comparison of models in NLoS scenario

TABLE 2: Simulated result on Line-of-Sight (LoS) scenario

S/N	Path Length (m)	Elevation (m)	Rain Attenuation (dB)	Path Inclination (mr)	Received Signal (dBm)	Path Loss in dB		
						Simulated Value	Predicted Value by the CI	Predicted Value by the 3GPP
01	1	462.54	53.05	42.28	-19.84	61.53	73.73	65.31
02	50	466.17	50.31	72.39	-23.69	87.29	97.62	91.34
03	100	465.30	44.30	27.56	-29.70	93.30	106.26	96.32
04	150	462.08	40.81	3.08	-33.19	96.79	112.46	99.31
05	200	463.07	38.30	2.61	-35.70	99.29	116.31	101.23
06	250	463.00	36.34	1.82	-37.66	101.25	119.36	104.12
07	300	463.82	34.79	4.27	-39.21	102.81	121.82	106.06
08	350	463.50	33.43	2.74	-40.57	104.17	123.90	108.27
09	400	461.08	32.28	3.68	-41.72	105.32	124.07	113.31
10	450	462.54	31.24	42.28	-42.84	106.85	126.81	114.63
11	500	466.17	30.33	72.39	-43.67	108.61	131.62	116.21

TABLE 3: Simulated result on Non-Line-of-Sight (NLoS) scenario

S/N	Path Length (m)	Elevation (m)	Rain Attenuation (dB)	Path Inclination (mr)	Received Signal (dBm)	Path Loss in dB		
						Simulated Value	Predicted Value by the CI	Predicted Value by the 3GPP
01	1	462.54	53.05	32.56	-21.89	57.61	68.34	62.24
02	50	463.21	51.56	45.54	-25.74	90.34	97.45	92.62
03	100	465.48	46.21	2.65	-31.75	97.35	104.93	99.24
04	150	463.37	42.58	2.06	-35.24	99.84	110.41	103.11
05	200	462.44	40.31	19.43	-37.75	104.34	114.29	105.86
06	250	463.21	38.91	3.32	-39.71	105.30	117.31	108.00
07	300	463.40	36.07	2.56	-41.26	107.86	119.77	109.74
08	350	463.14	35.37	1.69	-42.62	108.22	121.85	111.21
09	400	468.32	34.12	9.59	-43.77	110.37	123.65	112.49
10	450	468.73	32.54	3.44	-44.81	112.35	125.73	121.24
11	500	468.05	29.32	3.51	-45.72	113.33	126.57	137.62

TABLE 4: Performance indicator

Models	Condition	MAE (dB)	MAPE (%)	RMSE (dB)
3GPP	LOS	9.14	21.76	2.92
	NLOS	11.09	16.32	4.13
CI	LOS	16.32	13.29	5.55
	NLOS	19.21	12.16	7.04

On the simulated report in Table 2 for the 11 GHz channel prediction, it can be deduced that the CI model overestimated the prediction, while the 3GPP performed excellently on the prediction of path loss within this channel.

ACKNOWLEDGEMENTS

We give thanks to the 9Mobile Communication Limited for providing the licensed RF planning software tool for this work.

CONCLUSION

In this paper, we report 11 GHz channel simulation in an irregular environment in the central city of Abuja, Nigeria. The simulations are done in Line-of-Sigh (LoS) and Non-Line-of-Sight (NLoS) scenarios. The aim of this study is to have a better understanding of the suitability of 11 GHz 5G systems for mm-Wave deployment.

We evaluate the fit of two of the most widely used empirical models to the simulated data. In this analysis, the 3GPP model gives better prediction in LoS condition against the NLoS with MAE 9.14 dB and 11.09 dB. In both scenarios, the CI model overestimated the path loss, with MAE values of 16.32 dB and 19.21 dB, respectively. The models indicate that the CI model is superior for predicting path loss in the environment being studied at mmWave frequency. In future work, we plan to concentrate on an extensive physical measurement campaign for evaluating the map-based machine learning models, as other environments still need to be addressed.

REFERENCE

Bedda-Zekri, A., & Ajgou, R. (2022). Statistical Analysis of 5G/6G Millimeter Wave Channels for Different Scenarios. *Journal of Communication Technology and Electronics*, *67*(7), 854 - 875.

Chen, H., Ma, S., Lee, H., & Cho, M. (2021). Millimeter Wave Path Loss Modeling for 5G Communication Using Deep Learning with Dilated Convolution and Attention. *IEEE Access*, 62867 - 62879. https://doi.org/10.1109/ACCESS.2021.3070711

Daho, A., Yamada, Y., & Al-Samman, A. (2021). *Proposed path loss model for outdoor environment in tropical climate for the 28 GHz 5G system* 1st International Conference on

Emerging Smart Technologies and Applications (eSmarTA), Sana'a, Yemen.

Elmezughi, M. K., Afullo, T. J., & Oyie, N. O. (2021). Performance Study of Path Loss Models at 14, 18, and 22 GHz in an Indoor Corridor Environment for Wireless Communications. *SAIEE Africa Research Journal*, *112*(1), 32 - 45. https://doi.org/10.23919/SAIEE.2021.9340535

ITU. (2020). *Framework and Overall Objectives of the Future Development of IMT for 2020 and Beyond*. https://www.itu.int/rec/R-REC-M.2083

Juan-Llacer, L., Molina-Garcia-Pardo, J. M., Sibille, A., Torrico, S. A., Rubiola, L. M., Martinez-Ingles, M. T., Rodriguez, J.-V., & Pascual-Garcia, J. (2022). *Path Loss Measurements and Modelling in a Citrus Plantation in the 1800 MHz, 3.5 GHz and 28 GHz in LoS* 2022 16th European Conference on Antennas and Propagation (EuCAP), Madrid, Spain.

Landolsi, M. A., Almutairi, A. F., & Kourah, M. A. (2019). LOS/NLOS Channel Identification for Improved Localization in Wireless Ultra-wideband Networks. *Telecommunication Systems*, *72*, 441-456. https://doi.org/https://doi.org/10.1007/s11235-019-00572-w

Maccartney, G. R., & Rappaport, T. S. (2017). Rural Macrocell Path Loss Models for Millimeter Wave Wireless Communications. *IEEE Journal on Selected Areas in Communications*, *35*(7), 1663-1677. https://doi.org/10.1109/JSAC.2017.2699359

Maccartney, G. R., Rappaport, T. S., & Sun, S. (2015). Indoor Office Wideband Millimeter-Wave Propagation Measurements and Channel Models at 28 and 73 GHz for Ultra-Dense 5G Wireless Networks. *IEEE Access*, *3*, 2388-2424. https://doi.org/10.1109/ACCESS.2015.2486778

Oladimeji, T. T., Kumar, P., & Oyie, N. O. (2022). Propagation Path Loss Prediction Modelling in Enclosed Environments for 5G Networks: A Review. *Heliyon*, *8*, 1 - 16. https://doi.org/https://doi.org/10.1016/j.heliyon.2022.e11581

Rouphael, T. J. (2009). High-Level Requirements and Link Budget Analysis. In T. J. Rouphael (Ed.), *RF and Digital Signal Processing for Software-Defined Radio* (pp. 87-122). Elsevier Ltd. https://www.sciencedirect.com/science/article/pii/B9780750682107000047

Sasaki, M., Kuno, N., Nakahira, T., Inomata, M., Yamada, W., & Moriyama, T. (2021). *Deep Learning Based Channel Prediction at 2-26 GHz Band Using Long Short-Term Memory Network* 15th European Conference on Antenna and Propagation (EuCAP), Dusseldorf, Germany.

Sun, S., Rappaport, T. S., Rangan, S., Thomas, T. A., Ghosh, A., & Kovacs, I. Z. (2016). *Propagation Path Loss Models for 5G Urban Micro- and Macro-Cellular Scenarios* 2016 IEEE 83rd Vehicular Technology Conference (VTC Spring), Nanjing, China.

Wang, P., & Lee, H. (2021). *Indoor Path Loss Modeling for 5G Communications in Smart Factory Scenarios Based on Meta-Learning* 2021 12th International Conference on Ubiquitos and Future Networks (ICUFN), Jeju Island, Korea.

World, R. W. (2012). *Home of RF and Wireless Vendors and Resources*. Retrieved September 11 from https://www.rfwireless-world.com/Terminology/LOS-vs-NLOS-wireless-channel.html

ZEKRI, A. B., & AJGOU, R. (2019). *Study of mmWave channels for different scenarios* 2019 6th International Conference on Image and Signal Processing and their Applications (ISPA), Mostaganem, Algeria.

4th International Engineering Conference (IEC 2023)
Federal University of Technology, Minna, Nigeria

Effect of Remolded Density on the Pozzolanic Action of Zeolite on Calcium Carbide Residue (CCR) Treated Clay Soil

*Umar, K. G[1], Alhaji, M. M[2] & Musa, A[3],
[1]Federal Roads Maintenance Agency (FERMA), headquarters, Wuse II, Abuja, Nigeria
[2,3]Department of Civil Engineering, Federal University of Technology, Minna, Niger State, Nigeria

*Corresponding author a.mustapha@futminna.edu.ng +2348036133082

ABSTRACT
A clay soil collected from Niger State Polytechnic Zungeru classified under A-6 and clay of low plasticity (CL) based on AASHTO and unified soil classification systems respectively. The deficient clay was stabilized with calcium carbide residue (CCR) admixed with zeolite at five different compaction energy levels to evaluate the effect of molded density on the strength and pozzolanic action of zeolite in the presence of (CCR). The compaction energies are reduced standard proctor (RSP), standard Proctor (SP), West African standard (WAS), reduced modified Proctor (RMP) and modified Proctor (MP) compaction energy levels. At each compaction energy level, specimen were molded for untreated clay, clay treated with 5% CCR and clay treated with 5% CCR admixed with 2% zeolite. The clay, CCR, zeolite as well as the mixtures were tested for X ray diffraction (XRD), X ray florescence (XRF), scanning electron microscopy (SEM) and electro dispersive microscopy (EDS). Addition of CCR to clay remove the delayed ettringite peak in the untreated clay and introduced anorthite peak. Addition of 2% zeolite to clay-CCR mixture introduced microcline peak in addition to the anorthite peak. The SEM results of the clay, CCR and zeolite all showed particles with wide to small pores and occasional honeycomb structures. Specimen consisting of CCR and zeolite however, revealed compact structure whose pores are filled with cementitious calcium silicate hydrate (C-S-H) and calcium aluminate hydrate (C-A-H). For 7- and 60-days curing period, the UCS of clay mixed with CCR and clay mixed with CCR admixed with zeolite, were observed to increase with increase in compaction energy. At 120 and 180 days curing period, the UCS tend to reduce at intermediate energy levels and raised again at (MP) compaction energy level. This was attributed to the later reaction of ettringite in the system. The UCS increased from 52kN/m^2 for untreated clay to 2400kN/m^2 for clay treated with 5% CCR admixed with 2% zeolite after 120 days curing. This strength satisfies the requirement for soils to be used as subbase course material for highly trafficked roads based on Nigeria General Specification for Roads and Bridge Works (1992).

Keywords: Stabilization, Unconfined compressive strength, X-ray diffraction, Scanning electron microscopy, calcium carbide residue, Zeolite.

INTRODUCTION

Deficient soils are usually stabilized with cement (Bell, 1995; Stavridakis, 2005; Diana et al, 2019; Narloch et al, 2020;), lime (Amu et al, 2011; Harichane et al, 2019), bitumen (Zumrawi and Awad, 2017) e.t.c to increase their strength and stability. Though cement remain the most effective stabilizing material, its cost of production and environmental pollution resulting from its production have continued to discourage construction engineers from using cement for soil stabilization.

Calcium Carbide Residue (CCR) is a waste generated from acetylene welding which is usually disposed indiscriminately thereby causing environmental pollution. Some researchers have identified CCR as an effective stabilizing chemical consisting majorly of calcium ion. The work of Harichane et al (2019), Vichan and Rachan (2013), Horpibulsuk et al (2013), Isah and Sharmila (2015), Akinwumi et al (2019) and Majeed et al (2018) have studied the use of CCR or CCR admixed with pozzolanic chemicals to stabilize soils. Addition of pozzolana to CCR treated clay was observed to give prolonged strength gain due to Pozzolanic reaction.

It is a common knowledge that chemical stabilization of clay soil can be affected by two major factors: The compaction energy and the amount of chemical used. Researchers undertaking studies in chemical stabilization of deficient soils are usually faced with the problem of what compaction energy level to employ. This is because, even

though, higher energy level will result in to higher initial strength gains, it can result in to lower optimum moisture content (OMC) which affect prolonged strength development negatively. Compaction at lower energy level on the other hand, will give lower initial strength which is capable of long time strength development due to high OMC. Vichan and Rachan (2013) used standard Proctor compaction energy and achieved maximum unconfined compressive strength (UCS) value of about 1300kN/m^2, Horpibulsuk et al, 2013 used both standard Proctor and Modified compaction energy levels to mold clay mixed with CCR and fly ash. Isah and Sharmila (2015) used standard Proctor compaction energy to mold clay stabilized with CCR and Coconut shell ash. The author achieved 11.38 times the UCS of the untreated clay. Joel and Edeh (2014) employed West African Standard compaction energy level to mold laterite treated with cement and CCR. These authors used different compaction energy levels because there is no standard compaction energy specified for these various chemical stabilizations.

Ijimdiya et al (2014) studied the effect of compaction energy on the strength of soil. The author considered British Standard Light (BSL), West African Standard (WAS) and British Standard Heavy (BSH) energy levels. It was concluded that (BSH) compaction energy gave the highest UCS and California bearing ratio (CBR). Ikara et al (2016) worked on the use of Standard Proctor compaction energy and Modified Compaction energy to mold black cotton soil (BCS) with addition of up to 8% cement admixed with waste glass (WG). The modified Proctor compaction energy recorded the higher UCS of 1568 kN/m^2 after 7 days curing and 2005 kN/m^2 after 28 days curing. Consolidation and creep parameters of clay was studied at five different compaction energy levels (Alhaji et al, 2020). Reduced standard Proctor, Standard Proctor, West African standard, Reduced modified Proctor and modified Proctor energy levels. The consolidation properties were observed to be empirically related to compaction energy.

This study is therefore aimed at developing a balance among compaction energy level that will be required for efficient stabilization of clay using CCR and zeolite.

MATERIALS AND METHODOLOGY

MATERIALS

The materials used are for this experiment includes clay, cement, CCR and zeolite. The clay soil was collected from the premisses of Niger State Polyteechnics, Zungeru, Niger State. The clay was collected at depthof between 0.8m to 1.5m using the method of disturbed sampling. The clay soil was air-dried and pulverized as specified in BS 1377 (1992). The CCR was obtained from local acetyline welders in Keteren Gwari mechanic site, Minna, Niger State. It was collected in form of sludge, air-dried, pulverized and sieved through British sieve size 0.075mm and kept in a dry place to avoid moisture infiltration in to the CCR. The zeolite used for this study was obtained from a commercial market in Zaria, Kaduna State. It was also kept in a dry place to avoid moisture infiltration.

Figure 1: Materials used (a) clay, (b) CCR, (c) zeolite, (d) distilled water

The distilled water was obtained from a commercial medicine store opposite General Hospital gate, Minna, Niger State.

2.2 METHOD OF EXPERIMENTATION

Index properties test including Atterberg limits, grain size analysis, specific gravity, natural moisture content were conducted on the untreated clay soil so as to classify the soil. Clay, CCR, zeolite and a compacted mixture of clay, CCR and zeolite specimen were collected and sent to South Africa for X-ray diffraction (XRD) test, scanning electron microscopy (SEM) test and electron dispersive spectroscopy (EDS) tests. This tests will reveal the mineral, elemental and morphology characteristics of the clay, CCR and zeolite.

The clay was then compacted at five different energy levels (Reduced Standard proctor energy, Standard proctor

energy, West African standard energy, Reduced modified proctor energy and Modified Proctor energy levels). At each energy level, unconfined compressive strength (UCS) specimen were molded for untreated clay, clay treated with 5% CCR and clay treated with 5% CCR admixed with 2% zeolite. The UCS specimen were cured for 28, 60, 120 and 180 days before testing to determine the effect of long time curing on the strength of the specimen (see figure 2).

Figure 2: Unconfined compressive strength test

Figure 3: Immersion method of durability test

After 28 days curing, some specimen were waxed and immersed in water for another 7 days before testing to determine the durability of the molded specimen (see figure 3).

RESULTS AND DISCUSSION

3.1 INDEX PROPERTIES OF THE CLAY SOIL

The summary of the result of index properties of the clay soil is shown on table 2. The table showed that the clay classified as A-6 based on AASHTO soil classification system and clay of low plasticity (CL) based on unified soil classification system. Therefore, the clay cannot be used for any component of a road structure in its natural state unless the clay is stabilized to enhance its strength and stability.

TABLE 1: PHYSICAL PROPERTIES OF THE CLAY SOIL

Properties	Quantities
Gravel (%)	0.0
Sand (%)	19.4
Silt (%)	28.6
Clay (%)	53.0
Specific gravity	2.49
Liquid limit (%)	38.9
Plasticity Index (%)	19.3
Natural moisture content (%)	10.2
AASHTO soil classification	A-6
Unified soil classification	CL
Maximum unit weight (kN/m^3)	16.58
Optimum moisture cont. (%)	18.8
Color	Greyish brown

3.2 CHEMICAL COMPOSITION OF MATERIALS USED

TABLE 2: OXIDE COMPOSITION OF CLAY, CCR AND ZEOLITE

Oxide (%)	Clay	CCR	Zeolite
Fe_2O_3	6.4	0.3	0.1
TiO_2	1.04	0.05	0.04
CaO	3.9	62.6	0.4
K_2O	0.6	0.1	0.3
SiO_2	63.0	4.4	31.7
Al_2O_3	15.8	1.3	27.2
MgO	1.8	0.7	1.3
Na_2O	1.9	0.0	19.6

The oxide composition of the clay, calcium carbide residue and zeolite used in the study is presented on table 2.The clay and zeolite composed predominantly of silica followed by alumina and some iron oxide. Alumina and

silica are the two oxides that participate in cementitious compounds-calcium silicate hydrate (C-S-H) and calcium aluminate hydrate (C-A-H), in the presence of calcium oxide CCR contains high composition of calcium oxide which can produce the requisite calcium ion to react with the available silica and alumina in clay and zeolite to form cementitious (C-S-H) and (C-A-H).

3.3 COMPACTION CHARACTERISTICS

The result of compaction characteristics of the clay at varied compaction energy levels is shown in figure 3. The maximum dry density (MDD) increased from 1.765Mg/m3 at reduced Standard Proctor (RSP) energy level to 1.976Mg/m3 at West African Standard (WAS) energy level and further increase to 2.113Mg/m3 at Modified Proctor energy levels. The result of the Optimum moisture content (OMC) revealed values in reversed order. The values decreased from 17.6% at reduced Standard Proctor to 13.8% at (WAS) compaction energy levels after which it further reduced to 12.1% at modified Proctor energy level. This is in agreement with Proctor (1933) and Lambe (1958) who both observed increase in density with increase in compaction energy level and decrease in optimum moisture content with increase in compaction energy levels.

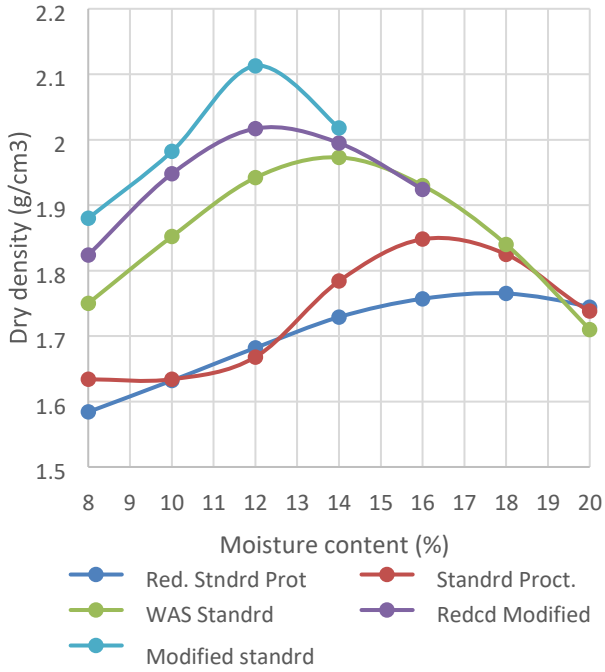

Figure 4: Compaction characteristics of clay at five energy levels

This trend can be explained along the line of lubrication theory (Proctor, 1933) who postulated that addition of water to dry soil particles began by lubrication of the particle surfaces which make it easier for lubricating particles to move and fill the pore spaces thereby increasing the density of the soil mass. When all the particles are fully lubricated, the remaining water will fill the pores and tend to reduce the density of the soil mass. This is because the specific gravity of water is less than that of soil particles. This assertion was overtaken by Lambe (1948) who explain this behavior along the line of clay structure.

3.4 MINERALOGICAL CHARACTERISTICS

The result of mineralogical characteristics of the clay, CCR, zeolite, clay treated with 5% CCR and clay treated with 5% CCR admixed with 2% zeolite are presented in figure 5 a-e. The natural clay consists of peaks for developing Ettringite at 2θ values of approximately 8 and 18, Albite at 2θ values of approximately 22 to 31, kaolinite at 2θ values of approximately 13, 20, 38 and 63, quartz at 2θ values of approximately 21, 26, 36, 39, 50 and 60 and calcite at 2θ values of 29.

Figure 4b showed the result of CCR peaks which are predominantly portlandite at 2θ values of approximately 18, 34.5, 47.1 and 51, calcite at 2θ values of approximately 23, 29.5, 36, 39.5 and 47 and quartz at 2θ values of approximately 21, 27 and 37. Portlandite and calcite are calcium rich minerals which contributes to the formation of cementitious composites.

Figure 4c represents the result of zeolite peaks which occurs at 2θ values of 7.5, 10, 12.5, 23, 27 to 59.

Figure 4d is the graph showing the peak values of clay treated with 5% CCR. The result showed anorthite peak at 2θ values of approximately 6 and 16, kaolinite peak at 2θ values of approximately 11.4, 19.5, 38 and 63, albite peak at 2θ values of approximately 13, 21.5 and 28, calcite peak at 2θ values of approximately 29 and quartz at 2θ values of approximately 21, 26.5, 37.5, 39 and 50.

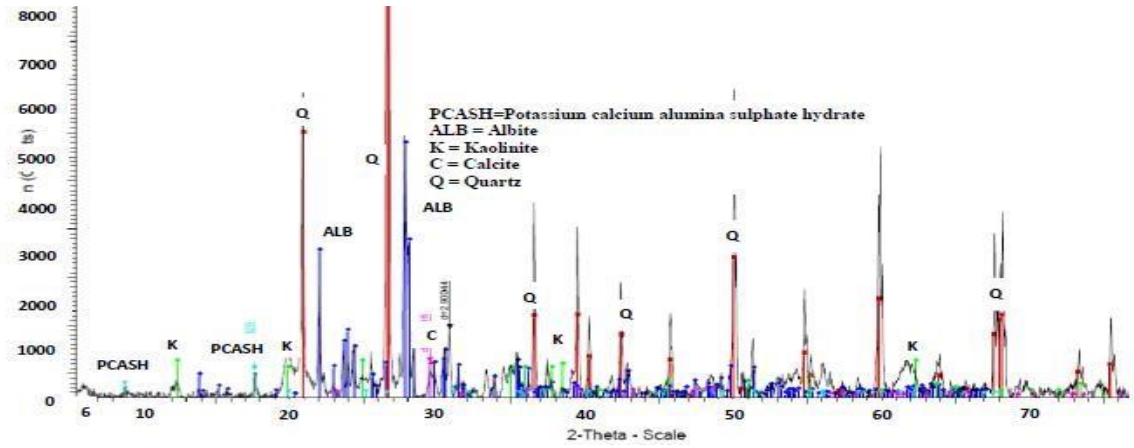

Figure 5a: XRD Pattern for Untreated clay

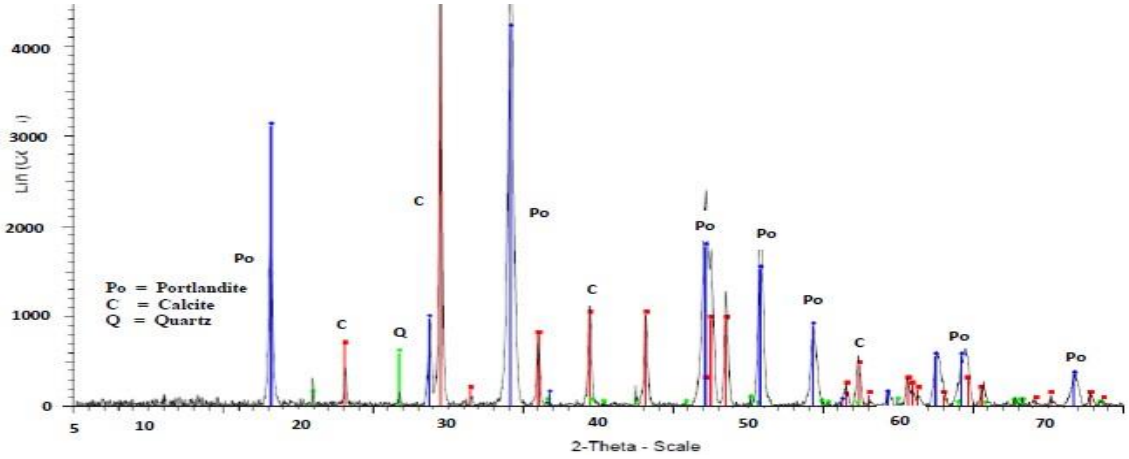

Figure 5b: XRD Pattern for Calcium Carbide Residue (CCR)

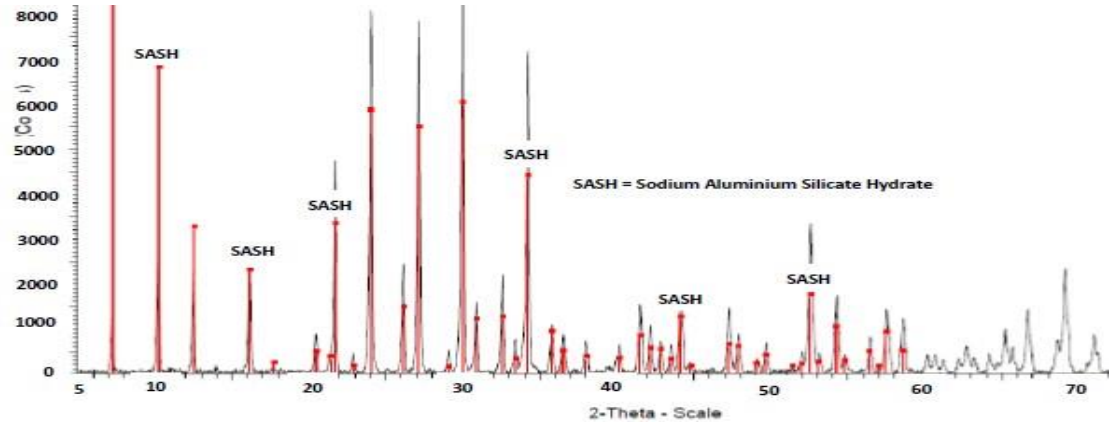

Figure 5c: XRD Pattern for Zeolite

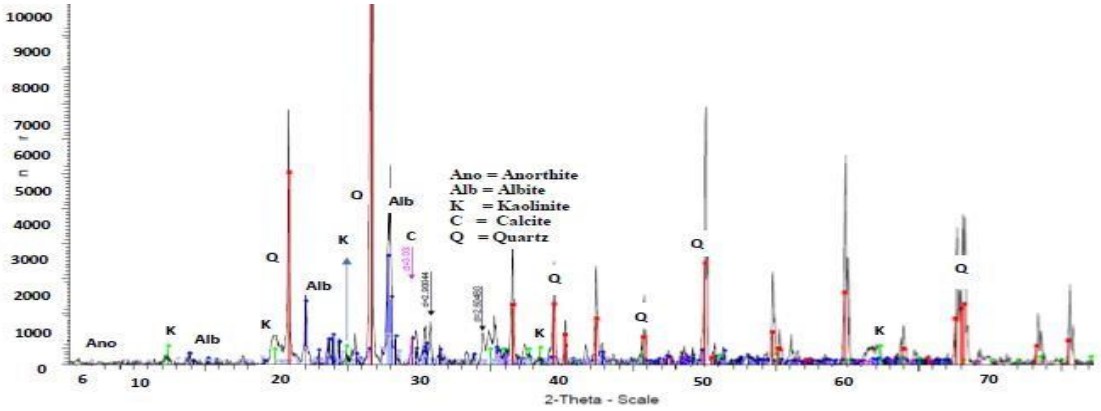

Figure 5d: XRD Pattern for Clay Treated with 5% CCR

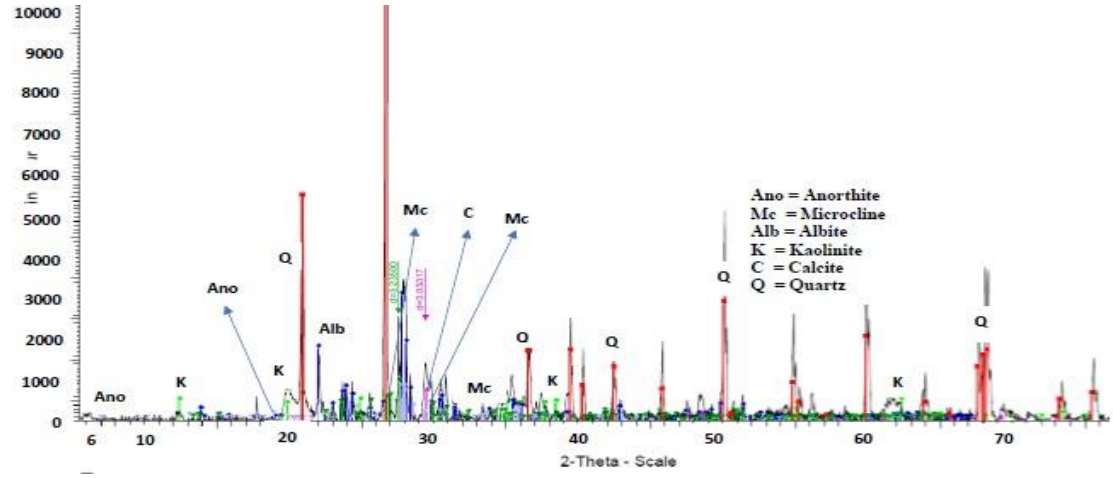

Figure 5e: XRD Pattern for Clay Treated with 5% CCR and 2% Zeolite

Addition of 5% CCR was observed to have disintegrated the developing Ettringite in the untreated clay and form anorthite mineral which is rich in calcium ion. Albite, kaolinite and calcite were retained in the mixture. Addition of both CCR and zeolite also disintegrate the developing Ettringite with formation of both anorthite and microcline. In all samples, no C-S-H compounds were identified by XRD. The poor crystalline structures of C-S-H compounds make them undetectable by XRD.

3.5 SCANNING ELECTRON MICROSCOPY

The morphology of the clay, CCR, Zeolite, clay treated with 5% CCR alone and clay treated with both the CCR and zeolite is shown on figure 6 a-e. The SEM image of clay reveal that soil particles are aggregated into lumps due to the cohesive nature of the clayey soil. However, it also shows the platy clay particles that make up the soil aggregates. The major elements revealed by the EDS test are carbon, oxygen and silicon. The micrograph of CCR and EDS (see figure 6b) also showed aggregated particles in form of honeycomb with pore spaces. The whitish portlandite minerals are visible on the

micrograph. The major elelments recorded by EDS are carbon, oxygen and calcium.

The micrograph of zeolite is shown on figure 5c. It consists of aggregation of particles with pore spaces. The major elements observed from EDS result are Carbon, oxygen, sodium, aluminium and silica for clay treated with 5% CCR showed whitish substance covering the particles which are suspected to be uncrystallized cementitious calcium silicate hydrate (C-S-H). However, large pore spaces were still observed in the specimen. The major elements recorded from EDS result are oxygen, aluminium, silicon and iron.

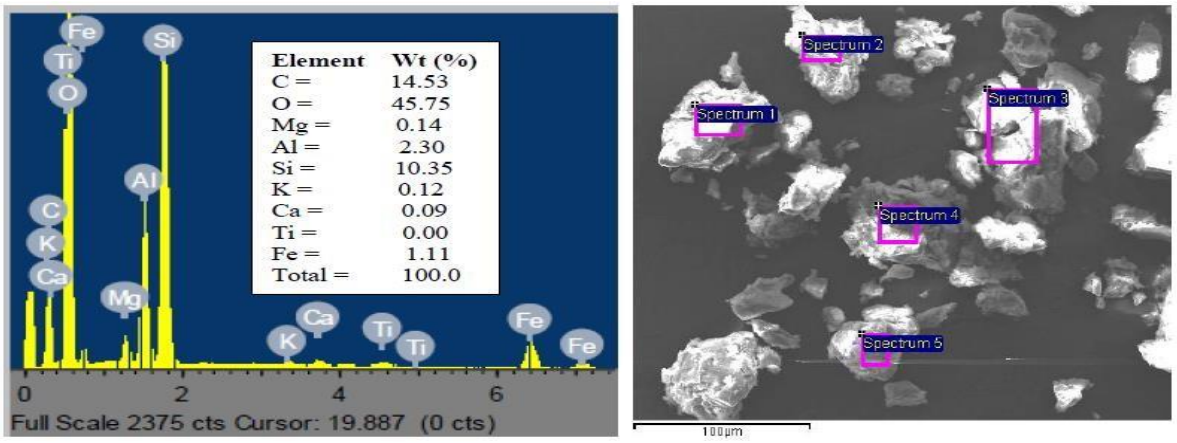

Figure 6a: SEM and EDS for untreated clay

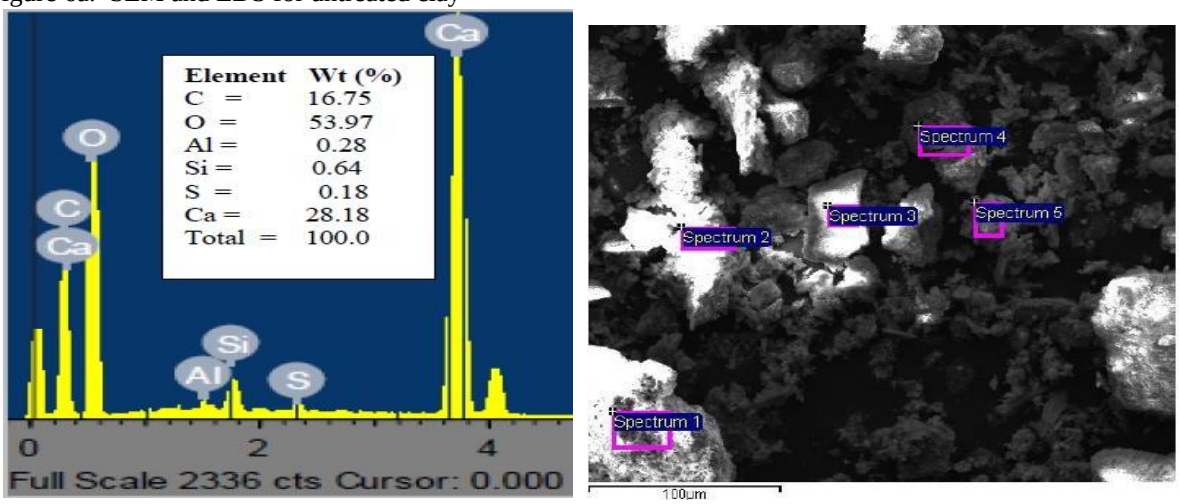

Figure 6b: SEM and EDS for CCR

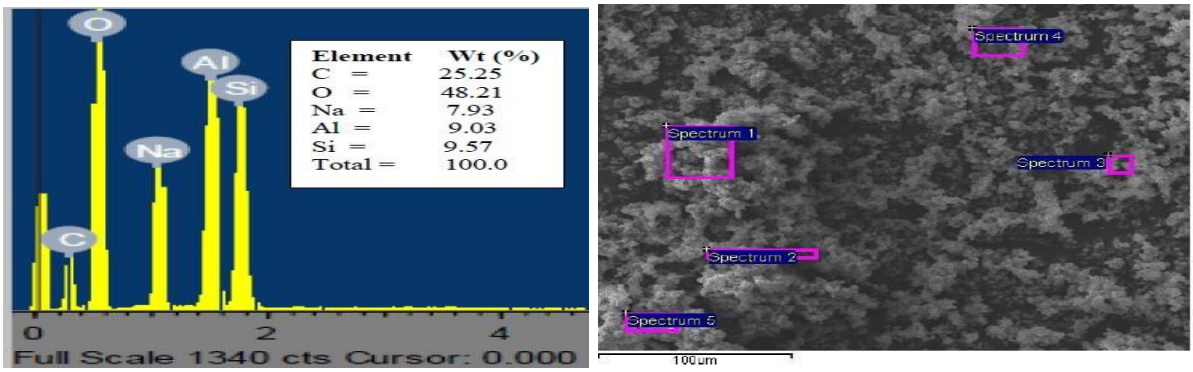

Figure 6c: SEM and EDS for Zeolite

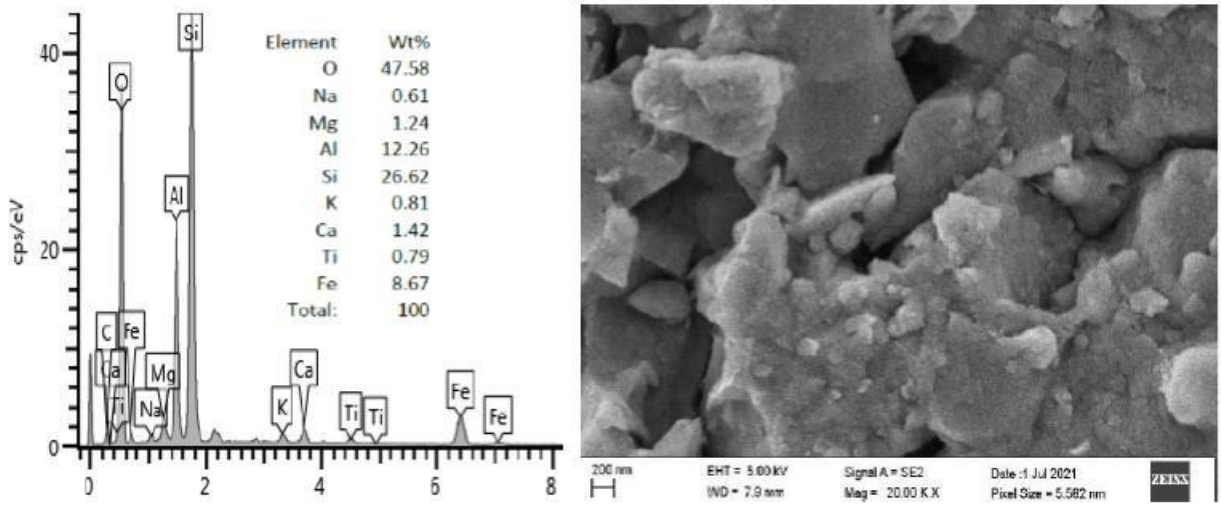

Figure 6d: SEM and EDS for clay treated with 5% CCR

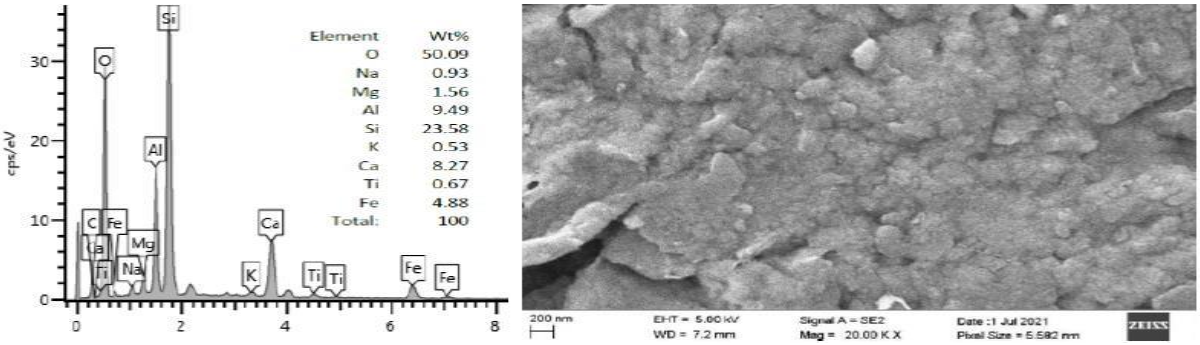

Figure 6e: SEM and EDS for clay treated with 5% CCR and 2% zeolite

The micrograph and EDS of clay treated with 5% CCR and 2% zeolite is presented in figure 6e. The micrograph showed compact structure whose pores are filled with whitish substances suspected to be cementitious calcium silicate hydrate and calcium illuminate hydrate. The major elements recorded by EDS result are oxygen, silica, alumina and calcium.

3.6 STRENGTH CHARACTERISTICS OF STABILIZED CLAY AT DIFFERENT ENERGY LEVELS

The result of UCS with variation in compaction energy level is presented in figure 7 a-d. Generally, the UCS result of the 7 days curing (see figure 7a) showed gentle increase in UCS with increase in compaction energy levels for untreated specimen, clay treated with 5% CCR and clay treated with 5% CCR and 2% zeolite. The UCS of untreated clay increased from 52kN/m^2 at reduced standard Proctor (RSP) compaction energy level to 243kN/m^2 at modified Proctor (MP) compaction energy level. Addition of 5% CCR gave UCS results increasing from 414kN/m^2 at (RSP) compaction energy to 1022kN/m^2 at (MP) compaction energy level. This increase must have resulted from the reaction of calcium hydroxide and calcium carbonate in CCR with the amorphors silica and alumina contained in clay to form cementitious calcium silicate hydrate (C-S-H) and calcium aluminate hydrate (C-S-H) and calcium aluminate hydrate (C-A-H). These two composites cemented the clay particles together thereby increasing the strength and stability. Addition of 2% zeolite to clay-CCR mixture increased the UCS further from 1109kN/m^2 at (RSP) compaction energy level to 1415kN/m^2 at (MP) compaction energy level.

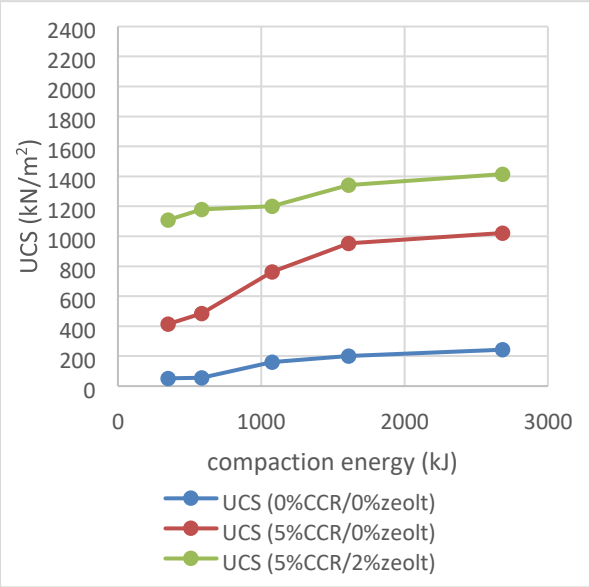

Figure 7a: UCS with Compaction energy at 7 days curing

This further increase resulted from the pozzolanic reaction between the portlandite in the CCR and silica and alumina contained in the zeolite as shown by the XRF and XRD results.

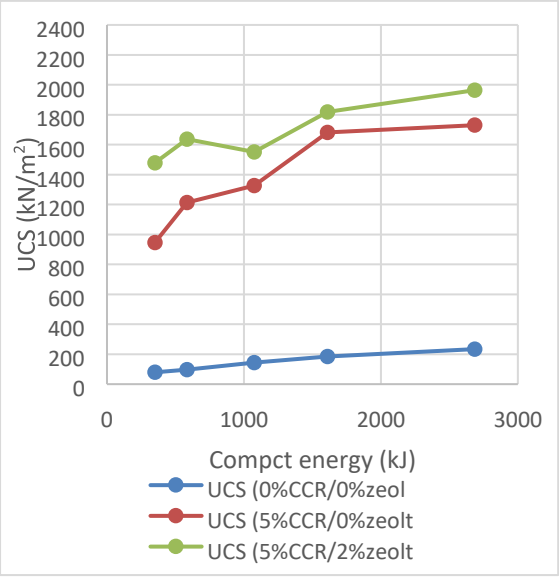

Figure 7b: UCS with Compaction energy at 60 days curing

The trend observed in the result of the 60 days curing (see figure 7b) is similar to that of 7 days curing with general increase in UCS with increase in compaction energy level for all the mixtures and compaction energy levels. The UCS results of clay treated with CCR and CCR admixed with zeolite recorded marginal increase compared to that of 7 days curing. The UCS of clay treated with 5% CCR recorded increase in UCS from 944kN/m^2 at (SP) compaction energy to 1730kN/m^2 at

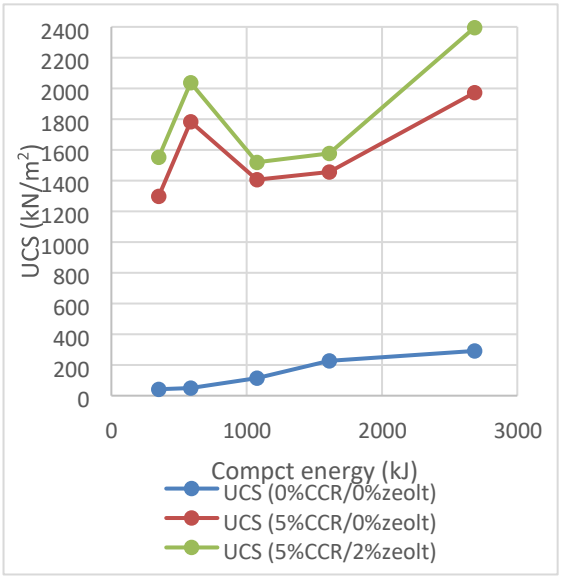

Figure 7c: UCS with Compaction energy at 120 days curing

(MP) compaction energy level. The UCS of clay treated with 5% CCR admixed with 2% zeolite increased from 1479kN/m^2 at (SP) compaction energy to 1964kN/m^2 at

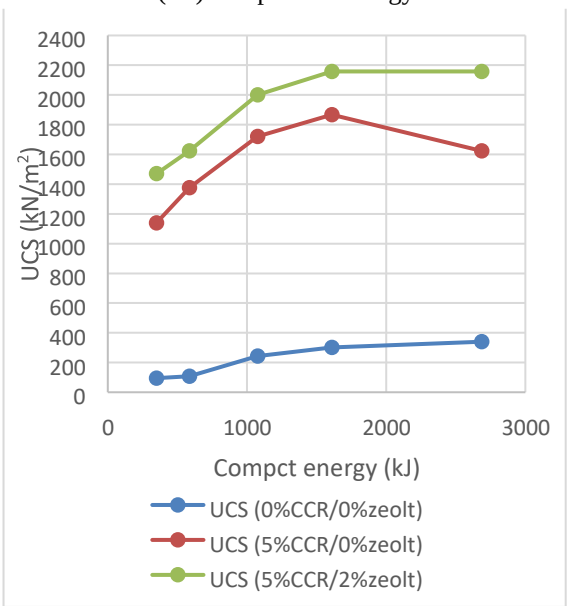

Figure 7d: UCS with Compaction energy at 180 days curing

(MP) compaction energy level. The UCS increase after 60 days curing is mainly due to pozzolanic reaction between the excess portlandite and calcite in CCR and the amorphous silica and alumina contained in the zeolite.

The trend of the UCS result for clay treated with 5% CCR as well as clay treated with 5% CCR admixed with 2% zeolite after 120 days curing (see figure 7c) revealed initial increase in UCS from (RSP) compaction energy level to standard Proctor (SP) compaction energy level. Thereafter, the UCS values reduced to West African standard (WAS) compaction energy levels and Reduced modified Proctor (RMP) compaction energy level after which the UCS values increased again to the maximum UCS value of 2400kN/m^2 at (MP) compaction energy level. The specimen compacted at lower compaction energy levels posseses higher optimum moisture content (OMC) which must have allowed for fast initial increase in strength. (WAS) and (RMP) compaction energy levels posseses moderate densities and lower (OMC) compared to (RSP) compaction energy level which must have resulted in to reduced chemical reaction to form cementitious compounds thereby reducing the strength. The sudden increase in strength at (MP) compaction energy level is caused by the higher density which control the strength of stabilized soils. The increase in strength due to addition of 2% zeolite due to pozzolanic reaction is also revealed in the general trend but was observed to be lower than that of 60 days curing.

After 180 days curing, there is decrease in the maximum UCS from the 2400kN/m^2 observed after 120 days curing to 2200kN/m^2. The trend in UCS of clay treated with 5% CCR and clay treated with 5% CCR admixed with 2% zeolite showed increase from (RSP) compaction energy to (WAS) compaction energy after which the UCS values reduced. The trend of clay treated with 5% CCR reduced to (MP) compaction energy level while the trend of clay treated with 5% CCR admixed with 2% zeolite tend to increase at (MP) compaction energy level. The eventual reduction of clay treated with 5% CCR can probably be attributed to the action of entriggite which can be formed in CCR by the sulphur and oxygen observed in the EDS result of CCR. The mineralogy of the clay also revealed delayed ettringite mineral which can easily be converted to ettringite with the removal of potassium in the delayed etrringite. Addition of 2% zeolite to clay-5% CCR mixture tend to neutralize the effect of the ettringite thereby undergoing the tendency to increase in UCS. The maximum UCS values of 2200kN/m^2 and 2400kN/m^2 both satisfy the specification for the clay material to be used as sub-base material for highly trafficked roads according to Nigeria General Specification for Roads and Bridge Works (1992).

3.7 DURABILITY TEST RESULTS

The result of the durability test is shown on figure 7 for the natural clay, clay treated with CCR only and clay treated with both CCR and zeolite. It was observed that resistance to loss in strength ranges between 27 and 43% for untreated clay for the five compaction energy levels studied. For clay treated with CCR alone, the resistance to loss in strength ranges from 70% to 77% while the clay treated with both CCR and zeolite recorded

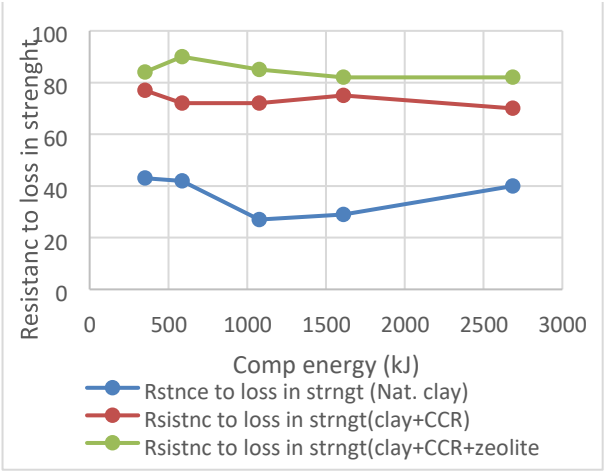

Figure 8: Durability result for clay, clay-CCR and clay-CCR-zeolite

resistance to loss in strength ranging between 82 to 90%. The values of resistance to loss in strength recorded for clay treated with both CCR and zeolite generally satisfied the 80% minimum resistance to loss in strength for cement stabilized soils to be used as base course material for road structures.

CONCLUSIONS

1 The clay used for this study classified under A-6 based on AASHTO soil classification system and clay of low plasticity (CL) based on unified soil classification system (USCS).

2 The oxide composition of the clay, CCR and zeolite showed predominance of silica, portlandite and calcite and zeolite respectively.

3 The mineralogical composition of CCR was mainly portlandite and calcite, zeolite minerals was observed in zeolite and quartzite, kaolinite and albite was recorded in untreated clay soil.

4 There is general increase in strength with increase in curing days to 60 days curing for clay treated with 5%

CCR and 5% CCR admixed with 2% zeolite. At 120 days curing, there was a marginal decrease in strength from (SP) compaction energy to (RMP) compaction energies after which the values increased at (MP) compaction energy level. After 180 days of curing, the strength increased to (WAS) compaction energy after which the values decreased to (MP) compaction energy due to probable reaction of ettringite.

5 The UCS increased from 52kN/m2 for untreated clay soil to maximum UCS value of 2400kN/m2 at 120 days curing. This value satisfy the requirement for soil material to be used as subbase material for highly trafficked roads based on Nigerian General Specification for Roads and Bridge Works (1992).

6 The trend of UCS with compaction energy level for all the compaction energy levels shows pozzolanic performance of zeolite when mixed with clay along side CCR. However, the pozzolanic action was more pronounced at lower curing days.

REFERENCE

Narloch, P., Woyciechowski, P., Kotowski, J., Gawriuczenkow, I. and Wojcik, E. (2020), The Effect of Soil Mineral Composition on the Compressive Strength of Cement Stabilized Rammed Earth, Materials, (13), 324-344.

Stavridakis, E. I. (2005), Evaluation of Engineering and Cement-Stabilization Parameters of Clayey-sand mixtures Under Soaked Conditions, Geotechnical and Geological Engineering, (23), 635-655

Bell, F. G. (1995), Cement Stabilization and Clay soils, with Examples, Environmental & Engineering Geoscience, (1) 2, 139-151

Diana, W., Hartono, E. and Muntohar, A. S. (2019), The Permeability of Portland Cement-Stabilized Clay Shale, IOP Conference Series: Materials Science and Engineering, 650, doi. 10.1088/1757-899X/650/1/012027

Amu, O. O., Bamisaye, O. F. and Komolafe, I. A. (2011), The Suitability and Lime Stabilization Requirement of Some Samples as Pavement, International Journal of Pure and Applied Sciences and Technology, (2)1, 29-46

Harichane, K., Ghrici, M. and Gadouri, H. (2019), Natural Pozzolana Used as a Source of Silica for Improving the Behavior of Lime-Stabilized Clayey Soil, Arabian Journal of Geosciences, (12), 447-452

Vichan, S. and Rachan, R. (2013), Chemical Stabilization of Soft Bangkok Clay Using the Blend of Calcium Carbide Residue and Biomass Ash, Soils and Foundations, (53)2, 272-281

Isah, B. W. and Sharmila, S. M. R. (2015), Soil Stabilization Using Calcium Carbide Residue and Coconut Shell Ash, Journal of Basic and Applied Engineering Research, Vol. 2, No. 12, Pp 1039-1044

Horpibulsuk, S., Phetchuay, C. Chinkulkijniwat, A. and Cholaphatsom, A. (2013), Strength Development in Silty Clay Stabilized with Calcium Carbide Residue and Fly Ash, Soils and Foundations, (53)4, 477-486

Akinwumi, I. I., Ajayi, O. O., Agarana, M. C., Ogbiye, A. S., Ojuri, O. O. and David, A. O. (2019), Investigation of Calcium Carbide Residue as a Stabilizer for Tropical Sand Used as Pavement Material, WIT Transactions on the Built Environment, (182), 285-294

Majeed, Z. H., Jawad, I. T. and Owaid, H. M. (2018), Fine Grained Soil Stabilization Using Binary Blending of Calcium Carbide Residue and Palm Oil Fuel Ash, International Journal of Civil Engineering and Technology, (9)4, 939-950

Joel, M. and Edeh, E. J. (2014), Stabilization of Ikpayongo Laterite with Cement and Calcium Carbide Waste, Global Journal of Pure and Applied Sciences, (20), 49-55

Ijimdiya, T. S., Sani, L., Isaac, A. L., Sani, J. E. and Osinubi, K. J. (2014), Effect of Compactive Effort on Properties of Cement Stabilized Black Cotton Soil Admixed with Groundnut Shell Ash, Proceedings of Nigerian Engineering Conference, Ahmadu Bello University, Zaria, Kaduna State, 392-403

Ikara, I. A., Kundiri, A. M. and Mohammed, A. (2016), Influence of Standard and Modified Proctor Compactive Efforts on Cement Stabilized Black Cotton Soil (BCS) with Waste Glass (WG) Admixture, IOSR Journal of Mechanical and Civil Engineering, (13)3, 716-726

Alhaji, M. M., Alhassan, M., Adejumo, T. W. and Jibrin, R. (2020), Effect of Density on Consolidation and Creep Parameters of Clay, Indonesian Journal of Science & Technology, (5)1, 31-44 .

Zumrawi, M. M. E. and E Abdalla, E. A. (2018). Stabilization of Expansive Soil Using Marble Waste Powder, 2nd Conference of Civil Engineering, Sudan, 266-271

BS 1377 (1992), Methods of Testing Soils for Civil Engineering Purposes, BSI Publications, 389, Chiswick High Road, London

4th International Engineering Conference (IEC 2023)
Federal University of Technology, Minna, Nigeria

Analysis of Soil Salinization on Groundwater Quality in an Irrigated Land

Abdullahi, J.[1*] and Abdullahi, S. A.[2]
Department of Agricultural Engineering and Irrigation,
National Agricultural Extension and Research Liaison Services, Ahmadu Bello University, Zaria, Nigeria[1]
Department of Water Resource and Environmental Engineering,
Faculty of Engineering, Ahmadu Bello University, Zaria, Nigeria[2]
*Correspondent author email: namallam05@yahoo.co.uk +2348068106008

ABSTRACT
Soil salinization is the most widespread form of groundwater contamination that is signified by the increase of total dissolved salts (TDSs) and specific chemical constituents. It is scientifically evidenced that irrigated agriculture inevitably caused salinization of soil either directly or indirectly has impact to the environment leading to destruction of natural vegetation; soil deterioration, surface water, and groundwater pollution. Kano River Irrigation Project (KRIP) has been in existing for over 40years with intense irrigated activities. The major problem pointed-out by this research and other various researches conducted within the area is soil salinization (sodicity), and also rises in water table which will eventually come into contact with such affected soil, and in turn become contaminated. This paper aims to highlight the basic stages in which soil salinization affects groundwater quality within this area, and bring-up with useful solutions. The results indicate the average salinity (ECe) within the soil samples collected as 0.278dS/m, TDS as 177.8mg/L, and pHe of 7.7 respectively. The correlation between the mass concentration of total dissolved solids (TDS) and that of soil salinity (ECe at 25^0C) has been established to represent soluble salts in the area with a regression model of $R^2 = 0.9998$. The soils in this area can be treated by applying gypsum or by reducing the salinity in the soil and irrigation water to increase infiltration into the surface soils and improve the productivity of the root zone.

Keywords: *Contaminants, Groundwater quality, Irrigation, Soil salinization, Salinity,*

1 INTRODUCTION

Salinization remains the major environmental adversity affecting soil and water resources, agriculture, and creating disturbances in the natural ecosystem. Groundwater contamination is also related to high concentrations of some elements like sodium, sulfate, boron, fluoride, selenium, arsenic, and high radioactivity *(Krishan, 2019)*. Soil salinization concerning irrigated agricultural activities is affecting the groundwater quality with the greatest environmental and economic impacts worldwide (*Morris et al. 2003; FAO 2016*).

Soil salinization signified the increase in the accumulation of total dissolved salts (TDSs) and specific chemical constituents, and these accumulated salts leach down to groundwater (*Yakirevich et al, 2013; Stephen et al, 2018)*. It is commonly a result of direct excessive exploitation, improper protection of land use *(Bocanegra et al, 2010*), and irrigation water mismanagement practices *(Postel 1989; Stephen et al, 2018*; *Blaylock, 1994; Mutasem, 2018; Stephen et al, 2018).*

Soil hydraulic conductivity especially in the unsaturated zone, remains as key factor in the downward displacement of the dissolved salts where various hydro-geochemical processes take place, including oxidation, reduction, ionic exchange, fixation, and precipitation (*Suarez 1989; Aragues and Tanji 2003; FAO 2016; Pulido-Bosch et al, 2018*). Salts transport to groundwater is a common problem in most agricultural areas, especially with its load concentration stored in the unsaturated zone, and its movement down into the saturated zone (*Suarez, 1989; Ferguson and Bateridge, 1982*).

Irrigated agriculture has caused inflicts specifically in areas with high evapotranspiration rates and low precipitation, which leads to the destruction of natural vegetation, soils deterioration, surface water bodies, and groundwater pollution (*Pulido-Bosch et al, 2018; AQUASTAT 2022*). Irrigated agriculture increases the quantity of water applied to the soils in most cases enhance the groundwater recharge (*Suarez 1989*; *Scanlon et al. 2007; Foster et al, 2018*).

Non-irrigated farming practices have also been referred to as the cause of serious groundwater deterioration. Evidence exists that; the crop-fallow farming system has been a major factor contributing to the increase in shallow groundwater build-up and its contamination (*Miller et al, 1980*). Analysis of the impact of soluble salt in crop-fallow farming by Ferguson and Bateridge (1982), indicates a significant reduction of salt in the root zone for most of the soils, however, 90t/ha of the salt has been moved in the soil toward the groundwater table causing groundwater contamination in the area studied *(Suarez, 1989*).

The major emphasis on the assessment of soil salinization and control measures has been on minimizing or reversing the increase in surface water deterioration

caused by agriculture with the fact that surface water quality is easier to characterize than groundwater.

Human activities involved in irrigated agriculture have been recognized as the cause of modification in soil properties, especially the degree of salinization (*Ferguson and Bateridge, 1982*), leading to irreversible groundwater contamination in many regions *(Aadhityaa et al, 2021*). This impact is compounded either through the concentration of salts due to plant water uptake, or the movement of salts already in the unsaturated zone down into groundwater (*Stephen et al, 2018; Suarez, 1989*).

Irrigation water quality substantially influences the extent of the groundwater deterioration process, ranging from freshwater to saline, when the contents of dissolved solids in terms of salts concentration level are above a predefined limit usually 1000mg/L. Soil textures influences salt accumulation ranging from clay to loam, with sandy textures having the tendency to show larger salinization other than coarser textures due to raise in residence time allowing more time for evapotranspiration (*FAO 2016; Pulido-Bosch et al, 2018).*

Groundwater deterioration is usually a slower process but one which deserves serious attention (*Suarez, 1989; Yakirevich et al, 2013).* In irrigated areas could be a result of higher concentrations of salts in the soil, which adversely affect both the chemical and the physical properties of the system leading to a long-term effect (*Burger, 2003; Aadhityaa et al, 2021*). In the process within salinized soils, salt reaches the groundwater when the pH increases over time and contaminates the aquifer. The degree and sternness of deterioration varied with the type and concentration of salt, climate geography and thus altering its physio-chemical properties and structure. Hence, soil salinization could contaminate groundwater at the same time harm crop growth (*De Craat et al, 2020*).

The consequences of irrigated activities on groundwater quality, have either direct or indirect consequences accompanying the application of water and agrochemicals (such as fertilizers, herbicides, and pesticides) to irrigated land (*Foster and Cherlet 2014; Pulido Bosch et al, 2018).*

The application of irrigation water in excess to satisfy crop water requirements and to leach the salts from the soil (FAO 2016) remains one of the processes that lead to the increase in the deterioration of groundwater quality (*Suarez 1989*). Salt concentration increases, resulting from crop transpiration and evaporation (i.e. water is evaporated and dissolved salts remained in the soil or accumulated in the unsaturated zone) (*Suarez 1989; Scanlon et al. 2005*).

Excessive groundwater abstraction for irrigation purposes can lead to groundwater quality deterioration and in-turn reduces the assimilative capacity of the aquifer. Hence, results in a decline in water levels with new hydraulic head distribution which changes the directions of groundwater flow (*Suarez 1989; Pulido Bosch et al, 2018*). Whenever saline water (low quality) is part of the subsurface system, it may gradually advance to freshwater zones relative to the aquifer (*Pulido Bosch et al, 2018*; *Baghvand et al. 2010*).

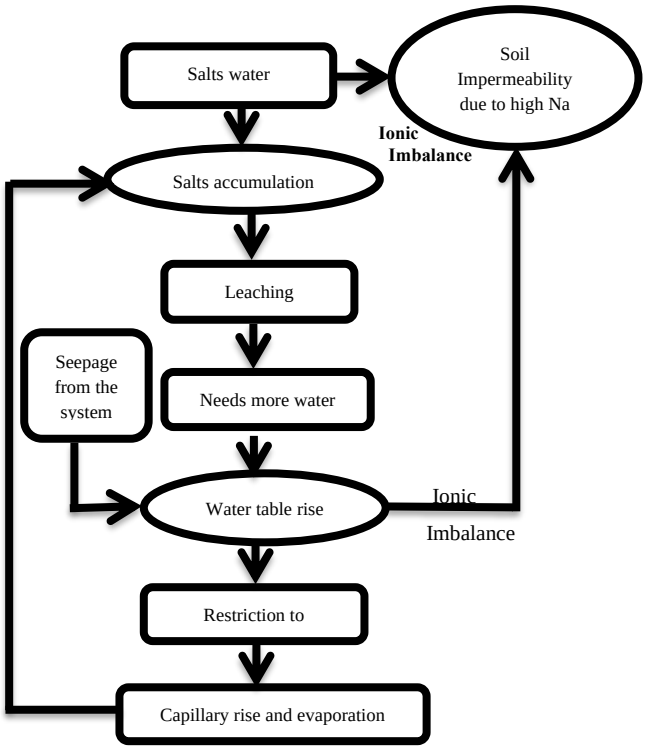

Fig 1: A hypothetical soil salinization cycle: ***(Adapted and modified from Shahid et al. 2010)***

Kano River Irrigation Project (KRIP) has been in existence for over 40years with intense irrigated activities. The major problem pointed-out by this research and other various researches conducted within the area is soil salinization (sodicity), and also rises in water table which will eventually come into contact with such affected soil. These will leads either directly or indirectly to the destruction of natural vegetation, soil deterioration, surface water, and groundwater pollution.

Thus, the main objective of this paper is to evaluate or assess the possible effects of soil salinization on groundwater quality in this area of study, KRIP and come up with a model of its transition using field data obtained in the course of this research.

2 METHODOLOGY

A salinity monitoring plan must be an integral part of any agricultural project and an effective salinity monitoring plan must be deployed in dealing with irrigation water so that salinity changes could be traced, more especially in the root-zone soil. The following methodology has been employed to accomplish the aim of this research as follows:

2.1 **Description of the sample location**

The data analyzed is obtained from the irrigation experimental field at the Kano River Irrigation Project (KRIP). The experiment aimed at reclaiming and management of saline/sodic soil in the area. Kano River Irrigation Project (KRIP) lies between latitude 11032`N to 11051`N and longitude 08040`E to 08040`E within the Sudan Savannah zone of Nigeria, a semi-arid climate with mean annual precipitation which is about 898 mm (maximum and minimum values are 1872 mm and 419.6 mm respectively). Evaporation is in the range of 3500mm to 4500mm per year and it is generally higher than precipitation *(KRIP, 1976; Tajuri, 2018*).

It is a scheme with irrigation facilities and almost 90% of its soil is suitable for irrigation. A well-drained sandy loam textured surface and sandy clay loam textured subsoil (i.e. alluvial deposit) of various thicknesses over laterite or bottom rock, while 10% is poorly drained sandy-loam (coarse and fine) dominated by older granites and younger metasediments of Precambrian to lower Paleozoic age (*KRIP, 1976; Malgwi et.al 2002*).

2.2 **Soil sampling**

The physicochemical properties of the soil were monitored within 90cm of the soil profile in each section of the area. In the soil profile, three soil horizons of 30cm interval: 0 – 30, 30 – 60, and 60 – 90cm is considered (FAO, 2006). The variations in the properties of the soil within the soil horizons are to be determined based on the physical and chemical analyses of the collected soil samples.

These include; saturated soil hydraulic conductivity (Ks), soil texture, the pHe and electrical conductivity of the saturated extract (ECe), soluble cation concentrations (Ca^{2+}, Mg^{2+}, Na^{+}), and the sodium adsorption ratio (SAR) (*Zeid et at, 2018*).

2.3 **pHe of the Saturated Soil Paste**

Soil pH remains part of the key influence on the physicochemical condition of the soil which determines the degree of acidity or alkalinity in its profile. This measurement was carried out using standard guidelines of the Food and Agricultural Organization (FAO, 2006).

2.4 **Electrical conductivity (ECe) of the Soil Sample**

The electrical conductivity (ECe) of the soil sample measures and evaluates the level of soil salinization. A high level negatively affects many soil physicochemical characteristics such as soil structure and soil porosity (*Huang et al. 2011; Shrivastava and Kumar 2015; Ray and Brady, 2017*). It is calculated using Equation 1, with the temperature correction factor and cell constant parameters calculated using Equations 2 and 3, respectively.

$$EC_{25} = EC_T \times K \times ft \quad \text{……. Equation (1)}$$

$$f_t = 0.4470 + 1.4034e^{-t/26.815} \quad \text{… ……Equation (2)}$$

$$K = \frac{Known\ conductivity\ of\ 0.01\ N\ KCL}{Conductivity\ of\ 0.01\ N\ KCL\ measured} \quad \text{Equation(3)}$$

Where;

EC_{25} is the conductivity of the soil sample at 25^0C.
EC_T is the apparent conductivity of soil-water extract as measured.
K is the cell constant
Ft is the temperature correction factor.

2.5 **Total Dissolve Salt (TDS)**

The total dissolved Salt (TDS) of the soil sample was obtained from Equations 4 and 5 depending on the level of Electrical conductivity (Ray and Brady, 2017 revised).

$$TDS(mg/L) = EC_e(dS/m) \text{ at } 25^0\text{C} \times 640$$

…….. Equation (4)
When ECe less than 5dS/m

$$TDS(mg/L) = EC_e(dS/m) \text{ at } 25^0\text{C} \times 840$$

…… Equation (5)
When ECe more than 5dS/m

2.6 **Sodium Adsorption Ratio (SAR) of the soil sample**

The sodium absorption ratio of the soil sample probed it is potentiality, especially the soil structure. These could be determined based on the composition of Ca^{2+}, Mg^{2+}, K^{+}, and Na^{+} of the soil extracted by adding Ammonium Acetate NH4OAC at pH 7, it can be read using Atomic Absorption Spectrophotometer (ASS) and Flame emission photometry (*Ray and Brady, 2017; Zeid et al. 2018*). The SAR is determined using Equation 6.

$$SAR = \frac{N_a^+}{\sqrt{\frac{Ca^{2+} + Mg^{2+}}{2}}} \quad \text{…… Equation (6)}$$

2.7 **Exchangeable Sodium Percentage (ESP) of the soil**

The Exchangeable Sodium percentage (ESP) of the soil is obtained as the ratio of sodium ions to the total cation capacity of the soil.

The exchangeable base of Ca^{2+}, $Mg^{2+,}$ K^{+}, and Na is determined using soil extracted by adding Ammonium Acetate NH4OAC at pH 7, and Ca^{2+} and Mg^{2+} are read using an Atomic Absorption spectrophotometer, while Na^{+} and K^{+} with Flame emission photometry. The ESP is calculated using Equation 7.

$$ESP = \frac{Na^+}{Na^+ + Ca^{2+} + Mg^{2+} + K^+} \times 100\% \quad \text{..... Equation (7)}$$

2.8 **Saturated Hydraulic conductivity of the soil sample**

Saturated hydraulic conductivity (K_{Sat}) quantitatively measures the soil's ability to transmit water when subjected to a hydraulic gradient. It is the ease with which pores of a saturated soil permit water solutes movement.

These can be measured with the use of the constant head method (*Blake and Hartge 1986*). The K_{sat} is calculated using Equation 8.

Soil saturated conductivity, $K_{Sat} = \frac{\Delta V}{\Delta T \times i \times A}$ Equation (8)

Where ΔV is the volume of the inflow or outflow, ΔT is the time step, i is the hydraulic gradient, and A is the cross-sectional area of the soil column.

3. RESULTS AND DISCUSSION

The total concentration (salinity) of all the soluble salts in the soil – water is usually expressed in terms of electrical conductivity (ECe). Therefore, analyzing the impact through the empirical relationship of the Total dissolved Solid (TDS) and electrical conductivity is judgmentally considered.

The laboratory analysis of soil samples collected in the field at various spot points worthy of this presentation is shown in Table 1.

Table 1: Field Soil TDS evaluated data – KRIP (2022)

Location	**Latitude: 11^{0}39'42.492''N Longitude.: 8^{0}24'59.952''E Altitude: 509.50m**		
Parameters	**pHe**	**ECe (dS/m) at 25^{0}C**	**TDS (mg/L)**
Point 1	7.8	0.146	93.57
Point 2	7.1	0.219	140.35
Point 3	7.9	0.465	297.28
Point 4	7.3	0.292	187.14
Point 5	7.7	0.245	156.93
Point 6	7.6	0.173	110.72
Point 7	7.5	0.223	142.98
Point 8	7.7	0.454	290.82
Point 9	7.5	0.278	178.18
Point 10	7.9	0.281	180.03
Average	**7.7**	**0.278**	**177.8**

The results of electrical conductivity (<4dS/m) indicate the soil salinization (sodicity) i.e. it is rich with sodium (Na+) which is widespread in KRIP, this agreed with the results obtained by Malgwi et.al, 2002, Jibrin et.al, 2008, and Maina et.al, 2012. The type of soil in the field as already established by other researchers is found to be the loamy sandy type which provides proper drainage of irrigation water but does not withstand the accumulation of sodium that might cause soil salinization (sodicity).

However, the result of potential salt accumulation beneath the soil in this area is of concern, which related to the negative influence of soil properties. This will consequently lead to low water infiltration rates and hydraulic conductivities due to clay swelling and dispersion (*Rhoades and Loveday 1990; Sheinberg 1990; Duan et.al, 2011*).

Furthermore, another salt accumulation in this area is certain through the application of fertilizer, and nitrogen when it exceeds the crop intake. The salt will be adsorbed by the soil particles, and accumulate in the root zone, then leached by irrigation water and rainwater deep into the soil layer and finally reaching the groundwater (*Libutti and Monteleone, 2017; Libutti et.al, 2018; Krishan, 2019*).

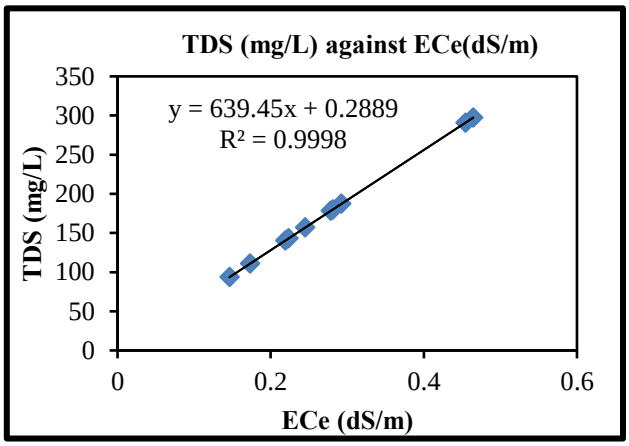

Figure 1:
Relationship between Total dissolved Solid (TDS – mg/L) and Electrical Conductivity (ECe – dS/m) in the soil samples analyzed.

Figure 1 shows the relationship between the mass concentration of total dissolved solids (TDS; in milligrams per liter) and that of soil salinity (ECe in micro siemens per centimeter at 25^{0}C) which is used to represent soluble salts in the soil. A regression model was obtained as shown in Equation 10 with a correlation coefficient of R^2 = 0.9998 (similar to R^2 = 0.9999 and R^2 = 0.9988 obtained by Omar et.al, 2006 and Duan et.al, 2011 respectively). This equation can be used to calculate the mass concentration of salt in the soil in the area as the concentration of TDS (mg/L).

$$y = 639.45x + 0.2889 \quad \ldots\ldots\ldots\ldots\ldots (9)$$

Where, x is the salinity in soil samples (micro siemens per centimeter), and y is the mass of TDS in a unit weight of a volume of soil sample (milligram per liter) in the research area.

The soils in this area can be treated by applying gypsum or by reducing the salinity in the soil and irrigation water to increase infiltration into the surface soils and improve the productivity of the root zone (Angela and Massimo, 2017). This treatment may alter the soil hydraulic properties well below the root zone leading to increased groundwater recharge and rising water tables.

Therefore, several kinds of research conducted by numerous authors on the relationship between soil salinization (soil salt migration) and groundwater quality such as Bing et.al, 2010; Xu et.al, 2012; Duan et.al, 2011; Wichelns et.al, 2015; Xia et.al, 2016; Haj-Amor et.al, 2017; Libutti et.al, 2018, are in agreement with the finding of this research.

4. CONCLUSION

In this study, the data analyzed indicate that salts are added to the soil through irrigation and other fertilization processes in the study area. The magnitude of the salt build-up depends on the water salinity, water composition, leaching requirement, soil type, drainage conditions, climate, management practices, and the consumptive use of crops to be grown. Soil salinization may cause groundwater quality deterioration problems directly and indirectly, as the salt build-up. Especially if the water available for leaching salts from the soil profile beyond the root zone is inadequate.

Furthermore, during the dry period as indicated by the field, there was a greater concentration of salts and total dissolved solids (TDS). This is due to intense irrigation activities that raise the groundwater level and add salts to the root zone, deteriorating the quality of the soil. Thus, there is a need for water resource agencies in collaboration with their agricultural counterparts to evaluate salt balances periodically, to assess the risk of soil salinization in groundwater quality for protection and enhancement of the environment.

ACKNOWLEDGEMENTS

We acknowledged Malam Shamsu Nafi'u Adam of KRIP Kadawa, Abdulhakim Adamu of Institute of Agricultural research (IAR) station Kadawa, Kabir Abdullahi Bindawa of Umar Musa Yar'adua University Katsina, Engineer Mustapha Khalil Usman of HJRBDA Headquarters, Kano for their support, advice and assistance during the trial activities and obtaining the field data.

REFERENCE

Anthony, J.J.; Olivier, B.; Randall, J.H.; Jean-Daniel, R.; Andrew, R (2016), Integrated Groundwater Management: Concepts, Approaches, and Challenges, Springer International Publishing, ISBN: 978-3-319-23575-2,978-3-319-23576-9, DOI 10.1007/978-3-319-23576-9_29

AQUASTAT (2022), FAO's Global Information System on water and agriculture, https://www.fao.org/land-water/databases-and-software/aquastat/en/

Arora, S. and Vanza, M. (2017), Microbial Approach for Bioremediation of Saline and Sodic Soils, Bioremediation of Salt Affected Soils: An Indian Perspective, 87–100. doi:10.1007/978-3-319-48257-6_5

Bernstein, L. (1975), Effects of Salinity and Sodicity on Plant Growth: Annual Review of Phytopathology, 13(1), 295–312. doi:10.1146/annurev.py.13.090175.001455

Bing, L; Zhao, W; Chang, X; Li, S; Zhang, Z; Du, M (2010), Water requirements and stability of oasis ecosystem in arid region, China, Environmental Earth Science, vol.59, Pp.1235

Bocanegra, E.M.; Custodio, E.; Silva Jr, G.C.; Manzano, M., and Montenegro, S. (2010), State of knowledge of coastal aquifer management in South America: Hydrogeology Journal, vol.18, Pp.261-267

Bouksila, F.; Bahri, A.; Berndtsson, R.; Persson, M.; Rozema, J.; and Van der Zee, T. M (2013), Assessment of soil salinization risks under irrigation with brackish water in semiarid Tunisia, Environmental and Experimental Botany, 92, 176–185. doi:10.1016/j.envexpbot.2012.06.002

Burger, F and Celkova, A (2003), salinity and sodicity hazard in water flow process in the soil, plant soil environment, Vol.49 (7), Pp.314-320, Institute of Hydrology, Slovak Academy of Science, Bratislava, Slovakia.

Dan'azumi, S.; Bichi, M.H. (2010), Industrial Pollution and Implication on Source of Water Supply in Kano, Nigeria, International Journal of Engineering & Technology IJET-IJENS, Vol.10(1)

Dikeogu, T.C.; Okeke, O.C.; Nwachukwu, H.G.O and Agbo, C.C (2021), Salinization and Waterlogging In Agricultural Lands: Causes, Effects, and Mitigation, Vol.9 (1), Pp.45-57, International Journal of Innovative Environmental Studies Research

Duan, R.; Fedler, C. B.; and Sheppard, C. D (2010), Field Study of Salt Balance of a Land Application System, Water, Air, & Soil Pollution, Vol.215 (1-4), Pp.43–54, DOI: 10.1007/s11270-010-0455-4

FAO, (2020), Mapping of salt-affected soils: Technical specifications and country guidelines, Rome.

FAOSTAT (2016), FAO Food and Agriculture Database, Statistics Division, Food, and Agriculture Organization of the United Nations, http://faostat.fao.org/, Accessed 25 Nov 2016

Ferguson, H., Bateridge, T. (1982), Salt Status of Glacial Till Soils of North-Central Montana as Affected by the Crop-Fallow System of Dryland Farming, Soil Science Society of America Journal, 46(4), 807–. doi:10.2136/sssaj1982.03615995004600040002

Foster, S., Pulido-Bosch, A., Vallejos, Á., Molina, L., Llop, A., & MacDonald, A. M. (2018). Impact of irrigated agriculture on groundwater-recharge salinity: a major sustainability concern in semi-arid regions, Hydrogeology Journal, DOI: 10.1007/s10040-018-1830-2

Guoqing, C; Yudong, L; Zheng, C; Zhiheng, L and Jiamei, S (2019), Relationship between Soil Salinization and Groundwater Hydration in Yaoba

Oasis, Northwest China, Natural Science Foundation of Shaan Xi Province (2017JQ4006)

Haj-Amor, Z.; Hashemi, H., and Bouri, S. (2018). The consequences of saline irrigation treatments on soil physicochemical characteristics, Euro-Mediterranean Journal for Environmental Integration, 3(1), DOI: 10.1007/s41207-018-0064-y

Haj-Amor, Z; Toth, T; Ibrahimi, M.K; Bouri, S (2017), Effects of excessive irrigation of date palm on soil salinization, shallow groundwater properties, and water use in a Saharan oasis, Environ. Earth Sci., 76, 590.

Jibrin, J.M., Abubakar, S.Z, and Sulaiman (2008), soil fertility status of the Kano River Irrigation Project Area in the Sudan savannah of Nigeria, Journal of Applied sciences, Vol.8(4), Pp.692-696, ISSN 1812-5654.

Krishan, G. (2019), Groundwater Salinity, Environmental Research Publishers, Vol. 14(2), Pp.186 – 188, ISSN: 0973-4929, Doi: http://dx.doi.org/10.12944/CWE.14.2.02

Libutti, A. and Monteleone, M. (2017), Soil vs. groundwater: The quality dilemma. Managing nitrogen leaching and salinity control under irrigated agriculture in Mediterranean conditions, Agricultural Water Management, vol.186, Pp.40 – 50, doi:10.1016/j.agwat.2017.02.019

Libutti, A; Cammerino, A.R.B; Monteleone, M (2018), Risk assessment of soil salinization due to tomato cultivation in Mediterranean climate conditions, water, vol.10, Pp.1503

Maina, M.M., Amin, M.S.M., Aimrun, W and Sani, I. (2012), soil salinity assessment of Kadawa Irrigation of Kano River Irrigation Project, journal of food, Agriculture and Environment, Vol.10 (3,4), WFL publisher.

Malgwi, W.B., Chude, V.O., Kparmwang, T and Raji, B.A. (2002), salinity and sodicity status of irrigation soils and irrigation and drainage waters of Jakara and Kano River Project in semi-arid Nigeria, Journal of soil science, Vol.III, Pp.63-71

Omar, A.A; Ghulam H; Mujtaba, K.M; Mohammaed, A.M and Ibrahim A.A (2006), Evaluation of Groundwater Quality and its Recharge by Isotopes and Solute Chemistry in Wadi Malal, Al-Madinah Al-Munawarah, Saudi Arabia, Pakistan Journal of Biological Sciences, 9: 260-269

Pulido-Bosch, A., Rigol-Sanchez, J. P., Vallejos, A., Andreu, J. M., Ceron, J. C., Molina-Sanchez, L., & Sola, F. (2018), Impacts of agricultural irrigation on groundwater salinity. Environmental Earth Sciences, 77(5), DOI: 10.1007/s12665-018-7386-6

Suarez, D.L (1989), Impact of agricultural practices on groundwater salinity, Agric Ecosystem and Environment, Vol.26, Pp.215–227, Elsevier Science Publishers B.V.

Tanji K.K; Kielen N.C (2002), Agricultural drainage water management in arid and semi-arid areas, FAO Irrigation and Drainage Paper No. 61, Food and Agriculture Organization of the United Nations, Rome.

United States Salinity Laboratory Staff (1954), Diagnosis and improvement of saline and alkali soil, Agriculture Handbook No. 60, Washington, D.C.

Van Dijk, G., Nijp, J. J., Metselaar, K., Lamers, L. P. M., & Smolders, A. J. P. (2016). Salinity-induced increase of the hydraulic conductivity in the hyporheic zone of coastal wetlands. Hydrological Processes, 31(4), 880–890. doi:10.1002/hyp.11068

Weil, R.R and Brady, N.C (2017), the nature and properties of soil, alkalinity, salinity and sodicity, 5th edition, Pearson Education Ltd, ISBN 10:1-292-16233-6, ISBN 13:978-1-1292-16223-2.

Wichelns, D; Qadir, M (2015), Achieving sustainable irrigation requires effective management of salts, soil salinity and shallow groundwater, Agricultural Water Management, vol.157, Pp.31–38

Xia, J.; Zhang, S.; Zhao, X.; Liu, J.; Chen, Y (2016), Effects of different groundwater depths on the distribution characteristics of soil-matrix water contents and salinity under saline mineralization conditions, Catena, Vol.142, Pp.166–176.

Yakirevich, A., Weisbrod, N., Kuznetsov, M., Rivera Villarreyes, C. A., Benavent, I., Chavez, A. M., & Ferrando, D. (2013), Modeling the impact of solute recycling on groundwater salinization under irrigated lands: A study of the Alto Piura aquifer, Peru. Journal of Hydrology, 482, 25–39. doi:10.1016/j.jhydrol.2012.12.029

Zaman, M., Shahid, S. A., and Heng, L (2018), Irrigation Water Quality: Guideline for Salinity Assessment, Mitigation, and Adaptation Using Nuclear and Related Techniques, 113–131. doi:10.1007/978-3-319-96190-3_5

Zaman, M., Shahid, S. A., and Heng, L (2018), Irrigation Water Quality: Guideline for Salinity Assessment, Mitigation, and Adaptation Using Nuclear and Related Techniques, 113–131. doi:10.1007/978-3-319-96190-3_5

4th International Engineering Conference (IEC 2022)
Federal University of Technology, Minna, Nigeria

Design, Fabrication and Performance Evaluation of a Melon Shelling Machine

Adebayo, S. E[1*], Lawal, M. I[1], Buremoh, O. O[1] & Tiamiyu, Q. O[1]

[1] Department of Agricultural and Bioresources Engineering, School of Infrastructure, Process Engineering and Technology, Federal University of Technology Minna.

***Corresponding Author: segun.emma@futminna.edu.ng**

ABSTRACT

Melon is a notable oil-seed crop widely planted in Tropical Africa for both consumer and industrial uses. Shelling is a very necessary postharvest practice prior to its vast applications. To address the problems associated with its shelling, a melon shelling and cleaning machine was developed using local materials. The machine consists of a frame, hopper, shelling and cleaning unit, prime mover, and chutes. The performance operation was carried out using "serewe" melon seeds. The processing involves different operations which include shelling and cleaning (separation of the seed from the chaff). The machine was tested at three different moisture content (12%, 16%, and 20%). The shelling speed was varied at 750rpm, 950rpm, and 1500rpm respectively. The machine's throughput Capacity per hour (C_{mph}) was 293.3 kg/hr and the grain recovery range of 87.8%. The optimum shelling and cleaning efficiencies were obtained at 20% moisture content at a shelling speed of 950rpm which gives shelling and cleaning efficiencies of 92.2 and 60.2% respectively.

Keywords: *Cleaning, Moisture, Melon, Seed, Speed*

1 INTRODUCTION

Melon (Citrullus Species), also known as "egusi" in Yoruba, is one of the significant oil-seed crops that are farmed and consumed in tropical Africa (Olaoye & Aturu, 2018). It is a tendril-climbing annual herbaceous crop that thrives in some areas of Nigeria's Savannah belt (Adekunle et al., 2009). Melon seed is incredibly nutritious and provides the human diet with high-quality proteins (Sobowale et al., 2015). It contains essential amino acids of about 41.51% and other essential nutrients. It is also a good source of vitamins, minerals, oil, and energy in form of carbohydrates. The seed contains 4.6g of carbohydrates, 0.6 of proteins, 33 mg of vitamin C, 230 mg of K, 17 g of Ca per 100 g edible seeds, 16 mg of P, 0.6 g of crude fiber, and unsaturated fatty acids. The seed kernel (Egusi) is the main ingredient in a number of soups, where it thickens, emulsifies, binds fat, and imparts flavor (Olaoye & Aturu, 2018).

Due to its ability to control weeds, crops including maize, okra, cassava, and yam can be grown alongside it as an intercrop. With proper management, it can be harvested between two and a half and three months after planting, with a potential seed yield of 350–400kg per hectare. Nigeria is home to the cultivars Bara, Serewe, and Sofin. Large brown seeds with thick black margins that thicken at the apex make up the 16 x 9.5mm bara, also known as papa, which is widely grown in northern and western Nigeria. While the smooth, light brown Serewe seeds are approximately 15 mm by 9 mm and have a thin, light whitish edge. The fruits have virtually spherical external surfaces and are formed of a white fleshy substance with a little, flat seed implanted inside (Nwosu, 1988). According to an examination of melon seeds conducted by Ajibola et al., (1990), melon seeds contain roughly 50% of oil by weight, 37.4% of protein, 2.6% of fiber, 3.6% of oil, and 6.4% of moisture. The seed's oil is composed of 50% of unsaturated fatty acids, such as linoleic acid (35%), oleic acid (15%), and 50% saturated fatty acids, such as stearic acid and palmitic acid. It is mostly grown for its shelled kernel, which is the intended usage. This can be crushed into a thick paste and added as a garnish to soups and stews. Additionally, it is incorporated into goods like "Ogiri" baby "Robocake," animal fodder, and its oil is used to make local pomade and soap (Shittu and Ndrika, 2012).

To further diversify melon's uses, processing is essential. This comprises drying, fermenting, drying, washing, coring, and oil extraction. Shelling is the process of removing the melon kernel's husk, or outermost layer. Consequently, the seed and prickly husk are separated. This procedure can be performed outside or at a storage environment (Nwakire et al., 2011). In Nigeria, melon shelling and winnowing are still done by hand, employing ancient methods like pounding the melon against a stone or hard surface to crack open the seeds (Olaoye & Aturu, 2018). Various studies on the creation and development of shellers have been conducted. Nevertheless, there is still a need for advancement in the mechanization of melon (egusi) shelling equipment. Due to their sophistication, poor output, and lack of a cleaning unit, the existing

devices are often not acceptable to consumers (Olaoye & Aturu, 2018). Therefore, the need for a simpler, more affordable device that can simultaneously clean and shell melons is still critical. Thus, determining a melon shelling machine that can efficiently shell and cleans the melon at the same time is the goal of this study.

2 MATERIALS AND METHODS

In order to accomplish the required aim, the material for the machine's design was selected based on accessibility, ergonomics, cost, the durability of materials, and ease of building. In order to match the working conditions of the shelling machine in use, these materials were also chosen based on an understanding of the chemical, physical, and mechanical qualities of the materials that were readily available.

2.1 DESIGN CONSIDERATION

A machine should be capable of serving the intended function in addition to being technically sound and operating as expected during the design process. However, it is preferable that a melon sheller should integrate design elements for durability and hygiene in addition to executing the suggested application as intended and meeting process requirements over the course of its service life (Sobowale et al., 2015). The availability of raw materials locally, the material's mechanical characteristics, such as strength and stiffness, the cost of the material, and its ease of manufacture, were all taken into proper consideration in the design of the melon seed sheller.

2.2 DESIGN CALCULATIONS

The primary design of this machine was influenced by the crucial characteristics of the melon seed (Bankole et al. 2005; Davies 2010). Evaluation of the crucial design parameters as well as the material selections for the construction process is the aim of the design calculations and other considerations (Olaoye & Aturu, 2018). As a result, basic considerations for the machine's capacity and scale, power consumption, rope length, shaft dimension, and other parameters were made in the design. Some of the variables for the numerous components of the Mellon sheller were calculated using the equations listed below.

2.2.1 BELT'S LENGTH & ANGLE OF CONTACT

The length of the belt was determined using equation 1 below as given by (Khurmi & Gupta, 2008).

$$L = 2C + \frac{\pi}{2}(D_1 + D_2) + \left[\frac{(D_2 - D_1)}{4c}\right] \quad (1)$$

Where;

D_1 = motor pulley's diameter

D_2 = shelling drum pulley's diameter

C = center distance between the major pulley and the shelling drum shaft pulley

thus, C = 146.3 mm and L = 568.2 mm.

The angle of contact of the belt was calculated using the equation 2 below as given by (Khurmi & Gupta, 2008).

$$\theta = (180 - 2\alpha) \times \frac{\pi}{180} rad \quad (2)$$

Thus, the angle of contact was calculated as 3.10 rad.

2.2.2 SHAFT DESIGN

The diameter of the shaft was calculated with equation 3 below as stated by (Khurmi & Gupta, 2008)

$$D^3 = \frac{16}{\pi s_s} \times \sqrt{\left(K_b {M_b}^2 + (K_t M_t)^2\right)}$$

(3)

Where,

D = shaft's diameter

S_s = allowable stress = 40 x $10^6 Nm^{-2}$ (Hall et al., 1980)

K_b = combined shock and fatigue factor applied to bending moment = 1.5 (Khurmi and Gupta, 2008)

M_b = bending moment

K_t = combined shock and fatigue factor applied to optional moment = 3.0 (Yusuf, 2012)

M_t = tension

Thus; shaft diameter d was calculated as 25 mm.

2.2.3 POWER REQUIREMENT

The minimum power required for the machine was calculated using equation 4 below as cited by (Olaoye & Aturu, 2018) at a speed of 800 rpm as used by (Ndirika, 2003).

$$P = T\omega \quad (4)$$

Where,

P = Power require

T = torque of the drum

ω = angular velocity (red/s)

$$\omega = \frac{2\pi N}{60} \quad (5)$$

N = Speed of the shelling drum given as 800rpm (Ndirika, 2003)

$$T = \omega r \quad (6)$$

r =Radius of the shelling disc (m)

Therefore, the power required for the shell melon from the panicle is expressed as 2.3Kw.

2.2.4 SHELLING DRUM'S DIAMETER

The diameter of the shelling drum was determined using the equation 7 below as reported by (Khurmi and Gupta, 2008)

$$D = \sqrt{\frac{4V}{\pi L}} \quad (7)$$

Where,

D = the shelling drum's diameter

L = the shelling drum's length

V = Volume of melon to be shelled in one minute

Thus; the shelling Drum Diameter was calculated to be 107mm.

2.3 MACHINE DESCRIPTION

Figures 1, 2, and 3 depict the graphical views of the machine. In order to achieve the intended result at the lowest possible cost, locally accessible and high-quality materials (angle iron, mild steel, shaft, pulley, motor, and belt) were employed. The hopper, the shaft, the shelling chamber, and the gear system, are the components that make up the melon shelling machine. Four mild steel metal sheets that have been welded together and are slanted toward the smaller hole make up the hopper. A respectable amount of unshelled melon seeds can fit through each of its two apertures, and an inlet throat joins the hopper to the shelling drum. The shelling drum, shelling vanes, shelling disc, and spacer make up the shelling chamber. While the shelling disc is composed of galvanized steel and has vane slots at the edges, the shelling drum is constructed of mild steel and has rods lining its inside. On the other hand, the gear that is used to manually operate the machine is composed of cast iron. When converting to automatic operation of the machine, a key (cone-like) attached to the shaft is easily detachable. Galvanized sheet is used to make the shelling vanes, which are stacked side by side at a 120° angle. Power is transferred from the drive shaft to the shelling portion via a bevel gear. The machine is supported by the frame, which also serves as a stand for the shelling drum and the bevel gear. The components utilized to build this machine are readily available, affordable, and have all the necessary qualities.

Fig 1: Pictorial side view of the melon shelling machine

Fig 1: Pictorial top view of the melon shelling machine

Fig 3: Pictorial front view of the melon shelling machine

2.4 OPERATION MODE

The machine operates on the theory that energy absorbed by the melon seeds beyond their elastic limit as a result of the impact force they receive upon collision with a stationary wall causes the seeds' shells to fracture and fall off. The machine receives unshelled melon seeds through a hopper that opens directly into the shelling unit. The shelling vanes are attached to the shelling disc at a 45° angle in order to increase the speed and rate of contact between the unshelled seeds and the rough body of the shelling unit, which causes the breakage and subsequent removal of the melon shells from the cotyledon. The cotyledon is separated from the unshelled seeds and peeled shells by gravity as the unshelled seeds and peeled shells are blown out of the shelling vanes and down the conveyor chute. The shelling vanes are attached at a 45° angle to the shelling disc via a shaft that is driven by a one-horsepower petrol engine that rotates at 1400 rpm. The rotary shaft was built to be stable and vibration-free with a ball-bearing housing and hanger. This prevented the rotating shelling disc from slamming into the stationary shelling drum wall, which in turn reduced the number of smashed melon seeds.

2.5 PERFORMANCE EVALUATION

The performance test was conducted following manufacture in order to meet the study's second objective and, if necessary, make improvements. The machine was first operated in a no-load condition using a petrol engine with 5.5 horsepower and a speed rating of 1500 rpm, while the shelling drum was operated in a no-load situation at a speed of 800 rpm. This was done to evaluate how well the machine's rotational components operated. The machine was put through testing to determine its percentage losses, shelling and cleaning efficiencies, and grain recovery range based on the following factors: moisture content, shelling drum rotation speed, and processing time for each operation. Specifically, the effects of their characteristics on the cleaning and shelling efficiency were examined overall. 55kg of melon seed was utilized to run the test throughout its entirety. The 15kg sample of melon seeds contains 5kg of each moisture content (12%, 16%, and 20%). The shelling drum's running speeds were 750 rpm, 950 rpm, and 1500 rpm, respectively, during the performance test. The table below shows the results that were achieved.

3 RESULTS AND DISCUSSION

TABLE 1: VARIABLES USED FOR THE EXPERIMENT.

Variables	**Values**
Seed moisture content (%)	12, 16 and 20
Shelling speeds (rpm)	750, 950 and 1500
Performance indicators	Shelling & Cleaning efficiency

The performance indexes and their corresponding values are displayed in Table 1. Table 2 displays the outcomes of cleaning and shelling at various moisture contents and the shelling rates. Using equation 4, a minimum power demand of 2300W was determined. The machine's throughput capacity was estimated to be 293.3 kg per hour. At different moisture concentrations of 12%, 16%, and 20%, the performance metrics were changed. For each wetness, the shelling speed was adjusted to 750, 950, and 1500 revolutions per minute. This melon shelling machine's optimal Shelling and cleaning efficiency were measured to be 92.2% and 60.2%, respectively, at 20% and 950 rpm. The shelling efficiency of the machine was better as compared to what was reported by Kilanko et al., (2019), Olaoye & Aturu, (2018), and Sobowale et al., (2015), while the cleaning efficiency was almost close to what was reported Olaoye & Aturu, (2018). Thus, moisture content of 20% and speed of 950 rpm were observed to be the conditions where the other performance indices in the table perform best.

TABLE 2: MELON SHELLER'S PERFORMANCE AT DIFFERENT VARIABLES.

Moisture content d.b (%)	Shelling speed (rpm)	Shelling efficiency (%)	cleaning efficiency (%)
12	750	86.5	60.6
	950	88	60.4
	1500	82	60
16	750	88.4	60.6
	950	91	60.4
	1500	84.5	61.2
20	750	92	60.2
	950	92.2	60.2
	1500	86.2	61.9

4 CONCLUSION

The melon cleaning and shelling device was created, built, and tested. The locally sourced resources were used to build the machine. According to the results of the tests, the operating speed of 950 rpm has the maximum shelling and cleaning efficiency at 20% moisture, with respective values of 92.2 and 60.2%. The machine is easy to operate, doesn't need specialized staff, and is not impacted by the regular power outages that plague developing countries like Nigeria. It may successfully address the needs of rural residents as well as small and medium-scale farmers in developing countries due to its lower production costs, and the difficulties associated with the conventional way of shelling melon will be resolved. Future works could investigate incorporating a heating device that may artificially dry the samples in the machine rather than waiting for samples to naturally dry before shelling can commence in order to boost the timeliness of operation.

REFERENCE

Adekunle, A. S., Ohijeagbon, I. O., & Olusegun, H. D. (2009). Development and Performance Evaluation of Manually and Motorized Operated Melon Shelling Machine using Impact Technique. *Journal of Engineering Science & Technology Review*, *2*(1).

Ajibola, O. O., Eniyemo, S. E., Fasina, O. O., & Adeeko, K. A. (1990). Mechanical expression of oil from melon seeds. *Journal of Agricultural Engineering Research*, *45*, 45-53.

Bankole, S. A., Osho, A., Joda, A. O., & Enikuomehin, O. A. (2005). Effect of drying method on the quality and storability of 'egusi\'melon seeds (Colocynthis citrullus L.). *African journal of biotechnology*, *4*(8), 799-803.

Davies, R. M. (2010). Engineering properties of three varieties of melon seeds as potentials for development of melon processing machines. *Advance journal of food science and technology*, *2*(1), 63-66.

Hall, A. S., Hollwen, K. O. A, and Laughum, H. (1980). Schaum's outline of theory and Problem of machine design. Metric selection. McGrac-Hill Books Company. New York, USA.

Khurmi, R. S., & Gupta, J. K. (2008). Theory of machines. 14th eds. *New Delhi, India: S. Chand and Company Ltd*.

Kilanko, O., Oko, A. I., Leramo, R. O., & Ilori, T. A. (2019). Development and performance evaluation of melon shelling and separating machine. *International Journal of Mechanical Engineering and Technology*, *10*(2), 440-450.

Kolawole, S. S., & Ndrika, V. I. O. (2012). Development and performance tests of a melon (egusi) seed shelling machine. *Agricultural Engineering International: CIGR Journal*, *14*(1), 157-164.

Ndirika, V. I. O. (2003). A simulation of optimum power requirements of selected grain threshers. Arid Zone Journal of Engineering, Technology and Environment, 3, 1-11.

Nwakaire, J. N., Ugwuishiwu, B. O., & Ohagwu, C. J. (2011). Design, Construction, and Performance Analysis of a Maize Thresher for Rural Dweller. *Nigerian Journal of Technology*, *30*(2), 49-54.

Nwosu, R. C. (1988). Engineering properties of egusi fruit and the design of egusi seeds extraction equipment. *B. Eng Project Report, Department of Agricultural Engineering, University of Nigeria*.

Olaoye, J. O., & Aturu, O. B. (2018). Design and fabrication of a mechanised centrifugal melon shelling and cleaning machine. *International Journal of Agricultural Technology*, *14*(6), 881-896.

Oloko, S. A., & Agbetoye, L. S. (2006). Development and performance evaluation of a melon depodding machine. *Agricultural Engineering International: CIGR Journal*.

Sobowale, S. S., Adebiyi, J. A., & Adebo, O. A. (2015). Design, construction and performance evaluation of a melon seeds sheller. *Food Process Technol*, *6*(7), 463.

Yusuf, M. B. (2012). Design and Fabrication of Millet Thresher (Doctoral dissertation).

4th International Engineering Conference (IEC 2022)
Federal University of Technology, Minna, Nigeria

Assessment of Hydrological Drought in Lower Benue River Basin (Hydrological Area II), Nigeria

*Nangkazah, R Y.[1], Jimoh O. D[2] & Adesiji, R[3]
[1]Civil Engineering Department, Federal University of Technology, PMB 65 Minna Niger State, Nigeria
[2] Afilation of First Author
[3]Afilation of Second Author
*Corresponding author email:nangkazahyusufu23@gmail.com +2348137349714

ABSTRACT
Drought is a natural phenomenon characterized by a decrease of water availability below a truncation threshold. Each drought differs from the other in severity, duration and spatial extends. The assessment of hydrological drought in Lower Benue River Basin (Hydrological Area HA Two) Nigeria was calculated using streamflow drought index (SDI) from streamflow a 30-year record at Donga and a 55-year record at Kastina Ala. Missing monthly stream flow was estimated average method, interpolation method, regression method and stochastic modelling method. Donga had 33% moderate drought, 10% moderate, 7% severe drought and 1% extreme occurrence. Kastina Ala had 39% moderate drought, 18% moderate, 4% severe drought and 1% extreme occurrence. The most extreme drought event at Donga had a magnitude of -3.4 (Quarter four Q4 1983) while Kastina Ala had an extreme drought magnitude of -2.46 (Quarter four Q4 2005). The longest dry spell at Donga lasted 11 quarters from Q3 1986 to Q1 1989 while at Kastina Ala it lasted 19 quarters from Q2 1991 to Q1 1996.

Keywords: *Drought, Hydrological Drought, Streamflow, Streamflow Drought Index.*

1 INTRODUCTION

Drought is a natural phenomenon characterised by a significant decrease of water availability during a significant period of time and over a large area. It occurs in parts of the Earth virtually every year thus affecting economic activities, human lives and various elements of the environment (Nalbantis, 2008). A drought is an event of prolonged shortages in water supply, where atmospheric (below average precipitation), surface water or ground water. A drought can last for months or years, or may be declared after as few as 15 days. Drought is a term that is employed for reflecting the situations where hydro-meteorological quantity such as water amounts may not satisfy a desired level of demand (IPCC, 2003). Droughts have a substantial impact on the eco system and agriculture of the affected area; it could harm the local economy. Annual dry seasons in the tropics significantly increase

Droughts have been occurring frequently in many parts of the world, and their impacts are being exacerbated by climate change (Dai, 2011). More specifically, global surface temperatures will continue to increase due increases in greenhouse gas emissions (FAO, 2007; Pachauri, et al., 2014; Qin, et al., 2007; IPCC I. P., 2007) A warming climate will also lead to an increase in extreme climatic events, such as floods and droughts worldwide (Pachauri, et al., 2014).

Droughts triggering mechanism in the atmosphere is not known definitely however ocean-atmosphere interaction had been a major cause of the changing weather patterns globally (Adejuwon & Dada, 2021). The ocean–atmosphere phenomenon of El-Nino/Southern Oscillation (ENSO) is associated with a lot of atmospheric disturbances as a result of the anomalously high or low temperature of the ocean surface known as 'El-Nino' and the tendency of a high- pressure build-up in a certain region of the globe to be compensated by a pressure fall in another referred to as 'Southern Oscillation'. ENSO is responsible for climatic perturbation and a major factor in short-term climatic change. The Southern Oscillation establishes a lot of atmospheric disturbances and responsible for heat sinks on the equatorial latitudes Walker circulation. The Walker circulation initiates aridity and partly accounts for rainfall variability in West Africa (FAO, 2007; Adejuwon, Balogun, & Adejuwon, 1990; Olaniran, 2002). The coastal decrease in upwelling process which weakens the south-westerly flow reduces the thermal contrast across the region leading to a reduction in the frequency of easterly disturbances and squalls, hence drought in the Sahel (Adejuwon & Dada, 2021).

Drought can be classified according to the perspective of the study or the period of occurrence, this can be attributed to the fact that there is no universally accepted clear definition of drought and opinion is divided on the terminology surrounding drought (Squires, 2016). Types of droughts are broadly divided in two with subdivisions. The classes are:

i. Based on perspective of study
ii. Period of occurrence

Based on perspective of study, drought is classified into five (5) categories, namely, meteorological, hydrological, agricultural, socioeconomic drought and

famine (Dalezios, et al., 2015). The first three approaches basically deal with physical phenomena such as rainfall, evapotranspiration, and streamflow, and the last two deals with the shortage of goods that depends on water (Wilhite & Glantz, 1985). The following are types of droughts based on the perspective of study:

1. Meteorological droughts
2. Hydrological droughts
3. Agricultural droughts
4. Socioeconomic drought
5. Famine

Hydrological droughts are more related to water demands and they appear whenever a marked reduction becomes appreciable in natural stream-flow or groundwater levels, plus the depletion of water storage in dams and lakes for water supply. Hence, hydrological droughts are very important and significant for urban areas or industrialized regions as well as for agricultural activities. The main impact of hydrological droughts is on water resources systems (Nabaltis & Tsakiris, 2009).

Hydrological drought is not attached to the precipitation decrease only, but additionally decreases in the surface flow and drops in the groundwater levels provide joint impacts. The magnitude of a drought is estimated using an index(Sirdas & Sen, 2003).

In general, practice a drought index is used to describes the magnitude, duration, severity, or spatial coverage extent of drought. They are based on meteorological and hydrological variables, such as precipitation, temperature, stream-flow, soil moisture, reservoir storage, and groundwater level. Several of them can be synthesized into a single indicator on a quantitative scale (Mishra & Singh, 2010). Although drought indices can provide ease of implementation, the scientific and operational meaning of an index value may raise questions, such as how each indicator is combined or weighted for an overall index derivation and how an arbitrary index value relates to hydro-meteorological and statistical characteristics of droughts (Sen Z. , 2014a.).

Hydrological droughts are more related to water demands and they appear whenever a marked reduction becomes appreciable in natural stream-flow or groundwater levels, plus the depletion of water storage in dams and lakes for water supply. Hence, hydrological droughts are very important and significant for urban areas or industrialized regions as well as for agricultural activities. The main impact of hydrological droughts is on water resources systems (Nabaltis & Tsakiris, 2009).

Hydrological drought is not attached to the precipitation decrease only, but additionally decreases in the surface flow and drops in the groundwater levels provide joint impacts. The magnitude of a drought is estimated using an index(Sirdas & Sen, 2003).

In general, practice a drought index is used to describes the magnitude, duration, severity, or spatial coverage extent of drought. They are based on meteorological and hydrological variables, such as precipitation, temperature, stream-flow, soil moisture, reservoir storage, and groundwater level. Several of them can be synthesized into a single indicator on a quantitative scale (Mishra & Singh, 2010). Although drought indices can provide ease of implementation, the scientific and operational meaning of an index value may raise questions, such as how each indicator is combined or weighted for an overall index derivation and how an arbitrary index value relates to hydro-meteorological and statistical characteristics of droughts (Sen Z. , 2014a.)

2 METHODOLOGY

The following research questions were raised to guide the study:

i. What are the mean monthly flows from historical records
ii. How can the missing streamflow discharge be estimated?
iii. What is the drought severity using Streamflow Drought Index (SDI)?

2.1 DESCRIPTION OF STUDY AREA

Nigeria is located on the western coast of Africa. Nigeria has a diverse geography, with climates ranging from arid to humid equatorial. It is situated in the northern latitudes between 4^0N and 14^0N and eastern longitudes 3^0E and 15^0E. Nigeria covers an area of 923,768 km^2. Nigeria is divided into 12 river basins for ease of managing the water resources that abound in her territories. The river basins are grouped based of the similarity of in the hydrology, geological, climatic and soil characteristics. 12 river basin development authorities were established in 1976 vie Decree No. 25 of 1976.

The study area chosen for this study is the Lower Benue River Basin (Hydrological Area IV) and it comprises Benue state, Nasarawa state, Plateau state and Kogi state (East of the River Niger). The lower Benue River basin covers an area of 74,500 km^2. Figure 1 shows a map of states that comprise the study area.

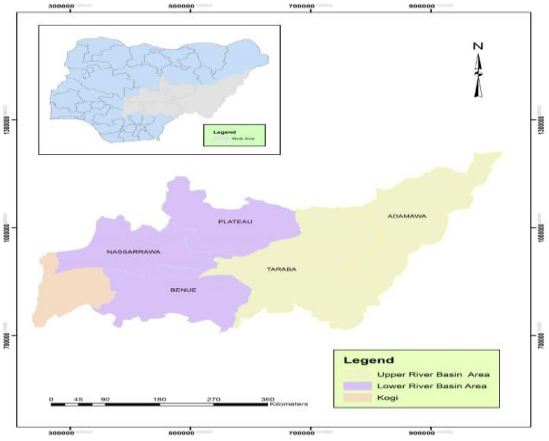

Figure 1 A map showing the area covering the lower Benue River basin

2.2 DATA COLLECTION AND ANALYSIS

Historical Data from The Nigeria Hydrological Service Agency (NIHSA) at two gauging stations within the basin was collected. The stations are located at Donga and Kastina Ala.

The data was inspected for consistency and processed using a cumulative discharge curve for each year are calculated using the following steps The following procedure and techniques and method is adopted for filling missing data for the data using MS Excel (Mohammad, Ali, & Andrew, 2016).. The techniques used are:

1. Average method
2. Interpolation method
3. Regression method
4. Stochastic modeling method

To carry out calculations for SDI, it is assumed that a time series of monthly streamflow volumes $Q_{i,j}$ is available where *i* denotes the hydrological year and *j* the month within that hydrological year (*j* = 1 for October and *j* = 12 for September). Based on this series we obtain equation (1)

$$V_{i,j} = \sum_{j=1}^{3k} Qi,j \qquad (1)$$

$$i = 1, 2, \ldots 12 \text{ and } k = 1, 2, 3, 4$$

Where:

$V_{i,k}$ = Cumulative stream flow volume for the *i*-th hydrological year and the *k*-th reference period,

For k = 1 for October–December,
k = 2 for October–March,
k = 3 for October–June, and
k = 4 for October–September.

Based on cumulative streamflow volumes $V_{i,k}$ the Streamflow Drought Index (SDI) is defined for each reference period *k* of the *i*-th hydrological year as follows

$$SDI_{i,k} = \frac{Vi,; - \overline{Vk}}{Sk} \qquad (2)$$

i = 1, 2, …. and *k* = 1, 2, 3, 4

$\bar{V}_k$ = the mean and

s_k = Standard deviation of cumulative streamflow volumes of reference period k as these are estimated over a long period of time.

For this study the truncation level is set to Vk

Based on SDI, the states of hydrological drought are defined which are identical to those used in the meteorological drought indices SPI and RDI. Five states are considered which are denoted by an integer number ranging from 0 (non-drought) to 4 (extreme drought) and are defined through the criteria of Table 1.

Table 1: Definition of hydrological drought state using SDI

State	SDI criterion	Drought type
0	SDI ≥ 0	Non-drought
1	-1 ≤ SDI < 0	Mild drought
2	-1.5 ≤ SDI < -1	Moderate drought
3	-2 ≤ SDI < -1.5	Severe drought
4	SDI < -2.0	Extreme drought

3 RESULTS AND DISCUSSION

3.1 RESULTS

The calculation was done following the steps illustrated by the flow chat in figure 2.

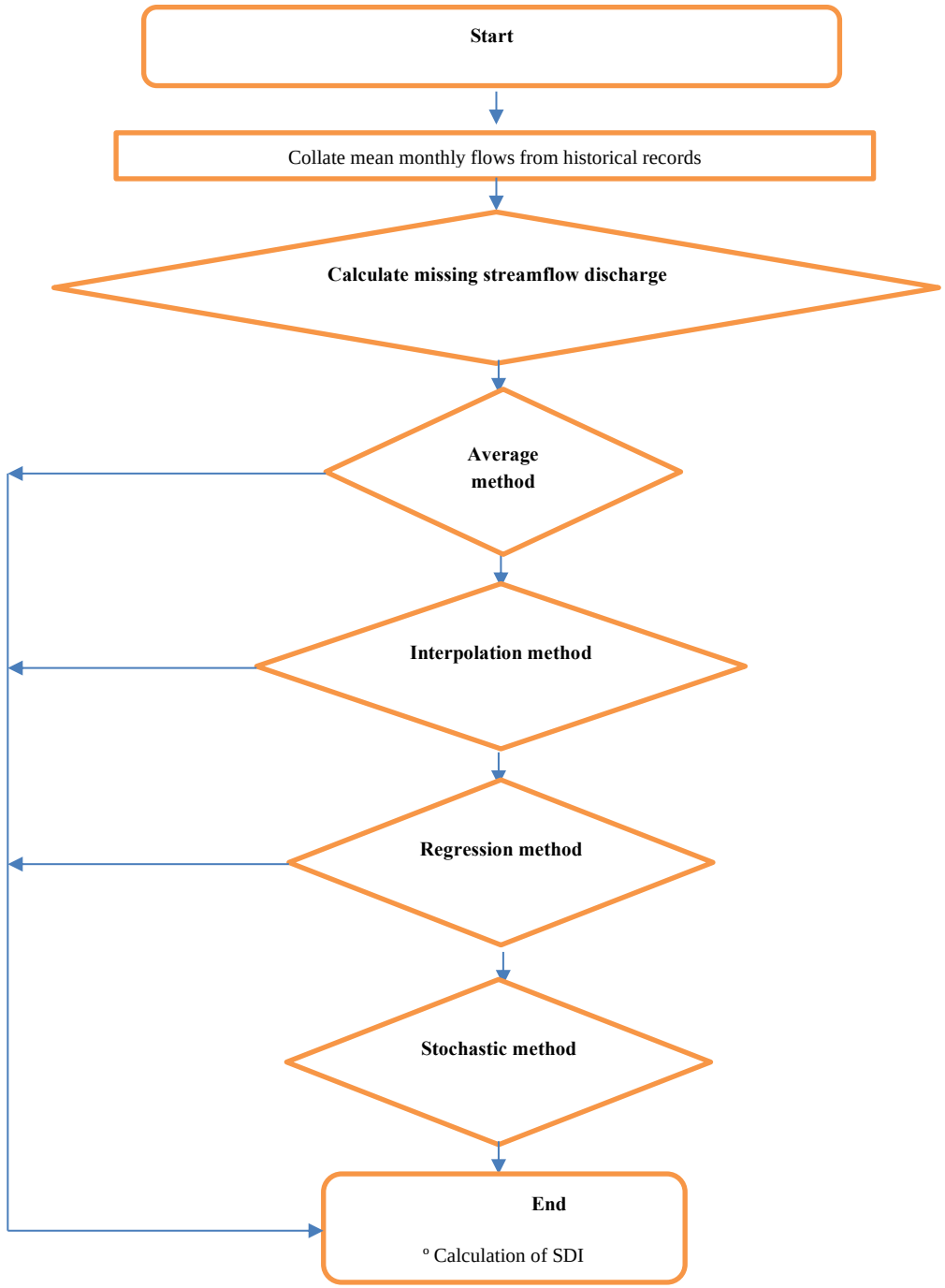

Figure 1: Flow chart for calculating SDI

The SDI was calculated using a Drought Indices calculator DrinC and the results are represented using the Legend table 2

TABLE 2: LEGEND FOR INTERPRETING DROUGHT SEVERITY FOR SDI

Drought type	Drought Class Range	Colour Code
None Drought	SDI ≥ 0	
Mild Drought	-1 ≤ SDI < 0	
Moderate Drought	-1.5 ≤ SDI < -1	
Severe Drought	-2 ≤ SDI < -1.5	
Extreme Drought	SDI < -2.0	

The results from the calculated SDI values are in figure three (3) to ten (10). The results show each figure having two sets of mostly ten year time of SDI values

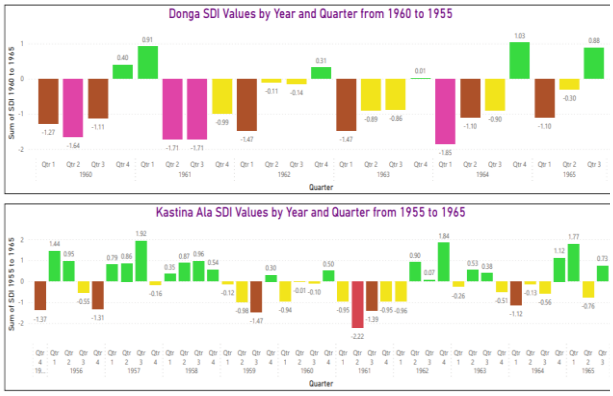

Figure 3: SDI Values for from 1959 to 1965 at Donga and 1955 to 1965 at Kastina Ala

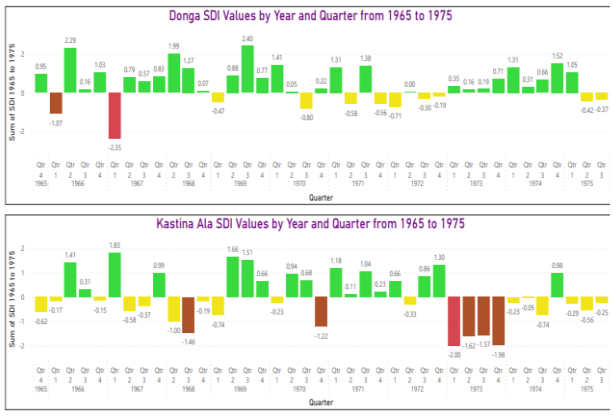

Figure 4; SDI Values for from 1965 to 1975 at Donga and 1965 to 1975 at Kastina Ala

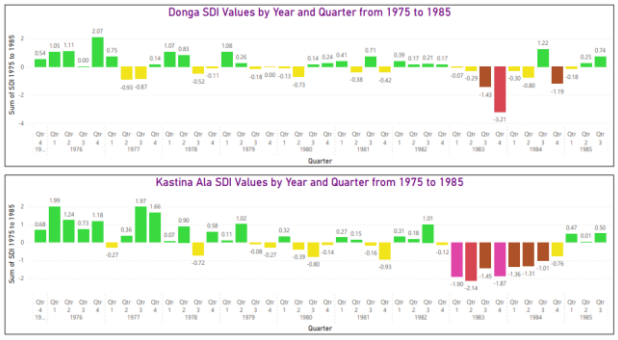

Figure 5: SDI Values for from 1975 to 1985 at Donga and 1975 to 1985 at Kastina Ala

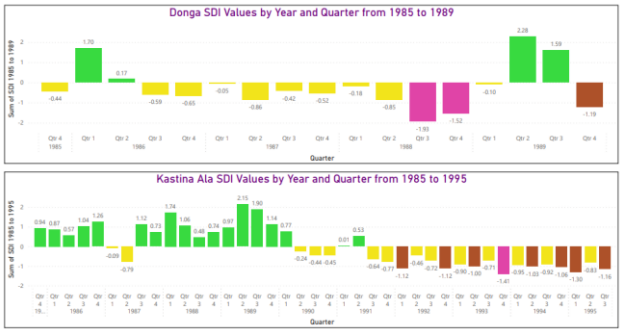

Figure 6: SDI Values for from 1985 to 1989 at Donga and 1985 to 1995 at Kastina Ala

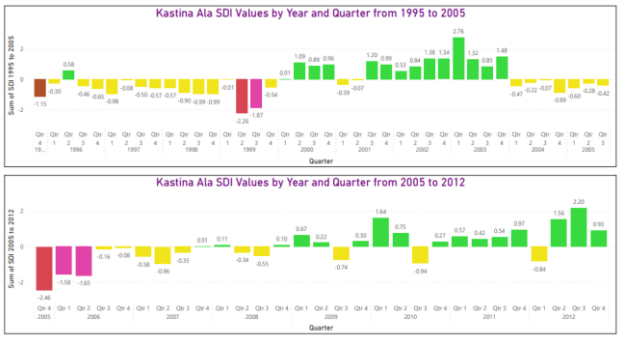

Figure 7: SDI Values for from 1995 to 2005 and 2005 to 2012 at Kastina Ala

3.2 DISCUSSION OF RESULTS

The drought events occurrence at Donga was found to be None Drought 50% Mild Drought 33% Moderate Drought 10% Severe Drought 7% and Extreme Drought 1% while at Kastina Ala it was found to be None Drought 47% Mild Drought 39% Moderate Drought 8% Severe Drought 4% and Extreme Drought 1%,, tthis is illustrated in figure 8

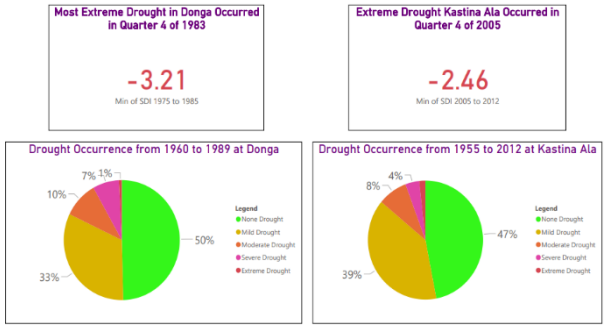

Figure 8: Dashboard showing worst drought and percentage occurrence at Donga and Kastina Ala

Most extreme drought event at Donga occurred in the 4th quarter of 1983 with a severe drought magnitude of -3.21 while Kastina Ala had a severe drought with a -2.46 magnitude in the 4th quarter of 2005.The worst drought occurrence is presented in Figure 9

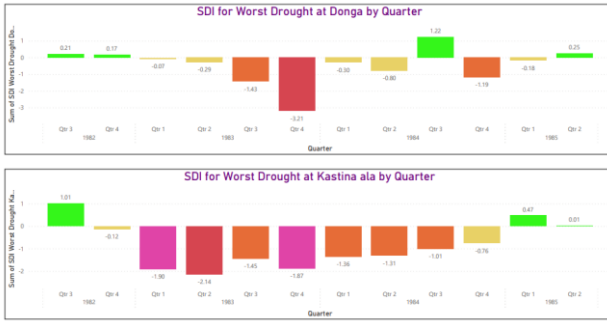

Figure 9: Worst drought Occurrence at Donga and Kastina Ala

The longest dry spell at Donga was recorded from quarter 3 of 1986 to quarter 1 of 1989 and spanned 11 quarters. At Kastina Ala the dry spell lasted 19quarters from quarter 2 of 1991 to quarter 1 of 1996. The longest dry spells at both donga and Kastina Ala are presented in figure 10

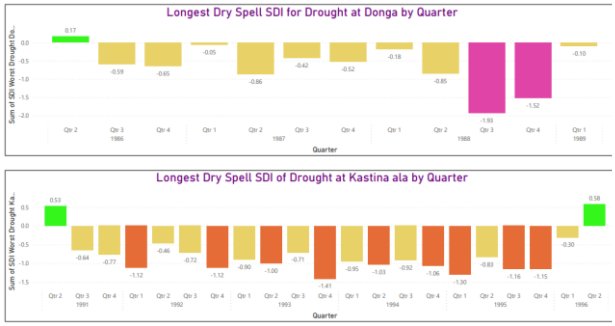

Figure 10: Longest Dry Spell at Donga and Kastina Ala

4 CONCLUSION

This study obtained mean monthly streamflow records from two gauging stations at Donga and Kastina Ala from historical records of NIHSA

The missing streamflow discharge was estimated using, average, interpolation regression and Stochastic modelling methods.

The SDI was calculated and classified. It was found that there was various degree of drought occurrence 50% from 1960 to 1989 at Donga and a 53% drought occurrence of varying severity at Kastina Ala from 1955 to 2012.

The following recommendations were made:

1. Adaptation of the drought occurrence in the basin in policy formulation for water management.
2. Further study into metrological and agricultural drought to have a more detailed assessment of drought in the basin.
3. Maintenance of existing gauging stations to make continuous data collation possible.
4. Creation of new gauging stations to have a more representative data for the whole basin.

ACKNOWLEDGEMENTS

I thank God almighty for the ability to carry out this study, I will like to thank Prof. O. D. Jimoh for creating time to contribute to this study. I thank my parents and sisters for their support. Thank you to my friends for their help in preparing this study

REFERENCE

Adejuwon, J. O., & Dada, E. (2021). Temporal analysis of drought characteristics in the tropical semi-arid zone of Nigeria. *Scientific African*, 28 35.

Adejuwon, J., Balogun, E., & Adejuwon, S. (1990). On the annual and seasonal patterns of rainfall fluctuations in sub-Sahara West Africa. *International Journal of Climatology* , 839-848.

Dai, A. (2011). Drought under global warming: A review. *Wiley Interdisciplinary Reviews Climatic Change, 2(1)*, 45–65.

Dai, A. (2013). Increasing drought under global warming in observations and models. *Nature Climate Change, 3:* , 52–58.

Dalezios, R, N., M, A., Alfonso, T., Saeid, & Eslamian. (2015). Drought Assessment and Risk Analysis. In S. Eslamian, & F. A. Eslamian, *Handbook of drought and water scarcity : environmental impacts and analysis of drought and water* (pp. 323-345). New York: CRC Press.

FAO. (2007, May 10). *State of the world's Forest 2007*. Retrieved Febuary 4, 2022, from Food and Agriculture Organization of the United Nations, Rome, 2007: http://www.fao.org/3/a-a0773e.pdf .

IPCC. (2003). Climate change 2001: the scientific basis. . *Contribution of Working Group I to the Third Assessment Report of the Intergovernmental Panel on Climate Change* (p. 944). Cambridge: Cambridge University Press.

IPCC, I. P. (2007). Climate Change 2007: Synthesis Report. *IPCC's Fourth Assessment Report (AR4).* Geneva, Switzerland: IPCC.

Mishra, A. K., & Singh, V. P. (2010). A review of drought concepts. *Journal of Hydrology*, 202-216.

Mohammad, T. S., Ali, R. J., & Andrew, K. (2016). Assessment of different methods for estimation of missing data in precipitation studies. *Hydrology Research*, 412-428.

Nabaltis, I., & Tsakiris, G. (2009). Assessment of hydrological drought revisited. *Water Resour. Manage*, 881–897.

Nalbantis, I. (2008). Evaluation of a hydrological drought index. *European Water*, 67–77.

Olaniran, O. J. (2002). Rainfall Anomalies in Nigeria: The Contemporary Understanding. *An Inaugural Lecture delivered on April 25, 2002* . Ilorin: University of Ilorin.

Pachauri, R., Allen, M., Barros, V., & Broome, J. (2014). *Climate change 2014: synthesis report. Contribution of Working Groups I, II and III to the fifth assessment report of the Intergovernmental Panel on Climate Change.* Copenhagen, Denmark: IPCC.

Qin, D., Solomon, S., Manning, M., Chen, Z., Marquis, M., Averyt, K. B., . . . Miller, H. L. (2007). Contribution of Working Group I to the fourth assessment report of the intergovernmental panel on climate change. . *IPCC 2007*, 966.

Sen, Z. (2014a.). *Applied and Practical Hydrogeology.* Amsterdam: Elsevier.

Sirdas, S., & Sen, Z. (2003). Spatio-temporal drought analysis in the Trakya region, Turkey. *J. Hydrology. Sci. 48*,, 809–819.

Squires, R. V. (2016). Desertification and Droughts.

Wilhite, D., & Glantz, M. (1985). Understanding the drought phenomenon: the role of definitions. *Water Int., 10*, 111–120.

Yevjevich, V., Cunha, L., & Vlachos, E. (1983). *Coping with Droughts.* Littleton, CO: Water Resources Publications.

4th International Engineering Conference (IEC 2022)
Federal University of Technology, Minna, Nigeria

CONCEPTUAL DESIGN OF AN IOT-BASED MULTI-SENSORY GAS LEAKAGE MONITORING AND CONTROL SYSTEM USING FUZZY LOGIC

*Mohammed, I. K[1], Kolo, J. G.[1], and Ohize, H.[1]
[1]Department of Electrical and Electronics Engineering, Federal University of Technology, PMB 65 Minna Niger State, Nigeria
*Corresponding author email:ibkingzy@gmail.com +2348037593744

ABSTRACT
Liquefied petroleum gas (LPG) is becoming increasingly popular for its clean energy properties, versatility, and affordability, but current methods for identifying and regulating leaks require improvement. This study investigates an approach for monitoring, detecting, and remediating gas leaks in a centralized gas supply system (a condominium) using a combination of IoT and fuzzy logic technology. The proposed solution utilizes multiple sensors connected to an IoT-based monitoring module that can be remotely tracked via Wi-Fi. Additionally, a fuzzy logic based corrective measure is implemented to activate a shut-off valve at various points of supply, making the process faster and safer. This study presents a promising solution to improve the safety and efficiency of centralized gas supply systems.
Keywords: *Artificial Intelligence , Fuzzy Logic, Gas Leakage Monitoring, Internet of Things, Wi-Fi*

1 INTRODUCTION

Natural gas is a non-renewable, odourless, colourless, and combustible hydrocarbon composed primarily of methane, a small quantity of carbon dioxide (CO2), and various amounts of other alkanes (Gordon, 2021). It is also known as the cleanest burning hydrocarbon since it emits half the carbon dioxide (CO2) and a tenth of the air pollutants generated by heavier hydrocarbons like coal and oil, resulting in fewer greenhouse gas emissions (Huntingford et al., 2015). Liquefied petroleum gas (LPG) is gaining popularity due to its several advantages, which include being a clean energy, having a wide variety of uses, and being less expensive than alternatives (Abubakar et al., 2020). While LPG is most commonly associated with cooking (Olorunfemi et al., 2020), it also has many other applications such as power generation, automotive fuels, industrial operations, refrigerants, and large-scale agricultural treatments (Khan, 2020; Adekitan et al., 2018).

Regardless of how beneficial gases are, inhaling them can be hazardous to one's health, and they can also cause explosions if leaks are not properly handled thus resulting in property damage, fatal injuries, and, in the worst-case scenario, death (Olorunfemi et al., 2020). As a result, gas leak detection, remediation, and control have become important innovations worthy of constant review.

With gas being used in nearly every aspect of our life (Liang et al., 2012), leakage might create negative consequences if not adequately controlled or remedied (Dadkani et al., 2021), and is thus predicted to be a major source of worry for consumers (Bhattacharyya et al., 2006). Despite multiple advancements in identifying and regulating these leaks, considerable work has to be done in developing systematic solutions toward a faster and safer process embedded with smart features that are self-sufficient in monitoring and correcting these leaks (Dewi and Somantri, 2018). To do this, it has been established that a system capable of real-time monitoring of LPG leakages at various sites and turning off its supply without human involvement is a superior strategy to controlling these leakages (Dewi and Somantri, 2018), hence preventing potential damages.

This study investigates a faster and more reliable approach to monitoring, detecting, and remediating gas leaks in a centralized gas supply system (a condominium) by utilizing a multiple sensing approach via an IoT-based monitoring module capable of remote tracking via Wi-Fi technology and a fuzzy logic based corrective measure capable of activating a shut-off valve at various points of supply. The rest of this paper is organized as follows: Section 2 presents a review of literature while the proposed research methodology is presented in Section 3. Section 4 presents preliminary results of the conceptual design while the conclusion and recommendation for future works is presented in Section 5.

2 LITERATURE REVIEW

With the increased use of liquefied Petroleum Gas (LPG) in our daily lives and the associated risks it poses to people and properties, the process of detecting gas leakages, gas flow monitoring, and leak remediation have become a topic of increased attention (Neri, 2021). The detection of gases has progressed from the use of canary birds to chemically infused papers to electronic sensors such as pellistor sensors, Non-Dispersive Infrared (NDIR) sensors, and Molecular Property Spectrometer (MPS) sensors (Brown, 2021), each incorporating novel approaches to better detect gases by improving miniaturization, precision, response time, life expectancy, power consumption, and maintenance requirements, as well as reducing cross-sensitivity, linearity, and cost (Nevadanano, 2022; Yi et al., 2015).

Numerous researchers have carried out studies and modelled systems aimed at fashioning out better ways to detect, monitor and remediate gas leakages. One such model is that of Simbeye, (2013), who developed a Gas Leakage Detection System to detect LPG combustible gases. The system comprised of a sensor for detection which was interfaced with a microcontroller. The system enabled a monitoring and remediation process made of an audible alarm to alert the user, an LCD screen that displayed the hazard information, and a message sent to the user's mobile device via a modem. The system also had a control mechanism that switched off the electric power if the leakage persists and there is no human intervention. However, constraints due to network availability, modem chip recharging, and leakage management without human involvement were identified as challenges that would affect the system's optimal operation.

Durán et al., (2016) developed a multisensory system for detecting toxic gases in an indoor environment. Their work which was based on the principles of multi-gas sensing was developed by building a detecting module that housed a set of six low-cost chemical gas sensors with overlapping sensitivities (so that each detected a distinct type of gas. The system which was proposed for underground coal mines used Principal Component Analysis (PCA) and Discriminant Function Analysis (DFA) from the data collected to assign statistical parameters that aided in its feature selection which determined the sensors data that was to be read. Despite incredible efforts, the system lacked simplicity because modern gas sensors can now detect numerous gases or a mixture of gases. Also, the system's functionality in monitoring and correcting gas leaks could not be evaluated because it wasn't applied in live scenarios.

The work carried out by Dewi and Somantri, (2018) could be considered an advancement to the system proposed by Duran et al., (2016). In contrast to Duran's work, which had different sensors housed in a detection module to detect different types of gases, Dewi proposed an Arduino-based gas leakage detection system and automatic gas regulator system which was made of multiple sensors each deployed at a probable leak spot and connected through a Wireless Sensor Network (WSN). They propounded that a smarter approach to detecting gas faster was to have multiple detectors at strategic locations; an edge point indeed. Their system was praised for its efficiency and sensitivity because it detected gas leaks faster in larger usage areas and was less prone to errors due to the minimal use of wired connections. The system harnessed the use of a wireless sensor network by using a Bluetooth HC–05 wireless connection to connect various detecting modules (the main system and a support system). While both systems comprised of a detection module and a Bluetooth communication device, the main system housed most of the system functionality such as a display unit, an alerting module, and a leak-stopping mechanism. Unfortunately, as amazing as the work is, there were drawbacks such as the connection range between the two subsystems and the support system's inability to operate for long hours because it was battery-powered.

Additionally, Adekitan et al., (2018) modelled a microcontroller-based gas leakage detection and evacuation system in response to the numerous household fires, injuries, and fatalities caused by gas leaks in Nigeria. The system which was christened a “smart system” by the researchers, combined elements of sensing, actuation, and control, as upon detection of a gas leak it activates a buzzer, sends an SMS to the user, shuts off the gas supply by the activation of a solenoid valve and evacuates the leaked gas through the operation of an evacuator fan. The system's highlight was the addition of remote monitoring, which allowed the user to check the system's operational status by sending SMS codes over a GSM network. Despite the impressive work done, the remote monitoring capabilities appear to be overblown as the user had to prompt the system each time he wished to observe it.

Omar et al., (2019) developed a system called MQ2-TECTOR that is quite comparable to the system developed by Adekitan et al., (2018). The device, which is an Arduino-based gas detector, was designed to prevent gas leaks and explosions, as well as evaluate the performance and responsiveness of the MQ-2 sensor. This was accomplished by measuring the time it took the system to detect gas leaks and activate other system functions when placed at both a fixed and variable distance. The MQ2-TECTOR was applauded for its versatility in use since it could detect both LPG and smoke, in addition to other features like an alarm system and LED for notification, an exhaust fan to evacuate leaked gases, and a mobile communication device for remote notification. While the system could be praised for being an improvement over existing works, the results of the analysis revealed a decrease in the system's response due to distance from the leak point. Other system flaws included the researchers' inability to employ a clear-cut process to stop gas supply when a leak is being detected and the GSM network's signal interruption.

While analyzing the inherent dangers accustomed to the extensive gas supply network in a hospital environment, Hussien et al., (2020) designed a smart gas leakage monitoring system in January 2020. The system took into account the variety of gases being transferred from a supply point to various sites of usage in a hospital environment, intending to detect leaks and inform hospital safety professionals for possible correction. This paper explored the use of multiple MQ-Series gas sensors and other external devices that alerted the users in the event of a gas leak, and all these were connected using an Arduino Uno microcontroller. The system's monitoring process was a high point because it allowed for remote monitoring via a GSM module, allowing a safety operator to easily

monitor the multiple detection points from a vantage point. A configuration was also done to ensure that the alarms and notifications would not stop until the system received a response from the safety personnel. Worthy of mention is also the inclusion of a manually operated push button at the user's end that acted as a fail-safe just in case the detection module fails to detect. While the system is near perfection, one flaw is that it lacks an automatic control measure in the event that the operator is too far away.

In addition, Abubakar et al., (2020) took cognizance of the growing level of patronage of LPG for domestic and industrial applications, as well as the accidents caused by its leakage, and proposed an alternative approach to preventing gas leaks by developing an Arduino based gas leakage control and temperature monitoring system. He developed two (2) prototypes utilizing different gas sensors (MQ5 and MQ6 gas sensors), and these configurations were designed to compare the detecting module's response to distance and the control system's responsiveness in order to select the best one for the desired usage area. The researcher also included a DHT 22 temperature sensor as he considered the impact of temperature in propelling a fire outbreak if there is a gas leak. The system was implemented using an Arduino Uno microcontroller and upon detection, it activated an alarm and a ventilation system while also displaying the leak status on an LCD and sending both an SMS and a voice message to either the user or a 3rd party. While the system proved to be a better alternative to earlier innovations, there was no inclusion of a control system to stop the gas leak.

Furthermore, Khan, (2020) focused on developing a low-cost sophisticated sensor-based gas leakage detector, alert, and control system that could be used in both industrial and residential areas. The study was a rudimentary set-up of a gas detection system with functions that are essentially similar to earlier developed systems covered in this chapter, albeit with a more skeletal concept. Even though his work was lacking in content, it was abundant in recommendations and could be used as a foundation for future works. The paper identified several key areas in this field that needs to be developed, which include the need for systems to distinguish between gas leaks and gas wastage, the inclusion of more software-based intelligent functions that would enable smart controls, a mobile and web-based app for real-time monitoring, the addition of more sensors and relays to simplify other system functionalities, and the need for data analysis that would aid both system analysis and prediction.

Harnessing a novel approach to detecting and managing gas leakage was the work done by Anika et al., (2021) wherein they developed a gas leakage with auto ventilation and a smart management system using IoT. The system was borne having noted the rapid adoption of gas use in households, the accustomed negative impact when its use is not properly monitored and the enormous advantages that sensor-based projects are used in solving complex day-by-day problems. Their work included the detection of gas leaks as well as fire outbreaks, and their focus was on gas use in compact spaces. They also praised the system for being an innovative approach to dealing with gas leak-related accidents because it provides both security and safety. The system consisted of a microcontroller-based module that housed the gas sensor and the fire detector and was programmed to activate an exhaust fan and a water system in the event of a fire. The system's high point was the attention paid to addressing gas leaks and fire outbreaks in compact spaces as well as the introduction of an IoT-based framework aimed at monitoring gas leakage. Notwithstanding the unique advantages of their approach, there was no clear process established to distinguish between a gas leak and a gas waste, a cut-off system for the gas supply upon detection, or specific solutions aimed at correcting a gas leak and a fire outbreak, as both corrective measures suggested are to be activated regardless of what is detected.

Baballe et al., (2021) came up with an automatic gas leakage monitoring system using an MQ-5 Sensor. The work emphasized the importance of adopting safe measures in the use of new technology. The system developed was aimed at raising awareness of the security actions that individuals can take in their daily lives in response to the rise in the outbreak of fires and explosions in the world today, and this was accomplished by providing a detailed process for developing a low-cost LPG leakage detection system. While the system developed used an Arduino microcontroller unit as the system's brainbox, with interconnected devices such as the MQ-5 sensor for detection and a buzzer alarm, LCD, and GSM Module for notification, the paper also highlighted unique features of other systems such as remote-control capabilities, gas supply control measures, acquiescence response to notifications, cost-effective prototypes, data collection for risk assessments, web-based applications. In spite of the extensive recommendations in the paper, the system was only a basic development of a gas leakage detection system.

Based on the aforementioned review, the following research gaps were identified:

i. Most of the earlier systems did not use a multi-point sensing approach to aid prompt detection of gas leakages.
ii. The earlier systems had restriction on the range of communication between interconnected modules.
iii. Earlier systems did not include mobile remote monitoring systems with remote control capabilities in their design.
iv. Prior systems did not characterize gas leaks, this limited the detection precision and caused false alarms.

v. There was no system that used a condominium as a case study.
vi. In the event of a leak, most systems did not include a cut-off valve for the gas supply network.

Based on the foregoing, our proposed system aims to address these research gaps highlighted above.

3 RESEARCH METHODOLOGY

3.1 SYSTEM OVERVIEW

To achieve the objectives of the research, the proposed system comprises of three major modules which are the detection module, the monitoring module and the gas supply control module. The detection module consists of a network of several sensors, each of which is installed in a housing unit and strategically placed so that any potential leak could be detected promptly. The gas supply control module is an interconnection of multiple valve systems and is responsible for cutting off the gas supply to the housing unit where a leak is detected. The monitoring module is enabled by a mobile application that will allow the user to remotely monitor the output parameters of the detection module, such as atmospheric levels, gas PPM detected, leak levels, valve operations, and the system's operational status. The application also has a manual override capability that allows the user to reactivate the valves and restart the system. As an extra feature, the mobile application includes an in-app notification that pops up to keep users informed about gas levels and potential leaks.

The use of IoT is employed for ease in communication and data collection amongst the multiple sensors, this would then be conveyed to the central processing unit and the remote monitoring unit. The data obtained is fed into the fuzzy logic inference system, after which instructions are set based on the specified rules so as to classify the different states of gas leakages. These operations determine the action of alerting the user and shutting off the gas supply to control the leakage. Figure 1 shows the flowchart of the system operation.

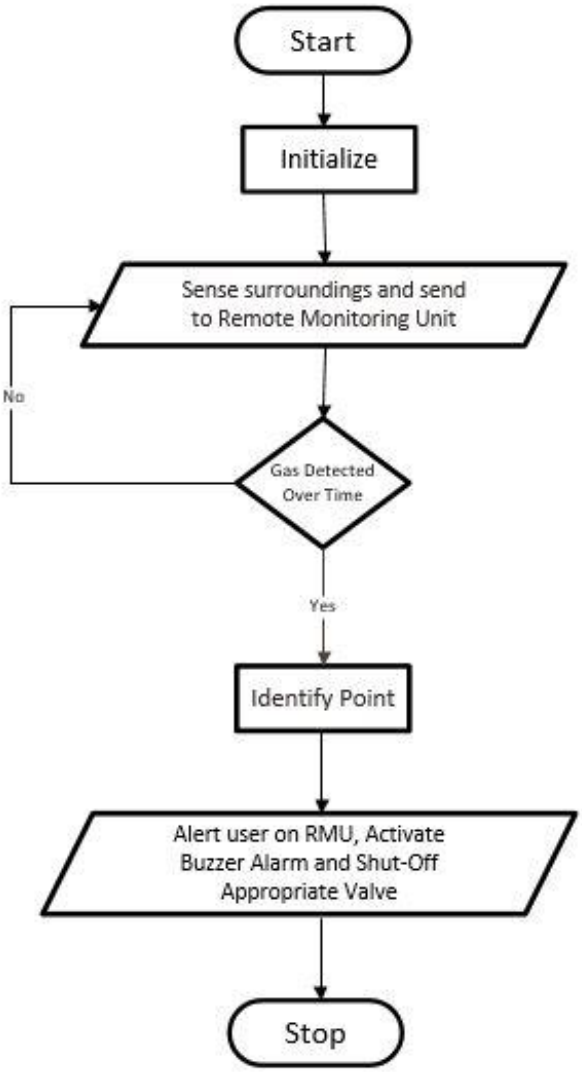

Figure 1: Flowchart of the IoT-based gas leakage monitoring and control system

3.2 IOT-BASED MULTI-SENSING GAS LEAKAGE MONITORING SYSTEM USING WI-FI TECHNOLOGY

The detection module is an interconnection of 3 MQ-6 sensors, each of which is positioned at a strategic location where the sensor's proximity to the usage area is close. A case study for 3 houses (making 9 MQ-6 sensors to make up the entire detection module) is used in this study. The detection module is based on the principles of the multisensory wireless network, which has been described as an important representative in the information technology space by (Zhang et al., 2021) having sparked a fresh wave of research around the world and opened up new areas of application in the military, environmental monitoring, traffic management, intelligent home, and other fields.

The use of the MQ-6 sensor for the multi-sensory wireless network was chosen for a variety of reasons, including its ability to detect LPG gas. For this study, three sensors are used to build up the multiple sensor networks (each deployed to a condominium unit), and they are integrated with a node MCU microcontroller to enable multiple sensor connections and communication with the monitoring module. Mapping the area of gas usage to determine the perfect detector placement position is done by taking into account potential gas discharge points, potential contact points and noise. The sensors are calibrated to detect gas between 200 and 1,000 Parts Per Million (PPM), and the output readings are relayed to the monitoring module in real-time. Figure 2 depicts the detection modules' architectural configuration and the interaction of the detecting modules with other modules using IoT.

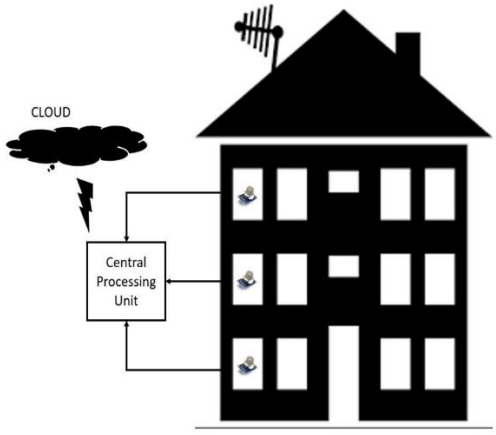

Figure 2: Architectural set-up of the detection module

The system is be remotely monitored and controlled via a mobile application. A Wi-Fi module enables the monitoring system as it is responsible for establishing the connection between the mobile application and the embedded system. In this study, the Blynk IoT Mobile application is used. This is an IoT platform for iOS and Android smartphones that can be used to control Arduino, Raspberry Pi, and NodeMCU via the internet, resulting in an interactive Graphical User Interface (GUI) or Human Machine Interface. Blynk is employed to monitor the gas levels in each detector module, as well as provide additional capabilities like data storage for analysis, remote management of the gas supply network, and overall system control. Figure 3 shows the architecture of Blynk in a sensor-based IoT monitoring system.

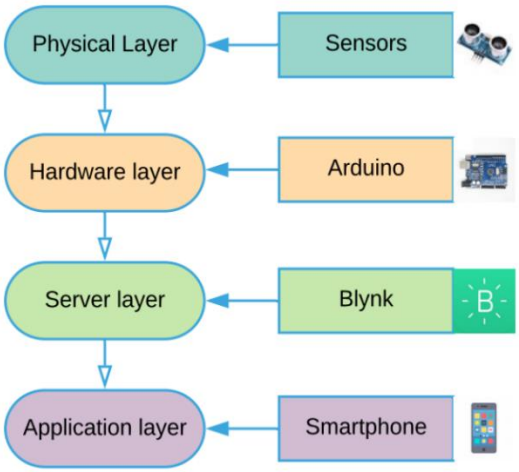

Figure 3: Architecture of the Blynk sensor-based IoT monitoring system (Karrupusamy, 2020)

3.3 FUZZY LOGIC CONTROL SYSTEM DESIGN

The gas supply control module is controlled by the principles of fuzzy logic by obtaining data from the sensors, analysing the obtained data using fuzzy logic and activating the shut-off valves based on the output from the analysis done using membership functions and the fuzzy rules. The fuzzy inference system employed in this study is presented in Figure 4.

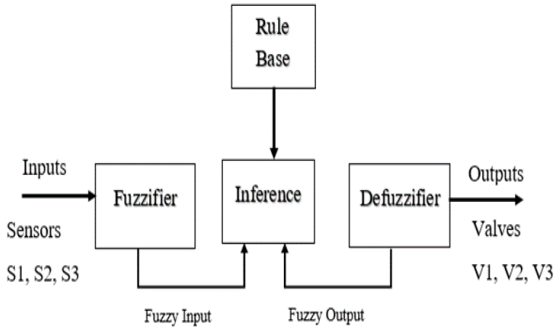

Figure 4: The fuzzy inference system for gas control

The Fuzzy Inference System (FIS) is designed using the fuzzy logic toolbox provided by MATLAB. The Mamdani FIS is used in this study due to its widespread acceptance, intuitiveness and suitability for human inputs (Bala et al., 2019). The FIS comprised of two inputs (gas quantity and time of leak) and one output (valve state). Defuzzification is achieved using the centroid technique which evaluates the area under a curve. This converts the fuzzy outputs to a crisp output. The output is then integrated to provide the final control signal.

The trapezoidal membership function (MF) is implemented for all the inputs and the output due to its simplicity, wide use and ease of implementation. The input variables are gas quantity and time of leak. The inputs have a range of 0 to 1000 and 0 to 5 for the gas quantity and time of leak respectively. The output variable is the valve state which has a range of 0 to 5. Equations 1, 2, and 3 show the range distribution according to the various individual membership functions for the inputs and outputs.

$$\mu_{gas\ quantity} = \begin{cases} 0 \le low \le 450 \\ 300 \le med \le 700 \\ 550 \le high \le 1000 \end{cases} \quad (1)$$

$$\mu_{time\ of\ leak} = \begin{cases} 0 \le low \le 2 \\ 1 \le med \le 4 \\ 3 \le high \le 5 \end{cases} \quad (2)$$

$$\mu_{valve\ state} = \begin{cases} 0 \le off \le 1 \\ 1 \le on \le 5 \end{cases} \quad (3)$$

From Equation 1, it can be observed that the 'gas quantity' variable has three membership functions. These are low, med, and high which have ranges of [0, 450], [300, 700], and [550, 1000] respectively. The 'time of leak' variable has three membership functions as well. These are low, med, and high which have ranges of [0, 2], [1, 4], and [3, 5] respectively. . The 'valve state' variable has two membership functions. These are off and on which have ranges of [0, 1], and [1, 5] respectively. Figures 5, 6, and 7 show the graphical representation of the membership functions.

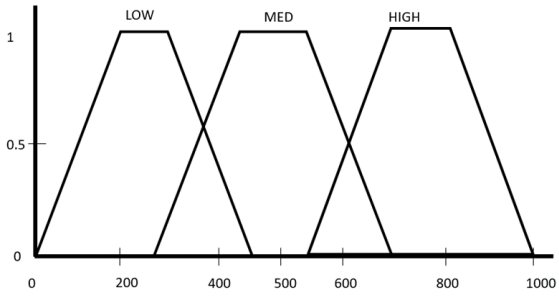

Figure 5: Membership Function for Gas Quantity

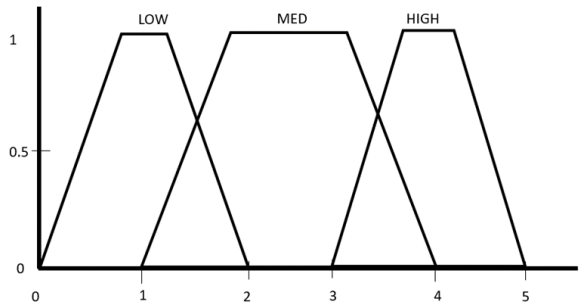

Figure 6: Membership Function for Time of Leak

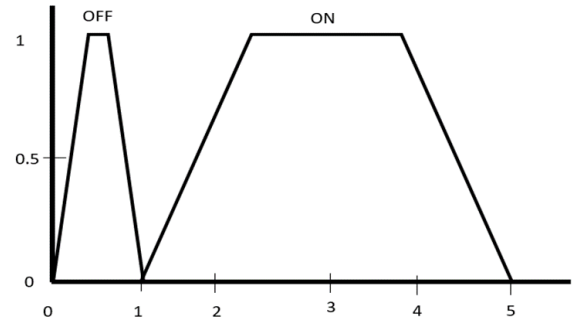

Figure 7: Membership Function for Valve State

The developed rule base is designed to specify classes for the actual gas leak and this is based on the classification of Table 1, and this is classified into normal class, ignition class, and gas leak class. The control system would be activated both intelligently by the system and manually through the Blynk IoT mobile application. This would serve as a fail-safe mechanism in the event that it is not automatically shut off. Based on the assumptions made in Table 1, the rule based was developed. The developed rules are presented in Table 2.

TABLE 1: CLASSIFICATION OF GAS LEAKS

S/No	The rate of gas leakage	Class
1	Consistently rising for more than 2 seconds	Gas Leak
2	Detected within 2 seconds	Ignition
3	No detection	Normal

TABLE 2: DEVELOPED RULE BASE

Valve State		Gas Quantity		
		LOW	MED	HIGH
Time of Leak	LOW	OFF	OFF	ON
	MED	ON	ON	ON
	HIGH	ON	ON	ON

3.4 System Prototype Development

The architecture of the system is represented by the block diagram presented in Figure 8. The system will be controlled by a node MCU microcontroller, which serves as the hub of the system. The instruction set, memory, and processing speed of the microcontroller will ensure fast processing power and handle computational complexities, while an inbuilt Wi-Fi module will provide internet access for remote monitoring and control.

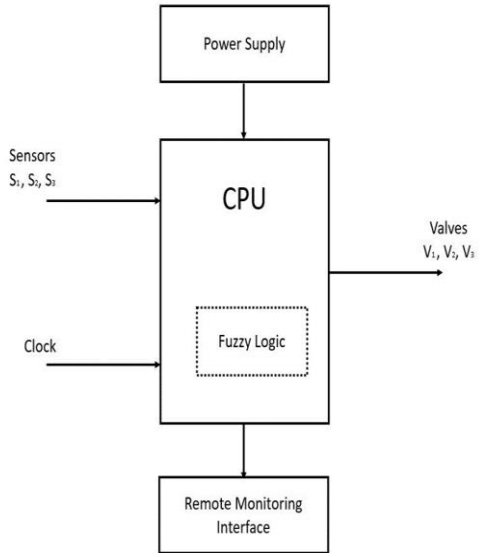

Figure 8: Architecture of the Multi-Point Gas Leakage Detection System

The inputs to the microcontroller are the signals from the gas sensors and the time from the clock. The gas sensor will be used to detect the quantity of gas, and the clock will provide the time of leakage. The output of the system is the valve state which is controlled by a servo motor, and is responsible for shutting of the gas supply valve. The inbuilt Wi-Fi module will form the base of the remote monitoring and control unit. This will be responsible for the transmission and receiving of data from the IoT platform which communicates with the mobile application.

4 RESULTS AND DISCUSSION

In this section, the results obtained from the development of the fuzzy logic control system are presented. Figure 9 shows the rule viewer of the developed Fuzzy Logic System.

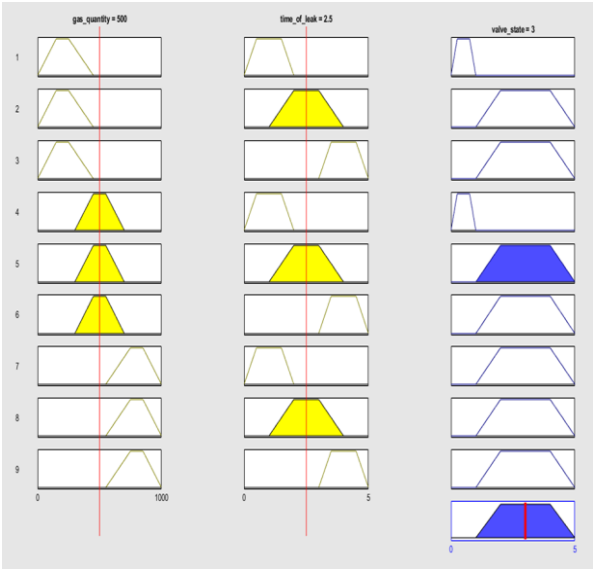

Figure 9: Fuzzy Logic System Rule Viewer

In Figure 9, the Rule Viewer of the Fuzzy Logic System is presented. This figure was obtained after developing the fuzzy inference system in MATLAB using the fuzzy logic toolbox. The figure is significant since it represents the relationships between the inputs and outputs of the fuzzy inference system for each of the developed rules. It can be observed from the figure that each rule is evaluated independently to get an output for that rule. At the end of the rule evaluations, the results from each rule is aggregated and defuzzified using the centroid technique discussed in section 3.3.2. From the figure, it can be seen that the rule viewer evaluates the fuzzy output for a gas quantity of 500 and a leak time of 2.5. Using these inputs, only rules 3, 4, and 5 cover the range for the first input (i.e. 500 falls within the membership function that covers that value). Similarly, rules 2, 5, and 8 cover the range for 2.5 in the second input. As a result of these conditions, only rule 5 triggered an output since the range for that rule covers both input values, thereby producing an output value of 3, representing a valve state of ON. This relationship between the inputs and outputs can be represented diagrammatically and Figure 10 shows the surface of the Fuzzy Inference System.

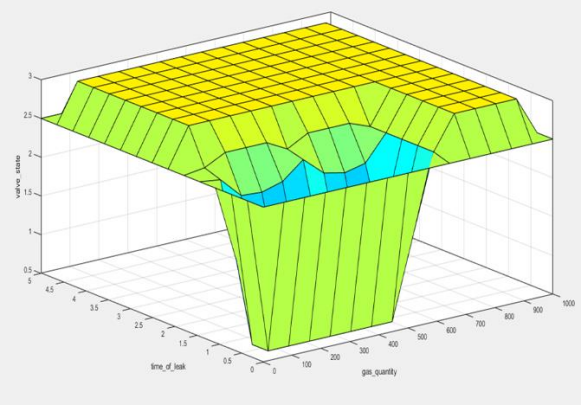

Figure 10: Surface of Fuzzy Inference System

In Figure 10, the surface diagram of the fuzzy inference system is presented. This diagram was obtained after developing the rules of the fuzzy logic control system. The importance of the figure lies in its representation of the relationship between the input and output values of the system. Since there are three elements in total (two inputs and one output), the surface diagram is a 3-dimensional figure. It can be observed from the figure that when values for both inputs on the x-axis and z-axis are traced to the output value of the y-axis, it provides an output which corresponds to the same output obtained from the fuzzy inference system for the same input values. Therefore, the surface diagram's lack of smoothness represents the intelligence associated with the inference process. The ability of the fuzzy system to infer the appropriate output based on given input values was evaluated using a combination of various inputs. The results of these experiments are presented in Table 3.

TABLE 3: RESULTS OF FUZZY LOGIC EXPERIMENTS

Gas Quantity (PPM)	**Time of Leak (secs)**	**Valve State**	**Obtained Output**	**Desired Output**
0	0	0.5	Valve Open	Valve Open
200	1	0.5	Valve Open	Valve Open
400	2	3.0	Valve Closed	Valve Closed
600	3	3.0	Valve Closed	Valve Closed
800	4	3.0	Valve Closed	Valve Closed
1000	5	3.0	Valve Closed	Valve Closed
0	5	3.0	Valve Closed	Valve Open
200	4	3.0	Valve Closed	Valve Closed
400	3	3.0	Valve Closed	Valve Closed
600	2	3.0	Valve Closed	Valve Closed
800	1	3.0	Valve Closed	Valve Closed
1000	0	3.0	Valve Closed	Valve Closed

Table 3 presents the experimental results obtained from the fuzzy inference system. This table was generated by feeding in various combinations of the input values into the system. The gas quantity values started from 0 and increased by an interval of 200, while the time of leak values started from 0 and increased with intervals of 1.

The table is significant since it shows the effectiveness of the developed fuzzy inference system in shutting off the gas supply in the event of a leakage. The results obtained are in line with the rule viewer and surface plots shown in Figures 9 and 10 respectively. The accuracy of the system can be evaluated as follows:

$$Accuracy = \frac{Total\ Number\ of\ Correct\ Predictions}{Total\ Number\ of\ Predictions} \times 100\%$$

$$Accuracy = \frac{11}{12} \times 100\% = 91.7\%$$

Therefore, it can be observed that based on the experiments carried out, the fuzzy inference system exhibited an accuracy of 91.7%. This implies that the developed system can be successfully implemented in gas leakage control with high accuracy.

5 CONCLUSION

In conclusion, this study presents a faster and more reliable method of monitoring gas leaks in a centralized gas supply system, specifically in a condominium setting. By utilizing a multiple sensing approach through an IoT-based monitoring module, gas leaks can be detected and remotely tracked via Wi-Fi technology. Additionally, the implementation of a fuzzy logic based corrective measure enables quick activation of a shut-off valve at various points of supply, minimizing the potential harm caused by gas leaks. This approach offers a promising solution to improving the safety and efficiency of gas supply systems.

REFERENCES

Abubakar, N. Y., Bature, U., Tahir, N. M., Babawuro, A. Y., and Systems, V. S. (2020). Arduino based gas leakage control and temperature monitoring system Arduino based gas leakage control and temperature monitoring system. December, 171–178. https://doi.org/10.11591/ijict.v9i3.pp171-178

Adekitan, A. I., Matthews, V. O., and Olasunkanmi, O. (2018). A microcontroller based gas leakage detection and evacuation system. IOP Conference Series: Materials Science and Engineering, 413(1). https://doi.org/10.1088/1757-899X/413/1/012008

Anika, A. M., Shoma, J. F., Akter, N., Sattar, A., and Hasan, M. N. (2021). Gas Leakage with Auto Ventilation and Smart Management System Using IoT. International Conference on Artificial Intelligence and Smart Systems, 1411–1415.

Baballe, M. A., Magashi, U. Y., Garko, B. I., Abdullahi, A., Umar, Magaji, Y. R., and Surajo, M. (2021). GAS LEAKAGE MONITORING SYSTEM USING MQ-5 SENSOR. 8(2), 64–75. https://doi.org/10.18488/journal.76.2021.82.64.75

Bala, J., Olaniyi, O., Folorunso, T., and Arulogun, O. (2019). Poultry Feed Dispensing System Control: A Case between Fuzzy Logic Controller and PID Controller. Balkan Journal of Electrical and Computer Engineering, 7(2), 171–177. https://doi.org/10.17694/bajece.536026

Bhattacharyya, T. K., Sen, S., Mandal, D., and Lahiri, S. K. (2006). Development of a wireless integrated toxic and explosive MEMS based gas sensor. Proceedings of the IEEE International Conference on VLSI Design, 2006, 4–7. https://doi.org/10.1109/VLSID.2006.72

Brown, E. (2021). Next-Generation MEMS Multi-Gas Sensing - Tech Briefs. Https://Www.Techbriefs.Com/. https://www.techbriefs.com/component/content/article/tb/supplements/st/features/applications/39240

Dadkani, P., Noorzai, E., Ghanbari, A. H., and Gharib, A. (2021). Risk analysis of gas leakage in gas pressure reduction station and its consequences: A case study for Zahedan. Heliyon, 7(5), e06911. https://doi.org/10.1016/j.heliyon.2021.e06911

Dewi, L., and Somantri, Y. (2018). Wireless Sensor Network on LPG Gas Leak Detection and Automatic Gas Regulator System Using Arduino. IOP Conference Series: Materials Science and Engineering, 384(1). https://doi.org/10.1088/1757-899X/384/1/012064

Durán, C. M., Monsalve, P. A. G., and Mosquera, C. J. (2016). Multisensor system for toxic gases detection generated on indoor environments. IOP Conference Series: Materials Science and Engineering, 157(1). https://doi.org/10.1088/1757-899X/157/1/012029

Ermi Media's, Syufrijal, and Rif'an, M. (2019). Internet of Things (IoT): BLYNK Framework for Smart Home. KnE Social Sciences, 3(12), 579. https://doi.org/10.18502/kss.v3i12.4128

Gordon, A. (2021). Natural Gas | Types, Discovery, Reserves, and Facts | Britannica. Britannica.Com. https://www.britannica.com/science/natural-gas

Huntingford, C., Lowe, J. A., Howarth, N., Bowerman, N. H. A., Gohar, L. K., Otto, A., Lee, D. S., Smith, S. M., den Elzen, M. G. J., van Vuuren, D. P., Millar, R. J., and Allen, M. R. (2015). The implications of carbon dioxide and methane exchange for the heavy mitigation RCP2.6 scenario under two metrics. Environmental Science and Policy, 51(0), 77–87. https://doi.org/10.1016/j.envsci.2015.03.013

Hussien, N. M., Mohialden, Y. M., and Ahmed, N. T. (2020). A smart gas leakage monitoring system for use in hospitals. July, 1048–1054. https://doi.org/10.11591/ijeecs.v19.i2.pp1048-1054

Karrupusamy, P. (2020). A Sensor based IoT Monitoring System for Electrical Devices using Blynk framework. Journal of Electronics and Informatics, 2(3), 182–187. https://doi.org/10.36548/jei.2020.3.005

Khan, M. M. (2020). Sensor-Based Gas Leakage Detector System †. 1–6. https://doi.org/10.3390/ecsa-7-08278

Liang, F.-Y., Ryvak, M., Sayeed, S., and Zhao, N. (2012). The role of natural gas as a primary fuel in the near future, including comparisons of acquisition, transmission and waste handling costs of as with competitive alternatives. Chemistry Central Journal, 6(S1), 1–24. https://doi.org/10.1186/1752-153x-6-s1-s4

Neri, G. (2021). Sensors | Topical Collection : Gas Sensors. Https://Www.Mdpi.Com/. https://www.mdpi.com/journal/sensors/special_issues/gas_sensors_collection

Nevadanano. (2022). NevadaNano Brings You The Next Generation Multi Gas Sensor. Https://Nevadanano.Com/. https://nevadanano.com/

Olorunfemi, B. J., Adenuga, D. E., and Olumilua, A. E. (2020). Development and Performance Evaluation of a Household Liquefied Petroleum Gas Monitoring and Leakage Detector. Covenant Journal of Engineering Technology (CJET), 4(2). http://journals.covenantuniversity.edu.ng/index.php/cjet

Omar, A., Ditual, A., Urot, J., Dimal, M., Mamco, N., and Sagarino, C. (2019). Mq2-Tector: an Arduino Based Gas Detector, Preventing Gas-Leak Explosion. Sensors Journal, April, 0–21. https://doi.org/10.13140/RG.2.2.15517.56808

Simbeye, D. S. (2013). Gas Leakage Detection System (GLDS) Daudi S. Simbeye Computer Studies Department, Dar es Salaam Institute of Technology, P. O. Box 2958, Dar es Salaam, Tanzania . 4, 36–43.

Yi, W. Y., Lo, K. M., Mak, T., Leung, K. S., Leung, Y., and Meng, M. L. (2015). A survey of wireless sensor network based air pollution monitoring systems. In Sensors (Switzerland) (Vol. 15, Issue 12). https://doi.org/10.3390/s151229859

Zhang, J., Hu, Y., and Li, H. (2021). Research on Wireless Sensor Network Positioning Based on Genetic Algorithm. Wireless Communications and Mobile Computing, 2021. https://doi.org/10.1155/2021/3996401

4th International Engineering Conference (IEC 2022)
Federal University of Technology, Minna, Nigeria

Determination of Physical and Mechanical Properties of Some Selected Varieties of Commonly Grown Maize in Nigeria

[1]Zubairu, M., *[2]Dauda, S. M.,[2]Balami, A.A.,[1]Gbabo, A. & [1]Mohammed, I.S.
[1] Agricultural Engineering Department, Kaduna Polytechnic
[2]Agricultural and Bioresources Engineering Department, Federal University of Technology, PMB 65 Minna Niger State, Nigeria.
*Corresponding author email:smdauda@futminna.edu.ng, +2348038964659

ABSTRACT
Knowledge of physical and mechanical properties of maize grains is significant in designing a processing machine whose energy depends on these properties**.** The aim of this study is to determine the physical and mechanical properties of some commonly selected varieties of maize grown in Nigeria, namely SAMMAZ/14, SAMMAZ/15, SAMMAZ/17, SAMMAZ/37, and SAMMAZ/50. Linear dimensions (length, width (W), thickness (T)) and moisture contents of Undehusked maize (leaf) kernel and seeds of each variety were determined. Angle of repose, bulk density, geometric mean diameter, deformation, compressive strength, and rapture energy measurements were also performed on each of the maize seeds varieties. Results shows the average linear dimensions of Undehusked maize (leaf) kernel and seeds varieties determined in terms of length, width (major, minor), thickness (major, minor) of SAMMAZ/14, SAMMAZ/15, SAMMAZ/17, SAMMAZ/37 and SAMMAZ/50 are 457.7mm, W(31mm, 27mm), T(6mm, 9.4mm), 565mm, W(40mm, 31mm), T(7mm, 5.5mm), 7.450mm, W(32mm, 19mm), T(5mm, 9mm), 426mm, W(29mm, 23mm), T(6mm, 3.4mm), 610mm, W(46mm, 19mm), T(4.1mm, 2.4mm) and 11mm, W(9.6mm, 7.4mm), T(4.4mm, 6mm), 9.5mm, W(9.3mm, 6.9mm), T(4mm, 3mm), 9.0mm, W(9.2mm, 7mm), T(4.1mm, 2.9mm), 9.3mm, W(8.8mm, 2.3mm), T(1.4mm, 3.4mm), 6.1mm, W(8.6mm, 7mm) T(4mm, 3.5mm), while moisture contents for both undehusked maize (leaf) kernels and seed varieties were 16%, 17%, 20%, 16%, 21% and 17%, 16%, 16%, 11%, 12% respectively. Average angle of repose, Bulk density, geometric mean diameters, deformation, compressive strength and rapture energy of the maize seed SAMMAZ/14, SAMMAZ/15, SAMMAZ/17, SAMMAZ/37 and SAMMAZ/50 varieties are 22.2^o, 0.71gcm^{-3}, 8.4mm, 1.201mm, 2.7N/mm^2, and 0.0840Nm, 20.1^o, 0.72gcm-^{3}, 8.1mm, 2.123mm, 6.6N/mm^2, and 0.1907Nm, 24.0^o, 0.70gcm^{-3}, 7.1mm, 0.825mm, 8.8N/mm^2, and 0.165Nm, 23.3^o, 0.8gcm^{-3}, 6.2mm, 0.132mm, 3.34N/mm^2, and 0.066Nm and 22.5^o, 0.76gcm^{-3}, 6.3mm, 0.456mm, 3.4N/mm^2 and 0.0228Nm. To prevent kernel damage during processing and handling, the measured rapture energy and compressive strength during compression can be used as the limit value for designing machine.

Keywords: *Animal Feed, Machine design, maize, mechanical, physical, varieties.*

1 INTRODUCTION

Corn (Zea mays L) ranks as the third most important cereals corps in the world. Asian countries are significant producers of sweet maize and more than 62% of their maize production is consumed in the form of animal feed, while the balance is for human consumption.

The knowledge of physical and mechanical properties of crops is essential in the design; fabrication and adjustment of machines utilize in processing, separation, cleaning, handling of Agricultural materials such as maize, and convert them into foods, feed, and fodder.

The properties which are useful during design must be known and these properties must be determined at laboratory conditions. The geometric properties such as size and shape are one of the most important physical properties considered during separation and cleaning of agricultural grains (Barnwal et al., 2012, Ganjeer & Banjare, 2020). Determination of physical properties as function of machine is important to the design of equipment for handling, conveying separation, drying, aeration, storage, and processing. The size and shape are for instance importance in their separation from undesirable material and in the development of sizing and grading machinery (Adesokan *et al.*.2019). Determination of physical and aerodynamic properties of some varieties of wheat, barly, chickpea and lentils, in terms of their length, width, thickness, geometric mean diameter, terminal velocities, drag coefficient of each grain were determined. Average experimental terminal velocity was found to be in the ranges of 7.52 to 8.14m/s for wheat varieties, 7.72 to 7.78m/s for lentil varieties and 11.15mto 12.01m/s for chickpea varies. S. Gursoy and E. Guzel (2010). Ahmadi and Mollazade. (2009) determined the physical and mechanical properties of funnel (seeds) as a function of moisture content. The angle of repose was used to select the angle at which the trapezoidal section of the hopper was slanted. The bulk density and moisture content were used to determine the uniformity of distribution of the maize seed, while the machine is in operations.

Adesokan (2019) cited criteria for evaluating performance of dehusking- shelling mechanism include dehusking-shelling efficiency grain loss, grain damage, output capacity, cleaning efficiency, power equipment and

dehusking shelling recovery. These criteria are measured against some variables namely crop moisture content, cylinder dehusking, shelling speed, crop federate, concave clearance, cylinder diameter and dehusking, shelling length. Crop material which are of importance include moisture content biometric properties such as size of grain spent cob ratio, grain bulk density, sphericity, angle of repose, terminal velocity, one thousand grain mass and porosity. For processing of maize product in general and dehusking – shelling in particular, (Isiaka *et al.* 2006) stated, it is necessary to determine some physical properties, which in most cases are dependent on moisture content. These properties include dimension (size shape), bulk density, and porosity, coefficient of static frictions, volume, surface area, angle of repose and angle of internal friction. Dula (2019) pointed out their practical utility in machine and structural design process and control engineering. Physical properties of agricultural product are studied by considering them individually due to their irregular shape and variability in sizes.

Understanding mechanical properties of maize kernel reduces mechanical damage through establishing and developing the mechanical system of harvesting, dehusking-shelling. Mechanical properties such as compressive strength, rapture forces, modulus of elasticity, rapture energy, deformations and others are important engineering data needed in studying size reduction of maize. Mechanical damage decreases seed corn viability and result in lower yields. Researchers have conducted many investigations to solve problems related to serial products through their mechanical properties (Wang, B. & Wang, 2019). Mechanical properties of fresh maize corn kernels were obtained for two varieties. White dent corn single hybrid 10 and yellow dent maize corn kernel single hybrid 155 at different moisture content ranged from 30.26 to 988 (w.b%).The mechanical properties obtained for white maize corn kernel include yield energy (YE), rapture energy (RE), at a moisture content of 9.81% and the yellow maize corn kernel obtained were yield energy (YE), and rapture energy (RE) at moisture content of 10.12% (Mohammed and Abdelmaksond (2009).

To determine some physical and mechanical properties of five selected varieties of commonly grown maize in Nigeria, was carried out.

2.0 LITERETURE REVIEW

Pradhan et al. (2008) stated that the repose angle of corn seeds increased with seed moisture content from 8.56% to 22.22%. The values were observed to rise from 27.69^0 to 37.33^0. The tendency towards the repose angle with moisture content takes place because of the surface layer of moisture around the particles, which holds the total seeds together by surface tension.

Esehaghbeygi et al. (2009) measured the shear stress of canola stalk for four levels of moisture content (35%, 43%, 50% and 57%, wet basis), with different cutting heights, two kinds of varieties, three levels of the fertilizer. The knife oblique angle of 30 ^{o} was found to apply the slightest shearing pressure.

Ince et al. (2005) reported that bending stress was less with increasing moisture content. The estimation of the compressing bending got was about two times at low moisture content compared with high moisture content. The mean compressing bending ranged from 9.71 to 47.49 MPa.

Batos et al. (2015) conducted a study on the wheat stalks. The cutting tests were done for two cutting velocities and two cutting angles. The moisture content of the samples ranged from 5.5% to 7.1%. The main cause for this difference was the greater friction at the larger cutting angle.

According to Miu (2016) the mechanical and physical properties of plant stalks affect their behavior under the impact of the mechanical forces exerted through the harvester combine, in terms of plant curvature (towards cutting unit), cutting (shear stress), and pick up cob. To assist modeling, emulation, and optimizing of combine operations, it is absolutely required to consider credible experiential data. For some properties after harvesting of the cereal stalks, these presented plant stalk data depends on ripeness of plant, and environmental conditions during harvesting. This means that consideration should be given to physical properties of the maize corn plant and the related mechanical properties of the plant components, which is crucial in the process of modeling and engineering design of agricultural machines.

Knowledge of all the mechanical properties of biological materials is necessary for the layout of technological processes as mentioned by Szymanek et al. (2006).

3.0 METHODOLOGY

Undehusked maize (leaf) kernel used in this study was purchase and experiment was conducted in Ahmadu Bello University (Zaria) Nigeria in 2019 include SAMMAZ/14, SAMMAZ/15, SAMMAZ/17, SAMMAZ/37 and SAMMAZ/50 varieties. The grain varieties were collected through the seed production unit of Instituted of Agricultural Research (IAR) Zaria. The Undehusked maize (leaf) kernel measuring 5kg of each variety was measured and their linear dimensions were taken, including their moisture content of each variety. Similarly, the seeds, of similarly varieties, measuring 5kg samples for each grain variety and randomly selected for the measurement of their linear dimensions (Length, width, and thickness) of each variety was measured. All the seeds were clean manually to remove all foreign matters, broken seeds, and dust e.t.c.

The dimensions of each seed, namely length, width and thickness were measured in three directions by using Vernier caliper with 0.001/mm accuracy.

3.1 Determination of geometric mean diameter. (d_g)

Geometric mean diameter measurement is used to for the design of concave sieve radius of the processing machine. Equations (1) was used to determine the geometric mean diameter of each variety of the maize seed (Mohsenin, 1980)

$$D_g = (abc)^{\frac{1}{3}} \quad (\mathbf{1})$$

$where$

$d_g = \ geometric\ mean\ diameter\ in\ mm$

$a \ = \ length\ of\ seed\ in\ mm$

$b \ = \ width\ of\ seed\ in\ mm$

$c \ = \ thickness\ of\ seed\ in\ mm$

3.2 Determination of Bulk density (ℓ_b)

Bulk density is used in determination of uniformity of distribution of Agricultural material while the machine is in operation. It is the ratio of mass to volume and express in g/m^3. The bulk density of the five varieties of maize were determined by weighing the grains in a measuring cylinder of known volume of (1000cm^3) and the weight of the seeds obtained as outlined by Waziri and Mittal (1983) using equation (2).

$$\ell_b \ = \ \frac{M_1 - M_2}{V} \quad (\mathbf{2})$$

$Where\ \ell_b \ = \ Bulk\ density\ in\ gcm3$

$M_1 \ = \ mass\ of\ filled\ container\ in, gram$

$M_2 \ = \ mass\ of\ empty\ container\ in\ gram$

$V \ = \ measured\ volume\ of\ container,\ 1000cm^3$

3.3 Determination of Angle of repose (O_F)

The angle of repose of the five varieties of maize was obtained. Angle of repose of grain is the angle the seed made with the horizontal at which the grain will stand when filled. It was obtained with the aid of an open container of 45cm and 20cm diameter and height respectively.

A container of 45cm diameter was filled with the grain after positioning it on a high round plat form. The container was removed gradually until the grain formed a shape of a cone. The height of the shaped cone was measured, and angle was computed as reported by Mustafa (2021) using equation (3). The same procedure was carried out for the remaining four varieties of the maize.

$$\Theta_F \ = tan^{-1}\frac{2H}{D} \quad (\mathbf{3})$$

$Where\ \Theta_F = \ Angle\ of\ repose$
$H \ = \ height\ of\ shape\ cone\ formed, m.$
$D \ = \ Diameter\ of\ shape\ cone\ form, m.$

3.4 Determination of Moisture content (M.C)

Moisture content is used in determination of uniformity of grains materials while the machine is in operation.

Moisture content of five varieties of Undehusked maize (leaf) kernel and the maize seed of each varieties of the selected maize of SAMMAZ/14, SAMMAZ/15, SAMMAZ/17, SAMMAZ/37, and SAMMAZ/50 at a moisture content of 16%, 17%, 20%, 16%, 21% of Undehusked maize (leaf) and of maize (seeds) at moisture content of 17%, 16%, 16%, 11%, and 12% was determined respectively (Mohsenin, 1980), using the same equation as stated in equation, 4.

$$M.C \ = \ \frac{W_1 - W_2}{W_1} \ \times 100 \quad (\mathbf{4})$$

W$here,$
$M.C. = \ moisture\ content$
$W_1 \ = \ weight\ of\ Undehusked\ (leaf)\ before\ heating, kg.$
$W_2 = \ weight\ of\ Undehusked\ (leaf)\ after\ heating, kg.$
$Similarly,$
$Moisture\ content\ of\ maize\ (seed)\ was\ determined\ using\ the\ equation$ (5)

$$M.C_1 = \ \frac{W_6 - W_7}{W_6} \ \ x\,100\% \quad (\mathbf{5})$$

$\boldsymbol{Where}$;

$M.C_1 = moisture\ content\ of\ maize\ seed$

$W_6 = weight\ of\ maize\ seed\ before\ heating\ (kg)$

$W_7 = weight\ of\ maize\ seed\ after\ heating\ (kg)$

3.5 Determination of compressive strength and rapture energy of maize seeds

The forces and deformation at the time of rapture of the grain samples between the base plate and the plunger head of universal materials testing machine (cat.Nr.261) was read directly from the universal testing machine, Ahmadu Bello University Zaria. The machine was operated in accordance with ASAE (2003). The values of the raptures forces, deformations were obtained directly from the machine. While the compressive strength, and the rapture energy was calculated using equation (6) and equation (7) from the results of rapture forces, and the deformation for the five varieties of the maize samples

$$Cs = \frac{F}{A} \quad (6)$$

$$E_a = \frac{FD}{2} \quad (7)$$

$Where\ C_s = compressive\ strength$

$F = rapture\ force, N.$

$A = x-sectional\ area, m^2$

$E_a = Rapture\ energy, joules$

$D = Deformation\ (mm)$

Table 1: Present the Linear Dimensions of the five selected varieties of Undehusked maize (leaf) kernel.

S/N	Sample	Length (L) mm	Width (w), mm		Thickness (t) mm	
			Major	Min	Major	Min
	SAMMAZ/14					
1		500	30	25	6.5	4.5
2		450	35	28	5.2	3.3
3		420	29	27	5.0	4.7
	Average value	457.7	31	27	6	9.4
	SAMMAZ/15					
1		605	40	35	7.5	5.8
2		550	45	30	6.0	4.7
3		540	35	28	7.0	5.5
	Average Value	565	40	31	7	5
	SAMMAZ/17					
1		400	35	20	6.5	5.6
2		430	30	22	4.5	2.5
3		520	32	15	4.7	3.2
	Average value	450	32	19	5	9
	SAMMAZ/37					
1		450	27	20	6.5	3.3
2		420	29	26	6.2	3.4
3		410	30	22	5.2	3.2
	Average Value	426	29	23	6	3.4
	SAMMAZ/50					
1		620	25	15	5.2	2.2
2		600	30	25	4.0	2.4
3		610	46	19	4.1	2.4
	Average Value	610	46	19	4.1	2.4

Table2. Presents the Linear Dimension, Angle of Repose, Bulk Density, and geometric mean

S/N	Sample	Length (L) mm	Width (w), mm		Thickness (t) mm		Angle of Repose (a)	Bulk density (g/cm^3)	Geometric diameter (g) mm
			Major	Min	Major	Min			
	SAMMAZ/14								
1		11.5	10.2	7.4	4.8	4.0			
2		10.8	9.9	8.0	4.4	3.0	22.2	0.71	8.4
3		9.4	8.6	6.8	4.0	2.9			
	Average value	11	9.6	7.4	4.4	6			
	SAMMAZ/15								
1		9.5	9.4	6.9	3.6	2.5			
2		10	9.2	7.6	3.8	2.8	20.1	0.72	8.1
3		9.0	9.2	6.3	4.7	3.7			
	Average Value	9.5	9.3	6.9	4	3			
	SAMMAZ/17								
1		9.0	9.4	7.9	4.0	3.1	24	0.70	7.1
2		9.0	9.1	6.8	4.0	2.5			
3		8.8	9.2	6.0	4.2	3.0			
	Average value	9.0	9.2	7	4.1	2.9			
	SAMMAZ/37								
1		10.2	10	2.2	6.5	3.3			
2		9.0	8	2.6	6.2	3.4	23.3	0.8	6.2
3		8.8	8.5	2.2	5.2	3.2			
	Average Value	9.3	8.8	2.3	1.4	3.4			
	SAMMAZ/50								
1		6.2	8.7	6.8	4.3	4			
2		6.0	8.0	6.2	4.2	3.8	22.5	0.76	6.5
3		6.1	9.0	7.9	3.4	2.6			
	Average Value	6.1	8.6	7	4	3.5	22.4	0.74	22.4

Table 3: illustrate the deformation, compressive strength, and rapture energy of the five Selected Varieties of Maize (Seeds)

S/N	Sample	Sample force (N)	Load (KN)	Deformation (mm)	Compression strength (N/mm^2)	Rapture Energy (NM)
1	SAMMAZ/14	140	0.14	1.201	2.7	0.0840
2	SAMMAZ/15	180	0.18	2.123	6.6	0.1907
3	SAMMAZ/17	400	0.4	0.825	8.8	0.165
4	SAMMAZ/37	100	0.1	0.132	3.34	0.0066
5	SAMMAZ/50	100	0.1	0.456	3.4	0.0228
Average Value		184	0.25	4.372	5	0.4512

3. RESULTS AND DISCUSSION

3.1 Physical Properties of the Undehusked Maize (leaf) Kernel.

Determination of the physical properties of undehusked maize leaf kernel is essential, as these parameters are required in the design and operation of harvesting machinery and postharvest machinery for the harvested undehusked maize and other plant biomass. The physical properties of maize plant reported in this study were from the samples taken from Ahmadu Bello University Farm Zaria Kaduna State, Nigeria.

Table 1 presents the five varieties of the physical properties data of undehusked maize (leaf) kernal. The average length of the undehusked maize (leaf) kernal of five varieties are 457.7 mm, 565 mm, 450 mm, 426mm and 610 mm which is higher than range indicated by Szymanek (2011) and Al-Mitewty et al. (2019) this increase may be due to soil type, environmental conditions and the varieties of the maize plant While, the average width (Major, minor) and thickness (Major, minor) of undehusked maize (leaf) kernal of five varieties are W(31mm, 27mm), W(40mm, 31cm), W(32mm, 19mm), W(29mm, 23mm), W(46mm, 19mm) which are within the range indicated by Szymanek (2011) and Al-Mitewty et al. (2019), and T(6mm, 9.4mm), T(7mm, 5.5mm), T(5mm, 9mm), T(4.1mm, 2.4mm) and T(6mm, 3.4mm) respectively.

The average value of the linear dimensions of maize (seed) varieties results (Table 2) shows that SAMMAZ/14 has the highest average length of 11mm, while SAMMAZ/15 has the least average length of 6.0mm which is within the range given by Balami et al. (2012). SAMMAZ/14 has the highest major width of 10.2mm while SAMMAZ/37 and SAMMAZ/50 have the least diameter of 0.8mm each. Minimum width diameter was recorded in SAMMAZ/37 as 2.0mm while SAMMAZ/14 has highest width diameter of 8mm which is within the range given by Szymanek (2011). thickness of maize seed was recorded with SAMMAZ/37 as the highest of 6.5mm major diameter, while SAMMAZ/50 has thickness to be 3.5mm. Minimum diameter of thickness was obtained in SAMMAZ/15 with 2.5mm. And maximum thickness and minimum diameter to be 4mm each in SAMMAZ/14 and SAMMAZ/50.

Moisture content of the Undehusked maize (leaf) kernel of SAMMAZ/14, SAMMAZ/15, SAMMAZ/17, SAMMAZ/37 and SAMMAZ/50 were found to be 16%, 17%, 20%, 16%, 21% respectively. With SAMMAZ/50 has highest moisture content of 21%, while SAMMAZ/14 and SAMMAZ/37 has least moisture content of 16%. Similarly, the various varieties of maize show that SAMMAZ/14 has the highest moisture content of 17%. While SAMMAZ/37 has least moisture content of 11%.

The average value of the load, deformation, compressive strength, and rapture energy of the five selected varieties of the maize seed are 0.25KN, 4.372mm, 5.0 N/mm^2 and 0.4512Nm which agreed with the results of Weronika et al. (2022)

4 CONCLUSION

Physical and mechanical properties of undehusked and maize seed are the most important properties in the design of agricultural machinery to determine standards of designed machine. The length, width, thickness, angle of repose, bulk density, geometric mean diameter, deformation, compression strength, and rapture energy

have a significant role in designing maize processing machine component parts which include hopper, concave clearance and holes, cylinder drum and sieve shaker. Knowing the angle of repose, is utilize in the design of the hopper while the bulk density is to determine the stability of flow of the seed when the machine is in operation. Whereas the mechanical properties of the undehusked and maize seed is considerable in designing the dehusked-shelling unit and grinding unit. The average load, deformation, compressive strength, and rapture energy of the five selected varieties of the maize seed are 0.25KN, 4.372mm, 5.0 N/mm^2 and 0.4512Nm.

Symbols

$L = length\ of\ Undehusked\ maize$

$(leaf)\ kernel, mm.$

$W = width\ of\ Undehusked\ maize$

$(leaf)\ kernel, mm.$

$t = thickness\ of\ Undehusked\ maize$

$(leaf)\ kernel, mm.$

$L_1 = length\ of\ maize\ seed, mm.$

$W_1 = width\ of\ maize\ seed, mm.$

$L_1 = length\ of\ maize\ seed, mm.$

$t_1 = thickness\ of\ maize\ seed, mm.$

$d_g = geometric\ diameter$

$maize\ of\ seed, mm$

$\ell_b = bulk\ density, gcm^3$

$v = measure\ volume\ of\ cylinder, cm^3$

$\Theta_f = Angle\ of\ repose\ of\ maize\ seed, o$

$M.C = moisture\ content\ of\ Undehusked$

$maize\ (leaf)\ \%$

$M.C_1 = moisture\ content\ of\ maize\ seeds$

$C_s = compressive\ strength$

$of\ maize\ seed, N/mm2$

$F = force, N$

$A = crossectional\ Area, m^2$

$E_a = rapture\ energy, NM$

$D = Deformation, mm$

$A.V = Average\ value$

SAMMA Z/14 = Sammaru Z/14

SAMMA Z/15 = Sammaru Z/15

SAMMA Z/17 = Sammaru Z/17

SAMMA Z/37 = Sammaru Z/37

SAMMA Z/50 = Sammaru Z/50

REFERENCE

Adesokan, M. A., Oriola, K. O., Ogundeji, B. A., & Bashir, O. W. M. (2019). Design, construction and performance evaluation of low cost maize dehusker-sheller in Nigeria. *British Journal of Applied Science & Technology*, *4*, 1-8.

Ahaneku I.E, kamal,A.R and ogunjiri , C.A (2003). Design,construction and performance evaluation of a multicrop thresher. Journal of Agricultural Engineering and Technology 11.17-23

Ahmadi, H and Mollazade (2009). Some physical and mechanical properties of fennel seed (foeneculartulgare.j.Agric,sci) : 66-75

ASE .ASAE (2003) Standard S352- 2FEBO3. Moisture measurement. Ungrounded Grain and Seeds. St Joshepmichegan. United States of America, pp. 606.

Al-Mitewty, M. I., A. Yahya, M. Razif, and N. Mat. 2019. Physical and mechanical properties of sweet corn plant. Agricultural Engineering International: CIGR Journal, 21(4): 152–160

Balami,A. A.,Adgidzi, D.,Kenneth, C. A., and Lamuwa, G. (2012) Performance Evaluation of a Dehusking and Shelling Machine for Castor Fruits and Seeds. IOSR Journal of Engineering (IOSRJEN).

Barnwal, P., Kadam, D. M., & Singh, K. K. (2012). Influence of moisture content on physical properties of maize. *International Agrophysics*, *26*(3).

Batos, A., and B. Ruepp, A. Jahr, and b. corves. 2015. Determination of the properties of cereal stalks

when being bent and cut with the aid of a universal test bench. Landtechnik, 70(4): 84-96.

Dula, M. W. (2019). Review on development and performance evaluation of maize Sheller. *International journal of engineering research and technology*, 471-481.

Esehaghbeygi, A., B. hoseinzadeh, and a. a. masoumi. 2009. Effects of moisture content and urea fertilizer on bending and shearing properties of canola stem. Applied engineering in agriculture, 25(6): 947-951.

Ganjeer, I., & Banjare, Y. K. C. C. (2020). Engineering properties of sorghum (Sorghum bicolor L.) and maize (Zea mays L.) grains. *IJCS*, *8*(2), 2760-2763.

Gursoy and E. GUZEL (2010). Determination of physical properties of some Agricultural grains research Journal of Sciences, Engineering and Technology 2 (5) 492 – 498, 2010.

Isiaka M.EL – Okene, A.M and Oyedele, T.A (2016). Determination of physical properties of Melon seed. Proceeding of Nigeria institution of Agricultural engineers .28:322:326

Mohammed A.F. ABDEI MAKSOND (2009). Determination of mechanical properties of white corn and yellow corn Jornal of M.S.T. Agr. Engr, 26 (4) 1901-1922.

Mohsenin N.N (1980): Physical properties of plants and animals materials. Gordin and breach sciences publishers, New York.

Mostafa, H. A. M. A. (2021). Manufacturing Engineering of Alternative Feeds.

Nimker,P.M and chattopahyay, P.K (2001). Some physical properties of green grain. Journal of Agricultural Engineering Reforms 80 (2):183-189

Miu, P. 2016. Combine Harvesters Theory, Modeling, and design. 1st ed. New York, USA: Taylor and Francis Group, LLC

Mohsenin, N. N. 1986. Physical Properties of Plant and Animal Materials. 2nd ed. New York, USA: GORDON and Breach Science Publishers.

Wang, B., & Wang, J. (2019). Mechanical properties of maize kernel horny endosperm, floury endosperm and germ. *International Journal of Food Properties*, *22*(1), 863-877.

Pradhan, R. C., S. N. Naik, N. Bhatnagar, and S. K. Swain. 2008. Moisture-dependent physical properties of Karanja (Pongamia pinnata) kernel industrial crops and products, 28(2): 155-161.

Szymanek, M. B. Dobrzanski JR, I. Niedziolka, and R. Rybcynski. 2006. Sweet corn harvest and technology physical properties and quality. 1st ed. Lublin, Poland, b. dobrzanski institute of agrophysics of polish academy of sciences.

Szymanek, M. 2011. Effects of blanching on some physical properties and processing recovery of sweet corn cobs. Food and Bioprocess Technology, 4(7): 1164–1171

Kruszelnicka,W.; Chen, Z.; Ambrose, K. (2022) Moisture-Dependent Physical-Mechanical Properties of Maize, Rice, and Soybeans as Related to Handling and Processing. Materials 2022, 15, 8729. https:// doi.org/10.3390/ma15248729

Ince, A., S Ugurluay, E. Guzel, and M. T. Ozcan. 2005. Bending and shearing characteristics of sunflower stalk residue. Biosystems Engineering, 92(2): 175-181.

4th International Engineering Conference (IEC 2022)
Federal University of Technology, Minna, Nigeria

Acid Value Reduction for Jatropha Oil using Wood Ash and Cocoa Pod Ash as Adsorbents

*Ajani, E. A[1], Bala, K. C[2], Lawal, S. A[3], Tsado, J[4]
[1,2,3] Mechanical Engineering Department, Federal University of Technology, PMB 65, Minna, Niger State, Nigeria
[4]Electrical and Electronics Engineering Department, Federal University of Technology, PMB 65, Minna, Niger State, Nigeria
*Corresponding author email: ajaniae@gmail.com +2348034128777

ABSTRACT
Mineral oil, commonly used as transformer oil, is environmentally-benign due to its non-biodegradability. Jatropha oil is a bio-degradable and eco-friendly vegetable oil and a potential alternative to mineral oil, however, like most other vegetable oils, its high acid number is a major drawback. The acid number of the crude jatropha oil used in this research is 35.9 mg KOH g^{-1} oil, which is about 600 times higher than the maximum standard limit of 0.06 mg KOH g^{-1} oil, as specified by the American Society for Testing and Materials, ASTM D 6871 Standard specification for natural (vegetable oil) ester fluids used in electrical apparatus. In this study, adsorption method was used for acid number reduction. Wood ash and cocoa pod ash were used as adsorbents. Cocoa pod ash performed better than wood ash as adsorbent for jatropha oil and was able to reduce the acid number low enough to satisfy the 0.06 mg KOH g^{-1} oil ASTM D 6871 standard specification. An optimum acid number reduction of 99.87 % (from 35.9 to 0.045 mg KOH g^{-1} oil) was achieved at 10 % cocoa pod ash adsorbent concentration, 80°C adsorption temperature and 30 minutes contact time.

Keywords: *acid number, adsorption, eco-friendly, jatropha oil, transformer oil*

1 INTRODUCTION

The negative impact of mineral oil-based transformer oil on the environment, due to its non-biodegradability has led to new researches into the development of eco-friendly alternatives using vegetable oils. While vegetable oils such as Jatropha oil are bio-degradable and environmental-friendly, one of the major drawbacks for the use of vegetable oils as base oil for the production of transformer oil is their high acid number. High acidity of dielectric fluids causes corrosion of ferrous component parts of the transformer, deteriorates the transformer windings (Adekoya and Adejumobi, 2017), leads to increase in the electrical conductivity of the oil-paper insulation system of the transformer (Wang *et al*, 2018) and increases the rate of sludge formation in the transformer oil. Thus, high acidity of oils used as transformer oil has a high potential for increasing the conductivity of the dielectric fluid, decreasing its dielectric strength and reducing its insulation capacity.

Jatropha oil has high potentials as an alternative to mineral oil transformer oil, however, the high free fatty acid content of jatropha oil requires refinement, to reduce its acid number and make it a suitable dielectric fluid. The acid number of jatropha oil, as reported by Abdulmumin *et al.* (2017), is 3.45 mg KOH g^{-1} oil. Evangelista *et al.* (2017) reported an acid number of 11.42 mg KOH g^{-1} oil for jatropha oil obtained from direct solvent extraction and 3.15 mg KOH g^{-1} oil from the one mechanically extracted. Farouk *et al.* (2016) reported an acid number of 8.99 mg KOH g^{-1} oil for crude jatropha oil mechanically extracted from jatropha seeds sourced from the Republic of Sudan and 15.99 mg KOH g^{-1} oil for the jatropha oil sourced from Bionas SDN Bhd Company in Kuala Lumpur. The lowest acid number of 3.15 mg KOH g^{-1} oil for jatropha oil is still about 53 times higher than the 0.06 mg KOH g^{-1} oil maximum limit as prescribed by ASTM D 6871 Standard specification for natural (vegetable oil) ester fluids used in electrical apparatus. Hence, the need to develop methods for efficiently and effectively reducing the acid number of jatropha oil.

In view of this, researchers have deployed several methods for reducing the acid number of vegetable oils to acceptable limits. Satpute *et al.* (2014) used esterification process to reduce the acid number of jatropha oil by 52.4 % from 17.0 to 8.1 mg KOH g^{-1} oil. Azeez *et al.* (2019) used the same process to achieve a 74.6 % acid number reduction from 4.56 to 1.16 mg KOH g^{-1} oil. Wu and Zhang (2020) deployed a six-step process for refining crude jatropha oil and reported a 99.87 % acid number reduction from 9.342 to 0.012 mg KOH g^{-1} oil. The six-step refining process included cold treatment, alkali (KOH) treatment, water washing (degumming), high temperature decompression, adsorption with activated clay and aluminium oxide (Al_2O_3). Evangelista *et al.* (2017) used three refining processes to achieve 99.4% acid number reduction from 6.8 to 0.04 mg KOH g^{-1} oil. Degumming the crude jatropha oil with 0.4 g of phosphoric acid per 100 g of oil, at 70°C reduced the acid number from 6.8 to 5.8 mg KOH g^{-1} oil. Treating the degummed jatropha oil with NaOH-water solution (2.0 g/g solid) at a concentration of (0.5 g/g oil) reduced the acid number from 5.8 to 0.5 mg KOH g^{-1} oil. Adsorption with a combination of activated carbon (5 % w/w oil) and MgO (1 % w/w oil) further reduced the acid number from 0.5 to 0.04 mg KOH g^{-1} oil,

which satisfies the ASTM D6871 maximum standard limit of 0.06 mg KOH g^{-1} oil.

Agricultural wastes such as wood shavings, sawdust, cocoa pod and coffee husk can be converted to useful adsorbents for the reduction of the acid number of vegetable oils. Chairgulprasert and Madlah (2018) reported a 100 % free fatty acid reduction from waste palm oil using adsorption method with a 10 % concentration of coffee husk ash as adsorbent, at an adsorption temperature of 30°C. Nuru and Getachew (2021) reported a 59.6 % acid number reduction from 8.31 to 3.36 mg KOH g^{-1} oil for waste Niger seed oil, used for deep frying of potatoes, treated with wood ash adsorbent. The aim of the current study, therefore, is to investigate the efficiency of acid number reduction for jatropha oil using wood ash and cocoa pod ash as adsorbents.

2 METHODOLOGY

2.1 MATERIALS

Crude jatropha oil used in this research was procured from AgriEnergy Nigeria Limited, Kano. The dried cocoa pods were sourced from Moses Jegede Farm, Akoko North West Local Government Area of Ondo State. Wood shavings and sawdust of Melina wood (*Gmelina arborea*) used for producing the wood ash was sourced from the lumberyard, popularly referred to as "Timber Shed" in Maitumbi, Minna, Niger State. The chemicals and reagent used in this research, including Absolute ethanol (C_2H_5OH, 99.5 % w/w, General Purpose Reagent, JHD Guangdong, Guanghua Sci-Tech Company Limited, Guangdong, China), Sodium hydroxide (Analytical Grade Reagent, JHD Guangdong, Guanghua Sci-Tech Company Limited, Guangdong, China), Phenolphthalein indicator (Kermel, China), and Hydrochloric acid (0.5 M, Analytical Grade Reagent, Atomic Scientific, Audcnshaw, Manchester) were sourced from the Centre for Genetic Engineering and Biotechnology Laboratory, Bosso Campus, Federal University of Technology, Minna, Niger State.

2.2 ADSORBENT PREPARATION

Wood ash and cocoa pod ash were used as adsorbents. Dried cocoa pods were crushed using a porcelain mortar and pestle. The pre-ashing process was carried out by placing a known weight of the crushed cocoa pods in a porcelain plate. The porcelain plate was placed on a hot plate, set at 200°C, inside a fume cupboard, until all the cocoa pod was charred and there was no more visible smoke. The weight of the charred cocoa pod was noted. The final ashing process was carried out by placing a known weight of the charred cocoa pod in a 500 ml crucible. The crucible was placed in a muffle furnace with the temperature set to 600°C for 3 hours until the black colour of the charred cocoa pod turned to whitish ash. The cocoa pod ash was stored in a desiccator to prevent it from absorbing moisture from the air. Similar process was carried out on the Melina wood sawdust to obtain the wood ash.

2.3 CHARACTERISATION OF THE CRUDE JATROPHA CURSUS OIL

The crude jatropha oil was stored in a dark laboratory shelf, away from sunlight to avoid oxidation. The oil was characterised to determine its electrical property (dielectric breakdown voltage), physical properties (viscosity, pour point, relative density, flash point and fire point) and chemical property (acid number).

The dielectric breakdown voltage (BDV) test was carried out based on the American Society for Testing and Materials ASTM D 1816 standard method for breakdown voltage for dielectric insulating liquids using a transformer oil breakdown voltage tester (KVTester Electronics Technology Company, ZC-210B), with Verband Deutscher Elektrotechniker (VDE) electrodes. The viscosity of the crude jatropha oil was determined based on the ASTM D 445 - 06 standard test method for kinematic viscosity of transparent and opaque liquids, using an Ostwald viscometer. The pour point of the jatropha oil was determine using the ASTM D 97 - 12 standard test method for pour point of petroleum products. The relative density was determined using a dry and clean 25 ml pycnometer. The flash point and fire point were determined using the ASTM D 92 – 05a standard test method for flash and fire points by cleveland open cup tester. The acid number of the crude jatropha oil was determined using the Association of Official Analytical Chemists AOAC 2000 standard methods for determining acid number of oils.

2.4 ADSORPTION EXPERIMENTS

Adsorption process was used to reduce the free fatty acid content of the crude jatropha oil, and in turn, the acid number of the oil. The adsorption experiments were carried out in two stages. The first set of adsorption experiments were conducted using the two different adsorbents (wood ash and cocoa pod ash) on the crude jatropha oil at two different temperatures: 30°C (ambient temperature at the time of the experiment) and 90°C. Each of the adsorbents was applied to the jatropha oil in two different concentrations: 1 % and 10 %. The three different contact times of the adsorbents in the oil used were 10, 30 and 60 minutes. The Design of Experiment for this study was based on One Variable at a Time (OVAT) method, as presented in Table 1. Twelve (12) experimental runs were conducted for each of the two (2) adsorbents, giving a total of twenty-four experimental runs for the first stage of adsorption experiments.

TABLE 1: DESIGN OF EXPERIMENT FOR FIRST SET OF ADSORPTION EXPERIMENT

Experimental Run No.	Concentration (%)	Contact time (mins)	Temperature (°C)	Response - Acid Number (mgKOH/g)
1	1	10	30	
2	1	30	30	
3	1	60	30	
4	1	10	90	
5	1	30	90	
6	1	60	90	
7	10	10	30	
8	10	30	30	
9	10	60	30	
10	10	10	90	
11	10	30	90	
12	10	60	90	

A known weight of the wood ash (2 g) was measured into an aluminium foil. 20 g of jatropha oil was weighed into a 50 ml beaker. The beaker was placed on a magnetic stirrer set at a temperature of 90°C and 1,200 rpm. A digital thermometer was clamped in position to touch the oil without making contact with the bottom of the beaker. The temperature of the oil was observed until a constant temperature of 90°C was attained. The weighed wood ash adsorbent was gently added into the oil and allowed to stir for 10 minutes. The beaker was removed from the magnetic stirrer and centrifuged at 5,000 rpm for 10 minutes to separate the treated oil from the adsorbent. The supernatant oil was decanted and the acid number of the treated jatropha oils was determined using the AOAC 2000 standard test method. This process was repeated for all the other 11 experimental runs. The entire process was repeated using cocoa pod ash as adsorbent.

The second set of adsorption experiments were conducted using only the cocoa pod ash adsorbent. The adsorbent concentration and contact time were kept constant at 10 % and 30 minutes respectively. The adsorption temperature was however varied in seven (7) steps: 30, 40, 50, 60, 70, 80, and 90°C. The adsorption experiments consisting of seven (7) experimental runs, as presented in Table 2, were conducted similar to the process described for the first set of adsorption experiments.

TABLE 2: DESIGN OF EXPERIMENT FOR SECOND SET OF ADSORPTION EXPERIMENT

Experimental Run No.	Concentration (%)	Contact time (mins)	Temperature (°C)	Response - Acid Number (mgKOH g^{-1})
1	10	30	30	
2	10	30	40	
3	10	30	50	
4	10	30	60	
5	10	30	70	
6	10	30	80	
7	10	30	90	

3 RESULTS

3.1 CHARACTERISATION OF THE CRUDE JATROPHA OIL

The result of the electrical, chemical and physical characterisation of the crude jatropha curcus oil is as presented in Table 3. The oil parameters were compared with the ASTM D6871 - 17 standard specification for natural (vegetable oil) ester fluids used in electrical apparatus. An acid value of 35.9 mg KOH g^{-1} oil was recorded for the crude jatropha oil, which is about 600 times higher than the maximum standard limit of 0.06 mg KOH g^{-1} oil.

TABLE 3: PROPERTIES OF CRUDE JATROPHA OIL AS COMPARED WITH ASTM D6871 STANDARDS

S/N	Transformer oil parameters	ASTM D6871 Standards	Crude Jatropha oil
1.	Dielectric breakdown voltage (kV), min.	35	31.8
2.	Pour point (°C), max.	–10	–3.5
3.	Viscosity at 27°C (cst), max.	50	16.9*
4.	Specific gravity at 20 °C, max.	0.96	0.88*
5.	Flash point (°C), min.	275	265
6.	Fire point (°C), min.	300	291
7.	Acid number (mg KOH g^{-1} oil), max.	0.06	35.9

** Values satisfies ASTM D6871 standard specification*

3.2 FIRST SET OF ADSORPTION WITH WOOD ASH AND COCOA POD ASH

The result of the acid number tests for the twelve experimental runs for the jatropha oil adsorption with wood ash adsorbent for the first set of adsorption experiments is as presented in Figure 1. The optimum reduction in acid number of the jatropha oil from 35.9 to 4.087 mg KOH g^{-1} oil (88.6 % reduction), was achieved at two points: at 10 % wood ash adsorbent concentration, adsorption temperatures 30 and 90°C and contact times of 30 and 60 minutes.

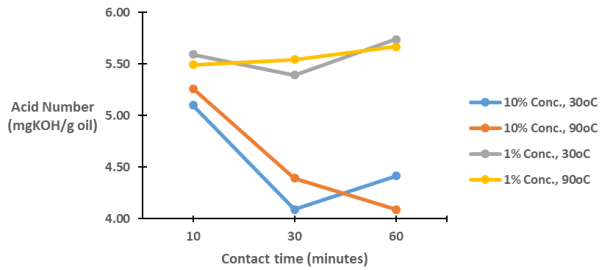

Figure 1: Jatropha oil adsorption with wood ash adsorbent

The result of the acid number tests for the twelve experimental runs for the jatropha oil adsorption with cocoa pod ash adsorbent for the first set of adsorption

experiments is as presented in Figure 2. The optimum reduction in the acid number of the jatropha oil from 35.9 to 0.093 mg KOH g^{-1} oil (99.7 % reduction), was achieved at 10 % cocoa pod ash adsorbent concentration, 90°C adsorption temperature and 30 minutes contact time. The 99.7 % acid number reduction, though very high, did not bring the acid number low enough to satisfy the ASTM D6871 maximum standard limit of 0.06 mg KOH g^{-1} oil.

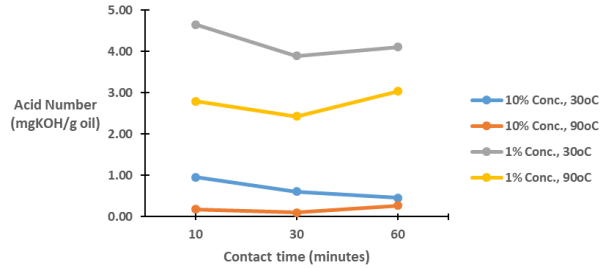

Figure 2: Jatropha oil adsorption with cocoa pod ash adsorbent

3.3 SECOND SET OF ADSORPTION EXPERIMENTS WITH COCOA POD ASH

The result of the acid number tests for the seven experimental runs for the second set of jatropha oil adsorption experiments with cocoa pod ash adsorbent is as presented in Figure 3. The optimum acid number reduction of the jatropha oil from 35.9 to 0.045 mg KOH g^{-1} oil (99.87 % reduction), was achieved at 10 % cocoa pod ash adsorbent concentration, 80°C adsorption temperature and 30 minutes contact time. The 0.045 mg KOH g^{-1} oil acid number falls within the ASTM D6871 maximum standard limit of 0.06 mg KOH g^{-1} oil. A second acceptable acid number value of 0.055 mg KOH g^{-1} oil for the treated jatropha oil was achieved at a lower adsorption temperature of 50°C.

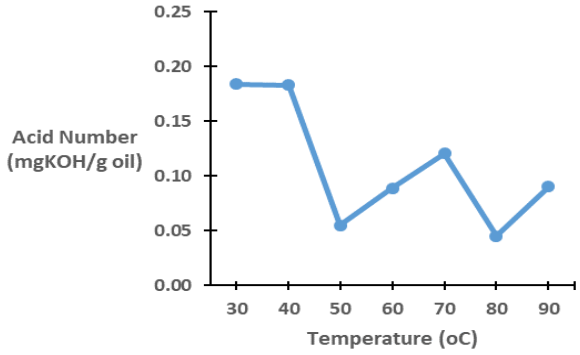

Figure 3: Second set of jatropha oil adsorption with cocoa pod ash adsorbent

4 CONCLUSION

An optimum acid number reduction of 99.87 % (from 35.9 to 0.045 mg KOH g^{-1} oil) was achieved for jatropha oil through adsorption method, using 10 % cocoa pod ash, adsorbent, at 80°C adsorption temperature and 30 minutes contact time. For acid value reduction for jatropha cursus oil, cocoa pad ash performed better than wood ash as an adsorbent and was able to reduce the acid number low enough to satisfy the 0.06 mg KOH g^{-1} oil standard specification for natural (vegetable oil) ester fluids used in electrical apparatus, as prescribed by ASTM D6871 – 17.

RECOMMENDATION

The study of the effect of the adsorption processes on other transformer oil parameters, such as dielectric strength, pour point, viscosity, specific gravity, fire point and flash point is recommended for further research.

ACKNOWLEDGEMENTS

The authors wish to acknowledge the contribution of Mr. Isaac Okorie and other staff of the Centre for Genetic Engineering and Biotechnology Laboratory, Bosso Campus, Federal University of Technology, Minna, Niger State, for their permission to use their laboratory space, equipment and materials for this research.

REFERENCES

Abdulmumin, S., Nana, B. I., Izom, I. I., Mamuda, A., Muhammad, A. & Abbas, A. M. (2017). Determination of Physicochemical Properties of Electric Transformer Oil Extracted from Selected Plant Seeds in Nigeria. *International Research Journal of Engineering and Technology (IRJET)*, 4(9), 760-767.

Adekoya, D. O. & Adejumobi, I. A. (2017). Analysis of acidic properties of distribution transformer oil insulation: A case study of Jericho (Nigeria) distribution network. *Nigerian Journal of Technology*, *36*(2), 563 – 570.

Azeez, A., Fasakin, A. & Orege, J. (2019) Production, Characterisation and Fatty Acid Composition of Jatropha curcas Biodiesel as a Viable Alternative to Conventional Diesel Fuel in Nigeria. *Green and Sustainable Chemistry*, 9, 1-10. doi: 10.4236/gsc.2019.91001.

Chairgulprasert, V. & Madlah, P. (2018). Removal of Free Fatty Acid from Used Palm Oil by Coffee Husk Ash. *Science & Technology Asia*, 23(3), 1 – 9. doi: 10.14456/scitechasia.2018.18

Evangelista, J. M. G., Coelho, F. E. B., Carvalho, J. A. O., Araújo, E. M. R., Miranda, T. L. S. & Salum, A. (2017). Development of a New Bio-Based Insulating Fluid from Jatropha curcas oil for Power Transformers. *Advances in Chemical Engineering and Science*, 7(2), 235-255.

Farouk, H., Prakoso, T., Jafar, M.N.M., Salih, S.M. (2016). Biodiesel Production from Crude Jatropha Oil (CJO) in Pilot Plant. *4th International Graduate Conference on Engineering, Science and Humanities*,

at: Universiti Teknologi Malaysia, Johor Bahru, Malaysia.

Nuru, Z. & Getachew, P. (2021). Improving the quality of used frying niger seed oil with adsorbent treatment, *Heliyon*,7(4),1-8. doi.org/10.1016/j.heliyon.2021.e06748

Satpute, S. R., Bhole, R. & Chavan, P. V. (2014). Acid Value Reduction of Jatropha Oil for High Quality Biodiesel, International Journal of Scientific and Engineering Research, 3(3), 228-232.

Wang, X., Tang, C., Huang, B., Hao, J. & Chen, G. (2018). Review of Research Progress on the Electrical Properties and Modification of Mineral Insulating Oils Used in Power Transformers. *Energies*, 11(487), 1-31.

Wu, J. & Zhang, J. (2020). Research and Development of Natural Vegetable Insulating Oil Based on Jatropha curcas Seed Oil. *Energies*, 13(17), 1-9. doi.org/10.3390/en13174319

4th International Engineering Conference (IEC 2023)
Federal University of Technology, Minna, Nigeria

Investigation Into the Tribological Properties of Shea Nut Shell Particles Reinforced Epoxy Composites

*Abdullahi, M.[1], Zubairu, P. T.[1], Gana, A[1], & Jabo, U[2]
[1] Department of Mechanical Engineering, Federal Polytechnic, PMB 55 Bida Niger State, Nigeria
[2]Estate and Municipal Services Department, Usman Danfodio University Sokoto, Sokoto State, Nigeria
*Corresponding author email:mohammedabdullahi047@gmail.com +2348035044103

ABSTRACT
Tribology is vital to modern machinery that involves sliding and rolling of surfaces. Epoxy resin has been widely used as binder in composite industry, due to its excellent adhesion to many reinforcements. Agricultural waste materials have been used as fillers/reinforcements for polymer matrices to obtain composites that exhibits a desirable tribological properties which would become an alternative material to the traditional fillers. In this study, tribological properties of shea nut shell particles (SNSP) reinforced epoxy composites have been investigated. Four different samples were produced by varying mass compositions of the SNSP. Sample A1 serve as clear epoxy (0 wt.% SNSP). Sample A4 has higher mass of SNSP (60 wt.%) and lower mass of epoxy resin (40 wt.%) while Sample A2 has lower mass of SNSP (40 wt.%) and higher mass of epoxy resin (60 wt.%). A mild steel mould was fabricated for compacting the formed composite. The characterization of the produced samples was investigated through Tribological studies, scanning electron microscope (SEM), surface morphology studies after wear rate, thermographic analysis (TGA/DTA) and laboratory test. The tribological study reveals uniform distribution coefficient of friction and wear rate. Highest coefficient of friction value of $\mu = 0.29$ at the sliding speed of 29.45 m was recorded by sample A4. Incorporation of high amounts of fine particle of shea nut shell (60 wt.%) into epoxy resin allows to prepare low-cost composites with acceptable tribological and thermo-mechanical properties that makes them applicable as materials for low-demanding parts and applications. Also, from the laboratory test results, shea nut shell particles can be effectively used to develop automobile brake pad with the addition of friction modifiers and abrasives.

Keywords: *Coefficient of friction: Composites: Epoxy resin: Shea nut shell particles: Wear rate.*

1 INTRODUCTION

The investigation of eco-friendly matrices for appliances and products is one of the most effective paths to accomplish the goal of sustainability (Ibrahim *et al*., 2020). Recently, both researchers and manufacturers are attempting to widespread the usage of renewable resources (such as agricultural waste e.g. natural fibers; industrial waste e.g., fly ash, red mud RM or postconsumer e.g., polymer bags, clothes) in a wide range of applications and processes to further replace the synthetic fibers with natural based fillers tuned polymer hybrids for different applications, particularly automotive applications owing to their lower cost and high strength to weight ratio (Clemons, 2008). The properly prepared waste material may be used as a filler or reinforcement for metal or polymer-based composites aimed at use in various applications, e.g., as tribological materials directly related to the wear processes due to friction (Sydow *et al*., 2021). Increased attention has been paid by researchers to the use of waste materials as fillers/reinforcements for metal or polymer matrices to obtain composites that exhibit desirable tribological properties which would become an alternative material to the traditionally used fillers (Sydow *et al*., 2021). The clear advantage of waste for composites fabrication compared to petroleum-based carbon filler are a transformation of waste into raw materials; improved mechanical and tribological properties, economic benefits, sustainability, biodegradability, and low environmental impact (Shivamurthy *et al.*, 2014). The epoxy-based composites have become potential candidates for application in different technological fields due to their excellent physical, chemical, and electrical performances. However, several researchers have reported a variety of reinforcement to explore mechanical, electrical, and tribological performances to predict their behaviour suitable for the technological viability of epoxy-based composites (Moharana *et al*., 2022). According to the literature, it has been reported that tribological characteristics of fiber-reinforced epoxy composites have shown improved resistance to friction and wear characteristics (Parameswaranpillai *et al*., 2022). Prabhu *et al.*, 2017 reported that frictional force increases as the load increases. As the percentage of reinforcement of coconut shell powder in the epoxy increases, the frictional force also increases this is because of the resistance offered by the coconut shell powder to the wear. The results of TGA and DTA analysis presented by Andezai *et al.*, 2020 showed that the pyrolysis of hemicellulose and cellulose was a maximum at 290˚C and 315˚C, respectively, while the signature for the pyrolysis

of lignin could be distinguished. Ganthia *et al*., 2022 investigated the tribological behaviour of Coconut shell–fly ash–epoxy hybrid composites and found out that their material could be used in short frictional applications. The aim of this research is therefore to investigate the tribological properties of shea nut shell particle-reinforced epoxy composites and to ascertain their applicability in various areas of engineering involving friction and wear.

2 MATERIALS EQUIPMENT METHODOLOGY

2.1 MATERIALS

The materials used in this study include Epoxy resin LY556 and hardener HY 951 supplied by Dongguan Haoyida Chemical Co. Ltd Guangzhou, China, Shea nut shell collected from shea nut processing center of the federal polytechnic Bid, candle wax, to increase the rate of curing, bonding strength and improve the surface finishing of the developed composites. The properties of the epoxy resin and hardener used are presented in Table 2.1.

TABLE 2.1: PROPERTIES OF EPOXY RESIN LY556 AND HARDENER HY951

Properties	Resin (LY556)	Hardener (HY951)
Appearance	Clear, colourles liquid	Brownish yellow liquid
Viscosity @25 °C (MPa)	9000-12000	500-1000
Density (g/cc)	1.13-1.16	0.946

2.2 EQUIPMENT

Some of the equipment used includes a Wooden mould, plastic cups, Vanier calliper, digital weighing machine (AR 1530, Adventurer OHAUS Corporation), Scanning electron microscope (JOEL JSM 6480 LV), EDXRF Machine (Model: Minipal 4 No. DY 1055 by PANalytical B.V.), Denver Cone Crusher, Standard tribometer/version 6.1.19 (ball-on-disc), Thermo gravimetric analyzer (Model TGA Q50), Laboratory test rig, Denver Roll Crusher, Grinding Mill (Made 4, Arthur H. Thomas Company, USA), and set of sieves.

2.3 METHODS

2.3.1 Fabrication of the composites

The collected shea nut shell was soaked in distilled water, washed with detergent to remove dirt and other contaminants, and sun-dried followed by an oven at 105 °C for five hours until the moisture is ensured to have greatly reduced toward zero presence. This was then charged into a Denver cone crusher to reduce its size to between 4mm to 3mm. It was further charged into a roll crusher that reduces the size of the shea butter shell to between 2-1mm. the product roll crusher was transferred into a ball milling machine and was left in the mill for two hours: after which the product was transferred into a set of sieves of +710 µm, + 500 µm, +355 µm +250 µm, +125 µm, and was sieved for 30 minutes using sieve shaker machine for 30 minutes. While the oversize at +710 µm was returned or recycled for regrinding until it passes through the sieves. Pre-determined quality of the sieved shea nut shell particles and epoxy resin were taken in a plastic container and stirred thoroughly to get a homogeneous mixture. After adding 10 % of hardener and 5 % of melamine, the mixture was stirred for 10 minutes and the mixture was poured into (180 × 140 × 10) mm mould, and allowed to cure for 24 hours at room temperature. After curing, the composites board were taken out from the mould and sun-dried for 3 hours. The composites were prepared with different volume fractions of shea nut shells as presented in Table 2.2. This was carried out according to the method of Manjunatha and Sabeel, 2017. Test samples were prepared from the composite boards using a pointed cutter.

TABLE 2.2: DESIGNATION AND VOLUME FRACTION OF THE COMPOSITES

Sample/ designation	Volume fraction of SNSP (%)	Volume fraction of Epoxy (%)
*A*1	0	100
*A*2	40	60
*A*3	50	50
*A*4	60	40

2.3.2 Tribological studies

A standard tribometer/version 6.1.19 (ball-on-disc) apparatus shown in Figure 1 was employed to conduct the tribological tests. Hardened steel (65 HRC) counter disc of 10 mm track diameter and 8 mm thick was used. Specimens of 14 mm diameter and 10 mm height

were prepared and the ball surface was polished with emery paper. The tests were conducted at 29 °C room temperature and 55 % relative humidity for 30 minutes. The variation of friction coefficient with time was continuously recorded during the tests. The tribological test parameters are summarized in Table 2.3.

Figure 1: Ball-on-disc Tribometer

TABLE 2.3: TRIBOLOGICAL PARAMETERS OF THE TEST SAMPLE

Parameter	Unit	Value
Normal load	N	90
Speed	Rpm	0.95
Acquisition rate	Hz	10
Abrasion time	Sec	1800
Disc diameter	m	0.005

Wear rate was determined using equations 1-2.

$$Wear\ rate = \frac{\Delta W}{L} \quad 1$$

$$L = 2\pi Ndt \quad 2$$

Where N is the machine speed (rpm), d is the disc diameter (m), t is the time of each sample to undergo abrasion (s), W_1 is the weight of sample before abrasion, W_2 is the weight of sample after abrasion.

2.3.3 Morphological Properties

A scanning electron microscope of Model JEOL JSM-6480LV was used to study the morphological properties of the composite surface. The samples are cleaned thoroughly, air-dried, and coated with 100 Å thick platinum in JEOL sputter ion coater and observed SEM at 20 kV. To enhance the conductivity of the composite samples a thin film of platinum is vacuum evaporated onto them. The worn microstructure of composites has been studied to reveal the effect of maximum testing conditions on the dry sliding wear of composites

2.3.4 Thermal analysis

Thermal decomposition was observed in terms of global mass loss by using a thermogravimetric analyzer Model TGA Q50. The apparatus detects the mass loss with a resolution of 0.1 as a function of temperature. The samples were evenly and loosely distributed in an open sample pan of 6.4 mm diameter and 3.2 mm deep with an initial sample weight of 8-10 mg. The temperature change was controlled from room temperature (25±3°C) to 900°C with a heating rate of 10 °C/min. High purity argon was continuously passed into the furnace at a flow rate of 60 mL/min at room temperature and atmospheric pressure. Before the starting of each run, the argon was used to purge the furnace for 30 min to establish an inert environment to prevent any unwanted oxidative decomposition. The TG and DTA curves were obtained from TGA runs using Microsoft software (Amaren, 2016).

2.3.5 Laboratory test

A laboratory test was carried out using a laboratory test rig by applying the brake at speeds of 100, 149, 225, and 250 rpm respectively until the system come to rest while the applied stopping pressure was recorded. The variation of speed with stopping pressure for the developed composites was determined.

3 RESULTS AND DISCUSSION

The results obtained after successfully conducting the tests are presented.

3.1 CHARACTERIZATION

3.1.1 Tribological studies

Figure 3.1 show the variations of the friction coefficients with a sliding distance of the developed composites. It can be seen from the figure that all the developed composite samples went through an initial increase in coefficient and became stable as the sliding distance increased. Samples A1, A2, A3, and A4 recorded an initial increase in coefficient friction at sliding distances of 0.20 at 1.11m, 0.19 at 1.02m, 0.07 at 2.93m,

and 0.06 at 4.91m respectively. Based on the comparison, sample A4 recorded the highest coefficient of friction value of μ = 0.29 at the sliding speed of 29.45 m. This may be due to the absence of reinforcement. Alotaibi *et al.*, 2021 recorded a similar slight decrease in friction coefficients with increased sliding distance before reaching a steady state.

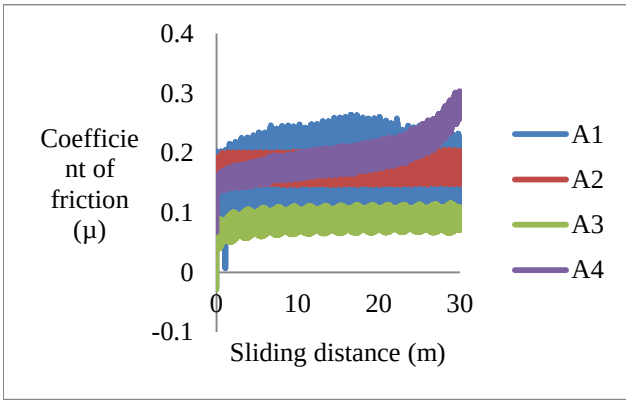

Figure 3.1: Variation of friction coefficient with sliding distance of the samples

Figure 3.2 shows the specific wear rates of test samples. The wear rates were calculated according to Equation 3.1. The increased addition of SNSP resulted in a decrease in the wear rate of the samples with the pure epoxy recording the highest wear rate of 0.93 mg/m while the sample with high SNSP reinforcement (A4) recorded the lowest wear rate of 0.19 mg/m. Algbory, 2011 also reported in his study that the wear rate of the composite specimen decreases with the increase in weight fraction.

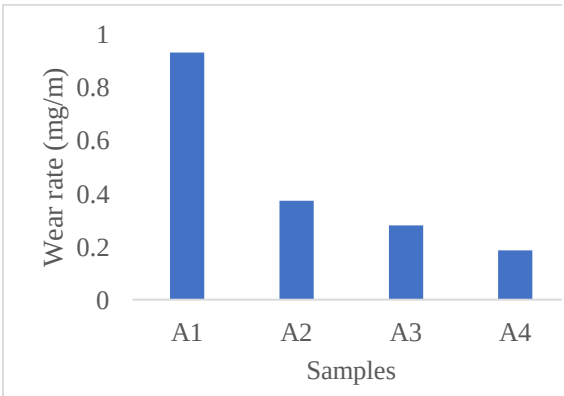

Figure 3.2: Variation of wear rate of the SNSP composite samples

3.1.2 Scanning electron microscopy (SEM)

Figures 3.3a-c show SEM images of the developed composites. The resin binder can be seen in the dark region on the images along with particle distribution in the white region. From the SEM study, it can be postulated in general that microstructures of SNSP-based composite samples showed homogeneous distribution. There are micro-voids on the surface of almost all the samples. It is seen from the Figures that larger micro-voids occurred in the samples due to detaching metallic particles. As seen, some particles are detached from the body causing micro-voids. The micro-voids on the surface of the samples can be classified as smaller and bigger. The bigger-sized micro-voids are due to the pitting of the metallic particles. In addition to micro-voids, there are some micro cracks on the surface. This finding agrees with the findings of Yawas *et al.*, 2016; Ramesh *et al.* 2014; Ahmet, 2011.

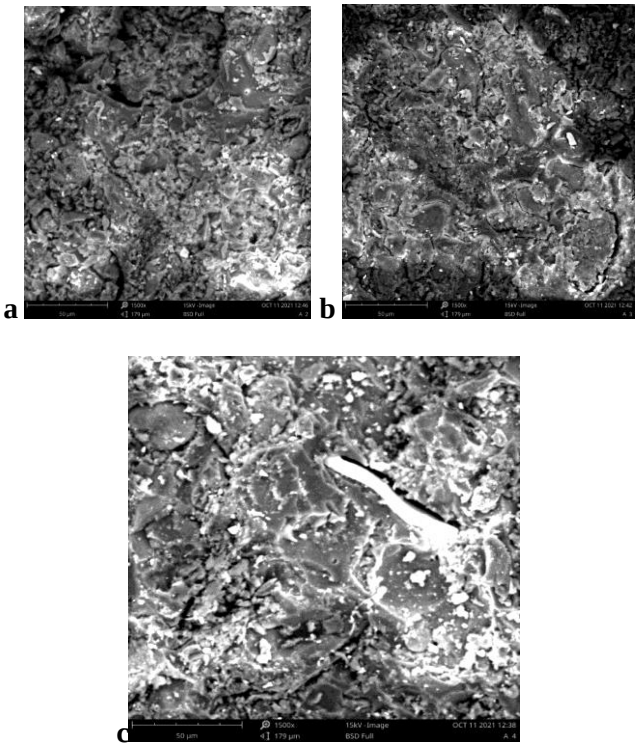

Figure 3.3: SEM Images of the developed brake pad materials for: (a) sample A2; (b) sample A2; (c) sample A3

3.1.3 Surface morphology

The fracture surfaces study of SNSP-reinforced epoxy composite after the wear rate test was presented in Figure 3.4. Figure 3.3a shows a sample with 100% epoxy resin. It is observed from the figure that the surface looks very smooth and has lesser void content as shown on the upper surface of the composite sample. On the addition of 40 wt.% of SNSP reinforcement the fractured surface of composite shows the breaking of matrix material under initial loading conditions (Fig. 3.4b). The surfaces of the

developed epoxy reinforced SNSP composites show a typical abrasive wear mode in which debris, scratches, and shallow and deep grooves are formed along the wear direction. Nassar *et al*., 2022 reported that a small amount of SiC up to 6 wt.% in the upper surface of their samples was subjected to a severe abrasive wear mechanism due to the appearance of large cracks and deep grooves

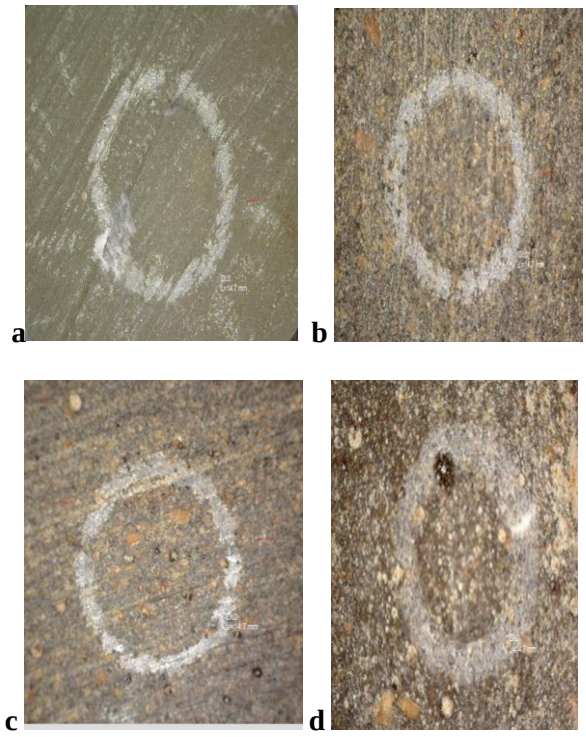

Figure 3.4: Fracture surfaces study of the developed composites after wear rate test for: (a) sample with 100% epoxy (A1); (b) sample with 60% epoxy (A2); (c) sample with 50% epoxy (A3) and (d) sample with 40% epoxy

3.1.4 Thermal analysis

Figures 3.5a-b shows the combined TGA and DTA curves obtained from the runs. The data from both curves were extracted and presented in Table 3.1. $D_{0.1}$ indicates the temperature at which the 10% of decomposition occurs, while $D_{1/2}$ indicates the temperature at which half of decomposition occurs and MRDT is the maximum rate of decomposition (MRD) temperature (Tiwari *et al.* 2004). It can be seen that all the curves have a similar appearance and decomposition patterns. It can be seen from Figure 3.4a, that all the samples start to lose weight earlier. This may be attributed to the higher moisture content, the presence of hemicelluloses has caused higher moisture absorption of the composite (Methacanon *et al.*, 2010). Evaporation of the moisture starts from the sample A1 at 88.91 ºC. The percentage of weight reduction at 500°C reflects the amount of residues left after the composites were degraded. Epoxy has the lowest residue due to the absence of char. Residue obtained after the complete decomposition of sample A2 to 900 °C was found to be 5.0 wt.%, this may be probably due to the formation of ceramic type of structure, while the residue in samples A1, A3 and A4 were 12.0, 18.50 and 18.60 wt.% respectively, which may be attributed to the formation of silica in form of SiO_2. All the developed materials exhibited almost the same initial mass loss with the first initial mass loss occurring between 88.74 °C to 310°C, and the second mass loss is between 310°C to 480°C.

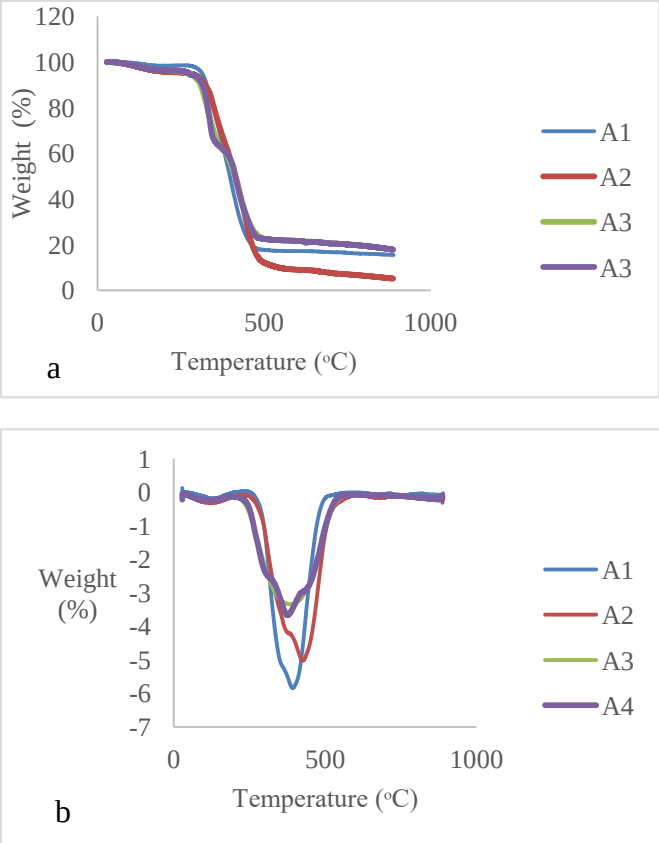

Figure 3.5 Combined TGA (a)/DTG (b) pattern of SNSP composites samples.

TABLE 3.1: DEGRADATION PARAMETERS FROM THE TGA PLOT

Samples	A1	A2	A3	A4
D_{01} Temperature (˚C)	88.74	88.76	88.74	88.74
$D_{1/2}$(˚C)	195.00	210.00	192.50	192.50
MRDT (˚C)	390.00	420.00	385.00	385.00

3.1.5 Laboratory test

Figure 3.6-3.8 shows plot of results of the laboratory test. Figure 3.6 presented the variation of

stopping pressure with speed of the developed composites. The results show that for the same speed, the laboratory developed composites requires less contact pressure to bring the system to a stop. This is because of its higher coefficient of friction. Effect of speed on composites mass loss at constant contact time of 1min is presented in Figure 3.7. The tests show that at a constant line pressure, the mass loss and reduction in thickness of composites increase with the increase in speed. For all the developed samples, initial mass loss begins at 100 rpm stoppage speed. Figure 3.8 shows the effect of disc temperature on speed. The results indicate that as the speed increases, the disc temperature rises due to the conversion of kinetic energy to heat energy as the brake is applied. The disc temperature rise is higher with the developed composites, this may be due to poor heat transfer properties of the developed composites.

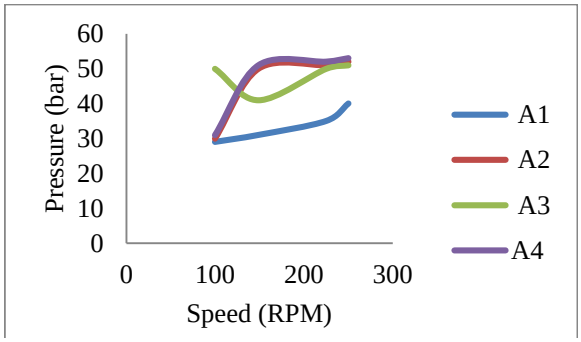

Figure 3.6 Variation of pressure with speed of the developed composites

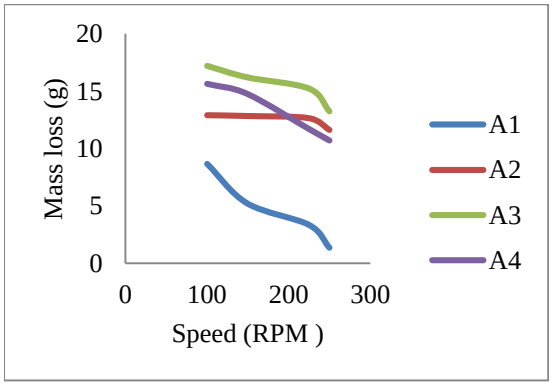

Figure 3.7 Variation of mass loss with speed of the developed composites

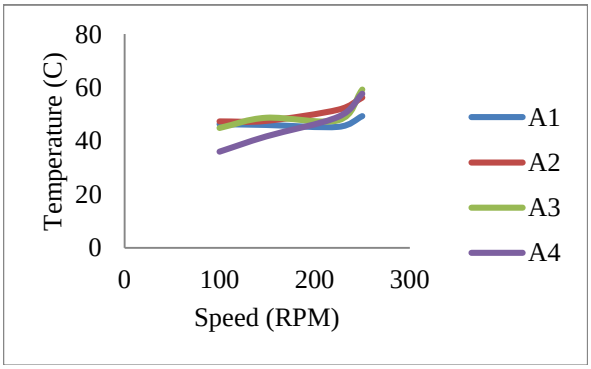

Figure 3.8 Variation of temperature with speed for developed composites

4 CONCLUSION

The tribological properties of the developed SNSP-reinforced epoxy composites have been investigated. The tribological study reveals a uniform distribution coefficient of friction and wear rate. The highest coefficient of friction value of μ = 0.29 at the sliding speed of 29.45 m was recorded by sample A4. All the developed materials exhibited almost the same initial mass loss with the first initial mass loss occurring between 88.74 °C to 310°C, and the second mass loss between 310°C to 480°C. The laboratory test was carried out by applying the brake at speeds of; 100rpm, 149 rpm, 225 rpm, and 250 rpm till the system comes to rest while applied the stopping pressure was recorded. Incorporation of high amounts of a fine particle of shea nut shell (60 wt.%) into epoxy resin allows for to preparation of low-cost composites with acceptable tribological and thermo-mechanical properties that make them applicable as materials for low-demanding parts and applications. Also, from the laboratory test results, shea nut shell particles can be effectively used to develop automobile brake pads with the addition of friction modifiers (graphite and ceramic) and abrasives (aluminium oxides, silica, etc.).

ACKNOWLEDGEMENTS

Authors would like to acknowledge Tertiary Education Trust Fund (TETFund), Nigeria and the Federal Polytechnic, Bida, Nigeria for sponsorship under the 2023 TETFund conference/workshop attendance.

REFERENCE

Ahmet, K. (2011). Investigation of using natural zeolite in brake pad. *Scientific Research and Essays*, *6*(23), 4893-4904.

Algbory, A. M. R. M. (2011). Wear Rate Behaviour of Carbon/Epoxy Composite Materials at Different Working Conditions. *Iraqi journal of mechanical and material engineering*, *11*(3).

Alotaibi, J. G., Eid Alajmi, A., Mehoub, G. A., and Yousif, B. F. (2021). Epoxy and polyester composites' characteristics under tribological loading conditions. *Polymers*, *13*(14), 2230.

Amaren S. G., Aku S. Y. and Yawas D. S. (2016). Effect of Periwinkle Shell Particle Size on Wear Behaviour of Asbestos Free Brake Pad. *Elsevier results in Physics*, 3, 109 – 114

Andezai, A. M., Masu, L. M., and Maringa, M. (2020). Chemical and Morphological Characterization of Coconut Shell Powder, Epoxy Resin and Coconut Shell Powder/Epoxy Resin Composites. *International Journal of Engineering Research and Technology*, 13(12), 4269-4275

Clemons, C. (2008) Raw materials for wood-polymer composites Wood-Polymer Composites ed K Oksman and M Sain (Boca Raton: CRC Press LLC) 1–22

Ganthia, B. P., Mallick, M., Sasmita, S., Utkal, K., & Mohanty, I. (2022). Tribological Behaviour of Coconut Shell-Fly Ash-Epoxy Hybrid Composites: An Investigation. In *Natural Polymers: Perspectives and Applications for a Green Approach*, 225-249. CRC Press.

Ibrahim, M. A., Hirayama, T. and Khalaf, D. (2020). An investigation into the tribological properties of wood flour reinforced polypropylene composites. *Material Research Express*, 7, 015313

Manjunatha chary G. H, and Sabeel Ahmed K. J., (2017). Experimental Characterization of Coconut Shell Particles Reinforced Epoxy Composite. *Environmental Science*. 8 (5), 1661-1667

Methacanon, P., Weerawatsophon, U., Sumransin, N., Prahsarn, C., and Bergado, D. T. (2010). Properties and potential application of the selected natural fibers as limited life geotextiles. *Carbohydrate Polymers*, *82*(4), 1090-1096.

Moharana, S., and Sahu, B. B. (2022). Synthesis and Properties of Epoxy-Based Composites. *Epoxy-Based Composites*, 59.

Nassar, A., Younis, M., Ismail, M., and Nassar, E. (2022). Improved Wear-Resistant Performance of Epoxy Resin Composites Using Ceramic Particles. *Polymers*, *14*(2), 333.

Parameswaranpillai, J., Gopi, J. A., Radoor, S., Dominic, C. M., Krishnasamy, S., Deshmukh, K., ... and Sienkiewicz, N. (2022). Turning waste plant fibers into advanced plant fiber reinforced polymer composites: A comprehensive review. *Composites Part C: Open Access*, 100333.

Prabhu, R., Rahul, M. P., Aeilias, A., Sunny, B., Alok, J., and Bhat, T. (2017). Investigation of tribological property of coconut shell powder filled epoxy glass composites. *American Journal of Materials Science*, *7*(5), 174-84.

Ramesh M. R., Nagesh S. N., Siddaraju C. and Prakash S. V. (2014). International Conference in *Advances in Manufacturing and Materials Engineering AMM*. Procedia Materials Science 5, 295-302.

Shivamurthy, B., Murthy, K., Joseph, P.C., Rishi, K., Bhat, K. U., and Anandhan, S. (2014). Mechanical properties and sliding wear behaviour of jatropha seed cake waste/epoxy composites. *Journal of Materials Cycles and Waste Management*, 17, 144–156

Sydow, Z., Sydow, M., Wojciechowski, Ł., and Bie ´nczak, K. (2021). Tribological Performance of Composites Reinforced with the Agricultural, Industrial and Post-Consumer Wastes: A Review. *Materials*, 14, 1863.

Tiwari A., Nema A. K., Das C. K. and Nema S. K. (2004). Thermal Analysis of Polysiloxanes, Aromatic Polyimide and their Blends Thermochimica Acta 417,133–142.

Yawas, D. S., Aku, S. Y., and Amaren, S. G. (2016). Morphology and properties of periwinkle shell asbestos-free brake pad. *Journal of King Saud University-Engineering Sciences*, *28*(1), 103-109.

4th International Engineering Conference (IEC 2023)
Federal University of Technology, Minna, Nigeria

Identification and Control of Heat Exchanger System

[1]S. H. Sulaiman, [2]K. S. Abubakar, [3]K. I. Dahiru, [4]I. M. Muhammad, & [5]S. A. Salisu
[1]Department of Electrical Engineering, Ahmadu Bello University, Zaria, Kaduna State, Nigeria
[2]Department of Electrical Engineering, School of Technology, Kano State Polytechnic, Kano, Nigeria
[3,4]Department of Computer Engineering, School of Technology, Kano State Polytechnic, Kano, Nigeria
[5]Department of Electrical Engineering, Nigerian Maritime University, Okerenkoko, Delta State, Nigeria

[1]shsulaiman@abu.edu.ng, [2]mksuleabubakar@gmail.com, [3]kabirudahiruibrahim@kanopoly.edu.ng,
[4]elmuazzam@kanopoly.edu.ng, [5]sasyalwa05@yahoo.com

ABSTRACT
Heat exchanger (HE) networks present an interesting control problem due to the existence of coupling between process streams. HE problems require an optimal controller design for better performance. The designed controller should be able to regulate the temperature of the outgoing fluid to a desired set point within a short period irrespective of load and process disturbances as well as equipment saturation and nonlinearity. This paper analyzed and compare the performances optimal PID and adaptive LQR control schemes for the HE. Reference temperatures 50℃ and 15℃ were selected for the hot and cold tanks respectively. The results obtained have indicated that LQR has a better performance and reference tracking than the PID in the control of the HE system.

Keywords: *Heat exchanger, LQR, PID, Process control.*

1 INTRODUCTION

Heat exchangers are devices that are employed for heat transfer between any two media. The media contact may be all fluids, a fluid and a solid surface, or solid particulate and a fluid that are in thermal contact but at differing temperatures (Dulău *et al.*, 2015). Temperature difference is of prime importance in HE systems as their main purpose is to transfer heat from a hot medium to a cooler one. For this purpose, HE is commonly used in chemical processes due to the production or absorption of heat energy usually associated with such processes (Hamze *et al.*, 2018). Varieties of HE systems exist, but their deployment depends on particular application. The main objective however is to maximize heat transfer while keeping cost of energy consumption at the minimum (Padhee, 2015; Oravec *et al.*, 2018). A hydraulic oil cooler for example, will remove heat from hot oil by using cold water or air. Also, a swimming pool HE uses hot water from a boiler or solar heated water circuit to heat the pool water. Process industries that produce light bulbs, dairy products, pharmaceuticals, incubators, etc., consider temperature control as an important factor and use HEs to achieve it. Principle of operation of HE is depicted in Figure 1.

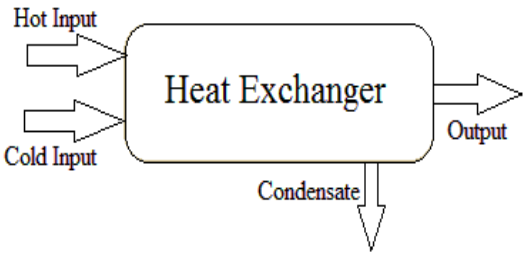

Figure 1: Operation of Heat Exchanger

Heat transfer is achieved in HE systems by conduction through the exchanger materials. There are basically two types of HEs: Shell and tube; and air-cooled type (Padhee, 2015). The former passes fluids through and over its tubes, whereas the latter passes cold air through a core of fins to cool a liquid. Plate type HEs operate in very much the same way as a shell and tube, except that a series of stacked plates is used rather than tubes. Air cooled heat exchangers are used in vehicles or other mobile applications where no provision for cold-water supply is made. Car radiator is a typical example of a HE system. Some industrial applications of HEs include agriculture, chemical and biotechnology industries, automobile industries, etc.

HE systems are highly nonlinear, design of their controller is a challenging task (Hamze *et al.*, 2018). In this work, design control system for the model developed in (Dulău *et al.*, 2015) was adopted to perform identification for HE test bench.

Temperature is the main parameter to be controlled in HEs. Hence, the temperature of the outlet fluid is measured and compared with the predetermined set point to produce the error signal that regulates the control valve. Proportional-Integral-Derivative (PID) control is the most commonly used control algorithm in industry and has been universally accepted in industrial control (Oravec *et al.*, 2018). This is in part due to their simplicity in design and robust performance under various operating conditions.

Cooling and heating are two essential processes in industrial settings and achieving them at the desired level leads to better output. In most industrial applications and processes, the former is often required than the latter (Jama & Syahputra 2016).

Fuzzy Logic based HE control was presented in (Khare & Singh, 2010). Because of non-linearity in the HE system

and the non-instantaneous fluid flow, the PDE model of the HE taken as a first order system with time-delay. Performance of feedforward, feedback and feedforward plus feedback control schemes were compared. The feedforward plus feedback controller exhibited the best output tracking response. However, the method is complex and requires a lot of computational effort in designing the membership function. The author in (Padhee, 2015) compared the conventional PID control and robust control applied on heat exchanger of second order with time delay. The controllers are tuned by Zeigler-Nichols experimental criteria and H-infinity synthesis. The simulation results showed that both controllers track the responses of the heat exchanger in the steady state. However, with PI controller, the responses are oscillatory and have considerable overshoot while the robust controller showed damped responses in time with reduced overshoot. Authors in (Dulău *et al.*, 2015) modeled temperature flow time-delay in HE using the method of moving average. Parameters of the time-delay system were estimated using gradient-decent optimization technique. The first order hyperbolic PDEs representing the HE model were decoupled and reformed into time-delay system. Results obtained were compared with ordinary PDE results in the literature, and system identification and validation were then carried out using the experimental data obtained from a test bench.

(Jamal & Syahputra, 2016) developed a simplified mathematical model for the comparison of performances of conventional PID and Advanced Artificial Neural Network NARMA L2 controllers in a shell and tube HE. The outlet cold water and the inlet hot water temperatures were taken as the controlled variable and manipulated variable respectively, while settling time, rise time, overshoot and steady state error were used as performance metrics. Simulation results indicated the superiority of the NARMA L2 controller over the conventional PID controller. However, performance of a neural network is mainly defined by the amount of training data. Thus, in processes were large volume of data is not available, the approach may be less effective. Reference (Saranya *et al.*, 2017) analyzed the transient performance and error detection capability of three different controllers: the feedback PID; feedback plus feed-forward; and inherent model controller to regulate the temperature of outlet fluid of a shell and tube HE. From the simulation results, the internal model control outperforms the other two controllers.

The authors in (Fatma *et al.*, 2017) studied the most effective controller among Proportional Integral and Derivative (PID), Self-tuning and Fuzzy logic controller. The controllers were applied in heat exchanger system and MATLAB Simulink was used for simulation. Moreover, overshoot, settling time and integral absolute error were the three criteria that had been considered to measure the effectiveness of the applied controllers. From the result obtained, PID controller has the fastest settling time compared to the Self-tuning and Fuzzy logic controller. However, it has the highest overshoot and integral absolute error. In (Hamze *et al.*, 2018), various control techniques were employed to study the dynamic behavior of HEs experimentally, and the values of the outlet cold water temperature used for regulating the hot water flow rate were simulated in MATLAB. Performances of PI and PID controllers for a noise free process with no delay were evaluated and the former was observed to have better control for the process than the latter. However, PID controller performs better when delay and noise were incorporated in the process.

2 METHODOLOGY

This section provides the methodology followed in carrying out the research in this paper.

2.1 MATHEMATICAL MODEL OF THE HE SYSTEM

In order to deal with distributed nature of heat exchanger process, it is represented by coupled first order hyperbolic differential equations given by (1) and (2).

$$\frac{\partial T^H}{\partial t}(x,t) + C_1 \frac{\partial T^H}{\partial x}(x,t) = d_1(T^H(x,t) - T^C) \quad (1)$$

$$\frac{\partial T^C}{\partial t}(x,t) + C_2 \frac{\partial T^C}{\partial x}(x,t) = d_2(T^H(x,t) - T^C) \quad (2)$$

C_1 and C_2 are characteristic parameters of the system, while d_1 and d_2 are the coupling parameters of the process.

The heat exchanger is a counter flow as shown in the Figure 1.

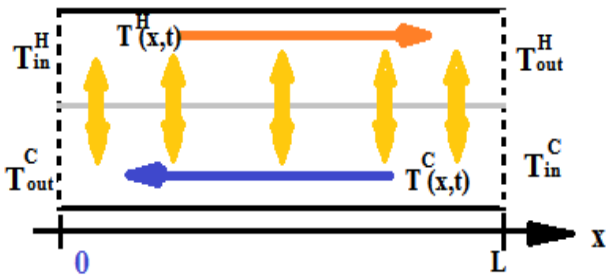

Figure 1: Output response of Pole Placement Controller

The boundary conditions of the system follow (3) and (4):

$$T^H(0,t) = U_1(t) \quad (3)$$

$$T^C(L,t) = U_2(t) \quad (4)$$

The system hot and cold outputs are respectively given by (5) and (6).

$$T^H(L,t) = y_1(L,t) \quad (5)$$

$$T^C(0,t) = y_2(t) \quad (6)$$

Equations (7) and (8) represent the initial conditions of the system.

$$T^H(x,0) = T_0^H(x) \quad (7)$$

$$T^C(x,0) = T_0^C(x) \quad (8)$$

2.1.1 State Space Representation of The System

The HE tube is divided into discretization steps to obtain state space equations of the system. Forward and backward Euler methods were respectively used for the hot flow and the cold flow of the working fluid as given in (9) and (10) respectively.

$$\partial_x T_j^H = \frac{T_{j+1}^H - T_j^H}{dx} \quad (9)$$

$$\partial_x T_j^H = \frac{T_j^H - T_{j-1}^H}{dx} \quad (10)$$

The N × N state matrix of the system was then formulated as in (11).

$$A = \begin{pmatrix} -\left(\frac{c_1}{dx}+d_1\right) & 0 & \dots\dots & 0 & d_1 & \dots\dots & 0 \\ -c_1 dx & -\left(\frac{c_1}{dx}+d_1\right) & \dots\dots & 0 & 0 & d_1 & 0 \\ 0 & -c_1 dx & \dots\dots & -\left(\frac{c_1}{dx}+d_1\right) & -c_2 dx & 0 & d_1 \\ d_2 & 0 & \dots\dots & 0 & -\left(\frac{c_1}{dx}+d_1\right) & -c_2 dx & 0 \\ 0 & d_2 & \dots\dots & 0 & 0 & -\left(\frac{c_2}{dx}+d_2\right) & -c_2 dx \\ 0 & 0 & \dots\dots & d_2 & 0 & 0 & -\left(\frac{c_2}{dx}+d_2\right) \end{pmatrix} \quad (11)$$

$$\mathrm{B} = \begin{pmatrix} c_1 dx & 0 \\ 0 & . \\ . & . \\ . & . \\ . & . \\ . & 0 \\ 0 & -c_2 dx \end{pmatrix} \quad (12)$$

$$C = \begin{pmatrix} 1 & 0 & 0 & 0 & 0 \\ 0 & 0 & 0 & 0 & 1 \end{pmatrix} \quad (13)$$

$$D = 0 \quad (14)$$

Control is achieved through the manipulation of c_1 and c_2.

2.2 PID CONTROL SCHEME

Figure 2 depicts the block diagram of a typical PID controller, while equation (15) is its mathematical representation.

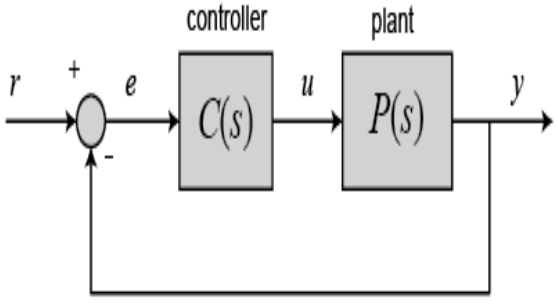

Figure 2: PID Control scheme

The control input to the plant, u, is sum of three products: the proportional gain K_p with the magnitude of the error; the integral gain K_i with integral of the error; and the derivative gain K_d with the derivative of the error.

$$u(t) = K_p e(t) + K_i \int e(t)dt + K_d \frac{de}{dt} \quad (15)$$

The output response of the PID controller was observed to be unstable. The parameters of the controller were then retuned, but the output failed to stabilize. As such, adaptive LQR was developed to address the problem.

2.3 ADAPTIVE LQR CONTROL DESIGN

An adaptive control is achieved through the adjustment of controller characteristics by automatically compensating the uncertainties in order to maintain the overall system performance at optimum level.

The dynamic of the extended state is defined by (16):

$$\dot{X} = A_e \begin{pmatrix} X \\ e_1 \end{pmatrix} + Be_1 U + Be_2 F \quad (16)$$

where Xe, e_1 and F are the extended state, integral of the error, and the boundary reference respectively, and are defined in (17).

$$\left.\begin{aligned} X_e &= \begin{pmatrix} X \\ e_1 \end{pmatrix} \\ e_1 &= F - \begin{pmatrix} T^H_{meas} \\ T^C_{meas} \end{pmatrix} \\ F &= \begin{pmatrix} T^H_r \\ T^C_r \end{pmatrix} \end{aligned}\right\} \quad (17)$$

Matrices A_e, B_{e1} and B_{e2} in (16) are defined in (18).

$$\left.\begin{aligned} A_e &= \begin{pmatrix} A & \begin{pmatrix} 0 & 0 \\ \vdots & \vdots \\ 0 & 0 \end{pmatrix} \\ \begin{pmatrix} 0 & \dots & 0 & -1 & 0 & 0 & \dots & 0 \\ 0 & \dots & 0 & 0 & -1 & 0 & \dots & 0 \end{pmatrix} & \begin{pmatrix} 0 & 0 \\ 0 & 0 \end{pmatrix} \end{pmatrix} \\ B_{e1} &= \begin{pmatrix} B \\ \begin{pmatrix} 0 & 0 \\ 0 & 0 \end{pmatrix} \end{pmatrix} \\ B_{e2} &= \begin{pmatrix} \begin{pmatrix} 0 & 0 \\ \vdots & \vdots \\ 0 & 0 \end{pmatrix} \\ \begin{pmatrix} 1 & 0 \\ 0 & 1 \end{pmatrix} \end{pmatrix} \end{aligned}\right\} \quad (18)$$

The Hamiltonian equation of the problem was analyzed beforehand to ascertain the necessary optimality conditions and the optimal control law in (19), while the optimal input is represented in (20).

$$H = \frac{1}{2}(X_e^T Q X_e + U^T R) + \lambda^T (A_e B_e + B_{e1} U + B_{e2} F) \quad (19)$$

$$Where \;\; Q = \begin{pmatrix} 0 & 0 \\ 0 & Q_r \end{pmatrix}$$

$$U' = G_{lqr} \,.\, X_e + G_F \,.\, F \quad (20)$$

$$where \; G_{lqr} = -R^{-1} B_{e1}^T (P B_{e1} R^{-1} B_{e1}^T - A_e^T)^{-1} P B_{e2}$$

P is a solution of the Ricatti equation in (21).

$$-Q = P A_e + A_e^T P - P B_{e1} R^{-1} B_{e1}^T \quad (21)$$

It could be seen that the gains G_{lqr} and G_F of the LQR controller are functions of Ae and $Be1$, which in turn are functions of A and B.

The system parameters K_1 and K_2 in matrices A and B can be evaluated either offline or online. In the former, a constant gain for the LQR controller is computed using their nominal values, while the latter involves assuming the availability of both estimator and observer for the system which represents an adaptive controller.

3 RESULTS AND DISCUSSION

3.1 PID CONTROL

When PID was deployed as the testbench system controller, the output did not settle despite several tuning of the controller gains. Figure 4(a) shows the input temperature profiles for both the hot and cold tubes while its output response is shown in Figure 4(b) for the PID controller.

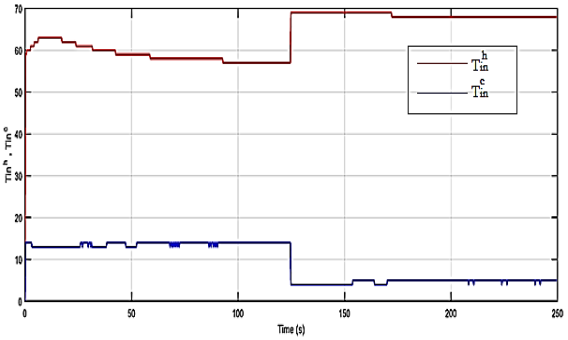

(a)

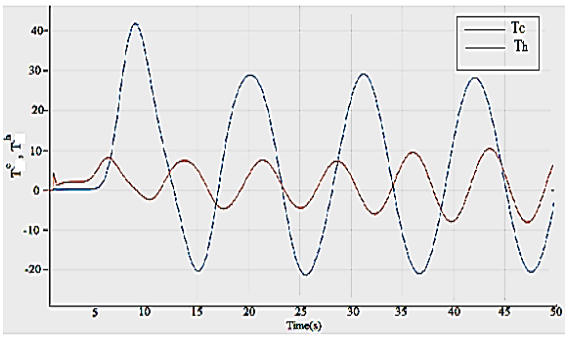

(b)

Figure 4: Temperature profile for PID controller (a) Input (b) Output

3.2 LQR CONTROL

As shown in Figure 4, the control scheme developed using PID controller was not satisfactory in tracking the reference points. Hence an adaptive LQR controller was developed. The adaptive LQR shows a better reference tracking performance than that of PID as depicted in Figure 5.

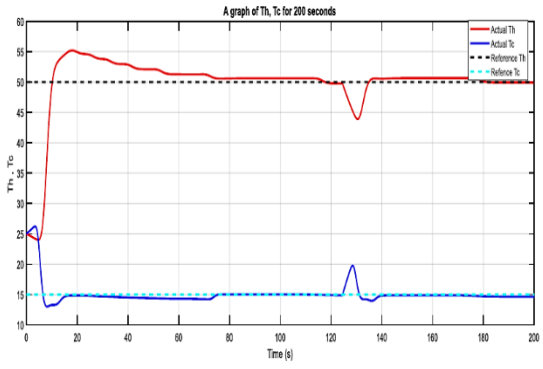

Figure 5: Temperature output profile for adaptive LQR controller

From Figure 5, it can be seen that the output closely tracked the set point. Hence the adaptive LQR shows a very good performance on the process.

4 CONCLUSION

In this paper, two controllers, PID and adaptive LQR were developed and their performances were tested on HE testbench for the fluid flow control. The designed PID was observed to exhibit poor performance in terms of reference tracking as compared to LQR controller. Hence adaptive LQR which performs better for both the hot tank and cold tank temperatures is preferred in the control of the HE system.

REFERENCE

Dulău, M., Oltean, S., & Gligor, A. (2015). Conventional Control vs. Robust Control on Heat-exchangers. *Procedia Technology*, *19*(5), 534–540. https://doi.org/10.1016/j.protcy.2015.02.076

Fatma, S., Karim, A., Jamaludin, A., Abdullah, Z., & Talib, N. (2017). Comparison Effectiveness of PID , Self-Tuning and Fuzzy Logic Controller in Heat Exchanger. *Journal of Applied Environmental and Biological Sciences*, *7*, 28–33.

Hamze, S., Witrant, E., Bresch-Pietri, D., & Fauvel, C. (2018). Estimating Heat-Transport and Time-Delays in a Heat Exchanger. *2018 IEEE Conference on Control Technology and Applications, CCTA 2018*, 1514–1519. doi.org/10.1109/CCTA.2018.8511359

Jamal, A., & Syahputra, R. (2016). Heat exchanger control based on artificial intelligence approach. *International Journal of Applied Engineering Research*, *11*(16), 9063–9069.

Khare, Y. B., & Singh, Y. (2010). PID Control of Heat Exchanger System. *International Journal of Computer Applications*, *8*(6), 22–27. https://doi.org/10.5120/1213-1742

Padhee, S. (2015). Controller Design for Temperature Control of Heat Exchanger System : Simulation Studies. *WSEAS TRANSACTIONS on SYSTEMS and CONTROL*, *9*(June 2014), 485–491.

Saranya, S. N., Sivakumar, V. M., Thirumarimurugan, M., & Sowparnika, G. C. (2017). An Analysis on Modeling and Optimal Control of the heat exchangers using PI and PID controllers. *International Conference on Advanced Computing and Communication Systems (ICACCS -2017)*, 1–8. Coimbatore, India.

Oravec, J., Bakošová, M., Trafczynski, M., Vasičkaninová, A., Mészáros, A., & Markowski, M. (2018). Robust model predictive control and PID control of shell-and-tube heat exchangers. *Energy*, *159*, 1-10.

4th International Engineering Conference (IEC 2022)
Federal University of Technology, Minna, Nigeria

EVALUATION OF RARE EARTH ELEMENTS MINERALIZATION POTENTIALS OF PARTS OF MINNA SHEET 164SW, NORTH CENTRAL NIGERIA

Akano T. O, and *Onoduku, U.S.

Department of Geology, Federal University of Technology, PMB 65
Minna Niger State, Nigeria
*Corresponding author email: onoduku.usman@futminna.edu.ng +2348035904399

ABSTRACT
The demand and prices for Rare Earth Elements (REEs) have risen in recent times as consequence of their new found applications in several industries including electronics and technology. However, supply has continued to be on the decrease due to non to minimal exploration data on these elements. This research presents the evaluation of the REEs Mineralization potential of parts of Minna sheet 164SW. A detailed geological fieldwork was carried out in which 4 rock types were identified- Granite, Schist, Quartzite and Granite-gneiss. 10 samples were obtained from rock exposures in the study area and were analyzed using ICP-MS. The average analyzed values in ppm - Gd- 4.8, Dy – 12.9, Ho – 3.3, Er – 10.9, Tm – 3.5, Y – 17.9, La – 34.4, Ce – 88.6, Nd- 19.7, Sm – 8.3, Eu- 10.4, Tb – 5.3, Yb – 3.5 and Lu- 1.7 were generated from the results and the resulting computed enrichment factors are Gd- 1.2, Dy – 3.3, Ho – 3.9, Er – 4.8, Tm – 11.5, Y – 0.9, La – 1.1, Ce – 1.4, Nd- 0.7, Sm – 1.8, Eu- 10.4, Tb – 7.6, Yb – 1.6 and Lu- 5.5 with elements like Tm, Tb, and Lu showing high enrichment status. The concentration of REEs in the rocks has shown the significant potentials for exploration in the study area.

Keywords: *enrichment, exploration, mineralization, REEs*

1 INTRODUCTION

Rare-earth elements (REEs) are a group of seventeen chemical elements in the periodic table- the fifteen lanthanides as well as yttrium and scandium according to the International Union of Pure and Applied Chemistry (IUPAC). Scandium and yttrium are considered REEs since they tend to occur in the same ore deposits as the lanthanides and exhibit similar chemical properties. Although Promethium, the rarest, only occurs in trace quantities in natural materials, all REEs occur in nature but not in pure metal form (Castor and Hendrik, 2006). Around 96% of the world's REE deposits are dominated by Ce, Y, La, and/or Nd (Jha *et al.*, 2016; Wall *et al.*, 2017 in Zhao *et al.,* 2022). The REEs in different geological materials have unique chemical characteristics and distribution patterns Zhao *et al.,* 2021a). The REE scarcely form economic mineral deposits (Migaszewski and Gałuszka, 2015). The largest deposits are primarily linked to carbonatites and peralkaline silicate rocks of hydrothermal origin, or affected by hydrothermal processes (Kynicky, Xu, & Smith, 2012).

Rare earth elements can be regarded as oil boom of the twenty first century (Dilioha *et al.* 2016). While many people are unaware of the huge effects of these elements, rare earth elements (REEs) are dictating how people live in the modern world- they have become become very critical to several modern technologies ranging from cell phones and televisions to LED light bulbs and wind turbines (Balaram, 2019). **Since** REEs play such a significant part in the development of modern industries and the transition to a green economy (Dushyantha *et al.*, 2020). Therefore, it has become crucial to pay attention to this unique group of metals in areas where they have not been traditionally exploited.

1.1 STUDY AREA

The Study area (Figure 1) is within Minna and is bounded by Latitudes 09º36ˈN to 09º38ˈN and Longitudes 06º 30ˈE to 06º 34ˈE in Minna Sheet 164NW. It is located in the middle of the Nigerian basement complex which houses metasedimentary and meta-igneous rocks that have undergone polyphase deformation and metamorphism that has been intruded by granitic rocks that are pan-African in age (Obaje, 2009).

2 MATERIALS AND METHODS

The material used for the studies are rock samples.

2.1 GEOLOGICAL MAPPING

The map of the study area was extracted from a base map of Minna sheet 164NW. The extract was on an

enlarged scale of 1:12,500 from the initial 1:50,000 scale map. Coordinates of rock outcrops location were taken using GPS (Global Positioning System), a detailed description of the each of the exposure was done and noted in the field note and measurements of strike, dip and joint directions were taken using a Compass clinometers. Samples were then taken from exposed outcrops using a sledge hammer and were labeled using a marker and masking tape. Geologic map of the area was produced by plotting the above information on the base map.

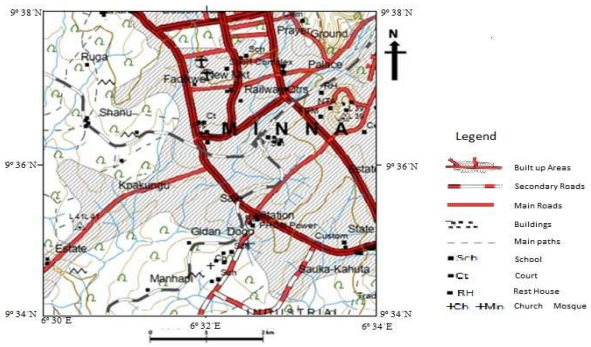

Figure 1: An extract of the study area from Minna Sheet 164NW

2.2 LABORATORY ANALYSES

Rock samples were crushed and pulverized and stored in sample bottles and sent to Activations laboratories, Ontario, Canada for Multi elemental analyses.

3 RESULTS AND DISCUSSION

All Figures and Tables inserted should be properly referenced in the discussion of the results. Results and discussion entails the use of words to describe the implication of the results expected/obtained. Often, Figures, Tables and Plates are powerful means for proper technical result reporting and discussion. Examples of Figures and Tables are given in Figure1 and Table1.

3.1 GEOLOGY

The geological map is shown in Figure 2. Three lithologic units were identified in the study area. The schist occurs as a flat-lying, thin band in the northeast with a short quartzite ridge parallel to it. The majority of the local rock types are granitic rocks, which come in different textures and compositions.

The granites found in the study area cover about 75% of the study area. They are mostly massive with several joints and faults, some of which are filled with quartz. Rose diagram of the measured joints is shown in figure 3. From this figure, the major joints direction is formed trending in the NNE/SSW and ENE/WSW directions. Exfoliation is quite common on the outcrops. In hand specimen, the grain sizes varies from medium, porphyritic to coarse grain size. The colour also ranges between light coloured to medium dark coloured. Some artisanal quarrying activities were observed in a location around Maitumbi.

The schist outcrops, are mainly N-S and NNE-SSW trending with greenish-blue color and of low - medium grade deformation suggesting that they were deformed and metamorphosed generally in the greenschist facies grade. The Quartzites appear elongated, displaying pod-like structures and are mostly foliated and undergoing intense weathering.

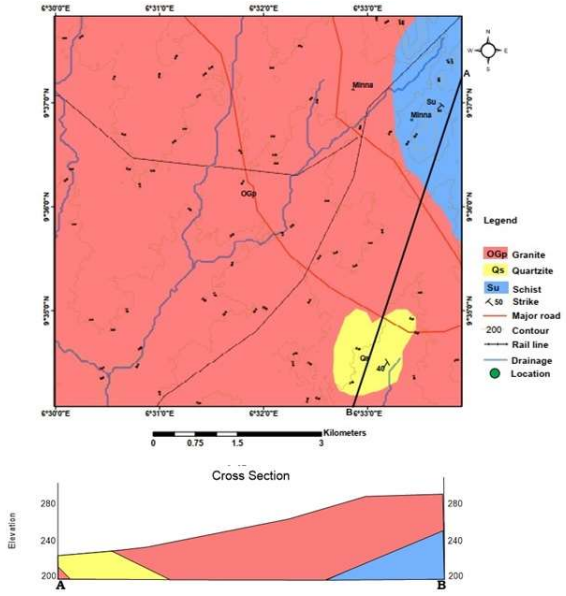

Figure 2: Geological map and Cross section of the study area

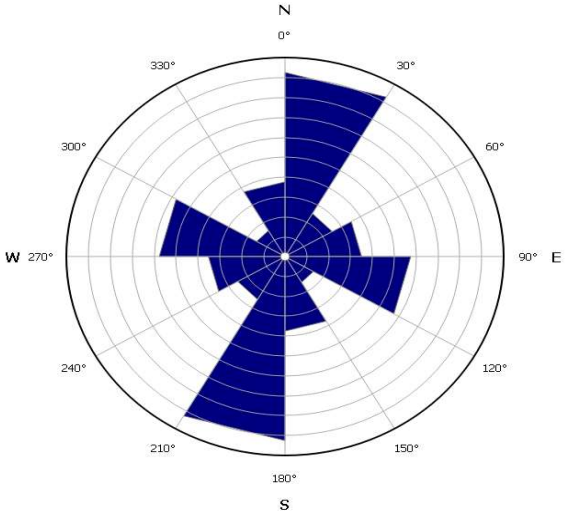

Figure 3: Rossete Diagram showing joint directions

3.2 WHOLE ROCK GEOCHEMISTRY

3.2.1 MAJOR OXIDES

The computed mean concentrations of the analyzed major oxides (Table I) show that the highest major oxide is SiO_2 which is followed successively in decreasing order by Al_3O_2, K_2O, Fe_2O_3, Na_2O and CaO. The rest are below 1 wt %. The high values of SiO_2 and Al_2O_3 is an indication of rocks derived from a Felsic protolith.

Granitic rocks of Minna are rich in alkalis (Mean = 6.89 wt %). This is supported by the provenance study's plot of SiO_2 versus $Na_2O + K_2O$ in the TAS Diagram (modified after Cox et al 1979) of the granites in Figure 4. The protolithic rock was identified as Granite-Granodiorite rocks by the TAS Diagram. The phase is characterized by high SiO_2 and low Al_2O_3, TiO_2, CaO, and MgO contents.

The schists and quartzites are also relatively rich in Al_2O_3 (10-12 wt%), Na_2O (approximately 2 wt%) K_2O (2-4 wt%) which is also an indication of rocks derived from a Felsic protolith.

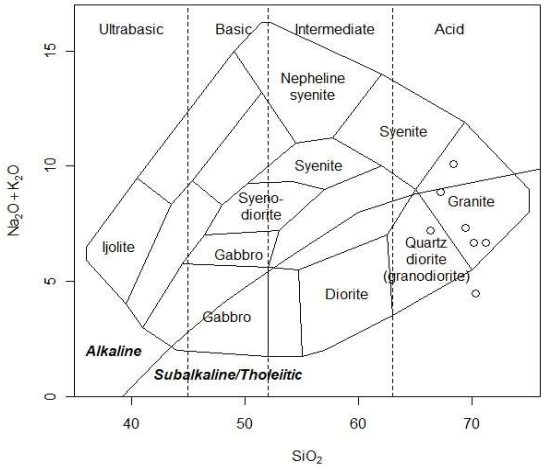

Figure 4: Classification of the protolith rock from Minna TAS Diagram (Modified after Cox et al., 1979)

3.2.2 TRACE ELEMENTS

Result of the trace elements analyses are as shown in Table II. The result of the analysis show the mean concentrations of the trace elements in decreasing order as Ba >Zr >Rb >Au >Sr >Hf >Zn >V >Nb >Th >Pt >Cu >U and Sn.

3.2.3 RARE EARTH ELEMENTS

The results of the Rare Earth Elements (REEs) analyses are shown in Table III. The result of the analysis show the mean concentrations of the REEs in decreasing order as Ce >La >Nd >Y> Dy> Er> Eu> Sm> Tb> Gd> Yb>Tm>Ho>L

Statistical analyses (Table IV) using Pearson Correlation Coefficient were carried out to show the degree and strength of association of the REEs so as to be able to determine their geochemical relationships or affinities within the study area. The relationships between elements are coherent in some cases and in-coherent in others (compatibility and in-compatibility respectively).

3.2.4 REES MINERALIZATION POTENTIALS OF THE STUDY AREA

The mineralization potential of the study area (Table V and Figure 5) was determined by dividing the average analyzed values of the REEs in the study area by their respective abundance in the upper crust after Dushyantha *et al.* 2020. This generated the Enrichment ratio and by extension, the enrichment status (Using a threshold of 1.5) of the study area. Elements Sm, Eu, Tb, Dy, Ho, Er, Tm, Yb and Lu show significant enrichment status while Elements La, Ce, Nd, Gd and Y show a relative depletion.

3.2.5 REE PATTERNS IN THE GRANITIC ROCKS

The REEs were normalized using values from Taylor and McLennan (1995) (Table VI). The Bulk Continental Crust-normalized REE patterns for the rocks are presented in Figure 6. They generally show depletion in the light REEs (LREEs) except for Eu and enrichment in the heavy REEs (HREEs). The ratios of LREEs to HREEs of the study area (approximately 1– 4 in the granites) are moderately enriched. REE patterns for the granite samples show enrichment in HREEs. LREE/HREE = 0.25–0.59 and positive Eu anomaly (0.9-3.1). The total REE contents of the studied rocks are 135–327 ppm. The REE contents in the 7 granitic samples exceed 200 ppm in 7 samples indicating localized REE enrichment in the study area which is consistent with when compared to the computed Enrichment ratio generated using the Average crustal abundances according to Dushyantha et al., (2020).

The increase in HREEs enrichment in the rocks of the study area could be as a result of an inherent HREE in the continental crust. This phenomenon depicts the differentiation pattern of the magma that gave rise to the rocks.

A positive relationship is identified between the ∑REE and SiO2 contents of the granitic rocks with high REE contents. These rocks are inferred to have been influenced by reactions with late magmatic F-, CO2–, and REE-rich fluids that altered magmatic minerals and crystallized as REE-fluorocarbonates and thorite. Similarly, the studied HREE-rich granites show high SiO2 contents, low Zr/Hf, and Rb/Ba, ratios, and positive Eu anomalies, indicating strong magmatic differentiation.

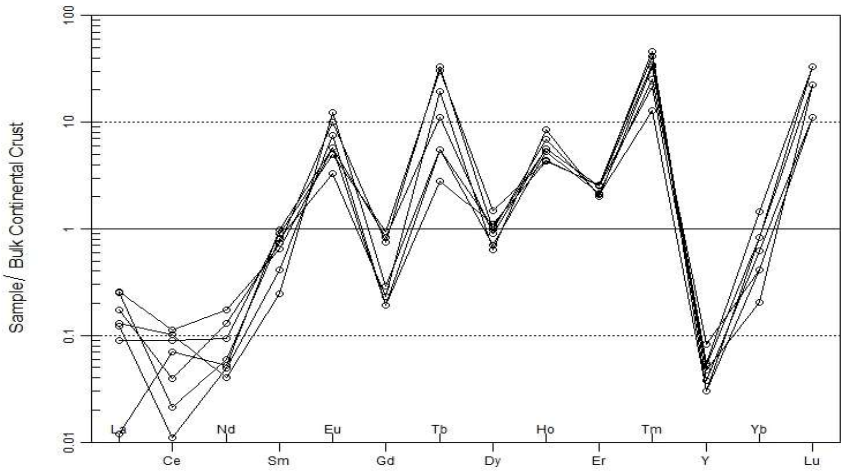

Figure 6: Spider plot of the Bulk Continental crust normalized REEs values after Taylor and McLennan (1995) for the granite rocks of the area.

TABLE I: CONCENTRATION OF MAJOR OXIDES (WT%) IN THE SAMPLES

Samples	**TA1**	**TA4**	**TA5**	**TA6**	**TA9**	**TA11**	**TA13**	**TA14**	**TA15**	**TA17**	**Mean**
Rock Type	Granite	Granite	Granite	Schist	Granite	Granite	Schist	Granite	Quartzite	Granite	
SiO_2	67.22	68.34	66.31	34.33	70.11	71.23	44.22	70.33	67.77	69.44	62.93
Al_2O_5	18.11	16.31	16.44	11.21	17.11	18.55	10.22	17.11	12.22	18.33	15.561
Fe_2O_3	3.11	2.12	2.13	1.88	3.21	2.12	2.43	1.77	1.98	2.22	2.297
MgO	0.22	0.54	0.65	1.01	1.04	0.55	0.21	0.44	0.73	0.33	0.572
Na_2O	2.55	2.98	1.99	2.23	2.11	1.33	1.51	2.33	2.13	2.1	2.126
K_2O	6.33	7.11	5.23	2.44	4.56	5.33	4.22	2.13	4.23	5.22	4.68
TiO_2	0.22	0.32	0.12	0.11	0.23	0.32	0.44	0.31	0.12	0.22	0.241
P_2O_5	0.11	0.12	0.21	0.1	0.33	0.25	0.26	0.23	0.12	0.17	0.19
MnO	0.01	0.06	0.01	0.05	0.12	0.11	0.04	0.03	0.05	0.06	0.054
CaO	2.11	2.1	1.44	1.34	1.23	0.44	0.87	0.76	0.28	1.11	1.168
$Na_2O + K_2O$	8.88	10.09	7.22	4.67	6.67	6.66	5.73	4.46	6.36	7.32	6.806

TABLE II: CONCENTRATION OF TRACE ELEMENTS (PPM) IN THE SAMPLE

Sample	**TA1**	**TA4**	**TA5**	**TA6**	**TA9**	**TA11**	**TA13**	**TA14**	**TA15**	**TA17**
Rock Type/ Trace elements	Granite	Granite	Granite	Schist	Granite	Granite	Schist	Granite	Quartzite	Granite
Au	112	94	66	224	77	101	333	87	23	82
Cu	5	8	2	6	8	13	14	11	22	12
Zn	33	23	29	44	56	32	21	20	14	22
Zr	102	122	234	222	301	111	98	121	120	78
Pt	10	12	15.3	12.5	17	18	11	12	11.8	10.2
Ba	666	432	111	213	67	222	110	78	95	12
Cs	2.1	2	3.1	2.1	2	2	3	3	3.1	3.4
Hf	33	53	23	76	11	23	42	22	17	21
Nb	8	23	11	44	22	27	23	33	20	21
Rb	111	121	123	201	231	222	133	140	130	66
Sr	112	98	144	162	100	77	120	98	104	77
Th	7	12	8	2.3	4.7	8	5	22	32	30
U	1	2	1	1	ND	5	3	1	2	1
V	33	22	14	56	21	34	10	55	12	11
Sn	2	3	3	1	ND	ND	ND	1	2	1
Rb/Ba	0.1667	0.2800	1.1081	0.9436	3.4478	1	1.2091	1.7948	1.3684	5.5
Zr/Hf	3.0909	2.3018	10.174	2.9211	27.364	4.8261	2.3333	5.5	7.0588	3.7143

TABLE III: CONCENTRATION OF REES (PPM) IN THE SAMPLES

	TA1	TA4	TA5	TA6	TA9	TA11	TA13	TA14	TA15	TA17
Rock Type/ REEs	Granite	Granite	Granite	Schist	Granite	Granite	Schist	Granite	Quartzite	Granite
La	66	44	23	40	65	31	17	33	22	3
Ce	122	43	98	55	23	12	222	111	123	77
Nd	44.6	33.1	23.8	12.4	15.2	12.7	12.9	10.2	11.7	13.4
Sm	8	9	11	12	10	5	7	3	6	12
Eu	7	12	6	11	4	9	21	15	12	7
Gd	9.11	8.23	10.22	4.11	2.55	2.12	2.43	3.12	3.45	2.12
Tb	4	12	11	9	7	2	4	2	1	1
Dy	12.22	13.44	20.12	12.22	8.77	9.56	11.23	14.12	12.22	15.12
Ho	3.4	4.2	2.7	2.9	5.2	3.2	1.3	3.4	4.2	2.6
Er	12.1	10.2	12.3	8.2	9.7	10.3	10.7	12.1	11.7	12.4
Tm	2.2	1.3	4.7	4.2	3.4	2.6	2.3	3.5	6.2	4.2
Y	21	12	15	18	22	33	11	19	16	12
Yb	4	4	3	8	7	2	3	1	1	2
Lu	3	2	1	1	3	1	2	2	1	1
ΣLREE	256.71	149.33	172.02	134.51	119.75	71.82	282.33	175.32	178.15	114.52
ΣHREE	61.92	59.14	69.82	63.52	66.07	63.66	45.53	57.12	53.32	50.32
ΣREE	318.63	208.47	241.84	198.03	185.82	135.48	327.86	232.44	231.47	164.84
HREE /LREE	4	3	2	2	2	1	6	3	3	2

TABLE IV: STATISTICAL ANALYSES USING PEARSON CORRELATION COEFFICIENT

	La	*Ce*	*Nd*	*Sm*	*Eu*	*Gd*	*Tb*	*Dy*	*Ho*	*Er*	*Tm*	*Y*	*Yb*	*Lu*
La	1													
Ce	-0.344	1												
Nd	0.5523	0.0022	1											
Sm	-0.013	-0.244	0.1772	1										
Eu	-0.369	0.6825	-0.3	-0.496	1									
Gd	0.3289	0.0259	0.8276	0.269	-0.29	1								
Tb	0.3418	-0.27	0.3992	0.5333	-0.188	0.6476	1							
Dy	-0.436	0.1843	0.1774	0.3088	-0.13	0.5925	0.324	1						
Ho	0.6222	-0.628	0.1556	-0.052	-0.53	0.0584	0.1491	-0.322	1					
Er	-0.358	0.4042	0.2115	-0.249	-0.078	0.2517	-0.422	0.5611	-0.173	1				
Tm	-0.41	0.0564	-0.498	0.1375	-0.199	-0.176	-0.258	0.3172	0.0823	0.2185	1			
Y	0.4022	-0.545	-0.074	-0.387	-0.359	-0.212	-0.26	-0.494	0.3071	-0.222	-0.112	1		
Yb	0.5921	-0.356	0.1462	0.6215	-0.301	0.1036	0.6026	-0.295	0.2349	-0.78	-0.177	0.0466	1	
Lu	0.7726	0.1003	0.5057	-0.137	-0.076	0.1656	0.094	-0.405	0.3702	-0.018	-0.558	0.0557	0.3134	1

TABLE V: REEs MINERALIZATION POTENTIALS OF THE STUDY AREA (THRESHOLD= 1.5)

S/N	REEs	Average Analysed Value (ppm)	Abundance in the upper crust (ppm) Dushyantha *et al.* (2020)	Enrichment Ratio	Enrichment Status
1	La	34.4	31	1.109677	Not Enriched
2	Ce	88.6	63	1.406349	Not Enriched
3	Nd	19.7	27	0.72963	Not Enriched
4	Sm	8.3	4.7	1.765957	Enriched
5	Eu	10.4	1	10.4	Enriched
6	Gd	4.746	4	1.1865	Not Enriched
7	Tb	5.3	0.7	7.571429	Enriched
8	Dy	12.902	3.9	3.308205	Enriched
9	Ho	3.31	0.83	3.987952	Enriched
10	Er	10.97	2.3	4.769565	Enriched
11	Tm	3.46	0.3	11.53333	Enriched
12	Y	17.9	21	0.852381	Not Enriched
13	Yb	3.5	2.2	1.590909	Enriched
14	Lu	1.7	0.31	5.483871	Enriched

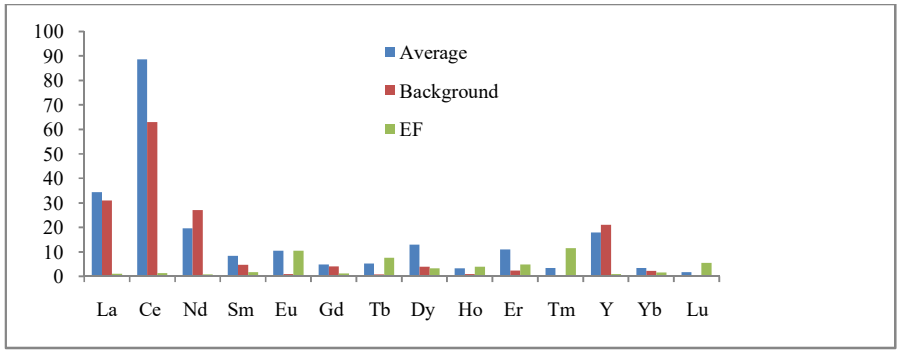

Figure 5: REEs Mineralization Potentials in the Study Area

TABLE VI: BULK CONTINENTAL CRUST NORMALIZED REEs VALUES AFTER TAYLOR AND MCLENNAN (1995)

REEs	TA1	TA4	TA5	TA9	TA11	TA14	TA17
La	4.13	2.75	1.44	4.06	1.94	2.06	0.19
Ce	3.7	1.3	2.97	0.7	0.36	3.36	2.33
Nd	2.79	2.07	1.49	0.95	0.79	0.64	0.84
Sm	2.29	2.57	3.14	2.86	1.43	0.86	3.43
Eu	6.36	10.91	5.45	3.64	8.18	13.64	6.36
Gd	2.76	2.49	3.1	0.77	0.64	0.95	0.64
Tb	6.67	20	18.33	11.67	3.33	3.33	1.67
Dy	3.3	3.63	5.44	2.37	2.58	3.82	4.09
Ho	4.36	5.38	3.46	6.67	4.1	4.36	3.33
Er	5.5	4.64	5.59	4.41	4.68	5.5	5.64
Tm	6.88	4.06	14.69	10.63	8.13	10.94	13.13
Y	1.05	0.6	0.75	1.1	1.65	0.95	0.6
Yb	1.82	1.82	1.36	3.18	0.91	0.45	0.91
Lu	10	6.67	3.33	10	3.33	6.67	3.33
LREE	22.03	22.09	17.59	12.98	13.34	21.51	13.79
HREE	39.58	46.8	52.95	50.03	28.71	36.02	32.7
LREE/HREE	0.55659	0.47201	0.3322	0.25944	0.46465	0.59717	0.42171
Eu/*Eu	2.51404	2.52968	3.11994	1.48398	0.95666	0.90388	1.48162

4 CONCLUSION

Geological mapping revealed the Minna Area to be is underlained by light to medium dark colored porphyritic to coarse grained granitic rocks, low - medium grade deformation N-S and NNE-SSW trending greenish-blue schist and elongated pod-like structures quartzite, with the granites occupying about 70% of the study area.

The area is considered to be a primary source of REEs, particularly the HREEs such as Sm, Eu, Tb, Dy, Ho, Er, Tm, Yb and Lu showing enrichment ratios ranging 3.3-11.5. The concentration of REEs in the rocks therefore shows a significant potential for exploration.

The Eu Positive anomaly of granitic rocks suggests an enrichment of plagioclase feldspar; this is corroborated by previous petrographic studies of the area (Alabi, 2011). Furthermore, the high SiO_2 content, low Zr/Hf, and Rb/Ba, ratios indicate strong magmatic differentiation.

ACKNOWLEDGEMENTS

Special appreciation to Dr. N.M Waziri of Department of Geology, Federal University of Technology, Minna for his immense contribution to this paper.

REFERENCE

Alabi, A. A. (2011). Geology and environmental impact assessment and benefits of granitic rocks of Minna area, Northwestern Nigeria. Ethiopian Journal of Environmental Studies and Management Vol. 4 No.4 2011 http://dx.doi.org/10.4314/ejesm.v4i4.5

Balaram, V. (2019). Rare earth elements: A review of applications, occurrence, exploration, analysis, recycling, and environmental impact. Geoscience Frontiers , 1285-1303.

Castor, S. B., & Hedrick, J. B., (2006). Rare Earth Elements. In: British Geological Survey, Natural Environment Research Council, pp: 1-5

Dahlquist, J.A. (2001). REE fractionation by accessory minerals in epidote-bearing metaluminous granitoids from the Sierras Pampeanas. Argentina. Mineral Mag.65 (4), 463–475. Dill,

Dilioha, I. I., & Onwualu-John, J. N. (2016) The Economic Potentials of the Rare Earth Elements in the Basaltic Rocks of Ameta, Southern Benue trough Nigeria. J Environ Anal Toxicol 6: 387. doi:10.4172/2161-0525.1000387

Dushyanthaa, N., Batapolaa, N., Ilankoonb, I. M .S. K., Rohithaa, S., Premasiria, R., Abeysinghea, B., Ratnayakea, N., & Dissanayakea, K. (2020). The story of rare earth elements (REEs): Occurrences, global distribution, genesis, geology, mineralogy and global production https://doi.org/10.1016/j.oregeorev.2020.103521

He, C., Xu, C., Zhao, Z., Kynicky, J., Song, W. & Wang, L., (2017). Petrogenesis and mineralization of REE-rich granites in Qingxi and Guanxi, Nanling region. South China. Ore Geol. Rev. 81, 309–325.

Jha, M. K., Kumari, A., Panda, R., Rajesh Kumar, J., Yoo, K. & Lee, J.Y. (2016). Review on hydrometallurgical recovery of rare earth metals. Hydrometallury. 165, 2–26.

Kynicky, J., Xu, C., & Smith, M. P. (2012). Diversity of Rare Earth Deposits: The Key example of China. Elements, An international Magazine of Mineralogy, Geochemistry and Petrology , 361-367.

Migaszewski, Z. M., & Galuszka, A. (2015). The Characteristics,Occurrence, and Geochemical Behavior of Rare Earth Elements in the Environment: A Review, Critical Reviews in Environmental Science and Technology, 45:5, 429-471, DOI: 10.1080/10643389.2013.866622

Obaje, N. G. (2009). Geology and Mineral Resources of Nigeria, Lecture Notes Earth Science, Pp. 120-221.

Taylor, S.R. & McLennan, S.M. (1995) The geochemical evolution of the continental crust American Geophysical Union., Reviews of Geophysics, 33, 2 / May 1995 8755-1209/95/95 RG-00262515.00 Pages 241-265

Wall, F., Rollat, A., & Pell, R.S., (2017). Responsible sourcing of critical metals. Elements 13, 313–318.

Zhao Y., Sanzhong Li W., Wang T., Zhang R., Somerville I., Santosh M., Wei H., Wu J., Yang J., Chen W., & Tang Z. (2021, May). Rare earth element geochemistry of carbonates as a proxy for deep-time environmental reconstruction. Article in Palaeogeography Palaeoclimatology Palaeoecology DOI: 10.1016/j.palaeo.2021.110443

Zhao Z., Wang D., Bagas L., & Chen Z., (2022). Geochemical and REE mineralogical characteristics of the Zhaibei Granite in Jiangxi Province, southern China, and a model for the genesis of ion-adsorption REE deposits, Ore Geology Reviews 140 (2022) 104579.DOI:https://doi.org/10.1016/j.oregeorev.2021.104579

Zhao, Z., Wang, D.H., Chen, Z.H. & Chen, Z.Y., (2017). Progress of research on metallogenic regularity of ion-adsorption type REE deposit in the Nanling Range. Acad. Geol. Sci 12, 2814–2827

4th International Engineering Conference (IEC 2022)
Federal University of Technology, Minna, Nigeria

Experimental study on the effect of Zeolite Inclusion on Stress – Strain Characteristics of Laterite soil Stabilized with Cement

*[1]James, O., [1]Sadiku, S., [1]Amadi, A.A., [2]Kovo, A.S., [1]Sanni, A. and [1]Agbese, E. O.
[1] Department of Civil Engineering, Federal University of Technology, Minna, Nigeria
[2] Department of Chemical Engineering, Federal University of Technology, Minna, Nigeria
*Corresponding author email:olayemi.james@futminna.edu.ng +2348034085752

ABSTRACT
The present laboratory investigation studied the effects of zeolite on the stress-strain characteristics of cement treated laterite soil. Four different cement contents (3, 6, 9 and 12%) and various percentages of cement replacement with zeolite (0, 15, 30, 45, 60, 75 and 90%) were constituted. Atterberg limits, compaction and unconfined compressive strength (UCS) tests were performed on soil mixtures. Specimens for UCS were compacted with British standard light (BSL) effort at optimum moisture contents and cured for 28 days. The results of the tests showed that the addition of cement and zeolite caused a decrease in the liquid limit and plastic index which indicated improved workability of soil after treatment. The maximum dry density (MDD) decreased initially between 0% - 45% zeolite replacement levels while the reverse is the case between 60% -90% zeolite replacement for all cement contents used in the study. Meanwhile, Optimum moisture contents (OMC) increased between 0% and 45% zeolite replacement level. Further increase in zeolite contents` (60% - 90%) resulted in an opposite trend. Finally, the peak stress values obtained from stress – strain curves of mixtures were recorded on specimens with 15% replacement level. Similarly, the lowest values of strain at failure were measured on specimens containing 15% zeolite which represents improvement in the ductile behavior of the mixtures compared to cemented specimens without zeolite.

Keywords: *Kaolin-based zeolite, Laterite soil, Ordinary Portland cement, Stress-strain Characteristics*

1 INTRODUCTION

Some classes of laterite/lateritic soils encountered on project sites are often problematic and gap graded having uneven amount of fines and unstable percentage of coarse particles. These deficiencies are associated with the differences in geological settings, prevailing weathering regimes and rock forming minerals (Sukkarak, 2021).Quite often, most of the areas where Civil Engineering construction projects are located are covered with fine grained laterite/lateritic soils that exhibit insufficient engineering properties needed to provide support for loads from construction equipment and the imposed structural loads during usage (Amadi, 2011). In order to make these deficient laterite/lateritic soils useful as construction materials, stabilization/improvement schemes to enhance their engineering properties are required (Ibrahim *et al*., 2020).

The use of soil stabilization techniques to improve the engineering performance of soils is quite wide spread across the globe (Kanyi, 2017; Alhaji *et al*., 2021).Overtime, cement and lime have been the two main materials used for stabilizing soils. The disadvantages of these stabilizers include environmental hazard due to promotion of green house gases which causes global warming and the high energy cost associated with the production process. In order to solve the problems identified above, Liew *et al*. (2011) as well as Alhaji et al. (2021) suggested the use of cement partially replaced with pozzolanic materials as stabilizer for soil improvement purposes. Among the various pozzolanic materials available, zeolite is being considered as a suitable replacement option for cement due to economic, environmental and technical advantages (Al-Swaidani *et al*., 2016; James *et al.*, 2019). Partial replacement of cement with zeolite can provide additional technical advantages by enhancing the physical and mechanical characteristics of soils through pozzolanic reaction with $Ca(OH)_2$, prevent undesirable expansion due to alkali-aggregate reaction, reduce the porosity of the soil mixtures and improvement in the interfacial microstructure properties of mixtures (Mola-Abasi and Shooshpasha, 2016; Mola- Abasi *et al*., 2020).

The main advantages in the use of stabilizers are its effects on physical properties such as reduced soil plasticity and higher maximum dry density as well as the mechanical properties of soil such as stress-strain, tensile strength, modulus of elasticity, hardness and fatigue limit. The stress- strain relationship represented by a stress-strain curve is a graph obtained by plotting the values of stresses and strains obtained in uniaxial compression test. Their characteristic is dependent on the strength, age at loading, rate of load and stabilizer properties and type as well as size of specimen. This parameter is used in analyzing the stability of materials (soils inclusive) as part of an engineering system. The curve consists of (i) the elastic phase (ii) plastic yield deformation phase and (iii) the failure deformation phase. The elastic phase is where

the material can be deformed and when released will return back to its original configuration, i.e., stress is proportional to strain. At this phase, materials obey the general Hook's law and the slope is defined as the Young's modulus. The plastic phase is the portion where some permanent deformation will occur, even if the load is removed, i.e. the strain is irreversible. Lastly, the failure deformation phase is where deformation is irreversible.

This study therefore presents the stress- strain characteristics of soil mixtures when various percentages of kaolin- based zeolite partially replaces cement in laterite soil- cement mixtures under laboratory conditions.

2 MATERIALS AND METHODS

2.1 MATERIALS

Laterite soil for the investigation was collected from an existing burrow pit located at Sauka-kahuta (longitude $06^0$28'11''E to $06^0$32'13'' and between latitude $09^0$35'22''N to $09^0$30'36''N) Minna, Nigeria. The cement used for this study is the Dangote brand of ordinary Portland cement designated as CEM II (adopting the terminology used in European standard) and was obtained from a cement depot in Minna, Nigeria. It is general purpose cement mostly used for concrete and soil stabilization (James *et al*., 2019).

The zeolite on the other hand was synthesized through beneficiation of kaolin obtained from Agbaja deposit from Kogi state, Nigeria in the Civil Engineering laboratory of Federal University of Technology, Minna, Nigeria.

The tap water used to prepare the specimens for the laboratory tests was collected from the Civil Engineering laboratory, Federal University of Technology, Minna.The water is fit for drinking and was also found to conform to BS 3148:1980.

2.1 METHODS

The physical property tests conducted in the laboratory include particle size analysis, Atterberg limits, specific gravity and compaction tests on the natural soil sample in accordance with the procedures outlined in BS 1377 (1990), while for soil mixtures, tests methods specified by BS 1924(1990) were followed. The soil mixtures were constituted with 3, 6, 9 and 12% Portland cements by weight of soil and cement contents were then replaced by zeolite in the order of 0, 15, 30, 45, 60, 75 and 90% by weight of cement.

Specimens for compaction were prepared using British Standard Light (BSL) compacting energy. The engineering test performed on the specimens was the unconfined compressive strength (UCS) tests. From the results, stresses and strains from each test were computed and presented in stress-strain curve.

Finally, X-ray fluorescence spectrometer was used to determine the oxide composition of laterite soil sample, cement and zeolite used in the study.

3 RESULTS AND DISCUSSION

3.1 PHYSICAL PROPERTIES OF THE LATERITE SOIL

The physical properties of the laterite soil were as summarized in Table 1. The natural moisture content of the untreated soil was found to be 17.01%. The particle size distribution curve of the soil shown in Figure 1 indicates that the percentage passing sieve No.200 is 81.38% while the sand fraction constitutes 18.62%. This indicates that the soil is fine-grained. The result of the Atterberg limits revealed that the liquid limit (LL) of the soil was 46.5%, the plastic limit (PL) 20.00% while the plastic index (PI) was 26.50%. These results together with the result of the sieve analysis allowed the classification of the soil sample in theA-7-6 group of American Association of State Highway and Transportation Officials (AASHTO) classification scheme. On the other hand, the soil is classified as CL according to Unified Soil Classification System (USCS). The specific gravity of the untreated (natural) soil was found to be 2.62, a value that is slightly lower than that reported by researchers like Amadi and James (2015) which recorded the value of 2.67 for lateritic soil, but fall in the range of values(2.6 - 2.75) for soils from the study location (Gbadamosi,2021). The low specific gravity of the soil is attributed to higher fines fraction and Alumina content (Gidigasu, 1976).

The oxide composition of the soil sample listed in Table 2 indicate that the major oxide compositions of the soil are SiO_2 (46.27%), Al_2O_3 (28.27%) and Fe_2O_3 (18.04%), all adding up to 66.53% of the total composition.

3.2 CEMENT

The cement used for the study was the Dangote brand of ordinary Portland cement conforming to BS 12:1991. The specific gravity of the cement is 3.15, while the oxide composition is as listed in Table 2.

3.3 ZEOLITE

The zeolite is non-plastic and classified as silt with specific gravity of 2.2. The percentage composition of iron oxide (Fe_2O_3), silica dioxide (SiO_2) and aluminum oxide (Al_2O_3) presented in Table 2 for the zeolite added up to 97.51% which is greater than 70% requirement for class F pozzolana. This confirms that the zeolite used in the study was a good pozzolanic material.

TABLE 1: ENGINEERING PROPERTIES OF LATERITE SOIL USED IN THE STUDY

Parameter Description	Value
Specific gravity	2.62
Percentage passing no. 200 sieve (%)	81.3
Liquid limit (%)	46.5
Plastic limit (%)	20
Plastic Index (%)	26.5
Classification (AASHTO)	A-7-6
Classification (USCS)	CL
Maximum dry density (kN/m^3)	1.59
Optimum moisture content (%)	18.48
Unconfined compressive strength (kN/m^2)	82.65
Colour	Reddish brown

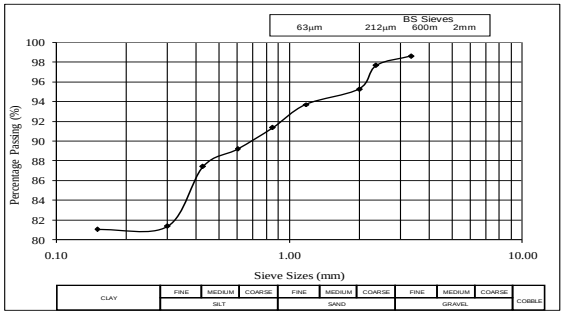

Figure 1: Particle size distribution of the laterite soil used in the study

TABLE 2: OXIDE COMPOSITION OF LATERITE SOIL, CEMENT AND ZEOLITE USED IN THE STUDY

Oxides	Composition (%)		
	Laterite soil	Cement	Zeolite
SiO_2	46.24	14.65	85.61
Al_2O_3	28.27	3.62	11.54
CaO	0.31	73.13	0.38
Fe_2O_3	18.04	3.74	0.36
K_2O	2.43	0.44	ND
MgO	1.10	1.07	ND
TiO_2	1.77	0.24	0.49
P_2O_5	0.47	0.09	0.57
SO_3	0.43	2.32	0.44
CL	0.26	0.13	0.30

3.4 EFFECTS OF CEMENT AND ZEOLITE ON INDEX PROPERTIES OF LATERITE SOIL

The effect of zeolite content on the Atterberg limits of the cement stabilized laterite soil is as presented in Figures (2-5). Generally, the results show a decreasing trend in the liquid limit (LL) values with higher cement and zeolite contents. At 0% zeolite replacement, the LL of soil-cement mixtures reached values ranging from 53-55.8% for all cement contents. By introducing and replacing cement with zeolite up to 90%, LL values were 47.9, 50, 43.8 and 48% for 3, 6, 9 and 12% cement contents respectively. The decrease may be linked to the flocculation and agglomeration arising from cation exchange reaction whereby Ca^{2+} in the additives reacted with ions of lower valency in the soil. This result agrees with the outcome of past studies like Yilmaz *et al*. (2007); Mola-Abasi and Shooshpasha (2016); Mola-Abasi *et al*. (2020) which reported that the addition of cement and zeolite to soil/sand led to reduction in the liquid limit. As can be seen in Figures (2-5), the plastic limit increased as the cement and zeolite contents increased. The increment in plastic limit (PL) recorded for all cement contents used in the study might not be unconnected with the flocculation and agglomeration of the clay particles occasioned by cation exchange at the surface due to the introduction of the cement and zeolite (Yilmaz *et al*., 2007; Rabab'ah *et al*., 2021). The variations of plastic index (PI) are as depicted in Figures (2-5). Generally, the PI decreased as both cements and zeolite contents increased. The plasticity index of 26.50% recorded for the natural soil decreased to16.89% when treated with 12% cement content replaced by 90% zeolite. This could be as a result of the reduction of the LL of soil mixtures.

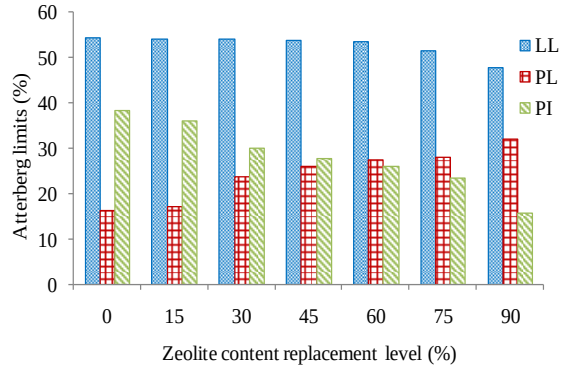

Figure 2: Changes in Atterberg limits of studied soil with 3% cement content

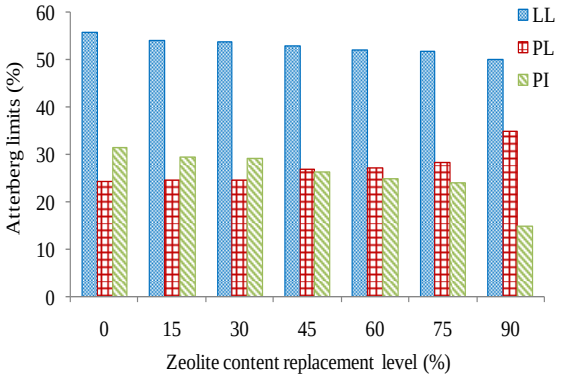

Figure 3: Changes in Atterberg limits of studied soil with 6% cement content

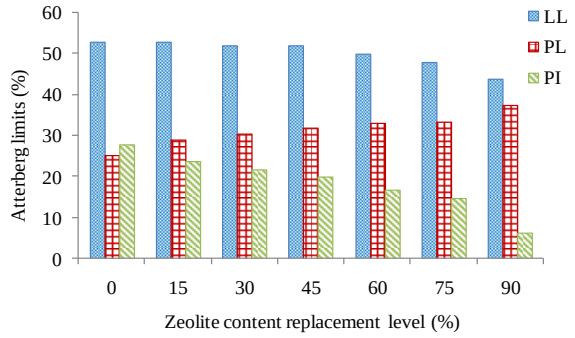

Figure 4: Changes in Atterberg limits of studied soil with 9% cement content

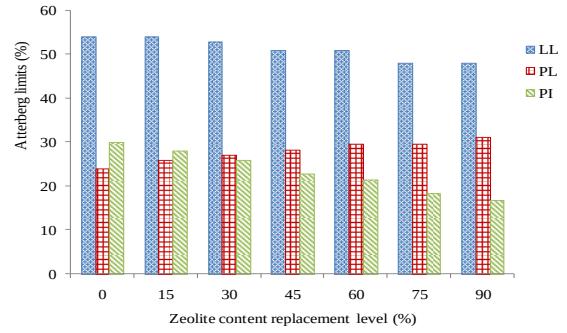

Figure 5: Changes in Atterberg limits of studied soil with 12% cement content

3.5 EFFECTS OF CEMENT AND ZEOLITE CONTENTS ON SPECIFIC GRAVITY

The specific gravity of the dry soil mixture reported in Figure 6 indicates that specimens with 0% zeolite replacement (i.e. soil+ cement mixtures) has specific gravity which ranged from 2.67 to 2.75 for cement contents of 3-12% representing an increase with higher cement content. The increase could be attributed to a material of higher specific gravity (cement- 3.15) replacing a lighter material (i.e. laterite soil) with a specific gravity of 2.62.

Generally, for the various soil-cement composites, increase in zeolite replacement level led to slight reduction in the values of specific gravities which recorded values between 2.40 and 2.47 at 90% zeolite content. The slight reduction is as a result of lighter material in terms of zeolite (specific gravity of 2.2) replacing heavy material in terms of cement (with specific gravity of 3.15) in soil mixtures.

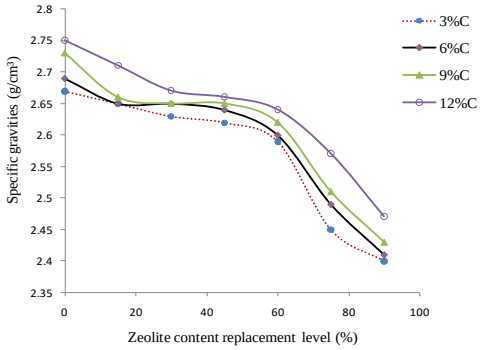

Figure 6: Variation of specific gravity of solid particle (Gs) with zeolite content (%) replacement level

3.6 EFFECTS OF CEMENT AND ZEOLITE CONTENTS ON MAXIMUM DRY DENSITY (MDD)

The variation of maximum dry density (MDD) of laterite soil-cement mixtures with zeolite contents for BSL compaction is as presented in Figure 7. It was observed that the MDD values decreases with increase in zeolite contents (from 0%-45% zeolite content) before increasing in values from 60%- 90% zeolite contents in the soil-cement mixtures and for all cement contents used for the study. The initial decrease in MDD can be attributed to the replacement of cement by zeolite which has a relatively low specific gravity of 2.2 when compared with that of cement that is 3.15. Between 60%-90% zeolite contents in the mixtures and for 3% C-12% C contents; there was increase in the value of MDD, i.e. from 1.629/cm^3 at 3% C content to 1.68g/cm^3 at 12% C content. The increase in MDD values can be attributed to a decrease in the surface area of clay fraction of the soil arising from the substitution of laterite soil with cement

and zeolite. In general, the result shows an increase for every percentage addition of cement. The increase in MDD with cement content is attributed to the relatively higher specific gravity of cement (3.15) to that of the soil (2.62) (Alhassan and Mustapha, 2006).

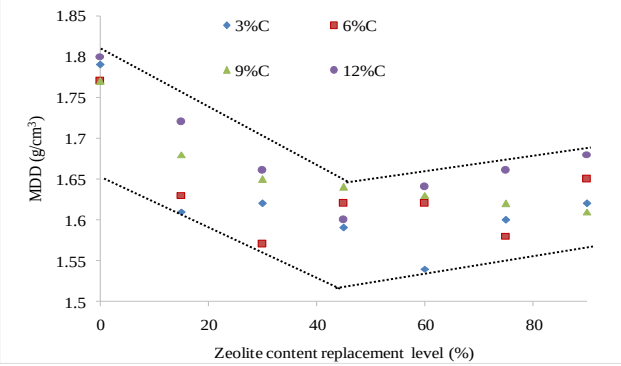

Figure 7: Variation of maximum dry density (MDD) of the soil-cement mixtures with zeolite content

3.7 EFFECTS OF CEMENT AND ZEOLITE CONTENTS ON OPTIMUM MOISTURE CONTENTS (OMC)

Figure 8 shows the variation of Optimum moisture content (OPC) of laterite soil-cement mixtures with zeolite contents for BSL compaction. It can be seen that the OMC increases with the increase in the zeolite content between 0% replacement and 45% replacement levels. Further increase in zeolite content (60- 90%) resulted in an opposite trend i.e., the OMC started decreasing. The increase in OMC of mixtures containing zeolite is expected as zeolite particles are finer with larger specific surfaces that require more water to saturate the particle surface (Mola-Abasi *et al.*, 2020; Rabab'ah *et al.*, 2021). The decrease in OMC between 60%-90%zeolite content replacement level might be attributed to reduction in water demanded for hydration purposes as the level of cement contents reduces greatly in all soil-cement mixtures as the level of zeolite increases to 90% replacement in various soil-cement mixtures.

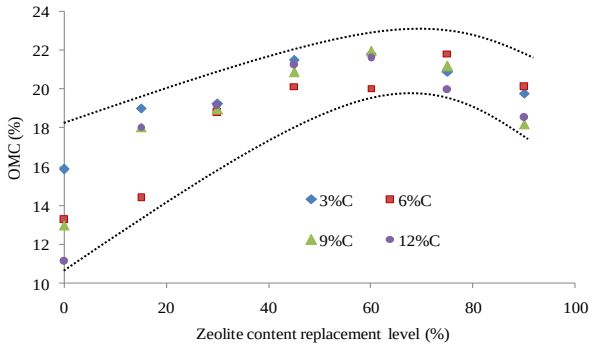

Figure 8: Variation of Optimum moisture content (OMC) of soil-cement mixtures with Zeolite content

3.8 STRESS-STRAIN CHARACTERISTICS OF MIXTURES

The stress-strain relationships obtained from UCS tests for mixtures stabilized with3% C, 6% C, 9 % C at 12% C at 0%, 15%, 30%, 45%, 60%, 75% and 90% zeolite replacement levels are presented in Figures (9-12).It is shown that the maximum axial stress increased significantly due to cement stabilization and the strain corresponding to the peak axial stress decreased. For example, at 3% C with 15% zeolite replacement level, the peak axial stress was 637.50 kN/m^{2}and strain at failure of 1.64%. When cement content was increased to 12%, at zeolite replacement of 15%, the peak stress increased considerably to 3480.90kN/m^2 with a corresponding strain of 0.66%. Thus, mixtures with the greatest strength were achieved at zeolite replacement levels of 15% for all cement content.

When additive contents were increased, large strength values were obtained for lower axial strain values. At high zeolite content (60-90%) the mixtures suffer from less effective cementation due to increase granular nature and hence yield low strength due to tensile cracking upon uniaxial loading.

The introduction of zeolite resulted in slight decrease of strain at failure. However, subsequent increase in zeolite content led to increase in the peak strain when compared to specimens treated without zeolite (Figure 13). Thus utilizing zeolite in cemented soil increases the strain at failure and reduces the brittleness of the mixtures.

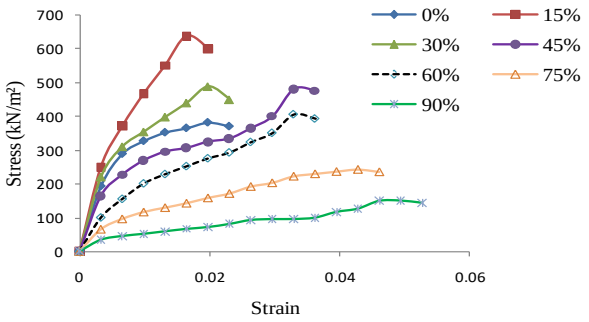

Figure 9: Stress-Strain behavior of laterite soil- 3% cement for varying zeolite content

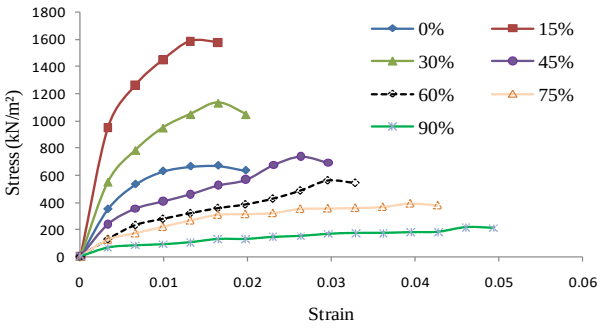

Figure 10: Stress-Strain behavior of laterite soil- 6% cement for varying zeolite content

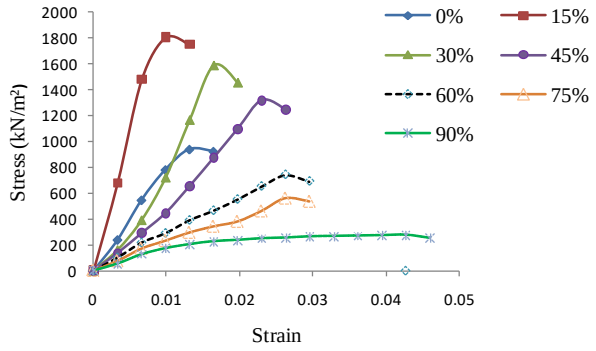

Figure 11: Stress-Strain behavior of laterite soil- 9% cement for varying zeolite content

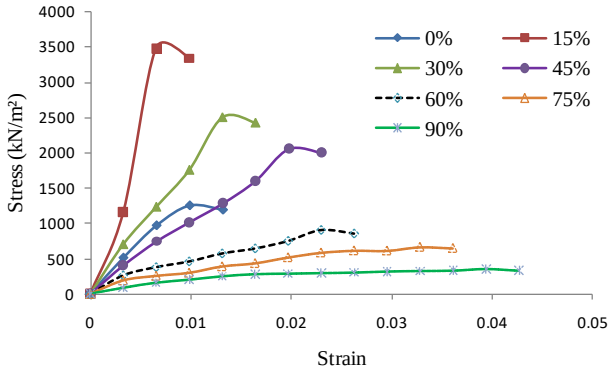

Figure 12: Stress-Strain behavior of laterite soil- 12% cement for varying zeolite content

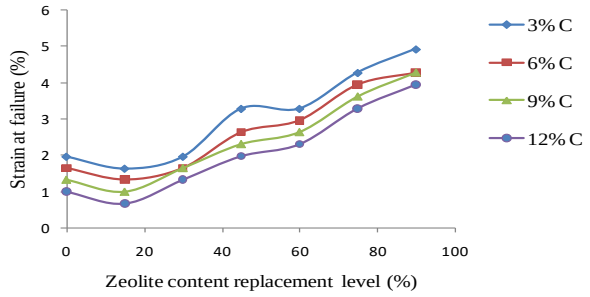

Figure 13: Variations of Strain at failure for different cement contents for varying zeolite content

4 CONCLUSION

Stabilization of a representative laterite soil was carried out using four cement contents that were replaced at 0, 15, 30, 45, 60, 75 and 90% zeolite content. From the results obtained, the following conclusions can be drawn.
The results of the tests showed that the addition of cement and zeolite improved the measured physical properties of the soilwhich indicates improved workability of mixtures after treatment. The maximum dry density (MDD) decreased between 0% - 45% zeolite replacement level and thereafter increased up to 90% replacement for all cement contents used in the study. Optimum moisture contents (OMC) on the other hand increased between 0% and 45% zeolite content at higher concentrations.

While the peak stress increased with increase in cement, the strain at failure decreased with increase in the amount of cement added to the mixture. Furthermore, both the peak stress and strain at failure were obtained in specimens containing 15% zeolite which represents remarkable improvement in the ductile behavior of the mixtures compared to the cemented samples without zeolite and this finds application in road pavement design.

REFERENCES

Amadi, A. and James, O. (2015). Lateritic soil stabilized with fly ash as a sustainable Structural material for flexible Pavement construction. 1st International Engineering Conference (IEC 2015). Book of Proceeding on Security and Environmental Challenges: The Engineering Perspectives, 277-282.

Alhaji, M. M.;Alhassan, M. Adejumo, T. E.Luka, M. H. and Abdulkadir, H. (2021). Microstructural and Strength Characteristics of Cement Treated Clay Stabilized with Zeolite for Road Base Application. IOP Conf. Series: Earth and Environmental Science 856 (2021) 012012, doi:10.1088/1755-1315/856/1/012012

Al-Swaidani. A., Hammoud. I. and Meziab. A. (2016). Effect of adding natural Pozzolana on Geotechnical properties of lime-stabilized clayey soil. *Journal of Rock mechanics and Geotechnical Engineering 8(5): 714-725, DOI:https://doi.org/10.1016/j.jrmge.2016.04.002*

Amadi, A. A (2011). Evaluating the Potential use of Lateritic soil mechanically stabilized with quarry fines for construction of road bases. Nigerian Journal of Engineering, 17(2), 1-12.

BS 3148 (1980). Standard for quality of mixing water, British Standard Institutions

BS 1377 (1990). Methods of Testing soil for Civil Engineering Purposes, British Standard Institute, London

BS 1924 (1990). Methods of tests for stabilized soils, British Standard Institute, London

BS 12 (1991). Specification for Portland cement, British Standard Institute, London

Gbadamosi, O. S.(2021). Improvement of Bearing Capacity of Lateritic Soil For Pavement Subgrade By Addition Of Rock Flour. Unpublished B.Eng Thesis in the Department of Civil Engineering, Federal University of Technology, Minna, Nigeria

Gidigasu, M.D. (1976). Lateritic soil Engineering, Elsevier scientific Publishing Co. New-York

James, O., Sadiku, S., Amadi, A.A.and Kovo, A. Effect of kaolin-based zeolite and cement on Physical Properties of Compacted Lateritic Soil. *Nigeria Journal of Engineering and Applied Sciences (NJEAS) vol.6, No. 2, 2019*

Kanyi, M. I. (2017). Cement Stabilization of Lateritic soil using Iron ore tailing as admixture. Unpublished MSC Thesis submitted to the Post-graduate school of Ahmadu Bello University Zaria, Nigeria

Liew, Y.M.; Kammarudin, H.A.; Mustapha Al Bakri, M. Luqman, M. Khairul Nizar, I. and Heah, C.Y. (2011). Investigating The Possibility Of Utilization of Kaolin And The Potential Of Met akaolin To Produce Green Cement For Construction Purposes. A Review. *Australian Journal of Basic and applied Sciences, 5(9):441-449, 2011*

Mola-Abasi, H and Shooshpasha, I (2016). Influence of zeolite and cement additions on mecha nical behaviuor of sandy soil. *Journal of Rock Mechanics and Geotechnical Engineering 8(5): 746-752, DOI:https://doi.org/10.1016/j.jrmge.2016.01.008*

Mold Khajeh, A. (2020). Triaxial behaviuor of zeolite-cemented sand. *Proceedings of the Institute of Civil Engineers- Ground Improvement 173(2): 82-92* https://doi.org/10.1680/jgrim.1800009

Rabab'ah, S.R., Taamneh, M.M., Adallah, H.M., Wusier, O.K., and Ibdah, L. (2021). Effect of Adding Zeolitic Tuff on Geotechnical Properties of Lime-Stabilized Expansive Soil. *KSCF J Civ Eng 25, 4596-4609. https://doi.org/10.1007/S 12205-021-1603-7*

Raksiri Sukkarak, Bordin Thangjaroensuk, Warat Kongkitkul and Pornkasen Jongpradist (2021). Strength and Equivalent Modulus of Cement Stabilized Lateritic with Partial replacement by Fly Ash and Rice Husk Ash. *Engineering Journal vol. 25 issue 10*

Yilmaz, B.; Uçar. A.; Öteyaka, B and Uz.V. (2007). Properties of zeolitic tuff(clinoptilolite) Blended Portland Cement, *Building and Environment, 42(11), 3808-3815*

4th International Engineering Conference (IEC 2022)
Federal University of Technology, Minna, Nigeria

EVALUATION OF HYDROLOGICAL DROUGHT IN THE UPPER BENUE RIVER BASIN

*Ogunnusi, A.[1], Jimoh, O. D[2] Adesiji, A. R[3]

[1,2,3]Civil Engineering Department, Federal University of Technology, PMB 65 Minna Niger State, Nigeria
*Corresponding author email:ogunnusialbert@gmail.com +2348056859622

ABSTRACT
Drought is a natural extreme event associated with reduced or total absence of precipitation. There have been various studies on drought occurrences in northern Nigeria that is based primarily on meteorological indices such as rainfall and evapotranspiration with little attention paid to hydrological indices such as streamflow. Nigeria, being a country with an elaborate hydrological system of rivers and streams occupying about 11.5% of the country's total surface area, indicates that the close analysis of the variations in the status of these hydrological systems can provide a veritable indication for drought events in the country. This study evaluated drought occurrence in the Upper Benue River Basin encompassing states in the North east such as Adamawa, Gombe, Taraba and parts of Borno using the Streamflow Drought Index methodology. Streamflow data was obtained from the Upper Benue River Basin Development Agency covering a period ranging between 35 to 41 years for four stations based along the river Benue and its tributaries. The quarterly SDI values was obtained for the period under review and an array of values indicating various drought intensities from mild to extreme was collated. It was observed that the years (1982, 1984, 1987, 1990) that indicated extreme droughts according to the array of SDI values obtained coincided with years that drought events were confirmed in various regions of the North. The results obtained increases the credence of the SDI methodology in ascertaining drought occurrence in the region and could serve as a veritable tool in the prediction of drought in the region.

Keywords: *Hydrological Drought, Streamflow, Streamflow Drought Index, Upper Benue River Basin.*

1 INTRODUCTION

Drought can be described as a naturally occurring extreme event that results in reduced or lack of water supply to meet the water demand of both flora and fauna in a location. The occurrence of drought, especially in the northern region of Nigeria, is well documented with records reflecting incidences in 1903/1905, 1912/1915, 1923/1924, 1942/1944, 1954/1956, 1972/1973, 1982/1983, and 1991/1995 (National Drought Plan, 2018). The devastating effect of drought is well captured by the report from Khalil (1974) on the 1973 drought which resulted in famines and the death of about 300,000 livestock in the northern region. Drought has variously been described as a creeping disaster since in most cases its effects are not sudden, resulting in the challenge of ascertaining its commencement and cessation. In order to adequately overcome this challenge various numerical indices have been evolved to capture various drought severities. According to the National Drought Plan Document for 2018, 'the frequency, severity, duration and spatial extent of drought are expected to further intensify in the coming decade because of climate change and associated risk'. Other studies have also identified the increasing threat of desertification with estimates of up to 15% of the country's total land mass being susceptible (Emodi, 2013).

Droughts can be classified into five major categories: Meteorological Drought, Agricultural Drought, Hydrological Drought, Ecological Drought and Socioeconomic Drought. Meteorological drought occurs when the natural climatic conditions of a region are distorted as a result of reduced quantity of precipitation as measured against some predetermined average, and in some cases, in combination with distortions in the normal temperature leading to increased evapotranspiration for long periods of time (Adefisan et al, 2015). Agricultural Drought occurs when reduced levels of rainfall and/or increased temperatures results in the reduction of soil moisture content thereby impacting the growth and germination of rain-fed crops and pastures (Adefisan et al, 2015). Ecological Drought results from the prolonged and widespread reduction or lack of precipitation that results in stresses in ecosystems thereby triggering feedbacks in natural and human systems (Mannocchi et al, 2004). Socio economic Droughts results from the ripple effect of the reduced or total absence of precipitation on the supply of socio-economic goods and services such as water supply, hydro-electricity, food (in terms of marine animals), agricultural products etc. Hydrological Drought relates to the long-term effect of reduced precipitation on hydrological systems such as surface and subsurface (Groundwater) water systems. Hydrological drought typically lags other forms of drought such as meteorological and Agricultural as it takes time for the effects of shortages to be noticed in hydrological systems (Abhishek et al, 2016). Whereas there are several variables

to quantify water, streamflow values remain the most significant (Nalbantis, 2008).

Typically, droughts in all its forms are characterised by severity, duration, areal extent and frequency. The SDI methodology as proposed by Nalbantis and Tsakiris (2008) reduces the four-dimensional drought severity-duration-frequency-area to a much simpler two dimensional relationship of severity versus frequency. The SDI typically transforms the streamflow values into z-scores from which the expected value (typically the mean) is set to zero and positive or negative values of the z-scores reflect corresponding states of wetness or dryness. One major challenge is identifying and selecting the ideal probability distribution function of the streamflow values (Morán-Tejeda, 2012). According to Nalbantis (2008), two probability distributions (Gamma Distributions and Log-normal Distributions) are normally considered to suitably model streamflows.

Most of the research carried out on drought in Nigeria have primarily made use of meteorological indices of rainfall and evapotranspiration (Aremu et al, 2014), (Adefisan et al, 2015), (Adakayi et al, 2016), (Ajayi et al, 2020). This research, in recognition of the elaborate hydrological system of rivers and streams in the country covering as much as 11.5% of the country's total surface area (Ita, 1993), made use of the Streamflow Drought Index (SDI) which relies solely on streamflow data of rivers and streams.

Nigeria is divided into 8 Hydrological Areas as follows: Upper Benue River Basin, Lower Benue River Basin, Niger North River Basin, Niger Central River Basin, Niger South River Basin, Western Littoral, Eastern Littoral and Lake Chad Basin.

This paper focused on the evaluation of Hydrological drought in the Upper Benue River Basin by analysing data from stations along the river Benue and some of its tributaries such Jimeta Bridge Station (River Benue), Chikito Station (River Faro), Numan Station (River Benue) and Dadinkowa Station (River Gongola).

2 METHODOLOGY

2.1 STUDY AREA

Nigeria is a country with a landmass covering about 923,769km^2 and lying between Latitudes 4° 16' N and 13° 52' N, and Longitudes 2° 49' E and 14° 37 'E (Taiwo et al, 2018) (Figure 1). The Global Positioning System coordinates indicate that the Upper Benue Hydrological basin, which covers an area of 154,328.9 km^2, is located between latitude 6°29′N to 11°46′N and longitude 8°55′E to 13°30′E. The basin is bound by the Lake Chad basin to the north, the Lower Benue and Upper Niger water shed to the west and the south and east by the Republic of Cameroun. It also has a mean elevation of 400m with a minimum and maximum elevation of 80m and 2034m respectively. (Odiji et al. 2021).

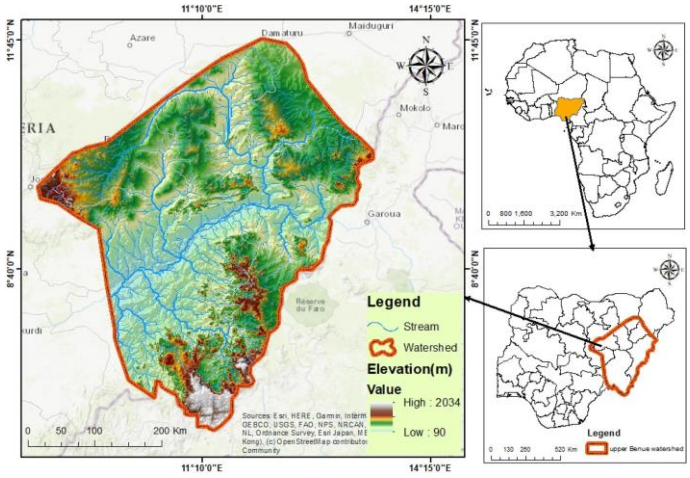

Figure 1: Location map of Upper Benue Hydrological Area culled from Odiji et al (2021)

The northern region with its mixture of tropical savannah and semi-arid climate receives rainfall for only 3-4 months annually (June - September) with a total annual precipitation of about 810mm and a relatively wide variability of precipitation values where some states, such as Kaduna, record precipitation of about 1218mm and others such as Nguru record values as low as 410mm (Adakayi et al, 2016). The region (North-East) has a mean annual rainfall in the basin ranging from 700mm to 1200 mm and a temperature range of 24℃ to 27 ℃ (Ishaku et al. 2015).

2.2 STREAMFLOW DROUGHT INDICES (SDI) CALCULATION

In calculating a Streamflow Drought Index (SDI), the indicator used is the historical monthly streamflow values of the basin. The set of data is fitted into a probability distribution function such as a Gamma function or Log normal function to define the relationship of probability to streamflow. The indices is typically a deviation from an agreed truncation level which often times is assumed to be the mean of long term historical records but other values can also be used. In order to calculate SDI, the following formula is used;

$$V_{i,k} = \sum_{i=0}^{3k} Q_{i,j} \quad i = 1, 2, 3 \ldots \quad j = 1, 2, 3 \ldots, 12$$

$$k = 1, 2, 3, 4 \ldots \ldots \ldots (1)$$

Where $V_{i,k}$ is the i th year volume of cumulative flow values. k=1 for October-December, k=2 for October-

March, k=3 for October-June, and k=4 for October-September. By using the cumulative streamflow volumes, SDI is calculated for each k and for ith hydrological year as given in Equation (2).

$$SDI_{i,k} = \frac{V_{i,k} - \overline{V_k}}{S_k} \quad i = 1, 2, \ldots,$$
$$k = 1, 2, 3, 4 \ldots\ldots\ldots\ldots (2)$$

$\overline{V_k}$ is the mean and S_k is the standard deviation of cumulative flow values for kth time period. For smaller Basins, streamflow may follow a skewed probability distribution which can be approximated by the family of Gamma distribution functions. The distribution is then normalised. (Nalbantis, 2008)

TABLE 1. DEFINITION OF STATES OF HYDROLOGICAL DROUGHT WITH SDI

State	Description	Criterion	Probability (%)
0	Non-Drought	SDI ≥ 0.0	50.0
1	Mild- Drought	-1.0 ≤ SDI <0.0	34.1
2	Moderate- Drought	-1.5 ≤ SDI <-1.0	9.2
3	Severe- Drought	-2.0 ≤ SDI <-1.5	4.4
4	Extreme- Drought	SDI < -2.0	2.3

3 RESULTS AND DISCUSSION

Streamflow data was obtained for four stations covering a period of between 35 – 41 years. As it is typically the case, the stations had various percentages of missing data as follows: Jimeta Bridge (6%), Chikito (16%), Numan (25%) and Dadinkowa (30%). In order to fill in these missing values, the Multivariate Imputation by Chained Equation (MICE) methodology was adopted. The result obtained for each of the stations are available on request from the corresponding author. However a chart of the average monthly streamflows for each of the stations is as shown in figure 1

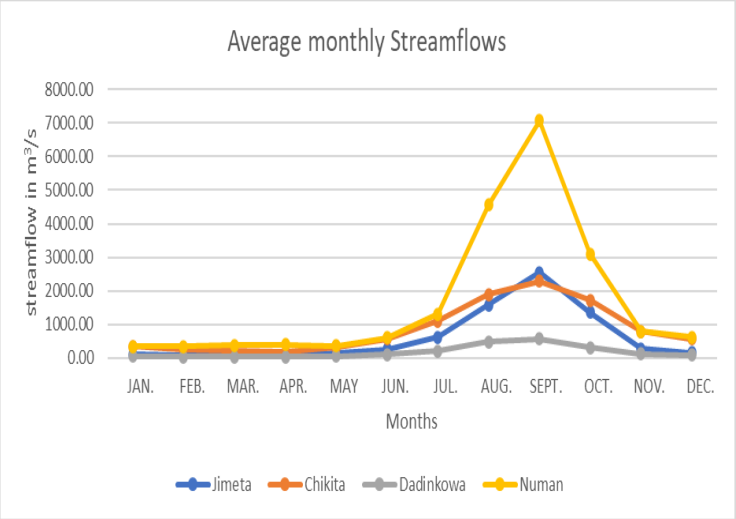

Figure 1: Average monthly streamflows for four select stations

The quarterly SDI values for each of the stations (Jimeta Bridge, Chikito, Numan and Dadinkowa) are as shown in the charts represented in figures 2 to 5.

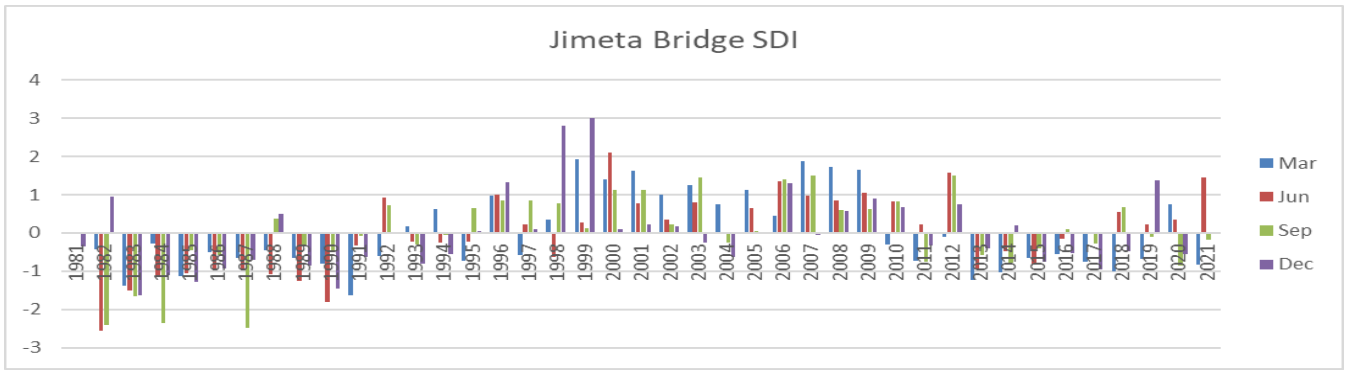

Figure 2: Quarterly SDI values for Jimeta Bridge Station

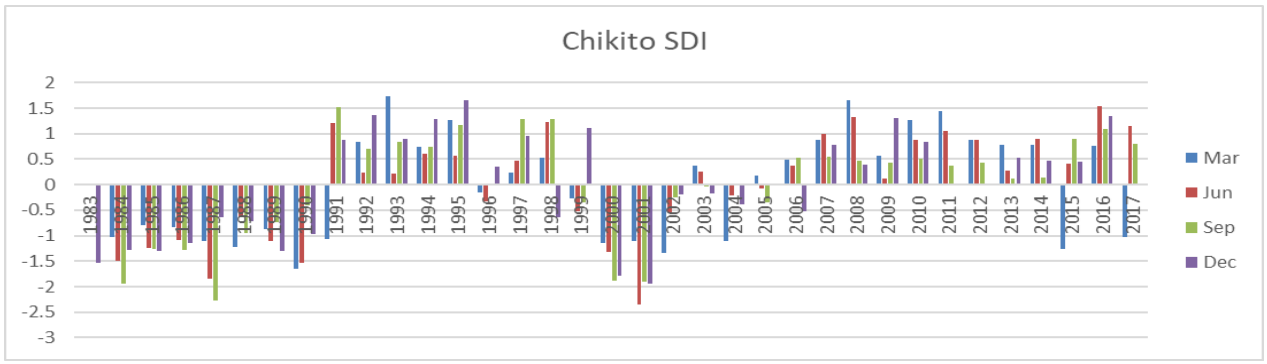

Figure 3: Quarterly SDI values for Chikito station

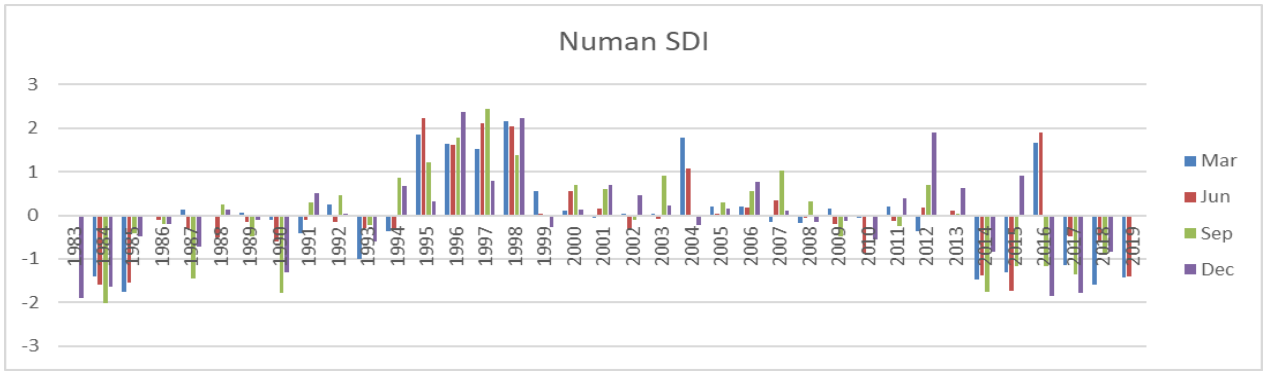

Figure 4: Quarterly SDI values for Numan station

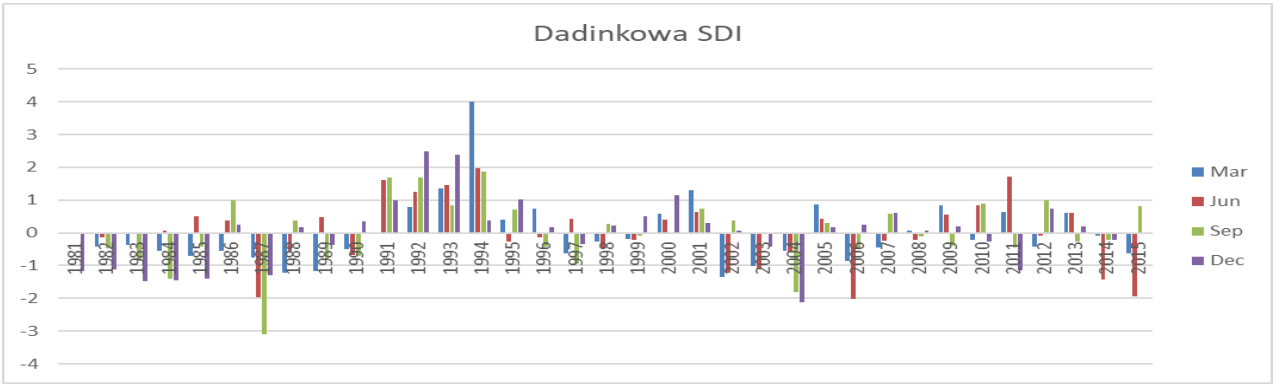

Figure 5: Quarterly SDI values for Dadinkowa station

The summary of results obtained from the four stations shown in table 6 reflects the years when various intensities of droughts, from moderate to extreme was observed, over the period under consideration.

TABLE 2: DISTRIBUTION OF STATIONS AND DROUGHT OCCURRENCES

Station	Years with extreme drought	Years with severe drought	Years with moderate drought
Jimeta Bridge	1982, 1984, 1987	1983, 1990, 1991	1983, 1984, 1985, 1988, 1989, 1990, 2014
Chikito	1987, 2001	1983,1984, 1987, 1990, 2000, 2001	1984, 1985, 1986, 1987, 1988, 1989, 2000, 2001, 2002, 2004, 2015, 2017
Numan	1984	1983, 1984, 1985, 1990, 2014, 2015, 2016, 2017, 2018	1984, 1987, 1990, 2014, 2015, 2016, 2019
Dadinkowa	1987, 2004, 2006	1987, 2004, 2015	1981, 1982, 1983, 1984, 1985, 1987, 1989, 2002, 2003, 2011, 2014

The results obtained across three of the stations (Jimeta Bridge, Chikito, Numan) indicate that severe to extreme droughts occurred in the region in the years 1983, 1984, 1987 and 1990. The result from the Dadinkowa station shows a deviation from the others as Dadinkowa is located in Gombe State along river Gongola as a dam outlet as shown on figure 5.

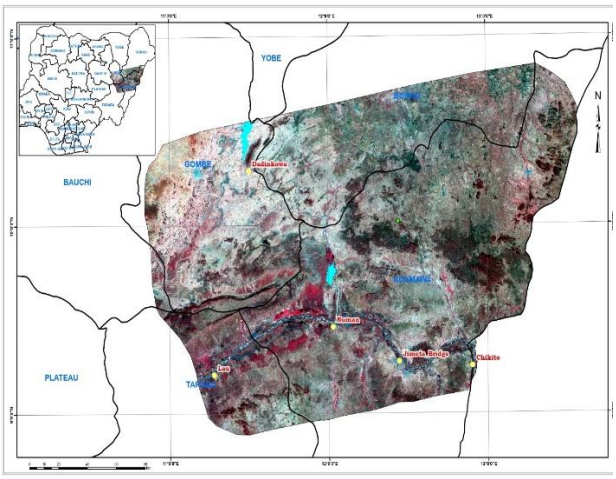

Figure 6: Map of region showing the location of stations along the river systems

The array of results reflected in the evaluation using the Streamflow Drought Index (SDI) methodology correlates with confirmed occurrences of droughts as reported by Mortimer, 1989 that the year 1987 recorded extreme droughts that led to huge crop losses in the Northern region. In a similar vein, Oladipo, 1993 in his paper titled 'Some Aspects of the Spatial Characteristics of Drought in Northern Nigeria' stated that the '1980s were characterised by more extensive, more severe and more persistent droughts than the previous decades. The decade witnessed persistent droughts in the region beginning in 1982. Severe droughts became more extensive covering about 40% of the region in 1983 and 1987. More than half of Northern Nigeria was affected by moderate to severe droughts in each of the years between 1982 to 1987'. Likewise, Eze, 2018 in his research on 'Drought occurrences and its implications on the households in Yobe state, Nigeria', using the Normalised Rainfall Index methodology identified that extreme droughts occurred from data sourced from Maiduguri, Potiskum and Nguru stations in 1987.

4 CONCLUSION

In conclusion, given the correlation of results obtained using the Streamflow Drought Index methodology for evaluating Hydrological Drought in the Upper Benue region with drought occurrences as confirmed by other researchers using other methodologies, which are primarily meteorological, the SDI methodology can serve as a veritable tool for drought prediction and management in the region.

ACKNOWLEDGEMENTS

This is to acknowledge the contribution of Bayo Omoyajowo and Caleb Odiji of the National Space

Research and Development Agency for provision of the regional map of the Upper Benue River Basin.

REFERENCE

Adefisan, E. A., & Abatan, A. A. (2015). Agroclimatic Zonning of Nigeria Based on Rainfall Characteristics and Index of Drought Proneness. Journal of Environment and Earth Science,5,115-128. http://www.iiste.org/Journals/index.php/JEES/article/viewFile/23310/24056

Emodi E. E (2013). Drought and Desertification as they affect Nigerian Environment. J. Environ. Manage. Saf. 4(1): 45-54.

Eze, Jude. (2018). Drought occurrences and its implications on the households in Yobe state, Nigeria. Geoenvironmental Disasters. 5. 10.1186/s40677-018-0111-7.

FME. (2018). National Drought Plan. Federal Ministry of Environment, Abuja (https://knowledge.unccd.int/sites/default/files/country_profile_documents/1%2520FINAL_NDP_Nigeria.pdf)

Idu A J (2015) Threats to Water Resources Development in Nigeria. J Geol Geophys 4: 205. doi:10.4172/2329-6755.1000205

Ishaku J M, Ankidawa B A, Abbo A (2015) Groundwater quality and hydrogeochemistry of Toungo Area Adamawa State North-Eastern Nigeria. Am J Min Metall 3(3):63–73. https://doi.org/10.12691/ajmm-3-3-2

Ita E O (1993). Inland Fishery Resources of Nigeria. CIFA Occasional Paper No 20. Rome, FAO. 1993. 120p (https://www.fao.org/3/t1230e/T1230E02.htm)

Khalil, I. M. (1974). North-Eastern State report on long term measure to combat drought. Government Printer, Maiduguri

Mannocchi, F. & Francesca, Todisco & Vergni, Lorenzo. (2004). Agricultural drought: Indices, definition and analysis. IAHS-AISH Publication. 246-254.

Morán-Tejeda, S. M.-S.-M.-L.-M. (2012). Accurate Computation of a Streamflow Drought Index. *Journal of Hydrologic Engineering, 17*, 318-332. doi:10.1061/(ASCE)HE.1943-5584.0000433

Mortimor, M. (1989). Adapting to Drought: Farmers, Farmine, Desertification in West Africa. Cambridge: Cambridge University Press.

Nalbantis I. (2008). Evaluation of a Hydrological Drought Index, European Water 23/24, 67-77.

Nalbantis, I., Tsakiris, G. (2008). Assessment of Hydrological Drought Revisited. Water Resources Management.; DOI 10.1007/s11269-008- 9305-1

Odiji, Caleb & Olaide, Aderoju & Eta, Joe & Shehu, Idris & Mai-Bukar, Adama & Onuoha, Hilda. (2021). Morphometric analysis and prioritization of upper Benue River watershed, Northern Nigeria. Applied Water Science. 11. 10.1007/s13201-021-01364-x.

Olatunde, Adewale & Aremu, J. K. (2014). The Extent and Intensity of Extreme Drought in Some Parts of the Savanna Region of Nigeria. Journal of Developing Countries. volume 4. 1-7.

Olukayode Oladipo, E. Some aspects of the spatial characteristics of drought in northern Nigeria. Nat Hazards 8, 171–188 (1993). https://doi.org/10.1007/BF00605440

Pathak, Abhishek & Channaveerappa, & Dodamani, B.M.. (2016). Comparison of two hydrological drought indices. Perspectives in Science. 8. 10.1016/j.pisc.2016.06.039.

4th International Engineering Conference (IEC 2022)
Federal University of Technology, Minna, Nigeria

A facile approach towards Hierarchical Zeolite Y Synthesis from Inexpensive Precursor

Usman, R. A.[1], Kovo, A. S.[1,2], Abdulkareem, A. S.[1,2] and Garba, M. U.[1]
[1]Department of Chemical Engineering, Federal University of Technology, PMB. 65, Minna, Niger State, Nigeria
[2]Nanotechnology Research Group, Africa Center of Excellence for Mycotoxin and Food Safety, Federal University of Technology, PMB 65, Minna, Niger State, Nigeria
*Corresponding author email: rukiyausman3@gmail.com +2348063320311

ABSTRACT
Microporous zeolite is one of the most utilized heterogeneous catalysts in many chemical reactions in process industries. It has a unique selectivity property, stability in high thermal reactions, and porosity to enhance the chemical reaction. The micropore associated with the conventional zeolites poses some constraints in a reaction involving a bulky reactant, thereby causing the deactivation of the zeolite catalyst. Therefore, a hierarchical structured zeolite catalytic material was proposed to overcome this constraint as it has pores of different dimensions that can overcome inaccessibility experienced in the smaller pore zeolites. This work synthesized a hierarchical zeolite Y catalyst using a poorly crystalline inexpensive Aloji Kaolin from Nigeria as an aluminosilicate material through a modified Top-down approach. The zeolite Y was initially prepared from the kaolin via the hydrothermal method and then followed by desilication using a mild sodium hydroxide solution. The synthesized hierarchical zeolite Y was characterized with the aid of powder X-ray diffraction (XRD), field emission scanning electron microscopy (FESEM), high-resolution transmission electron microscopy (HRTEM), and Brunauer-Emmett-Teller (BET) analysis. The synthesized hierarchical Y has a crystallite size of 35.67nm, 11.0112m^2/g, pore volume of 0.040299cm3/g, and pore size of 132.364Å or 13.236 nm.

Keywords: *Aloji Nigeria Kaolin (ANK); Conventional zeolites; Desilication; Hierarchical zeolites;Post-synthesis modification*

1 INTRODUCTION

Zeolite catalyst possesses unique structural patterns of regular arrays of pores, cages, channels, and cavities of dimensional molecular orders. Zeolite Y is mainly used as a catalyst due to its acidity, unique pore structures, and high thermal and hydrothermal stability (Sukrawati *et al.*, 2022). The application of zeolite catalysts depends mainly on their micropores which possess some constrain to bulky reactants and products. However, the small pore sizes restrict molecular diffusion and mass transport within zeolite crystals and prohibit large molecules from accessing the intra-crystalline active sites (Dorien *et al.*, 2020). Consequently, adsorption processes and catalytic reactions based on zeolites are often limited by slow diffusion, and zeolites cannot catalyze reactions involving large molecules.

Developing hierarchical Zeolite with qualities such as a longer lifetime, high catalytic performance, postponed coking, and deactivation will reduce the constrain observed in the conventional zeolite catalyst. Hierarchically structured zeolites combine the qualities of microporous zeolites and mesoporous materials to offer enhanced molecular diffusion and mass transfer without compromising the zeolites' inherent catalytic activities and selectivity. The difference in their physical properties, mainly pore size distribution, defines them. It contains more types of pores of different sizes (micropores, mesopores, and macro-pores) which can overcome the transport limitation of the smaller pore' zeolites. It encompasses Zeolite with at least a secondary pore–structure system (Dorien *et al.*, 2020). There are two methods of creating interconnectivity of mesoporous and microporous pore systems in zeolites. There are two main approaches in hierarchical zeolite production, top-down and bottom-up. Top-down methods are used when available, or commercial zeolites are treated to create additional pores by etching part of it. The bottom-up approach is the creation of an additional pore in the zeolites during the synthesis of the zeolites by incorporating a pore-directing substance (Mesoporogen) in the precursor gel. Hierarchical zeolites are synthesized mainly by either desilication or recrystallization of commercial zeolites (Neda *et al.*, 2021). Developing hierarchical Zeolite aims to obtain a catalyst with improved properties over the conventional microporous counterpart to enhance their performance (Vijaya *et al.*, 2020). The hierarchical type zeolite is essentially more active. It performs better in diffusion-constrained reactions, such as those involving the transformation of a larger substrate or in the liquid phase. They have activity, stability, selectivity, regenerability, longer lifetime, postponed coking, and deactivation. The post-treatment of microporous zeolites enhances the catalytic performance and lifetime (Zhang *et al.*, 2017). There are many approaches to introducing mesopores into zeolites in the post-treatment of parent zeolites. The top-down method includes dealumination steam treatment Dissolution-

Recrystallization) and desilication (Ming *et al.,* 2022). The zeolites have a nominal deactivation rate due to the high external surface area, mesopore volume, and pore mouth. Using NaOH to introduce mesopores in a zeolite through desilication has yielded a significant impact (Lingyu *et al.,* 2022; Tewdros *et al.,* 2021). The alkaline treatment of zeolites Y mostly at 1-2 wt% NaOH at room temperature has revealed incredible mesopores formation as detected in the modification that led to Si-O-(OH)-Al bond.

The silica extraction formed a framework structure, creating a different tetrahedral framework, lewis acidic aluminium (Ping et al., 2021). Other reagents have introduced mesopores in zeolites synthesis: Cetylmethlylammonium bromide (CTAB), Oxalic acid, NaHCO (Dongpong *et al.*, 2021). These reactions mainly occur in the presence of surfactants and involve high synthetic costs. Desilication processes to introduce mesopores have mainly been conducted using commercial zeolites (Hue-Tong *et al.,* 2020; Imbachi-Gamba *et al.,* 2021). Hierarchical zeolite Y in this work was synthesized by post-treatment of a conventionally synthesized zeolite Y from Aloji Nigeria kaolin (ANK) by mild sodium hydroxide solution and protonating with ammonium sulphate. Researchers in the past two or three decades have investigated the suitability of kaolinite minerals for zeolite catalyst synthesis. The synthesis of hierarchical mesoporous zeolites from kaolin is yet an unexplored area. Using kaolin for producing hierarchical zeolites catalyst is a research area that is just evolving. This work investigates ANK as a potential source of silica and alumina for developing hierarchical zeolites Y.

2 METHODOLOGY

2.1 Synthesis of Hierarchical Zeolite Y by Modified Top-down Approach (Desilication)

These procedures are modifications of the work of Van Aelst, *et al.* (2015) using a locally sourced, poorly crystalline kaolin Aloji kaolin as a source of aluminosilicate material and desilicating with a mild solution of NaOH. Raw Aloji kaolin was beneficiated and calcined at 650 ^{o}C for 3 hours. Sodium hydroxide pellets of mass 1.3 grams was dissolved in 2 grams of distilled water. The solution was divided into two halves. 2.46 grams of sodium metasilicate was added to one half and 1.0 gram of metakaolin to the other half. The two mixtures were stirred for complete dissolution. The combined aluminosilicate gel was aged at 10 hours and crystalline in a Teflon-line stainless steel autoclave at 80 ^{o}C crystallization temperatures for 9 h. The crystallized Zeolite was washed with deionized water to a pH of 9 and dried at 1100 C for 8 h. The as-synthesized Zeolite was desilicated to hierarchical Zeolite. A gram of synthesized conventional Zeolite from ANK was treated with a mild 0.2M Sodium hydroxide solution at 65 ^{o}C for 30 min. This hierarchical Zeolite was washed with deionized water to a pH of 9 and dried at 110 ^{o}C for 8h. This mesoporous zeolite Y was protonated by ion exchange with 10ml 1.0 M NH_2SO_4 solution per gram of synthesized Zeolite by soaking in the above solution for 24 h. The sample was filtered, dried in the oven at 100 ^{o}C for 3 h, and calcined at 550 ^{o}C for 3h. This hierarchical zeolite catalyst was denoted YT5 and characterized by XRD, SEM., and BET.

3 RESULTS AND DISCUSSION

3.1 Refining and Dehydroxylation of Kaolin

The SEM images show kaolinite and a considerably high amount of quartz. The angular orientation of SEM of raw ANK denotes the increased occurrences of quartz within the clay. Quartz is an insoluble mineral that exists within the kaolinite mineral. The SEM image of the refined ANK shows a platy morphology and hexagonal outline and is loosely packed, which are attributes of kaolinite clay. ANK's elemental composition has a Si/Al ratio of approximately I.12.as indicated by the EDX Spectrum in figure 1. The ANK a poorly crystalline kaolinite mineral with appreciable quartz content compared to kaolin sourced from Chokocho, Kankara, Egypt, Iraq and England with Si/Al ratio of 2.0, 1.23, 1.66, 1.53 and 1.17 respectively (Victor *et al.,* 2020).

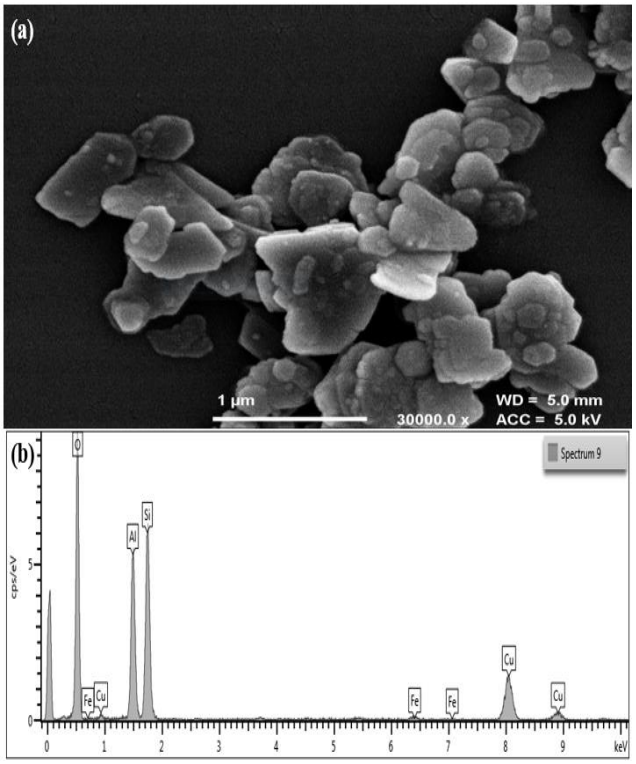

Figure: I SEM image and EDX spectra of Refined Aloji kaolin

3.2 Synthesis of Hierarchical Zeolite Y by modified Top Down Approach

The results obtained from the characterization of as-synthesized zeolites Y (YT5) were as follows. The XRD plots of as-synthesized Hierarchical zeolites Y obtained by top-down approaches with YT5 synthesized using 1.3 grams of NaOH, crystallized at 110 ºC for 9 hours after ageing 10 hours. The peaks at 2 theta values of 6,13º, 10.34º, 12.14º, 14.65º, and 15.97º, and more denotes zeolites Y, as depicted in figure 2. However, the peaks of 26.65º and 36.55º denote quartz, which is an impurity in synthesizing zeolites from kaolin. The crystallite size of 35.77nm was calculated from the XRD Pattern of YT5 Zeolite with a percentage crystallinity of 85.12%.

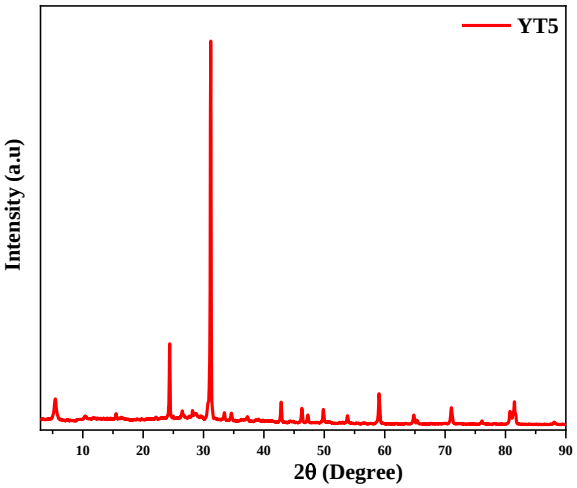

Figure 2: The XRD Pattern of Hierarchical zeolites Y (YT5).

SEM image of YT5 zeolites showing a plate-like morphology arranged in a cubohedral interlayered manner of hierarchical zeolites Y (Bastian *et al.*, 2022). A high silica layered zeolite Y and high Si/Al ratio (Dorien *et al.*, 2020). The EDX spectra revealed the elemental composition of YT5 Zeolite, showing the presence of Fe, Ti, S, and Na. These elements are the impurities in the kaolin, which depend primarily on the source of the kaolin. However, the high percentage of Si in YT5 Zeolite is expected of a faujasite zeolites framework (Dorien *et al.*, 2020). They observed that the zeolite catalyst's framework composition (Si/Al ratio) could be tuned from 1 to infinite by altering the hydrothermal synthesis or post-synthetic modifications. The diameter distribution was obtained. The higher distribution between 50 to 470nm gives an average crystallite diameter of 225.19nm.

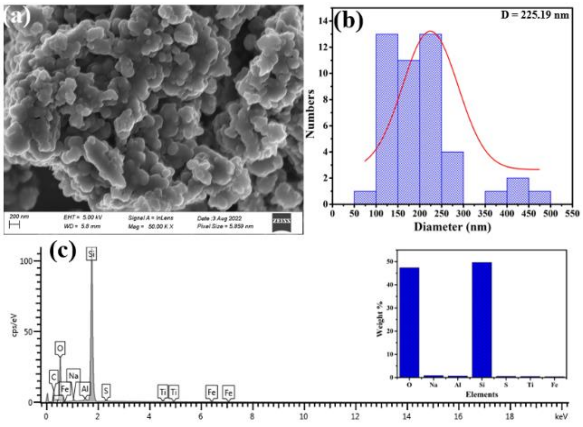

Figure 3: SEM image (a), crystallite diameter distribution (b) EDX spectra and Elemental percentage weight of YT5 Zeolite

Nitrogen adsorption has been used to analyze porous materials' surface area and pore size distribution. The pore size distribution, surface area, and pore volume are the catalyst's core characteristics determining the selectivity and accessibility of probing molecules during a catalyzed reaction. The catalyst's porosity determines the thermodynamics and transport of molecules in and out of the catalyst. The BET analysis of YT5 was conducted, and the following results were obtained. The gas adsorption-desorption isotherm was plotted and shown in the figure 4

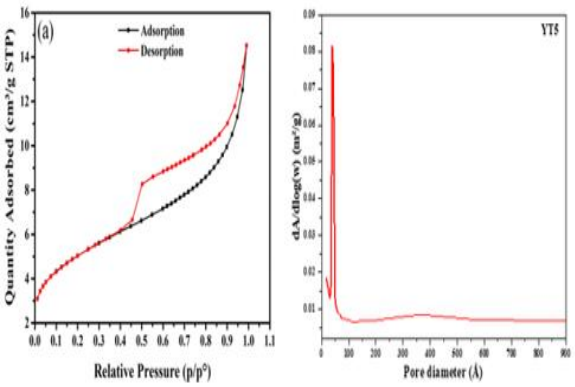

Figure 4: Nitrogen adsorption–desorption isotherm loops and BJH of YT5.

According to the IUPAC classification for a porous material, the adsorption isotherm is a type IV and hysteresis of H4. The hysteresis H4 is associated with narrow pores and connected internal voids of irregular shape. The narrow hysteresis loop observed at a low-pressure region of p/pº of less than 0.2 is evidence of the presence of mesopores (Younesse *et al.*, 2021). A hysteresis loop at a high-pressure region of p/po greater than 0.4-1. indicates mesopores and macropores in the as-synthesized zeolite YT5. This indicates silicon extraction

by the mild alkaline treatment of the synthesized hierarchical Zeolite. However, the adsorption capacity of YT5 is moderate due to the presence of quartz in the as-synthesized zeolites. The as-synthesized zeolite YT5 has a BET surface area of 11.0112m^2/g, pore volume of 0.040299cm^3/g, and pore size of 132.364Å or 13.236nm. The increase in the mesopores surface area of YT5 after the desilication steps proves there was a high dispersion of pore size in YT5 (Stephen *et al.*, 2021). However, the pore size and volume observed in YT5 zeolites are due to dissolution and partial amorphization during mild alkaline treatment. The etching and the partial amorphization of the framework lead to the blocking of pores with debris and silicon scraps etched from the framework. The Barret-Jovner-Halenda (BJH) pore size distribution derived from the desorption branch of the isotherm revealed the presence of multi-modal and hierarchical porosity. The sample YT5 has its highest peaks at <50Å and pore size ranging from 5nm to 90nm. The reduced micropore in YT5, due to the desilication with 0.2M NaOH solution, resulted in larger pores of 900Å. Aloji Nigeria kaolin has been utilized to develop a hierarchically structured zeolite Y.

4 CONCLUSION

Hierarchical zeolite Y was successfully synthesized from poorly crystalline Aloji kaolin for the first time by modified desilication of parent zeolite synthesized from Aloji kaolin using 0.2M of sodium Hydroxide solution at 65ºC for 30 minutes. The synthesized Zeolite's structure and morphology were characterized with BET, XRD, FESEM, and HRTEM. The results suggested that the modified top-down method could create pores ranging from 2 nm to 90 nm, as observed in the BJH plot for pore size distribution. A hierarchical zeolite Y with a micro-mesopore was synthesized with a spherical shape, polycrystalline structure, and numerous grains. The mesopores zeolites Y has a crystallite size of 35.67nm, average crystallite diameter of 225nm, BET surface area of 11.0112m^2/g, pore volume of 0.040299cm^3/g and pore size of 132.364Å or 13.236nm.

Funding

The author funded this research with no external funding

Conflict of interest

This research is solely the authors' work, and they declare no conflicts of interest.

REFERENCE

Bastian R., Tobias W., Wilhelm S. & Alexandra I. (2020). Layer-like FAU-type zeolites: A comparative view on different preparation routes. (Review) *Frontiers of Chemical Science and Engineering, 14,* 127–142

Dongping Z., Andac A., Yi C., Yinxu W. & Ruzhen X. (2021). Highly efficient removal of Cu(II) using mesoporous sodalite zeolite produced from industrial waste lithium-silicon-fume via reactive oxidation species route. *Journal of Cleaner Production, 319,* 128682

Dorien K., Brent S., Jonathan V. W., Qiang Z., Jihong Y. & Bert F. S. (2020). State of the Art and Perspectives of Hierarchical Zeolites: Practical Overview of Synthesis Methods and Use in Catalysis (Review). *Advanced Material,* 2004690

Hue-Tong V., Florian M. H., Michael G., Noemi L., Javier G. & Roger G. (2022). Enhanced activity of a bifunctional Pt/zeolite Y catalyst with an intracrystalline hierarchical pore system in the aqueous-phase hydrogenation of levulinic acid. *Chemical Engineering Journal, 430*(2), 132763

Imbachi-Gamba C. F. & Villa A. L. (2021). Statistical analysis of the influence of synthesis conditions on the properties of hierarchical zeolite Y. *Material today Chemistry, 20,* 100442

Lingyu T., Roya H., Benedettade C., Martina D., Laura P., Marco S., Ramin K. & Paolo D. F. (2022). Guaiacol hydrotreating with in-situ generated hydrogen over ni/modified zeolite supports. *Renewable Energy, 182,* 647-658

Ming L., Gen L., Shuo Z., Xionghou G., Bo Z., Xueyun B., Hongtao L. & Honghai L. (2022). Organic-Free Synthesis of Hierarchical ZSM-5 via a Combined Strategy of Unstable Precursors and Postsynthesis Steam Treatment. *Industrial & Engineering Chemistry Research, 61(17),* 6057-6064.

Neda K., Ali F., Nagihan D. & Aligholi N. (2021). Synthesis of multiple-template zeolites with various compositions and investigation of their catalytic properties. *Research on Chemical Intermediates 47*(12), 4957-4984.

Ping Z., Sebastian M., Shunmugavel S. & Anders R. (2021). Modification of commercial Y zeolites by alkaline-treatment for improved performance in the isomerization of glucose to fructose. *Molecular Catalysis, 510,* 111686

Stephen O., Chrispin K., Fredrick K. & Robert M. (2021). Effect of Kaolin Pre-treatment methods and NaOH level on the structure and properties of Kaolin derived Faujasite Zeolites. *Material Advance, 2,* 5997 -6010

Sukrawati A., Sumari S., Santoso A. & Tasya T. (2020). The Effect of Aging and Crystallization Time on the Synthesis and Characteristics of Zeolite-Y from

Malang-Quartzite Silica. *IOP Conference Series Materials Science and Engineering, 833*(1), 012060

Tewodros K., Dada M A., Islam A. K. & Vuppaladadiyam E. A. (2021). Thermo-catalytic co-pyrolysis of ironbark sawdust and plastic waste over strontium loaded hierarchical Y-zeolite. *Journal of Environmental Management, 299*, 113610

Van Aelst J., Verboekend D., Philippaerts A., Nuttens N., Kurttepeli M., Gobechiya E., Haouas M., Sree S., Denayer J., Martens J., Kirschhock C., Taulelle F., Bals S., Baron G., Jacobs P. & Sels B. (2015). Catalyst Design by NH4OH Treatment of USY zeolite. *Advanced Functional Materials, 25*, 7130-7144.

Victor P. M., Kenneth K. D. & Joshua L. K. (2020). Synthesis of Zeolite X from Locally Sourced Kaolin Clay from Kono-Boue and Chokocho, Rivers State, Nigeria. *Advances in Chemical Engineering and Science, 10*(4), 399-407.

Vijaya K., Ramesh K. & Vijayakumar V. (2020). Synthesis and characterization of stable ZnO nanoparticles using imidazolium-based ionic liquids and their applications in esterification reaction. *Indian Journal of Chemistry, 57A*, 1112-1120.

Younesse H., Hicham M., Said M., Youssef T., Rachid B., Mina O. & Hassan H. (2021). Effect of Sodium Hexafluorosilicate Addition on the Properties of Metakaolin Based Geopolymers Cured at Ambient Temperature. *Silicon 13*(5), 1441-1451.

Zhang J., Bai S., Chen Z., Wang Y., Dong L., Zheng H., Cai F. & Hong M. (2017). Core-shell zeolite Y with ant-nest like hollow interior constructed by amino acids and enhanced catalytic activity. Journal of Materials Chemistry. *Materials for Energy and Sustainability, 5*(39), 20757–20764.

4th International Engineering Conference (IEC 2022)
Federal University of Technology, Minna, Nigeria

Fuzzy Logic-Based Electrical Energy Management of Building

*Abdul-Azeez Dauda[1], Stephen Oyewobi[1], Umar Suleiman Dauda[2], & Farouq E. Shaibu[1]
[1]Department of Telecommunication Engineering, Federal University of Technology, Minna
[2]Department of Electrical and Electronic Engineering, Federal University of Technology, Minna

*Corresponding author email:abdulazeezdauda6@gmail.com

ABSTRACT
The modern trend in electrical energy distribution is the soft island system. Manual and conventional procedures struggle when dealing with multiple sources, loads, and constraints because they need intelligence to perform at their best. This work, therefore, proposes an intelligent fuzzy logic-based controller for building energy management system that controls solar panel and inverter, grid, battery and inverter, and generator in a way that prioritizes the use of the cleanest and most affordable source. To simulate the developed system in MATLAB Simulink, real data from offices in the engineering complex of Niger State Polytechnic Zungeru, Nigeria, was used. Results showed that when compared to the conventional distribution board, the developed algorithm conserved power by 33.71%.

Keywords: *Energy management system, Fuzzy logic control, energy efficiency.*

1 INTRODUCTION

From the time when people first started using stones and sticks to this current era of rapid industrialization, energy has been a vital resource. The world's energy consumption increased quickly, by 151%, from the final decade of the 20th century to the start of the 21st (Ibrahim *et al*., 2022). Nigeria is experiencing a severe lack of access to electricity. The issue is widespread across the majority of the nation; in rural areas, there are more power outages and supply seizures,(Dunmade, 2021). Due to the necessity of an uninterrupted electricity supply for socioeconomic development, electrical energy is essential to every aspect of modern life (Olanite and Nwohu, 2022).

Electrical energy management is becoming more significant as a result of worries about global warming and energy scarcity; this system aids in reducing the demand for electricity, particularly during times of peak load,(Saba *et al*., 2016). A wise and efficient use of electrical energy to maximize profits and minimize costs, thereby enhancing competitive position in the global economy, can be referred to as electrical energy management practices,(Saba *et al*., 2018) .

Decongesting the grid, allowing for alternative energy sources, creating distribution boards that can switch between power sources dynamically, and load segmentation are ways to accomplish this. Smart energy management systems (SEMS) have received a lot of attention recently due to their potential to autonomously control power consumption without human intervention. Though numerous studies on SEMS, including those on smart grid, smart meters, smart distribution algorithms, and various Internet of Things (IoT) applications on electric power management have been conducted, as discussed in the literature review section, this work aims to improve the current smart distribution algorithms in order to not only provide a dependable power supply but also significantly reduce energy consumption from the grid.

The remainder of this paper is divided into the following sections. Section 2 investigates some related works on smart energy systems, Section 3 discusses the methodology used in the design of the proposed fuzzy logic-based electrical energy management of buildings, The experiment's data are presented in section 4, the results are examined in section 5, and the paper is concluded in section 6.

This work suggests a fuzzy logic control that can intelligently select from the four sources—solar and inverter, grid, battery and inverter, and generator—to provide energy to the load while taking into account the preferred source that is currently available and the best combination in the event that multiple sources are used under various load conditions.

2 LITERATURE REVIEW

You This section discusses various research studies on smart energy systems. (Krishna *et al*., 2018) for example presented a smart energy management system to automatically switch over light and medium loads to it. A domestic consumer's daily energy consumption decreased to 35% because of a more than 50% reduction in the grid's midday energy consumption. Similarly, a smart home energy management system (SHEMS) was created by (Mubdir *et al*., 2016) to reduce energy consumption by identifying residential activity and categorizing it as either active, away, or asleep. The system has an energy efficiency of up to 18%.

(Uddin and Islam, 2018) proposed a fuzzy logic-based intelligent management controller that will be able to supply any excess power to the grid that is available. The system can function as a universal system and exchange power with the nearby grid. A fuzzy logic control (FLC) algorithm was created (Hettiarachchi *et al*., 2017), in

order to apply fuzzy logic in the AC and DC bus bar control to determines the constraints and identifies the required scenario.

For the hybrid energy storage system (HESS) based on batteries and supercapacitors to function as effectively as possible, (Gamage *et al*., 2018) develop algorithms. Depending on the battery's state of constraint, it determines the ideal HESS charging and discharging rate. The battery was used to balance the energy requirement over extended periods while the supercapacitors handled transient power primarily. a sophisticated control strategy for managing and regulating the flow of hybrid renewable energy (HRE) in rural applications was presented by (Meje *et al*., 2020). While meeting the needs of various loads and simultaneously storing extra energy in the battery, it regulates the power flow between the sources. The development of energy management system (EMS) to maintain the battery state of charge within a safe range while minimizing changes to the grid profile (Arcos-Aviles *et al*., 2018). In order for the EMS to react quickly to MG energy changes, the battery SOC is set to 75% of the rated battery capacity.

(El Zerk *et al*., 2018) proposed a robust control technique to supply load by ensuring the availability of power on demand, enhancing the quality of the generated power, and stabilizing the AC/DC Bus to improve the dynamic behavior of the hybrid system. By utilizing a combination of renewable energy sources PV/Wind and batteries as a storage system, the system's regulation of DC voltage, maintenance of the batteries at admirable intervals, and supply even with wind and irradiation fluctuation or load changes are all ensured.

In order to instantly and continuously monitor electrical data online, (Ramalingam *et al*., 2019) developed EMS. Both domestic and commercial users can easily set up its cloud-based embedded system-based communication gateway. It simultaneously reduces standby power consumption and the power outlet.

(Prathyush and Jasmin, 2018) developed a 25-rule FLC for use in an EMS for a grid to maintain the battery's state of charge within allowed bounds while lowering grid power profile deviations and lowering power variations. It lowers the microgrid's running expenses. (Zand *et al*., 2020) managed the power of a hybrid FC, battery, and capacitor using a wavelet conversion-based method. It is easy to manage the optimized power because the wavelet conversion can optimally distribute power at various frequencies to relevant sources. Supercapacitors and batteries are used as backup energy sources, with FC acting as the main source.

In order to give families comfortable services and boost uninterrupted electricity production, (Sultan *et al*., 2021) developed SHEMS. With demand rationalization, it provides a smooth, continuous electrification operation in housing developments, which facilitates a decrease in the price of energy generation. (Tuomela *et al*., 2021) proposed HEMS that can use renewable energy to shift energy demand to off-peak hours. Energy effectiveness increased.

3 METHODOLOGY

This describes the methodology and steps for the suggested fuzzy logic-based building electrical energy management system. There are four power sources that have been defined; solar panel power is source S1, grid power is source S2, battery power is source S3, which will be charged by solar panel through a DC-DC converter (Ghaffar *et al*., 2019), and generator power is source S4. E_{S1}, E_{S2}, E_{S3}, and E_{S4} are the corresponding source ratings for each of them in watts. Additionally, the wattage ratings for segment loads L1, L2, L3, and L4 are W1, W2, W3, and W4, respectively. All light fixtures, ceiling fans, 13-amp socket loads, 15-amp socket loads, and security lighting points together make up load L1, load L2, load L3, and load L4, respectively. L1 has the highest priority in the loading domain during the day (from 7 am to 6 pm) because it uses the least amount of power and is most important for buildings, while L3 has the lowest priority. L4 is the only priority at night (between the hours of 6 pm and 7 am). The system model is given in figure 1

Insert Figures and Tables after they have been cited in the text. Large Figures and Tables may span both columns. Place Figure caption below the Figures; place Table titles above the Tables. If your Figure has two parts, include the labels “(a)” and “(b)” as part of the artwork. Please verify that the Figures and Tables you mentioned in the text actually exist. Do not include captions as part of the Figures. Do not put captions in “text boxes” linked to the Figures. Do not put borders around the outside of your Figures. Do not use the abbreviation “Fig.” in the body text rather use Figure even at the beginning of a sentence. Do not abbreviate “Table.” Tables are numbered with Roman numerals. Use the Figure Label Style for all captions for Figure and the Table Head Style for all Table Caption.

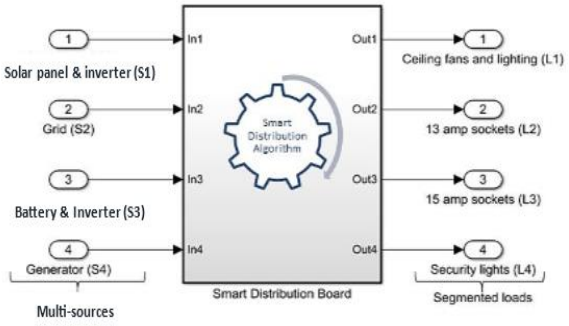

Figure 1: Smart Energy Management model

3.1 SMART ENERGY MANAGEMENT FLOWCHART

The flowchart of smart energy management is discussed in this section (see Figure 2).

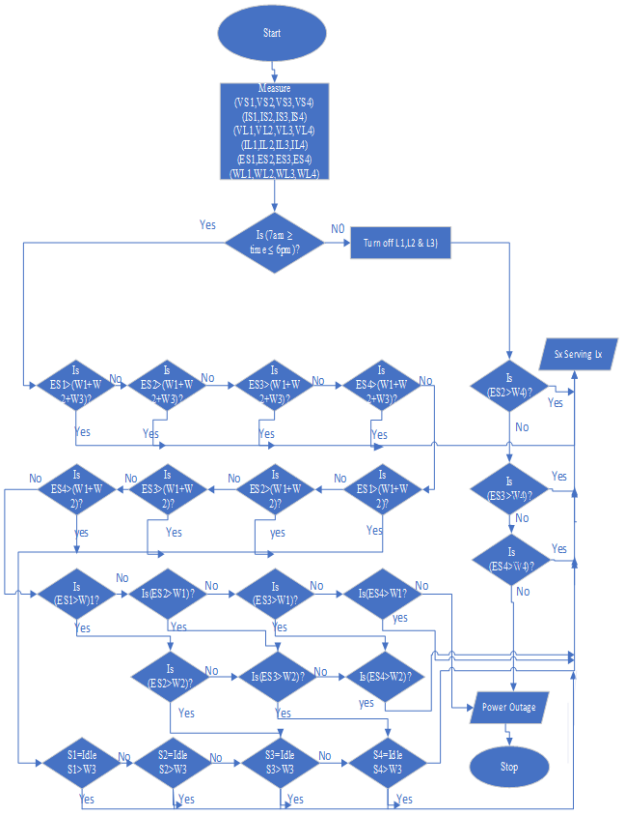

Figure 2: Flowchart of smart energy management

The distribution algorithm uses the flowchart to determine how to shut down the loads at night and choose an appropriate source to power the security lighting points from S2 to S4. Because there is no sunlight during the night, S1 is disregarded. The algorithm turns on the fuzzy logic system during the day to choose which load(s) and appropriate source(s) should be powered. The employed fuzzy logic system and its various components are covered in the section that follows.

3.2 FUZZY LOGIC SYSTEM

The fuzzy logic system used the Mandani Fuzzy Inference System (FIS) to dynamically map sources to load. Because of Mandani FIS's straightforward design and high level of accuracy, it was chosen. Figure 3 shows the model of the fuzzy logic system that was created in Matlab.

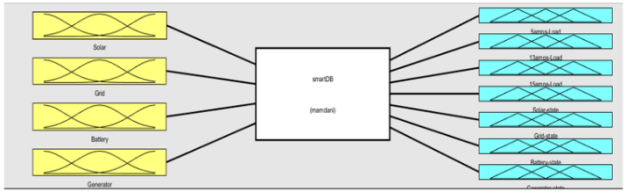

Figure 3: Fuzzy Logic Symbol Model

Figure 4 illustrates how the FIS determined the output using a total of 256 rules.

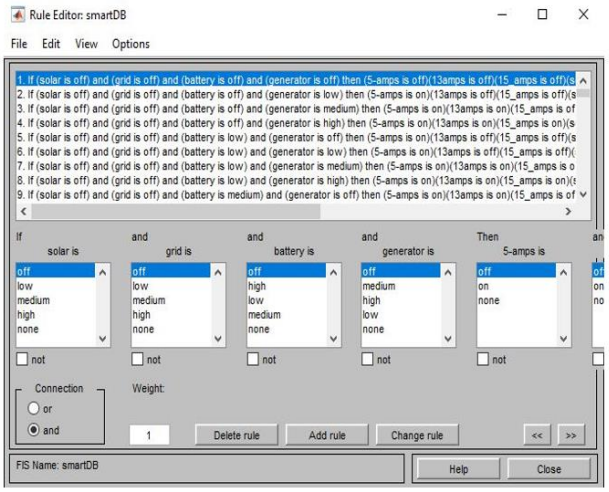

Figure 4: Fuzzy logic rules

4 ENGINEERING COMPLEX LOAD INFORMATION

In this section, Engineering complex load information of Niger State Polytechnic, Zungeru was in Table 1.

TABLE 1: ENGINEERING COMPLEX LOAD INFORMATION

Load Points	Average number of appliances	Rated power (W)	Total wattage (Kw)	Power consumption (11 hours) Daytime (Kw)	Power consumption (13 hours) Night (Kw)
Lighting point (5 Amp)	352	40	14.08	154.88	0
Ceiling fans (5 Amp)	321	60	19.20	211.86	0
13 Amp. socket outlet	447	600	26.68	2850.20	0
15 Amp socket outlet	74	1500	111.00	1221.00	0
Security lighting point	129	40	5.16	0	67.08
Total			176.18	4537.94	67.08

Prior to being fed into the algorithm, the measured values were normalized and converted to a percentage.

When a source's output or input power is less than 35 kW, the algorithm represents it as a value between 0 and 30. In this case, no output is sent to the load. The algorithm, however, indicates 30-50 when it is between 35 kW and 65 kW. Only the 5 Amp loads will be powered in this scenario. It represents 50-70 similarly when the source input or output is between 65 kW and 175 kW. This shows that the source is limited to 5 Amp and 13 Amp loads. The source is able to power all 5 Amp, 13 Amp, and 15 Amp loads, according to the algorithm, which interprets input or output above 175 kW as 70-100. In a Matlab environment, the developed algorithm was simulated.

5 RESULTS AND DISCUSSION

Table 2 shows how the algorithm operates when solar, grid, and battery outputs are high (i.e., >70%), the generator is off (i.e., 30%), and all loads are powered solely by solar energy while other sources are left unutilized.

TABLE 2: FLC RULES VIEW OF SOLAR POWER SERVE 5 AMP, 13 AMP AND 15 AMP

Energy sources	**State of sources**						**Loads**		
	High	Medium	Low	Off	Active	Idle	5 Amp	13 Amp	15 Amp
Solar and inverter	Yes	No	No	No	Yes	No	On	On	On
Grid	Yes	No	No	No	No	Yes	Off	Off	Off
Battery and inverter	Yes	No	No	No	No	Yes	Off	Off	Off
Generator	No	No	No	Yes	No	Off	Off	Off	Off

Similarly, Table 3 shows a medium solar source (50%–70%), a high grid and battery (>70%), and a low generator (30%). In this case, the 15 Amp loads are powered by the grid while the 5 Amp and 13 Amp loads are powered by solar.

TABLE 3: FLC RULES VIEW OF SOLAR POWER SERVE 5 AMP AND 13 AMPS, 15 AMP SERVE BY GRID

Energy sources	**State of sources**						**Loads**		
	High	Medium	Low	Off	Active	Idle	5 Amp	13 Amp	15 Amp
Solar and inverter	No	Yes	No	No	Yes	No	On	On	Off
Grid	Yes	No	No	No	Yes	No	Off	Off	On
Battery and inverter	Yes	No	No	No	No	Yes	Off	Off	Off
Generator	No	No	No	Yes	No	No	Off	Off	Off

Furthermore, the algorithm only supports 5 Amp and 13 Amp loads when the solar source is low (30%–50%), the grid is medium, the battery is low, and the generator is not running. As shown in Table 4, the 5 Amp loads are supplied by solar energy, while the 13 Amp loads are supplied by the grid.

TABLE 4: FLC RULES VIEW OF SOLAR POWER SERVE 5 AMP, 13 AMP SERVE BY GRID

Energy sources	**State of sources**						**Loads**		
	High	Medium	Low	Off	Active	Idle	5 Amp	13 Amp	15 Amp
Solar and inverter	No	No	Yes	No	Yes	No	On	Off	Off
Grid	No	Yes	No	No	Yes	No	Off	On	Off
Battery and inverter	No	No	Yes	No	No	Yes	Off	Off	Off
Generator	No	No	No	Yes	No	No	Off	Off	Off

The output of the distribution board with no algorithm (CDB) is presented in Figure 5. Results showed that on day 1, CDB was switched to solar source because all the sources except the generator were high and solar is the preference source. However, on day 2, only the grid and battery were high. The CDB was switched to grid because it is cheaper. This continued until day 7. The plot (Figure 5) shows that the CDB takes the preference source that can drive the most loads.

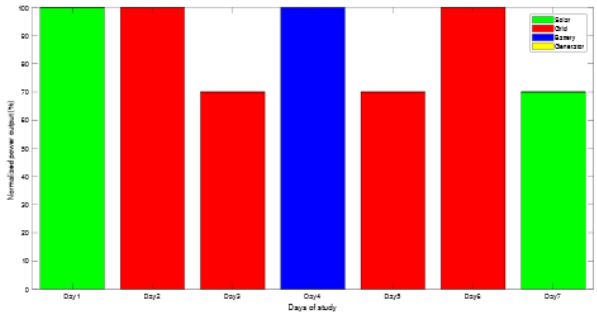

Figure 5: Output of distribution board with no algorithm (CDB)

On the other hand, the Smart Distribution Board (SDB) behaves differently. On the second day of the study, solar provided power for the 5 Amp and 13 Amp loads while the grid provided power for the 15 Amp loads, despite the fact that on the first day of the study solar was chosen as the preferred source to serve all the loads, including the CDB (see Figure 6). This is so that solar, which is in a medium state, can drive both 5 Amp and 13 Amp loads. The SDA assigned the 5 Amp and 13 Amp loads to solar and used the grid to drive only the 15 Amp load because the CDB would have used the grid to drive all of the loads because the grid is in high state. The CDB would have used the grid to drive all of the loads because the grid is in high state, but the SDA assigned the 5 Amp and 13 Amp loads to solar and only used the grid to drive the 15 Amp load.

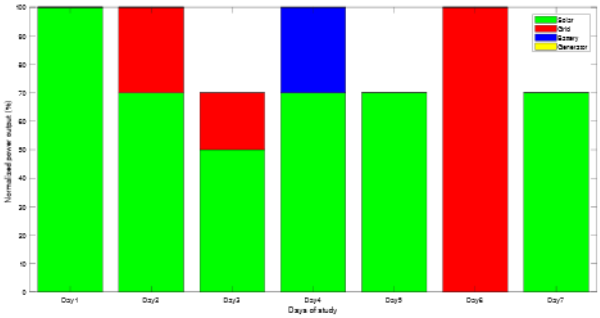

Figure 6: Output of Smart Distribution Algorithm (SDB)

5.1 ENERGY SAVING EFFICIENCY

This analysis looks at the distribution board's energy-saving effectiveness over the course of the experiment with no algorithm. The daily energy consumption for the loads using a distribution board without an algorithm is shown in Table 4. 15978.08KW is the total amount of energy consumed by the loads on the grid when using a distribution board without an algorithm.

TABLE 5: DAILY ENERGY CONSUMPTION BY THE LOADS USING DISTRIBUTION BOARD WITH NO ALGORITHM

Day	Load Points	Total wattage (KW)	Power consumption (11hours) Daytime (KW)	Power consumption (13 hours) Night (KW)
1	Lighting points	14.08	154.88	0
Solar	(5Amps)	19.20	211.86	0
	Ceiling fans (5Amps)	26.68	2950.20	0
	13 Amp. socket outlet	111.00	1221.00	0
Battery	15 Amp. Socket	5.16	0	67.08
(High)	outlet			
	Security lighting point			
	Total	**176.18**	**4537.94**	**67.08**
2	Lighting points	14.08	154.88	0
Grid	(5Amps)	19.20	211.86	0
(High)	Ceiling fans (5Amps)	26.68	2950.20	0
	13 Amp. socket outlet	111.00	1221.00	0
	15 Amp. Socket	5.16	0	67.08
	outlet			
	Security lighting point			
	Total	**176.18**	**4537.94**	**67.08**
3	Lighting points	14.08	154.88	0
Grid	(5Amps)	19.20	211.86	0
(Medium)	Ceiling fans (5Amps)	26.68	2950.20	0
	13 Amp. socket outlet	5.16	0	67.08
	Security lighting			

	point			
	Total	**65.14**	**3316.94**	**67.08**
4	Lighting points	14.08	154.88	0
Battery	(5Amps)	19.20	211.86	0
(High)	Ceiling fans (5Amps)	26.68	2950.20	0
	13 Amp. socket outlet	111.00	1221.00	0
	15 Amp. Socket outlet	5.16	0	67.08
	Security lighting point			
	Total	**176.18**	**4537.94**	**67.08**
5	Lighting points	14.08	154.88	0
Grid	(5Amps)	19.20	211.86	0
(Medium)	Ceiling fans (5Amps)	26.68	2950.20	0
	13 Amp. socket outlet	5.16	0	67.08
	Security lighting point			
	Total	**65.14**	**3316.94**	**67.08**
6	Lighting points	14.08	154.88	0
Grid	(5Amps)	19.20	211.86	0
(High)	Ceiling fans (5Amps)	26.68	2950.20	0
	13 Amp. socket outlet	111.00	1221.00	0
	15 Amp. Socket outlet	5.16	0	67.08
	Security lighting point			
	Total	**176.18**	**4537.94**	**67.08**
7	Lighting points	14.08	154.88	0
Solar	(5Amps)	19.20	211.86	0
(Medium)	Ceiling fans (5Amps)	26.68	2950.20	0
Battery	13 Amp. socket outlet	5.16	0	67.08
(Medium)	Security lighting point			
	Total	**65.14**	**3316.94**	**67.08**

According to Table 5, a distribution board using no algorithm consumed 15978.08KW of total energy on the grid, while SMES used 8910.38KW as shown in Table 6. This suggests that the SEMS saved 7067.70KW in energy during the research period.

The energy tariff of Niger State Polytechnic, Zungeru is charges on band A2, which is N48.37k per *Kwh* (AEDC,2023). 15978.08 x N48.37 = N772,859.73k is the amount of energy consumed from the grid through a distribution board with no algorithm. The SMES figure is 8910.38 x N48.37, which comes to N430,995.08k. For a week, using SEMS results in savings of N772,859.73 - N430,995.08 = N341,864.65k. N1,367,458.60k (for one month) = N341,864.65 multiplied by 4. While the annual equivalent is N16,409,503.20 (N1,367,458.60 x 12).

Table 6 compares the SMES's daily power usage for the grid and battery to the distribution board without an algorithm during the day.

TABLE 6: POWER CONSUMPTION ON THE GRID AND BATTERY

SN	Day 1	Day 2	Day 3	Day 4	Day 5	Day 6	Day 7	Total
DB with no algorithm (KW)	0	171.02	60.02	171.02	60.02	171.02	0	633.10
SMES (KW)	0	111.00	26.68	111.00	0	171.02	0	419.70

According to Table 6, the distribution board's total power consumption on the grid and battery with no algorithm is 633.10 kW, while the SEMS used 419.70 kW. This suggests that the SMES saved 213.40 kW of power during the study period. The efficiency of energy savings is 33.71%.

TABLE 7: DAILY ENERGY SAVING EFFICIENCY IN THE ENGINEERING COMPLEX

SN	Day 1	Day 2	Day 3	Day 4	Day 5	Day 6	Day 7
Efficiency (%)	100	35.1	55.5	35.1	100	0	100

From Table 7, the solar source serves the all loads in the first day being the preference source, which implies 100% of energy saving. Second day energy saving is 35.1%, third day is 55.5%, fourth day is 35.1%, fifth day is 100%, sixth day is 0%, because the grid serves all the loads and seventh day is 100%.

CONCLUSION

In this paper, an SMES that can operate on distribution boards with segmented multiple power sources and segmented loads in buildings was created. The SEMS turns the CDB into a smart device by dynamically allocating different sources to various loads in buildings in accordance with demand. According to simulation results, SEMS that use the developed algorithm are able to save 33.71% more electricity than CDBs.

REFERENCE

Arcos-Aviles, D., Pascual, J., Marroyo, L., Sanchis, P., & Guinjoan, F. (2018). Fuzzy logic-based energy management system design for residential grid-connected microgrids. *IEEE Transactions on Smart Grid*, *9*(2), 530–543. https://doi.org/10.1109/TSG.2016.2555245

Dunmade, I. (2021). Community/shared solar power option: A pathway to sustainable rural electrification in Nigeria. *Agronomy Research*, *19*(4), 1734–1746. https://doi.org/10.15159/AR.21.150

El Zerk, A., Ouassaid, M., & Zidani, Y. (2018). Energy management based fuzzy logic control of hybrid system wind/photovoltaic with batteries. *2018 Renewable Energies, Power Systems Green Inclusive Economy (REPS-GIE)*, 1–6. https://doi.org/10.1109/REPSGIE.2018.8488819

Gamage, D., Zhang, X., & Ukil, A. (2018). Fuzzy Logic Controller for Efficient Energy Management of a PV System with HESS. *IECON 2018 - 44th Annual Conference of the IEEE Industrial Electronics Society*, 3556–3561. https://doi.org/10.1109/IECON.2018.8592823

Ghaffar, M., Naseer, N., Sheikh, S. R., Naved, M., Aziz, U., & Koreshi, Z. U. (2019). Electrical energy management of building using fuzzy control. *2019 International Conference on Robotics and Automation in Industry, ICRAI 2019*. https://doi.org/10.1109/ICRAI47710.2019.8967381

Hettiarachchi, H. W. D., Hemapala, K. T. M. U., & Jayasekara, A. G. B. . (2017). A Fuzzy logic based power management system for an integrated AC-DC hybrid microgrid model. *2017 Moratuwa Engineering Research Conference (MERCon)*, 357–362. https://doi.org/10.1109/MERCon.2017.7980510

Ibrahim, R. O., Tambo, E., Tsuanyo, D., & Nguedia-Nguedoung, A. (2022). Modelling an Artificial Intelligence-Based Energy Management for Household in Nigeria. *Engineering Letters*, *30*(1), 140–151.

Krishna, P. N., Gupta, S. R., Shankaranarayanan, P. V., Sidharth, S., & Sirphi, M. (2018). Fuzzy Logic Based Smart Home Energy Management System. *2018 9th International Conference on Computing, Communication and Networking Technologies, ICCCNT 2018*, *July*. https://doi.org/10.1109/ICCCNT.2018.8493744

Meje, K., Bokopane, L., Kusakana, K., & Siti, M. (2020). Optimal power dispatch in a multisource system using fuzzy logic control. *Energy Reports*, *6*, 1443–1449. https://doi.org/https://doi.org/10.1016/j.egyr.2020.11.004

Mubdir, B., Al-Hindawi, A., & Hadi, N. (2016). Design of Smart Home Energy Management System for Saving Energy. *European Scientific Journal, ESJ*, *12*(33), 521. https://doi.org/10.19044/esj.2016.v12n33p521

Olanite, O. A., & Nwohu, M. N. (2022). Adoption of Photovoltaic Technologies in Nigeria: A Study of Issues, Problems and Solutions. *Proceedings of the 2022 IEEE Nigeria 4th International Conference on Disruptive Technologies for Sustainable Development, NIGERCON 2022*. https://doi.org/10.1109/NIGERCON54645.2022.

9803109

Prathyush, M., & Jasmin, E. A. (2018). Fuzzy Logic Based Energy Management System Design for AC Microgrid. *2018 Second International Conference on Inventive Communication and Computational Technologies (ICICCT)*, 411–414. https://doi.org/10.1109/ICICCT.2018.8473317

Ramalingam, G., Meikandasivam, S., Vijayakumar, D., & Govindarajan, R. (2019). Design and Implementation of Smart Energy Monitoring Systems Using Wireless Technology R.Govindarajan1,. *IOSR Journal of Engineering*, *09(10)*, *10.*, *09*(10), 2278–8719. www.iosrjen.org

Saba, T., Tsado, J., Bukar, B., & Raymond, E. (2016). Influence of Socio-demographic Variables on Electrical Energy Management Practices among Residents of Niger State, Nigeria. *British Journal of Economics, Management & Trade*, *13*(4), 1–10. https://doi.org/10.9734/bjemt/2016/25589

Saba,T.M.,Usman, G.A., Adamu, M.J.,& Daniel,B.C.(2018). Techniques for Enhancing Electrical Energy Management in Residential Buildings, Small and Medium Enterprises in Niger State, Nigeria. International Journal of Industrial Technology, Engineering, Science and Education(IJITESED) 1(1).

Shyni, S. M., & Ramadevi, R. (2019). Fuzzy Logic Controller Based Energy Management (FLCBEM) for a Renewable Hybrid System. *2019 11th International Conference on Advanced Computing (ICoAC)*, 333–337. https://doi.org/10.1109/ICoAC48765.2019.246862

Sultan, Y. AL, Sami, B. S., & Zafar, B. A. (2021). Smart Home Energy Management System: A Multi-agent Approach for Scheduling and Controlling Household Appliances. *International Journal of Advanced Computer Science and Applications*, *12*(3), 237–244. https://doi.org/10.14569/IJACSA.2021.0120329

Tuomela, S., de Castro Tomé, M., Iivari, N., & Svento, R. (2021). Impacts of home energy management systems on electricity consumption. *Applied Energy*, *299*(November 2020). https://doi.org/10.1016/j.apenergy.2021.117310

Uddin, N., & Islam, M. S. (2018). Optimal Fuzzy Logic Based Smart Energy Management System For Real Time Application Integrating RES, Grid and Battery. *2018 4th International Conference on Electrical Engineering and Information Communication Technology (ICEEiCT)*, 296–301. https://doi.org/10.1109/CEEICT.2018.8628057

Zand, M., Nasab, M. A., Hatami, A., Kargar, M., & Chamorro, H. R. (2020). Using Adaptive Fuzzy Logic for Intelligent Energy Management in Hybrid Vehicles. *2020 28th Iranian Conference on Electrical Engineering (ICEE)*, 1–7. https://doi.org/10.1109/ICEE50131.2020.9260941